All Text Search

Search

Please press this button

Proceedings of the 8th JFPS International
Symposium on Fluid Power, OKINAWA 2011
Oct. 25-28, 2011

S-1

SAVING THE WORLD'S ENERGY WITH FLUID POWER

Kim A. STELSON*

*Professor and Director, Center for Compact and Efficient Fluid Power
Department of Mechanical Engineering
University of Minnesota
111 Church Street, S.E., Minneapolis, MN 55455 U.S.A.
(E-mail: kstelson@umn.edu)

ABSTRACT

Fluid power transmits a surprisingly large amount of energy with remarkably low efficiency, providing an extraordinary opportunity to save energy, save money, improve the environment and create new businesses using more efficient fluid power technology. In this paper we will describe how new fluid power components and systems can significantly improve efficiency by creating more efficient systems and by improving the efficiency of individual components. This paper describes three applications; an excavator, a hydraulic hybrid vehicle, and a wind power generator; to demonstrate how fluid power saves energy in a cost effective way. In the excavator, elimination of throttling and regeneration can more than double fuel efficiency. Hydraulic hybrid vehicles are now entering the market where they are superior to electric hybrid vehicles for heavy applications such as refuse trucks and delivery vans. With improved technology, hydraulic hybrids could overtake electric hybrids as a cost-effective but efficient passenger vehicle. Wind is a rapidly growing power source, with the Department of Energy leading an effort to provide 20% of U.S. electricity from wind by 2030. Hydrostatic drives could replace mechanical gear boxes, extracting more power with higher reliability.

KEYWORDS
Efficiency, fluid power, excavator, hydraulic hybrid vehicle, wind power

INTRODUCTION

In 2010, Oak Ridge National Laboratory (ORNL) teamed with the National Fluid Power Association (NFPA) and with eighteen industry partners to quantify the impact of fluid power on the U.S. energy consumption [30]. The report on the study is still in draft form, but should be approved and published soon. The initiative for this study came from Lonnie Love of Oak Ridge National Laboratories, a member of the Center for Compact and Efficient Fluid Power (CCEFP) Scientific Advisory Board. The study was conducted by Eric Lanke and Pete Alles of NFPA. The goal was to quantify the amount of energy transmitted using fluid (hydraulics and pneumatics) and to predict potential energy savings from advancing fluid power technology. The study shows that there is a great potential to save energy in both industrial and mobile applications by using more efficient fluid power components and systems.

In 2008, fluid power systems transmitted 2.3 to 3.0 per cent of energy in the U.S.A. To put this in perspective, the U.S. consumes approximately 100 Quads (1 Quad is 10^{15} BTUs) of energy annually, with each Quad costing $20B if it is derived from petroleum. Since the U.S.A. represents approximately one third of the world's economy, the worldwide transmission of energy via fluid power is around 7 to 9 Quads valued at $14 to $18 billion or more that one trillion yen.

Moreover, the study revealed that fluid power systems are remarkably inefficient with efficiencies ranging from 6% to 40%, depending upon the application, with an average efficiency of 21%. The largest fluid power energy uses were mobile hydraulics and industrial pneumatics with the hydraulics typically being more efficient than the pneumatics. The large amount of energy used and the inefficiency of current systems make it clear that investing in more efficient hydraulics and pneumatics can reap significant savings in overall energy use.

A survey of the participating fluid power manufacturers predicts that a 5% improvement in efficiency is easily achievable with best practices over the next five years. This near term objective could consumers and industry over $9 to $11 billion per year in energy costs and reducing emissions by over 33 million metric tons of CO_2 per year. A longer term goal, through a strategic R&D program focusing on new controls, manufacturing and materials, could result in a 15% improvement in efficiency over the next fifteen years. Realizing this ambitious goal could save industry and consumers more than $19 to $25 billion per year in energy costs and reducing emissions by more than 90 million metric tons of CO_2 per year. Just as important, an ambitious program to develop energy efficient fluid power could invigorate the fluid power industry increasing our manufacturing capabilities and competitiveness in the growing world market.

In making these projections, it is important to note that we are considering current applications only. The expansion of fluid power into new applications can significantly increase the impact on energy savings, sustainability and economic development. Examples of new markets with significant energy savings are hydraulic hybrid vehicles and wind power transmission using hydrostatic transmissions.

TOWARD MORE COMPACT AND EFFICIENT COMPONENTS AND SYSTEMS

The Center for Compact and Efficient Fluid Power (CCEFP) [1-3, 31, 32] is conducting research aimed at significant energy savings. The CCEFP has four goals. The first goal is to dramatically improve the energy efficiency of fluid power in current applications; the second goal is to improve the efficiency of the transportation sector by developing fuel efficient hydraulic hybrid passenger vehicles; the third goal is to develop un-tethered portable human-scale fluid power devices; and the fourth goal is to make fluid power more acceptable and ubiquitous. Thus the first and second goals are explicitly addressing the energy issue.

Figure 1, below, shows power and weight of the CCEFP test beds. These test beds; medical devices, robots, passenger vehicles, excavators and wind turbines; are carefully chosen to span the range of power and weight of interest. Note that the plot uses log-log scales so that the range of power and weight considered spans many orders of magnitude. The most significant energy savings can be realized in the larger systems; the hydraulic hybrid passenger car, excavator and wind turbine. Improving the efficiency of these systems will have a very large impact on overall energy consumption of the economy. The smaller systems; the robot and medical devices; will not save significant amounts of energy when compared to the overall energy consumption of the economy, but energy efficiency is very important for improving the performance of smaller systems. In the next sections, some details are provided on ways to increase the efficiency of the three largest test beds, the energy efficient excavator, hydraulic hybrid passenger vehicle and hydrostatic transmission for wind power. Due to space limitation, emphasis will be put on CCEFP research activities recognizing that many others around the world are making important contributions toward making more efficient fluid power systems.

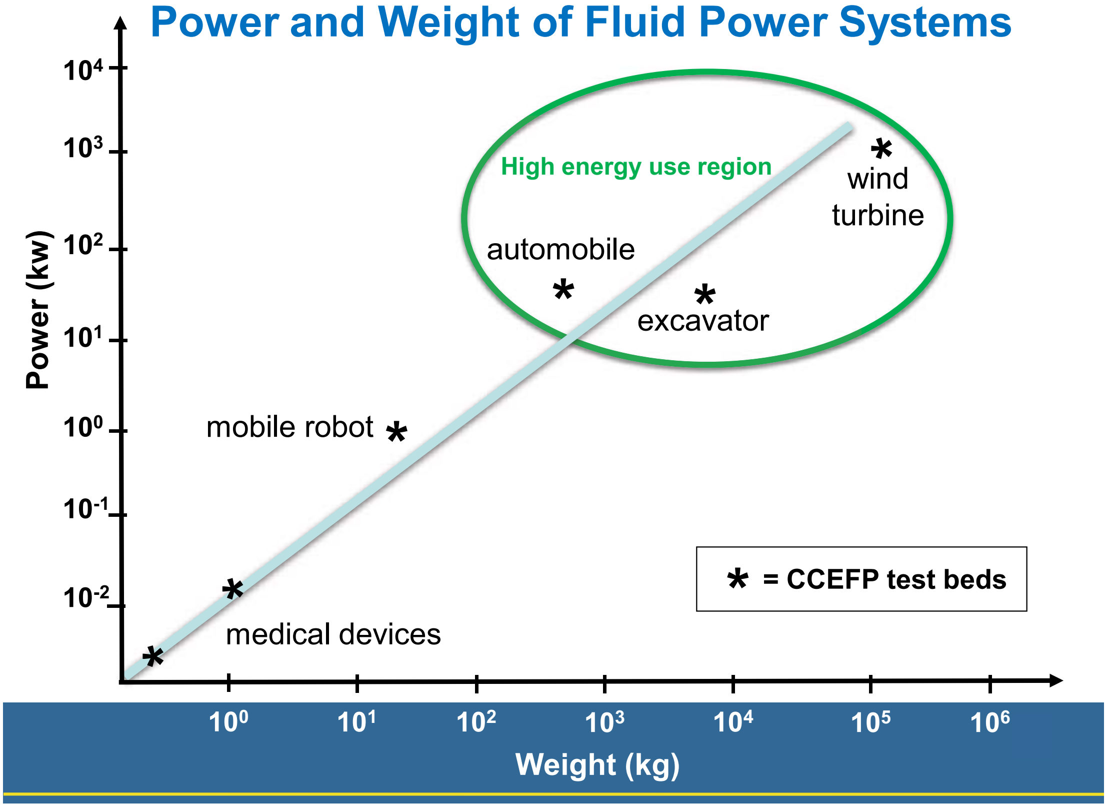

Figure 1: Power and Weight of Fluid Power Systems

ENERGY EFFICIENT EXCAVATOR

As an example of current application of fluid power in mobile hydraulics, consider the excavator. Excavators are important in their own right, but are also representative of off-road hydraulic applications more generally, with separate propel, steering and multiple work circuits that are used intermittently. Thus, approaches to making excavators more efficient have potential to be applied to other classes of machines.

An energy audit of a excavator executing typical dig cycles shows that over 40% of the energy is lost in the throttling valves with no possibility of recovery. Displacement control [43, 44, 45, 46] eliminates the dissipation from throttling by replacing control valves with variable displacement pumps. Displacement controlled actuation in reversible, allowing energy from one work circuit to be used to drive another work circuit instantaneously. With the addition of energy storage in an accumulator, even more energy can be saved.

The experimental displacement controlled mini excavator at Purdue has been independently tested at Caterpillar. The predicted reduction in fuel consumption of nearly one-half has been verified. Further, increases in digging productivity mean that the energy per unit earth moved, a more meaningful measure of efficiency, was reduced by more than half. The improvement in excavator efficiency has other benefits, notably the possibility of eliminating the cooling circuit [48]. With the transition from valve control to pump control, improving the efficiency of pumps with careful attention to all of the physical causes of loss becomes increasingly important [17]. Further improvements in efficiency can also be realized by carefully tailoring the hydraulic fluid to the application where high viscosity index fluids can increase efficiency be reducing the temperature sensitivity of the viscosity [16].

An alternative to controlling fluid power using throttling valves is to control fluid power using high speed on-off valves, sometimes called digital valves. The idea is to control the flow by rapidly opening and closing the valve. Since ideally the valve is very efficient in the fully open or fully closed state, a very efficient control is created, with most of the dissipation occurring during transitions. The improvement in efficiency is analogous to the improvement in the efficiency of lighting control when rheostats were replace by silicon controlled rectifiers (SCRs) enabling much more efficient control. Research of high-speed on off valves is using two approaches, a rotary valve [27, 28, 34, 40] and high speed poppet valves [5]. The development of high-speed on-off valves can also lead to digital pumps or pump-motors, an approach that promises to have broad applicability especially for vehicle applications where four-quadrant operation is needed [22, 23, 29, 41].

A promising but often overlooked opportunity to improve excavator efficiency is in developing more efficient and effective human-machine interfaces [10-15, 21]. Improved human-machine interfaces can improve productivity since getting a job done faster means less fuel will be used. Better human-machine interfaces have the added advantage of decreasing operator fatigue, reducing the frequency of mistakes and increasing safety. Machine characteristics play an important role in user interface design. For example, the replacement of throttling controls with displacement controls creates a machine with different dynamics. This change, if not properly understood and dealt with, can lead to instability, a situation that has recently been addressed by CCEFP researchers [38, 39, 45].

HYDRAULIC HYBRID PASSENGER VEHICLE

Since transportation uses about one third of our energy, improvement in transportation have an important effect on overall energy use. Hydraulic hybrid vehicles have been demonstrated to have greater efficiency and lower costs than electric hybrid vehicles in heavier applications such as refuse trucks and city buses. As an example of their expanding application, New York City is in the process of purchasing three hundred hydraulic hybrid refuse trucks.

The hydraulic hybrid passenger car is an example of a new application of fluid power. Hydraulic hybrid vehicles are clearly superior for larger sizes, and efficient and cost-effective solutions are currently coming on the market. The situation is more equal in the passenger vehicles, with several recent studies showing that hydraulic hybrid vehicles are competitive with electric hybrid vehicles [18, 37]. Crucial to the comparison is the efficiency of pumps and pump-motors, with future improvements in high-efficiency digital pumps and pump-motors tipping the balance in favor of hydraulic hybrid approaches. A recently between the U. S. Environmental Protection Agency (EPA) and Chrysler Corporation to develop a prototype Town and Country minivan hydraulic hybrid vehicle shows the commercial interest in migrating hydraulic hybrid approaches to the smaller passenger vehicle market.

There are four common hydraulic hybrid configurations, parallel, series, input coupled hydro-mechanical and output coupled hydro-mechanical, where hydro-mechanical transmissions are also called power-split transmissions. The parallel configuration is the simplest form where a hydraulic regenerative unit is added to a conventional mechanical power train. Parallel hydraulic vehicles have high transmission efficiency, but poorer engine management, limiting efficiency. Series hydraulic hybrid vehicles replace the mechanical transmission with a hydrostatic transmission. Since a hydrostatic transmission is continuously variable, the series configuration has better engine management than the parallel configuration, but losses in the hydrostatic transmission can be greater than the gain in engine efficiency. This is the reason that efficient pumps and pump-motors are needed to improve series hydraulic hybrid vehicles. Of the vehicles just coming on the market, parallel configurations are favored for the refuse truck application, while series configurations are favored for the delivery van application.

A hydro-mechanical or power-split transmission is an attractive alternative to the parallel or series configurations where these transmissions can be of the input coupled or output coupled type [6, 36, 42]. Hydro-mechanical transmissions have two power transmission paths, a mechanical path and a hydraulic path. Hydro-mechanical hybrid hydraulic vehicles can potentially have better fuel economy than either the parallel or the series configuration since can be both efficient and continuously variable.

Comparisons between hybrid vehicle concepts depend on many factors including component performance and sizing, duty cycle and control approach [19]. This makes valid comparisons difficult. Control based on dynamic programming is often assumed in comparative studies since it produces the optimum result theoretically, but dynamic programming cannot be used in practice because it requires future information [25, 33]. Real time control approaches that can prove effective are stochastic dynamic programming [24, 26] and model predictive control [7-9]. A three level decomposition with a Lagrange multiplier formulation has proven to be effective for the control of hydro-mechanical hydraulic hybrid vehicles [20].

HYDROSTATIC TRANSMISSION FOR WIND TURBINE

Wind power will become an increasing important renewable source of electricity in the future with the United States Department of Energy (DOE) setting the goal of receiving 20% of our electricity from wind by

2030 [4]. Since the electrical generator must turn much faster than the blades of the turbine, wind power generators require a speed-up transmission. The current approach is to use a fixed ratio mechanical gearbox, but mechanical gearboxes are heavy, costly and unreliable. The unreliability is caused by fatigue from the multi-axis dynamic loading of the wind.

Hydrostatic transmissions provide an attractive alternative to mechanical gear boxes for wind power [35]. Hydrostatic transmissions are lighter and cheaper than gear boxes and can be made more reliable than gear boxes by using hydrostatic bearings to avoid fatigue. Although hydrostatic transmissions are less efficient than gear boxes their use can cause higher overall efficiency since the variable ratio can be used to increase the aerodynamic efficiency of the rotor. The variable ratio also allows the use of a synchronous generator, eliminating the cost and inefficiency of power electronics. The hydrostatic transmission also has a cushioning effect that increases generator life by isolating the generator from shock loading of the wind. One novel approach is to split the hydrostatic transmission with the pump located in the nacelle but the hydraulic motor located at ground level along with the generator and controller. This approach reduces the weight in the nacelle and allows easy ground level access to all major components for maintenance, repair or replacement.

CONCLUSION

A recent survey has revealed that fluid power transmits large amounts of energy with low efficiency, providing an attractive opportunity to save energy, save money, improve the environment and create new businesses using more efficient fluid power technology. We have shown how significant efficiency improvements can be obtained for three examples, an energy efficient excavator, hydraulic hybrid passenger car and hydrostatic transmission for wind power. Efficiency improvements can come for more efficient components such as pumps and valves, but also from improved fluids. System architectures, controls and operator interfaces can also play a significant role in improving system efficiency.

ACKNOWLEDGEMENT

The work of the Center for Compact and Efficient Fluid Power is supported by the National Science Foundation under grant EEC#0540834.

REFERENCES

1. www.ccefp.org
2. http://www.erc-assoc.org/factsheets/ccefp/CCEFP_Factsheet_2007.html.
3. _____, Fluid Power Research Centres World-Wide: The Center for Compact and Efficient Fluid Power, University of Minnesota Minneapolis, Minnesota U.S.A, International Journal of Fluid Power, Vol. 9, No. 2, August 2008.
4. _____, 20% Wind Energy by 2030: Increasing Wind Energy's Contribution to U.S. Electricity Supply, U.S. Department of Energy Report DOE/GO-102008-2567, July 2008.
5. Andruch, J. and Lumkes, J., A Hydraulic System Topography with Integrated Energy Recovery and Reconfigurable Flow Paths Using High Speed Valves, Proceedings of the 51st National Conference on Fluid Power, Las Vegas, NV, 2008.
6. Cheong, K. L., Li, P. Y., Sedler, S. P., and Chase, T. R., Comparison Between Input Coupled and Output Coupled Power-Split Configurations in Hybrid Vehicles, Proceedings of the 52nd National Conference on Fluid Power, Las Vegas, NV, 2011.
7. Deppen, T.O., A.G. Alleyne, K.A. Stelson, J.J. Meyer, Model Predictive Energy Management of a Hybrid Hydraulic Vehicle, Proc. of the 6th FPNI PhD Symposium. 2010.
8. Deppen, T.O., A.G. Alleyne, K.A. Stelson, J.J. Meyer. "Predictive Energy Management for Parallel Hydraulic Hybrid Passenger Vehicle, Proc. of the ASME Dynamic Systems and Control Conference, 2010.
9. Deppen, T.O., A.G. Alleyne, K.A. Stelson, J.J. Meyer. "A Model Predictive Control Approach for a Parallel Hydraulic Hybrid Powertrain," Proc. of the American Control Conference. 2011.
10. Elton, M. and W. Book, Operator Efficiency Improvements From Novel Human-Machine Interfaces, Proceedings of the 6th FPNI-PhD Symposium, West Lafayette, IN, June 15-19 2010, pp.315-322.
11. Enes, A., Towards Shared Control of Hydraulic Excavators, in Fluid Power Net International 6th Annual PhD Symposium, West Lafayette, IN, July 2010.
12. Enes, A.Towards Shared Control of Hydraulic Excavators, in Fluid Power Net International 6th Annual PhD Symposium, West Lafayette, IN, July 2010.
13. Enes, A. and Book, W., A Hardware-in-the-Loop Simulation Testbed for Emulating Hydraulic Loads Representing the Complete Dig Cycle of a Construction Machine, in International Mechanical Engineering Congress and Exposition, Boston, Massachusetts 2008.
14. Enes, A., and W. Book, Recursive Algorithm for Motion Primitive Estimation, in proceedings of

IEEE International Conference on Robotics and Automation, Shanghai, China, May 2011.
15. Enes, A. and W. Book, Sharing Control Can Increase Excavator Productivity, Proc. of the 52nd National Conference on Fluid Power, Las Vegas, March 2011.
16. Herzog, S., Marougy, T., and Michael, P., Guidelines for Hydraulic Fluid Viscosity Selection to Improve Equipment Fuel Economy and Productivity, Proceedings of the 51st National Conference on Fluid Power, Las Vegas, NV, 2008.
17. Ivantysynova, M., Innovations in Pump Design - What are Future Directions?, Proceedings of the 7th JFPS International Symposium on Fluid Power, Toyama, Japan, 2008, pp. 59 -64.
18. Kumar, R. and M. Ivantysynova, The Hydraulic Hybrid Alternative for Toyota Prius - A Power Management Strategy for Improved Fuel Economy, Proceedings of the 7th International Fluid Power Conference Aachen 2010 (7IFK), Vol. 2, pp.329-341.
19. Kumar, R. and M. Ivantysynova, Investigation of Various Power Management Strategies for a Class of Hydraulic Hybrid Powertrains: Theory and Experiments, Proceedings of the 6th FPNI PhD Symposium, West Lafayette, IN, 2010, pp 87-99.
20. Li, P.Y. and F. Mensing, Optimization and Control of a Hydro-Mechanical Transmission based Hydraulic Hybrid Passenger Vehicle, Proceedings of the 7th International Fluid Power Conference, Aachen, Germany, 2010.
21. Liu, Y., X. Jiang, Z. Jiang, and E. Park, Predicting Backhoe Excavator Operator Performance Using Digital Human Modeling, Proceedings of the 2010 Industrial Engineering Research Conference, Cancun, Mexico, June 5-9, 2010.
22. Merrill, K., M. Holland, and J. Lumkes, Efficiency Analysis of a Digital Pump Motor as Compared to a Valve Plate Design, Proceedings of the 7th International Fluid Power Conference (7.IFK), Aachen, Germany, March 22-24, 2010.
23. Merrill, K. and J. Lumkes, Operating Strategies and Valve Requirements for Digital Pump/Motors, Proceedings of 6th FPNI-PhD Symp. West Lafayette 2010, pp. 249-258.
24. Meyer, J. J., K. A. Stelson, A. G. Alleyne and T. O. Deppen, Energy Management Strategy for a Hydraulic Hybrid Vehicle using Stochastic Dynamic Programming, in M. Ivantysynova, ed., Sixth Fluid Power Net International Ph.D. Symposium Proceedings, West Lafayette, IN, 15-19 June 2010.
25. Meyer, J. J., Stelson, K.A., Hencey, B. and Alleyne, A.G., Optimization of the Power Management Strategy for a Hydraulic Hybrid Vehicle, Fifth Fluid Power Net International Ph.D. Symposium Proceedings, Krakow, Poland, 2008, pp. 371-380.
26. Meyer, J. J., K. A. Stelson, B. Hencey and A. G. Alleyne, Power Management Strategy for a Hydraulic Hybrid Passenger Vehicle Using Stochastic Dynamic Programming, Proceedings of the 7th International Fluid Power Conference, Aachen, Germany, March 2010, pp. 22-24
27. Rannow, M., Li, P., Chase, T., Tu, H., and Wang, M., Optimal design of a high-speed on/off valve for a hydraulic hybrid vehicle application, Proceedings of the 7th International Fluid Power Conference, Aachen, Germany, 2010.
28. Rannow, M., Tu, H., Wang, M., Li, P. Y., and Chase, T. R., The Advantages and Feasibility of Externally Actuating a High-Speed Rotary On/Off Valve, 52nd National Conference on Fluid Power, LasVegas, NV, March 2011.
29. Rannow, M. B., Tu, H. C., Li, P. Y., and Chase, T. R., Software Enabled Virtually Variable Displacement Pumps - Theoretical and Experimental Studies, submitted to ASME Journal of Dynamic Systems, Measurement, and Control, in review.
30. Stelson, K. A., Saving Energy by Advancing Fluid Power Technology, Notable Words feature, Fluid Power Journal, March/April 2011, p. 4.
31. Stelson, K. A., Center for Compact and Efficient Fluid Power (CCEFP), A National Science Foundation Engineering Research Center, United States, Journal of the Japan Fluid Power Society, Vol. 41, No. 1, Jan. 2010, pp. 60-63.
32. Stelson, K. A., Engineering Research Center for Compact and Efficient Fluid Power (CCEFP). in D. N. Johnston and A. R. Plummer, eds., Fluid Power and Motion Control, Bath, England, 2008, pp. 265-275.
33. Stelson, K. A., Meyer, J.J., Alleyne, A.G., and Hencey, B., Energy Saving Control of a Hydraulic Hybrid Passenger Vehicle, Proceedings of the Seventh Japan Society of Fluid Power International Symposium on Fluid Power, Toyama, Japan, 2008, pp. 143-148.
34. Tu, H. C., Rannow, M. B., Wang, M., Li, P. Y., and Chase, T. R., "Design, Modeling and Validation of a High-Speed Rotary PWM On/Off Hydraulic Valve", ASME Journal of Dynamic Systems, Measurement, and Control, in review.
35. Thul, B., R. Dutta and K. A. Stelson, Hydrostatic Transmission for Mid-Size Wind Turbines, Proceedings of the 52nd National Conference on Fluid Power, Las Vegas, NV, 2011.
36. Van de Ven, J.D., Olson, M. and Li, P.Y., Development of a Hydro-Mechanical Hydraulic Drive Train with Independent Wheel Torque Control for an Urban Passenger Vehicle Hybrid,

International Fluid Power Exposition, Las Vegas, NV, 2008.
37. Wang, F., M. I. Ramdan and K. A. Stelson, Comparison Between Hydraulic Hybrid and Electric Hybrid Passenger Vehicles Using Advisor 2004 , 52nd National Conference on Fluid Power, Las Vegas, NV, 2011.
38. Wang, L. and W. Book, Applying Singular Perturbation Theory to Hydraulic Pump Control, IEEE/ASME Transactions on Mechatronics, in press.
39. Wang, L., W. Book and J. Huggins, A Hydraulic Circuit for Single-rod Cylinders, ASME J. Dynamic Systems, Measurement and Controls, in press.
40. Wang, M., Tu, H., Rannow, M., Li, P. Y., and Chase, T. R., Direct Displacement Control of Hydraulic Actuators Based on a Self-Spinning Rotary On/Off Vavle, 52nd National Conference on Fluid Power, Las Vegas, NV, 2011.
41. Wilfong, G., M. Batdorff, and J. Lumkes, Design and Dynamic Analysis of High Speed on/off Poppet Valves for Digital Pump/Motors, Proceedings of 6th FPNI-PhD Symposium West Lafayette 2010, pp. 259-269.
42. Williams, K. and Ivantysynova, M., Towards an Optimal Energy Management Strategy for Hybrid Hydraulic Powertrains Based on Dual Stage Power Split Principle, Proceeding of the 5th FPNI Ph.D. Symposium, Cracow, Poland, 2008, pp. 27–40.
43. Williamson, C. and M. Ivantysynova, Power Optimization for Multi-Actuator Pump-Controlled Systems, Proceedings of the 7th International Fluid Power Conference Aachen 2010 (7IFK), 2010. pp. 91-102.
44. Williamson, C. and Ivantysynova, M., Pump Mode Prediction for Four-quadrant Velocity Control of Valveless Hydraulic Actuators, Proceedings of the 7th JFPS International Symposium on Fluid Power, Toyama, Japan, 2008, pp.323-328.
45. Williamson, C. and M. Ivantysynova, Stability and Motion Control of Inertial Loads with Displacement Controlled Hydraulic Actuators, Proceedings of the 6th FPNI PhD Symposium, West Lafayette, USA, 2010, pp 499–514.
46. Williamson, C., Zimmerman, J. and Ivantysynova, M., Efficiency Study of an Excavator Hydraulic System Based on Displacement-Controlled Actuators. Proceedings of the Bath/ASME Symposium on Fluid Power and Motion Control (FPMC), 2008, pp. 291-307.
47. Zimmerman, J. and Ivantysynova, M., The Effect of System Pressure Level on the Energy Consumption of Displacement Controlled Actuator Systems, Proceedings of the 5th FPNI Ph.D. Symposium, Cracow, Poland, 2008, pp. 77-92.
48. Zimmerman, J. and M. Ivantysynova, Reduction of Engine and Cooling Power by Displacement Control, Proceedings of the 6th FPNI PhD Symposium, West Lafayette, IN 2010, pp 339-352.

S-2

A Fundamental Research of Cavitation in Hydraulic Component

Xin Fu
State Key Laboratory of Fluid Power Transmission and Control, Zhejiang University, Hangzhou, China

Keyword; Cavitation, Hydraulic valve, Gas nuclei

ABSTRACT

As the quality requirements of hydraulic products becomes much higher, the hydraulic cavitation related problems such as noise, erosion and flowrate saturation, is addressed with more concern [1]. A lot of work of structure optimization has been done on hydraulic components for the improvement of cavitation resistance by our research team. Furthermore, we have investigated the relation between the valve structure parameter and cavitation property, for example cavitation incipience, intensity, shapes etc., as well as the effects on the hydraulic system especially the flow characteristics. On the other hand, we have paid much attention to gas nuclei in liquid media, which weaken the tensile strength of liquid greatly [2]. We also explore the existence form of the gas nuclei in the liquid, and investigate the collapse process of gas nuclei by high speed camera, and measure the collapse intensity of a single cavitation bubble.

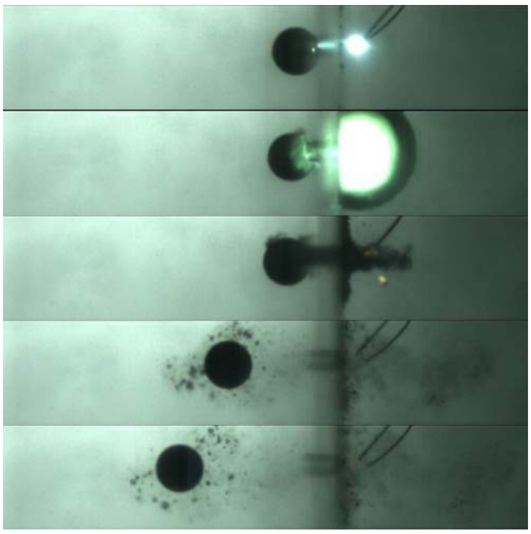

Fig.1 The force of the collapse of a single bubble measured by a drived ball

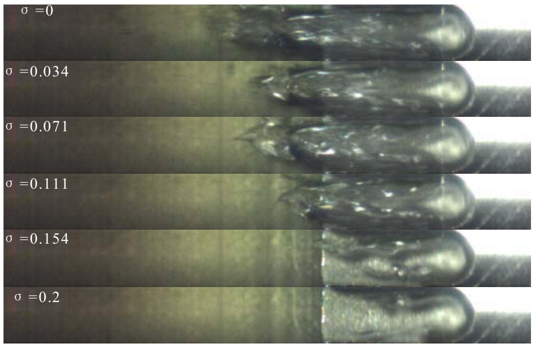

Fig.2 The cavitation morphology in U-type valve opening under different cavitation number σ

BIOGRAPHIES

FU Xin received his Ph.D degree in mechanical engineering from the University of Leoben, Austria, in 1998, He joined the faculty of mechanical engineering in Zhejiang University, China. He was appointed the director of the State Key Laboratory of Fluid Power Transmission and Control from 2005 to 2009 and vice dean of the Department of Mechanical Engineering in 2009. He is involved in research pertaining to the vibration and noise control in fluid power system, micro-fluidic system and flow measurement. He is the author or co-author of over 200 technical papers. He holds 50 patents and is a warded 5 national and provincial prizes of science and technology progress.

REFERENCES

1. Li, S. C., Cavitation of Hydraulic Machinery, University of Warwick, Imperial College Press, UK, 2000.
2. Morch, K. A., Reflections on Cavitation Nuclei in Water, Physics of Fluids, 2007, **19**, pp.0721041-0721047.

K-1

MASTER SLAVE ROBOT SYSTEM FOR LAPAROSCOPIC SURGERY WITH HAPTIC PERCEPTION USING PNEUMATIC ACTUATORS

Kenji Kawashima*, Kotaro Tadano*

* Tokyo Institute of Technology
4259 R2-46,Nagatsuta-cho,Midori-ku, Yokohama, Kanagawa, 226-8503 Japan
(E-mail: kkawashi@pi.titech.ac.jp)

INTRODUCTION

Minimally invasive laparoscopic surgery is an effective method as alternative to open surgery. However, the degrees of freedom (DOFs) of typical surgical instruments in such procedures are restricted due to the use of trocars. Hence it demands expert skill on part of the surgeon. In order to solve this problem, robotic manipulators with multi-DOF forceps, have been reported as alternative to conventional instruments [1].

There are two types of forceps manipulators: handheld ones that are highly compatible with conventional surgical tools [2,3] and master-slave systems [4-7]. The master-slave system, though a complex system, allows intuitive manipulation of surgical tools. To ensure more intuitive and much safer manipulation, haptic sensation to operators is an indispensable function of the system [8-11].

The master-slave system often uses an electric motor with a reduction gear having a high reduction ratio to realize precise positioning. Low back-drivability of the electric motor will require a force sensor at the tip of the forceps to detect minute forces. In practice, however, a force sensor at the tip of the forceps is not desirable in terms of miniaturization, sterilization, calibration, and cost. On the other hand, the use of direct-driven motors or geared motors with low reduction ratios will allow the estimation of external forces and the control of forces without the use of a force sensor. Such a motor, however, needs to be large enough to develop adequate drive torque, which makes it difficult to lighten or miniaturize the manipulator.

In such a context, we have worked on the development of a robotic system for laparoscopic surgery with 7-DOFs. In this system, pneumatic actuators, instead of electric motors, are used to detect external forces based on pressure values without a force sensor [12-14]. Pneumatic actuators with a high power-to-weight ratio obviates the need for a reduction gear in order to realize compatibility between adequate torque and high back-drivability, and it also makes the system smaller and lighter. The high backdrivability of the pneumatic actuator allows the detection of external forces from pressure data and compliance control of the system without the use of force sensors.

We have prototyped a model of surgical manipulators named IBIS IV, which has high performance in the estimation of external force. We have developed a master slave system with the manipulator and evaluated its performance in terms of force estimation. This paper introduces on the developments of and subsequent experiments with the system.

PNEUMATICALLY DRIVEN SURGICAL MANIPULATOR IBIS IV

Fig.1 shows the designed and developed pneumatic surgical manipulator named IBIS IV using pneumatic actuators The model consisting of a 3-DOF forceps manipulator including grasping and 4-DOF supporting manipulator has 7-DOF in total.

As shown in Fig.2, the supporting manipulator consisting of 3-DOF in rotation centered at the point of entry through a trocar cannula and 1-DOF in translation in the direction of forceps insertion. Pitch (joint 1) and yaw (joint 2) motions are achieved using pneumatic cylinders whereas roll (joint 3) motion is achieved using a rotary vane type pneumatic motor. The fourth prismatic joint is also actuated using a pneumatic cylinder. By combining two parallel link arrangements and a gimbal mechanism,

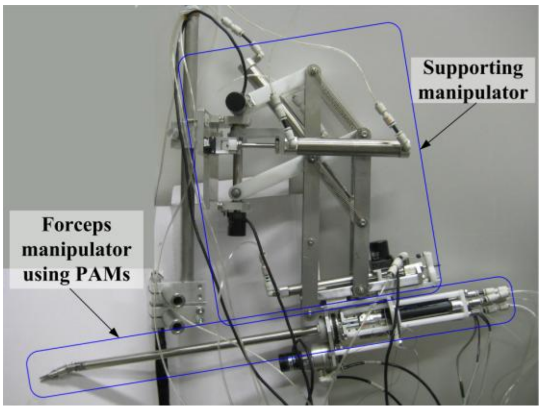

Fig.1. Developed slave-side surgical manipulator

the pivot point at the trocar cannula is rendered immovable mechanically without a large external force. This minimizes the load on the patient's body, and removes the need for the co-ordinates of the port position for kinematical calculations.
The forceps manipulator consists of a slender insert with a gripper at its extending tip and actuator housing for gripper, pitch and yaw at the other end, as shown in Fig.3. The two joints for pitch and yaw are tendon-driven with pneumatic cylinders or pneumatic rubber muscles. Most conventional multi-DOF-forceps use wire to drive the gripper; wire passed through over plural joints at the risk of interference with other joints. When especially strong gripping forces are to be generated, increased wire tension to drive the gripper will also increase loads on other joints over which the drive wire passes, resulting in changes in the joints' frictional characteristics, etc.
We have developed a new gripping mechanism in which a micro pneumatic cylinder and slider-crank mechanism are in combined use to generate strong gripping forces without causing interference to other joints, as shown in Fig.4. This prototype can generate strong gripping forces of 25 N or more with the gripper in almost closed conditions. Such strong gripping forces are generated without the use of wire for power transmission, hence no loads are generated on other joints.
As shown on the schematic drawing of a tendon drive with 1-DOF in Fig.5, two sets of such tendon-driving systems are installed at right angles to each other about the direction of the forceps insertion. The pressure sensors are installed into the valve side of the air tubes. Encoders and potentiometers are installed on rotational joints and tendon drive mechanism, respectively. Measured position and pressure signals are sent to a computer for control, and the computed voltage signals are provided to the servo valves. The signals from joint position encoders, potentiometers and pressure sensors are sampled at 1000Hz by a 16-bit A/D converter, resulting in a force resolution of 0.05N.

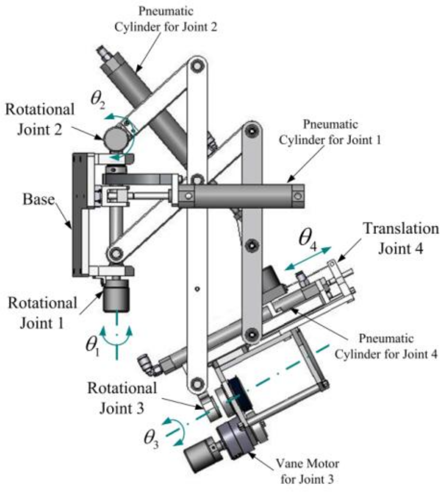

Fig.2 Supporting manipulator with 4-DOF

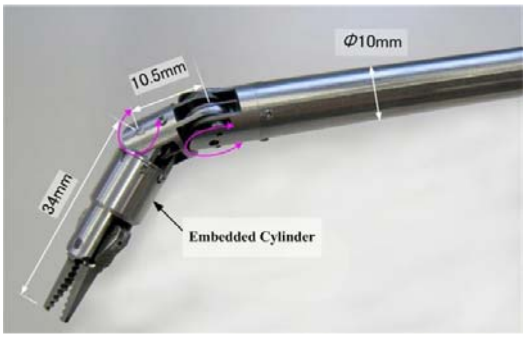

Fig.3 Tip of forceps manipulator

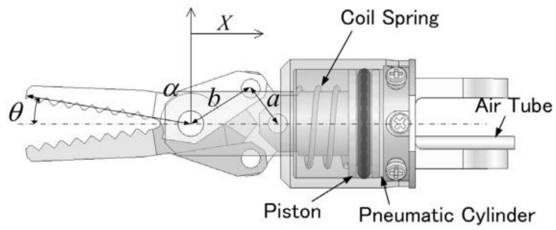

Fig.4 Schematic drawing of gripper at the tip of forceps

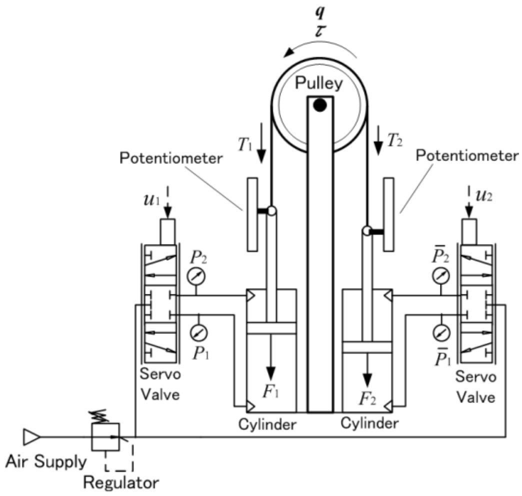

Fig.5 Schematic view of tendon drive of forceps using pneumatic cylinders

Master Slave System

System Configuration

We have developed a master manipulator capable of displaying sense of force with 6-DOFs. Fig.6 shows the developed master manipulator, in which a delta mechanism for translation and a serial gimbal mechanism for orientation are in combined use to realize a wide working range as well as compactness. As there are no constraints on the fitting sensors in the master manipulator, we have installed a 6-axis, force sensor at the rotational center of the gimbal and have used AC servo motors with built-in Harmonic Drive for the actuator. Thus, we have adopted admittance control for the master manipulator.

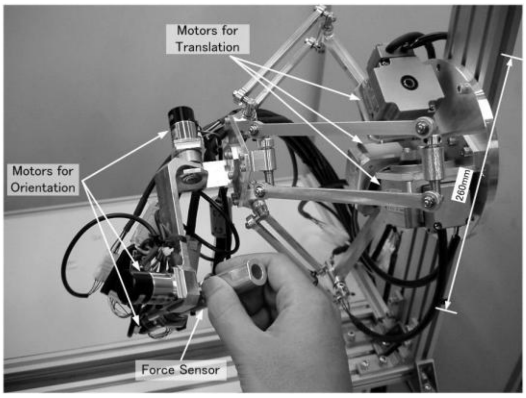

Fig.6 Developed master manipulator

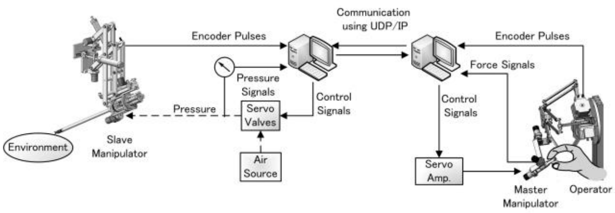

Fig.7 Schematic drawing of master slave system

The master-slave system consisting of these manipulators is shown in Fig.7. Communications between master and slave are based on UDP/IP, which we have confirmed may cause a delay of 1 ms or less on local networks.

Bilateral Control

In our master-slave system, we have applied compliance control to the slave manipulator to take advantage of flexibility and back-drivability of the pneumatic drive. This will help prevent excessive loads from generating in-vivo, but may cause positional deviations between the master and slave manipulators.

Generally, however, operators do not look at one's hands or the master manipulator during the task, but they get visual feedback on positions of the slave manipulator on the monitor, without any particular odd feelings. On the other hand, the master manipulator is provided with appropriate viscosity effects to constrain any trembling of the hands or the generation of excessive velocities.

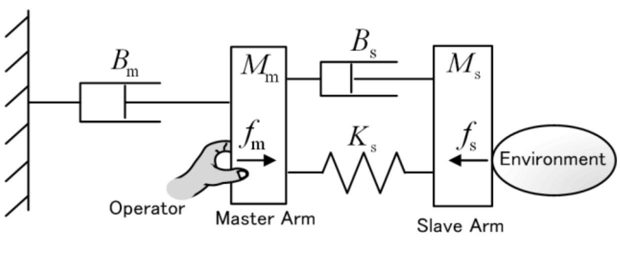

Fig.8 Conceptual model of impedance-controlled master-slave system

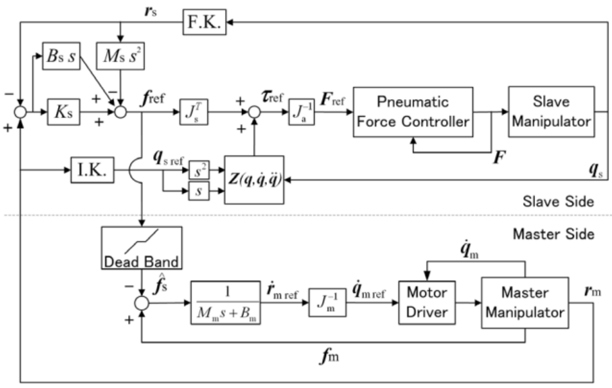

Fig.9 Block diagram of bilateral control

Based on the above-mentioned consideration, master and slave manipulators are so controlled as to be provided with the following impedance characteristics.

slave: $-f_s = M_s\ddot{r}_s + B_s(\dot{r}_s - \dot{r}_m) + K_s(r_s - r_m)$ (1)

master: $f_m - f_s = M_m\ddot{r}_m + B_m\dot{r}_m$ (2)

where,

$r_s \in R^{6\times 1}$: Positional vector of the forward tip of the slave

$r_m \in R^{6\times 1}$: Positional vector of the forward tip of the master

$f_s \in R^{6\times 1}$: Forces applied to environments by the forward tip of the slave

$f_m \in R^{6\times 1}$: Forces applied to the master by operators

$M_s \in R^{6\times 6}$: Set inertia for the slave

$M_m \in R^{6\times 6}$: Set inertia for the master

$B_s \in R^{6\times 6}$: Set viscosity for the slave

$B_m \in R^{6\times 6}$: Set viscosity for the master

$K_s \in R^{6\times 6}$: Set rigidity for the slave

Fig.8 shows a 1-axial conceptual model of an impedance-controlled master-slave system.

The impedance control is classified into a force-control type and a motion-control type. For pneumatic manipulators, impedance control based on force control is considered to be the most suitable because of the high back-drivability and flexible characteristics. Therefore, as shown in Fig.9, the slave manipulator is controlled by impedance control with internal force-control loops, and the master manipulator, by admittance control. "Pneumatic Force Controller" and "Motor Driver" in Fig. 9 respectively refer to the PI controller for the drive force of the pneumatic actuator and to the PID controller for angular velocities by the motor driver. Function Z represents an inverse dynamics model of the slave manipulator, where reference drive forces f_{ref} on the slave side are dealt with as estimated external forces to be transmitted to the master side.

EXPERIMENTAL RESULTS

We have conducted experiments with the system to evaluate its performance in estimating external forces.

Forceps Position Control

Firstly, in order to evaluate the performance of the slave manipulator, joint position tracking was performed with a sinusoidal reference input. Selection of a harmonic reference is guided by a simplistic approximation of the suturing operation during which we intend to measure the external forces. The range of amplitude and frequency is chosen based upon the practical bandwidth requirement during a master-slave laparoscopic surgery. For the first experiment, movement was unhindered with no contact with the external environment. The system was tested by varying the amplitude of the reference angles from 0 to 30 deg and frequencies between 0.1 to 4.5 Hz.

The control parameters are tuned manually for optimal results. Fig.10 shows the experimental result of position tracking at 0.5 Hz using pneumatic rubber muscles. It is clear that the error in position tracking for the tip joints is negligibly small.

Force Estimation

In the second experiment, the performance of the developed controller was calculated for its accuracy and sensitivity in external force perception. For this purpose, a suture thread bound to a rigidly fixed force sensor (BL AUTOTEC.LTD., NANO2.5/2) was gripped and pulled by the forceps manipulator while tracking a sinusoidal reference, as shown in Fig.11.

Fig.12 shows the combined plot of the magnitude of the estimated force and the joint force obtained from the output of the force sensor along Z axis direction. It is observed that errors in Z axis are within approximately 0.5 N that is around 16% of the maximum estimated force. The largest errors are observed during the unhindered motion when the output of the force sensor is zero. This error is attributed mainly to the inadequate modeling of the frictional forces in the mechanism which are dominant during unimpeded motion of the forceps.

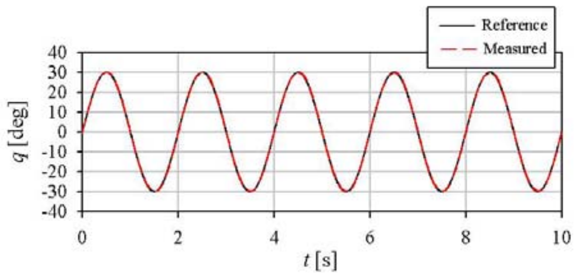

Fig.10 Position tracking of slave manipulator

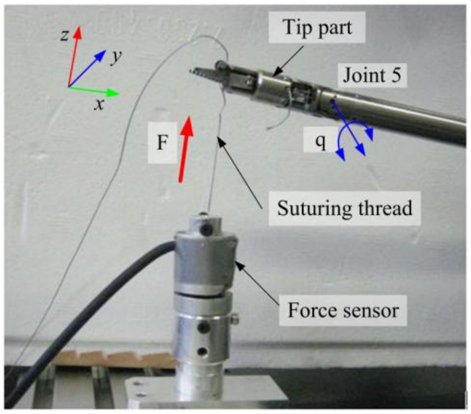

Fig.11 Experimental setup for force estimation at tip

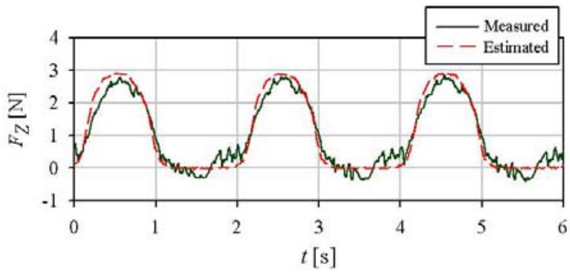

Fig.12 Experimental results of force estimation at tip joint

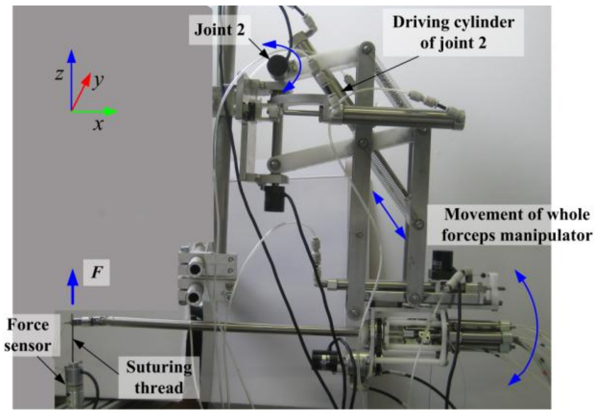

Fig.13 Force estimation set-up for supporting manipulator

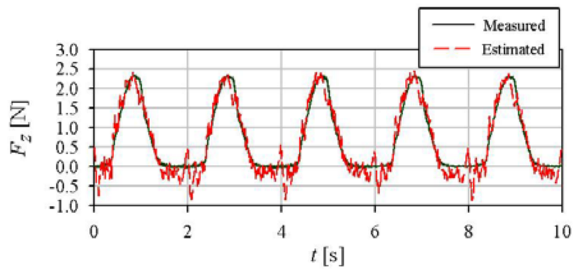

Fig.14 Experimental results of supporting manipulator

Table 1 Impedance parameters

M_s	0.02 Kg
M_m	1.0 Kg
B_s	0.02 Ns/mm
B_m	0.009 Ns/mm
K_s	0.6 N/mm

In the next experiment, the forces acting on supporting part are estimated during contact with the external environment. The experimental set-up is as shown in Fig.13. A sine wave driving signal with the frequency of 0.5 Hz is applied to a joint. The estimated forces are compared with those obtained from the force sensor.
The experimental results of forces estimation are shown in Fig.14. The experimental results indicate that IBIS IV estimates external forces with a sensitivity of 0.5 N

Experimental Results in Bilateral Controls
With the above-mentioned system in which impedance parameters are set as per Table 1, we have carried out a suturing task on a dummy organ, as shown in Fig.15.
Fig. 16 shows a part of the experimental results with respect to y-axial responses of positions and forces for the master and slave manipulators; the operator is handling the thread to form a knot until approximately 60s. During this time, there are almost no forces generated and the slave manipulator follows up the master manipulator very closely in positions. In the lapse of about 60 s, the operator has started pulling the thread and tightening knots, at which time there are forces of as much as 2 N generated. Positional deviations of the master and slave manipulators are proportional to external forces as per the set values of stiffness K_s, and the master and slave manipulators

In-vivo Experiments
We have conducted, using the developed master-slave system, in-vivo experiments on a pig, as shown in Fig. 17.

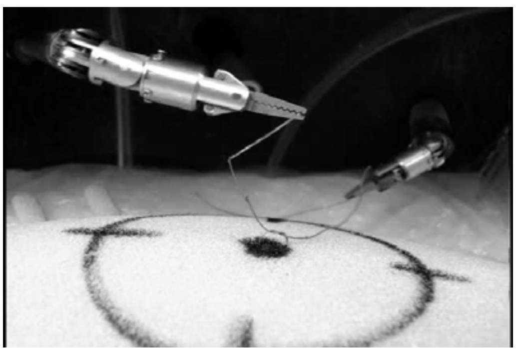

Fig.15 Suturing experiment

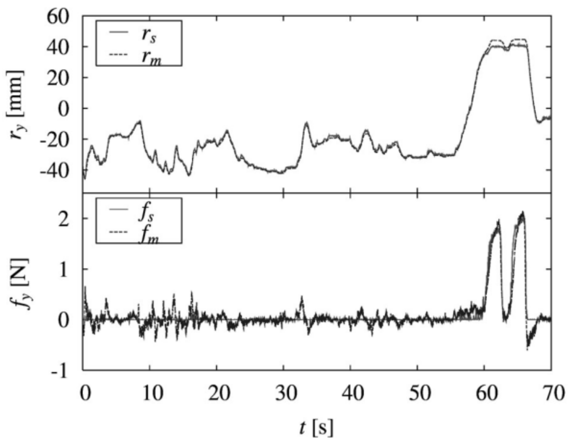

Fig.16 Experimental results of bilateral control

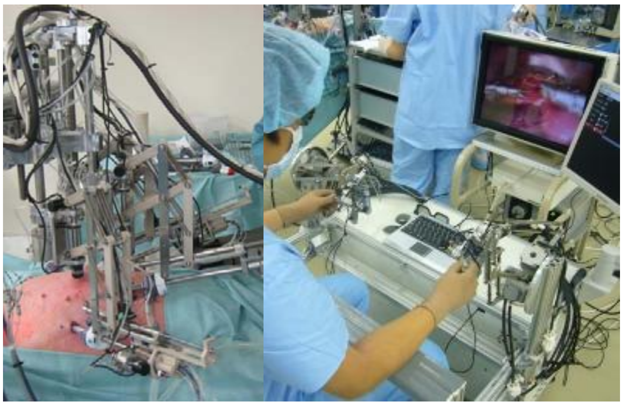

Fig.17 In-vivo experiment

The experiments had the following objectives:

(1) to confirm the motions of the manipulators in intra-abdominal environments,
(2) to confirm setting up procedures in surgical sites, and
(3) to obtain data on forces in in-vivo environments.

We have carried out the task of pushing a needle into the liver and intestines and then suturing them under pneumoperitoneum. We have found from the experiments that the forward tip of the manipulator, in particular the gripping mechanism, works very well in handling the curved needle at strong gripping forces without any adverse effects from body fluids. The suturing task in the abdomen was smoothly accomplished by the operator. Against concerns about possible deviations in positions between the remote center of motion of the manipulator and the actual insertion point due to respiration or changes in abdominal air pressure, in practice, no deviations in position have been observed when the forceps manipulator is inserted.

In the in-vivo experiments, we confirmed that the machine can successfully perform suturing tasks in the abdomen of the subject.

A sensitivity of 0.5 N is considered sufficient to sense the tensions in tightening suturing thread, according to reference [8] and in-vitro experimental results. This degree of sensitivity, however, is not enough to get a feel when soft organs are lightly pushed down. We therefore need to further improve force sensitivity of the manipulator in the future. Further miniaturization and lightening of the manipulator will enable it to estimate external forces to a much higher degree of sensitivity. At the same time, we may have to quantitatively evaluate and clarify the actual relations between force sensitivity and the efficiency safety of the task in the future.

CONCLUSIONS

In this paper, we introduced our work on the development of a master slave robotic system for laparoscopic surgery. In the system, pneumatic actuators, instead of electric motors, are used to drive the slave manipulator to detect external forces based on pressure values without a force sensor. We have developed a master slave system with the manipulator and evaluated its performance in terms of force estimation. The experimental results indicate that the manipulator named IBIS IV estimates external forces with a sensitivity of 0.5 N. Moreover, some in-vivo experimental results were demonstrated. We confirmed that the suturing task in the abdomen was smoothly accomplished by the operator.

ACKNOWLEDGEMENTS

The authors wish to thank Prof. Toshiharu Kagawa for his advices and the supports by Tokyo Medical and Dental University. This research was partially supported by the Ministry of Education, Science, Sports and Culture, Grant-in-Aid for Scientific Research (KAKENHI) No.21760190 and 21360114.

REFERENCE

[1] R. H. Taylor and D. Stioianovici, Medical Robotics in Computer-Integrated Surgery, IEEE Trans. on Robotics and Automation, Vol.19, No.5, pp. 765-780 (2003)

[2] N. Matsuhira et al., Development of a Functional Model for a Master-Slave Combined Manipulator for Laparoscopic Surgery, Advanced Robotics, Vol.17, No.6, pp. 523-539 (2003)

[3] H. Yamashita, D. Kim, N. Hata, and T. Dohi, Multi-Slider Linkage Mechanism for Endoscopic Forceps Manipulator," In Proc. of the 2003 IEEE/RSJ, Int. Conf. on Intelligent Robots and Systems, Vol.3, pp. 2577-2582 (2003)

[4] G. Hubens, H. Coveliers, L. Balliu, M. Ruppert, W. Vaneerdeweg, A performance study comparing manual and robotically assisted laparoscopic surgery using the da Vinci system, Surgical Endoscopy, Vol.17, pp.1595-1599 (2003)

[5] M. Hashizume et al., Early Experience of Endoscopic Procedures in General Surgery Assisted by a Computer-Enhanced Surgical System, Surgical Endoscopy, Vol.16, pp. 1187-1191 (2002)

[6] M. J. H. Lum et al., Multidisciplinary Approach for Developing a New Minimally Invasive Surgical Robotic System, In Proc. of the 2006 BioRob Conf. (2006)

[7] J. Arata, M. Mitsuishi, S. Warisawa, K. Tanaka, T. Yoshizawa, and M. Hashizume, Development of a Dexterous Minimally-Invasive Surgical System with Augmented Force Feedback Capability, In Proc. of Int. Conf. on Intelligent Robots and Systems, pp. 3738-3743, (2005)

[8] A.M. Okamura, L. N. Verner, C. E. Reiley, and M.Mahvash, Haptics for Robot-Assisted Minimally Invasive Surgery, In Proc. of the Int. Symposium Robotics Research, Hiroshima, Japan, November pp.26-29 (2007)

[9] J. T. Dennerlein, D. B. Martin, and H. Zak, "Haptic Force-Feedback Devices for the Office Computer: Performance andMusculoskeletal Loading Issues," Human Factors, Vol.43, No.2, 1996, pp. 278-286.

[10] G. Tholey, J. P. Desai, and A. E. Castellanos, "Force Feedback Plays a Significant Role in Minimally Invasive Surgery," Annals ofSurgery, Vol.241, No.1, 2005, pp. 102-109.

[11] M. Kitagawa, D. Dokko, A. M. Okamura, and D. D. Yuh, "Effect of Sensory Substitution on Suturemanipulation Forces for Robotic Surgical Systems," The J. of Thoracic and Cardiovascular Surgery, Vol.129, No.1, 2005, pp. 151-158.

[12] K. Tadano and K. Kawashima, Development of a Master Slave Manipulator with Force Display using Pneumatic Servo System for Laparoscopic Surgery, International Journal of Assistive Robotics and Mechatronics, Vol.8, No.4, pp.6-13 (2007)

[13] K. Tadano, K. Kawashima: Development of a Master Slave System with Force-Sensing Abilities Using Pneumatic Actuators for Laparoscopic Surgery, Advanced Robotics, Vol.24, No.12, pp.1763-1783 (2010)

[14] K. Tadano, K. Kawashima, K. Kojima and N. Tanaka, "Development of a pneumatic surgical manipulator IBIS IV", Journal of Robotics and Mechatronics, Vol. 22, No. 2, pp.179-188 (2010)

Proceedings of the 8th JFPS International
Symposium on Fluid Power, OKINAWA 2011
Oct. 25-28, 2011

K-2

Development of Hydraulic Controlled Bending Technology for Bent Pipe of Plant without Thickness Reduction

Ken Ichiryu*

*Mechatronics Laboratory, Kikuchi Seisakusho Company
2161-12, Miyama-cho, Hachioji, Tokyo, Japan
(E-mail: ichiryu@kikuchiseisakusho.co.jp)

ABSTRACT

This new pipe bending method was adopted as a strategic fundamental support program of government. In this program, original bending machine was manufactured using induction heating and tested 100A pipe bending for obtaining condition of pipe thickness without reduction. In this bending machine, because of accurate pipe thrust control is required, hydraulic servo control was successfully applied. Until now, we have been concerned with three dimensional cold bending machine using parallel link head. For large pipe application such as diameter of 50-60mm, hydraulic servo control was introduced. But more large size application for chemical, petroleum and power generation plant, hot induction heated bending is required. In the year of 2000-2008, new hot bending machine was developed by Miyasaka and Sato in Hachioji Branch Campus of KOGAKUIN University[1]. The bending machine is based on the new concept of without reduction of pipe thickness by applying axial compression thrust force.

KEYWORDS

Oil-hydraulic servo, Pipe Bending machine, Hot bending, High-frequency heating

OUTLINE OF NEWLY DEVELOPED BENDING MACHINE

Piping system of chemical, atomic power plant and so forth are composed of enormous number of welded pipe and elbow combination.

This study is aimed to replace this welded elbow-straight pipe combination by new bent pipe produced by local induction heating under compressive axial load.

This new bending principle is disclosed in Japanese patent #2010-131649.

Feature of the patent is to make it possible to determine neutral position of bending independent of pipe bending radius.

That is, by this invention, for example, if to assign neutral position toward the pipe outer or inner position, total section of pipe becomes under compression or tension stress, respectively.

Conceptual diagram is shown in Figure 1, where pipe thrust force is produced by the differential movement of pulley and carriage controlled by the velocity difference of pull and push wire rope.

In Figure 2, pipe bent state at induction heated zone is shown.

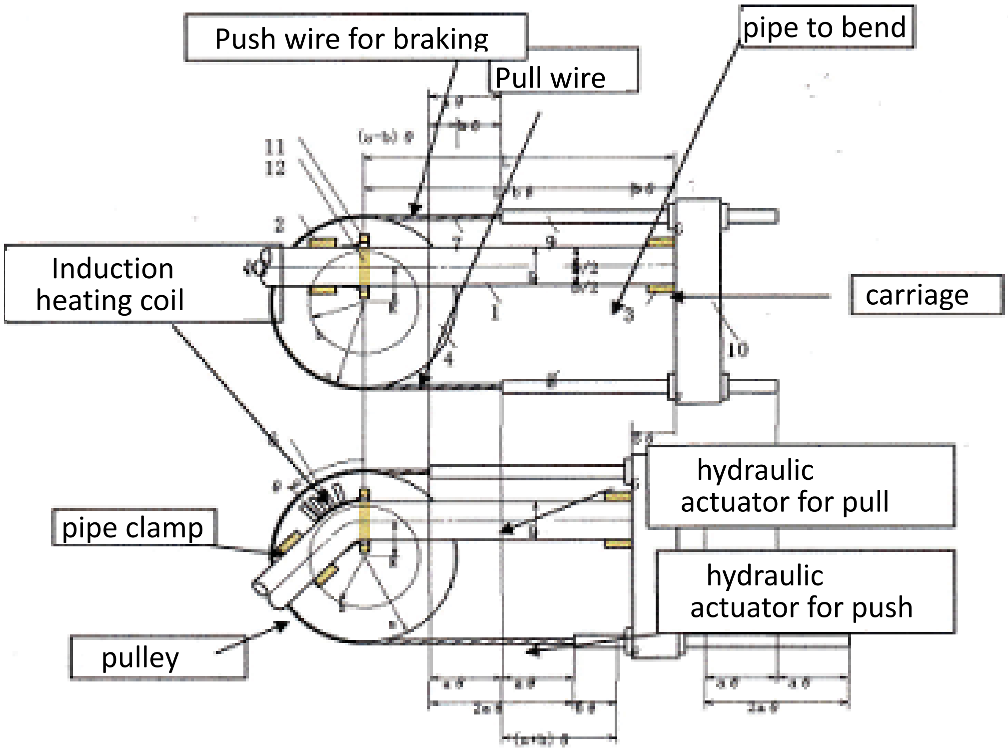

Fig. 1 Principle of new bending method

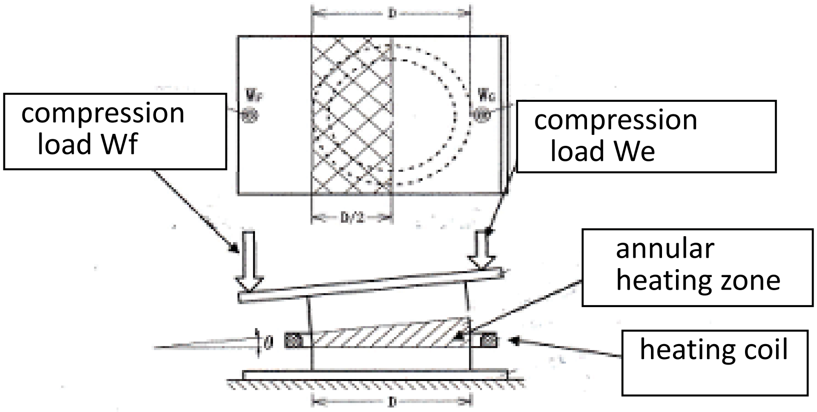

Fig. 2 Pipe bent state at induction heating zone

2

Applying W_f force by pull cylinder and W_g braking force by push cylinder, pipe heated zone is bent under axial load to create circular profile.

Figure 3 is a model diagram of hydraulic thrust control system. In Figure 4, detail diagram of pulley part is shown.

Designating V_f as pull relative velocity to the carriage and V_g as push backward velocity to the carriage, carriage relative velocity or pipe feed velocity is given as follows.

$$V_p = \frac{V_f - V_g}{2} \qquad (1)$$

Position where pulley rotational velocity relative to the pipe is zero, corresponds to the neutral position of pipe bending.

If defining $\sigma = V_f / V_g$ and pulley radius R_p, X / R_p is given as follows,

$$\frac{X}{R_p} = \frac{\sigma - 1}{\sigma + 1} \qquad (2)$$

For accurate control of X position, it is necessary to determine σ value precisely. So that electro-hydraulic flow control using servo valve is attempted for cylinder velocity V_f and V_g determination. Velocity diagram including gradation control is shown in Figure 5.

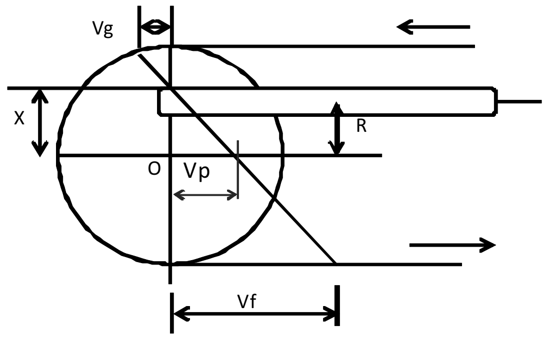

Fig. 4 Detail of Pulley Part

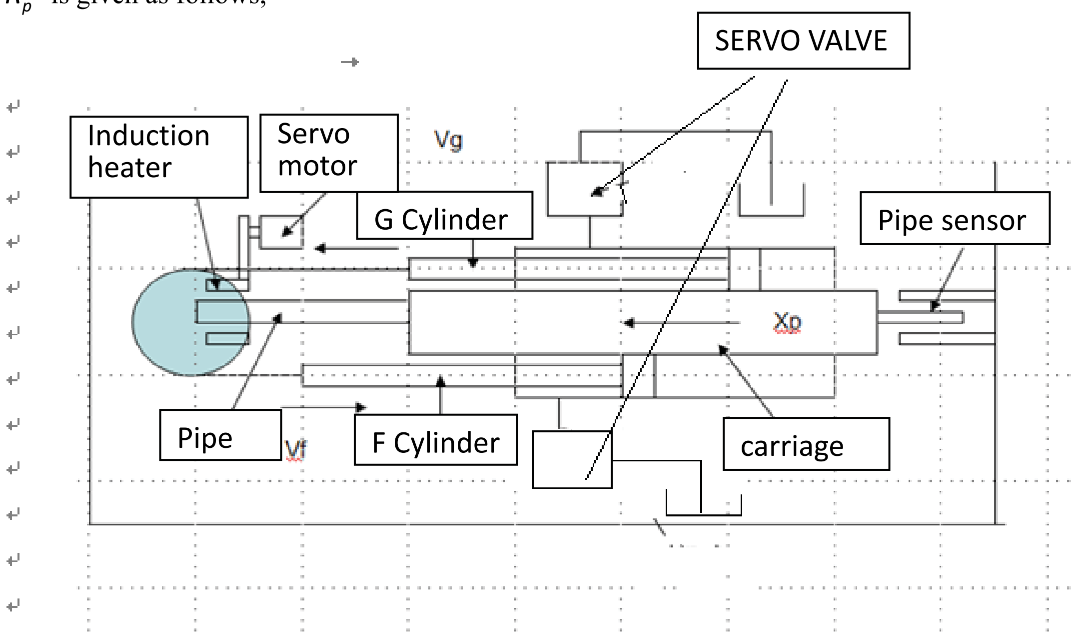

Fig. 3 Hydraulic Control System Model of Axial Thrust Force

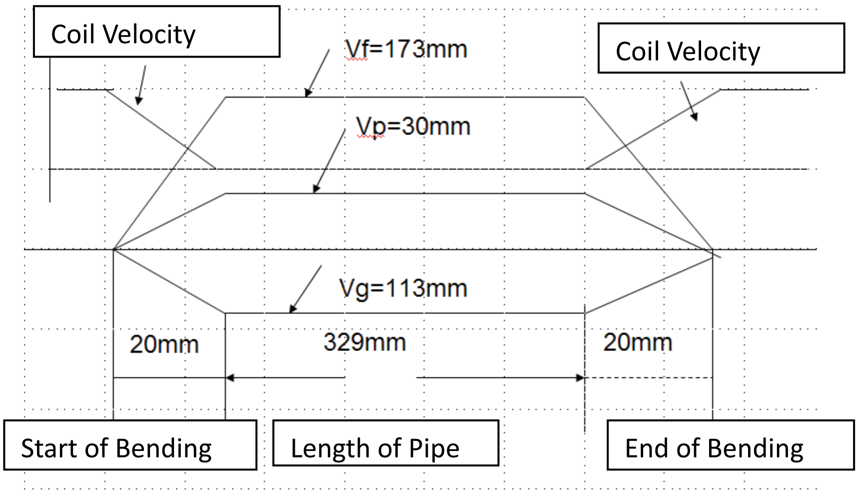

Fig. 5 Example of Velocity Diagram

OUTLINE OF EXPERIMENTAL APPARATUS

Bending machine is composed of A) machine base B) pipe clamp C) cylinder support box, F, G cylinders and pipe to bend D) pulley that is driven by wire rope coupled with F, G cylinders E) pulley support F) 3 axis induction heating coil moving table.

Incremental position sensor is incorporated in F, G cylinder rod end.

Bird eye view of bending machine is shown in Figure 6.

Hydraulic system is consisted of three components, such as hydraulic cylinder, hydraulic unit and servo pack as shown in Figure 3.

Main function of hydraulic system is accurate velocity control of V_f and V_g of F, G cylinder, respectively.

Both cylinder specifications are Φ200×Φ300×3000 stroke and 30 ton output force.

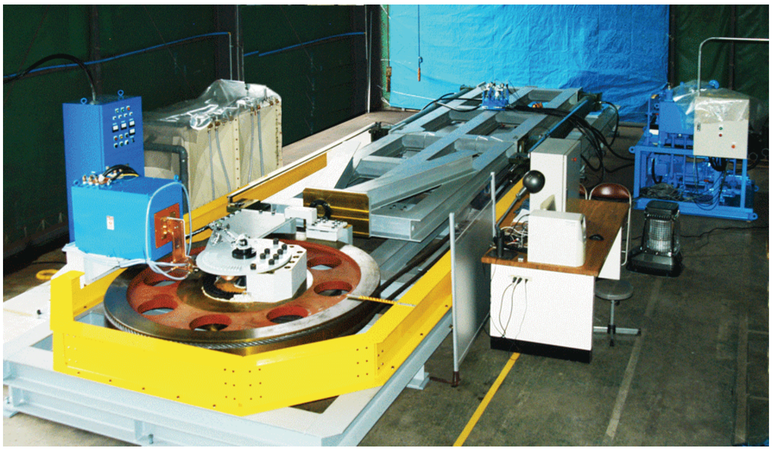

Fig. 6 Bird Eye View of Assembled Bending Machine

Controller is composed of FA-PC/windows attached to SPX motion controller. Main function is accurate control of V_f and V_g.

Controller block diagram is shown in Figure 7. Three input signals shown in Figure 5 are generated by four inputs of F, G cylinder position, pipe position and pulley rotational angle.

High frequency heating device is composed of high frequency oscillator, transformer and heating coil.

Bending system is classified in base part, bending main body composed of cylinder and pulley, transformer table and stroke measurement part, are shown in Table 1.

Table1 Bending machine specification

Bender main body	Base	composed of main frame and end frame L=10350mm, W=2760mm, H=430mm
	Carriage	two piece bolt structure (3425×1600ｍｍ) F, G cylinder are clamped in side wall
	Pulley	Diameter Φ2010 driven by wire coupled with F, G cylinder
Transformer table	3 axis drive 3 axis motor	X-Y-Z 3 axis movable Z=±80mm Y, Z=±10mm Z axis: AC servo motor X,Y; AC motor
Position sensing	pulse sensor 25µm pitch	F, G cylinder Stroke 3000mm ERGO JAPAN

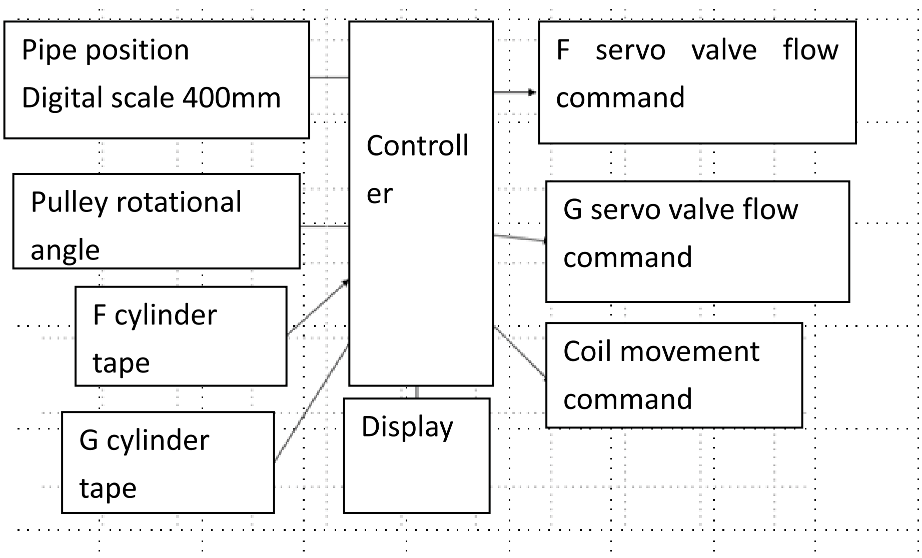

Fig. 7 Control block diagram

EXPERIMENT OF STEEL PIPE

At first, experiment of 1.33DR, so called, elbow bending was conducted using 50KVA high frequency power source. 1.33 DR means R/D =1.33, where R: radius of bending of pipe center, D: diameter of pipe.

90 degree bend of 5 samples was tried. Used pipe is STPG 370-E material, nominal outer diameter 114.3 mm, nominal thickness 8.6 mm. Bending radius is 152.4mm. Bending velocity is set as 0.75mm/s.

As shown in Figure 8, thickness decrease of tension side becomes small by giving strong compression force to the pipe, putting neutral axis outward by velocity ratio V_f/V_g large.

Measured values in Figures 8 and 9 are minimum thickness and mean thickness of measured domain, respectively.

Actual bent profile is shown in Figures 10 and 11, respectively. In the former case, no wrinkles were observed. But, in the latter case wrinkle was observed in the outlet domain.

If large compression force is imposed aiming zero thickness reduction, danger of wrinkle is difficult to avoid. Therefore, to allow a little reduction of thickness at the tension side is considered practical. If we consider pipe thickness variation, no thinning, reduction-less bending is not always effective.

By the thinning of bent pipe, plant designer is forced to select pipe thickness of one size up. Problem is how to avoid this situation. We could obtain practical solution by the optimum selection of velocity ratio $\sigma = V_f/V_g$.

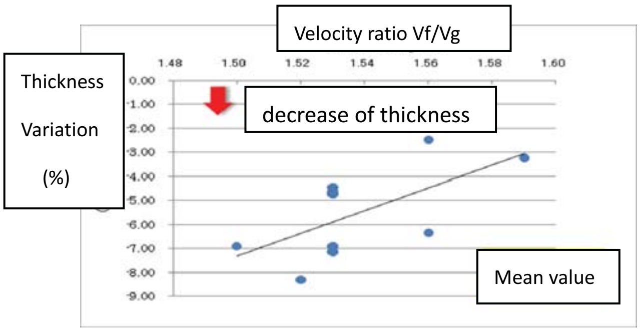

Fig. 8 Relationship between velocity ratio and thickness (minimum value comparison)

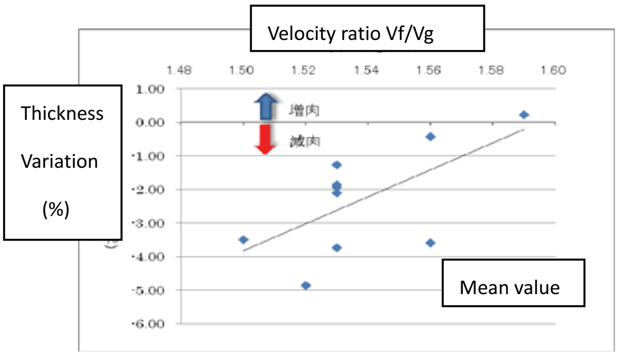

Fig. 9 Relationship between velocity ratio and thickness (mean value comparison)

Fig. 10 Right angle bent profile ,
Velocity ratio 1.53 thickness variation -2.7%

Fig. 11 Right angle bent profile velocity ratio 1.53 thickness variation -3.0%

CONCLUSIONS

New bending method without thickness reduction is realized by the joint work of T. Satoh and K. Miyasaka [1] under the sponsorship of Japanese government fund. This machine is hot bending machine of high frequency induction heating.

Performance of axial thrust force control was confirmed effective to prevent thinning of bent pipe.

By the experiment of 100A pipe, nearly thickness reduction-less bending was realized.

This bending method is anticipated to contribute to the large scale plant construction by the economical pipe usage.

In the end of this paper, I express my sincere thanks to Y. Ishikura for his cooperation of experiment and also I. Kikuchi of president of Kikuchi Company for his support of this development.

REFERENCES

1 K. Miyasaka; Dieless pipe bending by high frequency induction heating, Journal of Japan society for technology of Plasticity, 2010, **51**-591

Proceedings of the 8th JFPS International
Symposium on Fluid Power, OKINAWA 2011
Oct. 25-28, 2011

K-3

SMART FLUID POWER SYSTEMS UTILIZING ELECTRO-/MAGNETO-RHEOLOGICAL FLUIDS

Masami NAKANO*

* Intelligent Fluid Control Laboratory, Institute of Fluid Science
Tohoku University
2-1-1 Katahira, Aoba-ku, Sendai, 980-8577 Japan
(E-mail: m-nakano@fmail.ifs.tohoku.ac.jp)

ABSTRACT

Electro(ER)-/Magneto-rheological (MR) fluids typically undergo abrupt changes in their rheological properties in general when subjected to an external electric or magnetic field. In a hydraulic circuit system using the ER or MR Fluid, the ER or MR valve can be constructed to control the flow rate and the pressure drop, so that smart fluid power systems are realized by using the ER or MR fluid. In this paper, two typical smart fluid power systems utilizing the ER or MR fluid are introduced. One is a developed Braille display system driven by micro-diaphragm ER actuators controlled by micro ER valves fabricated by a photolithography technique. The other is a newly developed passive type MR damper using two permanent magnets, MR valves and check valves, which has variable damping characteristics as well as an existing semi-active damper, although it is fully passive device without any sensor, power supply and controller.

KEY WORDS

Electro-Rheological(ER) Fluid, Magneto-Rheological(MR) Fluid, Valve, Braille Display, Damper

INTRODUCTION

Electro(ER)- or magneto-rheological(MR) suspension is an exciting family of the functional fluids that behaves like a Bingham fluid having yield stress which can be rapidly changed in a reversible manner by applying electric or magnetic field [1, 2]. This rheological change is caused by the formation of fibrous structure consisting of the dispersed particles, which are polarizable under electric or magnetic field. In a hydraulic circuit system using ER or MR suspension, when the ER or MR suspension flows through the slit channel between two electrodes or magnetic poles, the dispersed particles are polarized and form many particle clusters, so that the flow rate and pressure drop across the channel can be controlled by changing the electric or magnetic field strength applied to the channel because the flow resistance due to the clusters changes with the electric or magnetic field strength. That is, the valve consisting of only electrodes or magnetic poles with no moving parts is realized using ER or MR suspension as a working fluid of the hydraulic circuit system. The ER or MR valve has some advantages such as simple and compact construction, high response rate and controllability, so that it is anticipated some smart applications to fluid power systems [3].

In this paper, firstly the rheological behaviors and some features of the ER and MR suspensions are briefly introduced. And then, typical two smart fluid power systems utilizing the ER and MR suspensions are described. One is a developed Braille display system driven by micro-diaphragm ER actuators controlled by micro ER valves fabricated by a photolithography technique. The other is a newly developed passive type

MR damper using two permanent magnets, MR valves and mechanical check valves, which has variable damping characteristics and excellent damping effect for single-degree-of-freedom vibration system, although it is fully passive device without any sensor, power supply and controller.

ER AND MR FLUIDS

Electro- and magneto-rheological fluids are suspensions that respond to an applied electric or magnetic field with a dramatic change in rheological behavior. The essential characteristics of these fluids is their ability to reversibly change from free-flowing, viscous liquids to semi-solids having a controllable yield stress in milliseconds when subjected to either an electric or a magnetic field. A simple Bingham-plastic model is effective in describing the essential field-dependent fluid characteristics. In this model, the total shear stress τ is given by

$$\tau = \tau_y(\text{field})\text{sgn}\dot{\gamma} + \eta_p\dot{\gamma} \qquad (1)$$

where τ_y is the yield stress caused by the applied field, $\dot{\gamma}$ is the shear rate and η_p is the field-independent plastic viscosity. The various different properties of the ER and MR suspensions are summarized in Table 1.

Table 1 Properties of ER and MR suspensions

	ER Suspension	MR Suspension
Max.yield stress	2-5 kPa	50-100 kPa
Max. field	～4 kV/mm	～250 kA/m
No-field viscosity	0.1-1.0 Pa·s	0.1-1.0 Pa·s
Operable temp. range	+10 to +90 ℃ (ionic, DC)	-40 to +150 ℃
Response time	<milliseconds	<milliseconds
Density	1-2 g/cm^3	3-4 g/cm^3
Power supply	2-5kV/1-10mA	2-25V/1-2A

ER FLUID BRAILLE DISPLAY SYSTEM

ER suspension is suitable for MEMS applications, because the electric field can be applied by two electrode plates which can be manufactured in small size. Nakano et al. developed three-port micro ER valves [4] by using ER suspensions. In order to support visually-impaired person, a Braille display system using the micro ER valves has been developed [5].

Micro-Diaphragm ER Actuator

The developed system displays Braille by changing each height of 6 dots. 6 tactile pins must be allocated in a 3.8 mm × 6.1 mm rectangle. Therefore, channels must be integrated in the narrow space. A micro-diaphragm

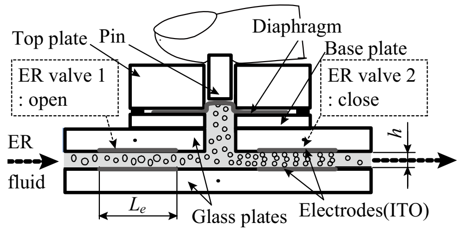

Figure 1 Actuation mechanism of ER micro-diaphragm actuator

actuator using a polyurethane film of 0.02 mm thickness and very low stiffness is developed. This actuator controlled by a pair of micro ER valves pushes up the dot as shown in Figure 1. The pressurized ER suspension pushes up a diaphragm when the valve 1 and 2 are respectively opened and closed. On the other hand, the diaphragm shrinks due to its elastic restoring force when the valve 1 and 2 are closed and opened, respectively. The diaphragm actuates a tactile pin on it and exerts force on a finger. The supply pressure which exerts the required display force of 0.15 N is measured to be 238 kPa. The length of an electrode L_e is calculated by the following equation :

$$L_e = \left(\frac{h}{2\tau_{ER}}\right)\Delta P_{ER} \qquad (2)$$

where h, τ_{ER}, and ΔP_{ER} are gap height between electrodes, yield stress and pressure drop of an ER valve, respectively. ER suspension containing 20 vol.% sulfonated polymer particles (Nippon Shokubai Co., Ltd.) of 5 μm in average diameter is used. E^2 and τ_{ER} have a correlative relationship of τ_{ER}=0.3271E^2. When the height h is 0.3 mm, electric field strength E is 2.5 kV/mm and ΔP_{ER} =238 kPa, the electrode length L_e is 17.5 mm.

Braille Display System Driven by Micro-Diaphragm ER Actuators

ER valves and flow channels are three-dimensionally fabricated by photolithography. Figure 2 shows an exploded view of the actuators. 12 valves are allocated parallel in a lower channel. The length of an electrode is 20 mm that includes the estimated length of 17.5 mm and margin. ER valves and rectangular channels are formed by ITO (Indium Tin Oxide) electrode film and photo resist. Height and width of a channel are 0.3mm and 1.5 mm, respectively. ER fluid is supplied from the inlet and flows an upper channels. The upper channels guide the fluid to 6 pins display part.

On the top of the actuator, 6 pins display part is mounted. As shown in Figure 3, two plates sandwich a diaphragm film and 6 pins inserted in the top plate's holes. In order to limit the pin height, a stopper mechanism is designed. A pin and a hole have stepped sections and there is 1.1 mm gap between the sections. When the pin is pushed up 1.1 mm in height, the stepped sections collides with each other and the height

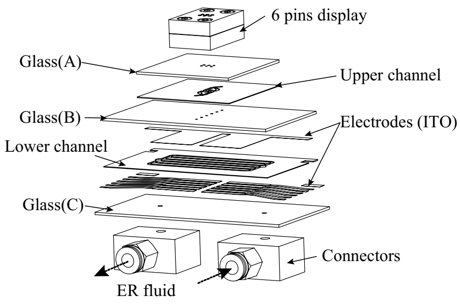

Figure 2 Exploded view of 6 units actuators

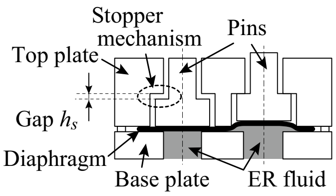

Figure 3 Tactile pin display mechanism of micro-diaphragm ER actuator

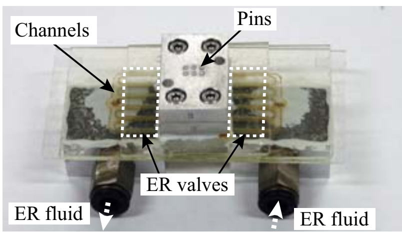

Figure 4 Photograph of a 6 units ER actuator for Braille display

(a) One pin (b) Six pins

Figure 5 Braille displaying by 6 units actuator control

is limited. And the top of the pin is raised 0.5 mm above the top plate.

Figure 4 shows the developed Braille display. The size of the 6 units actuator is 90 mm × 45 mm × 31 mm (width × depth × height). ER fluid is pressurized by P_s =230 kPa argon gas and electric field strength E =3.3 kV/mm applied to electrodes is controlled by a computer. Figure 5 shows a snapshot of controlling each height by 6 units ER actuator. The displacement of the top of the pin is measured by a laser displacement sensor. The maximum height is about 0.5 mm and the height is changed from 0 mm to 0.5 mm within 0.1 s. The transition from 0.5 mm to 0 mm is relatively slow since the pin is pulled by film's elastic restoring force. But still, the pin is returned under 0.1 mm in height within 0.5 s.

As described above, the developed 6 units ER actuator appropriates Braille display system. However, in order to develop the wearable device, the size of the actuator is not sufficient. Smaller actuators and a pump for supplying ER fluid will be developed in the next step.

PASSIVE TYPE MR DAMPER WITH VARIABLE DAMPING DEPENDENT ON DISPLACEMENT AND VELOCITY

A novel MR damper which has the same variable damping characteristics as an existing semi-active control but no active component has been proposed and developed [6]. The damping force changes in response to the sign of the displacement and the velocity, which is effective in reducing vibrations. Moreover, the damper has an advantage in high reliability, since the damper is composed of only passive components such as MR fluid, permanent magnets, and check valves.

Passive Type MR Damper

The schematic drawing and the photograph of the passive type MR damper are shown in Figure 6. The damper has the two permanent magnets on the ends of the cylinder in order to apply the magnetic field to the MR fluid, and some components consist of ferromagnetic materials such as low-carbon steel so as to transmit well the magnetic flux. In Figure 6, ferromagnetic components are drawn with light gray and non-magnetic materials are drawn with white, that is, the cylinder wall, piston head, and side flanges consist of ferromagnetic low-carbon steel and the piston rod is combined with ferromagnetic and non-magnetic materials. These magnetic structures provide magnetic circuits in response to the displacement of the damper. Moreover, a couple of the piston head have the annular orifice and the bypass orifice with the check valve in which the flow is one way, and hence, the passage of fluid flow depends on the sign of the damper velocity. These unique internal structures provide useful damping characteristics which are explained in Figure7.

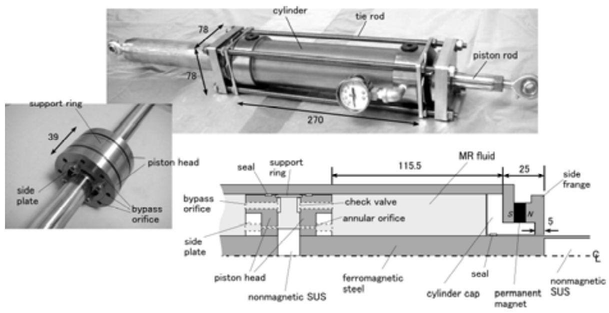

Figure 6 Schematic drawing and photo of developed passive type MR damper

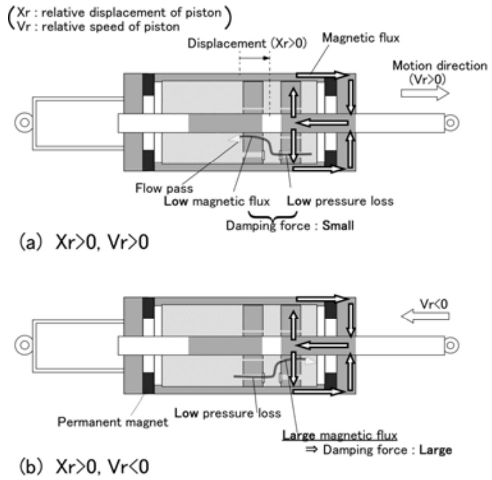

Figure 7 Mechanism of passive type MR damper

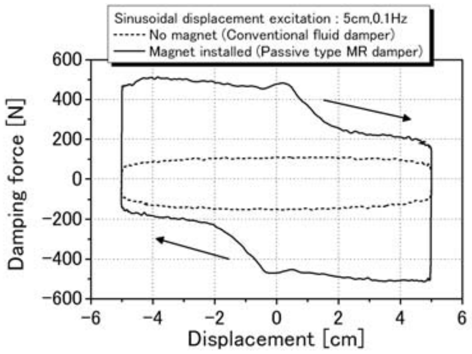

Figure 8 Damping force vs. damper displacement

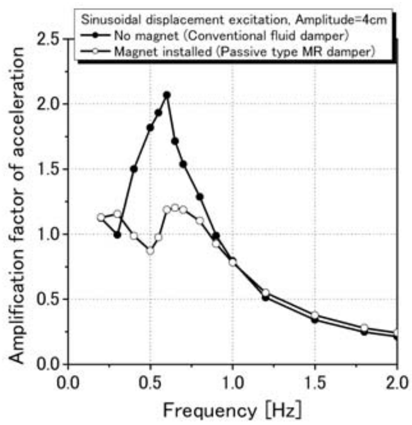

Figure 9 Acceleration response characteristics of SDOF system in base excitation test

When the piston is located at the right side as shown in Figure 7(a), (b), a magnetic circuit through the right side magnet and piston head is formed. Besides, if the piston moved to right as Figure 7(a), the fluid passes through the bypass orifice of the right piston head and the annular orifice of the left one. Here, the pressure drop through the bypass orifice is rather small because of its wide passage and that through the annular orifice at the left side is also small since the applied magnetic flux is quite small there. Therefore, the damping force in the case of Figure 7(a) becomes small. On the other hand, the damping force in the situation of Figure 7(b) becomes large, since the fluid flows in the right side annular orifice where the magnetic field is applied. Consequently, we can say that the damping force becomes larger when the sign of the product of the velocity and displacement is negative, and it becomes smaller when the sign is positive.

Damping and Response Characteristics

Figure 8 shows the damping characteristics under sinusoidal excitation with a frequency of 0.1Hz and amplitude of 5cm. Here, positive displacement means that the damper extends and the arrows show the direction of the motion. The damper without the permanent magnets behaves as an ordinary passive damper in which the damping characteristics depend on only velocity. On the other hand, the damper installed the magnets shows quite unique damping characteristics which are provided by the MR effect. The passive type MR damper changes the damping force at interval of 1/4 cycle, in other word, the force strength changes in response to the signs of displacement times velocity. The damping characteristics are in accordance with the expectation and with one of semi-active control proposed by Rakheja.

The response characteristics of single-degree-of-freedom (SDOF) system under a sinusoidal excitation are shown in Figure 9. The amplification factor of the acceleration is defined as the ratio of the measured maximum accelerations between the mass and the shaking table. the proposed MR damper can decrease the acceleration response around the resonance frequency, and besides the response at higher frequency is equivalent to that of no magnetic case. This result indicates that the proposed damper provides quite superior performance to ordinary passive dampers in a wide range of frequency.

REFERENCES

1. Winslow, W. M., Journal of Applied Physics, 1949, Vol.20, No.12, pp.1137-1140.
2. Nakano, M., Koyama, K. eds., Electro-Rheological Fluids, Magneto-Rheological Suspensions and their Applications, World Scientific, 1998, p.893.
3. Nakano, M. ed., Final Reports of Research Committee on Smart Fluid Power Systems utilizing Functional Fluids, The Japan Fluid Power Society, 2006, p.153.
4. Nakano, M., et al., Journal of Intelligent Material Systems and Structures, 2002, Vol.13, No.7&8, pp.503-508.
5. Tsujita, T., Nakano, M., Yoshida, K., ER Fluids and MR Suspensions, ed. R. Tao, World Scientific, 2011, pp.123-128
6. Murakami, M., Sakai, M., Nakano, M., Int. Journal of Applied Electromagnetics and Mechanics, 2010, Vol.33, No.3-4, pp.911-917.

Proceedings of the 8th JFPS International
Symposium on Fluid Power, OKINAWA 2011
Oct. 25-28, 2011

Aqua Drive System: a technology using tap water and its applications

Shimpei Miyakawa
Basic Technology R & D Center, KYB Co., Ltd.

1. Preface

In recent years, in the context of globalization, diversification, and complication of world markets and in terms of prevention of global warming, keywords such as "environment and energy-saving" are necessarily used when launching products onto the market. "**Energy-saving**" by improving efficiency and performance may reduce energy consumption, and eventually reduce the use of fossil fuels. "**Renewable energy**" such as wind power, water power, solar energy, and ocean energy may produce a similar effect. Examples of "**material recycling**" may include recycling and reuse.

"Recently, water shortages have become an international concern, particularly, shortages of drinking water. From this standpoint, the "water supply industry" has changed its business model from the public to the private sector. Several countries such as France, Singapore, and Korea are globally competitive in the market. It is has been called a "water major replacing an oil major." As in other countries, Japan intends to strengthen national commitment to increasing organizational competitiveness . Water is essential to human beings.

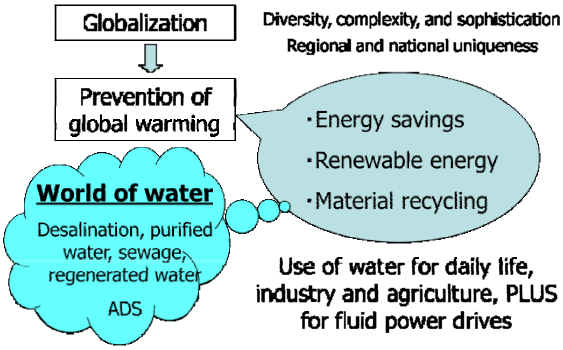

Fig. 1 Social context and "water use"

"Water" has properties that can be readily understood by combining the said three keywords (namely, energy-saving, renewable energy, and material recycling). Natural water exists in different forms, such as seawater, groundwater, well water, rainwater, mine water, vapor, and ice. It is reported that, of all the natural water available on the entire planet, only about 3% is fresh water, and the remaining 97% is seawater. Natural water is mainly used for daily life, industry, and agricultural use. The water problem varies by area. In advanced countries, water supplies for daily life and industrial use cannot keep up with demand, while in developing countries, degradation of water quality and especially shortage of drinking water are serious problems. Such social situations and "world of water utilization" are represented in Fig. 1.

Since water is such an important substance, it is urged that its effective use must be considered from every perspective. As well as using water itself directly for conventional purposes (such as for daily life, industrial, and agricultural use), a new approach, ADS (Aqua Drive System: a new water hydraulic system technology), is proposed to use "water for fluid power transmission." Technology research and development of Aqua drive systems or ADS began in the 1980's and the outcomes of that research have already been introduced in drives for industrial machines and equipment in various industries [(1)]. The graph in Fig. 2 shows the conventional "use of water itself" overlaying "ADS utilizing water as its working fluid" by placing flow rates in the horizontal axis and pressures in the vertical axis [2].

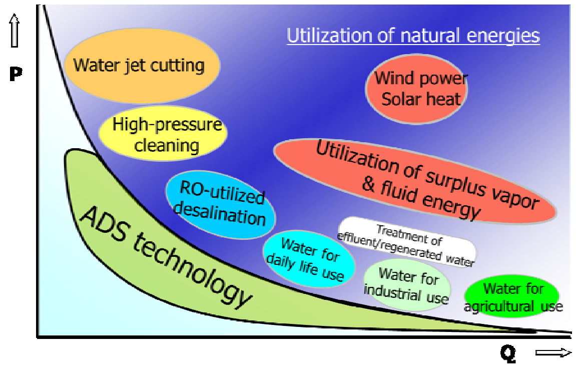

Fig. 2 "World of water utilization" expressed in a pressure-flow rate relationship

In a region where the flow rates are high and pressures are low, ADS incorporates "centrifugal pumps"; whereas, in regions where flow rates are low and pressures are high, it often uses "positive displacement pumps". Desalination technology that utilizes the reverse osmosis membrane (RO membrane) incorporates both pumps and ADS also actualizes its technology as a system.

This paper discusses this new dimension of ADS in terms of "market characteristics", component characteristics, technological challenges, performances and introduces "application examples" [3, 4, and 5].

2. Identifying ADS markets and developing the technology

Figure 3 describes processes for market and technology development.

First, identifying markets for ADS is vital for developing the technology. Markets that maximize benefits from the characteristics and added value of ADS are different from those for oil hydraulics, despite that they both provide the fluid power. As markets for ADS (water hydraulics), for example, the fields of food processing, semiconductor devices, packing devices, precision and clean molding and environmental/civil engineering are shown in the figure. The fields require products that have elements of hygiene, cleanness and washability, high temperature/humidity tolerance, and conformity with nature. Moreover, satisfying demands for ease of maintenance/servicing,

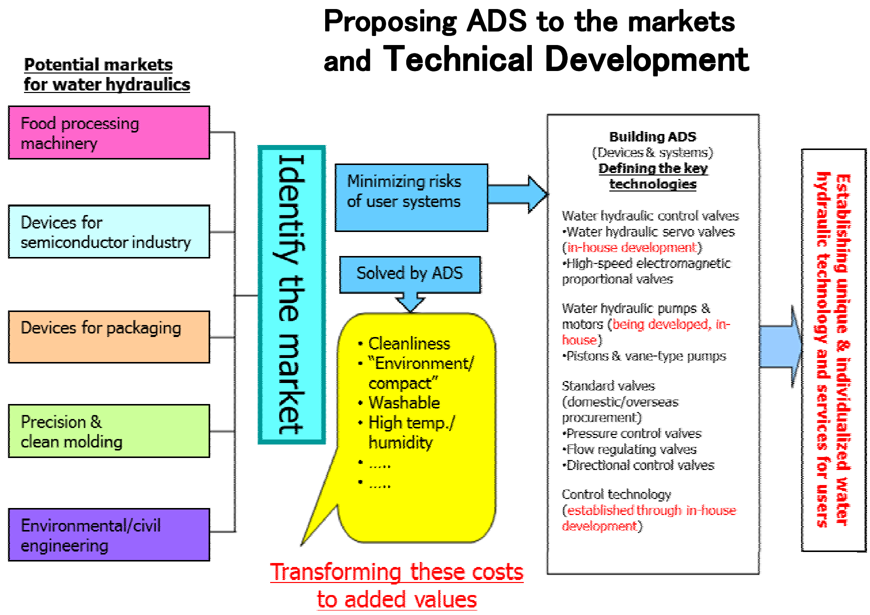

Fig. 3 Identifying ADS markets and developing the technology

interests in reducing overall costs for the purchase and disposal of working fluid (it means tap water here) and for system maintenance are the keys for introducing ADS in the markets. Once the target markets are specified, unique ADS technology to be developed to minimize risks in uses' systems shall be clarified.

In Figure 4, the idea of identifying the market is expressed as "Building ADS." In this phase, specifying the key technologies (ADS components and systems) is of great importance in component development.

This figure provides a snapshot of the "big picture" for ADS application fields focusing on "drives and environmental friendliness."

For drives for machines and equipment, mostly electric, oil hydraulic and pneumatic drives have been used. Fields where the required power density is high, oil hydraulic drives are advantageous. Those where the required power density is low, pneumatic drives have been applied, and electric drives have often been used to fill the gap between the power requirements. From the standpoint of fluid power levels, the author roughly grouped the drives-oil hydraulics, electrics and pneumatics-into high, middle and low pressure levels, respectively.

Provided that ADS produces working pressures that an oil hydraulic drive can provide, it offers the benefits of compactness, high speed and high power density inherent to fluid power, as well as superior environmental friendliness and ease of maintenance/service.

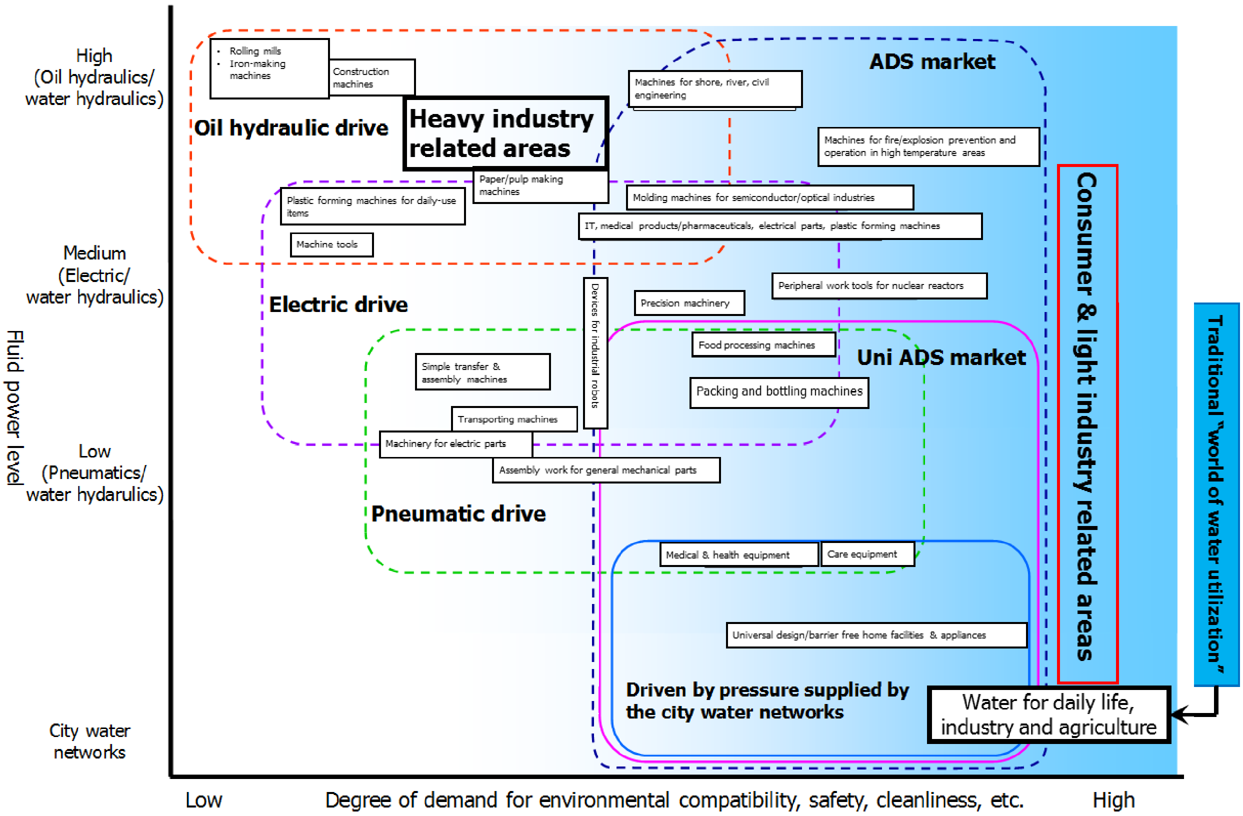

Fig. 4 Grouping of fluid power drives vs. environmental friendliness
(adding the "the world of traditional water use")

ADS offers a very wide range of driving pressure (0.3 MPa to 14 MPa), from high pressure at the level of oil hydraulics to very low pressure at the level of water supply and industrial water supply network pressures. The "world of water utilization" is added at the bottom right in the figure. Unlike oil hydraulic drives, which employ iron as their basic material and are often used in the iron-oriented heavy industry field, the market for ADS is basically made of clean stainless steel, is likely to expand globally in the future, and is compatible with the light industrial market, including, for instance, the medical and pharmaceutical markets, foods, cosmetic products, and consumer products industries, with increasing demand for "environmental friendliness", energy-saving and resource-saving. From now on, when selecting a driving source, it will be increasingly required to start with strong criteria for "environmental friendliness and ease of maintenance/service."

3. Technology development of ADS

The essential components in ADS technology are water hydraulic pumps, motors and valves. These components are built in such a way as to allow movement and clearance of component parts in applications which have important underlying tasks that must satisfy two functions simultaneously, "sliding and sealing." When introducing ADS, the technologies determine the "efficiency and durability" of the components, that is "the heart of the components."

The journey of fluid power development started in 1795 when an Englishman, J. Bramah, invented a water hydraulic press [(6)]. Later, the discovery of mineral oil solved difficulties associated with water hydraulics, and "oil film and corrosion control" has drastically changed technology for fluid power components from water hydraulics to oil hydraulics. Now, as we reconsider "water", the opposite of oil, as the fluid power in ADS, we are coming to realize that ADS technology is not a variant of oil hydraulic technology,

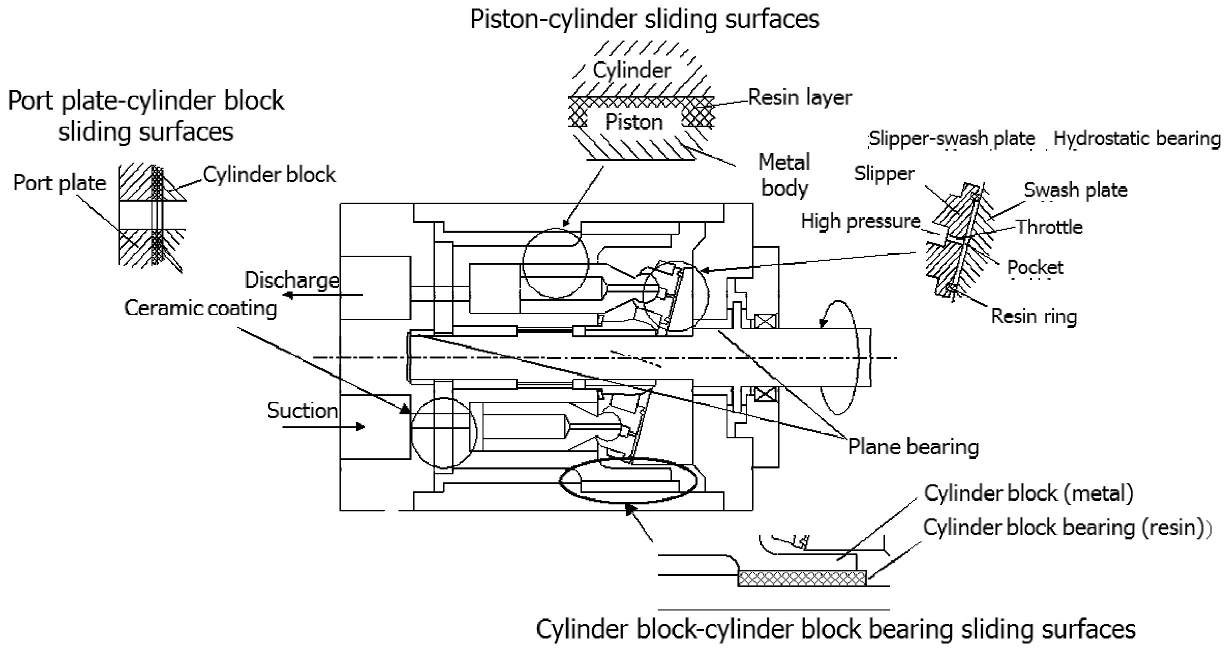

Fig. 5 Sectional view of the water hydraulic pump

and we are encouraged to rediscover the "property of water," which is the source of technology development. Only now can discussions regarding component structures and materials become meaningful. Starting from such a perspective, we can now begin to explain two approaches in ADS component development for incorporating technologies for "sliding and sealing" functions into the mechanism of ADS components.

1) Material selection and sliding mechanism for the sliding faces provide mostly mixed lubrication. This approach is used when a high load works between the two sliding surfaces, in a water hydraulic pump-motor structure, for example.
2) The two sliding surfaces are free of contact and the leakage from the clearance is used for other purposes, namely, the smooth movement required for the sliding type of water hydraulic control valves and for low working loads.

1) Case for a water hydraulic pump and motor

Figure 5 shows a sectional view of a water hydraulic pump [7]. A piston and a shoe, a cylinder block and a valve plate, the cylinder block and the inner surface of the casing, and the sliding bearing that supports the cylinder adopt sliding structures and materials, so that they can tolerate severe sliding action. However, the water film produced in the two sliding surfaces cannot be expected to act as a hydrostatic bearing to support the entire load. Under many operational conditions, the film is in a state of mixed lubrication; therefore, the load is partially supported by the materials. As seen in Figure 5, the basic inner structure of the modeled water hydraulic pump and motor is what we called a "hydrostatic bearing mechanism" intended to focus the sliding performance. The two sliding surfaces adopted are a combination of stainless steel and resin (PEEK: polyetheretherketone) or DLC.
The performance of the developed and then commercialized water hydraulic pump is exemplified in Fig. 6. The horizontal axis is the difference of the pump suction and discharge pressures and the pump speed is used as the parameter.

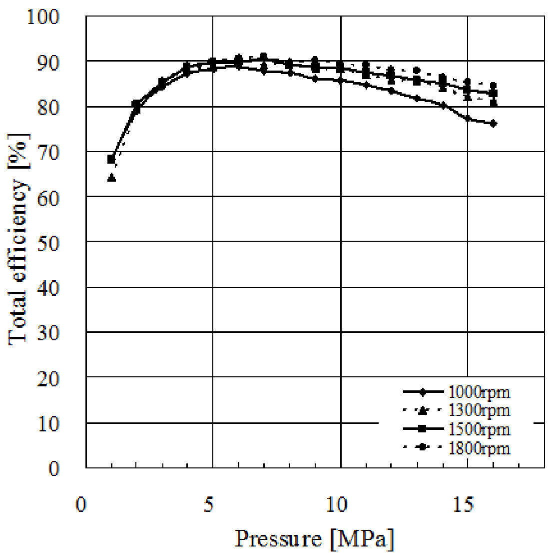

Fig. 6 Total efficiency of the water hydraulic pump

As the rotation speed increases (from 1000 to 1800rpm), the pump efficiency slightly improves. When the pressure differences in the clearance are the same, the leak flow rates should be constant; therefore, the increase of the theoretical flow rate along with the increase of the pump rotation speed indicates improvement in the pump efficiency. The standard specification of the pump is 15 cc/rev., 14 MPa, and 1800 rpm.
Figure 7 shows the torque loss. The horizontal axis indicates the bearing

parameters, μn/⊿P: μ is the viscosity coefficient of the fluid、 n is the pump rotation speed and ⊿p is the difference of the pump suction and discharge pressure. The pump was tested by giving the pump rotation speed and pressures in a range specified for practical use, and the torque loss was obtained as a curve of the negative gradient, as shown in Fig. 7.

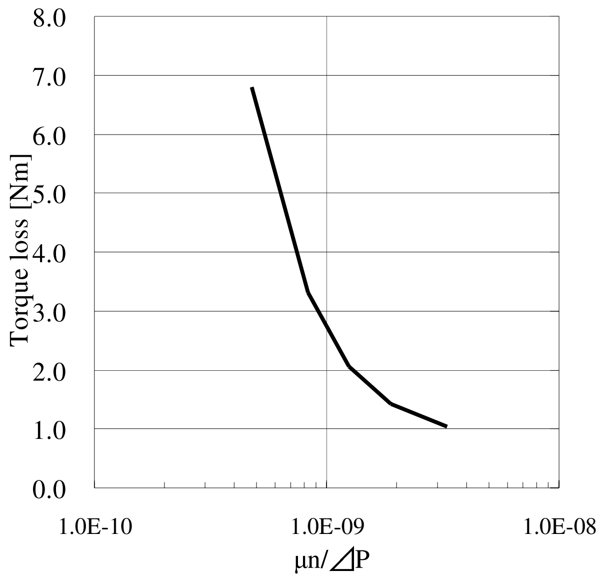

Fig.7 Relationship of the loss torque and the bearing

This is due to the behavior observed in the mixed lubrication region. For the bearing parameter, the torque loss falls mostly in one curve which shows a negative gradient toward a constant value. For the oil hydraulic pumps and motors, the negative gradient is a phenomenon observed in the region where the rotation speed is relatively low. For ADS, where the viscosity of the working fluid is extremely low and the water film is thin, the film behavior occurring on the sliding surfaces in the components is presumably governed by the mixed lubrication in the standard pump operation range (the maximum shaft rpm is from 1500 to 1800.) For some motor cases, the standard operation ranges are reported to be approximately 4000 rpm at maximum; therefore, the characteristic curve of torque loss in Fig. 7 is expected to show a phenomenon in which the curve leans toward the negative, reaches to the minimum value, and then goes to a region of fluid lubrication where the torque loss is in proportion to the motor rotation and finally ascends in a region where the torque loss increases due to water viscosity. On the other hand, the viscosity coefficient of the fluid in the bearing parameter is different from that of oil hydraulics. Since the coefficient is assumed to be almost constant within the practical operational temperature range (5 to 50 Centigrade), the torque loss is in proportion to the motor rotation, and inversely proportional to the difference of the pressures.

Since the torque loss curve in this study range shows a negative gradient, the torque loss is reduced when the motor rotation is increased and the loss is increased when the pressure difference in the pump increases. This phenomenon is assumed to happen due to water film formation as the motor speed increases. As the film starts to lubricate and the increase of the pressure difference is likely to encourage mechanical contact, eventually the torque loss increases.

Figure 8 shows the result of chronological wear and surface roughness observation of a piston sliding in the cylinder block.

The result shows the initial condition and the condition after 7000 hours of test operation. Both ends of the piston are worn by the severe sliding movement at the cylinder block ends.

The wear was approximately 4 μ m in the radial clearance. The average surface roughness was 0.65 μ m at the initial condition and was 0.40 μ m after 7000 hours of test operation. This suggests the surface was smoothed by the sliding. Observation of the efficiency change suggests that the piston surface at the initial condition was smoothed by time and smoothness was gradually improved and the surface condition stabilized around 1000 hours of test operation.

Decrease of the volumetric efficiency due to increase of the clearance is expected. However, the running-in contributes to improved smoothness of the piston surface, and the mechanical efficiency tends to increase. The overall efficiency is not affected

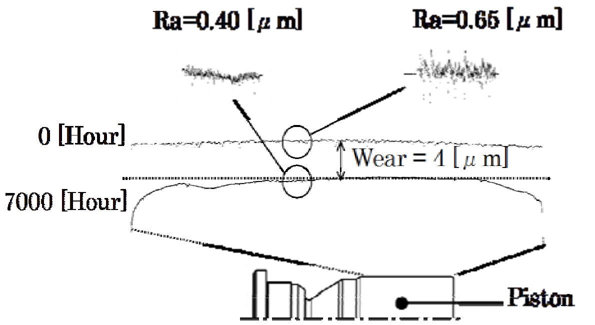

Fig. 8 Chronological changes of the piston conditions

by wear and surface roughness. The conditions for continuous operation are 14 MPa and 1800 rpm. Photo 1 depicts the appearance of the water hydraulic pump.

2) Case for a water hydraulic control valve

General valves which have controlling functions for pressures, flow rates and directions and electromagnetic proportional control valves and servo valves which accurately control fluid power are available. Poppet type valves and spool type valves ,valve bodies of which slide are available as general valves in the recent market. The former valve is prone corrosion from valve seat damage and offset of the valve body and seat that are likely to generate biased flow. In the spool type valve, elastic seals are often employed for the valve's sliding areas, which influence the valve and degrade valve performance by hysteresis.

Photo 1 Appearance of the water hydraulic pump

This phenomenon for general valves may be acceptable to some extent, although it is not intrinsically favorable. Again, "sliding and sealing" are the challenges, despite the fact that they hardly likely to cause serious problems. In a system which demands a precision control function for "drives and control," the mentioned valve structure cannot fulfill the requirements. We reinterpret the challenges of "sliding and sealing" as "leakage caused by sliding and effective use of the leakage", provided that some commercialized valve examples with innovative mechanisms can be introduced.

(1) Electromagnetic proportional control valve [8]

Figure 9 shows the internal structure of the valve.

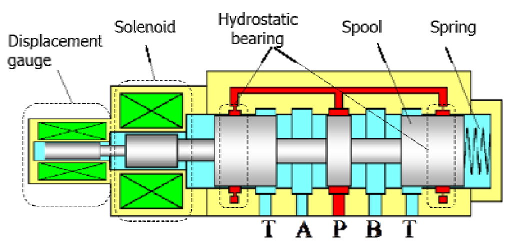

Fig. 9 Structure model and names of respective

The spool ends are supported by hydrostatic bearings. The viscosity coefficient of water is low; therefore, film formation in a clearance that occurs in an oil hydraulic valve cannot be expected in this water hydraulic valve. Thus, the hydrostatic bearings are used to support the spool to prevent the spool from contacting the surrounding wall. Since the bearings are working, the fluid in the clearance is used to channel the fluid, for example, so that the water does not stagnate. Water accumulation in the components is not favorable.

Photo 2 shows the appearance of the valve. The valve's rated pressure is 14 MPa and the rated flow rate is 20 L/min.

Photo 2 Appearance of the electromagnetic proportional solenoid valve

Figure 10 explains the flow characteristics without load. A slight flow rate difference between the two-way channels is observed near the point of origin; the controlled flow rate increases almost linearly to the electric input signals. Among factors that can seriously affect the characteristics, flow force is the factor affecting the spool. The spool may seize to the wall due to lateral stress to the spool produced by the interaction of the spring and the flow force, however, the mechanism of hydrostatic bearings is working effectively.

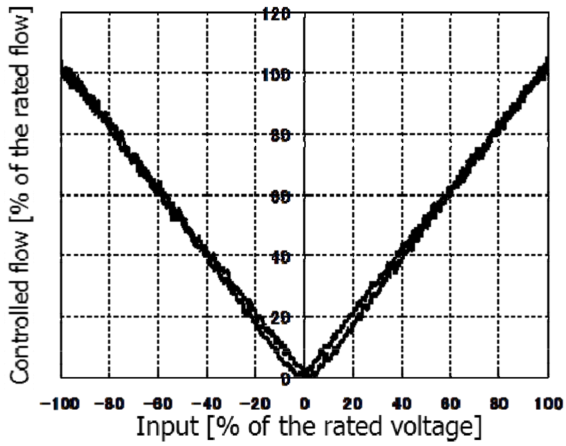

Fig. 10 Flow characteristics without load

Figure 11 shows the relationship of forces working on the spool displacement and the spool valve. A flow force of up to about 20 N is generated. The flow force balances the spool displacement, working together with the solenoid and spring forces, and the force is preferably weak.

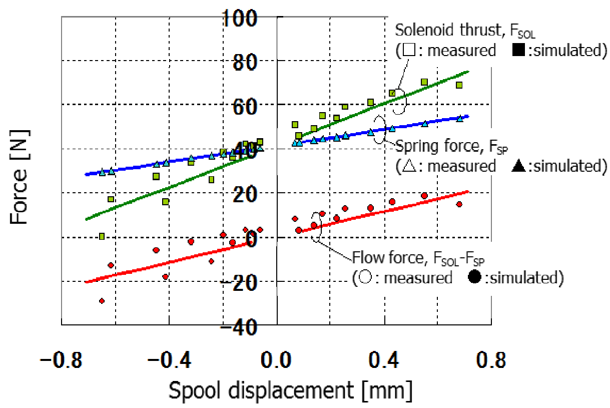

Fig. 11 Flow force that affects the spool displacement

(2) Water hydraulic servo valve [9,10]

Figure 12 shows the sectional model view of a water hydraulic servo valve. Again, the spool ends are supported by the set hydrostatic bearings and suppress the hysteresis phenomenon occurring when the spool is in motion. Since the lateral load is low, the effect of the bearings is utilized to float the spool. A part of the flow utilized for the hydrostatic bearing effect is channeled to the nozzle-flapper area and is then used to control the spool's back pressure.

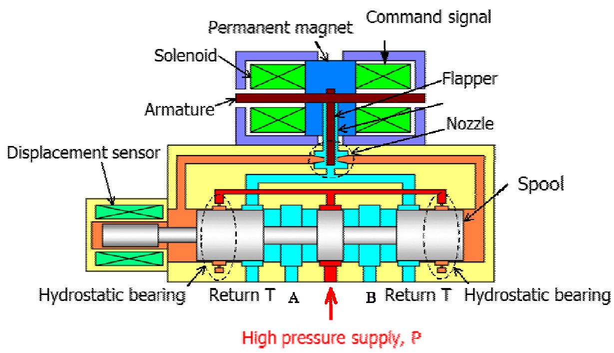

Fig. 12 Sectional model view of the water hydraulic servo valve

Fundamentally, the spool is free of contact from the surrounding wall; its durability is reliable. Some oil hydraulic control valves may be made of corrosion resistant materials for water hydraulic use; however, the valve durability is poor.

Photo 3 Appearance of the water hydraulic servo

Photo 3 shows the appearance of a servo valve. Figure 13 shows the pressure-flow characteristics when a load is given to the A-B port. When the load acts on the port, the controlled flow rate is reduced. Figure 14 shows the frequency characterristic. The result of the input frequency in the range of 25 to 100 % of the rated specifications is plotted.

The author has discussed the "mechanism of the two sliding surfaces" in the frame of ADS component development from the standpoint of "the sliding and effective use of fluid leakage."

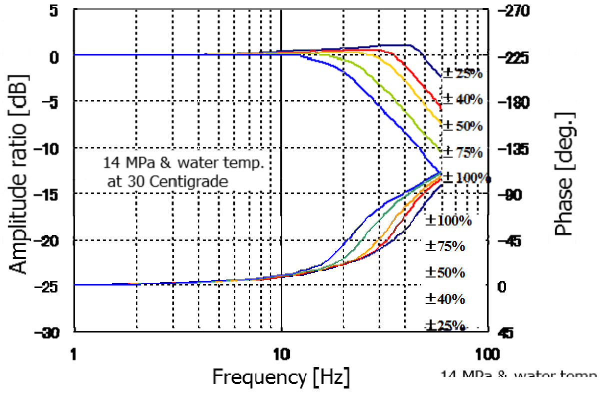

Fig. 13 Frequency characteristics

The loss torque and fluid leakage from sliding in the fluid power components should be minimized. However, in the new framework of the so-called "world of water utilization", the application of ADS for controlling fluid power drives can expand the world which adds further value.

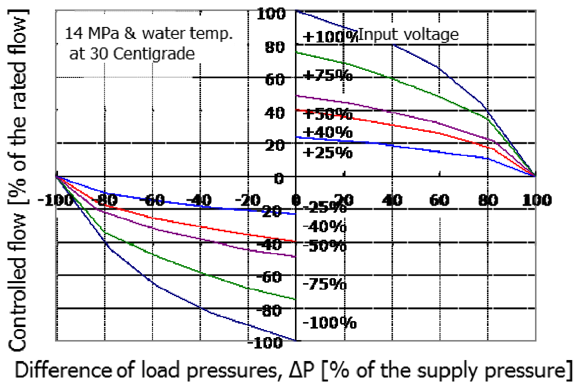

Fig. 14 Flow characteristics with load

4. New applications for ADS [11]

As the market begins to be identified, market-oriented water hydraulic pumps, electromagnetic proportional valves, and water hydraulic servo valves are beginning to be developed. The author intends to introduce some specific application examples employing these components.

1) Applications using the electromagnetic proportional valves

Photo 4 depicts a meat processing machine. It is a slicer intended to process hams and pork butt into thin slices. The slicer is composed of a water hydraulic motor (to drive the cutters) that rotates the cutters which thinly slices meat, a water hydraulic cylinder (to drive a slider) that moves the rotating cutters back and forth, and another water hydraulic cylinder (to drives the meat grip), and a water hydraulic unit that drives an

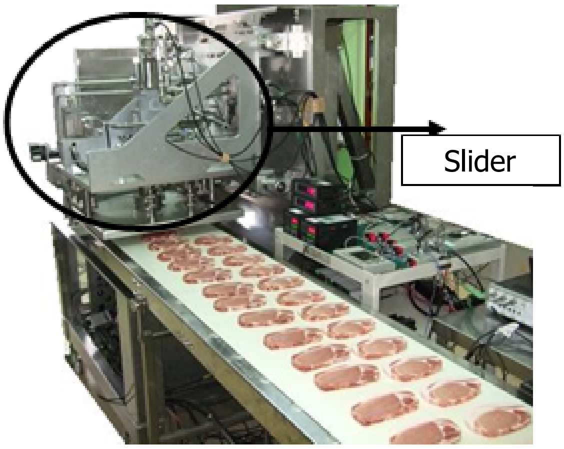

Photo 4 Appearance of the meat slicer (Watanabe Foodmach Co., Ltd).

actuator and is stored underneath of the slicer. The drive pressure is 5 MPa. The slider reciprocally moves and cuts 80 slices per minute. Adopting ADS to all drives makes the machine compact and enables the user to wash the entire meat processing machine without disassembling/assembling the machine, allowing for increased security and improved food safety. Cleaning required removing fat scattered in the machine during meat processing or lubrication will be greatly improved. Meanwhile, the time required for this repair work is shortened and thus reduces maintenance costs. Photo 4 shows the appearance of the slicer and Fig. 15 shows the supply pressure, the pressure on the cylinder rod for the slider, and the pressure on the cylinder head.

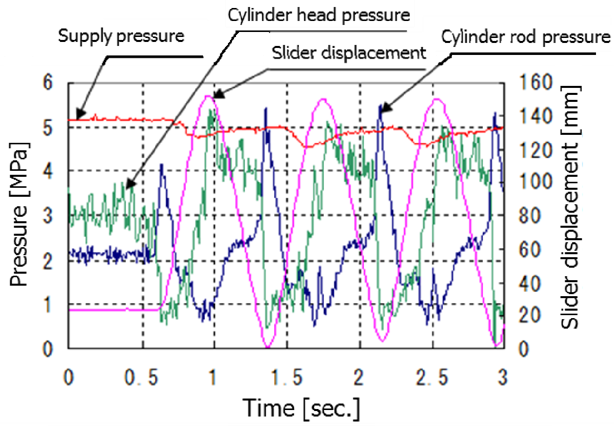

Fig. 15 Change of the slider displacement and the driving pressures

2) Applications using the water hydraulic servo valve

Photo 5 shows the application to general industrial machinery. This machinery generates pressure waves of certain patterns cyclically to meet the demand of the work. This application is suitable for production processes for rubber and resin products where cleanliness, hygiene and safety are demanded. This type of work process has increased in recent years, along with diversification of products.

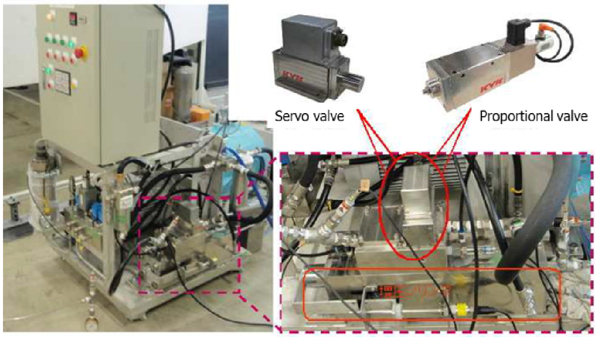

Photo 5 Device for generating predetermined pressure waves

Adopting machinery that uses a medium of fluid power makes this kind of work process easier as the work profile becomes more complex. Adopting oil hydraulics requires extra work for cleaning the produced parts. Pneumatics will provide insufficient power and the machine will tends to be large. This application example uses the ADS control valve (electromagnetic proportional valves and water hydraulic servo valves); therefore, accurate cyclic performance is achieved, and a booster mechanism facilitates generating a pressure to meet the requested and additional pressure. In this application, a water hydraulic power source of 14 MPa generates a cyclic pressure of 20 MPa by the booster. Thanks to the low viscosity of water, if the distance to the work is long due to the production line, the line pressure loss is minimized which contributes to energy-savings. The capability of handling parallel and multiple work processes, including machining, cleaning and simultaneous pressure tests in production lines, is a great advantage of ADS.

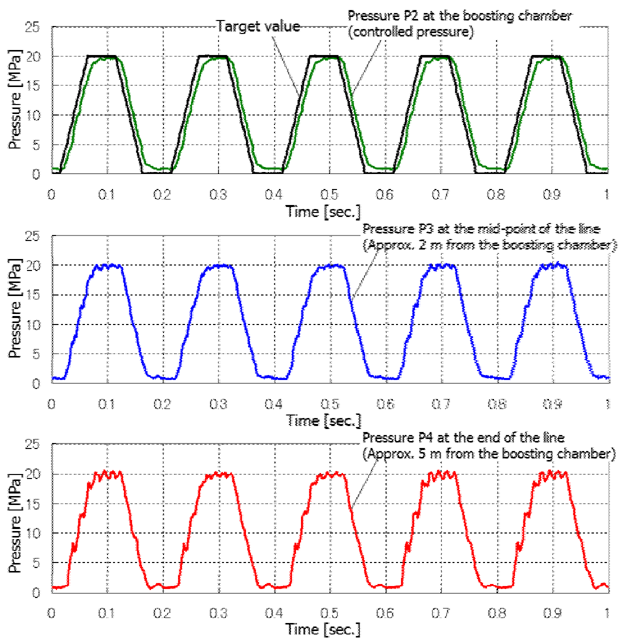

Fig. 16 Pressure waves for distances from the boosting chamber

Conventionally, this type of work process uses various drives, such as an oil hydraulic drive for molding, a pneumatic drive for blowing, electric drives for processes before and after the blow, and a water hydraulic drive for washing, thus making the work very complicated. Figure 16 shows the measured result of generated pressures at the source, and 2 m and 5m distant from the source, respectively. The pressure waves at the source and the redundant waves are clear.

5. Postscript

As means of driving machinery, electric, oil hydraulic and pneumatic drives have long been applied. The electric drive dominates the field of signals transmission and power, and its application range is truly broad. “Oil hydraulics and pneumatics”, in terms of fluid power drive, are mainly in the field of drives and control of machinery and equipment. ADS is one means of fluid power drive and control. Using “mostly pure water” for its working fluid, ADS does not simply remain in the field of “drive and control,” and further applications in other fields can be explored by merging it into technologies in the “world of water utilization, vapor and heat.” As an advanced form of ADS, applications focusing on “cogeneration” seem promising (12). This paper introduces technology of ADS by describing characteristics of the market, technological challenges, and applications from the standpoint of “fluid power drive and control.”

References

1) J. A. Currie: The Development of Raw Water Hydraulic Design, Modeling and Control of Pumps, Edited by C. R. Burrows and N. D. Vaugham, RESEARCH STUDIES PRESS LTD. 1988, 3, UK.

2) S. Miyakawa: New Application of ADS (PLENARY SESSION 2), Twelfth Scandinavian International Conference on Fluid Power, SICFE' 11, Tampere, Finland.
3) S. Miyakawa: Anwendugen von Wasserantriebsystemen, O+P Olhydraulik und Pneumatik 47, 2003, Germany.
4) New Water Hydraulic (Aqua Drive System), IFPEX08, <http://www.ifpex.net>
5) S. Miyakawa: Aqua-Drive-System, O+P Ölhydraulik und Pneumatik 11-12, 2010, Germany.
6) J. Bramah: BRAMAH APPLIED PASCAL'S THEORY, 30 April, 1795, in collection of The Science Museum in London, UK.
7) S. Miyakawa: Aqua-Drive-System market characteristics and recent technology development, KYB technical review, 37 (2008), 16, (in Japanese).
8) F. Yoshida and S. Miyakawa: Characteristics of Proportional Control Valve Using Tap Water, 7th International Fluid Power Conference, Group H, 445-456, 22-24 March, 2010, Aachen, Germany.
9) E. Urata, S. Miyakawa, et al.: Development of the water hydraulic servo valve, Transactions of the Japan Society of Mechanical Engineers, Part-B, 63, 610 (1997-6), 2078, (in Japanese).
10) Advancement of Aqua-Drive-System, 40th anniversary edition, the Japan Fluid Power System Society, April, 2011, (in Japanese).
11) S. Miyakawa, M. Watanabe: Development of a slicer with ADS (Aqua-Drive-System: New water hydraulic system technology), Technical Journal of Machinery, The Japan Food Machinery Manufacturers' Association, Vol. 8, No. , May, 2011 (in Japanese).
12) Report of the feasibility study on new dimensions of robotics by new water hydraulic technology (ADS: Aqua-Drive-System), March, 2010, (in Japanese).

Proceedings of the 8th JFPS International
Symposium on Fluid Power, OKINAWA 2011
Oct. 25-28, 2011

DEVELOPMENT OF A NOVEL PARALLEL PNEUMATIC WEIGHT BEARING WALKING ASSIST ROBOT

Haifan WU*, Congying HU*

* Department of Mechanical Engineering, Dalian University of Technology
2 Linggong Road, Ganjingzi District, Dalian, 116024 China
(E-mail: wuhaifan@dlut.edu.cn)

ABSTRACT

In this paper, for those patients who feels difficulties in walking caused by osteoarthritis of lower limb, a novel parallel pneumatic weight bearing assist robot is proposed. A relative simple prototype of such robot for one ill leg and a biomechanical force platform are developed. Experiments of weight bearing of 50% body weight are done. The experimental results prove that the concept of design is rational and the robot is effective in increasing the stability of the gait balance during walking.

KEY WORDS

Key words: Parallel Structure, Pneumatic, Partial Weight Bearing, Walking Assist, Robot

1. INTRODUCTION

Since our country is rapidly aging, there is an urgent need for the development of new walking assist devices for helping the elders. Osteoarthritis of lower limb is a common disease for the elders. It causes pain in leg joints (hip or knee) and often makes elders unable to walk outside for long. Although the elders can use wheelchair to go outside, it will make their legs totally rest for a long time and can led to disuse syndrome. Research has shown that water walking exercise can give leg valuable exercise while protect the joint from further overuse injury because the buoyancy partially support the body weight, but this method is too expensive and inconvenience since a swimming pool is always requested. In order to develop a land-based comfort walking assist device with rehabilitation function, partial weight bearing walking assist robot is believed an effective way.

In recent years, many new researches on powered walking assist robot have been done [1~4]. Among them, there are two kinds of robot that have partial weight bearing walking assist function even outdoor. One is a Walking Assist Device with Bodyweiht Support System which is developed by HONDA [5]. The HONDA's device is reported to be driven by electrical motors, and have the shortcoming of exerting too small assist force to support bodyweight very well. The other is a Pneumatic Power Assist Lower Limb which is developed by WU at Tokyo Institute of Technology [6]. Although the WU's device is light in weight and can exert assist force enough for supporting about 40% of the bodyweight, it can not improve gait balance during walking thus is not safe to the elders.

In order to overcome the shortcoming in walking assist robot mentioned above, a novel Parallel Pneumatic Weight Bearing Walking Assist Robot, called PWAR, is proposed. In this paper, the concept, structure, function and experiments involving the developed robot are described in detail.

2. BASIC CONCEPT

The concept of PWAR is illustrated in Fig.1. It comprises of a saddle supplied with a hip fastening device (a frame and two suspender band connected to the waist belt), 6 telescope rod sets (each comprises of an air cylinder, an outer slide rail, a lock mechanism, and an inner slide rail), and 2 foot plates(with force sensors inside) which band togther with 2 shoes.

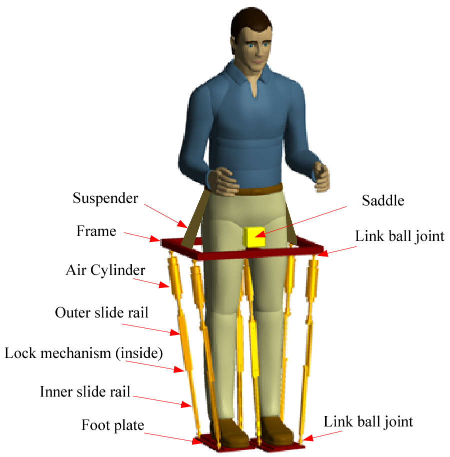

Figure 1 concept of the PWAR

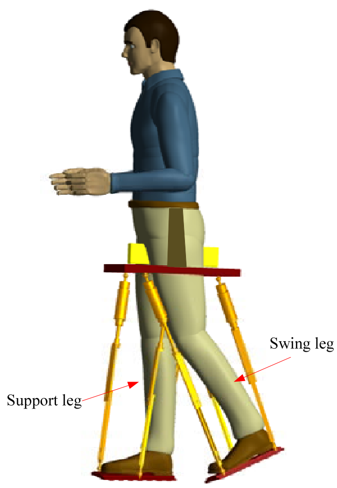

Figure 2 PWAR at walking assist

When PWAR provides walking assist (as illustrated in Fig.2), 3 telescope rod sets at the support leg side provide support force due to the extension of 3 cylinders rod and 3 lock mechanisms are in lock state. On the other hand, 3 telescope rod sets at the swing leg side lose their 3 lock mechanisms thus make no restriction on the swing leg movement.

The concept of PWAR's control algorithm is illustrated in Fig.3. When the foot touches the foot plate thus step on the ground, four force sensors inside the foot plate measure the leg force and the position data of the center of the pressure (COP) of the foot. Then the mearsured data is sent to a controller. The controller calculates the control signal and sends it to electro pneumatic transducing regulator thus controls the pressure send to the cylinder. By this way, the assist force from the prototype is controlled. However, in this paper, since a portable embedded controller has not been finished yet, a computer is used as the controller instead.

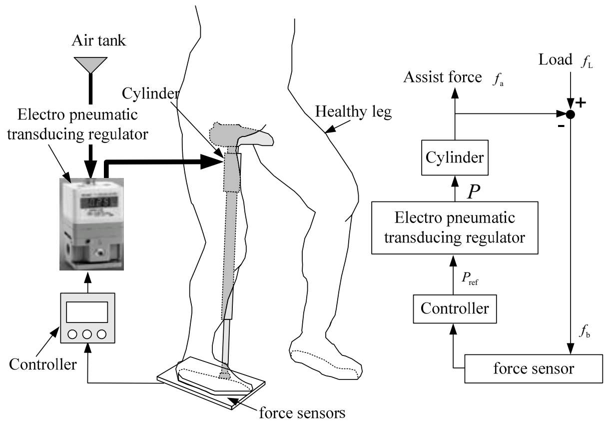

Figure 3 Concept of control algorithm(only single cylinder)

3. PROTOTYPE FOR TEST

Before PWAR is built, a relative simple prototype is developed and tested. The prototype design is illustrated in Fig.4. The purpose of the prototype is to verify the concept of PWAR, and search optimum control algorithm to maintain gait balance.

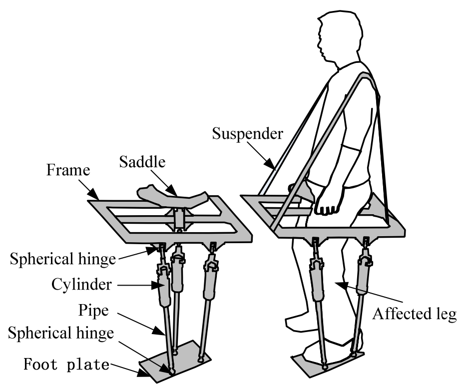

Figure 4 Simple prototype design for test

The prototype comprises a saddle supplied with a hip fastening device (two suspenders over the shoulders in this study), three air cylinder, three telescopic pipe, and a foot plate with four force sencors beneath it.

The relationship between leg force and assist force from the prototype can be expressed by positive force feedback relationship which is illustrated in Fig.5.

When the affected leg is in stance phase, the affected leg load f_b is measured by the force sensors beneath the foot plate. When the measured data is larger than load threshold c (c=20kgf in this study), air cylinder starts to extend to provide assist force. When the reference assist force f_{aref} to load increment ($f_b - c$) ratio is define as assist ratio, the following equation can be given.

$$f_{aref} = \begin{cases} K(f_b - c) & (f_b > c) \\ 0 & (f_b \le c) \end{cases} \qquad (1)$$

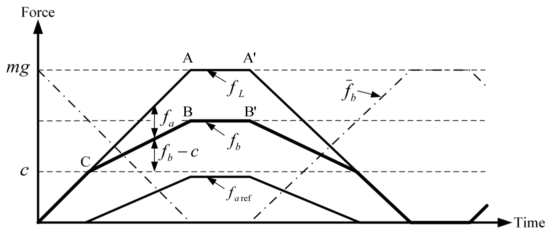

Figure 5 Concept of prototype’s control algorithm

In order to improve the gait balance during walking, a negative position feedback is also used. The layout of foot plate and four sensors is illustrated in Fig.6.

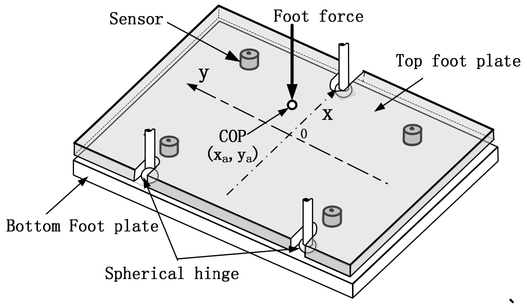

Figure 6 Layout of foot plate and four sensors

From the data of force sensors, the foot force and it’s position coordinate (x_a, y_a) can be calculated. Then the negative position feedback control algorithm can be obtained by changing equation (1) into equation (2).

$$f_{aref} = \begin{cases} K(f_b - c) - K_x x_a - K_y y_a & (f_b > c) \\ 0 & (f_b \le c) \end{cases} \qquad (2)$$

Where K_x and K_y are gains of negative position feedback control in x direction and in y direction.

Thus the reference pressure of air cylinder can be calculated by equation (3).

$$p_{ref} = \frac{f_{aref}}{A} \qquad (3)$$

Moreover, total affected leg side load f_L can be calculated by equation (4).

$$f_L = f_b + f_a \qquad (4)$$

In addition, assuming that walking speed is slow, and the influence from inertia force of bodyweight can be neglected, the relationship between healthy leg side load $\bar{f}_b$ and f_L can be given in equation (5).

$$f_L = mg - \bar{f}_b \qquad (5)$$

Such load threshold setting is because when the maximum affected leg load is reduced to a tolerable level, joint pain will be released. As shown in Fig.5 , affected leg load is reduced from A-A’ to B-B’ level. Only by adjusting two parameters of c and k , even to random human motion, a continuance walking assist control can be achieved. That is another merit for such settings.

4. DESCRIPTION OF THE STRUCTURE

Photo and construction of the developed prototype is illustrated in Fig.7. It comprises a saddle, three air cylinders, three support pipes, six spherical hinge and furniture, a foot plate with four force sensors beneath it.

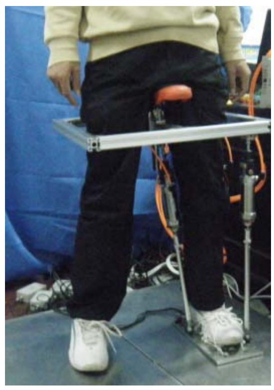

Figure 7 Photo of developed prototype

The photo of foot plate is illustrated in Fig.8. The force sensor is TJH-10 from Bengbu Tianguang Sensor co. LTD.

Figure 8 Photo of developed foot plate

Three electro pneumatic transducing regulator (SMC ITV2051-212s) is chosen for controlling the air cylinder for its small in size and electricity saving.

5. EXPERIMENT

The experimental setup for confirming the function of the developed prototype is illustrated in Fig.9. In order to examining the relationship between the foot load and the assist force, a biomechanical force plate is build. An 70kg weight person wears the prototype and marks time on the biomechanical force plate.

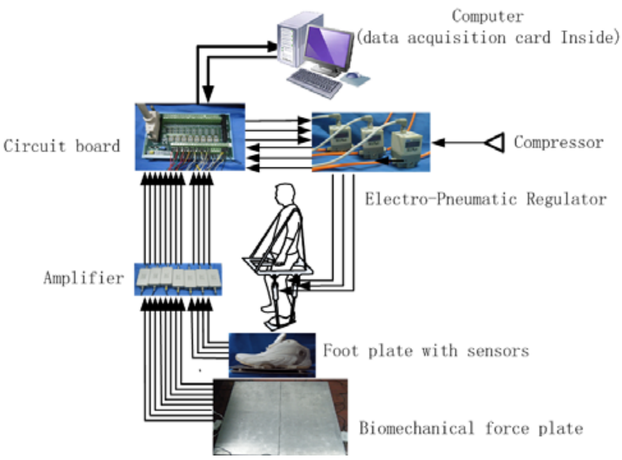

Figure 9 Experimental setup

In the experiments, a data acquisition card is used and Matlab with Realtime Windows Target toolbox is also used for real-time data acquisition and real-time control. The experiment of weight bearing of 50% bodyweight is done by a person. The control program is shown in Fig.10.

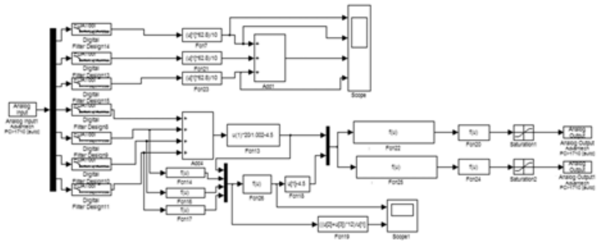

Fig 10 Control program using simulink in matlab

The experimental results are illustrated in Fig.11. The experimental results confirm the effectiveness of the prototype. With the help of the prototype, measured data from the foot plate is reduced from 70kgf to 35kgf, which shows 50% of the bodyweight smaller.

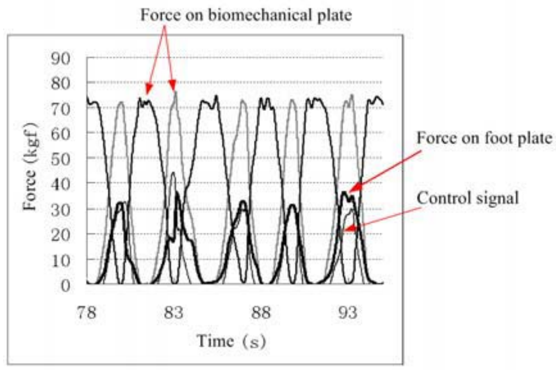

Fig 11 Experimental results of 50% bodyweight bearing

In addition to the above experiments, the experiment to improve the gait balance is also done. The experimental result proved the effectiveness of the negative position feedback control on prototype will increase the stability of the gait balance during walking.

6. CONCLUSIONS

In this study, a novel Parallel Pneumatic Weight Bearing Walking Assist Robot, called PWAR, is proposed. A prototype of the robot is built to confirm the function of the robot. The control algorithm of positive force feedback control together with negative position feedback control is also proposed. Experiment of 50% bodyweight weight bearing is done, and the experimental data is analyzed. The prototype robot is confirmed effective for those people whose muscle and balance remain in good condition but who have joint pain (hip or knee joint) in their leg and are unable to walk outdoors for long. The prototype is also confirmed effective in increasing the stability of the gait balance during walking.

Acknowledgements

This project is supported by the National Natural Science Foundation of China under the grant number 60875063 and Sponsored by the Scientific Research Foundation for the Returned Overseas Chinese Scholars, State Education Ministry.

References

1. Fabio Gazzani, Antonello Fadda, Marina Torre, and Velio Macellari, WARD: A pneumatic system for body weight relief in gait rehabilitation, IEEE Transactions on Rehabilitation Engineering, 2000, 8-4, 506-513.
2. Jerry E. Pratt, Benjamin T. Krupp, Christopher J. Morse, The roboknee: an exoskeleton for enhancing strength and endurance during walking, Proceedings of the 2004 IEEE International Conference on Robotics & Automation, 2004, 2430-2435.
3. H. Yamamoto, K., Ishii, M., Hyodo, K.,Yoshimitsu, T. and Matsuo, T., Development of power assisting suit for assisting nurse labor -miniaturization of supply system to realize wearable suit-, JSME International Journal, Series C, 2003, 46-3, 923-930.
4. Zoss, A., Kazerooni, H., Chu, A.,On the mechanical design of the Berkeley Lower Extremity Exoskeleton (BLEEX), IEEE/RSJ International Conference on Intelligent Robots and Systems, 2005,3132-3139.
5. http://corporate.honda.com/innovation/walk-assist/
6. Haifan WU, Ato KITAGAWA, Hideyuki TSUKAGOSHI, Canghai LIU, Development of a novel pneumatic power assisted lower limb for outdoor walking by the use of a portable pneumatic power source, 16th IEEE International

Proceedings of the 8th JFPS International
Symposium on Fluid Power, OKINAWA 2011
Oct. 25-28, 2011

1A1-2

PNEUMATICALLY ACTUATED EXOSKELETON FOR GAIT REHABILITATION

Natasa Koceska*, Saso Koceski*, Pierluigi Beomonte Zobel** and Francesco Durante**

*University "Goce Delce" – Stip, Faculty of Computer Science, Macedonia
**University of L'Aquila, Applied Mechanics Laboratory DIMEG, Italy

ABSTRACT

This paper describe the mechanical and control system design of a 10 DOF (Degrees Of Freedom) lower limbs exoskeleton for gait rehabilitation of patients with gait dysfunction. The system has 4 double-acting rod pneumatic actuators (two for each leg), that controls the hip and knee joints. Motion of each cylinder's piston is controlled by two pressure proportional valves, connected to both cylinder chambers. The pneumatic actuators are controlled by proportional-pressure valves. The control strategy has been specifically designed in order to ensure a proper position control guiding patient's legs along a fixed reference gait pattern. For this purposes Fuzzy controller with additional force compensator was developed. A numerical solution of the inverse kinematics problem based on video image analysis has been used. The controller was successively implemented and tested on embedded real-time PC104 system. Laboratory experiments without patient are carried out and the results are reported and discussed.

KEY WORDS

Exoskeleton, fuzzy logic, rehabilitation robotic, treadmill training

INTRODUCTION

Intensive training and exercise may enhance motor recovery or even restore motor function in people suffering from neurological injuries, such as spinal cord injury (SCI) and stroke. Repetitive practice strengthens neural connections involved in a motor task through reinforcement learning, and therefore enables the patients a faster and better re-learning of the locomotion (walking). Practice is most effective when it is task-specific [1],[2].
Thus, rehabilitation after neurological injury should emphasize repetitive, task-specific practice that promotes active neuromuscular recruitment in order to maximize motor recovery. Body-weight–supported treadmill training (BWSTT) is an emerging rehabilitation technique for gait rehabilitation of patients with locomotor dysfunctions in the lower extremities. Clinical studies have confirmed that individuals who receive bodyweight supported treadmill training following stroke [3], [4] and spinal cord injury [5]-[7] demonstrate improved electromyographic (EMG) activity during locomotion [8], walk more symmetrically [9], are able to bear more weight on their legs. BWSTT involves practice of stepping on a motorized treadmill while unloading a percentage of a person's body weight using a special suspension system. Manual assistance, from 2 or 3 physiotherapists, is provided as necessary to promote upright posture and lower-extremity trajectories associated with normal human gait. For therapists this training is labor-intensive; therefore, training sessions tend to be short because of the physical demands on the therapists, which

may limit the full potential of the treatment. Also, manually assisted treadmill training lacks repeatability and objective measures of patient performance and progress.

A promising solution for assisting patients during rehabilitation process is to design exoskeleton devices. It has already been shown that robot-assistive devices can be very helpful in training individuals to regain their walking ability following incomplete spinal cord injury [10].

In the general setting of these robotic systems, a therapist is still responsible for the nonphysical interaction and observation of the patient by maintaining a supervisory role of the training, while the robot carries out the actual physical interaction with the patient.

Several groups are working on development of exoskeletal devices for “gait training”. Lokomat is a motorized exoskeleton that can drive hip and knee flexion through the four rotary joints driven by dc motors via precision ball screws [11]. Mechanized Gait Trainer (MGT) is a one degree-of-freedom powered machine that moves a patient’s legs in a gait-like pattern by driving two foot plates connected to a double crank and rocker system that is actuated by a motor via a planetary gear system [12]. AutoAmbulator is a rehabilitation machine for the leg to assist individuals with stroke and spinal cord injuries. PAM is a device that can assist the pelvic motion during stepping using BWST, and it’s used in combination with POGO- the pneumatically operated gait orthosis [13]. Most of these devices are using electric motors as actuators.

The rehabilitation robot system presented in this work is developed in the Laboratory of Applied Mechanics at DIMEG of University of L’Aquila and is pneumatically actuated. The pneumatic actuators have been adopted in this work as an alternative solution to the widely used electric motors, due to their large power output at a relatively low cost. They are also clean, easy to work with, and lightweight. Moreover, the choice of adopting the pneumatic actuators to actuate the joints is biologically inspired. They provide linear movements, and are actuated in both directions, so the articulation structures do not require the typical antagonistic scheme proper of the biological joints.

However, pneumatic systems exhibit highly non-linear behaviors which are associated with the compressibility of air, the complexity of friction presence and the nonlinearity of valves [14]-[15]. Because of all these characteristics, it is very difficult to successfully apply the classical control theory on pneumatic systems. It is relatively easier to use a fuzzy logic control, even though there are difficulties in designing a fuzzy controller and determining its parameters by trial and test.

Applying fuzzy control to a continuous pneumatic positioning system is particularly advantageous in terms of simplicity of design and implementation, and thus significantly reduces the time required to develop the entire system [16]. Also fuzzy control has been demonstrated to provide highly satisfactory results in terms of accuracy, repeatability and insensitivity to changes in operating conditions [16].

This paper describes mechanical and control system design of the lower limbs exoskeleton for gait rehabilitation. Design choices for realization of the prototype are presented, the control architecture is described and experimental results, obtained without patient, are reported.

The evaluation of the system design and the proposed control architecture is foreseen in three experimental phases: experiments without patient, experiments with voluntary healthy patients and finally tests on disable persons.

EXOSKELETON STRUCTURE

Designing an exoskeleton device for functional training of lower limbs is a very challenging task. From an engineering perspective, the designs must be flexible to allow both upper and lower body motions, once a subject is in the exoskeleton, since walking involves synergy between upper and lower body motions. It must be also a light weight, easy wearable and must guarantee comfort and safety. From a neuro-motor perspective, an exoskeleton must be adjustable to anatomical parameters of a subject.

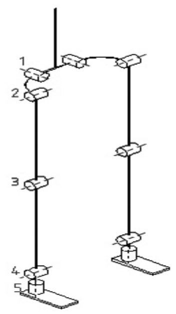

Fig.1. DOFs of the exoskeleton

Considering these characteristics an exoskeleton structure with 10 rotational DOF was studied and realized. An optimal set of DOF was chosen after studying the literature on gait, and in order to allow for subject to walk normally and safely in the device.

The degrees of freedom, all rotational, are: the number 1 with axis perpendicular to the front, the numbers 2, 3 and 4 with axes perpendicular to the sagittal plane, the number 5 with axis perpendicular to the ground; of these only DOF 2 and 3 are motorized (Fig.1).The robot moves in parallel to the skeleton of the patient, so that no additional DOF or motion ranges are needed to follow the patient motion. The mechanical structure of the shapes and the dimensions of the parts composing the exoskeleton are human inspired and have an ergonomic design.

The inferior limbs of the exoskeleton are made up of three links corresponding to the thighbone, the shinbone and the foot. The thighbone link is 463 mm long and has a mass of 0.5 kg and the shinbone link is 449 mm long and has a mass of 0.44 kg.

The prototype structure is adjustable to the patients which are tall from 175 cm up to 190 cm without any functional problems (Fig. 2a, 2b). For better wearability of the exoskeleton an adjustable connection between the corset of polyethylene (worn by the patient) and the horizontal rod placed at the pelvis level is provided. Moving the exoskeleton structure up for only 25 mm, the distance between the centre of the knee joint and the vertical axes of the hip articulation, is reduced to 148 mm (Fig.2c), while the corset remains in the same position.

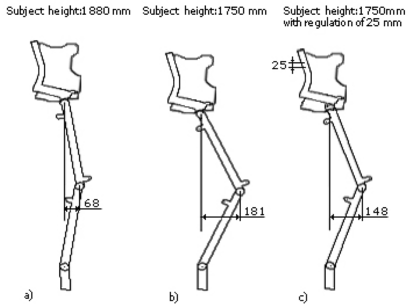

Fig.2. Adjustability of the realized prototype

In order to realize a prototype with anthropomorphic structure that will follow the natural shape of the human's lower limbs, the orientation and position of the human leg segments were analyzed. In the case of maximum inclination, the angle formed by the vertical axis and a leg rod is 2.6°, observed in frontal plane (Fig.3). The inclination of 1.1° was choosen for the stand position, while other 1.5° are given by a lateral displacement of 30 mm, when the banking movement occurs.

In this way the ankle joint is a little bit moved towards the interior side with respect to the hip joint, following the natural profile of the inferior limbs in which the femur is slightly oblique and form an angle of 9° with the vertical while for the total leg this angle is reduced to 3°. The other actuator which moves the knee joint is connected bellow the shinbone and has a rod stroke of 160 mm.

Both actuators are with bore diameter of 32 mm, capable to provide force of about 700 N under a supply pressure of 0.9 MPa coming by the external compressor (Fig.4).The motion of each cylinder's piston (i.e. supply and discharge of both cylinder chambers) is controlled by two pressure proportional valves (SMC-ITV 1051-312CS3-Q), connected to both cylinder chambers.

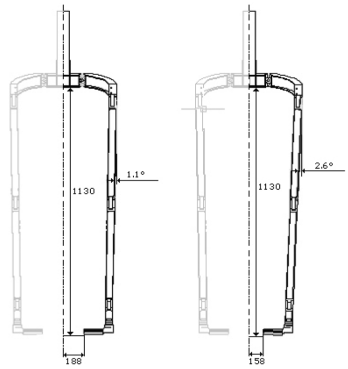

Fig.3. Positioning of the exoskeleton shinbone and thighbone link, realized following the human leg position

Fig.4. Mechanical structure of the exoskeleton with pneumatic actuators

The selection of the valve was due to the primary calculations for air flow through the valve. Each valve controls only one chamber of the actuator, therefore the calculations of the air flow is made only in one phase of the actuators cycle. Simulations done in Working Model 2D software showed that the outgoing speed of a piston (v) is 50 mm/s, which occurs during the pre-swing phase of the walking cycle when a force of about 700 N is required. As said before this force will be provided by a cylinder chamber's pressure of 0.9 MPa (relative).

The selected valve model satisfies these requirements.

The exoskeleton structure also has to guarantee the safety of the patient. As the joins motions of the robot directly correspond with that of a patient, it was relatively easy to implement the mechanical safety limits (physical stops), which are placed on extreme ends of the allowed range of motion of each DOF. For hip and knee joints in the sagittal plane, the stops can withstand the maximum torque that the actuators can apply. The structure of the exoskeleton is realized in aluminum which ensures a light weight and a good resistance.

In order to calculate the mechanical resistance, all exoskeleton components are imported in Visual Nastran, where Finite Element Analysis (FEA) was done.

The stresses measured (Von Mises stresses) are well below the yield strength of aluminum 6082 T6 (σ_y = 200 MPa) chosen as the material for realization of the exoskeleton.

Hip and knee angles, of our rehabilitation system, are acquired with the rotational potentiometers.

The overall exoskeleton structure is positioned on a treadmill and supported, at the pelvis level, with a space guide mechanism that allows vertical and horizontal movements. Space guide mechanism is connected with the chassis equipped with a weight balance system (Fig.5).

Fig. 5. Realized prototype of the overall rehabilitation system

KINEMATIC AND STATIC ANALYSIS

In the present section, the joints excursions have been analyzed for each articulation, making particular attention to the related actuators extensions and the forces they have to provide in order to move the articulations.

A. Knee articulation

In order to characterize the joint kinetic behavior, it is useful to analyze the actuator force necessary to counteract the gravitational load acting on the shinbone center of mass, varying the knee joint angular position. The knee articulation realized has only one DOF and thus it is actuated by only one pneumatic actuator as it can be seen on Fig.4. The knee articulation scheme is shown on the Fig.6a.

The p segment represents the pneumatic actuator, whereas the knee angle position is indicated by the θ angle.

The direct kinematic problem is easy to solve. In a few words, the process calculates the actuator length once known the rotation angle θ.

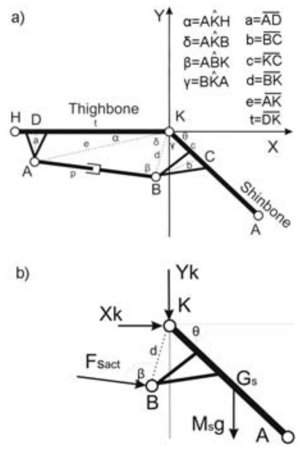

Fig. 6. a) Knee articulation scheme and b) free body diagram of the shinbone

The equations (1) show this process, considering the geometrical structure and the connections between different components.

$$\begin{cases} \gamma = cos^{-1}\left(\dfrac{d^2 + c^2 - b^2}{2dc}\right) \\ \alpha = cos^{-1}\left(\dfrac{t^2 + e^2 - a^2}{2te}\right) \\ \delta = \pi - \theta - \gamma - \alpha \\ p = \sqrt{e^2 + d^2 - 2ed\,cos\,\delta} \end{cases} \tag{1}$$

After the calculation of the actuators length p, the angle β can be easily deduced as in (3):

$$\beta = \sin^{-1}\left(\frac{e\sin\delta}{p}\right) \tag{2}$$

F_{Sact} represents the force supplied by the shinbone pneumatic actuator, whereas the arrow indicated by $M_S g$ shows the opponent force caused by the gravity. M_S is the approximate sum of the mass of the shinbone and the foot applied in the center of mass of the shinbone. Moreover, the segment d represents the arm of the cylinder force.

From a simple torque balance with respect to the point K, Fig. 6b, the relation between F_{Sact} and the knee angular position θ is derived as in (3).

$$F_{Sact} = \frac{M_S g L_{KGs} \cos(\theta)}{d\sin(\beta)} \tag{3}$$

From (1), (2) and (3) it can be seen that the force supplied by the shinbone pneumatic actuator can be expressed as a function of the θ angle, obtained by the knee rotational potentiometer.

B. Hip articulation

As the knee articulation also the hip articulation of our prototype has only one DOF and thus is actuated by only one pneumatic actuator as it can be seen on Fig.4. The hip articulation scheme is shown on the Fig.7a.

Analyzing the hip articulation torque, one can observe that the rod of the thighbone pneumatic actuator is connected to the segment c placed upon the thighbone. In particular, the segment b in this case, represents the arm on which the hip joint force acts.

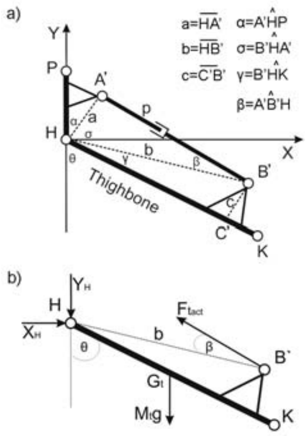

Fig. 7. a) Hip articulation scheme and b) free body diagram of the thighbone

The kinematic problem for this actuator, i.e. the process that calculates the actuator length knowing the rotation angle θ, is described with (4).

For a certain actuator length p, the angle β can be easily deduced as in (5). F_{Tact} indicates the force supplied by the thighbone pneumatic actuator, whereas the arrow indicated by M_Tg shows the opponent force caused by the gravity. M_T is the approximate sum of the weights of the thighbone, shinbone and the foot applied in the center of mass of the thighbone.

$$\begin{cases} \gamma = cos^{-1}\left(\dfrac{b^2 + L_{HC'}{}^2 - c^2}{2bL_{HC'}}\right) \\ \sigma = \pi - \gamma - \alpha - \theta \\ p = \sqrt{a^2 + b^2 - 2ab\,cos\,\sigma} \end{cases} \tag{4}$$

$$\beta = \sin^{-1}\left(\frac{a\sin\sigma}{p}\right) \tag{5}$$

From a simple torque balance Fig. 7b, the F_{Tact} value depending of the hip angular position is derived. Equation (6) shows the relation found for the hip articulation.

$$F_{Tact} = \frac{M_T g L_{HG_T} \sin\theta}{b\sin\beta} \tag{6}$$

From (4), (5) and (6) it can be seen that the force supplied by the thighbone pneumatic actuator also can be expressed as a function of the θ angle obtained by the hip rotational potentiometer.

So, analytic relations between the forces provided by the pneumatic actuators and the torques needed to move the hip and knee articulations have been found. In particular, in our case it is useful to analyze the forces necessary to counteract the gravitational load acting on the thighbone and shinbone center of mass, varying the joints angular position, because it offers the possibility of inserting a further compensation step in the control architecture in order to compensate the influence of the torques during the movement.

INVERSE KINEMATIC PROBLEM

To analyze the human walking, a camera based motion captured system was used. Motion capturing of a healthy subject walking on the treadmill, was done with one video camera placed with optical axis perpendicular in respect of the sagittal plane of the gait motion. The subject had markers mounted on hip, knee and ankle. An object with known dimensions (grid) was placed inside the filming zone, and it was used like reference to transform the measurement from pixel to the distance measurement unit. The video was taken with the resolution of 25 frame/s.

The recorded video was post-processed and kinematics parameters of limbs' characteristic points (hip, knee and ankle) were extracted.

After that, the obtained trajectory was used to resolve the problem of inverse kinematics of the lower limb rehabilitation system. The inverse kinematic problem was resolved in numerical way, with the help of Working Model 2D software. By the means of this software the target trajectory, which should be performed by each of the actuators, was determined.

FUZZY CONTROLLER

Fuzzy logic is basically a rule-based operation, in "if <condition> then <operation>". Compared with the traditional rule-based method, the condition and operation are fuzzy descriptions in a fuzzy controller. Thus the measured information is interpreted to fuzzy descriptions through the membership function. The output control signal is calculated from the operation by a defuzzification processing. Fuzzy control emulates human control strategy, and its principle is easy to understand.

The state variables of the pneumatic fuzzy control system are: the actuator length error E, which is the input signal and two output control signals U_{rear} and U_{front} which are control voltages of the valves connected to the rear chamber and front chamber respectively.

Actuator length error in the system is given by:

$$E(kT) = R(kT) - L(kT) \tag{7}$$

where, R(kT) is the target displacement, L(kT) is the actual measured displacement, and T is the sampling time.

Based on this error the output voltage, that controls the pressure in both chambers of the cylinders, is adjusted.

Seven linguistic values non-uniformly distributed along their universe of discourse have been defined for input/output variables (negative large-NL, negative medium-NM, negative small-NS, zero-Z, positive small-PS, positive medium-PM, and positive large-PL). For this study trapezoidal and triangular-shaped fuzzy sets are chosen for input variable and singleton fuzzy sets for output variables.

The membership functions were optimized starting from a first, perfectly symmetrical set. Optimization was performed experimentally by trial and test with different membership function sets. The membership functions that give optimum results are illustrated in Figs. 8, 9 and 10.

The rules of the fuzzy algorithm are shown in Table I in a matrix format. The max-min algorithm is applied and center of gravity (CoG) method is used for deffuzzify and to obtain an accurate control signal.

Since the working area of cylinders is overlapping, the same fuzzy controller is used for both of them.

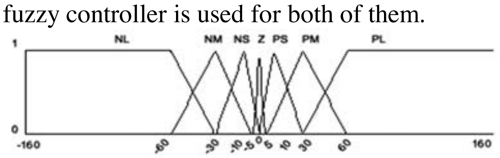

Fig. 8. Membership functions of input variable E

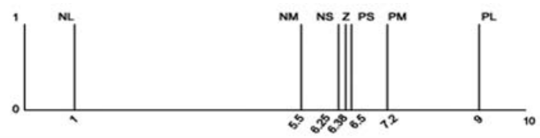

Fig. 9. Membership functions of output variable Ufront

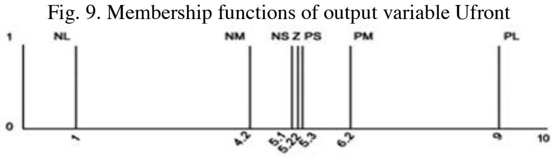

Fig. 10. Membership functions of output variable Urear

Rule n °	E	ANT	POS
1	PL	PL	NL
2	PM	PM	NM
3	PS	PS	NS
4	Z	Z	Z
5	NS	NS	PS
6	NM	NM	PM
7	NL	NL	PL

Table 1 Rule matrix of fuzzy controller

CONTROL ARCHITECTURE

The overall control architecture is presented on the Fig.11. In particular, it is based on fuzzy logic controllers which aim to regulate the lengths of thighbone and shinbone pneumatic actuators, described in *Fuzzy controller* Section.

The force compensators are calculating the forces necessary to counteract the gravitational load acting on the thighbone and shinbone center of mass, varying the joints angular position.

Target pneumatic actuators lengths obtained by off-line procedure described in the *Inverse kinematic problem* Section were placed in the input data module. In this way there is no necessity of real-time calculation of the inverse kinematics and the complexity of the overall control algorithm is very low.

The feedback information is represented by the hip and knee joint working angles and the cylinder lengths, calculated according to (2) and (5).

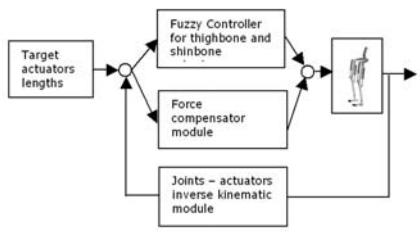

Fig. 11. Control architecture diagram

The global control algorithm runs inside an embedded PC104, which represents the system supervisor. The PC104 is based on Athena board from Diamond Systems, with real time Windows CE.Net operating system, which uses the RAM based file system. The Athena board combines the low-power Pentium-III class VIA Eden processor (running at 400 MHz) with on-board 128 MB RAM memory, 4 USB ports, 4 serial ports, and a 16-bit low-noise data acquisition circuit, into a new compact form factor measuring only 4.2" x 4.5". The data acquisition circuit provides high-accuracy; stable 16-bit A/D performance with 100 KHz sample rate, wide input voltage capability up to +/- 10V, and programmable input ranges. It includes 4 12-bit D/A channels, 24 programmable digital I/O lines, and two programmable counter/timers. A/D operation is enhanced by on-board FIFO with interrupt-based transfers, internal/external A/D triggering, and on-board A/D sample rate clock.

The PC 104 is directly connected to each rotational potentiometer and valves placed onboard the robot.

In order to decrease the computational load and to increase the real-time performances of the control algorithm the whole fuzzy controller was substituted with a hash table with interpolated values and loaded in the operating memory of the PC104.

EXPERIMENTAL RESULTS

To evaluate the performance of the exoskeleton structure together with the proposed control architecture experimental tests without patients were performed.

The experiments were conducted with a sampling frequency of 10 Hz, and a pressure of 0.6 MPa.

The movement was natural and smooth while the limb moves along the target trajectory.

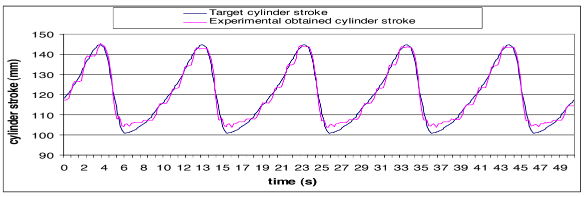

Fig. 12. Target and experimentally obtained thighbone actuator stroke during the gait cycle

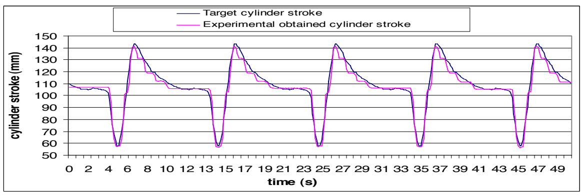

Fig. 13. Target and experimentally obtained shinbone actuator stroke during the gait cycle

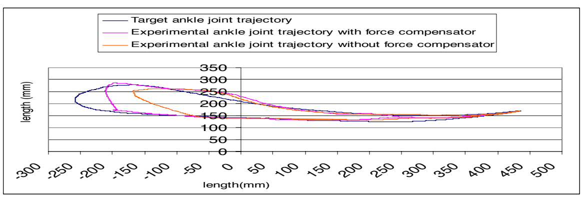

Fig. 14. Ankle joint trajectory (target, experimental without force compensator and experimental with force compensator)

Fig.12 and Fig.13 show the target and experimentally obtained stroke for thighbone and shinbone actuators, respectively.

As it can be observed from the graphs, the cylinders tracked the target trajectory well with the max. error of 5mm for the thighbone actuator, and 6mm for the shinbone actuator, which is accurate enough for the desired purpose. Results for the target and experimental ankle joint trajectory, for one cycle, with and without implementation of the force compensator, are shown in Fig.14.

From the graph we can observe that there is significant improvement of the gait trajectory when a force compensator is used.

During the gait training one of the most important goals to achieve is path repeatability. In order to test the path repeatability, ISO 9283 standard was used. According to this standard path repeatability expresses the closeness of the agreement between the attained paths for the same command path followed n times in the same direction. Path repeatability is expressed by RTp-the maximum RTpi which is equal to the radius of a circle in the normal plane and with its centre on the barycentre line (Fig. 15).

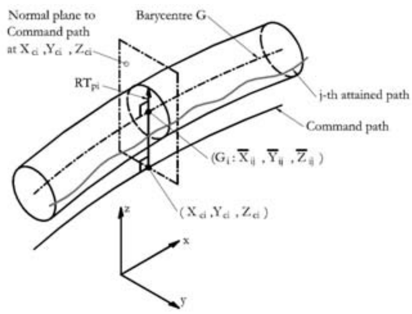

Fig. 15. Target and experimentally obtained thighbone actuator length during the gait cycle (RT represent repeatability; G represents the barycentre of a cluster of attained poses; X_{ci}, Y_{ci} and Z_{ci} are the coordinates of the *i*-th point of the command path; X_{ij}, Y_{ij} and Z_{ij} are the coordinates of the intersection *j*-th attained path and the *i*-th normal plane)

The path repeatability is calculated as follow:

$$RT_p = \max RT_{pi} = \max[\bar{l}_i + 3S_{li}] \quad ; \quad i = 1...m \tag{8}$$

where:

$$\bar{l}_i = \frac{1}{n}\sum_{j=1}^{n} l_{ij} \tag{9}$$

$$S_{li} = \sqrt{\frac{\sum_{j=1}^{n}(l_{ij} - \bar{l}_i)^2}{n-1}} \tag{10}$$

$$l_{ij} = \sqrt{(x_{ij} - \bar{x}_i)^2 + (y_{ij} - \bar{y}_i)^2 + (z_{ij} - \bar{z}_i)^2} \qquad (11)$$

$$\bar{x}_i = \frac{1}{n}\sum_{j=1}^{n} x_{ij}\ ;\ \bar{y}_i = \frac{1}{n}\sum_{j=1}^{n} y_{ij}\ ;\ \bar{z}_i = \frac{1}{n}\sum_{j=1}^{n} z_{ij} \qquad (12)$$

m is number of calculated points along the path, and n is number of measurement cycles.

Ten tests, with ten cycles, without load (the only load was the weigh of the exoskeleton structure), for the same command path, were conducted. The values for path repeatability were calculated and the corresponding results for all tests are shown in Table 2.

1	2	3	4	5	6	7	8	9	10
13.9	11.9	7.4	13.6	9.1	10.4	13.4	10.1	12.5	11.1

Table 2 Repeatability results (second row [mm])

Analyzing the results form Table 2, we can say that the path repeatability of our robot rehabilitation system is satisfactory.

CONCLUSION

Powered exoskeleton device for gait rehabilitation has been designed and realized, together with proper control architecture. Its DOFs allow free leg motion, while the patient walks on a treadmill with its weight, completely or partially supported by the suspension system.

The use of pneumatic actuators for actuation of this rehabilitation system is reasonable, because they offer high force output, good backdrivability, and good position and force control, at a relatively low cost.

The control strategy was designed to ensure that the patient's legs will be guided along a fixed reference gait pattern. The inverse kinematic problem was solved in a numerical way and fuzzy controller used to regulate the lengths of thighbone and shinbone pneumatic actuators was developed. Additional compensation module to eliminate the influence of the torques during the movement was added.

The effectiveness of proposed control architecture was confirmed by experiments. The experimental results show that the developed control architecture can be considered an appropriate option for the control of the developed prototype.

In order to increase the performance of this rehabilitation system a force control loop should be implemented as a future development. The future work also foresees two more steps of evaluation of the system: experiments with voluntary healthy persons and experiments with disable patients.

REFERENCES

1. F.M. Henry: Specificity vs. generality in learning motor skill, in *Classical Studies on Physical Activity*, R.C. Brown and G.S. Kenyon Ed. Englewood Cliffs, N.J., Prentice-Hall; 1968:331-340;
2. V.R. Edgerton, R.D. de Leon, N. Tillakaratne, M.R. Recktenwald, J.A. Hodgson, R.R. Roy: "Use-dependent plasticity in spinal stepping and standing," *Advances in Neurology* 1997, 72:233-247.
3. S. Hesse, C. Bertelt, A. Schaffrin, M. Malezic, and K. Mauritz, "Restoration of gait in non-ambulatory hemiparetic patients by treadmill training with partial body weight support," *Arch. Phys. Med. Rehabil.* 75, 1087–1093, October 1994.
4. S. Hesse, et al., "Treadmill training with partial body weight support: influence of body weight release on the gait of hemiparetic patients," *J. Neurol. Rehabil.* 11, 15–20, 1997.
5. A. Wernig, and S. Muller, "Laufband locomotion with body weight support improved walking in persons with severe spinal cord injuries," *Paraplegia* 30, 229–238, 1992.
6. A. Wernig, A. Nanassy, and A. Muller, "Laufband (treadmill) therapy in incomplete paraplegia and tetraplegia," *J. Neurotrauma* 16, 719–726, 1999.
7. V. Dietz, G. Colombo, L. Jensen, and L. Baumgartner, "Locomotor capacity of spinal cord in paraplegic patients," *Ann. Neurol.* vol. 37, no. 5, 574–582, May 1995.
8. M. Visintin, H. Barbeau, N. Bitensky, and N. Mayo, "Using a new approach to retrain gait in stroke patients through body weight support and treadmill training," *Stroke* 29,1122–1128, 1998.
9. E. Hassid, D. Rose, J. Commisarow, M. Guttry, and B. Dobkin, "Improved gait symmetry in hemiparetic stroke patients induced during body weight supported treadmill stepping," *J. Neurol. Rehabil.* 11, 21–26, 1997.
10. T.Hornby, D.Zemon and D. Campbell, "Robotic-assisted, body-weight-supported treadmill training in individuals following motor incomplete spinal cord injuri," *Physical Therapy*, vol. 85, no. 1, 52-66, Jan. 2005.
11. S. Jezernik, G. Colombo, T. Keller, H. Frueh, and M. Morari, "Robotic orthosis lokomat: A rehabilitation and research tool," *Neuromodulation*, vol. 6, no. 2, pp. 108–115, Apr. 2003.
12. S. Hesse and D. Uhlenbrock, "A mechanized gait trainer for restoration of gait," *J. Rehabil. Res. Development*, vol. 37, no. 6, pp. 701–708, 2000.
13. Daisuke Aoyagi, Wade E. Ichinose, Susan J. Harkema, David J. Reinkensmeyer, and James E. Bobrow, "A Robot and Control Algorithm That Can Synchronously Assist in Naturalistic Motion During Body-Weight-Supported Gait Training Following Neurologic Injury," *IEEE Transactions on neural systems and rehabilitation engineering*, vol.15, no. 3, Sep. 2007.
14. J. Y. Lai, C. H. Meng, and R. Singh, "Accurate position control of a pneumatic actuator," *Transactions of the ASME, Journal of Dynamic Systems, Measurement, and Control,* 112, 734-739, 1990.
15. J. Pu, R. H. Weston, and P. R. Moore, "Digital motion control and profile planning for pneumatic servos," *Transactions of the ASME, Journal of Dynamic Systems, Measurement, and Control,* 114, 634-640, 1992.
16. T.Raparelli, M.Velardocchia, P.Beomonte Zobel, "I controlli Fuzzy nella pneumatica", *1° Conv. Int. Trasmissioni di Potenza*, Milano, 20-21 giugno 1995, pp. 621-634.

Proceedings of the 8th JFPS International
Symposium on Fluid Power, OKINAWA 2011
Oct. 25-28, 2011

1A2-1

DEVELOPMENT OF HIGH PERFORMANCE SHOES WITH HUMAN COMPATIBILITY

Yasuhiro HAYAKAWA*, Yuuya TAGUCHI* and Yuuki TOOYAMA*

*Department of Control Engineering
Nara National College of Technology
22 Yata-cho, Yamato-Koriyama, Nara, 639-1080 Japan
(E-mail: hayakawa@ctrl.nara-k.ac.jp)

ABSTRACT

It is reported that the rate of elderly person in the total population of Japan is about 21.5% in 2007. Thus, the recent society of Japan is called as “Elderly Society”. In the society, many elderly people work or enjoy walking to keep health. However, some problems with respect to stumble over of elderly people are occurred. That is to say, in recent years, accidents of bone fracture with elderly people increase because of tendency to fall by a little step in a house. As one of this cause, it is considered that a center of gravity position with foot parts is changed. Therefore, in order to solve this problem, we propose a new type of high performance insole by making use of sponge-core-soft rubber actuator (SCSRA). In this study, we indicate the structure of the insole. Further, the basic characteristics of the insole are clarified through some experimental results.

KEY WORDS

High Performance Insole, Pneumatic, Care Prevention, Walking, Soft Rubber Actuator

NOMENCLATURE

F:	Pushing Force [N]
P:	Settling Pressure [kPa]
R:	Roll Angle of the Ground Plate [Deg]
T:	Torque[Nm]
Φ:	Roll Angle[°]
Θ:	Pitch Angle[°]

INTRODUCTION

In Japan, the number of elderly people increases. On the other side, the number of young people decreases. As the result, it is reported that elderly people have to care another elderly person. In order to solve this problem, many kinds of support machines have been developed. However, with respect to an elderly person who is not physically handicapped, the bone fracture in tendency to fall sometimes becomes a big issue. For example, when the elderly people fall in a little step, some of them sometimes have trouble of bone fracture. Especially, the number of aged person who comes to keep bed increases by reason of the bone fracture of thighbone cervix in the tendency to fall.

With respect to this problem, it is reported that the main cause of tendency to fall is change of gravity position with each foot[1]. That is to say, when elderly people walk on the road, the center of gravity position moves to edge side of the sole as shown in Fig.1. This is because that the angle between the innominate bone and the thighbone is decreased by the muscle force depression of lower extremities. As the result, the elderly people are easy to stumble over.

Therefore, in order to solve this problem, we propose a new type of insole. The insole is constructed with compound rubber elements that a sponge rubber is covered with silicon rubber[2]. With respect to the element, since the sponge is coated with silicon rubber, air can be charged into the sponge chamber. As the results, it is possible to control the stiffness of the actuator by controlling pressure in the sponge chamber. Therefore, when some actuators are arranged in parallel, the actuators can estimate the distribution of external force that acts on the actuators. Thus, by making use of control of inner pressure of each actuator, the actuator can adjust torque that acts on the insole.

In this paper, we explain about the structure of insole that is constructed with the elements. Further, a test device to clear the effectiveness of the proposed insole is explained. Moreover, by using the test device an adaptive shape of the insole to distinguish between a roll motion and a pitch motion of the foot part is cleared. This is because that the walking motion is mainly constructed with the pitch motion and the roll motion. From these experimental results, basic characteristics of the proposed insole are clarified.

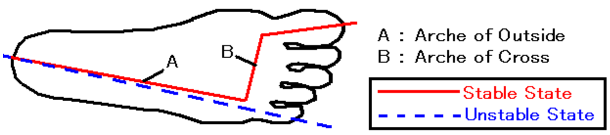

Fig. 1 Trajectory of Center of Gravity

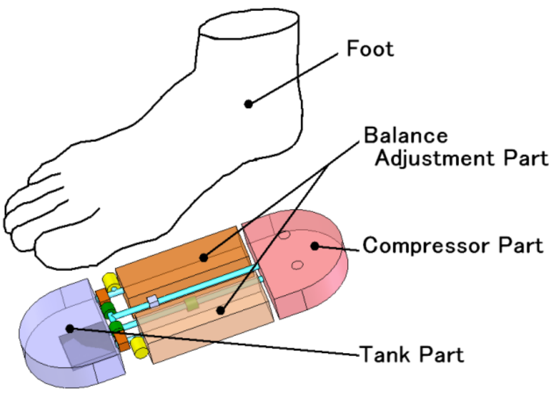

Fig. 2 Structure of High Performance Insole

HIGH PERFORMANCE INSOLE

Structure of the Insole

The structure of proposed insole is shown in Fig.2. The insole is constructed with compound rubber elements, a rubber compressor and a tank chamber.

When a subject walks on a road with shoes that has the proposed insole, air is compressed by the deformation of rubber compressor according to the motion of heels. Further, the compressed air is charged into the air chamber of the tiptoe part in the insole. Since pressure in the rubber element is measured by a small size pressure sensor, the stiffness of each rubber element can be controlled by pressure in the air chamber.

Rubber Element

In order to develop a new type of insole, we consider a pneumatic rubber element. The structure of the element is shown in Fig.3.

The actuator is made of two materials. One is silicon rubber and the other is sponge rubber. The sponge is coated with silicon rubber, and air can be charged into the sponge chamber. As the results, it is possible to control the stiffness of the element by controlling pressure in the sponge chamber.

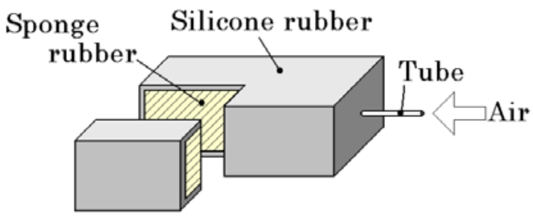

Fig. 3 Schematic View of Pneumatic Rubber Element

INSOLE TEST DEVICE

Structure of the Insole

When a person uses the shoes that have a high performance insole, the shape of the soft rubber element (SCSRA) is changed by external forces to the insole. This is because that the foot consists of a tiptoe, heel and the arch of a foot. Therefore, in order to clear the performance of the proposed insole, we developed a test device for an insole as shown in Fig.4. Figure 4(a) indicates a whole device and Fig.4(b) shows a foot plate (Ground) whose angles (a pitch angle and a roll angle) are controlled by pneumatic rotary actuators. Further, a foot model is attached to the 6-axis force sensor that is set to the tip of the cylinder rod to drive in the direction of z-axis as shown in Fig.4(c).

In the experiment, two pairs of SCSRA are put on the floor (Fig.4(b):Ground). Further the floor is driven by each rotary actuator. Thus, the inner pressure in the actuator is measured by a pressure sensor and the both torque and force in the direction of each axis that acts on the ankle part is measured by the 6-axis force sensor (Fig.4(c)).

By using the insole test device, we investigate an adaptive shape of the insole to distinguish the difference between a roll motion and a pitch motion of the foot. This is because that the main motion of falling down is a roll motion of the foot as shown in Fig.1. Therefore, we measure difference pressure between each element by using pressure sensors in the elements. Thus, we clarify the adaptive shape that the difference pressure does not be changed by a pitch motion but changes just only by a roll motion of the foot part.

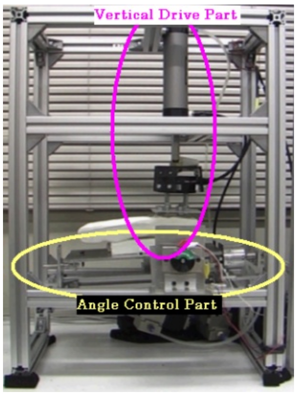

(a) Test Device

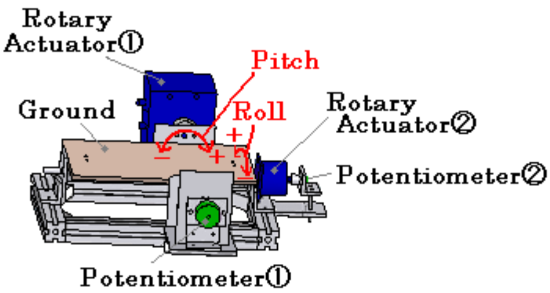

(b) Mechanism of Foot Plate

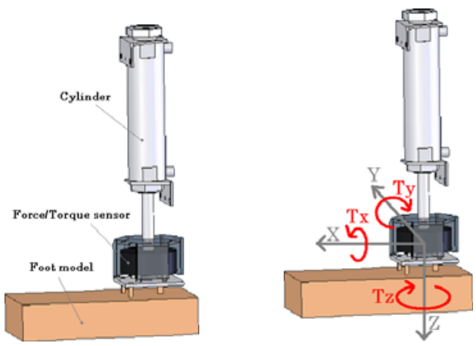

(c) 6Axis Sensor Part

Fig. **4** Structure of Test Device

Suitable Shape of the Element

In order to clear the adaptive shape of the element to distinguish between a roll motion and a pitch motion of the foot by value of pressure in the elements, we investigate the shape of the rubber element that the difference pressure between each rubber element is almost zero when the foot rotates in the direction of pitch motion. That is to say, variation of the inner pressure of the rubber element is measured by making use of the device that is shown in Fig.4.

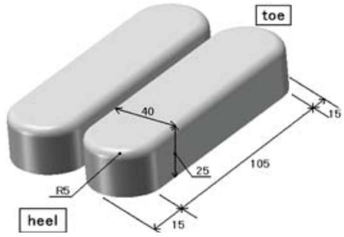

(a) Symmetric Type

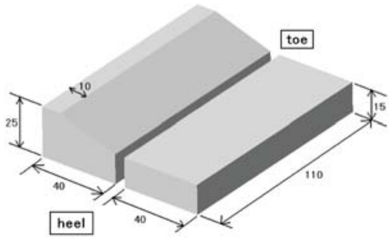

(b) One Side Inclination Type

Fig. 5 Rubber Element (Right Side)

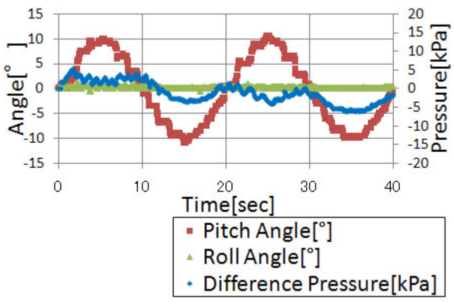

(a) Variation of Pitch Angle

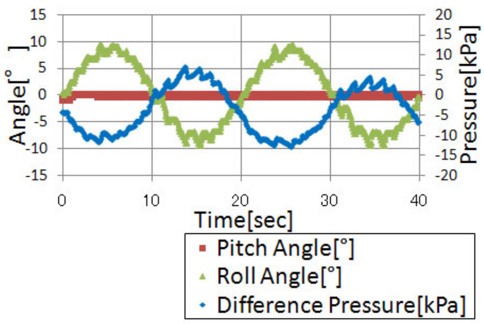

(b) Variation of Roll Angle

Fig. 6 Difference Pressure of Symmetric Type

In the experiment, we use 2 types of rubber element. Figure 5 shows each shape of the element. Figure 5(a) is symmetric type and Fig.5(b) is one side inclination type. By using these elements, we clear variation of the difference pressure between each element with respect to both a pitch angle and a roll angle.

Figure 6 shows the result with the symmetric type and Fig.7 is the result with the one side inclination type. The condition of each experiment is as follows.

[Condition]

(a): Force(60N), Pitch Angle (θ : -10°-10°)
Roll Angle(φ : 0°)

(b): Force(60N), Pitch Angle (θ : 0°)
Roll Angle(φ : -10°-10°)

From these results, it is cleared that in the case of the symmetric type, the difference pressure changes as the foot rotates in the direction of the pitch angle. On the other hand, in the case of one side inclination type, the value of difference pressure hardly changes when the foot rotates in the direction of pitch angle. As the result, it is clarified that the one side inclination type element can distinguish the motion of the foot by the change value of difference pressure between each element.

Further, the torque variation of the ankle part with respect to the one side inclination type element is shown in Fig.8. In this experiment the foot model is rotated in the direction of pitch motion. From this result, it is cleared that the variation of torque with roll motion is almost zero. Thus, by using the proposed element, the ankle is hardly damaged regardless of the shape of the one side inclination type.

EFFECTIVENESS OF THE ELEMENTS

In this chapter, we indicate the effectiveness of balance motion of the proposed element by adjustment of the pressure in each element. Figure 9 show torque values of ankle under each parameter.

With respect to Fig.9 (a), when the inclination angle between foot and ground (where, the inside point of the right side foot is a base point) increases, the sign of roll angle becomes positive. That is to say, the inside point of foot back (Arch of foot) comes in contact first with the ground. At this time, it is cleared that by the apophysis of the foot, the torque becomes positive at the latter half part of the torque result (latter half of walking motion).

Further, from Fig.9 (b), we verify that as the initial pressure of the outside element in the insole increases, the sign of torque in the direction of roll rotation becomes negative. That is to say, the elements of insole generate torque to the inside direction of the foot.

Moreover, through Fig.9 (c), it is confirmed that when the pushing force of the foot to the ground increases, the roll torque in the direction of negative increases (Where negative sign means inside direction of the foot).

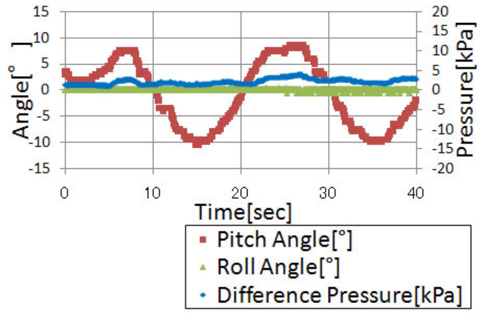

(a) Variation of Pitch Angle

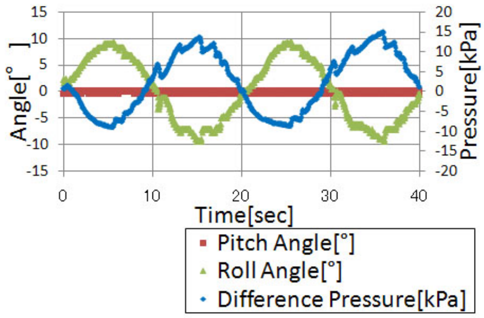

(b)Variation of Roll Angle

Fig. 7 Difference Pressure of One Side Inclination Type

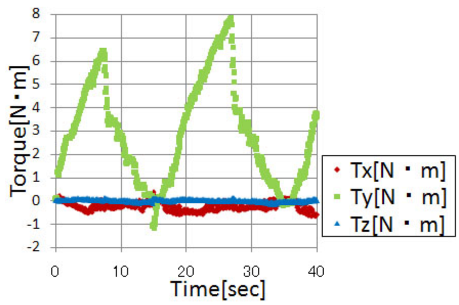

(a) Movement in the direction of Pitch Angle

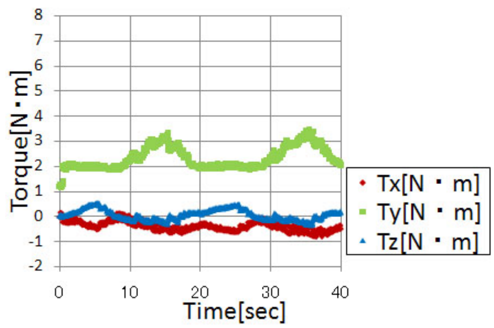

(b) Movement in the direction of Roll Angle

Fig. 8 Torque of Ankle Part (One Side Inclination Type)

HIGH PERFORMANCE SHOES TO ANALYZE WALKING MOTION

In this chapter, we explain about shoes that can measure pressure patterns of the insole. The sample shoes are shown in Fig.10. Further, we indicate a system diagram and a control circuit of the shoes in Fig.11 and Fig.12. As you can see the figures, the shoes have soft rubber elements (SCSRA1-4), an air pump, a battery, valves and control circuits. That is to say, the soft rubber elements in the insole are compressed when a subject walk on the ground. At this time, since pressure in the element is changed, the elements can be used as pressure sensors. Thus, by using the proposed insole, pressure patterns of the insole are measured. On the other hand, when pressure in the element is controlled by a computer, the stiffness of the element is adjusted. Further, with respect to the proposed shoes, each valve is driven by a battery and charge air is generated by a small size compressor (air pump). Further,

By using the shoes, we assume a trajectory of gravity position of the foot and analyze the walking patterns. In the experiment, subjects (students) equipped with the shoes walk on the walking machine as shown in Fig.13. We indicate sample results of walking motion in Fig.14. In the results, pressure values of each point of the foot are shown. Further, the trajectory of gravity position of each side foot is shown in Fig.15.

From the results it is clear that pressure in a heel point element is changed at the first time and the trajectory of gravity point moves to a tiptoe point (SCSRA4) from a heel point (SCSRA1). Thus, it is clear that we can analyze the walking pattern of the subjects by using the proposed shoes.

CONCLUSIONS

In this paper, we proposed a new type of insole using rubber elements. From some experimental results, we cleared performance of the proposed insole.

ACKNOWLEDGMENT

This research was partially funded by Grant-in-Aid for Scientific Research (c)(Project Number: 20500498). Additional support for this research was provided in part by SMC Co., Ltd.

REFERENCES

[1] M.P. Murray, et al. Walking Patterns of Healthy Old men, *J. Gerontology*, **24**, pp169-178, 1969

[2] Y. Hayakawa, H. Morishita, M. Aichi and R. Tsuda. Development of a Silicone Outer Fence Mold Actuator, *Journal of JSME*, Series C, **70**, pp. 433-439, 2004

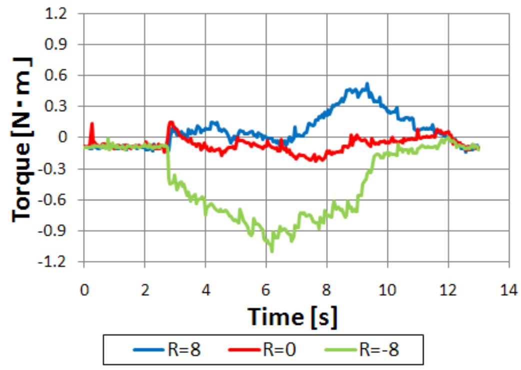

(a) Roll Angle(F=60, P=0)

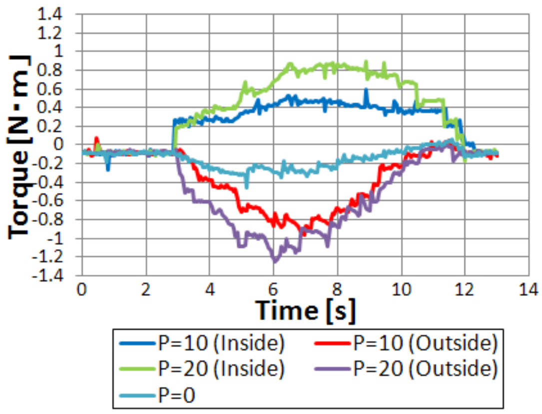

(b) Settling Pressure(F=50、R=0)

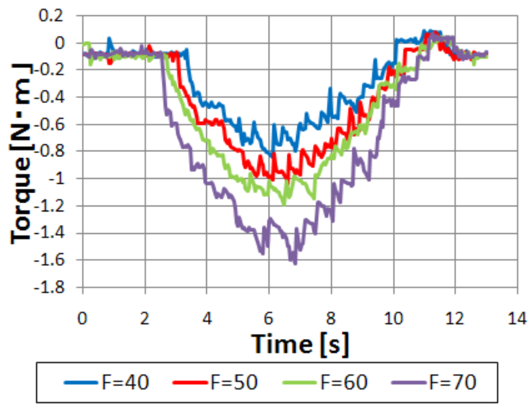

(c) Pushing Force(R=0、P=20(Outside) *)*

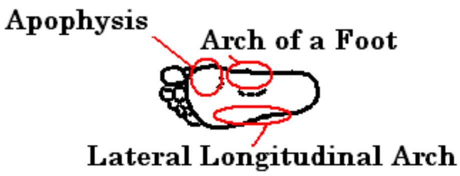

(d) Back of Foot

Fig.9 Experimental Results and Back of Foot

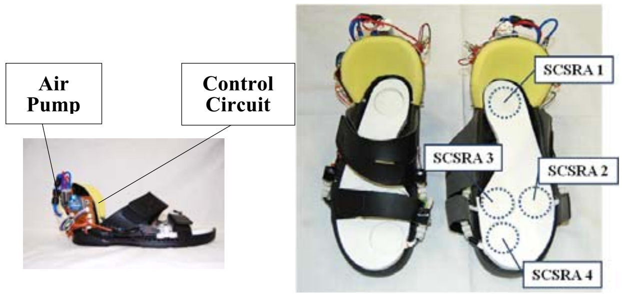

Fig. 10 Prototype shoes

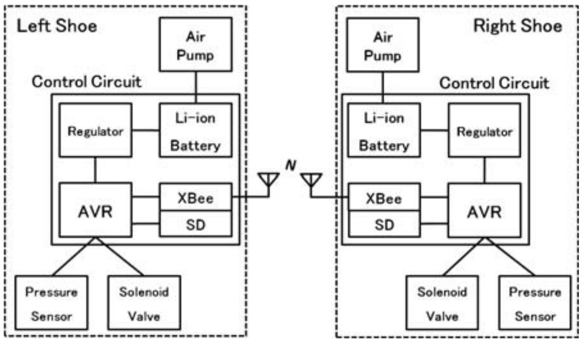

Fig. 11 System diagram

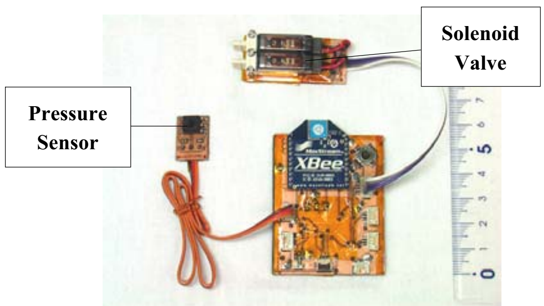

Fig. 12 Control circuit

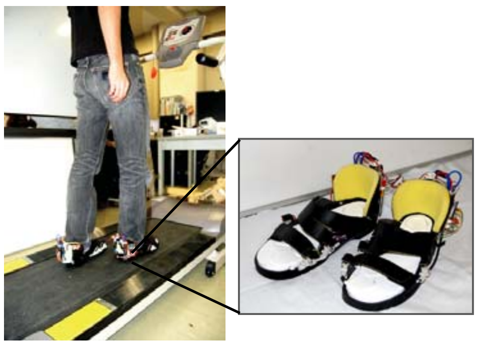

Fig. 13 Appearance of experiment

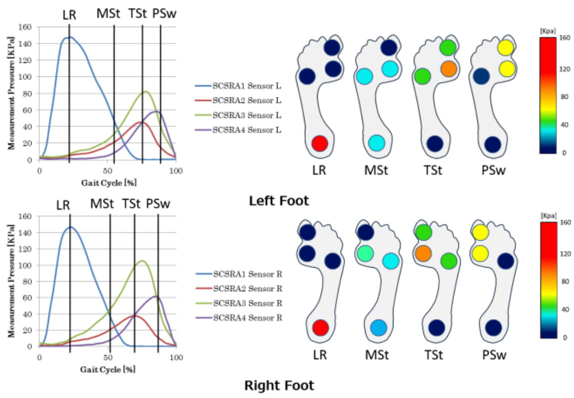

Fig.14 Experimental results

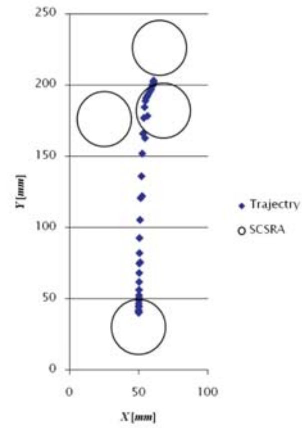

Left Foot

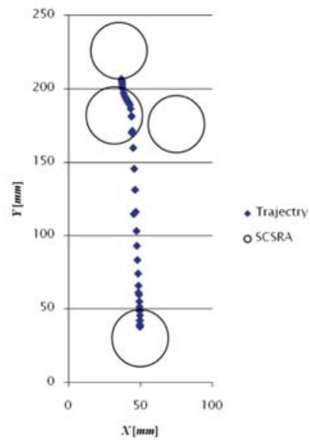

Right Foot

Fig.15 Trajectory of the center of gravity

Proceedings of the 8th JFPS International
Symposium on Fluid Power, OKINAWA 2011
Oct. 25-28, 2011

1A2-2

DEVELOPMENT OF WEARABLE MASTER-SLAVE TRAINING DEVICE FOR UPPER LIMB CONSTRUCTED WITH PNEUMATIC ARTIFICIAL MUSCLES

Daisuke SASAKI*, Toshiro NORITSUGU* and Masahiro TAKAIWA*

* Graduate School of Natural Science of Technology
Okayama University
3-1-1 Tsushimanaka, Kita-ku, Okayama, 700-8530 Japan
(E-mail: daisuke@sys.okayama-u.ac.jp)

ABSTRACT

The purpose of this study is to develop a wearable master-slave upper limb training device, which can be used to a passive training for a trainee who can not move by themselves. Developed device has 7 D.O.F by using three kinds of pneumatic artificial muscles, which are chosen as suitable actuators to move each human joint. In this paper, cooperated movements are experimented to verify a capability of slave device. It is confirmed from the result that a subject who uses the slave device can follow the trainer movement. Therefore, this device may be expected to be able to train all upper limb joints independently or cooperatively.

KEY WORDS

Pneumatic, Artificial muscle, Soft mechanism, Wearable robot

INTRODUCTION

Many kinds of power assist device have been developed to assist a hard work, rehabilitate a human body in recent years [1]-[5]. These devices are driven with various actuators such as a electric motor, a hydraulic cylinder and so on. Above all, a pneumatic artificial rubber muscle is effective to drive these devices[4][5]. Since these devices used by a human is required a safety and a light weight. This actuator has a mechanical flexibility according to the air compressibility, a rubber material, and has a high power weight ratio. Therefore, this rubber muscle can realize a flexible and a light weight device with a simple mechanism.
The purpose of this study is to develop a wearable master-slave upper limb training device for a trainer and a trainee. By realizing the wearable master-slave device, the trainer may be able to train the trainee easily since the trainer just moves the trainer's upper limb. A final goal of this study is shown in Fig.1. The trainer and the trainee use the devices, and the trainer moves the upper limb. By looking the trainee's condition and moving the

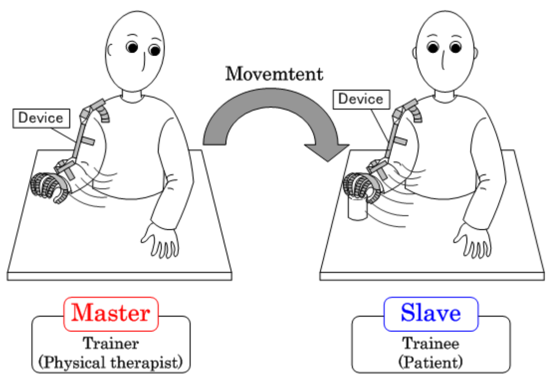

Fig.1 Image of final goal

trainer's upper limb, the trainer teaches the trainee an upper limb trajectory. The trainer can train the trainee only by moving the trainer's body.
Developed device has 7 D.O.F by using three kinds of pneumatic artificial muscles, which are chosen as suitable actuators to move each human joint. Therefore, this device can apply torques to each human upper limb joint independently. In addition the trainer can train easily without a complicated calculation since the trainer who uses the wearable master device only move a trainer's body intuitively.
In this paper, the structure of developed device is discussed, and then the cooperated movement is experimented. It will be confirmed through the above experiment that the slave subject who uses the slave device can follow the master subject's movement cooperatively by applying the torques to each joint independently.

MOVEMENT OF DEVELOPED DEVICE

Fig.2 shows an overview the developed master and slave devices. This device has 3 D.O.F at a shoulder and 1 D.O.F at an elbow, respectively. The same orthosis of the slave device in which the artificial muscle is not installed is used for a master device.
Developed device has 7 D.O.F, which is the same as the human upper limb. Therefore, this device can move the subject as shown in Fig.3, 4. The each elbow movement is shown in Fig.3. Similarly, the shoulder and wrist movement are shown in Fig.4, 5.

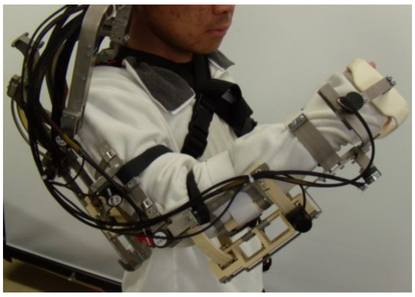

(a) Master device

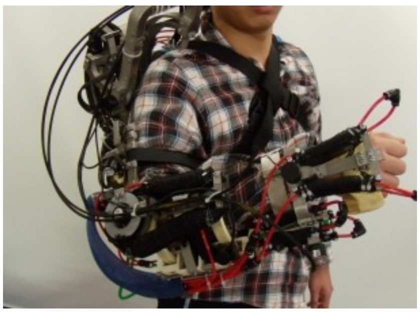

(b) Slave device

Fig.2 Overview of developed device

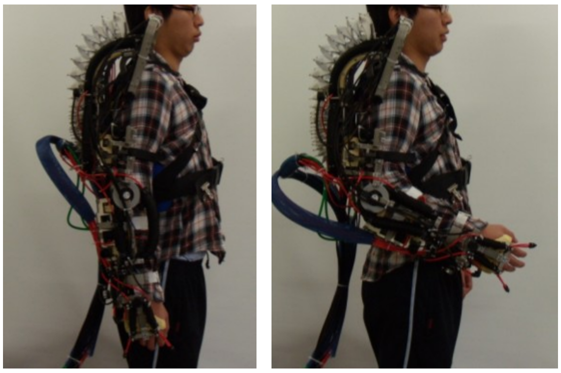

(a)Extension (b) Flexion

Fig.3 Movement of elbow device

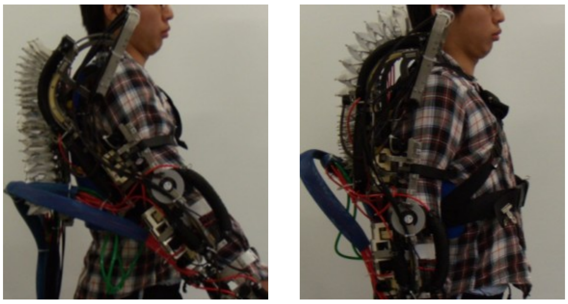

(a)Flexion/Extension

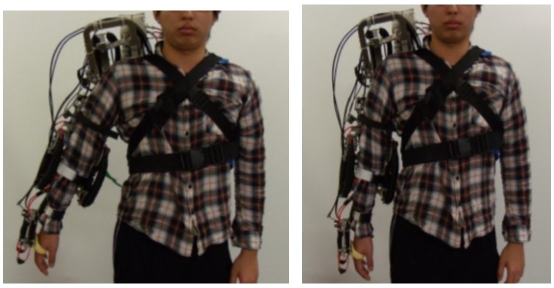

(b) Abduction/Adduction

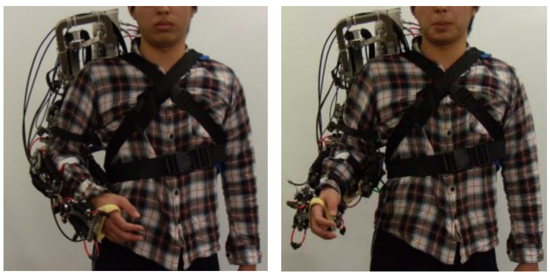

(c) Internal rotation/External rotation

Fig.4 Movement of shoulder device

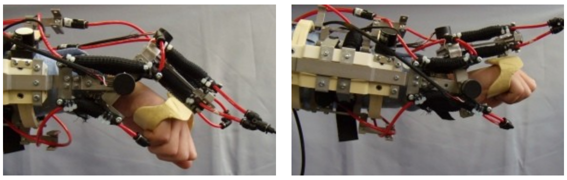

(a) Palmar flexion/Dorsal flexion

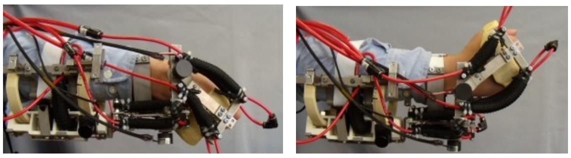

(b) Ulnar flexion/Radial flexion

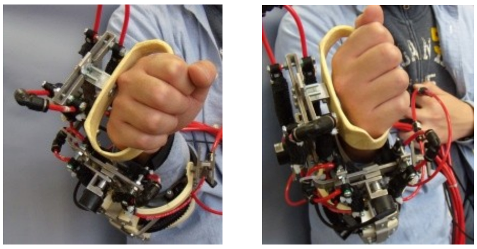

(c) Pronation/Supination

Fig.5 Movement of wrist device

STRUCUTURE OF DEVELOPED DEVICE

Fig.6 shows the structure of the slave shoulder and elbow device. Layer type pneumatic muscles as shown in Fig.7 are put on a back side through a slide rail. Layer type pneumatic muscle expands to the height direction when the compressed air is supplied into this muscle. This expansion force is converted to the shoulder flexion/extension torque by the slide rail and the shoulder joint via a nylon band in the slide rail as shown in Fig.8.

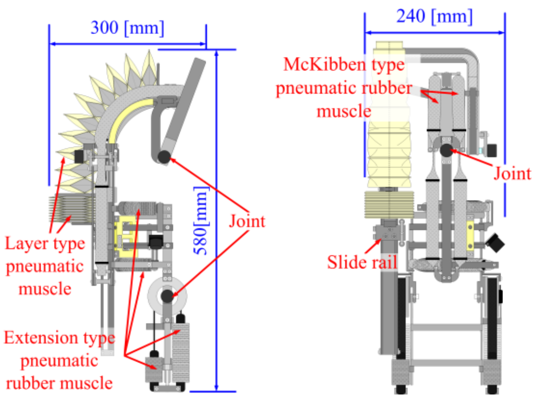

(a) Side view (b) Rear view

Fig.6 Structure of shoulder device

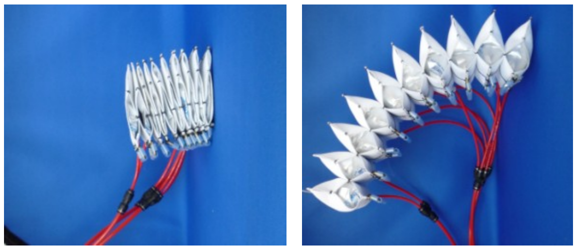

(a-1) Initial state (a-2) Pressurized state

(a) Pneumatic muscle for extension

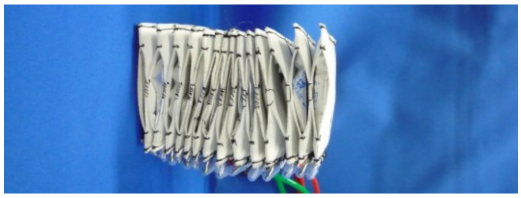

(b-1) Initial state

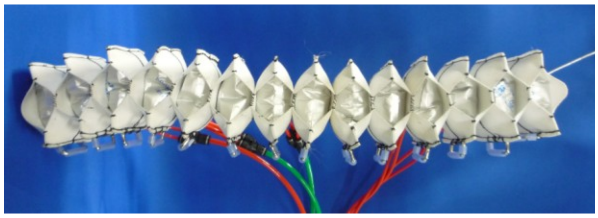

(b-2) Pressurized state

(b) Pneumatic muscle for flexion

Fig.7 Overview of layer type pneumatic muscle

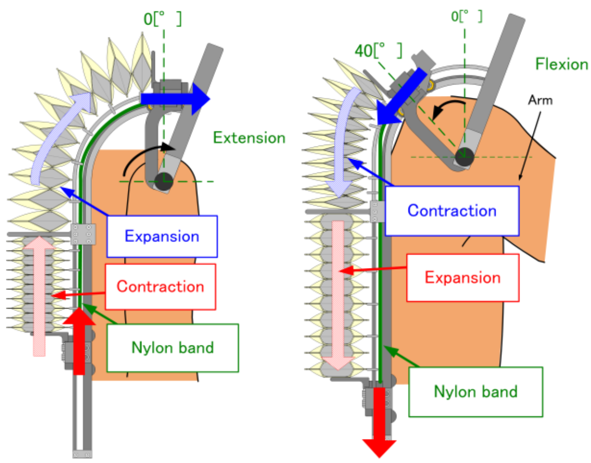

(a) Extension (a) Flexion

Fig.8 Principle of operation about shoulder flexion/extension

McKibben type pneumatic rubber muscles are used for generating an abduction/adduction torque. The contraction force from this muscle is also converted to the abduction/adduction torque by the shoulder joint.
A shoulder internal/external rotation and an elbow flexion/extension torques are generated by extension type pneumatic rubber muscles as shown in Fig.9. This artificial muscle is installed to the orthosis with this muscle extended from the initial length. The restoring force of the rubber increases by extending to the length direction. Conversely, the restoring force decreases by pressurizing, since this muscle extends to the length direction when the compressed air is supplied. This restoring force is used to generate the above torques in this device.
Two rubber muscles are installed on a slide rail alternately as shown in Fig.10. This slide rail is connected with the shoulder abduction/adduction device in which McKibben type pneumatic rubber muscles are installed as shown in Fig.7. Initially, both rubber muscles are supplied a balance pressures. In the case of external rotation, the rubber muscle for external rotation

(a) Initial state

(b) Pressurized state

Fig.9 Overview of extension type

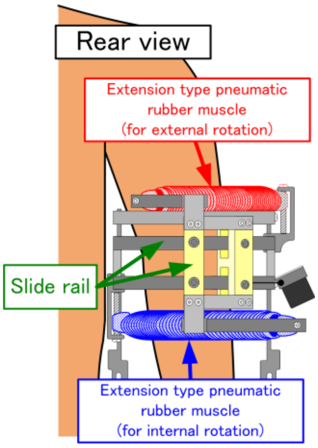

Fig.10 Structure of shoulder internal/external rotation device

shown as red line in Fig.11 is decreased from the balance pressure, and the rubber muscle for internal rotation shown as blue line is increased. The human can be done the external rotation by the restoring force from the rubber muscle for external rotation. In the case of internal rotation, the human can be also done the internal rotation by the same principle. The wrist pronation/supination device shown in Fig.5 (c) in the following description has the almost same structure and principle of operation.
Fig.12 shows the principle of operation about elbow device. The extension type pneumatic rubber muscles are put on the device so that both muscles are antagonized. When the rubber muscles for flexion and

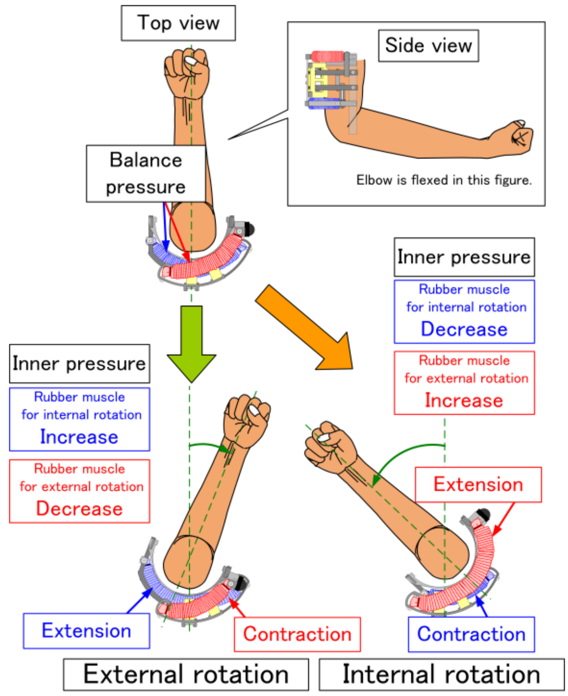

Fig.11 Principle of operation about shoulder internal/external rotation device

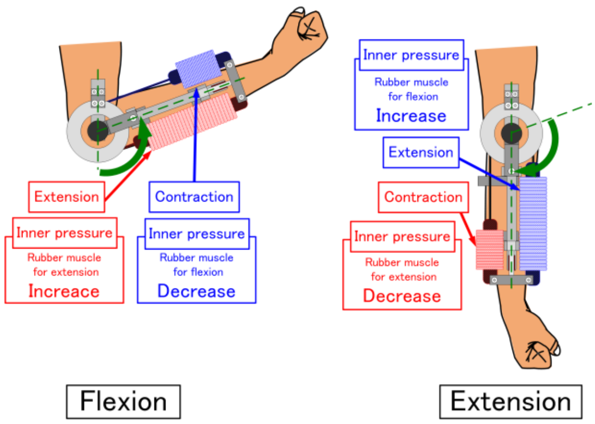

Fig.12 Principle of operation about elbow device

extension shown as blue and red lines are decreased and increased from the balance pressure, this device can flex a subject elbow. Conversely, when the rubber muscles for flexion and extension are increased and decreased from the balance pressure, a subject elbow is extended.
Fig.13 shows the structure of the wrist device. In the wrist device, all movements are also driven with the extension type pneumatic rubber muscles. The pronation/supination device has the almost same structure of shoulder internal/external rotation device as the above description. The principle of operation about the palmar/dorsal and ulnar/radial flexion devices also is the almost same one about the elbow device.

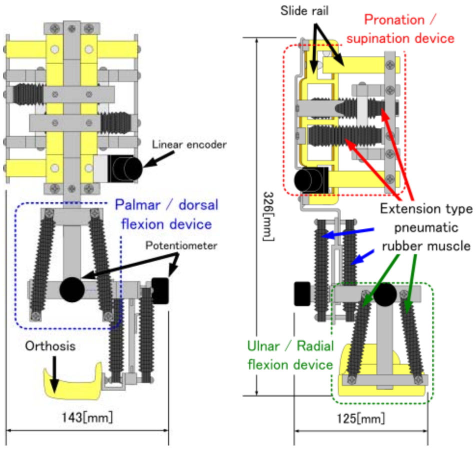

(a) Rear view (b) Side view

Fig.13 Structure of wrist device

COOPERATED MOVEMENT USING DEVELOPED DEVICE

In this section, the cooperated movement using the master and slave devices is experimented. The master and slave subjects use each device as shown in Fig.14. The master subject moves the hand at 10s in period by using all upper limb joints to draw a circle, which is about 300[mm] in diameter. The slave subject does not use muscular strength. In this experiment, the devices are controlled based on the unirateral master-slave control system. The each slave joint angle is controlled with the angle control system to follow the master joint angles, which are the reference angles in the slave angle control system. The inner pressure of the antagonized artificial muscle is calculated by the PI controller in the angle control system. Table 1 shows the main system parameters to show the each angle.

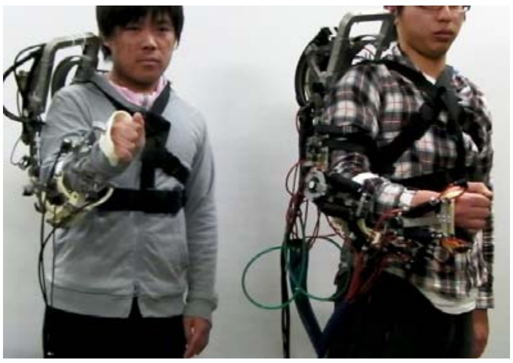

Fig.14 Image of experiment

Fig.15 show the experimental results and the definition of each angle. The master subject draw the circle three times. In flexion / extension and internal / external rotation shown in Fig15 (a), (c), the slave angles are saturated. This device has been designed as compactly as possible. Therefore, the generated torque from rubber muscle may be smaller than the required one to move the human body. It is the future work to cope with both the compactness and the increase in the generated torque. However, another slave angles can follow the master angles. It is another future work to improve the angle response against the master movement.

CONCLUSION

The purpose of this study is to develop a wearable master-slave upper limb training device for a trainer and a trainee. In this paper, the structure of developed device has been discussed, and then the cooperated movement has been described.

Table 1 Main system parameters

Parameter		Explanation about parameter		Unit
θ_s		Joint angle at slave device		rad
		Part	Movement	
	θ_{sh1}	Shoulder	Flexion/Extension	
	θ_{sh2}		Abduction/Adduction	
	θ_{sh3}		Internal rotation /External rotation	
	θ_{el}	Elbow	Flexion/Extension	
	θ_{wr1}	Wrist	Palmar flexion /Dorsal flexion	
	θ_{wr2}		Ulnar flexion /Radial flexion	
	θ_{wr3}		Pronation/Supination	
θ_m		Joint angle at master device		rad

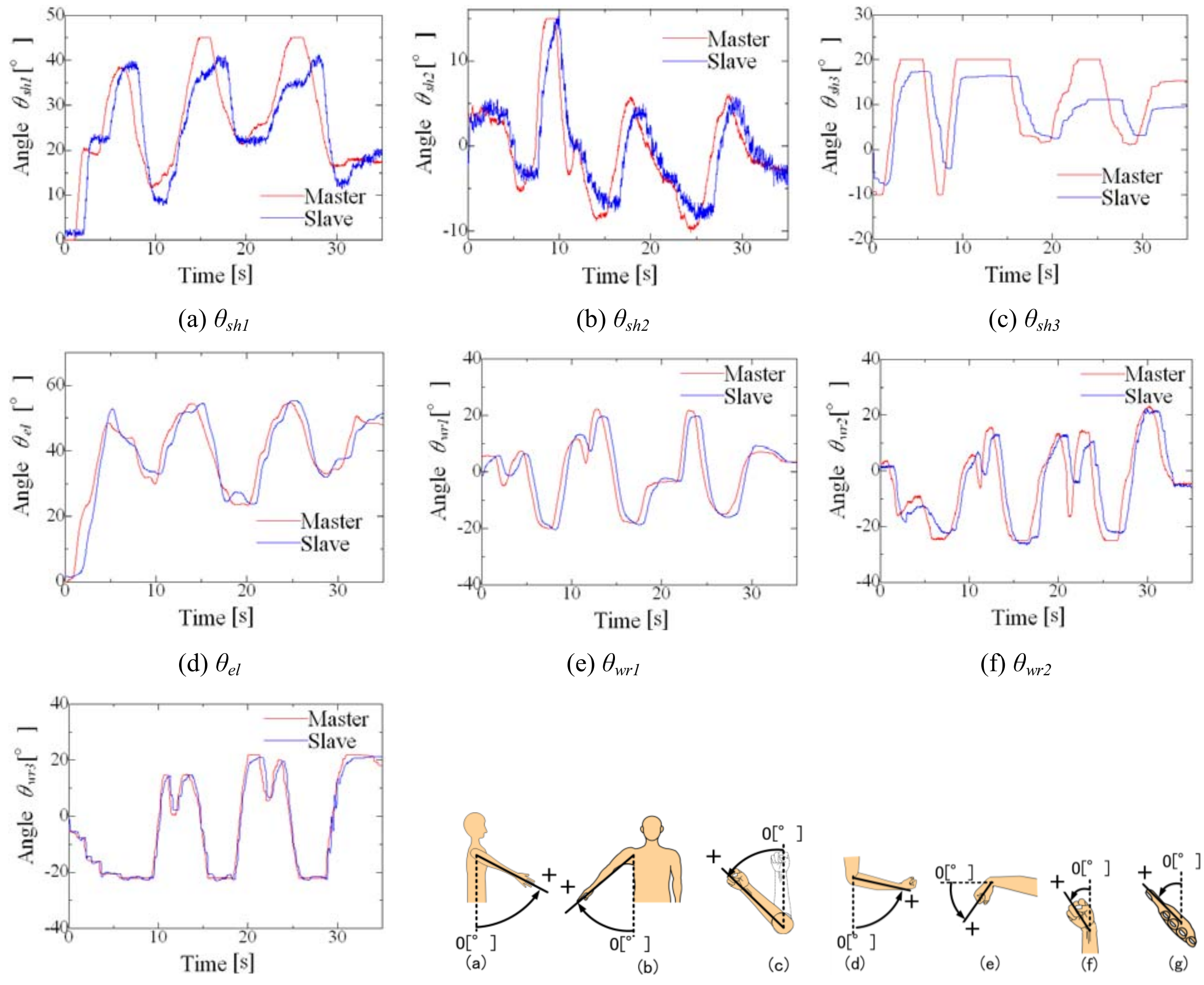

(a) θ_{sh1} (b) θ_{sh2} (c) θ_{sh3}

(d) θ_{el} (e) θ_{wr1} (f) θ_{wr2}

(g) θ_{wr3}

Fig.15 Experimental results and definition of each angle about cooperated movement

In flexion / extension and internal / external rotation, the generated torque from rubber muscle may be smaller than the required one to move the human body. It is the future work to cope with both the compactness and the increase in the generated torque.

However, another slave angles can follow the master angles. It is another future work to improve the angle response against the master movement.

REFERENCES

1. A.Chu, H.Kazerooni, A.Zoss, On the Biomimetic Design of the Berkeley Lower Extremity Exoskeleton(BLEEX), Proc. of the 2005 IEEE International Conference on Robotics and Automation, pp.4356-4363, 2005.
2. Y.Mori, K.Takayama, T.Zengo, T.Nakamura, Development of Straight Style Transfer Equipment for Lower Limbs Disabled: Verification of Basic Motion," Journal of Robotics and Mechatronics, Vol.16, No.5, pp.456-463, 2004.
3. J. Nikitczuk, B. Weinberg, C. Mavroidis, Rehabilitative Knee Orthosis Driven by Electro-Rheological Fluid Based Actuators, Proc. of the 2005 IEEE International Conference on Robotics and Automation, pp.2294-2300, 2005.
4. D.Sasaki, T.Noritsugu, Development of Wearable Master-Slave Training Device Constructed with Pneumatic Rubber Muscles, Proc. of the 18th IEEE International Symposium on Robot and Human Interactive Communication RO-MAN2009, pp.91-96, 2009.
5. H.Kobayashi, T.Siiba, Y.Ishida, Realization of All 7 Motions for the Upper Limb by a Muscle Suit, Journal of Robotics and Mechatronics, Vol.16, No.5, pp.504-512, 2004.

Proceedings of the 8th JFPS International
Symposium on Fluid Power, OKINAWA 2011
Oct. 25-28, 2011

1A2-3

DESIGN OF AN INNOVATIVE PNEUMATIC MASSAGE DEVICE FOR LOW BACK PAIN TREATMENT

Michele Gabrio ANTONELLI*, Pierluigi BEOMONTE ZOBEL*, Francesco DURANTE* and Terenziano RAPARELLI**
* DIMEG, Università degli Studi dell'Aquila
Via Giovanni Gronchi 18, 67100 L'Aquila, Italy
(E-mail: pierluigi.zobel@univaq.it)
** Dipartimento di Meccanica, Politecnico di Torino
Corso Duca degli Abruzzi 24, 10129 Torino, Italy
(E-mail: terenziano.raparelli@polito.it)

ABSTRACT

80% of healthy world population, with no sex distinction, suffers low back pain. Massage is an alternative method to pharmaceutical and surgical treatment for the low back pain. Massage is an hygienic and therapeutic method consisting of mechanical manipulation of human body surfaces. Traditionally, massage is practised manually; nevertheless several massage devices device can be found on market, sorted as regards method by which massage is exerted. Some robotic massage devicis can be found in scientific literature. This paper presents a new massage device for lumbar region in order to treat the low back pain. Massage is practised by air pocket actuators made of silicon rubber. The design of air pocket actuators, the design of the massage device frame and the control system design are described. Finally, experimental test on actuators and on the massage device prototype are described.

KEY WORDS

Massage device, pneumatic actuators, low back pain

INTRODUCTION

Spine can be affected by several pathologies: over 30 years old, it was demonstrated that spine elements are subjected to irreversible changes whose intensity is strictly correlated to subject age. Low back pain is certainly the more diffused. 80% of healthy world population, with no sex distinction, suffers low back pain whether the subject performs stressful activities or sedentary one. In order to treat low back pain, an alternative method to pharmaceutical and surgical treatment is represented by massage therapy [1]. Massage is an hygienic and therapeutic method consisting of mechanical manipulation of human body surfaces; specifically of back. Massage provides a relaxing effect on body: it acts directly on the local area in which is applied and acts indirectly on the nervous and vegetative systems [2].
Traditionally, massage is exerted by hands. It is possible to distinguish several kind of massage techniques on the basis of the region of the hand used for manipulation, of the exerted pressure intensity and of the movement performed by hands. Massage by hands requires patient to be relaxed on a bed, in order to avoid loads acting on the spine and to allow the physiotherapist to work better. The most common kinds of massage for low back pain treatment are: *surface palmar touch* (fingers exert light pressure on back, with both hands simultaneously

or alternately, from shoulders to lumbar region; movements can be in longitudinal, cross and diagonal direction as regards spine); *deep touch* and *deep palmar touch* (thumbs of both hands exert a heavy pressure on spine sides, from lumbar region to shoulders, and then fingers of both hands, simultaneously or alternately, exert a heavy pressure on back from shoulders to lumbar region, in longitudinal direction as regards spine); *hackning* (edges and dorsal surface of little fingers of both hands hit, alternately and sequentially, muscles on spine sides, from distal to proximal region, in order to provide a stimulant effect; movement has to be performed quickly and the exerted pressure has to be light); *kneading* (all fingers or only thumbs press and release muscles, performing a circular trajectory. Exerted pressure has to be heavy; each circular movement has to last about 3-4 seconds). Other kinds of massage techniques are applied to the back, but they are not suggested for low back pain treatment.

Nevertheless, it is possible to find, on market, massage devices [4]; they can be divided into four categories on the basis of the methods by which massage is exerted: *mechanical by pressure* (rigid elements are applied directly on the patient and moved on him; suitable shapes of the elements provides compression and manipulation of muscular tissues. A typical example is represented by rolls moved manually or electrically); *mechanical by vibration* (wearable devices or suitable carpets include eccentric electric motors; during functioning, eccentric kinematics develops vibrations exerting massage effects on the contact surface between device and patient); *pneumatic* (wearable device include chambers receiving pressurized air, to be inlet inside them; strains of air chambers provide compression of contact surfaces between devices and patients. Massage is exerted by sequences of compression and release of contact surfaces); *electric* (electric stimulators, by suitable electrodes, send electric currents to muscles, in order to provide muscle contractions).

Scientific literature refers to robotic massage device [5, 6, 7]: they are manipulators provided of end-effectors with suitable shapes able to perform massage. Although massage action is efficacious, these devices are too expensive, bulky and can not be used by a patient in domestic environments.

Among existing massage devices, it was not possible to find a massage device to be used only for low back pain treatment and able to perform the most common kinds of massage techniques exerted by hands, in terms of movements, time lengths and exerted pressure intensities, and user friendly.

In this paper a new massage device for lumbar region is presented: it is able to reproduce the most common kinds of massage techniques exerted by hands. Massage is exerted by air chamber actuators placed in order to realize a matrix of actuators. Actuators are placed on a wearable frame. Inlet and outlet of pressurized air is controlled by a Programmable Logic Controller (PLC). In this paper, technical specifications of the device will be defined and design of actuator, of device frame and of control system will be described. In particular, experimental activities in order to measure typical exerted pressure values and typical contact surfaces with patients, during the massage by physiotherapists, will be described; the design methodology of actuators, using finite element codes, will be described; components of device frame and functioning modes, managed by PLC, will be described. Finally, experimental activity for validation of finite model of the actuator and a first pre-clinic investigation, with healthy volunteer subjects, of the realized prototype will be described.

THE PROPOSED MASSAGE DEVICE

The objective of the presented research activity was the development of a suitable massage device for lumbar region of the spine. The definition of the technical specifications was the first step performed. In particular, the device has to be: able to reproduce most common kinds of massage techniques performed by hands; intrinsically safe; wearable and adaptable to the natural anatomical shape of patients, able to ensure the maximum adherence to the patient, usable for several patient sizes, light. Among them, device safety guided the choice of the actuation system: since device has to be used directly connected to the patient, it needs to avoid the use of rigid elements, rather compliant, and in the same time to be able to exert required pressure intensities. Since device has to reproduce the massage techniques performed by hands, it needs to be provided of a wide number of actuators to cover all the lumbar region. In order to satisfy specification of lightness, it was preferred pneumatic actuation because pneumatics is characterized by a high power/weight ratio; furthermore, pneumatics is a safe technology. On the basis of the cited requirements and of the expertise of authors in development of innovative pneumatic actuators [8], it was established to develop an air chamber actuator, to be realized in compliant material. The measurement of typical pressure values and typical contact surfaces during massage practice, by physiotherapist, was the next step. On the basis of the experimental results, actuator design, massage device frame design and control system design were performed.

Measurement of typical pressure values

An experimental set-up was realized in order to measure typical pressure values during massage by hands, because no data can be found in literature. The actuator to be designed has to reproduce the same pressure values exerted by physiotherapist.

The measurement chain was made by Bignardi et alii

[9] and consists of:
- a matrix, dimension equal to 80x85 mm, of eight resistive pressure sensors, connected to a data amplifier with eight input channels. Sensors are placed to realize a 4x2 matrix; each sensor is placed inside a silicon gel cell in order to spread uniformly pressure on sensor and to shield it from mechanical damages. Matrix frame is made of flexible material; its thickness is equal to 2,3 mm. The measurement error of each sensor is ± 50 mbar, equal to 5% of full scale (the full scale is equal to 2.000 mbar). Figure 1 shows sensors matrix;
- the XXGN 1.0400001 data amplifier of Medizintechnik Gmbh (Neubeuern, Germany). Each pressure sensor is connected to a channel; data of each channel can be read on the amplifier by means of a numerical display. By a selector it is possible to change data reading. The amplifier has eight input channels and eight output channels: sensibility is equal to 1V/100kPa;
- a data acquisition card, 16 bit resolution DAQ CARD 6036E of National Instruments (USA), to acquire output data of amplifier;
- a 2,4 GHz P4 personal computer to monitor and record acquired data.

Figure 1 Pressure sensors matrix

Experimental tests were performed using a silicon rubber pad, with the same dimensions of the lumbar region of a slim patient and with a similar compliance of the muscular tissue of a sport man. Pad thickness is equal to 2,5 mm, quite similar to sensors matrix thickness. In the centre of the pad a pocket was realized to place sensors matrix, as shown in Figure 2. A sheet of paper was used to cover pad and sensors matrix in order to hide sensors matrix: in this way, test performer was not influenced to exert different pressure on sensors rather than on silicon rubber. The pad-sensors matrix frame was fixed to the test bed (a fixed table) by two clamps, as shown in Figure 2. Sampling frequency of data acquisition was equal to 1.000 Hz; time length of data acquisition was 3 seconds; data acquisitions were performed in referenced single ended mode.

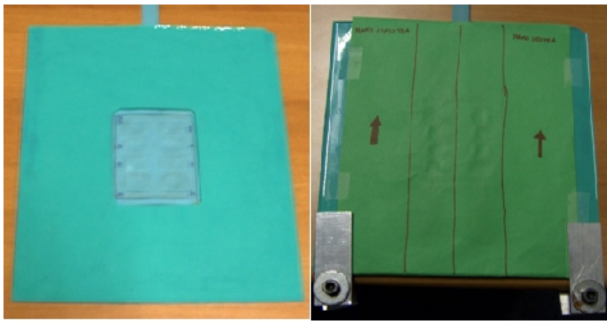

Figure 2 Pad-sensor matrix frame and test bed

Tests were performed by one physiotherapist. The kinds of massage techniques were: *surface touch by thumbs*, *deep touch by thumbs*, *surface palmar touch by fingers*, *hackning*. For each technique, 20 tests were performed for a total amount of 160 acquired signals. An example of acquired data is shown in Figure 3: data are referred to sensors 1, 3, 5 and 7, placed in the right side of the sensors matrix, as schematized in Figure 1.

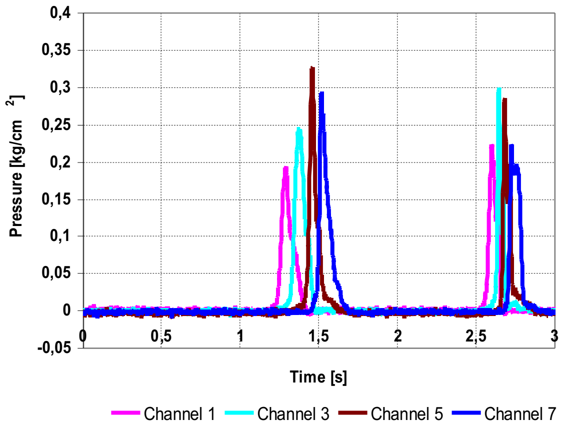

Figure 3 Example of acquired data

Pressure peak values of each sensor, as shown in Figure 3, are different in the same test. The final pressure value of each kind of massage technique test, to be used for actuator dimensioning, was assessed as described: for each test, pressure value was assessed as the mean value of the eight peak values acquired by each sensor; the final pressure value was assessed as the mean value of pressure value of each test. Table 1 shows the final pressure values assessed for each kind of massage technique. The maximum final pressure value (0,6 kg/cm^2) was adopted for actuator dimensioning.

Table 1 Pressure values assessed for each massage technique

Kind of massage technique	Pressure value [kg/cm^2]
surface touch by thumbs	0,35
deep touch by thumbs	0,60
surface palmar touch	0,40
hackning	0,20

Measurement of contact surfaces

In order to define actuator dimensions, measurements of contact surfaces between physiotherapist and patient were performed. Contact surfaces were considered as hands (fingers, thumbs and edges and dorsal surface of little fingers) imprints, left during a massage simulation. Test bed was realized by means of a black sheet of paper and a homogeneous layer of flour, placed on it. Tests were performed by one physiotherapist. Massage simulations were performed in order to measure: thumbs imprints surfaces; width of thumbs imprints, during a deep palmar touch; fingertips imprints surfaces; width of fingertips imprints, during a deep palmar touch; dorsal surfaces of fingers imprints.

After each simulation, a picture of each imprint was made; each picture was submitted to an image analysis, with a 2D CAD software, by which measurement values were obtained. Figure 4 shows some analyzed imprints. On the basis of the image analysis results, the lower imprint surface was practised by thumbs: it can be bounded inside a rectangle with a base value in the range 20-24 mm and a height value equal to 14 mm. The lower surface was chosen as actuator contact surface; hence, the actuator contact surface has to be in the range 280–336 mm^2. Wider surfaces can be obtained by joint more surfaces of more actuators.

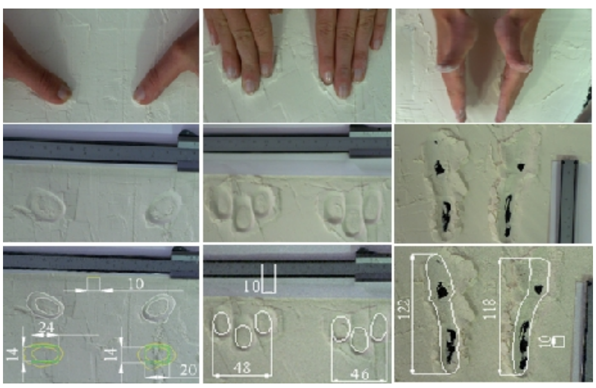

Figure 4 Analyzed imprints left during massage simulations: (from left to right) deep touch by thumbs; surface palmar touch by fingers; hackning

Actuator design

On the basis of the maximum final pressure value (0,6 kg/cm^2) and of the wider assessed contact surface (24x14 mm^2) in a deep touch massage simulation, technical specifications for actuator design were: pressure to be exerted equal to 0,7 kg/cm^2; contact surface equal to 336 mm^2; force developed equal to 23,5 N. Overestimation of pressure value was necessary to be sure to reach 0,6 kg/cm^2. Furthermore, during massage practice it was measured that compression of muscles, under hands, is less than 10 mm. As previously introduced, an air pocket actuator, in compliant material, was chosen to exert massage. Silicon rubber (Silastic E, Dow Corning) was chosen for its softness. The air pocket device was thought to be made by a chamber, constructed by two layers of silicon rubber linked each other on the edge, that can be pressurized. A hole has to be used to inlet and to outlet the air from the pocket. Pressurizing the air inside the pocket, the volume grows as a balloon, so that massage pressure is obtained by the contact with the lumbar region opposing to the volume expansion. A sheet metal is placed in correspondence of the lower layer of the chamber in order to perform volume expansion only in one side of the actuator. The air pocket device shows a strongly non linear behaviour by which output force depends on both the pressure inside the pocket and its volume. It is due to large strains to which it is subjected and to the constitutive material: silicon rubber, as all elastomeric materials, has a non linear σ-ε relationship. For this reason, before designing the air pocket device, it was useful to define a numerical model as a design tool able to predict the behaviour of air pockets. The principal aim was to obtain the geometrical parameters values of the air pocket and air pressure values to satisfy technical specifications. Two different models were implemented: one for the isometric test modelling and one for the isotonic test modelling. In the isometric test, consisting in constant deformation experiments, the force versus pressure inside the chamber is computed; in the isotonic test, consisting in constant force experiments, the displacement of the upper layer versus pressure is computed. In the isometric test modelling, input parameters, besides geometric ones, are pressure value and maximum admitted displacement value; in the isotonic test modelling, pressure value and force acting on the upper layer. Numerical models were implemented by a finite element models, developed by ANSYS code. Each model is a three dimensional and parametric model of a quarter of air pocket, in order to reduce the number of nodes and then the computing time. On the basis of previous validation model experiences [8], three different kinds of elements, chosen from ANSYS library, were used in the model: SOLID45 elements to model the sheet metal; LINK8 elements used as sensors to measure the exerted thrusts or as constrains of the maximum admitted displacement values; HYPER86 elements to model the silicone rubber. Due to the non linear behaviour of the silicone rubber, a non linear analysis by Newton-Raphson method was performed. The two coefficients Mooney-Rivlin formulation was applied to HYPER86 elements. Each model is made of 736 nodes and 434 elements. Figure 5 shows an example of numerical model.

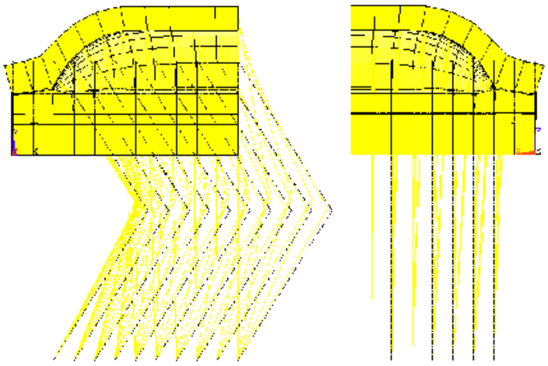

Figure 5 Example of numerical model of isometric tests. Link elements were used to control the admitted strain of the air pocket actuator model

By iterative methods, several numerical simulations were performed in order to find the right geometrical parameters values versus pressure values to satisfy technical specification. Obtained results were:
- chamber base dimensions: 34 x 26 mm (rectangle shape);
- thickness of chamber upper layer: 3 mm;
- maximum strain: 10 mm;
- air pressure value: 0,08 – 0,1 MPa;
- maximum exerted force value: 24 N.

Since dimensions of the chamber were too restrained, it was established to realize a frame made as a matrix 3x2 of chambers, for a total amount of 6 actuators.

Actuator protyping

Prototyping of actuators matrix frame required design and prototyping of a mould in order to strain silicon rubber inside it, silicon rubber, rectangle shape sheets of paper to realize chambers, a sheet metal to allow one side air pockets strains. Ducts for air inlet/outlet were obtained inside the mould; they were made in silicon rubber during the casting of it. Actuator prototyping expects the following phases: with reference to Figure 6, starting from the assembled mould (1), casting of a first layer of fluid silicon rubber for a height equal to 3 mm (2); deposition of 1 mm sheet metal, when the first layer of silicon rubber starts catalyst process (3); casting of a second layer of fluid silicone rubber for a height equal to 2 mm (4); deposition of six sheets of paper (each of them has dimensions equal to 34 x 26 mm), when the second layer of silicon rubber starts catalyst process (5); casting of the last layer of fluid silicon rubber for a height of 2mm (6). Inside mould, 4 pins were placed to create holes for screws in the actuators matrix frame. Screw were used to place actuators on massage device frame.

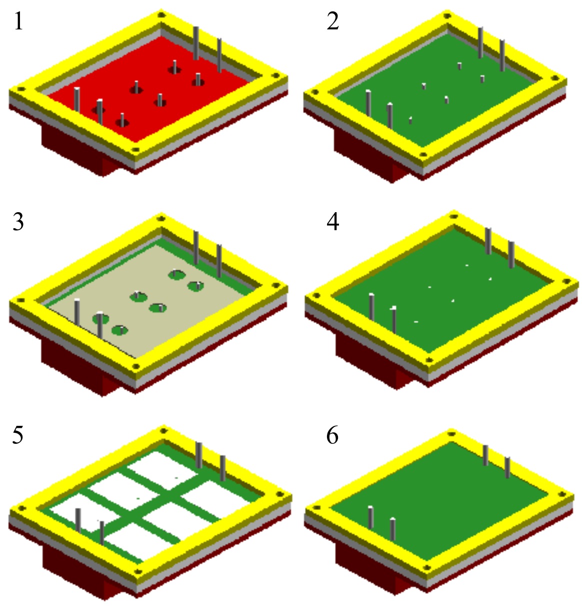

Figure 6 Actuator prototyping phases

Eight matrix frame were realized, for a total amount of 48 air pocket actuators. The final dimension of each actuators frame are equal to 83x104x9 mm. Figure 7 shows an example of actuators matrix frame.

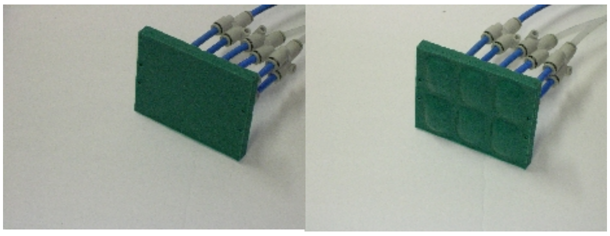

Figure 7 Actuators matrix frame in both configurations: unstrained and strained

Device frame

Massage device frame is made of a *central support frame*, two *support frames for actuators*, the *block system* and *actuators matrices*.

The *central support frame* is made of three components: an upper, a central and a lower module. The entire structure looks like vertebra of the lumbar region and it has two degrees of freedom (dof): rotations of upper and

lower modules around two horizontal axes, realized in the central module. Central module has to be placed in strictly contact with lumbar region; by means of rotation of the other modules it is possible to reproduce the normal curve of the spine, so that central support frame reproduce the anatomical shape of patients. Two buttonholes are realized respectively in upper and lower module: inside each buttonhole a pin is mounted and can move and rotate in it. At the endings of each pin there are two holes in order to install the support frames for actuators.
Each *support frame for actuators* is made of four sub-frames: two are used in the lower part of the lumbar region, two in the upper one. Two support frames for actuators are involved: one for the left part of the spine and the other for the right one for a total amount of eight sub-frames (each sub-frame requires one actuators matrix frame). Each sub-frames has three dof: one translation (the same of the pin inside the buttonhole), a rotation around a vertical axis, a rotation around the symmetry axis of pin. By means of dof it is possible to make support frames for actuators adherent to the patient. In particular: pin translation allows structure movements in order to consider possible presence of adipose layers; rotations allow to encircle all the lumbar region as regards the waistline and the patient curve of the spine. The final shape of the device is settled by manual regulation screws.
The *block system* provides device frame to be adherent to the patient, for a lot time length. It is made of: two lateral belts, joining the right and the left side of the device, to be tight in correspondence of the abdomen; a vertical belt, starting from the upper side of the upper module, divided in correspondence of the shoulders in two inextensible vertical belts to be connected to the lateral ones, on the abdomen. By means of the block system, massage device frame is put on as a rucksack. *Actuators* are mounted on the sub-frames by screws. Figure 8 shows massage device.

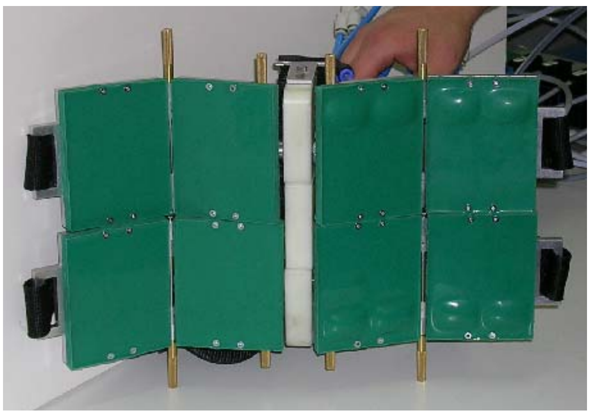

Figure 8 Massage device

Control system
Air inlet/outlet inside air pocket actuators is regulated by pneumatic monostable electro-valves 3/2. The valves control is manged by a CPU 224 S7-200 Siemens PLC. Control softwares were developed and implemented in order to reproduce the above mentioned massage techniques; in particular: surface palmar touch with both hands simultaneously or alternately, in longitudinal, cross and diagonal direction as regards spine; deep palmar touch; hackning; kneading. Figure 9 shows some functioning sequences of controller. Each picture shows the matrix of actuators (here a matrix 6x6 is described; the real device is made of a 6x8 matrix): numbers indicate compressed air inlet sequence, inside chambers. Air inlet in the next chambers means air outlet in the previous one.

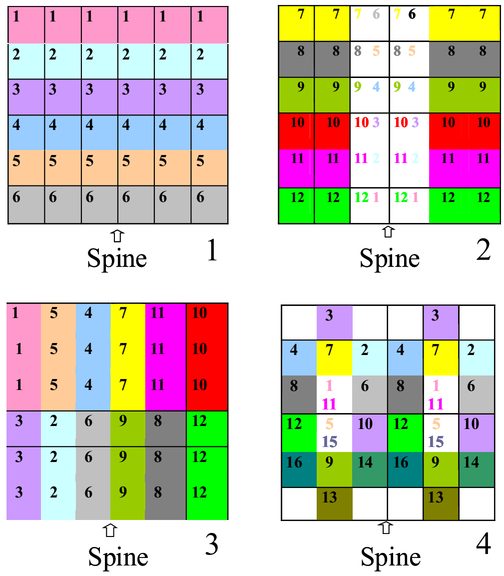

Figure 9 Some functioning sequences of massage: (1) surface palmar touch; (2) deep palmar touch; (3) hackning; (4) kneading

EXPERIMENTAL ACTIVITY

Experimental activity was divided in two phases. In the first phase, experimental validation of the numerical model of actuator was performed by means of isometric experimental tests; in the second one, a first pre-clinic investigation of the massage device was performed with healthy subjects.
In isometric tests, after fixing a strain value and the air pressure value, developed forces of all 48 air pocket actuators were measured; the force value to be referred to numerical model was assessed as the mean value of the 48 measured values. A test bed was realized by commercial profiles in aluminium in order to create a portal structure; in order to measure developed force

values, on the structure a CTCA10K5 load cell (AEP Transducers, Italy) was installed to work in compression mode. The full scale of the load cell is 10 kg; the nominal sensibility is 2mV/V. Strain is fixed by regulating the height of a moving plate, joined to the load cell, by a threaded rod. The same strain and the same pressure value were given as input of the numerical model. The comparison was made between the mean value of the measured force values of the experimental models in its ±2σ range with the output force value of the numerical model.
Figure 10 shows results comparison between the experimental and numerical models.

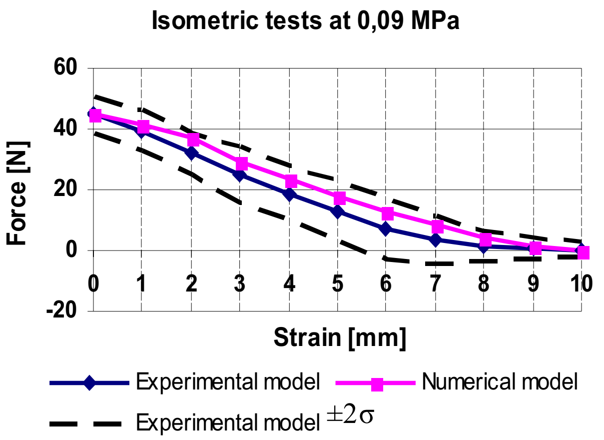

Figure 10 Comparison between results of experimental and numerical models in an isometric test at a pressure value equal to 0,09 MPa

As shown in Figure 10, the behaviour of two models is quite similar: numerical model results are major than experimental ones but they are in the range ±2σ. It means that numerical model is validated.
The pre-clinic investigation was focused on the functional validation of the massage device. Five volunteer healthy subjects, aged between 24 and 40 years, with no low back pain diseases were involved in the investigation. It was performed with PLC software able to reproduce the surface and deep palmar touch massage with both hands, in longitudinal direction as regards spine. Six electro-valves were used: each valve provided air inlet/outlet of each row of the 6x8 actuators matrix. Air pressure value was regulated in the range 0,03 – 0,1 MPa, by a pressure regulator and read by a manometer: qualitative, under 0,03 MPa massage action was inappreciable; over 0,1 MPa massage was felt as fastidious. Massage time length, defined as spent time between two subsequent activations of the same air pocket actuator, was changed in the range 3–9 seconds: qualitative, under 3 seconds massage action was felt as fastidious; over 9 seconds massage was felt as ineffective. No discomfort was recorded as regards device weight equal to about 2 kg. Block system guaranteed adherence to subjects, even after a long time period of about 30 minutes. Sub-frames can be moved very easily. Figure 11 shows the conformability of the massage device put on.

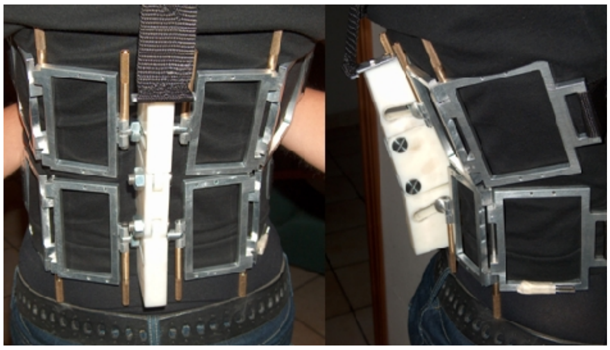

Figure 11 Massage device put on

CONCLUSIONS

An innovative massage device for lumbar region was presented. Device is able to reproduce the traditional massage techniques by means of a 6x8 matrix of air pockrt actuators made of silicon rubber. Too attention was spent for the design of actuators. The upper value of pressure exerted by each actuator is equal to 0,7 kg/cm^2 on a surface equal to $336mm^2$. These values are concordant with values of exerted pressures by physiotherapist and contact surfaces between physiotherapist and patient, measured by test bed realized and described in the present work. Air pocket actuators are placed on a frame able to be adapted to the anatomical shape of patient, for several sizes. Device weight is equal to about 2 kg. Air inlet/outlet inside actuators is controlled by a PLC. The activation of only one air pocket actuator allows to reproduce the massage by thumb; the activation of much more than one air pocket actuator allow to reproduce deep or surface palmar touch, hackning and kneading. Control system can change time length of massage; by a pressure regulator it is possible to set the air pressure value. A pre-clinic investigation on healthy subjects was performed: under 0,03 MPa massage action was inappreciable; over 0,1 MPa massage was felt as fastidious; under 3 s massage action was felt as fastidious; over 9 s massage was felt as ineffective. Subjects submitted to pre-clinic investigation appreciated the use of massage device. Results were encouraging: they suggest to extend experimental investigations to subjects affected by low back pain in order to check the effectiveness of the massage action and, eventually, to obtain precious indication in order to improve the massage device.

ACKNOWLEDGMENTS

Authors wish to thank Piera Giansante, for her precious help during all the activities of the presented research project, and Cristina Bignardi, for the pressure's measurement apparatus.

REFERENCES

1. Ernst, E, Massage therapy for low back pain: a systematic review, Journal of Pain and Symptom Management, 1999, 17-1, pp. 65-69
2. Bell, J., Massage Therapy helps to increase range of motion, decrease pain and assist in healing a clint with low back pain and sciatica symptoms, Journal of Bodywork and Movement Therapies, 2008, 12, pp. 281-289
3. Dario Fiandesio, Massofisioterapia, Utet Torino, 1996
4. Chul-goo Kang; Bong-ju Lee; Ik-xu Son and Ho-yeon Kim, Design of a Percussive Massage Robot Tapping Human Backs, Robot and Human interactive Communication, 2007. RO-MAN 2007. The 16th IEEE International Symposium on , vol., no., pp.962-967, 26-29 Aug. 2007
5. Kume, M.; Morita, Y.; Yamauchi, Y.; Aoki, H.; Yamada, M. and Tsukamoto, K., Development of a mechanotherapy unit for examining the possibility of an intelligent massage robot, Intelligent Robots and Systems '96, IROS 96, Proceedings of the 1996 IEEE/RSJ International Conference on , vol.1, no., pp.346-353 vol.1, 4-8 Nov 1996
6. Jones, K.C. and Winncy Du, Development of a massage robot for medical therapy, Advanced Intelligent Mechatronics, 2003. AIM 2003. Proceedings. 2003 IEEE/ASME International Conference on , vol.2, no., pp. 1096- 1101 vol.2, 20-24 July 2003
7. Koga, H.; Usuda, Y.; Matsuno, M.; Ogura, Yu.; Ishii, H.; Solis, J.; Takanishi, A. and Katsumata, A., Development of Oral Rehabilitation Robot for Massage Therapy, Information Technology Applications in Biomedicine, 2007. ITAB 2007. 6th International Special Topic Conference on , vol., no., pp.111-114, 8-11 Nov. 2007
8. M.G. Antonelli, P. Beomonte Zobel, P. Raimondi, T. Raparelli and G. Costanzo, An innovative brace with pneumatic thrusts for scoliosis treatment, Int. J. of Design & Nature and Ecodynamics, 2010, 5-4, pp 354–367
9. C. Bignardi, P. G. Bondente, V. Rosso, Dispositivo di misura delle pressioni esercitate dai corsetti ortopedici, XXVIII Convegno Nazionale AIAS, Vicenza, Italy, 8-11 settembre 1999

Proceedings of the 8th JFPS International
Symposium on Fluid Power, OKINAWA 2011
Oct. 25-28, 2011

1A2-4

EMG BASED WRIST REHABILITATION USING PNEUMATIC PARALLEL MANIPULATOR

Masahiro TAKAIWA* , Toshiro NORITSUGU*, Daisuke SASAKI*

* The Graduate School of Natural Science and Technology
Okayama University
3-1-1 Tsusimanaka Kitaku Okayama, 700-8530 Japan
(E-mail:takaiwa@sys.okayama-u.ac.jp)

ABSTRACT

To support wrist rehabilitation mechanically, we propose introducing a pneumatic parallel manipulator that provides enough degrees of freedom (D.O.F.)corresponding to wrist motion and is inherent by compliant thanks to air compressibility. We also propose electromyographically based training in which a payload set between the joint angle and the muscle to be trained strengthens this muscle directly. We further propose detecting muscle fatigue based on EMG frequency analysis. The effectiveness of our proposals is confirmed in experiments.

KEY WORDS

Wrist Rehabilitation, Pneumatic Parallel Manipulator,EMG,MPF

INTRODUCTION

Although 2008 physical therapy white paper[1] states that about 12,000 of rehabilitation facilities and 35,000 of physiotherapist (P.T.) are currently available in Japan, at least 80,000 P.T. are needed to serve all rehabilitation facilities equally. The use of robot technology is expected to cope with the shortages of nursing labors in a medical/welfare fields and some mechanical rehabilitation devices have been developed up to now[2][3][4][5][6].

In our focus on mechanical wrist rehabilitation devices motion of human wrist joint and aim at developing a mechanical device to support a rehabilitation training instead of P.T. A pneumatic parallel manipulator[7] is introduced from a view that it has 6 D.O.F. sufficient to correspond to complex wrist motion and has back-drivability resulted from air compressibility, which works as safe function.

In generally, wrist rehabilitation with mechanical system is implemented by giving a payload between joint torque and joint angle/joint angular velocity. We introduce a surface electromyogram (hereafter called EMG) signal instead of a joint torque into the wrist rehabilitation[9][10]. Owing to a rehabilitation based on an EMG, we can select a corresponding muscle and give it a training intensively. EMG signal is also well known to be used as an index of a fatigue, which means a possibility of a rehabilitation with fatigue consideration.

In Japan, medical services under health insurance were limited to 180 days. Using a mechanical device with the proposed scheme, patients can continue the training even in their home. The validity of the proposed system are confirmed through some experiments.

DEVELOPED WRIST REHABILITATION DEVICE

A pneumatic parallel manipulator shown in Figure 1 (a) is introduced as a wrist rehabilitation device[11] from view that its multiple D.O.F. can correspond to the motion of human wrist joint[12][13]. 6 low friction type pneumatic cylinders(Airpel Co. Ltd., 9.3 mm in internal diameter, 150 mm in rod stroke) are employed as driving actuators to form so called Stewart type platform[14]. Figure 1(b) shows the pneumatic driving circuit. The pressure in each cylinder's chamber, p_1, p_2 are detected by a pressure sensor and the

(a)overview

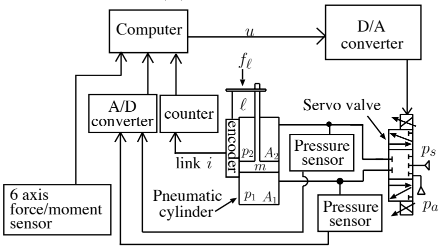

(b)pneumatic driving circuit

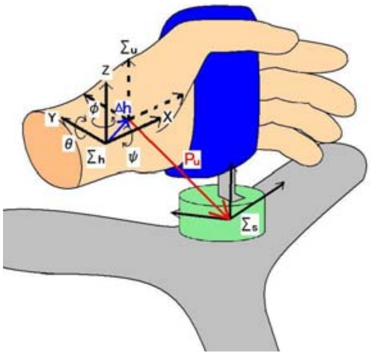

(c)schematic diagram

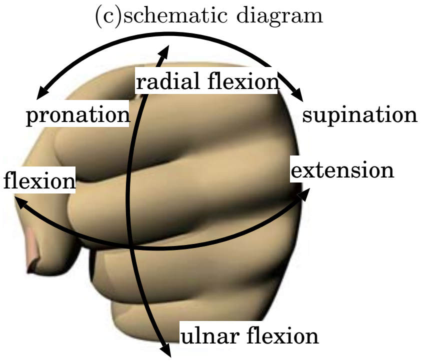

(d)wrist motion

Figure 1: Wrist rehabilitation device

displacement of a piston rod ℓ is measured by a wire type rotary encoder(0.025mm in resolution). A pressure in chambers are regulated by a flow control type servo valve(FESTO MPYE-5), where a supply pressure is set to 500 kPa. Control algorithm is implemented on RTAI a real-time extension of Linux with sampling interval of 5 ms.

Table 1: Control parameters

$\boldsymbol{T_p}, \boldsymbol{T_{pn}}$	Time constant of pressure response
$\boldsymbol{K_p}, \boldsymbol{K_{pn}}$	Steady gain of pressure response
$\boldsymbol{K_v}$	Steady gain between piston velocity and pressure
$\boldsymbol{m}, \boldsymbol{m_n}$	Equivalent mass for one cylinder
$\boldsymbol{b}, \boldsymbol{b_n}$	Viscous coefficient
$\boldsymbol{f_h}$	Force/moment applied by patient
$\boldsymbol{f_{pt}}$	Force/moment applied by P.T.
$\boldsymbol{f_e}$	Force equivalently applied on a link
$\boldsymbol{f_s}$	Force/moment measured by a sensor
$\boldsymbol{A_1}, \boldsymbol{A_2}$	cross sectional area of head/piston side
$\boldsymbol{p_1}, \boldsymbol{p_2}$	air pressure in head/piston side
$\boldsymbol{\ell}$	displacement of piston rod
$\boldsymbol{J}$	Jacobi matrix
$\boldsymbol{T_q}, \boldsymbol{T_{pq}}$	Time constant of filter
$\boldsymbol{u}$	control input (input voltage of valve)

Figure 1 (c) shows the schematic diagram of the manipulator. The position/orientation of the upper platform is expressed by a hand coordinate frame $\boldsymbol{h} = [x, y, z, \phi, \theta, \psi]^T$ using roll-pitch-yaw angle notation. The origin of hand coordinate frame $\boldsymbol{h}$ is set at an above of a center point of an upper platform of a manipulator, which is the same with that of the wrist joint. A patient put its forearm above the upper platform along with x axis of manipulator and receive rehabilitation exercise by holding a jig mechanically attached with a 6-axis force/moment sensor equipped on an upper platform.

Similarly a link vector is defined as $\boldsymbol{\ell} = [\ell_a, ..., \ell_f]^T$ with an element of a displacement of each piston rod.

Force/moment vector at an origin of $\boldsymbol{h}$ is defined as $\boldsymbol{f_h} = [\boldsymbol{f_{he}}^T | \boldsymbol{\tau_{he}}^T]^T = [f_x, f_y, f_z, |\tau_\phi, \tau_\theta, \tau_\psi]^T$, which is obtained through coordinate transformation based on the measured force/moment with a force/moment sensor. Also, $\boldsymbol{f_h}$ acts on a piston rod as an external force $\boldsymbol{f_e}$, which satisfy the following relation from a principle of a virtual work.

$$\boldsymbol{f_h} = \boldsymbol{J}^T \boldsymbol{f_e} \tag{1}$$

, where J is a Jacobi matrix which forms the next relation.

$$\frac{d\boldsymbol{\ell}}{dt} = \boldsymbol{J}\frac{d\boldsymbol{h}}{dt} \tag{2}$$

Figure 1(d) shows a wrist motion, where pronation/supination, radial flexion/ulnar flexion and flexion/extension motion correspond to ψ, θ and ϕ, respectively.

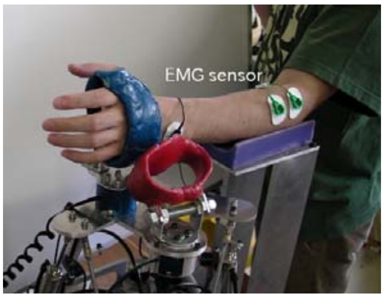

Figure 3: Aspect of rehabilitation based on EMG

WRIST REHABILITATION BASED ON EMG

In generally, rehabilitation is implemented based on the relation between an applied torque and a joint angle/angular velocity.

In this study, we introduce an EMG for a wrist rehabilitation. The EMG based rehabilitation allow us to train a muscle we want to train and evaluate a property of a muscle directly, which is said to be effective in the early period of rehabilitation after a stroke.

Figure 2 (a) shows a control system for an EMG based rehabilitation. The position based impedance control system is employed and the input signal to the impedance model I_{mp} is an integral of EMG shown in Eq.(3) as the index of muscle force. Figure (b) shows a force generation control system included in figure (a).

$$iEMG(t) = \int_{t-T}^{t} |EMG(p)|dp \qquad (3)$$

where an integral time T is set to be 1.0 s. The control parameters are described in Table 1.

Figure 3 shows an aspect of wrist rehabilitation based on EMG, where a patient with EMG sensor put their palm into a mechanical jig attached on the manipulator. Figure 4 shows the align of muscles in a forearm, which are explained in Table 2.

EXPERIMENTAL RESULTS

Stiffness as payload

Figure 5 shows experimental results for setting stiffness ($I_{mp} = K$) between extension/flexion (ϕ) angle and the antagonist muscle (extensor carpi radialis longus and flexor carpi ulnaris), which are dominant muscles for that direction. Figure (a) (b) correspond to the extention/flexion joint angle and iEMG of the both muscles, respectively. In figure (b), we can see the antagonist muscles are activated in tern. In figure (a), red line shows the desired angle calculated

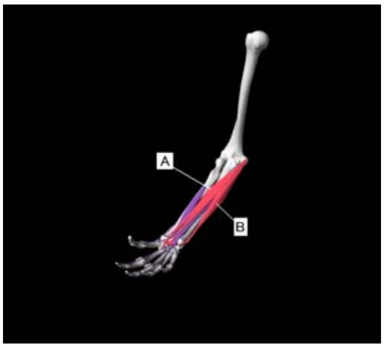

(a)Muscle for Flexion

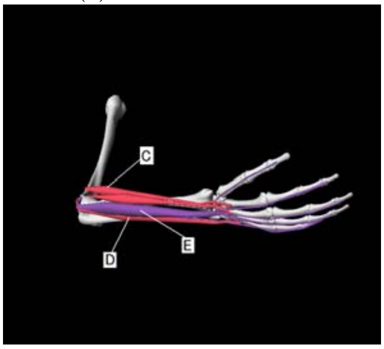

(b)Muscle for Extension

Figure 4: Muscle for Flexion/Extension

by dividing $iEMG$ with stiffness K. An actual angle shown by blue line agrees with its desired one, which shows the reference stiffness is well realized.

Figure 6 shows the results of the same experiment with Figure 5, except for the motion direction is changed to radial flexion/ulnar flexion. The proposed training method correspond to the various direction in wrist motion.

EFFECTIVENESS FOR AVOIDING OF TRICK MOTION

A trick motion sometimes becomes matter in a rehabilitation training. A trick motion means a motion which is implemented not by correct muscle but by another muscle. For example, wrist extension motion is implemented by a motion of whole forearm without using a corresponding muscle. This kind of trick motion occurs sometimes due to the fatigue and it is not easy to avoid under the general torque based rehabilitation.

Figure 7 shows the same experiment with Figure 5 except that the input of impedance model is not an $iEMG$ but a wrist joint torque. In the Figure 7, we can confirm the proper $iEMG$ since trick motion is not occurred in this case.

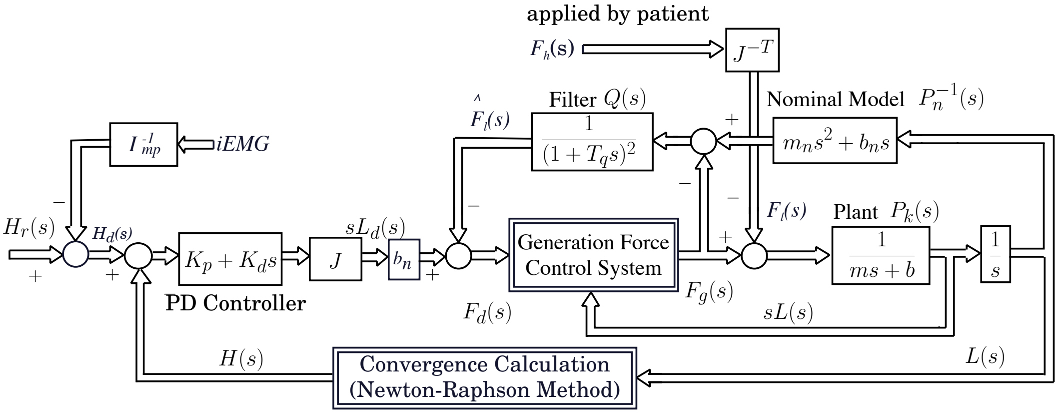

(a) EMG based rehabilitation control system

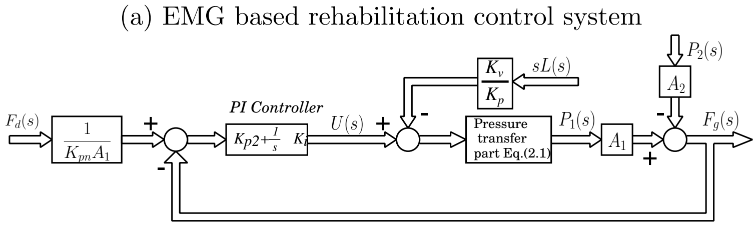

(b) generation force control system

Figure 2: EMG based rehabilitation control system

Table 2: Muscles in forearm

motion	dominant muscle	symbol	support muscle	symbol
Flexion	Flexor carpi ulnaris Flexor carpi radialis etc.	A B	Flexor digitorum superficialis Flexor pollicis longus etc.	
Extention	Extensor carpi radialis longus Extensor carpi ulnaris etc.	C D	Extensor digittorum Extensor pollicis longus etc.	E
Radial flexion	Extensor carpi radialis longus Extensor carpi rasialis brevis	C	Flexor carpi radialis Flexor pollicis longus etc.	B
Ulnar flexion	Flexor carpi ulnaris Extensor carpi ulnaris	A		

In the mean while, Figure 8 shows the case of trick motion, where $iEMG$ is low since the muscle is not activated in spite that angle and torque are large value. Apparently it seems to be a correct rehabilitation motion, but actually there is little effectiveness. Therefore it is not easy to avoid trick motion if the torque based control system is employed.

Figure 9 shows the case of trick motion but the control system is based on $iEMG$ as proposed in Figure 2. In the figure (b), large joint torque is applied but the joint angle shown in the figure (a) is not produced since the $iEMG$ is low (muscle is not activated). Basically, in the EMG based system, rehabilitation motion is not executed even in case of trick motion.

EFFECTIVENESS FOR FATIGUE EVALUATION

In generally, a rehabilitation training is carried out for a long time, therefore it is required for a control system to consider a fatigue of a patient. It is well known that a mean power frequency (MPF) of EMG shifts to the low frequency range along with an increase of fatigue of a muscle[15].

Figure 10(a) shows a MPF of a EMG of the extensor digitorm muscle during continuous squeezing for about 2 minute. A black line is the MPF of EMG calculated using a FFT function in a GSL (GNU Science Library), where the calculation is implemented ev-

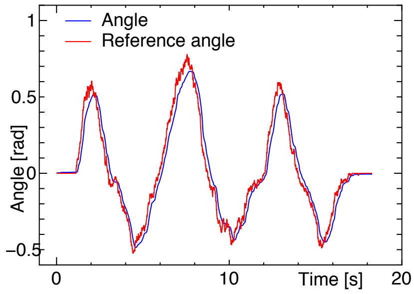

(a) extention/flexion joint angle

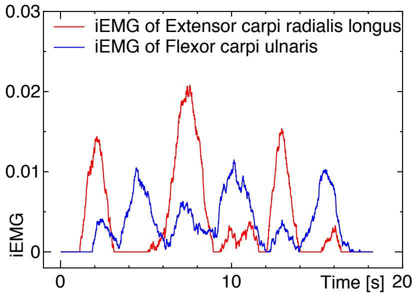

(b) iEMG of antagonist muscle

Figure 5: Rehabilitation with stiffness control (for flexion/extention: ϕ)

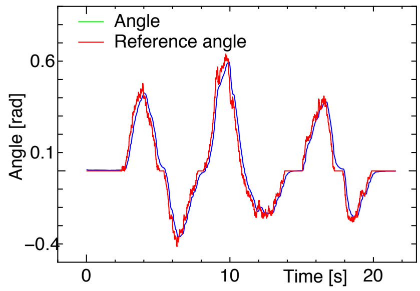

(a) radial flexion/ulnar flexion joint angle

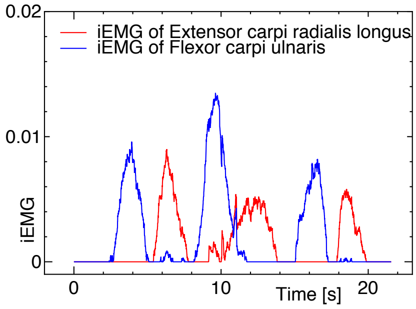

(b) iEMG of antagonist muscle

Figure 6: Rehabilitation with stiffness control (for radial flexion/ulnar flexion: θ)

ery 200 sampling period(=1.0s). A GLS can be used by calling from rehabilitation program implemented with C code and owing to the multi-task function of real time Linux. A gray line shows the raw EMG

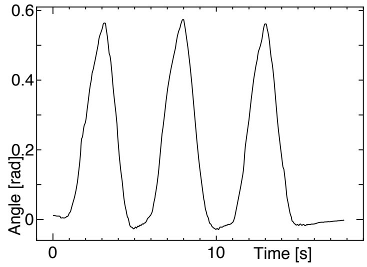

(a)Angle

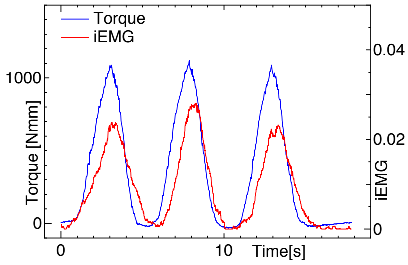

(b)Torque and $iEMG$

Figure 7: Rehabilitation without trick motion (control with torque)

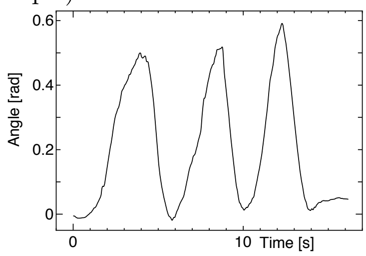

(a)Angle

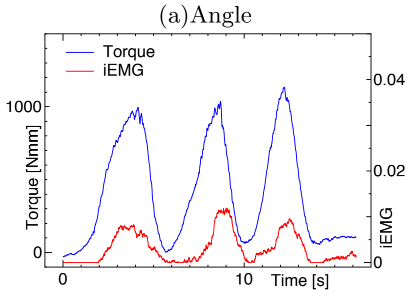

(b)Torque and $iEMG$

Figure 8: Rehabilitation with trick motion (control with torque)

data indicates that a muscle produce a force continuously for 2 min. We can confirm MPF deteriorates gradually to the low frequency range according to the time.

This 2 min. trial is repeated 5 times with 1 min. interval. Figure 10(b) shows the comparison with the result of 5th time. The slope of the line in the case of 5th trial is larger than that of first one, which means the fatigue is increased according to the progress of

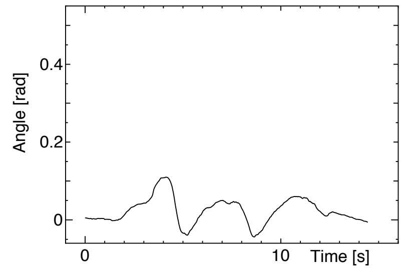

(a)Angle

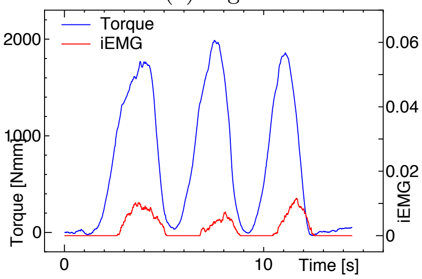

(b)Torque and iEMG

Figure 9: Rehabilitation with trick motion (control with EMG)

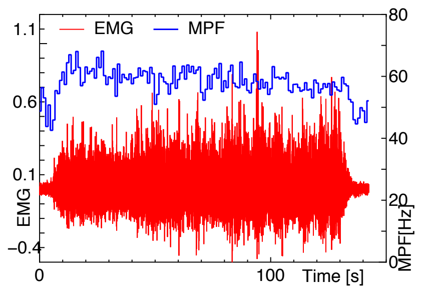

(a)EMG and MPF

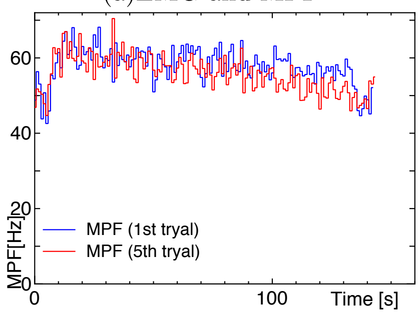

(b)Variation of MPF

Figure 10: Fatigue index with MPF

training motion.

Using the proposed scheme, a P.T. and a patient can confirm the current fatigue property without stopping the rehabilitation training quantitatively and it shows the possibility of regulating a rehabilitation motion based on a fatigue index.

CONCLUSION

In this study, a pneumatic parallel manipulator is introduced as a rehabilitation equipment for human wrist joint from a view point of its remarkable features, such as, multiple D.O.F. suitable for complex wrist motion and safety property due to the air compressibility.

We propose a rehabilitation system based on an EMG in order to give training to a muscle directly. Using the proposed EMG based rehabilitation, the following effectiveness are obtained.

1. We can train a muscle selectively and intensively for variable payload.

2. We can select the pair of a motion and a muscle owing to the multiple D.O.F. robotic mechanism, which allow us to train a muscle even for a motion which the muscle is not dominant for.

3. We can avoid the trick motion since it is not basically occurred in the proposed EMG based rehabilitation.

4. We can evaluate the fatigue of a patient quantitatively in parallel with a rehabilitation training using a real time frequency analysis of EMG.

A concrete evaluation of the proposed system at a rehabilitation facility and the more improvement of rehabilitation method based on EMG are the matter to be settled at present as future works.

REFERENCES

1 Physical therapy white paper, Japan Physical Therapy Association Ed., 2008

2 T. Neuritis, T.Tan-aka, Application of Rubber Artificial Muscle Manipulator as a Rehabilitation robot,IEEE/ASME Trans. on Mechatronics, 1997, **2**-4 pp.259-267.

3 T. Kikuchi, J.Furusho and K.Oda, Development of Isokinetic Exercise Machine Using ER Brake, Proc. of the 2003 IEEE ICRA, 2003, pp.214-219.

4 K. Koyanagi, J.Furusho, U.Ryu and A.Inoue, Development of Rehabilitation System for the Upper Limbs in a NEDO Project, Proc. of the 2003 IEEE ICRA, 2003, pp.4016-4021.

5 S. Hesse, G.S.Tigges, M.Konrad, A.Bardelebem and C.Werner, Robot-assisted arm trainer for the passive and active practice of bilateral forearm and wrist movements in hemiperetic subjects, Archives of Physical Medicine and Rehabilitation, 2003, **84**-6, pp.915-920.

6 H.I.Krebs, B.T.Volpe,D.Williams,J.Celestino, S.K.Charles,D.Lynch, and N.Hogan, Robot-Aided Neurorehabilitation: A Robot for Wrist Rehabilitation, IEEE Trans. on Neural System and Rehabilitation, Vol.15,No.3,2007,pp.327-335

7 M.Takaiwa, T.Noritsugu, Position Control of Pneumatic Parallel Manipulator, Int. J. of Automation Technology,Vol.2,No.1,2009,pp49-55 Positioning Control System

8 M.Takaiwa,T.Noritsugu,D.Sasaki,Y.Masago, Development of Wrist Rehabilitation Equipment Using Pneumatic Parallel Manipulator -Acquiring training motion of P.T. and multiple D.O.F. measurement of wrist property-, Journal of the Robotics Society of Japan, 2007, **25**-8, pp.1251-1258.

9 T.Su.Buchanan,M.J.Moniz,J.P.A.Dewald and W.Z.Rymer,Estimation of Muscle Force about The Wrist Joint During Isometric Using an EMG Coefficient Method, Journal of Biomechanics,Vol.26,No.4/5,pp.547-560,1993

10 T.Ando,M.Watanabe,M.Seki,and M.G.Fujie,Myoelectric Controlled Exoskeletal Robot to Suppress Essential Tremor:Extraction of Elbow Flexion Movement Using STFTs, Proc. of the 5th Int.Conf.of the Advanced Mechatronics,pp.756-760,2010

11 T. Noritsugu, M. Takaiwa and D. Sasaki, Development of Wrist Rehabilitation Equipment Using Pneumatic Parallel Manipulator, Proc. of the 2005 IEEE International Conference on Robotics and Automation, 2005, pp.2313-2318.

12 J.A.Saglia,N.G.Tsagarakis,J.S.Dai,and D.G.Galdwell,A High Performance 2-dof Over-Actuated Parallel Mechanism for Ankle Rehabilitation, Proc. of IEEE ICRA,pp.2180-2186,2009

13 A.Gupta,M.K.O'Malley,Design of a Haptic Arm Exoskeleton for Training and Rehabilitation, IEEE/ASME Transaction on Mechatronics,Vol.11,No.3,pp.280-289,2006

14 D.Stewart, A platform with Six Degrees of Freedom, Proc. Inst. Mechanical Engineers,1965, **180**-15,pp.371-386.

15 Mamaghani Nasser Koleini et.al, Changes in Surface EMG and Acoustic myogram Parameters During Static Fatiguing Contractions until Exhaustion : Influence of Elbow Joint Angles, Journal of physiological anthropology and applied human science 20(2), 2001, pp.131-140.

Proceedings of the 8th JFPS International
Symposium on Fluid Power, OKINAWA 2011
Oct. 25-28, 2011

1A3-1

STUDY ON N-LEVEL PRESSURE HYBRID POWER SUPPLY HYDRAULIC SERVO SYSTEM WITH HIGH EFFICIENCY AND HIGH RESPONSE

Jinshi LU*, Changhai LIU*, Ato KITAGAWA*
Michihito SAITO**, Kazuhito OSAKA***, Kouichi OBA***

* Department of Mechanical and Control Engineering,Tokyo Institute of Technology
2-12-1 Ookayama, Meguro-ku, Tokyo, 152-8550 Japan
(E-mail: ro_ks@cm.ctrl.titech.ac.jp)
** Nippon Accumulator Co., Ltd.
415 Shimizu, Nishikubo, Shizuoka, 424-0038 Japan
***Yuken Kogyo Co., Ltd.
4-4-34 Kamitsuchidana-Naka, Ayase, Kanagawa, 252-1113 Japan

ABSTRACT

In a constant pressure valve-controlled hydraulic servo system, the response is excellent but the efficiency is deteriorated. In a load-sensing pump-controlled hydraulic servo system, the efficiency is excellent but the response is desired to be improved. In this study, an N-level pressure hybrid power supply is proposed to realize high efficiency and high response simultaneously. In this paper, the characteristics and the working principle are described. An experimental setup of a 2-level pressure hybrid power supply is used to conduct the experiments. Experimental results show that the efficiency is improved compared with a conventional constant pressure valve-controlled hydraulic servo system. And another high response type of the N-level pressure hybrid power supply is also proposed. Finally, a new 'Active Charge Accumulator' (ACA) which realizes compact N-level pressure power supply is proposed. The effective area of the piston in the ACA is controlled by switching the On/Off valves to realize the load sensing.

KEY WORDS

Hybrid power supply, High efficiency, High response, Accumulator, ACA

INTRODUCTION

As a control method of the hydraulic servo system, valve-controlled and pump-controlled method are the two conventional methods. In a constant pressure valve-controlled hydraulic servo system, a relief valve is used to keep the supply pressure for the servo valve to be constant. It is well known that the response of a constant pressure valve-controlled hydraulic servo system is excellent. However, because excess flow rate with high pressure is always dumped to the tank through the relief valve, the efficiency of the system is deteriorated. Also the constant supply pressure generates the excess throttling loss in the servo valve when the load varies. Consequently, the efficiency of the constant pressure valve-controlled hydraulic servo system is worse than a load-sensing pump-controlled hydraulic servo system. Regarding a load-sensing pump-controlled hydraulic servo system, several approaches have been widely used, such as the displacement control of a variable displacement piston pump, and the rotational speed control of a fixed displacement pump, etc, to varying load conditions. However, how to realize the high response of a load-sensing pump-controlled hydraulic

servo system is still in the progress [1].
In order to realize high response, it is necessary that there are the valve-control and a high response power supply in the hydraulic system. In order to realize high efficiency, the load-sensing is important. In the paper, a hydraulic servo system by the use of N-level pressure hybrid power supply is proposed to realize high efficiency and high response simultaneously.

N-LEVEL PRESSURE HYBRID POWER SUPPLY

As mentioned above, to achieve high response, the valve-controlled and a high response power supply are essential. And to achieve high efficiency, supply pressure and flow must adapt to the load. N-level pressure hybrid power supply has not only the high response characteristic, but also can adapt to the load. So a hydraulic servo system with N-level pressure hybrid power supply has high efficiency and high response. It is more efficient than the constant pressure valve-controlled hydraulic servo system. At the same time its response is faster than the load-sensing pump-controlled hydraulic servo system.
As shown in dash box in figure 1, a pump with unload valve, N accumulators with different applied pressure and N On/Off valves at the inlet of N accumulators are used to consist of an N-level pressure hybrid power supply. Comparing with the constant pressure hydraulic power supply as shown in dash box in figure 2, it has some differences. First, an unload valve is connected to the side of the fixed-displacement pump. Second, N accumulators are used instead of the relief valve. According to the load, the applied pressures of the N accumulators are set to be in N pressure levels (i.e. p_1, p_2,…, p_n) from low to high.
During the time system running, when an accumulator whose pressure adapt to the load is chosen, the On/Off valve at the inlet of the selected accumulator is opened, and the selected accumulator is connected to the servo valve. Then supply pressure to the servo valve will reach to the pressure of the selected accumulator in a moment. Consequently supply pressure adapt to the load very fast. Moreover, at the beginning period of the selected accumulator connected to the servo valve, the pump supplies the oil to both the servo valve and the accumulator. And the pump is unloaded after the pressure of the selected accumulator reaches to the maximum value. After the pump is unloaded, the selected accumulator supplies oil to the servo valve.
The hydraulic servo system with N-level pressure hybrid power supply has no excess oil flow back into the tank from the relief valve. And because N-level supply pressure to the servo valve by N accumulators can adapt to the load, there is no excess throttling loss in the servo valve. So the efficiency of the hydraulic servo system with N-level pressure hybrid power supply is very high.
And also, in the hydraulic servo system with N-level pressure hybrid power supply, supply pressure will reach

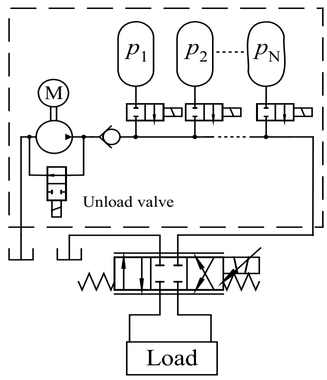

Figure 1 N-level pressure valve-controlled hydraulic servo system

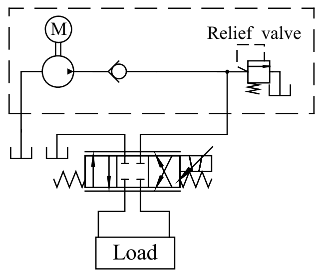

Figure 2 Constant pressure valve-controlled hydraulic servo system

to the appropriate pressure to the load in a moment by switching the accumulator, the response of the system is very high.

ANOTHER TYPE OF N-LEVEL PRESSURE HYBRID POWER SUPPLY

There are N ON/OFF valves at the inlet of the accumulators in the N-level valve-controlled hydraulic servo system as shown in figure 1. The construction of this type of the N-level pressure hybrid power supply is simple. But in this type, supplying flow from an accumulator to the system and filling flow from pump to an accumulator are controlled by the same ON/OFF valve. So that, an accumulator can be filled only the period the pump supplies the oil to the servo valve. Therefore, on the occasion when input signal frequency is very fast, such as 20Hz, accumulators cannot be filled sufficiently.
So another type of N-level pressure hybrid power supply is proposed in this paper. As shown in figure 3, new type has two ON/OFF valves at the inlet of each accumulator. Pressurized oil is supplied from the accumulators to

servo valve through ON/OFF valves (V_{AV1},V_{AV2},…, V_{AVN}). Also, accumulators are filled by pressurized oil from pump through ON/OFF valves (V_{PA1},V_{PA2},…,V_{PAN}). The supply circuit from an accumulator to servo valve is separated from the filling circuit of an accumulator. Consequently, the accumulator can be filled, regardless of whether the accumulator supplies oil to the servo valve or not. It means that the accumulators in new type N-level pressure hybrid power supply can be filled sufficiently in high-frequency switching condition.

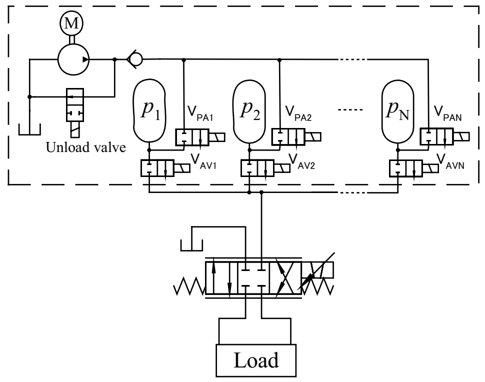

Figure 3 N-level pressure valve-controlled hydraulic servo system (another type)

Because the purpose of experiments in this paper is to verify high efficiency of the N-level pressure hybrid power supply, switching frequency of accumulators is not so high. Therefore, the N-level pressure hybrid power supply as shown in figure 1 is used in this paper.

ACTIVE CHARGE ACCUMULATOR

A new ACA (Active Charge Accumulator) is proposed as illustrated in figure 4 to realize a compact N-level pressure hydraulic servo system.

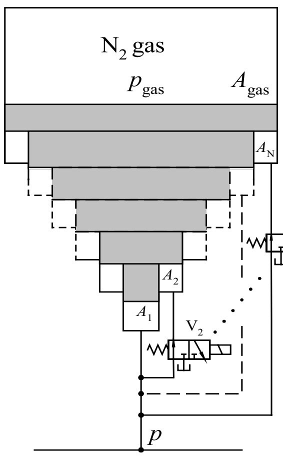

Figure 4 Schematic of the ACA

In a common accumulator, no matter a bladder type or a piston type, the output pressure of the accumulator is determined by the nominal gas pressure charged and the volume of the oil charged and therefore cannot be controlled actively in a moment.
If the output pressure of the ACA can be controlled in N level actively, the proposed N-level pressure system will be very compact just by replacing the N accumulators with the ACA.
The proposed ACA is basically composed of a piston type accumulator. The effective area of gas side A_{gas} is constant. On the other hand, the effective area of oil side A_{oil} is divided in N parts. There are N rooms in oil side. As shown in the figure, the areas of the N rooms are named as A_1, A_2, …, A_N. N rooms except room No.1 are switched to connect with room No.1 or tank by ON/OFF valves.
For example, if all the N-1 rooms except room No.1 are connected to the tank, the effective area of oil side A_{oil} is equal to A_1 and the output pressure of the ACA is calculated as $p_{gas}(A_{gas}/A_1)$. In this case, the output pressure of the ACA will be in the highest level.
If all the N-1 rooms are connected to room No.1, the effective area of the oil side A_{oil} is equal to the sum of A_1, A_2, …, A_N and the output pressure of the ACA is calculated as $p_{gas}A_{gas}/(A_1+A_2+\ldots+A_N)=p_{gas}$. In this case, the output pressure of the ACA will be in the lowest level. In the ACA, by controlling the N-1 valves appropriately, the output pressure of the ACA can be controlled in N levels between the minimum p_{gas} and the maximum $p_{gas}A_{gas}/A_1$. By using the ACA, the proposed N-level pressure system can be realized compactly.

2-LEVEL PRESSURE HYBRID POWER SUPPLY

To illustrate action principle of the N-level pressure valve-controlled hydraulic servo system, a 2-level pressure valve-controlled hydraulic servo system as shown in figure 5 is constructed. As shown in figure 5, there are a high pressure accumulator and a low pressure accumulator. Pressure of the high pressure accumulator is p_H. Its range is 8.4MPa to 8.7MPa. Pressure of the low pressure accumulator is p_L. Its range is 2.6MPa to 2.77MPa. The parameters of the devices are shown in table 1. To switch quickly, two servo valves at the inlet of accumulators are used as the ON/OFF valves. Input signals of two servo valves are -10V to 10V. They are produced by Yuken Kogyo Co., Ltd. (Type: F-LSVG-10-60-10. Frequency: 330Hz@-3dB/410Hz@ -90 °).
To illustrate the system action principle and verify high efficiency of the system, the input signal as shown in figure 6 is used. There are the target displacement and the target force in the period of 20s. As shown in figure 6, when the cylinder reaches 50mm after 9s, it begins to compress the spring. It begins to press on the fixed wall as reaching 67mm at 13.5s. It runs back after 16.5s. So

force control is used from 13.5s to 16.5s in pressing on the fixed wall (Force target: 5700N), and position control is used in other period.

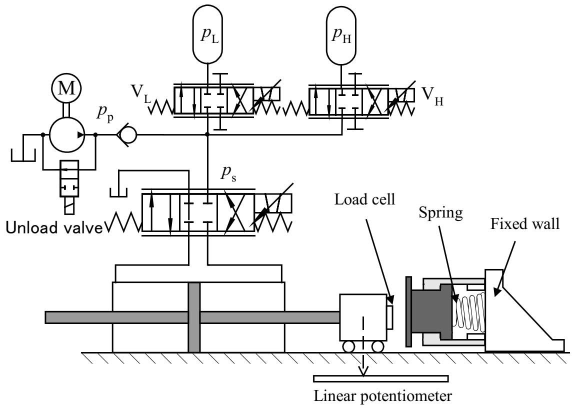

Figure 5 Schematic of experimental setup

Table 1 Specification of the experimental setup

Press force	5700N, max
Cylinder	Piston diameter: 22mm Head diameter: 40mm Stroke: 150mm
Spring	26.1 N/mm
Low pressure accumulator	Volume: 4L
High pressure accumulator	Volume: 4L
Pump	6L/min, 1500rpm

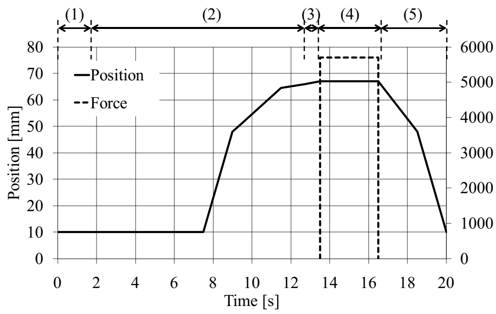

Figure 6 Target position and force

According to unload valve and two valves at the inlet of two accumulators, there are four states in the 2-level pressure valve-controlled hydraulic servo system as shown in table 2. In the state "LL" and "LU", the low accumulator is connected to the system, and p_s (supply pressure to the servo valve for controlling load) is equal to p_L(pressure of the low accumulator). In the state "LL", pump is loaded. It means pump supplies oil to the low accumulator and the servo valve. In the state "LU", pump is unloaded. It means the low accumulator supplies oil to the servo valve. In the state "HL" and "HU", the high accumulator is connected to the system, and p_s is equal to p_H (pressure of the high accumulator). In the state "HL", pump is loaded. It means pump supplies oil to the high accumulator and the servo valve. In the state "HU", pump is unloaded. It means the high accumulator supplies oil to servo valve. So, it can supply two pressures to the servo valve for adapting load by switching V_L and V_H (two valves at the inlet of two accumulators).

To keep the efficiency to be high, the phases of force control are in the high pressure mode and the phases of position control are in the low pressure mode.

Table 2 Four states of power supply

State	Control valve of accumulator	Pump
LL	V_L: 10V; V_H:-10V	Load
LU	V_L: 10V; V_H:-10V	Unload
HL	V_L: -10V; V_H:10V	Load
HU	V_L: -10V; V_H:10V	Unload

Table 3 Switching conditions of valves

	Switching conditions	Change of valve state
Phase(1)→Phase(2) (LL→LU)	p_L > 2.77MPa	Unload valve: unload
Phase(2)→Phase(3) (LU→HL)	Displacement increases to 66mm	1.Unload valve: load 2.V_L: -10V 3.V_H: 10V
Phase(3)→Phase(4) (HL→HU)	p_H > 8.7MPa	Unload valve: unload
Phase(4)→Phase(5) (HL→LU)	Displacement decreases to 66.9mm	1.V_H: -10V 2.V_L: 10V

There are five phases in the position signal as shown in figure 6. The states are shown in table 2. In the initial state, p_L is 2.6MPa and p_H is 8.4MPa. At first, there is the state "LL" in the phase(1). Because the pump is supplying oil to the low accumulator and system, p_s and p_L are rising. After p_L >2.77MPa, it reaches the phase(2) on the state "LU". The low accumulator is supplying oil to the servo valve and the pump is unloaded. Before the force control, it reaches the phase(3) on the state "HL" when the piston reaches 66mm. The pump is loaded and p_s and p_H are rising. After p_H >8.7MPa, it reaches the phase(4) on the state "HU". The high accumulator is supplying oil to the servo valve and the pump is unloaded. When the cylinder returns to 66.9mm after force control, it reach the phase(5) which is the same case as the phase(2). The switch conditions and valve changes between phases are shown in table 3.

As mentioned above, hydraulic power supply can be quickly converted between two accumulators and pump by controlling unload valve and two high-speed valves (V_L and V_H). So it can be achieved that high response and high efficiency of the hydraulic servo system by the use of 2-level pressures hybrid power supply.

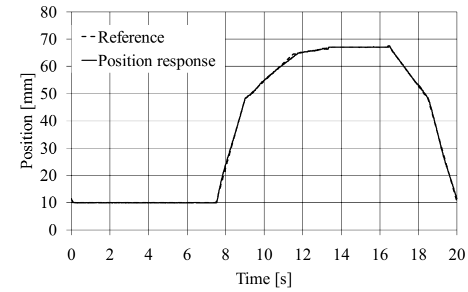

(a) Position

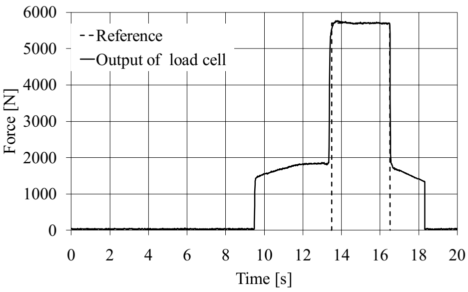

(b) Force

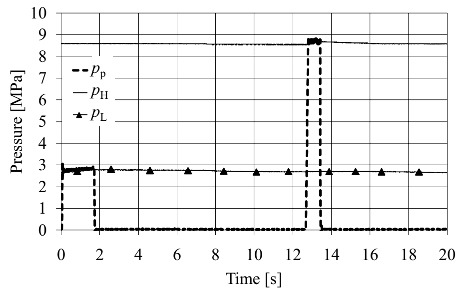

(c) Pressure of pump and two accumulators

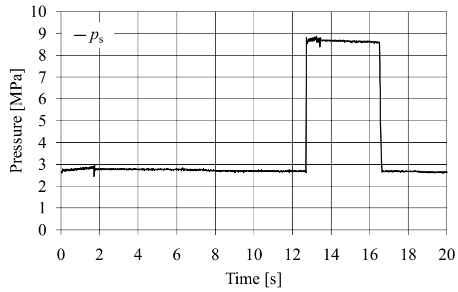

(d) Supplied pressure to the servo valve

Figure 7 Results of experiment I

EXPERIMENTS

Experiment I

To verify the efficiency of the 2-level pressure valve–controlled hydraulic servo system, experiment is preformed. Hydraulic circuit and experimental devices are the same as that shown in figure 5. Position signal is the same as that shown in figure 6.

The servo valve to control the load is produced by Yuken Kogyo Co., Ltd. (Type: LSVG-10-10-10, frequency: 350Hz@-3dB 450Hz@-90 °). The unload valve is produced by Hirose Valve Industry Co., Ltd (Type: HSO-T03-A10F-21). When the servo system is running, p_L is kept between 2.6MPa and 2.77MPa and p_H is kept between 8.4MPa and 8.7MPa.

Experimental results are shown in figure 7. The position response is shown in figure 7(a). The output force is shown in figure 7(b). It is verified that position response and force response are very good by the 2-level pressure valve-controlled hydraulic servo system. The supply pressure for the servo valve to control the load, shown in figure 7(d) adapt to the load. The pump pressure (p_p) and the pressures of two accumulators (p_H, p_L) are shown in figure 7(c). The pump is loaded just when accumulators are filled. Loaded time of the pump in the 2-level pressure valve-controlled hydraulic servo system is very short. It can be concluded that fluid power generated by the pump in the 2-level pressure valve-controlled hydraulic servo system is 93% less than that in a constant pressure valve-controlled hydraulic servo system.

Experiment II

Hydraulic circuit and experimental devices of experiment II are the same as that of experiment I. The pump flow is 15L/min. As shown in figure 8, the sinusoidal signal is used as the position signal. The period is 2s and amplitude is 25mm. When the cylinder reaches 10mm, it begins to compress the spring. The spring force becomes maximum in 25mm which is the maximum position of the cylinder. The spring force is shown in the dotted line in figure 8.

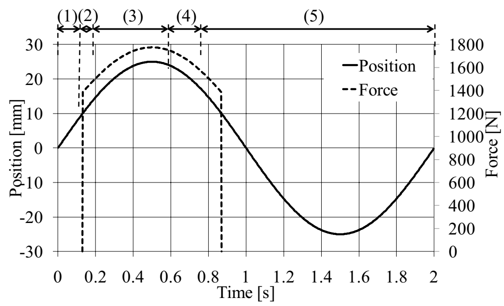

Figure 8 Target position and force in experiment II

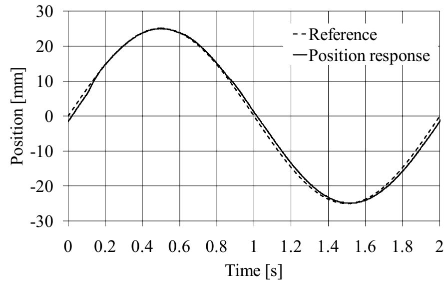

(a) Position

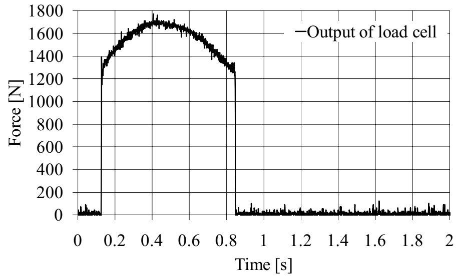

(b) Force

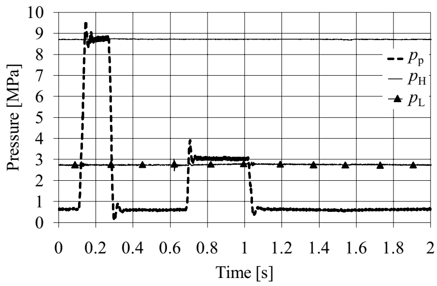

(c) Pressure of pump and two accumulators

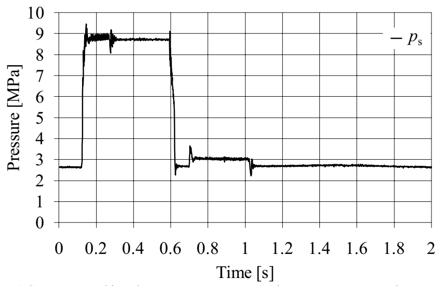

(d) Supplied pressure to the servo valve (p_s)

Figure 9 Results of experiment I

To get high efficiency and good response, the servo system runs on the high pressure mode between 9mm (before compressing the spring) and 24mm (after returning from 25mm). As shown in figure 8, there are the high pressure mode in the phase(2) and phase(3) and the low pressure mode in the phase(1), phase(4) and phase(5).

In the initial state, p_L is 2.7MPa and p_H is 8.4MPa. States of the 2-level pressures hybrid power supply and valve changes between phases are the same as that shown in table 2 and table 3.

There are five phases in the position signal as shown in figure 8. At first, there is the state "LU" in the phase(1). It reaches the phase(2) on the state "HL" when the piston reaches 9mm. After p_H >8.7MPa, it reaches the phase(3) on the state "HU". When the cylinder returns to 24mm, it reaches the phase(4) on the state "LL". After p_L>2.77MPa, it reaches the phase(5) which is the same case as phase(1). The states and switching condition between states are like experiment I.

Experimental results are shown in figure 9. As shown in figure 9(a) and figure 9(b), it is verified that position response and force response is very good by the 2-level pressure valve-controlled hydraulic servo system. From p_s as shown in figure 9(d), it is verified that supply pressure to the servo valve adapt to the load. From p_p, p_H and p_L as shown in figure 9(c), it is verified that the pump is unloaded just when accumulators are filled.

It can be concluded that fluid power generated by the pump in the 2-level pressure valve-controlled hydraulic servo system is 80% less than that in a constant pressure valve-controlled hydraulic servo system.

From two experimental results, it is concluded that the efficiency of the servo system proposed in this paper is greatly improved compared with a constant pressure valve-controlled hydraulic servo system.

CONCLUSION

In this paper, two types of N-level pressure hybrid power supply are proposed. The hydraulic servo system by the use of the N-level pressure hybrid power supply is constructed and its characteristics are described. To realize a compact N-level pressure hybrid power supply hydraulic servo system, a new "Active Charge Accumulator" (ACA) is proposed and the concept is explained. Finally, the efficiency of the hydraulic servo system by the use of 2-level pressure hybrid power supply is verified to be very high experimentally.

Verification of the high response of the hydraulic servo system by the use of N-level pressure hybrid power supply and the characteristics of ACA are under study.

REFERENCES

1. Jinshi LU, Changhai LIU, Michihito SAITO, Kazuhito OSAKA, Kouichi OBA, Ato KITAGAWA, A Study on N-level Pressure Power Supply and its Application in High Response and High Efficiency Hydraulic Servo System (1st Report: Proposal of N-level Pressure Hybrid Power Supply and its Effectiveness in Improving Efficiency), Transactions of the Japan Fluid Power System Society, 2011, 42-3, 46-52.(in Japanese)

Proceedings of the 8th JFPS International
Symposium on Fluid Power, OKINAWA 2011
Oct. 25-28, 2011

1A3-2

DEVELOPMENT OF A NOVEL HYDROSTATIC TRANSMISSION SYSTEM FOR BRAKING ENERGY REGENERATION

Hoang Thinh DO *, Quang Truong DINH **, Kyoung Kwan AHN**, Triet Hung HO ***

* Graduated School of Mechanical and Automotive Engineering
University of Ulsan,
San 29, Muger 2dong, Nam-gu, Ulsan, 680-764, Korea
(E-mail: dohoangthinh2010@gmail.com)
** School of Mechanical and Automotive Engineering
University of Ulsan,
San 29, Muger 2dong, Nam-gu, Ulsan, 680-764, Korea
*** Mechanical Engineering Department
Hochiminh University of Technology
268 Ly Thuong Kiet Strt, Dist. 10, Hochiminh City, 70000, Vietnam

ABSTRACT

A novel hydrostatic transmission (NHST) system is proposed in this paper. The proposed system reduce the energy consumption by recovering the braking energy A hydraulic accumulator, the key component of an energy regenerative system is used in a novel way to recover the braking energy without reversion of fluid flow. Both variable displacement hydraulic pump /motors are used when the system operates in the flow coupling configuration so it is able to match meet the difficult requirements of some industrial and mobile applications. Simulations and experiments were investigated with regard to using primary energy sources and recovering the energy potential of the system. The simulation results indicated that the round-trip efficiency of the system in energy recovery testing varied from 32% to 66% while the experimental results showed that the round-trip efficiency varies from 22 % to 59%.

KEY WORDS

Hydrostatic Transmission, Constant Pressure System, Energy Saving, Flywheel, Hydraulic Accumulator

NOMENCLATURE

A_w	:	Accumulator heat convection area	[m^2]
C	:	Viscous friction coefficient	[Nm.s/rad]
J	:	Moment of inertia of flywheel	[kg.m^2]
K_{sv}	:	DC gain of the mechanism	
n	:	Adiabatic coefficient	[-]
p_0	:	Pre-charged pressure	[Pa]
p_i	:	Pressure at port of accumulator	[Pa]
Q_a	:	Flow rate into accumulator	[m^3/s]
Q_i	:	ideal flow rate of pump/motor	[m^3/s]
Q_l	:	loss flow rate of pump/motor	[m^3/s]
T_{ex}	:	External torque	[Nm]
T_l	:	loss torque of pump/motor	[Nm]
T_m	:	Torque of hydraulic motor	[Nm]
$u(t)$	:	Electric signal control	[V]
u_2	:	Displacement ratio of pump/motor PM_2	
V_0	:	Volume of hydraulic accumulator	[m^3]
V_f	:	Fluid volume in the accumulator	[m^3]
x	:	Relative swivel angle of swash plate	[rad]

α : Displacement ratio [-]
Δp : Pressure difference [Pa]
η_{ac} : Efficiency of accumulator [-]
$\eta_{fl,a}$: Acceleration efficiency of flywheel [-]
$\eta_{fl,d}$: Decelerating efficiency of flywheel [-]
$\eta_{m/p}$: Efficiency of pump/motor PM_2 [-]
ω : Pump/motor speed [rad/s]

INTRODUCTION

Nowadays, the demand of energy is more and more increasing while the natural resources have been exhausted. Besides, the pollution of environment caused by vehicles has been being a serious problem. Therefore, researches about saving energy have been done, especially focus on braking energy regeneration of mobile vehicles, in order to save energy as well as reduce emission. In hydraulic systems, hydrostatic transmissions (HST), constant pressure systems (CPS), electro-hydraulic actuators (EHA) and secondary control systems with two common rails (CPR) have been considered as energy-saving systems. In a HST system, the velocity of the motor is continuously controlled by adjusting the pump flow rate. Thus, it is suitable for earth moving machines such as wheel loaders, tractions and forklifts, etc. [1]. However, the HST system cannot recover kinetic energy of the load, consequently, restricting its energy-saving potential. A CPS system employs a flywheel with an auxiliary hydraulic pump/motor so that it is able to recover kinetic energy of the load and reuse recovered energy. The CPS system studies in [2-3] have shown that these systems are adequate for mobile applications, such as vehicles. In an EHA system, batteries or super-capacitors are employed to store kinetic energy of the load [4]. The EHA system has high recovery efficiency and good performance but its applicability is restricted due to its low specific power and high price. In a CPR system, two common rails are employed: a high-pressure line connected with high-pressure accumulators and a low-pressure line connected directly to a tank. The CPR system is applied to vehicles and shows great energy consumption reduction, according to [5-6].

To inherit the advance of above hydraulic systems, a novel closed-loop hydrostatic transmission system with two hydraulic accumulators is proposed. A high pressure accumulator functions as power source as well as energy storage to absorb the braking energy from the pump/motor PM_2 in braking phase for reusing later.

The remains of this paper are organized as following: section 2 describes the proposed system and its operation; section 3 presents the mathematical model of the system; section 4 shows the analysis of simulation and experiment results. Finally, conclusions are presented in the last section.

DESCRIPTION OF THE PROPOSED HYDROSTATIC TRANSMISSION SYSTEM

In comparison to a traditional HST, two directional control valves (V_1, V_2) and two hydraulic accumulators (HA_1, HA_2) are added, shown in Figure 1.

Table 1 Configurations of the system

V_1	V_2	Configuration
OFF	OFF	Flow coupling config.
ON	---	Pressure coupling config. Driving or reusing phase
OFF	ON	Pressure coupling config. Braking phase

The high pressure accumulator functions as a storage system or a power supply, while the low pressure accumulator functions as a low pressure, high-flow source for the hydraulic pump during recovery time, and boosts the system during driving time. The functions of the two pilot check valves and two relief valves are discussed later for each particular configuration. The flywheel functions as an external load. By controlling the two directional valves V_1 and V_2, the system is able to operate in distinct configurations, shown in Table 1.

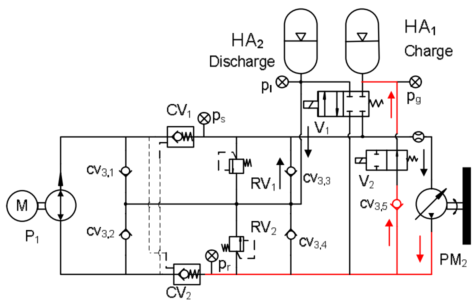

Fig. 1 Braking phase

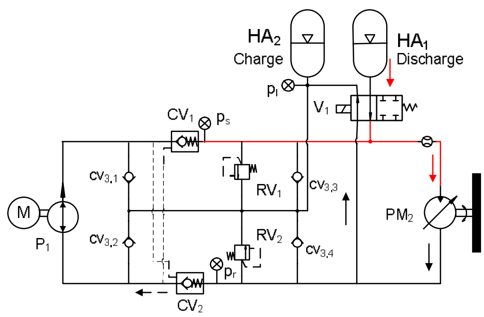

Fig. 2 Reusing phase

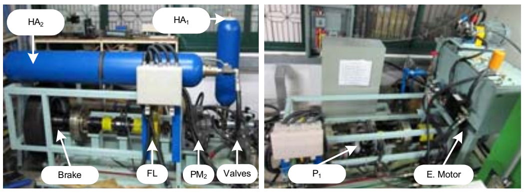

Fig. 3 Photograph of the test bench system

The pump P1 is operated to supply the fluid pressure of the accumulator HA_1. In braking phase, the pump/motor PM_2 functions as a hydraulic pump to transfers the kinetic energy of the flywheel FW to hydraulic energy stored in HA_1 (Figure 1). In driving phase or reusing phase, the hydraulic energy of the accumulator HA_1 is supplied to the pump/motor PM_2, which functions as a hydraulic motor to accelerate the flywheel (Figure 2).

MATHEMATIC MODEL DESIGN

Hydraulic accumulator

The hydraulic accumulator plays an important role in the system. The hydraulic accumulator here is modeled based on its physical attributes. According to [8], the nitrogen gas was assumed to compress and expand based on the adiabatic gas law:

$$pV^n = p_0 V_0^n = p_{\max} V_{\min}^n \tag{1}$$

Then the fluid volume in the hydraulic accumulator HPA was derived as:

$$V_f = \begin{cases} 0, if\ p_i \le p_0 \\ V_0 (1 - \dfrac{p_0}{p_i})^{\frac{1}{n}}, else \end{cases} \tag{2}$$

Hydraulic Pump/Motor

Pump mode

The ideal flow rate, volumetric and mechanical efficiencies of the piston hydraulic pump are expressed in Eq. (3) , (4) and (5), respectively:

$$Q_i = \alpha \omega D_{\max} \tag{3}$$

$$\eta_{vP} = \frac{Q_i - Q_l}{Q_i} \tag{4}$$

$$\eta_{tP} = \frac{\alpha D_{\max} \Delta p}{\alpha D_{\max} \Delta p + T_l} \tag{5}$$

Thus, the actual output flow rate and torque input of the pump are expressed in Eq. (4) and (5), respectively:

$$Q_p = Q_i \eta_{pV} \tag{6}$$

$$T_i = \alpha \Delta p D_{\max} \eta_{tPM} \tag{7}$$

Motor mode

The volumetric efficiency, mechanical efficiency, actual flow rate and actual output torque of the piston hydraulic motor are expressed by Eq. (8) ~ (11), respectively:

$$\eta_{vM} = \frac{\alpha D_{\max} \omega}{\alpha D_{\max} \omega + Q_{loss}} \tag{8}$$

$$\eta_{tM} = \frac{\alpha D_{\max} \Delta p - T_{loss}}{\alpha D_{\max} \Delta p} \tag{9}$$

$$Q_m = \frac{Q_i}{\eta_{vM}} \tag{10}$$

$$T_m = \alpha \Delta p D_{\max} \eta_{tM} \tag{11}$$

Electro-hydraulic displacement control mechanism (DCM)

This mechanism is a fifth-order mechanism, although in practical applications a reduced order model is usually used. We considered it as a first-order system and expressed as:

$$u(t) = \frac{\tau}{K_{sv}} \dot{\alpha} + \frac{1}{K_{sv}} \alpha \tag{12}$$

where $u(t)$ is the electric signal control, τ is the time constant, and K_{sv} is the DC gain of the DCM.

The connecting lines

This mechanism is a fifth-order mechanism, although in practical applications a reduced order model is usually used. We considered it as a first-order system and expressed as:

$$Q_a = v_1 \left(Q_{pa} - Q_{r1} - Q_{ma} \right) + v_2 \left(Q_{mi} - Q_{r2} \right) \tag{13}$$

If the dynamic characteristics of the directional control valves are ignored, v_1 and v_2 are only integer values, as:

$$v_i = \begin{cases} 0 & if\ V_i : OFF \\ 1 & else,\ i = 1,2 \end{cases} \tag{14}$$

Pressure values in the high and low lines are expressed by Eqs. (15) and (16), respectively,

$$p_s = \begin{cases} p_g & if\ V_1 : ON \\ p_l & V_1 : OFF \end{cases} \tag{15}$$

p_g and p_l are the pressure of HPA and LPA, respectively.

$$p_r = \begin{cases} p_l & \text{if } V_1 : ON \\ p_g & \text{if } V_1 : OFF \text{ and } V_2 : ON \end{cases} \quad (16)$$

$$\Delta p = p_s - p_r \quad (17)$$

Flywheel

The dynamic equation of the flywheel is obtained by applying Newton's second law:

$$T_m = J\dot{\omega} + C\omega + T_{ex} \quad (18)$$

SIMULATIONS & EXPERIMENTS

In this study, the HST with flywheel at FPMI Lab at University of Ulsan is used for simulation. Thus, the main parameters of the system are brought in for simulation, shown in table 2.

Table 2 Setting parameters of the system

Components	Capacity	Unit
Hydraulic pump P_1		
Displacement	[-55 55]	cc/rev
Max pressure	250	bar
Hydraulic pump/motor PM_2		
Displacement	[-55 55]	cc/rev
Max pressure	250	bar
Flywheel		
Viscous friction coefficient	0.01	Nm.s/rad
Moment of inertia	4.5	$Kg.m^2$
Hydraulic accumulator HA_1		
Volume	20	Liter
Gas-pre-charge	120	bar
Max pressure	280	bar
Hydraulic accumulator HA_2		
Volume	50	Liter
Gas-pre-charge	2	bar
Directional valve (V_1)		
Max flow rate	140	LPM
Pressure drop slope	15	L/bar
Electric motor		
Power	25	Hp
Speed	1160	rpm

Influence of components on the overall efficiency

A cycle of energy recovery is defined as follows. The kinetic energy of the flywheel is transferred to potential energy in the accumulator in the form of high pressure fluid, which then transfers the stored energy back into kinetic energy in the flywheel. Five components participate in the recovery cycle that consists of flywheel – pump – accumulator – motor – flywheel. Round trip efficiency is defined as the fraction of energy available after reuse and before recovery from the flywheel. This relationship is expressed by Eq. (19):

$$\eta_{rt} = \eta_{fl,d}\eta_p\eta_{ac}\eta_m\eta_{fl,a} \quad (19)$$

Efficiencies of the flywheel caused by friction forces and the accelerator are assumed to be constant and similar in both the deceleration and acceleration times. Determination of the efficiency based on Figure 4 is as follows: Assuming a deceleration time of 3 seconds, the energy of the flywheel decreases from $E_0 = \frac{1}{2}J\omega_0^2$ to $E_3 = \frac{1}{2}J\omega_3^2$ after 3 seconds, so the efficiency η_{fl} is estimated by:

$$\eta_{fl} = \frac{E_3}{E_0} = 0.9 \quad (20)$$

The efficiency of the accumulator was assumed to be a constant of 0.95 in this section. Figure 5 shows the round trip efficiency versus the variation in the pump/motor efficiency. The round trip efficiency of the test bench varied from 32% to 66% when the motor efficiency was in the interval [0.6 0.94] and the pump efficiency was in the interval [0.68 0.92].

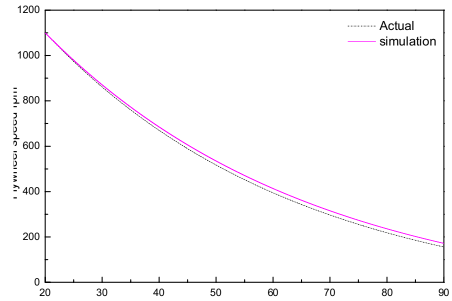

Fig. 4 Flywheel test result

Influence of the pump/motor displacement

The energy recovery procedure is presented as follows. First, the displacement of the PM_2 was fixed for each test, and low pressure accumulator HA_2 was charged to 3bar by an auxiliary pump that is not shown here. The flywheel was driven at 1100rpm to guarantee that the system achieved a steady state condition. Next, the pump P_1 was shut off and valve V_2 was ON instantaneously, while valve V_1 was still OFF. The flywheel ran continuously because of its kinetic energy. Pump/motor PM_2 functioned as a hydraulic pump. Pressure in the driving line was decreased, and pilot check valve CV_2 was closed. Fluid was pumped from the low accumulator HA_2 to the high accumulator HA_1. When the speed of the flywheel reached zero, V_1 was switched to ON. HA_1 became the high pressure power source, powering PM_2 which functioned as a hydraulic motor. The speed of the flywheel increased while the pressure in HA_1 decreased gradually. During this time, fluid moved from HA_1 to HA_2. When HA_1 was out of energy, the speed of the flywheel was reduced. Then, directional valve V_1 was switched OFF, but valve V_2 was ON for the next recovery cycle. After some recovery cycles, the reuse maximum speed of the flywheel was reduced due to the characteristic of the flywheel, and the testing program was stopped. Four motor displacement ratios of 1, 0.75, 0.50 and 0.25 were used in four tests numbered 1, 2, 3, and 4, respectively. To estimate the energy recovery potential of the system, a parameter called round trip efficiency is defined again as:

$$\eta_{rt} = \frac{\frac{1}{2} J\omega^2_{\max(i+1)}}{\frac{1}{2} J\omega^2_{\max(i)}} = \frac{\omega^2_{\max(i+1)}}{\omega^2_{\max(i)}} \qquad (21)$$

where $\omega_{\max(i)}$, $i = 0,1,2\ldots$ is the maximum speed of the flywheel at recovery cycle i.

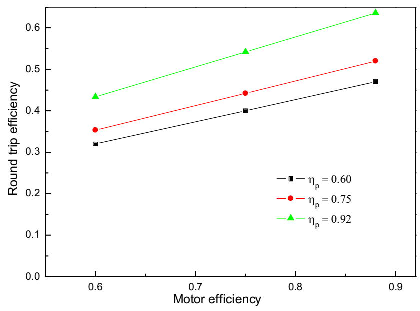

Fig. 5 Round trip efficiency versus pump/motor

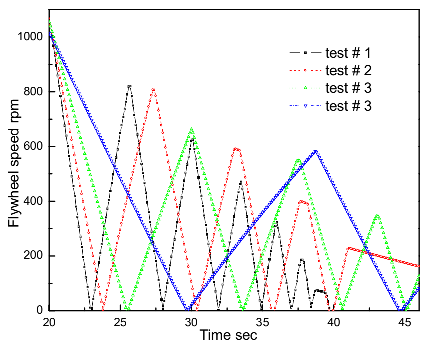

Fig. 6 Round trip efficiency versus motor displacement

The times needed to decelerate the flywheel from maximum speed to zero and to accelerate it from zero to maximum speed are called the braking and accelerating times, respectively. Figure 6 shows the speed curves of the flywheel from our four tests. The braking and accelerating times of the flywheel increased from 2.5 seconds to 10 seconds, respectively, as the displacement ratios decreased from 1 to 0.25.

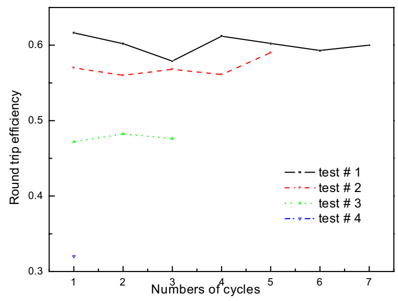

Fig. 7 Round trip efficiency versus cycling numbers

Figure 7 shows the round trip efficiencies of the system versus the cycle number of the four tests. Test number 4 is not illustrated because only one cycle was conducted, and its value of 0.32 matched that of the previous analysis. The round trip efficiencies in tests 1 and 2 were quite high, and varied from 55% to 64%.

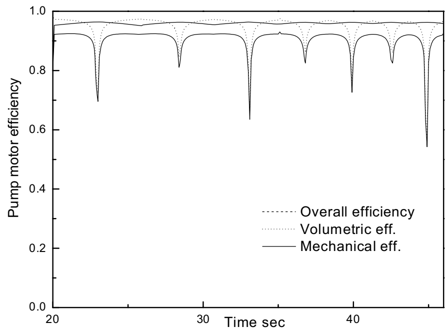

Fig. 8 Pump/motor efficiencies

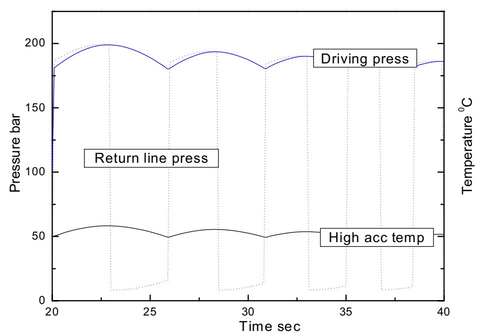

Fig. 9 Parameters of the high accumulator

Figure 8 shows estimates of the volumetric and mechanical efficiencies of the pump/motor in test 1. In this test, both mechanical and volumetric efficiencies of the hydraulic pump/motor were high. Figure 9 shows the simulation values of temperature and pressure in the high pressure accumulator.

Experimental results

This test was used to evaluate the validity of the employed mathematical model. Experimental round-trip efficiency was defined by Eq. (21). The speed of the flywheel in the equation was measured value. The test was conducted with four initial speeds of the flywheel corresponding to four displacement ratios. For each test, when speed of the flywheel reached the setting value, the pump P_1 was shut off and the valve V_2 was ON. When speed of the flywheel was nearly to zero, V_2 was OFF and V_1 was ON and the speed of the flywheel increases again. Figure 10 shows speed curve of the flywheel in two cycles of energy-recovery. The figure also shows that the simulation model was validity in the test.

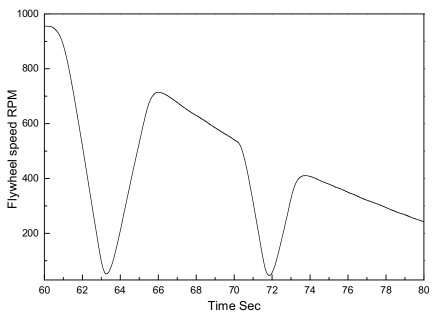

Fig. 10 Speed of the flywheel (u2 = 0.75)

Figure 11 shows simulation and experimental results of pressure in the accumulator HA_1. From the figure, pressure in the accumulator increased from 60^{th} second to 63^{rd} second and it decreased again until 65^{th} second. The next recovery cycle was taken in interval [70^{th} 73^{rd}] second. Obviously, the initial kinetic energy of the flywheel was small the cycle of recovery was short. The measured pressure was a little lower than the simulation pressure, so the measured round-trip efficiency of the test bench would be lower than the estimated value in the previous subsection.

Figures 12 and 13 show more detail about energy transformation in the system. Pressure in the accumulator increased from 120 bar to 130 bar corresponding to the flywheel speed decreased from 100 rad/s to nearly 0 rad/s at 63^{rd} second. Then, speed of the flywheel increased again but the pressure decreased from 130bar down to 120 bar at 65^{th} second. The maximum flywheel's speed was 73 rad/s and the round-trip efficiency was 53 percents.

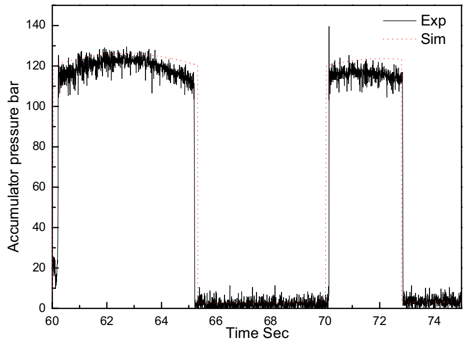

Fig. 11 Pressure in high pressure line

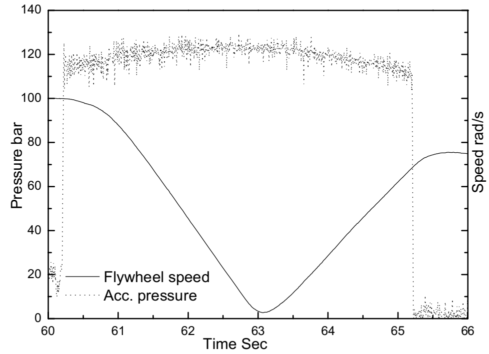

Fig. 12 Measured speed and pressure during regeneration braking

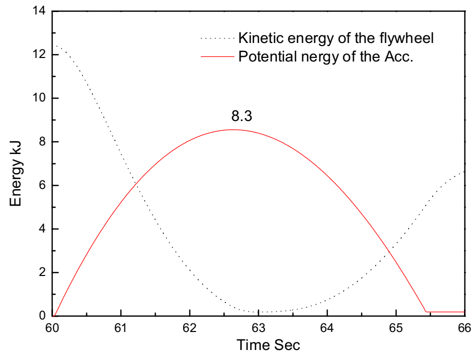

Fig. 13 Measured energy of the system

Figure 13 indicated that the accumulator recovered 8.3 kJ of 12.5 kJ of the kinetic energy of the flywheel and generated again 6.7 kJ kinetic energy of the flywheel in the next cycle. Thus, recovery efficiency in this case was 66.4 % while reuse efficiency was 80.7%.

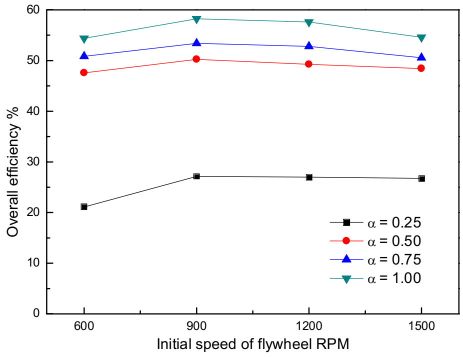

Fig. 14 Measured round-trip efficiency versus initial speed and displacement

Figure 14 showed the measured round-trip efficiency of the system versus initial speed and displacement ratio of PM_2. Experimental results in this subsection confirm the validity of the employed mathematical model of the system. In the test bench the round-trip efficiency varies from 22 % to 59% according to the displacement ratio of the pump/motor PM_2 varies from 0.25 to 1 and the initial speed of the flywheel varies from 600 rpm to 1500 rpm. Pressure p_2 is lightly increases when the directional switches its states.

CONCLUSIONS

A novel energy saving hydraulic system based on HST combined with a hydraulic accumulator was investigated through analysis and modeling.
A model of the hydraulic pump/motor efficiencies was developed and was used to estimate the energy utilization and recovery of the system under different conditions.
The energy utilization of the system was analyzed for three control strategies, which indicated that ON/OFF control achieves a high efficiency with low speed and high torque ratio, and that the HST mode dominates the others with high values of both speed and torque ratios.
Model validation indicated that the recovery energy potential of the system varied from 32% to 66 % depending on the pump/motor displacement. Greater motor displacement ratio corresponded to a greater energy recovery potential.
Experimental results confirmed the validity of the employed mathematical model of the system. In the test bench the round-trip efficiency varies from 22 % to 59% according to the displacement ratio of the pump/motor PM_2 varies from 0.25 to 1 and the initial speed of the flywheel varies from 600 rpm to 1500 rpm.

ACKNOWLEDGEMENTS

This work was supported by grant No. (R01-2006-000-11390-0) from the basic research program of the Korea Science and Engineering Foundation.

REFERENCES

1. Martelli, M. and Zarotti, L., Hydrostatic Transmission with a Traction Control, 22nd ISARC, 2005.
2. Shimoyama, H., Ikeo, S., Koyabu, E., Ichiryu, K. and Lee, S., Study on Hybrid Vehicle Using Constant Pressure Hydraulic System with Flywheel for Energy Storage, Powertrain & Fluid Systems Conference & Exhibition, 2004, 10.4271/2004-01-3064.
3. Ho, T. H. and Ahn, K. K., A Study on Energy Saving Potential of Hydraulic Control System Using Switching Type Closed Loop Constant Pressure System, Proc. of the Int. Conf. JFPS, 2008, **1**-12, pp. 317-322.
4. Yang, H., Sun, W. and Xu, B., New investigation in energy regeneration of hydraulic elevators, IEEE/ASME trans. on Mech., 2007, **12**-5, pp. 519-526.
5. Johri, R. and Filipi, Z., Low-cost pathway to ultra efficiency car: Series hydraulic hybrid system with optimized supervisory control, SAE International Journal of Engines, 2010, **2**-2, pp. 505-520.
6. Matheson, P. and Stecki, J., Modeling and simulation of a fuzzy logic controller for a hydraulic hybrid powertrain for use in heavy commercial vehicles, SAE Powertrain & Fluid Systems Conference & Exhibition, 2003, 10.4271/2003-01-3275.
7. Jen, Y.M. and Lee, C.B., Influence of an accumulator on the performance of a hydrostatic drive with control of the secondary unit, IMechME, 1993, **207**-13, pp. 173-184.
8. Surampudi, B., Nedungadi, A., Ostrowski G. and Montemayor, A. Design and Control Considerations for a Serial Heavy Duty Hybrid Hydraulic Vehicle, SAE, 2009-01-2717.
9. Hao, J., Ikeo, S., Sakurai, Y. and Takahashi, T., Energy saving of a hybrid vehicle using a constant pressure system, Proc. of the Int. Conf. JFPS, 1999, **30**-1, pp. 20-27.
10. Pinches, M.J. and Ashby, J.G. Power Hydraulics, Englewood Cliffs, NJ: Prentice-Hall, UK, 1988, pp.58-62.
11. Ho, T. H. and Ahn, K. K., Modeling and simulation of hydrostatic transmission system with energy regeneration using hydraulic accumulator, KSME, 2010, **24**-5, pp. 1163-1175.

Proceedings of the 8th JFPS International
Symposium on Fluid Power, OKINAWA 2011
Oct. 25-28, 2011

1A3-3

PERFORMANCE TEST OF AN AC SERVOMOTOR DRIVE PUMP CONTROL VALVELESS POWER STEERING FOR HEV COMMERCIAL VEHICLE BY USING A PASSIVE TYPE ELECTRO-HYDRAULIC LOAD SIMULATOR

Hirohisa TANAKA*, Ken-ichi HIRANO* and Yasukazu SATO*

*Department of Mechanical Engineering

Yokohama National University

(Email:tanaka-h@ynu.ac.jp)

79-5 Tokiwadai, Hodogaya, Yokohama, kanagawa, 240-8501 Japan

ABSTRACT

Recent passenger cars have been equipped with electric power steering (PS) for both saving energy and safety cruise assistance such as lane keep or vehicle distance control, however heavy-duty commercial vehicles are still steered by hydro-mechanical PS due to larger steering torque. It is necessary to develop high efficient electro-hydraulic control PS for hybrid commercial vehicles due to saving battery power. The authors presented a new type of AC-servomotor drive pump control valveless PS and showed the efficiency improvement on the power consumption compared to current valve-control PS from 2.5kW to 340W at full slalom steering in 14s of a 4-ton pay-load vehicle. Following to this study, steering feel, restoring performance and insensitivity against kick back torque are examined by using a passive type load simulator with maximum torque capacity of 1500Nm on the basis of the Fiala's two-wheel tire model.

KEY WORDS

Power steering, AC servomotor, Pump control, Hybrid vehicle, Load simulator

NOMENCLATURE

I_z: vehicle inertia in yaw motion
K_a: Control gain of controller
K_f: Front tier cornering power
K_r :Rear tire cornering power
K_s: Servomotor control gain
K_u: Gain of handle wheel torque to steering angle [deg/Nm]
l: wheelbase
l_f: distance from the vehicle center to front tire wheel
l_r: distance from the vehicle center to rear tire wheel
m: vehicle mass
M_s: self-aligning torque
P_l: load pressure in cylinder
Q_l: load flow rate in cylinder
T_h: handle wheel operating torque
T_L: load torque
u: vehicle speed element in x direction
v: vehicle speed element in y direction
V: vehicle speed
y :displacement of hydraulic piston
β:side-slip angle of vehicle
β_f:side-slip angle of front tire
β_r:side-slip angle of rear tire
γ:yaw rate of vehicle
θ:sector gear rotating angle
θ_h: handle wheel operating angle

θ_0:sector gear command angle
μ:dry road-tire friction coefficient
φ:non dimensional side-slip angle

INTRODUCTION

Recent passenger cars have been equipped with electric motor assist power steering for both saving energy and safety cruise assistance such as lane keep or vehicle distance control, however heavy-duty commercial vehicles are still steered by hydro-mechanical PS due to larger steering torque. It is necessary to develop high efficient electro-hydraulic control PS for hybrid commercial vehicles due to saving battery power. In 2008 JFPS Int. conference [1], the authors presented a new type of AC servomotor drive pump control PS and showed the power waste reduction compared to a current valve-control PS from 2.5kW to 340W at full slalom steering in 14s of a 4-ton pay-load vehicle [2]. This simulator is low cost and simple compared to high performance simulators [3]. It is possible to be set up by combining same steering units through the sector gear shafts. The load is controlled by hydraulic piston pressure with using an electro-hydraulic pressure proportional valve.
This paper shows mechanism, steady-state and dynamic characteristics of the AC servomotor drive pump control valveless PS for HEV commercial vehicles with using the electro-hydraulic load simulator.

AC SERVOMOTOR DRIVE PUMP CONTROL PS AND LOAD SIMULATOR

Figure 1 shows schematic figure of the AC servomotor drive pump control valveless PS combined with an electro-hydraulic control load simulator. The PS is a modified type of a current IPS without control valves. Figure 2 is a control system of the valveless PS. The handle wheel steering torque T_h is converted to the command signal of the sector gear shaft rotary angle θ_0 through the torque sensor. The sector gear rotating angle θ is controlled in relation to θ_0 by the 10cc/rev axial piston pump driven by the AC servomotor with maximum rotational speed of 2000rpm and power of 1.3kW.
The output shaft of the PS in Fig.1 is connected to the sector gear shaft of the load simulator through a high torque sensor. The load is controlled by the pressure of the load piston as shown in Fig.3. In Fig.3, a trochoid pump charges to the piston at pressure of 0.2MPa for avoiding cavitation.

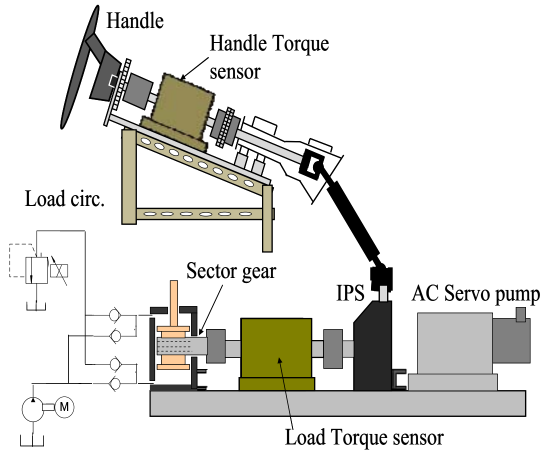

Figure 1 AC Servomotor drive pump control PS and passive type hydraulic simulator

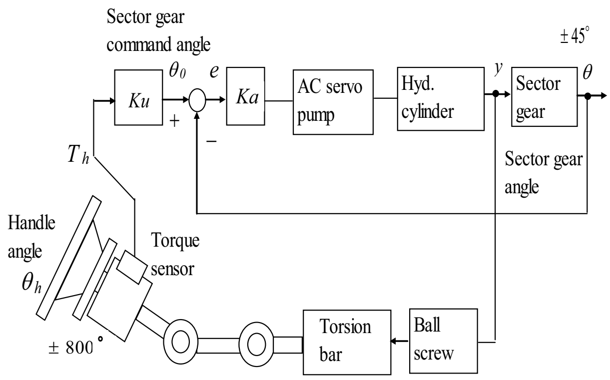

Figure 2 Control system of AC servomotor drive pump control PS

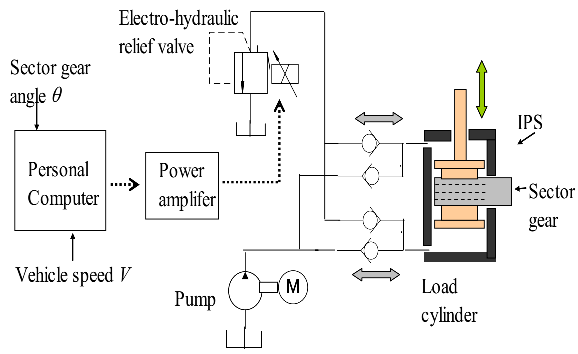

Figure 3 Hydraulic circuit of the load piston

MODELLING OF SELF-ALIGING TORQE OF TIRE

The vehicle motion is expressed by using a simple two-wheel model [4,5] in Fig.4, and slip angle β_f of front tire is modeled as shown in Fig.5.
The self-aligning torque M_s is expressed according to the Fiala's theory [6,7].
For $\theta \geqq 0$,

$$Ms = -\frac{\mu mgl}{2}\left(\frac{1}{6}\varphi - \frac{1}{6}\varphi^2 + \frac{1}{18}\varphi^3 - \frac{1}{162}\varphi^4\right) \quad (1)$$

and $\theta \leqq 0$,

$$Ms = \frac{\mu mgl}{2}\left(\frac{1}{6}\varphi - \frac{1}{6}\varphi^2 + \frac{1}{18}\varphi^3 - \frac{1}{162}\varphi^4\right) \quad (2)$$

where

$$\varphi = \frac{4Kf}{\mu mg} tan\left|\beta_f\right| = \frac{4Kf}{\mu mg} tan\left|\frac{m}{4lK_f}V^2\theta\right|$$

and

$$\beta_f = -\frac{m}{4lK_f}V^2\theta$$

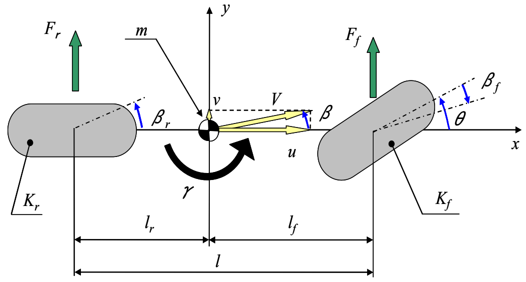

Figure 4 Vehicle turning motion simplified by two wheel model

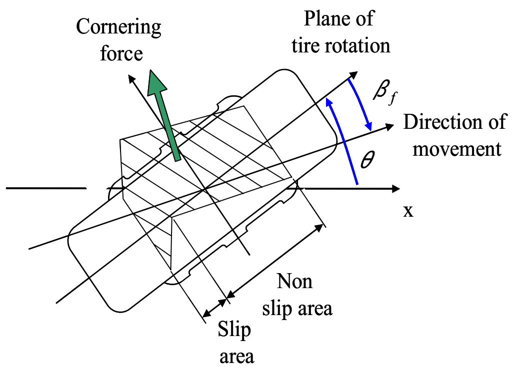

Figure 5 Front tire slip angle of β_f

MEASUREMENT OF SELF-ALIGNING TORQUE

Theoretical self-aligning torque characteristics, θ to Ms, of a 4t truck with m=2000kg and 4000kg at vehicle speed of V=50km/s, and their measurements are shown in Fig.6 and Fig.7, respectively. On the measurement of Ms, the conversion coefficient from load piston pressure P_L to Ms is set to be 229Nm/MPa. The load pressure P_L of the simulator at V=50km/h is 0.5MPa at maximum, of which value is small compared to the stationary steering load pressure of 5MPa.
The parameters of vehicle and road friction are listed in Table1.

Table 1 Parameters of vehicle and tire friction

m	Vehicle mass at no load	2000kg
	Vehicle mass at full load	4000kg
K_r	Cornering power of front wheel at no load	42000N/deg
	Cornering power of front wheel at full load	84000N/deg
l	Length of wheel base	4.6m
μ	friction coefficient of dry asphalt road	0.8

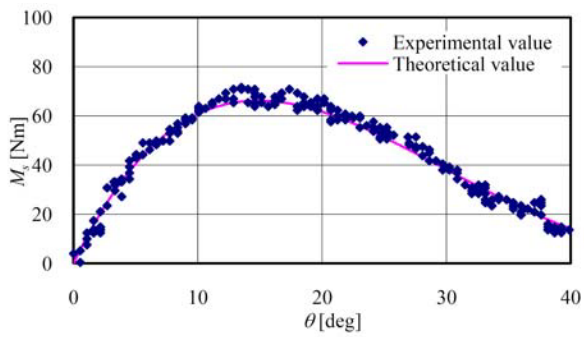

Figure 6 Measurement of self-aligning torque M_s of load simulator at m=2000kg, V=50km/h

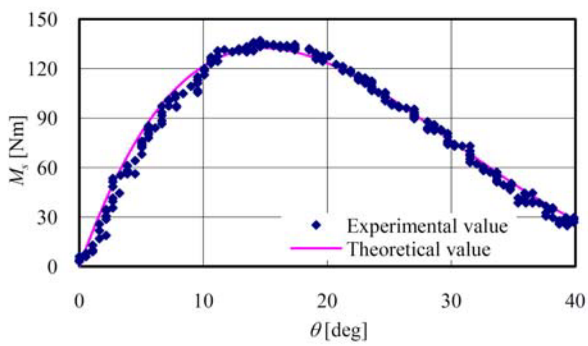

Figure 7 Measurement of self-aligning torque of load simulator at m=4000kg, V=50km/h

HANDLE WHEEL STEERING TORQUE CHARACTERISTICS

The AC servomotor drive pump control PS is easy to set the handle wheel steering torque characteristics. Figure 8 is an example of steering characteristics; relation between steering angle θ_h and handle wheel torque T_h.

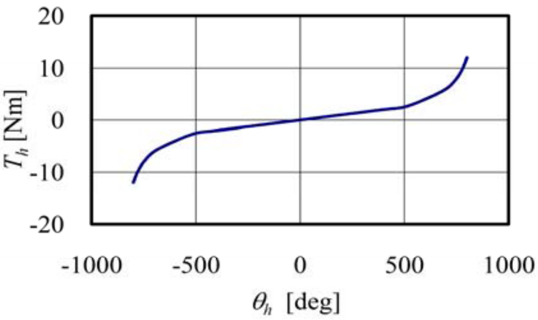

Figure 8 Example of steering characteristics; steering angle θ_h and handle wheel torque T_h

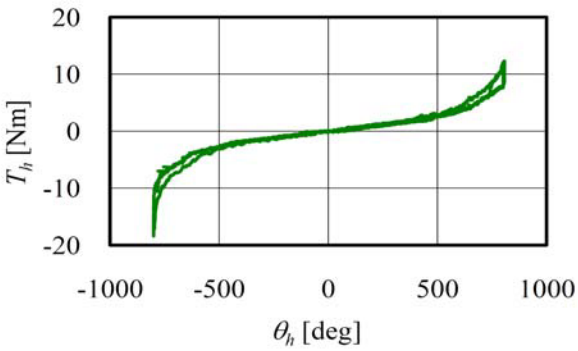

Figure 9 Measured handle wheel torque characteristics of AC servo motor pump control valveless PS; handle angle θ_h to handle torque T_h at a handle wheel steering speed of 30 degs/sec

Figure 9 is measured handle wheel torque characteristics at a handle wheel steering speed of 30 degs/s. We can see low hysteresis of the characteristics.

VEHICLE SPEED COMPENSATING TORQUE FOR HIGHWAY CRUIISING

Handle wheel steering torque is better to be set heavier for stable cruising on highway [8]. In this paper, it is achieved by giving variable stiffness around the handle wheel neutral position in relation to the vehicle speed.
The stiffness is expressed by the slope of the compensating torque T_v/θ_h in the range of neutral to operating angles of 90 degs. The compensating torque T_v is set to be in relation to the vehicle speed V as shown in Fig.10.

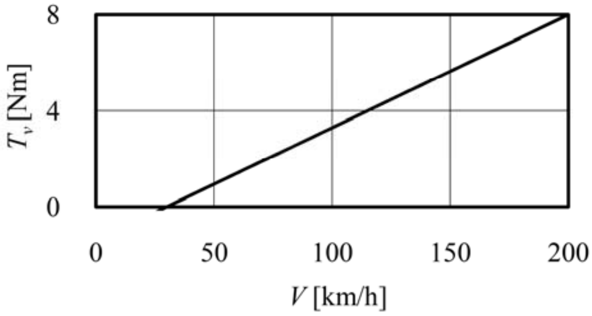

Figure 10 Vehicle speed compensation torque T_v for giving stiffness from neutral to 90 degs around handle wheel neutral position

Figures 11 and 12 are measured examples of the vehicle speed compensated handle wheel torque T_{hv} at low speed of V=20km/h and high speed of V=80km/h. The former is same characteristics shown in Fig.9, but precise expression around the neutral position.

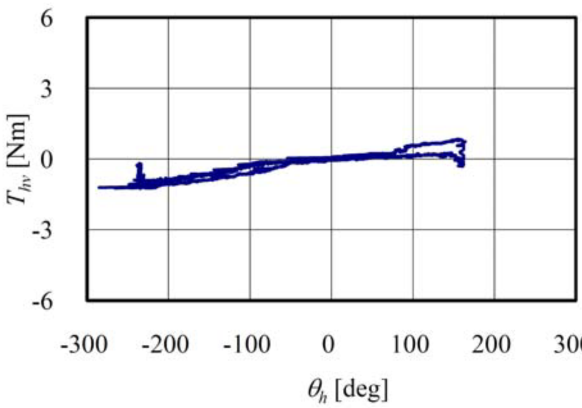

Figure 11 Measured handle wheel torque T_{hv} characteristics at V=20km/h

On the other hand, we can see higher stiffness at V=80km/h in Fig.12.

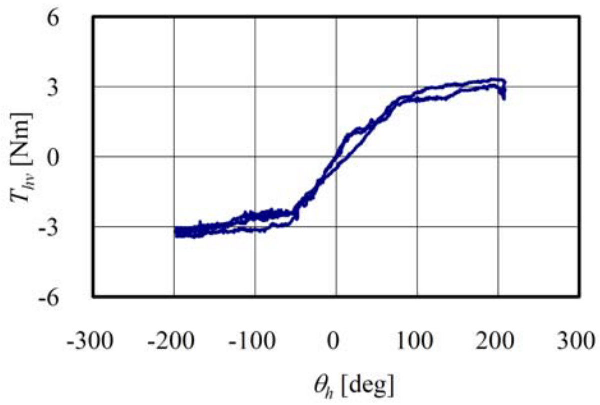

Figure 12 Measured handle wheel torque characteristics at V=80km/h; higher stiffness around neutral position

STEERING WHEEL RESTORING CHARACTERISTICS

Steering wheel restoring characteristics [9] are measured for evaluating PS restoring feeling. Figures 13 and 14 are measured and simulated transients of handle wheel restoring from 720 and 360 degrees to neutral position at V=20km/h, respectively. We can see adequate turning speed in both tests.

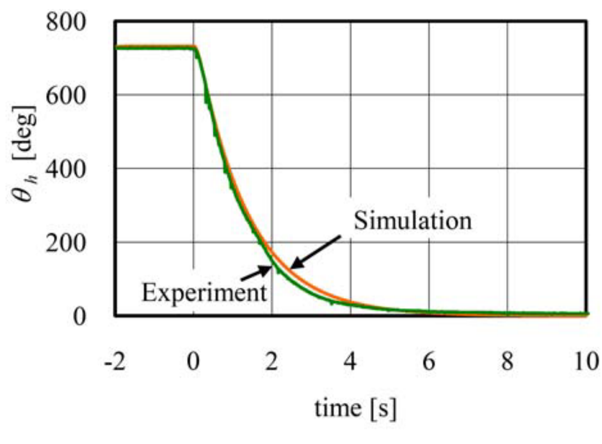

Figure 13 Measured and simulated restoring transients of handle wheel to the neutral position from 720 degrees with steering torque of 8 Nm at 20km/h of vehicle speed

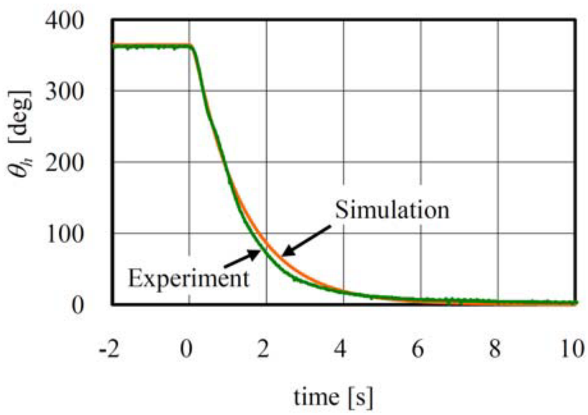

Figure 14 Measured and simulated restoring transients of handle wheel to the neutral position from 360 degrees with steering torque of 3.2 Nm at 20km/h of vehicle speed

INSENSITIVITY AGAINST KICK BACK TORQUE

Heavy duty vehicles require insensitivity against sudden load torque change from tire. As this simulator is a passive type, power is not supplied from outside, the insensitivity is measured by giving step change of pressure in the hydraulic load cylinder. In Fig.15, the steering wheel is operated in slow speed from -400 degrees to neutral.

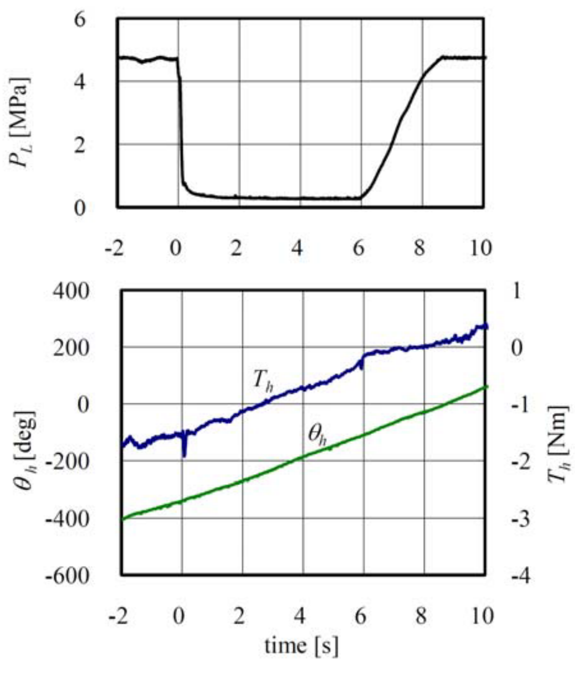

Figure 15 Insensitivity test of the handle wheel torque T_h against kick back torque on the sector gear shaft from 1029 Nm (P_L=4.8MPa) to 64Nm (P_L=0.3MPa)

The load pressure P_L=4.8MPa is equivalent to the sector gear torque of 1029Nm. We can see that the handle wheel steering torque T_h reduces continuously without any sudden change against the step-like pressure changes from 4.8 to 0.3MPa at time t=0.

CONCLUSIONS

This paper shows performance of the AC servomotor drive pump control valveless PS for a heavy duty HEV by using a passive type electro-hydraulic load simulator. The simulator is coupled with same size hydraulic PS units through the sector gear shafts with torque capacity of 1500Nm. The load torque acting on the tire is simulated by the two wheel steering model according to the Fiala's theory, and is controlled by the pressure of hydraulic cylinder of the simulator. By using this test rig, steering feel, steering restoring responsibility, vehicle speed compensation torque characteristics and insensitivity against kick back torque are measured. The AC servomotor drive pump control valveless PS reduces power waste from 2.5kW to 0.34kW for a 4ton pay load commercial vehicle compared to the current valve control hydraulic PS, and gives easy setting of the steering wheel torque characteristics.

ACKNOWLEDGEMENT

Authors would like to thank Mr.Shogo Yokoi for assisting experiment and Yuken Kogyo Co.Ltd for supporting experiments.

REFERENCES

1. K. Hirano and H. Tanaka: Performance of AC servomotor Control Electro-Hydraulic Valve-less Servomechanism, Proceedings of 7th JFPS Int. Symposium on Fluid Power, TOYAMA, P2-08,p.623-628 (2008)
2. K. Hirano and H. Tanaka: A Study on Valve-less Electro-Hydraulic Power Steering for Commercial Vehicles, Transaction of Japan Fluid Power System Society, Vol.40, No.6, p.111-116 (2009)
3. M. Segawa, S. Azuma, S. Nakano, M. Kotake, M. Nagai: Development of Simulator for Evaluation of Steering Systems, Koyo Engineering Journal, No. 168, p.31-34 (2005)
4. JSAE: Technical Handbook of Automobile (No.2 separate volume, Design), p.540-543 (1991)
5. M. Abe: Automotive Vehicle Dynamics (Theory and Applications) , Tokyo Denki University Press., p.10-74 (2008)
6. E. Fiala: Seitenkräften am rollenden Luftreifen, V.D.I.,Bd. 96,Nr.29,11,Okt., p.973-979 (1954)
7. H. Sakai: Engineering of Tire, Grandprix Press., p.159-194 (1987)
8. KYB Corporation: Steering and Dynamics , Sankaidou Press., p.85-102 (1996)
9. T. Miyamoto, F. Momiyama and T. Fujioka: Steer-Restoring Torque Controlled Driving Simulator for Developing Steering Road Feel, SAE paper No.912690, p.549-554 (1991)

Proceedings of the 8th JFPS International
Symposium on Fluid Power, OKINAWA 2011
Oct. 25-28, 2011

1A3-4

PERFORMANCE ANALYSIS OF TURBO-CORER FOR DEEP-SEA DRILLING

Yuichi SHINMOTO* and Eigo MIYAZAKI*

* Technology Development Group, Center for Deep Earth Exploration
Japan Agency for Marine-Earth Science and Technology (JAMSTEC)
3173-25 Showa-machi, Kanazawa-ku, Yokohama, 236-0001 Japan
(E-mail: shinmotoy@jamstec.go.jp)

ABSTRACT

The deep-sea drilling vessel (*D/V*) *Chikyu* is a riser-equipped, dynamically positioned scientific drill ship built for the purpose of scientific research and exploratory expeditions. The vessel is designed to access scientific targets deeper than previously attempted, to depths of 7000 m below the seafloor, in order to recover core samples in the deep oceanic crust. Innovations and improvements of the drilling systems will be vital in order to withstand such extreme environments as temperatures of over 250 degree Celsius (deg. C) and pressures greater than 1000 atm. Efforts are also focused on the development of new types of coring systems including a turbo-corer as part of research into key technologies of national strategic importance. This study introduces the present status in development as well as new conceptual designs and technological work being carried out for coring systems that can achieve high performance and efficiency even under extreme drilling environments.

KEY WORDS

Key words, Turbine, Circulation, Fluid Analysis, Fluid Power, Drilling

INTRODUCTION

The deep sea drilling vessel (*D/V*) *Chikyu* (**Figure 1**) was completed in July, 2005 and measures 210 m in overall length, 38 m in breadth, and has a gross tonnage of approximately 57,000. The top of the derrick is located approximately 121 m above sea level. The vessel has been built for the purpose of scientific research and can carry out deep sea drilling up to a depth of 7000 m below the seafloor to recover core samples in deep underwater formations. The core samples are investigated for scientific analysis in elucidating the factors involved in environmental change, earthquake outbreak mechanisms, and deep biosphere and solid earth cycles below the seafloor [1]. Our work is also part of multinational investigations in these areas under an international scientific effort called the Integrated Ocean Drilling Program (IODP). The *D/V Chikyu* is equipped with a riser subsea system and riser-pipes, currently of 2500 m and in the future 4000 m, along with two heave compensation systems, i.e., passive and active, which allow stable drilling and coring under rough sea conditions. Presently, the *D/V Chikyu* can drill to a vertical maximum depth of 9500 m (in 2500 m water depth) while aiming to eventually reach up to 11000 m (4000 m water depth).

Scientists have recently found remarkable differences in the kinds of rocks present within the upper mantle. While typical mantle rocks appeared in the drilled holes, mantle rock in combination with a significant amount of gabbro, a rock that makes up the lower layer of the ocean crust, has also been cored. Gabbro forms from molten rock, or magma, that rises out of the mantle and hardens deep within the crust. The finding of this rock in the mantle has led researchers to believe they have penetrated a fossilized conduit through which mantle magma has risen into the crust. Researchers have also drilled a major hole into the gabbro rocks of the deep crust. The *D/V Chikyu* is involved in groundbreaking work to reach deep into the earth's crust with the eventual goal of reaching the earth's mantle and, in order to carry out this goal, improved and new drilling technologies are presently under development [2].

Figure 1 Scientific riser equipped deep-sea drilling Vessel *Chikyu*

TURBO-CORER

When drilling to extreme depths, the drill pipes will encounter intense friction so that drill bit efficiency will be lost as power from the rig-surface top drive system lessens. Core recovery can also be expected to decrease and the core samples damaged by problems such as the stick-slip phenomenon. More power at the bottom of the borehole will, thus, be required for extremely deep underwater formations. A conventional core barrel would no longer be effective in vertical holes of up to 7000 m below the seafloor (BSF). A conceptual design for a more powerful and effective turbo-corer is now under development, as shown in **Figure 2**. This turbo-corer consists of a power section (turbine, reduction gear), transmission section (spline coupling, shaft), and bearing section. The turbine motor assembly and inner core tube are retrievable using a rig-equipped wire-line (core line) latch on the pulling neck so that the cores can be continuously recovered. The new method combines an adjustable bent housing sub which is located between the outer barrel, just above the inner core tube.

Most conventional turbo-corers lack reduction gear especially for the smaller size of the BHA, however, we have developed turbo-corers that control and maintain appropriately high torque for efficient drilling. In the past, several types of conventional turbo-corers have been used [3]. With the most commonly used hollow type turbo-corers, the turbine motor section is located in the outer core barrel and is non-retrievable, remaining downhole even when damaged. Development of a corer which allows retrieval of the turbine motor section and reduction gear have enabled constant maintenance and repair at the surface, significantly, during coring operations.

Figure 3 shows the turbine motor assembly and turbine blades (rotors and stators). There are a total of 40 turbine stages on the turbo-corer. The turbine blades rotate at a maximum of 8000 revolutions per minute (RPM) and 100 ~ 400 RPM actual operating rotary speed with an expected operating torque of up to 7500 N-m with the reduction gear. A turbine motor was found to be better for high bottom hole temperatures of over 300 deg. C as well as extended use compared to a positive displacement motor (PDM) which uses elastomer components to prevent vibrations while turning but has a maximum temperature capacity of only 175 deg. C or so and, thus, is prone to friction, melting and bending out of shape [4]. The core bits are especially prone to damage and wear when drilling in extremely hard formations. Hard formations in a deep vertical section create a drilling environment with the risk of increased vibrations which can cause catastrophic damage to the bit components and cutting structure. Thus, special core bits which have passed several land drilling tests have been developed specifically for deep sea scientific and exploratory drilling in soft to hard formations. Analysis of bit performance under various conditions was carried out to determine core bit selection, high core recovery and core quality from ultra deep formations. The newly developed core bits are shown in **Figure 4**. Two types of core bits, the impregnated diamond bit and polycrystalline diamond compact (PDC) bit, were designed particularly for hard formations at extreme seafloor depths. The size of the core bits is 8-1/2 inches. They differ in cutter shape, matrix body, number of diamond tips and total flow area depending on the different formation strata and hardness encountered during coring expeditions. Initial target specifications of the turbo-corer are shown in **Table 1**. The specifications were proposed based on the design of our standard rotary core barrel (RCB) which is retrievable by wireline. A borehole size of 8-1/2" is currently expected for drilling in deeper sections.

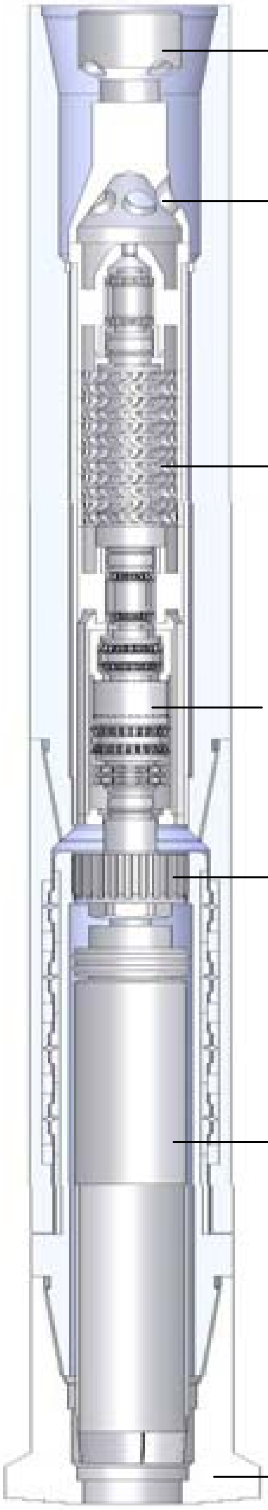

Figure 2 Schematic of Turbo-corer

Figure 3 Turbine motor assembly
Top: turbine motor unit,
Bottom: turbine blades (stators and rotors)

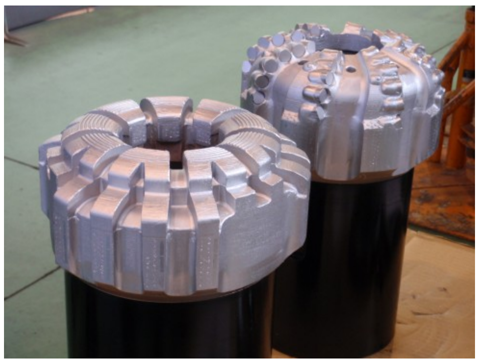

Figure 4 Core bits
(Left: Impregnated diamond, Right: PDC)

Table 1 Initial design specifications of the turbo-corer

Coring Depth (m-BSF)	Up to 7000
Formation hardness	Medium ~ Hard
Core Bit OD (in.)	8.5
Core Sample Size (in.)	3.25
Core Sample Length (m)	4.5
Operating WOB (kN)	10 ~ 100
Operating Torque (N-m)	2000 ~ 7500
Rotary Speed (RPM)	100 ~ 400
Max. Operating Temp. (deg.C)	300
Flow rate (*l* / min)	600 ~ 1800
Mud Weight (g/cm^3)	1.0 ~ 1.8

TURBO-CORER PERFORMANCE TESTS

Turbo-corer tests were carried out to estimate its capability for maintaining the required torque and how much drilling fluid pressure can be reduced with the turbine reduction gear as well as other tests to fine tune the smaller components.

Model experiments

A model of the turbine motor which is a 1/2 scale size of the actual turbo-corer is shown in **Figure 5**. The conceptual design has 40 turbine stages of rotors and stators. However, component tests were carried out for just 5 stages using this scaled model which includes the reduction gear and spline coupling to estimate the performance of an actual size turbine motor. The mud weights in the tests were 1.35 g/cm^3.

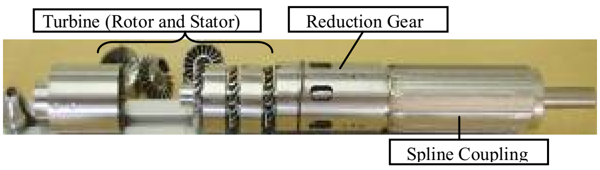

Figure 5 1/2 scale Turbine motor

The actual operating torque required is 3500 N-m with a rotary speed of 100 RPM for the turbine motor including reduction gear. The fluid flow rates into the turbine stages were as high as 600 ~ 1100 *l*/min which are about the same flow rates for a RCB coring system and is, thus, effective for borehole stability and bringing the formation cuttings to the surface. The reduction gear was assembled with the spline coupling connected to the shaft to generate appropriate torque which was then measured by a torque meter.

Results of the model experiments

Experiments of 1/2 scale size were carried out in order to obtain the performance curves for the power section. The actual turbine motor power, efficiency factor and torque can be converted using the Equation below. A specific speed for the waterwheel formula can convert the 1/2 scale size test to the actual turbine motor performance curves. The following Equation (1) can calculate the specific speed of the turbine while Equation (2) is used to calculate torque and power in the full size turbine.

$$N = \frac{\Delta P^{\left(\frac{5}{4}\right)}}{P_t^{\left(\frac{1}{2}\right)}} N_s \qquad (1)$$

$$P_t = \frac{\pi}{30} * T * \left(\frac{N}{1000}\right) \qquad (2)$$

N_s: Specific speed of turbine ($N_s = 66.7$)
N: Rotation (RPM) of 1/2 scale turbine
P_t: Power by one stage of turbine
ΔP: Pressure drop of turbine.
T: Torque

The characteristic curves of the turbine motor are shown in **Figure 6**, as plotted using the Equations. The curves indicate the performance for power P_t, torque T, efficiency factor η and pressure drop ΔP. The turbo-corer is designed for 100 RPM, thus at present, 3500 N-m torque can be generated.

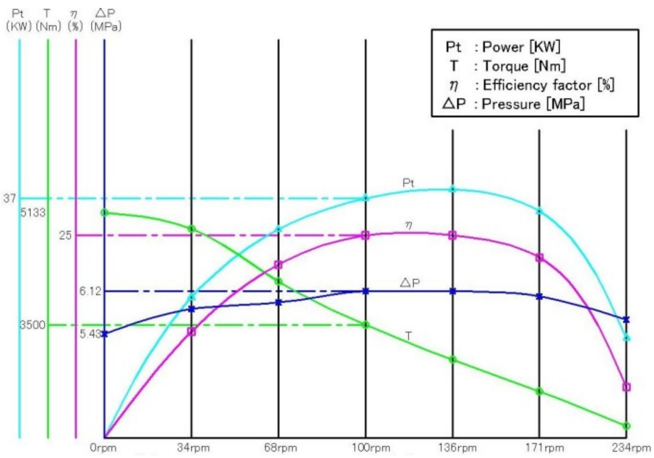

Figure 6 Characteristic curves of the turbine motor

Prototype performance tests

A turbine motor prototype (scale 1/1) was manufactured (Figure 3) and performance tests were carried out using the rotary and torque measurement system assembled with the circulating casing pipe (over 20 m). The instrumented system used at the site is shown in **Figure 7**. The turbine motor assembly (2 ~ 3 units) was installed in the casing pipe and latched. The circulating pump shown in **Figure 8** for an oil-gas field was brought to the site to circulate a maximum flow rate of more than 1000 *l*/min with pressure at approx. 5 MPa.

Such factors as the stall torque *T or* rated torque, rotary speed of turbine motor *R*, flow rate of circulating fluid Q_1, and pump pressure of circulating fluid *P* were recorded. The unit houses a computer as well as data logger. The data scan rate is 100 msec. All of the drilling parameters can be monitored on a display.

Figure 7 Experiment site
(Left: torque measurement system)

Figure 8 Circulation pump for the experiments

In order to evaluate core bit adoptability for various flow rates as well as to investigate turbine motor capability and durability, circulating tests were carried out. The field tests for instrumented circulating were carried out in Hitachi-Omiya city, Japan. The experiments were carried out for a total of 20 days. Fresh water (1.0 g/cm^3 density) was circulated using the pump systems. Test components of 1/1 size scale were also manufactured and further tests carried out. The turbine motor was combined as 2~3 units. The pressure sensors were also installed both above and below the turbine motor section, as shown in **Figure 9,** in order to assess pressure loss.

Figure 9 Pressure sensors above and below the turbine motor section

Results of the experiments

Figure 10 shows the results of the turbine motor performance tests. The reduction gear performance was not included in these results since the gear shaft was damaged during the experiment. The parameters were as follows: Q_1: 450 ~ 1000 *l*/min, *P*: 1.0 ~ 4.2 MPa, *R:* 600 ~ 1020 RPM, and *T*: 100~300 N-m. The rotation speed as well as stall torque increased with regard to the flow rate. Due to overly fast rotation speed, the thrust and radial bearings were damaged, showing the material to be too fragile, so that testing had to stop while fixing the damage and redoing the tests. The fast rotation made the turbine rotor and stator to come into contact, causing severe damage. The bearing section of the turbine motor, thus, requires modification. However, overall, experiments with the turbine motor could be successfully carried out to reach the initial specification torque and rotation speed.

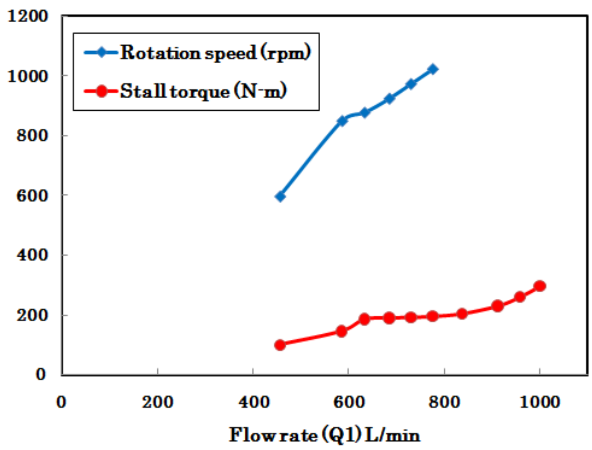

Figure 10 Turbine performance curve
(Torque and RPM with regard to flow rate)

CONCLUSIONS

This paper presents an overview of the technological developments being carried out in our coring systems and equipment as well as an outline of a conceptual study for deep sea drilling to retrieve core samples from the Earth's mantle.

The turbo-corer is presently under development for more power under high temperature conditions. Tests were carried out on a 1/2 scale size model and results were obtained to estimate the power, efficiency factors and torque required for efficient drilling operations.

Prototype performance tests using a turbine motor were also carried out. Component testing against extreme deep sea drilling conditions were carried out in order to clearly define the required improvements and modifications. A specially developed turbine motor section was also evaluated.

REFERENCE

1. Kyo, M. and Isozaki, Y.: Status Report on Deep-sea Drilling Vessel *Chikyu* - The Design and SIT Operation, *Proceedings*, The Seventh The International Society of Offshore and Polar Engineers (ISOPE) Ocean Mining Symposium, Lisbon, Portugal, (2007).

2. Shinmoto, Y. and Wada, K.: Effect of Drill Ship Motions on Core Sample Conditions during the Nankai Trough Seismogenic Zone Experiment, *Proceedings*, the ASME 28th International Conference on Ocean, Offshore and Arctic Engineering, Honolulu, (2009).

3. Tiraspolsky, W.: Hydraulic Downhole Drilling Motors - Turbodrills and Positive Displacement Rotary Motors, III.8 Turbocorers, the Institut Francais du Petrole (IFP), (1985), 204-209.

4. Saito, S., and Sakuma, S.: Frontier Geothermal Drilling Operations Succeed at 500 deg. C BHST, SPE Drilling & Completion, Vol 15, No 3, (2000), 152-161.

Proceedings of the 8th JFPS International
Symposium on Fluid Power, OKINAWA 2011
Oct. 25-28, 2011

1B1-1

AN INDIRECT MEASUREMENT METHOD OF TRANSIENT PRESSURE AND FLOW RATE IN A PIPE USING STEADY STATE KALMAN FILTER

Akira OZAWA*, Kazushi SANADA**

* Department of Mechanical Engineering, Graduate School of Mechanical Engineering
Yokohama National University
79-5 Tokiwadai Hodogayaku, Yokohama, Kanagawa, 240-8501 Japan
(E-mail: d09sb101@ynu.ac.jp)
** Department of Mechanical Engineering
Yokohama National University
79-5 Tokiwadai Hodogayaku, Yokohama, Kanagawa, 240-8501 Japan

ABSTRACT

The purpose of this study is to estimate fluid transients in a pipe using measured pressure values of three points. In this study, method of estimating fluid transients by combining a steady-state Kalman filter and an optimized finite element model of pipeline dynamics was proposed. In this paper, fluid transients in a pipe were estimated off-line by using experimental values in order to show basic performance of the Kalman filter. For comparison, the method of characteristics and was applied to the same data. Estimation results of the Kalman filter show good agreement with the result of the method of characteristics. In addition, Steady flow rate estimated by the Kalman filter was compared with the flow rate measured by flow meters. In this comparison, it was confirmed that the estimated result is proportional to the measurement result.

KEY WORDS

Kalman Filter, Pipe Flow, Optimized Finite Element Model, Simulation

NOMENCLATURE

A	: Cross section of the pipe line
$\boldsymbol{A_p}$, $\boldsymbol{B_p}$	: coefficient matrix of OFEM model
A, B, E, F	: coefficient matrix
c	: wave speed
$\boldsymbol{C}$	: output matrix
G	: coefficient matrix
K_T	: Kalman Filter gain
P	: Solution of Riccati eqation
$\boldsymbol{p}$	: pressure vector
$\bar{\boldsymbol{p}}$	: input vector of OFME model
p_f	: a function of flowrate
$\boldsymbol{Q}$	: covariance vector of system noise
$\boldsymbol{q}$	: flow rate vector
R	: covariance of sensor noise
t	: time
v	: sensor noise
w	: system noise
x	: state variable of OFEM model
ρ	: Density

Subscript

N	: number of grid point
up	: upstream end
mid	: mid point
$down$	: downstream end

INTRODUCTION

Two major methods of understanding fluid transients are measurements and simulations. However, pressure and flow rate of a point which is not a measurement point cannot be obtained by the measurement with a sensor. Moreover, the simulation that uses the approximate expression includes error margin. Recently, the study on the technique for combining two techniques, the measurement and the simulation, is done. For example, in measurement of the flow rate in a pipe, remote measurement of instantaneous flow rate was proposed by Yokota (1991)[1)] and a real time measuring method of unsteady flow rate and velocity employing a differential pressure in a pipe was proposed by Zhao(1986)[2)]. In these techniques, the flow rate of one point was obtained from the measurement of the pressure of two points by using the hydraulic pipeline dynamics.
On the other hand, Measurement-Integrated Simulation was proposed by Funamoto and Hayase (2004)[3)] .In these techniques, a lot of calculations are required, because fundamental equations of three dimensional or two dimensional flow are solved.
In this study, method of estimating fluid transients by combining a steady-state Kalman filter and an optimized finite element model (OFEM model) of pipeline dynamics was proposed. In this estimation, it is expected that not only flow rate of various points but also pressure of various points can be measured indirectly from measured pressure of three points without accurate setting of initial condition.

OUTLINE OF INDIRECT MEASUREMENT METHOD

OFEM model is based on the equation of motion of fluid flow in a circular pipe and the continuity equation. Based on an interlacing grid system as shown in Fig.1, assuming one-dimensional flow, and neglecting a convection term, the equation of motion of fluid flow in a circular pipe is written as follows [4)]

$$\frac{\mathrm{d}\boldsymbol{q}}{\mathrm{d}t} + \frac{A}{\rho}\boldsymbol{Bq} + \frac{A}{\rho}\boldsymbol{F}\bar{\boldsymbol{p}} + \boldsymbol{p_f} = 0 \tag{1}$$

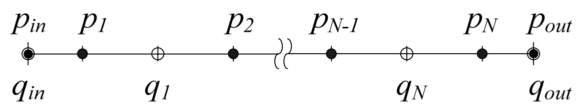

Fig.1 Interlacing grid system

The continuity equation is written as follows.

$$\frac{\mathrm{d}\boldsymbol{p}}{\mathrm{d}t} + \frac{\rho c^2}{A}\boldsymbol{Eq} = 0 \tag{2}$$

Where, the matrices $\boldsymbol{B}$, $\boldsymbol{E}$ and $\boldsymbol{F}$ are calculated from the finite element approximation. Elements of the vector $\boldsymbol{p}$ and $\boldsymbol{q}$ are flow rate variable and pressure variable at the grid points

$$\boldsymbol{q} = \left[q_{up}, q_1, \ldots q_{N-1}, q_{down}\right]^T \tag{3}$$

$$\boldsymbol{p} = \left[p_1, p_2 \cdots p_N\right]^T \tag{4}$$

$\bar{\boldsymbol{p}}$ is pressure input of OFEM model and $\boldsymbol{p_f}$ is a function of flowrate at grid point.

$$\bar{\boldsymbol{p}} = \left[p_{up}, p_{down}\right]^T \tag{5}$$

$$\boldsymbol{p_f} = \left[p_f\left(q_{up}\right), p_f\left(q_1\right) \ldots p_f\left(q_{N-1}\right), p_f\left(q_{down}\right)\right]^T \tag{6}$$

OFEM model can be written as follows by a state space equation[4)]

$$\frac{\mathrm{d}\boldsymbol{x}}{\mathrm{d}t} = \boldsymbol{A_p x} + \boldsymbol{B_p}\bar{\boldsymbol{p}} \tag{7}$$

Where, the state variable vector is

$$\boldsymbol{x} = \left[\boldsymbol{q}^T, \boldsymbol{p}^T\right]^T \tag{8}$$

When the measurement noise is considered, OFEM model can be written as follows by a state space equation[4)]

$$\frac{\mathrm{d}\boldsymbol{x}}{\mathrm{d}t} = \boldsymbol{A_p x} + \boldsymbol{B_p}\bar{\boldsymbol{p}} + \boldsymbol{Gw} \tag{9}$$

$$p_{mid} = \boldsymbol{Cx} + v \tag{10}$$

Filer equation of Kalman Filter is written as follows.

$$\hat{x}[n] = \boldsymbol{A_p}\left(\boldsymbol{I} - \boldsymbol{K_T C}\right)\hat{x}[n-1] + \boldsymbol{A_p K_T} p_{mid} + \boldsymbol{B_p}\bar{\boldsymbol{p}} \tag{11}$$

Where, $\boldsymbol{K_T}$ is Kalman Filter gain, $\boldsymbol{P}$ is solution of Riccati eqation.

$$\boldsymbol{K_T} = \boldsymbol{PC}^T\left(R + \boldsymbol{CPC}^T\right)^{-1} \tag{12}$$

$$\boldsymbol{P} = \boldsymbol{A}(\boldsymbol{P} - \boldsymbol{PC}^T[\boldsymbol{CPC}^T + R]^{-1}\boldsymbol{CP})\boldsymbol{A}^T + \boldsymbol{GQG}^T \tag{13}$$

Where, $\boldsymbol{Q}$ is covariance vector of system noise, R is covariance of sensor noise

$$\boldsymbol{Q} = E(\boldsymbol{w}[n]\boldsymbol{w}[n]^T) \tag{14}$$

$$R = E(v[n]^2) \tag{15}$$

A block diagram for estimation is illustrated in Fig.1. Three sensors are attached at a pipe to pick up transient pressure at the upstream-end p_{up}, the mid-point p_{mid}, and the downstream-end p_{down}. In this study, sensor noise of p_{mid} is considered as measurement noise. The steady state Kalman Filter is used to estimate the fluid transition. In OFEM model, after the observation time passes enough, the Kalman filter is settled to the filter of a fixed coefficient. Therefore, it only has to request the steady state Kalman filter gain, and the Riccati equation need not be solved in real time.

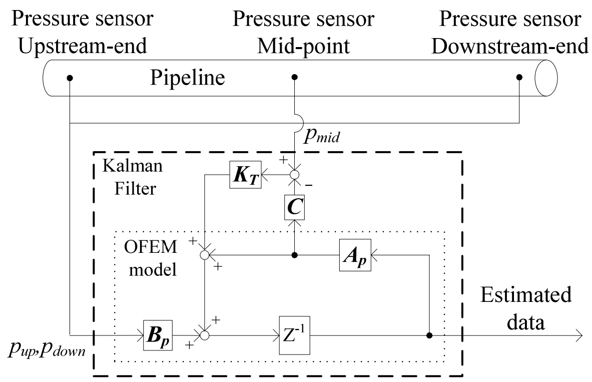

Fig.2 Schematic diagram of a proposed Kalman filter

COMPARISON WITH A METHOD OF CHSRACTERISTICS

Fluid transients in a pipe were estimated off-line by using these experimental values in order to show the basic performance of the Kalman filter. Fig.2 shows experiment instrument. Test parameters are listed in Table 1. Working fluid was tap water of 16 degree Celsius. Three pressure sensors were attached at the pipe to pick up the transient pressures at upstream-end, the mid-point, and, the downstream-end. The experimental data is shown in Fig.4. By switching the spool valve, the upstream pressure was increased quickly. Because of pressure wave travelling along the pipe, the mid-point pressure and the downstream-end pressure showed oscillations.

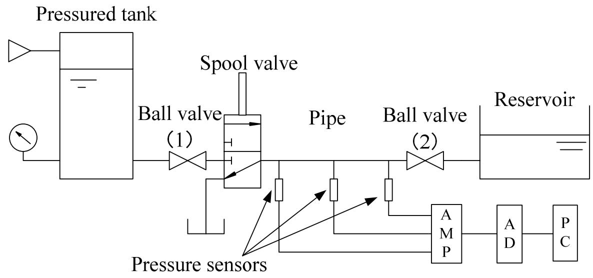

Fig.3 Experimental pipeline and measurement system

Table1 Parameters for experiment and simulation

Wave speed	1310 m/s
Tank pressure	0.2 MPa
Length of pipe	36 m
Number of elements	5
Diameter of pipe	10 mm
Kinematic viscosity	1.05 cSt
Density	999 kg/m^3
Sampling time	2 ms

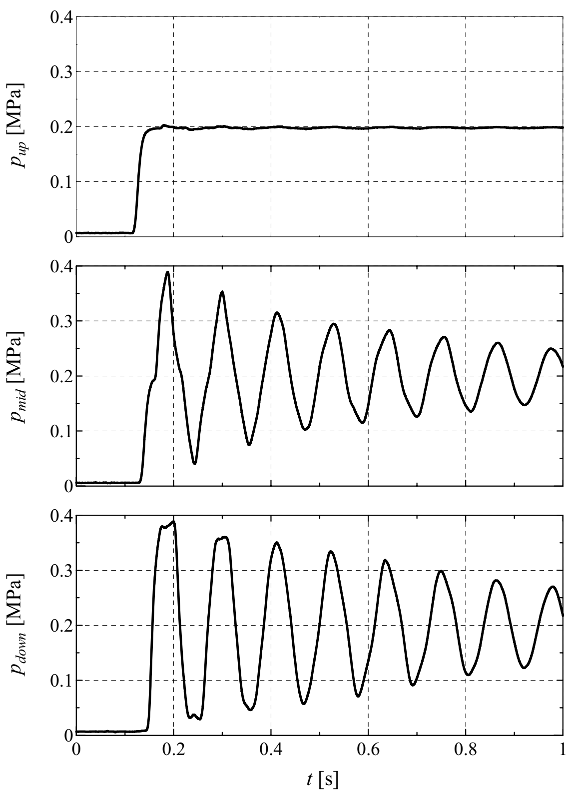

Fig.4 Experimental results of pressures p_{up}, p_{mid} and p_{down} used for the Kalman filter

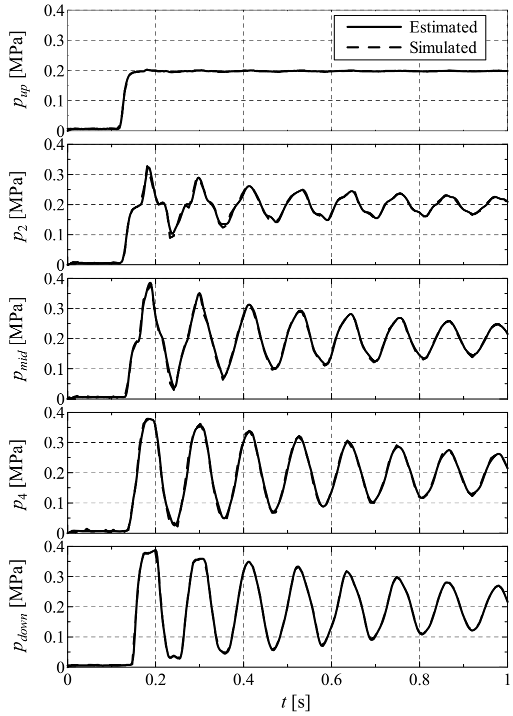

Fig.5 Transient flow rates obtained by the Kalman filter and the method of characteristics

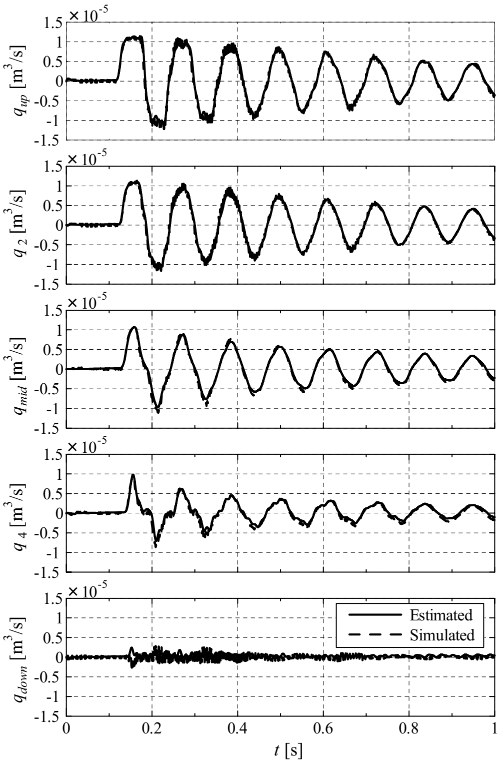

Fig.6 Transient flow rates obtained by the Kalman filter and the method of characteristics

Fig.5 shows the pressure at uniformly spaced grid points in a pipe and Fig.6 shows the flow rate at same points. For comparison, it was also simulated by the method of characteristics using the same data. The estimation results showed good agreement with the simulation results. Therefore, it was confirmed that the time spatial distributions of pressure and flow rate can be precisely estimated by the Kalman Filter.

COMPARISON WITH FLOW RATE OBTAINED BY A FLOW METER

Steady flow rate estimated by the Kalman filter was compared with the flow rate measured by flow meters in order to confirm the static characteristics of the Kalman Filter. Fig.6 shows experiment instrument. Test parameters are listed in Table 2. The pipe (1) was made of a stainless pipe of 20mm in inner-diameter and 2.5mm thickness. The total length of estimated section was 3.2m. Working fluid was hydraulic oil of 30 degree Celsius. The upstream of the estimated section was connected the relief valve (2), pressure gauge (3) and pump unit (4). At first, the throttle valve (5) was closed. Then, the hydraulic fluid is discharged by the pump unit (4) and returns to a tank through a relief valve (3). Pressure was set as 4MPa by the relief valve (3). Secondly, when a throttle valve (5) was opened, the hydraulic oil is discharged from the pump unit (4), and back to tank through the pipe (1), throttle valve (5), and flow meter (6). Then, the pressure falls so that flow rate increases. Three pressure sensors were attached at the pipe to pick up the pressures at upstream-end, the mid-point, and, the downstream-end. In this experiment, distance of each sensor was 1.6m. In addition, a flow meter is attached to the down stream side of the throttle valve. Therefore, estimation value of the steady flow rate can be compared with the measured value.

Table 2 Parameters for experiment and simulation

Wave speed	1310 m/s
Relief pressure	4 MPa
Length of pipe	3.2 m
Number of elements	5
Diameter of pipe	20 mm
Kinematic viscosity	40 cSt
Density	850 kg/m^3
Sampling time	1 ms

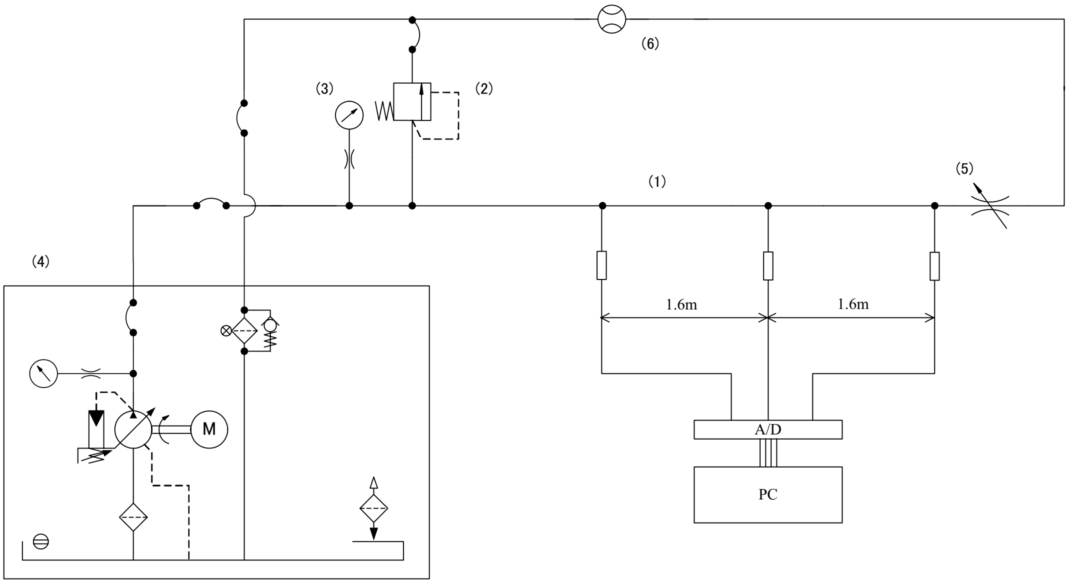

Fig.6 Experimental pipeline and measurement system

Fig.7 shows an example of measured pressure. The pressure at mid-point p_{mid} was shown. Pressure showed oscillations in this figure. In this instrument, noise of amplifier is 0.06MPa. Therefore, it was thought that these oscillations were pressure pulsations caused by a pump unit. Fig.8 shows the flow rate estimated by the Kalman filter, and Fig.9 shows the flow rate obtained by the flow meter. Estimated flow rate shows oscillation. The oscillation of measured flow rate was less than the oscillation of estimated flow rate. It was thought that a cause of the oscillation of estimated flow rate was the pressure pulsation. Therefore, flow rate pulsation was possible to be estimated by Kalman Filter. Estimation results of the Kalman filter show good agreement with the result of measurement.

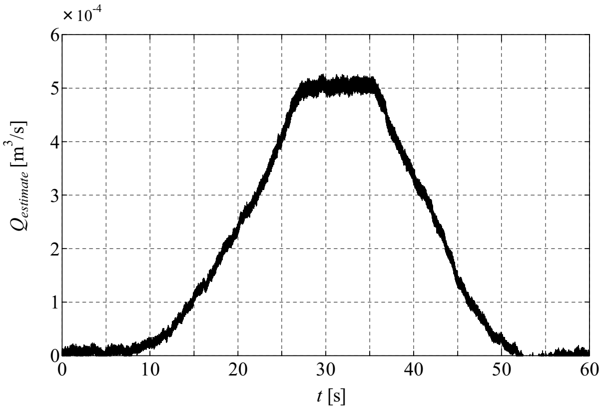

Fig.8 Estimated flow rate at mid point

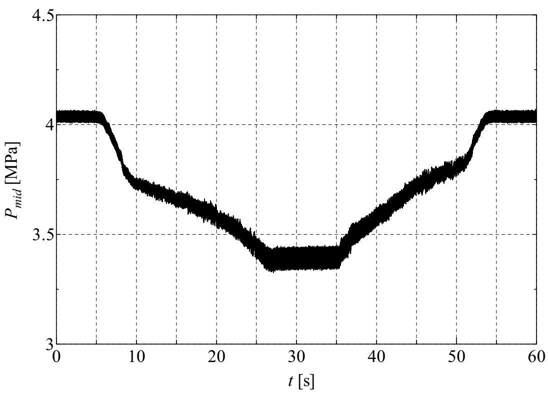

Fig7 Measured pressure at mid-point

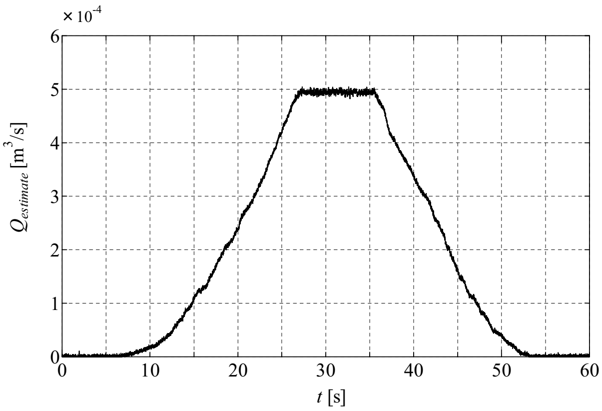

Fig.9 Measured flow rate by flow meter

Fig.10 shows relation between estimated flow rate and measured flow rate. The horizontal axis shows the measured flow rate and the vertical axis shows the estimated flow rate. The oscillation of estimated flow rate influences the results. Moreover, the hysteresis was slightly confirmed. However, it was confirmed that the estimated result is good proportional to the measurement result.

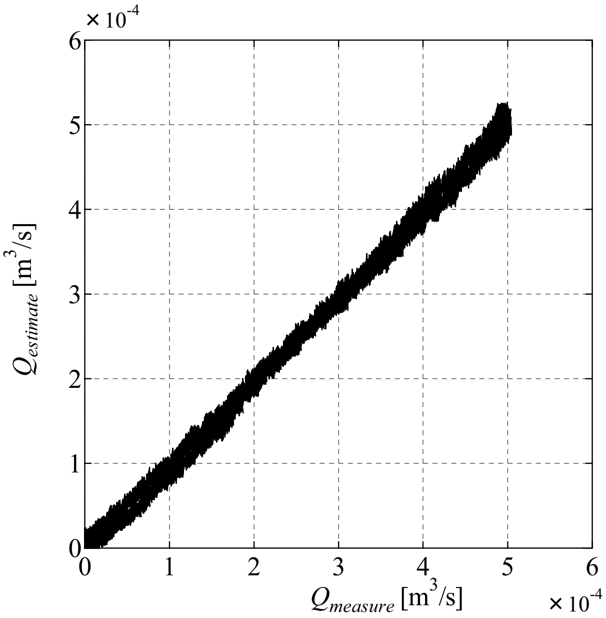

Fig.10 Relation between estimated flow rate and measured flow rate

CONCLUSION

In this paper, method of estimating fluid transients by combining a steady-state Kalman filter and an optimized finite element model of pipeline dynamics is discussed. Pressure and flow rate in a pipe are estimated from measured data of an experiment. As a result, it is confirmed that the estimation results of the Kalman filter show good agreement with the result of the remote measurement method for unsteady flow.

In addition, Steady flow rate estimated by the Kalman filter was compared with the flow rate measured by flow meters. In this comparison, it was confirmed that the estimated result is proportional to the measurement result.

REFERENCES

1. YOKOTA, S., Do-Tae KIM, etc, An Approach to Unsteady Flow Rate Measurement Utilizing Dynamic Characteristics between Pressure and Flow Rate along Pipeline, Trans. JSME. C (in Japanese), vol. 57, No. 541, pp.2872-2876.
2. Tong Zhao, KITAGAWA, A., etc, A Real Time Measuring Method of Unsteady Flow Rate and Velocity Employing a Differential Pressure, Trans. JSME. B (in Japanese), vol. 57, No. 541, pp.2851-2859.
3. HAYASE, T, Ultrasonic-Measurement-Integrated Simulation of Blood Flows, Journal of the Japan Fluid Power System Society, vol. 37, No. 5, pp.302-305,2006.
4. SANADA, K., KITAGAWA, A., A Finite-Element Model of Pipeline Dynamics Using an Optimized Interlacting Grid System, Trans. JSME. C (in Japanese), vol. 60, No. 578, pp3314-3321.

Proceedings of the 8th JFPS International
Symposium on Fluid Power, OKINAWA 2011
Oct. 25-28, 2011

1B1-2

REFLECTION OF FLOW FORCE TO SIMULATION MODEL OF PROPORTIONAL DIRECTIONAL/FLOW CONTROL VALVES WITH SPOOL POSITION FEEDBACK

Ill-yeong LEE*, Je-mok Son** and Ju-sung Kam**

* Dept. of Mechanical & Automotive Engineering
Pukyong National University
San 100, Yongdang-dong, Nam-gu, Busan, Korea
(E-mail: iylee@pknu.ac.kr)
** Graduate School, Pukyong National University

ABSTRACT

In establishing a simulation program for hydraulic valves, it is always a big obstacle to incorporate correctly flow forces on valve body into the simulation program. This paper suggests a method to estimate flow forces on spool in proportional directional/flow control valves with spool structure. Furthermore, suggests a way to obtain simulation program for spool valves, in which the flow force acting on the spool is fully reflected.

KEY WORDS

Spool Valve, Flow Force, Proportional Directional/Flow Control

INTRODUCTION

Fluid force in spool type hydraulic valves is one of major physical parameters that have great influence on characteristics of the valves. Although spool valves have been used for a long time, researches on the fluid force in spool valves are very rare. There were researches on flow force analysis based on momentum principle[1], flow force compensation methods[2, 3], and computational fluid dynamics analysis for evaluating thrust force on spools[4, 5, 6]. However, research reports on precise measuring/identification of flow force by sensing electric signals in electrically controlled spool valves has not to be found in reference surveys. So, the authors develop a method of precisely identifying the flow force on spools by an experimental process in this study.

In the first stage of this study, the authors devise a method for identifying flow force in spool type proportional directional/flow control valves with spool position feedback. Finally, a simulation program for the valve performance analysis reflecting the flow force acting on the spool is suggested.

FLOW FORCE ON SPOOL(AN APPROXIMATE EQUATION BASED ON MOMENTUM PRINCIPLE)

Fig. 1 shows the flow pattern in a spool type hydraulic valve. The lower part of the figure describes the flow situation in the C_1 chamber of the upper part of the figure, where the fluid flow into the chamber with the angle of 90°and flow out with the angle of ϕ to the spool axis.

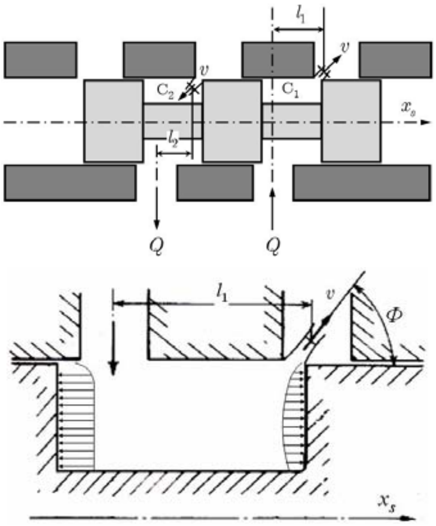

Fig. 1 Flow force in spool valve chamber

Now we shall consider a spool type hydraulic valve with matched and symmetrical control orifices. The flow force f to the spool axial direction is represented as

$$
\begin{aligned}
f &= -2\rho Q v\cos\phi + \rho(l_2 - l_1)\frac{dQ}{dt} \\
&= -4C_d A(x_s)(\frac{\Delta p}{2})\cos\phi + \rho(l_2 - l_1)\frac{dQ}{dt} \qquad (1) \\
&= f_s + f_t
\end{aligned}
$$

In Eq. (1), C_d is flow coefficient, Δp is pressure drop in the valve(sum of pressure difference in each control orifice), x_s is spool displacement, $A(x_s)$ is opening area of the orifices, f_s is steady state flow force, and f_t is unsteady state flow force.

MODELING OF THE VALVE

Short description on the object valve

Fig. 2 shows the object valve for study, the electronic amplifier and the inside shape of the valve. The valve is a spool type proportional directional/flow control valves with spool position feedback, and with nominal flow 16 L/min at Δp = 10 bar. The maximum operating pressure of the valve is 315 bar.

The control orifices of the valve are formed by the circular grooves shown in Fig. 2(b), thereby the flow vs. displacement relation of the valve show a nonlinear

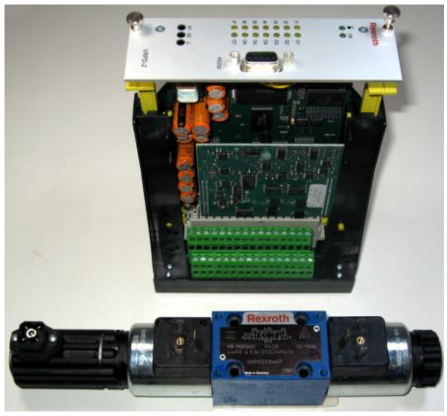

(a) the valve and amp. for test

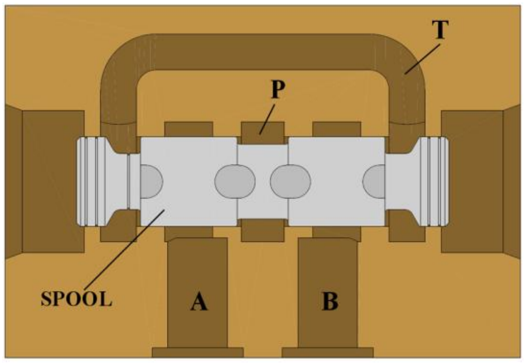

(b) shape of the valve inside

Fig. 2 The valve and amp.

characteristics.

Mathematical model of the valve

Fig. 3 shows the block diagram for describing the operation of the valve/amplifier assembly. The transfer function of the valve/amplifier assembly is written as

$$
\begin{aligned}
X_s(s) &= \frac{HK_a G_c(s) G_{sol}(s) G_s(s)}{1 + K_a K_{pos} G_c(s) G_{sol}(s) G_s(s)} R(s) \qquad (2) \\
&\quad - \frac{G_s(s)}{1 + K_a K_{pos} G_c(s) G_{sol}(s) G_s(s)} F(s)
\end{aligned}
$$

SIMULATION AND EXPERIMENT

Experimental setup and simulation program

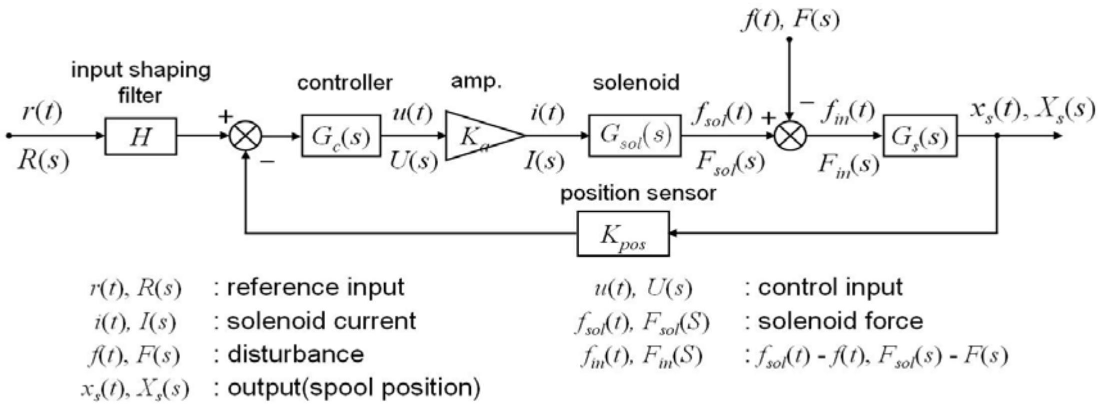

Fig. 3 Block diagram of the spool valve

Fig. 4 shows the setup for experiments of the steady-state characteristics of the valve.
The simulation program displayed in Fig. 5 for the analyses of the valve is composed on a commercialized software package 'AMESim', where the characteristics of the proportional solenoid shown in Fig. 6 is

Fig. 4 Test bench of the experiment

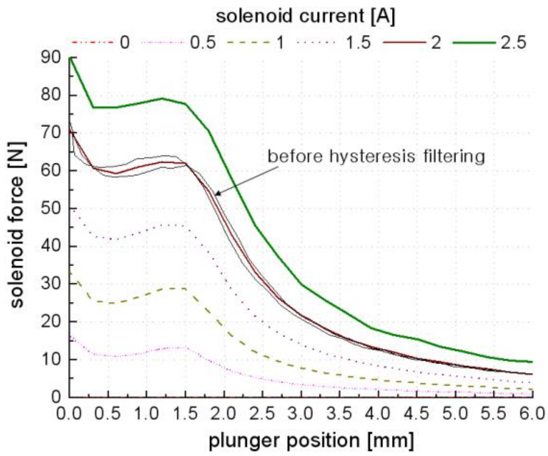

Fig. 6 Steady state characteristics of the proportional solenoid (hysteresis filtered)

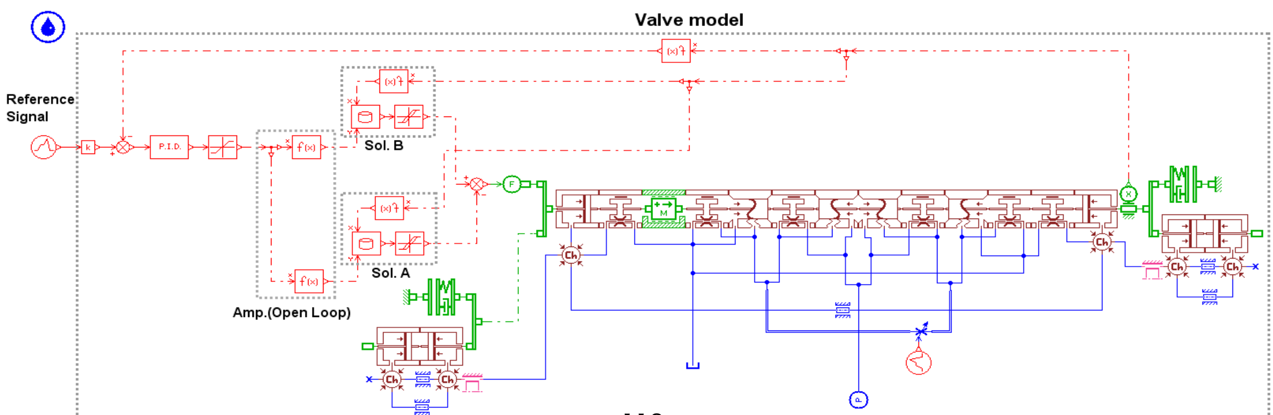

Fig.5 Simulation program(AMESim-based) reflecting the steady-state flow force by Eq. (1)

reflected with a data file obtained in a preliminary test. For the control of the spool position, a PI controller with gains of $K_p = 6$ and $K_i = 20$ was implemented in both the experiment and the simulation.

Steady state characteristics of the valve

Experiments and simulations of steady-state characteristics were performed using the experimental setup and the simulation program described above. The results of experiments and simulations are shown in Fig. 7 ~ Fig. 10.

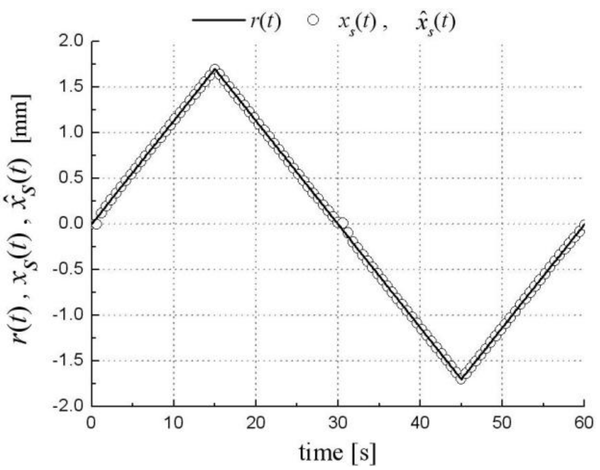

Fig. 7 Steady-state response of $x_s(t)$, $\hat{x}_s(t)$ under the variation of reference $r(t)$

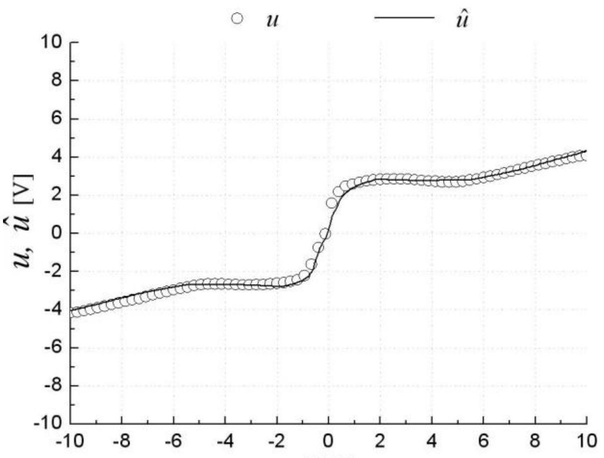

Fig. 8 Comparison of u and $\hat{u}$ under $\Delta p = 0$

Fig. 7 shows the steady-state response of spool displacement x_s (experiment) and $\hat{x}_s$ (simulation) under $\Delta p = 100$ and the experimental time of 60s, which exhibits good control(input following) performance of x_s, and good agreement between x_s and $\hat{x}_s$.

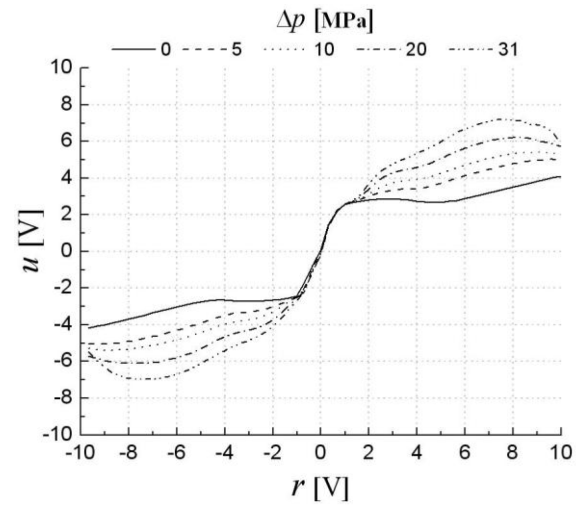

Fig. 9 Effect of Δp on u: experiment (hysteresis filtered)

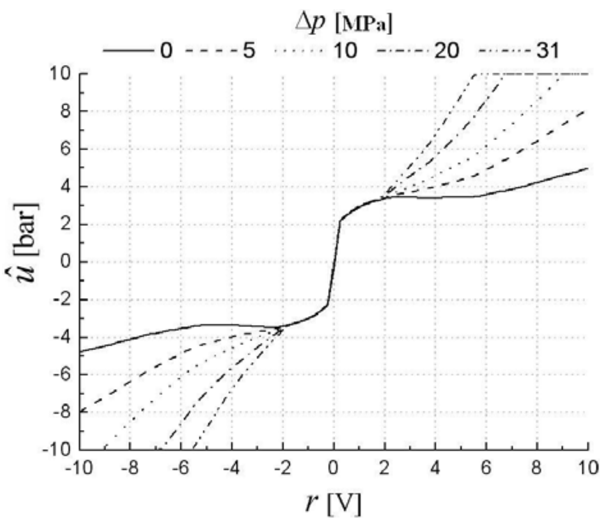

$$^* f_s = 4C_d A(\hat{x}_s)(\frac{\Delta p}{2})\cos\phi$$

Fig. 10 Effect of Δp on $\hat{u}$: simulation using eq. (1) with $C_d = 0.7$, $\phi = 69°$

In Fig. 8, control input u (experiment) and $\hat{u}$ (simulation) under the control shown in Fig. 7 with $\Delta p = 0$ (therefore no fluid flow and no flow force condition) are compared. u and $\hat{u}$ in Fig.8 appeared to be in a good agreement.

Fig. 9 and Fig. 10 shows u and $\hat{u}$ under the control action in Fig. 7, where u and $\hat{u}$ do not agree well with each other except the case of $\Delta p = 0$ bar.

REFLECTING THE STEADY STATE FLOW FORCE IN THE SIMULATION PROGRAM

The authors suggest an algorithm for identifying the steady state flow force on the spool in a spool type proportional control valve with spool position feedback. The suggested algorithm is shown as a block diagram form in Fig. 11, which consists of 'actual valve', 'valve model' and 'f_s identifier' parts. The 'valve model' and 'f_s identifier' parts are implemented in a computer(PC). The 'f_s identifier' performs control action using a PI controller, so as to make the error u - $\hat{u}$ to be zero, and compute flow force $\hat{f}_s$ that identifies f_s precisely.

The 'f_s identifier' is implemented using the following equations.

$$K = K_{pe}(u - \hat{u}) + K_{ie}\int (u - \hat{u})dt \tag{3}$$

$$f_s = -K \cdot 4C_d A(x_s)(\frac{\Delta p}{2})\cos\phi \tag{4}$$

Fig. 12 shows an AMESim-based simulation program for identifying f_s using the algorithm depicted in Fig. 7 as a block diagram. In fig. 12, the relationships between u and r (data shown in Fig. 9) depending on constant Δp values are reflected as a data file.

Fig. 13 presents good agreements between control input u (experimental) and $\hat{u}$ (identified) under ramp input r shown in Fig. 7, and various Δp values. This result(very good agreement between u and $\hat{u}$) is the evidence of excellent identification of f_s in the simulation.

Fig. 14 shows the identified results of steady state flow force under various Δp values together with spring force in the valve.

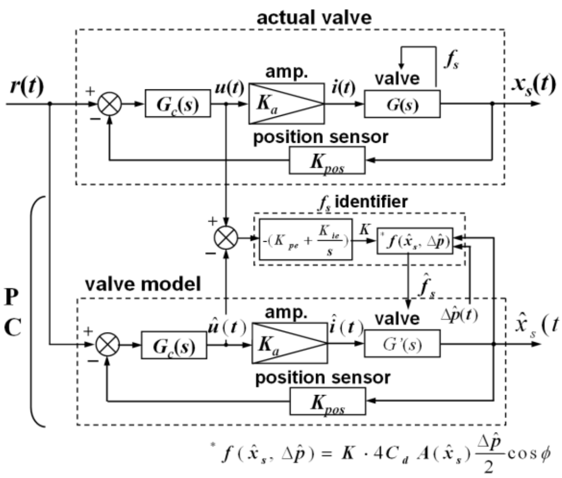

Fig. 11 Block diagram to identify f_s

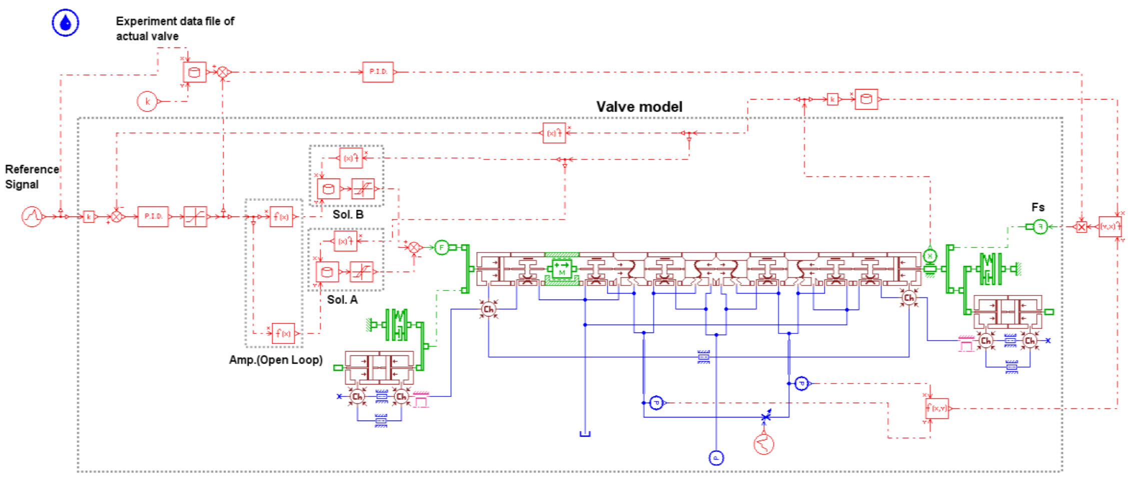

Fig. 12 Simulation program(AMESim-based) including f_s identifier

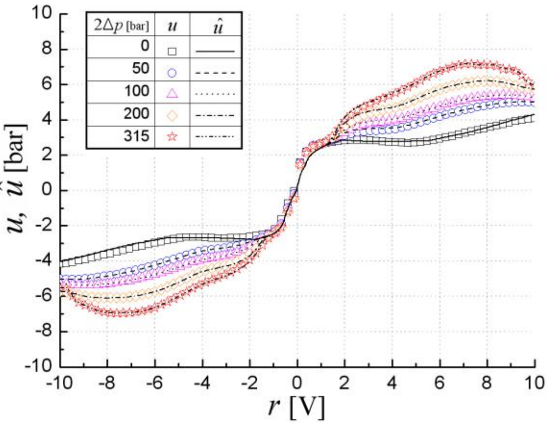

Fig. 13 u and $\hat{u}$ under various Δp (hysteresis filtered)

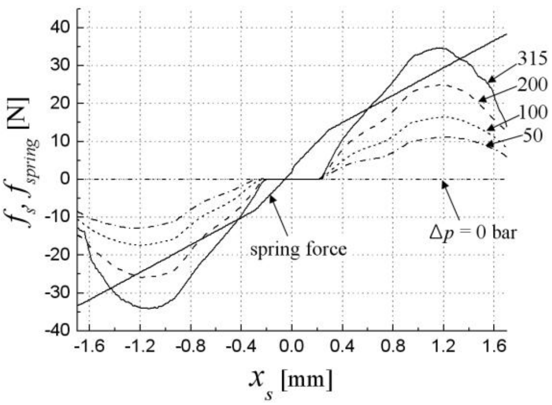

Fig. 14 Identified f_s under various Δp and spring Force

CONCLUSIONS

In this paper, the authors suggested a method of flow force identification in spool type proportional directional/flow control valves with spool position feedback. It was ascertained that the suggested identification method gives very precise identified results on steady state flow force.

ACKNOWLEDGEMENT

This work is the result of the “Human Resource Development Center for Economic Region Leading Industry” project, supported by the Ministry of Education, Science & Technology and the National Research Fund(NRF) of Korea.

REFERENCES

1. Takenaka, T. and Urata, E., Oil Hydraulics, Yogendo, Tokyo, 1970.
2. Merritt, H. E., Hydraulic Control Systems, John Wiley & Sons, Inc. 1967, pp. 101-105.
3. Lee, S.Y. and Blackburn, J.F., Contribution to Hydraulic Control 1. Steady State Axial Forces on Control-Valve Pistons, T. ASME, 1952, **74**, pp. 1005-1011.
4. Guo, M. and Nakano, K., Numerical Analysis for the Flow in a Spool Valve by a Boundary Element Method(1st, 2nd Report), JFPS, 1989, **20**-6.
5. Amirante R., Moscatelli, P.G. and Catalano, L.A., Evaluation of the flow Force on a Direct(Single Stage) Proportional Valve by computational Fluid Dynamic Analysis, Energy conversion & Management, 2007, Vol. 48, pp. 942-953.
6. Tanaka, K., Tomioka K., Shimizu F. and Fuchiwaki M., A Study of Flow Force on a Spool Valve, Trans. of JFPS, 2011, Vol. 42, No. 1, pp. 13-18.

Proceedings of the 8th JFPS International
Symposium on Fluid Power, OKINAWA 2011
Oct. 25-28, 2011

1B1-3

EVALUATION OF CAVITATION EROSION UNDER SUBMERGED JET WITH CFD

Kento KUMAGAI*, Shohei RYU*, Kazuo FUJISHIMA *
Toshiharu KAZAMA**, Jian KE***

* Department of Technical Research Lab.
Hitachi Construction Machinery Co.,Ltd.
650, Kandatsu-machi, Tsuchiura-shi, Ibaraki-ken, 300-0013 Japan
(E-mail: k.kumagai.kq@hitachi-kenki.com)
** College of Design and Manufacturing Technology
Muroran Institute of Technology
27-1 Mizumoto-tyo, Muroran-shi, Hokkaido, 050-8585 Japan
(E-mail: kazama@mmm.muroran-it.ac.jp)
*** Mechanical Department, Southwest Jiaotong University
1-111 2huanlu,Chengdu, 610031, China
(E-mail: kjian@home.swjtu.edu.cn)

ABSTRACT

This paper proposed a new method for evaluation of cavitation erosion in hydraulics based on CFD (Computational Fluid Dynamics) and experiment. A simulation model is made, which has same geometry of a submerged jet experiment system. According to the analysis of flow and pressure distribution characteristics from CFD and the erosion map in experiment, it is found that the erosion has close relationship with the distribution of cavitation number σ which is calculated from flow and pressure. The relation makes possible that with only calculating the distribution of σ on surface of specimen by CFD, the erosion risk can be evaluated. Erosion map for different jet distance are predicted with the method, and they fit well with erosion experiment results.

KEY WORDS

Cavitation, Cavitation Number, CFD, Erosion, Hydraulic Valve

NOMENCLATURE

L	: [mm]	... Stand-off distance
p	: [MPa]	... Gauge pressure
p_d	: [MPa]	... Downstream gauge pressure
p_u	: [MPa]	... Upstream gauge pressure
p_v	: [MPa]	... Vapor gauge pressure
t	: [hr]	... Experiment time
u	: [m/s]	... Velocity magnitude
ρ	: [kg/m^3]	... Density
σ	:	... Cavitation number

$= (p- p_v)/(1/2\,\rho u^2)$

INTRODUCTION

Cavitation is a serious problem which causes noise, vibration, performance decline and cavitation erosion in hydraulic system [1]. The erosion is a kind of fatigue damage, it is difficult to predict before hand, and needs long time to find out in practice. An effective method which can predict the erosion risk in design stage is quite important.

The most popular reason of erosion in hydraulic components is impingement of cavitating jet, which is generated when the flow pass throw an orifice with large pressure drop. Lichtarowicz [2-4] proposed a submerged cavitating jet apparatus to evaluate erosion of materials. Many researchers had used similar type of experiment apparatus to study the influence of various flow parameters on erosion. For example, Yamaguchi and Shimizu [5-10] reported the influence of pressure, temperature, stand-off distance, nozzle design etc. Kazama and their colleagues [11-14] reported the relationship between erosion and Liquid type, down stream pressure, nozzle outlet geometry, impinged surface geometry etc.

In other field, Sato et al [15-17] reported the relation between the erosion and cavitation number σ around screw blade and cylinder.

In this paper, authors try to develop a method to predict the erosion in hydraulic components according to the analysis of flow characteristics with CFD.

EXPERIMENT

Test Method

The apparatus and test procedure used for this research are referred to ASTM standards G134-95 [18], with only some difference in size and test conditions. And detailed experiment condition can be referred to the paper of Kazama et al [19].

Experimental Apparatus

The hydraulic circuit for experiment is shown in Fig.1. The pump 2 is driven by an electric motor 1 to provide high pressured oil to the test chamber. A cooling system is set to keep the system temperature in constant, a filter with nominal filtration size of 3 μm is used to remove contaminants from the test liquid. Pressure sensors at in and out ports of chamber, flow sensor, oil temperature sensor are installed to monitor the experiment state.

The schematic of test chamber is shown in Fig.2. The steel chamber included a long-orifice nozzle, its holder, the specimen, holder, mount, and spacers. The inner

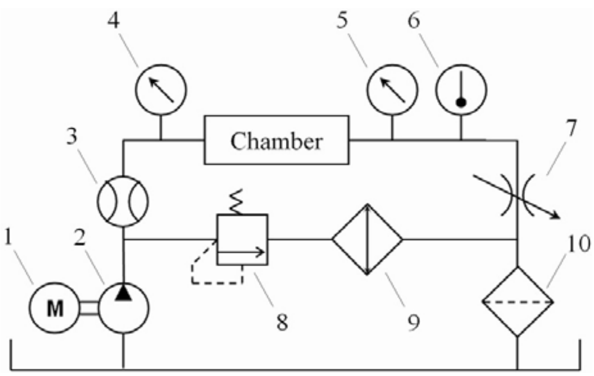

1: electric motor, 2: pomp, 3: flow sensor, 4: upstream pressure gauge, 5: downstream pressure gauge, 6: temperature, 7: throttle valve, 8: relief valve, 9: cooler, 10: filter

Figure 1 Hydraulic Circuit of Experimental

chamber is cylindrical type with diameter of 170 mm. Two transparent windows are provided at both sides of the chamber, so that the cavitating jet can be observed and photographed. The nozzle diameter is 1.0 mm and its length is 4.0 mm. The nozzle is bored cylindrically; its edge is machined carefully, so to keep the edge in sharp.

Specimen

The specimen diameter d is 15 mm. it is made of aluminum alloy designated as A5056 by Japanese Industrial Standards (JIS). The average surface roughness is less than 0.8 μm. The physical and mechanical properties are as follow: Vickers hardness 91.7 Hv5, breaking strength 313 MPa, tensile strength 217 MPa, elongation 28.7 %. The chemical composition was Cr: 0.06 %, Cu: 0.01 %, Fe: 0.11 %, Mg: 4.8 %, Mn: 0.06 %, Si: 0.04 % and Zn: 0.01 %.

Experimental Conditions

The experiment condition is shown as Table 1. The stand-off distance L is defined as the distance from the edge of the nozzle outlet to the specimen surface, as indicated in Fig.2. L can be set in range of L = 10〜30 mm by adjusting of annular spacers.

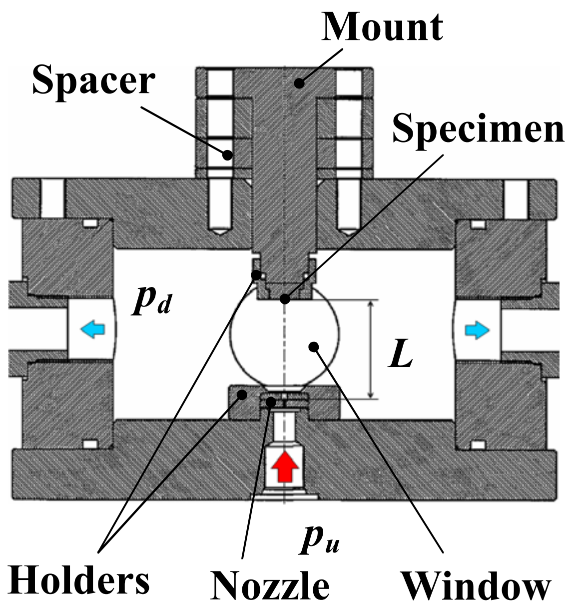

Figure 2 Schematic of Test Chamber

Table 1 Experiment and Analysis Conditions

Test Liquid	Mineral Oil VG46
Up-Steram Pressure [MPa]	10 (gauge)
Down-Steram Pressure [MPa]	0.1 (gauge)
Stand-off Distance [mm]	10 ～ 30
Temperature [℃]	50±1

ANALYSIS

Analysis Method

Fig.3 shows the 3-D simulation model which has same geometry with the submerged jet experiment chamber, shown in Fig.2. CFD is carried out with STAR-CD.

Analysis Conditions

The analysis condition is same with the experiment shown in Table 2. The assumption in CFD is steady flow, no bubble exists in fluid, and the turbulent model is k-ε high Reynolds number.

The assumption for analysis is obviously different from the experiment state, because in experiment the bubble is always full of chamber. But since the erosion is integration effect of time, the steady analysis can provide more essential flow characteristics in apparatus. And in practice, the steady analysis is easier to be applied in engineering design.

EVALUATION METHOD

Relation of Erosion and Flow Characteristics

Fig. 4 shows the CFD result when the stand-off distance L = 25 mm, the contour map shows velocity, contour line shows pressure distribution. Fig.5 shows a photograph of the specimen surface after the experiment in same condition with Fig.4, the experiment time t = 12 h. The specimen is eroded as a ring-like figure. Fig.6 shows the average depth to radius of specimen.

To explain the reason of the ring-like figure, we can find the relation between the erosion and flow characteristics.

At the point ①, says the center of the jet flow, there is nearly no erosion in experiment photo, and from Fig.4, the pressure at the point is quite large, and velocity is small. It can be explained as that at this point, since the pressure is too large, bubble has less opportunity to come near the wall, and so less erosion appear there.

At the point ②, says the edge of the specimen, there is also less erosion, and from Fig.4, the pressure there is small, and velocity is high. It can be explained as that when the pressure is too small, it has not enough power to crash the bubble, and quick flow bring the bubble leave away, so even there maybe a lot of bubbles around the point but it not create damage there.

At the point ③, says the point at the maximum eroded ring, where pressure and velocity are in middle. Bubbles may have more opportunity to come near to the wall and

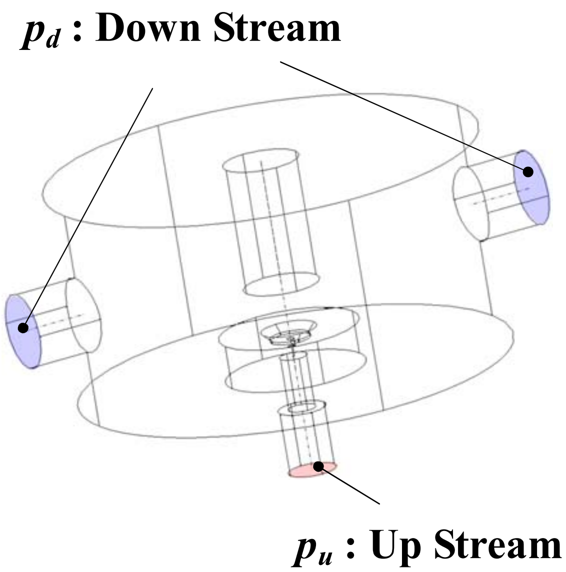

Figure 3 3D Analysis Model

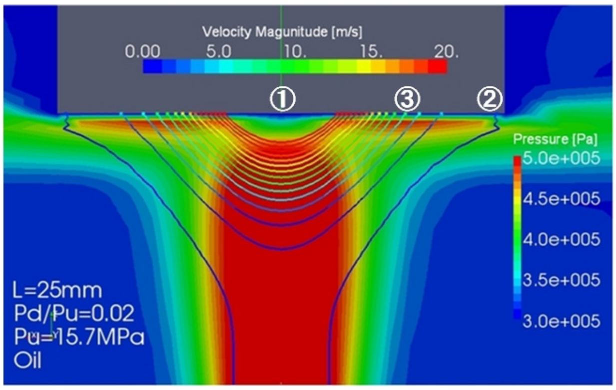

Figure 4 Relationships of Pressure and Velocity Magnitude on Specimen Surface

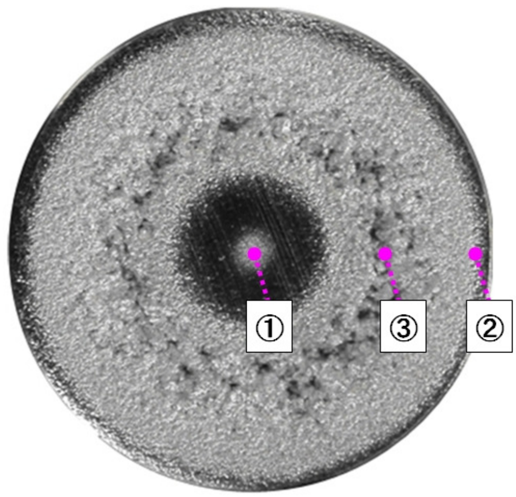

Figure 5 Specimen's Surface (L = 25 mm, t = 12 h)

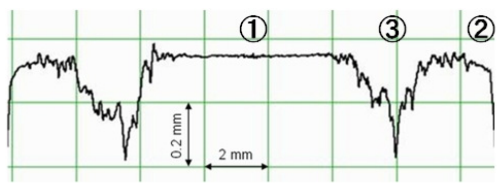

Figure 6 Cross Section of Eroded Specimen

be crashed there, so they create large erosion.

From the explanation above, it can be known that the erosion has close relation with the pressure and velocity near the surface of the specimen, and so it is assumed that the erosion under submerged jet may have same kind of relation between the erosion and cavitation number σ which has appeared in screw blade[15].

Cavitation Number and Impact ratio

The cavitation number σ is defined in following equation:

$$\sigma = \frac{p - p_v}{1/2 * \rho u^2} \tag{1}$$

p: pressure at any point; u: velocity at same point; p_v : liquid vapor pressure; ρ: density of fluid.

The cavitation number σ at any point can be calculated by bringing the pressure and velocity which are get from CFD to Eq. (1). Fig. 7 shows the distribution σ near the surface of the specimen in above experiment. And the pink line with triangle mark in Fig.8 shows the cavitation number σ to radius of specimen.

It can be noticed in Fig.5, that different depth shown in specimen surface actually means the different impact which is received at the position, so according to the depth of erosion, the impact force can be indirectly obtained.

The impact ratio is defined for expressing the damage power of erosion, and calculated in following equation

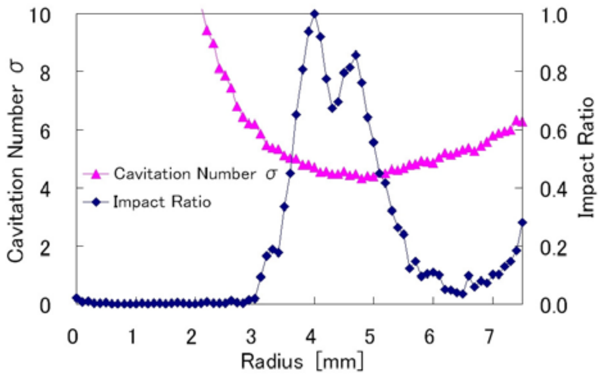

Figure 8 Cavitation Number σ, Impact Ratio vs. Radius of Specimen

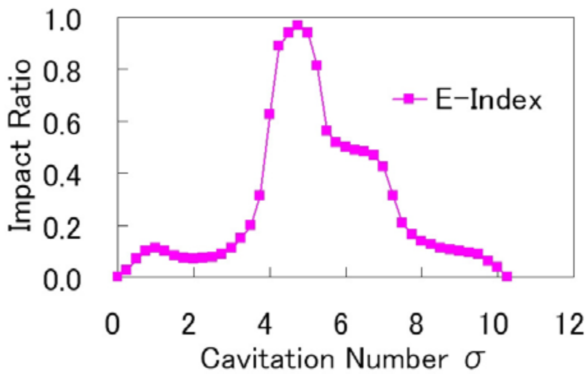

Figure 9 Cavitation Number σ vs. Impact Ratio

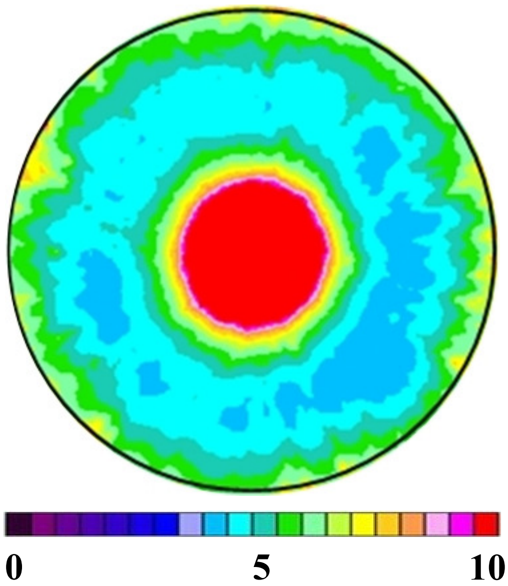

Figure 7 Cavitation Number σ Distribution on Specimen Surface (L = 25 mm)

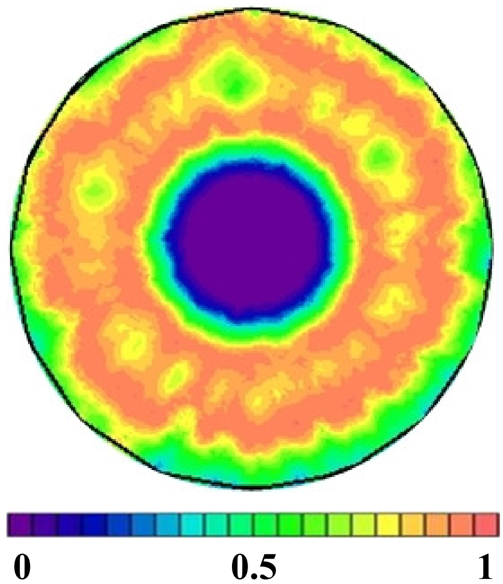

Figure 10 Distribution of Erosion Possibility

$$Ie = \frac{depth(r)}{deepest} \quad (2)$$

Bring the data in Fig.6 to Eq. (2), the impact ratio at any radius is obtained and shown as the blue line with dot in Fig.8.

Erosion Index

According to Fig.8, to take the cavitation number σ at any radius position as X axis, and impact ratio at the position as Y axis, the relation between the impact ratio and σ can be shown as Fig.9. The curve is defined as E-Index (Erosion Index), which have similar style with the impulsive acceleration appeared in screw blade.

Applying the E-index to σ distribution in Fig.7, the E-index distribution can be obtained as Fig. 10, when the color near to red, it means high possibility of erosion, when it near to violet, it means low possibility.

By comparing the Fig.5 and Fig.10, it can be found that both the experiment and E-index evaluation shows same kind of ring-like figure.

EVALUATION OF EROSION

According to the paper of Kazama [11], the erosion under submerged jet has relation with the stand-off distance shown in Fig.11. When L is less than 20mm, the erosion is quite small, when L near to 25, the erosion become quite large, and when L get further increase as over 30 mm, the erosion will turn weak.

In order to verify the applicability of the proposed erosion evaluation method, three point (a): L = 10 mm, (b): L = 25 mm, (c): L = 30 mm are chosen out, at which both the analysis and experiment are carried out. Fig.12 shows comparisons of pictures from experiment, and E-index results from analysis.

In analysis result, the violet color means low erosion possibility; and in the experiment photograph at left, the dark black part is original color of the specimen, which also means less erosion appeared there.

In Fig.12 (a), there are two violet rings in analysis results, and there are also two black rings in experiment photo. The small green ring near the center of the analysis fits the erosion mark in the center of specimen, and the blue ring in analysis fits the white ring of experiment. According to the color bar at the bottom of Fig.12, the blue is near the violet, which means the erosion is not so large, and the experiment also shows same fact.

In analysis result of Fig.12 (b), the center part is violet color, and around of it is bright orange, which means high erosion possibility. The experiment also shows the same distribution of erosion.

In analysis result of Fig.12 (c), it has a larger violet center than that when L = 25 mm, and the color around

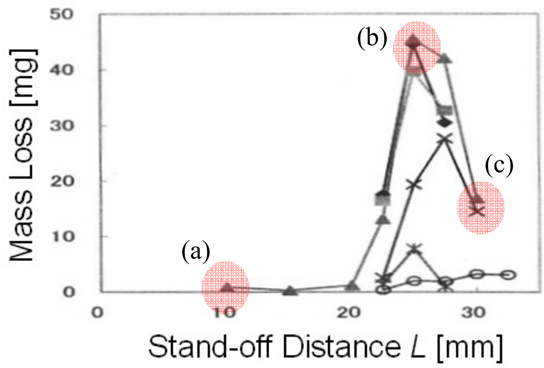

Figure 11 Mass Loss vs. Stand-off Distance L from Muroran Institute of Technology [11]

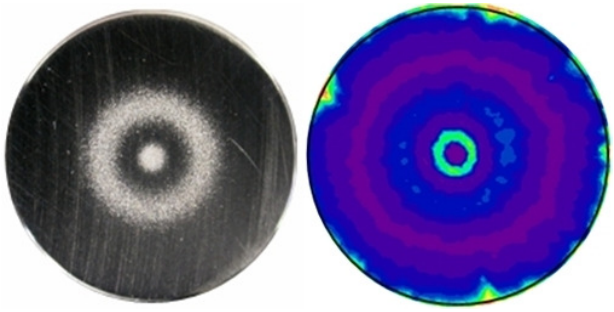

(a) L = 10 mm

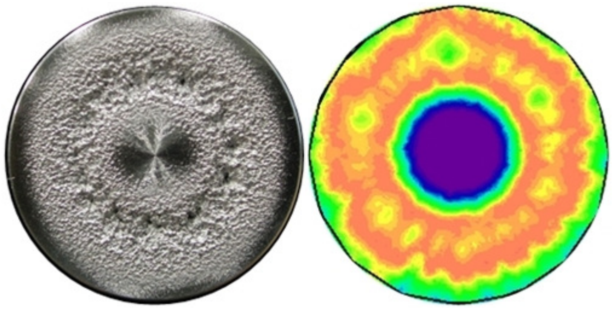

(b) L = 25 mm

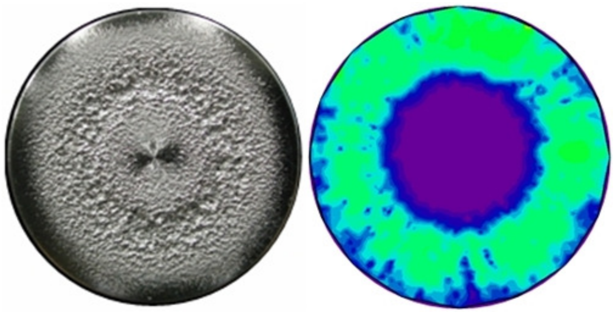

(c) L = 30 mm

Figure 12 Eroded Regions on Specimen (Left Experiment, Right Analysis)

the center turn to light green, and that means the erosion will be less than that at L = 25 mm, but larger than L = 10 mm. The experiment photo also shows erosion is larger than L=10, but smaller L=25

From above comparisons, it can be known, that E-index method can well predict the risk map of erosion. But since bubble movement is not considered in analysis, the erosion mark position and size maybe a little different between analysis and experiment.

CONCLUSION

This paper proposed an evaluation method for hydraulic components in submerged jet. Both CFD and erosion experiment are carried out for same experiment device, and it is found that:

1) Erosion map and the eroded depth have close relationship with the cavitation number distribution near the surface of the specimen.

2) The E-Index (Erosion Index) is defined, which takes cavitation number obtained from CFD as X-axis, and erosion impact ratio from experiment as Y-axis. It can be used to translate the CFD result to erosion risk evaluation map.

3) The evaluation method is applied to evaluate the change of erosion with different stand-off distance of the submerged jet. The results show predicted erosion map is well agreed with the real erosion photo from experiments.

REFERENCES

1. Knapp, T.T., Daily, J.W. and Hammitt, F.G., Cavitation, McGraw-Hill, 1970.
2. Lichtarowicz, A., Use of a Simple Cavitating Nozzle for Cavitation Erosion Testing and Cutting, Nature physical science, 1972, 239, pp.63-64.
3. Lichtarowicz, A., Cavitation Jet Apparatus for Cavitation Erosion Testing, ASTM Special Technical Publication, 1979, 664.
4. Lichtarowicz, A., and Kay, P., Proceedings of the 6th International Conference on Erosion by Solid and Liquid Impact, 1983, pp.15.1-15.4.
5. Shimizu, S., and Yamaguchi, A., Erosion due to impingement of cavitating jet, Journal of the Japan Hydraulics & Pneumatics Society, 1988, 19(1), pp.68-75.
6. Shimizu, S., Yamaguchi, A., and Kazama, T., Erosion due to Impingement of a Cavitating Jet 2nd Report, Journal of the Japan Hydraulics & Pneumatics Society, 1991, 22(1), pp.57-62
7. Yamaguchi, A., and Kazama, T., Erosion due to Impingement of a Cavitating Jet 3rd Report, Journal of the Japan Hydraulics & Pneumatics Society, 1993, 24(4), pp.90-97
8. Yamaguchi, A., Wang, X., and Kazama, T., Erosion due to Impingement of a Cavitating Jet 4th Report, Journal of the Japan Hydraulics & Pneumatics Society, 1997, 28(3), pp.353-358.
9. Yamaguchi, A., Kazama, T., and Wang, X., Erosion due to Impingement of a Cavitating Jet 5th Report, Journal of the Japan Hydraulics & Pneumatics Society, 2000, 31(7), pp.1-6
10. Yamaguchi, A., and Shimizu, S., Erosion Due to Impingement of Cavitation Jet, Trans. ASME, J. Fluids Engineering, 1987, 109(4), pp.442-447
11. Kazama, T., and Miura, Y., Reduction in Submerged Jet Cavitation Erosion, Trans. Japan Fluid Power System Society, 2007, 38(6), pp.77-82
12. Kazama, T., and Shimizu, K., Erosion due to Impingement of Submerged Cavitating Jets in Tap Water, Biodegradable and Mineral Oils, SICFP’07, 2007
13. Kazama, T., Kumagai, K., Miura, Y., and Narita, Y., Reduction and Enlargement of Erosion by A Submerged Cavitating Jet with Geometric Control, PRIC-WJT2009, 2009, pp.123-131
14. Kazama, T., Kumagai, K., and Narita, Y., Effect of Nozzle Outlet Geometry and Impinged Surface Geometry on Erosion Casued by Cavitating Jets for Hydraulic Equipment, TJIEME-CME-MuroranIT-2010, 2010
15. Sato, K., and Sugimoto, Y., Bubble Collapsing Behavior of Vortex Cavitation Relative to Erosion Especially in the Near Wake behind a Triangular Cylinder, Trans. of the Japan Society of Mechanical Engineers, Ser. B, 1997, 63(616), pp.3815-3821.
16. Sato, K., Study on Transition of Flow Regime in the Cavitation Process of a Circular Cylinder, Trans. of the Japan Society of Mechanical Engineers, Ser. B, 1994, 60(574), 1876-1882.
17. Sato, K and Kakutani, K., Suppression of Bubble Occurrence and Transition of Flow Regime in the Cavitation Process of a Circular Cylinder, Trans. of the Japan Society of Mechanical Engineers, Ser. B, 1993, 59(559), 671-676.
18. ASTM, Standard Test Method for Erosion of Solid Materials by a Cavitating Liquid Jet, G134, 1995, 95, pp.529-540.
19. Akiyama, Y., Kazama, T., and Narita, Y., Erosion due to Cavitating Jets, Trans. of the Japan Society for Design Engineering, 2011, pp.13-15

Proceedings of the 8th JFPS International
Symposium on Fluid Power, OKINAWA 2011
Oct. 25-28, 2011

1B1-4

TEMPERATURE MEASUREMENT OF A CAM-RING AND SIDE-PLATES IN A VANE PUMP

Toshiharu KAZAMA*, Yukihito Narita*

* College of Design and Manufacturing Technology
Muroran Institute of Technology
27-1, Mizumoto-cho, Muroran, Hokkaido, 050-8585 Japan
(E-mail: kazama@mmm.muroran-it.ac.jp)

ABSTRACT

The effects of operating conditions on the temperatures of a cam-ring and the side-plates of a hydraulic vane pump were examined. Four thermocouples were embedded in the side-plate and four were implanted in the cam-ring. Mineral-oil-type and water-glycol-type hydraulic oils with VG32 were used as the test fluids. The maximum discharge pressure was 20 MPa and the maximum rotational speed was 25 rps. The inlet oil temperature was specified at 30 to 50°C. At pressures ranging from the atmospheric pressure to the maximum discharge pressure, the temperature changes were monitored. As the discharge pressure increased, the temperatures of both the cam-ring and the side-plates increased. The temperature change of the cam-ring at the suction port was largest. The temperature increase with the water-glycol-type oil was markedly less than that observed with the mineral oil.

KEY WORDS

Fluid power, Tribology, Vane pump, Temperature, Experiment

NOMENCLATURE

N : Rotational speed
p_d : Discharge pressure
t : Temperature
t_{in} : Inlet oil temperature
Δt : Temperature rise or change = $t - t_{in}$

Subscripts
1, 2, 3, 4 : Temperature measuring points on the side-plate
5, 6, 7, 8 : Temperature measuring points in the cam-ring

INTRODUCTION

Hydraulic vane pumps [1, 2] and motors are used in many industrial applications, such as workshops and automobiles. The pumps and motors are expected to operate under medium pressure and a wide range of speed conditions, and to have a long and useful life while maintaining high reliability and high efficiency. Many researchers and engineers have studied and revealed the characteristics of vane pumps and motors from the viewpoints of, for example, reduction of frictional torque [3] and the jumping behavior of the vanes [4].
In some applications, the size is enforced to be compact, which often results in a higher operating pressure. Higher power density forces severe operation at the tribological

parts of the pumps and motors, resulting in heat generation and seizure. The need exists for a tool of optimum design and precise estimation including the influence of heat generation and thermal lubrication.

Wilson [5] pointed out that the optimum clearance based on isothermal theory is insufficient to design displacement pumps, addressing the importance of the thermal effects. As regards axial piston pumps, Yamaguchi et al. [6] experimentally investigated the effects of operation conditions and working fluids on the performance and temperature of a test pump in which the thermocouples were installed in the cylinder block. Ivantysynova [7] and Olems [8] measured the temperature distributions around the cylinder bores using a test pump with thermocouples installed in the cylinder block. In that study, they obtained the temperature distributions by the experiment and compared with the thermohydrodynamic lubrication (THL) analysis, however, the specification of the test pumps and the condition of the experiment differed from those of actual hydraulic pump operation.

Kazama et al. [9] examined the thermohydrodynamic performance of a slipper model, including the effect of the changes in physical properties of fluids as functions of temperature and pressure. Later, he and his colleagues experimentally measured the temperature of the swash plate, the cylinder block, and the valve plate of the piston pumps [10, 11] under actual operating conditions. Furthermore, Kazama and Oguma [12] measured the temperature of the side-plate of a compact gear pump under the actual operating conditions.

In this report, the temperatures of the cam-ring and the side-plate of a compact vane pump were measured. The results were compared and discussed.

EXPERIMENTAL APPARATUS AND METHODS

The hydraulic circuit of the test rig [10–12] consisted of test pumps, a three-phase induction motor (7.5 kW), an electric inverter, a strain-gauge-type torque sensor (20 N·m), flow-rate meter (4 kl/h), a pressure transducer, thermistors, thermocouples, valves, an oil cooler, and a reservoir. The pump tested was a single-stage vane pump with a theoretical discharge volume of 9.4 mL/rev, a maximum working pressure of 21 MPa, and a rated rotational speed of 13 to 30 rps.

The locations of the thermocouples installed in the side-plate and the cam-ring are illustrated in Figs. 1 and 2, respectively and were numbered 1 through 8. Thermocouples 1-4 were embedded close to at the suction port, the delivery port, the bottom-dead center, and the top-dead center of the side-plate; thermocouples 5-8 were embedded close to the delivery port, bottom-dead center, suction port, and top-dead center of the cam-ring, respectively.

The induction motor drove the test pump through the torque sensor. Thermistors were placed at the pump inlet and the flow meters were installed in the discharge line and the drain line. The test oils were mineral-oil-type hydraulic fluids with the viscosity grade (ISO VG) 32 (designated as MO) as well as a water–glycol-type hydraulic fluid (designated as WG) with ISO VG32 (50% water content). The fluid densities of MO and WG were 869 and 1069 kg/m^3, and the kinematic viscosities at 40/100°C of MO and WG were 33/5.5 and 33/7.4 mm^2/s, respectively.

The experiment was conducted as follows: the oil temperature at the test pump inlet and the rotational speed of the pump were set; the discharge pressure was increased from atmospheric pressure to 20 MPa (or the feasible maximum pressure) by 1 MPa, then decreased from the maximum pressure to atmospheric pressure by 1 MPa. At each setting, the pressure, discharge flow-rate, torque, and temperatures were measured.

RESULTS AND DISCUSSION

Experiment for mineral-oil-type hydraulic oil

Figures 3 and 4 show the effect of the discharge pressure p_d on the temperature change Δt ($= t - t_{in}$) at each measurement point (Nos. 1 to 8), where the locations of Nos. 1 to 4 were in the side-plate and the locations of Nos. 5 to 8 were in the cam-ring. The test oil was the mineral-oil-type hydraulic oil with VG32, the rotational speed (target level) N was 25 s^{-1}, and the oil temperature at the inlet of the pump (target level) t_{in} was 40°C. The individual variability of the temperature was measured by each sensor, and the deviation of the inlet temperature t_{in} and the temperatures t_1 through t_8 were compensated by the standard thermometer.

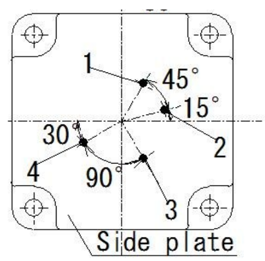

Figure 1 Location of thermocouples installed in the side-plate

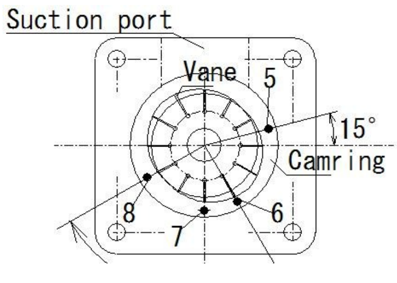

Figure 2 Location of thermocouples installed in the cam-ring

As the pressure p_d increased, the temperature change Δt at all measurement points rose monotonically. This is mainly because the contacting loads between the tip of the vanes and the inner surface of the cam-ring as well as the side surface of the vanes and the inner surface of the side-plates increased by the back pressures introducing the discharge pressure. The heat generation H was caused by friction of these sliding and mating parts, which was basically given by

$$H \propto f \times p \times v \tag{1}$$

where f is the friction coefficient, p is the contact pressure, and v is the sliding speed.

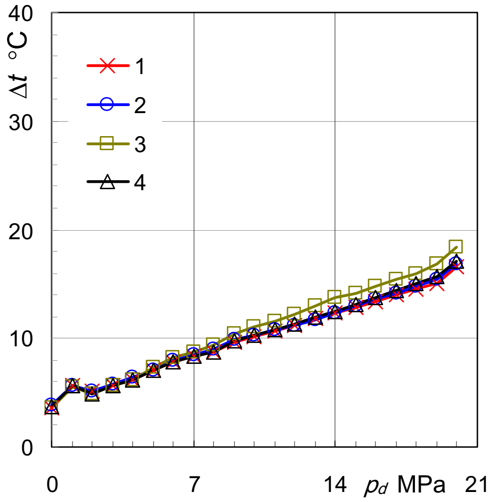

Figure 3 Effects of discharge pressure p_d on temperature change Δt of the side-plate (MO, $N = 25$ s^{-1}, $t_{in} = 40$°C)

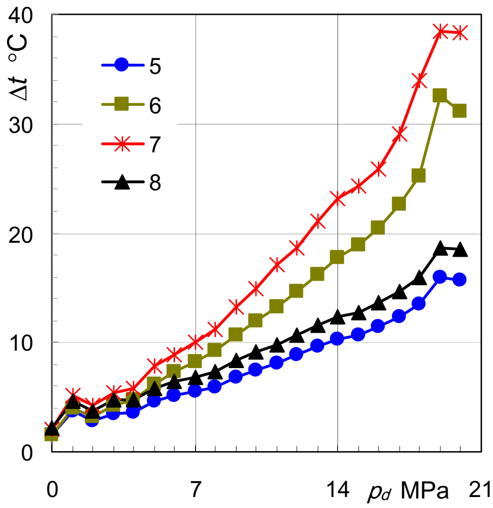

Figure 4 Effects of discharge pressure p_d on temperature change Δt of the cam-ring (MO, $N = 25$ s^{-1}, $t_{in} = 40$°C)

The increases in Δt of the cam-ring were markedly larger than the increases in Δt of the side-plate as shown in Fig. 4. The rise Δt close to the suction port of the cam-ring (No. 7) was highest, and the rise Δt close to the delivery port of the cam-ring (No. 5) was lowest. The difference between Δt_5 and Δt_7 became about 23°C at $p_d = 20$ MPa. In contrast, for the side-plate (in Fig. 3), the rises Δt of Nos. 1 to 4 were low, and the differences in Δt between Δt_7 and Δt_5 were up to about 2°C at the largest.

The vane tips were lubricated elastohydrodynamically and the lifting force was generated, which resulted in hydrodynamic lift and separation force between the vane and the cam-ring. To avoid separation, the back pressure, which was proportionally increased with the discharge pressure, acted on the vanes. The contact pressure of the vane tip close to the suction port was large and the pressure to the delivery port was small. Therefore, the temperature change Δt of No. 7 was high, and Δt of No. 5 was low.

Repeatability of the measured temperatures was examined in Figure 5, where t_3 and t_6 were the temperatures at the bottom-dead-center of the side-plate and at that of the cam-ring, respectively. The experimental conditions were the same as the conditions of Figures 3 and 4. The upward arrows imply the data of the increase process of the discharge pressure, and the downward arrows imply the data of the decrease process. Based on these results, one can see that the repeatability was good.

Figure 6 illustrates the effects of the rotational speed N on temperature change Δt; the temperature of the mineral oil under the inlet, t_{in}, was 40°C. The temperature change Δt at No. 7 of the cam-ring was shown because this value of Δt was highest. Under the lower speed conditions ($N =$

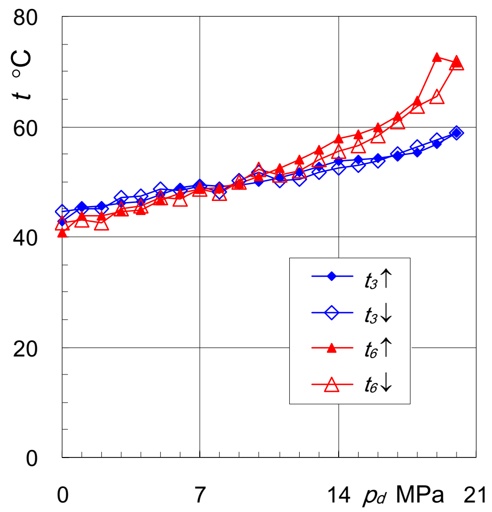

Figure 5 Repeatability of measured temperatures t_3 and t_6 (MO, $N = 25$ s^{-1}, $t_{in} = 40$°C)

15 and 20 s^{-1}) the data was missing because of the limitation of the specification of the electric inverter-driven test rig. The rotational speed N had less affected the temperature difference Δt_7 in this experiment.

Figures 7 and 8 depict the effects of inlet oil temperature t_{in} on the temperature change Δt of No. 5 at the lowest temperature difference, and No. 7 at highest temperature difference of the cam-ring under the conditions of MO and $N = 25$ s^{-1}. The temperature changes Δt of Nos. 5 and 7 similarly increased with increasing the discharge pressure p_d. The value of Δt of $t_{in} = 40$°C was highest, and Δt of $t_{in} = 30$°C was lowest; however, the differences in Δt were very small, and therefore, not very significant. The frictionally heating would be increased as the sliding speed increased, but the discharge flow rate was also increased, which contributed to transforming the heat and cooling of the sliding parts of the pump.

Experiment for water-glycol-type hydraulic oil

Figures 9 and 10 show the effect of the discharge pressure p_d on Δt of the side-plate and the cam-ring, respectively, using the water-glycol-type hydraulic oil with VG32. The experimental conditions were a rotational speed N of 25 s^{-1} and an inlet oil temperature t_{in} of 40°C. Due to low lubricity caused by the use of water-glycol-type oil (WG), the experimental condition was limited up to the discharge pressure p_d of 10 MPa.

Under these experimental conditions, the temperature change Δt was less pronounced. It is noteworthy that using the water-glycol hydraulic oil from atmospheric pressure to the maximum discharge pressure p_d=10 MPa, the temperature Δt_7 at No. 7 elevated only 5°C from the inlet temperature t_{in}. In particular, the values of Δt of the cam-ring were smaller and the differences between Δt of the side-plate and the cam-ring were indistinct.

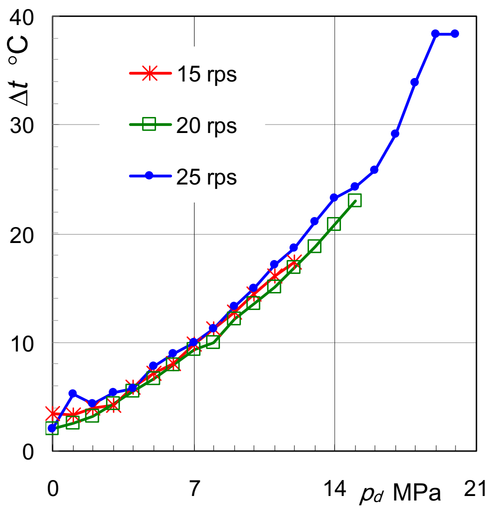

Figure 6 Effects of the rotational speed N on temperature change Δt at No. 7 of the cam-ring (MO, $t_{in} = 40$°C)

Figure 11 portrays the effects of the rotational speed N on Δt at No. 7. At higher speed $N = 25$ s^{-1}, the increase in Δt was highest, but the differences in Δt were slight.

Figure 12 shows the effects of the inlet oil temperature t_{in}. As with the mineral oil, the temperature change Δt in the case of the temperature $t_{in} = 40$°C was highest. In particular, Δt of $t_{in} = 30$°C was lowest, being approximately less than 1°C in the range of $p_d \leq 10$ MPa.

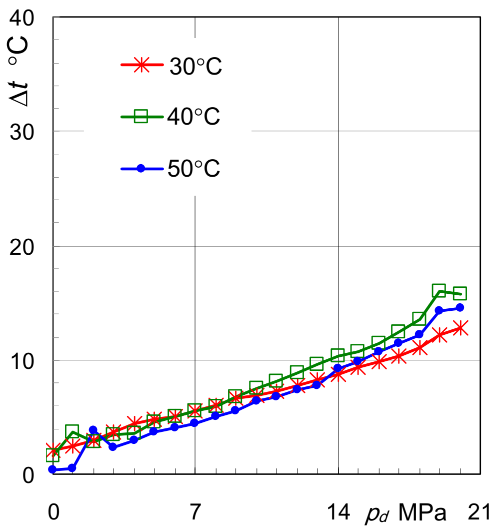

Figure 7 Effects of inlet oil temperature t_{in} on Δt at No. 5 of the cam-ring (MO, $N = 25$ s^{-1})

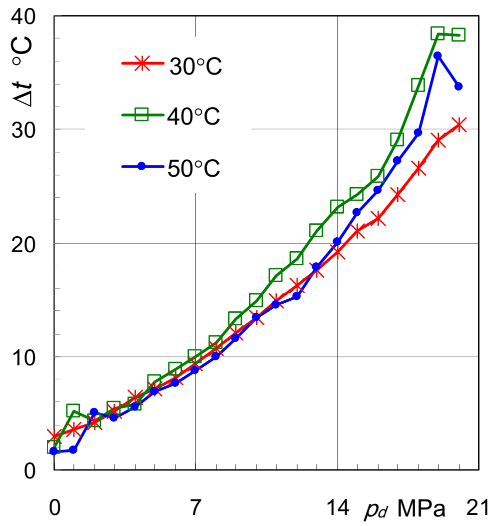

Figure 8 Effects of inlet oil temperature t_{in} on Δt at No. 7 of the cam-ring (MO, $N = 25$ s^{-1})

Figures 13 and 14 portray the comparison of temperature changes Δt at Nos. 5 and 7 of the cam-ring for mineral oils (MO) and water-glycol oils (WG). The temperature increase in Δt of WG was markedly less than that in Δt of MO for both the delivery and suction ports.

CONCLUDING REMARKS

Using a small hydraulic vane pump, the temperatures of the cam-ring and the side-plates were measured. The hydraulic fluid type, inlet fluid temperature, discharge pressure, and rotational speed were selected as the parameters, and the thermal lubrication characteristics of the pumps were examined experimentally under field operating conditions.

The temperatures of the cam-ring and the side-plates increased almost linearly as the discharge pressure increased. The temperature rise of the cam-ring was larger than the rise of the side plates. The temperature greatly increased at the suction port of the cam-ring, while the temperature did not exhibit a distinguished increase at the delivery port of the cam-ring. The differences in the temperature changes of the side-plates were slight.

The temperatures with the water-glycol-type oil were elevated less than the temperatures observed in the

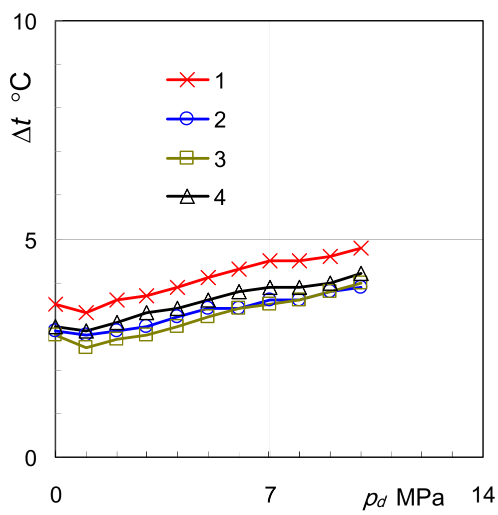

Figure 9 Effects of discharge pressure p_d and on Δt of the side-plate (WG, $N = 25\ s^{-1}$, $t_{in} = 40°C$)

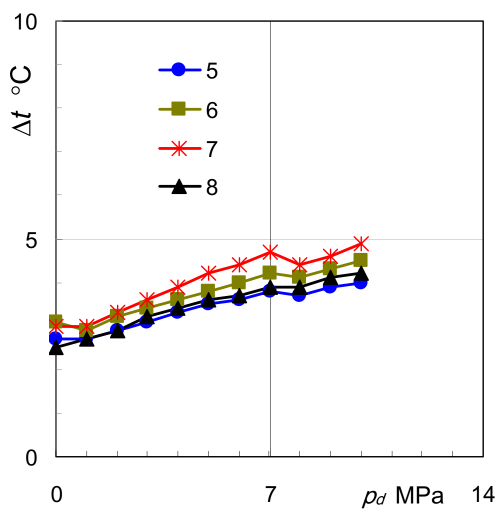

Figure 10 Effects of discharge pressure p_d and on Δt of the cam-ring (WG, $N = 25\ s^{-1}$, $t_{in} = 40°C$)

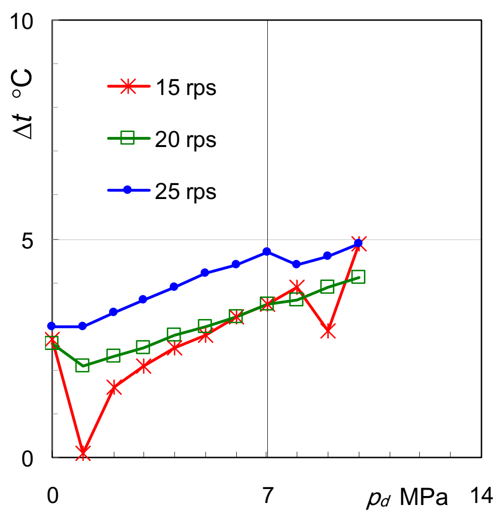

Figure 11 Effects of rotational speed N on Δt at No. 7 of the cam-ring (WG, $t_{in} = 40°C$)

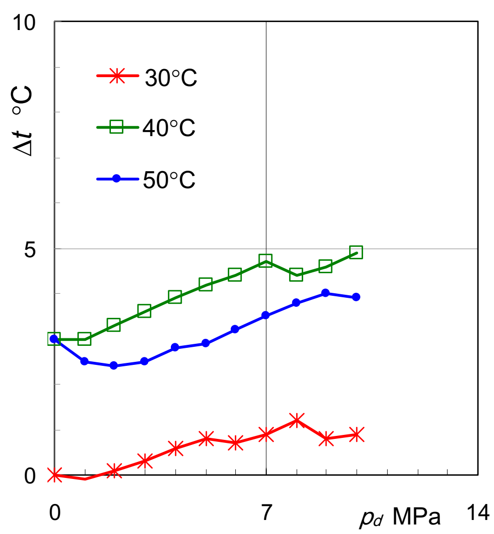

Figure 12 Effects of inlet oil temperature t_{in} on Δt at No. 7 of the cam-ring (WG, $N = 25\ s^{-1}$)

experimental setup with the mineral oil. The differences in the temperature changes of the cam-ring as well as the side-plates were insignificant.

In this experiment, the effects of the rotational speed and the inlet oil temperature on the sliding surface temperatures were unclear.

ACKNOWLEDGEMENTS

The authors would like to express their appreciation to Mr. K. Ohba, Mr. H. Kawahara, and Mr. T. Kitamura of Yukenkogyo Co., Ltd., and Mr. M. Anzai, a former student at the Muroran Institute of Technology.

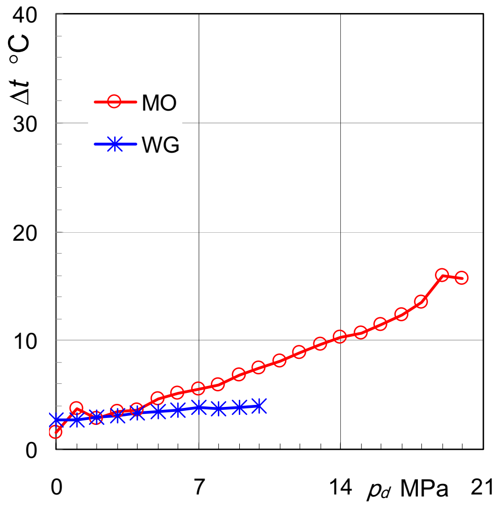

Figure 13 Comparison of Δt at No. 5 of the cam-ring for mineral oil (MO) and water-glycol oil (WG) (t_{in} = 40°C, N = 25 s^{-1})

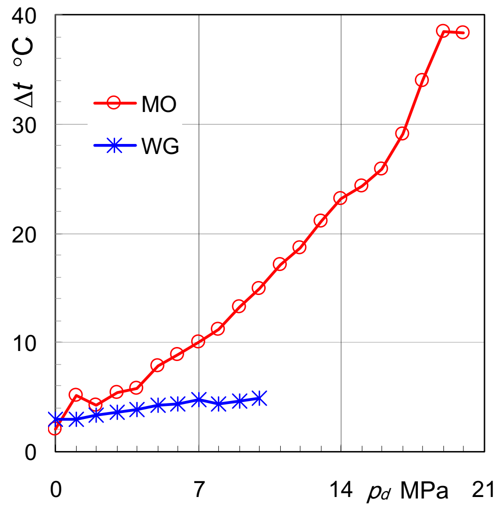

Figure 14 Comparison of Δt at No. 7 of the cam-ring for mineral oil (MO) and water-glycol oil (WG) (t_{in} = 40°C, N = 25 s^{-1})

REFERENCES

1. JIS B 8351, Vane Pumps for Hydraulic Use, 1999.
2. ASTM D6973, Standard Test Method for Indicating Wear Characteristics of Petroleum Hydraulic Fluids in a High Pressure Constant Volume Vane Pump, 2008.
3. Inaguma, Y. and Hibi, A., Reduction of Friction Torque in Vane Pump by Smoothing Cam Ring Surface, Proceedings of the Institution of Mechanical Engineers, Part C: Journal of Mechanical Engineering Science, 2007, 221–5, pp.527–534.
4. Nishiumi, T., Konami, S., and Maeda, T., Vane Jumping and Its Prevention in a Dual-Vane Pump (in Japanese), Transactions of Japan Hydraulics and Pneumatics Society, 2002, 33–7, pp.156–161.
5. Wilson, W. E., Design of Optimum Clearances in Positive-Displacement Pumps and Motors, Transactions of American Society of Mechanical Engineers, 1956, pp. 117–122.
6. Yamaguchi, A. and Tsuchimoto, M., Bearing Seal Characteristics of the Oil Film Between a Valve Plate and a Cylinderblock of Axial Piston Pumps (in Japanese), Journal of Japan Hydraulics and Pneumatics Society, 1982, 13–1, pp. 55–60.
7. Ivantysynova, M., A New Approach to the Design of Sealing and Bearing Gaps of Displacement Machines, Proceedings of 4th JHPS International Symposium on Fluid Power, Tokyo, 1999, pp.45–50.
8. Olems, L., Investigations of the Temperature Behaviour of the Piston Cylinder Assembly in Axial Piston Pumps, International Journal of Fluid Power, 2000, 1–1, pp.27–38.
9. Kazama, T., Thermohydrodynamic Lubrication Analysis of Hybrid Thrust Bearings: Modeling of a Slipper Used in Swashplate Type Axial Piston Pumps/Motors (in Japanese), Transactions of Japan Hydraulics and Pneumatics Society, 2007, 40–2, pp. 30–35.
10. Kazama, T. and Tsuruno, T., Thermal Lubrication Characteristics of Swash-Plate Type Axial Piston Pumps (Temperature Measurement of Swash-Plate and Cylinder-Block) (in Japanese), Transactions of Japan Society of Mechanical Engineers, Ser. C, 2004, 74–738, pp. 425–430.
11. Kazama, T., Tsuruno, T. and Sasaki, H., Temperature Measurement of Tribological Parts in Swash-Plate Type Axial Piston Pumps, Proceedings of the 7th JFPS International Symposium on Fluid Power, Toyama, 2008, CD-ROM, P1-16.
12. Kazama, T., Oguma, S., and Huang, R., Tribological Approach to Side-Plates in External Gear Pumps (Temperature Measurement, Vibration Analysis, and Geometry Design), Proceedings of the 2nd International Conference on Design Engineering and Science, Tokyo, 2010, pp. 235-240.

A ROBUST POSITION CONTROL OF ELECTRO-HYDROSTATIC ACTUATOR SYSTEMS

In Seok Seo*, Ji Min Lee**, Sung Hwan Park*** and Jong Shik Kim ****

* PhD candidate in School of Mechanical Engineering, Pusan National University, Korea.
(e-mail : s76024515@nate.com)
** PhD candidate in the School of Mechanical Engineering, Pusan National University, Korea.
(e-mail : j2002@pusan.ac.kr)
*** Research assistant professor in the School of Mechanical Engineering, Pusan National University, Korea. (e-mail : shpark@pusan.ac.kr)
**** Professor in the School of Mechanical Engineering, Pusan National University, Korea.
(e-mail : jskim@pusan.ac.kr)

ABSTRACT

In this paper, an adaptive PID sliding mode controller is proposed for the position control of electro-hydrostatic actuator(EHA) systems with system uncertainties and saturation in the motor. An EHA prototype is developed and system modeling and parameter identification are executed. Then, adaptive PID sliding mode controller and optimal anti-windup PID controller are designed and the performance and robustness of the two control systems are compared by experiment. It was found that the adaptive PID sliding mode control system has better performance and is more robust to system uncertainties than the optimal anti-windup PID control system.

KEY WORDS

Robust control, Electro-Hydrostatic Actuator, Position control

NOMENCLATURE

Q_a, Q_b	:	pump in/out flows
p_a, p_b	:	pump in/out pressures
Q_1, Q_2	:	cylinder in/out flows
ω_p	:	angular velocity
p_{pipe}	:	pressure drop
B	:	viscous friction coefficient
β_e	:	effective bulk modulus

INTRODUCTION

Recently, lots of hydraulic servo systems have been replaced to electric motor driven systems to overcome the problems of traditional hydraulic servo systems such as oil leakage, maintenance and complex pipe laying. In spite of these drawbacks, hydraulic systems are still used in the fields where large force and high power are required. In order to solve these drawbacks of hydraulic systems, electro- hydrostatic actuator (EHA) systems are in the process of development for industrial use. The

EHA system is a kind of compactly high power actuator module through the integration of electric motor, pump, accumulator and oil tank in a component. Therefore, EHA systems do not need complex pipe lines. Moreover, EHA systems are environment- friendly driving systems which can realize no oil leakage. Also, energy efficiency of EHA systems is extremely high because they can supply the only necessary energy in the plant.

Hydraulic servo systems, in general, have some system uncertainties such as internal leak and friction in the cylinder and pump. These uncertainties also affect to the performance of the position control system for EHA. On the other hands, EHA systems have the closed loop structure which can use relatively a little working fluid. Therefore, the performance of EHA systems can be sensitive to the variation of system parameters of the working fluid such as the effective bulk modulus and the viscosity due to the variation of circumstance environment.

In order to obtain the desirable performance of EHA systems, a number of control strategies have been investigated in the literature including inner and outer loop controllers based on the PID control scheme[1][2], classic quantitative feedback theory (QFT)[3], sliding mode controller with variable structure filter[4]. S. Habibi et. al. proposed PID controller with inner-outer loop structure for position control of EHA to compensate the dead zone of the electric motor which occurs when the rotational direction of the electric motor is changed [2][3]. Uncertainties of the position control system for EHA can be compensated by selecting the control gains of the inner-loop which controls the velocity of the electric motor as large as possible. However, the inner loop PID controller cannot compensate system uncertainties effectively because the magnitude of the control gains has a limitation physically. The outer loop PID controller for the position control has no desired robustness to system uncertainties.

In addition, E. Sampson et. al. applied a sliding mode controller to the variable structure filter for the robust position control of EHA systems[4]. The variable structure filter has been designed to estimate the states of a system. However, this control scheme has complex structure because both estimator and controller are designed and implemented respectively. Also, it is unpractical to constitute the bypass for the high frequency loop to transfer states estimated by the variable structure filter to the sliding mode controller.

The problem of the saturation in the electric motor has not been considered in the previous research. Therefore, in the paper, an EHA prototype was developed in order to apply it in industrial fields such as servo press, steering gear, injection molding machine and etc. The experiment was executed in order to verify the control performance of the developed EHA prototype with PID controller. From experimental results, it was found that overshoot occurred due to the saturation in the electric motor when fast response is required.

In this paper, an adaptive PID sliding mode control scheme is applied for the position control of EHA systems which can achieve desirable performance and robustness. Also, an optimal anti-windup PID controller was designed and implemented in order to compare with the adaptive PID sliding mode controller.

This paper is organized as follows: Composition and details of the position control test rig of an EHA prototype are included in section 2. System modeling and parameter identification of the EHA system are presented in Section 3. In Section 4, position controllers for the EHA system using traditional anti-windup PID control scheme and adaptive PID sliding mode control scheme are presented. Section 5 presents comparative results of the experimental tests executed on the position control test rig of EHA applying both anti-windup and adaptive PID sliding mode control schemes. Finally, conclusions are provided in Section 6.

EXPERIMENTAL SETUP OF ELECTRO-HYDROSTATIC ACTUATOR PROTOTYPE

The EHA system consists of electric motor, hydraulic pump, hydraulic cylinder, accumulator, check valves and relief valves for safety. The cylinder is controlled by the electric motor which is directly connected to the hydraulic pump. The direction change of the cylinder depends on the rotation direction of the electric motor. Also, an electric motor installed in the EHA system controls the flow rate and pressure of the working fluid by regulating the velocity and torque of the motor.

In this paper, an EHA prototype is developed which can be used for various purposes in industrial fields such as servo press, steering gear, injection molding machine and etc. The specifications of the EHA prototype are shownin Table 1. Figure 1 shows the hydraulic circuit of the hydraulic position control test rig for the developed EHA prototype. The test rig is used for the dynamic performance test of position control systems. It consists of two hydraulic cylinders: a main cylinder which is a

Table 1 Specifications of the EHA prototype

Specification	Value
Stall force	15,705kg
Stroke	± 33.7 Wb/m2
Velocity	123.0~142.5 mm/s
Power	9.0 kW

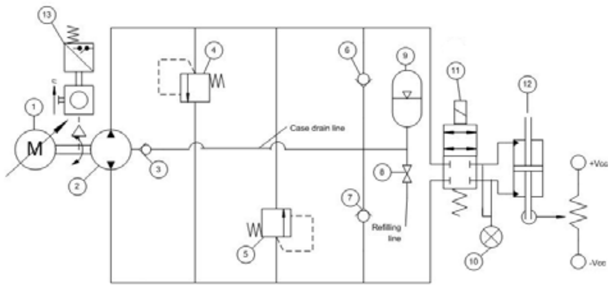

Figure 1 Hydraulic circuit of the EHA system

part of EHA and a load cylinder. Two cylinders are coupled by a shaft. The main cylinder is controlled by the electric motor which is also a part of EHA. The load cylinder is controlled by the Moog servo valve and it controls the meter-out flow from the load cylinder to simulate the load.

The flow of the hydraulic fluid to the main cylinder is controlled by the electric BLDC servo motor operated through a driver by a controller. The position of the main cylinder along its stroke is measured by a linear variable displacement transducer (LVDT) mounted in the hollow of the main cylinder rod. The signal from the LVDT is used for the closed-loop control of the main cylinder via controllers. The load force is measured by the load cell installed at the linkup between two cylinders.

In addition, there is the main control device DS1104 dSPACE board which is used to implement position controllers: anti-windup PID controller and adaptive PID sliding mode controller. The real-time control system is programmed by MATLAB/ Simulink. The real-time control system is transferred to the board through the Real-Time Workshop. The parameters of the controller implemented on the board can be changed and monitored through the Control-Desk software in real time. Figure 2 shows the position control test rig of the EHA system.

Figure 2 Position control test rig of the EHA system

MODELLIMG AND IDENTIFICATION OF EHA SYSTEMS

In order to design the position control systems of EHA using the optimal anti-windup PID controller scheme and adaptive PID sliding mode control scheme, a mathematical model of EHA systems is derived and system parameters are identified by the signal compression method (SCM).

A. Mathematical Model of EHA Systems

The pump in/out flows (Q_a, Q_b) can be represented with pump in/out pressures (p_a, p_b) and angular velocity (ω_p) as follows:

$$\begin{aligned} Q_a &= D_p\omega_p - \xi(p_a - p_b) - \frac{V_a}{\beta_e}\frac{dp_a}{dt} \\ Q_b &= D_p\omega_p - \xi(p_a - p_b) + \frac{V_b}{\beta_e}\frac{dp_b}{dt} \end{aligned} \tag{1}$$

where D_p is the pump displacement. In addition, the cylinder in/out flows (Q_1, Q_2) can be represented with the cylinder in/out pressure (p_a, p_b) and the cylinder displacement (x) as follows:

$$\begin{aligned} Q_1 &= A\dot{x} + \frac{(V_0 + Ax)}{\beta_e}\frac{dp_1}{dt} + Lp_1 \\ Q_2 &= A\dot{x} - \frac{(V_0 - Ax)}{\beta_e}\frac{dp_2}{dt} - Lp_2 \end{aligned} \tag{2}$$

The pipe between the pump and the cylinder can be represented with a pressure drop (p_{pipe}) on the assumption that the pipe is rigid [1].

$$\Delta p_{pipe} = 2K_{pipe}D_p^2(\Delta\omega_p) \tag{3}$$

Then, the relationship between the pump port pressures and cylinder chamber pressures can be expressed as

$$\begin{aligned} p_a &= p_1 + p_{pipe}, \\ p_b &= p_2 - p_{pipe}. \end{aligned} \tag{4}$$

It is assumed that $\frac{dp_{pipe}}{dt}$ is negligible compared with $\frac{dp_1}{dt}$ and $\frac{dp_2}{dt}$, then

$$\begin{aligned} \frac{dp_a}{dt} &= \frac{dp_1}{dt}, \\ \frac{dp_b}{dt} &= \frac{dp_2}{dt}. \end{aligned} \tag{5}$$

Since the shape of the cylinder chamber is symmetric, the following equation for the cylinder chamber pressures can be established.

$$\frac{dP_1}{dt} = -\frac{dP_2}{dt} \tag{6}$$

By combing Eqs. (1) and (6), a simplified pump/cylinder model equation can be obtained as

$$D_p \omega_p = A\dot{x} + \frac{V_0}{\beta_e}\dot{p}_L + \xi p_L + 2\xi p_{pipe} + \frac{L}{2}p_L \tag{7}$$

where $p_L = p_1 - p_2$ The actuator force and the displacement of the load can be represented as

$$F = p_L A = M\ddot{x} + B\dot{x} \tag{8}$$

By combining Eqs. (7) and (8), the transfer function between the angular velocity of the pump and the displacement of the load can be expressed as

$$\frac{x(s)}{\omega_p(s)} \approx \frac{\dfrac{2D_p\beta_e A}{MV_0}}{s^3 + s^2\left(\dfrac{B}{M} + \dfrac{C_T\beta_e}{V_0}\right) + s\left(\dfrac{2\beta_e A^2}{MV_0} + \dfrac{C_T B\beta_e}{MV_0}\right)} \tag{9}$$

From Eq. (9), it is found that the variation of the effective bulk modulus of the working fluid can increase or decrease the compressibility of the working fluid and then the natural frequency of the EHA system can be varied. The viscosity of the working fluid also affects the dynamic characteristics of the EHA position control system. Therefore, the EHA system with fixed control gains may not obtain the desirable response characteristics.

B. Parameter Identification

In general, the unknown system parameters of the linear elements in a non-linear system can be identified by the SCM. In practice, hydraulic servo systems exhibit significant non-linear behaviour due to system uncertainties such as line losses, leakages, and parameter variations of the working fluid. In the identification process by the SCM, some of those uncertainties have to be neglected because the SCM can only identify the linear part of the system. The unknown parameters of the linearized mathematical model of the position control system for EHA are identified by the SCM.

As shown in Fig. 3, the test signal that has the same amplitude up to 4 Hz in the frequency domain is applied to the position control system of EHA by constructing a close-loop proportional control system to obtain a more accurate equivalent impulse response for the precise identification of unknown parameters. Figure 4 shows the comparison of the frequency response of the pressure control system between the closed-loop nominal model and the closed-loop actual system with a proportional controller, whose gain is 1000.

From the identified nominal model for the closed-loop position control system for EHA with the proportional controller, the parameters of the position control system can be acquired by eliminating the effect of the proportional controller mathematically.

After eliminating the effect of the proportional controller mathematically, the identified transfer function of the position control system for EHA is as follows:

$$G(s) = \frac{11.8\times10^4}{s^3 + 2231s^2 + 71.8\times10^5 s} \tag{10}$$

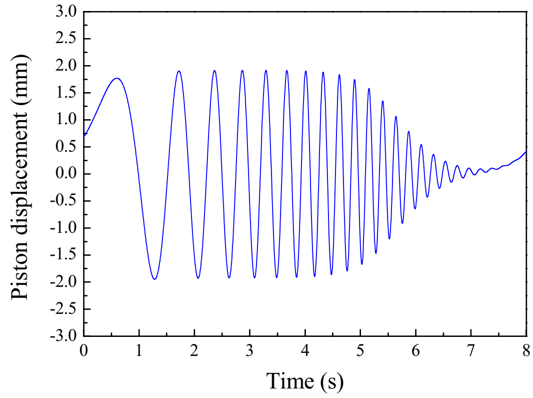

Figure 3 Test signal

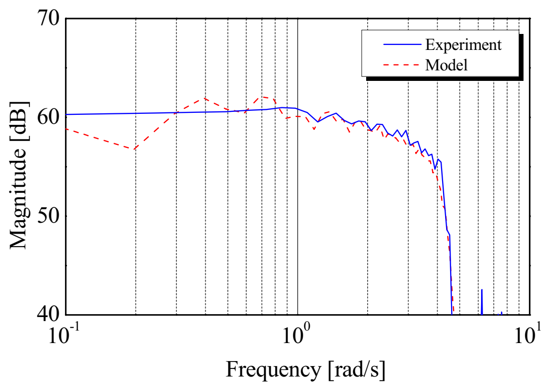

Figure 4 Bode-plots of the closed loop nominal model and the closed loop actual system with a proportional controller

The identified system parameters were verified on the time domain. Figure 5 (b) shows the step responses of the nominal model and actual system. The validations of the estimated parameters are estimated by the cross-correlation.

$$corr = \frac{\sum_{k=1}^{N}(Y_p(k)-\overline{Y}_p)(Y_m(k)-\overline{Y}_m)}{\sqrt{\sum_{k=1}^{N}(Y_p(k)-\overline{Y}_p)}\sqrt{\sum_{k=1}^{N}(Y_m(k)-\overline{Y}_m)^2}} \qquad (11)$$

where $Y_p(k)$ and $Y_m(k)$ are the responses of the real and nominal model in time train k, respectively. $\overline{Y}_p$ and $\overline{Y}_m$ are the mean values of $Y_p(k)$ and $Y_m(k)$, respectively. N is the acquired data number. The value of the cross-correlation is 0.904 which can calculate from the identification results.

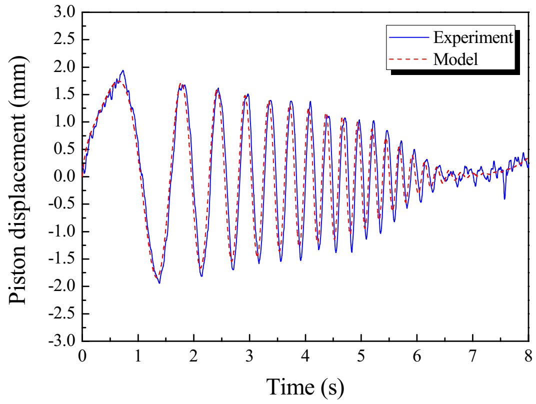

(a) Response for the test signal

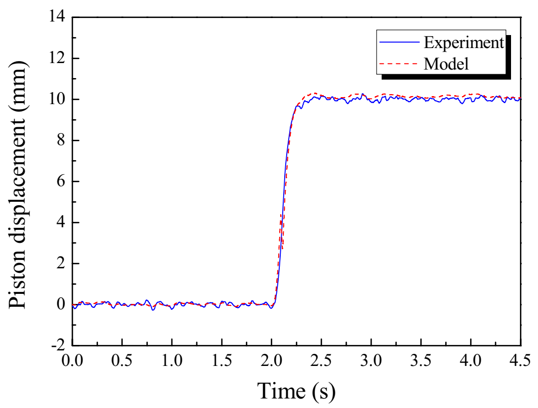

(b) Step response

Figure 5 Time responses of the position control system obtained by the experiment and nominal model

POSITION CONTROL SYSTEM DESIGHN FOR EHA

A. Optimal Anti-windup PID Control System

An optimal anti-windup PID control system for the EHA with saturation in the electric motor is designed which can obtain desirable performance. In the time domain, performance for a control system design involves certain some requirements associated with the time response of the system. The performances are expressed in terms of the rising time, settling time, overshoot and steady-state error in step response. The identified transfer function in Eq. (10) is considered to obtain optimal control gains of the anti-windup PID controller.

In order to realize desirable performance, the performance function is considered during the design of the anti-windup PID controller as follows:

$$J(K_p, K_i, K_d) = \sum_{t=0}^{\infty}(y_{step}(t) - y_{step}^{d}(t)) \qquad (12)$$

where $y_{step}^{d}(t)$ is the desired step of the optimal anti-windup PID control system response and $y_{step}(t)$ is the step response by the identified transfer function in Eq.(10). The optimal PID controller design can be stated as

$$\min_{K_p, K_i, K_d} J\left(K_p, K_i, K_d\right) \qquad (13)$$

where K_p, K_i and K_d are the proportional, integral and differential control gains, respectively.

There are many optimization algorithms in the optimization toolbox for use with MATLAB/Simulink. The reference step input is the same as used in the design procedure of the PID controller. The cost function is

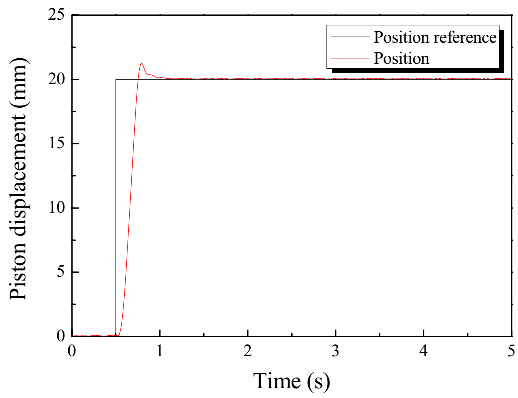

Figure 6 Step response of the optimal anti-windup PID control system

given by $J(K_p, K_i, K_d)$ and the optimal PID controller gains K_p, K_i, K_d can be found by using the optimization toolbox. The saturation in the electric motor and system parameter uncertainties due to the modeling error are reflected in the optimization process for the controller parameters. The step response of the optimal anti-windup PID control system is shown in Fig. 6.

B. Adaptive Sliding Mode Control System considering PID Sliding Surface

The position control system for EHA with saturation in the electric motor is designed by the adaptive PID sliding mode control scheme to achieve desirable response characteristics of EHA systems. In the controller design process, the effective bulk modulus and viscous friction coefficient are considered as system parameters with variation.

The sliding surface s for the design of the adaptive sliding mode control system is defined as

$$s = k_1 e + k_2 \int e dt + k_3 \dot{e} \tag{14}$$

where the tracking error of the position $e = r_d - r$, r_d is the desired position and k_1, k_2 and k_3 are positive design parameters. By combining Eqs. (9) and (14) and considering the noise term in the acceleration $\ddot{x} = \ddot{x}_m + \ddot{x}_n$ where the subscripts m and n denote the nominal and noisy values, respectively. The derivative of the sliding surface $\dot{s}$ can be written as

$$\dot{s} = -\frac{2D_p \beta_e A}{MV_0}\omega_p + \left(\frac{B}{M} + \frac{C_T \beta_e}{V_0}\right)(\ddot{x}_m + \ddot{x}_n) + \beta_e\left(\frac{2A^2 + C_T B}{MV_0}\right)\dot{x} \\ - 2\lambda\ddot{e} - \lambda^2\dot{e}. \tag{15}$$

The derivative of the sliding surface which can satisfy the reaching condition and solve the chattering problem of the control input is selected as

$$\dot{s} = -Ds - K\,\mathrm{sgn}(s) \tag{16}$$

where D and K are positive design parameters. In Eq. (15), the magnitude of the uncertainty related to $\ddot{x}_r$ is assumed as

$$\kappa_{\min} < \left| k_3\left(\frac{MV_0}{BV_0 + C_T \beta_e}\right)\ddot{x}_n \right| < \kappa_{\max} \tag{17}$$

where $\kappa_{\min}$ and $\kappa_{\max}$ are constants.

From Eq. (16) and the reaching condition, the equivalent control law can be selected as

$$u_{eq} = k_1\dot{e} + k_2 e + k_3\ddot{x}_r + k_3\frac{MV_0}{2D_p\beta_e A}(\ddot{x}_m + \ddot{x}_n) \\ + k_3\left(\frac{2\beta_e A^2 + C_T B\beta_e}{2D_p\beta_e A_0}\right)\dot{x}. \tag{18}$$

In order to determine the robust control term of the sliding mode controller, it is assumed that

$$D_0|s| + K_0 > \left| k_3\left(\frac{MV_0}{BV_0 + C_T\beta_e}\right)\ddot{x}_n \right| + \eta \tag{19}$$

where $K_0 = \left(k_3\frac{2D_p A\hat{\beta}_e}{BV_0 + C_T\hat{\beta}_e M}K\right)$, $D_0 = \left(k_3\frac{2D_p A\hat{\beta}_e}{BV_0 + C_T\hat{\beta}_e M}D\right)$ and η are positive design parameters. On the assumption of Eq. (19), the robust control law is determined as

$$U_r = Ds + K\,\mathrm{sgn}(s) \tag{20}$$

If the viscous friction coefficient B and the effective bulk modulus of EHA systems β_e are considered as unknown and variation parameters, respectively, then the uncertainty ψ is defined as

$$\psi = k_3\left(\frac{MV_0}{BV_0 + C_T\beta_e}\right)\ddot{x}_m + k_3\left(\frac{2\beta_e A^2 + C_T B\beta_e}{2D_p\beta_e A_0}\right)\beta_e\dot{x} \tag{21}$$

where $\theta^T = \left[k_3\left(\frac{MV_0}{BV_0 + C_T\beta_e}\right) \quad k_3\left(\frac{2\beta_e A^2 + C_T B\beta_e}{2D_p\beta_e A_0}\right)\right]$ $\varphi = \begin{bmatrix}\ddot{x} \\ \dot{x}\end{bmatrix}$.

The parameter vector $\hat{\theta}$ is considered as an unknown parameter vector and it can be estimated by using the update law.

In order to obtain the update law for the unknown parameters, the Lyapunov candidate is defined as

$$V = \frac{1}{2}s^2 + \frac{1}{2k}\tilde{\theta}^T\tilde{\theta} \tag{22}$$

where $\tilde{\theta} = \theta - \hat{\theta}$ and θ and $\hat{\theta}$ are the nominal and estimated parameter vectors, respectively, and k is a positive parameter. From the derivative of the Lyapunov included sliding dynamics, the update law for the unknown parameters is selected as

$$\dot{\hat{\theta}} = ks\varphi \tag{23}$$

Therefore, the derivative of the Lyapunov is given by

$$\dot{V} = -Ds^2 - Ks\,\mathrm{sgn}(s) \le 0 \tag{24}$$

By applying the Lasalle's theorem for Eq. (24), the asymptotical stability of the EHA position control system is guaranteed [3].
Finally, the sliding mode control law can be selected as

$$\hat{u} = \frac{BV_0 + C_T\hat{\beta}_e M_0}{k_3 2D_p\hat{\beta}_e A}\left(\hat{\theta}^T\varphi + k_1\dot{e} + k_2 e + k_3\ddot{x}_r\right) + K\,\mathrm{sgn}(s) + D(s) \quad (25)$$

where $\hat{\beta}_e(t+T_s) = \frac{d\hat{\beta}_e(t)}{dt}T_s + \hat{\beta}_e(t)$ and T_s is the sampling time.

EXPERIMENTAL RESULTS AND DISCUSSION

In order to demonstrate and compare the performance of two control systems, some experimental results are represented in this section. Figure 7 shows the performance of the optimal anti-windup PID and adaptive PID sliding mode position control systems for EHA. It is shown from experiments carried out in the test rig that the closed-loop position control system of EHA with anti-windup PID control system gives unexpected overshoot, long settling time and big steady state error. On the other hand, no overshoot, short settling time and small steady state errors are obtained to the various reference positions by the adaptive PID sliding mode control system.

In addition, the optimal anti-windup PID control system does not achieve robustness to the load disturbance as shown in experiments with a load (See Fig. 7). Despite of the modeling error, uncertainties and load disturbance in the position control system for EHA, the adaptive PID sliding mode control system has better performance and robustness than the optimal anti-windup PID control system. The time-domain performances are presented in Table 2 for anti-windup PID and adaptive PID sliding mode control systems.

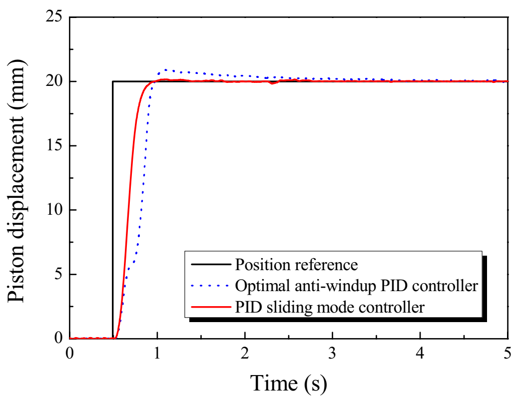

(a) Step response

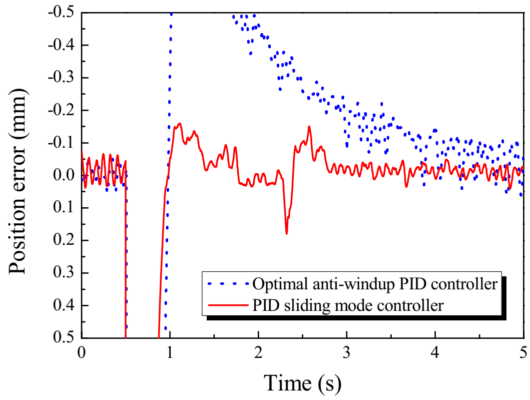

(b) Error

Figure 7 Position errors of EHA control systems with a load

TABLE 2 comparison of the performance of optimal anti-windup PID and adaptive PID sliding mode control systems

Performance	optimal anti-windup PID	adaptive PID sliding mode
Overshoot	4.5%	0.5%
Settling time	3sec	0.5sec
Time delay	0.31sec	0.18sec

CONCLUSION

In this paper, optimal anti-windup PID controller and adaptive PID sliding mode controller have been adopted to control the position of EHA systems. With saturation in the electric motor an identified third order plant model is used to design controllers based on the mathematical model of EHA systems. Based on the experimental results and the time domain specifications, it can be concluded that the performance of the EHA position control system can be improved and robustness to the load which can be implemented by using the adaptive PID sliding mode controller compared with the optimal anti-windup PID controller.

REFERENCES

1. S.R. Habibi and A. Goldenberg, Design of a new high-performance electro-hydraulic actuator, IEEE/ASME Trans. Mechatron. 2000, pp. 158–164.
2. Sampson E, Habibi S, Chinniah Y, Burton R. Model identification of the electro-hydraulic

actuator for small signal inputs. In: Bath workshop on power transmission and motion control (PTMC 2005), 18th. University of Bath, United Kingdom; September 7–9, 2005
3. M. Pachter, C. H. Houpis, K. Kang., "Modeling and control of an electro-hydrostatic actuator" ISA Transactions., vol. 7, No.6, pp. 591-608, 1998.
4. Ilyas Eker., "Sliding mode control with PID sliding surface and experimental application to an electromechanical plant " ISA Transactions., vol. 45, No.1, pp. 109-118, Jan 2006.
5. N. Aoshima, "Measurement of nonlinear vibration by signal compression method," Proc. of the Acoustical Society of America, vol.76, no.3, pp. 794-801, 1984

Proceedings of the 8th JFPS International
Symposium on Fluid Power, OKINAWA 2011
Oct. 25-28, 2011

1B2-2

FORCE EQUALIZATION FOR REDUNDANT ACTIVE/ACTIVE POSITION CONTROL SYSTEM INVOLVING DISSIMILAR TECHNOLOGY ACTUATORS

Lijian WANG*, Jean-Charles MARE*, Yongling FU**, Haitao Qi**

* Institut Clément Ader, INSA-UPS, Université de Toulouse
135 Avenue du Rangueil, 31077, Toulouse, France
(E-mail: lijian.wang@insa-toulouse.fr)
** Department of Mechanical Engineering and Automation, Beihang University
37 Xueyuan Road, Haidian District, 100191, Beijing, China

ABSTRACT

The purpose of this communication is to develop the suitable control strategies to solve the force fighting of redundant active/active position control system involving dissimilar technology actuators. The research work is based on one redundant actuation test bench composed by one electro-mechanical actuator (EMA) and one servo-hydraulic actuator (SHA). One numerical model of this test bench is developed and detailed, and the sources for force fighting are studied based on it. Then three static force equalization control strategies are advanced. In the first one, both actuators are at position control and with quasi static force equalization. In the second one, the SHA is at position control but the EMA is at force control to compensate the force fighting. In the third one, the SHA is controlled to drive the position load while the EMA is controlled to output zero force. With both simulations and experiments, these three strategies are compared and concluded.

KEY WORDS

Active/Active, Actuator, Dissimilar, Force equalization, Redundant

NOMENCLATURE

A_t [m²]	: SHA piston effective area
a [null]	: SHA friction mean coefficient of external applied force
B_s [Ns/m]	: SHA viscous damping coefficient
b [null]	: SHA friction quadrant coefficient
B_e [Nm/(rad/s)]	: EMA viscous damping coefficient
c [null]	: EMA friction mean coefficient of external applied force
d [null]	: EMA friction quadrant coefficient
E_e [m]	: EMA position sensor offset
E_s [m]	: SHA position sensor offset
E_y [Pa]	: hydraulic oil bulk modulus
F_L [N]	: total external load force
F_{LE} [N]	: external force working on EMA
F_{LS} [N]	: external force working on SHA
F_e [N]	: EMA output force
F_{ex} [N]	: external force working on the rod of actuator
F_{fc} [N]	: SHA Coulomb friction force
F_{fs} [N]	: SHA Stribeck friction force
F_s [N]	: SHA output force
F_{sf} [N]	: SHA friction force
f_v [Ns/m]	: SHA friction viscous coefficient

I_{sv} [A] : SHA servovalve input current
J_m [Kgm²] : EMA equivalent rotation inertia
K_c [(m^3/s)/Pa] : SHA total flow/pressure gain
K_{ac} [(m^3/s)/Pa] : cylinder inner leakage coefficient
K_{eb} [N] : EMA controller proportional gain
K_{sb} [A/m] : SHA controller proportional gain
K_{sc} [(m^3/s)/Pa] : servovalve flow/pressure gain
K_{sg} [(m^3/s)/A] : servovalve flow/current gain
K_{so} [m/A] : servovalve opening/current gain
K_{sp} [Pa/m] : servovalve pressure/opening gain at null flow
l [m] : EMA roller-screw lead
M_t [Kg] : load equivalent mass
M_e [Kg] : EMA equivalent mass
P_f [Pa] : SHA load pressure
Q_{sv} [m^3/s] : servovalve output flow
S_e [N/m] : EMA position closed loop stiffness
S_{et} [N/m] : EMA overall structural stiffness
S_s [N/m] : SHA position closed loop stiffness
S_{st} [N/m] : SHA overall structural stiffness
S_t [N/m] : overall transmission stiffness
T^* [Nm] : EMA torque demand
T_e [Nm] : roller-screw output torque
T_{ef} [Nm] : EMA friction torque
T_{fc} [Nm] : EMA Coulomb friction torque
T_{fs} [Nm] : EMA Stribeck friction torque
T_m [Nm] : EMA DC motor output torque
t_v [Ns/m] : EMA friction viscous coefficient
V_t [m^3] : SHA cylinder effective volume
v_r [m/s] : SHA friction reference velocity
X_e [m] : EMA piston displacement
X_s [m] : SHA piston displacement
X_t [m] : aerodynamic surface displacement
x_{tc} [m] : transmission compression
ω_h [Hz] : redundant system natural frequency
ω_m [rad/s] : EMA motor rotation velocity
ω_r [rad/s] : EMA friction reference velocity
ω_s [Hz] : SHA natural frequency
γ [N] : actuators force fighting

INTRODUCTION

In current aircrafts, most actuation devices used for flight control and landing gear systems are servo-hydraulic actuators (SHA) which are supplied hydraulically and involve a servovalve as the power control element interfacing with electrical control. However, the aircraft industry has engaged in the evolution towards the “More Electric Aircraft” (MEA) in recent years, and the hydraulic power networks are being progressively replaced by the electrical ones. In the field of actuation, Power-by-Wire (PbW) involves electro-hydrostatic actuators (EHA) and electro-mechanical actuators (EMA) [1].
Due to the safety issues and the lack of maturity of PbW for application in normal mode, the new aircraft framework could only combines EHAs and EMAs with SHAs: the Airbus A380 involves 14 EHAs/EBHAs and the Boeing B787 involves 4 EMAs. And all these PbW actuators are being used only as backup actuators. However, for the MEA, the ultimate type of actuator could be the EMA, because it removes the hydraulics totally [2].
In a transition period, the actuation systems combining one SHA and one EMA in an active/active mode, shown as Figure 1, generate a main issue that is the force fighting between the two actuators. Because of their dissimilar technology and setting/manufacturing tolerances, their static and dynamic behaviors are so different that they do not share the load equally and often fight one against another to position the load. So, in order to improve the system energy efficiency and reliability, the force equalization must be addressed. In this communication, the new control strategies will be advanced, studied and compared.

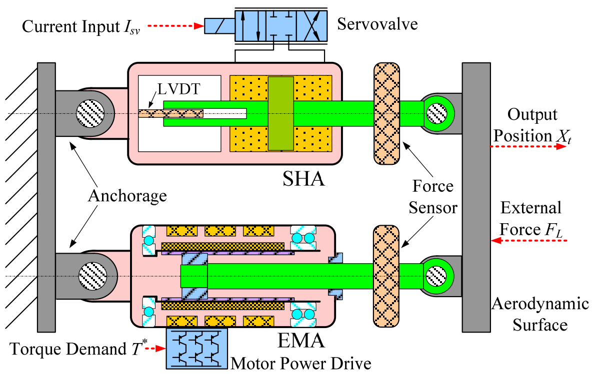

Figure 1 Schematic of redundant actuation system

The actuation system under study is sized for the roll control of single aisle aircrafts. It includes one industrial SHA that is set to reproduce the aircraft one and one prototype of EMA combining a brushless DC motor with an inverted roller-screw.
As the base of all the research work, the linear models of SHA and EMA forming the redundant system are studied in the first part. Then a virtual prototype of this redundant actuation system is developed and detailed in the LMS-AMESim simulation environment. With this virtual system, the reasons of static force fighting are studied. Then based on the former results, three quasi static force equalization control strategies are proposed and tested by simulations and experiments. Finally the conclusion is drawn for the work in this communication.

LINEAR MODEL BUILDING

This part is focused on the linear model building and analyzing in order to support the synthesis of controller for load position control and force equalization later. In addition to the pure position control performances, a particular attention is paid to the segregation of signaling the SHA and EMA (for safety issues) and the quasi closed loop static stiffness.

SHA Linear Model

As shown in Figure 1, the SHA combines one flow control servovalve and one symmetrical jack to drive the load. From the control point of view, the inputs of SHA are the current I_{sv} to servovalve and the external force F_{LS} working on the load. The functional output is the piston displacement X_s (that equals the air surface displacement X_t in linear models because the structural stiffness is neglected). The block diagram of the SHA is displayed in Figure 2 [3].

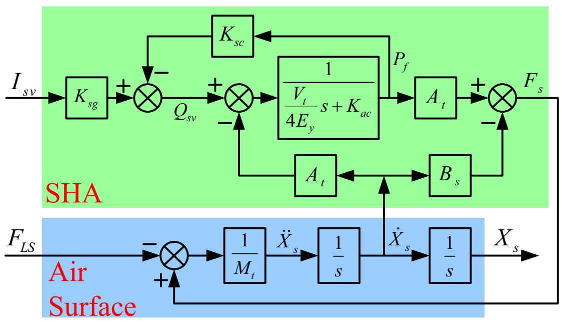

Figure 2 Linear model of SHA

This linear model takes into consideration the servovalve flow/current gain K_{sg} and flow/pressure gain K_{sc}, the jack inner leakage K_{ac}, the equivalent fluid compliance E_y (in control domains), the jack equivalent viscous friction and the load inertia effect. The transfer function of single SHA system based on Figure 2 is:

$$X_s(s) = \frac{A_t K_{sg} I_{sv}(s) - (\frac{V_t}{4E_y} s + K_c) F_{LS}(s)}{s[\frac{V_t M_t}{4E_y} s^2 + (M_t K_c + \frac{V_t B_s}{4E_y}) s + (B_s K_c + A_t^2)]} \qquad (1)$$

where $K_c = K_{ac} + K_{sc}$, is the SHA total flow/pressure gain. As shown in Eq. (1), this is a three order system with one integrator which is located downstream the loads disturbance. Therefore even with a pure proportional control in position closed loop, there is no static error in the pursuit mode and a constant error under static external force. The parameters in Eq. (1) are assigned with the values in Table 1 (these values are gotten from the manufacture datasheets).

Table 1 The values of SHA system parameters

A_t [m²]	B_s [Ns/m]	E_y [Pa]	K_c [(m³/s)/Pa]	K_{sg} [(m³/s)/A]	M_t [Kg]	V_t [m³]
3.1×10^{-3}	2300	8.0×10^{8}	7.94×10^{-8}	8.3×10^{-3}	600	3.1×10^{-4}

The open loop hydro-mechanical natural frequency with jack position centered can be calculated as:

$$\omega_s = \sqrt{\frac{4E_y(B_s K_c + A_t^2)}{V_t M_t}} = 64.7\ [\text{Hz}] \qquad (2)$$

The SHA natural frequency is principally determined by the jack mechanical structure, load equivalent mass and hydraulic oil characteristics, and less influenced by the inner leakage and friction. So this calculated value is very close to the experiment measurement one. For the controller design, this frequency value can be used to set filter parameters to improve the system stability.

Then the SHA quasi closed loop static stiffness with one pure P position controller can be calculated as:

$$S_s = \frac{A_t K_{sg} K_{sb}}{K_c} \approx A_t K_{so} K_{sp} K_{sb} = 3.24\times10^7 K_{sb}\ [\text{N/m}] \qquad (3)$$

where K_{so}=0.0142[m/A], K_{sp}=7.18×10^{11}[Pa/m].

In Eq. (3), the first equation is gotten from the transfer function and the second one comes from the physical characteristics of servovalve about pressure/opening gain. For the static stiffness calculating, the two results are very close.

EMA Linear Model

As illustrated in Figure 1, the EMA is composed by one motor power drive, one brushless DC motor and one roller-screw. The inputs of EMA are torque demand T^* and the external force F_{LE}. The output is the rod displacement X_e (also equals the load displacement X_t because the structural stiffness is neglected). The block diagram of EMA is shown in Figure 3.

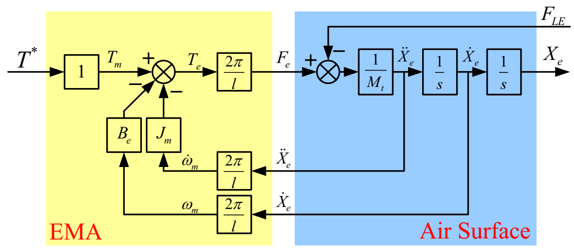

Figure 3 Linear model of EMA

In the upper model, it is assumed that the current loop dynamics is sufficiently high (about 600Hz) to be neglected in comparison with the other dynamics (a few tens Hz). Consequently, the motor output torque T_m equals the torque demand T^* exactly. Meanwhile the equivalent viscous friction and equivalent inertia J_m are considered at the motor shaft level. The transfer function of single EMA system is obtained as Eq. (4):

$$X_e(s) = \frac{T^*(s) - \frac{l}{2\pi} F_{LE}(s)}{s[(\frac{M_t l}{2\pi} + \frac{2\pi J_m}{l}) s + \frac{2\pi B_e}{l}]} \qquad (4)$$

which parameters are summarized in Table 2.

Table 2 The values of EMA system parameters

l [m]	J_m [Kgm²]	B_e [Nm/(rad/s)]
3×10^{-3}	9.2×10^{-3}	7.5×10^{-3}

The EMA quasi closed loop static stiffness with one pure P controller can be calculated as:

$$S_e = \frac{2\pi K_{eb}}{l} = 2.094\times10^3 K_{eb}\,[\text{N/m}] \tag{5}$$

In Eq. (5), the lead of roller-screw is changeless, so the stiffness is mainly determined by the P controller gain. Then the most important characteristic of EMA is the equivalent mass reflected at the rod level. It can be calculated with the following equation:

$$M_e = M_t + \frac{4\pi}{l^2} J_m = 40956\,[\text{Kg}] \tag{6}$$

Through Eq. (6), it is clear that the kinetic energy of moving mass is principally determined by the EMA. Compared with the single SHA system, the increased effective mass due to the EMA itself will induce a significant reduction of the system natural frequency (without considering the structural compliance).
So for a well designed EMA controller, the system performance shall be hardly affected by the load mass change. For example, if both SHA and EMA are under position control and the operation mode changes from active/active to SHA passive/EMA active under special situation, it is not necessary to change the EMA controller because the additional SHA equivalent mass is much less than the original one of EMA.

Redundant Actuation System Linear Model

Then the linear models of SHA and EMA are combined to get the transfer function of this redundant actuation system indicated in Figure 1 as the Eq. (7):
Similar to the single SHA system, the redundant actuation system is also a three order system with one integrator. But its main characteristics have been greatly changed, like the system equivalent mass and the system natural frequency. In Eq. (7), the first term of the denominator polynomial points out that the redundant system equivalent mass equals the EMA equivalent mass M_e in Eq. (6), which is a very large value and mostly fixed by the EMA rotation inertia reflected through the roller-screw.
The redundant actuation system natural frequency can be calculated with the following equation:

$$\omega_h = \sqrt{\frac{4E_y(K_cB_s + \frac{4\pi^2}{l^2}K_cB_e + A_t^2)}{V_t(M_t + \frac{4\pi^2}{l^2}J_m)}} \approx \sqrt{\frac{E_yA_t^2l^2}{V_tJ_m\pi^2}} = 7.84\,[\text{Hz}] \tag{8}$$

It is clear that a direct result of large system equivalent mass is the decreasing of the system natural frequency.

VIRTUAL ACTUATOR BUILDING

With the researches on linear models, many important characteristics of redundant actuation system have been gotten. These results are very helpful for designing the controllers for single or redundant actuation systems. However, a reality, the non linear virtual prototype of this redundant actuation system must be established and detailed to virtually validate the controllers design. It must be noticed that reproducing the major defects with accuracy is of prime importance for force fighting studies, opposite to only take care of the position signals that are low frequency state variables. This is performed easily in the LMS-AMESim.
The process of developing the virtual actuation system is based on the progressive introduction of the non linear or higher order parasitic effects in accordance with the real test bench, as detailed below.

SHA Friction

The SHA friction is mainly generated between rod and cylinder, and influenced by the sliding velocity and the pressure difference between two chambers because of the seals deformations [4]. In order to identify the friction representation model accurately, both constant and sine wave velocity experiments have been run. In the constant velocity experiments, the piston moves at series constant speed, and the external force F_{ex} is generated by the EMA that is under force control mode. On basis of experimental results, the friction model is proposed and parameters identified as:

$$F_{sf} = \left(F_{fc} + F_{fs}e^{\left(-|\dot{X}_s|/v_r\right)} + |F_{ex}|\left(a + b\,\text{sgn}(F_{ex}\dot{X}_s)\right)\right)\text{sgn}\left(\dot{X}_s\right) + f_v\dot{X}_s \tag{9}$$

where F_{fc}=590[N], F_{fs}=860[N], v_r=7.2×10^{-3}[m/s], f_v=800[Ns/m], a=0.0087 and b=0.0197.
After that, the parameters values are tuned with the results from the sine wave velocity experiments. In this friction model, the piston relative velocity and the external force F_{ex} which is linked to the two chambers pressure difference signal are considered as the input variables. The Coulomb friction and Stribeck friction

$$X_t(s) = \frac{A_tK_{sg}I_{sv}(s) + \frac{2\pi}{l}\left(\frac{V_t}{4E_y}s + K_c\right)T^*(s) - \left(\frac{V_t}{4E_y}s + K_c\right)F_L(s)}{\frac{V_t}{4E_y}\left(M_t + \frac{4\pi^2}{l^2}J_m\right)s^3 + \left(\frac{V_t}{4E_y}B_s + \frac{\pi^2V_t}{l^2E_y}B_e + K_cM_t + \frac{4\pi^2}{l^2}K_cJ_m\right)s^2 + \left(K_cB_s + \frac{4\pi^2}{l^2}K_cB_e + A_t^2\right)s} \tag{7}$$

are the main parts of this model.
Now the friction model is implemented, the non linear simulations results and the experiments measurements are compared at system level.

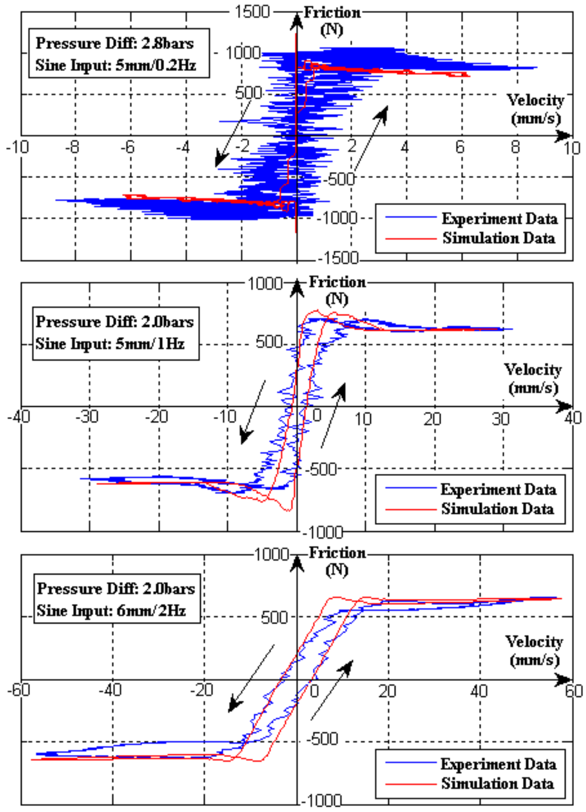

Figure 4 Comparison of simulations and experiments about SHA friction

In Figure 4, the relative error between simulations and experiments is smaller than 10%, which shows the excellent performances of this friction model. And the delay effect appearing in the graph is caused by the digital filter for data processing.

EMA Friction

The EMA friction mainly comes from the roller-screw which has a lot of mechanical contacting points. Same to the SHA friction, the EMA friction is also influenced by the external force F_{ex} working on the end of screw although the original physical phenomenon is different. The EMA friction which has been studied in a former work [5] is proposed as the Eq. (10) with the associated identified values of its parameters.

$$T_{ef} = \left(T_{fc} + T_{fs} e^{(-|\omega_m|/\omega_r)} + |F_{ex}|\left(c + d\,\mathrm{sgn}(F_{ex}\omega_m)\right)\right)\mathrm{sgn}(\omega_m) + t_v\omega_m \quad (10)$$

where T_{fc}=3.624[Nm], T_{fs}=-2.245[N], ω_r=70.55[rad/s], t_v=0.016[Nm/(rad/s)], c=1.04×10^{-4}[m], d=-6.21×10^{-5}[m]. The upper model presents the EMA overall friction torque reflected at motor shaft level. When the friction is considered at rod level, the value shall be magnified by $2\pi/l$ (2094[1/m]). So, when the EMA and SHA are coupled by the load and operate under the same conditions (same velocity and external force), the EMA needs much more energy to offset the friction.

Transmission Stiffness

In linear models, the transmission stiffness between actuators and load has not been considered. However, this effect plays a significant role on the force fighting. Moreover, when both the SHA and EMA operate in an active/active position control mode to pursuit the position demand without force fighting compensation, the actuators final stable positions cannot be identical due to the manufacturing, setting or even temperature drift differences. This position difference causes the deformation at the actuator anchorage to the frame and at the transmission to the load, which itself influences the force fighting.
In order to measure the transmission compliance, the EMA is asked to operate as force control to load the SHA, which is under position control.

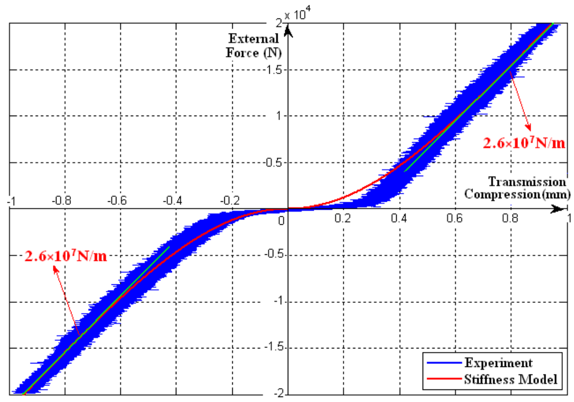

Figure 5 The overall transmission stiffness

As shown in Figure 5, the overall transmission stiffness plot is not linear because of the backlash existing in the mechanical linkages (about 0.6[mm] in the present measurements). Then based on the experiment results, the stiffness model Eq. (11) is gotten by a curve fitting approach and included in the figure.

$$S_t = 2.6\times10^7 abs\left(\tanh\left(1200 x_{tc}\right)\right) \text{[N/m]} \quad (11)$$

The value of transmission stiffness changes with the variation of external force. When the external force is small, the transmission compression is around zero, where the stiffness value is much lower than the biggest one 2.6×10^7[N/m]. This will significantly decrease the system natural frequency.

Anchorage Stiffness

The same approach is applied to the anchorage stiffness which experimental and simulated characteristics are displayed on Figure 6 (the anchorages of SHA and EMA are same, and here the SHA anchorage is tested).

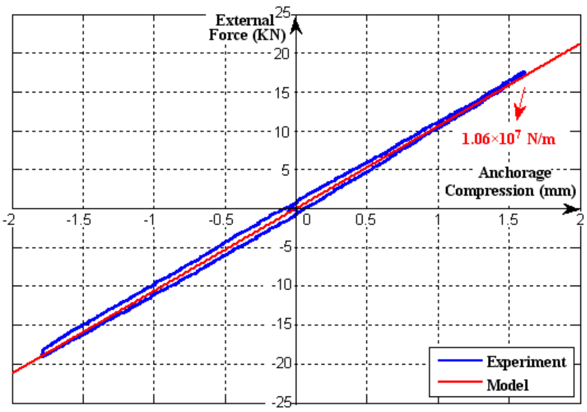

Figure 6 Anchorage stiffness of SHA

In Figure 6, the hysteresis of experiment results comes from the backlash of linkages between position sensor and test bench. The magnitude of backlash is about 0.15[mm]. Therefore the anchorage stiffness can be globally considered as constant (about 1.06×10^7[N/m]). Compared with other stiffness, the anchorage stiffness is much lower, but this can supply more buffering during the experiments.

Virtual Actuation System

The complete model of this redundant actuation system on active/active mode is summarized in Figure 7. The overall transmission stiffness in Figure 5 is divided into two parts to calculate the output force of each actuator more accurately. The SHA servovalve in this virtual system is a home-built model because the standard servovalve model cannot describe well the valve pressure/flow and leakage characteristics [6]. The actuators frictions are calculated on basis of Eq. (9) and Eq. (10), and transferred to mechanical models to generate the required amount of friction. Each actuator has its own position sensor to measure the relative displacement between rod and housing. Two force sensors are installed to measure the SHA and EMA output force, but no sensor for the external load force.

The accuracy of this virtual test bench has been found to be excellent, in particular when it was necessary to analyze and explain the unexpected results during the development of position control with force equalization strategies. As there is no mean to generate an external load when both actuators are operated in position control, the virtual system will be used advantageously as a substitute of reality. The particular attention paid to the simulation of load effects, servovalve gains, friction and structural compliances contributes significantly to the realism of the simulated responses.

STATIC FORCE FIGHTING ANALYSIS

Before developing force equalization control strategies, it is necessary to make clear the reasons that cause

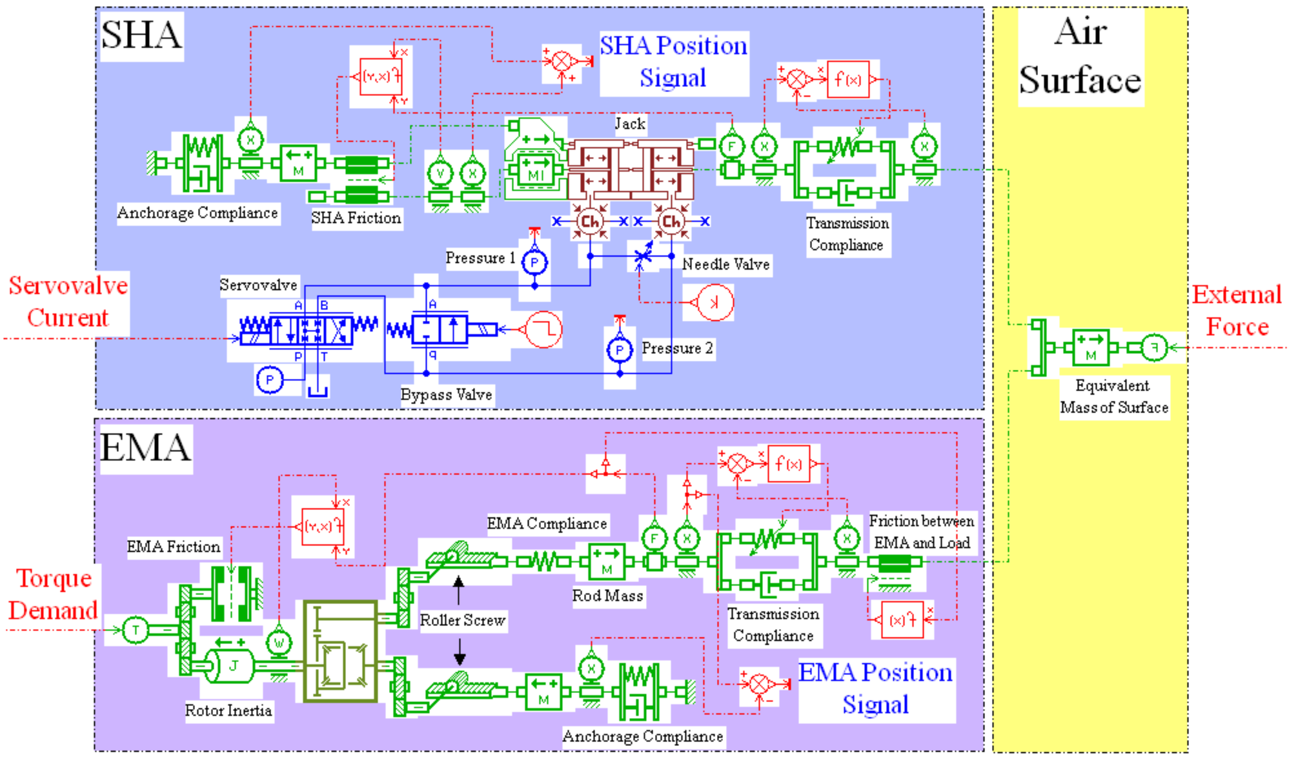

Figure 7 The virtual redundant actuation system

force fighting, which is defined to be presented as:

$$\gamma=F_s\text{-}F_e \tag{12}$$

when γ equals zero, it means no force fighting.
Then two simulations are carried up to help study the reasons. Here, the actuator controllers in simulations come from the designs for single SHA system and single EMA system. These position controllers are all pure proportional controllers and asked to satisfy the requirements (position static error is smaller than 0.5[mm] in cases of 10[KN] external forces; frequency response is smaller than -3dB/-45° in case of 3Hz sine position input). The integral control is not recommended because it will aggravate the force fighting.
In the first simulation, the SHA and EMA are all controlled to zero displacement, and the external force is continuously and slowly varying from -20[KN] to 20[KN]. The static load sharing is shown in the upper graph of Figure 8. In the second simulation, the external force is kept to null while a continuously and slowly varying position offset from -2[mm] to 2[mm] is introduced to the SHA control loop. The result is displayed in the lower graph of Figure 8.

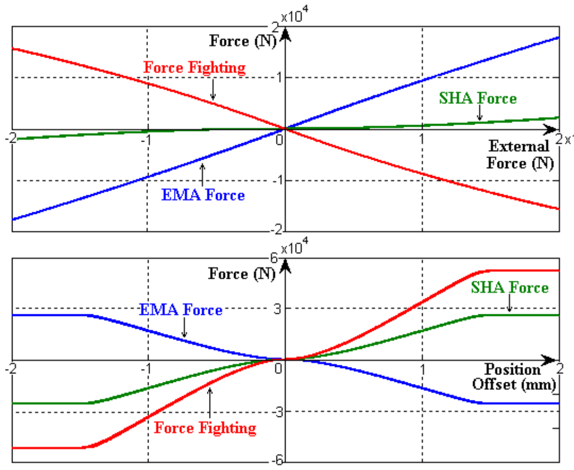

Figure 8 Simulations about static force fighting

On basis of the simulations results, one equation used to calculate the static force fighting of redundant active/active position control system without force equalization is gotten as Eq. (13):

$$\begin{cases} S_s^{-1}(F_s)+S_{st}^{-1}(F_s)-E_s=S_e^{-1}(F_e)+S_{et}^{-1}(F_e)-E_e \\ F_s+F_e=F_L \end{cases} \tag{13}$$

The theory of Eq. (13) is that the SHA static position error plus actuator structural deformation (transmission and anchorage) plus position sensor offset should equal the one of EMA because the coupled load is considered as stiff. The functions about actuators static closed loop stiffness and structural stiffness all have been gotten during the model building in previous parts.
In Eq. (13), the stiffness functions are globally constant when the actuator controllers are fixed, so one idea to solve the static force fighting is to compensate the E_s and E_e in the first equation to get a balanced status.

REDUNDANT SYSTEM CONTROL STRATEGY

Three static force equalization control strategies are introduced below, based on the upper analysis.

SHA Position Control/EMA Position Control

In this strategy, both the actuators are under position control, and the force fighting signals are introduced to compensate the position feedback signals as tuning the E_s and E_e in Eq. (13) to balance the actuator output force. An integrator is added to the compensation path to remove the static error.

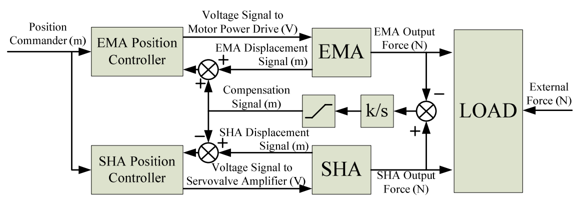

Figure 9 Static force equalization strategy 1

SHA Position Control/EMA Force Control

In this strategy, there is no change to the SHA position controller, but the EMA is changed to force control. The EMA output force is asked to track the SHA output force to reduce the force fighting.

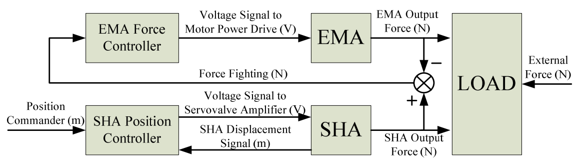

Figure 10 Static force equalization strategy 2

Here the EMA is chosen as force control because that its output force is corresponding to the motor current control, which dynamics are much higher than the ones of SHA servovalve. So, for the future work on dynamic force equalization, choosing EMA is better.

SHA Position Control/EMA No-Load Control

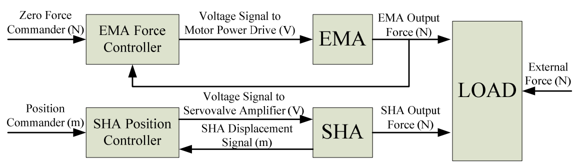

Figure 11 Static force equalization strategy 3

In the third one, the EMA is asked to always output zero force, and the static load is balanced exclusively by the SHA. Because the EMA has no direct influence on the load position, the force fighting is cancelled in statics [7].

Simulation and Experiment

The efficiency of these force equalization strategies are compared by simulating firstly in the virtual prototype and then taking experiments. The position set point is kept null while a continuously and slowly varying position offset is introduced to the SHA channel. The effects of structural compliances are simulated and activated in the real test bench. The corresponding responses are displayed on Figure 12.

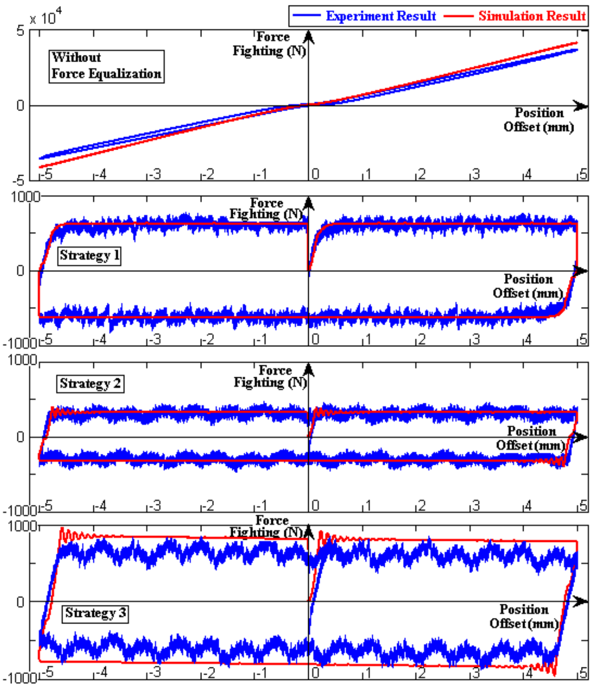

Figure 12 Comparison of force equalization strategies

In Figure 12, these three control strategies all have good effects on static force equalization, the magnitude of force fighting reduces from 4.0×10^4 [N] to smaller than 1.0×10^3 [N]. The first strategy is more stable than the other ones under the function of integrator, but the response speed is slower because the force fighting compensation is added to the position loop which dynamics are poor. But for the second strategy, the compensation is working on the EMA force control loop which dynamics are much quicker because it is corresponding to the motor current control. For the third strategy, the effect is poorer compared to the second one, that is because the SHA operating information is not used in the control law of EMA, they are two segregated actuators totally, but this is better for the safety issue of aircraft.

CONCLUSION

The research work presented in this communication aimed at providing suitable control strategies for static force equalization of redundant actuation system involving dissimilar technology actuators. For that one virtual system corresponding to the redundant actuation test bench was built, detailed and proved work well on describing the system performances by comparing with the experimental results. Based on this virtual system, the reasons causing static force fighting were studied and three force equalization control strategies were advanced. With the simulations and experiments, these three strategies were confirmed producing significant effects on static force equalization. Now the static force fighting problem of redundant actuation system has been well studied, the future work will be focused on the dynamic force equalization and the virtual system built in this paper will still play an important role.

ACKNOWLEDGMENT

The research work in this communication is one part of the cooperation project between Institut Clément Ader, France and Beihang University, China, and it is supported by the Ministry of Science and Technology of the People's Republic of China, the contract number is 2010DFA72540.

REFERENCES

1. S. L. Botten, C. R. Whitley, and A. D. King, Flight Control Actuation Technology for Next Generation All-Electric Aircraft, Technology Review Journal - Millennium Issue, Fall/Winter, 2000, pp.55-68.
2. O. Cochoy, S. Hanke, and U. B. Carl, Concepts for Position and Load Control for Hybrid Actuation in Primary Flight Controls, Aerospace Science and Technology, 2007, Nov, pp.194-201.
3. P. Cheng, Automatic Control Theory, Higher Education Press, Beijing, 2003, pp.15-57.
4. J. C. Maré, System Level Modeling of Mechanical Losses in Actuators, The 20th International Conference on Hydraulics and Pneumatics, Prague, Sep. 2008, pp.20-30.
5. W. Karam and J. C. Maré, Modeling and Simulation of Mechanical Transmission in Roller-Screw Electromechanical Actuators, Aircraft Engineering and Aerospace Technology, Vol.81, 2009, pp.288-298.
6. J. C. Maré, Contribution to the Modeling, Simulation, Identification and Control of the Eletro-hydraulic Actuators, PhD thesis, 1993, pp.83-97.
7. H.T. Qi, J.C. Maré and Y.L. Fu, Force Equalization in Hybrid Actuation Systems, 7th International Conference on Fluid Power Transmission and Control, Hangzhou, 2009, pp.342-347.

Proceedings of the 8th JFPS International
Symposium on Fluid Power, OKINAWA 2011
Oct. 25-28, 2011

1B2-3

ON-BOARD DATA TRANSFER OF AUTOMATED HEAVY MACHINERY

Otso KARHU and Kalevi HUHTALA

Department of Intelligent Hydraulics and Automation
Tampere University of Technology
PO Box 589, 33101 Tampere, Finland
(E-mail: otso.karhu@tut.fi)

ABSTRACT

In heavy machinery, maintaining the control system architecture modular, robust and generic can prove difficult. The problem becomes more complex when functions of a machine are automated: New types of sensors and computation devices are needed. These devices often use means of data transfer that have been designed for entirely different operating conditions. In this study, these means of data transfer are discussed in sense of modularity and life cycle management. The suitability of different buses and networks are debated. An automated wheel loader with remote control is discussed as an example. Localization is based on code differential GPS and wheel odometry. An embedded computer calculates automated functions such as a path-following controller. Design objectives of the loader are presented and the hardware architecture of the on-board control system is described and discussed. Guidelines for implementing on-board data transfer of an automated machine are proposed.

KEY WORDS

Networked control systems, Distributed control, Land vehicles, Robotics and automation

INTRODUCTION

Heavy machinery applications are challenging for electronic control systems. In addition to demanding operating conditions, the machines can have life cycles of several decades. Therefore, the control system should be robust and flexible to enable maintenance and possible future extensions. Electronic components that are used in controllers and sensors often become obsolete during the life cycle of a machine. These problems can be solved with a modular distributed system. Standardized interfaces and configurable generic devices make the system maintenance less dependent on suppliers of control electronics.

The problem with automated machinery, however, is the lack of standardization. Some sensors and controllers required for automated functionality are quite new and have no well-established interfaces. Others may have interfaces but they are targeted at office environment, for example.

In this paper, the typical ways of digital communication are discussed and applicability to automated heavy machinery is considered. A wheel loader is studied as an example.

BUSES AND NETWORKS

Digital communication has undisputable advantages compared to analogue signals: Digital signals have a strong tolerance of interference and noise, it is possible to transfer several control signals and configuration data in one conductor, and transmission errors can be detected and corrected, for example. When arranged as a network, digital communication enables efficient distributed control and minimizes cabling.

A device with a digital interface usually has an embedded microprocessor (typically as the core of a microcontroller) unless both functionality and communication interface are very simple. This makes the devices more expensive. On the other hand, as computation of a system can be distributed, the main controller can be less expensive. The key problem with microprocessors, however, is their relatively short life cycle. There are different compilers, software development tools and hardware programming and debugging interfaces for each family of processors or microcontrollers. As workstation hardware and operating systems tend to become obsolete within years, maintaining configuration tools for older devices is often challenging.

Digital communication can be optimized for data rate, transfer delay, distance, cost or reliability. The solution is always a trade-off between some of these design parameters. Since one bus or network cannot be optimal for everything, there are dozens of standardized and established ways of digital communication. Furthermore, the rapid development of electronics and the industrial competition constantly produce new digital buses and networks. Updated specifications are usually backwards compatible but rapid introduction of entirely new buses and networks tends to make many of the older ones obsolete.

In addition to physical specifications, a communication protocol has to be defined. Depending on the system, different levels of the Open Systems Interconnection (OSI) model [1] are implemented. There are usually several competing higher layer protocols for each physical layer. Some of these protocols conflict with each other and therefore require separate physical layers.

Considering system integration, production and maintenance of heavy machinery, it would be ideal to have the same digital interface for all the devices. Due to application-specific optimization, many devices only have the interface that best suits the device type. Therefore, actual machines with advanced automation include several digital buses and networks.

ISO 11898 (Controller Area Network)

Controller area network (CAN) was originally developed for automotive applications. Since the control systems and operating conditions of cars and heavy machinery are alike in many ways, CAN is nowadays the most common network in distributed control of heavy machinery.

CAN cabling can be implemented at low cost as the only key parameter is a characteristic impedance of 120 Ω [2]. For most operating environments, unshielded twisted pair copper cable is sufficient. Care has to be taken, however, to minimize mismatches in characteristic impedance all over the network. Typical mismatch problems are related to connectors and termination.

CAN controller integrated circuits (IC) implement data link layer of the OSI model according to [3]. Most CAN controller ICs have configurable data signaling rate up to 1 Mb/s. However, many devices cannot take full advantage of this feature: An application layer protocol or the functionality of the device may require a certain rate. Moreover, a device may have a limited message processing capacity, which either restricts the maximum data signaling rate or tolerates only low bus loads at high data signaling rates. Because all the devices of a CAN need to have the same data signaling rate, this limitation alone may require dividing the devices of a system into several CANs.

The main limitation with CAN is the maximum data signaling rate of 1 Mb/s. Therefore, in a control system with several closed loops the data transfer capacity of CAN is often insufficient. Another problem in some control applications is that the common CAN protocols are not deterministic: A message with a higher priority may cause extra communication delay at any time. This can be avoided to some extent by careful node configuration and synchronous message transmission. [4] A deterministic time-triggered communication has been specified [5] but not widely implemented so far.

When CAN is operated at 1 Mb/s, the maximum bus length is only 25–40 m [2,4]. Since the bus topology requires short stubs, the trunk may become surprisingly long. An example of this is illustrated in Figure 1.

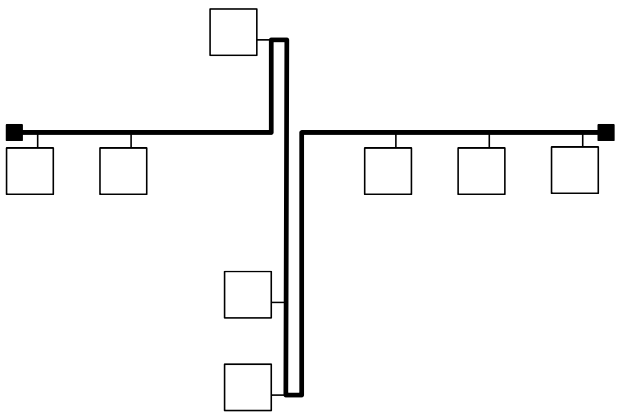

Figure 1 Example of bus layout

The number of devices has a considerable effect on the bus length as well: Devices need to be spaced sparsely enough to keep the mismatch of the bus characteristic impedance low [6]. If minor extra delays can be tolerated, some of the limitations can be avoided by grouping devices into separate buses and using switches [7].

There are several application layer protocols that cannot usually be used in the same physical network. SAE J1939 is the only CAN protocol generally supported by heavy duty diesel engine manufacturers. Because J1939 was originally developed for trucks, it does not cover the communication of a machine, in general. Therefore, machines with such an engine often have one CAN for J1939 devices and another for controlling the hydraulic system, for example.

Some of the application layer protocols are designed to be more flexible. CANopen and Common Industrial Protocol (CIP) are the most common general-purpose CAN protocols. CANopen specifications are maintained by CAN in Automation (CiA). In addition to general protocol specification, CiA has defined profiles for several device types and applications. Therefore, many CANopen devices can be replaced with a similar product from another manufacturer rather easily. Conformance tests are not mandatory, which has contributed to extending the CANopen product range. On the other hand, some of the devices that have not been tested for conformance do not fully meet CANopen specifications. CIP is the application layer protocol of DeviceNet which is managed by ODVA, Inc. Manufacturers are closely linked to ODVA to maintain product conformance. This, in contrast, makes developing new products more difficult. Most DeviceNet products are targeted at industrial automation.

Because CAN frame is simple and many networks have only a few devices, implementing light system-specific protocols is often fast and easy. However, considering the life cycle of a machine, a commonly used protocol makes maintaining and extending the control system more efficient. Because most application layer protocols have minimal overhead and flexible options for timing, system-specific protocols have no performance benefit.

Although CAN is the current industry standard in control systems of heavy machinery, it is likely to be replaced with a faster network, eventually. CANopen and CIP are already available as deterministic real-time protocols on IEEE 802.3, for example [8,9].

IEEE 802.3 (Ethernet)

Ethernet is the most actively developed and supported local area network (LAN) technology. The development started in the 1970s and the first Ethernet standard was published in 1985. The first implementations used a thick coaxial cable as physical medium. Several new physical layers have been standardized since but most specifications have remained valid. [10]

In addition to ongoing strong development and standardization, Ethernet has an extremely strong position on office, consumer and industrial market. IEEE standards for Ethernet cover the physical and the data link layer of the OSI model [10,11]. Since Ethernet was originally developed for office environment, there are features that are not optimal for industrial applications, not to mention heavy machinery.

Nowadays the physical layer of Ethernet is mainly implemented according to 100BASE-TX or 1000BASE-T specifications of [10]. The 8P8C modular connector that is used in these specifications (often erroneously called RJ45) has very limited strain relief and poor protection against dust and water [12]. For 10BASE-T and 100BASE-TX there is an optional, properly protected industrial connector: a 4-pole M12 with D-coding. The 8-pole version of the same connector can be used for 1000BASE-T and even 10 Gigabit Ethernet. [13,14] These connectors are not specified for Ethernet by IEEE but especially the 4-pole version is strongly supported by several manufacturers of high protection rating Ethernet devices.

The 8P8C modular connector is, however, often the only option in an industrial device, probably due to strong standardization and low cost. With devices like this, an extra enclosure is needed if there is no dust and waterproof control cabinet available for installation. The connector type can be changed from 8P8C into M12 on the enclosure panel with an adapter [14,15]. However, even inside the extra enclosure, 8P8C connectors may still be vulnerable because of mechanical vibrations and shocks of the machine. There are robust 8P8C products [14,16] but both the plug and the receptacle need to be of the same product series, there is no well-established solution and they are more expensive than M12 connectors. These robust receptacles, however, usually accept the regular 8P8C jack which makes testing and configuration easier as no special cables are needed.

Excluding obsolete coaxial implementations, Ethernet usually has a star topology with a switch or a hub in the center. A linear bus is also possible if all the devices have two Ethernet ports. Regardless of the topology, the physical layer of Ethernet is more expensive to implement than CAN, for example.

At the moment there are not many Ethernet devices available for motion control of heavy machinery. However, considering embedded computers, wireless communication modules and various advanced sensor systems, Ethernet is often the only reasonable option.

Internet Protocol Suite

Internet protocol suite (often called TCP/IP) is the most common set of protocols used in Ethernet systems. Although the internet protocol suite is a layered set of protocols, it does not strictly comply with the OSI model. Most of the suite is divided into application layer, transport layer, internet layer and link layer protocols [17]. These layers do not have strict definitions. Part of the data link layer of the OSI model is covered by the link layer of the internet protocol suite. One of the key protocols of the link layer is address resolution protocol (ARP) which finds an Ethernet address for a destination internet address. The pairs of Ethernet and internet addresses are stored into a translation table which is typically cleared at shutdown. Therefore, after boot-up, ARP communication takes place before the first transmission to each destination address. [18]

The main protocol of the internet layer is called internet protocol (IP). Its main functions are addressing and fragmentation of data packets from higher layers. IP has a header checksum which makes sure the packet is addressed and fragmented correctly. The data of the packet, however, is not checked for errors in this layer. IP has no mechanisms for acknowledgment, retransmission or flow control, either. [19]

Most application level protocols are based on transmission control protocol (TCP) [20] which corresponds to a transport layer protocol in the OSI model. As a connection-oriented protocol, it has features that are not needed in control applications. A more suitable option is another transport layer protocol, the user datagram protocol (UDP). A lost or duplicated packet is not detected by UDP. [21] In a small, properly configured on-board network transmission errors are unlikely and typically originate from a hardware fault. Therefore, a separate detection of fault situations is usually implemented.

Industrial Ethernet

Neither Ethernet specifications nor internet protocol suite definitions are deterministic: Although frame collisions can be avoided by using switches instead of hubs, the communication delay cannot be predicted if transmissions of several devices overlap. There are several competing solutions that implement a deterministic industrial Ethernet. Most of these, however, require modified Ethernet hardware for real-time performance [22] and are therefore not IEEE 802.3 compliant. The ones that are implemented with standard Ethernet hardware only replace the internet protocol suite with a real-time protocol stack. Conventional internet protocols are, however, supported as the real-time protocol stacks have separate time slots for non-real-time communication.

Many automation devices, nevertheless, still have only a standard Ethernet interface and regular internet protocol suite. Therefore, it should be easy to add standard Ethernet devices into an industrial Ethernet system. Unfortunately this is usually not the case. The networks that use non-standard hardware require a special bridge between the industrial and standard parts of the network. A bridge is also needed with an IEEE 802.3 compliant industrial Ethernet if the firmware of the standard Ethernet devices in the system cannot be updated.

Most industrial Ethernet devices are not designed to tolerate operating conditions of heavy machinery. However, as the level of automation is increasing, industrial Ethernet may well replace CAN in heavy machinery applications. Due to relatively long machine lifecycles and small production volumes, the industrial Ethernet protocols that are based on standard Ethernet hardware seem most applicable. For example, in CANopen-dominated applications POWERLINK is a likely successor, having the same application layer protocol [8].

V.24 and Related

V.24 and V.28 recommendations specify a serial link that was originally designed to interface a teletypewriter with a modem. For compatibility reasons, a V.24/V.28 compatible serial port was included in practically every personal computer till it was replaced by Universal Serial Bus (USB). The V.24/V.28 interface is light to process and the hardware is low-cost. Therefore, it is still very common in embedded devices. The serial interface is usually controlled by a universal asynchronous receiver/transmitter (UART).

UARTs do not have addressing or error detection apart from rarely used simple bit parity check. Therefore, proprietary serial protocols are very common. There are also several well-established protocol specifications for certain applications.

A V.24/V.28 serial link has a point-to-point topology. Therefore, a computer usually has a separate serial port for each V.24/V.28 device in the system. Maximum cable length depends mainly on the total capacitance of the cable. V.28 specifies single-ended signalling which is sensitive to interference. Therefore, especially long cables should be shielded.

The V.24/V.28 devices usually have quite low data rates. The V.28 recommendation covers signalling rates only up to 20 kb/s [23] but devices supporting up to 115.2 kb/s are quite common nowadays. In any case, the maximum signalling rate has to be checked for each device separately.

A point-to-point serial link can also use differential signalling [24]. The specification enables longer cables and higher data signalling rates. Similar transceivers can also form a half-duplex multi-point network [25] if the transmitters can be switched off. This type of serial bus is common in traditional industrial automation.

IEEE 1394

IEEE 1394 is a high-performance serial bus for computer peripherals, for example. Depending on interface generation, an IEEE 1394 interface may use a data signalling rate of up to 3 Gb/s. The interface is often called FireWire, according to the brand name of Apple Inc., the original developer. The specification includes different physical transfer mediums but the most common is the short-haul copper cable. It usually has a maximum length of 4.5 m, although longer cables are possible in simple network layouts. [26]

A short-haul IEEE 1394 network with more than two devices has to be daisy-chained or branched using

devices that have more than one port. In addition, since the cable shielding specification is quite complex, the hardware cost of a network easily becomes high. [26]
The IEEE 1394 specification is targeted at indoor applications. There is no well-established industrial connector outside the specification, either. Therefore, protected and robust plugs and receptacles no not usually mate unless they are of the same product series.
An IEEE 1394 interface is usually not included in embedded computers. A separate adapter board is therefore needed. Although integrated IEEE 1394 interfaces are quite low-cost, adapter boards for embedded computers tend to be quite expensive.

Universal Serial Bus

USB was designed for interfacing peripherals with a personal computer. Latest version of the specification, USB 3.0, has a maximum data signaling rate of 5 Gb/s. At the moment, however, most devices only support USB 2.0 that has a maximum data signaling rate of 480 Mb/s. The USB network has a tiered star topology which requires a host that is connected to devices directly or via hubs. The devices do not communicate with each other but with the host, only.
USB 3.0 has more complicated cable and connector specifications than USB 2.0. Neither specification states maximum length of a cable but a limit for signal propagation delay and insertion loss. With typical cables, these result in a maximum length of a couple of meters. [27,28] In heavy machinery applications, USB has connector limitations similar to IEEE 1394.

AUTOMATED WHEEL LOADER

Functional Objectives

An automated wheel loader was developed to be used as a generic research platform. The machine is used in research and demonstration of automated path-following, short-range remote control and digital working hydraulics. The control system also needs to support operation as a member of a fleet of automated machines. In addition, different optimizations of the power train control may be researched. Moreover, the control system should support modifications of the hydraulic system. Overall, the control system has to be flexible in terms of updating control algorithms and adding or replacing devices.

Construction

The wheel loader is shown in Figure 2. Although the frame of the machine is from a commercial loader, the engine and the hydraulic system have been replaced. The machine has a mass of 4000 kg, a 100 kW common rail diesel engine and articulated frame steering. Since pure drive-by-wire is needed, the steering cylinder is controlled with an electrically actuated proportional valve. The front attachment can be changed. A pallet fork has been used so far.

Figure 2 Automated wheel loader

The machine has a closed-loop hydrostatic transmission with a variable displacement pump and four parallel fixed displacement hub motors. Working hydraulics circuit has been implemented with digital hydraulics. There are 20 seat type on/off-valves for both lift and tilt, 5 in parallel for each control edge. [29]

Control System Architecture

The layout of the control system is presented in Figure 3. The devices are divided into three levels. The automated functions are calculated with an advanced computing module which is an embedded computer. The computer runs an Ethernet boot loader for Mathworks xPC Target. New software can therefore be developed using MATLAB/Simulink and downloaded via the wireless interface.
For flexibility and extensive product range, CANopen was chosen as main network technology. Many components of the hydraulic system have integrated electronics with a CANopen interface. To enable possible future modifications, the main PLC has extra analog and digital inputs and outputs for hydraulic components with conventional electric connections. The PLC also measures analog signals from pressure and temperature transducers, and controls the pump of the working hydraulics.
In addition to the main PLC, the motion control level of the control system has a separate controller for controlling the digital working hydraulics. Since digital working hydraulics have probably never been implemented on a machine, flexible control algorithm development and real-time monitoring are required. Therefore, a dSPACE MicroAutoBox with easy access from MATLAB/Simulink is used.
Some of the CANopen devices are designed, built and programmed at the department since no applicable commercial products are available. These include the digital hydraulic valve drivers and the modules for remote control, emergency stop and wheel odometry. All of these deploy the same hybrid microcontroller, a Freescale 56F8323.

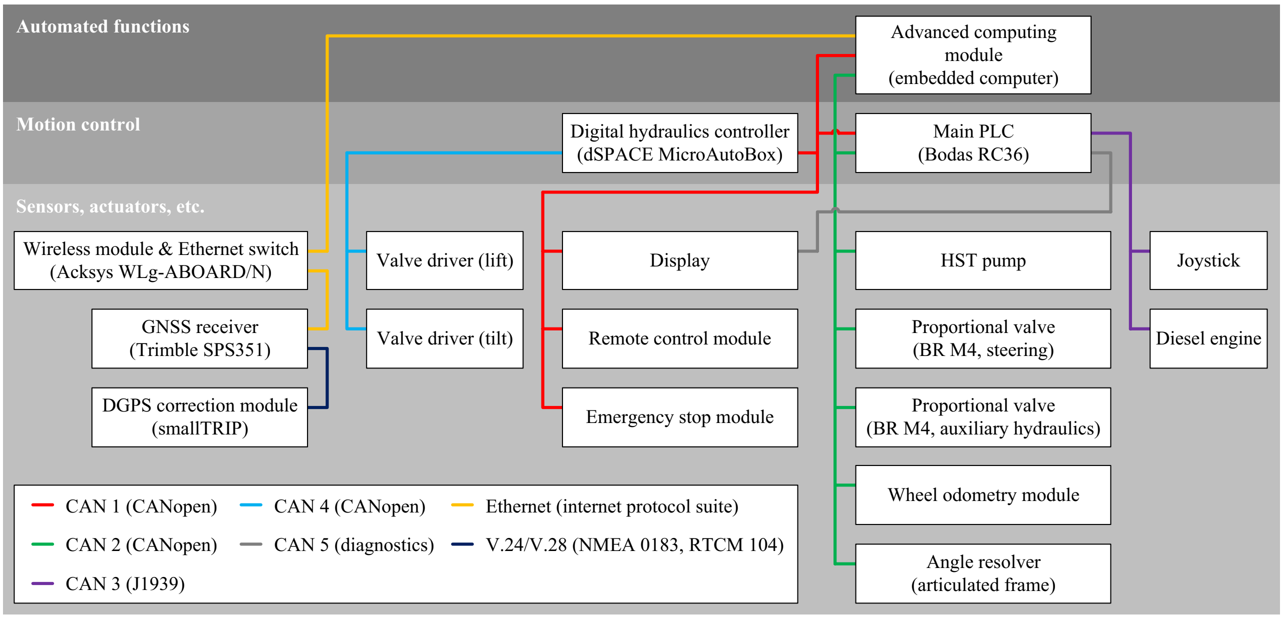

Figure 3 Control system layout

The CAN devices are grouped into four busses. Since the only SAE J1939 devices are the diesel engine and the joystick, they are connected to the same bus. The CANopen devices are divided into three busses based mainly on device functionality to balance the bus loads.
A separate IEEE 802.11a/b/g/h compliant wireless module with an integrated Ethernet switch was selected for high-performance wireless communication. Another solution could have been a wireless adapter board for the embedded computer. A separate module was preferred because of independence from operating system, easy hardware updates, and a quick and simple configuration procedure via a web browser interface.
The GNSS receiver had to be chosen on the grounds of localization performance and cost. Fortunately, it also has diverse options for communication. Ethernet was chosen since there was a spare port in the switch integrated into the wireless module. The receiver was configured to transmit position data to the embedded computer in UDP packets.
Since there are several sources of drifting systematic error in GNSS signals, a fixed reference station is usually used to cancel the drift. To make the machine more independent of working area, a network-based correction service (Trimble VRS DGPS) is used. The position data of the GNSS receiver is transmitted to the correction server over the Internet every 10 seconds. An optimal set of correction data for the current working area is then received from the server every second. For this communication, an embedded mobile Internet module (smallTRIP) was installed. The module has a V.24/V.28 compliant serial port. It communicates directly with the GNSS receiver in NMEA 0183 and RTCM 104 protocols which are well-established in GNSS applications. The GNSS receiver can communicate with the correction server also via the Ethernet interface if the wireless module has access to Internet. A separate module, however, means that the correction signal can be received almost anywhere without IEEE 803.11 compliant wireless Internet access. Moreover, with the external module it is possible to keep the embedded computer and the GNSS receiver entirely separated from the Internet for improved security.

CONCLUSION

There are several possible solutions for on-board networking of a machine. Applicable products for automated functionality, however, are not widely available. For cost and availability reasons, a CAN-based general-purpose protocol is a good choice for most devices. In addition, automated functionality usually requires a network with a high data rate, Ethernet being the only practical solution. For configuration and maintenance, an ideal combination of technologies would be CANopen and POWERLINK or DeviceNet and Ethernet/IP. However, since industrial Ethernet protocols are not widely supported by GNSS receivers, laser scanners, machine vision cameras etc., a standard Ethernet with conventional internet protocol suite is almost mandatory. Special attention needs to be paid to scheduling analysis and connector solutions. Keeping the number of software tools reasonable may prove difficult.

REFERENCES

1. ISO/IEC 7498–1, Information technology – Open Systems Interconnection – Basic Reference Model: The Basic Model, Geneva, Switzerland 1994, International Organization for Standardization, 59 p.
2. ISO 11898–2, Road vehicles – Controller area network (CAN) – Part 2: High-speed medium access unit, Geneva, Switzerland 2003, International Organization for Standardization, 21 p.
3. ISO 11898–1, Road vehicles – Controller area network (CAN) – Part 1: Data link layer and physical signalling, Geneva, Switzerland 2003, International Organization for Standardization, 45 p.
4. CiA Draft Standard 301, CANopen – Application Layer and Communication Profile, Erlangen, Germany 2002, CAN in Automation, 135 p.
5. ISO 11898–4, Road vehicles – Controller area network (CAN) – Part 4: Time-triggered communication, Geneva, Switzerland 2004, International Organization for Standardization, 32 p.
6. Corrigan, S., Controller Area Network Physical Layer Requirements, Dallas, Texas, USA 2008, Texas Instruments, SLLA270, 15 p.
7. Saha, H., Some Methods to Improve Life Cycle Manageability of Low-Volume Mobile Processing Platforms, Dissertation, Tampere, Finland 2010, Tampere University of Technology, Publication 899, 175 p.
8. EPSG Draft Standard 301, Ethernet POWERLINK – Communication Profile Specification, Berlin, Germany 2008, Ethernet POWERLINK Standardization Group, 349 p.
9. The CIP Advantage Technology Overview: Ethernet/IP, Ann Arbor, Michigan, USA 2008, ODVA, 8 p.
10. IEEE 802.3, Information technology – Telecommunications and information exchange between systems – Local and metropolitan area networks – Specific requirements – Part 3: Carrier sense multiple access with Collision Detection (CSMA/CD) Access Method and Physical Layer Specifications, New York, USA 2008, Institute of Electrical and Electronics Engineers, 597 p.
11. IEEE 802.2, Information technology – Telecommunications and information exchange between systems – Local and metropolitan area networks – Specific requirements – Part 2: Logical Link Control, New York, USA 1998, Institute of Electrical and Electronics Engineers, 239 p.
12. IEC 60603–7, Connectors for electronic equipment – Part 7: Detail specification for 8-way, unshielded, free and fixed connectors, Geneva, Switzerland 2008, International Electrotechnical Commission, 92 p.
13. IEC 61076–2, Connectors for use in d.c., low-frequency analogue and digital high speed data applications – Part 2: Circular connectors with assessed quality – Sectional specification, Geneva, Switzerland 1998, International Electrotechnical Commission, 51 p.
14. Ethernet cabling, Espelkamp, Germany 2010, HARTING, 209 p.
15. EF12RJ45 OCTOPUS, Product information, Neckartenzlingen, Germany 2011, Hirschmann Automation and Control, 2 p.
16. Buccaneer For Data, Romford, Essex, UK 2010, Elektron Components, 6 p.
17. RFC 1122, Requirements for Internet Hosts – Communication Layers, 1989, Internet Engineering Task Force.
18. RFC 826, An Ethernet Address Resolution Protocol, 1982, Internet Engineering Task Force.
19. RFC 791, Internet Protocol, 1981, Internet Engineering Task Force.
20. RFC 793, Transmission Control Protocol, 1981, Internet Engineering Task Force
21. RFC 768, User Datagram Protocol, 1980, Internet Engineering Task Force.
22. Felser, M. and Sauter, T., Standardization of Industrial Ethernet – the Next Battlefield?, Proceedings of the 5th IEEE International Workshop on Factory Communication Systems, Vienna, Austria, Sep 22-24, 2004, Vienna University of Technology, pp. 413-421.
23. V.28, Electrical Characteristics for Unbalanced Double-current Interchange Circuits, Helsinki, Finland 1993, International Telecommunication Union, 10 p.
24. V.11, Electrical Characteristics for Balanced Double-Current Interchange Circuits Operating at Data Signalling Rates up to 10 Mbit/s, Geneva, Switzerland 1996, International Telecommunication Union, 18 p.
25. TIA-485-A, Electrical Characteristics of Generators and Receivers for Use in Balanced Digital Multipoint Systems, USA 2003, Telecommunications Industry Association.
26. IEEE 1394, High-Performance Serial Bus, New York, USA 2008, Institute of Electrical and Electronics Engineers, 906 p.
27. Universal Serial Bus Specification, 2000, Compaq, Hewlett-Packard, Intel, Lucent, Microsoft, NEC and Philips, 622 p.
28. Universal Serial Bus 3.0 Specification, 2008, Hewlett-Packard, Intel, Microsoft, NEC, ST-NXP Wireless and Texas Instruments, 482 p.
29. Backas, J., Ahopelto, M., Huova, M., Vuohijoki, A., Karhu, O., Ghabcheloo, R. and Huhtala, K., IHA-Machine: A Future Mobile Machine, Proceedings of the 12th Scandinavian International Conference on Fluid Power, Vol. 1, Tampere, Finland, May 18-20, 2011, Tampere University of Technology, pp. 161-176.

Proceedings of the 8th JFPS International
Symposium on Fluid Power, OKINAWA 2011
Oct. 25-28, 2011

1B2-4

Application of fuzzy fault feature extraction approach on hydraulic system of mini-excavator

Xiangyu He, Shanghong He and Yiming Shao

College of Automobile and Mechanical Engineering,
Changsha University of Science and Technology
Changsha, Hunan, 410083 China

ABSTRACT

With the automation development of excavator, fault diagnosis for hydraulic system has become one of the key techniques of modern excavator. By analyzing the excavator's hydraulic system, this paper presents a fault feature approach based on fuzzy ARX (Auto-Regressive with eXtra outputs) model to extract of the excavator's hydraulic system. Compared with classical ARX model, fuzzy ARX model is capable to extract nonlinear features. On the basis of target fault features, RBF (Radial Basis Function) network is served as fault classifier and the output of the RBF network is the result of diagnosis. Several typical faults of hydraulic system were used to test the fault diagnosis approach. Experimental results show that 80% of the test faults were correctly identified, and the fault diagnosis approach proved feasible and effective on construction machinery hydraulic system.

KEYWORD

Hydraulic system, construction machinery, fault diagnosis, fuzzy logic, auto-regressive with extra outputs (ARX) model

NOMENCLATURE

R^r : Fuzzy relation rule
A^r : Fuzzy set for input
B^r : Fuzzy set for output
x : Input variable
y : Output variable

INTRODUCTION

In order to meet the increasing demand of fast and efficient construction, mechanic and electric technology has been widely employed on the excavator. Hydraulic system is becoming more and more complex [1]. Therefore, there is an important significance to develop an effective fault diagnosis approach for the excavator's hydraulic system.

Faults in an excavator's hydraulic system can take many forms, such as pump faults, valve faults, cylinder faults and so on. Hydraulic faults are generally sorted in several grades according to severity. Complete failures and abrupt faults are comparatively easy to detect. Fault detection techniques related to complete failures of control and equipment components of hydraulic system were proposed. Gradually generating faults are hard to detect early using limit-checking methods with simple residuals because fault effects are often masked by control actions. On the other hand, the hydraulic system is nonlinear with dynamic property. It is difficult to develop a fault feature extraction technique based on linear model[2]. Fuzzy ARX model has been proposed for the nonlinear process, which can effectively describe the nonlinear property of a process [3][4]. The fuzzy ARX model is valid for dealing with data from dynamic process[5][6]. In this paper, an online fault feature extraction approach based on fuzzy ARX model was put forward. This approach was effectively applied on SWE50 excavator and could accurately diagnose faults.

SYSTEM OVERVIEW

A hydraulic excavator consists of a boom, stick, and bucket, and move via tracks or wheel. The motion of boom, stick and bucket are driven by corresponding hydraulic cylinders. A basic operating cycle involves a digging pass through the bank, a loaded swing to dump position, a dump into a haul truck, empty swing back to the digging and repositioning or spotting of the bucket at the face. To fulfill those complex operations, an excavator usually equipped with various hydraulic components including variable pump, proportional valve and cylinder. Variable pump converts mechanical energy to hydraulic energy and proportional valves distribute hydraulic energy to cylinders to drive boom, stick and bucket. Hence, we can simplify an excavator's hydraulic system to several similar basic hydraulic loops in spite of the functional difference. A basic hydraulic loop of the excavator can be demonstrated as Figure 1.

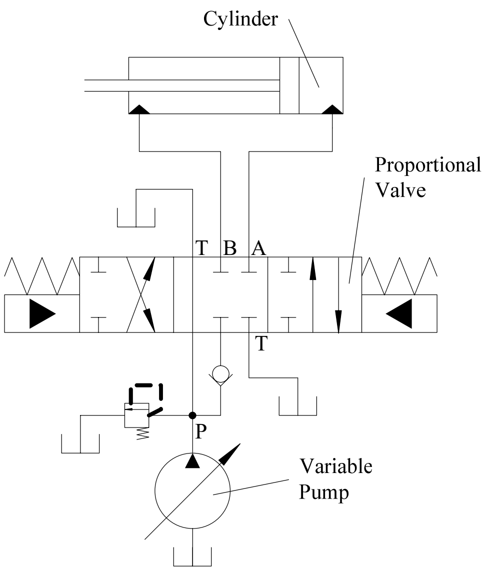

Figure 1 A basic hydraulic loop of the excavator

This paper focuses on a SWE 50 mini excavator. This excavator's hydraulic system mainly involves a load-sensing variable pump integrated with two piston pumps, a gear pump and a trochoid pump, a piloted electric-hydraulic proportion valve series, and working attachments including boom, arm, bucket and cylinders corresponded.

FAULT FEATURE EXTRACTION

Structure of fuzzy ARX

Let us consider a single-input-single-output nonlinear system which can be configured as following fuzzy relational equations

$$\begin{aligned} &\underset{\sim}{R}^1: \text{ IF } x \text{ is } \underset{\sim}{A}^1, \text{ THEN } y \text{ is } \underset{\sim}{B}^1 \\ &\vdots \\ &\underset{\sim}{R}^r: \text{ IF } x \text{ is } \underset{\sim}{A}^r, \text{ THEN } y \text{ is } \underset{\sim}{B}^r \end{aligned} \tag{1}$$

The system can be described by a system of disjunctive rules, we could decompose the rules into a single aggregated fuzzy relational equation as follows

$$\begin{aligned} y = \left(x \circ \underset{\sim}{R}^1\right) \text{AND} \left(x \circ \underset{\sim}{R}^2\right) \text{AND} \\ \cdots \text{AND} \left(x \circ \underset{\sim}{R}^r\right) \end{aligned} \tag{2}$$

or

$$y = x \circ \underset{\sim}{R}$$

where, $\underset{\sim}{R} = \underset{\sim}{R}^1 \bigcap \cdots \bigcap \underset{\sim}{R}^r$.

We can incorporate ARX model into fuzzy relational equations. The fuzzy ARX model can be written as following equations

$$\begin{aligned} &\underset{\sim}{B}^1: \text{ IF } y(t-1) \text{ is } \underset{\sim}{B}^1, \text{ THEN} \\ &y(t) = -a_1^1 y(t-1) - \cdots - a_{n_a}^1 y(t-n_a) \\ &+b_1^1 u(t-1) + \cdots + b_{n_b}^1 u(t-n_b) + e^1(t) \\ &\vdots \\ &\underset{\sim}{B}^n: \text{ IF } y(t-1) \text{ is } \underset{\sim}{B}^n, \text{ THEN} \\ &y(t) = -a_1^n y(t-1) - \cdots - a_{n_a}^n y(t-n_a) \\ &+b_1^n u(t-1) + \cdots + b_{n_b}^n u(t-n_b) + e^n(t) \end{aligned} \tag{3}$$

Above equations can be represented in an aggregated fuzzy relational equation as follows

$$y(t) = \underset{\sim}{\mathbf{B}}^T \left(y(t-1)\right) \Theta \boldsymbol{\varphi}(t) + e(t) \tag{4}$$

where,

$$\begin{aligned} \boldsymbol{\varphi}(t) = \big[y(t-1), \cdots, y(t-n_a), \\ u(t-1), \cdots, u(t-n_b) \big]^T \end{aligned}$$

$$\boldsymbol{\Theta} = \begin{bmatrix} a_1^1, \cdots, a_{n_a}^1, b_1^1, \cdots, b_{n_b}^1 \\ \vdots \\ a_1^n, \cdots, a_{n_a}^n, b_1^n, \cdots, b_{n_b}^n \end{bmatrix} = \begin{bmatrix} \boldsymbol{\theta}^1 \\ \vdots \\ \boldsymbol{\theta}^n \end{bmatrix}$$

$$\underset{\sim}{\mathbf{B}}\left(y(t-1)\right) = \left[\mu_{\underset{\sim}{B}^1}\left(y(t-1)\right), \cdots, \mu_{\underset{\sim}{B}^n}\left(y(t-1)\right) \right]^T$$

Then Equ. (4) could be simplified as follows

$$y(t) = \boldsymbol{\varphi}^T(t) \underset{\sim}{\boldsymbol{\theta}} + e(t) \tag{5}$$

where, $\underset{\sim}{\boldsymbol{\theta}} = \underset{\sim}{\mathbf{B}}^T \left(y(t-1)\right) \boldsymbol{\Theta}$.

Fault feature extraction approach

The fault feature extraction approach could be given as following steps:

(1) Define membership functions.

Five Gaussian membership functions were used to represent the output y as shown in Figure 2.

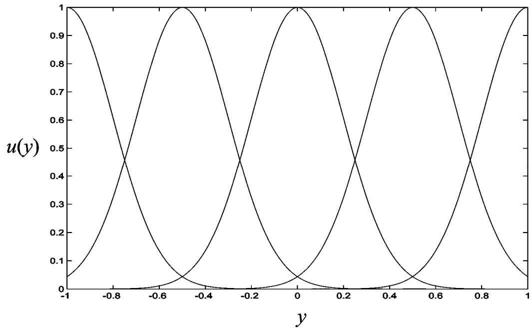

Figure 2. Memship function for the output y

(2) Define the fuzzy relational rules.

Fuzzy relational rules were consisted of five equations which can be given by

$$\begin{aligned}
&\underset{\sim}{B}^1: \text{ IF } y(t-1) \text{ is } \underset{\sim}{B}^1, \text{ THEN} \\
&y(t) = -a_1^1 y(t-1) - \cdots - a_{n_a}^1 y(t-n_a) \\
&+b_1^1 u(t-1) + \cdots + b_{n_b}^1 u(t-n_b) + e^1(t) \\
&\vdots \\
&\underset{\sim}{B}^5: \text{ IF } y(t-1) \text{ is } \underset{\sim}{B}^5, \text{ THEN} \\
&y(t) = -a_1^5 y(t-1) - \cdots - a_{n_a}^5 y(t-n_a) \\
&+b_1^5 u(t-1) + \cdots + b_{n_b}^5 u(t-n_b) + e^5(t)
\end{aligned} \tag{6}$$

(3) Establish the Fuzzy ARX model

We can establish a corresponding ARX model for each fuzzy rule. The parameters of fuzzy ARX model is estimated by applying the least square method and is given by

$$\begin{aligned}
\hat{\boldsymbol{\theta}}^i &= \left[\sum_{t=1}^{N} \left(\mu_{\underset{\sim}{B}^i} \left(y(t-1) \right) \right)^2 \boldsymbol{\varphi}(t) \boldsymbol{\varphi}^T(t) \right]^{-1} \\
&\sum_{t=1}^{N} \mu_{\underset{\sim}{B}^i} \left(y(t-1) \right) \boldsymbol{\varphi}(t) y(t)
\end{aligned} \tag{7}$$

and

$$\hat{\boldsymbol{\Theta}} = \begin{bmatrix} \hat{\boldsymbol{\theta}}^1 \\ \vdots \\ \hat{\boldsymbol{\theta}}^5 \end{bmatrix} \tag{8}$$

(4) Extract the fault feature vector

Generally, dimension of parameter matrix is so big that fault classifier can not properly determine the fault condition. To improve efficiency of fault diagnosis, we use weighted vector as the fault feature vector as follows

$$\mathbf{f} = \lambda_1 \hat{\boldsymbol{\theta}}^1 + \cdots + \lambda_5 \hat{\boldsymbol{\theta}}^5 \tag{9}$$

where, $\lambda_1 + \cdots + \lambda_5 = 1$.

FAULT DIAGNOSIS ON HYDRAULIC SYSTEM OF MINI EXCAVATOR

Fault classifier based on RBF networks

The structure of an RBF networks includes three layers with input layer, hidden layer and output layer. An RBF networks can be written as following form

$$g(x) = \sum_{j=1}^{k} \omega_j \varphi \left(\frac{\left\| \mathbf{x} - \mathbf{c_j} \right\|}{h} \right) \tag{10}$$

where, k is the number of basis function, $\mathbf{x} \in R^p$ is the input vector, φ is basis function, h is the smooth coefficient, c_j is centroid of cluster j, ω_j is the weight and $\|*\|$ is the Euclidean norm. Here we choose Gaussian form as the basis function by

$$\phi(z) = \exp\left(-z^2\right) \tag{11}$$

We can define a objective function as following form

$$\mathbf{c_j} = \frac{\sum_{i=1}^{n} u_{ij} \cdot \mathbf{x_i}}{\sum_{i=1}^{n} u_{ij}} \tag{12}$$

To minimize the criterion J_m, namely $\min(J_m)$, an iteration algorithm is implemented by following steps:

1) Randomly initialize the c-partition matrix according to

$$\sum_{i=1}^{C} u_{ij} = 1, \forall j = 1, ..., N \tag{13}$$

and $U^{(0)}$ is generated.

2) Calculate centroids of clusters using

$$c_j = \frac{\sum_{i=1}^{N} u_{ij}^m \cdot x_i}{\sum_{i=1}^{N} u_{ij}^m} \tag{14}$$

3) Compute dissimilarity between centroids and data points by

$$u_{ij} = \frac{1}{\sum_{k=1}^{C} \left(\frac{\left\| x_i - c_j \right\|}{\left\| x_i - c_k \right\|} \right)^{\frac{2}{m-1}}} \tag{15}$$

4) Stop iteration when

$$\left\| U^{(k+1)} - U^{(k)} \right\| \le \varepsilon \tag{16}$$

5) Update $U^{(k)}$ and go to step 2).

6) Construct a k-dimension space vector

$$\mathbf{y}_i = \begin{bmatrix} \exp\left(-\frac{\left\| \mathbf{x}_i - \mathbf{c}_1 \right\|^2}{h^2} \right) \\ \vdots \\ \exp\left(-\frac{\left\| \mathbf{x}_i - \mathbf{c}_k \right\|^2}{h^2} \right) \end{bmatrix} \tag{17}$$

Where the variances are also considered to be known, and

$$g(x_i) = \boldsymbol{\omega}^{\mathbf{T}} \mathbf{y} \tag{18}$$

7) By implementing LMSE (Least Mean Square Error) method, we can obtain estimated matrix of weight

$$\hat{\boldsymbol{\omega}} = \begin{bmatrix} \hat{\omega}_{11} & \hat{\omega}_{12} & \cdots & \hat{\omega}_{1N} \\ \hat{\omega}_{21} & \hat{\omega}_{22} & \cdots & \hat{\omega}_{2N} \\ \vdots & \vdots & \vdots & \vdots \\ \hat{\omega}_{k1} & \hat{\omega}_{k2} & \cdots & \hat{\omega}_{kN} \end{bmatrix} \tag{19}$$

Fault diagnosis

Firstly, samples of N target faults and a test fault are collected at certain sample frequency. Then these sample data should be preprocessed to satisfy the requirement of fuzzy ARX model. The fuzzy ARX models for each fault are established.

Then we can extract fault feature vectors according to equation (7), (8) and (9). Considering N types of target faults, a dataset composed of N eigenvalue vectors can be obtained

$$\mathbf{F} = \begin{bmatrix} \mathbf{f}_1^T \\ \mathbf{f}_2^T \\ \vdots \\ \mathbf{f}_N^T \end{bmatrix}^T \tag{20}$$

In order to determine the condition of a test fault, its eigenvalue vector is incorporated into the dataset above and a new dataset generates

$$\mathbf{F}_{new} = \begin{bmatrix} \mathbf{f}_1^T \\ \mathbf{f}_2^T \\ \vdots \\ \mathbf{f}_N^T \\ \mathbf{f}_{N+1}^T \end{bmatrix}^T \tag{21}$$

Firstly target fault dataset were used to train RBF networks classifier, and then the output of the classifier is the result of fault diagnosis.

(1) Training of the RBF network

1) Initialize parameters and construct N discriminants $g_1(x), g_2(x), \cdots, g_N(x)$;

2) Calculate k centroids $\mathbf{c_1}, \mathbf{c_2}, \cdots, \mathbf{c_k}$ using $\mathbf{U}^{(r)}$;

3) Compute n k-dimesion $\mathbf{y_1}, \mathbf{y_2}, \cdots, \mathbf{y_n}$ while fault feature vectors $\boldsymbol{\theta}_1, \boldsymbol{\theta}_2, \cdots, \boldsymbol{\theta}_N$ and centroids $\mathbf{c_1}, \mathbf{c_2}, \cdots, \mathbf{c_k}$ were carried into the basis function;

4) Estimate weight matrix $\hat{\boldsymbol{\omega}} \in R^{(k+1)\times N}$ by LMSE, and obtain RBF networks classifier.

(2) Classification of the test fault sample

1) Obtain $g_1\left(\boldsymbol{\theta}_f^{test}\right)$, $g_2\left(\boldsymbol{\theta}_f^{test}\right) \cdots$, $g_N\left(\boldsymbol{\theta}_f^{test}\right)$

according to equation (10).

2) if

$$g_i\left(\boldsymbol{\theta}_f^{test}\right)=\max\left(g_1\left(\boldsymbol{\theta}_f^{test}\right),g_2\left(\boldsymbol{\theta}_f^{test}\right),\cdots,g_N\left(\boldsymbol{\theta}_f^{test}\right)\right)$$

and then we can determine that the test fault sample is the i fault; Else, we cannot determine the fault type.

4. Experiment

With the SWE50 experimental excavator, sample data is generated from three single fault cases including piston wear, spool stroke and spool wear. The observation vector at time *t*, which is composed of the variables from the simulation model, may be written as follows

$$x(t)=\left[P_P(t),P_A(t),P_B(t),Q_P(t)\right]^T$$

where P_P and Q_P are the pressure and the flow rate at pump outlet respectively. P_A and P_B are the pressure at port A and port B of valve respectively. The fuzzy ARX model can be rewritten as follows

$$\begin{cases} Q_P(t)= \\ \text{FARX1}\left(Q_P(t-1),Q_P(t-2),P_P(t-1),P_P(t-2)\right) \\ P_A(t)= \\ \text{FARX2}\left(P_A(t-1),P_A(t-2),P_B(t-1),P_B(t-2)\right) \end{cases}$$

With the SWE50 experimental excavator, sample data is generated from three target fault cases as follows:

Fault 0: No faults
Fault 1: piston wear
Fault 2: spool stroke
Fault 3: spool wear

The cases that more than one fault occur at the same time were not under consideration in this study. To obtain adequate resolution of the hydraulic system, the sample frequency can be taken as 100Hz. The computation and analysis of sample data to verify the online fault detection approach were implemented in Matlab environment. In order to avoid particular variables inappropriately dominating the procedure, the training data should be normalized before developing a fuzzy ARX model. The normalization consisted of two steps: the first step was to subtract the mean from each variable in the data; the second step was to divide each mean-centered variable by its standard deviation. This scaled each variable in the sample data to zero mean and unit variance. Sample data should be scaled with mean and variance vector of the sample data of the normal condition.We can extract fault feature vectors from model FARX1 and model FARX2 of Fault0, Fault1, Fault2 and Fault3 as shown in Table1.

Several test faults were introduced to verify the classification performance of RBF network classifier. Fault feature vectors were used to train RBF network classifier, Then RBF network classifier was used to classify the test fault. The classification result shows that all the test faults were correctly classified as shown in Table 2. The fault diagnosis using fuzzy ARX and RBF networks classifier proves feasible and effective on excavator's hydraulic system. A SWE50 excavator was used to verify the online fault detection approach. Experimental results show that the proposed approach could be effectively applied to the fault extraction of the excavator's hydraulic system.

CONCLUSION

Aiming at the hydraulic system of excavator, a fault extraction approach using fuzzy ARX was put forward in this paper. With this approach, fuzzy ARX models were developed using sample data for target faults; Fault feature vector was extracted from the model; RBF network classifier was used as the fault classifier to sort the test fault to the target faults.

The hydraulic system of SWE50 excavator was developed to verify the fault detection approach. The proposed fault extraction approach was verified via this experimental excavator. Experimental results show that the proposed approach could be effectively applied to the fault detection of the excavator's hydraulic system.

ACKNOWLEDGEMENT

This work is a project supported by Scientific Research Fund of Jiangxi Provincial Education Department under Grant No. GJJ11479. It is also a project supported by Huxiang Scholar Fund of Changsha University of Science and Technology under grant No. 200807. Finally, the authors are grateful to Qinghua He, Ying Jiang and Ping Jiang for helpful discussions on this topic, and valuable comments on earlier drafts of this paper.

Table 1 Fault feature vectors of three single fault cases

Fault type	Fault feature vector							
FAULT0	4.249	-0.536	1.421	-2.504	5.271	0.731	0.537	0.256
FAULT1	4.341	-0.318	0.669	-1.772	-2.030	7.389	0.491	-0.600
FAULT2	4.187	-0.440	-0.619	0.286	6.099	-0.798	0.105	-0.152
FAULT3	4.620	-1.132	0.384	-1.516	4.866	0.145	0.119	-0.091

Table 2 Output of RBF network classifier

Fault type	Target fault				Result of classification
	$g_1(x)$	$g_2(x)$	$g_3(x)$	$g_4(x)$	
(1)FAULT0	**0.137**	0.000	0.033	-0.006	FAULT0(√)
(2)FAULT1	0.000	**0.120**	0.000	0.000	FAULT1(√)
(3)FAULT1	0.000	**0.203**	0.000	0.000	FAULT1(√)
(4)FAULT2	-0.015	0.000	**0.591**	-0.043	FAULT2(√)
(5)FAULT2	-0.014	0.000	**0.405**	-0.027	FAULT2(√)
(6)FAULT3	-0.004	0.000	0.047	**0.599**	FAULT3(√)
(7)FAULT3	-0.004	0.000	0.046	**0.389**	FAULT3(√)

REFERENCES

1. J. M. Lattin, J. D. Carroll, and P. E. Greeen, Analyzing Multivariate Data. Beijing, Mechanical Industry Press, 2003.
2. D. Zogg, E. Shafai, H. P. Geering, Fault diagnosis for heat pumps with parameter identification and clustering, Control Engineering Practice, 2006, 14-12, pp.1435-1444.
3. Lennart Ljung, System Identification : Theory for the User(2nd Edition), Tsinghua University Press, Prentice Hall PTR, 2002.
4. M. Mahfoufa, S. Kandiahb, D.A. Linkensa, Fuzzy model-based predictive control using an ARX structure with feedforward, Fuzzy Sets and Sstems, 2002, 125, pp.39-59
5. Haojun Sun , Shengrui Wang , Qingshan Jiang, FCM-Based Model Selection Algorithms for Determining the Number of Cluster, Pattern Recognition, 2004, 37-10, pp. 2027-2037.
6. Z. Hilal İnan, Mehmet Kuntalp, A study on fuzzy C-means clustering-based systems in automatic spike detection, Computers in Biology and Medicine, 2007, 37-8, pp.1160-1166.
7. Francisco de A . T, de Carvalho, Fuzzy c-means clustering methods for symbolic interval data . Pattern Recognition Letters , 2007 , 28-4, pp.423-437.
8. Gleb Beliakov, Matthew King, Density based fuzzy c-means clustering of non-convex patterns, European Journal of Operational Research, 2006, 173-3, pp.717-728.

Proceedings of the 8th JFPS International
Symposium on Fluid Power, OKINAWA 2011
Oct. 25-28, 2011

1B3-1

EXPERIMENT ON SLIPPERS BEHAVIOR IN SWASHPLATE-TYPE AXIAL PISTON MOTORS

Motoshi SUZUKI*, Hideki AKITA*, Tatsuya SAITO**, and Toshiharu KAZAMA**

* Technical Research Center, Hitachi Construction Machinery Co., Ltd.
650 Kandatsu, Tsuchiura, Ibaraki, 300-0013, Japan
(E-mail:m.suzuki.jz@hitachi-kenki.com)
** Muroran Institute of Technology
27-1 Mizumoto-cho, Muroran, Hokkaido, 050-8585, Japan

ABSTRACT

The slippers behavior in swashplate-type axial piston motors was measured by the test rig. The operating conditions were supply pressure of up to 35 MPa and rotational speeds of 0–26.7 s^{-1}. A petroleum-type hydraulic oil with a viscosity grade of 46 was used as the test fluid, and the temperature was maintained at value between 30 and 60 ºC. The experiment examined the influences of supply pressure, rotational speed and oil temperature. The displacement between a slipper and a rotational disk, tilt angle, azimuth angle of a slipper and frictional torque are reported. As the supply pressure increased, the clearance between the slipper and the disk, the slipper tilt angle and the slipper azimuth angle decreased, and the frictional torque increased. As the rotational speed increased, the displacement and the slipper tilt angle increased. As the oil temperature increased, the displacement decreased and the slipper tilt angle increased.

KEY WORDS

Axial piston motor, Slippers, Hydraulics

NOMENCLATURE

d_p	: Diameter of pistons [mm]
h	: Center displacement of slippers [mm]
N	: Rotational speed [s^{-1}]
p_s	: Discharge pressure [MPa]
r_1	: Diameter of the inner sealing land [mm]
r_2	: Diameter of the outer sealing land [mm]
t_c	: Hydraulic fluid temperature [ºC]
α	: Tilt angle of slippers [deg]
η	: Static pressure balance ratio of slippers
φ	: Azimuth angle of slippers [deg]

INTRODUCTION

Hydraulic fluid power systems are used in construction machinery, automobiles, fabrication machinery and other industrial equipment, because of their high energy density, responsiveness, and the good method of transmitting large amount of power. Gear type, vane type, screw type, and piston type pumps and motors are used as pressure sources and actuators in fluid power systems. One of these, the swashplate-type axial piston pump or motor has a variable volume mechanism, and is widely used because of its small size. Figure 1 shows the structure of a swashplate-type axial piston pump. There has been demand for higher efficiency and reliability in pressure sources and actuators, and swashplate-type

axial piston pumps and motors are no exception. Static pressure bearing mechanisms have been mounted on parts to support the fluctuating high loads that occur during the operation of these pumps and motors. The slippers that support the relative sliding motion between the pistons and the swash plate are extremely important components, as they have a significant affect on mechanical function.
Many reports on research into slippers have been published. Kazama [1] analytically calculated the tribological characteristics of an over-clamped slipper. The other, Manring, Wray and Dong [2] [3], Iboshi and Yamaguchi [4] [5], Tanaka, Nakahara, Kyogoku and Fujita [6], Yabe and Kubo [7] have studied the motion and tribological characteristics of slippers theoretically and experimentally. However, the behavior of slippers has not been studied under real-life operating conditions with a focus on application to hydraulic motors and pumps, particularly those used in construction machinery.
In this study, the slipper was evaluated the behavior with a slipper test rig developed by the authors. The displacement and frictional torque of slippers were measured under a supply pressure of up to 35 MPa and rotational speed up to 26.7 s^{-1}, and the results are discussed in this report.

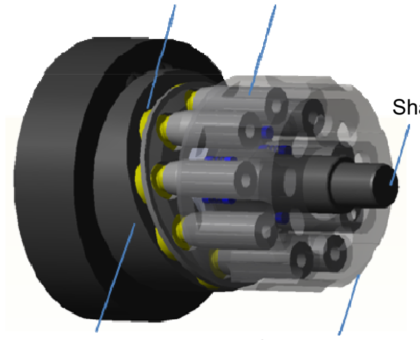

Figure 1 Mechanism of swashplate-type piston pump and motor

APPARATUS AND PROCEDURE

Figure 2 is a schematic view of the test rig for slippers in swashplate-type axial piston pumps and motors [9]. The device was mounted in an oil chamber with a rotational disk and two cylinders. Two piston assemblies were mounted inside the cylinders. One of the piston assemblies was used to measure behavior, and the other was included to balance the load on the rotational disk. The chamber was filled with an ISO viscosity grade 46 (density: 862 kg/m^3 @ 15 ºC, kinematic viscosity: 48.85/7.67 mm^2/s @ 40/100 ºC). The oil temperature was monitored by a thermocouple in the chamber and the oil was heated with two heaters (input power: 2 kW). The rotational disk was rotated by a servo motor (rated output: 4.4 kW, rated torque: 28.4 N•m, maximum speed: 50 s^{-1}). The rotational disk was set to zero tilt, perpendicular to the cylinders. A torque sensor (rated torque: 100 N•m, hysteresis: ±0.3%) was attached to the shaft.

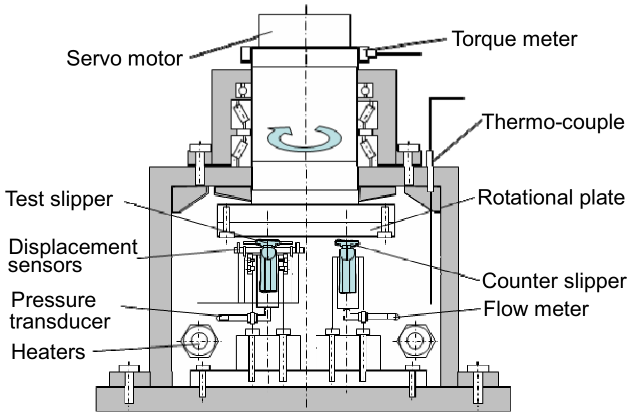

Figure 2 Diagram of slipper test rig

Figure 3 shows the hydraulic circuit. The oil flow rate to the cylinders was measured with a gear type flow meter (range: 0.083-16 ml/s, maximum pressure capacity: 62 MPa). A pressure sensor (maximum range: 50 MPa, non-linearity: 0.3% RO) was placed upstream of the flow meter, the measured value was feedback to the servo valve to control the pressure. A piston pump (maximum pressure: 72 MPa, flow rate at maximum pressure: 8.3 ml/s) was used as the pressure source.

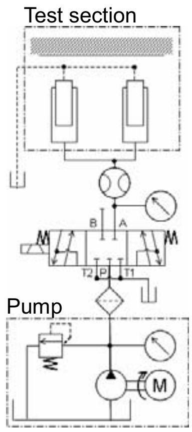

Figure 3 Diagram of hydraulic circuit

Figure 4 shows how the displacement meters were placed. Six contact sensors (range: ±0.5 mm, resolution: 0.1 μm) were used, three inner sensors for displacements of the slipper, and three outer sensors for the rotational disk. The sensors on the inner and outer sides were placed in pairs. The differences between the two sensors in each pair enabled us to calculate the changes in displacements between the slipper and the rotational disk. As displacement values were obtained at three points, their values enabled us to estimate the displacement h at the center of the slipper, the tilt angle α, and the azimuth angle φ.

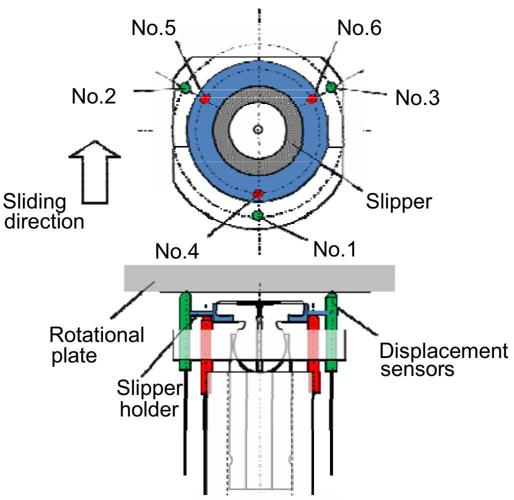

Figure 4 Locations of displacement sensors

The experiment was conducted as follows. Test piston assemblies were placed in the cylinders. The chamber was filled with test oil and the chamber was purged of air. The test oil in the chamber was heated to the test temperature. The cylinders were pressurized at 1 MPa and the displacement meters were zeroed. The rotational disk was driven at a constant rotational speed. The supply pressure was increased from 5 MPa to 35 MPa in 5 MPa increments and then lowered. The pressure changes were accomplished in 5 seconds, and 20 seconds were allowed for the pressure to stabilize. The supply pressure, flow rate, frictional torque and slipper displacement were recorded on a PC. The increase and decrease in pressure were carried out twice, and the data taken during the second cycle were used as a basis for comparison. The rotational speed of the disk was controlled by feeding back the signals of a tachometer to the electric servomotor to maintain a constant rotational speed under operating conditions ranging from low and high load.

The experimental conditions were as follows. The rotation rate N was 0, 3.33, 6.67, 10.0, 13.3, 16.6, 20.0 and 26.7 s^{-1}, and the operating temperature t_c for the hydraulic fluid was 30, 40, 50 and 60ºC. The diameter of the piston used was 25 mm, and the static pressure balance ratio η of the slipper found in the following expression was 0.03.

$$\eta = \frac{d_p^2 \ln(r_2/r_1) - 2(r_2^2 - r_1^2)}{d_p^2 \ln(r_2/r_1)} \quad \cdots\cdots(1)$$

RESULTS

Figure 5 illustrates the process for calculating the center displacement using the measured displacement data. Figure 5 (a) shows all the sampling data for the slipper and the rotational disk. Figure 5 (b) shows the values obtained by dividing the displacements of the slippers and the rotational disk by the corresponding data. These are the dimensions of the displacement between the slipper and the rotational disk in three positions. Figure 5 (c) shows the center displacement calculated as the mean of the displacements in the three directions.

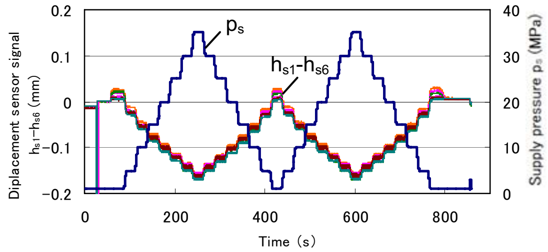

(a) Sampling data

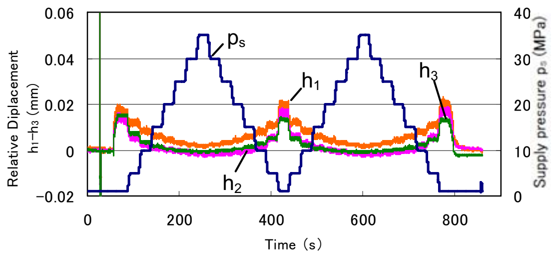

(b) Displacement between slipper and disk

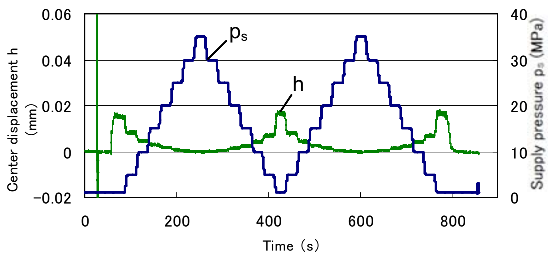

(c) Center displacement of slipper

Figure 5 Change in displacement h and supply pressure p_s (N = 3.33 s^{-1}, t_c= 30ºC)

Figure 6 shows the influence of supply pressure p_s and rotational speed N on the center displacement as the oil temperature t_c = 30 ºC. As the supply pressure p_s increased, the displacement h decreased. As the rotational speed N = 0 s^{-1}, the center displacement h was negative because high pressure caused the slipper deformation.

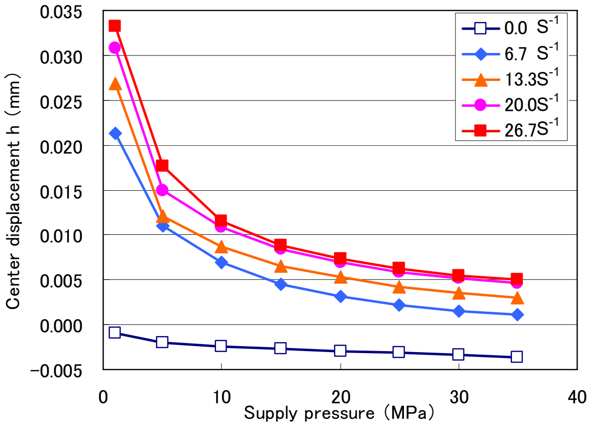

Figure 6 Influences of supply pressure p_s and rotational speed N on center displacement (t_c= 30ºC)

Figure 7 and 8 show the effect of rotational speed N and p_s on the center displacement h under low (t_c = 30 ºC) and high (t_c = 60 ºC) oil temperatures, respectively. The displacement h was large at low oil temperatures, due to the contribution of the hydrodynamic effect based on oil viscosity; the viscosity was higher at lower oil temperature. The center displacement h increased with rotational speed N, because a hydrodynamic (wedge) effect is obtained as a result of the rotation of the rotational disk. The force of the piston assemblies pushing the slippers to the rotating disk at higher supply pressure was larger than that at lower; hence, the slipper was compressed onto the disk and the displacement became smaller. As supply pressure p_s increased, the displacement h tended to decrease the effect by rotational speed N.

Figure 9 and 10 show the effects of rotational speed N and supply pressure p_s on tilt angle α under low (t_c = 30 ºC) and high (t_c = 60 ºC) oil temperatures, respectively. As the supply pressure p_s increased, the tilt angle α became small, indicating that the pad inclination was suppressed by the acting load. As the rotational speed N increased, the tilt angle α became large, owing to the hydrodynamic effect. This trend was a remarkable at high oil temperature.

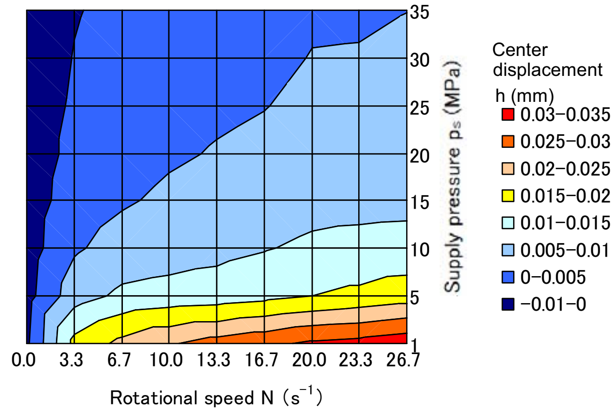

Figure 7 Influence of supply pressure p_s and rotational speed N on central displacement h (t_c = 30 ºC)

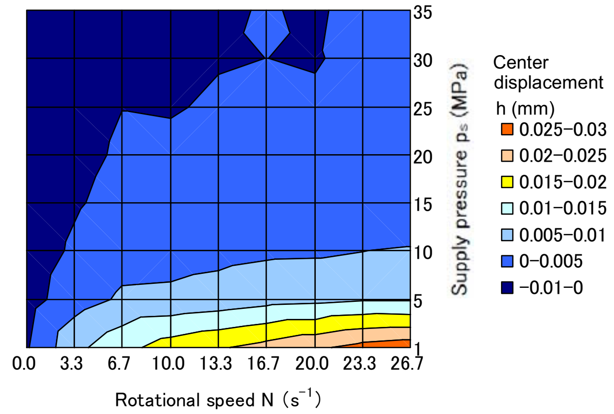

Figure 8 Influence of supply pressure p_s and rotational speed N on central displacement h (t_c = 60 ºC)

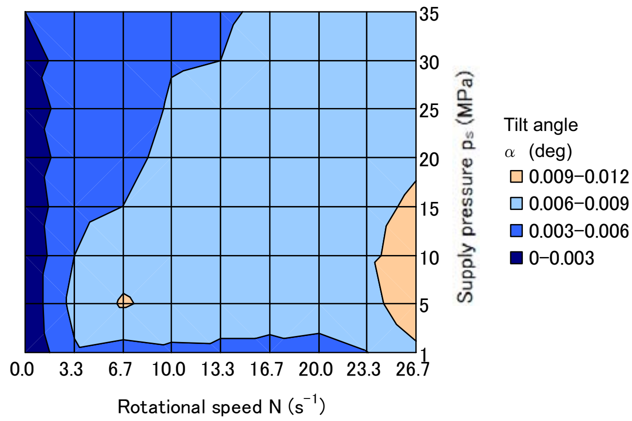

Figure 9 Effect of supply pressure p_s and rotational speed N on tilt angle α (t_c = 30 ºC)

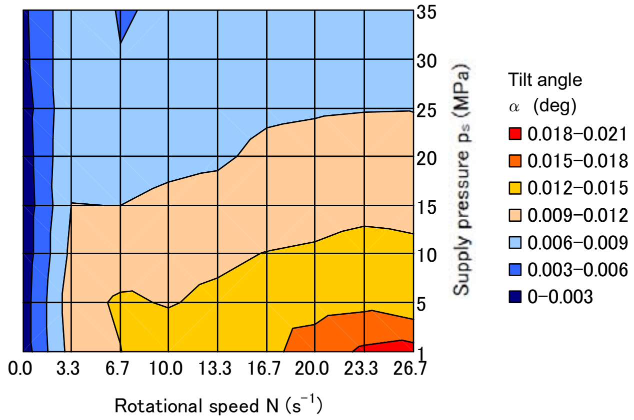

Figure 10 Effect of supply pressure p_s and rotational speed N on tilt angle α (t_c = 60 ºC)

Figure 11 and 12 show the effects of rotational speed N and supply pressure p_s on azimuth angle φ under low (t_c = 30 ºC) and high (t_c = 60 ºC) oil temperatures, respectively. The azimuth angle means the slipper pad direction of the maximum clearance. The azimuth angle φ is expressed with the clockwise direction being positive. The φ = 180 º was toward the center of the rotational disk from the center of test slipper, and the φ = 0 º was the opposite. As the supply pressure p_s increased, the azimuth angle φ was rather decreased, and vice versa.

Figure 13 and 14 show the effects of rotational speed N and supply pressure p_s on the frictional torque T under low (t_c = 30 ºC) and high (t_c = 60 ºC) oil temperatures, respectively. As the supply pressure ps increased, the frictional torque increased. At the low oil temperature, the frictional torque T tended to be lower depending on the rotational speed N; on the other, at the high oil temperature, this trend was not.

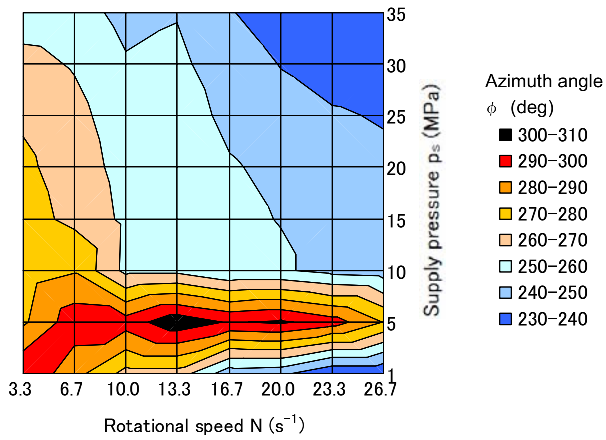

Figure 11 Effect of supply pressure p_s and rotational speed N on azimuth angle φ (t_c = 30 ºC)

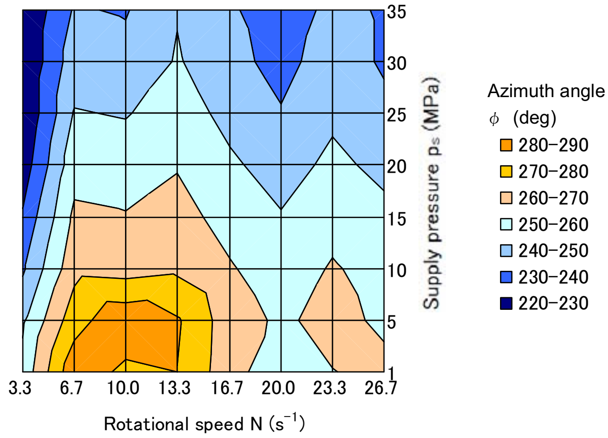

Figure 12 Effect of supply pressure p_s and rotational speed N on azimuth angle φ (t_c = 60 ºC)

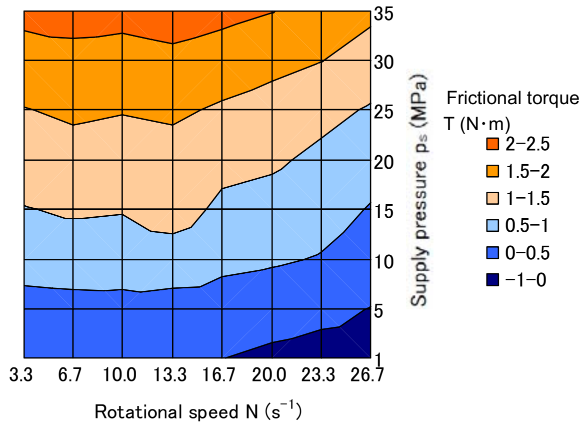

Figure 13 Effect of supply pressure p_s and rotational speed N on friction torque T (t_c = 30 ºC)

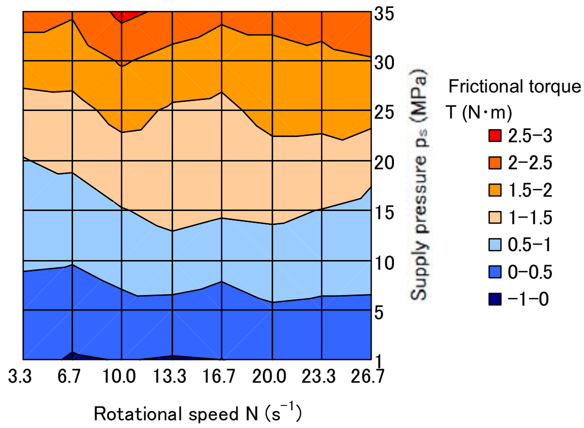

Figure 14 Effect of supply pressure p_s and rotational speed N on friction torque T (t_c = 60 ºC)

At fast and high oil temperature condition, the high torque was estimated caused by the low displacement due to the lower viscosity.

CONCLUSIONS

The behavior of the slippers used in swashplate-type piston motors was measured in a slipper test rig. The experiment was carried out under the conditions of a maximum supply pressure of 35 MPa and a maximum rotational speed of 26.6 s^{-1}. The following results were obtained. i) As the supply pressure increased, the displacement between the slippers and the disk, the slipper tilt angle and the slipper azimuth angle decreased, and the frictional torque increased. ii) As the rotational speed increased, the displacement and the tilt angle increased. iii) As the oil temperature increases, the displacement decreased and the tilt angle increased.

REFERENCES

1. T. Kazama,Numerical Analysis of Motion of A Slipper in Swash plate Type Axial Piston Pumps and Motors (Tribological Characteristics of An Over-Clamped Slipper), Proceedings of 11th Symposium “Dynamics, Measurement and Control Division” of JSME, No.09-30, 2009, pp.466-469.
2. N.D.Manring, R.E.Johnson, H.P.Cherukuri, The Impact of Linear Deformations on Stationary Hydrostatic Thrust Bearings, Jornal of Toribology, Transaction of ASME, vol.124, 2002, pp.874-877
3. N.D.Manring, C.L.Wray, Z.Dong, Experimental Studies on the Performance of Slipper Bearings Within Axial-Piston Pumps, Jornal of Toribology, Transaction of ASME, vol.126, 2004, pp.511-518
4. N. Iboshi and A. Yamaguchi, Characteristics of a Slipper Bearing for Swash Plate Type Axial Piston Pumps and Motors (1st Report, Theoretical Analysis), Transactions of JSME. B, 48(428), 1982, pp.695-706
5. N. Iboshi and A. Yamaguchi, Characteristics of a Slipper Bearing for Swash Plate Type Axial Piston Pumps and Motors (2nd Report, Experiment), Transactions of JSME. B, 49(437), 1983, pp.164-171
6. K. Tanaka, T. Nakahara, K. Kyogoku, K.Fujita, Motion Characteristics of Slipper Bearing in Swash Plate Type Piston Pump and Motor, Transactions of JSME. C, 73(728), 2007, pp.1236-1244
7. H.Yabe, A.Kubo, Fundamental Characteristics of Slipper Bearings in Swash Plate Type Axial Piston Pumps and Motors (1st Report, Fundamental Bearing Characteristics), Transactions of JSME. C, 63(608), 1997, pp.1350-1356
8. J. M. Bergada, J. Watton, Optimization of the Lift Characteristics of an Axial Piston Pump Grooved Slipper, Proceedings of 6th JFPS International Symposium on Fluid Power, Tsukuba, 2005 , pp 700- 704
9. T. Kazama, Trial Manufacture of A Tribological Characteristics Tester for Slippers Used in Hydraulic Piston Motors, Proceedings of Annual Meeting of JSDE Hokkaido Branch, No. 1-2008, 2009

PRINCIPLE AND METHOD TO IMPROVE THE DYNAMIC STIFFNESS OF THE ELECTRO-HYDRAULIC SERVO SYSTEM

Yanhong BAI[1,2] and Long QUAN[1,*]

1. Institute of Mechanical and Electronics Engineering
Taiyuan University of Technology
Taiyuan, Shanxi, 030024 China
(E-mail: yanhong.bai@163.com)
2. School of Electronics Information Engineering
Taiyuan University of Science and Technology
Taiyuan, Shanxi, 030024 China

ABSTRACT

The conception of raising dynamic stiffness of electro hydraulic position servo system by flow feedforward compensation is put forward. First, the elementary principle of maintaining piston position unchanged under sudden external force load change by charging additional oil volume is analyzed. Then, a scheme using double servo valves to realize flow feedforward compensation is presented, in which another servo valve is adopted specially to compensate the compressed oil volume in time. The two valves are arranged in parallel to control the cylinder jointly. Furthermore, the model of the flow feedforward compensation is derived, which is the key technique of this scheme. Using co-simulation of AMESim and Simulink, simulations are conducted under sudden external load force. And the results show that system dynamic load stiffness is improved with decreased maximal dynamic position deviation and shorted settling time.

KEY WORDS

Electro-hydraulic servo system, Flow feedforward compensation, Dynamic load stiffness, Double valves actuation

INTRODUCTION

In electro-hydraulic servo system application cases with large load force impact, in order to improve finished product rate and diminish the equipment vibration caused by the impact, not only high steady state control precision is required, but also high dynamic load stiffness is demanded. Let us consider the hydraulic screw-down system in a steel rolling mill. The rolls, which process steel, are subjected to large load changes or disturbances. As a steel bar approaches the rolls, the rolls are empty. However, when the bar engages in the rolls, the load on the rolls increases immediately to a large value. So a considerable abrupt force load change is exerted on the hydraulic screw-down system, which leads to the piston position of the hydraulic actuator seriously deviated from the desired point. Plus its high travel speed, the steel plate's head length beyond the permissible error is very long, which leads to higher fault product rate. Moreover, a greater impact is imposed on the mill equipment, which

* Corresponding author. E-mail: quanlong@tyut.edu.cn
This project is supported by National Natural Science Foundation of China (Grant No. 51075291)

causes system vibration and therefore shortens the equipment lifespan.

Researchers in Institute for Fluid Power Drives and Controls in RWTH Aachen University have been devoted to increasing the dynamic load stiffness by changing system structure. They amounted a piezo-actuator in the piston rod of the hydraulic cylinder specially to generate counterforce to balance the external force [1-2]. They also developed a hybrid valve, of which the sleeve is actuated by a piezo actuator [3]. With movable spool and sleeve in reverse directions, the valve's dynamic characteristics can be improved in the range of small valve openings. They utilized this hybrid valve in the position control system to improve the dynamic stiffness. With the above mentioned methods, the dynamic stiffness can be improved under given conditions. The first one can only be used in small load force cases owing to the limited driving force of the piezo actuator. The second one makes the valve's structure complicated, especially in large flow cases.

More research works on improving the performance against force disturbance are focused on the use of different control theories, such as adaptive backstepping sliding mode control[4], adaptive control[5], immune PID[6], delay control based on evolution strategies[7], fuzzy control[8], H_∞ robust control[9], and so forth. No matter which control theory is adopted, essentially the control accuracy and load stiffness is improved by increasing the open-loop dc gain. It is well known that low stiffness of the hydraulic system is owing to the compressibility of the oil. When a sudden force change is exerted on the system, the oil will be compressed and a position deviation will be caused. And to make the system return to the desired position, the compressed oil volume must be charged. But for the closed-loop control system regulating according to the error, it's difficult to charge enough oil in short time with limited gain. So the dynamic performance against disturbance and the dynamic load stiffness can't be improved evidently by advanced control algorithms.

In this paper, based on the essential reason of low stiffness of the electro hydraulic position servo system, the conception of raising dynamic stiffness by flow feedforward compensation is put forward. According to the detected force magnitude in real time, an appropriate amount of oil is charged as fast as possible by flow feedforward compensation. The new method is suitable for different magnitudes of force load and the valves existed in the markets can meet the requirement.

PRINCIPLE OF DYNAMIC STIFFNESS IMPROVEMENT BY FLOW COMPENSATION

Basic principle

The working process schematic of the hydraulic differential cylinder disturbed by external force is shown in Figure 1. A, V and p represent effective area of the piston, volume of the chamber and oil pressure in the chamber, respectively. And subscript 1 and 2 are used to distinguish variables of the two chambers. x denotes displacement of the piston. F_L is external force load.

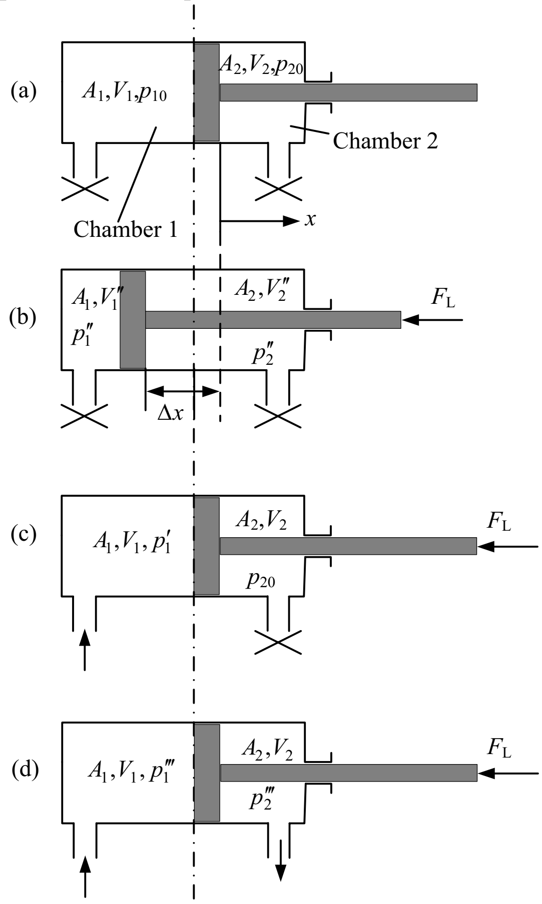

(a) Two plugged chambers, without external force.
(b) Two plugged chambers, with external force.
(c) One charged chamber and one plugged chamber, with external force.
(d) One charged chamber and one discharged chamber, with external force.

Figure 1 Working process schematic of hydraulic differential cylinder

In Figure 1(a), the two chambers are full of high pressure oil and the oil ports are plugged. In steady state, the actuator piston stays in a certain position and the pressures in the two chambers are represented by p_{10} and p_{20}. When an external force F_L is exerted (see Figure 1(b)), the actuator gets balanced in another piston position, and the displacement change is denoted by Δx. For chamber 1, the volume is dwindled and the pressure is upgraded owing to oil compression. For chamber 2, in contrary, the volume is expanded and the pressure is degraded due to oil release. Thereby, the corresponding driving force is produced to balance the external force.

If chamber 1 is opened and is charged and chamber 2 is still kept plugged, the piston could return to the original position by charging an appropriate amount of oil, as shown in Figure 1(c). In this case, the pressure in chamber 2 is unchanged and still is p_{20} and that in chamber 1 is upgraded to p_1'. Similarly, if chamber 1 is plugged, and chamber 2 is opened and is discharged, the piston could also return to the original position. If chamber 1 is charged and chamber 2 is discharged simultaneously under the control of a servo valve, the piston could also be actuated back to the initial position when an external force is imposed, as shown in Figure 1(d). But in this case, the pressures in both chambers are different from those in other conditions and will be discussed in the following section.
In summary, when a hydraulic actuator in equilibrium state is disturbed by an external force, the corresponding counterforce can be generated and the piston can be kept in the original position by charging oil to the pressure-down chamber or by discharging the pressure-up chamber.
For the electro-hydraulic position servo system with closed-loop feedback control, when the external force disturbance is applied, the actual position deviates from the desired position, and then the controller generates adjusting output according to the position error to maintain the prescribed position. The controller takes effect only after the position is deviated, so the control action is lagged. Moreover, to quickly build the counterforce against the force disturbance, large controller gain is required to yield large control value when the error is small, which is not possible owing to the limitation of stability. Therefore, the dynamic settling time is long and the dynamic error is large when the system is disturbed by external force, that is, the dynamic stiffness is poor.
To improve the dynamic stiffness, according to the operating process of the hydraulic actuator disturbed by external force, it is necessary to charge or discharge a certain amount of oil as soon as possible when force disturbance appears. So, on the basis of the regular electro-hydraulic position servo system, flow feedforward compensation is suggested. Its function is to charge or discharge a certain amount of oil quickly according to the magnitude of the load force.

Realization scheme
The prerequisite to improve the electro-hydraulic servo system performance against force disturbance by flow feedforward compensation is "rapid compensation", which is to make sure that the needed oil volume is charged before large position error occurs.
The step response curves of the servo valve D634 and D765 made in Moog Inc. are shown in Figure 2 and 3. In our study, the rated flow of the selected D634 and D765 is 100 L/min and 38 L/min respectively, with full valve opening and under the rated pressure drop 3.5 MPa. From Figure 2 and 3, when 20 L/min flow is through the two valves under pressure drop 3.5 MPa, the response time of D634 (20% of the total stroke) is 7 ms and that of D765 (52.5% of the total stroke) is 1.5 ms. It can be concluded that the response time of the ordinary valve D634 is much longer than the fast-response valve D765 in the case of small flow. Evidently, D634 can not meet the requirement of "fast compensation", and D765 can be used for flow feedforward compensation.

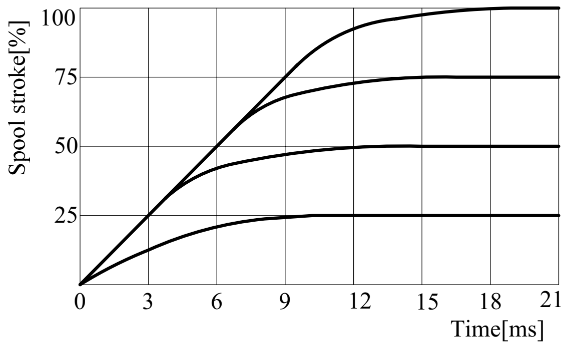

Figure 2 Step response of servo valve D634

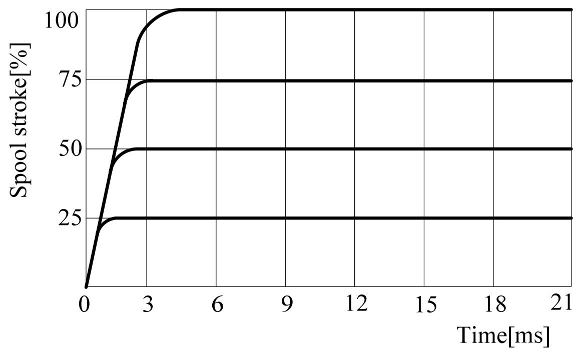

Figure 3 Step response of servo valve D765

But due to its small rated flow, the fast-response valve D765 can not replace the regular large-flow servo valve in the position servo system. So double valves-control scheme is put forward to realize flow feedforward compensation, with which a fast-response valve for flow compensation is added to the regular electro-hydraulic position control system. The schematic diagram of the double valves-controlled hydraulic position servo system with flow compensation is shown in Figure 4. The system is mainly composed of three parts: position closed loop control, flow feedforward compensation and force load compensation.
The compensation servo valve is specially used to control the compensation oil flow, which is arranged in parallel with the main servo valve.

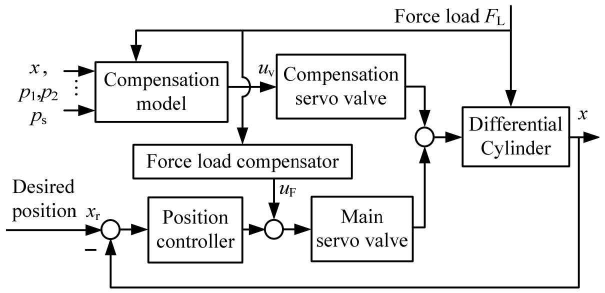

Figure 4 Schematic diagram of double valves-controlled electro-hydraulic position servo system with flow compensation

Proportional control algorithm is used in position closed-loop control. With this simple method, the steady state error caused by load force couldn't be reduced. To improve control accuracy, force load feedforward compensator is adopted. The compensator's output is the valve's control value u_F needed to generate counterforce to balance force load, which is added to the command signal of the main valve. And the force load compensation model can be easily obtained by experimental data fitting method.

FLOW COMPENSATION MODEL

The key to realize flow compensation is to design the compensation model which reflects the relationship between the command signal of the compensation valve and the magnitude of the load. In this section, the compensation model in the simple case only with flow feedforward control is discussed firstly. On this basis, the compensation model is obtained by considering the effects of the feedback control.

Simple case

For the case that one chamber of the actuator is plugged and the other is controlled by a servo valve, the piston position can be kept unchanged under external force, see Figure 1(c). For this simple case, we analyze the required charging oil volume first, and then determine the command signal of the compensation valve.

Suppose the volume change of chamber 1 from Figure 1(a) to Figure 1(c) is ΔV_1. From Figure 1(a) and Figure 1 (c), the following expression can be obtained

$$\begin{cases} A_1 p_1' - A_2 p_{20} = F_L \\ A_1 p_{10} - A_2 p_{20} = 0 \end{cases} \tag{1}$$

For the sealed chamber 1, the pressure can be upgraded from p_{10} to p_1' by decreasing its volume and compressing the oil. And the piston displacement deviation Δx should follow the formula

$$\Delta x = -\frac{V_1}{\beta_e A_1}(p'_1 - p_{10}) \tag{2}$$

And the dwindled volume can be expressed as

$$\Delta V_1 = A_1 |\Delta x| = \frac{V_1}{\beta_e}(p'_1 - p_{10}) \tag{3}$$

Where β_e is the equivalent bulk modulus of the oil.

The pressure in the sealed chamber 1 can also be upgraded from p_{10} to p_1' by charging high pressure oil without changing the volume (see Figure1(c)). In this case, the oil volume of chamber 1 can be considered as two parts: the compressed oil and the charged oil. If the pressure of the charged oil is p_1', the charged oil volume should be equal to the dwindled volume ΔV_1 expressed by equation (3).

From equation (1), the following equation can be derived

$$F_L = A_1(p'_1 - p_{10}) \tag{4}$$

Substitute equation (4) in equation (3), yields

$$\Delta V_1 = \frac{F_L V_1}{\beta_e A_1} \tag{5}$$

The oil volume needed to charge into the chamber to keep the piston position unchanged under external force can be obtained from equation (5).

The control signal of the servo valve to charge oil volume of ΔV_1 into the chamber 1 is determined in the following. To meet the requirement of fast compensation, pulse signal is adopted as valve's command signal. The signal's amplitude and width are represented by U_v and Δt respectively.

Port A of the servo valve is connected to chamber 1, so its flow equation can be expressed as

$$Q_A = u_v Q_N \sqrt{\frac{p_s - p_1}{\Delta p_N}} \tag{6}$$

Hence, the oil volume through port A is

$$\Delta V_A = \int_0^\infty u_v Q_N \sqrt{\frac{p_s - p_1}{\Delta p_N}} dt \tag{7}$$

Where Δp_N is the rated valve pressure drop [MPa], p_s is the pressure in port P [MPa], Q_N is the rated valve flow [m^3/s], u_v is the command signal of the valve ($-1 \le u_v \le 1$).

As a pulse signal, u_v can be expressed as

$$u_v = \begin{cases} U_v & t_0 \le t \le t_0 + \Delta t \\ 0 & others \end{cases} \tag{8}$$

If the fluctuation of the pressure in chamber 1 and the supply pressure p_s is ignored, and the pressure in chamber 1 is kept at p_1', substituting equation (8) into equation (7) yields

$$\Delta V_A = \frac{Q_N \sqrt{p_s - p'_1}}{\sqrt{\Delta p_N}} U_v \Delta t \tag{9}$$

The oil volume charged into chamber 1 is equal to that flowing through port A, so

$$\Delta V_A = \Delta V_1 \tag{10}$$

Substituting equation (5) and (9) into (10), the relationship between the amplitude U_v and the width Δt of the pulse command signal of the servo valve can be deduced as follows

$$U_v \Delta t = \frac{F_L V_1 \sqrt{\Delta p_N}}{\beta_e A_1 Q_N \sqrt{p_s - p_1'}} \tag{11}$$

Just like that in pushing force, in the case of pulling force (F_L<0), chamber 1 is plugged and chamber 2 is controlled by the servo valve. And port B of the valve is connected to chamber 2. The relationship between the amplitude U_v and the width Δt of the pulse command signal can be deduced similarly as follows

$$U_v \Delta t = \frac{F_L V_2 \sqrt{\Delta p_N}}{\beta_e A_2 Q_N \sqrt{p_s - p_2'}} \tag{12}$$

Where p_2' represents the steady-state pressure of chamber 2 with external pulling force F_L.
Equation (11) and equation (12) show that the product of the amplitude and the width of the valve's pulse command signal is a constant for a given external force.

Flow compensation model

For the proposed electro-hydraulic servo system shown in Figure 4, when external force is exerted, not only the flow feedforward compensation takes effects, but also the feedback control does. Moreover, the two chambers are controlled by the compensation valve simultaneously. So equation (11) and equation (12) need to be modified. First consider the case of F_L>0.
Figure 1(d) is used to discuss the situation that two chambers are controlled by a servo valve. When chamber 1 is charged to upgrade its pressure to reject external force, chamber 2 will be discharged and its pressure will be decreased. So the steady-state pressure p_2''' is less than p_{20}. Compared with the case that one chamber is controlled, the pressure increment in chamber 1 needed to reject load force is decreased and the charging oil volume should also be reduced.
In addition, with position deviation caused by force load, closed-loop position control also takes actions through the main servo valve. Hence, compared with the system in Figure 1(d), for the system shown in Figure 4, the compensation oil volume to chamber 1 should be reduced.
Therefore, the extra oil volume injected by flow feedforwad compensation should be less than the calculated results by equation (5). This is taken into consideration by modifying equation (10) as

$$\Delta V_A = \alpha \Delta V_1 \tag{13}$$

where 0<α<1.
Moreover, the pressure in chamber 1 does not remain unchanged during oil charging process by compensation valve. But its value varies from lower than p_1''' to higher than p_1''', so the average value can be considered as p_1''' approximately. Therefore, the assumption that the pressure in chamber 1 is kept at constant p_1''' is reasonable and equation (9) can still be adopted by replacing p_1' with p_1'''. Thus, equation (11) can be modified as

$$U_v \Delta t = \alpha \frac{F_L V_1 \sqrt{\Delta p_N}}{\beta_e A_1 Q_N \sqrt{p_s - p_1'''}}, \quad F_L \geq 0 \tag{14}$$

Similarly, equation (12) can be modified as

$$U_v \Delta t = \beta \frac{F_L V_2 \sqrt{\Delta p_N}}{\beta_e A_2 Q_N \sqrt{p_s - p_2'''}}, \quad F_L < 0 \tag{15}$$

where 0<β<1.
Equation (14) and (15) illustrate that the product of the amplitude U_v and width Δt of the valve's pulse command signal depends on external force magnitude and piston position. And this value is constant for a given external force and piston position.

Simulations

Using AMESim and Simulink co-simulation, the scheme proposed above is verified. Hydraulic system model is constructed in AMESim according to the double-valves control principle shown in Figure 4. The parameters of the cylinder are 63 mm piston diameter, 45 mm piston rod diameter and 300 mm total stroke. The main servo valve and the compensation servo valve are regular valve D634 and fast-response valve D765 made in Moog Inc. In simulation experiments, the proportional factor of the position controller is 12 1/m.

Figure 5 gives the response curves under a sudden change force load of 20 kN, including the exerted force load curve, the pulse command signal of the compensation valve, the compensating flow curve and the piston displacement curve. In simulation, the amplitude U_v and width Δt of the valve's pulse command signal is 1 and 0.005 s respectively. To compare, the displacement response curve without flow compensator is also given in Figure 5

From Figure 5 it can be seen that the max dynamic position deviation with flow compensation is almost 50% of that without flow compensation. That is, dynamic stiffness is largely improved by the flow compensation.

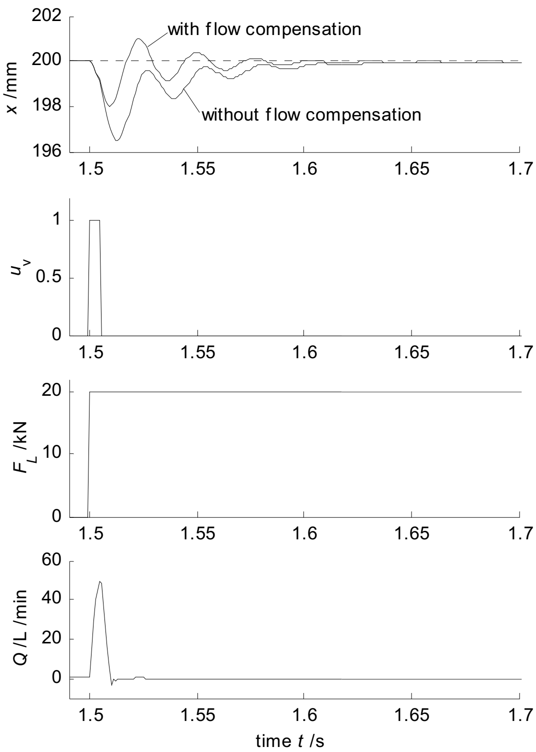

Figure 5 Response curves with sudden load change

DETERMINATION OF THE PUSLE CONTROL SIGNAL

Performance index against disturbance

In general, for disturbance input, dynamic performance is measured by maximal dynamic error and settling time. Since flow feedforward compensation control is adopted in the system under consideration, the second dynamic peak absolute error B_2 may be more large and even over the first peak absolute error B_1. The definition of B_1 and B_2 is shown in Figure 6. Hence, the comprehensive index SAE (sum of absolute error) is used to measure the dynamic performance against disturbance.

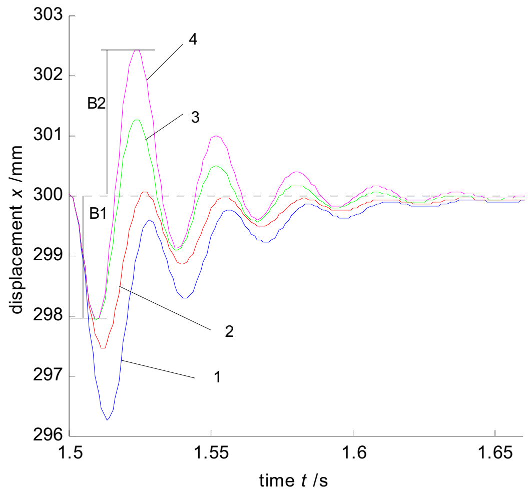

Figure 6 Response curves with different pulse signals

With the same load change, simulations are carried out under different pulse signals. Response curves are given in Figure 6. SAEs corresponding to curve 1 to 4 are 113.58 mm, 69.112 mm, 56.145 mm and 73.057 mm, respectively. Comparing the four curves, we can conclude that curve 3 has good performance for its smaller B_1 and B_2 and shorter settling time. And its SAE is the smallest. Evidently, adopting SAE as performance index is suitable.

Verification of the compensation model

Pulse signal calculation equation (14) and (15) will be verified by simulation experiments in the following.

When piston position x is 200 mm and external force F_L is 20 kN, according to equation (14) there exists

$$U_v \Delta t = 8.76\alpha \times 10^{-3}$$

Let α=0.6, then $U_v \Delta t \approx 0.005$.

At the piston position x=200mm, for the same load change and with U_v=1, simulations are carried out with different Δt, including 0.003 s, 0.005 s and 0.008 s. Response curves are shown in Figure 7 and the corresponding SAEs are 60.46 mm, 48.21 mm and 59.96 mm, respectively. For $\Delta t = 0.003$s, $\Delta t \cdot U_v = 0.003$, SAE is the largest and B_1 is the largest too. This manifests that the injecting oil volume is less than that needed to reject load force, which is called under-compensation. For $\Delta t = 0.008$s, $\Delta t \cdot U_v = 0.008$, B_1 is the smallest, but B_2 is the largest and the SAE is also more larger, nearly equal to that with $\Delta t = 0.003$s. This indicates the injecting oil volume exceeds that needed, which is called over-compensation. For $\Delta t = 0.005$s, $\Delta t \cdot U_v = 0.005$, both B_1 and B_2 are smaller and SAE is the smallest, and settling time is the shortest. This suggests that the injecting oil volume approaches to that needed.

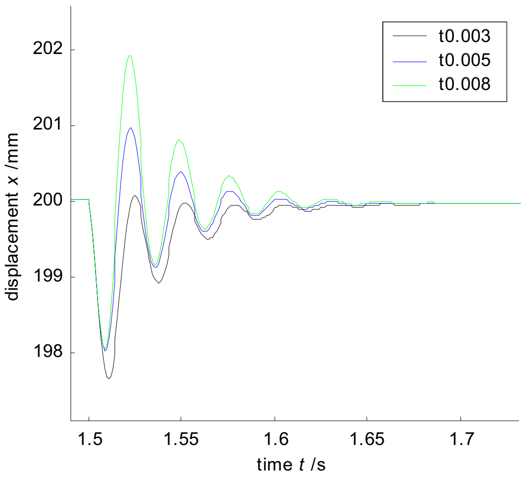

Figure 7 Response curves with different Δt and identical U_v

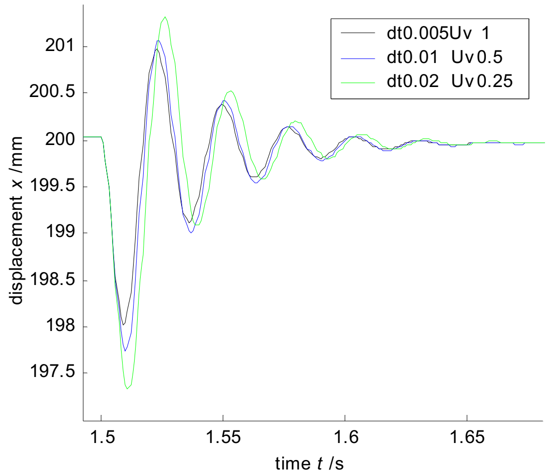

Figure 8 Response curves with same $\Delta t{\cdot}Uv$ and different U_v

The analysis above shows that the system has good transient performance against disturbance when $\Delta t{\cdot}U_v$ is equal to the calculated value. This conclusion just verifies the correctness of equation (14) and (15). The factors that affect α or β are complex, including piston position, position controller's proportional coefficient, operating pressure and so on. So α or β can't be defined exactly. We suggest the values range between 0.5 and 0.9. Thus the appropriate value of $\Delta t{\cdot}U_v$ is also not a determined value but just in a range.

Determination rules of pulse command signal

With the determined product value of amplitude U_v and width Δt of the valve's pulse command signal, the determination rules of U_v and Δt are discussed in this section.

Rule 1: to inject compensation oil as quickly as possible, the amplitude of pulse signal should be large, and the width should be small.

According to the above section, as piston position x is 200 mm and external force F_L is 20 kN, good control performance can be achieved with $\Delta t{\cdot}U_v = 0.005$. Figure 8 gives response curves with different (Δt, U_v) pairs, including (1, 0.005 s), (0.5, 0.01 s) and (0.25，0.02 s). And the corresponding SAEs are 48.21 mm, 55.19 mm and 63.98 mm.

It can be concluded that the performance is different with different U_v even with same $\Delta t{\cdot}U_v$. When the amplitude U_v takes the maximal value, i.e. $U_v = 1$, both the first peak absolute error B_1 and the second one B_2 are the smallest and the SAE is also the smallest, which shows that the control performance is the best.

Rule 2: considering sampling time and response speed of compensation servo valve, the minimal width of the pulse signal is limited. Here 0.003 s is taken as minimal pulse width.

For small $\Delta t{\cdot}U_v$, if let U_v=1 in terms of rule 1, then Δt will be very small. For instance, when piston position x is 20 mm and external force F_L is 10 kN, equation (14) yields

$$U_v \Delta t = 2.229\alpha \times 10^{-3}$$

Let α=0.8, then $U_v \Delta t \approx 0.0018$

Figure 9 shows response curves with (U_v, Δt) pairs as (1, 0.002 s), (0.6, 0.003 s) and (0.45, 0.004 s), and the corresponding SAEs are 16.27 mm, 12.2 mm and 12.86 mm.

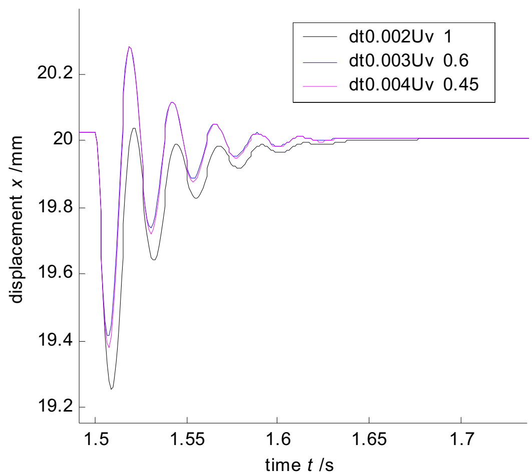

Figure 9 Response curves with smaller $\Delta t{\cdot}U_v$ and different $\Delta t{\cdot}$

It can be seen that with Δt = 0.002s and U_v = 1, the best control performance cannot be obtained. The reason is that the actual injecting oil volume is less than the expected since the desired opening of the servo valve couldn't be completely opened due to shorter pulse actuating time, though the actual value of $\Delta t \cdot U_v$ is larger than the calculated value. With Δt = 0.003 s and U_v = 0.6, better performance can be obtained. But with Δt = 0.004 s and U_v = 0.45, the performance is a little worse than the former. Thus rule 1 is further proved.

Rule 3: if injecting oil process continues after the first peak time, the second peak error would be increased, and the control performance would get worse. Hence the maximal width of the pulse signal is also limited and should be shorter than the first peak time.

With rule 3 when the calculated width of the pulse signal exceeds the maximum, the practical width will take the maximal value. Thus, the practical injection oil volume will be less than the expected and under-compensation will occur, which would affect the control performance. Therefore, when selecting compensation servo valve, the capacity to charge the required oil volume during the limited pulse actuating time under maximal load force should be considered.

CONCLUSIONS

Based on the principle of rejecting force load by injecting extra high-pressure oil, the conception of double valves-controlled electro-hydraulic position servo system with flow feedforward compensation is proposed. The product expression of the amplitude and width of the compensation servo valve's pulse command signal, that is, flow compensation model is derived and its correctness is verified by simulations. Three determination rules of the amplitude and the width of the pulse signal are concluded by analysis and simulations. Simulation results show that dynamic load stiffness can be improved with this scheme.

REFERENCES

1. Meuser MARCELL, Vollmer FRANK. Using piezo actuators to improve the load stiffness of servohydraulic drives[J]. Ölhydraulik und Pneumatik, 2003,47(10):1-6.
2. Vollmer FRANK. Hydraulic actuators with high load stiffness[J]. Ölhydraulik und Pneumatik, 2001, 45(7): 675-682.
3. Reichert MAXIM, Murrenhoff HUBERTUS. Stiff electro hydraulic drives using a hybrid valve[C]. Proceedings of the 7th JFPS International Symposium on Fluid Power, TOYAMA, 2008: 585-590.
4. Yiqun WANG, Shurong NING, Jian LIU. Adaptive fuzzy approach to control the electro-hydraulic servo on the plate width in hot plate mills[J]. Chinese Journal of Mechanical Engineering, 2007, 43(12):1-4.
5. Jun ZOU, Xin FU, Huayong YANG, et al. Application of immune PID controller in hydraulic servo control system[J]. Chinese Journal of Mechanical Engineering, 2005, 41(1):1-5.
6. Gang CHEN, Yi CHAI, Baocang DING, et al. Multiple sliding mode neural network control of electro-hydraulic position servo system[J]. Control and Decision, 2009, 24(2):221- 225.
7. Minyoung KIM, Chungoh LEE. An experimental study on the optimization of controller gains for an electro-hydraulic servo system using evolution strategies[J]. Control Engineering Practice, 2006, 14(2): 137-147.
8. Xi LI, Xiaoqi TANG, Yunfei ZHOU. Study and application on model-free motion control scheme of electro-hydraulic servo systems[J]. Chinese Hydraulics & Pneumatics, 2003(2):6-8.
9. Jian YANG. Control of hydraulic press machine using model reference adaptive control[J]. Machine Tool & Hydraulics, 2009,37(6):83-85.

Proceedings of the 8th JFPS International
Symposium on Fluid Power, OKINAWA 2011
Oct. 25-28, 2011

1B3-3

THE HYDRAULIC EFFECT OF DIFFUSER VANES IN AN ANNULAR CASING

Pengfei WANG, Xiaodong RUAN, Jun ZOU* and Xin FU

State Key Laboratory of Fluid Power Transmission and Control
Zhejiang University
38 Zheda Road, Hangzhou, 310027, China
*E-mail: junzou@zju.edu.cn

ABSTRACT

Annular casing can be adopted to achieve higher strength, better processability and easier inspection than the volute casing. Since there is enough space between the impeller discharge and the casing, diffuser vanes can be assembled in the casing, help to transform the velocity energy into pressure. The hydraulic effect of vanes in the annular casing is then studied by means of fluid dynamic calculations.
Cases are carried out involving the variation of the number of vanes, the wrapping angle, the attack angle and the circumferential distribution of vanes and are compared with the case without diffuser vanes. Surprisingly, the results reveal that the adopting of diffuser vanes has negative effect on the hydraulic efficiency in the annular casing. From the velocity distributions we find the reason lies in that since the volute tongue area is very large, there exists a large recirculation flow region in the casing, and vanes in this region will hinder the flow back to the outlet.

KEY WORDS

Annular Casing; Diffuser Vane; Hydraulic Efficiency

INTRODUCTION

The structure of water pumps usually consists of an extruding chamber, which is used to gather water and convert high velocity kinetic energy of the flow from the impeller discharge to pressure in order to minimize the hydraulic loss [1]. Annular casing is one type of extruding chamber, and due to its structural symmetry, can be adopted to achieve higher strength, better processability and easier inspection than the popular volute casing. However, the hydraulic efficiency of annular casing is usually much lower than that of volute casing, due to the severe impacting of the constant flow from the impeller to the mean flow in the annular casing whose velocity varies as it passes though the casing[2]. Since there is enough space between the impeller discharge and the casing, diffuser vanes can be assembled in the casing, in order to weaken this kind of velocity impacting, and help to change the velocity energy into pressure. Its overall hydraulic effect is studied in this paper by means of fluid dynamic calculations.

MODEL

Since the blades are rotating with a high speed, the time-averaging velocity profile can be treated as uniform at the outlet of the blades i.e. the inlet of the vanes. Then, if we focus our attention on the flow in the casing, the blades can be omitted, and a uniform velocity inlet boundary can be used. Besides, the problem can be reduced to 2-D if the side effects of the vanes are neglected. Hence the following geometry without diffuser vanes is drawn (Fig.1).

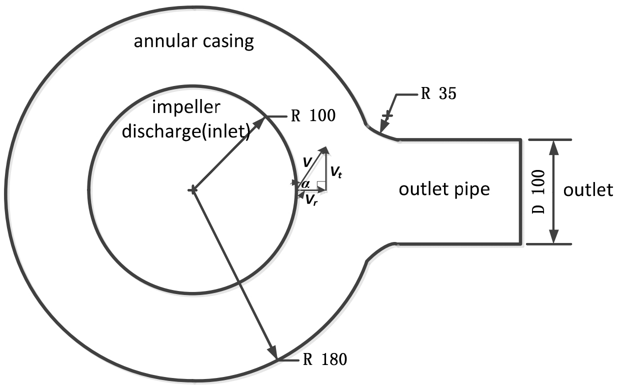

Fig.1 sketch of the simplified geometry without diffuser vanes.

The steady state of the flow in the casing is under study, and since water is pumped, incompressibility is assumed. Then the continuity equation under the Cartesian coordinates writes

$$\frac{\partial u_i}{\partial x_i} = 0 \tag{1}$$

where u_i is the x_i component of velocity. And the momentum equation is

$$u_k \frac{\partial u_i}{\partial x_k} = -\frac{1}{\rho}\frac{\partial p}{\partial x_i} + \mu \frac{\partial^2 u_i}{\partial x_k \partial x_k} \tag{2}$$

where p is the static pressure and μ is the dynamic viscosity.

In addition, due to the turbulence of the flow, the standard k-ε turbulent model with the standard wall function is adopted.

The boundary conditions are set as follows: at the inlet, uniform velocity is set with the radial component $V_r=V\cdot\sin\alpha$, and the circumferential component $V_t=V\cdot\cos\alpha$, where V is the magnitude of discharging velocity from the impeller which is set to be 10m/s throughout the calculations, and α is the tangent flow angle, which is set to be 20 degree in the calculations; at the outlet, pressure boundary condition is used; at the wall, no slip boundary condition is set.

The fluid region is discretized using the quadrilateral elements with the pave scheme. The above problem can be directly solved by means of the commercial software FLUENT.

RESULTS and DISCUSSION

To investigate the hydraulic effects of the diffuser vanes, various factors are involved in, namely the number of vanes, the wrapping angle, the attack angle and the circumferential distribution of vanes.

Throughout of the investigation, the case without diffuser vanes is used as the reference. The flow without diffuser vanes is shown in Fig.2, and the hydraulic loss is 4.9m. From the velocity distribution we can figure out that there exists a large recirculation region in the casing.

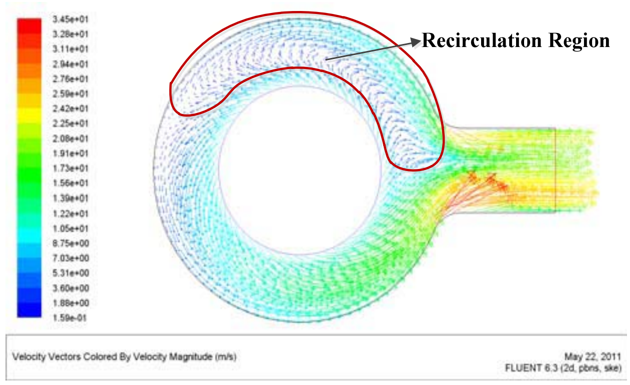

Fig.2 the velocity distribution without diffuser vanes, used as the reference.

Variation of the number of diffuser vanes

Two cases are carried out with the number of diffuser vanes of 7 and 17 respectively. The vane is designed as a logarithmic spiral and no flow attack at the inlet. The wrap angle of each vane is chosen to be 20 degree. The vanes are mounted equidistantly along the circumferential direction.

The velocity distribution of the two cases is shown in Fig.3, and the hydraulic loss is 5.6m and 6.8m respectively, all of which is higher than the reference (Fig.2).

From the velocity distributions, we can see that in the guide region, where flow passes through the vanes, the flow is much more uniform. However, the recirculation region still exists, in which the vanes hinder the flow back to the outlet. More the number of vanes, more serious of hindered.

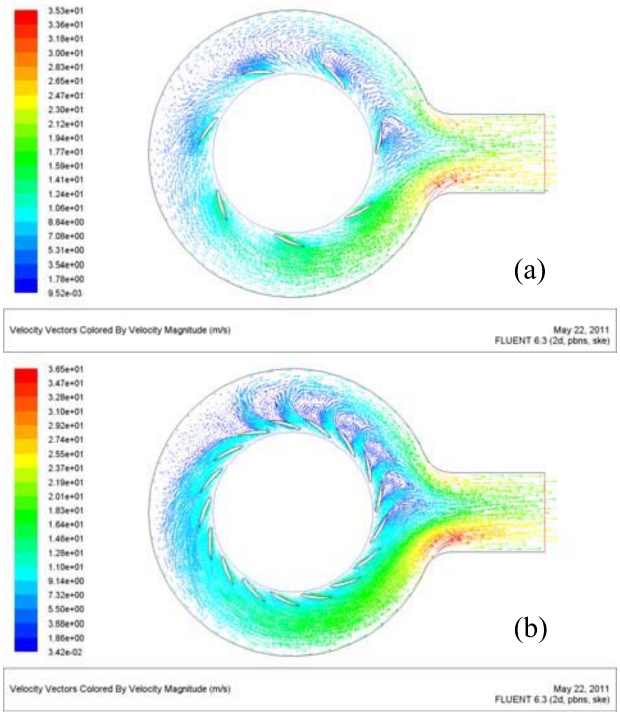

Fig.3 the velocity distribution with the number of vanes varied: (a) 7 vanes; (b) 17 vanes.

Variation of the wrap angle of diffuser vanes

Two wrap angles are chosen, 10 and 30 degree respectively. The larger the wrap angle, the longer the vane. The velocity distributions shown in Fig.4 reveal that with the increase of wrap angle the guide region of the flow is enlarged, however, the flow in the recirculation region is hindered more seriously. The hydraulic loss is found to be 5.4m and 6.6m respectively, still higher than the reference (Fig.2).

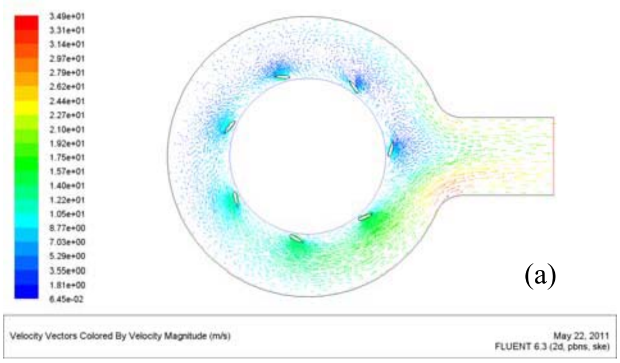

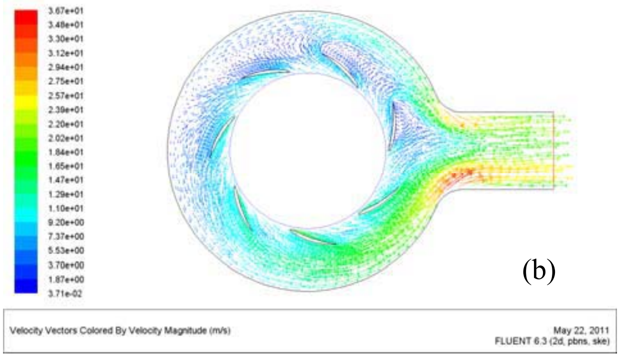

Fig. 4 the velocity distribution with the wrap angle varied: (a) 10 degree; (b) 30 degree.

Variation of the attack angle

The attack angle is determined by the difference of the inlet flow angle and the vane stagger angle. Two attack angles are chosen, -10 and 10 degree respectively. The velocity distributions shown in Fig.5 reveal that with the increase of attack angle the guide region of the flow is enlarged as well, however, the flow in the recirculation region is hindered more seriously. The hydraulic loss is found to be 6.4m and 8.0 m respectively, much higher than the reference (Fig.2) and the case without attack (Fig.3a).

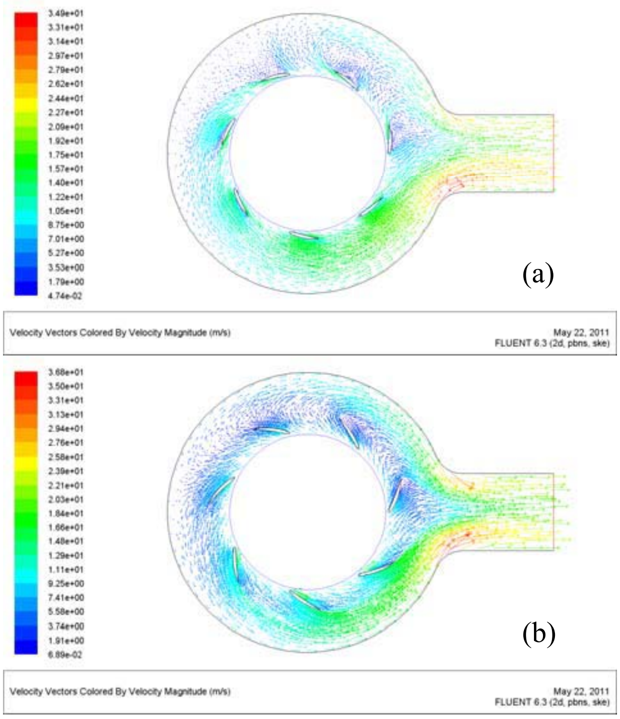

Fig.5 the velocity distribution with the attack angle varied: (a) -10 degree; (b) 10.

Variation of the circumferential distribution

The diffuser vanes are generally assembled equispaced circumferentially. Here we consider two special cases where the vanes are assembled as a geometric sequence along the circumferential direction; one common ratio is 0.9, and the other is 1.1.

The velocity distributions shown in Fig.6 reveal that the larger the common ratio, the more number of vanes will appear in the recirculation region, then the flow is hindered more seriously. The hydraulic loss is 5.5m and 5.9m respectively, still higher than the reference (Fig.2).

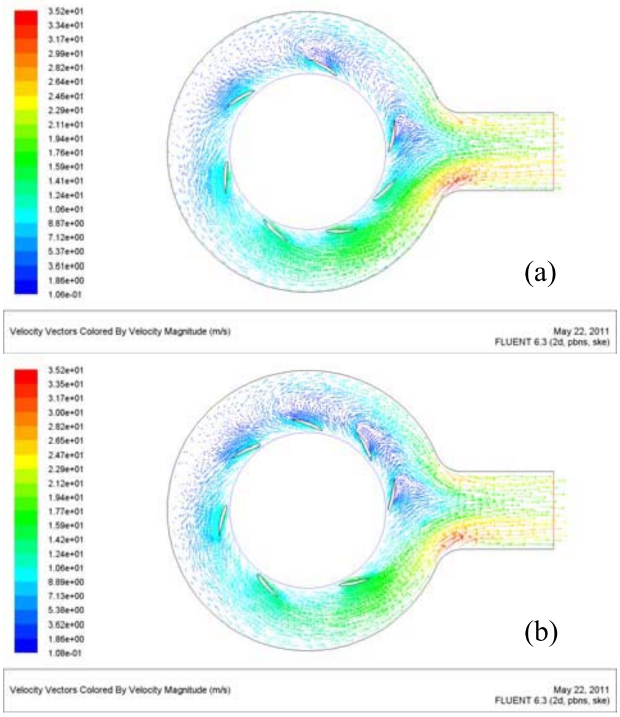

Fig.6 the velocity distribution with the circumferential common ratio varied: (a) 0.9; (b) 1.1.

CONCLUSION

The hydraulic effect of diffuser vanes in the annular casing is studied by means of fluid dynamic calculations. Cases are carried out involving the variation of the number of vanes, the wrapping angle, the attack angle and the circumferential distribution of vanes and are compared with the case without diffuser vanes.

Despite the flow is even in the guide region, the overall flow becomes surprisingly much worse. From the velocity distributions we find that there is a large recirculation flow region in the casing due to the large area of volute tongue. Hence the vanes in the recirculation region will hinder the flow back to the outlet. Therefore the hydraulic loss increases.

Through the numeric experiments we get to the point that for the annular casing we considered it's not suitable to add diffuser vanes in the casing. However, for the case where no recirculation region exists, there's still the possibility that the adopting of diffuser vanes will enhance the overall hydraulic performance.

ACKNOWLEDGEMENT

This work has been supported by the National Basic Research Program of China (Grant No. 2009 CB724300) and National High Technology Research and Development Program (863) of China (2010AA045401).

REFERENCES

[1] Stepanoff, A. J., Centrifugal and Axial Flow Pumps: theory, design, and application, New York, Krieger Publishing Company, 1957.

[2] Cha, S., Pump: Principle and Design, Beijing, China Machine Press, 1988.

Proceedings of the 8th JFPS International
Symposium on Fluid Power, OKINAWA 2011
Oct. 25-28, 2011

1C1-1

MATHEMATICAL MODELING, EXPERIMENTAL RESEARCH AND OPTIMIZATION OF CHARACTERISTIC PARAMETERS OF THE VALVE PLATE OF THE AXIAL PISTON PUMP/MOTOR

Radovan Petrovic[*], Miroslav Zivkovic[**], Milomir Gasic[***]

[*] *College of Applied Engineering Trstenik; Center for Power Control Hydraulics (CPCH), Serbia*
(E-mail: radovanfvk@yahoo.com)
[**] *College University of Kragujevac, Faculty of Mechanical Engineering Kragujevac, Serbia*
[***] *College University of Kragujevac, Faculty of Mechanical Engineering Kraljevo, Serbia*

ABSTRACT

Modern design of the axial piston pump/motor, based on computer aided design, requires description of all processes and parameters in the pump/motor. The hydrodynamic and dynamic processes in the axial piston pump (cylinder, intake and discharge chambers, discharge valve, and high pressure pipeline) are very complex, so they demand a thorough physical and mathematical analysis. Compression losses, which are caused by sudden pressure changes in the cylinders of cylinder block, result in energy loss and increased noise. The compression losses can be decreased by identification of optimal dimensions and shapes of the port at the valve plate. The experimental research is based on the ultra speed measurement system, mathematical modeling of non-stationary high dynamic processes, and optimization method. The paper also includes the analysis of the influence of working and design parameters of the axial piston pump/motor on the position of intake and discharge ports of the valve plate. To solve the problem the special program (AKSIP) has been developed and presented in the paper.

KEY WORDS

Piston pump, dynamic processes, experiment

NOMENCLATURE

A_1 - geometrical flow section of the intake pipe
μ_1 - flow coefficient of the intake pipe
A_u- geometrical flow section of the intake split organ
μ_u - flow coefficient
E - modulus of elasticity
φ - the driving shaft angle
x_k - immediate displacement of the piston
z_c - the numbers of cylinders
A_2 - geometrical flow section of the discharge pipe line
D_c - diameter of cylinder
Δr - radial clearance between the piston and the

cylinder
η - dynamic viscosity
$x_k(\varphi)$ - immediate displacement of the piston
p_c - the pressure in the cylinder
p_s - the pressure in the intake space
ρ_c - the density of the fluid in the cylinder
ρ – density of fluid per cross section of the pipe
w – velocity of fluid per cross section of the pipe
f_r – friction force per mass unit

1. MATHEMATICAL MODEL OF A PUMP PROCESS

Mathematical model is given for each element, considering the complexly of some processes and their mutual dependence as well as the need for further mathematical modeling [1] to [2].
This makes programming module and their further improvement and monitoring much easier [1]. Piston axial pump are shown in Fig. 1.
Mass flow through the opening 1, on the entrance place into the intake space of the pump of fluid, Fig. 1:

$$\frac{dm_1}{dt} = \sigma_1 \mu_1 A_1 \sqrt{2\rho_s |p_u - p_s|} \tag{1}$$

where: $\sigma_1=1$ for $p_u \geq p_s$, $\sigma_1=-1$ for $p_u < p_s$
Mass flow of fluid through the split pump organ during filling one of the pump cylinders:

$$\frac{dm_u}{dt} = \sigma_u \mu_u A_u \sqrt{2\rho_s |p_s - p_c|} \tag{2}$$

where: $\sigma_u=1$ for $p_s \geq p_c$, $\sigma_u = -1$ for $p_s < p_c$

Mass balance of the intake space is:

$$\frac{dm_s}{dt} = \frac{dm_1}{dt} - \sum_{j=1}^{z_c} \frac{dm_{u,j}}{dt} \tag{3}$$

where: j=1,2,..., zc order number of cylinder, zc the numbers of cylinders.
Differential pressure equation in the intake pump space:

$$\frac{dp_s}{d\varphi} = \frac{E}{V_s \rho_s}\left(\frac{dm_1}{d\varphi} - \sum_{j=1}^{z_c} \frac{dm_{u,j}}{d\varphi}\right) \tag{4}$$

Technical data:
- Speed:1000 min-1
- Pressure: 210 bar
- Specific volume: 75cm3
- Number of pistons: 8

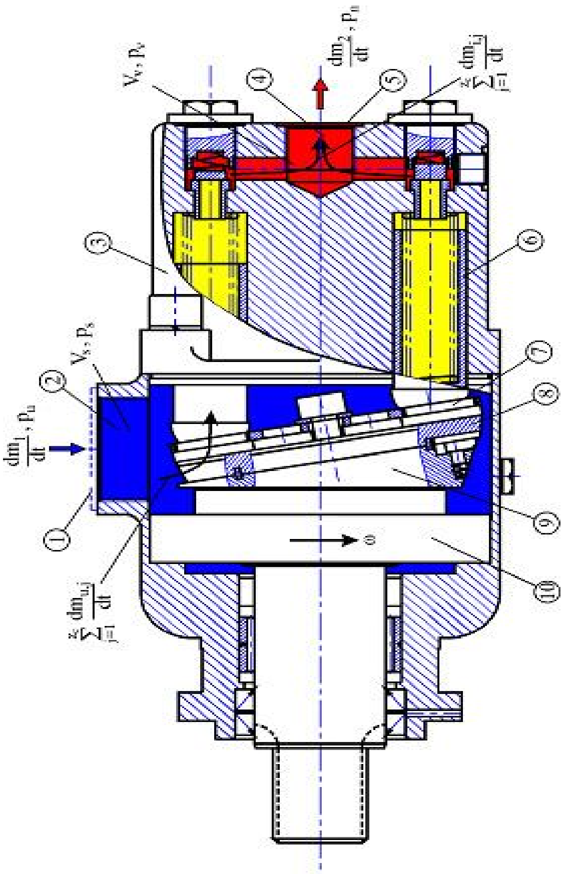

Fig. 1. Piston axial pump type PPT 3112. 750.02C/1DL, Firm PPT, Trstenik, Serbia

1. intake pipe line connection
2. intake space of the pump
3. cylinder block
4. discharge space of the pump
5. discharge pipeline connection
6. piston
7. split panel
8. acute panel
9. the pump shaft
10. in bearing the pump shaft

Differential pressure equation in the pump cylinder:

$$\frac{dp_c}{d\varphi} = \frac{E}{V_c}\left[\frac{A_c v_k}{\omega} + \frac{1}{\rho_c}\left(\frac{dm_u}{d\varphi} - \frac{dm_i}{d\varphi}\right)\right] \tag{5}$$

Where:

$V_c = V_{c\min} + V_{cx}; V_{cx} = A_c \cdot x_k$ - immediate volume of the cylinder;

the change of the volume of the pump cylinder caused by piston moving $\frac{dV_c}{dt} = -A_c v_k$, Mass balance of the discharge space is:

$$\frac{dm_v}{dt} = \sum_{j=1}^{z_c} \frac{dm_{i,j}}{dt} - \frac{dm_2}{dt} \qquad (6)$$

where: j=1,2,..., z_c order number of cylinder
Mass flow streaming out of the discharge space into the discharge pipe is:

$$\frac{dm_2}{dt} = \sigma_2 \mu_2 A_2 \sqrt{2\rho_t |p_v - p_n|} \qquad (7)$$

where:

$\sigma_2 = 1$ for $p_v \geq p_n$, $\sigma_2 = -1$ for $p_v < p_n$
Differential pressure equation in the discharge pump space:

$$\frac{dp_v}{d\varphi} = \frac{E}{V_v \rho_v} \left(\sum_{j=1}^{z_c} \frac{dm_{i,j}}{d\varphi} - \frac{dm_2}{d\varphi} \right) \qquad (8)$$

Mass flow through a concentric clearance between the cylinder and the piston:

$$\frac{dm_z}{dt} = \frac{\pi \cdot D_c \cdot \Delta r^3}{12 \cdot \eta \cdot x_k(\varphi)} \cdot (p_c - p_s) \cdot \rho_c \qquad (9)$$

1.1. Modeling the streaming in the intake and discharge pipe line of the pump

During mathematical modeling of a process in a pump, it is also necessary to include and consider a series of suppositions for a process modeling occurring in the intake and discharge pipe line of the pump.
For the most general model the following suppositions for streaming of the operational fluid in the intake and discharge pipe line are taken and considered:
The fluid streaming is one-dimensional. The pipes are of a constant cross section. Temperature and streaming fields per cross section of the pipe are homogeneous. Velocity vector laps the direction of the axis of the pipe at any moment and in any section.
Viscosity friction between some layers of the fluid inside the pipe is neglected. The friction forces appear on the inside walls of the pipe.
The processes in the pipes are isentropic. The change of entropy caused by friction, heat and mixing of fluid parts are neglected. Forces of the field (gravitational, magnetic, etc) are neglected.
In the scope of dynamic of one-dimensional streaming, such streaming is considered as “non stationary streaming in a streaming fiber”.

1.2. Continuity Equations

The equation of continuity of pressed fluid with functions p, w, ρ at the isentropic change of the state:

$$\frac{\partial p}{\partial t} + w\frac{\partial p}{\partial x} + a^2 \rho \frac{\partial w}{\partial x} = 0 \qquad (10)$$

- where:
- $a = \sqrt{\left(\frac{\partial p}{\partial \rho}\right)_s}$, the velocity of sound in the fluid, where:
- $p = p(t,x)$ and $\rho = \rho(t,x)$ are functions of time t and coordinate x.

1.3. Momentum Equations

- $$w\frac{\partial \rho}{\partial t} + \rho\frac{\partial w}{\partial t} + w\frac{\partial}{\partial x}(\rho w) + \rho w \frac{\partial w}{\partial x} + \frac{\partial p}{\partial x} = -f_r \rho \qquad (11)$$

2. EXPERIMENTAL TESTING THE PROCESS IN THE AXIAL PISTON PUMP

The pressure changes in the cylinder, discharge chamber and discharge pipeline were measured within the experimental research work. The vibrations of the pump housing were also analysed depending on the shaft angle. All pressures and vibrations were simultaneously measured at cca 0.09o of the pump shaft (exactly 4096 times per shaft rotation).
The incremental angle sensor is an optical sensor with 1024 pulses per rotation. The pulses of the angle sensor were quadrupled by the interface of the ADS 2000 system [5]. Thus, 4096 pulses per shaft rotation were achieved. Ten consecutive cycles were measured in order to repeat the consecutive cycles with the continuous performance. At the same time, the period from one angle to the next one was also measured in order to identify the uniformity of the shaft speed and to control the incremental angle sensor.
All analogous signals (pressures, vibrations) were simultaneously converted into cipher form by four ultraspeed convertors working simultaneously. The total number of measured data was (4+1) x 4096 = 20480 per rotation, i.e. 204800 for ten consecutive cycles. The number 4096 was not chosen by chance; it was chosen in order to apply Fast Fourier's Transformation (FFT) of measured signals.
The testing was done in the Laboratory for Development and Research in College of Applied Engineering - Center for Power Control Hydraulics (CPCH), which is situated in Trstenik, Serbia and in cooperation with the Institute for Motors in the Faculty of Mechanical Engineering in Belgrade University.
The pump was, for the purpose of this experiment processed, to ensure that the necessary measuring up

converter needed for measuring the characteristic parameters of the axial piston pumps with a combined distribution of working fluid.

2.1. Testing devices and system for data acquisition

The axial piston pump was tested by the devices which are made especially for this experiment done at the testboard in the Laboratory for Development and Research.Basic component of the testboard is driving electromotor whose power is 137 kW and whose number of revolutions and torque are controlled by electromotive drive. Figure 2 shows the testboard used for testing the characteristic parameters of the axial piston pump having the following components: electromotor whose power is 137kW, speed 1450min-1 ,with controlled number of revolutions(1); redactor(2); axial piston pump 3112 -750.020/02, (3); angle marker(4); measuring converter of vibrations(5); measuring converter of pressure in discharge chamber(6); measuring converter of pressure in cylinder(7); system for measuring and acquisition ADS 2000 – CADEX(8) [5].

used to measure pressure. These converters are based on measuring tapes and they are made by the company "Hottinger", Germany; their measuring range is 500bar, class of accuracy is 0.1 and transmission range is 100 kHz. Flow was measured by measuring turbine, type RE2 25/180 l/min. Its class of accuracy is 0.4 and it is made by the company "Hydrotechnik", Germany.
Incremental sensor, type ROD 426E, made by the company "Heidenhain", Germany, was used to measure the rotation angle of the pump shaft. It has 1024 optical markers and its maximum number of rotation is 12000 min-1. The accelerometer whose measuring range is up to 5 [m/s2] and is made by the company "Brüel&Kjaer", Denmark, was used to measure the vibrations of the pump housing.
Ultra speed measuring system ADS 2000-CADEX was used for acquisition. The system provides continual measurement and calculation of characteristic parameters of working cycle in real time.

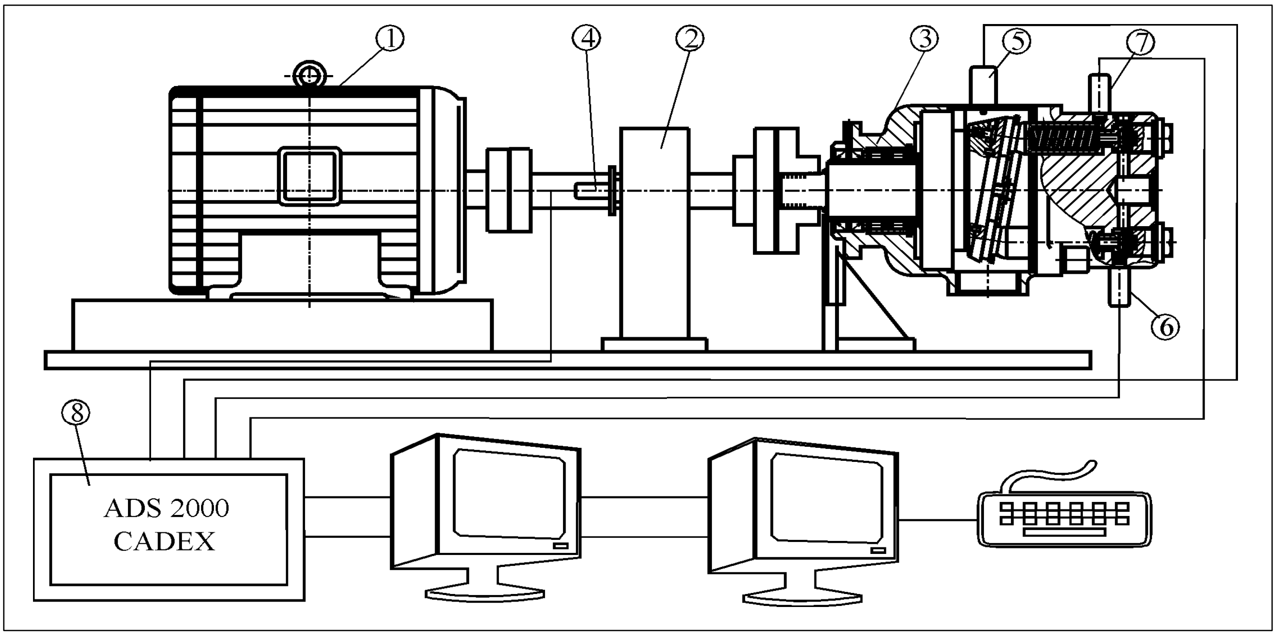

Fig. 2. *Testboard used for testing the the axial piston pump*

The following quantities were measured: pressure in the cylinder which depends on the angle of driving shaft; pressure in the vale chamber which depends on the angle of driving shaft; pressure in the discharge pipeline which depends on the angle of driving shaft; vibrations of the pupm housing which depends on the angle of driving shaft; angle of driving shaft; pump flow; temperature of working fluid; number of revolutions of driving shaft.
Measuring converters of pressure, type P3MA, were

The system ADS 2000-CADEX, which is used to develop highly dynamic mechanical objects by integrated measuring and calculating technique, is based on the following components: VME-bus CPU with graphics, VME-bus ADC, VME-bus PGA and CDM Interface.The processor receives data from A/D converter in real time directly in CPU-DRAM. The processor simultaneously controls the amplyfing and multiplexer cards in real time. The software was developed especially for this system in order to measure

cyclic and non-cyclic processes with graphical on-line display. Statistic processing of measured data is done with graphical display. 50.000.000 data were measured at maximum speed of 3MHz by 6...12 simultanous A/D converters. Up to 4 VME-CPU cards with processors Motorola 68020...68060, Intel Pentium, Digital Alpha or Motorola Power PC, can be integrated into the system. VME-bus ADC contains two A/D converters with simultaneous working speed of 2 · 350 kHz at 1bit and 1 timer. Start of each conversion is done by pulses of angle sensor or timers with hardware registration of referent mark of incremental angle sensor in order to 100% control the proper work of angle sensor in real time. It is possible to integrate up to six A/D cards into the system. i.e. 12 A/D converters. Two VME-bus ADC modules were installed into this system.
VME-bus PGA multiplexer and amplifier modul has six fast instrumental amplifiers used for direct connection between the sensor and measuring tapes tied in full bridge with DC supply of 5V (options 12 or 15). Maximum speed of conversion is 150 kHz. Four VME-bus PGA modules were integrated in this system.
The system has an interface for incremental angle sensors with DC supply and for multiplying the pulses of angle sensor. Up to four interfaces can be integrated into the system.
The applied measuring system enables simultaneous measuring at four fast analogous canals with parallel measuring of time periods from the angle mark to the mark of incremental angle sensor.

2.2. Results of measuring of parameters of working processes of the piston axial pump

In the scope of performed experimental testing was done a measuring of the pressure flow in the cylinder, discharge space and intake pipeline as well as vibration of the pump housing in dependence of the passed angle of the pump shaft.
All pressures and vibrations were measured completely parallel on each cca 0.09o of the pump shaft (exactly 4.096 times per shaft rotation).
As incremental giver of the angle an optical giver with 1024 pulses per rotation was used. Pulses of the giver of the angle were 4 times increased by the interface for the angle givers on the ADS 2000 system and so 4096 pulses per shaft rotation were obtained. In order we might see the repetitions of the consecutive cycles with the unchanged work regime 10 consecutive cycles were measured. At the same time, a time interval from angle to angle was measured as well in order to determine an even angle speed of the shaft and work control of the incremental giver of the angle.
All the analogue signals (pressure, vibrations) were converted into cipher form by means of four ultra speed converters working simultaneously (parallel). The total number of measured data was (4+1) x 4096 = 20480 per rotation (cycle), that is, 204800 for ten consecutive cycles. The number of samples of 4096 was not chosen by chance, but purposely with the aim of the application of the fast Furrier’s transformation (FFT) of measured signals. Measures were done for seven working regimes.
Fig. 3÷7, shows the measured pressure flow for individual, that is, ten consecutive cycles of the piston axial pump. Big similarity of measured pressures for the first of ten consecutive cycles (MERF) in relation to the middle of ten consecutive cycles (MERM).
Fig. 3 show the measured pressure flow in the cylinder (pc) for one, that is the middle of ten consecutive cycles in the function of the angle of the shaft. The diagram shows the visual pressure gradients at the pressure stage and expansion as well as the appearance of peaks during intake.
Fig. 3 also show the pressure flow in the discharge space (p_v) for one, that is middle of the ten consecutive cycles in the function of the angle of the shaft.
The pressure pulses in the discharge space depend on the number of the cylinders what is obvious in this case, because it deals with the pump with 8 cylinders. The appearance of peaks at the intake stage for one, that is, middle of ten consecutive cycles, is shown in Figures 4. and 5.
Figures 6. and 7. present the measured pressure flow in the cylinder (p_c) for one, that is middle for ten consecutive cycles with the aim to analyze in detail the gradient growth of pressure at the stage of pressing. The same diagram, at the same interval, shows the pressure pulses in the discharge space. The Figures 3÷7, stand for diagrams of measured pressure at the work regime n=875.6 min-1 and p_c=210 bar.

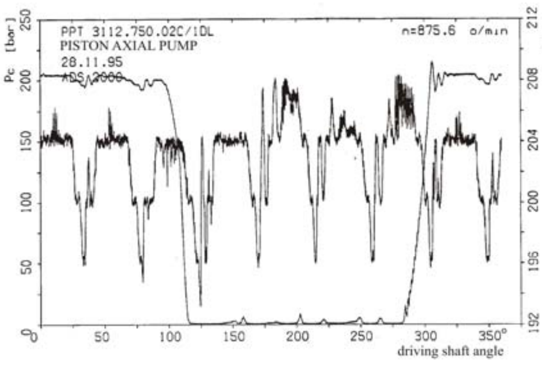

Fig. 3. The pressure history in the cylinder (p_c) and delivery chamber (p_v) for the average cycle

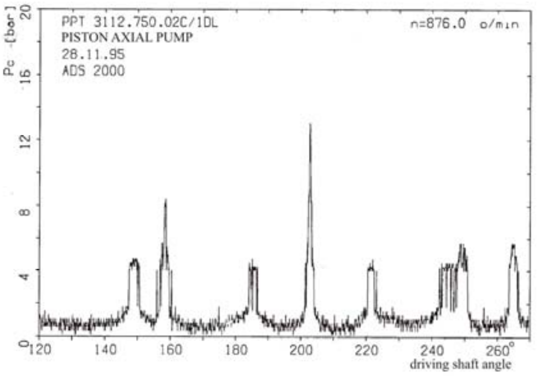

Fig. 4. The pressure history in the cylinder (p_c) in the $120^o \div 270^o$ interval for one cycle

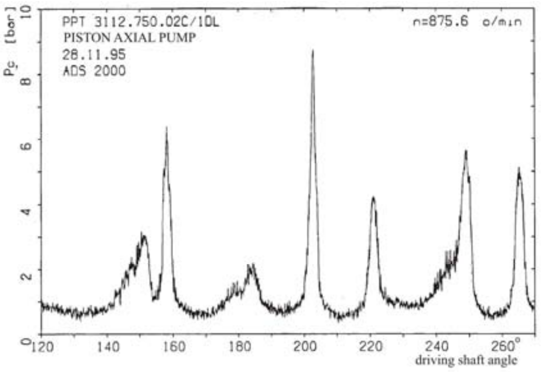

Fig. 5. The pressure history in the cylinder (p_c) in the $120^o \div 270^o$ interval for the average cycle

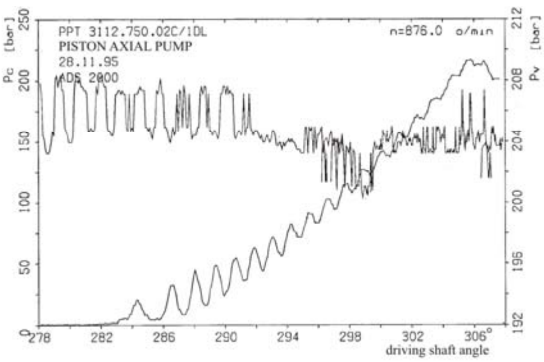

Fig. 6. The pressure history in the cylinder (p_c) and delivery chamber (p_v) in $278^o \div 307^o$ interval for one cycle

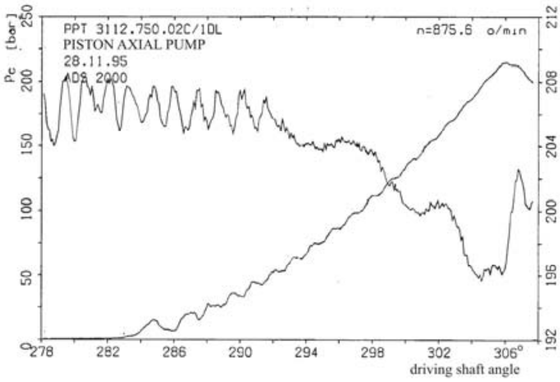

Fig. 7. The pressure history in the cylinder (p_c) and delivery chamber (p_v) in $278^o \div 307^o$ interval for the average cycle

3. CONCLUSION

It is not possible to give a precise determination of parameters of hydrodynamic processes of a piston axial pump neither experimentally nor by a mere mathematical modeling only. Sufficiently exact parameters can be obtained by combining the application of measuring the pressure flow in the cylinder, mathematical modeling of a real hydrodynamic process and the method of nonlinear optimization which enables, at the same time, the determination of systemic measuring errors and unknown parameters. The computer AKSIP program gives possibilities to combine 56 influential pump parameters in order to achieve optimal solution, in regard to flow losses, flow inlet etc. Further research is possible in the construction of the piston-axial pumps with a bent cylinder block and splitting of working fluid by means of a split panel. Mathematical model would be, in that case, expanded by a dynamic cylinder block and hydrodynamic processes in clearances between the cylinder block and the split panel. General conclusions of the presented results relate to all tested working regimes of the axial piston pump. It is not possible to define precisely the parameters of hydrodynamic processes in the axial piston pump by experiments only, or by mathematical modeling only. Precise parameters can be obtained if the following methods are combined: measurement of pressure changes in the cylinder, mathematical modeling of real hydrodynamic process and nonlinear optimization. At the same time, systematic errors of measuring and unknown parameters can be defined this way.

4. ACKNOWLEDGEMENT

The part of this research is supported by Ministry of Education and Science, Republic of Serbia, Grant TR 32036 and Grant TR 35038.

REFERENCES

[1] Petrovic,R. Mathematical modeling and identification of multi cylindrical axial piston pump parameters. PhD Thesis, Faculty of Mechanical Engineering, Belgrade, 1999.

[2] Bergemann,M. Systematic research of noise of piston pumps with odd number of cylinders. Edition Mainz, Wissenschaftsverlag, Aachen, 1994.

[3] Darling J. Piston-Cylinder Dynamics in Oil Hydraulic Piston Pumps. Dissertation Universität Bath, 1985.

[4] Petrović R., Jankov R., Lazović M.: " Experimental study of hydraulic and vibration axial piston pumps " - Scientific Conference "Heavy Machinery", 1996.

[5] Jankov R.: ADS 2000-CADEX, system for the development of facilities mechanical application of integrated measurement and calculation techniques, Faculty of Mechanical Engineering Belgrade.

[6] Petrović,R. Mathematical Modeling and Experimental Research of Characteristic Parameters of Hydrodynamic Processes of an Axial Piston Pump, Strojniški vestnik - Journal of Mechanical Engineering 55(2009)4, UDK 621.785.4.

[7] Petrović,R. Mathematical Modeling and Experimental Verification of Operating Parameters of Vane Pump With Double Effect, Strojniški vestnik - Journal of Mechanical Engineering 55(2009)1 UDC 621.9.04

[8] Petrovic,R.,Glavcic,Z. Systematic research of characteristic parameters of the piston axial pump . III International Workshop on Computer Software for Design, Analysis and Control of Fluid Power Systems, September 2003. Ostrava-Malenovice, Czech-Republic.

Proceedings of the 8th JFPS International
Symposium on Fluid Power, OKINAWA 2011
Oct. 25-28, 2011

1C1-2

OPTIMAL DESIGN OF BUBBLE ELIMINATOR BY NUMERICAL AND EXPERIMENTAL INVESTIGATION

Sayako SAKAMA*, Ryushi SUZUKI**, Yutaka TANAKA* and Nobuyuki TANAKA***

*Graduate School of Engineering and Design
Hosei University
2-17-1 Fujimi, Chiyodaku, Tokyo, 102-8160, Japan
(E-mail: y_tanaka@hosei.ac.jp)
** Opus System Inc.
3-18-7 Asagayaminami, Suginamiku, Tokyo, 166-0004, Japan
***TNK CORPORATION'LTD
1-18 Hirai, Hinodecho, Nishitama, Tokyo, 190-0182, Japan

ABSTRACT

Air bubbles in working oil influence stiffness and efficiency of hydraulic systems, thus it is important for technical issues to eliminate the air bubbles actively from the hydraulic oil. Bubble eliminator is a device that removes air bubbles by using a swirling flow. In this paper, we investigate flow behavior in the bubble eliminator by means of laboratory experiments with a transparent bubble eliminator and numerical analysis. We especially focus on the diameter of vent port and analyze the relation between the parameter and removal performance of bubbles. The validity of numerical simulation is verified by comparing the results of the numerical simulation with flow patterns obtained from image photos of the experimental flow visualization. Moreover, we evaluate the optimal dimension of the diameter of the vent port from numerical analysis.

KEY WORDS

Bubble, Bubble eliminator, CFD, Flow visualization, Hydraulic system

NOMENCLATURE

D_3	:	diameter of vent port
E_b	:	rate of bubble removal
E_o	:	rate of oil flow
Q	:	flow rate
$_{A}$, $_{O}$	:	air, oil
$_{i}$, $_{o}$, $_{v}$	:	inlet, outlet, vent

INTRODUCTION

In recent year, hydraulic systems have advanced high pressure and high output power [1]. However, thermal load and cavitation occurrence increase with increasing pressure. Bubbles which are generated by cavitation remain submerged in the hydraulic oil [2] and deteriorate the stiffness of the hydraulic oil. Moreover, bubbles drive deterioration of oil by causing oil temperature rise by adiabatic compression [3], and cause failure by reduction of lubricating film.

To solve these problems, our project team has been developed an active bubble eliminating device called a bubble eliminator [4] and applied to construction machinery to get high efficiency of the systems and long life time of oils [5]. It has been verified that this device efficiently removes the bubbles from the working oil by experimental and numerical analysis, and that temperature rise of fluids can effectively reduce and oxidation of oil can be prevented [6] [7] [8]. Moreover, it has been clarified that the shape of the device influences the removal performance of bubbles [9]. So the selection of shape parameters is the most important for optimal design of the device. In this paper we focus on evaluating diameter of the vent port of the bubble eliminator by comparing between experimental result and simulation result.

DESIGN AND PRINCIPLE OF BUBBLE ELIMINATOR

Figure 1 illustrates a design and principle of the bubble eliminator. The tapered-tube type device is designed such that a chamber of cross-sectional round shape becomes gradually smaller and connected to a cylindrical chamber [4]. Working oils with bubbles flow tangentially into the tapered-tube from inlet ports and form a swirl flow that circulates fluid through the flow passage. The swirl flow accelerates towards the downstream. Bubbles are trapped in the vicinity of the central axis because of a difference in the specific gravity of the oil and the bubble, and collected near the range of a vent port where the pressure is lowest. When some back pressure is applied by a check valve or an orifice located at the downstream side of the bubble eliminator, the bubbles are ejected oneself through the vent port. The dissolved gas in the fluid is also eliminated through the bubbles extracted at the pump suction side under the negative pressure. In the previous study [8], it is experimentally confirmed that the bubble eliminator has been able to eliminate efficiently the entrained bubbles and dissolved gases from the working fluid. Geometric parameters of a standard device used for experimental and numerical investigations are illustrated in Figure 2 and dimensions are tabulated in Table 1. In this paper we analyze effects that difference of diameter of the vent port D_3 makes on performance of the bubble elimination.

EXPERIMENTAL FLOW VISUALIZATION

A full scale transparent model of the bubble eliminator is fabricated for flow visualization in order to understand the situation of the collected and eliminated bubbles. Figure 3 illustrates the transparent bubble eliminator for experimental flow visualization. The transparent bubble eliminator consists of nine blocks made from acrylic resin. The blocks are stacked and placed with its four corners accurately fitted by screw rods and nuts. The blocks are convertible to change the shape parameters of the inlet port, the tapered tube and the vent port.

Figure 4 illustrates an experimental fluid circuit for the flow visualization. Working oil in a 30L reservoir fed by a piston pump driving by a variable speed motor flows to the transparent bubble eliminator. A needle valve and a restrictor at the pump suction side are used experimentally to bleed air intentionally from a

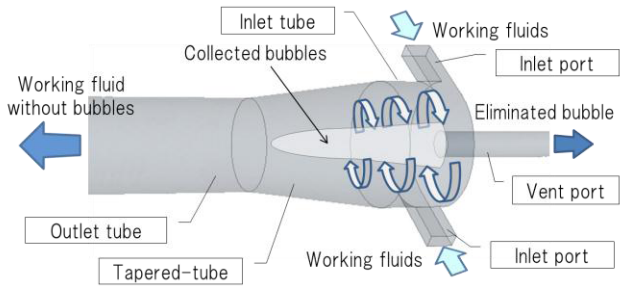

Figure 1 Design and principle of bubble eliminator

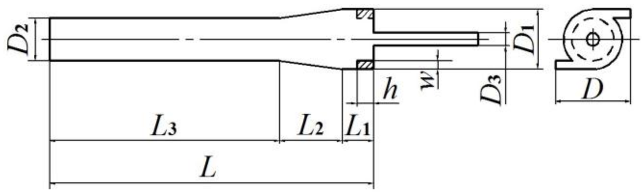

Figure 2 Geometry of bubble eliminator

Table 1 Dimensions of standard model

D	D_1	D_2	D_3	w	h	L	L_1	L_2	L_3	[mm]
36	28	20	6	3	6	265	15	30	220	

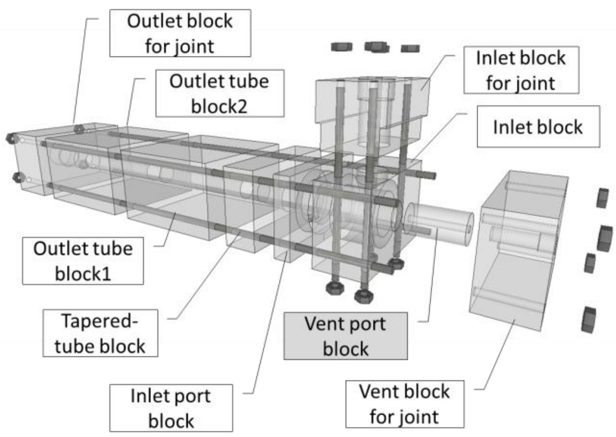

Figure 3 Transparent bubble eliminator for experimental flow visualization

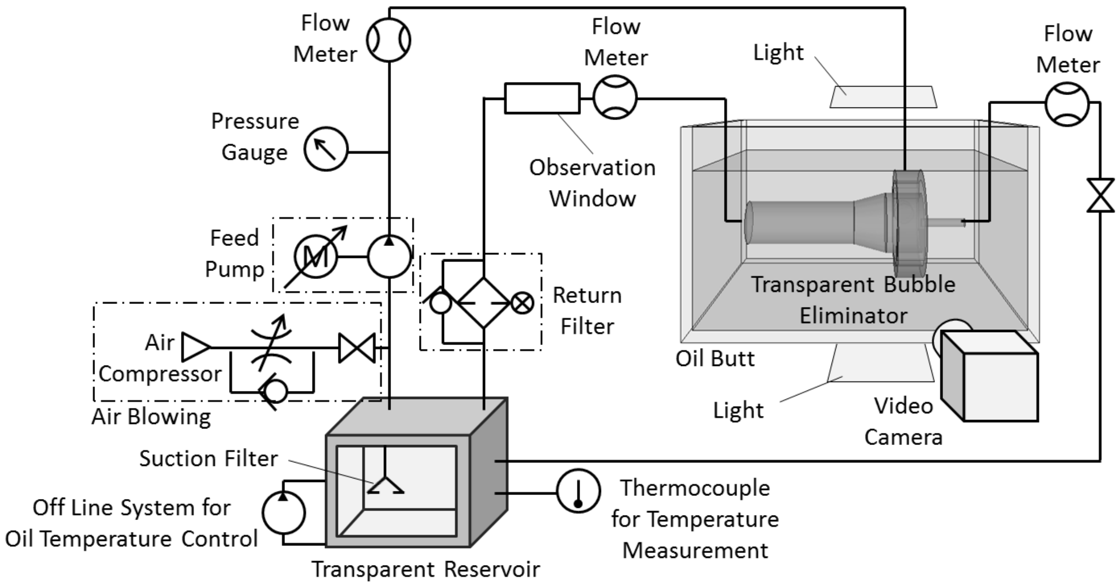

Figure 4 Experimental fluid circuit for flow visualization

compressor into the working oil. The restrictor is slightly opened and compressed air is admitted in the oil for bubbling. The flow rate is measured by a flow meter in the upstream and downstream side of the bubble eliminator. A needle valve is installed on the vent port side of the bubble eliminator. In the usual case, the needle valve is opened, and the trapped and collected bubbles are ejected through the vent line. When the needle valve is closed, the trapped bubbles merge and make a large air column in a flash time. The whole transparent bubble eliminator is submerged in an oil butt removed a cause of refractor effects by the acrylic pipe wall for the flow visualization. A digital video camera is set at a flank of the transparent bubble eliminator. A growth pattern of the trapped bubbles by the swirling flow in the tapered tube of the bubble eliminator can be observed. The working oil for hydraulic systems is used in the experiments of the flow visualization. The working fluid has a kinetic viscosity of 31.3 mm^2/s at the oil temperature of 40°C. The fluid flow rate is set at 20 L/min. For the flow rate of 20 L/min, the outlet side of the downstream tube has a fluid average velocity of 1.06 m/s and a Reynolds number of 707.

The bubbles are collected along the central axis in the transparent bubble eliminator. A snapshot of the digital video camera which shows a close-up photograph of the transparent bubble eliminator is shown in Figure 5. When the needle valve at the vent line is closed, the trapped bubbles started to be collected and to form a large air column which extends along the central axis of the tube toward downstream. The photograph shows that

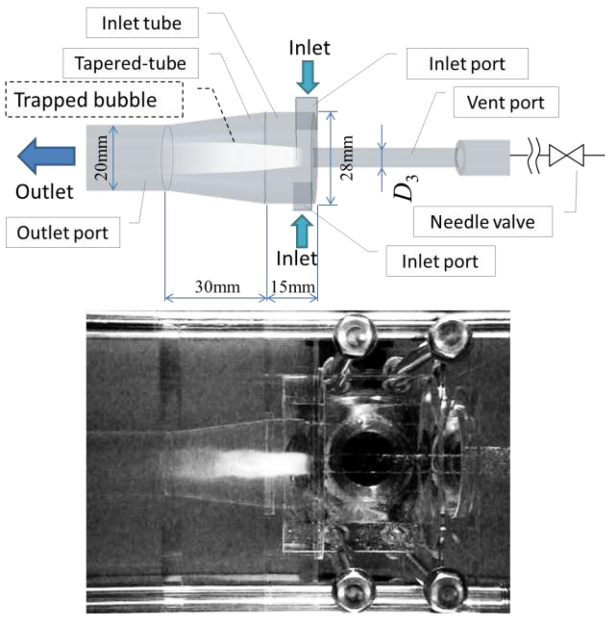

Figure 5 Photograph of transparent bubble eliminator

the air column grows into its maximum length within the first 500 ms. The length of the air column increases to 45 mm through the series of frame digital images in accordance with the elapsed time. The growth process of the trapped bubbles with the elapsed time can be experimentally clarified through the flow visualization.

When the needle valve at the vent line is opened, the trapped bubbles are instantaneously pushed out from the vent port. The elimination of the trapped bubbles depends on the diameter of the vent port. A series of monochrome photograph frames obtained with the change of the diameter of the vent port D_3 is shown in Figure 6. The inlet flow rate Q_i and outlet flow rate Q_o are monitored with the flow meter installed at the side of the inlet port and outlet port, respectively. In case of small diameter of the vent port, the trapped bubbles remain in the inlet port and the tapered tube block. The diameter of the vent port is larger, performance of the bubble elimination pushed out from the vent port is higher. A comparison between the experiments and the numerical results will be discussed in the next section.

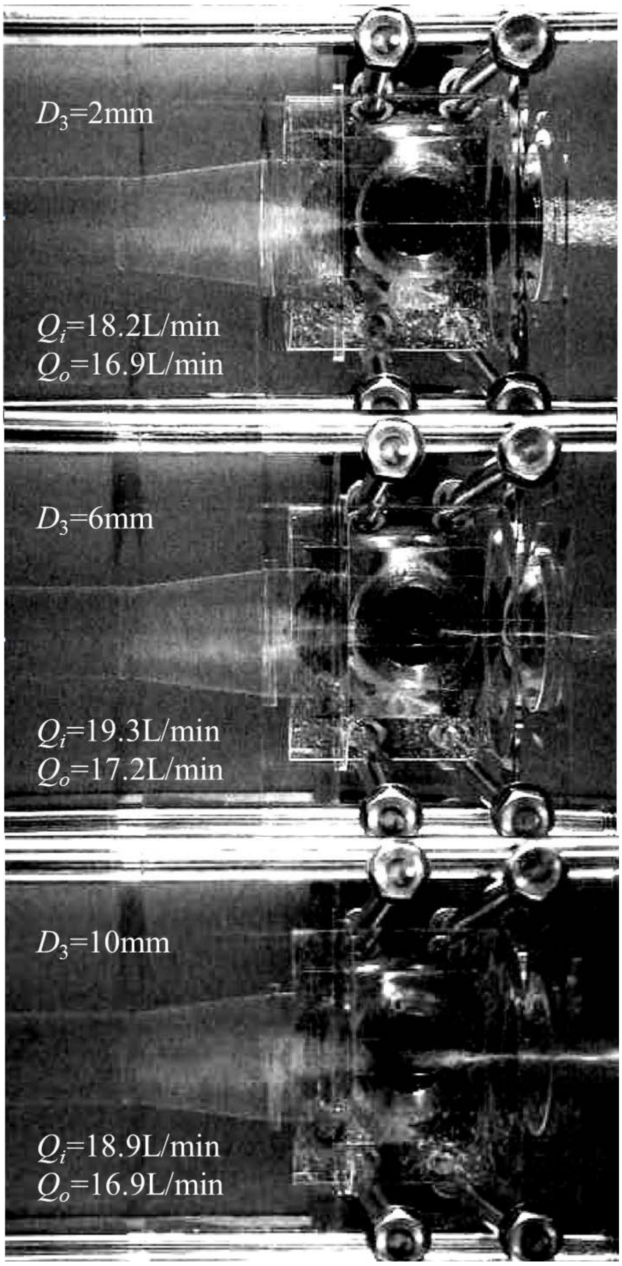

Figure 6 Photograph frames with change of vent port diameter

NUMERICAL ANALYSIS

In this paper, we perform flow analysis of air-liquid two-phase flow using the commercially numerical calculation software; STAR-CD. The established meshes and definition of the coordinate are shown in Figure 7. A utilized mesh is the polyhedral which typically has an average of 14 cell faces and is characterized by good convergence. The central axis of the device is coincident with z-axis, making the positive direction of the z-axis downward and the origin of coordinates is located at the entrance of the vent port. We assume that conditions of bubbles have the diameter of mixed air particles of 0.3 mm and the volume ratio of the air contained in the oil of 5 %. In addition, it is assumed that bubbles are particle, and deformation and merge of bubbles are neglected.

Firstly, we compare between the experiments and the numerical results in various diameters of the vent port. Condition of working oils for numerical analysis has the same that experimental value: the kinetic viscosity of 31.3 mm^2/s at the oil temperature of 40°C and inlet and outlet flow rates of that is monitored with the flow meter. Volume fraction of bubbles in the cross section of the device is shown in Figure 8. It is confirmed that the deepest area of the gray scale image moves from the inlet tube to the vent port as diameter of the vent port becomes larger. The numerical simulation has qualitatively good agreement with the experimental flow visualization. The simulation results describe the flow pattern in the bubble eliminator well.

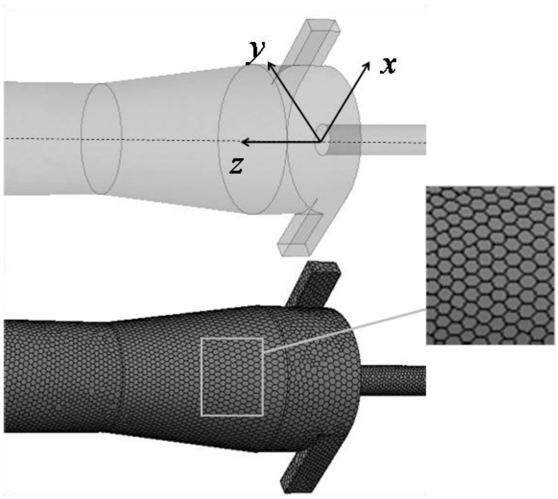

Figure 7 Mesh and coordinate definition for CFD

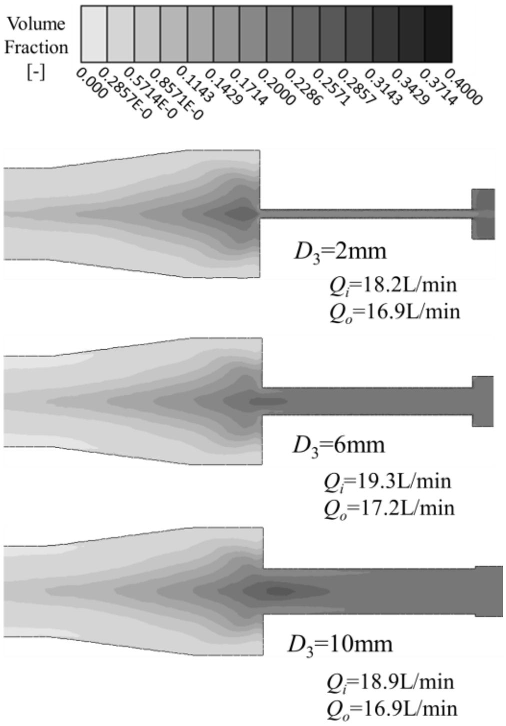

Figure 8 Volume fraction of bubbles for comparison with experiments

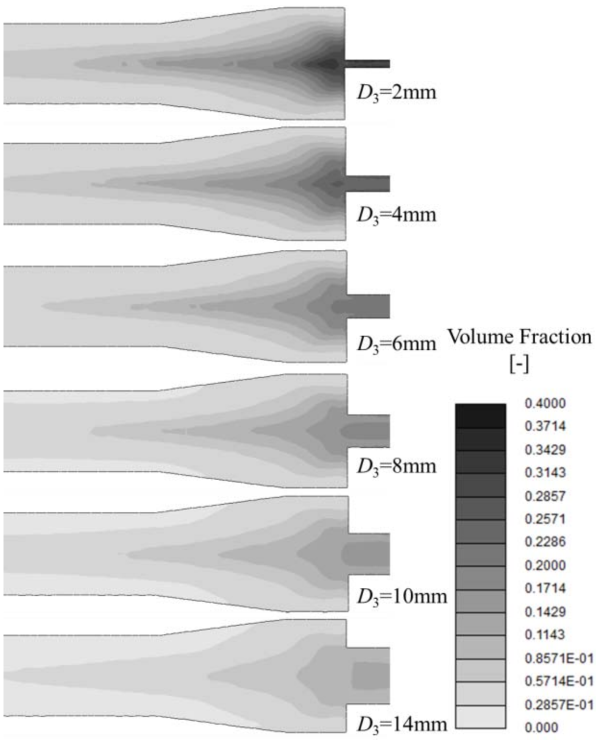

Figure 9 Volume fraction of bubbles in various diameter of vent tube

Next, based on the above results, we perform the numerical analysis in various diameters of the vent port on the same condition of working fluid. The working fluid has the inlet flow rate of 20 L/min and the kinetic viscosity of 31.3 mm^2/s. Outlet flows from the outlet port and the vent port are set by the area ratio between the outlet port and the vent port. Volume fraction of bubbles is shown in Figure 9. It is confirmed that the gray scale image becomes deeper around the close inlet of the vent port as diameter of the vent port becomes smaller. Figure 10 shows flow velocity of bubbles seen in the cross section of the device. It is also confirmed that the flow velocity to the vent port becomes larger and the bubbles easily flow out from the vent port as diameter of the vent port becomes larger.

We quantitatively evaluate performance of the bubble elimination through an index of bubble removal. In order to evaluate it, the rate of bubble removal E_b and the rate of oil flow E_o are defined as follows:

$$E_b = \frac{Q_{Av}}{Q_{Ai}} \times 100 \tag{1}$$

$$E_o = \frac{Q_{Oo}}{Q_{Oi}} \times 100 \tag{2}$$

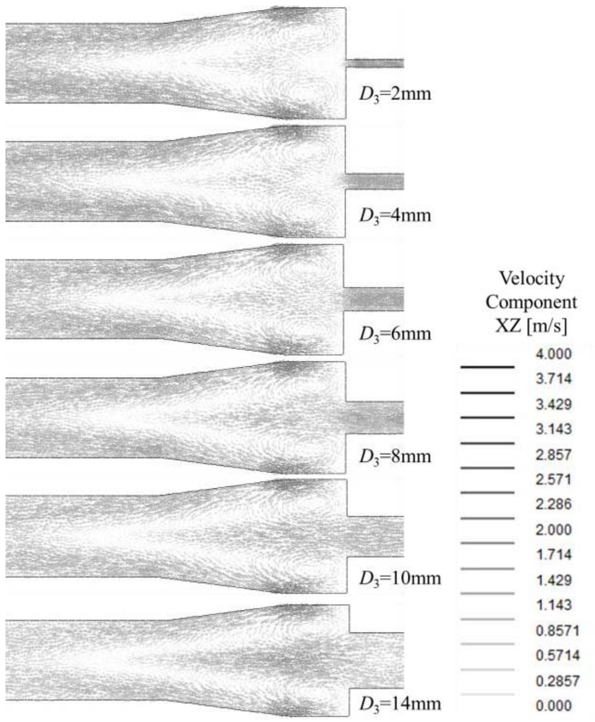

Figure 10 Velocity of bubbles in various diameter of vent tube

where Q_{Ai} is volumetric flow rate of bubbles from the inlet port to the inlet tube, Q_{Av} is one of bubbles flowing from the vent port, Q_{Oi} is one of oil from the inlet port to the inlet tube and Q_{Oo} is one of oil flowing from the outlet port, respectively. Thus if both index of E_b and E_o becomes larger, it can be evaluated that performance of the bubble elimination becomes higher. The comparison with performance of the bubble elimination in various diameters of the vent port is shown in Figure 11. As diameter of the vent port becomes larger, the rate of bubble removal increases but the rate of oil flow decreases. It is confirmed that there is the trade-off problem between E_b and E_o and that the position of an intersection point of the two lines which show the rate of bubble removal and outlet flow of oil is around 70% at the diameter of the vent port between 13mm and 14mm. It is needed that diameter of the vent port is set smaller to aggregate bubbles, but that should be set larger to push out the bubbles from vent port. This means there is an optimal diameter of the vent port to remove the bubbles efficiently, and this point can be obtained by considering the relationship between the rate of bubble removal and oil flow.

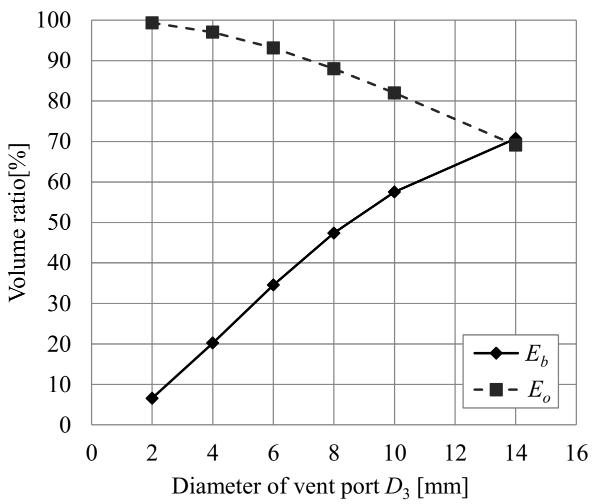

Figure 11 Volume ratio in various diameters of vent port

CONCLUSIONS

In this paper, the experimental flow visualization using the full scale model of the transparent bubble eliminator and the numerical simulation have been carried out to evaluate the performance of bubble elimination. The results of numerical simulation have qualitatively good agreement with the results of experimental flow visualization. It has been verified that the bubble eliminator efficiently removes the bubble from the working oil through the experimental flow visualization and the numerical simulation. The performance evaluation of the bubble eliminator has been studied through the numerical simulation by modifying diameter of the vent port. It is clarified that the selection of the diameter of the vent port influences the performance of the bubble elimination.

ACKNOWLEDGMENT

The numerical calculations were performed at the Research Center for Computing and Multimedia Studies of Hosei University. Our research project has been supported by the grant in aid by the Small and Medium Enterprise Agency, Japan.

REFERENCES

1. Brendan Casey, Mobile Hydraulic Equipment: Increasing the Pressure, Machinery Lubrication Magazine. January 2008.
2. Totten, G.E., Sun, Bishop, Hydraulic Fluids: Foaming, Air Entrainment, and Air Release –A Review, SAE Technical Paper No.972789, 1997.
3. Backe and Lipphardt, Influence of the Dispersed Air on the Pressure, CI Mech. Eng., C97/76, pp.77-84, 1976.
4. K. Nagaishi, Y. Tanaka and R. Suzuki, Bubble Elimination for Hydraulic Systems –New Design of Hydraulic System for Environmental Compatibility-, Proceedings of 5th FPNI PhD Symposium Krakow, pp.254-262, 2008.
5. R. Suzuki and S. Yokota, Bubble Elimination by Use of Swirl Flow, IFAC Int. Workshop on Trends in Hydraulic and Pneumatic Components and Systems, Poster Paper 2, 1994.
6. R. Suzuki and Y. Tanaka, Downsizing of Oil Reservoir by Bubble Eliminator, Proceedings of the 6th JFPS International Symposium on Fluid Power, Tsukuba, pp.7-10, November 2005.
7. R. Suzuki, Y. Tanaka and S.Yokota, Reduction of Oil Temperature Rise by Use of a Bubble Elimination Device in Hydraulic Systems, Journal of the Society of Tribologists and Lubrication Engineers, Vol. 54, No. 3, pp.23-27, March 1998.
8. Y. Tanaka and R. Suzuki, Solution of Air Entrainment for Fluid Power Systems, Proceedings of the 49th National Conference on Fluid Power, IFPE2002, pp.57-62, March 2002.
9. R. Suzuki, Y. Tanaka and H. Goto, Bubble Elimination from Hydraulic Fluids for Reduction of Environmental Burdens, Proceedings the twelfth Scandinavian International Conference on Fluid Power, SICFP'11, Vol.2, pp341-353, 2011.

Proceedings of the 8th JFPS International
Symposium on Fluid Power, OKINAWA 2011
Oct. 25-28, 2011

1C1-3

CFD ANALYSIS OF INLET FLOW AROUND AN IMPELLER OF AN OIL-HYDRAULIC PUMP

Kazushi SANADA* and Naohiro YAMAGUCHI**

* Professor, Department of Mechanical Engineering, Graduate School of Engineering,
Yokohama National University
79-5, Tokiwadai, Hodogaya, Yokohama, Kanagawa, 240-8501 Japan
(E-mail: ksanada@ynu.ac.jp)
** Master Student, Department of Mechanical Engineering, Graduate School of Engineering
Yokohama National University
79-5, Tokiwadai, Hodogaya, Yokohama, Kanagawa, 240-8501, Japan

ABSTRACT

An impeller is used to prevent cavitation by increasing pressure in a suction port of an axial piston pump. Oil flow around the impeller is analyzed using CFD. A 3D model of an inlet chamber, an impeller disk and the outlet port of the impeller is build. Pressure/velocity distributions and pressure increase across the impeller are calculated. The pressure increase well agrees with experimental results. Visualization of stream lines around the impeller gives important information on the impeller characteristics, such as reverse flow which occurs both at the inlet chamber and at the downstream of the impeller. Modification of the flow path is proposed to prevent the reverse flow.

KEY WORDS

Oil hydraulics, CFD, Axial piston pump, Impeller, Visualization

NOMENCLATURE

p : pressure (Pa)
t : time (s)

INTRODUCTION

Construction machineries are used at severe locations, such as open-air mining of highlands. Pumps and motors are required to be reliable when used at difficult conditions. Cavitation is one of important technical subjects to be solved. Low suction pressure may cause cavitation in the pump and may damage some parts of the pump, for an example a valve plate of an axial piston pump. Tsukiji et. al. studied about jet flow from an orifice of a valve plate with a groove in an axial piston pump [1]. For estimation of flow characteristics of a notch of a valve plate, visualization of flow have been investigated by Oyama and Tanaka [2]. Computational fluid dynamics (CFD) is a powerful tool in order to investigate flow inside oil-hydraulic components. Park and Hwang applied CFD to study effects of groove shape on lubrication characteristics of a spool valve [3]. Tsukiji et. al. proposed a useful method to improve an oil-hydraulic ball valve using visualization techniques including CFD [4]. J. Watton wrote a paper summarizing progress of servo vales using CFD [5]. Cavitation in a plunger pump was studied using CFD by K. Edge et. al. [6]. In addition, a trial to predict the characteristics of the pump was performed by CFD [7].
One method to prevent cavitation at the inlet port of the pump is to increase the inlet pressure by use of an impeller disk. Inlet pressure may be increased by installing an impeller disk at the inlet port just before the valve plate. In

this paper, an impeller disk installed in the inlet port of an axial piston pump is studied by CFD analysis. At first, a 3D CFD model is build focusing on the impeller disk. Through CFD analysis, flow pattern around the impeller disk is visualized and pressure/flow rate distributions are obtained. Pressure increase due to the impeller disk is discussed comparing CFD analysis and experimental results. In order to improve pressure increase, flow path around the impeller disk is modified. Finally, results of this paper are summarized.

AXIAL PISTON PUMP

An axial piston pump is treated in this paper. The pump has a rated displacement of 180cc. The maximum pressure is 30MPa. An impeller disk is installed in the inlet port (suction port) of the pump just before a valve plate. It has 13 impellers located in radial direction. The impeller disk diameter is 150mm. The impeller disk is directly connected with a drive shaft of the pump and it rotates at the same speed as the pump.

CFD ANALYSIS

A 3D CFD model of the impeller disk is shown in Fig. 1. An inlet port (suction port), a top cover (an inlet chamber), an impeller disk, and a flow path to a valve plate are modeled. An inlet port is the left side section of the model. A valve plate is located at the bottom of the model. Therefore hydraulic oil comes into the pump from the left-side inlet port. It is twisted in a right angle and goes downward to the valve plate. A top view of the 3D model is shown in Fig. 2. A transparent model is shown in Fig. 3. These figures are provided for better understanding of the 3D model.

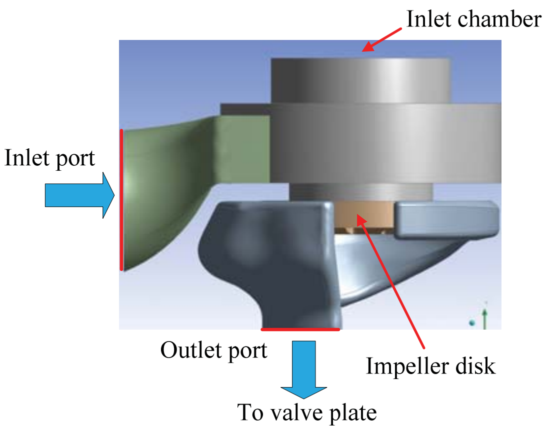

Fig. 1 3D CFD model of an impeller disk

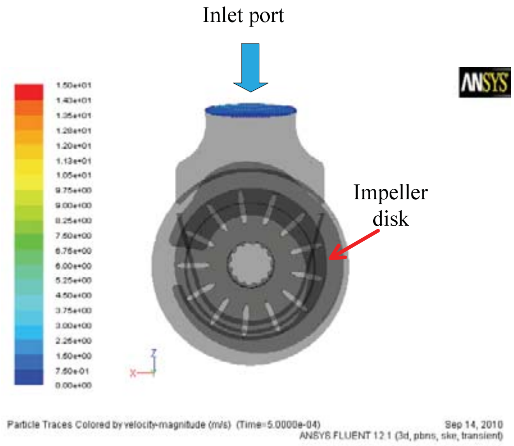

Fig. 2 Top view of the 3D model

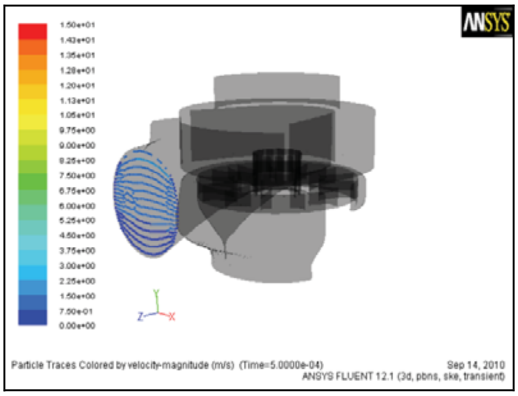

Fig. 3 Transparent model

CFD software

Commercial software was used for CFD analysis. As a flow model, mixed-phase flow was assumed, that is, liquid flow including air bubbles including a small amount of oil vapor. When pressure is decreased, the gas bubble is expanded according to circumferential pressure. It may suggest outbreak of cavitation. However in this study, pressure stays over the certain level and cavitation is not important for the CFD analysis. As a friction model, $k-\varepsilon$ turbulent model was used.

Computational grids

For CFD analysis, an ideal computational grid is sphere shape. However it is impossible to make grid pattern using the sphere grid. Instead of the sphere, cubic grid and tetrahedron grid are used in practice. The tetrahedron grid is useful to model complicated shape. However the tetrahedron grid may result in increase of the number of meshes. On the other hand, cubic grid is suitable for simple shape. Usage of grid type is important in terms of accuracy of CFD analysis. In this model, flow around the impeller disk was modeled by the tetrahedron grid system and other parts were modeled by cubic grid system as shown in Fig. 4.

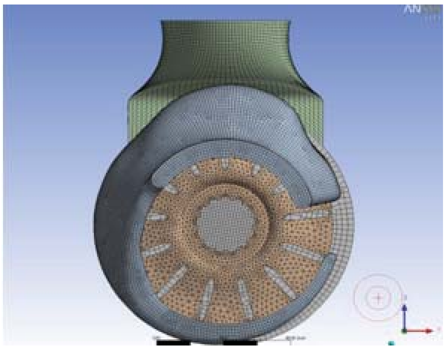

Fig. 4 Tetrahedron grid system for the impeller disk

Boundary conditions

Pressure increase across the impeller disk is one of the targets of the CFD analysis. In order to calculate the pressure increase, it is necessary to set boundary conditions at the inlet and at the outlet port of the model. A boundary condition of "pressure inlet" was applied to the inlet port. This means that pressure in the cross sectional area of the inlet port is uniform and that it is specified as a condition of calculation. Another boundary condition of "velocity inlet" was applied to the outlet port. This condition corresponds to determination of uniform velocity distribution at the cross sectional area of the outlet port. When pump speed is specified, flow rate of the pump is known and flow rate at the outlet of the impeller model is the same as that of the pump. Therefore velocity at the outlet port is calculated by dividing the flow rate by the cross sectional area of the outlet port.

RESULTS OF CFD ANALYSIS

A number of computations by the CFD analysis were carried out for various conditions using a desktop personal computer. One case of computation took eight hours to get animation for flow visualization. In the following analysis, pump speed was set as 1800rpm. Rotation of the impeller disk was considered in the CFD analysis. The CFD software provided animation video files for visual understanding of flow pattern.

Velocity distribution

An example of stream lines calculated by the CFD analysis is shown in Fig. 5. Velocity distributions are shown in Fig. 6. Velocity of the flow is classified by colors. Red color is 15m/s and dark blue is 0m/s as indicated in the left color bar. The oil flow has the highest velocity of about 14m/s at the outer edge of impeller dsik.

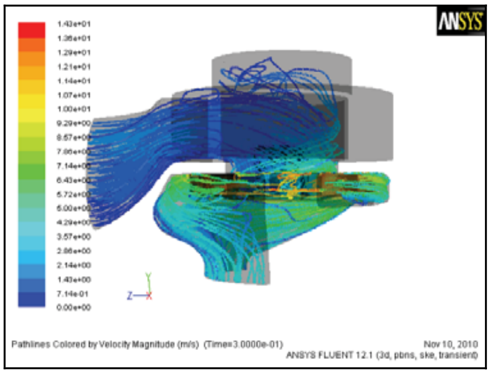

Fig. 5 An example of stream lines

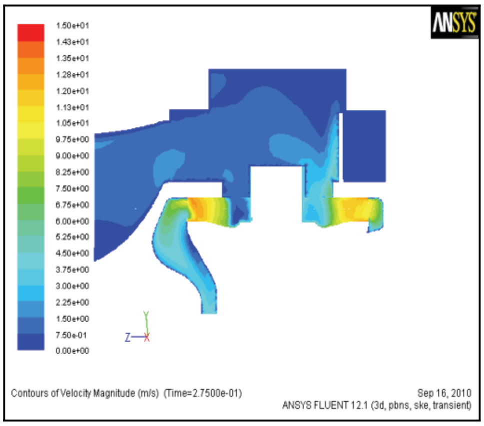

(a) Side view

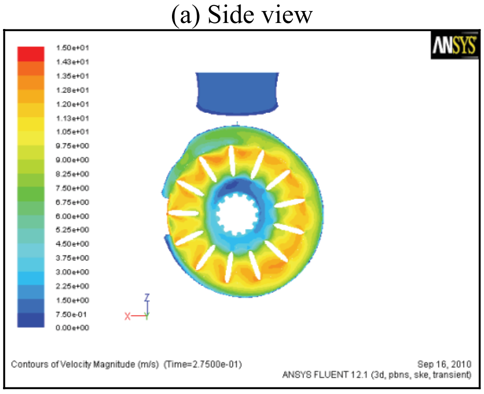

(b) Top view

Fig. 6 An example of velocity distribution

Pressure distribution

Pressure distribution calculated by the CFD is shown in Fig. 7. Red color indicates pressure level of 0.1MPa and dark blue is 0MPa. In the figure, the impeller rotates in a counterclockwise direction. Pressure is increased according to the rotation of the impeller disk. At the outlet of the impeller indicated by a red arrow in the figure (b), pressure reaches the highest value. In the downstream path in the figure (a), the highest pressure was observed in the middle of the flow path between the impeller disk and the outlet port (valve plate). As an ideal design, pressure may reach the highest value at the valve plate.

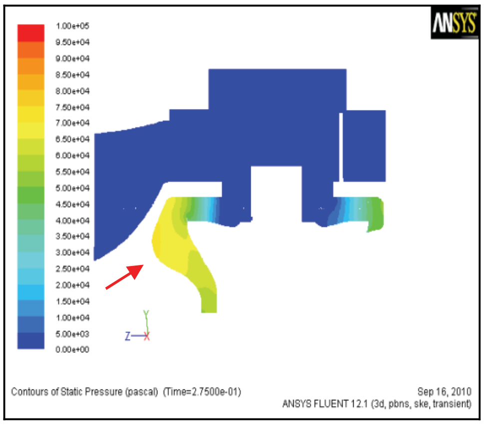

(a) Side view

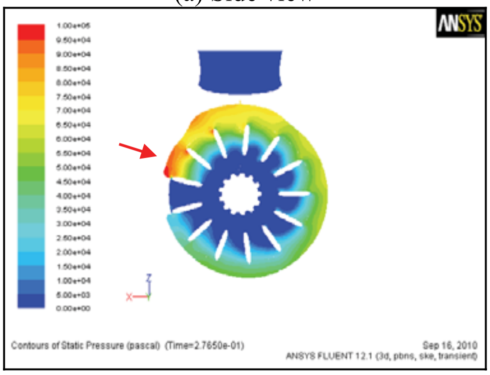

(b) Top view

Fig. 7 An example of pressure distribution

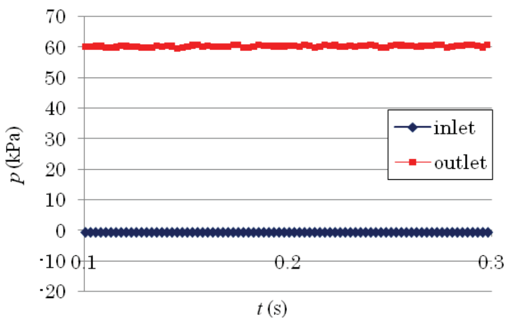

(a) Calculated results

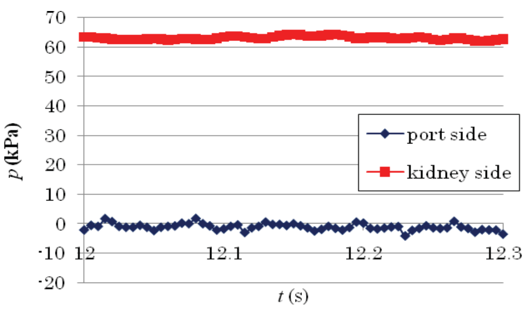

(b) Experimental results

Fig. 8 Inlet and outlet port pressures

Pressure increase across the impeller disk

Inlet and outlet pressure obtained by the CFD are plotted as a function of time in Fig. 8 (a). Pressure increase across the impeller was about 60kPa. An example of experiments carried out on a test bench is plotted in the figure (b). The port side pressure and the kidney side pressure of the experiments correspond to the inlet pressure and the outlet pressure of the model, respectively. The CFD results agreed with the experimental results.

MODIFICATION OF FLOW PATH

Reverse flow in the inlet chamber

When looking at flow pattern in the inlet chamber at the top of the impeller disk, reverse flow is observed, as indicated by red circles in Fig. 9. Around the reverse flow region, oil flow may lose velocity and pressure may increase locally. Flow path of the inlet chamber was modified in order to prevent the reverse flow, as shown in Fig. 10. The top of the inlet chamber was rounded and the corner connecting the chamber with the impeller disk housing was tapered.

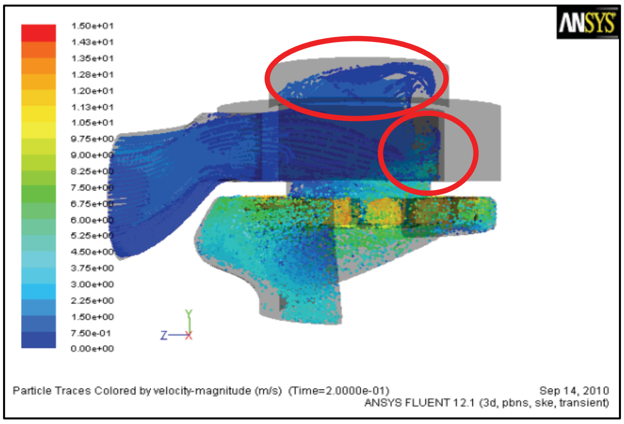

Fig. 9 Reverse flow at the inlet chamber

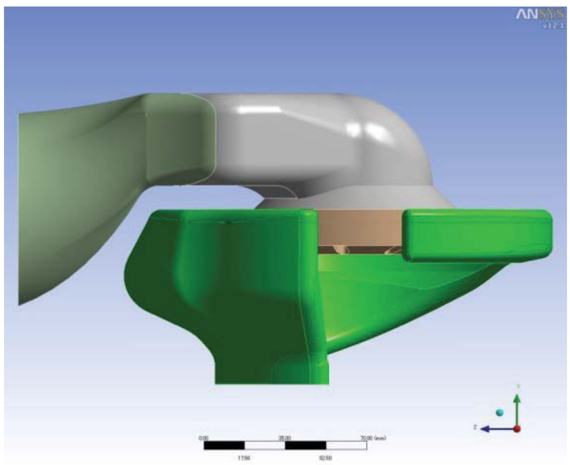

Fig. 10 Modification of inlet chamber

CFD results of stream lines of the modified inlet chamber are shown in Fig. 11. Because of the modification, the hydraulic oil flows smoothly along the rounded flow path and the reverse flow is significantly reduced.

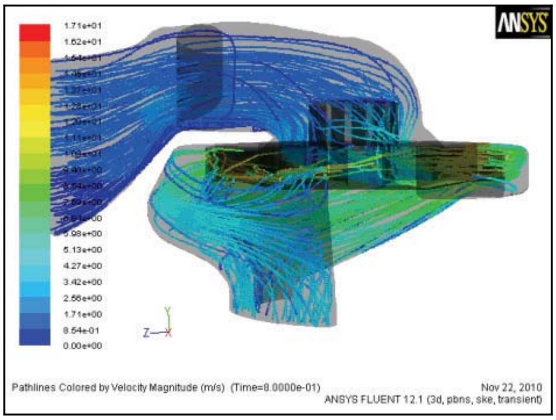

(a) Side view

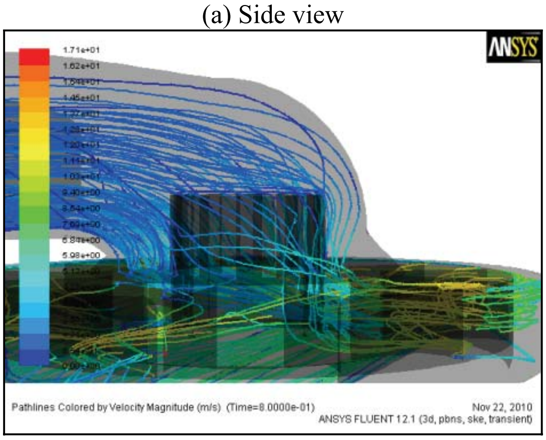

(b) Close-up view

Fig. 11 Streamlines of the modified inlet chamber

Modification of outlet flow path

At the downstream of the impeller, oil flow also has reverse flow region indicated by a red allow shown in Fig. 12. To prevent the reverse flow, the outlet flow path was modified as shown in Fig. 13. A part of the flow path at downstream of the impeller disk was cut out diagonally. A CFD example of stream lines is shown in Fig. 14. The reverse flow region is diminished and the oil flows along the modified flow path smoothly.

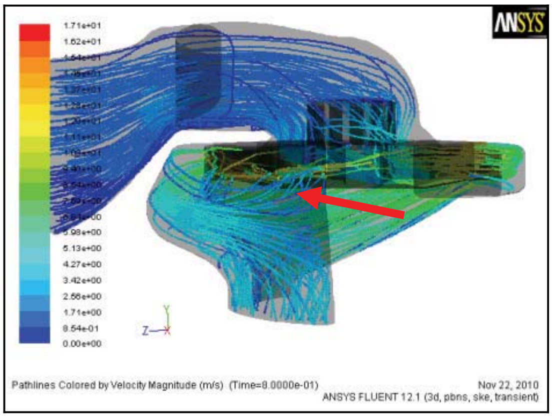

Fig. 12 Stagnation at the outlet port

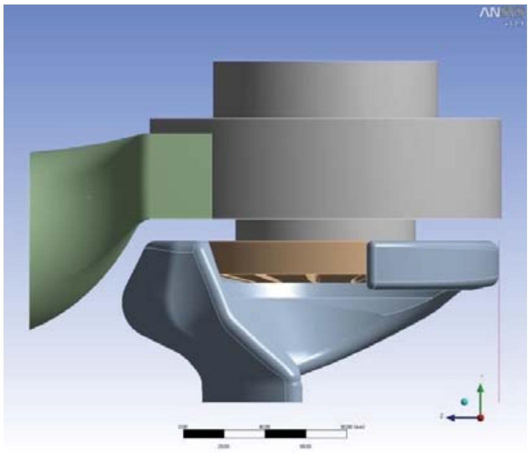

Fig. 13 Reshaping of the outlet port

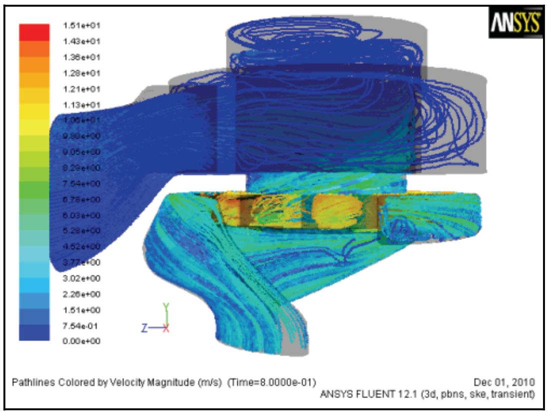

Fig. 14 Stream lines of modified outlet flow path

Combination of the modifications

Combining both modifications at the inlet chamber and at the outlet port, a revised model is proposed as Fig. 15. An example of CFD results of stream lines is shown in Fig. 16. Reverse flow regions at the inlet chamber and at the outlet port are not observed. Calculated results of pressure increase of the original model, the modification of the inlet chamber (modification 1), the modification of the outlet flow path (modification 2), and the combined modification are summarized in Table 1. An experimental result of the inlet port pressure was -0.6kPa. For CFD analysis, pressure at the inlet port was set as the same value of -0.6kPa. Calculated results of the outlet pressure are listed in the table and pressure increase is obtained from the difference between the inlet and the outlet pressures. Compared with the original model, the modification 1, 2 and combined modification improve the pressure increase. The pressure increase of the modification 2 is larger than that of the modification 1. Furthermore the pressure increase of the modification 2 is similar to that of the combined modification. Among the modifications, the modification 2 is enough effective to improve pressure increase.

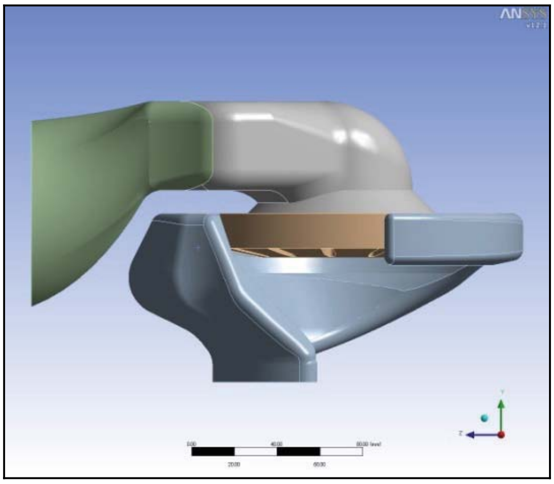

Fig. 15 Combined modification

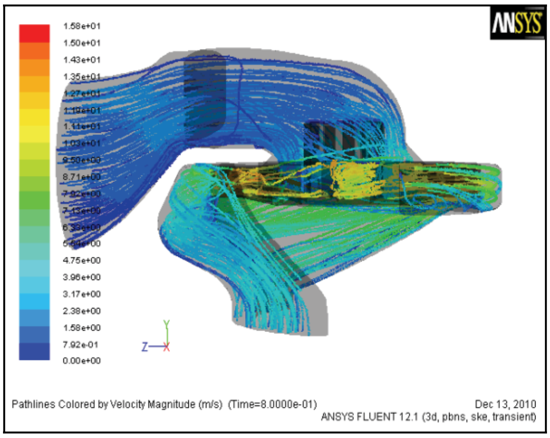

Fig. 16 Stream lines of the combined modification

Table 1 Summary of modifications

	Pressure (kPa)		Pressure Increase (kPa)	Increase Rate
	Inlet (fixed)	Outlet (calculated)		
Original	-0.6	60.4	61	100%
Mod. 1		62.6	63.2	104%
Mod. 2		68.6	69.2	113%
Combined		69.3	69.9	115%

Particle trace analysis

When hydraulic oil flows in the reverse direction inside the model, a certain part of oil may stay inside the model. The CFD software used for this study has a function of particle trace. As shown in Fig. 17 (a), a certain amount of tiny particles is put at the cross section of the inlet port. Mass of the particles is negligibly small. The total number of the particles is known. The particles may move along the stream lines. Fig. 17 (b) shows the particle distribution entering to the impeller disk. In Fig. 17 (c), the particles are driven by rotation of the impeller disk. In Fig. 17 (d), some part of the particles has gone out of the impeller disk and reaches at the outlet port. When the number of particles that have passed through the cross section of the outlet port is counted, the number of particles remaining in the model between the inlet port and the outlet port is obtained. The ratio of the number of particles remaining in the model for the initial total number of particles is shown in Fig. 18. The graph shows how many particles remain inside the impeller model. Original, modification 1, modification 2 are indicated by red, light-blue, and dark-blue lines, respectively. It takes about 0.15s for the first particles passed the cross section of the outlet port in all three cases. Then the ratios of remaining particles began to decrease. In the case of the original model, even after 0.8s, some part of the particles still remains inside the model. In the cases of the modifications 1 and 2, almost all particles pass the outlet port within 0.8s. In the case of the modification 2, the remaining particles inside the impeller decreased the fastest among them. This means that the modification 2 is the most effective in terms of smoothing stream lines.

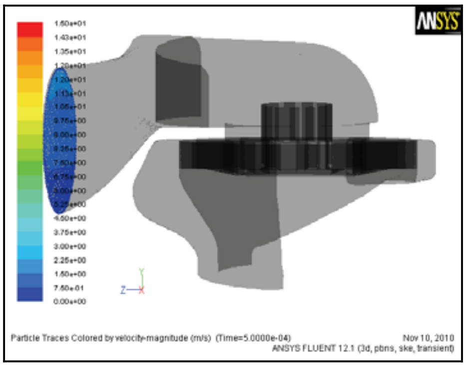

(a) Initial position

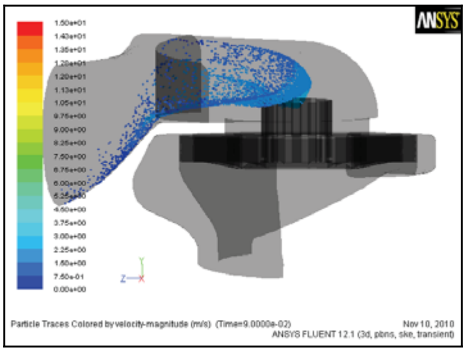

(b) To the inlet chamber

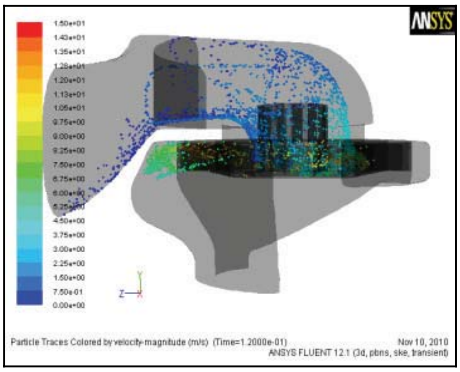

(c) Through the impeller disk

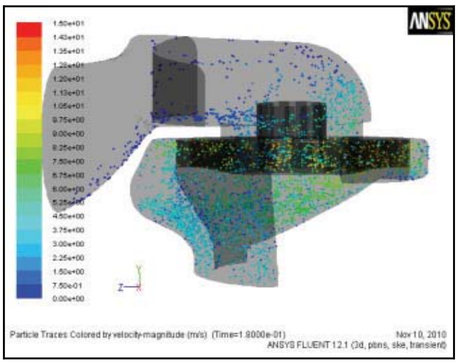

(d) Out of the outlet

Fig. 17 Particle trace

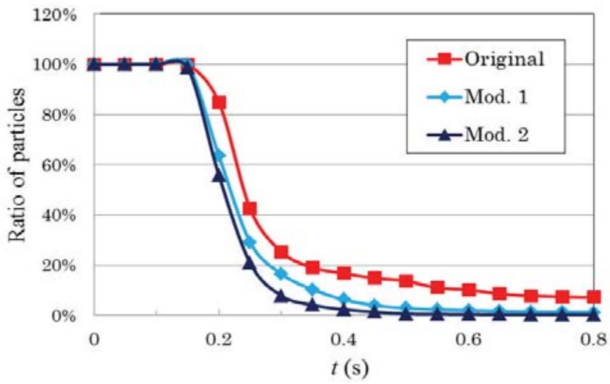

Fig. 18 Ratios of particles remaining inside the model as a function of time

CONCLUSIONS

CFD was applied to analysis of inlet flow around the impeller disk installed between the inlet port and the valve plate of an axial piston pump. The rotation of the impeller disk was considered when computing the flow pattern by the CFD software. Velocity and pressure distribution were calculated and animations of the flow dynamics gave us visual understanding of the flow characteristics of the impeller disk. CFD results of pressure increase across the impeller disk agreed with experimental results. From investigation of stream lines, reverse flow regions were observed in the inlet chamber and in the flow path downstream of the impeller disk. Modifications of flow path both in the inlet chamber and in the outlet port were proposed. Pressure increase was improved by the modifications. A promising modification is the modification of the outlet port. Investigation by use of the particle-trace function of the CFD software supported the study of improvement of pressure increase. The CFD analysis is very useful to improve the impeller performance and efficiency.

REFERENCES

1. Tetsuhiro Tsukiji, Shozo Sakura, Kiyokazu Nagata, Eishin Noguchi, Study on Jet Flow from an Orifice of a Valve Plate with a Groove in an Axial Piston Pump, Transactions of the Japan Fluid Power Systems Society, Vol.38 No.4, p.60/64, 2007
2. Masahiro Oyana and Kazuhiro Tanaka, Visualization of hydraulic flow on sliding part with notch in an oil hydraulic equipment, JSME annual meeting 2008(2), 123-124, 2008
3. Tae-Jo Park and Yun-Geon Hwang, Effect of Groove Sectional Shape on the Lubrication Characteristics of Hydraulic Spool Valve, Tribology Online, Vol. 5 No. 5, pp.239-244, 2010
4. Tetsuhiro Tsukiji, et. al., Improvement of an oil hydraulic ball valve using visualization technique, Transactions of the Japan Fluid Power System

Society, Vol.35, No.6, p.103/108, 2004
5. J. Watton and J.M. Bergada, Progress towards an understanding of the pressure/flow characteristics of a servovalve two-flapper/double-nozzle flow divider using CFD modeling, Preprints of FLUCOME '94, p.47/52, 1994
6. K. Edge, C. Burrows, and M. Lecky Thompson, Modelling of Cavitation in a Reciprocating Plunger pump, Proceedings of the Third JHPS International Symposium on Fluid Power Yokohama 1996, Vol.3, p.473/478, 1996
7. P.-E. Wiklund, G.C. Svedberg, Numerical Analysis of the inflow dynamics of a fluid power axial piston pump, Fith Trienial International Symposium on Fluid Control, Measurement and Visualization, p.403/408, 2007.

Proceedings of the 8th JFPS International
Symposium on Fluid Power, OKINAWA 2011
Oct. 25-28, 2011

1C1-4

RIDE COMFORT WITH SELF-ORGANIZING FUZZY SLIDING MODE CONTROLLER FOR SEMI-ACTIVE SUSPENSION OF A PERSONAL CAR

Yu-Hsien Wang* and Ming-Chang Shih *

Department of Mechanical Engineering, National Cheng-Kung University,
Tainan City, 701 Taiwan, R.O.C
(E-mail: mcshih@mail.ncku.edu.tw)

ABSTRACT

The semi-active suspension system can instantly change the damping coefficient depending in order to 'stiffen' or 'soften' the system. It will effectively and timely eliminate road disturbances on the car body. Thus, research on the semi-active suspension system is necessary. According to the performance test of the proposed adjustable damper, the different damping coefficients can be selected by using a stepping motor. After that, the proposed adjustable damper was installed in the 1/4 car. Besides, a self-organizing fuzzy sliding controller was used in the experiments to verify its feasibility. This study also investigates ride comfort of a 1/4 vehicle for the semi-active suspension system according to the ISO2631-1 standard. The experimental results show that the proposed controller demonstrates effective improvements in the vibration suppression of the vehicle body and ride comfort that is better than the compared fuzzy sliding mode controller design.

KEY WORDS

Semi-active suspension system, Fuzzy sliding controller, Ride comfort, Self-organizing

NOMENCLATURE

α	:	Scaling factor of sliding surface
G_e, G_v, G_u	:	Gain value of FSMC
M	:	Direct forward system gain
W_i	:	Excitation intensity of FSMC
$S(\Omega_0)$	:	Roughness coefficient
Ω	:	Spatial frequency
a_v	:	Ride comfort level
ζ	:	Weighted factor
γ	:	Learning rate
$\dot{Z}_{bu}$	:	Suspension velocity

INTRODUCTION

Most vehicles are equipped with passive suspensions. However, these suspensions are made up of only passive elements such as the shock absorbers or the springs that do not supply external energy to the system. As a consequence, it is usually difficult to obtain both good ride comfort and driving quality with the use of passive suspensions. Besides, without extra external control to inhibit external disturbances, the damping coefficient will not be altered with road condition. Therefore, the ride comfort is completely subject to the design of component parameter of the suspension system.

Meanwhile, due to car body structure aging, the effectiveness of the suspension system changes with the increase in car age. The semi-active suspension system can immediately change the damping coefficient depending in order to 'stiffen' or 'soften' the system. It will effectively reduce road profile disturbances on the car body. Subsequently, it will improve the comfort; moreover, it is competitive price and has simpler structures.

In recent years, the design and development of semi-active suspension systems has attracted increased interest, and the various techniques and the methodologies for their design have been proposed [1]. Techniques such as H_∞ control [2], linear quadratic control [3], robust control [4] and fuzzy logic control [5-6]. The implementation of fuzzy control still needs time-consuming adjustments of fuzzy parameters and fuzzy rules, especially for a system with nonlinear time-varying properties. Furthermore, an optimal fuzzy logic controller cannot be achieved by trial and error. In order to solve these problems, Procky et al. [7] proposed a self-organizing fuzzy controller (SOFC). This control scheme established control rules through on-line learning instead of human knowledge based approaches. It simplified the design processes and facilitates the implementation of a fuzzy controller. Shao [8] designed the modified learning schemes for a SOC. The error and error rate were used to calibrate the control inputs, instead of the performance.

This study adopts the proposed adjustable shock absorber that is applied to a semi-active suspension system of a quarter-car. According to the control commands of the proposed controller, the microcomputer can judge suitable damping level to suppress vibration of the car body. Besides, the random road surface can be generated by using the hydraulic servo system. Experiments on a test rig with the proposed controllers are performed for investigating its dynamic responses and ride comfort analyses.

ADJUSTSBLE SHOCK ABSORBER

The minimum to maximum damping coefficients are defined from 0^o 0 to 100^o by changing the rotation angles of the rotary valve. It can be shown that the 100^o is the stiffest level of the damping force from the F-D diagram which is equipped with the largest surrounding area in Figure 1, while 0^o is equipped with the least one. F-V diagram can be also shown that the variances of the different damping coefficients. Among it, the minimum damping coefficient is 1626 Ns/m, and the maximum one is 4156.7 Ns/m.

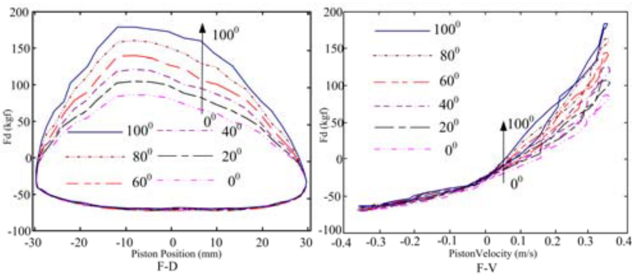

Figure 1 Experimental results of adjustable damper of 2Hz.

QUARTER CAR MODEL DESCRIPTION

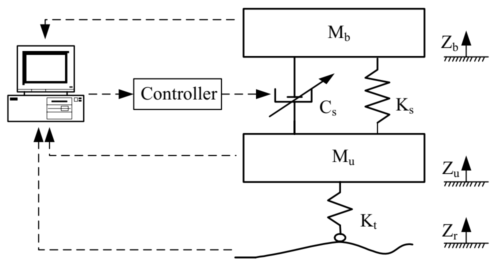

Figure 2 Scheme of semi-active suspension system

The scheme of the semi-active suspension is shown in Figure 2. The assumption is that the wheel always contacts the road surface and the wheel is hypothesized by a spring with constant coefficient. The dynamic equations of the quarter-car system can be obtained as follows:

$$M_b\ddot{Z}_b = -K_s(Z_b - Z_u) - C_s(\dot{Z}_b - \dot{Z}_u) \quad (1)$$

$$M_u\ddot{Z}_u = K_s(Z_b - Z_u) + C_s(\dot{Z}_b - \dot{Z}_u) - K_t(Z_u - Z_r) \quad (2)$$

where M_b and M_u are the sprung mass and the unsprung mass, respectively; Z_b and Z_u are the displacements of the sprung mass and the unsprung mass, respectively; K_s and K_t are the spring coefficients of the spring and the tire, respectively; $F_d = C_s(\dot{Z}_b - \dot{Z}_u)$ is the damping force of the adjustable damper; Z_r is the road irregularity, and the controllable damping force u representing F_d. Thus, the dynamic equations of the quarter-car system can be described as follows:

$$\dot{\boldsymbol{x}} = \mathbf{A}\boldsymbol{x} + \mathbf{B}u + \mathbf{D}Z_r \quad (3)$$

where the state vector is $\boldsymbol{x}=[Z_b \quad \dot{Z}_b \quad Z_u \quad \dot{Z}_u]^T$

$$A=\begin{bmatrix} 0 & 1 & 0 & 0 \\ -\frac{K_s}{M_b} & 0 & \frac{K_s}{M_b} & 0 \\ 0 & 0 & 0 & 1 \\ \frac{K_s}{M_u} & 0 & -\frac{(K_t+K_s)}{M_u} & 0 \end{bmatrix}, B=\begin{bmatrix} 0 \\ -\frac{1}{M_b} \\ 0 \\ \frac{1}{M_u} \end{bmatrix}, D=\begin{bmatrix} 0 \\ 0 \\ 0 \\ \frac{K_t}{M_u} \end{bmatrix}$$

RIDE COMFORT ANALYSES

This section presents the three types of different ride comfort analyses: PSD, Meister chart, and vibration-weighted acceleration.

(1) PSD

The spectral density captures the frequency content of a stochastic process and helps identify periodicities. In this study, it is applied towards determining the frequency composition of acceleration and can be regarded as an indicator of ride comfort.

$$a_k=\sum_{n=0}^{N-1} a[n]\exp(-j\frac{2k\pi n}{N}) \tag{4}$$

$$G(f_{req})=\frac{1}{N}|a_k|^2 \tag{5}$$

(2) Meister chart

The Meister chart represents a person can endure the vibrations during the time for acceleration. However, ISO uses a weighted curve $W(f_{req})$ to revise it for the Meister chart in the 2631-1 standard nowadays. The equation is shown as follows:

$$a_{RMS}(k)=\sqrt{\int_{f_{lk}}^{f_{uk}} W(f_{req})G(f_{req})\, df_{req}} \quad , k= 1,2,3...20 \tag{6}$$

where

$$W(f_{req})=\begin{cases} 0.5 f_{req}^{1/2} & 0.9<f_{req}\le 4 \\ 1 & 4<f_{req}\le 8 \\ 8/f_{req} & 8<f_{req} \end{cases}$$

(3) Vibration-weighted acceleration

This is to use the time domain to evaluate the effects of acceleration on ride comfort. The formula for calculating the vibration-weighted accelerations a_v of the three axes can be shown as follows:

$$a_v=(k_x^2 a_{wx}^2+k_y^2 a_{wy}^2+k_z^2 a_{wz}^2)^{\frac{1}{2}} \tag{7}$$

However, the vibrations only occur on the Z-axis for the 1/4 vehicle; the vibrations from the X and Y-axes can be temporarily ignored. Therefore, the equation is modified as follows:

$$a_v=(k_z^2 a_{wz}^2)^{\frac{1}{2}}, \quad k_z=1 \tag{8}$$

where $a_{wz}=(\frac{1}{T}\int_0^T a_w^2(t)\,dt)^{\frac{1}{2}}$

where a_w is the filtered accelerations of Z-axis. For a more detailed description of the theorem, see Ref.[11].

SELF-ORGANIZATION FUZZY SLIDING MODE CONTROLLER

The proposed controller is shown in Fig. 3. It is comprised of two parts: fuzzy sliding mode controller (FSMC) and self-organizing learning mechanism.

1. Fuzzy sliding mode controller

The traditional fuzzy logic control theory involves fuzzification, a fuzzy rule base, a fuzzy inference engine and defuzzification. The fuzzy rule base is dependent on error e and error rate $\dot{e}$ that complicate both fuzzy rules and membership functions.

To replace those, the fuzzy sliding surface is introduced. The sliding surface function is designed as

$$S=\mathbf{C}\boldsymbol{x}=[-\alpha \ \ -1 \ \ 0 \ \ 0]\boldsymbol{x} \tag{9}$$

where α is a positive constant. The fuzzy sliding surface $S=\text{zero}$ is a straight line with slope α in the phase plane. Next, consider the reaching condition ($\dot{V}=S\dot{S}<0$) which is based on the Lyapunov function ($V=S^2/2$). If the control u can be chosen to satisfy the reaching condition, the control system will converge to the sliding surface. Computing the derivative of S in Eq. (9) and substituting Eq. (3) into $\dot{S}$ as

$$\dot{S}=\mathbf{C}(\mathbf{A}\boldsymbol{x}+\mathbf{B}u+\mathbf{D}Z_r) \tag{10}$$

Then, the Lyapunov stability condition

$$V=S\dot{S}=S(\mathbf{CA}\boldsymbol{x}+\mathbf{CB}u+\mathbf{CD}Z_r) \tag{11}$$

In terms of Eqs. (10), (11), (9) and (3), yields **CB** >0. According to Eq. (11), we know that the coefficient of u in Eq. (10) is positive. Eq. (10) denotes that decreasing u

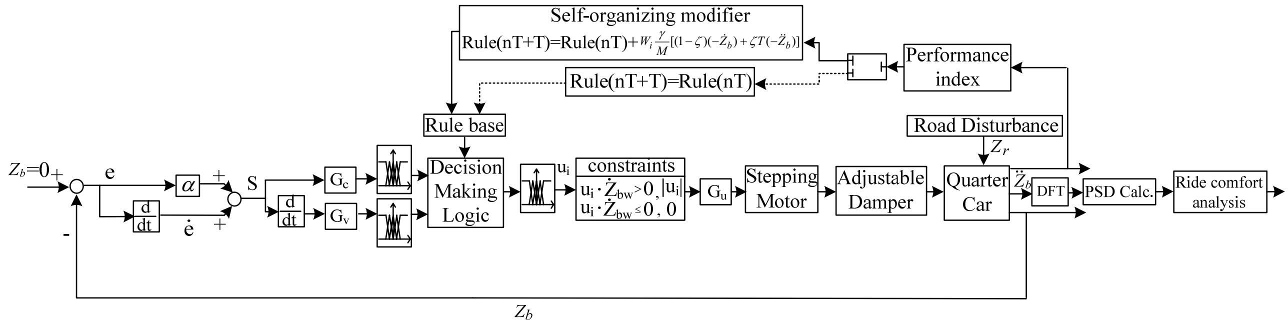

Figure 3 Block diagram of proposed controller

will result in decreasing $S\dot{S}$ as S is positive and increasing u will result in decreasing $S\dot{S}$ as S is negative. Based on this above method, the control input u can be designed in an attempt to satisfy the sliding mode reaching condition $S\dot{S}<0$. The relating theory about the convergence and stability of the adaptation process on the basis of the minimization of $S\dot{S}$ can be found in [9-10]. Besides, a fuzzy sliding mode controller based on sliding mode reaching condition is designed to attenuate vibration caused by external disturbance. S and $\dot{S}$ are chosen as the input linguistic variables and u is chosen as the output linguistic variable. This study is applied to triangular membership function to simplify complexity. The membership function can be described that is shown in Figure 4. Besides, the output and input membership functions are normalized between -1 and 1. The center of area method is selected for defuzzification. The designed fuzzy rule base is illustrated in Table 1.

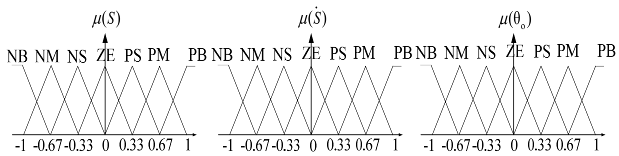

Figure 4 Diagram of membership functions

Table 1 Rule base for FSMC

	θ_o						
	$\dot{S}$=NB	$\dot{S}$=NM	$\dot{S}$=NS	$\dot{S}$=ZE	$\dot{S}$=PS	$\dot{S}$=PM	$\dot{S}$=PB
S=NB	PB	PB	PM	PM	PS	PS	ZE
S=NM	PB	PM	PM	PS	PS	ZE	NS
S=NS	PM	PM	PS	PS	ZE	NS	NS
S=ZE	PM	PS	PS	ZE	NS	NS	NM
S=PS	PS	PS	ZE	NS	NS	NM	NM
S=PM	PS	ZE	NS	NS	NM	NM	NB
S=PB	ZE	NS	NS	NM	NM	NB	NB

The controller θ mentioned above is designed in an active actuating mode. However, the proposed damper applied in the suspension system, as shown in Figure 2, is desired to be a semi-active actuator. Thus, the control input should be modified in terms of the below actuating condition. This condition physically implies that the actuating of the controller θ only assures the increment of energy dissipation of the stable system.

$$\theta^*=\begin{cases}|\theta_o| & , \quad \theta_o\cdot\dot{Z}_{bu}\geq 0\\ 0 & , \quad \theta_o\cdot\dot{Z}_{bu}<0\end{cases} \tag{12}$$

In this study, G_u is chosen to be 100 so that the control commands θ=($\theta^*\cdot 100$) can be mapped to the rotation angles.

2. Self-organizing learning mechanism

The self-organizing learning mechanism is applied to modify on-line the 7x7 fuzzy sliding rule base. To design the SOFSMC learning mechanism, the system dynamic response feature can be represented as an auto-regression and moving average (ARMA) model.

$$Y(k)=A(z^{-1})Y(k-1)+Mq(k-d)+B(z^{-1})q(k-d-1) \tag{13}$$

where $A(z^{-1})=a_0+a_1z^{-1}+...+a_{r-1}z^{-(r-1)}$,

$B(z^{-1})=b_0+b_1z^{-1}+...+b_{s-d-1}z^{-(s-d-1)}$

, M can be obtained by the projection algorithm, q is the control signal and Y is the angle output. If the past condition is constant, another input $q^{'}(k-d)$, which is not the same as $q(k-d)$, will produce an output $Y^{'}(k)$ as

$$Y^{'}(k)=A(z^{-1})Y(k-1)+Mq^{'}(k-d)+B(z^{-1})q(k-d-1) \tag{14}$$

Then, ΔY and Δq are described as follows:

$$\Delta Y(k)=Y^{'}(k)-Y(k) \tag{15}$$

$$\Delta q=q^{'}(k)-q(k) \tag{16}$$

Substitute Eq.(15) for Eqs.(13), (14) and (16) to obtain

$$\frac{\Delta Y(k)}{\Delta q(k)}=M \tag{17}$$

Similar procedures are utilized to obtain $\Delta\dot{Y}$ as

$$\frac{\Delta\dot{Y}(k)}{\Delta q(k)}=\frac{1}{T}M \tag{18}$$

where T is the sampling time that is small. Here, the limitations of Eqs.(17) and (18) are $\Delta Y \approx 0$ and $\Delta\dot{Y} \approx 0$, respectively. If they are not satisfied, the input reinforcement Δq would become incorrect. When Y and $\dot{Y}$ are departures, a single control input does not allow Y to approach the desired point Y_d and $\dot{Y}$ to approach the desired point $\dot{Y}_d$, similarly. Thus, the input reinforcement should be redefined.

Here, Δq_c and Δq_{ce} are defined as the correction values to compensate for ΔY and $\Delta\dot{Y}$, respectively. Thus, Δq_c and Δq_{ec} are defined as follows:

$$\Delta q_c = \frac{1}{M}\Delta Y(k) \tag{19}$$

$$\Delta q_{ce} = \frac{T}{M}\Delta\dot{Y}(k) \tag{20}$$

In general cases, the following form is chosen:

$$\Delta q(k)=(1-\zeta)\Delta q_e(k)+\zeta\Delta q_{ce}(k), 0 \le \zeta < 1 \tag{21}$$

where ζ is a design parameter representing the weighting distribution between Δq_c and Δq_{ce}. If there is a significant difference between Y and the desired output point Y_d, Eq.(19)is not suitable for calculating the input correction Δq_c. Eq.(20)has the same problem when calculating Δq_{ce}. A reasonable approach is to choose a Y' between Y and Y_d. Then the system output Y will approach the desired value Y_d gradually with a factor of the learning rate γ:

$$Y'(k) = (1-\gamma)Y(k)+\gamma Y_d(k),\ 0 < \gamma \le 1 \tag{22}$$

Then ΔY and $\Delta\dot{Y}$ are rewritten as

$$\Delta Y(k) = [Y_d \text{-} \gamma Y(k)] = \gamma E(k) \tag{23}$$

$$\Delta\dot{Y} = \gamma\dot{E}(k) \tag{24}$$

Then, substitute Eq. (21) for Eqs. (19), (20), (23), (24) to obtain

$$\Delta q(k) = \frac{\gamma}{M}[(1-\zeta)E(k)+\zeta T\dot{E}(k)],\ 0 \le \zeta < 1 \tag{25}$$

Since the fuzzy sliding rule base provides the control signal q, modifying q also means modifying the fuzzy sliding rule base. Every output state can be excited by four modules. The correction of each rule is modified by its excitation intensity W_i, which can be obtained by the linear interpolation technique. In this study, $\dot{Z}_b$ and $\ddot{Z}_b$ are selected for $E(k)$ and $\dot{E}(k)$. Thus, the input q_i of the i^th^ rule is

$$q_i(k+1)=q_i(k)+W_i\frac{\gamma}{M}[(1\text{-}\zeta)(\text{-}\dot{Z}_b)+\zeta T(\text{-}\ddot{Z}_b)] \tag{26}$$

This equation is the basic learning algorithm. According to the linguistic approach, the rule base can be expressed in the following vector form:

$$\text{RULES}_i(k+1)=\text{RULES}_i(k)+W_i\frac{\gamma}{M}[(1\text{-}\zeta)(\text{-}\dot{Z}_b)+\zeta T(\text{-}\ddot{Z}_b)] \tag{27}$$

If the performance of the suspension system reaches the desired control effect, the compensation term of the self-organizing learning mechanism should be closed immediately to avoid over learning. Thus, for the performance index, RMS of the power spectral density (PSD) of the sprung mass acceleration, the vibration weighted acceleration a_v [11], and the integrated square error (ISE) of the sprung mass displacement are adopted. The former two mathematical terms can be considered values quantifying comfort. The last term is designed to diminish the changes in car body displacement. The performance index follows larger-the-better (LTB); it can be expressed as follows:

$$PI=1/(0.2\cdot(PSD)_{RMS,acc}+0.3\cdot a_v+0.5\cdot ISE(\text{-}Z_b)) \tag{28}$$

LAYOUT OF EXPERIMENTAL DEVICES

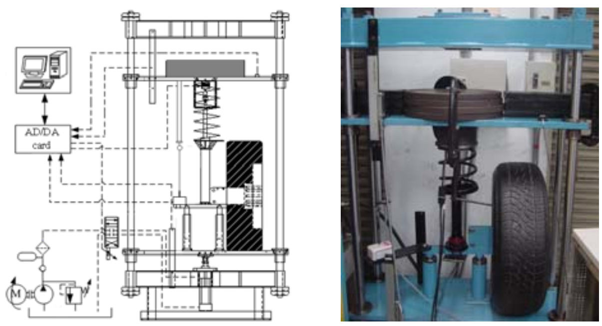

(a) (b)

Figure 5 Experimental devices for quarter vehicle suspension system: (a) schematic diagram and (b) photograph

The Experimental devices are shown in Figure 5, which consists of the suspension mechanism part and the electrical control part. The suspension mechanism part includes the mass, the spring, the proposed adjustable damper, the hydraulic cylinder, the stepping motor and the wheel. The hydraulic cylinder is used to generate the road profiles. The flow rate of the hydraulic cylinder is controlled by a servo valve. The linear scales are applied to measure the car body displacements and the road profile vertical displacements, respectively. The suspension travels are obtained by a LVDT. To evaluate ride comfort, an accelerometer is set up on the sprung mass to measure the vertical acceleration. A microcomputer which in the study acts as controllers is used for the experimental data acquisition.

EXPERIMENTAL RESULTS

According to the ISO 8608 [12] standard, the road surface types can be divided into eight levels. In this study, the road roughness is used according to the ISO Level E ($S(\Omega_0)=256\cdot 10^{-6}$ m^3/cycle) standard. Thus the random road surface irregularities in the time domain can be determined and calculated [13]. Thus, the dashed line indicates performance based on random road profile from figure 6(a).

The dynamic responses are obtained by applying both FSMC and SOFSMC control strategies to the experimental devices, shown in Figures 6~9. The time responses which compare FSMC of the two kinds of the scaling factors for the sliding surfaces with the passive suspension system can be shown as Figures 6 and 7. On the basis of Table 2, FSMC ($\alpha = 1.8$) improves the improvement rate of the sprung mass displacement by 10.6 %, while that with a scaling factor of 0.7 enhances it by 6.3 %. Figure 6(b) shows that the FSMC ($\alpha = 1.8$) can also effectively suppress the sprung mass acceleration. Due to PSD of the sprung mass acceleration is an important index of ride comfort. This study transforms the accelerations into PSD by using discrete Fourier transform. The peak PSD acceleration demonstrated by FSMC ($\alpha = 1.8$) in Figure 7(a) is 4.21. The FSMC with a scaling factor of 1.8 prolongs the comfortable time for more than 1hr at 8 Hz in Figure 7(b), while the comfortable time for both the passive suspension system and the FSMC with a scaling factor of 0.7 are less than 1 hr, respectively.

The time responses which contrast the different learning cycles of self-organizing fuzzy sliding controller (SOFSMC) with the passive suspension system can be shown as Figures 8 and 9. Figure 8(b) shows that SOFSMC with a scaling factor of 1.8, in comparison to the passive suspension system, effectively improves the RMS value of the acceleration to 0.5312 for the 3rd cycle. The semi-active suspension system with SOFSMC control strategy can also demonstrate obvious improvements in the vibration suppression for the 3rd cycle. The improvement rate of the PSD peak value by SOFSMC for the 3rd cycle is 49.52% and the vibration weighted acceleration is reduced to 0.4589 with SOFSMC from Table 2. Thus, the proposed controller which demonstrates effective improvements in ride comfort is better than the FSMC.

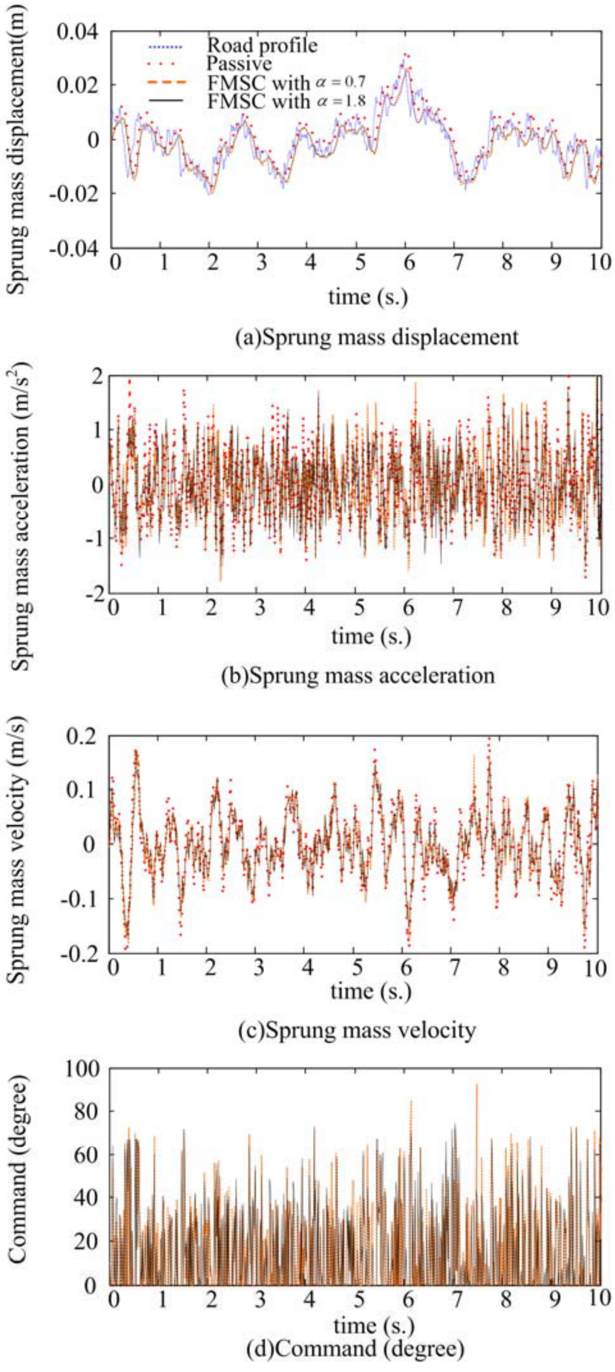

Figure 6 Time response of suspension with FSMC

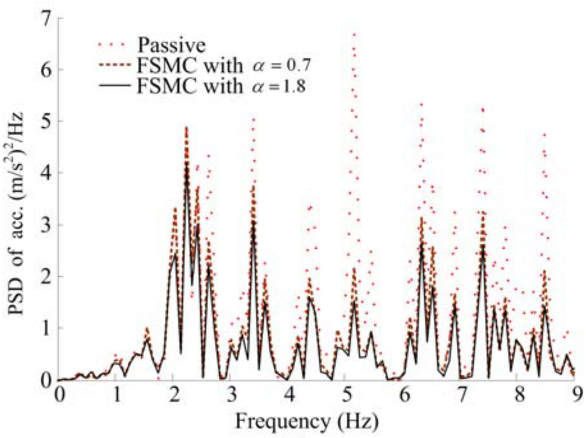

(a)

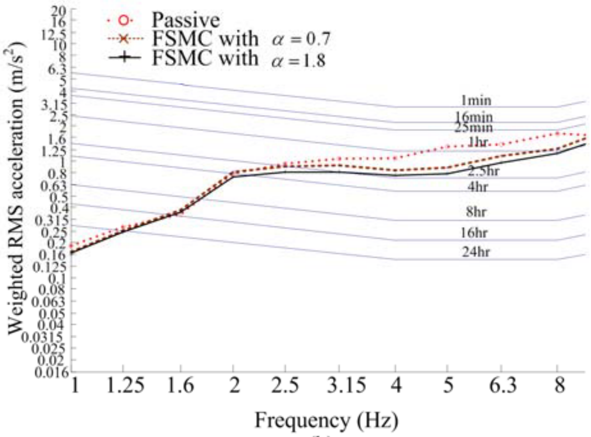

(b)

Figure 7 (a) PSD of acc. (b) Meister chart with FSMC

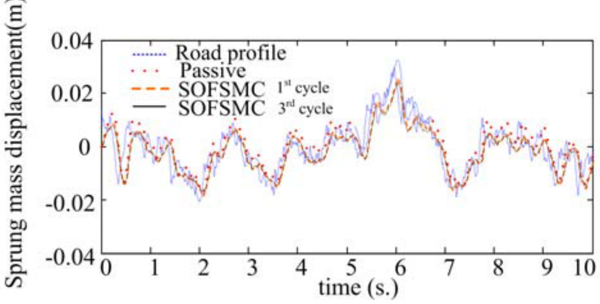

(a)Sprung mass displacement

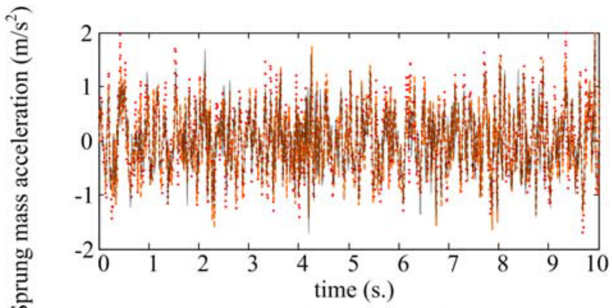

(b)Sprung mass acceleration

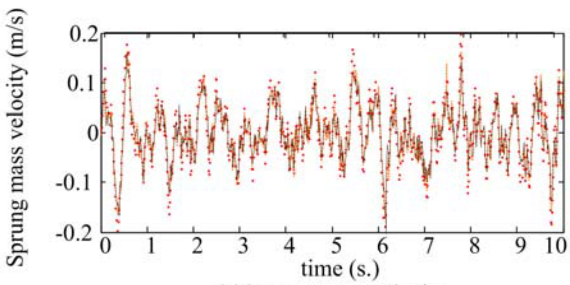

(c)Sprung mass velocity

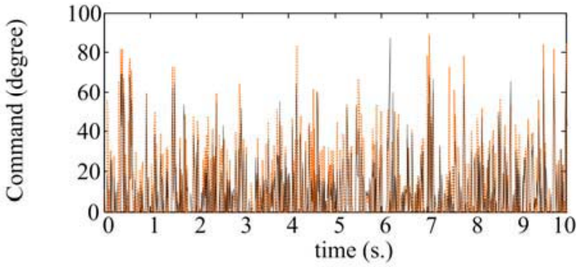

(d)Command (degree)

Figure 8 Time response of suspension with SOFSMC

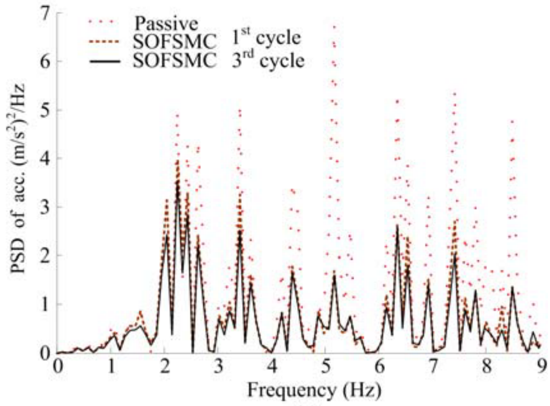

(a)

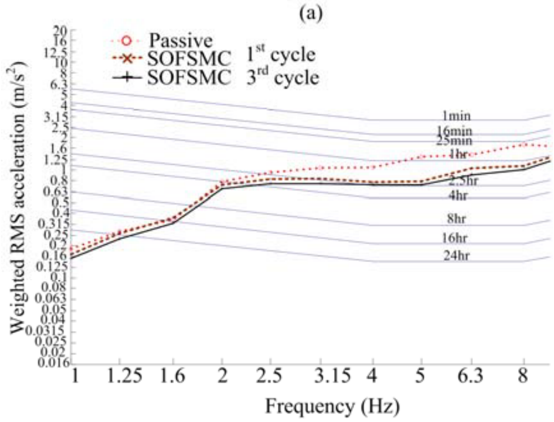

(b)

Figure 9 (a) PSD of acc. (b) Meister chart with SOFSMC

Table 2 Comparison of response characteristics of passive and semi-active designs

ISO level E road surface	Passive 100°	FSMC $\alpha=0.7$	FSMC $\alpha=1.8$	SOFSMC $\alpha=1.8, 3^{rd}$ cycles
$Z_{b,RMS}$ (m)	0.0094	0.0088 (-6.3%)	0.0084 (-10.63%)	0.008 (-14.89%)
$\ddot{Z}_{b,RMS}$ (m/s^2)	0.6462	0.6153 (-4.8%)	0.5723 (-11.43%)	0.5312 (-17.8%)
$PSD_{acc,peak}$ ((m/s^2)^2/Hz) (0 ~ 9 Hz)	6.736	4.91 (-27.1%)	4.21 (-37.5%)	3.4 (-49.52%)
a_v	0.5897	0.5304 (-10.05%)	0.4931 (-16.38%)	0.4589 (-22.18%)

CONCLUSION

The conclusions of this study are shown as follows:

1) A testing rig of the quarter car was built to evaluate the control performance. The hydraulic system was used to generate random road surface. A stepping motor in the study was used to adjust the damping coefficient to evaluate the dynamic responses and characteristics of the semi-active suspension system.

2) The learning strategy in the form of fuzzy sliding rules can be continually updated by using SOFSMC. If the performance of the suspension system reaches the desired control effect, the compensation term of the self-organizing learning mechanism should be closed immediately to avoid over learning in real time.

3) The experimental results show that the proposed control scheme for semi-active suspension system obviously suppresses the position oscillation amplitude of the sprung mass and ride comfort is improved effectively.

ACKNOWLEDGEMENTS

This research was partially supported by the National Science Council of the Republic of China government under the contract no. NSC-97-2221-E-006-052-MY2.

REFERENCES

1. Tomizuka, M. and Hedrick, J.K., Advanced control methods for automotive applications, Vehicle System Dynamics, 1995, Vol. 24, pp 449–468.
2. Damien Sammier, Olivier Sename and Luc Dugard, Skyhook and H∞ Control of Semi-active Suspensions: Some Practical Aspects, Vehicle System Dynamics, 2003, Vol.39 , pp279-308.
3. Elmaciany, M.M. and Abduljabbar, Z., Linear quadratic Gaussian control of a quarter car suspension, Vehicle System Dynamics, 1999, Vol. 32, pp 479–497.
4. Son, H.Y., Jeong, S.G., Choi, J.Y. and Kim, J.K., A robust controller design for performance improvement of a semi-active suspension system, IEEE International Symposium on Industrial Electronics, 2001, Vol. 3, pp 1458–1461.
5. Liu, H., Nonami, K. and Hagiwara, T., Semi-active fuzzy sliding mode control of full vehicle and suspensions Semi-active fuzzy sliding mode control of full vehicle and suspensions, Journal of Sound and Vibration, 2005, Vol.314, pp39-52.
6. Sung, Kum-Gil, Han, Young-Min, Cho, Jae-Wan and Choi, Seung-Bok, Vibration control of vehicle ER suspension system using fuzzy moving sliding mode controller,Journal of Sound and Vibration, 2008, Vol. 311, pp1004-1019.
7. Procyk, Tom J. and Mamdani, Ebrahim H., A linguistic self-organizing process controller, Automatica, 1979, Vol.15, pp. 15-30.
8. Shao, S., Fuzzy self-organizing controller and its application for dynamic processes, Fuzzy Sets Syst., 1988, Vol.26, pp. 151-164.
9. Hwang, G.C. and Lin, S.C., Stability Approach to Fuzzy Control Design for Nonlinear Systems, Fuzzy Sets and Systems, 1992, Vol.48, pp269−278.
10. Li, T.H.S. and Shieh, M.Y., Switching-type Fuzzy Sliding Mode Control of a Cart-pole System, Mechatronics, 2000, Vol.10, pp 91−109.
11. International Organization for Standardization ISO 2631-1, Mechanical vibration and shock - evaluation of human exposure to whole-body vibration - part 1: general requirements, 1997.
12. International Organization for Standardization ISO 8608, Mechanical vibration – Road surface profiles - Reporting of measured data, 1995.
13. Sun, Lu, Simulation of pavement roughness and IRI based on power spectral density, Mathematics and Computers in Simulation, 2002, Vol. 61, pp77-88.

Proceedings of the 8th JFPS International
Symposium on Fluid Power, OKINAWA 2011
Oct. 25-28, 2011

1C2-1

PRESSURE DROP OF PIPE FLOW IN A MANIFOLD BLOCK

Osamu ABE*, Tetsuhiro TSUKIJI*, Takeshi HARA*, and Kazutoshi YASUNAGA**

* Faculty of Science and Technology
Sophia University
7-1 Kioi-cho, Chiyoda-ku, Tokyo, 102-8554 Japan
(E-mail: t-tukiji@sophia.ac.jp)
** TOKYO KEIKI INC.

ABSTRACT

We deal with a solid manifold block and a laminated manifold block that are used for connecting hydraulic components. They are useful for reducing the space and weight of hydraulic systems. We investigate pressure drops of their pipe flow with computational fluid dynamics (CFD) and compare those of two types. The majority of all pressure drops in both types is pressure drop at corners. In solid type, pressure drop is affected by the distance between two corners and angle of corner against upstream corner. Solid type has round sectional area ,but laminated type has a square one. So, pressure drop of laminated type is smaller than that of solid type. By experiment of visualization with an acrylic manifold block and comparison of pressure drop of CFD results with experimental results, the validity of CFD results is proved unless heavy cavitation occurs.

KEY WORDS

Manifold block, Pressure drop, CFD, Pipe flow

NOMENCLATURE

ρ	:	Density
v	:	Kinetic viscosity
Q	:	Volumetric flow rate
p	:	Pressure
p_e	:	Pressure at exit
θ	:	Angle
L	:	Length
ζ	:	Pressure loss coefficient
p_{all}	:	All pressure loss
p_A	:	Pressure loss at corner A
p_B	:	Pressure loss at corner B
p_f	:	Friction loss of pipe flow
u	:	Flow velocity
d	:	Pipe diameter

INTRODUCTION

Hydraulic machines have many valves and piping parts. So there are problems that much space is needed and plumbing is more troublesome. Recently, as one of the methods to reduce the space and piping parts, manifold system is developed. This system is the method of connecting valves and actuators by using steel blocks that have pipelines inside. These blocks are called 'Manifold Block'. It is said that pressure drop of pipe flow in the block because it has many curved section. However, pipe flow in the block has hardly been researched ever though curved pipe flow such as bend or elbow is researched by many workers.

Manifold block is generally classified into two types by way of machining. One is a solid manifold block (solid type) that has some holes by drilling as shown in figure 1.

The other is a laminated manifold block (laminated type) that is composed of some blocks grooved and drilled in advance. In solid type, design of pipeline is relatively simple since its pipeline only connects some holes, but it is impossible to design pipeline freely. On the other hand, in laminated type, it is possible to design pipeline freely because it has pipes of rectangular groove, but it is difficult to weld blocks. So it takes much time to manufacture laminated type.

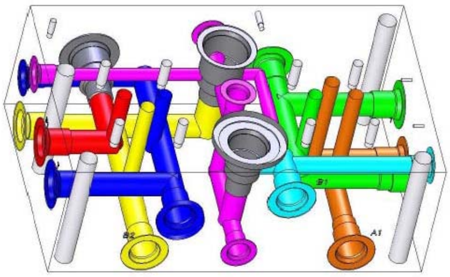

Figure 1 Solid manifold blocks

This study focuses on estimating pressure drop of pipe flow in two types as follows with CFD. And by using these results, we aim obtainment of guidelines for pipeline design in a manifold block. Furthermore, we also verify the validity of the CFD results by comparison of CFD results with pressure measurement. In this paper, however, we deal with a manifold block as port converter in case of substituting a valve as shown in figure 2(a) for another valve as shown in figure 2(b) when we compare two types.

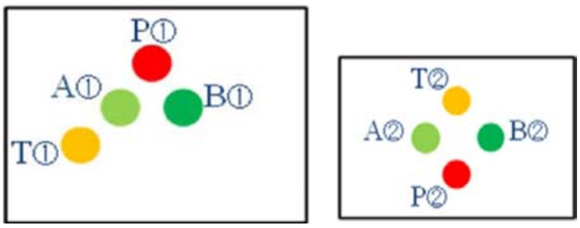

(a) One port of valve (b) Another port of valve

Figure 2 Port standard of valves

NUMERICAL ANALYSIS

Objects of Analysis

Figure 3 shows a port converter of solid type. And figures 4(a), (b) show flow channels in the block connecting T1 with T2 (solid-T) and P1 with P2 (solid-P). These channels go around because they must avoid tapped holes for attachment and other channels. Pipe diameter is 6[mm], partially 10[mm]. Red arrows in figures show flow direction. Figure 5(a) shows a port converter of laminated type (laminated 1). This is composed of three blocks shown in figure 5(b). In the same, figures 6(a), (b) show flow channels in the block (laminated 1-T and laminated 1-P, respectively). Unlike solid type, it is possible to connect ports by curved channel. To compare with solid type, we deal with flow channels that are the same length as solid type channel as shown in figures 7(a), (b) (laminated 2-T and laminated 2-P, respectively). Cross section of groove is 6[mm] square.

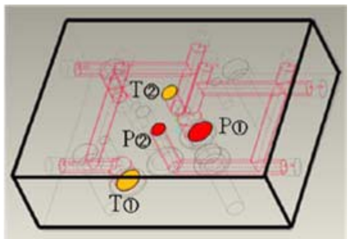

Figure 3 Port converter of solid manifold block

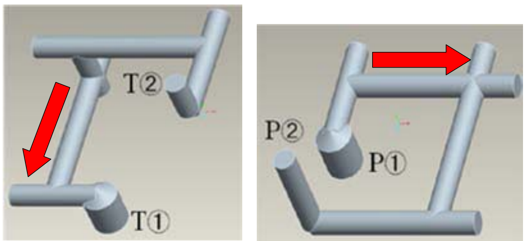

(a) Solid-T (b) Solid-P

Figure 4 Flow channels in solid manifold block

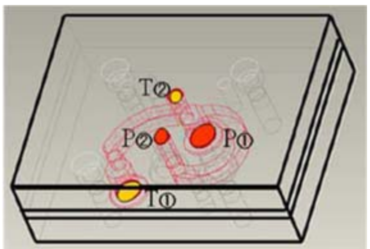

(a) Block after attached

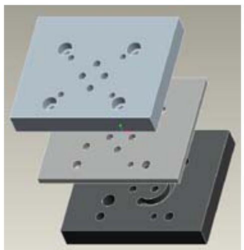

(b) Three blocks before attached

Figure 5 Port converter of laminated manifold block (laminated 1)

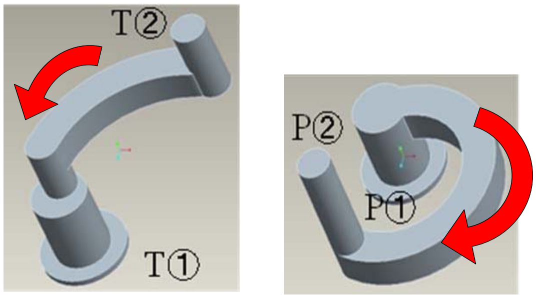

(a) Laminated 1-T (b) Laminated 1-P

Figure 6 Flow channels in laminated 1

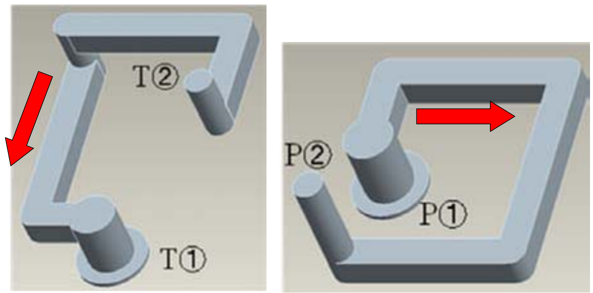

(a) Laminated 2-T (b) Laminated 2-P

Figure 7 Flow channels in laminated 2
(like solid type)

Analysis objects are the above six flow channels. In this paper, we analyze them by FLUENT6.3. SST k-ω model is used for turbulence model along the lines of the study in last year [1]. Inflow boundary condition is set to velocity inlet (uniform flow), and outflow boundary condition is set to pressure outlet (0[MPa]). Those flow channels contain tetrahedral and hexahedral cells. Properties of working fluid is ρ=870[kg/m^3], and ν is =32[mm^2/s] where T=317[K] (40 degrees).

Results of Analysis

Figures 8 (a), (b) show pressure on central axis of flow channel in Q=50[L/min]. The vertical axis shows the remainder of pressure (p) on central axis and outlet pressure (p_e). Central axis of solid type is shown in figures 9 (a), (b). From figures, pressure drop at corners is the majority of pressure drop of flow channel in all types. Pressure drop of solid type at corners is different from each other, so it is found that the distance to previous corner and the bend angle of previous corner affect pressure drop in solid type. Laminated 1 and 2 have less pressure drop than solid type. When laminated 2 is compared with solid type, pressure drops of laminated 2 at corners are smaller than that of solid type. This is because laminated type has lager sectional area than solid type even if their flow channels have the same width.

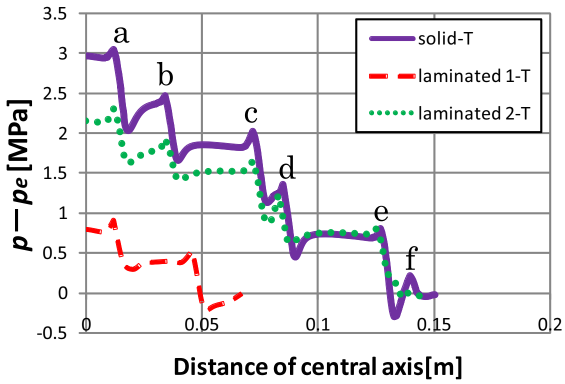

(a) Pressure of flow channels T

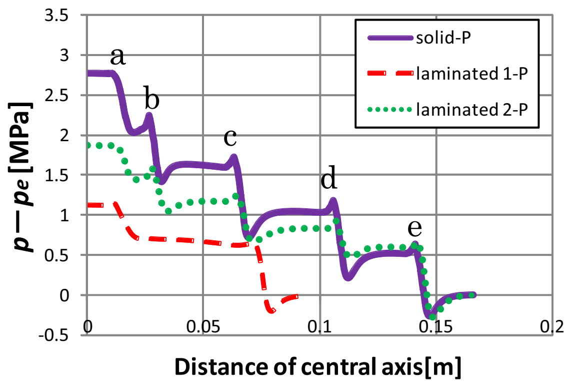

(b) Pressure of flow channels P

Figure 8 Pressure on central axis of flow channels

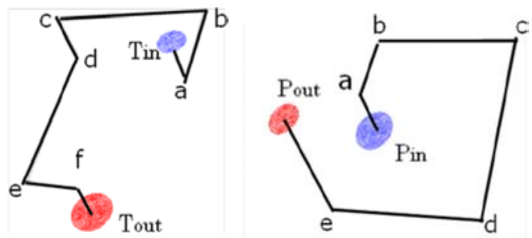

(a) solid-T (b) solid-P

Figure 9 Central axis of solid type

Figures 10 (a), (b) show velocity vectors of entire flow channels of solid type in Q=50[L/min]. Figures 11 (a), (b) show velocity vectors on cross sections of corner d and e in figure 10 (a). Figures.12 (a), (b) also show velocity vectors on cross sections of corner b and d in figure 10 (b).

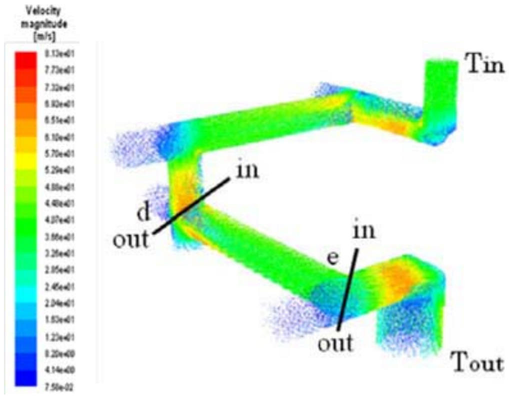

(a) Velocity vectors of solid-T

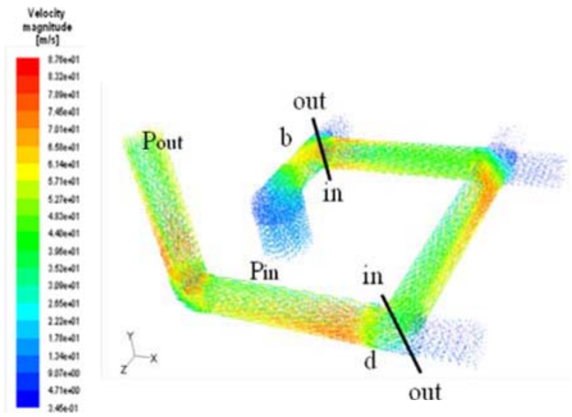

(b) Velocity vectors of solid-P

Figure 10 Velocity vectors of solid type

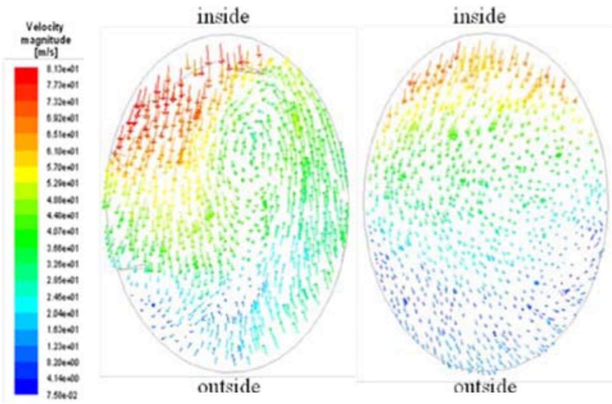

(a) Cross section b (b) Cross section d

Figure 11 Velocity vectors on cross section of solid-T

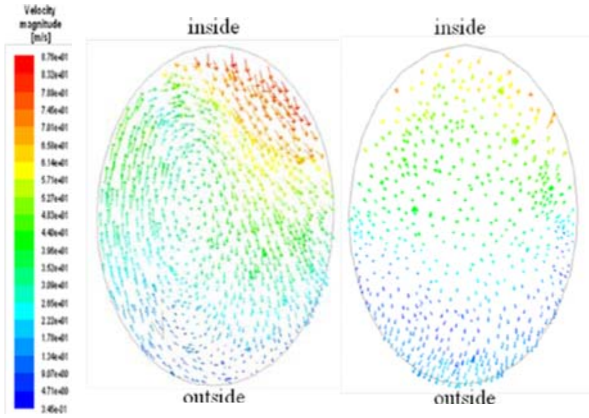

(a) Cross section P1 (b) Cross section P2

Figure 12 Velocity vectors on cross section of solid-P

It is found that there are regions of large velocity (red regions in figures) after corners from figure 10, and velocity vectors like vortex are seen in figure 11 (a), figure 12 (a), but not seen in figure 11 (b), figure 12 (b). This is because the distance from corner c to d is shorter than the distance from corner d to e in Solid-T, and the bend angle of upstream corner is different from each other in corners b and d of Solid-P.

Influence of the upstream corner on pressure drop at the downstream

To investigate the influence of the upstream corner on flow pattern described above, we propose three flow channels as shown in figure 13. These channels have two corners. In this paper, the upstream corner is named corner A and the downstream corner is named corner B. They are different from the angle θ between inlet and outlet pipeline. Moreover, by varying the length L between corner A and B, we examine the influence of θ and L on pressure drop at corner B, where volumetric flow rate is Q=50[L/min] and all pipe diameter is d=6[mm].

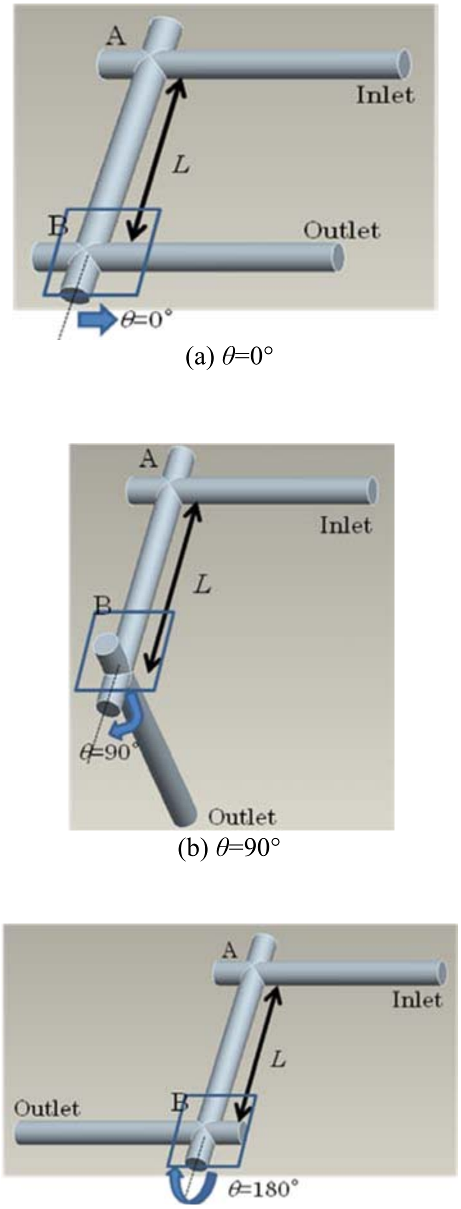

(a) θ=0°

(b) θ=90°

(c) θ=180°

Figure 13 Flow channels with two corners

To evaluate the influence of θ and L on pressure drop, pressure drop at corner B p_B is defined as follows.

$$p_B = p_{all} - (p_A + p_f) \quad (1)$$

where p_{all} is the pressure loss of all pipeline, p_A is the pressure loss at corner A, p_B is the pressure loss at corner B, and p_f is the friction loss of pipeline. Furthermore, pressure loss coefficient ζ, which is dimensionless quantity, is defined as follows.

$$\zeta = p_B / \{(1/2)\rho u^2\} \quad (2)$$

where ρ is the density of fluid (oil), u is the mean flow velocity, and u=29.47[m/s] for volumetric flow rate Q=50[L/min] and pipe diameter d=6[mm].

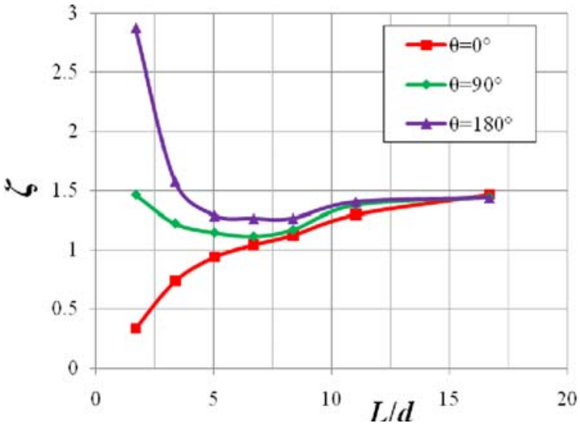

Figure 14 Relations between ζ and L/d for each θ

The results is shown in figure 14. Horizontal axis L/d shows ratio between L and d. From figure 14, it is found that the transition of ζ differ by θ, especially in case of L/d<5,and ζ approach a constant value for L/d>13 in any θ. In case of θ=90° and 180°, ζ is minimized for $L/d \approx 6$, while, in case of θ=0°, the smaller L/d is, the smaller ζ is.

EXPERIMENT

Experimental Apparatus and Method

We manufacture port converter of manifold blocks (test piece) that have the same flow channel that is used in CFD analysis, and prepare experimental apparatus for measuring pressure shown in figures.15 (a), (b). These manifold blocks are attached to blocks for connecting electronic pressure sensors, a block for returning oil flow from B to T or from P to A, electronic pressure sensors, A/D converter, and 24 [V] power supply.

Data of voltage are transmitted from pressure sensor to A/D converter and converted to pressure data. In this paper, pressure drop of each flow channel is defined as the pressure gap of upstream data and downstream data. By comparing with experimental results, we verify the validity of the CFD results. Temperature of working oil is about 40 degree to fit condition of CFD analysis.

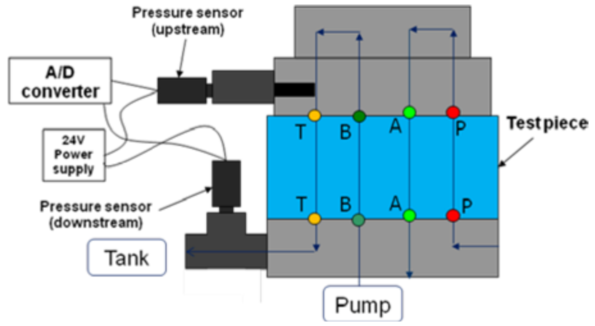

(a) Pressure measurement of flow channels of T

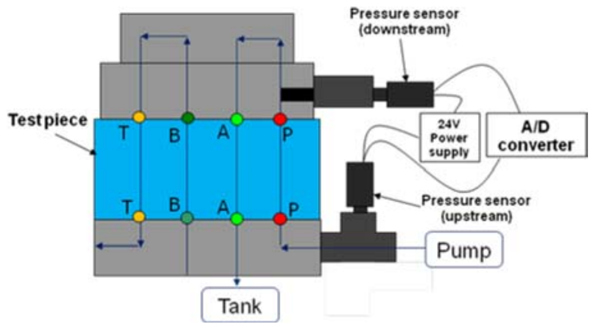

(b) Pressure measurement of flow channels of P

Figure 15 Experimental apparatus for measuring pressure

Comparison of Analysis with Experiment

Figures 16 (a), (b) show the relations between volumetric flow rate and pressure drop of solid type. Figures 16 (c), (d) show the relations between flow rate and pressure drop of laminated type.

In solid type, there is a tendency that experimental values are about 15 percent smaller than CFD results from 20[L/min] (Reynolds number is about 2,200) to 70[L/min] (Reynolds number is about 7,700). Reynolds number is based on pipe diameter, the mean velocity of flow, and kinetic viscosity. So it is found that it is possible to regard pipe flow in solid type as turbulent flow even if Reynolds number is small in case flow channel has many corners. In laminated type, experimental values show good agreement with CFD results except laminated 1-T. In laminated 1-T, the more the flow rate increase, the larger the error between experimental values and CFD results.

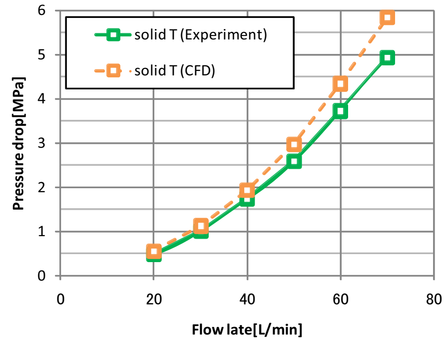

(a) Solid-T

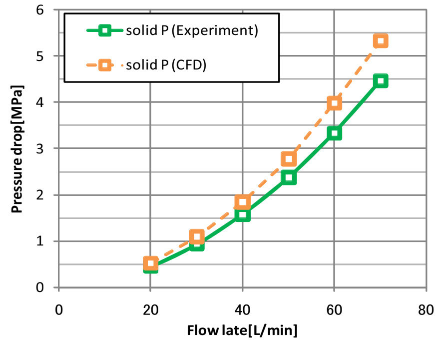

(b) Solid-P

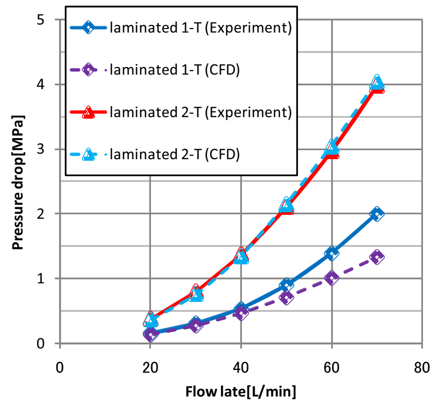

(c) Laminated 1-T and 2-T

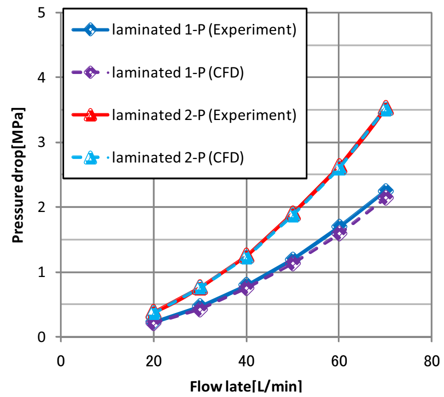

(d) Laminated 1-P and 2-P

Figure 16 Relations between flow rate and pressure drop

So when we manufacture an acrylic test piece of laminated 1 and observe oil flow in laminated 1 to investigate factors, luminescence by heavy cavitation [2] is seen at a red circle in figures 17(a), (b) in case of more than 50[L/min]. This is the factor of the error. Figure 17 (a) shows a direction for visualization of laminated 1-T. A picture of cavitation is shown in figure 17 (b).

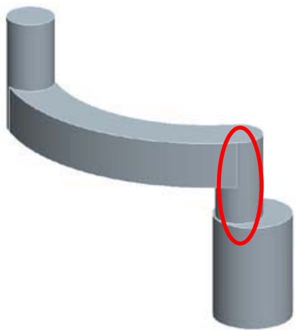

(a) Direction for visualization of laminated 1-T

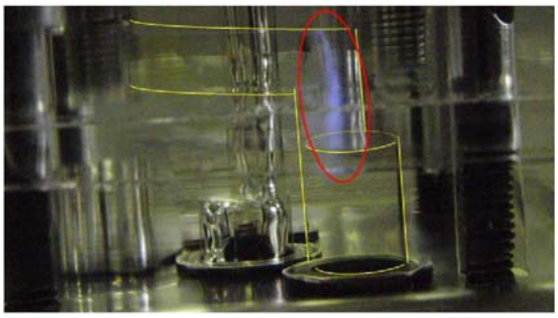

(b) Picture of cavitation

Figure 17 Luminescence by heavy cavitation

CONCLUSIONS

This paper focuses on estimation of pressure drop of pipe flow in two types of manifold block with CFD analysis, verification of the validity of CFD results by comparison with experimental results, and obtainment of guidelines for pipeline design in a manifold block. Also, we investigate pipe flow from velocity vectors, pressure distribution, and pressure drop. The conclusions of this paper are as given below.

(1) Pressure drop at corners is the majority of pressure drop of pipe flow in manifold block.
(2) At corners of solid type, pipe flow pattern is varied by the distance L and the angle θ, which affect pressure drop at corners.
(3) Pressure drop of laminated type is smaller than that of solid type because laminated type has lager sectional area than solid type even if their flow channels have the same width.
(4) Unless heavy cavitation occurs, it is proved that estimate of pressure drop with CFD is valid by comparison with experimental results.

REFERENCES

1. Takeshi Hara, Research on pipe flow in a manifold block, The Proceedings on Spring Conference of Fluid Power System Society, 2010, pp 4-6.
2. T. G.LEIGHTON, M.FARHAT, J. E.FIELD and F.AVELLAN, Cavitation luminescence from flow over a hydrofoil in a cavitation tunnel, Journal of Fluid Mechanics, No.480, pp.43-60 (2003)

Proceedings of the 8th JFPS International
Symposium on Fluid Power, OKINAWA 2011
Oct. 25-28, 2011

1C2-2

A STUDY ON THE RELATION BETWEEN UNPREDICTABLE VIBRATION OF HYDRAULIC EXCAVATOR AND DESIGN PARAMETERS OF TRAVEL MOTOR USING 1-D HYDRAULIC SYSTEM ANALYSIS

Jae-Seok LEE*, Pan-Young KIM*, Lim-Gook CHOI**, and Min-Hee LEE**

*Construction Equipment Research Department, Product Development Research Institute,
Hyundai Heavy Industries Co., Ltd., Korea
(E-mail: jaeseok@hhi.co.kr)
**Advanced Technical Department, Construction Equipment Division,
Hyundai Heavy Industries Co., Ltd., Korea

ABSTRACT

A travel motor is the main component of an excavator as an energy translator from hydraulic to mechanical system. Abnormal vibration tends to happen when the excavator starts to travel downward on the slope. It is expected that the vibration is subjected to the reciprocating motion of the main spool in the counter balance valve which is designed to control the flow rate to the travel motor. In this paper, the relation between the abnormal vibration and main design parameters of counter balance valve is evaluated based on 1-D analysis method. As a result, it is found that the abnormal vibration mainly depends on the spring stiffness coefficient and the opening area of the main spool notch and can be controlled by the appropriate combination of the parameters. Optimum design parameters are determined from the analysis and verified with the test results.

KEY WORDS

Excavator, Travel motor, Counter balance valve, Abnormal vibration, 1-D hydraulic system analysis

INTRODUCTION

The travel motor, which directly transmits torque to the travel reduction gear, takes an important role in driving stability and ride comfort of an excavator as shown in Figure 1. Because of its importance, there is a counter balance valve in the travel motor while most other hydraulic components are just controlled by the main control valve. In general, while the excavator is travelling downhill slowly, the counter balance valve makes the rotating speed of the traveling motor stable by controlling translation motion of the main spool in the counter balance valve.

Figure 1 Travel motor of an excavator

The translation motion of the main spool is determined by the combination of hydraulic pressure, spring stiffness coefficient, and cushion spool. Therefore, in design consideration of the counter balance valve, the spring, the cushion spool for main spool movement control and the opening area of the main spool notch for the flow path will be the main design parameters. In addition, the interference between the parking brake and counter balance valve shall be determined as well. In this paper, by using the 1-D hydraulic analysis method, the abnormal vibration mechanism during the downward travelling of an excavator will be determined and the contribution of the main design parameters to the overall performance enhancement will be analyzed as well.

HYDRAULIC SYSTEM MODELING

The flow diagram of the working fluid to operate the travel motor is shown as Figure 2(a). In brief, the discharge flow rate from the main pump, which is determined by the spool stroke in the main control valve operates the travel motor and is returned to the tank through the main control valve again. The spool stroke, which makes the travel motor work by controlling the opening area, is controlled by the pilot pressure of the remote control valve. Figure 2(b) shows the schematic diagram of the path for the energy transfer from the engine to travel motor via the hydraulic system.

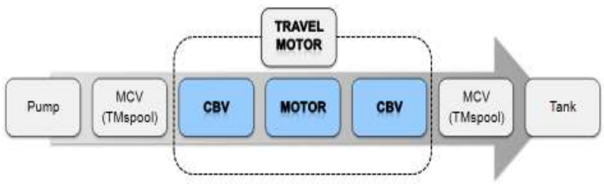

(a) Schematic of hydraulic circuit

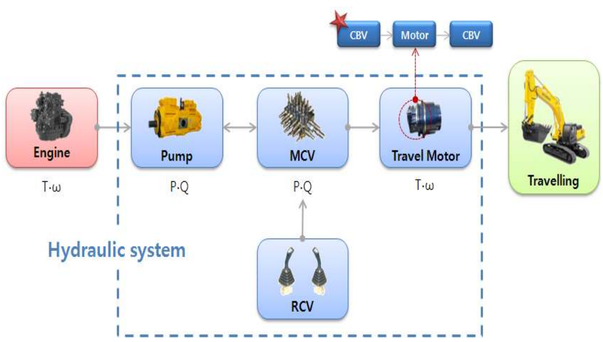

(b) Path for the energy transfer

Figure 2 Flow line of working fluid

Figure 3 shows the hydraulic system model which consists of hydraulic components from the main pump to the travel motor. In this 1-D analysis model, the counter balance valve has been modeled in detail using the hydraulic component design (HCD) library in AMESim because it governs the characteristic of the travel motor when the excavator travels downhill. In addition, in order to express the condition for downhill travelling, the torque value caused by the weight of the excavator was applied to the travel motor as an external input condition.

The flow rate of the main pump in an excavator is basically controlled by a regulator which consists of negative flow control, total horsepower control, and power shift control system. In negative flow control, the discharge flow rate decreases as the pilot pressure rises. In total horsepower control, the discharge flow rate is simultaneously controlled by the sum of the load pressure of the two pumps in tandem double arrangement. In this analysis model, the main pump is simply modeled by handling the negative control and total horsepower control as signal processing.

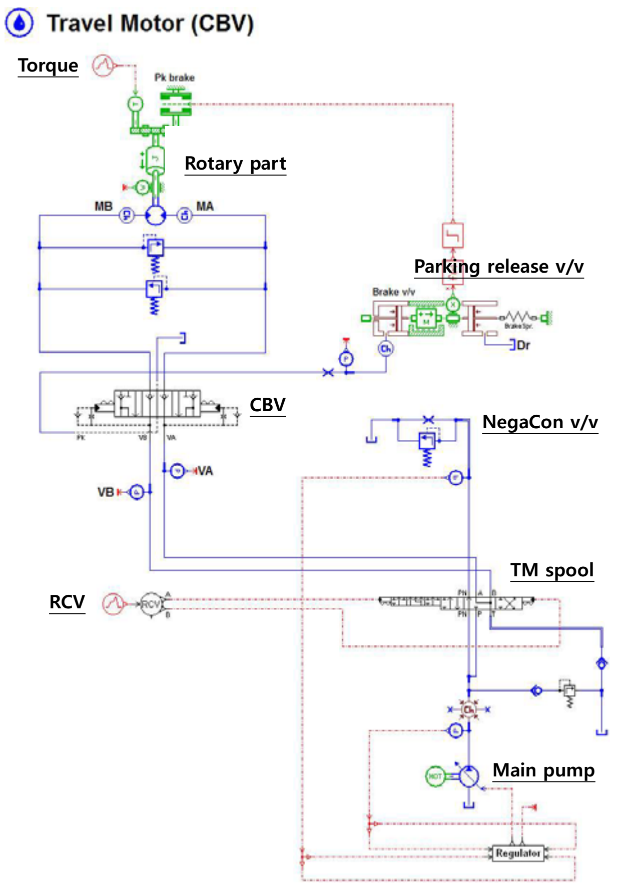

Figure 3 Analytical model of the hydraulic system using AMESim

Details of the counter balance valve modeling

The main roles of the counter balance valve are as follows: parking brake release, motor control when driving on the slope, rapid response in sudden stop. All of the features of the counter balance valve are related to safety, because the travel motor is located far distant from the main control valve, and as a sequence, the compressibility of the working fluid may cause accidents. Therefore, the design process of counter balance valve is the most important part for achieving an excellent performance of the travel motor. In order to accurately simulate the characteristics of the counter balance valve, the HCD modeling was carried out using AMESim based on the sectional drawing as shown in Figure 4(a). As shown in Figure 4(b), it can be inferred that the main design parameters of the counter balance valve could be the stiffness coefficient of the main spring, the opening area of the main spool notch, the characteristics of the cushion spool and the orifice diameter from main chamber to pressure sensing chamber, etc. By using this HCD modeling, the dimensions of the main design parameter can be easily controlled and the parametric study for performance enhancement can be carried out as well.

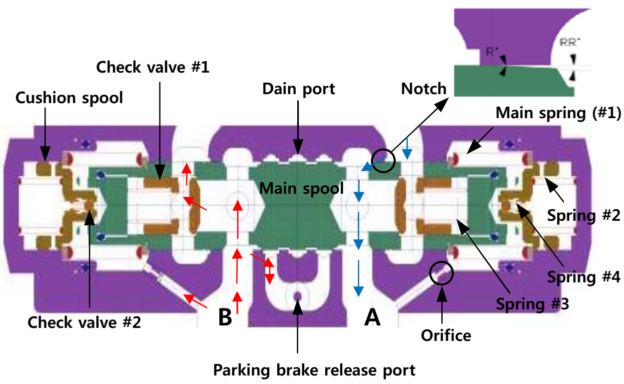

(a) Sectional drawing

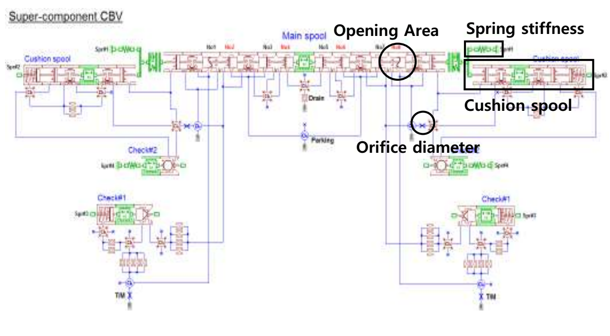

(b) AMESim modeling

Figure 4 Hydraulic modeling of the counter balance valve

RESULTS OF THE ANALYSIS

Verification of the hydraulic system model

First of all, in order to validate the hydraulic system model, pre-analysis was performed for Mode 1, as shown in Table 1, where the remote control valve signal is almost same to the one from the experiment. Every simulation condition is set up to the 2nd gear mode, which is more sensitive to inertia force of an excavator than the 1st gear mode. Especially, on the slope the abnormal vibration can occur on the 2nd gear mode. The simulation results were compared with the experimental results as shown in Figure 5. The estimated results for the initial pressure when the motor just starts moving, and the brake pressure when the motor suddenly stops moving, show good agreements with the experimental results. In those plots, inlet pressure of the travel motor is drawn as red line and outlet pressure of the travel motor is drawn as blue line.

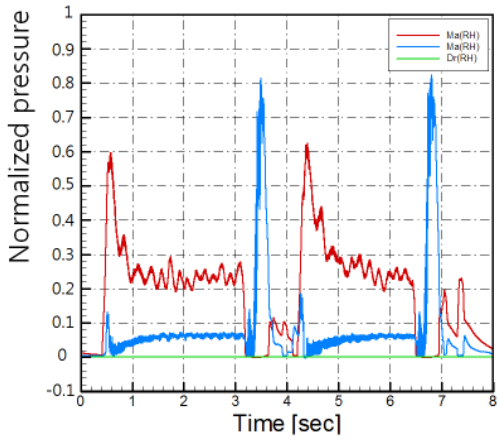

(a) Experiment

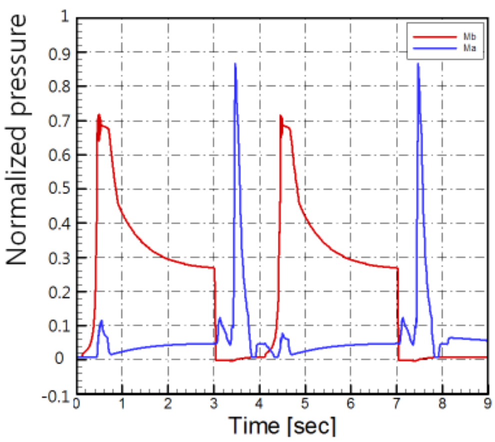

(b) Simulation

Figure 5 Comparison of pressure history in the ground traveling condition

Abnormal vibration mechanism

In order to reveal the mechanism of the abnormal vibration caused by the weight of excavator on the downhill, the unstable condition was studied by using the proven system model. In this analysis, the torque corresponding to 20 degrees inclination was applied to the travel motor and the constant pressure signals of the remote control valve were applied as shown in Mode 2 of Table 1.

Table 1 Boundary conditions of the hydraulic system analysis

Traveling (2^{nd} gear mode)		RCV input signal	Torque
Mode 1	Ground	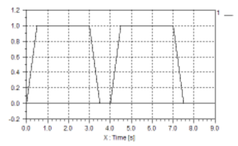	0
Mode 2	Slope	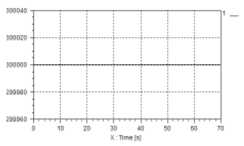	500 (θ=20˚)

Figure 6 shows the two simulation results of the specific cases. The abnormal vibration, caused by applying improper design parameters, is simulated in Case1 and a modified model to remove the abnormal vibration is simulated in Case 2 as well. From the analysis results of Case 1, the abnormal vibration is considered to be caused by the external torque, occurred by the reciprocating motion of the main spool in the counter balance valve in a specific operating range. For the reciprocating motion of the main spool, the opening area of the main spool notch determines the rotating speed of the travel motor. In addition, if the reciprocating motion is larger as shown in Figure 6(a), the interference with parking brake occurs and it makes the parking brake ON/OFF by transferring the parking brake release pressure signal as shown in Figure 6(b). Therefore, the abnormal vibration of the travel motor occurs as shown in Figure 6(c) causes negative effects on the driving stability and ride comfort of an excavator. Inspiritingly, the abnormal vibration does not occur in Case 2 as a sequence of modifying the main design parameter such as main spring stiffness, opening area of the main spool notch, and cushion spool. Consequently, the abnormal vibration phenomena of a traveling motor can be prevented by controlling the main design parameters. Finally, by the hydraulic system analysis, the specific and unstable condition was successfully simulated and the contribution of the design parameters to the counter balance valve was analyzed.

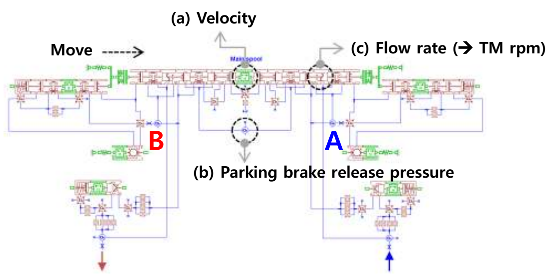

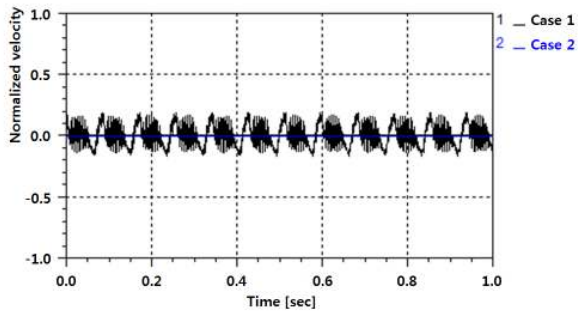

(a) Velocity of the main spool

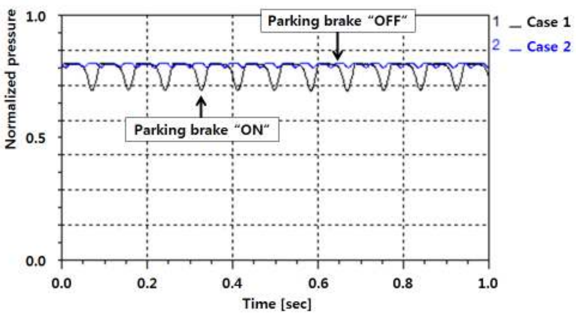

(b) Parking brake release pressure

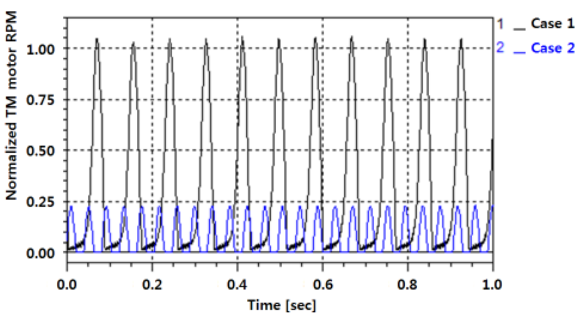

(c) Rotating speed of the travel motor

Figure 6 Comparison of simulation results in the slope traveling condition

CONCLUSION

By using the hydraulic analysis method, the abnormal vibration mechanism during the downward travelling of a mid-class excavator was revealed.

- In order to predict the performance of the travel motor, the hydraulic system has been modeled and was verified by comparing with the experimental results.
- For the abnormal vibration which can happen on the downhill, the contribution of the main design parameters to the overall performance enhancement has been analyzed.
- By using the hydraulic system analysis in the basic design process, the overall performance of the excavator travel motor can be evaluated and especially, the abnormal vibration on the downhill can be simulated and prevented in advance.

REFERENCES

1. D. S. Jang and Y. L. Cho, Improvement of Excavator Rode Comfort through Test and Analysis, Journal of the Korea Fluid Power System Society, 2004, pp.8-15.
2. ISO 2631-1, Mechanical vibration and shock-Evaluation of human exposure to whole-body vibration, 1997.
3. E. C. Fitch and I. T. Hong, Hydraulic Component Design and Selection, BarDyne, Inc., 1997.
4. E. C. Fitch and I. T. Hong, Hydraulic System Modeling and Simulation, BarDyne, Inc., 1997.
5. AMESim User's Manual, 2009.

Proceedings of the 8th JFPS International
Symposium on Fluid Power, OKINAWA 2011
Oct. 25-28, 2011

1C2-3

RESEARCH ON A PARAMETER SELF-TUNING ELECTRO-HYDRAULIC PROPORTIONAL CONTROLLER

Yong NIE and Qingfeng WANG

The State Key Lab of Fluid Power Transmission and Control
Zhejiang University
Room402, State Key Lab of Fluid Power Transmission and Control, Zhejiang University,
Hangzhou, Zhejiang Province, 310027 P. R. China
(E-mail: nyong168@126.com)

ABSTRACT

The proportional controller is widely employed in the electro-hydraulic control system. Because of various proportional solenoids have different resistance and inductance, a proportional controller can't matching them very well. In order to improve the application range of proportional controller, a parameter self-tuning electro-hydraulic proportional controller is proposed, which can auto identify the proportional solenoid parameter and control the current very well.

KEY WORDS

Proportional amplifier, System identification, Internal mode control (IMC)

NOMENCLATURE

L	*the equivalent inductance of proportional solenoid*
R	*the equivalent resistance of proportional solenoid*
i(t)	*current of proportional solenoid*
u(t)	*u(t) is the voltage of proportional solenoid*
T	*PWM period* ...
K_{PWM}	*gain of PWM modulator*
U	*power volatage*
e(t)	*the steady-state error*
Γ	*the total time..*

INTRODUCTION

The electro-hydraulic proportional controller is an important part of an electro-hydraulic proportional system. It's used to provide specific current for proportional solenoid, and control the proportional valve. Because various proportional solenoids have different resistance and inductance, a traditional controller which does not allow user to adjust the current control loop parameters can't match them very well. This dissert proposes a parameter self-tuning electro-hydraulic proportional controller for improve the application range of proportional controller.

PROPORTIONAL SOLENOID CURRENT

CONTROL LOOP PARAMETER SELF-TUNING SCHEME

Model of proportional solenoid current control loop

The structure of proposed proportional solenoid current control loop is show in Fig.1, and the main parts are linearly modeled as follow.

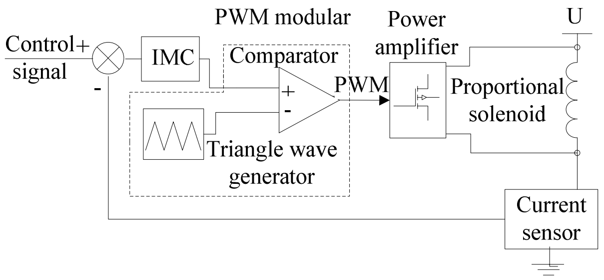

Figure1 the structure of proportional solenoid current control loop

1) Proportional solenoid model: because the response of the proportional current is faster than the armature movement, the EMF caused by the armature motion can be ignored. The model of the proportional solenoid is

$$\mathrm{Gs}(s)=\frac{\mathrm{I}(s)}{\mathrm{U}(s)}=\frac{1}{\mathrm{L}s+\mathrm{R}} \tag{1}$$

2) PWM modulator: the duty of PWM is changed once in a control period, and the modulation frequency is high. The transfer function of the PWM modulator is[1]

$$\mathrm{G}_{\mathrm{PWM}}(s)=\frac{\mathrm{K}_{\mathrm{PWM}}}{\mathrm{T}s+1} \tag{2}$$

The PWM signal is produced by input signal compared with the triangular wave generator. The amplitude of the triangular wave generator is form 0 to A_1. When the input signal are 0 or A_1, the output PWM duty are 0 or 1, so there is

$$\mathrm{K}_{\mathrm{PWM}}=\frac{1}{\mathrm{A}_1} \tag{3}$$

3) Power amplifier: because the control objective of the system is average current, and the PWM modulation frequency is high. The ratio of the average voltage and the PWM duty can be written as

$$\mathrm{K}_{\mathrm{u}}=\mathrm{U} \tag{4}$$

Design of Internal Model controller (IMC)

In order to facilitate tuning parameters, the internal model control (IMC) algorithm is applied to control the proportional solenoid current. The IMC structure of a signal input and output (SISO) system is show in Fig.2, where R(s) is control signal input, C(s) is the controller, P(s) is controlled plant, $\tilde{\mathrm{P}}(s)$ is the Denoting model of the controlled, Y(s) is the measurement signal. [2][3]

$$F(s)=\frac{C(\mathrm{s})}{1-C(\mathrm{s})\tilde{P}(s)} \tag{5}$$

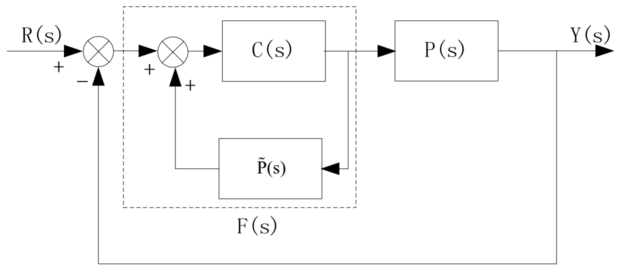

Figure 2 Structure of IMC

Base on the Eq. (1) ~ (4), the proportional solenoid, PWM modulator and power amplifier are merged,

$$\tilde{P}(s)=\frac{\mathrm{b}_0}{s^2+\mathrm{a}_1 s+\mathrm{a}_2} \tag{6}$$

where $\mathrm{b}_0=\frac{\mathrm{U}}{\mathrm{A}_1\cdot\mathrm{T}\cdot\mathrm{L}}$, $\mathrm{a}_1=\frac{\mathrm{T+L}}{\mathrm{T}\cdot\mathrm{L}}$ and $\mathrm{a}_2=\frac{\mathrm{R}}{\mathrm{T}\cdot\mathrm{L}}$.

Based on the properties of the ideal IMC, the controller is designed as

$$\mathrm{C}(s)=1/\tilde{\mathrm{P}}(s)=\frac{s^2+\mathrm{a}_1 s+\mathrm{a}_2}{\mathrm{b}_0} \tag{7}$$

To ensure that the controller can be realized and improve the robustness of the control system, a second-order low-pass filter is in series before Eq. (7), which is

$$L(s)=\frac{1}{(\lambda s+1)^2} \tag{8}$$

The Eq. (7) and Eq. (8) were merged as the IMC of the current loop, which is

$$C'(s)=\frac{s^2+a_1 s+a_2}{b_0\lambda^2 s^2+2b_0\lambda s+b_0} \quad (9)$$

where just the parameter λ needs to tuning. The parameter λ impact on the rapidity and robustness of the system. Reduced the λ can speed up system response speed, and increasing the λ can enhance the robustness. Parameter λ is the selection which is the robustness and rapidity trade-off. The controller requires that improving the response speed under the premise of small steady-state error, so parameter optimization index is integral of the product of the time and the absolute error (ITAE)

$$J=\int_0^{\Gamma} t\left|e(t)\right|\mathrm{d}t \quad (10)$$

The parameter λ is optimization by the NLJ method. [4]

Proportional solenoid Current loop control parameter self-tuning algorithm

Step 1: Applied a constant power voltage across the proportional solenoid, sampling the voltage and current, and according Eq. (1), then the L and R of the proportional solenoid can be identified.

Step2: The a_1, a_2 and b_0, which are calculated by the U, A_1, T, R and L, are substituted into Eq. (9). Then, the parameter λ is optimization by NLJ method.

Step3: The parameter which has been tuning is applied to control the proportional solenoid for step response. Recording the control signal and the actual current value, the ITAE index is studied. If the ITAE index meets the requirement ,the controller parameter has been finished tuning; if that does not meet the requirement, the difference between the model parameters identified and the real value are too large, then we need to return to step 1.

EXPERIMENTAL INVESTIGATION

The purpose of this experiment is to study the performance of current control which was proposed based on internal model control. The type of proportional solenoid employed in the experimental investigation is '045' (GP61-4-A) from Ningbo HOYEA Machinery Manufacturer Co., ltd. The main parameters are that: the PWM period is 2kHz, current control period is T=0.0005s, the control parameter is λ=0.05, the power voltage is U=24v. The proportional solenoid parameters identification results are that: resistance is R=13.504, and inductance is L=0.201H. The above parameters are assigned to the proposed parameter self-tuning control algorithm. The up-step from 100 mA to 800 mA is done. The results are shown in Fig. 3, we can conclude that: the current steady-state error is ± 6mA, and the overshoot is small.

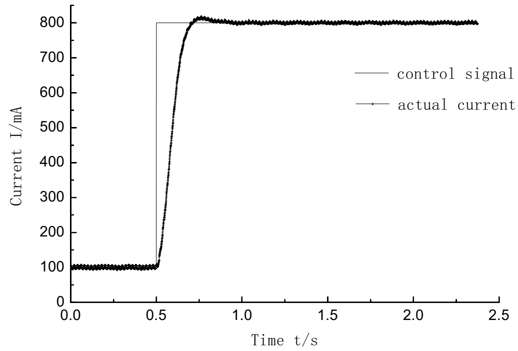

(a) step response

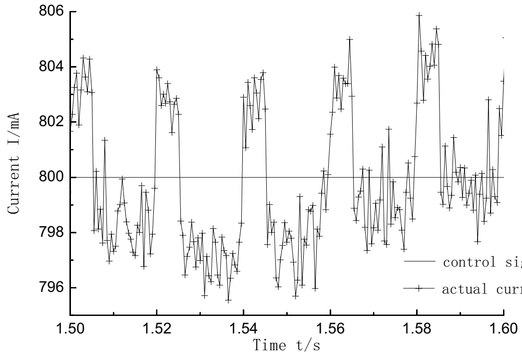

(b) Local Enlargement

Figure 3 Current step response

CONCLUSIONS

Based on internal model control principle, a parameter self-tuning electro-hydraulic proportional controller structure and a parameter self-tuning algorithm were proposed. Finally, the proposed structure was experimentally researched on the test bench and the results showed that: the proposed proportional controller can automatically identify the parameters of proportional solenoid coil, and the control parameter can be automatically tuning. The proposed controller can automatically match the different types of proportional solenoid.

REFERENCES

1. Zhang Chongwei, Zhang Xing. PWM Rectifier and Control. Beijing,China Machine Press, 2002
2. Carlos E.Garcla, Manfred Morarl. Internal Mode Control-1. A Unifying Review and some new results. Ind. Eng. Chem. Process Des. 1982, 21
3. Danlel E. Rivera, Manfred Morarl, Slgurd Skogestad. Internal Model Control- 4. PID Controller Design.

Ind. Eng. Chem. Process Des. 1986, 25
4. Pan Lideng. An improvement in optimal tuning method with Least Performance Index. Control and Instruments In Chemical Industry. 1985, 12(1)

Proceedings of the 8th JFPS International
Symposium on Fluid Power, OKINAWA 2011
Oct. 25-28, 2011

1C2-4

AN EXPERIMENTAL INVESTIGATION ON SWASH PLATE CONTROL TORQUE OF A PRESSURE COMPENSATED VARIABLE DISPLACEMENT INLINE PISTON PUMP

Rathindranath MAITI and Paritosh NARAYAN

Department of Mechanical Engineering
Indian Institute of Technology, Kharagpur
721302, India
(Email : rmaiti@mech.iitkgp.ernet.in)

ABSTRACT

To avoid or to reduce the costs of experiments, analysis by simulation is preferred to predict the performance in design and development stages. However, accurate modeling and then remodeling after part experiments are usual practice. In in-line piston swash plate type variable displacement pump with pressure compensation swash plate dynamics has a crucial role on pump performance – particularly at the vicinity of operation at set pressure. The present investigation is targeted at understanding the reasons of such dynamics. A commercially available pump was chosen for study. The swash plate control torque and relevant data were measured experimentally in a proven test rig. Analysis was made to identify the various forces that give rise to the cradle or swash plate torque about its pivot in a pump. A simplified and concise model was finally developed and simulation was carried out in MATLAB-SIMULINK environment. Analytical results had good agreement with experimental results.

KEY WORDS

Inline Piston Pump, Pressure Compensated, Swasplate Control Torque

INTRODUCTION

In line linear piston pumps with swash plate are widely used in both military and civil fluid drive applications. For accurate flow control, particularly in sophisticated applications, the swash plate yawing torque has a great role. Over last fifty years several investigations are carried out globally to understand, assess and optimize the swash plate contol torque.

Lewis & Stern [1], Green & Crossley [2], and Zaki & Baz [3] have analyzed the dynamic response of various types of conventional control systems for in-line linear piston pumps (hence forth mentioned only as pump / pumps) following Merritt's [4] approach and using linear transfer function analysis. Most of the models were devoted to the specific control system with simplified linear model representation for the pump. Such models did not incorporate the effect of different geometrical features or the variations in operating conditions.

Yamaguchi [5, 6] investigated considering more complex parameters of the hydraulic pump model. The subject of loads on the swash plate was treated from the point of view of power losses. However, he too presented a linear model of a hydraulic pump. He considered the effect of load pressure on the pump dynamics, although based on a pump with simplified configuration.

Zeiger & Akers [7] and later with Lin [8] presented a comprehensive mathematical model for the average torque on the pump swash plate. The analysis was limited to steady state conditions only.

Zeiger & Akers [9] also analyzed the pump dynamics as an open loop plant to be controlled. The analysis followed a state variable approach in place of a simpler classical approach of transfer function.

Schoenau, Burton & Kavanagh [10, 11] investigated in detail the characteristics of such a pump with pressure compensated swash plate control (Vickers PVB5 Model). They developed a comprehensive mathematical model capable of predicting both steady state and dynamic responses. Inertial and viscous damping terms as well as the control-piston and return-spring dynamics were considered in details. Experiments were conducted in support of the theoretical analysis.

Manring [12] developed a mathematical model to depict the dynamic characteristics of torque exerted on the input shaft of the pump. The approach used was different from understanding this torque with traditional macro input-output perspectives. In his analyses he considered all basic forces within the machine to compute the instantaneous torque exerted on the shaft. Manring further analyzed the control and containment forces and moments acting on the swash plate of an axial-piston pump [13].

Later Zhang , Cho & Nair with Manring [14] presented a new, open-loop, reduced order model for the swash plate dynamics of an axial piston pump. The proposed reduced order model is validated by comparing with a complete nonlinear simulation of the pump dynamics over the entire range of operating conditions.

Zeliang [15] in association with Burton [11] worked on condition monitoring of an axial piston pump (Vickers model) for his M.Sc. thesis. Results of this investigation are very useful to understand the pump as well as swash plate performances.

To understand the swash plate control torque in a better way we considered a Vickers PVB5 model, apparently the same model that was used by Kavanagh et al. [10, 11]. Experiments were conducted following civil and military specifications [16]. Later we have also tried to present a concise mathematical model and carried out simulation, following some of the investigations referred above, in support of our experimental results [17]. The experiments have been conducted on a proven test rig which is regularly used to test such hydrostatic units for civil as well as military applications. This paper is a brief report of the investigation.

MATHEMATICAL MODEL FOR SWASH PLATE CONTROL TORQUE

A schematic view of the pump, considered for study, is illustrated in Figure 1. The total torque which acts on the swash plate yoke assembly consists of several components, namely torque due to pressure differences and locations of pistons (T_{ap}), the yoke damping torque (T_d), (in the negative direction), the return spring torque (T_{sp}) and the torque applied to the yoke by the control piston (T_{sp}) (in the negative direction). Therefore, taking a summation of the torques that act on the swash plate yoke assembly yields –

$$\sum T_y = -\vec{T}_{ap} - T_d + T_{sp} - T_c = I\ddot{\alpha} \quad (1)$$

where I is the mass moment of inertia of the swash plate yoke assembly. [17]

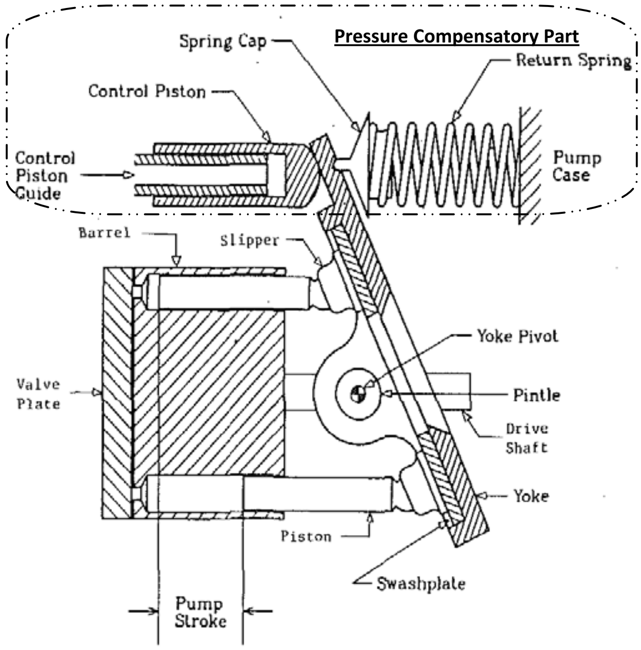

Figure 1 Model Feature of the Pump [11]

Substituting all expressions derived [17] for different torques and grouping of similar terms yields an equation of the form:

$$-P_c A_c b + K_{pr2}\Delta P_p + K_{pr3}\Delta p_p \alpha + C_1 + C_2\dot{\alpha} + C_3\dot{\alpha}^2 = I_e\ddot{\alpha} \quad (2)$$

Coefficient C_1 includes all terms that depend only on the angular position of the swash plate. C_2, the coefficient of angular velocity and C_3, the coefficient for the square of the angular velocity term [17].

I_e represents the total effective mass moment of inertia.

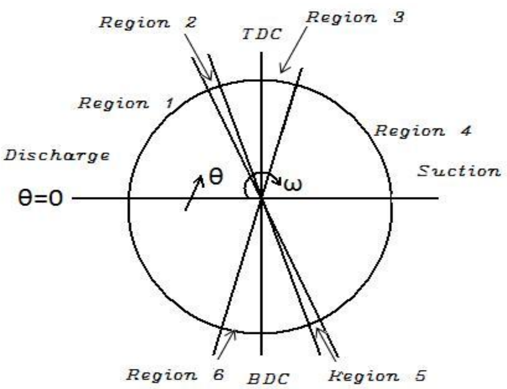

(a) Pressure regions as seen by piston centers [11].

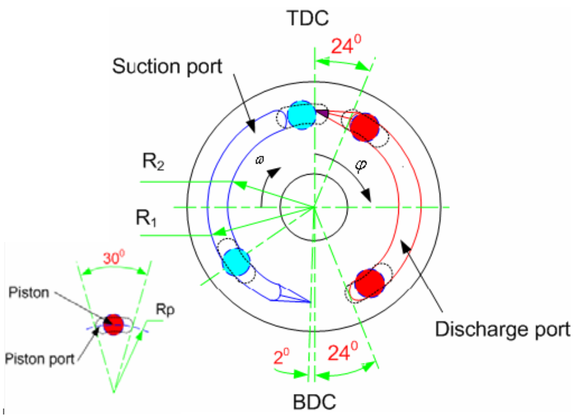

(b) Detail of valve port plate as in [15].
(It is almost similar to that
in the pump under study.)

Figure 2 Uni-Pressure Regions on Valve Plate

Simplified model.

Equation 2 is highly nonlinear if all terms are considered. However, it can be solved using numerical techniques although very unwieldy and cumbersome to.. The comprehensive developed model can be simplified by linearizing the equation set for torque due to piston pressure and the coefficient terms in the remaining describing equations by comparing the various terms in the coefficients and neglecting those terms deemed to have an insignificant effect.
The terms in the coefficient equations used in this study have been determined using the physical data of the pump (Vickers PVB5). Certain coefficients in the equation depend on the specific type of pump being used and some of these have to be experimentally measured. Based on the values over a range of swash-plate angles, equations of coefficients have been significantly simplified using linear regression techniques. The approach is justified at this stage because the dynamics of the swash plate have already been considered in their nonlinear form. Only the coefficients are simplified.
The coefficients C_1 and C_2 were fit using the equations

$$C_1 \approx S_1 - S_2\alpha \qquad (3)$$

and $$C_2 \approx S_3 \qquad (4)$$

where S_1, S_2 and S_3 are simplified Pump model Constants whose values have a maximum difference of less than 1 percent with Complete pump model Constants C_1, C_2 etc.

Value of C_2 is found to be a 0.549, thus $IC_2 >> IC_3(d\alpha/dt)I_{\max}$ implying that the term $C_3(d\alpha/dt)^2$ can be neglected and hence $C_3 \approx 0$.

Variation of the coefficient, I_e with α is small and can be neglected. Thus, the effective inertia can be assumed constant and equal to the average effective inertia

$$I_e \approx \bar{I}_e \qquad (5)$$

Substituting these results from equations (3) to (5) into equation (2) yields,

$$-P_c A_c b + K_{pr2}\Delta P_p + S_1 = (S_2 - K_{pr3}\Delta p_p)\alpha - S_3\dot{\alpha} + \bar{I}_e\ddot{\alpha} \qquad (6)$$

Above equation (6) represents the simplified mathematical model of the pump.
To verify the dynamic response of the model, Simulation of the Simplified Mathematical Model (equation 6)) has been done using MATLAB – SIMULINK ® and the simulated dynamic responses of the pump have been compared to those obtained experimentally.
While estimating the swash plate torque, pressure variations in the valve port and slipper pad were considered in detail [Figure - 2]. The developed equations are solved in light of the physical model of a pump to assess and estimate swash plate motions, in the dynamic and the steady state conditions. A SIMULINK block diagram is presented in Figure 3. The rig tests on pump model were carried out to examine the swash plate behavior. Finally, theoretical and experimental results were compared.

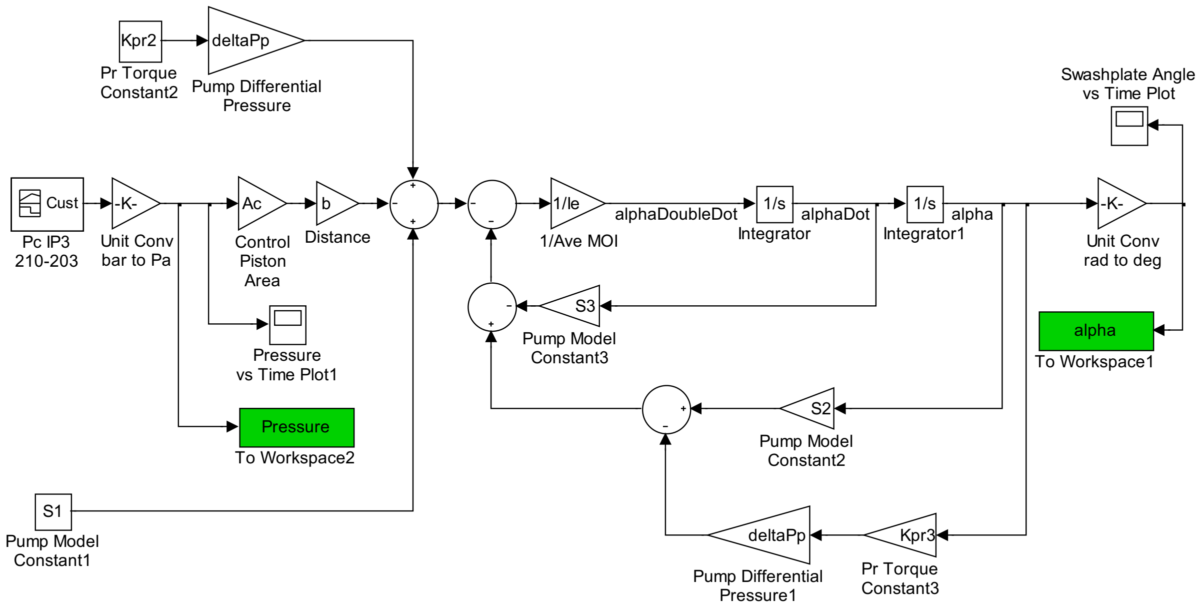

Figure 3 SIMULINK Model to Estimate the Swash Plate Torque.

Table – 1 Some specification of the pump (a commercial model).

Parameter		Numerical value
Delivery Pressure	Full flow	203 bar
	Zero flow (At set pressure)	210 bar
Flow rate		28 LPM
Inlet Pressure		2-3 bar
Case Drain Pressure		4.5 bar
Rated Speed		3600 RPM

Experimental Results

As stated earlier a well established and equipped test rig, which is regularly used to test such hydrostatic units for civil as well as military applications, is used for conducting experiments. Variation in Piston chamber pressure and change in port area (theoretically estimated) are shown in Figure 4 and Table 2 & Figure 5 respectively.

It is observed that the swash-plate angle α varied from 14 degree inclination to 0 degree inclination in almost 0.1 seconds where pressure varied from 210 bar to 203 bar respectively. The set pressure was 210 bar in pressure compensator. This means that when system pressure was raised to 210 bar the swash plate inclination was move to 0 degree by the control piston force [Figure 1] and the final position was maintained at 203 bar at main system line. With a slight reduction in set pressure the swash plate returned to its original inclined position (14 degree) and the system pressure was increase to new set pressure (close to 210 bar). The nature of change in swash-plate angle with time and pressure is shown in Figure 6.

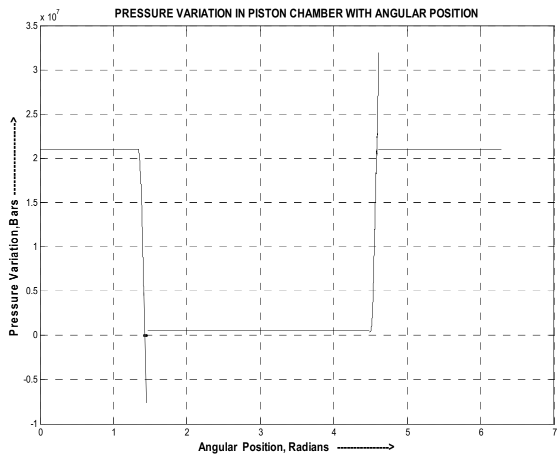

Figure 4 Variation in piston chamber pressure with shaft rotation.

The variation of swash plate angle has shown an expected trend. The initial sluggishness is expected for a change of system flow of the order of zero LPM to 28 LPM or vice-versa. This behavior may be observed for possible co-relation during steady-state loading-unloading of pump assembly.

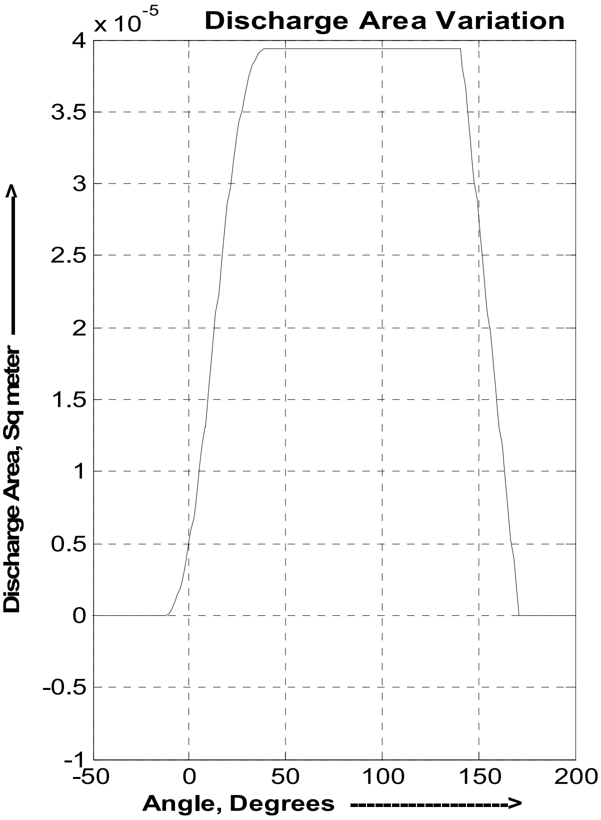

Figure 5 Port area opening with shaft rotation.

The preliminary analysis of response parameters of pump obtained during experimentation has been done. The comparison of response parameters with their limiting values for three pressure cycles is summarized below in Table 3.

It is observed that pressure pulsation (oscillation in steady state pressure value during operation) is moderately low and perhaps well within tolerable limits. The frequency associated with pump rotation and its higher multiples did not affect the steady-state behavior. The response time (response of a system to perturbation) is relatively high.

Table 2 Cumulative valve port opening area

Angle, Degrees	Discharge Area X 10^{-4} (m^2)
-13^0 to 9^0	0.0003 – 0.1314
9^0 to 17^0	0.1314 - 0.2492
17^0 to 39^0	0.2492 - 0.3934
39^0 to 141^0	0.3934
141^0 to 171^0	0.3934 - 0

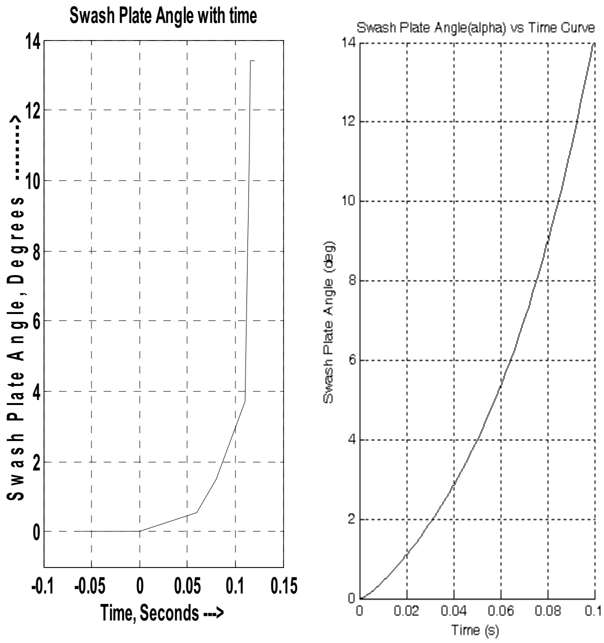

Experimental Analytical

Figure 6 Swash Plate Angle with respect to time.

The range of response time for full flow to zero flow is 70 to 100 seconds and for zero flow to full flow, when pressure is regulated, is 298 seconds to 400 seconds. The settling time (time taken to settle down when switched from one to another steady state) within limits for full flow to zero-flow but beyond limits for zero flow to full flow.

The overshoot and the undershoot in percentage (maximum and minimum transient pressures during dynamic response) are within limits for full flow to zero flow. However, these are beyond limits for zero flow to full flow operation.

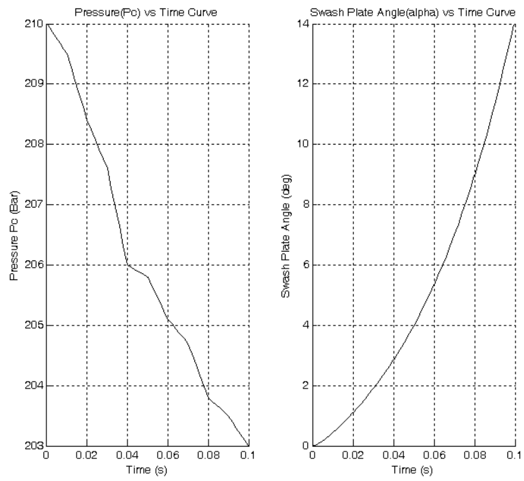

Experimental Analytical

(a) Swash Plate angle Increasing

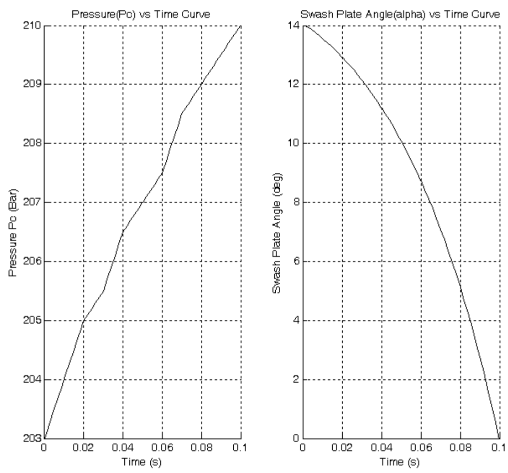

Experimental Analytical

(b) Swash Plate angle Decreasing

Figure 7 Variation of swash-plate angle for pressure regulation

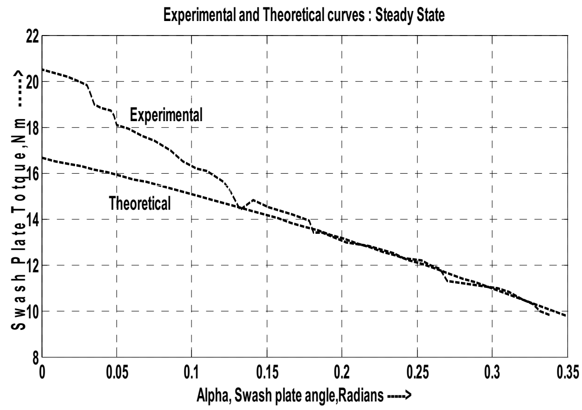

Figure 8 Swash Plate Control Torque
(Set Pressure 210 bar)

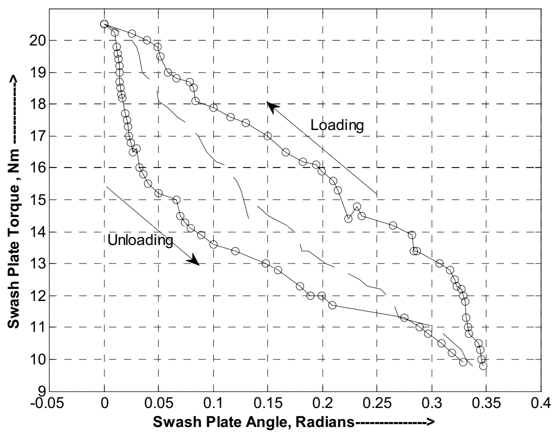

Figure 9 Hysteresis observed experimentally.

Table- 3 Some Measured Data of the Pump

Parameter	Limiting value	Full to Zero Flow			Zero to Full		
		2200 100-150	2500 145-210	3600 100-210	2200 150-100	2500 210-145	3600 210-100
Response Time (sec)	0.05 max	0.076	0.07	0.102	0.404	0.374	0.298
Over and Undershoot	± 35%	18%	13%	11%	75%	69%	53%
Settling Time (sec)	1 max	0.480	0.2	0.228	1.5	1.946	1.258

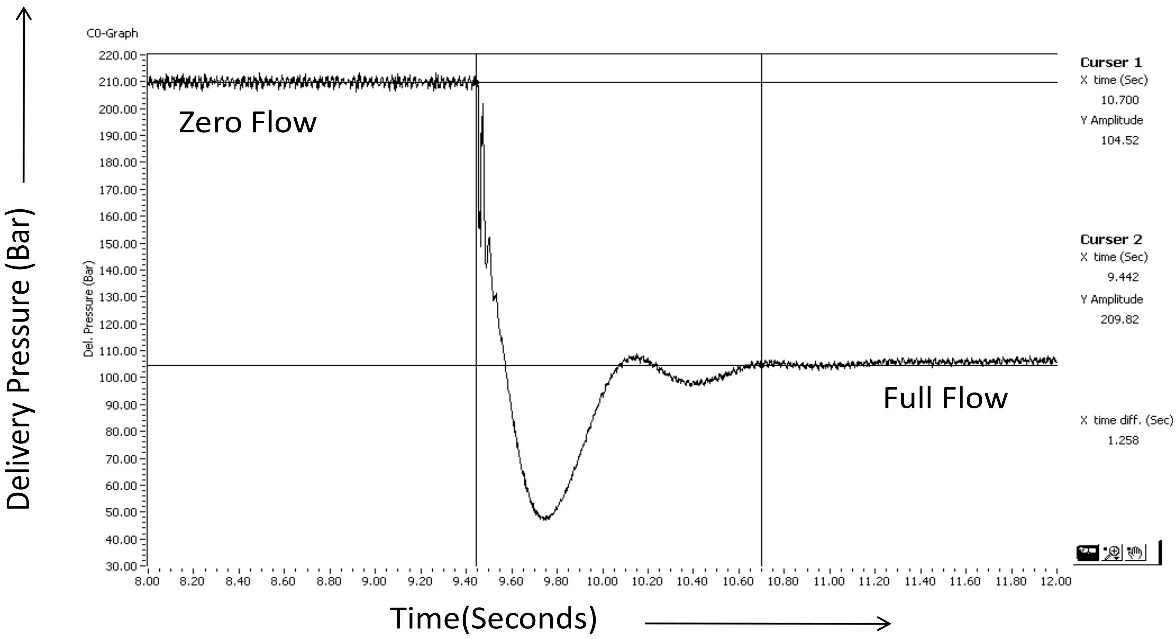

Figure 10 A typical record of experimental results (Delivery pressure, flow rate and time response)

Theoretical response

During simulation, pressure-time history (203 to 210 bar and 210 to 203 bar) as obtained during experimental work has been used as input. The variation of swash-plate angle for pressure regulation of 203-210 bar has been estimated theoretically and compared with experimental response. The variation of swash plate angle in both the cases has been from 0-14 degrees. The general shape and trend of the theoretical curve agrees with the experimental results, though the experimental values of swash plate angle were derived from flow. Figure 7 shows the respective results.
A sample result of the variation in torque when the swash plate start moving at the vicinity of set pressure zone, is shown in Figure 8. The estimated torque has good agreement with the experimental result except at the low flow zone. This is apparently due to the increase in mechanical resistances when swash plate approaches zero angle inclination. Usually such mechanical resistance leads to a hysteresis in forward and backward operation which is also realized during experiments as shown in Figure 9. Some recorded data and specifications of the pump during a test are shown in Table 3 and Figure 10.
It is apparent that the theoretical model is well established to estimate the swash plate torque. Such model can be incorporated in on-line control although possibly the model needs further refinements.

SUMMARY

The investigation was targeted to study and analyze the behavior of swash plate of a variable displacement, pressure compensated, in-line piston pump when subjected to a pressure control signal. The equations have been developed to formulate the equation of motion of swash plate. An important consideration in developing the equations has been the net torque which acts on the swash-plate. In the derivation of the equations care has been taken to include as many parameters as possible viz. reciprocating piston torque, return spring torque, control piston torque and yoke viscous damping torque [7, 8 & 11] for carrying out precise steady state and dynamic analysis. Inclusion of inertial terms, viscous damping terms, torque terms for control piston and return spring, has made the mathematical model apt for dynamic analysis. Towards simplification of theoretical simulation, the comprehensive model developed was simplified by linearizing the equation set for torque due to piston pressure and the coefficient terms in the remaining describing equations [11].
It is observed during the preliminary analysis of the model under steady-state load conditions that the torque induced by the line pressure on the swash plate is quite significant. The pump assembly has been observed to respond in a sluggish manner to load input at extreme swash plate positions, either loading or unloading type.

The assembly load-deflection was found to be more or less linear, with intermediate zones of non-linearity. Large hysteresis was observed between loading and unloading. The origin of such losses could not be related to load-deflection characteristics of return–spring in isolation. Therefore, the phenomena has its co-relation with friction (stiction, Coulomb and viscous shear) associated with the pump assembly.

Based on the correlation between the experimental and theoretical transient responses, it can be concluded that the simulation using simplified model and physical pump parameters does represent the dynamic response behavior of a variable displacement pump. The response of swash plate to dynamic and steady-state pressure inputs or perturbations is linear. Load–Deflection characteristics (Spring rate) of return spring play an important role because linearity of the spring has significant influence on the dynamic behavior. The transient period between the steady-states is very much influenced by nonlinearities associated with the pump-assembly as a whole.

Acknowledgement

Authors gratefully acknowledge HAL and DRDO, Lucknow, India who sponsored the second author for Masters program at IIT, Kharagpur and provided the experimental and research facilities.

References

1. Lewis, E., and Stern, H., Design of Hydraulic Control Systems, McGraw-Hill, New York, N.Y., 1962.
2. Green, W., and Crossley, T., “An analysis of control mechanism used in variable delivery hydraulic pumps”, Proceedings of the Institution of Mechanical Engineesrs,Vol.185, No.6 ,1971, pp. 63-72.
3. Zaki, H., and Baz, A., “ On the dynamics of pressure compensated Axial Piston Pumps,” Journal of Fluid Control/fluidics Quarterly, Vol. 11, No.2, 1979, pp. 73-87.
4. Merrit, H., Hydraulic Control Systems, Wiley, New York, N. Y.1967.
5. Yamaguchi. A.,“Study on the Characteristics of Axial Plunger Pumps and motors,” Bulletin of JSME, Vol. 9, No. 34, 1966, pp. 305-313.
6. Yamaguchi. A., and Ishikawa, T., “Characteristics of Displacement Control Mechanism in Axial Pistons Pumps,” Bulletin of JSME, Vol.22, No. 165, 1979, pp.356-361.
7. Zeiger, G., and Akers, A., “Torque on Swash plate of an Axial piston pump,” ASME Journal Dynamic Systems, Measurement and Control Vol.107, No 3, September 1985, pp.220-226.
8. Lin, S. J., Akers, A., and Zeiger, G., “Oil Entrapment in an Axial piston pump and its effect upon pressures and swash plate torques,” Proceeding of the 42nd national conference on fluid power, Chicago, Mar.1987, pp. 113-114.
9. Zeiger, G., and Akers, A., ”Dynamic analysis of an axial piston pump swash plate control,” Proceedings of Institution of Mechanical Engineers, Vol. 200, No C1,1986, pp 49-59.
10. Kavanagh, G. P., “The Dynamic Modeling of an Axial Piston Hydraulic Pump,” M.Sc thesis, Dept. of Mechanical Engineering, Univ. of Saskatchewan, May 1987.
11. Schoenau, G. J., Burton R. T., Kavanagh G. P., “Dynamic Analysis of a Variable Displacement Pump,” Journal of Dynamic Systems, Measurement, and Control, March 1990, Vol. 112, pp 122-132.
12. Manring, N. D.,” The Torque on the Input Shaft of an Axial-Piston Swash-Plate Type Hydrostatic Pump,” Journal of Dynamic Systems, Measurement and Control, Mar 1998, Vol. 12, pp 57-62.
13. Manring, N. D., “The Control and Containment Forces on the Swash Plate of an Axial-Piston Pump, ”Journal of Dynamic Systems, Measurement, and Control, December 1999, Vol. 121, pp 599-605.
14. Zhang, X., Cho, J., Nair, S. S., Manring N. D., “New Swash Plate Damping Model for Hydraulic Axial-Piston Pump,” Journal of Dynamic Systems, Measurement and Control Sept 2001, Vol. 123, pp 463-470.
15. Zeliang, Li., “Condition Monitoring of Axial Piston Pump,” M.Sc. Thesis, Department of Mechanical Engineering, University of Saskatchewan, Saskatoon, Nov. 2005.
16. Military Specification MIL-P-19692E, General Specification for variable flow hydraulic pumps, 199.
17. Narayan, P., “Studies on Swash Plate Behavior of Variable Displacement, Pressure Compensated, In-Line Piston Pump. MTech Dissertation, Mech. Engg. Dept., IIT, Kharagpur, India, May 2010.

Proceedings of the 8th JFPS International
Symposium on Fluid Power, OKINAWA 2011
Oct. 25-28, 2011

1C2-5

AN INVESTIGATION OF THE IMPACT OF ELASTOHYDRODYNAMIC DEFORMATION ON POWER LOSS IN THE SLIPPER SWASHPLATE INTERFACE

Andrew SCHENK, Prof. Monika IVANTYSYSNOVA

Maha Fluid Power Research Center
Department of Mechanical Engineering, Purdue University
225 S. University Street, West Lafayette IN 47907, USA
E-mail: mivantys@purdue.edu

ABSTRACT

This paper presents a new fluid-structure-thermal model of the slipper swashplate lubricating interface in axial piston machines. A combination of modeling techniques including finite volume and finite element methods are utilized to solve for the conditions of the thin fluid film, critical to machine operation. Nonlinearities present between physical domains pose a challenge for numerical convergence and therefore considerable detail is given on the algorithms used to achieve stable solutions. The developed model is then used to compare power loss from the lubricating interface both considering and neglecting solid body deformation for two different sizes of hydraulic units.

KEY WORDS

Axial-piston, Slipper, Elastohydrodynamic

NOMENCLATURE

B	Shape matrix	
C	Constitutive matrix	
c_p	Oil Heat Capacity	J/kg·K
d_{DG}	Orifice diameter	m
F	Force	N
F_{fZ}	Fluid force	N
F_{HD}	Slipper hold down force	N
F_{SK}	Piston reaction force	N
F_{TG}	Viscous friction force	N
$F_{\omega G}$	Centrifugal force	N
h	Film thickness	m
p	Fluid pressure	Pa
p_{case}	Case pressure	Pa
p_{DC}	Displacement chamber pressure	Pa
p_G	Pocket pressure	Pa
P	Power	W
r	Radial coordinate	m
Q_{SG}	Fluid leakage	m^3/s
t	Time	s
V_{NF}	Nodal force energy potential	Nm
v_{gr}	Radial velocity	m/s
$v_{g\theta}$	Tangential velocity	rad/s
u	Nodal displacement	m
U_ε	Strain energy	Nm
z	Gap height coordinate	m
α_D	Orifice coefficient	
ε	Strain	
λ_f	Fluid Thermal Conductivity	W/m·K
μ	Fluid dynamic viscosity	Pa·s
Π	Total potential energy	Nm
ρ	Fluid density	kg/m^3
τ	Shear stress	N/m^2

INTRODUCTION

Axial piston pumps and motors are critical components in many hydraulic systems. Additionally, today more than ever before, the importance of improving hydraulic system efficiency is not just necessary but demanded by customers and economics. Modern system architectures such as pump controlled actuation eliminate valve losses which is a vast improvement over older systems in itself. However, in these valveless systems, the efficiency of the pump, especially over a wide range of operating conditions, becomes of significant importance.

The most critical components of an axial piston machine are the lubricating interfaces – these fluid films separate heavily loaded movable parts from each other. Additionally, the fluid film fulfills a double function sealing the regions of high and low pressure fluid from each other and bearing the pressure loads acting on the solid parts. This particular work will investigate one interface, the slipper swashplate interface as illustrated in Fig 1.

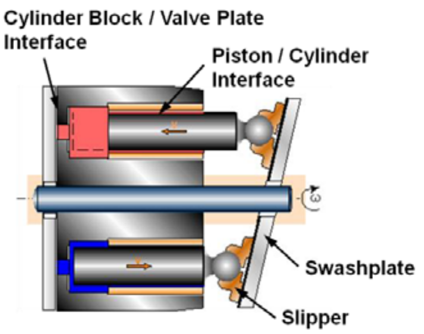

Figure 1 Cross section of an axial piston hydraulic pump

To improve the efficiency of the slipper interface and more generally, axial piston pumps, the underlying physical phenomena at play must be understood. To facilitate this understanding, numerical models have been developed. As new physical effects are incorporated into the model, it is also important to characterize the impact they have on one of the primary parameters of interest: power loss. Many works in the past have modeled the slipper swashplate interface for a variety of reasons and considered various physical effects [1-3]. This work aims to utilize and extend the past numerical models and then compare the effect pressure deformation of the slipper body has on power loss.

NUMERICAL MODEL

The slipper swashplate interface is assumed to operate under full film lubrication during steady state operation of the pump or motor. Although the macro motion of the slipper is governed by main pump kinematics, additional degrees of freedom are present on the micron scale. These micro motions allow the slipper to behave as a load adaptive bearing and respond to changing external loads. This adaptability is critical to the performance of the interface.

Partitioned Fluid Model

The slipper swashplate fluid model is divided into three regions as illustrated in Fig. 2. The displacement chamber pressure, p_{DC}, is solved in a separate model by considering the continuity equation, fluid bulk modulus, and a dynamic orifice area derived from valve plate geometry. The displacement chamber pressure results are then used as a transient boundary condition for the slipper model. Pocket pressure, p_G is modeled using a lumped parameter approach considering the continuity and orifice equations. Finally, the fluid film in the gap is modeled using the lubrication equation.

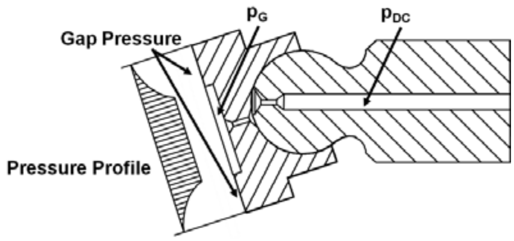

Figure 2 Partitioned fluid regions in the slipper-swashplate

Fluid flow in the lubricating gap is characterized by a low Reynolds number and assumed to be laminar with viscous forces dominating and inertial forces negligible. Additionally, the length and width of the fluid film are significantly greater than its height, thus in the gap height direction pressure is assumed constant and fluid velocity is neglected. Considering these assumptions, the Reynolds equation, Eq. (1), in polar coordinates is used to solve for the pressure distribution in the lubricating interface [4,5].

$$\frac{\partial}{\partial r}\left(h^3\frac{\partial p}{\partial r}\right)+\frac{1}{r}\left(h^3\frac{\partial p}{\partial r}\right)+\frac{1}{r^2}\frac{\partial}{\partial\theta}\left(h^3\frac{\partial p}{\partial\theta}\right)= 6\mu\left(v_{gr}\frac{\partial h}{\partial r}+v_{g\theta}\frac{\partial h}{\partial\theta}+2\frac{\partial h}{\partial t}\right) \quad (1)$$

Special consideration is given to the $\partial h/\partial t$ term which will be discussed later. The partial differential equation is discretized using the finite volume method (FVM) and the resulting linear system is solved using the BiConjugate Gradient Stabilized numerical method with an incomplete LDL^T preconditioner [6,7]. Pocket and case pressure are used as inner and outer boundaries,

respectively.
Notice in Eq. (1) that pressure is a function of the local viscosity of the fluid. Because the viscosity of oil is quite temperature dependent, and the oil temperature is non-uniform throughout the fluid film, the resulting temperature distribution must be considered. The convective-diffusive form of the energy equation, Eq. (2), is used to solve for fluid temperature [5,6]. The convective term in the gap height direction is neglected because fluid flow in that direction is assumed negligible as stated earlier.

$$\rho c_p \boldsymbol{V} \cdot \nabla T = \lambda_f \nabla \cdot \nabla T + \mu \Phi \tag{2}$$

The second term on the right hand side of Eq. (2) represents the heat generation due to viscous friction where:

$$\Phi = \left(\frac{\partial v_r}{\partial z}\right)^2 + \left(\frac{\partial v_\theta}{\partial z}\right)^2 + \frac{4}{3}\left(\frac{v_r}{r}\right)^2 + \left(\frac{v_\theta}{r}\right)^2 \tag{3}$$

Equation (2) is discretized using the FVM and the resulting linear system is solved using a Gauss-Seidel successive over-relaxation (SOR) method. An empirical fluid model is used to correlate fluid pressure and temperature to viscosity for use in Eq. (1).
Pressure in the slipper pocket is solved using a conservation of mass approach [5]. Thus, flow leaving the pocket through the lubricating gap must equal flow entering the pocket from the displacement chamber. Fluid flow leaving the pocket is given by Eq. (4), and can be solved once Eq. (1) has found the fluid pressure field.

$$Q_{SG} = \iint \frac{1}{2\mu} \frac{\partial p}{\partial r}\left(z^2 - hz\right) r \, dz \, d\theta \tag{4}$$

Fluid flow into the pocket is dependent on the hydraulic resistance and pressure difference between the displacement chamber and the pocket. Since fluid flow in and out of the pocket is considered equal and the displacement chamber pressure is known, the appropriate fluid resistance equation can solve for the pocket pressure. Assuming an orifice of diameter d_{DG}, the pocket pressure is calculated using Eq (5).

$$p_G = p_{DC} - 8\rho\left(\frac{Q_{SG}}{\pi d_{DG}^2 \alpha_D}\right)^2 \tag{5}$$

Linear Elastic Structural Model
Large pressures can develop in the fluid film between the slipper and swashplate due to both hydrostatic and hydrodynamic effects. Because of the amplitude of pressure acting on the swashplate, linear deformation of the solid slipper body occurs on an order of magnitude comparable to that of the fluid film height. This effect has been known for some time and is referred to in the tribological community as elastohydrodynamic deformation (EHD) [8,9].
The solid geometry of the slipper is meshed with first order tetrahedron elements using a commercial software package. The nodal locations and element connectivity are then imported into an internally developed linear elastic deformation model. The deformation model uses the finite element method and the minimum potential energy principle to formulate the stiffness matrix [10]. The total energy in an element, Π, is defined according to Eq. (6). This equation is differentiated with respect to the nodal displacements, u, and set equal to zero, minimizing the total potential energy in each element.

$$\boldsymbol{\Pi} = \mathbf{U}_\varepsilon + \mathbf{V}_{\mathrm{NF}} = \frac{1}{2}\int_V \left(\mathbf{B}\,\boldsymbol{u}\right)^T \mathbf{C}\left(\mathbf{B}\,\boldsymbol{u}\right) dV - \boldsymbol{u}^T \begin{Bmatrix} F_{x1} \\ F_{y1} \\ F_{z1} \\ \vdots \\ F_{xn} \\ F_{yn} \\ F_{zn} \end{Bmatrix} \tag{6}$$

Numerical Gaussian quadrature integration is used to solve the volume integral and the result is a system of linear equations representing the stiffness of an element. Each local stiffness matrix is assembled to form a single sparse global stiffness matrix. Nodes are constrained removing degrees of freedom from the solid model and the singularity from the stiffness matrix. The applied boundary conditions are shown in Fig 3. A preconditioning conjugate gradient method is used to solve the resulting linear system and find the nodal displacements.

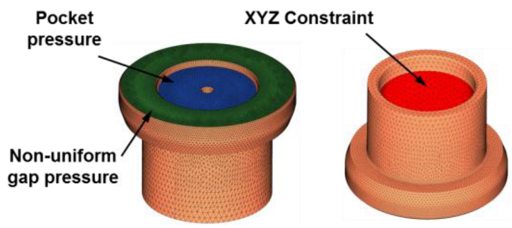

Figure 3 Slipper deformation boundary conditions

To decrease the computational effort required, influence matrices for the gap surface and pocket are generated prior to simulation. This reduces the deformation problem from solving a sparse linear system to computing a weighted sum, Eq. (7) [11-13].

$$u = \sum_{i=1}^{n} p_n I_n \tag{7}$$

Rigid Body Dynamics Model

The macro motion of the slipper is constrained by the ball-socket joint of the piston and the surface of the swashplate [1]. Due to these constraints, the slipper orbits the pump shaft as it rotates and follows the swashplate inclination. These motions are used to prescribe the necessary boundary velocity conditions in Eq. (1).

In addition to the constrained macro motion, the slipper also exhibits what is termed micro motion. This motion is on the order of micrometers in magnitude and occurs in three degrees of freedom. Specifically, the slipper is able to slightly vary the fluid film thickness between the swashplate (Z) as well as rotate slightly about the x_G and y_G axes using the coordinate system illustrated in Fig 4. This micro motion enables the load adaptivity of the slipper interface. Through constantly varying the velocity and thus position of the micro degrees of freedom, the pressure field generated by the slipper is able to change and respond to external loads [4].

A number of external forces act on the piston as shown in Fig. 4. To satisfy Newton's law of motion, all forces acting on the slipper must be balanced. Thus the rigid body dynamics problem of solving for slipper micro-motion can be reformulated as a zero finding of net slipper forces [5]. Specifically, a Newton-Raphson method is used to solve for an instantaneous $\partial h/\partial t$ vector which yields net forces within a toleranced zero. Recall the presence of a $\partial h/\partial t$, or squeeze term in Eq. (1). As the Newton method varies this squeeze term, the hydrodynamic pressure field changes affecting the slipper net force balance; in this way a force balance is achievable. Because a zero finding method is already required, a second order Adams Moulton implicit method is used to integrate the velocity with respect to time solving for the new slipper position. Since the slipper position now changes within each timestep thanks to the implicit method, the h term in Eq. (1) also varies with $\partial h/\partial t$ resulting in a more stable scheme.

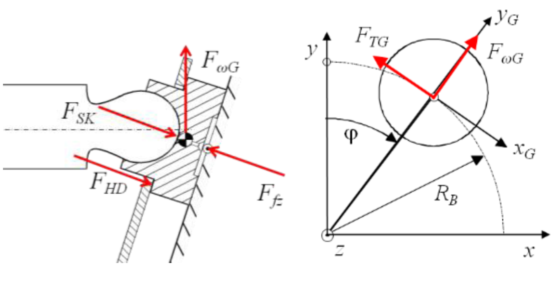

Figure 4 Coordinate system and forces acting on the slipper

Non-Linear Coupling Solver

The ability to combine all of the individual models and numerical schemes into a fully coupled and converging simulation is frequently one of the largest challenges in fluid structure interaction (FSI) problems. In this problem, the coupled nonlinearities present in Eqs. (1), (2), (5), and (6) are solved. Because the problem is formulated using a partitioned approach with each physical quantity being solved separately, an under relaxed fixed point iteration method is employed to achieve convergence [11,12,14]. This process is illustrated in Fig. 5.

Gap Pressure

$$-\nabla \cdot \left(\frac{h^3}{12\mu}\nabla p\right) - \frac{\boldsymbol{V}}{2} \cdot \nabla h + \frac{\partial h}{\partial t} = 0$$

Temperature

$$\rho c_p \boldsymbol{V} \cdot \nabla T = \lambda \nabla \cdot \nabla T + \mu \Phi$$

Pocket Pressure

$$p_G = p_{DC} - 8\rho\left(\frac{Q_{SG}}{\pi d_{DG}^2 \alpha_D}\right)^2$$

Gap Deformation

$$u = \sum_{i=1}^{n} p_n I_n$$

Deformation Squeeze

$$\frac{\partial h}{\partial t} = \frac{\partial h_{rigid}}{\partial t} + \frac{u - u_{t-\partial t}}{\partial t}$$

Figure 5 Inner loop to solve for nonlinearities between domains.

Deformation Squeeze Pressure

It was found through simulation that special attention needs to be given to the transient effect of solid body deformation. The interdependence of pressure, p, on gap height, h, and then gap height on pressure is clear from examining Eqs. (1) and (7). However, for a given timestep there is not an apparent influence of deformation on the Reynolds squeeze term. This of course is because in the strict sense the deformation model is linear static. Yet, since the deformation varies between timesteps, it is clear the deformation must be transient. To account for this, a first order backwards difference method is used to compute the $\partial u/\partial t$ for every volume. This $\partial u/\partial t$ is then added to the $\partial h/\partial t$ from the Newton method and used in the source term of the Reynolds equation. For a majority of the pump revolution, the deformation squeeze effect is actually quite small because of similar pressures and thus deformations from timestep to timestep. However, during the switch from high to low pressure and low to high pressures the magnitude of deformation can change significantly between timesteps. It is in these instances where the deformation squeeze effect becomes important to provide the necessary hydrodynamic pressure.

Once the inner fixed point loop converges, the net force balance is computed and that value is returned to the Newton method. As the Newton method varies the squeeze velocities searching for a velocity vector which will balance the external loads, the inner fixed point loop must again converge for the new squeeze velocity values.

Power Loss

The power loss in the slipper-swashplate interface comes from two sources: viscous friction between the slipper and swashplate, and fluid leakage through the slipper from the displacement chamber. These two sources are illustrated in Fig. 6.

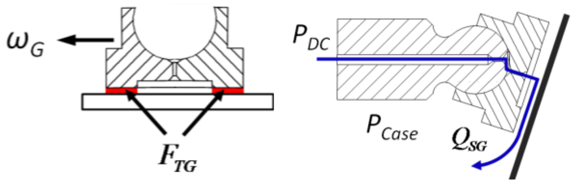

Figure 6 Viscous friction and leakage in the slipper swashplate interface

The instantaneous power loss is calculated with Eq. (8).

$$P = Q_{SG}\left(p_{DC} - p_{case}\right) + \int\left(\tau_r v_r + \tau_\theta v_\theta\right)dA \tag{8}$$

RESULTS

To investigate the impact of slipper deformation on power loss, two different pump sizes (18 and 75 cc/rev) were simulated. These simulations were conducted considering a range of operating conditions both with and without slipper pressure deformation. The operating conditions are expressed as the difference in pressure between the high and low pump ports, the shaft rpm speed, and the swashplate angle as a percentage of its maximum displacement.

18 cc Pump

Figure 7 is a comparison of the modeled power loss for the 18 cc pump under six different operating conditions considering an EHD versus rigid slipper model. (Note the power loss over a shaft revolution is plotted starting with the pumping stroke from 0-180 deg. and then the suction stroke from 180-360 deg.) For some operating conditions there is a marked difference between the two models. More can be understood by comparing Fig. 7 with Fig. 8 which are the average gap heights of the slipper. Notice the rigid modeled gap heights are rather low, all below 1.5 µm. Because the EHD model at times doubles the height of the small gap, viscous friction is reduced lowering the predicted power loss.

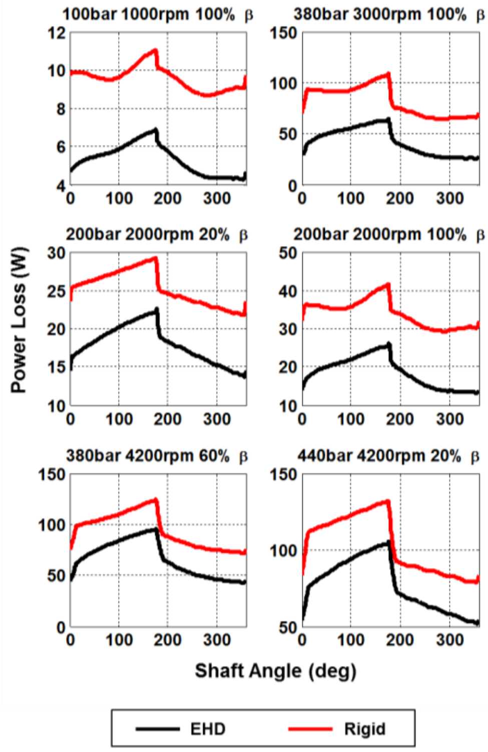

Figure 7 Comparison of slipper power loss in EHD and rigid models for an 18 cc/rev pump

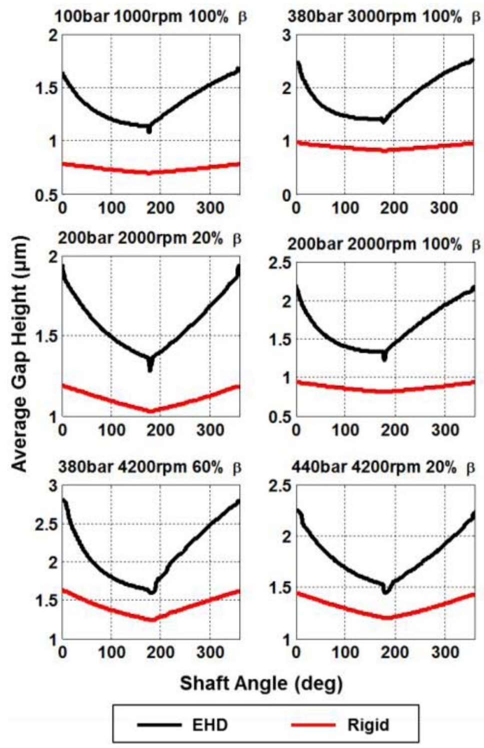

Figure 8 Comparison of slipper average gap height in EHD and rigid models for an 18 cc/rev pump

To understand why the EHD model predicts higher gaps in this instance, it is necessary to delve deeper into the physics. Figure 9 illustrates the typical deformation mode of the slipper during the pumping stroke; note how the lubricating surfaces bow outwards. As the slipper translates over the swashplate, the fluid film on the leading and trailing edges will experience an increase and decrease in pressure respectively from the deformation shape. The pressure effect from the bowing is commonly referred to as the physical wedge effect of the Reynolds equation.

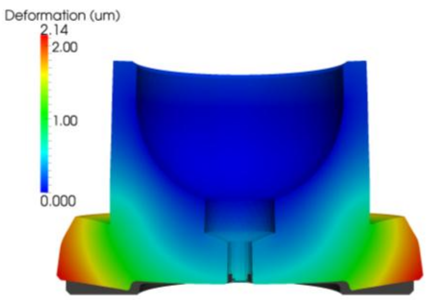

Figure 9 EHD deformation shape (scaled 300x)

In actual slipper operation, the leading and trailing pressures must be nearly equal to maintain net force equilibrium on the slipper body. To achieve equal pressures now with a deformable slipper body, the slipper must adjust its micro motion. A comparison between rigid and EHD gap sections is shown in Fig. 10. (Note the pocket height is not shown)

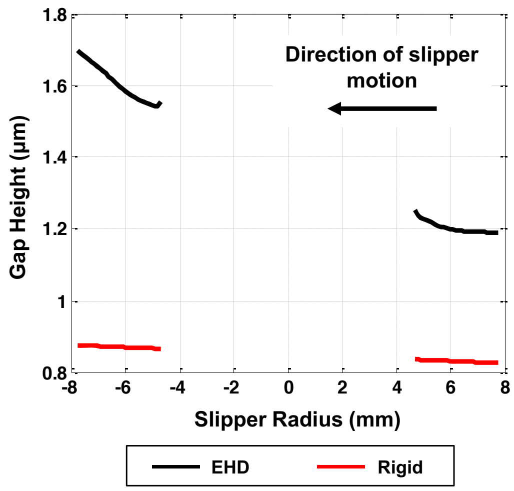

Figure 10 Section cut of slipper gap height normal to the x-axis for EHD and rigid models

The EHD model rotated the slipper so the trailing edge is either converging or parallel to the swashplate. This allows pressures to build on the trailing edge while lifting the leading edge so the wedge effect from the deformation is less pronounced. The net effect of this action is a balance of pressure between the leading and trailing surfaces which in turn lifts the slipper slightly away from the swashplate.

75 cc Pump

The 75 cc/rev pump was modeled and simulated in the same fashion as the 18 cc/rev unit. Aside from obvious geometrical size differences, the 75cc unit had a fixed slipper hold down device as opposed to the spring type in the 18cc unit. To model this difference, the F_{HD} force is zero until the slipper reaches the fixed hold down clearance. Beyond that height, a stiff linear spring is used to represent the fixed holder.

Figures 11 and 12 are comparisons of the modeled power loss and average gap height for the 75 cc pump under four different operating conditions considering an EHD versus rigid slipper model.

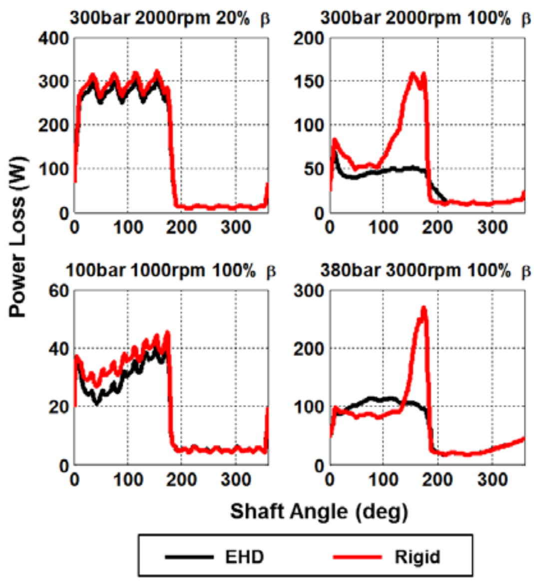

Figure 11 Comparison of slipper power loss in EHD and rigid models for a 75 cc/rev pump

In Fig. 11, the power loss between the EHD and rigid models for the left operating conditions are very similar, and for the right conditions only differ in the 90-180 deg. range. The reason pressure deformation has less impact on this larger unit when compared to the 18cc one lies in the magnitude of interface gap heights. The gap heights for the 75cc pump vary between 5-25 µm, significantly greater than the 18cc unit. Because the pressure deformation is on the magnitude of 1-2 µm, the ratio of deformation to rigid gap height is much greater on the 18cc unit, thus the effect is also larger. Recognize the property of larger gap heights on larger pumps is not a rule, but rather a coincidence in this study.

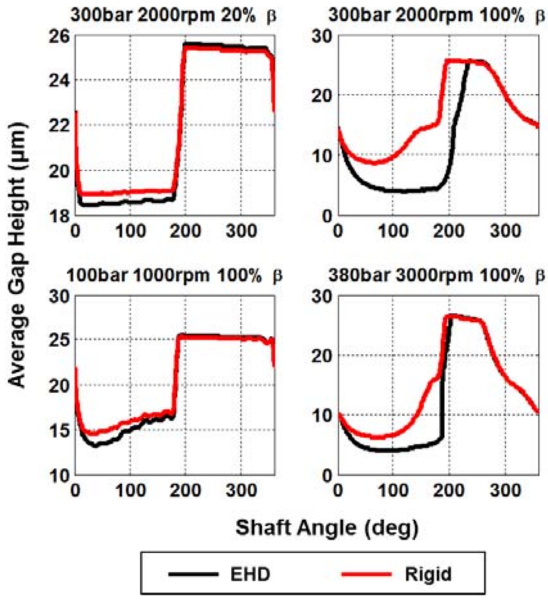

Figure 12 Comparison of slipper average gap height in EHD and rigid models for a 75 cc/rev pump

CONCLUSIONS

This paper used an advance fluid-structure-thermal, rigid body dynamics model to investigate power loss in the slipper-swashplate interface of two different axial piston pumps under a range of operating conditions. It was found that considering the deformation due to fluid pressure has a significant impact on the modeling power loss, especially on units where the deformation magnitude becomes comparable to the overall gap height. Moreover, the pressure deformation magnitudes in actual pumps are on a similar scale to the gap height.

It was found that considering the squeeze pressure buildup due to changing pressure deformation is also important, especially during the switch between pumping and suction strokes. In these time periods, the bowing of the slipper changes rapidly with displacement chamber pressure and the additional hydrodynamic squeeze pressure enables successful operation.

REFERENCES

1. Ivantysyn J. and Ivantysynova M., Hydrostatic Pumps and Motor, Principles, Designs, Performance, Modeling, Analysis, Control and Testing, Academic Books International, New Delhi, 2001.
2. Pelosi, M. and Ivantysynova, M., “A New Fluid Structure Interaction Model for the Slipper-Swashplate Interface” Proc. of the 5th FPNI PhD Symposium, Krakow, Poland, 2008, pp. 219-236.
3. Kumar, S., Bergada, J., Watton, J., “Axial piston pump grooved slipper analysis by CFD simulation of three-dimensional NVS equation in cylindrical coordinates” Computers & Fluids, Vol. 38, 2009, pp. 648-663.
4. Hamrock, B., Schmid, S. and Jacobson, B., Fundamentals of Fluid Film Lubrication, 2nd ed., Marcel Dekker, New York, 1994.
5. Wieczorek, U. and Ivantysynova, M., “Computer Aided Optimization of Bearing and Sealing Gaps in Hydrostatic Machines - The Simulation Tool CASPAR” International Journal of Fluid Power, Vol. 3, No.1, 2002, pp. 7-20.
6. Patankar, S., Numerical heat Transfer and Fluid Flow, Hemisphere Publishing Corporation, New York, 1980, Chap. 3-5, pp-25-109.
7. Renard, Y., “Gmm++ user documentation” http://download.gna.org/getfem/html/homepage/gmm.html, Release 4.1.1, April 2011.
8. Kim, K. and Sadeghi, F., “Three-dimensional temperature distribution in EHD lubrication: Part I - circular contact” ASME Journal of Tribology, Vol. 114, 1992, pp. 32-41.
9. Fatemi, A., Wohlers, A. and Murrenhoff, H., “Simulation of Elastohydrodynamic Contact between Piston and Cylinder in Axial Piston Pumps” Proc. of the 6th International Fluid Power Conference, Dresden, 2008, pp. 539-552.
10. Hartley G., Fundamentals of The Finite Element Method, Macmillan Publishing Company, New York, 1986.
11. Pelosi, M. and Ivantysynova, M., “A Simulation Study on the Impact of Material Properties on Piston/Cylinder Lubricating Gap Performance” Proc. of the 6th FPNI PhD Symposium, West Lafayette, IN, 2010.
12. Schenk, A. and Ivantysynova, M., “Design and Optimization of the Slipper-Swashplate Interface Using an Advanced Fluid Structure Interaction Model” Proceedings of the 52nd National Conference on Fluid Power 2011, NCFP I11-4.2.
13. Xiong, S., Lin, C., Wang, Y., Liu, W., Wang, Q., “An Efficient Elastic Displacement Analysis Procedure for Simulating Transient Conformal-Contact Elastohydrodynamic Lubrication Systems” ASME Journal of Tribology, Vol. 132, April 2010.
14. Pelosi, M. and Ivantysynova, M., “A Novel Fluid-Structure Interaction Model for Lubricating Gaps of Piston Machines” Proc. of the 5th Fluid Structure Interaction Conference, Crete, 2009, pp. 13-24.

1C2-6

RESEARCH ON THE HELMHOLTZ TYPE VARIABLE RESONANCE ATTENUATOR FOR THE FLUID POWER SYSTEM

Takayoshi ICHIYANAGI*, Tetsuya KURIBAYASHI**, Masaki ITO**
and Takao NISHIUMI*

* Department of Mechanical Systems Engineering
National Defense Academy
1-10-20Hashirimizu, Yokosuka, Kanagawa, 239-8686 Japan
(E-mail: ichiyana@nda.ac.jp)
** Graduate School of Science and Engineering
National Defense Academy

ABSTRACT

Vibration and noise caused by pressure pulsation, known as fluid borne vibration or fluid borne noise, are one of detrimental problems in the fluid power system. The Helmholtz type variable resonance attenuator called the multi-degree of freedom type Helmholtz resonator has been designed to attenuate several harmonic frequencies. The resonator consists of one cylindrical vessel and some chokes inside the vessel. The development of the multi-degree of freedom type Helmholtz resonator applying to hydraulic systems operated under the variable speed condition is a final goal of this research project. The aim of this report is to establish the design criteria of the resonator specifications. In particular, the effect of diameter and length of the choke and cylindrical cavity for the attenuation performance is investigated analytically.

KEY WORDS

Pressure pulsation, Hydraulic system, silencer, Helmholtz resonator

NOMENCLATURE

$\mathbf{A}_i$	:	Transfer matrix of the ith divided cylindrical cavitiy
$\mathbf{B}_i$	:	Transfer matrix of the ith divided choke
C_{fi}	:	Viscous damping coefficient of the ith divided choke
c	:	Speed of sound
D_h	:	Diameter of cylindrical cavity of standard Helmholtz resonator
d_0	:	Diameter of cylindrical cavity
d_4	:	Diameter of main line
d_i	:	Diameter of the ith divided choke
d_h	:	Diameter of choke of standard Helmholtz resonator
f_n	:	Resonance frequency of standard Helmholtz resonator
$f_{r.i}$	:	the ith resonance frequency of resonator
$f_{r.i}^*$	:	Desired value of $f_{r.i}$
K	:	Gain factor
k_i	:	Spring coefficient of the ith divided cylindrical cavity
L_i	:	Length of the ith divided cylindrical cavity
L_h	:	Length of cylindrical cavity of standard Helmholtz resonator

Copyright © 2011 by JFPS, ISBN 4-931070-08-6

l_i : Length of the ith divided choke
l_h : Length of choke of standard Helmholtz resonator
m_i : Mass of the ith divided choke
P : Pressure pulsation
P_d : Discharge mean pressure
Q : Flow pulsation
s : Laplace operator
$\mathbf{T}$: Transfer matrix of resonator
TL : Transmission loss
V_h : Volume of cylindrical cavity of standard Helmholtz resonator
W_i : Incident energy of pulsation into silencer
W_i : Transmitted energy of pulsation through silencer
$\mathbf{X}$: Design variables
$Z_{c.4}$: Characteristics impedance of main line
$Z_{c.i}$: Characteristics impedance of the ith divided cylindrical cavity
Z_h : Entry impedance of standard Helmholtz resonator
Z_r : Entry impedance of resonator

ε : Ratio of transmission loss at resonance frequency
κ : Bulk modulus of oil
ν : Kinematic viscosity of oil
ρ : Density of oil
ω_n : Resonance angular frequency of standard Helmholtz resonator
ξ : Complex coefficient for unsteady viscous friction effect
ζ : Damping coefficient

INTRODUCTION

It is well known that all positive displacement pumps generate flow pulsation, which interacts with the hydraulic circuit to produce pressure pulsation. The pressure pulsation is usually the primary noise source of the hydraulic circuit because it is very easily transmitted throughout the entire system and then excites the mechanical parts that generate audible noise. The pressure pulsation is a periodic function of time and its frequency characteristics is comprised of a fundamental frequency and higher harmonics. The amplitudes of the first, the second and the third harmonics are often dominant components in the pressure pulsation. Therefore attenuating the amplitude of these harmonics is an effective way of reducing the system noise.
The attenuator called “the multi degree of freedom type Helmholtz resonator” has been developed in the past [1]. Unlike a conventional standard type Helmholtz resonator, this device has a feature that it is possible to adjust freely the resonance mode to the desired resonance mode, i.e. the desired resonance frequencies and mode shapes, with a single closed-end cylindrical vessel configuration. However the multi degree of freedom type Helmholtz resonator can be only applied to the system which runs at a constant pump rotational speed. The hydraulic systems such as an excavator or an injection molding machine are operated under the constant speed condition. But the attenuator which covers wider frequency range is desired. Therefore the final goal of this research project is that the present Helmholtz resonator can be applied to the hydraulic systems operated under the variable speed condition. This will be achieved by adding some variable resonance mechanism to the resonator. The past work has been clarified the present resonator have the capability of the variable resonance attenuation performance by changing the dimensions of the resonator continuously [2].
In this report, we focus on the design criteria of these dimensions. The relationship between the dimensions and the attenuation characteristics is discussed. In particular, the effect of length and diameter size of the standard type Helmholtz resonator is examined in order to clarify how these dimensions have an influence on the attenuation performance. This information will be important to design the dimension of the multi degree of freedom type Helmholtz resonator.

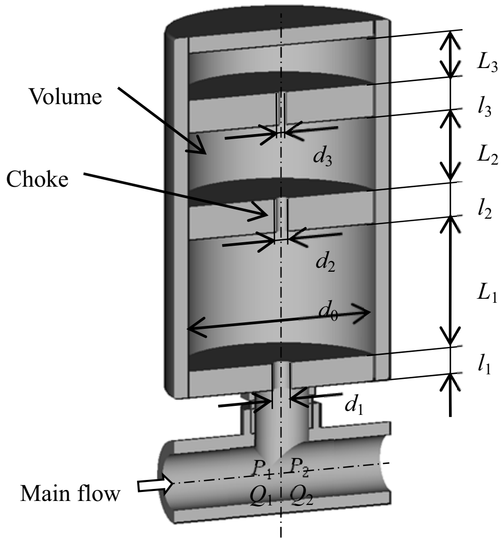

Fig.1 The multi degree of freedom type Helmholtz Resonator

MULTI DEGREE OF FREEDOM TYPE HELMHOLTZ RESONATOR

Fundamental principle and Structure

Fig.1 shows the structure of the multi degree of freedom type Helmholtz resonator. Some chokes (e.g., three chokes in Fig.1) are inserted in a closed cylindrical vessel. These chokes divide the vessel into some cylindrical cavities. Fig.2 shows the physical model of this resonator. The fluid in each chokes acts as a mass due to the inertia effect of fluid, and each divided cylindrical cavities act as a spring due to the capacitive

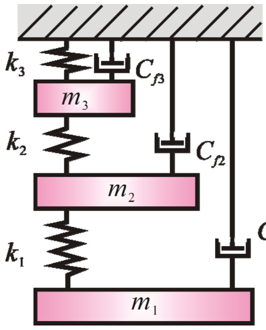

Fig.2 Physical Model of The multi degree of freedom type Helmholtz Resonator

effect of fluid. The viscous friction in each chokes acts as a dashpot effect. In the case of Fig.1, the resonance phenomena of three degree of freedom system, which is based on the three spring-mass systems in Fig.2, are utilized for attenuation of pressure pulsation. Resonance frequencies of this multi degree of freedom type Helmholtz resonator can be tuned freely by appropriately adjusting the lengths and diameters of each chokes and cavities.

Mathematical model

For modeling of the resonance phenomena of the multi degree of freedom system, the lumped parameter model that considers only the compressibility (capacitive effect) of the fluid in the cavity can be approximately used (it is described in the next chapter). But, in this work, the distributed parameter model has been used also for the fluid in the cavity of this Helmholtz resonator in order to improve the design accuracy. Assuming the fluid flow in the cylindrical cavity to be two-dimensional, compressible and laminar one, the Laplace transfer matrix between the upstream and the downstream for the ith divided cylindrical cavity $\mathbf{A}_i$ is given by the following equation [3].

$$\mathbf{A}_i = \begin{bmatrix} \cosh\left\{\dfrac{\xi_i(s)s}{c}L_i\right\} & Z_{c.i}\sinh\left\{\dfrac{\xi_i(s)s}{c}L_i\right\} \\ \dfrac{1}{Z_{c.i}}\sinh\left\{\dfrac{\xi_i(s)s}{c}L_i\right\} & \cosh\left\{\dfrac{\xi_i(s)s}{c}L_i\right\} \end{bmatrix} \tag{1}$$

where s is Laplace operator, c is the speed of sound in oil, L_i is the length of the ith divided cylindrical cavity. $\xi(s)$ and $Z_{c.i}$ are the complex coefficient for unsteady viscous friction effect and the characteristic impedance of the ith divided cylindrical cavity respectably. These parameters are expressed as follows.

$$\xi_i(s) \cong 1 + \sqrt{\frac{4\nu}{d_i^2 s}} + \frac{4\nu}{d_i^2 s} \tag{2}$$

$$Z_{c.i} = \frac{4\rho c\,\xi(s)}{\pi d_i^2} \tag{3}$$

ρ and ν are the density and kinetic viscosity of oil. For the cylindrical cavity, all diameters of divided parts are the same as d_i=d_0.

The transfer matrix of choke is also given by the same equation as Eq.(1). But this equation can be simplified like Eq.(4) because the length of choke l_i is generally far shorter than the wave length.

$$\mathbf{B}_i = \begin{bmatrix} 1 & \dfrac{4\rho l_i s\,\xi_i(s)^2}{\pi d_i^2} \\ 0 & 1 \end{bmatrix} \tag{4}$$

Therefore, for the Helmholtz resonator with three chokes shown in Fig.1, the transfer matrix between the inlet and the closed-end of cylindrical vessel can be described by the following equation with the transfer matrix **C**

$$\mathbf{C} = \mathbf{B}_1 \cdot \mathbf{A}_1 \cdot \mathbf{B}_2 \cdot \mathbf{A}_2 \cdot \mathbf{B}_3 \cdot \mathbf{A}_3 \equiv \begin{bmatrix} C_{1.1} & C_{1.2} \\ C_{2.1} & C_{2.2} \end{bmatrix} \tag{5}$$

Since this resonator are branched off from the main line, The relationship between the variables P_1, Q_1 at the inlet and P_2, Q_2 at outlet of the resonator in the main line can be derived using Laplace transfer matrix **T** as follows

$$\begin{bmatrix} P_1 \\ Q_1 \end{bmatrix} = \mathbf{T}\begin{bmatrix} P_2 \\ Q_2 \end{bmatrix} \tag{6}$$

$$\mathbf{T} \equiv \begin{bmatrix} T_{1.1} & T_{1.2} \\ T_{2.1} & T_{2.2} \end{bmatrix} = \begin{bmatrix} 1 & 0 \\ C_{2.1}/C_{1.1} & 1 \end{bmatrix} = \begin{bmatrix} 1 & 0 \\ 1/Z_r & 1 \end{bmatrix} \tag{7}$$

Z_r is the entrance impedance of the resonator. Once the transfer matrix is determined, Transmission Loss can be calculated from the Eq.(8). Transmission Loss is a measure of the attenuation performance of hydraulic silencer under the anechoic termination condition. It means the ratio of the incident and transmitted pulsation wave energy of hydraulic silencer.

$$TL = 10\log\left|\frac{W_i}{W_t}\right| = 20\log\left\{\frac{1}{2}\left|2 + \frac{Z_{c.4}}{Z_r}\right|\right\} \tag{8}$$

where $Z_{c.4}$ is the characteristic impedance of the main line and is obtained from Eq.(2) and (3) (in this case d_i=d_4). Fig.3 shows the transmission loss characteristics of an example design of the three degree of freedom type Helmholtz resonator.

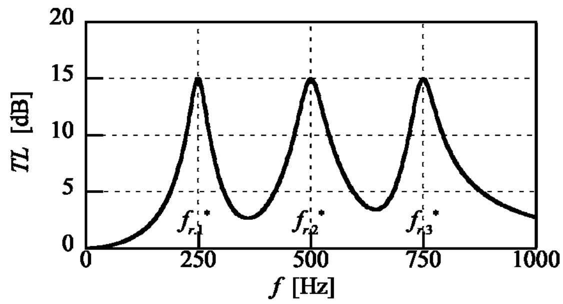

Fig.3 Typical transmission loss characteristics of the multi degree of freedom type Helmholtz Resonator

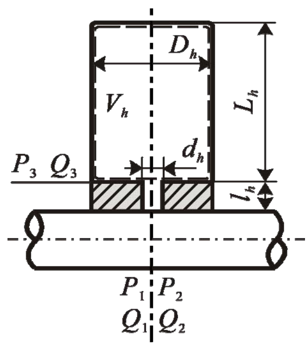

Fig.4 Structure of standard type Helmholtz Resonator

SIZING HELMHOLTZ RESONATOR

The main feature of the multi degree of freedom type Helmholtz resonator is that it can make up the resonance phenomenon at any desired frequencies. In order to achieve the desired attenuation performance, the diameter and length of each chokes and cylindrical cavities must be appropriately determined. In this report, to understand how these design parameters affect the attenuation performance, the dimension study of the standard one degree of freedom type Helmholtz resonator are carried out.

Standard Type Helmholtz Resonator

The structure of a standard type Helmholtz resonator is shown in Fig.4. The inverse of the entrance impedance of this standard type Helmholtz resonator can be given by Eq.(9) using the lumped parameter model [see the appendix].

$$\frac{1}{Z_h} = s\frac{K\omega_n{}^2}{s^2 + 2\zeta\omega_n s + \omega_n{}^2} \qquad (9)$$

This model includes the well-known standard second order lag element. K is the gain factor, ζ is the damping coefficient and ω_n is the resonance angular frequency. These parameters are described by the following relational expressions.

$$\left.\begin{aligned} K\omega_n^2 &= \frac{\pi}{4\rho}\frac{d_h^2}{l_h} \\ \zeta &= 32\nu\sqrt{\frac{\rho}{\pi\kappa}}\frac{\sqrt{V_h l_h}}{d_h^3} \\ \omega_n &= \frac{1}{2}\sqrt{\frac{\pi\kappa}{\rho}}\frac{d_h}{\sqrt{V_h l_h}} \end{aligned}\right\} \qquad (10)$$

where d_h is the diameter of choke, l_h is the length of choke, V_h ($=\pi D_h^2 L_h/4$) is the volume of cylindrical cavity, κ is the bulk modulus of oil. The resonance angular frequency ω_n can be rewritten in frequency unit.

$$f_n = \frac{1}{4}\sqrt{\frac{\kappa}{\pi\rho}}\frac{d_h}{\sqrt{V_h l_h}} \qquad (11)$$

Transmission loss for the standard Helmholtz resonator is also derived from Eq.(8) and (9).

$$TL = 20\log_{10}\left\{\frac{1}{2}\left|2 + \frac{Z_{cA}}{Z_h}\right|\right\} \qquad (12)$$

From above equations, the attenuation performance, i.e. the resonance frequency f_n and the peak value of transmission loss TL, can be related to the design parameters as follows.

$$\left.\begin{aligned} f_n &\propto \frac{d_h}{\sqrt{V_h l_h}} \\ TL &\propto \frac{d_h^2}{l_h} \end{aligned}\right\} \qquad (13)$$

These relations are very important to design the multi degree of freedom type Helmholtz resonator as well as the standard Helmholtz resonator. It can be said that the diameter of the choke d_h is more sensitive to the attenuation performance of the resonator. The interesting knowledge from Eq.(13) is that the volume of the cylindrical cavity is independent from transmission loss characteristics. The maximum attenuation performance is determined only by the dimension of the choke.

The distributed parameter model is also examined for the standard type Helmholtz resonator and is compared to the lumped parameter model. The model can be derived from the same manner as the multi degree of freedom type Helmholtz resonator, which was mentioned in the previous chapter, but the standard Helmholtz resonator

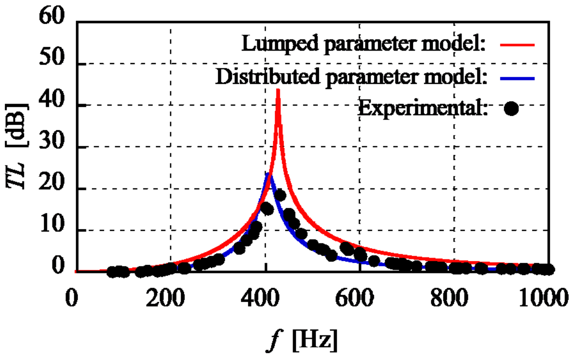

Fig.5 Comparison of lumped parameter model, distributed parameter model and experimental results (For experimental result, P_d =10MPa)

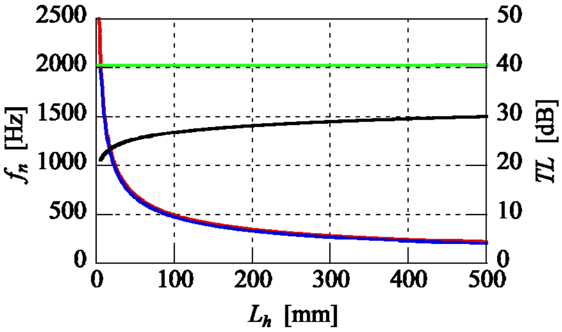

Fig.6 Influence of length of cylindrical cavity L_h (Lumped parameter model, f_n: ——, TL: ——, distributed parameter model, f_n: ——, TL: ——)

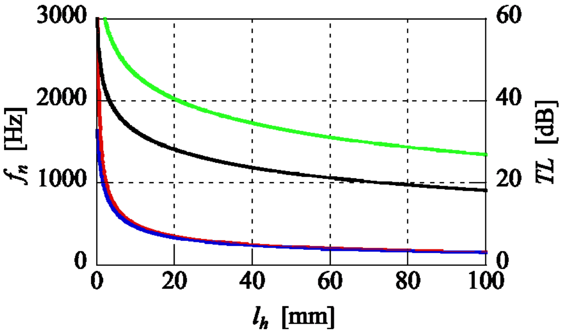

Fig.7 Influence of length of choke l_h (Lumped parameter model, f_n: ——, TL: ——, distributed parameter model, f_n: ——, TL: ——)

only uses a set of the choke and cylindrical cavity in Eq.(5). Fig.5 shows the comparison between the lumped parameter model and the distributed parameter model together with the experimental result. The dimension of the resonator is chosen as d_h=6 mm, l_h=20 mm, V_h=3.93 $\times 10^{-4}$ m^2 (D_h=50 mm, L_h=200 mm). The experimental result was calculated from the experimentally acquired transfer matrix of the standard Helmholtz resonator [4]. It can be seen from this figure that there are difference between two models in terms of the resonance frequency and its peak value of transmission loss. Since the experimental result agrees better with the distributed parameter model than the lumped parameter model, the distributed parameter model should be used to design the Helmholtz resonator. This is mainly because the inertia effect of the cylindrical cavity cannot be neglected, while the lumped parameter model only takes into account the compressibility effect. Nevertheless, the lumped parameter model can be also utilized to roughly design the resonator since it is expressed in the simple form as in the Eq.(13), which give us the idea how the design parameters relates to the attenuation performance.

The influence of dimensions change is investigated. This study helps us how to size the choke and cylindrical cavity of the Helmholtz resonator. Firstly, the volume of cylindrical cavity V_h is varied by changing the length of cylindrical cavity L_h. The calculated results for both the lumped and distributed parameter models are shown in Fig.6. As expressed in Eq.(13), the cylindrical cavity has no effect on the transmission loss characteristics in the lumped parameter model. It can be said that the result of the distributed parameter model has also little influence on the transmission loss compared with dimensions of the choke. Concerning about the resonance frequency f_n, both results shows the relation of $f_n \propto 1/\sqrt{V_h}$. These results imply the fact that varying the volume of the cylindrical cavity makes it possible varying the resonance frequency without changing the peak value of transmission loss. Therefore, any mechanism which varies the size of volume is enough to realize a variable resonance type Helmholtz resonator.

Secondly, the length of choke l_h is chosen as the parameter. Fig.7 shows the influence of the choke length change. The difference between the transmission losses of two models are came up in the figure, however this difference is not important in this report as explained in Fig.5. The significant derivation from this figure is that the relations between the length of choke l_h and both the resonance frequency f_n and transmission loss TL are appeared identically as it is expressed in Eq.(13). These are $f_n \propto 1/\sqrt{l_h}$ and $TL \propto 1/l_h$, respectably. It should be noted that tuning the resonance frequency f_n by varying the length of choke l_h has limitation since the frequency f_n will reach the minimum value within a practical range of choke length (l_h <100 mm).

Finally, the influence of choke diameter d_h is examined in Fig.8. In this figure, the result of a side branch resonator is added to the two models. The side branch resonator is only a branch pipe installed in the main flow

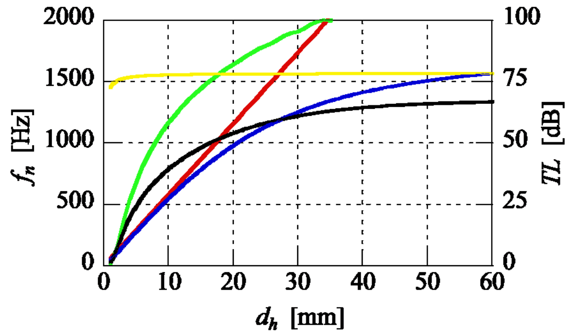

Fig.8 Influence of diameter of choke d_h
(Lumped parameter model, f_n: ——, TL: ——,
distributed parameter model, f_n: ——, TL: ——,
side branch, f_n: ——)

line. The pressure pulsation is attenuated by utilizing the reflection of pulsation wave in the branch pipe. The resonance frequency of the side branch resonator is dependent only on the length of branch pipe. In the case of this figure, the length of side branch becomes $l_h + L_h$ =220 mm and the diameter of choke d_h corresponds to the diameter of side branch. It can be pointed out that the resonance frequency result of the distributed parameter model starts to deviate from the lumped parameter model at d_h =10 mm, and this deviation becomes large with a increase of the diameter d_h. The result of transmission loss shows a same tendency as the result of the resonance frequency. These deviations can be explained that the Helmholtz resonator begins to act as the side branch resonator when the diameter of choke is close to the diameter of cylindrical cavity. Then when the diameter of choke and cylindrical cavity is the same, the attenuation characteristics become completely that of the side branch resonator. In practice, however, the diameter of cylindrical cavity is usually larger than the choke diameter (the maximum diameter of choke will be the diameter of main line). Regarding the resonance frequency f_n of the distributed model (blue line), f_n makes a transition from the lumped parameter model to the side branch model.

DESIGN EXAMPLE OF THREE DEGREE OF FREEDOME TYPR HELMHOLTZ RESONATOR

An example of the three degree of freedom type Helmholtz resonator which has the variable resonance ability is designed by the optimum design method. Based on the knowledge from the previous chapter, the variable resonance phenomenon is realized by varying the length of the cylindrical cavity, i.e. varying the volume of the cylindrical cavity. Hence the optimum design method is used to determine the unknown lengths of three cylindrical cavities. The purpose of this calculation is to search the unknown values so that the resonance frequencies $f_{r.i}$ of the resonator coincide with the desired values $f_{r.i}^*$. The ratios of transmission loss at the resonance frequencies ε are constrained while searching the unknown lengths (as ε=1.0). The following equations represent the design variables, the objective function and the constraint condition.

Design variables:

$$\mathbf{X}=\{L_1, L_2, L_3\}^T \tag{14}$$

Objected function:

$$f(\boldsymbol{X})=|f_{r.1}-f_{r.1}^*|+|f_{r.2}-f_{r.2}^*|+|f_{r.3}-f_{r.3}^*| \tag{15}$$

Constraint condition:

$$\frac{TL(f_{r.2})}{TL(f_{r.1})}=\frac{TL(f_{r.3})}{TL(f_{r.1})}=\varepsilon \tag{16}$$

The lengths and diameters of chokes are set to l_1=12.9 mm, l_2=7.3 mm, l_3=4.6 mm, d_1=6 mm, d_2=4 mm, d_3=2.5 mm, and the diameters of cylindrical cavity is d_0=49.5 mm. For the optimum design algorithm, Powell's conjugate directions method is adopted to search for the design variables [5]. Fig.9 shows the searched lengths of cylindrical cavities when the resonance frequencies are varied. The horizontal axis of the figure is the desired first resonance frequency $f_{r.1}^*$. The second and third resonance frequencies are twice and three times of $f_{r.1}^*$. It is obvious from the figure that the lengths of all three cylindrical cavities are varied continuously with the resonance frequency change. Therefore varying the lengths of three cylindrical cavities makes it possible the variable resonance ability at the desired frequencies. The transmission loss characteristics of this example design is shown in Fig.10.

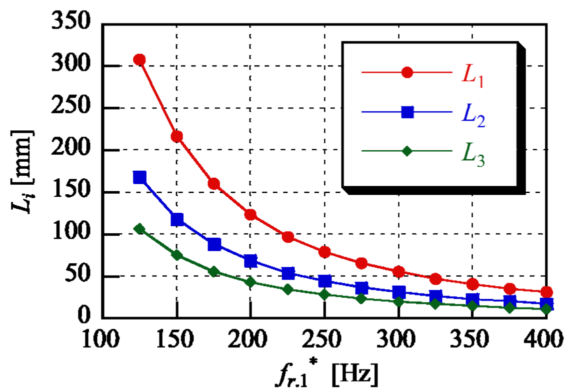

Fig.9 Example design of present resonator

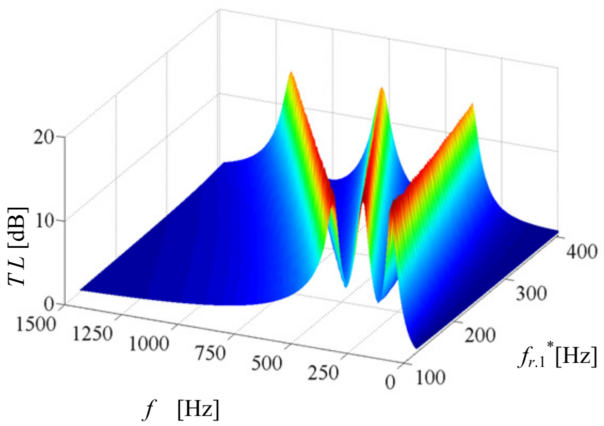

Fig.10 Transmission loss characteristics of example design

The figure clearly indicates the design variables are well searched with the given constraint condition ε=1.0 for all the frequency range 125 Hz < $f_{r.1}{}^*$ <400 Hz. The peak values of transmission loss at each resonance frequencies are almost constant when the lengths of cylindrical cavities are varied. As discussed before the change of these lengths have little influence on the transmission loss.

CONCLUSIONS

The final aim of this research is the development of the multi degree of freedom type Helmholtz resonator which can be applied to the hydraulic systems operated under the variable speed condition. In this report, in order to establish the design criteria of the present Helmholtz resonator, the transmission loss characteristics was theoretically investigated with respect to the design parameters for a conventional one degree of freedom type Helmholtz resonator. From these results the relationship between the design parameters such as the length and diameter and the attenuation performance was clarified. It is also confirmed that these information can be used to design the multi degree of freedom type Helmholtz resonator.

REFERENCES

1. Kojima, E. and Ichiyanagi, T., Development Research of New Types of Multiple Volume Resonators, Proc. of 1st Bath workshop on PTMC, 1998, pp. 193-206
2. Kribayashi, T., Ichiyanagi, T., Nishiumi, T., and Kikuta, K., Research on the Attenuation Characteristics of a Multi-degree of Freedom Type Helmholtz Resonator for Hydraulic Ssytems, Proc. of Mechanical Engineering Congress 2010 Japan, 2010, Vol.7, pp.79-80.
3. Brown, F. T., Nelson, S. E., Step Response of Liquid Lines with Frequency Dependent Effects of Viscosity, Journal of Basic Engineering, Transactions of ASME, 1965, Series D, **87-**2, pp. 504-510.
4. Kojima, E., and Ichiyanagi, T., Generation and Propagation of Fluid-borne Pressure Ripple in Fluid Power Systems Caused a Pump (2nd Report, Experimental Determination of Transfer Matrix Parameters of Hydraulic Silences and Assessment of its Attenuation Performance), Transaction of JSME, 1995, Ser. B, **61-**583, pp. 1014-1022.
5. Powell, M.J., An Efficient Method for Finding the Minimum of a Function of Several Variables Without Calculating Derivatives, The Computer Journal, 1964, Vol.7, pp.155-162

APPENDIX

The motion equation of oil inside the choke in Fig.4 can be expressed in the following equation.

$$\rho a_c l_h \frac{d}{dt}\left(\frac{Q_3(t)}{a_c}\right) = a_c\left(P_1(t) - P_3(t)\right) - a_c \frac{128\mu l_h}{\pi d_h^4} Q_3(t) \tag{A.1}$$

a_c is the cross sectional area of choke. Using the Laplace transform with respect to P and Q, the Eq.(A.1) becomes

$$(ms + C)Q_3 = P_1 - P_3 \tag{A.2}$$

where m is the inertial mass of fluid and C is the damping coefficient caused by viscous friction in the choke. These are defined as m=$\rho l_h/a_c$ and C=$\dfrac{128\mu l_h}{\pi d_h^4}$, respectably. The continuity equation considering the compressibility of oil in the cylindrical cavity can be given by

$$Q_3(t) - 0 = \frac{V_h}{\kappa}\frac{dP_3(t)}{dt} \tag{A.3}$$

The Laplace transform of Eq.(A.3) becomes the following equation with the elastic coefficient k=κ/V_h.

$$Q_3 = \frac{s}{k} P_3 \tag{A.4}$$

Hence, the inverse entrance impedance can be derived as follows.

$$\frac{Q_3}{P_1} = \frac{1}{Z_h} = \frac{s}{ms^2 + Cs + k} \tag{A.5}$$

Proceedings of the 8th JFPS International
Symposium on Fluid Power, OKINAWA 2011
Oct. 25-28, 2011

1C3-1

APPROXIMATE SIMULATION OF PNEUMATIC STEADY FLOW CHARACTERISTICS IN TUBES WITH FRICTION

Takeshi SHIRAISHI*, Eiji MURAYAMA**,
Yukio KAWAKAMI*, Kazuo NAKANO***

* Graduate School of Engineering, Shibaura Institute of Technology
307 Fukasaku, Minuma-ku, Saitama, 337-8570, Japan
(E-mail: kawakami@shibaura-it.ac.jp)
** Neorium Technology Co., Ltd
(E-mail: murayama@ neorium.co.jp)
*** Tokyo Institute of Technology
(E-mail: nakanokazu@jcom.home.ne.jp)

ABSTRACT

The conventional analysis of the Fanno flow is applicable for the air flow through the uniform adiabatic rigid pipe with friction losses. But it has the short-coming that the numerical method is inevitable in the analysis. In this paper we present the simple methods to calculate approximate characteristics for the Fanno flow in considering the dependency of the friction factor on the Reynolds number. And the usefulness of the simulation is shown by comparing the calculations to the experimental results.

KEY WORDS

; Pneumatic pipeline, Steady flow, Friction, Choking, Simulation

NOMENCLATURE

C: Sonic conductance (M_2=1)
C_e: Conductance (M_2<1)
c : Speed of sound
c_p: specific heat at constant pressure
D : Inner diameter of tube
f : Friction factor
K : Loss coefficient
L : Length of tube
M : Mach number
p : Static Pressure
q_m : Mass flow rate
R : Gas constant
R_{eD}: Reynolds number
T : Static Temperature
v : Axial speed of flow
κ : Specific heat ratio
μ :Viscosity
ν : Kinematic Viscosity
ρ : Density of air

Subscripts
0: Stagnation state
1: Upstream end
2: Downstream end
a :Approximate value
c : Critical or Choking condition
sra : Standard reference atmosphere
*:State at the section where M=1

INTRODUCTION

The steady flow of the air through the uniform adiabatic rigid tube with friction losses can be modeled by the Fanno flow.[1],[2],[3] But its analytical solution is not available and so the numerical method is inevitable in the analysis. We presented the paper [4] on the simulation for the Fanno flow. In the paper the friction factor f was treated as the constant factor and chosen so that the simulation results fit to the experimental results.

Now we take into considerations the dependence of the friction factor on the Reynolds number and introduce the new method to calculate approximate characteristics for Fanno flow.

BASIC EQUATIONS

The basic equations for the Fanno flow are written as followings.

Equation of conservation of mass

$$\frac{d\rho}{\rho}+\frac{dv}{v}=0 \tag{1}$$

Equation of motion

$$vdv=-\frac{dp}{\rho}-\frac{4f}{D}dx\frac{v^2}{2}=-\frac{dp}{\rho}-dK\frac{v^2}{2} \tag{2}$$

Energy equation

$$vdv+c_p dT=0 \tag{3}$$

Gas state equation

$$p=\rho RT \tag{4}$$

APPROXIMATE SOLUTIONS

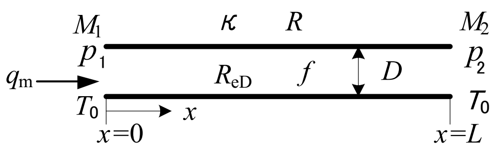

Figure1 Variables and parameters of a tube

1) M_2<1 (Subsonic condition)

We assume that the effects of compressibility are negligible with regards to the relationship between the friction factor and the Reynolds number. As the result incompressible formulas on the friction factor may be applicable for the Fanno flow in the subsonic region.

The Reynolds number is written by Eq. (5)

$$R_{eD}=\frac{vD}{\nu}=\frac{\rho vD}{\mu}=\frac{4q_m}{\pi D\mu} \tag{5}$$

The viscosity μ of the air is evaluated by the following Sutherland equation.

$$\mu=\mu_r\frac{T_r+S}{T+S}\left(\frac{T}{T_r}\right)^{3/2} \tag{6}$$

T_r=291.2K, μ_r=18.27×10^{-6} Pas and S= 120 K.

We assume that the temperature T of the air near the adiabatic wall of the tube is nearly equal to the stagnation temperature T_0. We substitute T_0 for T in Eq. (6) through this paper. From these assumptions we considered that the Reynolds number R_{eD} and the friction factor f do not change their value along the tube.

The loss coefficient K is given

$$K=\int dK=\int_0^L\frac{4f}{D}dx=\frac{4fL}{D} \tag{7}$$

Solving Eq.(1) to Eq.(7) the friction factor f is obtained

$$f=\frac{D}{4L}\left\{\frac{1-(M_1/M_2)^2}{\kappa M_1^{\,2}}+\frac{\kappa+1}{2\kappa}\ln\left[\left(\frac{M_1}{M_2}\right)^4\cdot\left(\frac{p_1}{p_2}\right)^2\right]\right\} \tag{8}$$

The static pressure ratio p_2/p_1 is expressed as a function of the Mach number ratio M_1/M_2 for a fixed value of the Mach number M_2 as shown in Eq. (9).

$$\frac{p_2}{p_1}=\left(\frac{M_1}{M_2}\right)\sqrt{\frac{2+(\kappa-1)M_1^{\,2}}{2+(\kappa-1)M_2^{\,2}}}=\left(\frac{M_1}{M_2}\right)^2\sqrt{\frac{2+(\kappa-1)M_1^{\,2}}{2\dfrac{M_1^{\,2}}{M_2^{\,2}}+(\kappa-1)M_1^{\,2}}} \tag{9}$$

Solving Eq. (9), the Mach number ratio (M_1/M_2) is expressed as the function of the Mach number M_1 for the given static pressure ratio p_2/p_1 as follows.

$$\frac{M_1}{M_2}=\left[\frac{1+\sqrt{1+\left(2+(\kappa-1)M_1^{\,2}\right)(p_1/p_2)^2(\kappa-1)M_1^{\,2}}}{\left(2+(\kappa-1)M_1^{\,2}\right)(p_1/p_2)^2}\right]^{0.5} \tag{10}$$

Substituting Eq. (10) into Eq. (8), the friction factor f is expressed in a functional form as follows,

$$f=f_{p21}(M_1) \tag{11}$$

Simultaneously the friction factor f is related to Reynolds number R_{eD} as followings.

$1\times10^4\le R_{eD}\le5\times10^6$ Filonenko's equation

$$f=\lambda/4=0.25\times\left[1.82\log_{10}(R_{eD})-1.64\right]^{-2} \tag{12a}$$

$3\times10^3\le R_{eD}\le1\times10^5$ Blasius formula

$$f=\lambda/4=0.0791R_{eD}^{\;-1/4} \tag{12b}$$

The mass flow-rate q_m is also the function of M_1 for the given value of the static pressure p_1 and the stagnation temperature T_0.

$$q_m=\frac{\pi D^2}{4}\sqrt{\frac{\kappa}{RT_0}}M_1\sqrt{\frac{2+(\kappa-1)M_1^{\,2}}{2}}p_1 \tag{13}$$

From Eq. (5), (6), (12) and (13), we get the function

$$f = f_{\mathrm{Re}}(M_1) \tag{14}$$

The simultaneous equations Eq. (11) and Eq. (14) are solved numerically for the given parameters D, L, R, κ and boundary conditions p_1, p_2, T_0.

Since $f_{p21}(M_1)$ and $f_{\mathrm{Re}}(M_1)$ are monotonously decreasing functions of M_1 like an example as shown in Figure 3, it is straightforward to find the cross point of these curves.

Let f_s and M_{1s} be the solution of the simultaneous equations. Substituting the solution M_{1s} into Eq. (13), the flow rate can be determined for the static pressure p_1 and the stagnation temperature T_0.

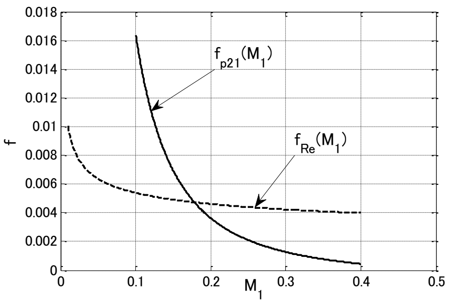

Figure.2 An example case of $f_{p21}(M_1)$ and $f_{\mathrm{Re}}(M_1)$

We adopted MATLAB and Simulink as the one of the simulation tools. The numerical searching the cross point is programmed as the MATLAB Function. It is integrated in the Simulink as shown in Figure 3.

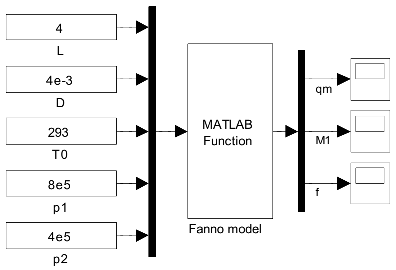

Figure.3 Simulink block

Solving Eq. (9), the Mach number M_2 is expressed on the given static pressure ratio p_2/p_1 and the Mach number M_1.

$$M_2 = \sqrt{\frac{-1+\sqrt{1+\dfrac{(\kappa-1)M_1^2\left(2+(\kappa-1)M_1^2\right)}{(p_2/p_1)^2}}}{\kappa-1}} \tag{15}$$

We can estimate the Mach number M_2 by substituting the Mach number M_{1s} into Eq. (16) for the given static pressure ratio. Since the range of the Mach number M_2 in Eq. (15) is less than the unity for the subsonic flow, the domain of the static pressure ratio p_2/p_1 and the related Mach number M_{1s} has to be restricted within the relevant extent.

2) M_2=1 (Critical condition)

To simplify a discussion we assume that the air blows directly into the atmosphere or a large chamber from the outlet of the tube shown in Figure 1.

Let p_2 be the static pressure at the adjacent interior side of the cross section of the outlet. The static pressure p_2 may be nearly equal to the static back pressure p_b in the downstream chamber if the Mach number M_2 is lesser than unity.

The Mach number unity is reached at the outlet by the choking due to friction. In this critical condition we assume that the static pressures p_2 is equal to the static back pressure p_b.

Specifying the stagnation temperature T_0 and the static pressures p_2^* first, the static temperature T_2^*, the velocity of sound c_2^*, the density ρ_2^* and the mass flow rate q_{mc} are given as follows:

$$T_2^* = \left.\frac{2}{2+(\kappa-1)M_2^{*2}}T_0\right|_{M_2^*=1} = \frac{2}{\kappa+1}T_0 \tag{16}$$

$$c_2^* = \sqrt{\kappa R T_2^*} = \sqrt{\frac{2\kappa R}{\kappa+1}T_0} \tag{17}$$

$$\rho_2^* = \frac{p_2^*}{RT_2^*} = \frac{(\kappa+1)p_2^*}{2RT_0} \tag{18}$$

$$q_{mc} = \frac{\pi D^2}{4}\rho_2^* c_2^* = \frac{\pi D^2}{4}\sqrt{\frac{\kappa(\kappa+1)}{2RT_0}}\,p_2^* \tag{19}$$

From Eq. (5), Eq. (6), Eq. (12), and Eq. (19), we can estimate the friction factor f_c.

From Eq. (8) and Eq. (9), the loss coefficient K_c at the choking condition is written as the function of the Mach number M_{1c} at the inlet.

$$K_c = \frac{4f_cL}{D} = \frac{1-M_{1c}^2}{\kappa M_{1c}^2} + \frac{\kappa+1}{2\kappa}\ln\left\{\frac{(\kappa+1)M_{1c}^2}{2+(\kappa-1)M_{1c}^2}\right\} \tag{20}$$

We proposed the inverse functions to compute the approximate Mach number M_{1ca} in our former paper [4] as followings.

$$M_{1ca} = a_1 \times \exp\left(-a_2 K_c^{a_3}\right) + a_4 \tag{21}$$

The parameters a_i (i=1 to 4) are listed for several intervals of the loss coefficient K_c in Table 1.

Table 1 Parameters in Eq.(22)

K_c	a_1	a_2	a_3	a_4
$0.1<K_c\leqq 1$	0.95	0.728	0.415	0.05
$1<K_c\leqq 25$	0.9	0.787	0.386	0.1
$25<K_c\leqq 110$	0.4	0.29	0.475	0.052
$110<K_c\leqq 200$	0.405	0.349	0.39	0.0333
$200<K_c\leqq 700$	0.33	0.28	0.38	0.0223

The Mach number M_{1c} and M_{1ca} are shown on the same plane (K_c, M_{1c}) and (K_c, M_{1ca}) in Figure 4. They coincide on the one line.

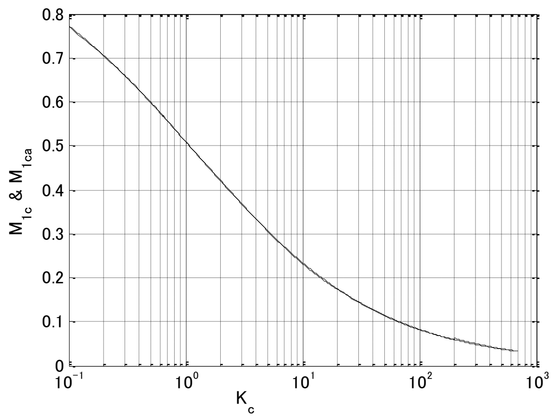

Figure 4 Comparisons of Eq. (20) and Eq. (21)

Substituting p_2^*, M_{1ca} and M_2=1 in Eq. (9), the critical static pressure ratio b_{21} is obtained.

$$b_{21}=\frac{p_2^*}{p_{1c}}=M_{1ca}\sqrt{\frac{2+(\kappa-1)M_{1ca}{}^2}{\kappa+1}} \tag{22}$$

The critical stagnation pressure ratio $p_{02}*/p_{01c}$ and the critical hybrid pressure ratio p_2^*/p_{01c} are related to the critical static pressure ratio b_{21} as follows.

$$\frac{p_2^*}{p_{1c}}=\left(\frac{2+(\kappa-1)M_{1ca}{}^2}{\kappa+1}\right)^{\frac{\kappa}{\kappa-1}}\frac{p_{02}*}{p_{01c}}=\left[\frac{2+(\kappa-1)M_{1ca}{}^2}{2}\right]^{\frac{\kappa}{\kappa-1}}\frac{p_2^*}{p_{01c}} \tag{23}$$

Figure 5 is a numerical example which show the boundaries of the critical conditions on the static pressure p_2^* and the static pressure p_{1c} for different length of tubes. The pair of $p_1$and p_2 in the left upper side of each boundary line belongs to the un-choking region and the pair of $p_1$and p_2 in its right down side belongs to the choking region respectively.

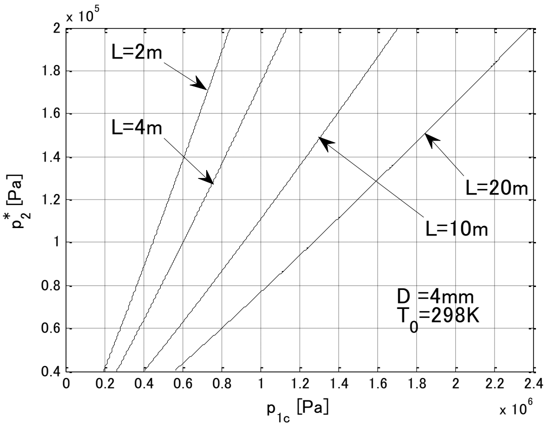

Figure 5 Boundaries of the critical conditions

3) M_2=1 (Choking condition)

When the inlet stagnation pressure is constant and the static back pressure is reduced from the critical value, the Mach number M_2 maintains unity and the choking continues. In this state the static pressure p_2^* is higher than the static back pressure. Similarly when the static back pressure is maintained at a certain constant value and the inlet stagnation pressure is increased from the critical value, the choking state continues and the static pressure p_2^* becomes higher than the static back pressure. In these states the flow at the downstream side of the outlet is highly affected by the shape of the downstream path and so one dimensional flow models are not appropriate to exact simulations.

On the choking state we assume that the static pressure p_2^* is related to the choking flow in the tube and independent of the static back pressure which is specified as the static pressure in the large chamber or the atmosphere.

EFFECTS OF FRICTION FACTOR

The conductance in the subsonic region is defined as follows,

$$C_e=\frac{q_m}{\rho_{sra}p_{01}}\sqrt{\frac{T_{01}}{T_{sra}}} \tag{24}$$

We considered two representative boundary conditions of flows through tubes.

Case1: The static pressure p_1 is constant and the static pressure p_2 is variable. (Constant upstream)

Case2: The static pressure p_2 is maintained at the atmospheric pressure and the static pressure p_1 is variable. (Variable upstream)

Numerical examples of conductance on two cases are shown in Figure 6.

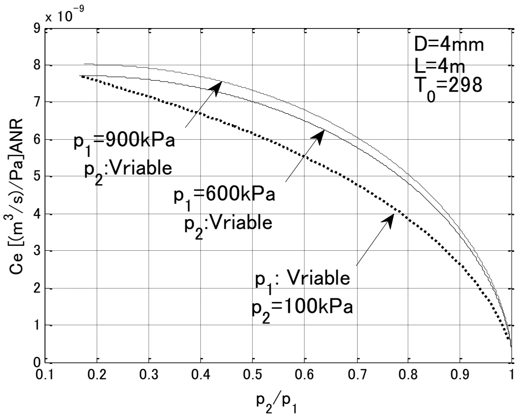

Figure 6 Conductance to static pressure ratio

The solid and broken lines show Case 1 for the different upstream static pressure p_1 and the dotted line shows Case 2 for the atmospheric downstream static pressure p_2. The left end of each line shows the critical condition. The big deference is shown between Case 1 and Case 2.

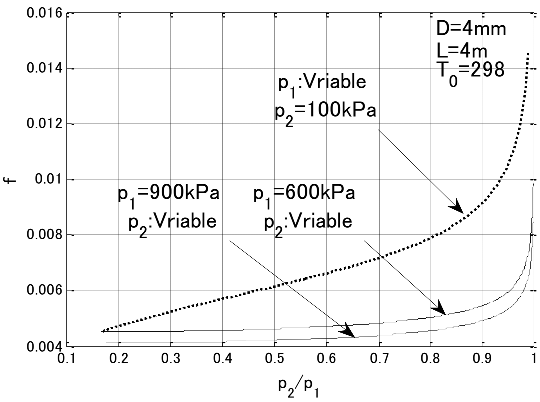

Figure 7 Friction factor

Figure 7 shows the friction factors which are obtained by the simulator shown in Figure 3. In Case 2 the friction factor, shown by the dotted line, varies remarkably in the full range of the static pressure ratio. On the contrary the variations of Case 1, shown by the solid and broken lines, are small within the wide range of the static pressure ratio as in Figure 7.

In the former report [4], we assumed that the friction factor f was uniform along tubes and equal to a certain constant value which was chosen so as to minimize the difference between simulation results and experiments in the corresponding range of the pressure ratio.

In this constant friction factor model, the simulation results of the conductance for Case1 and Case2 become same and they are shown on a single line in the (p_2/p_1, C_e) plane. For example, they are shown as three broken lines which correspond the friction factors f=0.004, f=0.0045 and f=0.005 respectively in Figure 8. The solid line in the Figure 8 shows the conductance for Case 1 (p_1=600kPa) of the variable friction factor model. The solid line coincides the broken line for f=0.0045. It is considered that the constant friction models may be good candidates to model Case 1 on the variable friction factor model but not for Case 2.

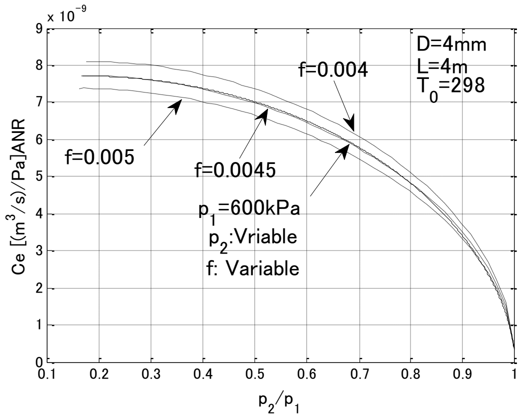

Figure 8 Conductance for the constant friction model

COMPARISON WITH EXPERIMENTS

We calculated the conductance for several tubes by making use of our simulation program and compared with experimental results which were done at SMC Co.

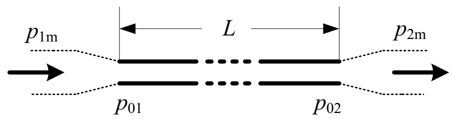

Figure 9 Test line and connected tubes

Test lines are connected to the pressure measuring tubes by each transition connectors at the inlet and outlet of test lines according to the test procedure of ISO-6358 as shown in Figure 9. The static pressure p_{1m} and p_{2m} at the pressure measuring tubes are measured. It is considered that p_{1m} and p_{2m} are nearly equal to the stagnation pressure at the inlet and outlet of the test line due to the effect of each tapered transition connector respectively. We compared the calculated stagnation pressure ratio p_{02}/p_{01} to the static pressure ratio p_{2m}/p_{1m}. In the simulations the stagnation pressure at the inlet or the outlet are adjusted to fit the boundary conditions.

In Figure 10 to Figure 12 we show the calculated results of Case 1 by solid and broken lines and Case 2 by dotted lines respectively. The measured values are shown by the marks ○ and ・ for Case 1 and the marks □ for Case 2.

For large ratio of L/D, for example 10000 or 1000, the simulation results are very similar to the measured results as in Figure 10 to Figure 11. Figure 12 for L/D=100 shows the big differences between them.

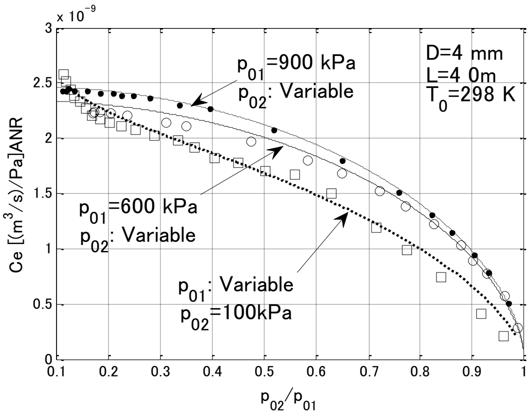

Figure 10 Conductance D=4 mm, L=40m

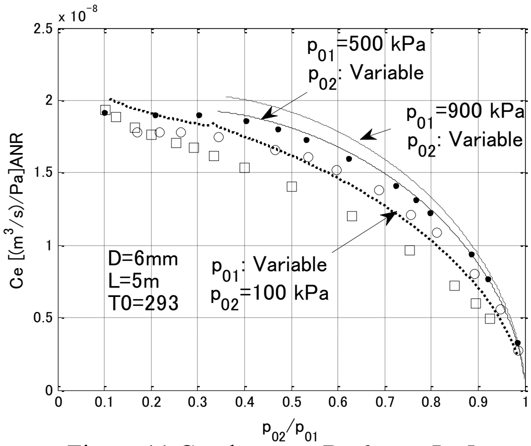

Figure 11 Conductance D=6 mm, L=5m

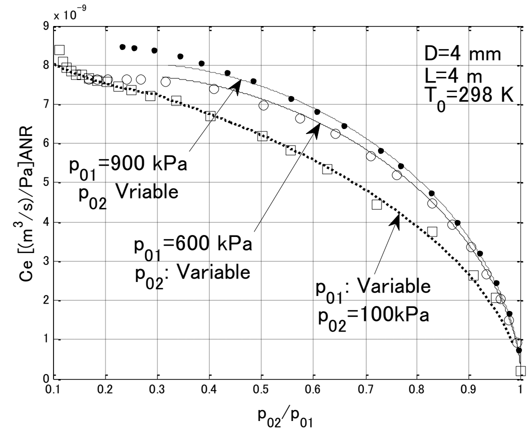

Figure 11 Conductance D=4 mm, L=4m

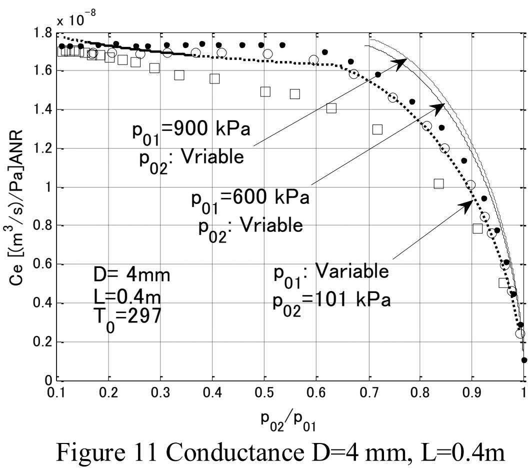

Figure 11 Conductance D=4 mm, L=0.4m

We also checked up on our simulation results by comparing them with the results of the reference [5]. The experimental results which are picked up from the data in the reference are shown by marks in Figure 12. The lines are corresponding results of our simulation. Our simulation results shift to the greater direction of the conductance from the real experimental results [5].

We also checked on the combination [5] of D=2mm and L=3m. The tendencies were similar to Figure 11.

CONCLUSION

On the discrepancy between simulations and measurements, many reasons are considered. For example the velocity distribution is not uniform and so the average velocity is not equal to the speed of sound at the outlet in the choking condition. And also it is difficult to measure the stagnation pressure at the outlet and the exact estimation of the difference between p_{02} and p_{2m} is impossible. One dimensional modeling has to be modified for better simulations.

It is confirmed that our simulation model is useful for practical calculations in the design of pneumatic systems.

ACKNOWLEDGEMENT

We wish to thank Mr. N. Oneyama and his colleague in SMC Co. for furnishing their data to us. We also wish to thank Dr. S. Sesmat in INSA and his colleague for the permission to cite their data.

REFERENCES

1. Shapiro, A.H.: The Dynamics and Thermodynamics of Compressible Fluid Flow, Vol. I , Ronald Press, 1954
2. Benedict, R.P. et al: A Generalized Approach to One-Dimensional Gas Dynamics, Trans. ASME, J. E. Power, January ,1962, pp49/68
3. Wartelle, C.: Caractéristiques de débit des apparreils á fluides compressibles, Les Mémoires Techniques du CETIM, No.13, September, 1972, pp1/54
4. Kawakami,Y. et al: Proc. 7th JFPS Int. Symp. On Fluid Power, 2008, P1-29, pp413/416
5 D. Gaitier, S. Chabane, S. Sesmat and D. Hubert: Long Pneumatic Tubes, Experimental Approach, ISO French Delegation Report 14 June (2010), pp1/11.

Proceedings of the 8th JFPS International
Symposium on Fluid Power, OKINAWA 2011
Oct. 25-28, 2011

1C3-2

RATE- AND STATE-DEPENDENT FRICTION MODEL FOR ELASTOMERIC SEALS

Oliver Heipl*, Hubertus Murrenhoff*

* Institute for Fluid Power Drives and Controls (IFAS)
RWTH Aachen University
Steinbachstraße 53, 52072 Aachen, Germany
(E-mail: oliver.heipl@ifas.rwth-aachen.de)

ABSTRACT

Seals are crucial for the functionality of pneumatic linear actuators. They separate chambers with different pressure levels. Little air leakage which leads to reduced volumetric efficiency is often accepted. More important is the role of friction which decreases the efficiency caused by tribological contacts between seals and counter surfaces. Furthermore, friction leads to reduced precision. Static friction models are state of the art within the designing of pneumatic systems including cylinder devices. These friction models are based on a description of the Stribeck curve. But they are not able to predict dynamic friction instabilities like stick-slip, increasing break-away force due to dwell-time and hysteretic friction phenomena. The paper shows a simulation approach based on a powerful rate- and state-dependent friction model. Loads on the tribological contact between seal and rod are realised by a structural mechanics method. The numerical results are compared with experimental investigations.

KEY WORDS

Friction, Seal, Pneumatics, Elastomer, Thermo-Viscoelasticity

NOMENCLATURE

A	:	Area
B	:	Left Cauchy Green strain tensor
b	:	Contact width
C_1, C_2	:	WLF parameter
C_{10}, C_{01}	:	Mooney-Rivlin parameter
e, τ	:	Relaxation parameter
F	:	Force
I	:	Invariant
m	:	Mass
p	:	Pressure
T	:	Temperature
t	:	Time
v	:	Velocity
W	:	Strain energy density
x	:	Stroke
α, τ, γ	:	Carlson-Batista parameters
θ	:	Frictional state variable

INTRODUCTION

Due to the simple and robust design pneumatic linear devices are often used for automation purposes to generate reciprocating motion. To ensure the functionality seals are applied, see Figure 1. They are located at the piston to separate the cylinder chambers, in the area of the end cushioning and at the rod to enable a pressure difference between chamber and ambience. At the rod additional wipers are used to avoid a contamination of the pneumatic system by dust. They can be carried out as single element or combined with the seal.

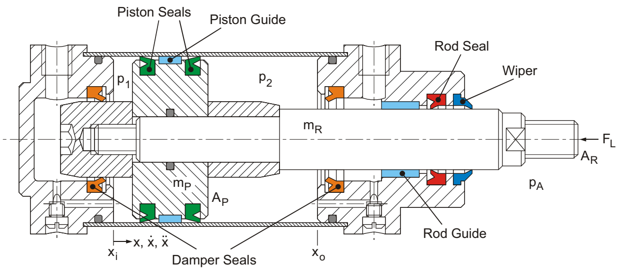

Figure 1: Schematic of a pneumatic linear device

A little air leckage which results in a decrease of the volumetric efficiency is often accepted. In contrast, friction is one of the main problems of pneumatic cylinder devices. In consequence of the contact between the seals, wipers and guidance elements with the counter surfaces, friction is induced when relative motion occurs. The dissipative character of friction (kinetic energy is transferred to thermal energy) causes a decline of the pneumatic-mechanical efficiency as well as an interaction with the dynamics of the piston.
An established tool in the design and development stage of pneumatic systems is the one-dimensional system simulation of the fluidic circuit. Hereby the dynamic properties of a pneumatic linear device can be investigated in an early stage of the development process. With ease, interaction between fluidic, mechanical and control system can be optimised.
The mathematical description of the piston motion is based on a differential equation of second order, see Equation 1. The pressures in the cylinder chambers can be easily described by the pressure build up as a result of mass flow, volumetric changes as well as heat generation and transfer. However, the implementation of the friction into the simulation is very insufficient.

$$(m_P + m_R)\ddot{x} = p_1 A_P - p_2 (A_P - A_R) - p_A A_R - F_L - F_F \qquad (1)$$

State of the art in present system simulation tools are static friction models. Normally, the so called Stribeck model is used which describes the fundamental relationship between friction and velocity. In Equation 2 a possible form to reproduce a Stribeck curve is shown [9].

$$F_{F,0} = \begin{cases} F_C\, sgn(v) + (F_S - F_C)\, e^{-\left|v/v_S\right|^{\delta_S}}\, sgn(v) + F_v v & ;\ v \neq 0 \\ F_e & ;\ v = 0 \ and \ \left|F_e\right| < F_S \\ F_S\, sgn(F_e) & ;\ otherwise \end{cases} \qquad (2)$$

In addition a linear scaling factor f to describe the influence of the pressure on the friction is generally considered, see Equation 3.

$$F_F = F_{F,0}\,(1 + \Delta p\ f) \qquad (3)$$

By investigating measured friction of a pneumatic seal a more complex behaviour including hysteretic effects, frictional memory and non reversible friction characteristic is detectable, see Figure 2 and 3. Static linking between friction and velocity is insufficient for a realistic description [2,3,5,7,8]. Rather, a change in the friction characteristic is detectable due to the change off the operating conditions. Among others a significant influence of the temperature appears.

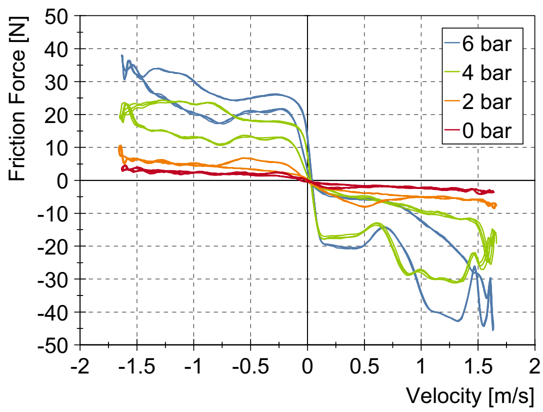

Figure 2: Pressure-dependent friction force

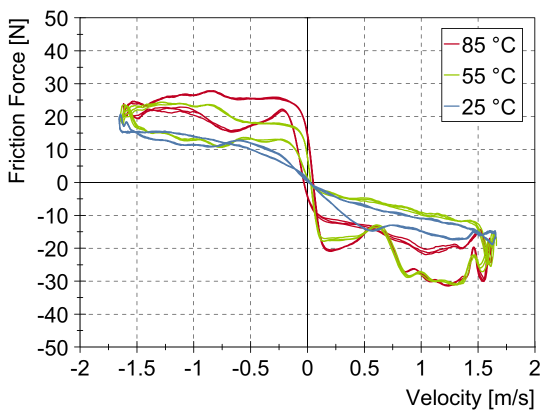

Figure 3: Temperature-dependent friction force

OBJECT OF RESEARCH

Static friction models which are implemented in present one-dimensional system simulation tools do not allow considering the dynamic friction phenomena as well as the influence of the design of the sealing system. Furthermore the influence of the temperature on friction is neglected.
Enhancing the description of friction within the system simulation by a novel approach based on a coupled simulation between system simulation, dynamic friction model and structural mechanics, a more accurate modelling including friction instabilities and time dependent effects is possible.
Integration of structural mechanics allows considering the influence of the seal shape, the dimension of the groove as well as the seal material on friction.

MODELLING APPROACH

The modelling approach is based on a system simulation model, a friction model and a structural mechanics model. The interaction between the three partial models is figured out in Figure 4.

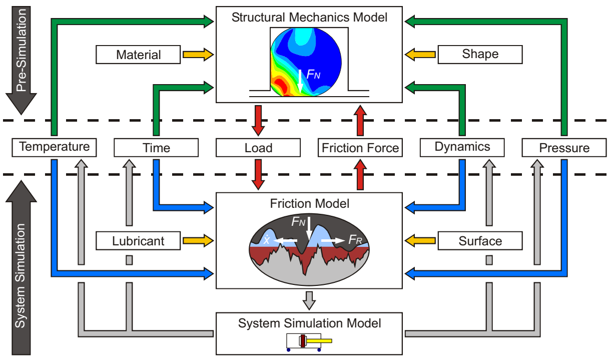

Figure 4: Modelling approach

The system simulation model describes the fluidic, mechanical and control properties of the investigated system. For this purpose the commercial system simulation tool DSH*plus* is used. An exemplary system simulation model is shown in Figure 5. A pneumatic cylinder without any internal friction models is controlled by a valve. The programmable logic controller (PLC) triggers the valve with a typical driving cycle. A signal input is used as well as a signal output to couple the system simulation model with the friction model. Separating system simulation and friction model allows using different system simulation tools. To determine the friction force, values (e.g. temperature, pressure and velocity) from the system simulation are transferred to the friction model via the signal output. Loading of the pneumatic cylinder by a friction force occurs via the signal input.

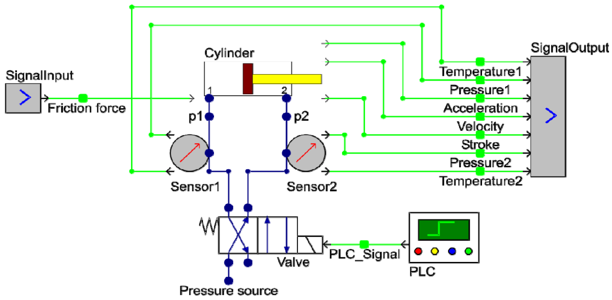

Figure 5: System simulation model

The friction model uses the values from the system simulation tool and calculates the friction forces based on empirically and physically motivated equations. This partial model characterises the friction in a microscopic way which means that the description is limited to the contact area.
The implemented rate- and state-dependent friction model is based upon the model by Carlson and Batista [1,4,10] which describes the fundamental physics in the easiest possible way. The basic principle of this model is a frictional state variable Θ to model the transition from dry friction to a full hydrodynamic friction. The change of the frictional state variable in a range from 1 (dry friction) to 0 (hydrodynamic friction) satisfies Equation 4. The state term on the left side implies melting of the film defined by a time constant τ. The rate term on the right side describes the change of the film due to shear stresses. The factor α correlates to a characteristic length in which the changes take place. In addition a load on the contact is taken into account by the factor F_N. The load is dependent on the installation situation, the shape and the material of the seal as well as the operating conditions like pressure and temperature.

$$\dot{\Theta} = \frac{\Theta}{\tau}(1-\Theta)\,F_N - \alpha\frac{1}{F_N}\Theta\,\dot{x} \qquad (4)$$

A progression of the frictional state variable for a simple periodic motion is shown in Figure 6. With increasing velocity a transition between dry friction and hydrodynamic friction occurs (lower loop) while with decreasing velocity the value of the frictional state variable increases again and the portion of boundary friction grows. The transition between the different states effects a hysteretic behaviour. By increasing the load F_N a rather weakly developed transition between dry and hydrodynamic friction occurs (upper loop).

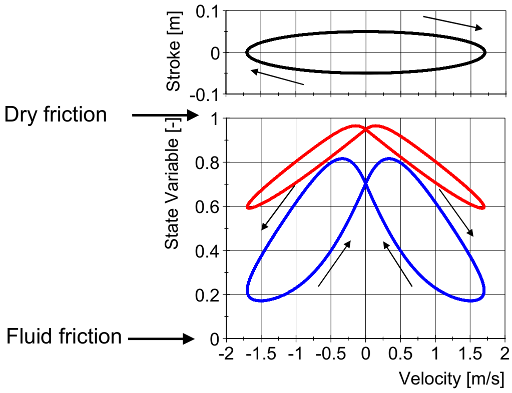

Figure 6: Progression of the frictional state variable

The friction force is calculated based on the frictional state variable, see Equation 5. A distinction between static F_a and dynamic frictional components F_b takes place. In addition, the third term of the equation provides the viscous friction which is assumed as linearly dependent to the piston velocity. The parameter γ describes the fluid properties, primarily the (equivalent-)viscosity of grease. The factor F_N and the contact width b are interfaces to the structural mechanics again.

$$F_F = \left(F_a - F_b\right)\,\Theta\; + F_b + F_N\;b\;\gamma\;\dot{x} \tag{5}$$

The structural mechanics model is the third partial model and provides the loading on the tribological contact in a macroscopic way using a Finite Element Method (FEM). First geometrically simple O-ring seals are applied to simplify the modelling. Due to this a fully parameterisable axial symmetric seal model was build up. The FE-model is able to consider the fundamental physics of elastomeric seals.
In contrast to steel elastomeric materials does not possess a linear stress-strain relation even at low loading. Measured quasi-static stress-strain relations are shown in Figure 7 for two typical sealing materials for pneumatic applications.

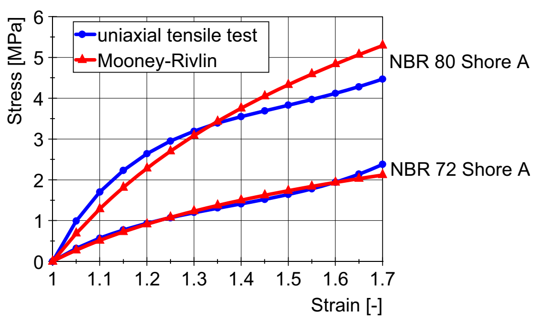

Figure 7: Stress-strain relation for elastomers

The hyperelastic material behaviour can be modelled by using a widely spread approach by Mooney and Rivlin [10,11] which bases on a strain energy function, see Equation 6. B is the left Cauchy Green strain tensor and $tr(B)$ represents the first principal invariant I_1 of that tensor, while $tr(B^{-1})$ stands for the second principal strain invariant I_2. The parameters C_{10} and C_{01} have to be determined by curve fitting for each material.

$$W^0 = C_{10}^0\left[tr(B) - 3\right] + C_{01}^0\left[tr\left(B^{-1}\right) - 3\right] + k\left(det(B) - 1\right)^2 \tag{6}$$

The third term of the strain energy function represents a thermal expansion which is equivalent to a change in the third invariant I_3, see Equation 7.

$$I_3 = det(F) = 1 + 3\alpha(T)\left[T - T_0\right] \tag{7}$$

If temperature is varied and especially when temperature is low relative to the glass transition temperature the thermo-viscoelasticity of the sealing material has to be taken into account [6,12]. In this case the history-dependent behaviour requires a strain energy function which considers not only the actual but also the past values of loading, see Equation 8 and 9.

$$\hat{W} = W^0\left(\hat{I}_1;\hat{I}_2\right)\left[1 - \sum_{i=1}^{N} e_i\{1 - exp(\frac{\hat{t} - t}{\tau_i a_{T,T_G}})\}\right] \tag{8}$$

$$log\; a_{T,TG} = \frac{C_1\left(T - T_G\right)}{C_2 + T - T_G} \tag{9}$$

Using this constitutive framework for elastomeric seals FE analysis can be performed. As an exemplary result a cooling process is shown in Figure 8. The temperature of an O-ring seal which is assembled in a groove is going down from room temperature to -90 °C. The cooling rate is small enough that the sealing forces are in a thermodynamic equilibrium until the glass transition temperature T_G. Below the glass transition temperature the thermal shrinkage is less adapted which leads to a much stronger sealing force reduction. At about -80 °C the contact between seal and groove disappear and a gap results. Afterwards the forces at the rod increases due to thermal shrinkage. A more detailed discussion of the thermo-viscoelastic properties of sealing materials can be found in [6].

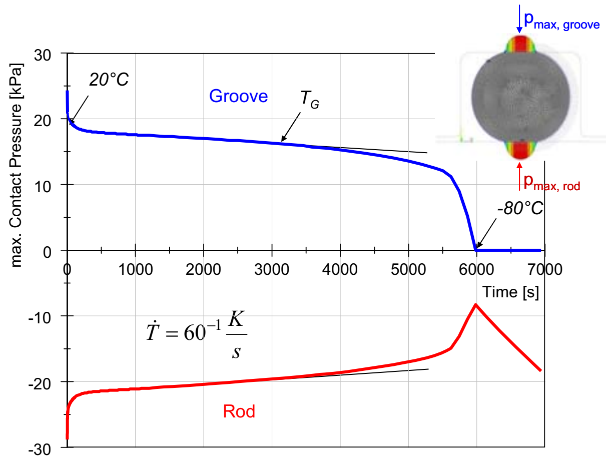

Figure 8: Cooling process

The three introduced partial models (system simulation model, friction model and structural mechanics model) are integrated in a coupled simulation using MATLAB/Simulink, see Figure 9. Due to the reason that a finite element simulation would dominate the calculation time compared to the system simulation the structural mechanics is solved by using characteristic diagrams. These characteristic diagrams are generated in a pre-simulation.

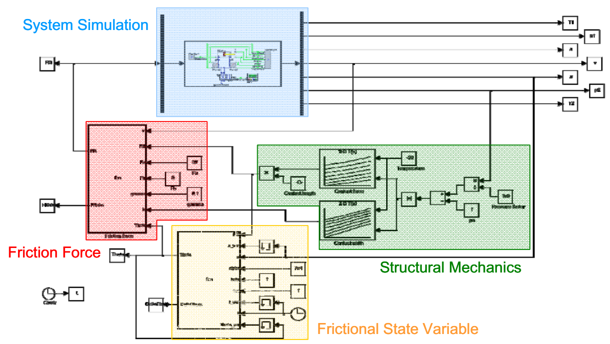

Figure 9: Coupling of the partial models

A result of a coupled simulation is shown in Figure 10. A differential cylinder where the friction is only located at the rod seal is controlled with a rectangular signal. The motion characteristic changes as well as the sealed pressure dependent on the loading with different temperature levels. At low temperature the piston reacts a little bit faster and more dynamic due to lower contact forces and in succession lower friction as shown before compared to a higher temperature.

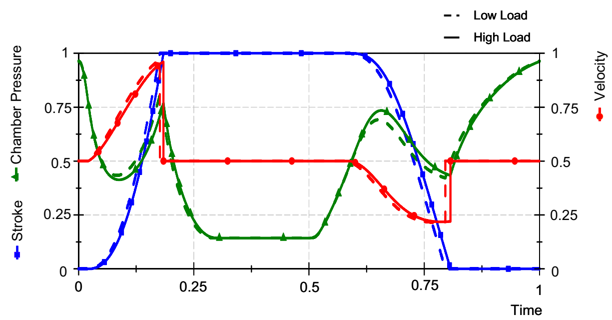

Figure 10: Simulation at different loads

VALIDATION

Experimental investigations are necessary to parameterise and validate the friction model. For this purpose a test rig for pneumatic piston seals was used. The measurement principle is shown in Figure 11. The piston including the test seal is at rest and the tube is driven by a crank mechanism. To pressurise the test seal a second piston is applied. Measuring at different temperature levels is possible by heating the complete test assembly.

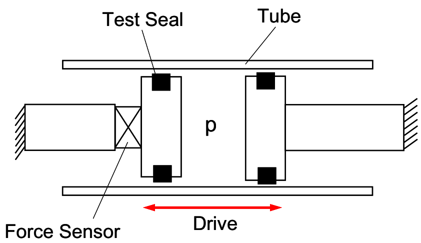

Figure 11: Measurement principle

Comparisons between simulated and measured friction forces are shown in Figure 12 for room temperature and Figure 13 for a temperature of 55 °C. The simulated friction forces are much smoother then the measured one. Reasons are small form deviations of the tube and vibrations of the test assembly caused by the crank mechanism.

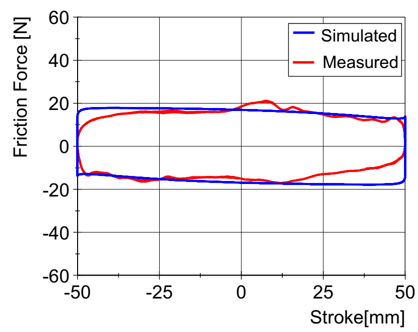

Figure 12: Comparison at room temperature

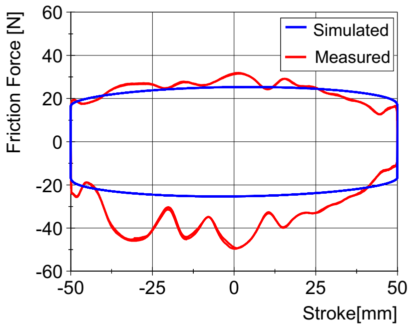

Figure 13: Comparison at 55 °C

CONCLUSION

The motion characteristics of pneumatic cylinder devices are significantly influenced by seal friction. In present one-dimensional system simulation tools static friction models are state of the art. To consider rate- and state-dependent friction a dynamic friction model is presented. Coupling of system simulation with a powerful friction model and a structural mechanics model shows accurate results. Especially influences on the friction process (e.g. temperature and seal shape) can be considered with this novel method. Using measurements with different parameters of the tribosystem like different roughnesses will be necessary to expand the database which is used for parameterising the friction model.

ACKNOWLEDGEMENT

The IGF-project 16229 N/1 of the Forschungs-vereinigung Forschungskuratorium Maschinenbau e.V. – FKM, Lyoner Straße 18, 60528 Frankfurt am Main is supported via the AiF in the context of the program to support the Joint Research and Development (IGF) by the Federal Ministry of Economics and Technology because of an enactment of the German Federal Parliament.

REFERENCES

1. Achenbach, M. and Papatheodorou, T.: Modeling of Friction Phenomena in Pneumatic Cylinders. In: Proceedings of the 6th International Fluid Power Conference (IFK), Volume 2, 2008, pp. 279-288
2. Al-Bender, F. ; Lampaert, V. and Swevers, J.: Modeling of dry sliding friction dynamics - From heuristic models to physically motivated models and back. In: Chaos 14 (2004), No. 2, pp. 446-460
3. Canudas de Wit, C. ; Olsson, H. ; Åstrom, K. J. and Lischinsky, P.: A New Model for Control of Systems with Friction. In: IEEE Transations on Automatic Control 40 (1995), No. 3, pp. 419-425
4. Carlson, J. M. and Batista, A. A.: Constitutive relation for the friction between lubricated surfaces. In: Physical Review E 53 (1996), No. 4, pp. 4153-4165
5. Dahl, P.: A solid friction model. In: Technical Report TOR-0158, The Aerospace Corporation, El Segundo (1968), pp. 3107-3118
6. Heipl, O. ; Murrenhoff, H. ; Achenbach, M.: Friction Modelling for Pneumatic Actuator Seals Regarding Structural Mechanics. In: Proceedings of the 16th International Sealing Conference (ISC), Stuttgart, 2010, pp. 141-152
7. Hess, D. and Soom, A.: Friction at a Lubricated Line Contact Operating at Oscillating Operation Conditions. In: Journal of Tribology 112 (1990), No. 1, pp. 147-152
8. Olsson, H. ; Åström, K. ; Canudas de Wit, C. ; Gäfvert, M. and Lischinsky, P.: Friction Models and Friction Compensation. In: European Journal of Control 4 (1998), No. 3, pp. 716-195
9. Persson, B. N.: Theory of friction: on the origin of the stick-slip motion of lubricated surfaces. In: Chemical Physics Letters 254 (1996), No. 1-2, pp. 114-121
10. Rivlin, R. S., Saunders, D. N.: Large Elasticity Deformations of Isotropic Materials VII: Experience on the Deformation of rubber. In: Phil. Trans. Roy. Soc. Lond. Math. Phys. Sci. 243 (1951), No. 865, pp. 251-288
11. Treloar, L. R.: The Physics of Rubber Elasticity. Third Edition. Oxford : Clarandon Press, 1975
12. Williams, M. L. ; Landel, R. F. and Ferry, J. D.: The Temperature Dependence of Relaxation Mechanisms in Amorphous Polymers and Other Glass-forming Liquids. In: Journal of the American Chemical Society 77 (1955), No. 14, pp. 3701-3707

Proceedings of the 8th JFPS International
Symposium on Fluid Power, OKINAWA 2011
Oct. 25-28, 2011

1C3-3

VISUAL CONTROL OF A PNEUMATIC DRIVEN MANIPULATOR FOR THE BIOMEDICAL TECHNOLOGY

Hung-Yi Chen, Ming-Chang Shih*

* Department of Mechanical Engineering, National Cheng-Kung University, Taiwan
(E-mail:mcshih@mail.ncku.edu.tw)
Department of Mechanical Engineering, National Cheng-Kung University, Taiwan
(E-mail: n1895153@mail.ncku.edu.tw)

ABSTRACT

This study described a two axes pneumatic driven manipulator, which is driven by the servo cylinder. Through visual image technology, the position between the tip of the probe and the target was determined. Therefore, the visual servo can be produced the control command. A fuzzy controller with a dead zone compensator was designed to improve the position precision of a nonlinear pneumatic driven manipulator. From the experimental results, the position error stayed within 254nm.

KEY WORDS

Visual Servo, Fuzzy Control, Manipulator, Pneumatic Cylinder

NOMENCLATURE

e_i : position error of pneumatic driven manipulator
G_{cei} : scaling factors of fuzzy set
G_{ei} : scaling factors of fuzzy set
Gui : scaling of controller output
u_{fi} : output signal of fuzzy controller
u_{di} :compensation command of dead zone
V_f : positive constants
V_b : positive constants
y_c : target position
y_{m_i} : probe position of the pneumatic driven manipulator
y_i : the center of tracking image
ρ : the scale factor and image resolution

INTRODUCTION

In the advanced scientific applications, the manipulation systems are widely applied such as the biomedical technology and the semi-conductor technology. In the biomedical technology research, the manual manipulation systems were earlier utilized to the cell punctures, cutting, and injections which require fine control of both the position and the force in executing various processes. Human operator is difficult to accomplish. The speed of penetration enables the micropipette to quickly pierce without causing excessive deformation to the cell .The success rate of manual manipulations were low [1]. Combining the high position accuracy of the manipulation system and the automatic operation can be improved the success rate of the manual

manipulation. Visual technology was often applied to determine the position of the object and track the object increasing the probability of the automatic operation. Through image processing and image recognition, the distance between the tip of a micropipette and the cell is calculated in the image plane. Therefore, researchers have developed many types of the automatic manipulation system using visual servo [1-6]. Yasser et al. [1] developed a robotic manipulation system for automated selection using vision-based feedback control. Ouyang et al. [5] designed and developed automatic bio-micromanipulator system with visual control, which moving velocity is 10um/s. It can be applied to puncture cells. Various image processing and image recognition methods was used to determine and to measure the position of an object accurately. Zhang [6] utilized the image processing to cell injection and called Hough cell detection algorithm. Another aspect, the success rate of manipulation process depends on the high position accuracy of the manipulation system. Thielecke H et al. [7] used a stepper motor-based system for the cell manipulation with the 40 nm of position accuracy. Ouyang et al. [5] designed a manipulation mechanism which is driven by DC servomotors and a PZT actuator.
This paper presents the pneumatic driven manipulator based on servo pneumatic technology. The advantages of a pneumatic driven system include large stroke and low cost. However, because of the compressibility, the air leakage, the friction force and the load force, the pneumatic system is highly nonlinear [8]. The PVA/PV control and friction compensation, used in the pneumatic servo positioning system, can achieve ±0.01mm of the position accuracy [9].Utilizing conventional PD and Fuzzy controller with a velocity compensator, a pneumatic cylinder driven table was controlled to achieve 20nm of the position accuracy. The velocity compensator can be reduced to overcome the stick-slip effective of the pneumatic cylinder driven table [10].The hybrid self-tuning fuzzy controller with dead zone and velocity compensator is used to control the low friction pneumatic XY table embedded with aerostatic bearings, can achieve ±40nm of the position accuracy [11].

SYSTEM DESCRIPTION

A visual control system was built, shown in Fig. 1. The system is constructed of three subsystems: a microscope, a two axes pneumatic driven manipulator, and a control interface. The microscope and the two axes pneumatic driven manipulator are integrated to enable both position control and automatic manipulation through the designed of a control interface.

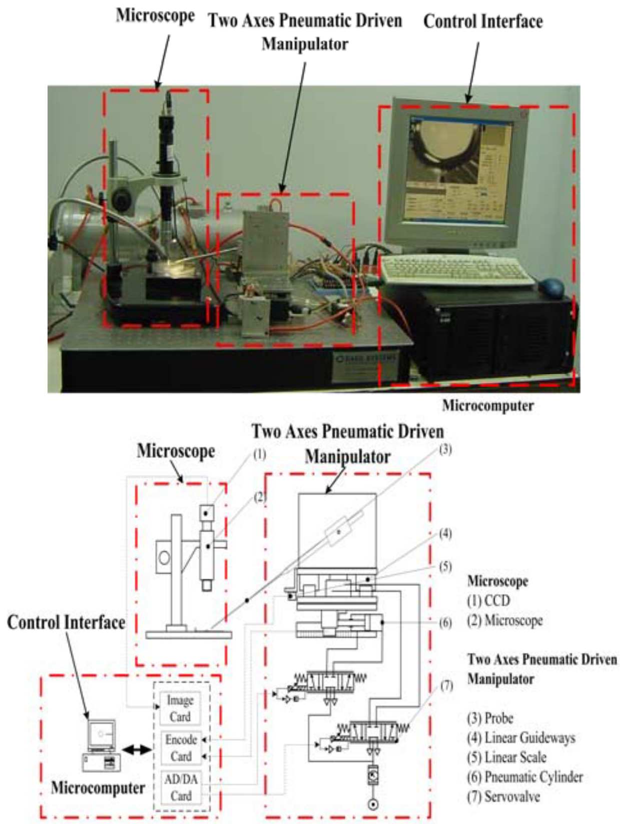

Figure 1 Photo and scheme of the proposed system

The microscope includes an optical microscope (NAVITAR Zoom 6000), a CCD camera (WAT-525EX, 30 FPS), an image processing card (PICLO, 30 FPS) and light Source (150W). The magnification of an optical microscope is adjusted from 3.48 to 78. The image resolution is from 2.87 to 0.127 micrometer.
The two axes pneumatic driven manipulator consists of the position tables, the servo valves (FESTO MPYE,0 to 100 l/min, 0.6MPa), the linear scale (JENA, resolution: 20nm), the pneumatic cylinders (SMC, 40mm) and linear guideways. The position table is pushed by air cylinders and moves along the linear guideways. The platform is set horizontally driven by the pneumatic cylinder. The 3/5-port proportional control valve which operates at 6 bar is used. It can adjust the flow-rate from -100 1/min to 100 1/min with the input voltage (0 to 10V). When input voltage is half of the nominal voltage (5 V) so that the flow rate is zero. A microcomputer acts as a controller and is used for the experimental data acquisition. The displacement of the tables is measured

by a linear scale and feedback to the microcomputer through the AD/DA card and the encode card. The control signal is calculated in the microcomputer through designed the control interface and passed to the 3/5-port proportional control valve by the D/A capability of the data acquisition and the control card.

The control interface includes the capturing image and the displacement of the manipulator, the image recognition, calculating and sending the control signal through the AD/DA card, the encode card and the image processing card. Visual C++ code from the MFC is used to finish the control processing and the control interface, which Multi thread technology ensured the processing program of the control interface can be synchronized to proceed in real time.

In this study, the visual image is captured using a CCD camera in the proposed system. Through the image processing and the image recognition, the distance between the object and the tip of the probe can be determined in the image plane. Therefore, the command signal can be calculated. The control signal is produced to the servo valve, the displacement of the servo pneumatic manipulation system is measured by the linear scale and feedback to the computer through the AD/DA card and the encode card. The air mass flow rate is regulated by the servo valve. The pressure difference of the cylinder can be built up to drive the manipulation system. This system can be controlled to target position. The block diagram is shown in Fig. 2.

CONTROLLER DESIGN

Considering the stroke of the pneumatic actuator and the field of view of the microscope, visual servo is applied to calculate and produce the control command to the fuzzy controller with the dead zone compensator in the field of view of the microscope. To avoid the area of motion of the two axes pneumatic driven manipulator being outside the field of view of the microscope, the control interface can be used to produce the control command, and implemented to the positioning control of the servo pneumatic manipulator. A block diagram of the system is shown in Figure 3.

Visual Servo

Visual servo is used to the image tracking and recognition and calculated the distance between the target position and the tip of the probe in the image plane, Control command be described as

$$\begin{bmatrix} r_{m_x}(k) \\ r_{m_y}(k) \end{bmatrix} = \rho \begin{bmatrix} \cos\theta - \sin\theta \\ \sin\theta \quad \cos\theta \end{bmatrix} \begin{bmatrix} r_{ix}(k) \\ r_{iy}(k) \end{bmatrix} \tag{1}$$

where y_c is the target position, y_i is the center of tracking image, in this study is utilized tracking tip, ρ is the scale factor and image resolution which is adjusted with the microscope .

Position error of the pneumatic driven manipulator can be represented as

$$e_i(k) = r_{m\,i}(k) - y_{m_i}(k) \qquad i = x, y \tag{2}$$

where e_i is the position error of the pneumatic driven manipulator, y_{mi} is the probe position of the pneumatic driven manipulator.

Control signals can be written as

$$U_i(k) = u_{di}(k) \qquad i = x, y \tag{3}$$

where u_d is the fuzzy control with the dead zone compensation command

Fuzzy Control

Fuzzy controller has the advantage of being a man-made design, adjustable by means of rule tables to compensate for physical phenomena. Thus, fuzzy controllers are often utilized in nonlinear systems such as the ones addressed in this study. The structure of the fuzzy control includes four parts: fuzzification interface, knowledge base, decision logic and defuzzification . The proposed design applies the Mamdani control rules algorithm, and uses the “center of the gravity” to defuzzify and to get the accurate control signal.

The variables E_i DE_i and u_i are chosen to be the two input and output of the controller, respectively. The error E_i and the change of error DE_i are defined by

$$E_{\mathrm{i}}(k) = e_{\mathrm{i}}(k) \times G_{e\mathrm{i}} \tag{4}$$

$$DE_{\mathrm{i}}(k) = \frac{1 - z^{-1}}{T_s} e_{\mathrm{i}}(k) \times G_{ce\mathrm{i}} \tag{5}$$

where G_{ei} and G_{cei} are the scaling factors of error and change of error.

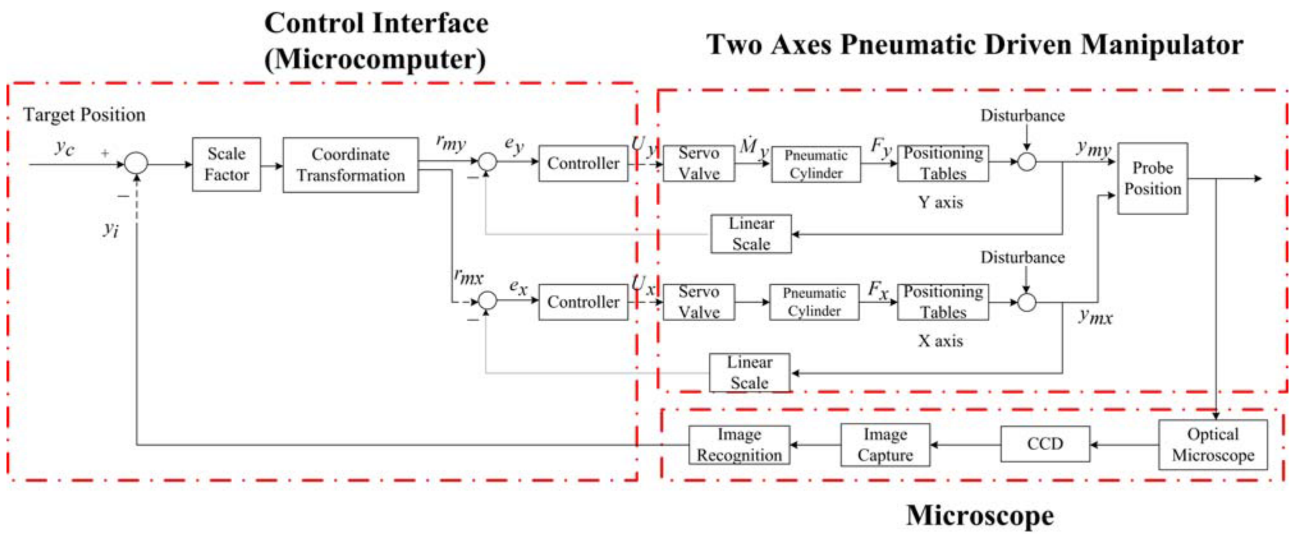

Figure 2 Block diagram of the proposed system

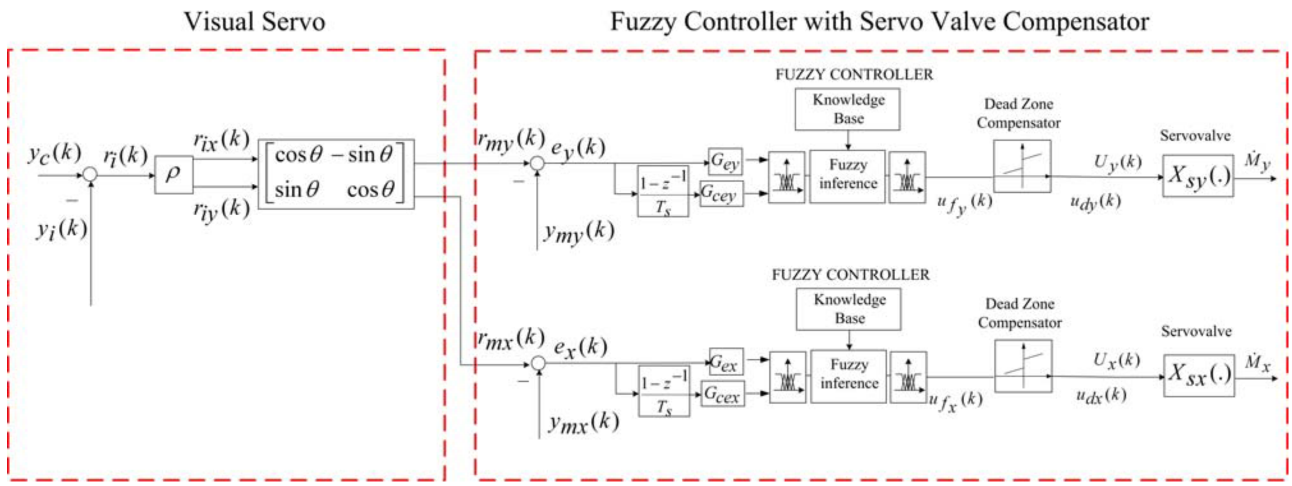

Figure 3 Scheme of the control structure

The output signal $u_{fi}(k)$ form the microcomputer is defined as:

$$u_{f_i}(k) = u_i(k) \times Gu_i \qquad i = x, y \tag{6}$$

where $u_i(k)$ and Gui denote the controller output and the scaling of the controller output.

The triangular membership functions are applied to define the fuzzy sets of the inputs and the outputs, as illustrated in Figure 4. The input boundary of membership function is based on positioning precision. From the experimental results, is adjusted the output boundary of the membership function. Because the characteristics of the two axes are not the same, the output boundary of the membership function is different. The value of the control signal depends on the flow rate of the servo valve and friction force. Since the friction force of Y-axis is the large then X-axis, the control law of the Y-axis is the large. Considering different cross-section of the piston of the pneumatic cylinder, a non-symmetric way of the membership function is used.

The rule table is according to the practical phenomenon. The table below shows that if the position error and the error differentiation are both negative big, then the output is negative big. In this case, the happening of the big overshoot in this system must be prevented. Therefore, the control signal should be "Negative Big." The system can be driven backward to the target position by the pneumatic cylinder. This method thus completes the rule table.

Dead Zone Compensator

The friction force and the characteristics around the mid-position of the servo valve create a dead zone in the proposed system. To avoid the effect of the dead zone influence on position accuracy, the control signal must add "V_f" to the forward motion of the system and subtract "V_b" from the backward motion of the system.
The dead zone compensator was designed as shown in Fig. 5. and express as:

$$u_{di}(k)=\begin{cases}u_{fi}(k)+V_{fi}, & if\ u_{fi}(k)>5\\ u_{fi}(k)-V_{bi}, & if\ u_{fi}(k)<5\end{cases} \qquad (7)$$

$$i=x,y$$

where V_f and V_b are positive constants and their values are obtained through measurement of the dead zone.

Table 1 Fuzzy rules for computation of $u_i(k)$

$\dot{E}_i$ \ E_i (u_i)	NB	NS	ZE	PS	PB
NB	NB	NB	NS	NS	ZE
NS	NB	NS	NS	ZE	PS
ZE	NS	NS	ZE	PS	PS
PS	NS	ZE	PS	PS	PB
PB	ZE	PS	PS	PB	PB

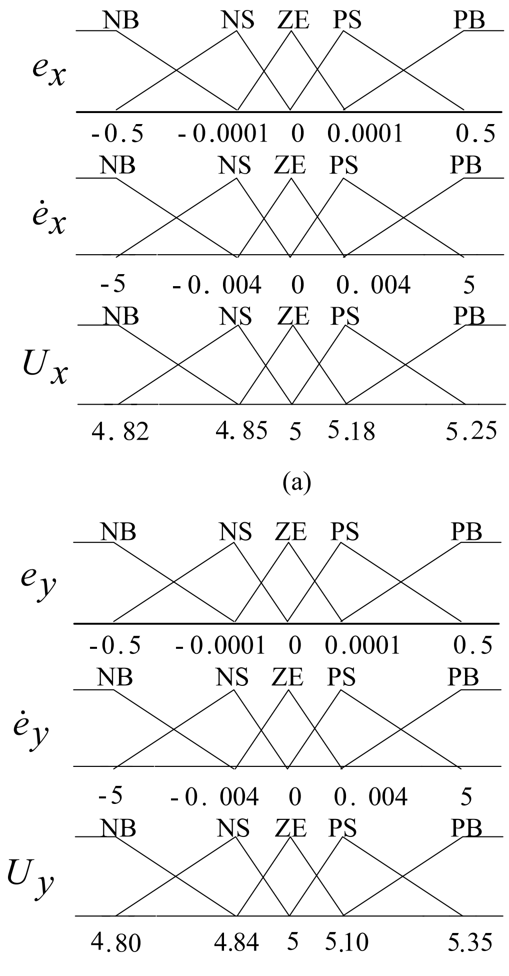

Figure 4 Membership function and rules table

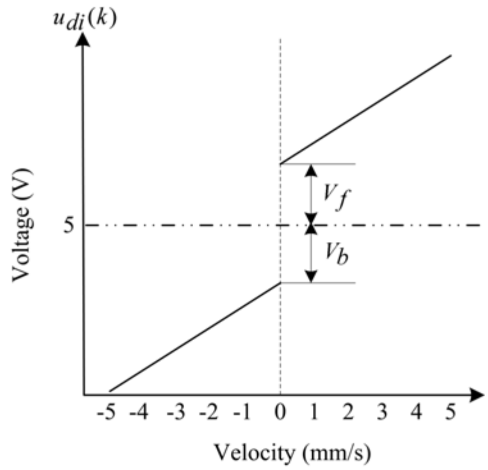

Figure 5 Compensation command of the dead zone

CONTROL INTERFACE

The control process is performed according to the following step:

1. The image is captured with a CCD camera . After the image is processed using the Sobel operator, the invert image, and the threshold
2. Image recognition and image tracking are employed to determine the position, and the distance between the target position and the object position is calculated.
3. The control command is produced and used to control the position of the pneumatic driven manipulator.

Steps (1) to (3) of the control process are repeated and using the control interface, the manipulation process or the position control is achieved.

Image process

A 640*480 pixel image was used to measure and define the position the object and the tip of a probe. Fig. 6 shows that the proposed design applies various image processing methods including the Sobel operator, the invert image, and the threshold methods. Sobel operator performs a 2-D spatial gradient measurement on an image, and thus emphasizes regions to edges. Threshold processing converts a grey image into a binary image and to differentiate the sample contour in an image from the background in the study.

Equation (8) is an expression of the binary image $I(u, v)$.

$$I(u,v) = \begin{cases} 1 & \text{if } f(u,v) \geq k \\ 0 & \text{otherwise} \end{cases} \quad (8)$$

where $f(u,v)$ is the grey value of a pixel in gray image, $I(u,v)$ is the corresponding binary value of that pixel, k is the threshold value, the histogram can be analyzed, image and selected fit for threshold value k.

Object Recognition

In this paper, the object matching based on Normalized Cross Correlation. In object recognition or matching applications, one finds an instance of a small reference template in a large scene image by sliding the template window in a pixel-by-pixel basis, and computing the normalized correlation between them [12], as shown in Fig. 7. The NCC used for finding matches of a reference template $t(i, j)$ of size $m \times n$ in a scene image $f(u,v)$ of size $M \times N$ is defined as

$$N(i,j) = \frac{\sum_{u,v}[f(u,v) - \bar{f}_{u,v}][t(u-i, v-j) - \bar{t}]}{\sqrt{\sum_{u,v}[f(u,v) - \bar{f}_{u,v}]^2 \sum_{u,v}[t(u-j, v-j) - \bar{t}]^2}} \quad (9)$$

where $\bar{t}$ is the mean of the reference template, $\bar{f}_{u,v}$ is the mean of $f(u,v)$ in the region under the template. The template size $m \times n$ is smaller than the scene image size $M \times N$.

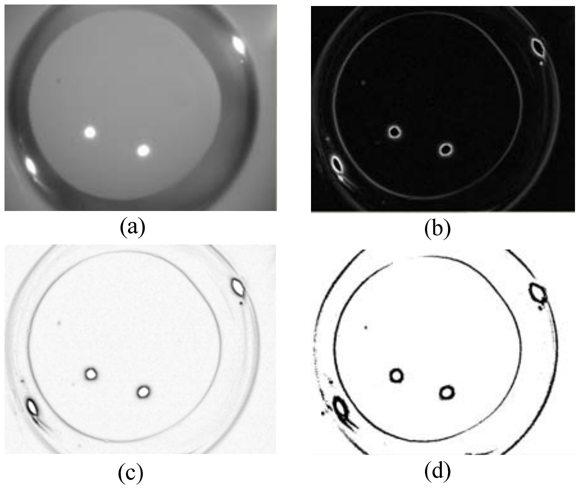

Figure 6 Image processing methods (a) Gray image (b) Sobel image (c) invert image (d) Threshold

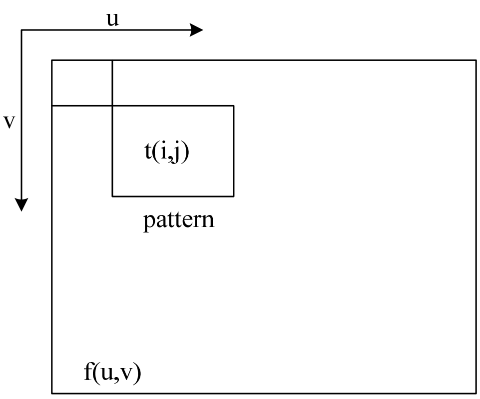

Figure 7 Object recognition

EXPERIMENTAL RESULTS

Online of the Distance Measurement

In this study, the visual image is used to measure the distance between the glass pipette and the probe tip with a control interface, which includes the image processing, the image recognition, the image tracking and the distance calculating. The control interface can be used to measure the distances in the real time, as shown in Fig. 8. Green and red grids represent the target object and the tip of the probe, respectively. The cross mark is the center of the feature tracking in the image plane. The user can select the matching image size using the control interface. After the Sobel operator, the image inversion, and threshold process, the recognition and measuring time is 0.053 seconds. The contour of the glass pipette and the probe tip is clearly shown in Fig. 8.

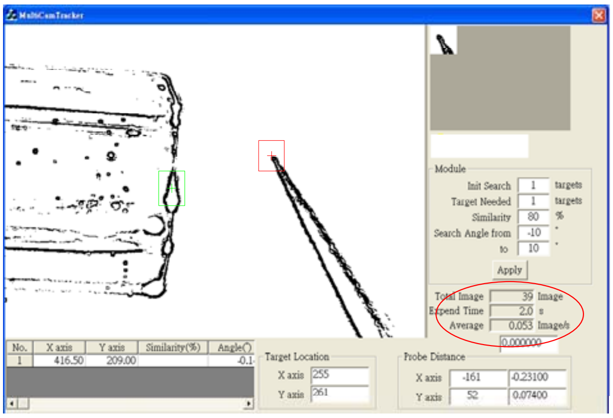

Figure 8 Photo of distance measurement

Automatic Puncturing Operation

Proposed system ensures that it can be applied on realistic process. The proposed system was implemented for the automatic puncturing operation of a fish egg, as shown in Fig. 9. In this study, a fish egg was fixed on a petri-dish. The user could select the puncturing position with the control interface in the proposed system. From the experimental results, the automatic puncturing operation was successfully completed.

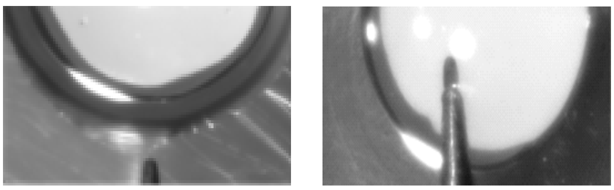

(a) (b)

Figure 9 Photo of automatic puncturing operation
(a) before puncture (b) after puncture

Position Control

Figure 10 and Figure 11 show the time responses of the step input with 127nm image resolution of the microscope. The manipulator is controlled forward to 50 pixels. The visual sensor captures the image speed with 30 frame/s. Therefore, the displacement output looks like a saw toothed line. From the experimental results, the steady state errors stayed within 254nm(2 pixels).

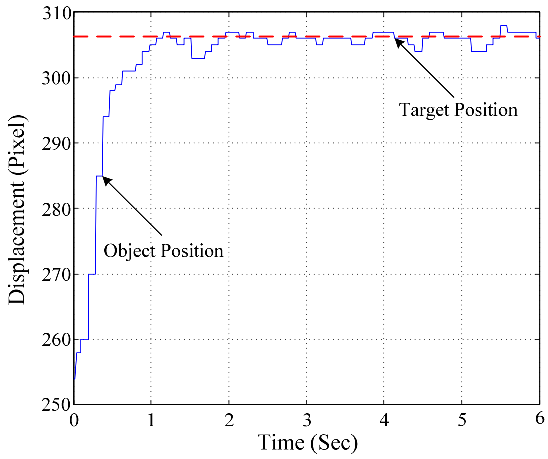

(a)

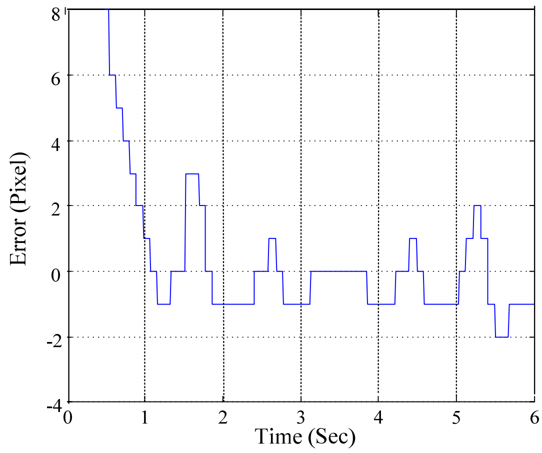

(b)

Figure 10 (a) time response of the x axis (b)error

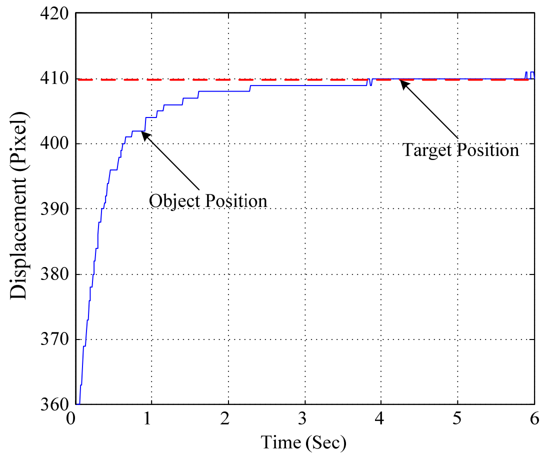

(a)

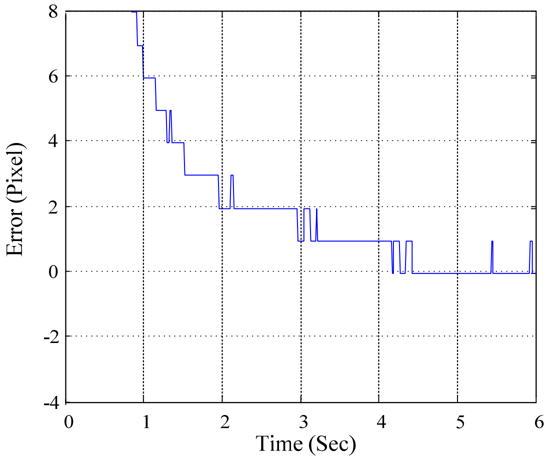

(b)

Figure 11 (a) time response of the y axis (b)error

CONCLUSION

This paper presents the two axes pneumatic driven manipulator with visual control. Through the experimental results, the performance of the system can be described in the following:

1. A visual image was used to calculated the error between the target position $y_c(k)$ and the object position $y_i(k)$ in the image plane, after the control command of the system $r_{mi}(k)$ are produced.
2. A microscope and a two axes pneumatic driven manipulator were integrated by a control interface
3. A fuzzy controller with a dead zone compensator was designed to improve the position precision of a nonlinear pneumatic driven manipulation system.
4. From the experimental results, the position error stayed within 2 pixels (image resolution :127nm).

ACKNOWLEDGMENT

The support provided by National Science Council of Taiwan (NSC99-2221-E-006-255) is appreciated.

REFERENCES

1. Anis, Y.H., Holl, M.R. and Meldrum, D.R., Automated Selection and Placement of Single Cells Using Vision-Based Feedback Control, IEEE Trans. on Automation Science and Engineering, 2010, vol.7, no. 3, pp. 598-606.
2. Kudoh, K.I., Tabuchi, S., Higuchi, T., Kakusho, N. and Sato, K., Development of Automatic Micromaipulation System for Biological Cell Sorter, J. Mamm. Ova Res, 1998, vol. 15, pp.167-172.
3. Zhou, Y., Nelson, B.J. and Vikramadita, B., Interagting Optical Force Sensing with Visual Servoing for Microassembly, Journal of Intelligent and Robotic Systems, 2000, vol. 28, pp. 259-276.
4. Yamamoto, H. and Sano, T., Study of Micromanipulation Using Stereoscopic Microscope, IEEE Trans. on Industrial and Measurement, 2002, vol. 51, no. 2, pp. 182-187.
5. Ouyang, P.R., Zhang, W.J., Madan, M. and Zhao, W., Overview of the development of a visual based automated bio-micromanipulation system, Journal of Mechatronics, 2007, vol. 17, pp. 578-588.
6. Zhang, Y. and Tan, K.K., Vision-Servo System for Automated Cell Injection, IEEE Trans. on Industrial electronics, 2009, vol. 56, pp. 231-238.
7. Thielecke,H., Zimmermann, H. and Fuhr, G.R., Gentle cell handling with an ultra-slow instrument: creep-manipulation of cells, Microsyst Technol, 2005, vol. 11, pp. 1230-1241.
8. Shearer, J.J., The Study of Pneumatic Process in the Continuous Control of Motion with Compressed Air-I, ASME Trans., 1956, pp. 233-242.
9. S. Ning and G.M. Bone, "High Steady-State Accuracy Pneumatic Servo Positioning System with PVA/PV Control and Friction Compensation, Washington, DC, 2002,pp. 2824-2829.
10. Shih, M.C. and Pai, K.R., Nanoaccuracy Position Control of A Pneumatic Cylinder Driven Table, Int. Journal of JSME, Series C, 2003, vol. 46, no. 3, pp. 1062-1068.
11. Shih, M.C., Tsai, M.H., Hsu, T.Y. and Pai, K.R. Precision Position Control of Pneumatic Servo Table Embedded with Aerostatic Bearing, Journal of System Design and dynamics, 2008, vol. 2, no. 4, pp. 940-949.
12. Tsai, M.D. and Lin, C.T., Fast normalized cross correlation for defect detection, Pattern Recognition Letters,2003, vol. 24, pp. 2625-2631.

Proceedings of the 8th JFPS International
Symposium on Fluid Power, OKINAWA 2011
Oct. 25-28, 2011

1C3-4

A DISPATCH METHOD OF AIR COMPRESSORS BASED ON FORECASTING CONSUMPTION

Dewen KONG*,Weiqin LIN*, Maolin CAI*

* School of Automation Science and Electrical Engineering, Beijing University of Aeronautics and Astronautics,BUAA
Beijing, 100191,China
(kongdewen01@163.com)

ABSTRACT

Pneumatic system operation status and problems were analyzed in the industrial production site; Considering the 24 hours as a time unit, the feature of compressed air consumption was studied every 20 seconds in 24 hours in the industrial production site. Then, presenting a forecasting method, which is workable and the overall mean in line with air consumption changes in the law. This forecasting method is for the purpose of the operation dispatching of air compressors in the industrial site, and Its forecasting accuracy meets the requirement of air compressors operation dispatching. Finally, with forecasting consumption of compressed air , a optimal scheduling algorithm of compressor group is given.

KEYWORDS

Pneumatic system, Energy-saving, Forecast model, Neural network, Optimal scheduling

NOMENCLATURE

Q : the air consumption[L/min]
A_1 : the effective front area of the piston[cm^2]
A_2 : the effective back area of the piston[cm^2]
L : the pison stroke[cm]
p : the working pressure[kg/cm^2]
N : the cylinder stroker per minute
K : the safety factor,K=2
p_0 : air pressure inside the connecting pipeline[bar]
p_b : air pressure in the outlet of hole[bar]
T_0 : air temperature inside the connecting pipeline[K]
u_0 : the flow rate of compressed air in pipeline[m/s]
u_2 : the flow rate of compressed air outside the hold [m/s]
A_h : the the sectional area of a small hole[m^2]
G : mass flow rate under Standard Reference Atmosphere [kg/s(ANR)]
C : the sonic conductance[$dm^3/(s\bullet bar)$]
ρ_0 : air density in the air pipeline[kg/dm^3]
$Q(t)$: the historical air consumption

INTRODUCTION

Entering into the 2l century, energy conservation and environmental protection has receviced more and more attention in China. The Chinese government has promulgated a series of energy-saving policies and measures. Especially in Copenhagen climate change conference at the end of 2009,our country government solemnly declared that the 2020 carbon dioxide emissions per unit of GDP would drop 40% to 45% compaired to 2005.The pneumatic systems which occupy the total elctricity consumption of the national factories by 10% to 20% (even as high as 35%) will inevitably become the energy conservation object[1].People started to focus on waste issues in the use of the pneumatic system, such as the unscientific use and excessive leakage problem, so energy saving is becoming an important and urgent task in pnematic system in China.

At present, Energy-saving research is focused on a single pneumatic device in the field of pneumatic system. For example, the authors focused on how to improve efficiency of compressor drive motor and how to change compressor drive motor speed to change its volume flow[2][3] ,etc. But Energy-saving research on the whole pneumatic system is relatively small, especially energy-saving research on air supply compressor group running has not yet been carried out in-depth study.

This paper argues that the important reason for these problems, pneumatic system with high energy consumption and low resource utilization in our country, is unreasonable dispatching of air compressors in industrial site. This leads to a problem, That is, compressors' air production does not match the air need of industrial production site. It pushes up pressure in air supply pipeline and increases the energy consumption of pneumatic system. All these make the air consumption forecasting very important in industrial production site. Only the authors obtain air consumption forecasting values which comply with the requirements of precision, the authors can provide a reasonable basis for air compressors' dispatch and improve pneumatic system operation efficiency.

PNEUMATIC SYSTEM OF INDUSTRIAL SITE

A. The Composition of Pneumatic System

Fig 1 shows a typical compressed air system, which can be divided into the four main parts: compressor, dryer and filter, receiver and pipe network and end uses.Compressed air which is generated by air compressor is fed into the air purification device to remove moisture, oil and other purification. Clean air is sent to the air devices through air pipeline, such as spray gun, cylinder and so on[4].

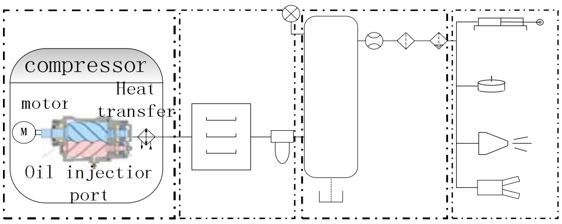

Fig.1 A typical compressed air system

In the pneumatic system, the energy conversion process is that air compressor motor output shaft power is converted into pneumatic power and stored in the compressed air , and then transmitted through the air pipeline to the cylinder, spray gun and other pneumatic devices. Energy is consumed in air compressor, air pipeline and terminal pneumatic devices in the whole process[5].In the whole process, Air compressor power consumption is about 96% of the whole process. Air purification device is about 3% of the whole process. The other process is about 1% of the whole process[6]. Nowadays, the prudent users have been becoming aware of the fact that pneumatic system is not low-cost to operate. Among compressed air system, compressed air is produced by air compressors. Air compressors consumed the most electricity of the pneumatic system. The production of compressed air can be one of the expensive processes in the manufacturing facilities.Therefore, Efficient operation of air compressor group is great significant to reduce the energy consumption of the pneumatic system.

B. Pneumatic System Problems in Operation

There are many problems in the course of air users using the pneumatic system in our country, which cause a lot of waste. The main waste is that air compressor group were dispatched in the unreasonable way , which is only to guarantee air minimum pressure required by industrial production. In addition, there are many minor waste with high pressure in air pipeline, larger leakage, Inefficient spray gun, weak awareness of air costs for workers etc.And there are also many irrational phenomena of pneumatic devices in use. Such as, air back pressure test to determine whether the parts stick to place, vacuum generator with compressed air when they are not at work. Factories often reduce 0.7MPa high pressure to 0.1~0.2MPa to use, Especially Stirring the chemical liquid tank or pneumatic tire manufacturing in the shape[7].For all waste, which need to enhance the management awareness of air cost to avoid some waste. More importantly, the authors should develop techniques to optimize the operation of air compressors and improve operation efficiency of the pneumatic system.

C. Classification of Compressed Air Consumption in Industrial Site

1) Air consumption of the pressure stable-supply device

The pressure stable-supply device in industrial production site is mainly the actuator cylinder, which moves objects from point to point. These cylinders are divided into reciprocating motion cylinder, the swing movement cylinder, air claws etc. Their role is to convert the air pressure energy into mechanical energy to drive objects reciprocating, swing and rotating motion.

The authors can calculate air consumption of a common cylinder by equation 1 as follows 1:

$$Q = \frac{(A_1 + A_2)L*(p+1)N}{1000} * K(l/\min) \tag{1}$$

The authors can see from the equation 1. Air consumption of cylinder is affected by its own intrinsic parameters and air supply pressure. When cylinder is at work, air pipeline is Installed pressure regulator to stabilize the cylinder working pressure. Therefore, the air consumption of cylinder will not change with the whole pipeline pressure fluctuations.

2) Air consumption of the pressure unstable-supply device

The pressure unstable-supply device is mainly spray gun, which directly connects to the air pipeline without the pressure regulator. In addition, leakage points in the air pipeline are caused by aging and damage. These air devices are of the same air consumption feature, and the flow characteristics can be basically equivalent to a small hole. Fig. 2 shows the schematic flow of hole[8].

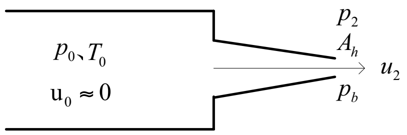

Fig. 2 Contraction of the flow through the nozzle

Ideal air flow through the contraction, which is considered as one-dimensional isentropic flow. The hole flow curve is shown as Fig.3, when the outlet of hole is under the same pressure.

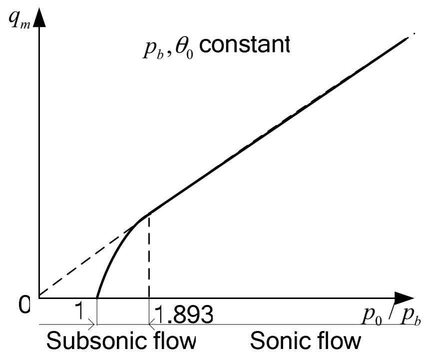

Fig. 3 The flow curve of ideal air flowing through contraction nozzle

Pressure is equal to atmospheric pressure(0.1MPa) at the outlet of hole. The authors can see from the Fig.3, when pressure higher than 0.1893MPa in the air pipeline, flow of compressed air has reached the speed of sound. The flow rate is proportional to its change in supply pressure. When air is in the sonic flow condition, the mass flow is calculated by equation 2[9].

$$G = Cp_0\rho_0\sqrt{\frac{\theta_0}{\theta_1}} \tag{2}$$

D. Air Consumption Characteristics of Industrial Site

Air consumption of industrial production site has its own characteristics and is greatly affected by the production. Based on production in the industrial site, the authors conduct air consumption forecasting in a 24-hour. Only the authors fully grasp the characteristics and variation of air consumption, the authors can establish realistic forecasting model and improve forecasting accuracy.

1) Uncertainty

Future need of air consumption in industrial site is uncertainty, which is affected by a variety of complex factors. For example, Reduction in air consumption caused by devices failure, the number of devices running at the same time is not the same and so on. Various factors are constantly changing. Some changes can be forecasted in advance, but some changes are difficult to forecast in advance. Coupled with the impact of temporary change of condition, these lead to the inaccuracy of air consumption forecast in industrial production site.

2) Periodicity

Compressed air consumption of industrial production site fluctuates in a day, week cycle, and big cycle contains small cycle. Generally, in the course of normal industrial production, air consumption changes of weekdays have similar law and air consumption changes of weekend have similar law. Usually, air consumption variation is not the same between workday and weekend. Monday to Friday is the peak production of industrial production. Air consumption is relatively large and small differences in weekday. Saturday and Sunday are the rest days, and relatively small industrial production. Therefore air consumption is relatively small. Taking air consumption of information product workshops of Haier Group for example, the authors analyze feature of air consumption in industrial production site. Compressed air consumption week curve from August 9 to August 15 in 2010 is shown as Fig.4.

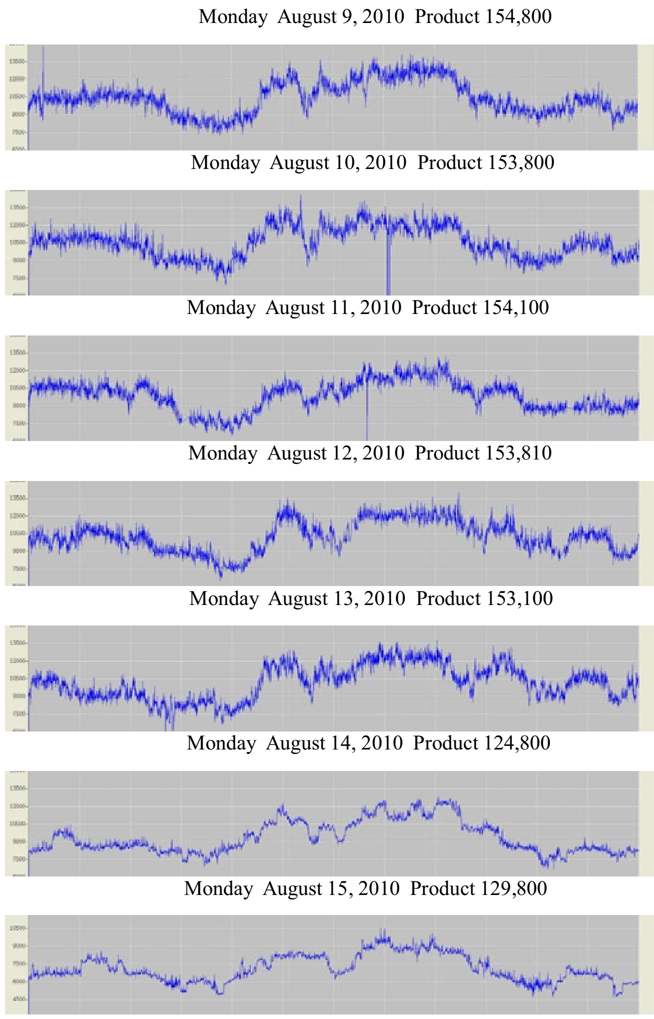

Fig.4 air consumption curve of workshops of Haier Group in a week

As can be seen from the Fig.4. Air consumption changes of Haier Workshops are with periodic law. Curves are significantly similar in a 24-hour cycle. At the same time , air consumption is not a simple repetition of the previous 24-hour cycle, but there is a random value in each cycle.

FORECASTING ALGORITHM OF AIR CONSUMPTION IN INDUSTRIAL SITE

Forecasting algorithm is the core of air consumption forecasting in industrial site. This section will focus on forecasting algorithm and construct forecasting model based on forecasting algorithm. The authors propose a real-time air consumption forecasting model with feedback and recursive. In this model, the authors obtain the forecasting values through similar day air consumption value plus a correction value.

A. Data pre-processing of Historical Air Consumption

The authors deal with historical air consumption of different air pressures by way of benchmarking; The authors repair historical air consumption data; The authors vertically and horizontally deal with anomalous historical air consumption data to smooth the historical air consumption curve.

1) Dealling with historical air consumption of different air pressures by way of benchmarking

Air consumption historical data consist of two parts. One part is flow values, and another part is pressure values. Because the compressors' air production does not match the need of air flow in industrial production site, so the air pressure fluctuates in the pipeline. This makes air device, air consumption affected by pressure in pipeline, produce a pseudo-flow requirements, when air supply pressure is higher than the rated pressure. Such as leakage points, spray gun etc. The authors can deal with the historical air consumption by equation 3,4,5.

$$Q(t) = (1-\alpha)Q(t) + \frac{p_t}{p_0}Q_0(t) \tag{3}$$

$$Q_0(t) = \alpha \cdot \frac{p_0}{p_t} \cdot Q(t) \tag{4}$$

$$Q_r(t) = (1-\alpha)Q(t) + \alpha \cdot \frac{p_0}{p_t} \cdot Q(t) \tag{5}$$

Where: $Q(t)$ is the historical air consumption; $(1-\alpha)Q(t)$ is the air consumption of the stable supply pressure device; p_t is the pressure value at t time; p_0 is the rated pressure of air devices; $Q_0(t)$ is the air consumption of the unstable supply pressure device under p_0; α is the scale factor(0~1); $Q_r(t)$ is the actual need of air consumption in the production site at t time.

By the above equation 3,4,5, the authors convert historical air consumption into effective air consumption value under p_0 by way of benchmarking.

2) Repairing historical air consumption data

If there are a large number of missing or bad data in historical air consumption data, the authors can consider this day's data invalid. The authors use two similar day's normal data, one similar day before this day and another day after this day, to repair the missing data. Because there is quite different law in different similar day's air consumption, so the authors must use similar day's data to repair the missing data. In this paper, the authors use the following equation 6 to process data.

$$x(d_n, t) = \omega_1 x(d_{n-1}, t) + \omega_2 x(d_{n+1}, t) \tag{6}$$

Where: $x(d_n, t)$ is the effective air consumption value at t time in d_n day; $x(d_{n-1}, t)$ is the effective air consumption value at t time in d_n day; $x(d_{n+1}, t)$ is the effective air consumption value at t time in d_n day; ω_1 , ω_2 are weight values, here, ω_1 =0.5, ω_2 =0.5.

3) Filtering the historical air consumption data

In sequence of historical air consumption data, it may produce abnormal values of air consumption. These abnormal values may be caused by major leaks or workshop unexpected suspending production. This abnormal data, mixed into normal air consumption data, will increase the overall noise of air consumption data sequence and reduce similarity of air consumption curve. it increases the forecasting uncertainty, so the authors must remove the abnormal data from air consumption data to smooth the historical air consumption curve.

Air consumption is cyclical in a 24-hour,so Air consumption should have similarity and air consumption value should maintain at a certain range at the same time in similar day. The authors use the following method to revise bad values, which are out of range.

Assuming air consumption sequence with $x(n,t)$, and t=0, 20, 40……86400 represent the 4320 time points in a day. n=1, 2, ……N, N represents N day's air consumption. The authors take N=10 of same kind day, which are weekdays. The authors take N=6 of same kind day, which are weekend. The mean and variance of air consumption can be calculated by the following equation 7,8,9[10].

$$E(t) = \frac{1}{N}\sum_{n=1}^{N} x(n,t) \tag{7}$$

$$V(t)=\frac{1}{N}\sum_{n=1}^{N}(x(n,t)-E(t))^2 \tag{8}$$

Suppose deviation rate of air consumption $\rho(n,t)$,then.

$$\rho(n,t)=\frac{|x(n,t)-E(t)|}{\sqrt{\frac{1}{N}\sum_{n=1}^{N}(x(n,t)-E(t))^2}} \tag{9}$$

Where:t=0,20,40,…..,86400;n=1,2,…N. In the data processing, the authors set η deviation rate of air consumption. If $\rho(n,t)\geq\eta$, the authors think this air consumption value is abnormal points; On the contrary, the authors think this air consumption value is normal points. Deviation from the air consumption can be adjusted by changing the η value. The authors use $\overline{x}(n,t)$ to replace the abnormal values $x(n,t)$.

$$\overline{x}(n,t)=\frac{1}{N}\sum_{n=1}^{N}x(n,t) \tag{10}$$

Dealing with historical air consumption by this way, the historical original air consumption value became more reasonable.

B. *Air Consumption Forecasting Model*

Air consumption in a 24-hour in industrial production consists of two parts. The authors divided into two parts: One part is the overall trend and another part is random variation.

1) *Overall air consumption trend forecasting*

It can be seen from Fig.4, air consumption at a time is different degree of correlation with the air consumption at the same time of the same kind day. Correlation is relative to the distance of two points. When the historical air consumption is closer to the current forecasting value, the correlation is stronger. Otherwise, the correlation is weaker. With this rule, the authors forecast the overall air consumption trend by way of multiple linear regression model with variable coefficients. The following equation 11.

$$y(d_n,t)=\frac{1}{N}\sum_{x=1}^{N}b_x\cdot y(d_{n-x},t) \tag{11}$$

Where: $y(d_n,t)$ is the forecast value of air consumption at a time on d_n day; b_1, b_2…. b_N are variable coefficients. This model has the advantage of simple principle and fast computing speed. This model is suitable for overall air consumption trend forecasting.

2) *Random variation forecasting of air consumption*

In this model, correction value and forecasting error of air consumption are feedback to input layer to be as learning data. Compared to air consumption forecasting by way of the traditional neural network[11][12],this model is with a smaller sample set, which can reduce the structure and learning frequency of neural network. In addition, this method forecast air consumption by way of online and real-time learning. It can reflect the impact of devices suspending in real time and greatly reduce the forecasting error. The forecasting model is shown as Fig.5.

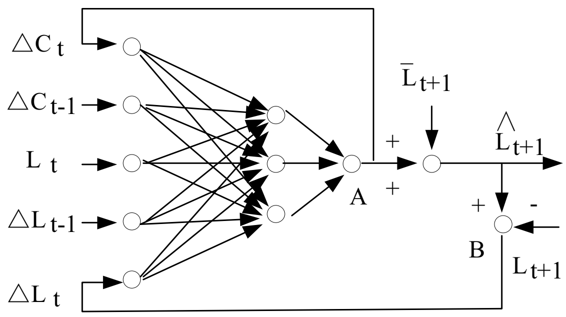

Fig.5 Air consumption improving model in industrial site

Feedback value ΔC_t:In the neural network learning process, input variable ΔC_t feedback from A network node's output value ΔL_{t+1},and the model can be corrected in time to learn the air consumption forecasting error which may affect air consumption forecasting.

Feedback value ΔL_t : Supposing B network node's output value ΔL_{t+1}, ΔL_{t+1} is the difference between forecasting and actual air consumption. That can be calculated by the following equation 12.

$$\Delta L_{t+1}=\hat{L}_{t+1}-L_{t+1} \tag{12}$$

Where: $\hat{L}_{t+1}$ is the air forecasting consumption at t+1 time; L_{t+1} is the actual air consumption. Taking $\Delta L_t=\Delta L_{t+1}$,it feedback to the input layer as input variable, which can correspondingly adjust the air consumption according to forecasting error in time.

Recursive value ΔC_{t-1}:Input variable ΔC_{t-1} is the value of previous time(ΔC_t).

Recursive value ΔL_{t-1}: Input variable ΔL_{t-1} is the value of previous time(ΔL_t).

Direct input L_t : Direct input L_t is the air consumption at t time. Because of taking the value of real-time air consumption to forecast, it greatly improve the accuracy of the air consumption forecasting.

EXAMPLE CALCULATION AND ANALYSIS

The authors use the above real-time forecasting model to forecast the air consumption of the weekday, here N=10. And the authors forecast air consumption of information product workshops of Haier Group on August 16 in 2010.The forecasting curve is shown as Fig.6.

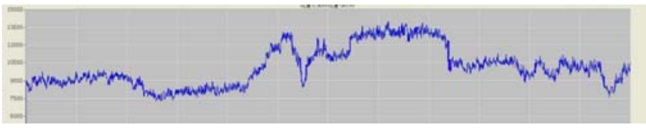

Fig.6 air consumption of information product workshops of Haier Group on August 16 in 2010

The actual air consumption curve on August 16 in 2010 is show as Fig.7.

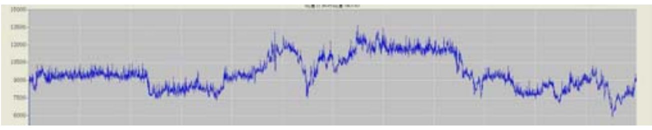

Fig.7 the actual air consumption of information product workshops of Haier Group on August 16 in 2010

Forecasting error curve is shown as Fig.8.

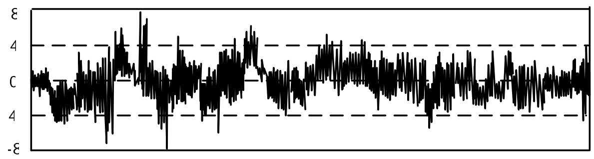

Fig.8 Forecasting error curve

As can be seen from Fig.8,error of the model in the range -4% to 4%.And error of the model is not subject to variation of air consumption. The forecasting air consumption meet the requirement of dispatching of air compressors.

CONTROL METHOD BASED ON LOAD/UNLOAD QUEQE

with the air consumption forecasted using the method mentioned before and the current air supply, the air demand is calculated and some compressor is loaded or unloaded to achieve flow match as to minimize energy consumption.

A. Generation of load/unload queqe

Using decision-making[12] and assessing the affect of air compressor energy consumption, the comprehensive evaluation of compressor is obtained as to determine each compressor's priority of load/unload.

1) Establishment of factor set

a variety of factors affect the compressor run compose a fact set, with U as $U=\{u_1,u_2,\cdots,u_{\mathrm{m}}\}$,where u_i is the i-th factor, m is the number of factors. Considering energy consumption and healthy operation of compressor, efficiency, priority and cumulative running time are focused on the paper, and compose the factor set $U=\{u_1,u_2,u_3\}$ ={efficiency, priority, running time}.

2) Establishment of weight set

Generally, as the importance of each factor is different, a weight a_i is given corresponding to u_i to make the importance stand out while reduce the affect of unimportant factor. a_i is required to satisfy by the following equation 13:

$$a_i \geq 0, \sum_{i=1}^{m} a_i = 1 \tag{13}$$

Where: $i = 1,2,3....m$.

When determining the weight set, the most critical is to correctly identify the relative importance of the air compressor rather then the specific values of the weights. If the information is insufficient, make sure the relative importance among using fuzzy ordering factors and then assign the appropriate weights.

Thus, a fuzzy set on U is composed of each weight a_i by the following equation 14:

$$\underset{\sim}{A} = (a_1, a_2, \cdots, a_m) = \frac{a_1}{u_1} + \frac{a_2}{u_2} + \cdots + \frac{a_m}{u_m} \tag{14}$$

In this article, the authors took $\underset{\sim}{A} = (0.5, 0.3, 0.2)$.

3) Single factor fuzzy evaluation

Suppose that r_{ij} is the single evaluation according to u_i which is the i-th factor in set U, the evaluation corresponding to u_i can be expressed as the following equation 15:

$$\underset{\sim}{R_i} = \frac{r_{i1}}{(u_i, v_1)}, \frac{r_{i2}}{(u_i, v_2)}, \cdots, \frac{r_{in}}{(u_i, v_n)} \tag{15}$$

Where: $\underset{\sim}{R_i}$ is the single evaluation set, simply expressed as

$\underset{\sim}{R_i} = (r_{i1}, r_{i2}, \cdots, r_{in})$.

So, single-factor evaluation matrix is obtained as the following 16:

$$\underset{\sim}{R}=\begin{bmatrix}\underset{\sim}{R_1}\\ \underset{\sim}{R_2}\\ \vdots\\ \underset{\sim}{R_m}\end{bmatrix}=\begin{bmatrix}r_{11} & r_{12} & \cdots & r_{1n}\\ r_{21} & r_{22} & \cdots & r_{2n}\\ \vdots & \vdots & \cdots & \vdots\\ r_{m1} & r_{m2} & \cdots & r_{mn}\end{bmatrix} \tag{16}$$

Each compressor can be seen as a matrix corresponding to the factor set *U*, a fuzzy relationship, that between the object and evaluation of factors affecting the "reasonable relationship."

In this article, setting the priority for the air compressor is divided into priority loading and unloading, loading priority, normal priority to unload, it's set with the type of air compressor and reliability-related, for example, centrifugal air compressor general are not started after the start and stop frequently, so the set to normal, that is, generally do not start it, do not start the uninstall. For the machine can be set to phase out the priority loading and unloading, such as plus unloading machine conditioners, accelerated aging. Given respectively 4,3,2,1.

Assuming the efficiency of the air compressor 4, respectively 0.8,0.75,0.6,0.8; set priorities were 3,4,2,1; run time was 1000h,800h,400h,600h. For the cumulative run time, the more priority to the less loaded, so you can make the machine up time balancing purposes. Commentary on the value of the normalization processing, the evaluation can be set to load the queue as the following 17.

$$\underset{\sim load}{R}=\begin{bmatrix}1 & \frac{3}{4} & 0 & 1\\ \frac{2}{3} & 1 & \frac{1}{3} & 0\\ 0 & \frac{1}{3} & 1 & \frac{2}{3}\end{bmatrix} \tag{17}$$

For the unloading queue, the lower the operating efficiency, the higher the priority; running time of more and more to uninstall. Can also be set as the evaluation of unloading queue as the following 18 :

$$\underset{\sim unload}{R}=\begin{bmatrix}0 & \frac{1}{4} & 1 & 0\\ 0 & 1 & \frac{1}{3} & \frac{2}{3}\\ 1 & \frac{2}{3} & 0 & \frac{1}{3}\end{bmatrix} \tag{18}$$

4) *Fuzzy comprehensive evaluation*

Equation 19, that is to be compared with each compressor comprehensive evaluation of factors affecting the value. The greater the priority the higher the row in front of the queue.

$$\begin{aligned}\underset{\sim}{B}=\underset{\sim}{A}\bullet\underset{\sim}{R}&=(b_1,b_2,\cdots,b_n)\\ &=(a_1,a_2,\cdots,a_m)\bullet\begin{bmatrix}r_{11} & r_{12} & \cdots & r_{1n}\\ r_{21} & r_{22} & \cdots & r_{2n}\\ \vdots & \vdots & \cdots & \vdots\\ r_{m1} & r_{m2} & \cdots & r_{mn}\end{bmatrix}\end{aligned} \tag{19}$$

Where b_i is the comprehensive evaluation which the larger is, the higher priority compressor has the compressor with the largest b_i is in front of the queue, the rest be deduced by analogy.

According to Eq.19, comprehensive evaluation of the load queue can be obtained as:

$$\begin{aligned}\underset{\sim}{B}=\underset{\sim}{A}\bullet\underset{\sim load}{R}&=(0.5,0.3,0.2)\bullet\begin{bmatrix}1 & \frac{3}{4} & 0 & 1\\ \frac{2}{3} & 1 & \frac{1}{3} & 0\\ 0 & \frac{1}{3} & 1 & \frac{2}{3}\end{bmatrix}\\ &=\begin{bmatrix}0.7 & 0.74 & 0.3 & 0.56\end{bmatrix}\end{aligned} \tag{20}$$

That is to say,the load queue is [2 1 4 3].

As the same the unload queue comprehensive evaluation can be calculated as:

$$\begin{aligned}\underset{\sim}{B}=\underset{\sim}{A}\bullet\underset{\sim unload}{R}&=(0.5,0.3,0.2)\bullet\begin{bmatrix}0 & \frac{1}{4} & 1 & 0\\ 0 & 1 & \frac{1}{3} & \frac{2}{3}\\ 1 & \frac{2}{3} & 0 & \frac{1}{3}\end{bmatrix}\\ &=\begin{bmatrix}0.2 & 0.56 & 0.6 & 0.27\end{bmatrix}\end{aligned} \tag{21}$$

So, the unload queue is [3 2 4 1].

Once the configuration parameters of air compressors are modified, the load and unload queue change also. Considering a matter of running time, a new load/unload queues are automatically generated each week.

B. *Control process*

the compressor whose product flow match or is a little more than the air demand, which is got by subtracting the air supply from the forecasting consumption in the third part, is found from the load/unload queue from from the beginning to the end to load or unload. The control process is shown as Fig.9.

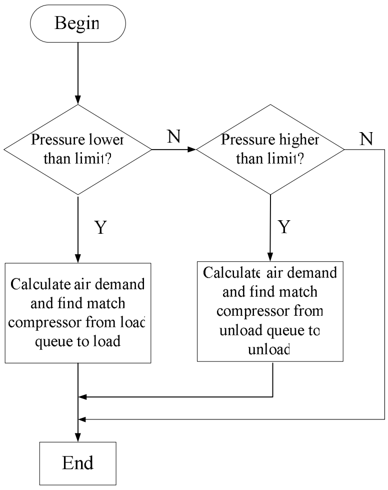

Fig.9 process chart of control method based on load/unload

CONCLUSION

Summary, during the actual operation of the pneumatic system in the industrial production site, it is impossible and unnecessary to establish a fully accurate model to forecast air consumption. It is feasible and practical to establish a modle to meet the requirement of dispatch of air compressors, which is applicable within a certain range. The calculation results truly reflect the inherent characteristics of the system, the law and stability, which is very good.

REFERENCES

1. MAOLIN CAI, TOSHIHARU KAGAWA: Energy consumption assessment and energy loss analysis in pneumatic system[J], *Chinese Journal of Mechanical Engineering*, 2007, 43(9):69-74.
2. Schmidt C,Kissock K.Modeling and simulation of air compressor energy use.ACEEE Summer Study on Energy in Industry,The authorsst point,NY,July 19-22:2005
3. Akbaba M.Energy conservation by using energy efficient electric motors.Applied Energy 1999:64(1999):149-58
4. R.Saidur,N.A.Rahim,M.Hasanuzzaman:A review on compressed-air energy use and energy savings,Renewable and Sustainable Energy Reviews[J],2010,4,1135-1153.
5. MAOLIN CAI, TOSHIHARU KAGAWA: Energy consumption assessment and energy loss analysis in pneumatic system[J], *Chinese Journal of Mechanical Engineering*, 2007, 43(9):69-74.
6. MAOLIN CAI.: Modern pneumatic technology theory and practice, lecture 10: Energy-saving of pneumatic system [J], *Hydraulics Pneumatics & Seals*, 2008,5:59-62.
7. MAOLIN CAI:Modern pneumatic technology theory and practice, lecture 10: Energy-saving of pneumatic system [J], *Hydraulics Pneumatics & Seals*, 2008,5:59-62.
8. SMC(China)Ltd.Modern and Practic Technique of Pneumatic[M],China Machine Press, 2009,44–46.
9. SMC(China)Ltd.Modern and Practic Technique of Pneumatic[M],China Machine Press, 2009,54–46.
10. Kuihe YANG, "Research on Intelligent Forecasting Method of short-term Electricity Load" J. Xidian University,2004,31-32.
11. Khotanzad A,Afkhami-Rohani R, Lu TL. ANNSTL-A Neural-Network-Based Electric Load Forecasting System.IEEE T.Neural Nets,1997,8(4):835-846
12. ZhuJinjun,YangKuihe,ZhaoLngiling.Two Grade bus-Mastering Temperarure Detecting System of Multi-Points and Long Distance.Preceeds of the Sixth International Conference on Electrical Measurement and instruments,2003,Vol.3,2434-2437.

1D1-1

NEW STRATEGY FOR DESIGN AND FABRICATING OF A GRAIN SORTING SYSTEM USING HIGH-SPEED PIEZOELECTRIC VALVES

So-Nam Yun*, Hwang-Hun Jeong**, Dong-Gun Kim**, Eun-A Jeong** and Hong-Hee Kim***

* Department of Energy Systems, Korea Institute of Machinery and Materials
Shinseongno 104, Yuseong-gu, Daejeon, 305-343 Korea
(E-mail: ysn688@kimm.re.kr)
** Department of Energy Systems, Korea Institute of Machinery and Materials
Shinseongno 104, Yuseong-gu, Daejeon, 305-343 Korea
(E-mail: hhjeong@kimm.re.kr)
*** Technology Institute, Kyungwon Ferrite Ind. Co. Ltd.,
2-na-205, Jeongwang-dong, Shiheung, Kyunggi, Korea

ABSTRACT

The purpose of this paper is to develop a new type pneumatic valve which has a multilayered bender type piezo actuator and is used for a grain sorting system. In this study, a new type high-speed pneumatic valve with a piezo actuator for a grain sorting system was analyzed, designed and fabricated, and performances of the fabricated pneumatic valve were evaluated. Finally, an endurance test was conducted, and it was confirmed that the new type piezo pneumatic valve is possible to use to the ejector for grain sorting system.

KEY WORDS

Key words, PZT valve, Piezoelectric valve, Piezo actuator, Grain sorting system, Color sorter

INTRODUCTION

Figure 1 shows the structure and an operating principal of the grain sorting system. Grains in the Hopper run down through the Feeder and the Chute. Foreign bodies, which are found by the lamp and the image sensor, are removed by an air ejector. In this case, not only the distinction capability of foreign bodies but also the fine removing ability is very important. The response characteristics of an air ejector are also one of important design parameters. An air ejector consists of an air gun with a small volume and a pneumatic valve. So they want the high-speed pneumatic valve. Many kinds of methods for overcoming the above-mentioned problems such as response characteristics and low power consumption one have been suggested.

Figure 2 shows the pressure lag characteristics by input voltage wave to the object pneumatic valve, and these characteristics are differ from the used solenoid valve such as Solenoid_1 and Solenoid_2. If we use the Solenoid_1 and the Solenoid_2 of figure 2, we can't help the precise control to remove the foreign bodies in grains because the lag response characteristics.

Figure 3 shows the schematic diagram with cross sectional view of a solenoid valve for a grain sorting system which had been studied by Z. Xiang. The valve was designed as a 2/2-way electro-magnetic solenoid operated on-off valve, and this consists of four major

bodies and armature and stator with a coil. To realize the long lifecycle requirement, an air pressure return structure valve was adopted and there is no spring for avoiding the spring fatigue problem in the traditional spring return valve.
The other method is to make one stationary core with two parallel coils. This was suggested by Tomohiko Katagiri, and it was known to have some characteristics like very short displacement and adoption of a plate type plunger for high-speed performance.
The purpose of this paper is to develop a new type pneumatic valve which has a multilayered bender type piezo actuator and is used for a grain sorting system. In this study, a new type high-speed pneumatic valve with a piezo actuator for a grain sorting system is analyzed, designed and fabricated, and performances of the fabricated pneumatic valve are evaluated. Finally, an endurance test is conducted..

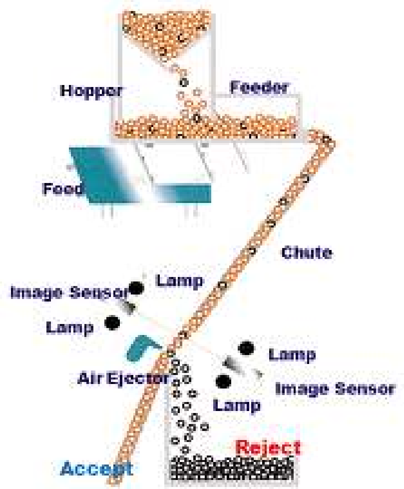

Figure 1 Structure and operating principal of a grain sorting system (1 chute and 1 ejector with a PZT valve)

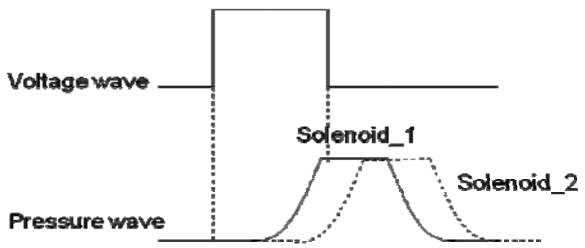

Figure 2 Input voltage and output pressure wave a pneumatic valve for a grain sorting system

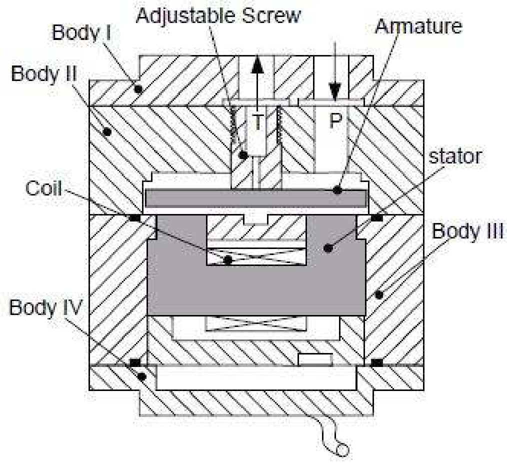

Figure 3 Schematic diagram with cross sectional view of a solenoid valve for a grain sorting system (from Z. Xiang)

PIEZOELECTRIC ACTUATOR DESIGN AND MANUFACTURING

Figure 4 shows the structure of a designed and manufactured piezoelectric actuator. Dimensions of the manufactured actuator are 50L x 10W x 0.80t (㎣) and dimensions of ceramics are 38L x 10W x 0.40t. Ceramic sheet thickness is 40 ㎛ and number of layers is 9. And the capacitance of the manufactured piezoelectric is 1.26 ㎌.

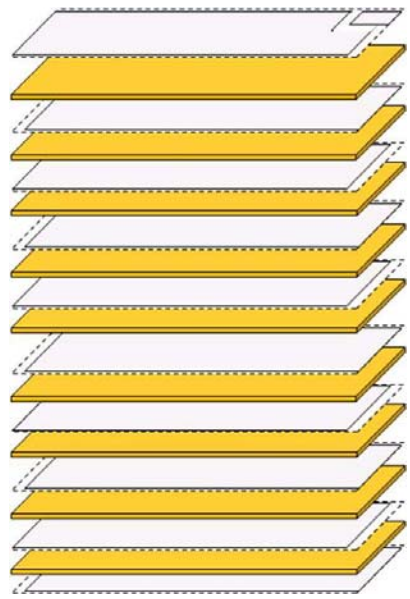

a) Exploded view

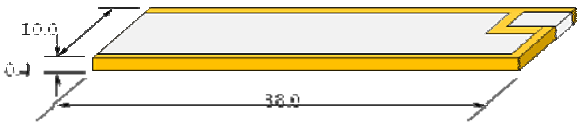

b) Fabricated piezoelectric actuator

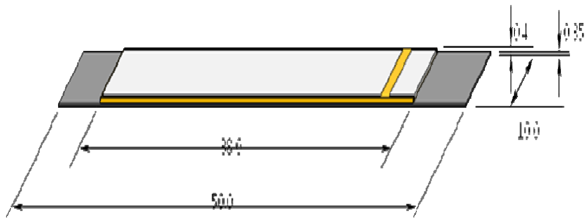

c) Assembled actuator with CFRP

Figure 4 Manufactured piezoelectric actuator

Figure 5 and figure 6 show the photo view and the operating principal of the manufactured piezoelectric actuator, respectably. To realize the long lifecycle requirement like Z. Xiang's study, an air pressure stops the flow out orifice and there is no spring for avoiding the spring fatigue problem.

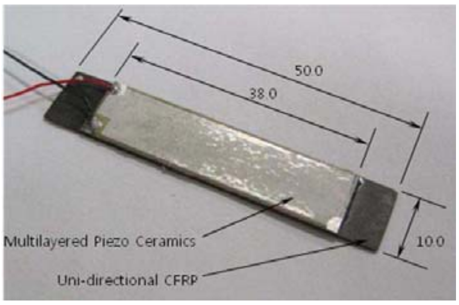

Figure 5 Photo view of the manufactured actuator

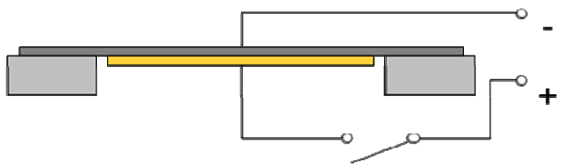

a) Off state

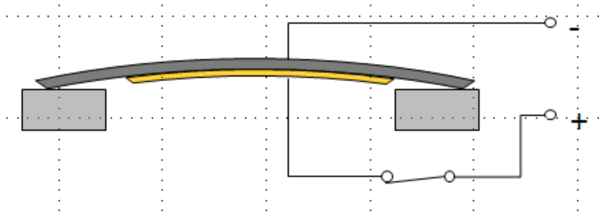

b) On state

Figure 6 Operating principal of the manufactured piezoelectric actuator

In figure 5 and figure 6, the CFRP elastic material is also used for improvement the dynamic characteristics. Figure 7 is the experimental setup for the performance measurement of the fabricated piezoelectric actuator and general solenoid actuator. The experimental setup consists of a fixed jig, a laser sensor, a force sensor and a frequency analysis equipment.

Figure 8 shows the experimental results of the actuator displacement and blocking force. In the experimental results, x-axis is the voltage inputted to the actuator, and left-y-axis and right-y-axis are the displacement and the blocking force of the manufactured actuator. The minimum and the maximum value of the actuator displacement are 150 μm at 50 V input and 350 μm at 120 V input, respectably. We can know that the output displacement of the manufactured actuator is proportional to the input voltage and displacement results are very linear. The blocking forces of the actuator are from 300gf to 470 gf and over when input voltages are 80 V and 120V, respectably.

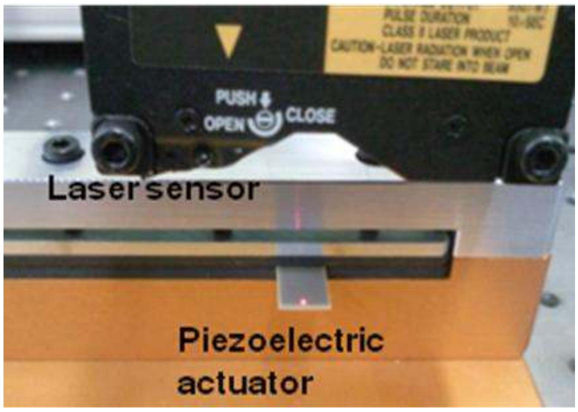

a) Experimental setup for the piezoelectric actuator

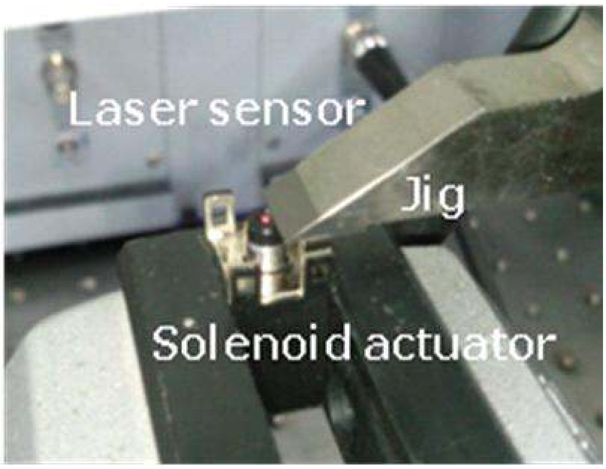

b) Experimental setup for the frequency response characteristics measurement for solenoid actuator

Figure 7 Experimental setup for the fabricated piezoelectric actuator test

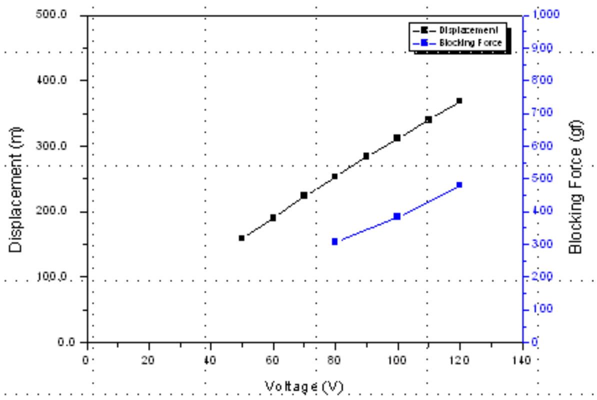

Figure 8 Experimental results of displacement and blocking force

PIEZOELECTRIC VALVE FOR THE GRAIN SORTING SYSTEM

Figure 9 shows the assembled piezoelectric valve and its controller. The prototype piezoelectric valve of figure 9 is for controlling the air ejector and tube plumbing having a small volume doesn't need for high-speed response characteristics.

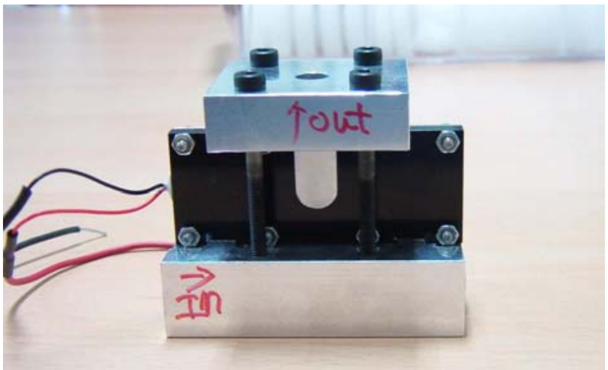

a) Assembled piezoelectric valve

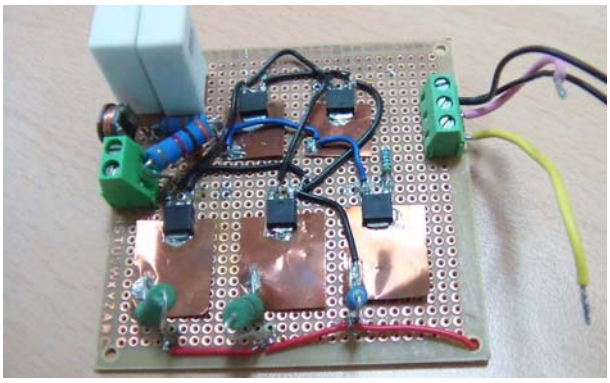

b) Controller for piezoelectric valve

Figure 9 Assembled piezoelectric valve and its controller

Figure 10 shows the two kinds of control method for solenoid and piezoelectric valve. In case of solenoid valve of a) of figure 10, the attraction force is greater when the length between core and plunger is short. So, low input voltage makes operate the solenoid valve in case of reasonable range between core and plunger. This means that the maximum input voltage doesn't need for low energy consumption. The other method is to control the piezoelectric valve using PFM method. The PFM method is very important control strategy because the grain arrangement is unity and the drop down speed of the grain is only changed by the feeder and the chute.

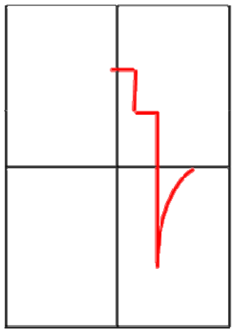

a) Control strategy using solenoid controller

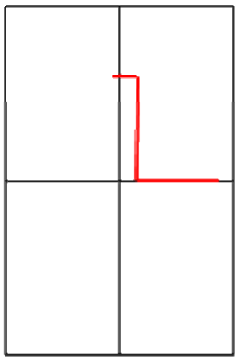

b) PFM control strategy for piezoelectric valve

Figure 10 Control strategies for solenoid valve and piezoelectric valve using controller

Figure 11 is the experimental circuit and the experimental setup for performance evaluation of the manufactured piezoelectric valve, and the test circuit of the figure 11 was built according to the ISO 6358. In this study, a matter of concern is to check of pressure variation at the outlet port because the manufactured valve is better or not than the conventional type solenoid valve. So, pressure sensors were equipped to the air tank and outlet port of the tested valve. The b) of figure 11 presents the experimental setup for performance and endurance test for the fabricated valve.

The PC with AD converters and some amplifiers for data measurement were installed and the function generator for PFM control is also equipped to experimental setup. The endurance test was conducted under the condition of no-load and 0.4 MPa-load.

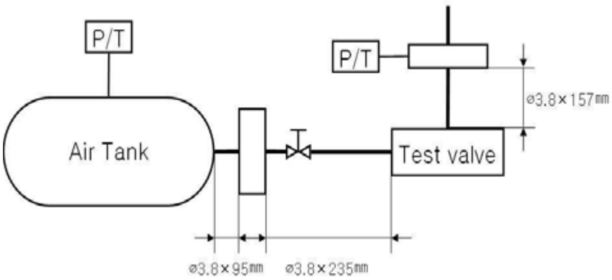

a) Pneumatic circuit for experiment

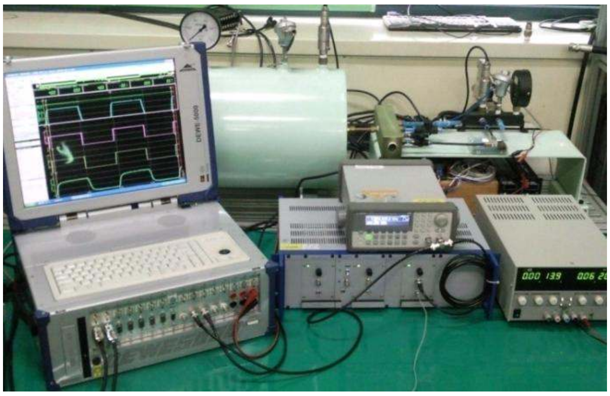

b) Experimental setup for performance & endurance test for the fabricated valve

Figure 11 Experimental circuit and setup for performance test of the manufactured piezoelectric valve.

Figure 12 shows the experimental results of the pressure characteristics of the valve outlet port. The x-axis is the time and y-axis is the output voltage which means the pressure variation. And the symbol, DW224, means the solenoid valve, and KW 2nd and KW 3rd mean the 2nd and 3rd prototype piezoelectric valve, respectably. The meaning of the same pressure peak result is that the flow rate at outlet port is also the same because of the same orifice and the same volume. In case of 2nd prototype of figure 12, a), the on-process, such as the delay time and peak time, is equivalent to the conventional type solenoid actuator but the off-process is a few late about 150 μs. We can know from the figure 12, a) that the on-off characteristics of the manufactured piezoelectric valve are equivalent to the conventional type solenoid valve one and that the manufactured valve has a possibility to use for the grain sorting valve. Figure 12, b) shows the results comparison between the 3rd prototype piezoelectric valve versus conventional type solenoid valve.

It was confirmed from figure 12, b) that the flow performance of the 3rd prototype valve is superior to the conventional type solenoid valve. This means that the 3rd prototype valve can remove the more heavy foreign body in the grain sorting system.

Finally, we had operated the endurance test using the 3rd prototype valve, and we confirmed that the endurance number is 10 billion and over.

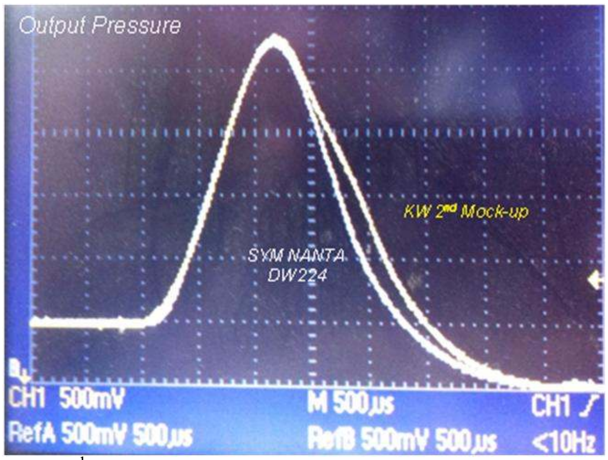

a) 2nd prototype piezoelectric valve vs. conventional type solenoid valve

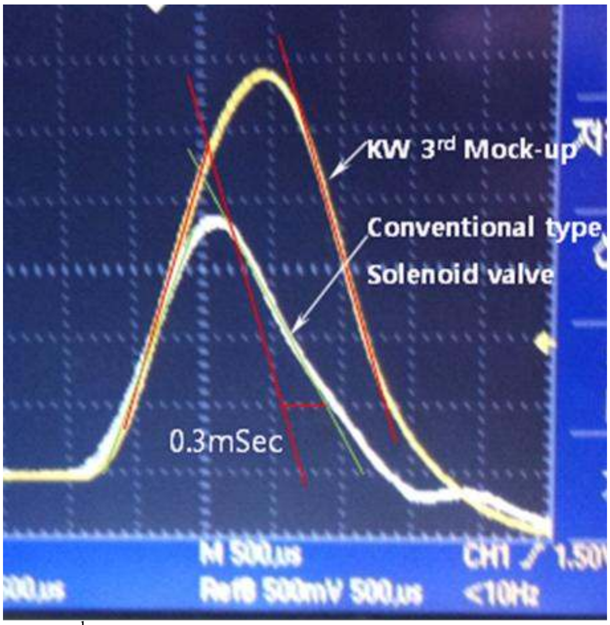

b) 3rd prototype piezoelectric valve vs. conventional type solenoid valve

Figure 12 Experimental results of the outlet pressure (DW224 means the solenoid valve and KW 2nd KW 3rd mean the prototype piezoelectric valve)

CONCLUSIONS

In this study, the 2nd and the 3rd prototype piezoelectric valve for an ejector of the grain sorting system were designed and fabricated, and the experimental setup for the performance evaluation was manufactured. The results of this study are as follows;

1. The maximum displacement and the maximum blocking of the fabricated actuator of which ceramic sheet thickness of 40 ㎛ and layers of 9 for overcoming the input pressure of 0.4MPa are 350 ㎛ and 470gf, respectably.

2. The piezo valve and the controller were suggested and PFM control method was conducted.

3. We had operated the endurance test using the 3rd prototype valve, and we confirmed that the endurance number is 10 billion and over.

4. It was confirmed that the new type piezo pneumatic valve is possible to use to the ejector for grain sorting system.

REFERENCES

1. Zhong Xiang, Hao Liu and Guoliang Tao, Development and investigation of high-speed pneumatic jet valves by lumped parameter modeling, 7th International Fluid Power Conference, 2010, pp.1-12.
2. Tomohiko Katagiri, High-speed strategy of solenoid valve, Fluid power system, Vol.41, No.5, 2010, pp.30-33.
3. M. Weinmann, A. J. Schmid, M. Fuss, Piezoelectric pneumatic valves, Actuator 2006-A5.2, 2006, pp.181-184.
4. So-Nam Yun, Kyung-Woo Lee, Hong-Hee Kim and Hyung-Jong So, Development of the pneumatic valve with bimorph type piezoelectric actuator, Materials chemistry and physics, 2006, pp.1-4.
5. So-Nam Yun, Young-Bog Ham, Jung-Ho Park, Woo-Seok Seo and Kyung-Woo Lee, Electro-pneumatic regulator strategy using two PZT actuator, ATEM'07, 2007, p208.
6. M. Weinmann, M. Muth, M. Giousouf, C. Hanisch and P. Post, State of the art in pneumatic microvalves, Actuator 2002-B 1.0, 2002, pp.217-222.
7. P. Mandurino and P.M. Weaver, Electronic domestic gas valve proportionally controlled using piezo actuators, Actuator 2004-A4.7, 2004, pp.152-155.
8. Hubertus Murrenhoff, Innovative designs and control circuits for proportional valves, NCFP 102-27.2/SAE OH 2002-01-1458, 2002, pp.691-701.

Proceedings of the 8th JFPS International
Symposium on Fluid Power, OKINAWA 2011
Oct. 25-28, 2011

1D1-2

PARAMETERS IDENTIFICATION AND ANALYSIS OF PNEUMATIC CYLINDERS FRICTION MODEL BASED ON EXPERIMENTS

Hao Liu*, Jianfeng Chen*, Guoliang Tao*

* State Key Laboratory of Fluid Power Transmission and Control,
Zhejiang University
38 Zheda Road, Hangzhou ,310027,China
(E-mail: hliu2000@zju.edu.cn)

ABSTRACT

Although LuGre Model is considered as a nice friction model that can describe the friction phenomenon of pneumatic cylinders comprehensively, its parameters are hard to be defined in the real cases. In this paper, a new experimental bench, on which the moving of pneumatic cylinder is driven by a servo motor accurately, is developed to study the friction characteristics of the cylinders. Based on this bench, a method of how to identify parameters of the LuGre Model is proposed, using a single-rod cylinder as examples. Meanwhile the influences on the parameters that arise from running conditions such as working pressure and differntial pressure are discussed. As simulation results agree with the ones obtained from experiments well, the model and the parameters identification method are proved to be effective in actual processes.

KEY WORDS

Pneumatic cylinder, Friction model, Parameters identification, Pressure, Experimental Analysis

NOMENCLATURE

A_1	:	Piston area of the cylinder chamber that along the direction of the cylinder driving force (m^2)
A_2	:	Piston area of the cylinder chamber that opposite the direction of the cylinder driving force (m^2)
F	:	Friction force (N)
F_c	:	Coulomb friction force (N)
F_{c0}	:	Coulomb friction force in pressure 0kPa (N)
F_d	:	Driving force on the testing cylinder (N)
F_s	:	Maximum stiction friction force (N)
F_{s0}	:	Maximum stiction friction force in pressure 0kPa (N)
F_{ss}	:	Steady-state friction force (N)
k_1~k_8	:	Proportion coefficients
g	:	Stribeck effect function
m	:	Total mass of the moving parts
p_1	:	Pressure of the cylinder chamber that along the direction of the cylinder driving force (kPa)
p_2	:	Pressure of the cylinder chamber that opposite the direction of the cylinder driving force (kPa)
p_s	:	Working Pressure of the cylinder chamber(kPa)
Δp	:	Differential pressure between the two chambers of pneumatic cylinder
t	:	Time (s)
v	:	Relative velocity between two surface (mm/s)
v_s	:	Stribeck velocity (mm/s)
v_{s0}	:	Stribeck velocity in pressure 0kPa (mm/s)
v_{ss}	:	Steady-state velocity (mm/s)
x	:	Cylinder displacement
z	:	Average deflection of the bristles (mm)
σ_0	:	Stiffness of the bristles (N/m)
σ_1	:	Damping coefficient of the bristles (N·s/m)
σ_2	:	Viscous friction coefficient (N·s/m)

σ_{20} : Viscous friction coefficient in pressure 0kPa(N·s/m)
ξ : Relative damping ratio of the seal ring

INTRODUCTION

Recently with the rapid development of microelectronics technology, the pneumatic position servo control systems have become more and more widespread application in many industrial fields. The characteristics of the pneumatic cylinder, which is the key actuator of the servo system, have great influence on the system's control precision. Among these characteristics, the friction force of the actuator is the most complex non-linearity element. So learning more about the friction force in pneumatic cylinder is an important step to build up a high precise pneumatic position control system, or optimize a pneumatic cylinder.

In recent years, many researchers, such as Dalh [1], Bliman [2], Haessig [3], Canudas de Wit C [4], had proposed many models to describe the friction. Among them, the LuGre friction model built by Canudas de Wit C has been accepted as an accurate model that can describe the real friction phenomenon in most of experiments. It can describe the friction well both in the steady state and transient state, with a compact mathematical form. But, before the model can be used for the control system, there are several parameters in it to be identified by experiments firstly. The pneumatic cylinder friction testing method had been studied by many researchers. Most of them, such as L. E. Schroederl [5], B. H. Zhang [6], and P. L. Andrighetto [7], studied the cylinder friction with the test rig in which the testing cylinder drives a load cylinder directly. This method is simple and low cost, but it is hard to obtain a stable speed of the cylinder to test friction under very low velocity, or obtain a data without the interference of the pressure under high velocity. G.Belfore [8] developed a test rig in which the pneumatic cylinder was dragged by a hydraulic cylinder, which ensured the pressure in the cylinder and the speed of the cylinder can be controlled individually. This method avoided the problems encountered by the previous mentioned one, but it was much more complex and high cost.

In this paper, a new pneumatic cylinder friction experimental apparatus is developed. Here, the moving of pneumatic cylinder is driven by a servo motor accurately. Based on this bench, a method of how to identify parameters of the LuGre Model is proposed. Furthermore, experiments were performed to determine the influnces of speed and working pressure on the parameters, using a rodless cylinder and a single-rod cylinder as examples.

FICTION MODEL

The LuGre friction model built by Canudas de Wit C has been accepted as an accurate model that can describe the real friction phenomenon in most of experiments. In the model, the friction contact surface is identified as a group of elastic bristles with random behavior in the micro-scale. Friction is generated by the deflection of bristles. It can be described as

$$F = \sigma_0 z + \sigma_1 \frac{\mathrm{d}z}{\mathrm{d}t} + \sigma_2 v \tag{1}$$

$$\frac{\mathrm{d}z}{\mathrm{d}t} = v - \frac{|v|}{g(v)} z \tag{2}$$

In the Eq. (2), the function $g(v)$ describes the Stribeck effect [9]. Usually, $g(v)$ is expressed as

$$\sigma_0 g(v) = F_C + (F_S - Fc) e^{-(v/v_S)^2} \tag{3}$$

In the steady state, the average deflection of the bristles z approaches the value

$$v_{ss} = \frac{v}{|v|} g(v) = g(v)\mathrm{sgn}(v) \tag{4}$$

It follows from Eq. (2) to Eq. (4) that for steady-state motion the relation between velocity and friction force is given by

$$F_{ss}(v) = F_c \,\mathrm{sgn}(v) + (F_s - F_c) e^{-(v/v_s)^2} + \sigma_2 v \tag{5}$$

With this description, the LuGre model is characterized by six parameters F_c, F_s, v_s , σ_0, σ_1, and σ_2. Among them, parameters such as F_c, F_s、v_s and σ_2 can be identified by the means of measuring the steady-state friction of the cylinder when its velocity is held constantly. However, the identification of the dynamic-state parameters σ_0 and σ_1 is much more complicated for the state variable z in Eq. (1) is immeasurable.

EXPERIMENTAL APPARATUS

To obtain accurate data for the parameters identification of the LuGre model, a new pneumatic cylinder friction experimental bench is developed. The schematic diagram of the system is as Figure 1 shows. In the diagram, 1 is servo motor, 2 is gear, 3 is lead screw, 4 is grating displacement sensor, 5 is force sensor, 6 is testing cylinder, 7 and 8 are pressure sensors, 9 and 10 are buffer tanks, 11 and 12 are precise pressure regulating valves, 13 is AD/DA card.

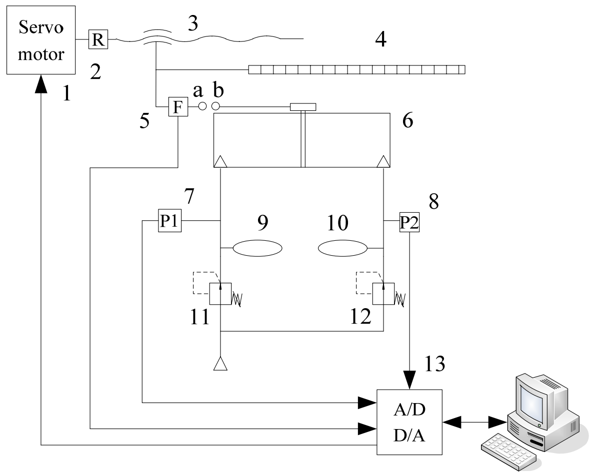

Figure 1 Schematic diagram of the servo motor drived friction experimental bench

The motion of the testing cylinder is driven by a servo motor, separating the influnce of the pressure in the chambers of the cylinder. The moving range of the servo motor driving system is 3m, which guarantees the effective testing displacement and the possibility of high velocity testing. The speed of the servo motor is precisely controled and the lead screw can transfer the driving force to testing cylinder smoothly. The lowest speed of the system is below 0.5 mm/s and the highest is 150 mm/s.

The pressure in the two chambers of the testing cylinder are controled by precise pressure regulatinng valves individually. And two big volume baffer tanks are installed near the inlet and outlet of the cylinder to stable the pressure when the cylinder is in high speed moving.

The realtime displacement of the cylinder is got by grating displacement sensor, with measurement accuracy of ± 5um and range up to 2m. The force sensor's range is 100Kg and its non-linear error is less than 0.05% FS. And the pressure sensor's range is 10bar, with the accuracy of 0.05% FS.

All the signals of the sensors are collected by a AD/DA card and transferred to the control computer. The system control program in the computer handles the whole experiment process and reports the results when the process is over. The friction force is calculated with the experiment data in the program as follow:

$$F = F_d - (p_2 A_2 - p_1 A_1) \quad (6)$$

MODEL PARAMETERS IDENTIFICATION WITH THE EXPERIMENT DATA

Steady-state Parameters Identification

The steady-state parameters of the LuGre model can be identified by the means of measuring the relationship between steady-state friction and velocity curves, as we can see in the following example.

Here, a single rod low-friction cylinder had been tested with the bench. The pistol diameter of the cylinder is 32mm and the stroke of it is 500mm.

Because the moving speed of the cylinder and the pressure in the chambers are relatively more stable when the cylinder is running in the middle section of the test stroke, which can ensure the accuracy of data measured by the sensors. The mean value of the data collected in this section are taked as the experiment data for the friction force calculating under this specific working pressure and moving velocity. As several different moving velocity experiments are carried out under the same chamber pressure, a steady-state friction-velocity curve can be obtained. In Figure 2, we can see the steady-state friction-velocity curve of the single rod low-friction cylinder with its both chambers connecting to atmosphere directly.

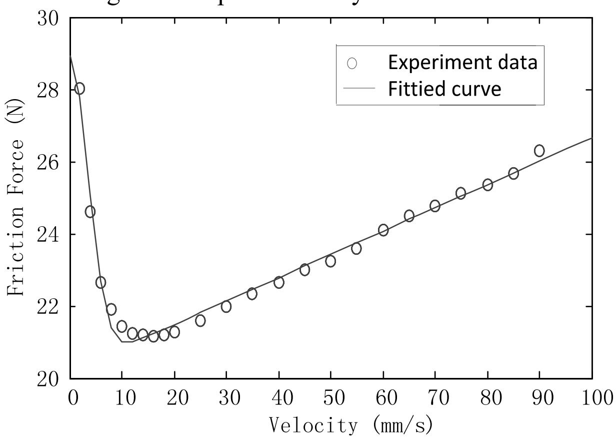

Figure 2 Experiment data and fittied steady-state friction-velocity curve of the single rod low-friction cylinder with zero chamber pressure

Considering the Eq. (5), which is a non-linear function and is hard to derivate its coefficients with the least square method, we use the function named Fminsearch in the MATLAB® program to find the resolvers. Function Fminsearch works are based on the theory of simplex method and has the ability to find the minimum value of a scalar function from a specified initial value. While used for the parameter estimation, it is described as:

[*x, fval, exitflag, output*]
= fminsearch (*fun, x0, options, p1, p2,* ……) (7)

where *x* is the parameters to be identified, *fval* is the returned value of the object function at the optimum solution point *z*, *exitflag* is the returned ending flag of the calculation process, *output* is a returned data structure of the calculation process, *fun* is the object function that represents Eq. (5) here, *x0* is the initial value of x, *options* is parameters for optimizing the calculation process, *p1, p2,* ⋯ are the arguments matrix and output values matrix of the object function, representing the velocity matrix and friction force matrix come from the experiment data.

The initial values demanded by Eq. (7) can be derived from the experiment data in Figure 2 as follow. The relation of friction force and velocity is nearly a line when the velocity is above 30mm/s. The intersecting point of the line and the y-axis is the initial value of the coulomb friction force F_c. The slope of the line is the initial value of the viscous friction coefficient σ_2. The maximum stiction friction force F_s can be valued with the mean value of the friction force while the speed of cylinder is below 0.5mm/s. And the initial value of the stribeck velocity v_s can be replaced by the velocity at the time when the friction force is the minimum one.

Using the above identification method, the steady-state motion friction force of the single rod low-friction cylinder can be calculatied by the following equation:

$$F_{ss}(v) = 2.856\mathrm{sgn}(v) + (3.904 - 2.856)e^{-\left(\frac{v}{2.3892}\right)^2} -0.0185v \quad (8)$$

The simulation results that calculated with Eq. (8) are showed in Figure 2 as fitted curve. It can be seen that the error between the experiment data and simulation results is very small.

Dynamic-state Parameters Identification

There are two dynamic-state parameters in the LuGre model. One is stiffness of the bristles σ_0 and the other is damping coefficient of the bristles σ_1. Because they have the relation with the average deflection of the bristles z, while the deflection always appears at the time the cylinder speed changes, we focus on the dynamic processes such as start and stop.

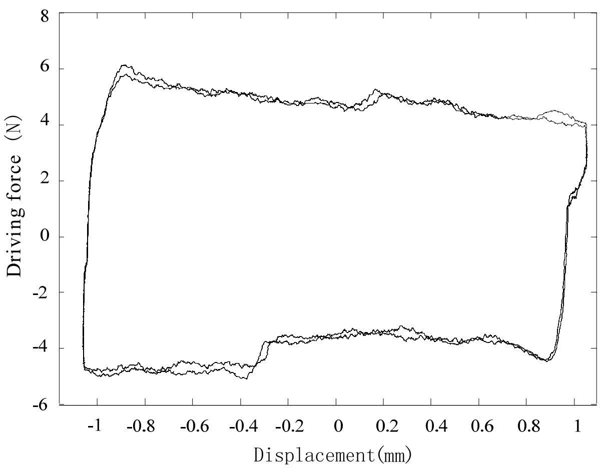

Figure 3 Driving force-displacement curve of the single rod low-friction cylinder in the reciprocating motion

We let the cylinder do a short-stroke reciprocating motion with a low speed 0.5mm/s. To pick up the rapidly changing data in the dynamic process, the grating was replaced with a high precise and high frequency laser displacement sensor here. And the sampling frequency was also increased to 2000Hz.

The friction force and the displacement of the cylinder in two running cycles are measured as Figure 3 shows.

As we can see in the Figure 3, there is a very short displacement on which the friction keeps the linear relationship with the displacement. So it can be determined that the cylinder does not move, but the deforming of the seal ring makes the displacement appear. It is called pre-move period. In this period, the average deflection of the bristles z can be regarded as cylinder displacement. Hence

$$\frac{\mathrm{d}z}{\mathrm{d}t} = \frac{\mathrm{d}x}{\mathrm{d}t} \quad (9)$$

Taking the mass acceleration into account, Eq. (1) and Eq. (9) then give

$$F_d = \sigma_0 x + (\sigma_1 + \sigma_2)\frac{\mathrm{d}x}{\mathrm{d}t} + m\frac{\mathrm{d}^2x}{\mathrm{d}t^2} \quad (10)$$

Eq.(10) indicates that the dynamic-state characters of the cylinder in the pre-move period are similar to the second-order damping system in forced vibration process. So it can be given similarly

$$\sigma_1 + \sigma_2 = 2\xi\sqrt{m\sigma_0} \quad (11)$$

Usually, the value of ξ is given greater than 0.2 and less than 0.7,P. Z. Li[10].

And because the speed and acceleration is very small in the pre-move period of the experiment, Eq. (10) can be simplified as

$$\Delta F_d = \sigma_0 \Delta x \quad (12)$$

Therefore, we can get σ_0 as 4.48×10^5N/m with the experiment data. Then, from the Eq. (11) the value of σ_1 can be determined as 6.42×10^2N/m.

PARAMETERS MODIFICATION OF THE LUGRE MODEL

With the previous method, the parameters of LuGre model can be identified succesfully under the working condition with zero chamber pressure. But as we know, chamber pressure will change the stress state of the seal ring, then the friction force will be different. The parameters of the LuGre model have to be modificated to fit the influences of the pressure.

The influence of working pressure on steady-state parameters

Setting both chambers of the cylinder stable on the the same pressures with the precise pressure regulators, we test the single rod low-friction cylinder under different steady speed and working pressure. The experiment results are given in Figure 4.

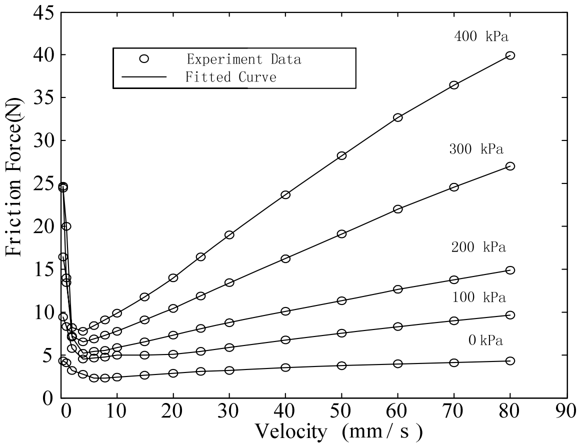

Figure 4 Experiment data and fittied steady-state friction-velocity curve of the single rod low-friction cylinder with changing working pressures

Based on the experiment data, the steady-state parameters of the model under differet working pressure are calculated and show in Figure 5~8.

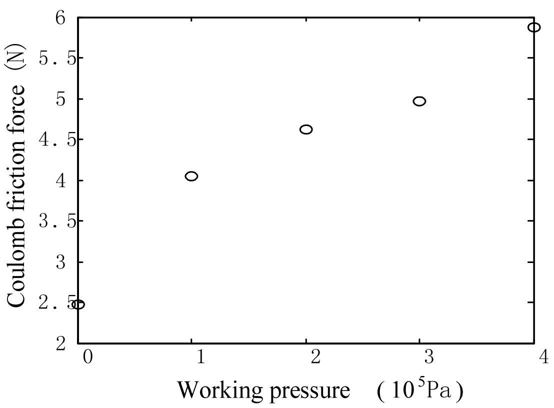

Figure 5 Relation between Coulomb friction force and changing working pressures

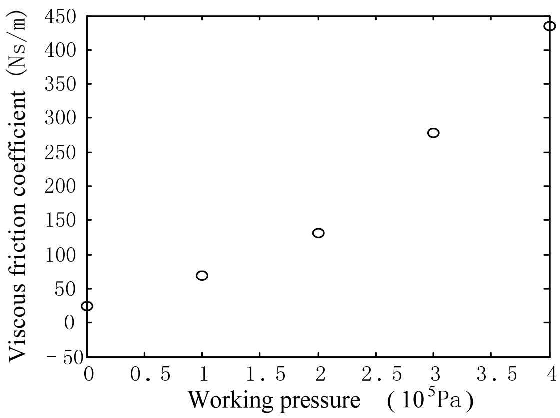

Figure 6 Relation between viscous friction coefficient and changing working pressures

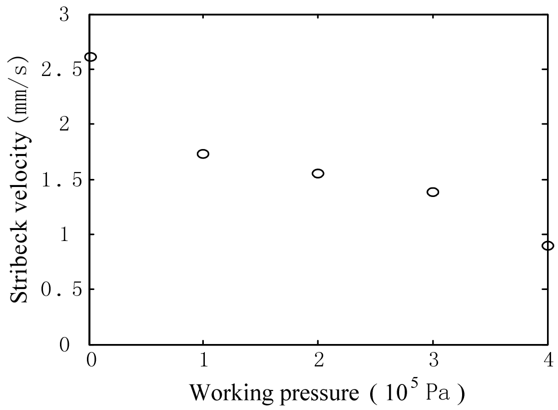

Figure 7 Relation between Stribeck velocity and changing working pressures

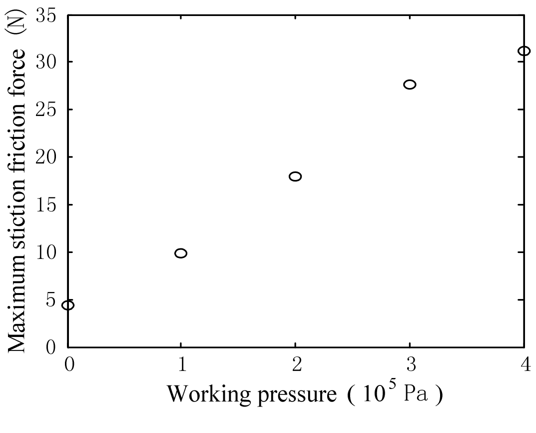

Figure 8 Relation between maximum stiction friction force and changing working pressures

Figure 5, Figure 6 and Figure 8 indicate individually that Coulomb friction force, viscous friction coefficient and maximum stiction friction force are all increasing with the raising working pressure nearly linear. But Figure 7 indicates that Stribeck velocity is decreasing with the raising working pressure. Those results can be explained with the analysis on the physical characteristics of cylinder friction process. The seal rings are pushed more firmly against the cylinder wall and the piston rod while working pressure increasing, which causes the positive pressure of the seal ring increasing near proportionally and the boundary lubrication condition become worse for the oil film is forced out.

The influence of differential pressure on steady-state parameters

With the same single rod low-friction cylinder, we test the relationship between the friction force and the variable differential pressure under different steady speeds. The pressure in the rodless chamber of the cylinder is fixed to 300KPa while the pressure in the rod chamber is changing in the expreriments. The results are given in Figure 9. where, differetial pressure Δp is defined plus when the pressure in the rod chamber is below the pressure in the rodless chamber.

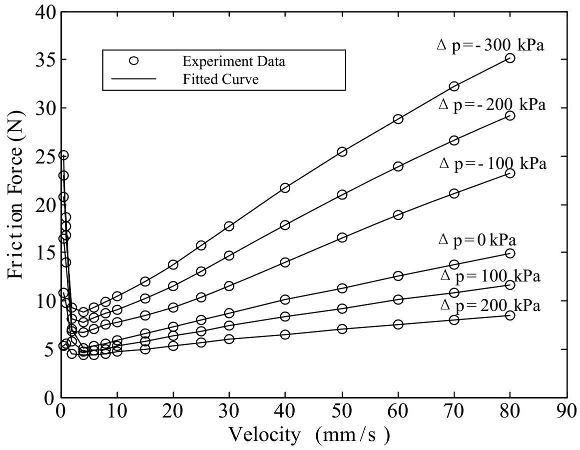

Figure 9 Experiment data and fittied steady-state friction-velocity curve of the single rod low-friction cylinder with changing differential pressures

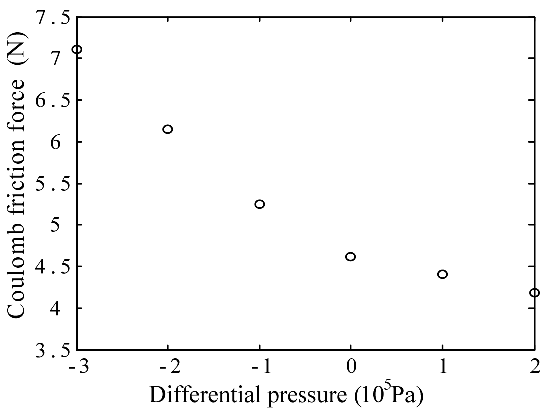

Figure 10 Relation between Coulomb friction force and changing differential pressures

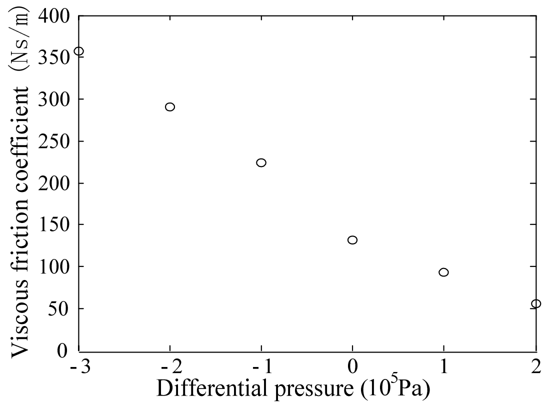

Figure 11 Relation between Coulomb friction force and changing differential pressures

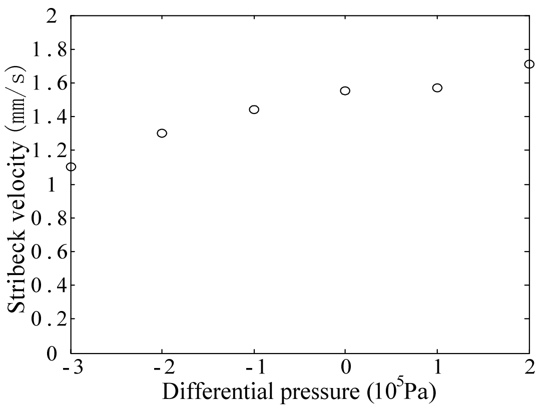

Figure 12 Relation between Stribeck velocity and changing differential pressures

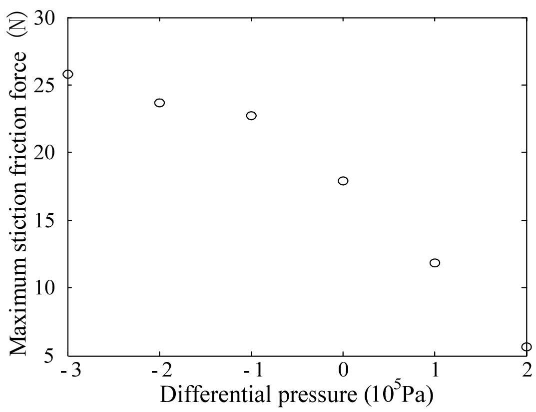

Figure 13 Relation between maximum stiction friction force and changing differential pressures

Based on the experiment data, the steady-state parameters of the model under variable differentila

pressure are calculated and shown in Figure 10~13.
Figure 10, Figure 11 and Figure 13 indicate individually that Coulomb friction force, viscous friction coefficient and maximum stiction friction force are all decreasing with the raising differential pressure nearly linear. While, Figure 12 indicates that Stribeck velocity is decreasing with the raising working pressure. Those results can be explained that the total pressure acting on the seal rings is decreasing with the rising differential pressure. Therefore, the force of the ring against the cylinder wall and the piston rod becomes smaller almost proportionally and the boundary lubrication condition is improved.

The influence of working pressure on dynamic-state parameters

In this section, the cylinder is driven to do a short-stroke reciprocating motion with a low speed 0.5mm/s, while its both chambers of the cylinder stable on the the same pressures with the precise pressure regulators. After every three cycles, the pressure in the chambers changes. The results are given in Figure 14.

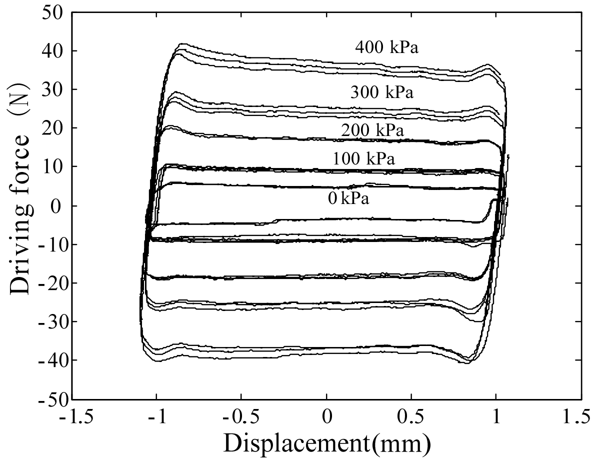

Figure 14 Driving force-displacement curve of the cylinder in reciprocating motion under different working pressure

As it shows, the slopes of the driving force-displacement curves in the pre-move period of very cycle almost rarely change. That means, according to Eq. (12), the parameter Stiffness of the bristles σ_0 can be regarded as a constant while working pressure changes. Then, according to Eq. (11), the parameter Damping coefficient of the bristles σ_1.can also be regarded as a constant, because the parameter Viscous friction coefficient σ_2 is too small to be considered in comparison.

The influence of differential pressure on dynamic-state parameters

Here, the cylinder is driven to do a short-stroke reciprocating motion with a low speed 0.5mm/s too. The pressure in the rodless chamber of the cylinder is fixed to 300KPa while the pressure in the rod chamber is changing in the expreriments. The results are given in Figure 15. where, differetial pressure Δp is defined plus when the pressure in the rod chamber is below the pressure in the rodless chamber. After every three cycles, the pressure in the rod chamber changes.
The results are given in Figure 15.

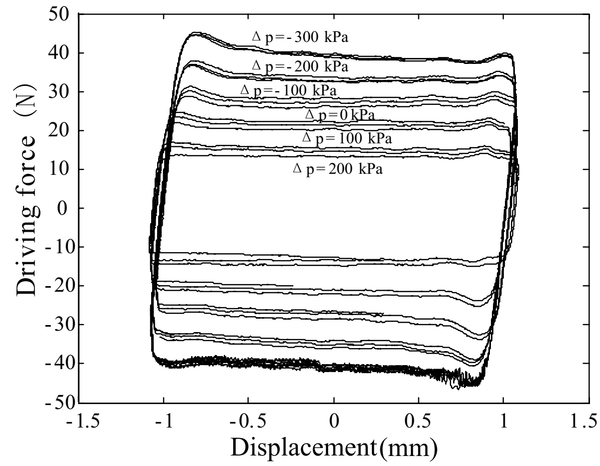

Figure 15 Driving force-displacement curve of the cylinder in reciprocating motion under changing differential pressure

As slopes of the driving force-displacement curves in the pre-move period of very cycle in Figure 15 also change little just like those in Figure 14, it can be said that the influence of differential pressure on the parameter σ_0 and $\sigma_1$is small too.
Those results can be explained into that the dynamic parameter σ_0 represents the axial stiffness coefficient of seal rings indeed. Therefore, the value of it is only associated with the material characteristics of itself and the ambient temperature, but has nothing to do with the pressure. And because the dynamic parameter σ_2 represents the damping coefficient of the rings indeed, its value may also has little relation with the pressure too.

Modify the parameters of LuGre model

With the experiment results above, it is clear that the working pressure and the differential pressure do have influence on the steady-state parameters but less on the dynamic-state parameters. It is needed to introduce these influencing factors into LuGre model to make it fit the practical application.
As it has been discussed, both the working pressure and the differential pressure almost have linear relation with the value of parameters F_c, F_s, v_s andσ_2, the proportional coefficient can be added to define the parameters. In this way, the LuGre model is now given as:

$$
\begin{cases}
F = \sigma_0 z + \sigma_1 \dfrac{\mathrm{d}z}{\mathrm{d}t} + \sigma_2 v \\
F_{\mathrm{ss}}(v) = F_{\mathrm{c}} \,\mathrm{sgn}(v) + (F_{\mathrm{s}} - F_{\mathrm{c}}) e^{-(v/v_{\mathrm{s}})^2} + \sigma_2 v \\
F_{\mathrm{c}} = F_{\mathrm{c0}} + k_1 p_{\mathrm{s}} + k_2 \Delta p \\
F_{\mathrm{s}} = F_{\mathrm{s0}} + k_3 p_{\mathrm{s}} + k_4 \Delta p \\
v_s = v_{s0} + k_5 p_{\mathrm{s}} + k_6 \Delta p \\
\sigma_2 = \sigma_{20} + k_7 p_{\mathrm{s}} + k_8 \Delta p
\end{cases} \tag{13}
$$

The parameters F_{c0}, F_{s0}, v_{s0}, σ_{20}, σ_0, and σ_1 can be identified by the means of the experiment data on the condition that the pressure in both chamber of the cylinder keep on 0kPa. Then, the parameters k_1~k_8 can be identified with the experiment data with variant working pressure p_s and differential pressure Δp. The relation between p_s and Δp The relationship between p_s and Δp is defined as:

$$
\begin{cases}
p_1 = p_s \\
p_2 = p_1 - \Delta p
\end{cases} \tag{14}
$$

EXPERIMENTAL VERIFICATION

With the previous experiment data, we have identified all the parameters of the LuGre model for the single rod low-friction cylinder, as Eq. (15) shows.

$$
\begin{cases}
F_{\mathrm{ss}}(v) = F_{\mathrm{c}} \,\mathrm{sgn}(v) + (F_{\mathrm{s}} - F_{\mathrm{c}}) e^{-(v/v_{\mathrm{s}})^2} + \sigma_2 v \\
F_{\mathrm{c}} = 2.856 + 0.772 p_{\mathrm{s}} - 0.5843 \Delta p \\
F_{\mathrm{s}} = 3.904 + 7.152 p_{\mathrm{s}} - 4.0386 \Delta p \\
v_s = 2.3892 - 0.3782 p_{\mathrm{s}} + 0.1134 k_8 \Delta p \\
\sigma_2 = -0.0185 + 0.1032 p_{\mathrm{s}} - 0.0627 \Delta p
\end{cases} \tag{15}
$$

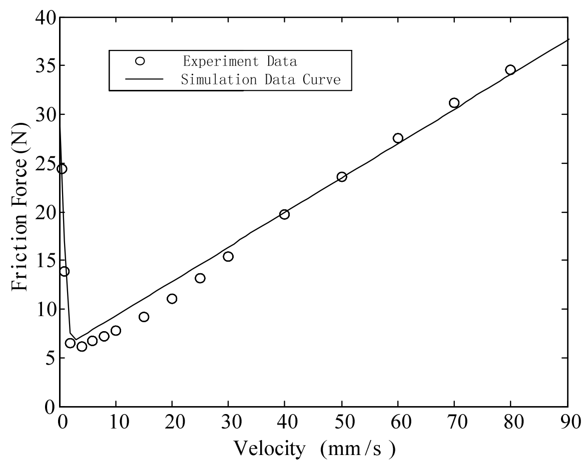

Figure 16 Comparing simulation data from the modified LuGre model with experiment data

Suppose it is needed to find out the friction-velocity characteristics of the cylinder with the condition p_1 is 300kPa and p_2 is 400kPa, which has not been tested before, we can get it soon by simulation based on Eq. (15). Comparing the simulation data with the experiment data we got later, the Figure 16 is obtained. As figure 16 shows, the simulation data curve is very close to the experiment data. The maximum error between then is less than 2N. It is validated that the modified LuGre model with the parameters indentified can describes the friction characteristics of the pneumatic cylinder with high precision.

CONCLUSIONS

A new method of identifying parameters of the LuGre Model, which is a nice friction model that can describe the friction phenomenon of pneumatic cylinders comprehensively, is presented. Corresponding to the method, a new experimental bench, on which the moving of pneumatic cylinder is driven by a servo motor accurately, was developed to obtain precise experiment data for the parameters identification. As experiment data shows that the working pressure and the differential pressure both almost have linear relation with the value of steady-state parameters Coulomb friction force F_c, Maximum stiction friction force F_s, Stribeck velocity v_s and viscous friction coefficientσ_2, but have little influence on the dynamic-state parameters Stiffness of the bristles σ_0 and Damping coefficient of the bristles σ_1, the LuGre Mode was modified to introduce the influence of pressure. A following experiment was carried out and its results verified that the modified model is precise and the parameters identify method is effective.

REFERENCES

1. P. R. Dahl. Solid friction damping of mechanical vibrations. AIAA Journal, 1976, 14(12):1675−82.
2. P.A. Bliman, M. Sorine. Easy-to-use realistic dry friction models for automatic control . In Proceedings of 3rd European Control Conference, Rome, Italy, 1995: 3788−3794.
3. D.A. Haessig, B. Friedland. On the modelling and simulation of friction. Dyn Syst Meas Control Trans ASME, 1991, 9, 113(3): 354−362.
4. Canudas de Wit C, P . Lischinsky . Adaptive friction compensation with partially known dynamic friction model. International Journal of Adaptive Control and Signal Processing, 1998, 11(1):65-80.
5. Lee E. Schroederl. Experimental Study of Friction in a Pneumatic Actuator at Constant Velocity.

Journal of Dynamic Systems, Measurement, and Control, 1993, 9,Vol. 115: 575-577.
6. B. H. Zhang, H. F. Chen, Y. F. Ma, The characteristics of Friction Force in Pneumatic Cylinders, Journal of Beijing Institute of Technology, 2005, (6): 483~487.
7. Pedro Luís Andrighetto, Antonio Carlos Valdiero, Leonardo Carlotto. Study of the friction behavior in industrial pneumatic actuators . ABCM Symposium Series in Mechatronics, 2006, 2 : 369-376.
8. Belforte, G., Mattiazzo,G, Mauro,S., Tokashiki,L. R. Measurement of Friction Force in Pneumatic Cylinders. Tribotest journal, 2003,20(2): 33-48.
9. Armstrong B. Control of Machines with Friction. Boston: Kluwer Academic Publishers, 1991: 24~26.
10. P. Z. Li, Y. L. Ying, Z. L. Gu, Application of Pneumatic technology and development of Pneumatic components, Science & Technology Information, 2007, No. 19: 28.

Proceedings of the 8th JFPS International
Symposium on Fluid Power, OKINAWA 2011
Oct. 25-28, 2011

1D1-3

MODELING OF PNEUMATIC EJECTOR SYSTEM WITH RESTRICTIONS AT EXHAUST AND VACUUM PORTS

Chongho YOUN*, Masahiko ITO**, Kenji KAWASHIMA*, Toshiharu KAGAWA*

* Tokyo Institute of Technology, Precision and Intelligence Laboratory
4259 Nagatsuta, Midori-ku, Yokohama 226-8503, Japan
(E-mail: youn.c.aa@m.titech.ac.jp)
** Tokyo Institute of Technology, Department of Mechano-Micro Engineering, Japan

ABSTRACT

In this study, the characteristic of a flow type ejector and a pressure type ejector with flow restrictions at the exhaust and vacuum ports is examined by the experiment. The characteristic change of this ejector affects the performances of a vacuum system. it is necessary to take into consideration the vacuum characteristic change to design vacuum system. the semi-experimental model that can predict the vacuum characteristic is proposed. This model can calculrate the vacuum characteristic with restrictions at the exhaust and vacuum ports, when the vacuum characteristic by an exhaust pressure, supply pressure, and the characteristic of flow resistance are known. The calculation value of the vacuum characteristic when the orifices are connected with both sides of the vacuum port the exhaust port has a good agreement with experimental results. The pressure response experiment of the chamber is conducted, and the effectiveness of the simulation is confirmed.

KEY WORDS

Pneumatic ejector, Vacuum characteristic, Flow restriction

NOMENCLATURE

b	:	critical pressure ratio [-]
C	:	sonic conductance [m^4･s/kg]
d	:	diameter [m]
m	:	mass [kg]
P	:	pressure [Pa(abs)]
Q	:	flow rate [L/min(normal)]
R	:	gas constant [J/(kg･K)]
V	:	chamber volume [m^3]
ρ	:	density [kg/m^3]
θ	:	temperature [K]
Subscript		
a	:	atmospheric condition
b	:	exhaust port
c	:	vacuum port
m	:	mixing chamber
n	:	nozzle
s	:	supply port

INTRODUCTION

Ejectors are widely used in industrial field to make vacuum pressure. Schematic diagram of ejector is shown in Fig.1. An ejector has three ports: supply port, exhaust port and vacuum port. It has a nozzle and a diffuser part. It doesn't have a mechanical driving part, and a comparatively simple structure. It is cheap, small and light as compared with a vacuum pump.

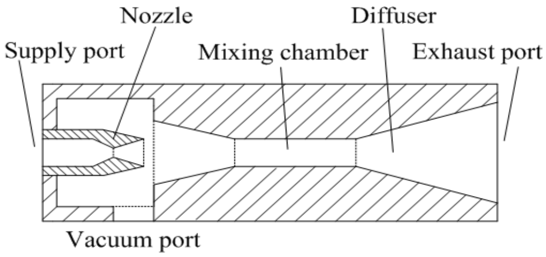

Figure 1 Schematic diagram of ejector

Generally the exhaust port of an ejector is an atmospheric pressure, and there is no flow resistance at the exhaust port. However, some valves and pipes are connected to exhaust port and the vacuum port in the some industrial field.
As an example of application, ejector is used in the vacuum toilet system of railway vehicles. The vacuum toilets system is used for high performance and energy saving, because it can reduce uncomfortable odor and also reduce loading water. The exhaust and vacuum ports of an ejector are connected to some valves and pipes in the vacuum toilet system. Then, the characteristic of an ejector changes with flow resistances of the exhaust and vacuum ports. The change of the vacuum characteristic affects the performances of a vacuum toilet system. Then, it is necessary to take into consideration the vacuum characteristic change to design vacuum system.
In the previous study, Watanabe et al. [1] measured the internal pressure distribution of the pneumatic ejector in an experiment. Matsuo et al. [2] visualized double-Vacuum Phenomenon. However, as for the experimental measurement, exhaust port is atmospheric pressure. As well as an experiment, a lot of theoretical analysis is studied. B. J. Huang et al. [3], Hisham El-Dessouky et al.[4] , R. Yapici et al.[5] and Zhu YH et al.[6] suggested a mathematics model about the ejector in the frozen system. To our knowledge, the research on ejector with resistance at the exhaust port and the vacuum port is few in a pneumatic system.
In this study, the characteristic of the ejector with flow restrictions at the exhaust and vacuum ports is examined by the experiment, and the semi-experimental model is proposed.

PNEUMATIC EJECTOR

The operation principle of an ejector is explained as follows. A compressed air is supplied from a supply port. When air passes the nozzle, it becomes a high-speed. The negative pressure occurs by high speed flow. Air is sucked from the vacuum port by the negative pressure. The mixed air passes along diffuser and the pressure is recovered.
There are "Constant-area mixing ejector" and "Constant- pressure mixing ejector" by the position of a

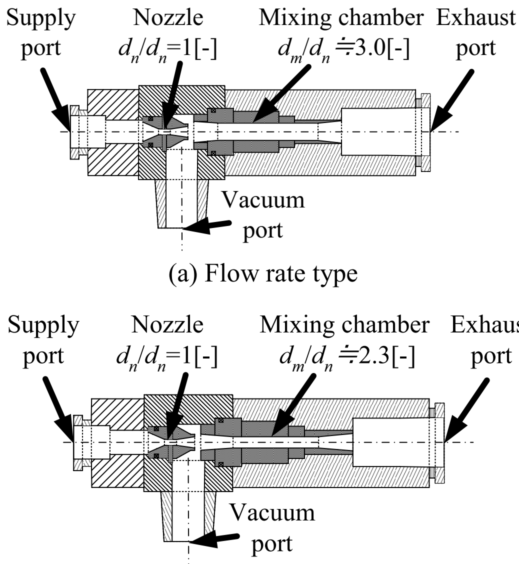

(a) Flow rate type

(b) Pressure type

Figure 2 Ejector type

jet nozzle. The one that the exit of the nozzle is located in suction chamber is called "Constant-pressure mixing ejector". The other that the exit of the nozzle is located in constant-area section is called "Constant-area mixing ejector"."Constant-pressure mixing ejector" is used widely because it may show better performance than "Constant-area mixing ejector".
"Constant-pressure mixing ejector" can be divided roughly into a flow type and a pressure type. A flow type ejector and a pressure type ejector are shown in Fig.2. As for the area of the mixing section, the flowing quantity type is wide, and the pressure type is narrow. However, the nozzle diameter is the same. The characteristic is very different according to the difference of the area of the mixing section. The difference of the characteristic is experimentally shown in the next chapter.

CHARACTERISTIC OF THE EJECTOR

In case of no fluid resistance at exhaust and vacuum port

The characteristic in case of no fluid resistance at exhaust and vacuuim port is examined. The circuit of an experimental setup is shown in Fig.3. The buffer tank (5L) is located at supply port of ejector to stabilize supply pressure and the supply pressure is controlled by regulator. Specifications of the sensor are shown in Table 1. The pressure sensor is installed in the supply port, vacuum port and the exhaust port of the ejector. The variable restriction and the flow meter are installed in the vacuum port.

The experiments are conducted with the flow type ejector and the pressure type ejector. The experimental method is as following. The supply pressure P_s is fixed to 600 kPa(abs). The vacuum port pressure P_c and the flow rate Q_c are measured by varing restriction.

An experimental result is shown in Fig.4. In this study, the relation between the vacuum port pressure P_c and flowing quantity Q_c of the vacuum port is called a vacuum characteristic. In case of the flow type ejector, a maximum flow rate is about 120 L/min(normal)

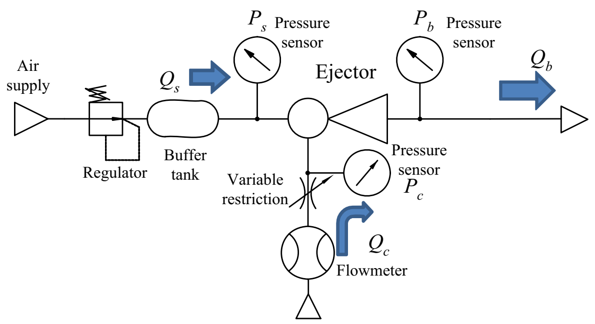

Figure 3 Experimental setup

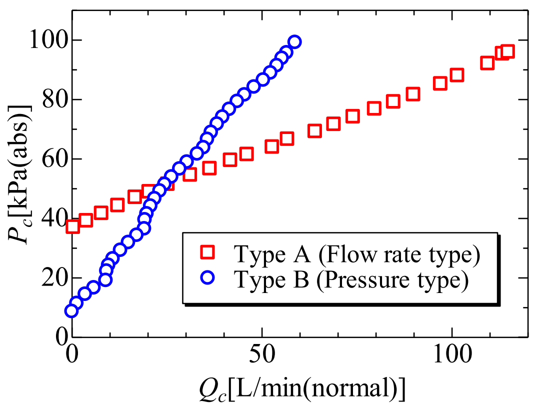

Figure 4 Vacuum characteristics

Table 1 Specifications of sensors

Component		Specification	
Pressure sensors (Kenyence Corp.)	P_s	Model	AP-13S
		Range	0-1MPa
		Accuracy	± 0.5% F.S.
	P_b	Model	AP-13S
		Range	0-1MPa
		Accuracy	± 0.5% F.S.
	P_c	Model	AP-10S
		Range	±100kPa
		Accuracy	± 0.5% F.S.
Flow sensor	Q_c	Type	Laminar flow
		Accuracy	± 0.5% F.S.

and the maximum vacuum degree is about 40 kPa(abs). In case of the pressure type ejector, a maximum flow rate is about 60 L/min(normal) and is lower than the flow type ejector, but the maximum vacuum degree is about 10 kPa(abs).

In case of fluid resistance at exhaust and vacuum port

In this section, the vacuum characteristic with flow resistance at exhaust and vacuum port is experimentally examined. An experimental setup is shown in Fig.5. An orifice is connected to an exhaust port or a vacuum port as a flow resistance. The diameter of an orifice is shown in Table2. Other experimental devices are same as the previous section. The experiment is conducted in case of orifice in the exhaust port and in case of orifices in the exhaust and vacuum port.

An experimental results are shown in Fig.6. When an orifice is connected only to an exhaust port, the flow rate and vacuum pressure are varing. When an orifice is added to a vacuum port, a maximum flow rate is only varied, but the maximum vacuum degree is not varied. The reason is that the pressure difference at an orifice is not produced when a flow rate is zero. Therefore, the maximum vacuum degree does not change. It was confirmed that the vacuum characteristic of the ejector was varied by connecting the restrictions at exhaust and vacuum port.

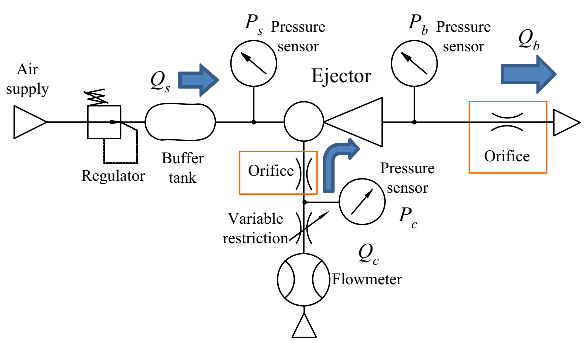

Figure 5 Experimental setup

Table 2 Diameters of orifices at both ports

	Diameter[m]	
	Exhaust port	Vacuum port
Flow rate type	4.5	2.5
Pressure type	3.8	2.5

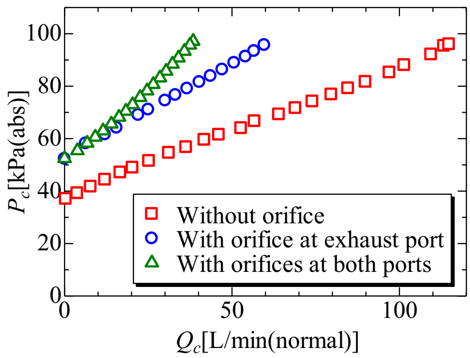

(a) Flow rate type

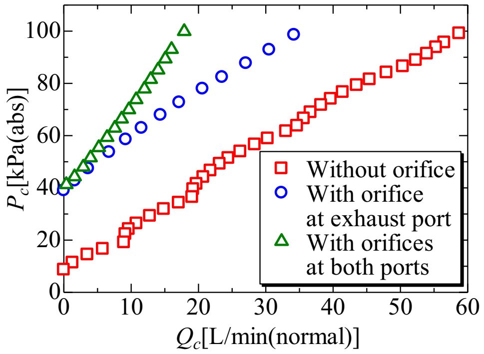

(b) Pressure type

Figure 6 Vacuum characteristics

INFLUENCE OF AN EXHAUST PRESSURE

To predict the vacuum characteristic with a flow resistance is very useful in design of the vacuum sysem. This chapter examines the influence of an exhaust pressure by the experiment, and proposes the approximate equations to make the modeling of the vacuum characteristic.

Experimental result

The experimental setup is same as Fig.3, and in order to set exhaust pressure, the variable resistance was added at the exhaust port. The experimental method is as following. The supply pressure P_s is fixed to 600 kPa(abs). The vacuum characteristic is measured when an exhaust pressure is an atmospheric pressure. The exhaust pressure is increased by 10kPa intervals, and the vacuum characteristic is measured at each case. The experiment is conducted until flow rate is minus value.

An experimental result is shown in Fig.7. The vacuum characteristic of a flow type and a pressure type are different. As for a flow type, the vacuum characteristic changes when an exhaust pressure is increased. On the other hand, in case of pressue type, the vacuum characteristic does not change up to P_b=110kPa (abs). The maximum suction flow rate does not change up to P_b=130kPa (abs). The flow type causes the backflow from P_b =160kPa(abs) and the pressure type causes the backflow from P_b =190kPa(abs).

Approximation

The experimental result of the vacuum characteristic is approximated. Inclination [(L/min (normal)) / (kPa (abs))], and an intercept of vertical axis [L/min (normal)] are approximated with the secondary function of the exhaust pressure P_b, respectively. Inclination can be expressed as an equation (1) and an intercept of vertical axis can be expressed as an equation (2).

$$A'P_b^2 + B'P_b + C' \tag{1}$$

$$D'P_b^2 + E'P_b + F' \tag{2}$$

Therefore, flow rate Q_c is expressed with the function of the vacuum pressure P_c and the exhaust pressure P_b. as an equation (3).

$$Q_c = (A'P_b^2 + B'P_b + C')P_c + (D'P_b^2 + E'P_b + F') \tag{3}$$

A´～F´is obtained from experimental result. the approximate equations of flow rate type and pressure type is like this.

$$Q_c = (-2.96\text{e-}05\ P_b^2 + 3.70\text{e-}02\ P_b - 1.46)\ P_c$$
$$+(-2.43\text{e-}02\ P_b^2 + 8.70\text{e-}01\ P_b + 8.46\text{e+}01) \tag{4}$$

$$Q_c = (1.81\text{e-}04\ P_b2 - 3.23\text{e-}02\ P_b + 1.99)\ P_c$$
$$+(-3.40\text{e-}02\ P_b^2 + 7.06\ P_b - 3.69\text{e+}02) \tag{5}$$

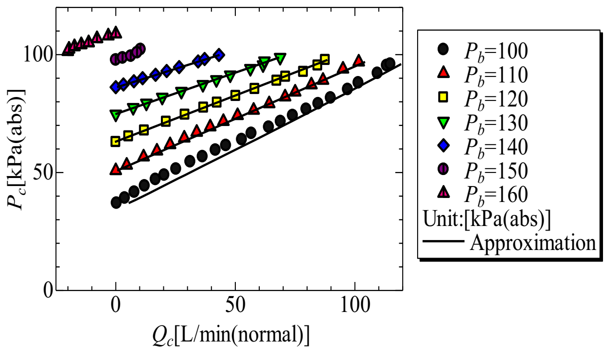

(a) Flow rate type

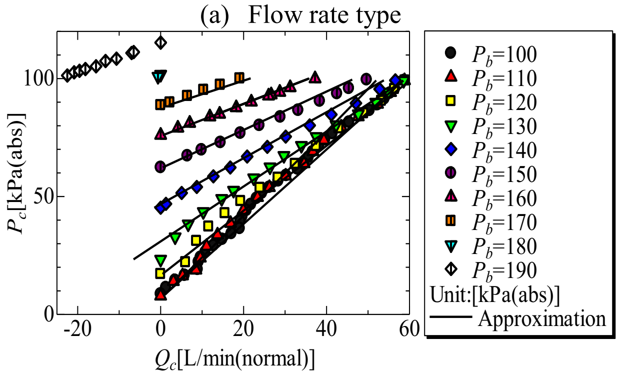

(b) Pressure type

Figure 7 Vacuum characteristics with increased exhaust pressure

MODELING

This chapter proposes a semi-experimental model to simulate the vacuum characteristic with a flow resistance. This model can predict the vacuum characteristic with a flow resistance, when the vacuum characteristic by an exhaust pressure, supply pressure, and the characteristic of flow resistance are known

The proposal of a semi-experimental model

The flow rate relation of the ejector is following.

$$Q_s + Q_c = Q_b \quad (6)$$

Q_s and Q_b is flow rate of the nozzle and the orifice in the exhaust port. It is necessary to obtain the flow rate characteristic of the ejector nozzle and the orifice in the exhaust port. Approximate equation of vacuum flow rate Q_c is obtained in the previous chapter. Q_s is calculated from the flow rate characteristic of the nozzle. Q_b is calculated from the flow rate characteristic of the orifice in the exhaust port.

The flow rate characteristic of an ejector nozzle and an exhaust port orifice is obtain by experimental result. The experiment is conducted according to the ISO6358. The flow rate of the ejector nozzle and the exhaust port orifice can be expressed like the equation (7) and (8).

$$Q_s = C_s P_s \sqrt{\frac{293}{\theta_a}} \quad (7)$$

$$Q_b = C_b P_b \sqrt{\frac{293}{\theta_a}} \phi_b \quad (8)$$

When $P_a/P_b \le 0.528$

$$\phi_b = 1 \quad (9)$$

When $P_a/P_b > 0.528$

$$\phi_b = \sqrt{1 - \left(\frac{P_a / P_b - b_b}{1 - b_b}\right)^2} \quad (10)$$

From equation (3), (6), (7), (8), following equation is obtained.

$$C_s P_s \sqrt{\frac{293}{\theta_a}} + \{(A' P_b^2 + B' P_b + C')\, P_c + (D' P_b^2 + E' P_b + F')\} = C_b P_b \sqrt{\frac{293}{\theta_a}} \phi_b \quad (11)$$

Algorism of calculation

The algorism of calculation is shown in Fig.8. At first, the vacuum characteristic with the flow resistance at the exhaust port is calculated. Then, the flow rate characteristic of the orifice in the vacuum port is added and the vacuum characteristic with restrictions at the exhaust and vacuum ports is calculated.

The algorism of calculation is explained as follows.

1. An arbitrary P_c is given to equation (11). equation (11) becomes the function of P_b and ϕ_b
2. Equation (11) becomes the secondary function of P_b when assuming $P_a/P_b \le 0.528$. P_b is calculated from the Equation (11).
3. If $P_a/P_b \le 0.528$ is approved, Q_c are calculated from equation (3) .
4. $P_a/P_b \le 0.528$ is not approved, it is assumed $P_a/P_b >$ 0.528. P_b is calculated from equation (11).
5. Q_c are calculated from equation (3) .
6. The relation between Q_c and P_c is calculated.
7. The following algorism is added when there is a flow resistance at the vacuum port. The orifice characteristic of the vacuum port is substituted for the relation between Q_c and P_c of previous result and the new relation of Q_c and P_c is obtained

The calculation results are shown in Fig.9. The calculation results has a good agreement with experimental results.

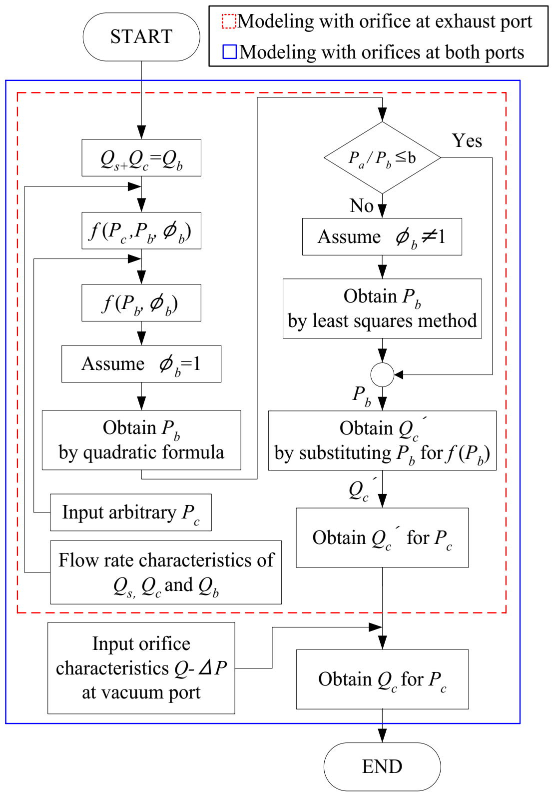

Figure 8 Calculation flowchart

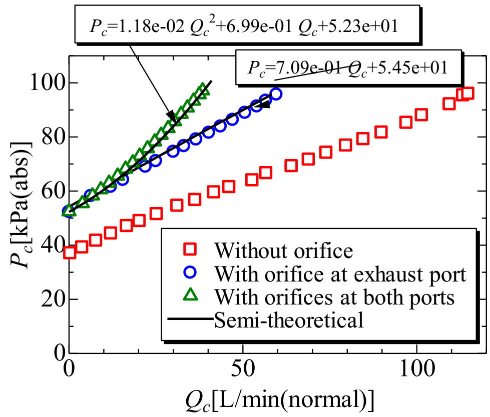

(a) Flow rate type

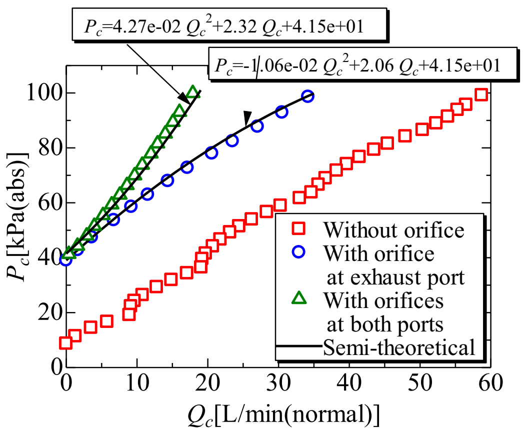

(b) Pressure type

Figure 9 Vacuum characteristics

THE PRESSURE RESPONSE OF A CHAMBER

Generally, a chamber is connected to the vacuum port of an ejector. The pressure response of a chamber is conducted by the experiment and the simulation.

Experimental setup

An experimental setup is shown in Fig.10. The solenoid controlled valve was connected to the supply port, and the isothermal chamber[7] is connected to the vacuum port. It can be assumed that the temperature in the chamber is constant.
The supply pressure is set P_s=600kPa(abs). A solenoid valve is opened and the pressure of chamber P_c is measured.

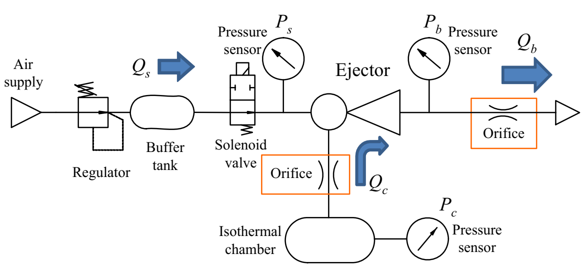

Figure 10 Experimental setup

Simulation and result

The block diagram is shown in Fig.11. An experimental results and a simulation results are shown in Fig.12. When the orifice is connected to the exhaust port, the average error of a simulation in flow rate type and pressure type is 0.6% and 1.1%. As a reason of the error, the approximate equationn of the vacuum flow rate, the temperature change of a chamber, etc. can be considerd. When the orifice is connected to both ports , the average error of a simulation in flow rate type is 0.9%, and pressure type is 1.0%. average error of a simulation in flow rate type is 0.9%, and pressure type is 1.0%. It was comfirmed that it was possible to calculate a pressure response with sufficient accuracy with a simulation.

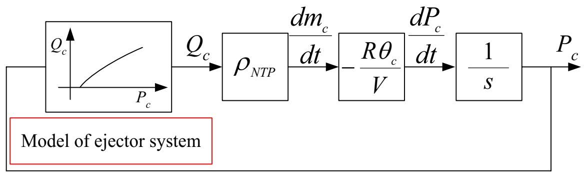

Figure 11 Block diagram for simulation

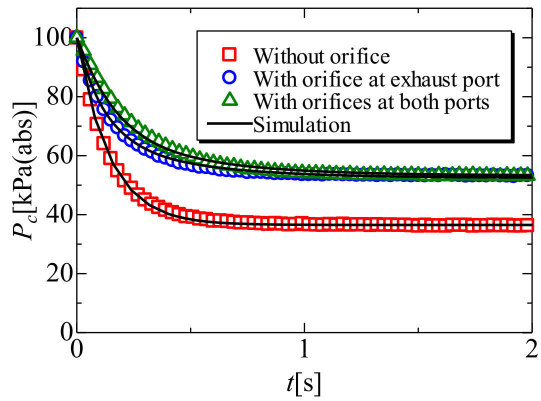

(a) Flow rate type

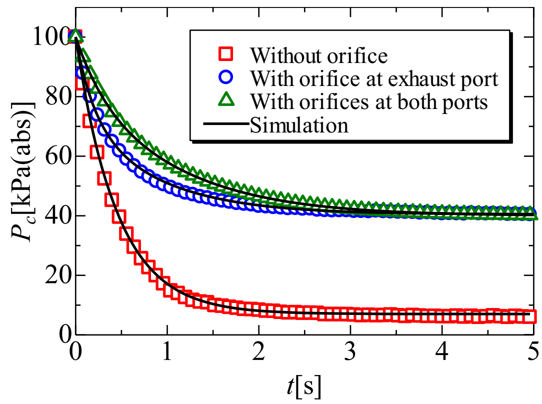

(b) Pressure type
Figure 12 Pressure response

CONCLUSION

In this study, the characteristic of a flow type ejector and a pressure type ejector with restrictions at the exhaust and vacuum ports is examined by the experiment. the semi-experimental model that can predict the vacuum characteristic is proposed. This model can calculrate the vacuum characteristic with a flow resistance, when the vacuum characteristic by an exhaust pressure, supply pressure, and the characteristic of flow resistance are known. The pressure response experiment of the chamber is conducted, and the effectiveness of the simulation is confirmed.

REFERENCES

1. WATANABE Itiro, WATANABE Takeo, ISO Shunya, KAWAHITO Takeki : Experimental Study on Pneumatic Ejector, with Special Reference to the Effect of Area Ratio on Performance Characteristics (1st Report) , The Japan Society of Mechanical Engineers, 58(434), 280, 1955
2. ATSUO Kazuyasu, MOCHIZUKI Hiroaki, KOBAY-ASHI Akinobu: On the Double-Vacuum Phenome-non of a Supersonic Air Ejector, The Japan Society of Mechanical Engineers, 51(469), 2813-2819, 1985
3. B.J.Huang, J.M.Chang, C.P.Wang, V.A.Petrenko: A 1-D analysis of ejector performance, International Journal of Refrigeration, Vol.22, No.5, pp.354-364, 1999
4. El-Dessouky H, Ettouney H, Alatiqi I, Al-Nuwaibit G: Evaluation of steam jet ejectors, Chemical Engineering and Processing, Vol.41, No.6, pp.551 -561, 2002
5. Yapici R, Ersoy HK: Performance characteristics of the ejector refrigeration system based o nthe constant area ejector flow model, Energy Conversion and Management, Vol.46, No.18-19, pp.3117- 3135, 2005
6. Zhu YH, Cai WJ, Wen CY, Li YZ: Shock circle model for ejector performance evaluation, Energy Conversion and Management, Vol.48, No.9, pp.2533 -2541, 2007
7. Kenji KAWASHIMA, Yukio ISHII, Tatsuya FUNAKI, Toshiharu KAGAWA: Determination of Flow Rate Characteristics of Pneumatic Solenoid Valves using An Isothermal Chamber, Journal of Fluids Engineering-transactions of the ASME, Vol. 126, No.2, pp.273-279, 2004

Proceedings of the 8th JFPS International
Symposium on Fluid Power, OKINAWA 2011
Oct. 25-28, 2011

1D2-1

RESEARCH ON THE SPHERICAL JOINT ROBOT DRIVEN BY THE PNEUMATIC MUSCLE ACTUATOR

Yu LIU*, Tao WANG* and Wei FAN*

* School of Automation, Beijing Institute of Technology
Beijing, 100081 China
(E-mail: liuyu@bit.edu.cn)

ABSTRACT

This paper describes a robot with a spherical joint that imitates the shoulder joint of humans. The robot with a spherical joint is developed considering structural features of a human's shoulder joint. The spherical joint has three degrees of freedom: abduction or adduction, flexion or extension and internal rotation or external rotation. Furthermore, this robot is actuated by a group of pneumatic artificial muscles (PMA), which have high power to weight ratio and an effective passive compliance characteristic. Basic characteristics of the artificial muscle are presented. Finally, because of the strong nonlinear and time lags of the PMA, model-free adaptive control which is an advanced control method and does not require building an off-line mathematical model. At last, sufficient accuracy of 0.5 degrees is obtained experimentally.

KEY WORDS
Spherical joint, PMA, Model-free adaptive control

I. INTRODUCTION

Generally, for traditional robots, motors are used as drivers and installed in joints. This arrangement can enhance the control precision, but increase the inertia and weight of the joints and limit its carrying capacity. Meanwhile, robots with these joints usually can't possess high flexibility. In order to overcome these shortcomings of traditional robots in high speed movement and rapid response, cable-driven robots come into being. Compared with the traditional robots, cable-driven robots are light in weight and possess higher flexibility of movement[1].

In this paper, a robot with a spherical joint that imitates the shoulder joint of humans is designed. The spherical joint has three degrees of freedom: abduction or adduction, flexion or extension and internal rotation or external rotation.

Compared with actuator actuated hydraulically or by motor, Pneumatic Muscle Actuator (PMA) has many super properties, such as easy installation, higher flexibility, without pollution, lower costs, higher ratio of power to weight and so on. In recent years, more attention has been paid to PMA all over the world[2].

Since the Pneumatic Muscle Actuator has the features of strong nonlinear and time lags, it is hard to establish a precise mathematical mode. Model-Free Adaptive Control (MFAC) is an advanced control method that does not require building an off-line mathematical model. MFAC is an ideal method for time-varying nonlinear systems which are difficult to identify the actual parameters. The basic idea of Model-Free Adaptive Control, MFAC)[3] is to introduce a new concept of pseudo-partial derivative; to change the ordinary nonlinear systems by a series of dynamic linear time-varying models; and to estimate the pseudo-partial vector of the by the I/O data from the controlled system. Finally, the system realizes a model-free learning of the nonlinear self-adaptive control.

II. THE CHARACTERISTICS OF ARTIFICIAL MUSCLE

The pneumatic artificial muscle actuator that we developed is an actuator strengthened by of the woven mesh with a certain length. A latex tube is inserted into the woven mesh in the axial direction. The operating principle of the PMA is that: when the compressed air is charged into the PMA, the latex tube will inflate in the radial direction. Because of the woven mesh, the expansion force in radial direction is changed to shrinkage force in the axial direction. Meantime, the PMA can lead to a amount of shrinkage displacement[4]. The pneumatic artificial muscle actuator used in this paper is shown in Figure 1:

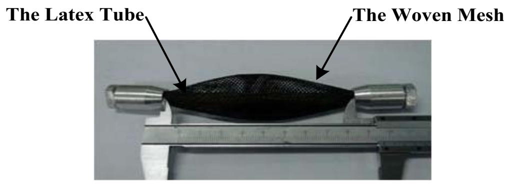

Fig.1 PMA

There are three critical parameters: pressure, shrinkage force and shrinkage displacement of this PMA. For the better application of PAM, it is necessary to obtain the relationship among the three parameters precisely. By testing the static characteristics of the PMA(The structural parameters is shown in Table 1), Three group of curves is obtained and shown in Figure 2(a), (b), (c)

Table 1 Structural parameters of the PMA

Length	250 mm
Outer diameter	20 mm
Inner diameter	16 mm
Mass	30 g

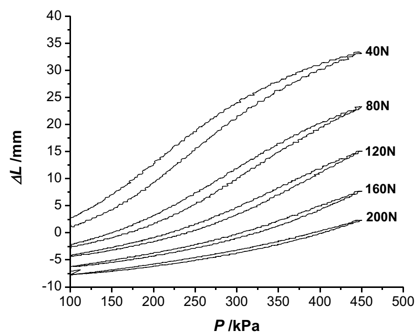

Figure 2(a) Relation curve between pressure and shrinkage displacement under constant shrinkage force

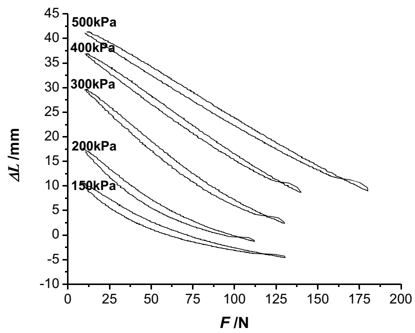

Figure 2(b) Relation curve between shrinkage force and shrinkage displacement under constant pressure

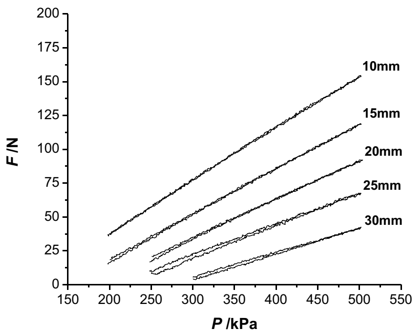

Figure 2(c) Relation curve between shrinkage force and pressure under constant shrinkage displacement

III. THE SPHERICAL JOINT ROBOT

A. Structure of the spherical robot

In this paper, a spherical joint using a spherical bearing is proposed, as shown as Figure 3. The spherical joint has three degrees of freedom: abduction or adduction, flexion or extension and internal rotation or external rotation. The centers of rotation of all directions are in the center of the spherical bearing. An overview of the spherical robot is presented as Figure 4. The spherical joint, which includes the spherical bearing, is driven by three PMA groups. The rotations in three degrees of freedom are caused by these three PMA groups respectively. The spherical joint and these three PMA groups are connected by three metal wires.

Figure 3 Spherical bearing

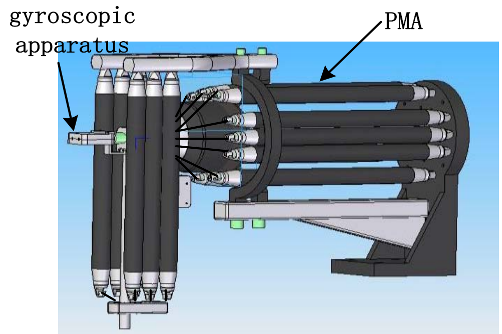

Figure 4 Overview of the spherical robot

B. Control System

PMAs are control by the SMC ITV0050 proportional pressure valve. Gyroscopic apparatus LCG50 from SILICON SENSING company are used for the measurement of joint angles. The structure of the control system diagram is shown in Figure 5.

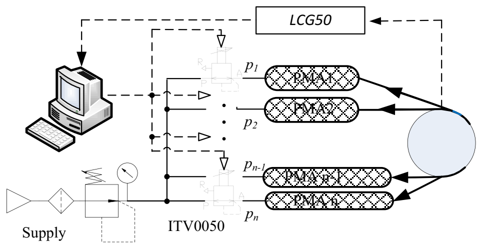

Figure 5 Control system diagram

IV. MODEL-FREE ADAPTIVE CONTROL OF

THE SPHERICAL JOINT ROBOT

The basic idea of Model-Free Adaptive Control, MFAC)[5] is to introduce a new concept of pseudo-partial derivative; to change the ordinary nonlinear systems by a series of dynamic linear time-varying models; and to estimate the pseudo-partial vector of the by the I/O data from the controlled system. Finally, the system realizes a model-free learning of the nonlinear self-adaptive control.

A. Estimate of the pseudo-partial derivative

Considering the following estimation criterion function

$$\Delta y(k+1) \le \emptyset(k) \cdot \Delta u(k) \quad (1)$$

$$J[\emptyset(k)] = [y^*(k) - y(k-1)]^2 + \mu[\emptyset(k) - \emptyset^\wedge(k-1)]^2 \quad (2)$$

According to (1) and (2), making the derivative of $\emptyset(k)$ equal to zero and according to the minimized algorithm

$$\emptyset^\wedge(k) = \emptyset^\wedge(k-1) + \frac{\varepsilon_k \cdot \Delta u(k-1)}{\mu + |\Delta u(k-1)|^2} \cdot [\Delta y(k) \ - \Delta\emptyset^\wedge(k-1) \cdot \Delta u(k-1)] \quad (3)$$

that $\emptyset^\wedge(\mathrm{k})$ is the estimated value of the pseudo-partial derivative $\emptyset(\mathrm{k})$, ε_k is the learning rate, μ is the penalty factor.

B. Model free adaptive control law

Considering the following input criterion function

$$J[u(k)] = [y^*(k+1) - y(k+1)]^2 + \gamma[u(k) - u(k-1)]^2 \quad (4)$$

Where $y^*(k+1)$ is the desired output; γ is the penalty factor; $\gamma[u(k) - u(k-1)]^2$ restricts the control input and overcomes the steady-state tracking error.

According to (1) and (4), to make the derivative of $u(k)$ equal to zero and refer to the minimized algorithm.

$$u(k) = u(k-1) + \frac{\rho_k \cdot \emptyset(k)}{\gamma + |\emptyset(k)|^2} \cdot [y^*(k+1) \ - y(k)] \quad (5)$$

Here ρ_k is the learning rate and γ is the penalty factor. It limits $\Delta u(k)$ and restricts the linear substitution confine that the dynamic linear system substitutes the nonlinear system, so it restricts $\emptyset(k)$ indirectly. Besides, it avoids denominator of (5) becoming zero.

According to (3) and (5), we can obtain the model free adaptive control low. The structure of the model free adaptive control law is shown in Figure 6:

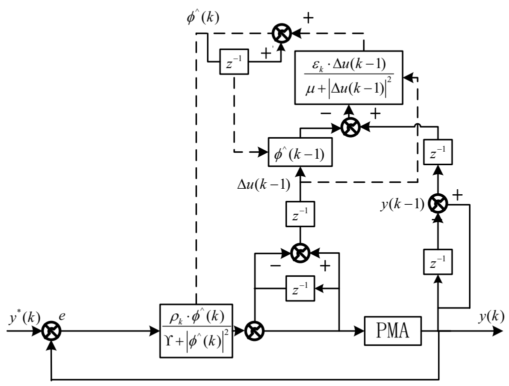

Figure 6 Structure of the model free adaptive control law

V. EXPERIMENT

In this section, we demonstrate the posture control of the spherical robot.

A. The rotation of single-degree-of-freedom

In this section, The rotation of abduction or adduction is taken as an example. The sampling time is 0.01s, and the parameters are set as following: $\varepsilon_k = 0.7$, $\rho_k = 0.03$, $\mu = 1.2$, $\gamma = 1.4$

Experiment 1: The adaptability performance: The desired output is: $y^* = 50^\circ$, The experiment result is shown in Figure 7.

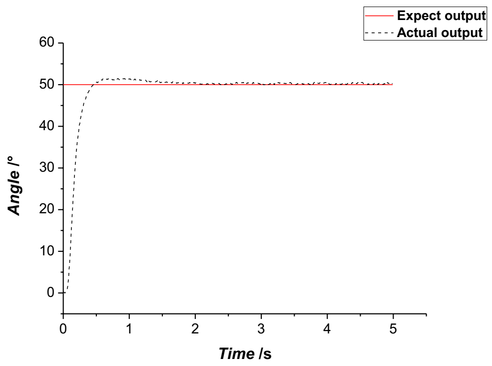

Figure 7 Adaptability performance

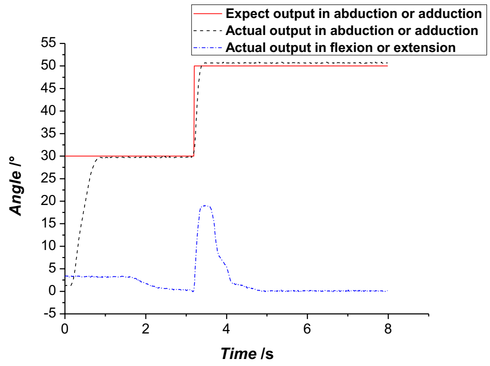

Figure 9 Rotations of double-degree-of-freedom

Experiment 2: The tracking performance: The experiment result is shown in Figure 8.

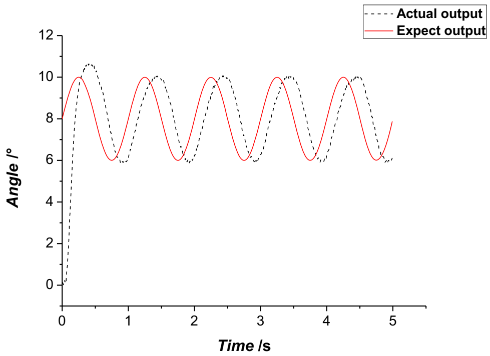

Figure 8 Tracking performance

B. The rotations of double-degree-of-freedom

In this section, the rotations of abduction or adduction and flexion or extension are taken as an example. The sampling time is 0.01s, and the parameters are set as following: $\varepsilon_{k1} = 0.7$, $\rho_{k1} = 0.03$, $\mu_1 = 1.2$, $\gamma_1 = 1.4$; $\varepsilon_{k2} = 0.5$, $\rho_{k2} = 0.07$, $\mu_2 = 1.5$, $\gamma_2 = 1.3$.

First, for 0–3s, the desired output of rotation in abduction or adduction is 30°. After that, for 3–8s, the desired output of rotation in abduction or adduction is 50°. At the same time, the desired output of rotation in flexion or extension is 0°. The experiment result is shown in Figure 9.

C. The conclusion of experiments

According to the result of the experiments, for the rotation of single-degree-of-freedom, the spherical robot controlled by the model-free adaptive control has fast response and the steady-state error is less than 1°. However, for the rotations of double degree of freedom, because of the coupling between the two rotations, a sudden change of one rotation will bring the disturbance to the other.

VI. CONCLUSION

In this paper**,** a robot with a spherical joint that imitates the shoulder joint of humans is designed. The spherical joint has three degrees of freedom and is actuated by a group of PMA. Because of the strong nonlinear and time lags of the PMA, model-free adaptive control is introduced to this system, At last, sufficient accuracy of 0.5 degrees is obtained experimentally.

In the future study, a de-coupling control should be introduced is this spherical robot for better performance.

REFERENCES

[1] Yangyi Yang, Weihai Chen, Xingming Wu, Quanzhu Chen. Stiffness Analysis of 3-DOF Spherical Joint Based On Cable-Driven Humanoid Arm[C]. 2010 5th IEEE

Conference on Industrial Electronics and Applicationsis 1998(3)100-103.
[2]Yugui Yang, Research on the Robot Dual Arm Driven by the Pneumatic Muscle Actuator[D]. Bei Jing Institute of technology. 2009.
[3] Ma Ping, Li Wei, Zheng Guiwen and Niu Yuguang, “The Application of Model Free Adaptive Control”, Beijing: IMACS Multi-conference on "Computational Engineering in Systems Applications"(CESA), October 2006. (in Chinese)
[4] K. Yaegashi, T. Nakamura, N. Saga, “Study on Biological Characteristics of Pneumatic Artificial Muscle Reinforced by Fiber in the Axis Direction” SICE System Integration Division Annual Conference, 2003, pp.872-873
[5] C.P. Chou, B. Hannaford, “Static and Dynamic Characteristics of McKibben Pneumatic Artificial Muscles”, Proceedings IEEE International Conference on Robotics and Automation, Vol.12, No.1, 1994, pp.281-286.
[6] F. Daerden, D. Lefeber, “The Concept and Design of Pleated Pneumatic Artificial Muscles, International Journal of Fluid Power, 2001, Vol.2, No.3, pp.41-50.

Proceedings of the 8th JFPS International
Symposium on Fluid Power, OKINAWA 2011
Oct. 25-28, 2011

1D2-2

DEVELOPMENT AND APPLICATION OF ALTERNATIVE DIRECTION AIR COMPRESSOR

Takuya FUJIKAWA*, Osamu OYAMA* and Toshihiro YOSHIMISTU**

* Department of Mechanical Engineering, School of Science and Technology
Meiji University
1-1-1 Higashimita, Tamaku, Kawasaki city, Kanagawa, 214-8571 Japan
(E-mail: ce02088@meiji.ac.jp)
** Department of Mechatronic Robot
Kanagawa Institute of Technology
1030 Shimoogino, Astugi city, Kanagawa, 243-0292 Japan

ABSTRACT

This paper deals a new type of compressor that can deliver the air directions alternatively. This compressor is made by replacing the location of inhalation/exhalation air port into proper position of ordinary vane type air compressor. By using the compressor the direction or speed of cylinder can be selected changing the clockwise/counterclockwise rotational direction and the rotational speed of compressor and the extensional solenoid valves are not needed. In this report, we choose components of this compressor. The air motor that composes this compressor is paid to attention, and a new sample is examined.

KEY WORDS

Key words, Alternative Direction Air Compressor, Air Motor, Energy Saving

INTRODUCTION

In recent years, the global environmental problems, for example the global warming, have become increasingly serious. Therefore, we must always develop the machine which is designed in consideration of energy saving. In the field of pneumatics, to improve energy conservation and efficiency of the air compressor is a problem to be solved in the near future, because the source of power supply like air compressor use a huge energy. Incidentally as the case may be the pneumatic system requires the air compressor that can deliver the air both directions, that is, inhalation and exhalation from the viewpoint of energy saving. The reason is because it is possible to control the behavior of the pneumatic actuator by selecting the compressed air directions. Such air compressor can be seen in the literature, but is currently not given.

Accordingly, the purpose of this study is the development of alternative direction air compressor and the verification of its fundamental characteristics. Furthermore, this study provides the new system which is configured by the alternate direction air compressor.

ALTERNATE DIRECTION AIR COMPRESSOR

The alternate direction air compressor is a new compressor that can switch the inlet and outlet and change the direction of air flow each other. In previous studies, the compressor that was designed to meet such a functional specification was producted by hand made but the compressor could not get enough pressure because of the lack of precision of composed parts. So we focused an air motor that is commercially used as an actuator by using the air motor. Fig.1 shows the schema of the alternate direction air compressor. As shown in Fig.1, the compressor is made by air motor driven by the shaft of the electric motor. When the electric motor rotates the clockwise, the port 1 becomes the exhalation port and the port 2 is the inhalation port. On the other hand, when the electric motor rotates the counterclockwise the port 1 becomes inhalation port and the port 2 is exhalation port. This compressor can select the moving direction of cylinder by changing the clockwise or the counterclockwise rotational direction and the speed of cylinder is continuously changed by the rotational speed of compressor. This compressor needs no additional solenoid valve, speed controller and so on, not as the conventional pneumatic system.

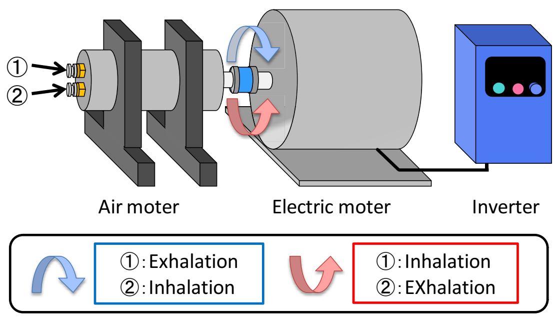

Figure 1 The alternate direction air compressor

Air Motor

In a past study, we suggested air motors which were constructed as the alternate direction air compressor. Table 1 shows specifications of the air motor. The internal structure of this air motor is a complete symmetry, and it may be said that it is the ideal construction for the alternate direction air compressor.

Table 2 shows the Output characteristic of the alternate direction air compressor is made by this air motor.

Table 1 Specifications of the previous air motor used for compressor

Type code		TAV2R-030
Rated pressure (MPa)		0.5
At max output (0.5 MPa)	Output (W)	220
	Torque (N・m)	1.7
	Revolution (rpm)	1250
	Air consumption (L/min)	650
Min starting torque (N・m)		3.3
Mass (kg)		5

Interior volume (mm^2)	44

Table 2 The Output characteristic of the previous air motor used for compressor

Pressure (MPa)	Exhalation	0.13
	Inhalation	0.073
Flow rate (L/min)	Exhalation	49.7
	Inhalation	60.0
Total mass (kg)		12

We see from Table 2 that the output pressure of weak and does not sufficient for compressor. TAV2R-30 is the smallest air motor in this series. Therefor we developed the alternate direction air compressor using two types of air motors newly for improvement of the output. Table 3 shows specifications of the new air motors for the alternate direction air compressor. These two air motors differ in the size, but mechanism is a same.

Table 3 Specifications of new air motors

Type code		P1V-S03 0A0E50	P1V-S06 0A0E00
Rated pressure (MPa)		0.6	0.6
At max output (0.5 MPa)	Output (W)	300	600
	Torque (N・m)	0.40	0.82
	Revolution (rpm)	7250	7000
	Air consumption (ℓ/min)	480	900
Min starting torque (N・m)		0.60	1.2
Mass (kg)		1.0	2.0

Electric Motor

The alternate direction air compressor is driven by the shaft of the electric motor. The electric motor which we used is an AC motor. We used inverter to control the direction of rotation and the rotational speed of motor, in order to control the pressure and flow rate. Table 4 shows specifications of the electric motor. And Table 5 shows specifications of the inverter.

Table 4 Specifications of the electric motor.

Type code	EFOU-K
Rated output (W)	200[4-pole]
Rated torque (N・m)	1.3
Rated speed (rpm)	1430[50Hz]
Mass (kg)	6.7

Table 5 Specifications of the inverter.

Type code	L100-002MFR
Applicable motor	4-pole ,200W
Rated capacity	0.6kVA
Rated input voltage	100-115V
	50/60Hz
Rated output voltage	3-phase 200-230V
Rated output current	1.4A
Control method	Line to line sine wave PWM
Output frequency range	0.5-360Hz

Output Characteristic for The Alternate Direction Air Compressor

We show the performance of the alternate direction air compressor using these air motors with electric motor in Table 6. The figure 2 shows the pressure in each rotational speed and the figure 3 shows the Flow rate in each rotational speed.

Table 6 Output characteristic for the compressor

			P1V-S030A0E50	P1V-S060A0E00
Revolution (rpm)	Exhalation	CW	4880	3160
		CCW	4860	3330
	Inhalation	CW	5870	3160
		CCW	5870	3330
Pressure (MPa)	Exhalation	CW	0.185	0.153
		CCW	0.188	0.151
	Inhalation	CW	-0.081	-0.073
		CCW	-0.078	-0.074
Flow rate (L/min)	Exhalation	CW	35.3	51.8
		CCW	33.2	51.0
	Inhalation	CW	35.1	43.0
		CCW	33.9	44.8
Air capacity par a roll (mL/rev)	Exhalation	CW	7.16	16.4
		CCW	6.83	16.2
	Inhalation	CW	5.98	12.9
		CCW	5.78	13.4
Compressor efficiency (%)			54.4	66.0
Total mass			7.7	8.7

CW ; Clockwise CCW ; Counter-Clockwise

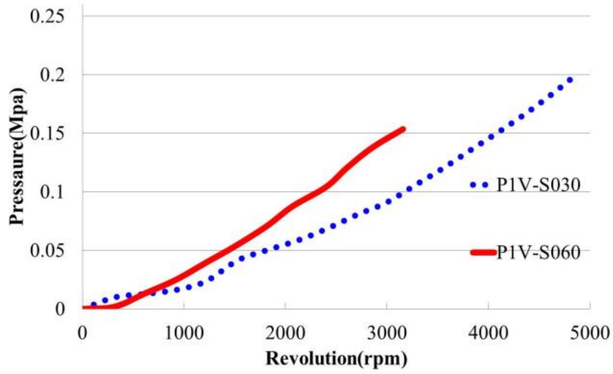

Figure 2 Pressure in each rotational speed

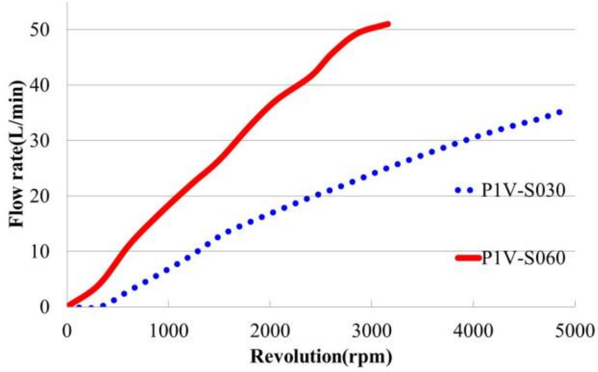

Figure 3 Flow rate in each rotational speed

Compressor Efficiency

Because the internal volume and revolution levels of compressor are different, we compared it with the performance as the each compressor. We calculated efficiency from following expressions (1) (2) and show the result in table 7.

$$L_0 = \frac{P \cdot Q}{60} \tag{1}$$

$$\eta = \frac{L_0}{L_i} \times 100 \tag{2}$$

L_0 : Output of the compressor (kW)
P : pressure (MPa)
Q : Flow rate (L/min)
η : Compressor efficiency (%)
L_i : Shaft input of the compressor (kW)

We decided to use for calculation with a value of the biggest exhalation pressure of Table 6. In addition, a value of Shaft input of the compressor [L_i] is used consumption power energy of AC motor which we connected.

Table 7 Compressor efficiency comparison

Air motor	Output (kW)	Efficiency (%)
TAV2R-030	0.108	53.8
P1V-S030A0E50	0.110	54.4
P1V-S060A0E00	0.132	66.0

The Present Problems

We aim at the development of the compressor that needs downsizing and the high output. This is contradicting performance. Thus we prepare samples about air motors and AC motor and choose it. About the air motor, the structure of the compression room chooses the samples of methods different conventionally. We adopted the compression method of the vane type, but plan improvement of the output using the compression method of the piston type as the thing which the high output can expect airtightness from highly more. About the AC motor, we prepare a sample with high output power and plan output improvement about the air motor of the vane type.

Comparison about The Air Motor

We show air motor to use for the choice of the compressor in Table 8. Sample 1 and 2 are the air motor of a vane type suggested conventionally. About the air motor of the radial piston type, we prepared for the thing of the standard that start torque and mass were close in because we compare it with the vane type. There are sample 3 and 4. We inspect each characteristic using these sample, we choice the most suitable component.

Table 8 Comparison of air motor's specifications

Sample	Compression method	Max power [w]	Min start torque [Nm]	Weight [kg]
No.1	Vane	600	1.23	2.0
No.2	Vane	300	0.60	1.0
No.3	Radial piston	135	1.96	2.5
No.4	Radial piston	73.5	0.686	1.45

Results

About each sample, we constitute an interactive model compressor using the same AC motor and measure pressure, flow quantity and the number of revolutions of the verge (See Figure 9). And we show the each sample efficiency comparison in the Table 9. In the figure 4 is exhalation pressure of each sample and in the figure 5 is Inhalation flow rate of each sample.

Table 9 Evaluation of characteristics experiment result of compressor

sample	Revolution [rpm]		Pressure [MPa]		Flow rate [L/min]	
	Ex.	In.	Ex.	In.	Ex.	In.
No.1	3160	3160	0.153	0.073	51.8	43.0
No.2	4880	58700	0.185	0.081	35.3	35.1
No.3	1460	2670	0.185	0.083	47.2	52.9
No.4	2800	4540	0.255	0.097	36.2	39.3

Table 10 Efficiency comparison of each sample

Sample	Output (kW)	Efficiency (%)
No.1	0.132	66.0
No.2	0.110	54.4
No.3	0.146	72.8
No.4	0.154	77.0

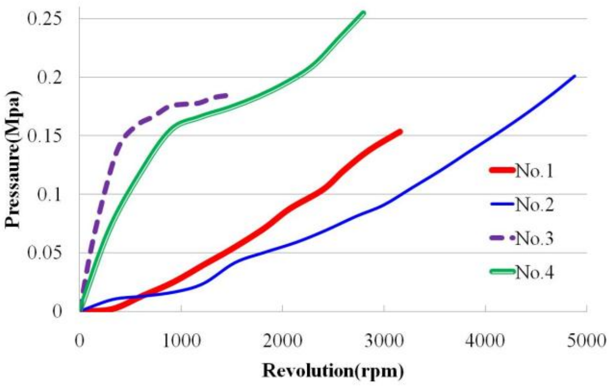

Figure 4 Exhalation pressure of each sample

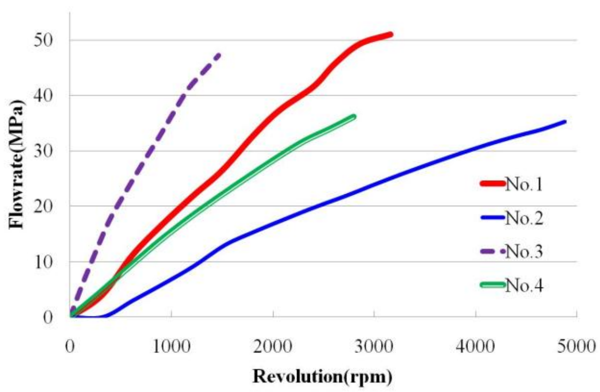

Figure 5 Inhalation flow rate of each sample

About the pressure, the difference by the air motor's exhalation was of particular note. Though all samples became more lightweight than the air motor which we used, we were able to get high pressure. About the air motor of the vane type, getting high pressure is thought that we were able to put it up to high rotational speed. About the air motor of the radial piston type, getting high pressure is thought that the air tight of the compression room is superiority. In the flow rate, we were not able to get ever-impressive flow rate by the capacity of the compression room having decreased for smaller and lighter air motor. A decrease in flow rate, however, is approximately 30%. It is not a big loss, because weight is lightweight approximately 50%.

We prepared near samples of the weight in each compression method, but we did not see different in the pressure or flow rate.

New AC Motor

We suggest that we use new AC motor for output improvement about the alternate direction air compressor. It is a problem, however, how we choose new AC motor. So we chose an AC motor not to lose the advantage to be able to carry itself of the alternate direction air compressor. Actually, we were based on 11.7[kg] which is total mass of the first alternate direction air compressor and chose an AC motor not to surpass it. Table 11 shows specifications of the electric motor. And Table 12 shows specifications of new inverter that is used to turn new AC motor.

Table 11 Specifications of new AC motor.

Type code	TFO-FK
Rated output (W)	400[4-pole]
Rated torque (N・m)	1.3
Rated speed (rpm)	1410[50Hz]
Mass (kg)	8.2

Table 12 Specifications of new inverter.

Type code	WJ200-004L
Applicable motor	4-pole ,400W
Rated capacity	1.0kVA
Rated input voltage	200-240V 50/60Hz
Rated output voltage	3-phase 200-240V
Rated output current	3.0A
Control method	Line to line sine wave PWM
Output frequency range	0.10-400.00Hz

To aim at the high output and rotary level we constituted the alternate direction air compressor using P1V-S060 and AC motor of 400[W] and we examined output characteristic from it. In addition, we compared it about each compressor. We show the combination of air motor and AC motor that was compared in table 13

Table 13 Combination of air motor and AC motor

The alternate direction air compressor			Total mass
	Air motor	AC motor	
Sample 1	P1V-S060 A0E00	[400W]	10.2[kg]
Sample 2	P1V-S060 A0E00	EFOU-K [200W]	8.7[kg]
Sample 3	P1V-S030 A0E50	EFOU-K [200W]	7.7[kg]

Results

First, we show below result of a measurement about Sample 1. We show output characteristic for Sample 1 in Table 11. In addition, we show the pressure in each number of revolutions in Figure 5 and Figure 6 and the flow rate in each number of revolutions in Figure 7 and Figure 8.

Second, we compare sample 1 to the others. Figure 9 shows pressure and Figure 10 shows flow rate each sample in exhalation when each sample turns clockwise. Furthermore, we show compressor efficiency comparison about each sample in Table 12.

Table 11 Output characteristic for Sample 1

		Sample 1
Revolution (rpm)	Exhalation	3920
	Inhalation	5183
Pressure (MPa)	Exhalation	0.254
	Inhalation	-0.085
Flow rate (L/min)	Exhalation	54.8
	Inhalation	50.3
Compressor efficiency (%)		58.0
Total mass		10.2

CW ; Clockwise CCW ; Counter-Clockwise

Table 12 Compressor efficiency about each sample

Air motor	Output (kW)	Efficiency (%)
Sample 1	0.232	58.0
Sample 2	0.132	66.0
Sample 3	0.110	54.4

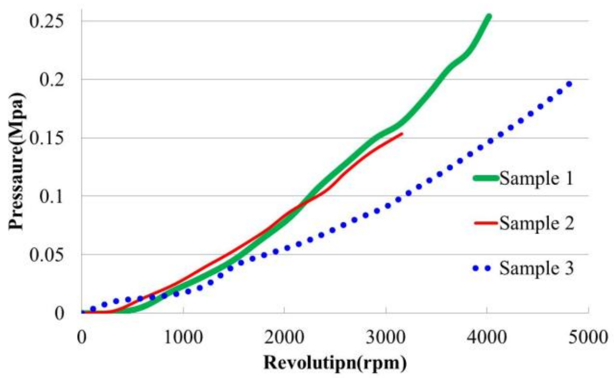

Figure 6 Pressure of each sample

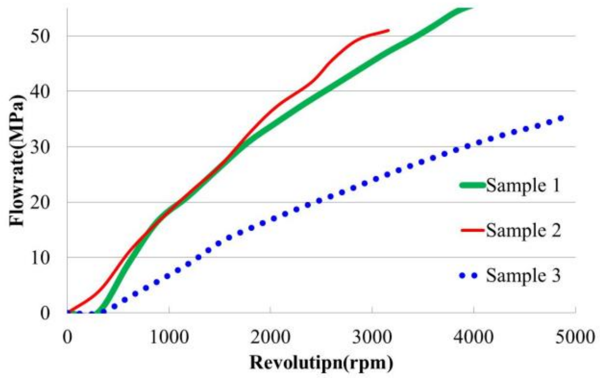

Figure 7 Flow rate of each sample

First, we have verified that the pressure is 0.254 [MPa], the flow rate is 54.8 [L/min] and the revolution is 3920 [rpm] in exhalation when sample 1 turns clockwise by this experiment. And we identified the compressor efficiency that is 58.0 [%] by these results. The difference of output by the rotatory direction is not seen.
Second, in figure 6 and figure 7, the sample 1's performance is higher than sample 2's in a high rotary level. Sample 1's compressor efficiency is lower than sample 2. We would suggest that it is caused by the development of fever in the alternate direction air compressor.

CONCLUSION

In this study, we developed a new-type alternate direction air compressor is constructed by a air motor or a new AC motor. About air motor, we prepared near samples of the weight in each compression method, but we did not see the difference by the air motor's exhalation was of particular note in the pressure or flow rate. About AC motor, we succeeded in using the compressor at a high rotary level and succeeded in measurement of the max pressure and flow quantity together. The important part of this argument is that the compressor is useful as a movable small compressor. But we have a problem that the compressor produces heat when we operate it at a high rotary level. Because it is thought that this leads to loss of the energy, the construction of the system which can remove heat effectively is necessary.
In addition, because compressor efficiency falls by the improvement of the rotary level, we think about the changes of the compression method of the air motor and want to develop a more efficient interactive model compressor.

REFERENCES

1. Takeyuki Sasaki, Osamu Oyama and Toshihiro yoshimitsu, Development and Application of Alternate Direction Air Compressure, The JFPS Symposium on Fluid Power, 2010
2. Takeyuki Sasaki, Osamu Oyama and Toshihiro yoshimitsu, Development and Application of Closed system, 2011.

Proceedings of the 8th JFPS International
Symposium on Fluid Power, OKINAWA 2011
Oct. 25-28, 2011

1D2-3

DEVELOPMENT OF QUADRUPED ROBOT WITH PNEUMATIC ACTUATOR

Zilei ZHAO*,Toshiro NORITSUGU*,Masahiro TAKAIWA* and
Daisuke SASAKI*

* Okayama University,The Graduate School of Natural Science and
Technology,Japan
3-1-1,Kitaku Tsushimanaka,Okayama,700-8530,Japan
(E-mail:cyousirai@mcrlab.sys.okayama-u.ac.jp)

ABSTRACT

We develop a quadruped walking robot, assuming human cooperative tasks in a construction building or rescue activity in disaster environment. Pneumatic cylinders are employed as driving actuators since it has explosion proof and inherent compliance. Owing to the compliance feature external force is easily estimated based on inner pressure of cylinder. We compose compliance control system on each leg based on the estimated floor reaction force with disturbance observer. After mentioning overview of the developed quadruped walking robot, we describe kinematics, statics and control system of each leg. We propose motion control strategy based on the floor reaction force estimated using disturbance observer. The validity of the proposed control system is verified through some experiments.

KEY WORDS

Pneumatic actuator, Quadruped robot, Disturbance observer

INTRODUCTION

In order to make a robot to perform several services in an outer field, its moving mechanism is important issue. The legged mechanism is indispensable especially for the rough terrain environment since it can select a contact point arbitrary. Researches for the multi-legged robots have been classified to the walking mechanism, such as ZMP based walking[1] or CPG one[2] and its application, such as, forestry[3], demining[4], steep slope operation[5], volcano investigation[6] and entertainment one[7].

Viewing from the point of size, most of the developed multi-legged robot are small one except for the some huge robot. One of the application of multi-legged robot is a task with human, such as cooperative carrying objects in a construction building or rescue victims in a disaster area. Such a robot should be the same with human from the view point of the size and the power level and also it should hold a compliance property.

We develop a quadruped robot using pneumatic actuators on the assumption of applying it to the above mentioned human friendly tasks. Employing pneumatic actuators bring some advantages as follows. As you know, compliance is necessary not only for the flexible property as human friendly robot but also for a stable gait. Therefore we compose position based compliance control system on each leg. In this case, force/moment sensors are generally required but it is not realistic from a view of cost and reliability especially for a field robot. In a pneumatic actuator, the control variable (stroke of piston) is easily affected by the external force, which means simultaneously that the external force is easily estimated based on the pressure. We propose a compliance control system using an estimated floor reaction force with disturbance observer.

The validity of the proposed control system is verified through some experiments.

PNEUMATIC QUADRUPED ROBOT

Fig.1(a) show overview of the developed quadruped robot and schematic diagram of a leg, respectively. A leg has 3 D.O.F. , which are driven by pneumatic cylinders. A base plate is 1114[mm] in length and 773[mm] in width and the total weight of the robot is about 209[kg]. The position and orientation of the base plate and the position of each leg is described with coordinate frame Σ_{body} placed at the center of base plate and hand coordinate is defined as $h = [x, y, z]$. As shown in (a), the legs are placed being symmetry with respect to the front and the rear considering the same motion property for the both direction.

Fig.1(b) shows detail mechanical structure of a leg. A leg is connected to the base plate with a 2 D.O.F. gimbal mechanism (joint-1,joint-2). At joint-1,a rotational shaft is inserted and mechanically fixed and the shaft is held by a base plate with bearings. Therefore a cylinder-1(80[mm] in diameter)drives a whole leg around joint-1 by rotating the shaft. The head side of a cylinder-2(80[mm] in diameter) is also mechanically attached to a shaft with a bearing and it gives a rotational motion around joint-2 axis. A cylinder-3(100[mm] in diameter) is mounted on the Leg1 to yield rotation motion around joint-3. An ankle joint has also 2 D.O.F gimbal mechanism and they are equipped with passive dampers.

Here we introduce a joint coordinate θ=$[\theta_1, \theta_2, \theta_3]^T$ corresponding to the rotational angle around joint-1,2,3 and they are measured by rotary encoders. Figure(c) shows the moving area of forward right side leg in $y-z$ plane, where an origin point of h is set at the joint-1,2 for simplicity. It can be seen that about 700 mm stroke for y direction(forward direction) is obtained at the standard height shown by a dashed line in the figure.

Fig.2 shows driving circuit for one pneumatic cylinder. Pressure in both chambers are measured by pressure sensors and each chambers regulated by pressure control valve, respectively. These 2 control valves are controlled with one control signal to behave as a SISO system. A joint angle is detected by a rotary encoder. The control system must be implemented as a real-time control system. Real-time control system is composed based on Linux (kernel 2.6) real-time extension (RTAI 3.8). An operator control the robot by remote login (SSH) function via wireless LAN.

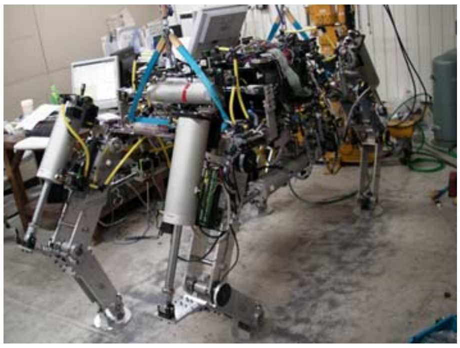

(a) side view

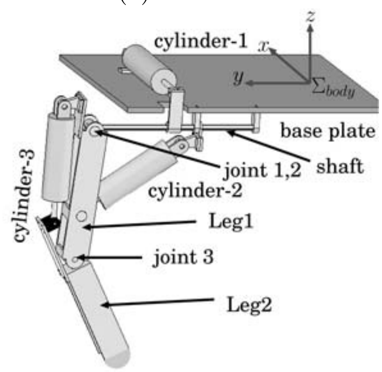

(b) joint of leg

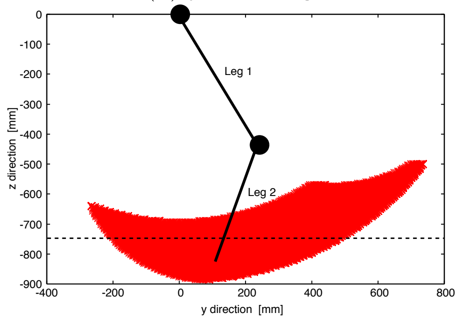

(c) moving area

Fig. 1: Picture of Robot

CONTROL SYSTEM

Kinematics

Fig.3 shows a schematic diagram of forward right side leg. Owing to the mechanical simplicity of a leg, the kinematics can be easily solved.

$$\begin{cases} \theta_1 = \sin^{-1}\frac{x}{L} \\ \theta_2 = \cos^{-1}\frac{L_1^2+L^2-L_2^2}{2L_1L} + \sin^{-1}\frac{y}{L} \\ \theta_3 = \cos^{-1}(-\frac{L_1^2+L_2^2-L^2}{2L_1L_2}) \end{cases} \tag{1}$$

, whereL_1,$L_2$are length of leg-1 and leg-2, respectively and $L = \sqrt{x^2+y^2+z^2}$ is distance between a center point of universal joint(joint-1,joint-2) and a tip of leg-2.

Compliance control system

In generally, a position control is composed on legs for this kind of walking robot and mostly 1-type controller(one integrator in an open-loop control system)

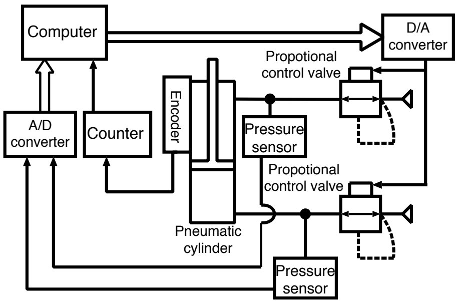

Fig. 2: Pneumatic driving circuit

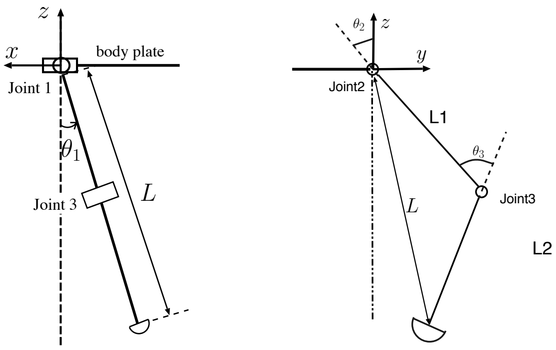

(a) Front view

(b) Side view

Fig. 3: Kinematics

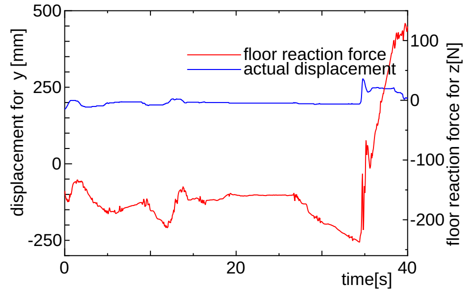

Fig. 4: Floor reaction force

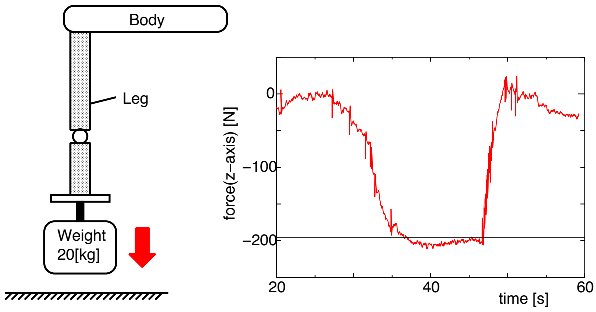

(a) experimental setup

(b) force estimation

Fig. 5: Image of experiment

is employed. In this case, if a deviation between the reference position and current one is occurred under the state of contact with ground, the position controller, of course, works to eliminate the deviation by integral effect. Consequently, an inner force affects each other among legs, which may lead the robot be unstable. Fig.4 shows this phenomenon. A red line shows a estimated floor reaction force (described later) for y direction and blue one shows an actual position of leg tip for y. We can see that from 26s, floor reaction force gradualy increase and at 35s a leg suddenly slip on the ground when floor reaction force overtakes the maximum friction force. There fore we introduce compliance control on legs control system.

In order to implement a compliance control, a force/moment sensor is necessary to mount at the ankle joint of a leg, however, it is not practical from a view of a cost and maintenance for the field working robots. In a pneumatic actuator, the control variable(stroke of piston) is easily affected by the external force which enables us to estimate the external force based on the pressure. Therefore we propose compliance control system using not a force/moment sensor but a estimation function of disturbance observer.

Fig.7 shows the proposed compliance control system, where τ is a estimated external torque and and it is fed back as floor reaction force F through a transpose of Jacobi matrix J^T from a principle of virtual work. K^{-1}=diag$\{K_x^{-1}, K_y^{-1}, K_z^{-1}\}$ is a stiffness matrix. $F_g(s) = P_1(s)A_1 - P_2(s)A_2, r, J, D$ are a generated force of cylinder, moment arm, inertial moment, damping coefficient, respectively. First, a disturbance observer is applied to the mechanical transfer part $P_s(s)$. If the nominal model $P_n(s)$ is the same with $P_k(s)$, then the estimated disturbance $D(s)$ contains external force and external torque τ is derived as $rD(s)$. A doubled line box in the figure is generation force control system and it is concretely described in the figure(b). A disturbance observer is also applied to this control system, which works the closed loop transfer function from the reference F_r to F_g to match the nominal model $P_{pn}(s)$ and reduce the influence of piston velocity which works as a disturbance.

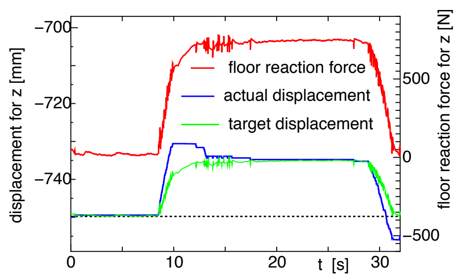

Fig. 6: Compliance control property

Fig.5 shows the property of force estimation using disturbance observer. In the state the robot is sus-

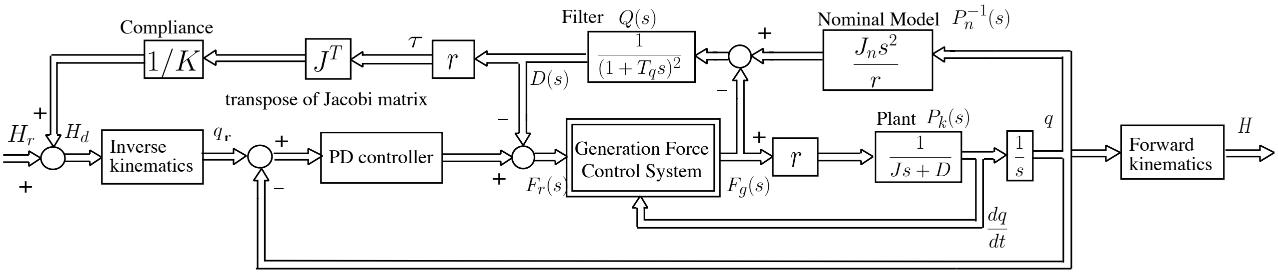

(a) Joint servo system

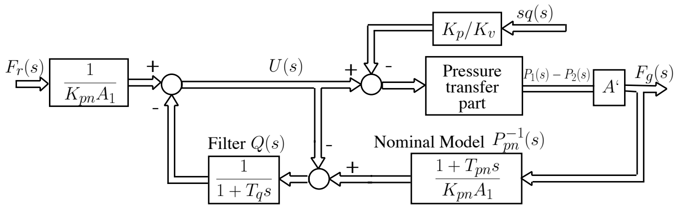

(b) Generation force control system

Fig. 7: Compliance control system

pended by a crane as shown in the figure (a), a mass of 20 kg hangs from a tip of a leg and then it is removed. Figure (b) shows the element for z direction of the estimated floor reaction force. Almost satisfactory estimating performance can be seen.

Fig.6 shows a compliance control property of a forward right side leg. From the initial state suspended by a crane, the robot is slowly lowered on a ground and stands with 4 legs for a while and then lifted up again. A red line shows a floor reaction force normal for the ground. Green line indicates a reference displacement for z direction of the leg tip and blue one shows an actual z position of leg tip. In a steady state, the blue line agrees with green one, which shows the given compliance is well realized.

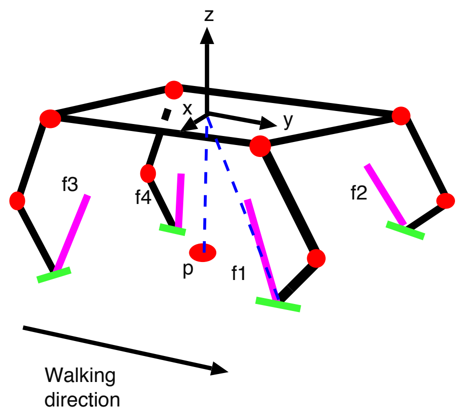

Fig. 8: Floor reaction force

ZMP

As shown in Fig.8, moment applied at point p is expressed as eq.(2), where $h_j = [h_{jx}\ h_{jy}\ h_{jz}]^T (j = 1,2,3,4)$ is position vector of leg and $f_j = [f_{jx}\ f_{jy}\ f_{jz}]^T (j = 1,2,3,4)$ is estimated floor reaction force. Zero moment point (ZMP), widely used in legged robot,

$$\tau_j = \sum_{j=1}^{4} (h_j - p) \times f_j \tag{2}$$

is calculated by setting $\tau = 0$ in eq.(2) as eq.(3).

$$\begin{cases} p_x = \sum_{j=1}^{4} h_{jx} f_{jz} / \sum_{j=1}^{4} f_{jz} \\ p_y = \sum_{j=1}^{4} h_{jy} f_{jz} / \sum_{j=1}^{4} f_{jz} \end{cases} \tag{3}$$

Estimation of body orientation

In order to carry out a locomotion, it is important to estimate the relative posture of the base plate against a ground. In a static gait, 3 legs are always contact with ground. Now we select position vectors h_1, h_2, h_3 for the contacting 3 legs. Then a unit normal vector n for the plane composed by the 3 position vectors is described as follows.

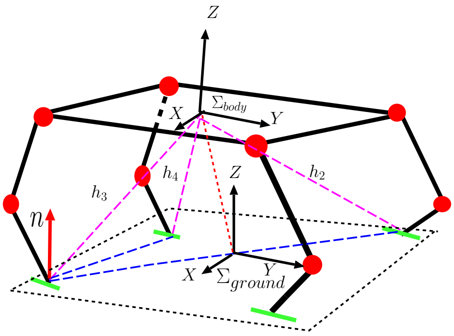

(a) orientation detection

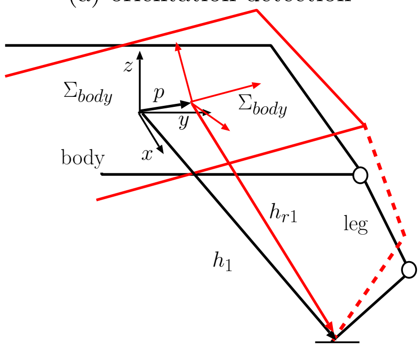

(b) orientation compensation

Fig. 9: Orientation detection and compensation

$$n = \frac{(h_2 - h_3) \times (h_4 - h_3)}{|h_2 - h_3||h_4 - h_3|} \tag{4}$$

We define the posture of base plane with roll(ϕ)-pitch(θ)-yaw(ψ) notation, then the following relation is obtained.

$$R \cdot n = [0 \;\; 0 \;\; 1]^T \tag{5}$$

,where R is a rotational matrix. Eq.(6) is calculated as follows with roll angle $\phi = 0$.

$$\begin{cases} \cos\theta n_x + \sin\theta \sin\psi n_y + \sin\theta \cos\psi n_z = 0 \\ \cos\psi n_y - \sin\psi n_z = 0 \end{cases} \tag{6}$$

Solving eq.(6), the posture angle is obtained as

$$\begin{cases} \psi = \tan^{-1} \dfrac{n_y}{n_z} \\ \\ \theta = \tan^{-1} - \dfrac{n_x}{\sin\psi n_y + \cos\psi n_z} \end{cases} \tag{7}$$

Fig.9(b) shows the compensation of the position and orientation, where red line is the reference posture and black one shows the current one. The reference position vector is described as follows.

$$h_r = R^T(h - p) \tag{8}$$

, where p is a deviation from reference position.

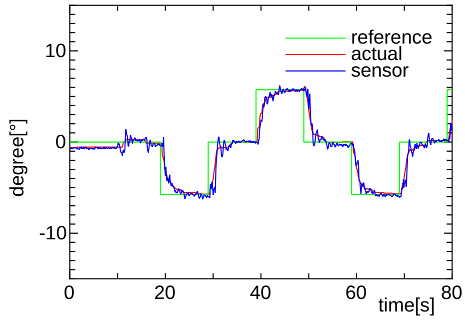

(a) around x-axis (ψ)

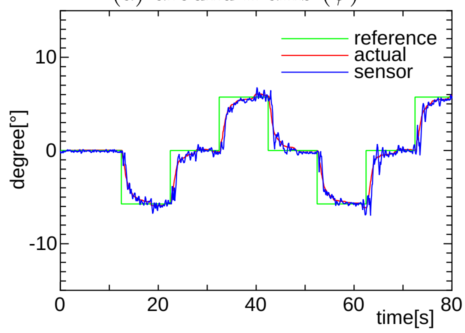

(b) around y-axis (θ)

Fig. 10: step response

EXPERIMENTAL RESULTS

Fig.10 (a), (b) show step responses around x and y axis, respectively. Owing to the detection and compensation scheme of the position and orientation of a robot shown in Fig.9, tracking error almost can not be seen in the steady state. In the current strategy, posture estimation shown in eq.(7) the detected orientation of the body is just a relative one for the ground. Therefore we introduced an acceleration sensor to detect absolute posture of the body. Combining the estimation scheme of the relative posture of the body with the acceleration sensor, we can detect an inclination of ground. The blue line in Fig.10 is the posture of the body detected by acceleration sensor. Fig.11 shows the ability to detect the inclination of ground. As shown in figure (a), (b), we made an inclination on the ground by inserting oil jack under the forelegs intentionaly. In Fig.11 (c), a red line shows y of ZMP and blue line shows x of ZMP. Green line indicates relative posture of body for the slope calculated in eq.(7) and light blue one shows the measured by sensor. We can know the inclination of ground by the value of acceleration sensor.

Static gait

We employ the intermediate crawl gait[10],[11] which is the most stable static gait as shown in Fig.12. This walking style has feature that swing phase and motion phase for changing of center of gravity is completely divided. In the situation(a), we make a body move so

(a)upward

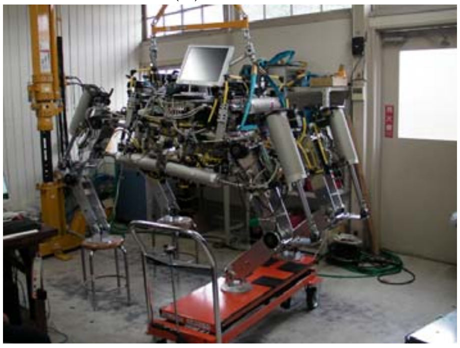

(b)downward

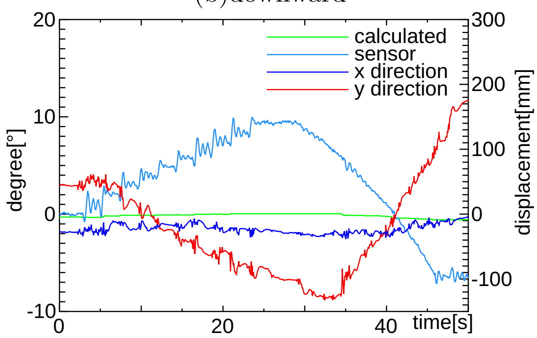

(c) around x-axis (ψ)

Fig. 11: experiment

that the center of gravity stay in the triangle composed with the supporting legs and then move the swing leg to the proper position. After then we continue the similar motion as (c),(d) and (e). Fig.13 shows the static picture of intermittent crawl gait, where (a)(b)(c)(d) indicate the scene of each leg in swing period in tern. One cycle(4 legs complete the motion) takes about 25 seconds, to travel about 40cm. Improvement of walking speed is a challenge for the future.

CONCLUSION

In this study, we developed a quadruped robot with pneumatic actuators with assumption to apply for the human cooperative tasks.

A compliance control system is composed on the leg without using force/moment sensor but with estimating the floor reaction force by introducing a disturbance

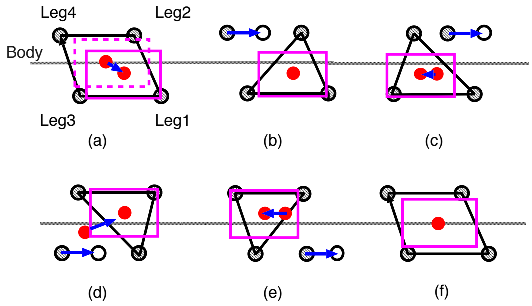

Fig. 12: Intermittent crawl gait

(a) Leg4 in swing period

(b) Leg2 in swing period

(c) Leg3 in swing period

(d) Leg1 in swing period

Fig. 13: Intermittent crawl gait

observer. If the servo system of an actuator has enough stiffness, then the position control of legs will be able to attain the static gait. But making robot hold compliance for the purpose of above mentioned application, the dynamics change must be compensated. The disturbance observer is also expected as dynamics compensator.

The improvement of gait motion through the enhancement of control performance of leg motion is under the current investigation.

REFERENCES

[1] H.Montes,S.Nabulsi,M.Armada,"Detecting Zero-Moment Point in Legged Robot",proc. of the 7th Int. Conf. CLAWAR 2004

[2] H.Kimura,Y.Fukuoka,A.H.Cohen,"Biologically inspired adaptive walking of a quadruped robot", Philosophical Transactions of The Royal Society A, 365,pp.153-170,2007

[3] S.Salmi, A.Halme,"Implementating and Testing a Reasoning-based Free Gait Algorithm in the Six-

legged walking Machine""MECANT"",Control Eng.Practice,vol.40,no.4,pp.487-492,1996

[4] J.Estremera,J.A.Cobano,P.Gonzalez de Santos,"Continuous free-crab gaits for hexapod robots on a natural terrain with forbidden zones:An application to humanitarian demining",Robotics and Autonomous System,58,pp.700-711,2010

[5] Ryuichi Hodoshima,Takahiro Doi,Yasushi Fukuda,Shigeo Hirose,Toshihito Okamoto,Junichi Mori,"Development of a Quadruped Walking Robot TITTAN XI for Steep Slope Operation", it J. of Robotics and Mechatronics,vol.19,no.1,2007

[6] John E.Bares,David S.Wettergreen,"Dante II:Technical Description,Results,and Lessons Learned",The Int.J.of Robotics Research,vol.18,no.7,pp.621-649,1999

[7] Stephan K.Chalup,Craig L.Murch,Michael J.Quinlan,"Machine Learning with AIBO Robots in the Four-Legged League of RoboCup",IEEE Trans.on System, Man, and Cybernetics,partC,vol.37,no.3,pp.297-310,2007

[8] Shigeo Hirose,Akihiko Nagakubo,Ryosei Toyama,"Machine That Can Walk and Climb on Floors,Walls and Ceilings", prroc. of Int. Conf. Advanced Robotics,vol.l,pp.753-738,1991

[9] K.Ohnishi,"Robust Motion Control by Disturbance Observer", Journal of the Robotics Society of Japan,vol.ll,no.4,pp.486-493,1993,(in Japanese)

[10] Heeseon Hwang, Youngil youm,"Steady Crawl Gait Generation Algorithm for Quadruped Robots", Advanced Robotics,vol.22,pp.1539-1558,2008

[11] Hideyuki Tsukagoshi, Shigeo Hirose,"Proposal of the Intermittent Crawl Gait and Its Generation", it Journal of the Robotics Society of Japan,vol.17,no.2,pp.301-309,1999,(in Japanese)

Proceedings of the 8th JFPS International
Symposium on Fluid Power, OKINAWA 2011
Oct. 25-28, 2011

1D3-1

MASTER-SLAVE CONTROL FOR A CONSTRUCTION ROBOT TELEOPERATION SYSTEM
(EVALUATION OF AN OPERATION SYSTEM WITH VIDEO CAMERAS AND FORCE FEEDBACK)

Lingtao HUANG*, Hidetoshi KATO**, Takuya KAWAMURA***and Hironao YAMADA***

* Mechanical and Civil Engineering Division
Gifu University
1-1 Yanagido, Gifushi, Gifu, 501-1193 Japan
** Denso Corporation Company
*** Human and Information Systems
Gifu University
1-1 Yanagido, Gifushi, Gifu, 501-1193 Japan
(E-mail: yamada@gifu-u.ac.jp)

ABSTRACT

The purpose of this study is to evaluate a construction robot master-slave teleoperation system with video cameras and force feedback based on behavioral and subjective measures. The system can provide an operator with a realistic force feeling according to the actuator condition using the velocity-driving force characteristics. The teleoperation system comprises two joysticks on the master side, and a robot arm with four degrees of freedom on the slave side. In this study, we have introduce the control method to actual tasks of conveying and piling up concrete blocks in order to evaluate the operability based on work efficiency, danger indexes, as well as evaluation of mental strain using NASA-TLX. As a result, it is verified that the control method in this system could contribute to improving safety in teleoperation work, and alleviate the operator's mental strain.

KEY WORDS

Construction Machinery, Robot, Hydraulic Actuator, Master-Slave Control, Force Feedback

NOMENCLATURE

The main nomenclature used in this paper is given below. The subscript i in expressions such as f_{prei} is a number i=1-4 corresponding to swing, fork glove, boom or arm, respectively.

F_c	:	Average force	[-]
F_t	:	Sum of excess force generated in actuator	[s]
f_{pre}	:	Threshold driving force for feed back to reaction force	[N]
f_s	:	Slave force	[N]
k_{pm}	:	Master proportional	[Nm]
k_{dm}	:	Master differential gain	[Nm/s]
k_{ps}	:	Slave proportional	[m]
k_{ds}	:	Slave differential gain	[m/s]
k_{tm}	:	Master torque gain	[m]
T	:	Master overall gain	[-]
y_m	:	Master displacement	[m]
y_{0m}	:	Standard master displacement (y_{0m}=0.06)	[m]
Y_m	:	Nondimensional quantity of y_m(=y_m/ y_{0m})	[-]
$\dot{Y}_m$	:	Nondimensional quantity of master velocity	[-]
y_s	:	Slave displacement	[m]
$\dot{y}_s$	:	Slave velocity	[m/s]

y_{0s}	:	Standard slave displacement (y_{0s}=0.3)	[m]
Y_s	:	Nondimensional quantity of y_{0s} ($= y_s / y_{0s}$)	[-]
$\dot{Y}_s$	:	Nondimensional quantity of $\dot{y}_s$	[-]
τ_r	:	Reaction force (torque) to joystick	[Nm]
τ_{0r}	:	Standard reaction torque to joystick (τ_{0r} =0.57)	[Nm]
T_r	:	Nondimensional reaction torque to joystick ($=\tau_r / \tau_{0r}$)	[-]
t_c	:	Contact time	[s]

INTRODUCTION

Remote-control robotics is an effective technique in machine work at certain locations where are considered difficult and dangerous for human to enter, such as disaster sites. In Japan, unmanned construction was first introduced on a practical level in the disaster recovery work after the eruption of Mt. Unzen Fugen Dake, and numerous examples of practical application were reported from that time. In 2001, the Ministry of Land, Infrastructure and Transport (MLIT) worked out guidelines for full-scale introduction of unmanned construction in public works projects. These trends suggest that unmanned construction will become increasingly familiar in the future [1,2]

The main trend in a teleoperation system for construction machinery currently applied in practical use is an operation method in which feedback is limited to visual information obtained by onboard cameras mounted on the construction machine. But site information gathered with this method is limited, and there have been reported that work efficiency is considerably inferior to that in direct operation [3].

In order to enable safe, high-level teleoperation work, it is important to provide site information for an operator to perceive a realistic feeling of force, or force feedback (FFB), in addition to visual information. The following is an overview of past research on the FFB function for construction machinery.

First, Takasu carried out a basic study of FFB technology with a master-slave operating system using a master that was geometrically similar to the slave. The results confirmed that it is possible to give an operator a feeling of a force generated in the slave by compensating for the self-weight and frictional force of the slave mechanism and using the force reflecting-type control method. Next, Yoshinada evaluated an operability of a master-slave operating system for handling manipulators used with heavy weights. The results confirmed that even novices can achieve the same level of operation as a skilled operator after brief trial-and-error operation when a symmetric positioning and force reflection control methods were used in combination and FFB was provided for three drive axes. However, the shortcomings of these systems included the facts that a separate master with a geometry similar to that of the slave was necessary, and FFB was given even when the device dose not touch the object.

The authors previously investigated the FFB function when performing various tasks (e.g., grasping an object, etc.) using a hydraulic power shovel (hereinafter, “construction robot”) with a master-slave system comprising two joysticks (a right-and-left pair) as the master and all drive axes (fork glove, swing, boom, arm) of the construction robot as the slave. As the first stage in those researches, we proposed control methods [4-6] for the fork glove and swing using a symmetric positioning and force reflection control methods in combination, in which a threshold value for force representation was variable by measured velocity-driving force characteristics. Because external forces caused by a self-weight of the links act on the boom and arm, a method [7] with gravitational compensation was proposed for the control method for these parts. Experiments and simulations had confirmed that realistic representation of the feeling of the task was possible in a wide range of tasks.

As a result of these studies, the effectiveness of FFB for the construction machinery is gradually becoming clear. However, this research has not reached a stage where operability can be adequately evaluated when the FFB function is applied to actual work. Thus, more detailed study is desired in the future.

Due to the high adaptability of human subjects, there are cases where operability cannot be evaluated adequately on the basis of work efficiency or work results alone [8]. In such cases, an evaluation that also includes the mental strain on an operator becomes necessary. Therefore, in this research, the control method is applied to an actual task, and its effectiveness is verified by NASA-TLX, which is a representative subjective evaluation method, in addition to work efficiency and danger indexes.

TELEOPERATION CONSTRUCION ROBOT

Figure 1 shows a schematic diagram of the experimental teleoperation/presence representation construction robot system treated in this research.

As shown in the figure, the system comprises two joysticks (Side Winder Feedback 2 manufactured by Microsoft Co., Ltd.) as the master and a construction robot (A modified version of a Hitachi LandyKID-EX5, which is a commercially-available backhoe) as the slave. The joysticks enable forward/reverse and right/ left movement. To supply an operator with a sense of grasping an object by the fork glove and the work reaction force (force sense) generated by the swing, boom, and arm in teleoperation, two DC motors are installed in each joystick. In slave system, a robot arm with four degrees of freedom is used; the hydraulic cylinders (the fork glove, swing, boom, and arm) are operated by manipulating the joysticks in four directions.

The four cylinders are operated by feedback control by proportional valves. Pressure sensors are installed on the head side and cap side of each cylinder for detection of its load pressure. These pressure signals can be used as force-sense signals

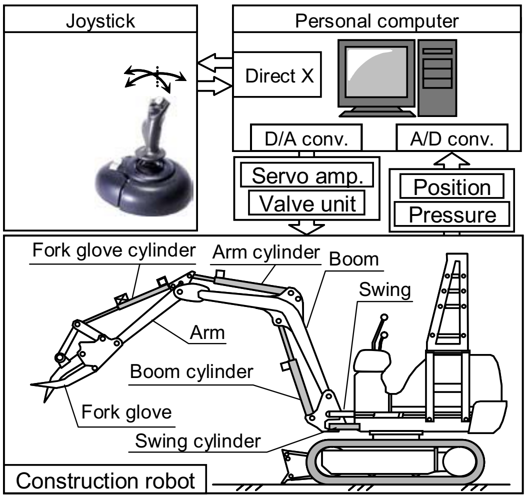

Figure 1 Schematic diagram of experimental apparatus

MASTER-SLAVE SYSTEM

A control method have been proposed for the fork glove, which enables realistic representation of a feeling of grasping with the fork glove in a wide range of grasping tasks. The features of the control method are briefly described in the following.

This control method uses a driving force threshold f_{prei} for representation of driving force, and the threshold can change continuously depending on the actuator drive condition using measured velocity-driving force characteristics ($\dot{y}_s$ - f_s characteristics). Figure 2 shows the $\dot{y}_s$ - f_s characteristics of the fork glove.

The points plotted in this figure show a relationship between velocities and driving force measured by experiment. The threshold f_{pre2} obtained by the least squares method from these results is expressed as a function of velocity, and shown by a solid lines in the figure. Considering minor variations in the measured $\dot{y}_s$ - f_s characteristics due to the oil temperature, etc., a certain degree of vertical offset is given to these lines, as seen in the figure. The functional equations for the threshold f_{pre2} of the fork glove obtained from Figure 2 are as Eq. (1).

In this control method, a reaction force (torque) to joysticks comprises items that depend on a position, velocity deviation between the master and slave, and an item ($T_2 k_{tm2} f_{s2}$), which depends on driving force. The reaction force (torque) τ_{r2} to the joysticks at this time is expressed by Eq. (2).

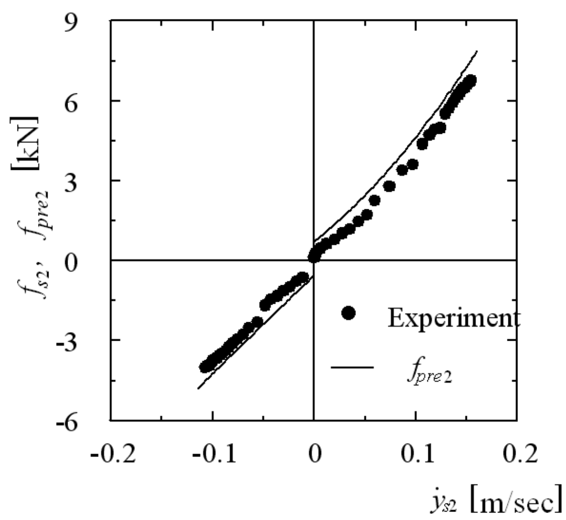

Figure 2 Characteristics of $\dot{y}_s$ - f_s

$$
\begin{cases} f_{pre2} = (49.4\dot{y}_{s2}{}^2 + 8.20\dot{y}_{s2} + 0.8)\times 10^3; (\dot{y}_{s2} \geq 0) \\ f_{pre2} = (-31.2\dot{y}_{s2}{}^2 + 11.2\dot{y}_{s2} - 0.8)\times 10^3; (\dot{y}_{s2} < 0) \end{cases} \quad (1)
$$

$$
\tau_{r2} = T_2\left\{k_{pm2}(Y_{s2} - Y_{m2}) + k_{dm2}(\dot{Y}_{s2} - \dot{Y}_{m2}) + k_{tm2} f_{s2}\right\} \quad (2)
$$

Gain T in Eq. (2) is given by the following equation:

$$
T_2 = \begin{cases} 0 & (|f_{s2}| \leq |f_{pre2}|) \\ 0 < \dfrac{f_{s2} - f_{pre2}}{f_{e\_\max} - f_{pre2}} \leq 1 & (f_{s2} > 0 \cap f_{s2} > f_{pre2}) \\ 0 < \dfrac{f_{s2} - f_{pre2}}{f_{c\_\max 2} - f_{pre2}} \leq 1 & (f_{s2} < 0 \cap f_{s2} < f_{pre2}) \end{cases} \quad (3)
$$

f_{e_max}, f_{c_max} expresses a maximum driving force of the piston in the expansion and contraction directions (f_{e_max}=11.7kN, f_{c_max}= -6.8kN). A block diagram of the control system configured from above is shown in Figure 3.

As a concrete example of a task in which the control method was applied, Figure 4(a)-(c) shows the results of an experiment in which a rubber tire is grasped. First, Figure 4(a) shows a change over time in the displacement Y_{m2}, Y_{s2} of the joystick and fork glove, respectively. As shown in the figure, in this task, grasping of the tire begins from point A, and then the grasping force is strengthened in steps at intervals of approximately 4 seconds. As a result, a condition in which the tire is completely crushed is reached at point B. Next; Figure 4(b) shows the change in the driving force f_{s2} of the fork glove. Driving force f_{s2} increases in steps accompanying the tire grasping operation, and reaches a large value at point B, where the tire is completely crushed.

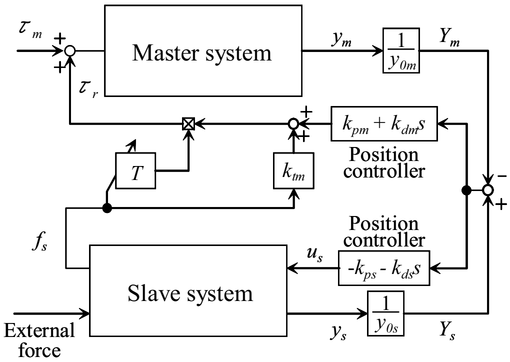

Figure 3 Block diagram of this method control

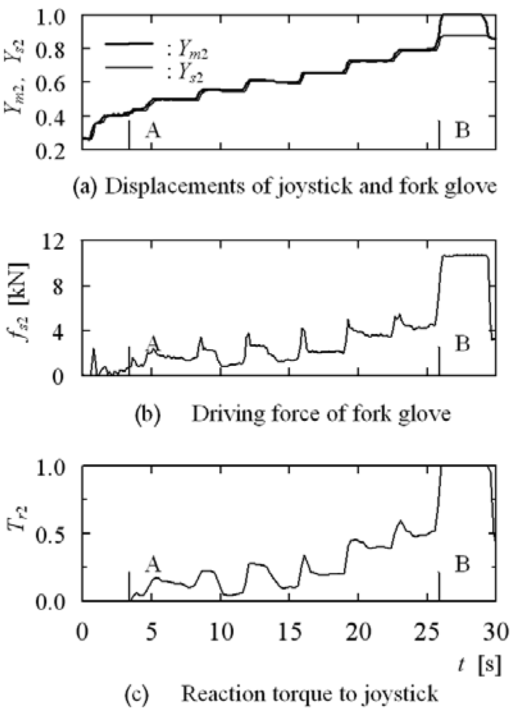

Figure 4 Grasping a tire step by step

Figure 4(c) shows the change in the nondimensional reaction torque to the joystick T_{r2}. According to this figure, between points A and B, T_{r2} increases in steps corresponding to the grasping operation, and after point B, where the tire is completely crushed, a large reaction force occurs instantaneously. These results show that the feeling of this task can be transmitted satisfactorily to the operator, even in a grasping task involving a comparatively soft object.

Next, extension of the control method to all drive axes was attempted, including the boom and arm. However, because cylinder driving force was measured in this research using pressure sensors mounted on each cylinder, the measured driving force included load forces caused by the self-weight of the respective links (hereinafter, simply called “load force”), particularly in the boom and arm. Accordingly, in application of the control method, it was necessary and indispensable to compensate for load force in the respective measured driving forces. Therefore, an equation of motion for the robot arm was derived by the Lagrange method, and a relational equation was calculated for joint angle, joint torque, and load forces due to self-weight of the respective links when displacements of the boom and arm were given. Application of the control method was possible by estimating the external forces due to self-weight from these results, and compensating for these forces in the measured driving force. As a result, the feeling of the task could be communicated to the operator satisfactorily for the boom and arm, with the fork glove and swing.

EXPERIMENTAL EVALUATION OF OPERABILITY

Up to this point, this research has examined the force representation function when performing various tasks for all drive axes of the construction robot. Therefore, an operability evaluation experiment is conducted to verify the effectiveness of the FFB function in an actual task.

EXPERIMENTAL METHOD

The operability evaluation experiment is conducted with 11 subjects with and without FFB. Figure 5 shows the composition of the system used in the operability evaluation experiment.

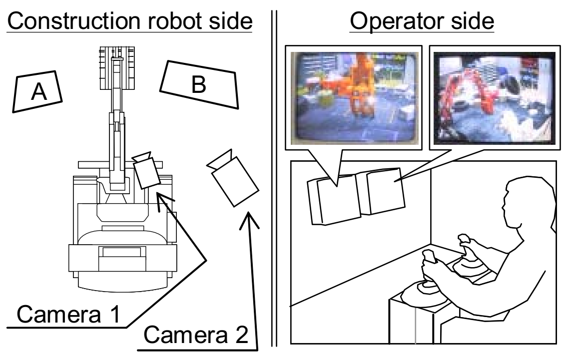

Figure 5 Composition of system used in operability evaluation experiment

A “block stacking task” which could be reproduced in the experimental facilities used by the authors is adapted, referring to the volcanic mudflow countermeasures work on Miyakejima, which is performed by remote operation. This task involves conveying multiple blocks arranged at point A in the figure to point B, where the blocks are to be arranged. The blocks are two sizes, comprising 4 large blocks (approx. 200mm×260mm×100mm) and 2 small blocks (approx. 200mm×130mm×100mm). The subjects select 4 large blocks and 1 small block from among these, move them to point B, and arrange them by stacking in two levels. The remaining small block plays a role of an unnecessary block, which the subjects must avoid while performing the task. Accordingly, the task includes not simply a block stacking task, but also a sorting task. Five block arrangement patterns at point A at the start of the task are prepared in advance in order to minimize the effect of familiarity with the conditions. Considering human fatigue, the operability evaluation experiment is divided over a 2-day period.

As shown in the figure, 2 CCD cameras are installed on the construction robot side to provide visual information to the operator. The first camera which is mounted on the boom attachment part of the construction robot, photographs the tip of the fork glove at all time, while the second one which is located at an angle to the right of the robot, photographs the work site as a whole. To simulate teleoperation work, operators perform operation from a different room from the laboratory where the robot is located.

EVALUATION METHOD

In this research, the evaluation of operability with/without FFB is performed by (1) work efficiency, (2) danger indexes, and (3) a mental strain evaluation (NASA-TLX). The subjects performed the task 5 times with FFB and 5 times without FFB. Details of the respective evaluation methods are described in the following.

(1) Work efficiency

The number of blocks conveyed and arranged at point B per unit of time (Obj./min) is used as an index of work efficiency.

(2) Danger indexes

When a construction robot continues work in an unstable condition, there is a danger of accident due to overturning and the like. This condition occurs in cases where the fork glove forcibly presses the ground or a different drive axis is operated while in a pressing condition. In particular, these conditions tend to occur easily in teleoperation using only visual information. The danger indexes used in this research are contact time t_c (hereinafter, "contact time") in a dangerous condition, e.g., when the fork glove is forcibly pressing the ground, and average force F_c (hereinafter, "average force") generated by the boom, arm, and swing of the construction robot while in this condition. Figure 6 shows the method of calculating the danger indexes.

In this figure, the horizontal axis shows time, and the vertical axis shows the excess force F_t generated by boom, arm, and swing. Based on the action-reaction relationship, the excess force generated by the piston during contact with the ground surface, etc. can be treated as equivalent to an external force acting on the piston. Therefore, the excess forces generated in the each cylinder can be expressed non-dimensionally by introducing the aforementioned gain T, and the generated force F_t is obtained as the sum of these individual forces. A threshold is set for the generated force F_t obtained by the above, as shown by a broken line in the figure, and conditions that exceed this threshold are regarded as unstable conditions. According to this figure, the generated force F_t exceeds the set threshold in all sections except t_1, therefore, contact time t_c can be obtained as the total of sections t_2-t_4. The average force F_c is then obtained by dividing the integral value of the generated force F_t in the given section by the contact time t_c.

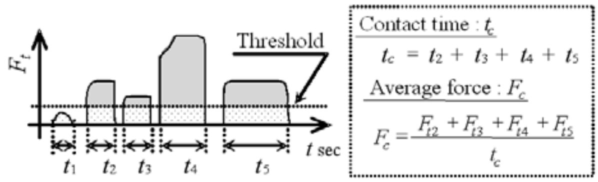

Figure 6 Danger indexes

(3) Mental strain evaluation (NASA-TLX)

The best-known methods of metal strain evaluation are SWAT (Subjective Workload Assessment Technique) and NASA-TLX (NASA Task Load Index). In this research, NASA-TLX is used as the mental strain evaluation method as there are numerous examples of application and introduction is relatively easy.

NASA-TLX was developed by NASA (National Aeronautics and Space Administration) to evaluate workloads, and it comprises 6 criteria, mental demand, physical demand, temporal demand, own performance, effort, and frustration level. The flow of mental strain evaluation by NASA-TLX is shown in the following.

First, the importance of the 6 NASA-TLX criteria is judged by a pair comparison test. This test is carried out for all criteria in order to determine which items appear more important when performing teleoperation. Because the results of the pair comparison obtained here have a large influence on the results of the subsequent evaluation of workload, the pair comparison is performed twice to minimize this problem. At this time, the subjects make comparative judgments referring to the explanations of the criteria in Table 1. (The Japanese explanations were prepared referring to a translation of the English version of NASA-TLX by Haga et al [9]. A slightly modified version was used here, as required by the evaluation of this system).

Next, the experiment described in the preceding section is performed 5 times. After completion of the experiment, the subjects assign evaluation scores from 0 to 100 to the 6 criteria. The mean weighted workload (WWL) score, which is obtained as a weighted average of the scores given to the 6 criteria and the weights of the criteria obtained in the aforementioned pair comparison test, is used as the result of evaluation of work load by the NASA-TLX technique. Here, smaller values of the evaluation scores given and the WWL

Table 1 Explanations of NASA-TLX criteria

Criterion	Explanation
Mental demand (MD)	· Difficulty of sensory grasp of site information and construction machine condition. · Requires greater than necessary intellectual activity (thought, decision, etc.). · Difficulty of the given task.
Physical demand (PD)	· Requires physical activity (control, movement, etc.). · Requires rapid work.
Temporal demand (PD)	· Time restrictions on the given task.
Own performance (OP)	· Requires accurate achievement of the given task.
Effort (EF)	· Requires more than necessary effort to accomplish the task. · Task requires hard physical and mental effort
Frustration level (FR)	· Feel frustration (toward operation) during work. · Feel dissatisfaction during work.

score indicates lower loads.

EXPERIMENTAL RESULTS

The block stacking task described above was performed by 11 subjects. The results for work efficiency, the danger indexes, and evaluation by NASA-TLX are described below.

(1) Work efficiency

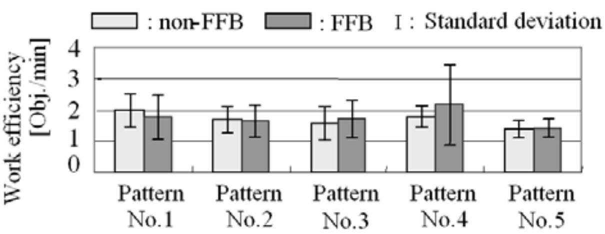

Figure 7 Work efficiency

Figure 7 shows the average values and standard deviations for the 5 block stacking patterns as work efficiency results for all subjects. In this figure, FFB and non-FFB mean the cases with force feedback and without FFB, respectively. The horizontal axis shows the block stacking patterns, and the vertical axis shows work efficiency. Larger values on the vertical axis mean higher work efficiency. According to this figure, there is no difference in work efficiency without and without FFB. Thus, no meaningful difference depending on FFB is found.

(2) Danger indexes

Figure 8 shows the average values and standard deviations for the 5 block stacking patterns as danger index results for all subjects.

As in Figure 8, the horizontal axis shows the block stacking patterns. Here, the left vertical axis shows contact time t_c when the construction robot was in an unstable condition, and the right one shows the average force F_c in the actuators during t_c. Smaller values of t_c and F_c mean work is being performed in a safe condition. According to the figure, the values of t_c and F_c decrease with FFB in all patterns, in particular, contact time t_c is approximately half that without FFB. This is considered because, without FFB, the operator must judge the condition of the construction robot solely by images from the cameras, whereas with FFB, the condition of the robot can be grasped directly as a feeling of force. This result confirmed that subjects can avoid such situations in which the construction robot falls into a dangerous operating condition, such as contact between the fork glove tip and the ground or object being handled, when FFB is provided.

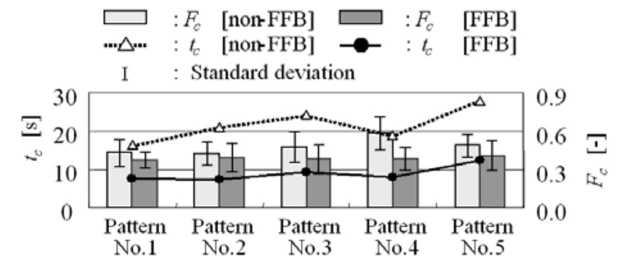

Figure 8 Danger indexes

(3) NASA-TLX

Figure 9 shows the NASA-TLX results as an evaluation of mental strain. Because NASA-TLX is a subjective evaluation method, judgment standards and evaluation scores differ depending on the subject. Therefore, the figure presented here shows a typical example rather average value for all subjects. In the figure, the black circles (●) and triangles (Δ) show the scores for the criteria with and without FFB, respectively. According to the figure, the scores for most individual items and WWL, which represents the total score, are both smaller with FFB. Therefore it can be understood that the subject's mental strain is alleviated. Furthermore, the trend for all subjects revealed that FFB reduced mental strain associated with the criteria of mental demand (MD), effort (EF), frustration (FD), and own performance (OP). In particular, when new operation systems are evaluated, there are many cases in which only effort (EF) is considered as an evaluation index, and reduction of effort is equated with reduction of the workload as a whole. Here, however, it was found that the score for physical demand (PD) tends to increase slightly with FFB. The above results confirmed that FFB makes it possible to grasp the condition of the construction robot directly, which is difficult with only visual information, and this reduces mental strain

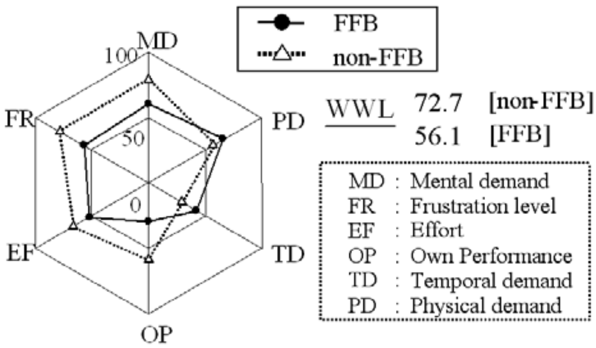

Figure 9 NASA-TLX

.

CONCLUSION

The purpose of this research was to provide a realistic sense of work when using a construction robot by providing force feedback (FFB) to an operator. The actual object of the research was a teleoperation system of a hydraulic power shovel. In previous work, the authors proposed a method of expanding the FFB function to all drive axes of a construction robot and verified the effectiveness of the control method in various types of tasks. However, this research did not reach the stage of evaluation of effectiveness when the FFB function was applied to actual work. Therefore, in the present research, the FFB function was applied to an actual task, and the effectiveness of the control method was evaluated by NASA-TLX, which was a representative subjective evaluation method, in addition to work efficiency and danger indexes. The results are summarized as follows:

(1) Work efficiency is evaluated by the number of blocks conveyed per minute. No meaningful difference related to FFB is found. This may be attributable to the comparatively simple nature of the task in this experiment.

(2) The danger indexes used in evaluations are contact time t_c when the construction robot is in an unstable condition and average force during this time, F_c. Both contact time t_c and average force F_c are reduced by providing FFB. This means that it is possible to avoid dangerous conditions because the work condition of the construction robot can be grasped directly by the joystick. This confirmed that the safety of work involving teleoperation could be improved by providing FFB.

(3) In the evaluation of mental strain, a subjective evaluation by NASA-TLX was used. As a general trend, it was found that FFB is associated with lower scores for mental demand, effort, frustration, own performance, and the total score, WWL (weighted workload), while conversely, the score for physical demand increases. These results confirmed that, although physical demand tends to increase slightly with FFB, the mental strain on operators can be reduced. This is attributed to the fact FFB makes it is possible to grasp the condition of the construction robot, which had been difficult when feedback was limited to visual operation.

We applied the control method to carry out a block stacking task. As a result of experiment, the effectiveness of the control method was verified by NASA-TLX, in addition to work efficiency and danger indexes.

REFERENCES

1. Muramatsu, T., Construction Using Information Technology and a future trend Vol.1, Construction Machinery, 2002, Vol.38, No.1, pp.8-19.
2. What's new about Movement of the River Bureau, PORTAL, foundation river information center, 2001, No.11.
3. Kanno, S., Okada, T., Kitahara, S., Unmanned construction technology by remote control, The mechanization of construction, 1994, No.8, pp.17-20.
4. Yamada, H., Takeichi, K., Muto, T., Master-Slave Control for Tele-Operation Construction Robot System, Society of mechanical Engineers, Series C, 2000, Vol.66, No.651, pp3664-3671.
5. Kato, H., Yamada, H., Muto, T., Master-Slave Control for a Tele-Operation System of Construction Robot, Proceeding of the 5th JFPS International Symposium on Fluid Power, 2002, Vol.2, pp.513-518.
6. Kato, H., Yamada, H., Muto, T., Master-Slave Control for a Tele-Operation System of Construction Robot, Fluid Power System Society, 2003, Vol.34, No.2, pp.27-33.
7. Kato, H., Yamada, H., Muto, T., Master-Slave Control for Tele-Operation System for a Construction Robot (2nd Report: Expansion of Force Feedback to Articulated Arm by Gravity Compensation), Fluid Power System Society, 2003, Vol.34, No.4, pp.85-91.
8. Ebe, K., Okuwa, M., Inagaki, H., Evaluation of Driver's Mental Workload Due to Visual and Auditory Cognition, R&D Review of Toyota CRDL, 1999, Vol.34, No.3, pp55-62.
9. Haga, S., Theory and Measurement of Mental Workload, Japan Publication Service, 2001, pp.39-46

Proceedings of the 8th JFPS International
Symposium on Fluid Power, OKINAWA 2011
Oct. 25-28, 2011

1D3-2

RESEARCH ON HARDWARE-IN-THE-LOOP SIMULATION SYSTEM OF HYDRAULIC EXCAVATORS

Qiang Feng*, Qingfeng Wang*, Wen Gong*

*The State Key Laboratory of Fluid Power Transmission and Control,
Zhejiang University, Hangzhou, China
(E-mail: qiangf1987@163.com)

ABSTRACT

Hydraulic excavators are widely used around the world and control strategies play an important role in improving the performance of excavators, reliability, energy consumption and exhaust. A hardware-in-the-loop (HIL) simulation system of the hydraulic excavator is established, which can provide high performance in simulation environment, improvement in efficiency and safety, and lower cost. The HIL simulation system contains several parts, e.g., 3D real-time display platform, model of the hydraulic excavator and real physical components. With the hydraulic excavator HIL simulation system, some experiments have been done. Also some applying plans with the HIL simulation system are proposed.

KEY WORDS:

Hydraulic excavator, Hardware-in-the-loop simulation, Real-time model, Three-dimensional display, dSPACE

INTRODUCTION

Earthmoving machines are widely used all over the world and excavators are one of the most important parts in the heavy duty machine's field[1]. So hydraulic excavators have been paid much attention. As the rapid development of technologies and the requirements of consumers and environment, manufacturers of construction machinery are more than ever aware of the importance of improving the quality of the product, reducing cost and shortening the period of study and develop new products. Traditional process of developing new construction machinery is a serial of design processes, which contain theory research, engineering design, sample machinery manufacture and debugging, and so on. These process consume a lot of money, human power and time. The technology of hardware-in-the-loop simulation has introduced a new method to design new construction machinery in a parallel process. Also, the proposed technology can provide a reliable environment for designing and testing a new product, which makes several processes, e.g., the manufacturing of mechanical structures, the testing of hydraulic and electric systems and the debugging of control algorithms to be carried out at the same time. Hence, it is beneficial to shorten the period of design, improve the quality and reliability, and reduce the cost and risk.

1. The configuration of the HILS platform

The HIL simulation system is a real-time simulation system, which contains some real physical parts and virtual simulation models[2]. It can be seen from **Fig. 1** that the HIL simulation platform of the hydraulic excavator is made up of four parts: dSPACE real-time simulation system[3], multifunctional physical experiment system, three-dimensional (the "3D") real-time display unit and model of the hydraulic excavator[4]. Part A is the dSPACE real-time system, which plays an important role in the whole simulation system. It is installed in the host computer and exchanges data with the host computer through ISA bus. While changing the simulation model into real-time codes and downloading them into dSPACE system, the real-time system receives signals from handles or controllers and the dSPACE system begins to calculate the model. Part B is the multifunctional physical experiment system. It contains power system, sensors, hydraulic control unit and so on. Part C is the 3D real-time display unit[5], which is used to display the real-time motion state of the virtual hydraulic excavator actually and intuitively to make the human-machine environment better. Part D is the real-time model of the hydraulic excavator. It consists of power system model, hydraulic system model, mechanical system model and load model of the hydraulic excavator.

As shown in Fig. 1, when the HIL simulation system is used to simulate the working condition of the hydraulic excavator[6], the signal of control sticks are delivered to dSAPCE to control proportional directional valves of physical system and directional control valves of the excavator model. At the same time, the signal of pressure sensor of the physical system is imported to dSPACE system. Then it can be achieved that the data transmits between the physical system and the model.

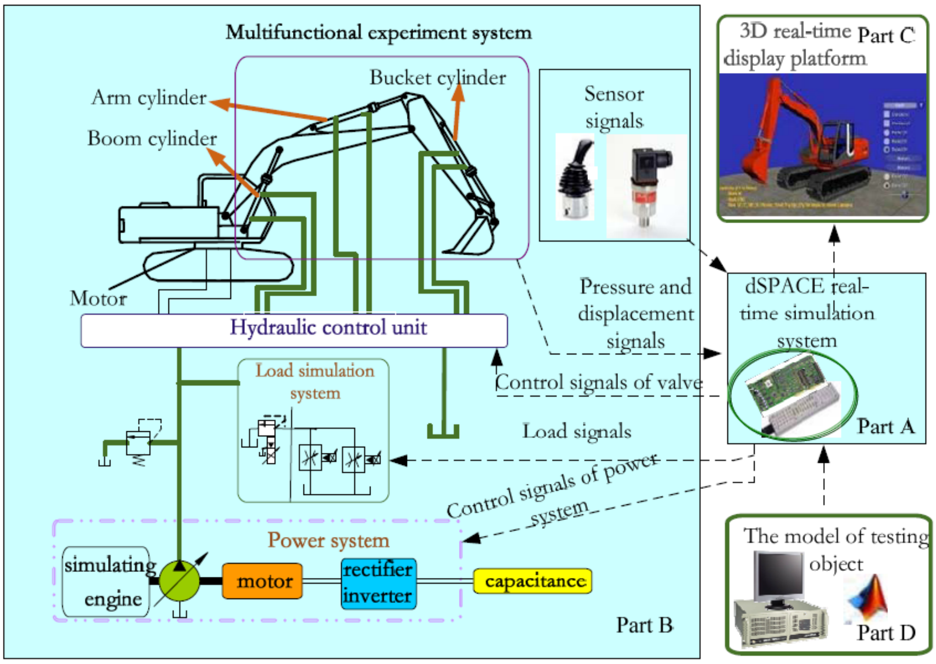

Fig. 1 The configuration of the HIL simulation platform

2. The three-dimensional real-time animation of the hydraulic excavator

A 3D real-time animation software of the hydraulic excavator has been designed to display the real-time motion state of the virtual hydraulic excavator. The software displays three advantages: (1) It can be used to simulate the motion process of hydraulic excavator. (2) It can improve the simulation accuracy and intuitiveness. (3) It can make the human-machine environment better[7].

As shown in Fig. 2, there are four steps to develop the 3D real-time animation software. Firstly, the geometric models of the hydraulic excavator components, which are made up of base, rotation body, boom and boom cylinder, arm and arm cylinder, bucket and bucket cylinder and so on, are built with 3DS MAX software. Secondly, the file type of these geometric models is changed into .X. With the particular file type, the model files can be identified with DirectX software. DirectX SDK is a set of APIs which provides a set of multimedia development tools for Windows system applications and hardware associated itself with strong three-dimensional graphics display ability. So the 3D real-time animation software of hydraulic excavator is programmed with VC++ and DirectX. At last, the motion state data of the hydraulic excavator model is transmitted from dSPACE system to the 3D real-time animation software by serial port.

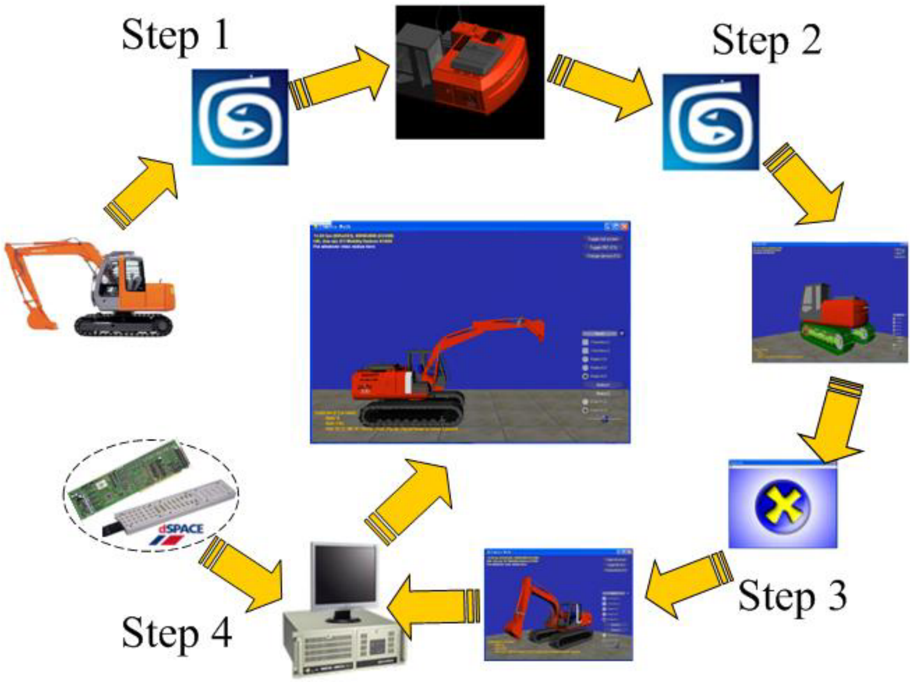

Fig.2 Steps of developing the 3D animation software

Fig. 3 The HIL simulation system of the hydraulic excavator

3. The experiment study with the HIL simulation system

Fig. 3 shows the HIL simulation system of the hydraulic excavator. The left part of **Fig.3** is the control platform and researchers can control the simulation process through the control sticks or the Controldesk software of dSPACE. The right part is the hydraulic simulator system, which contains power system, control units and so on.

In general, the HIL simulation system has two characteristics, which are real-time and accuracy. The real-time performance depends on the hardware as well as the software. For example, the calculating speed of controller and communication speed can affect the real-time performance of the whole system. In order to guarantee the real-time performance, the excavator model is built with MATLAB carefully and the simulation step is chosen appropriately. The performance of accuracy mainly depends on the accuracy of model. Besides, with some real physical components in the HIL simulation system, so it’s more accurate than off-line.

In order to test the real-time and accuracy performance of the HIL simulation system, an experiment is designed: The sticks are manipulated to control the proportional directional valves of real physical system and the directional valves of the hydraulic excavator model at the same time; then signals of sensors are acquired and transmitted to dSPACE to compare with the simulation values calculating from the excavator model. The result is shown in **Fig. 4~6**.

Fig. 4 expresses the boom cylinder displacement of the realistic system and the simulation model. It illustrates that the boom cylinder is stretching from 10s to 30s while the cylinder is retracting from about 47s to 72s. The two curves of the HIL simulation and experiment are nearly the same, which indicates that the HIL simulation system is accurate enough and in real-time. Similarly, the cylinder speed curves in **Fig. 5** support the conclusion.

Fig. 6 shows the pressure of two cylinder chambers. Comparing these curves, the HIL simulation results fit with the experiment curves most of time. It proves the accuracy of models and real-time performance of the HIL simulation system again.

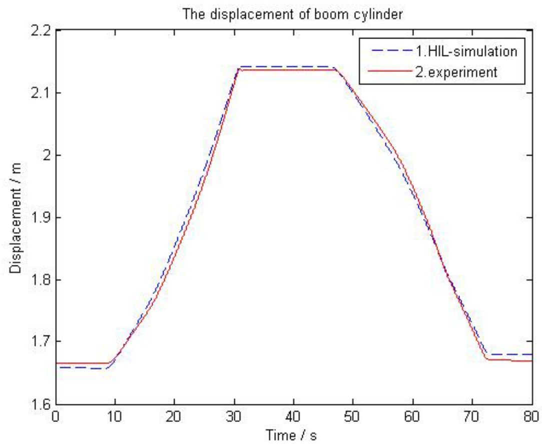

Fig. 4 The boom cylinder displacement of experiment and HIL simulation

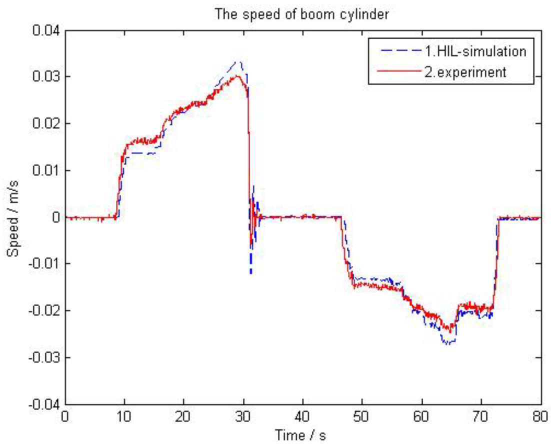

Fig. 5 The boom cylinder speed of experiment and HIL simulation

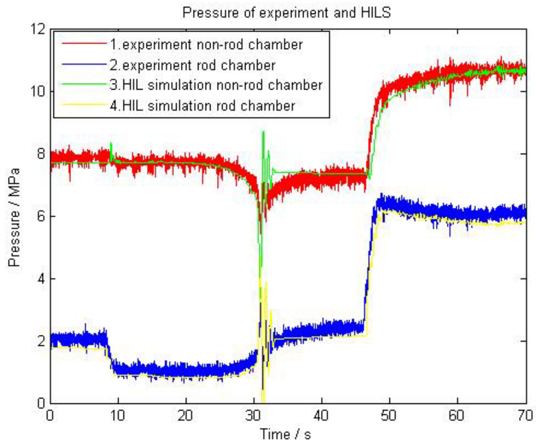

Fig. 6 The pressure of rod chamber and non-rod chamber of the boom cylinder

4. The applications of the HIL simulation system

In general, the HIL simulation system is intended for use in four applicable situations. First, the HIL simulation can be used to test the accuracy of models; second, it is suitable for debugging the subsystem, especially the controller, before the real physical experiment; third, it is available when some parts of the system are too complex to build these models[8]; fourth, usually it is used to imitate some components, the costs of which are too high. Then in our hydraulic excavator HIL simulation system, the four applications are carried out.

4.1 The application of testing model accuracy

As **Part 3** described before, it is an application of testing the model accuracy. The sticks are manipulated to control the real physical system and the hydraulic excavator model at the same time; then signals of real sensors are acquired and transmitted to dSPACE to compare with the simulation values calculating from the excavator model. From the comparing results, it is easy to judge whether the models are accurate.

4.2 The application of debugging controller

The controller and control strategies of the hydraulic excavator play an important role in reducing the fuel consumption and improving the performance of manipulation. Then the debugging of control strategies and controller is important[9]. Usually the controller is connected with control object—the real excavator to test its performance directly. But this traditional method has some disadvantages: Firstly, it’s maybe dangerous to debug the machine when the control strategies have not been proved whether they are true. Then, it’s needed to run the excavator in the process of debugging, which will consume a lot of energy. At last, it costs a lot of time to debug the controller.

These three disadvantages can be compensated with HIL simulation system. When our HIL simulation system and real-time model of the hydraulic excavator have been established, it's just needed to connect the controller with the dSPACE and control the real-time model to debug the controller. it is convenient and beneficial to shorten the design period, improve quality and reliability and reduce the cost and risk.

4.3 The application of improve simulation accuracy

Hydraulic systems are strong nonlinear systems and hard to establish their model. Besides, the excavator hydraulic system is too complex to build the accurate model. So in the HIL simulation system, a real hydraulic system is built in instead of hydraulic model. Then the whole HIL simulation system runs with real-time model and real hydraulic system, which increases the simulation accuracy.

4.4 The application of diesel engine imitation

Usually some subsystems cost high and have some other weak points. Then components with similar function are chosen to instead of the subsystem in experiment rig. With the difference of performance between subsystems and their substitutes, the experiment rig can't imitate the real system accurately and completely. Hence, HIL simulation system can solve this problem. **Fig. 7** illustrates the function and structure of HIL simulation system. The upper block diagram is the real subsystem and the input is x while output is y. Actually our imitation item with the substitute is that the substitute output is y when input is x like the real system. As the under block diagram shows, a model of real system has established and its output y is the input of substitute closed cycle. Then the substitute output y_i is very similar with y.

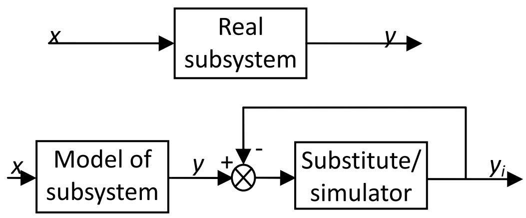

Fig.7 The simulator based on HIL simulation system

Take our HIL simulation system as an example. Usually the diesel engine is the power system of hydraulic excavator. But its price is too high and the noise is too loud. So an electric motor is used to imitate the diesel engine in the hydraulic excavator HIL simulation system. The structure is showed in the Fig. 8. The load curve is imported to the dSPACE system to control the pressure and flow rate of the system. Then the torque feed back to the diesel model and the rotational speed is imported to control the electric motor .Then the electric motor can simulate the diesel work condition.

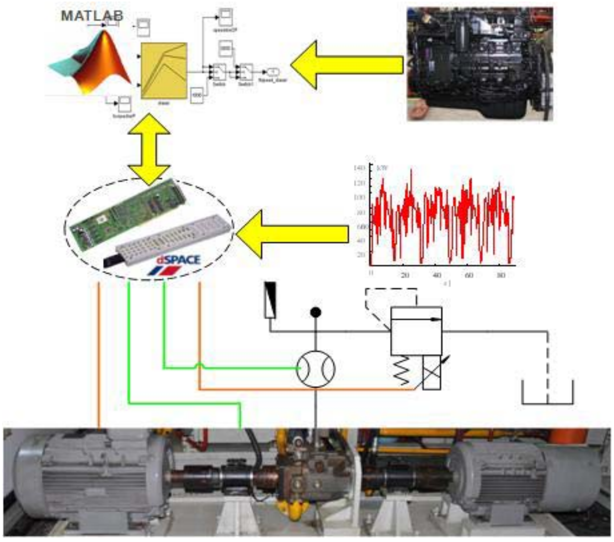

Fig. 8 The configuration of diesel engine simulation system

5. Conclusions

Hydraulic excavators are widely used around the world and control strategies play the important role on improving excavators' performance, reliability, energy consumption and exhaust. A hardware-in-the-loop(HIL) simulation system of the hydraulic excavator is established, which can provide high performance simulation environment, improve efficiency and safety and reduce cost. The HIL simulation system contains several parts, like 3D real-time display platform, model of the hydraulic excavator and real physical components. With the hydraulic excavator HIL simulation system, the experiment is done to prove the accuracy and the real-time performance. At last, some application plans with the HIL simulation system are proposed.

Reference:

[1] Liu Jian-min. Overview of Key Technology of Hydraulic Excavator. Technology & Management For Construction Machinery. 2001, (12):26~28

[2] Hughes K, Jiang XC. Using Discrete Event Simulation to Model Excavator Operator Performance. Human factors and ergonomics in manufacturing& service industries. 20(5)(2010): pages 408-423.

[3] dSAPCE Real-Time Interface Implementation Guide. dSAPCE Gmbh, 2004

[4] Imanishi, Etsujiro, Nanjo, Takao, Hiroka, Eiko. Dynamic simulation of flexible multibody

system with the hydraulic drive . Nippon KikaiGkakai RonbunshuC，2003，69(9)：2336~2343

[5] DiMaio SP，Salcudean SE，Reboulet C，et al．A virtual excavator for controller development and evaluation . IEEE International Conference on Robotics and Automation，1998：52~58

[6] Tae-Hyeong Lim，Hyun-Chul Cho，Hong-Sun Lee and Soon-Yong Yang．Development of Hardware In the Loop System(HILS) for Hydraulic Excavator . 22nd International Symposium on Automation and Robotics in Construction，2005

[7] Gong W, Wang QF. A real-time simulation system for excavator controller. Proceedings of the 2nd international conference on advanced computer theory and engineering(ICACTE 2009), VOLS 1 and 2(1999): pages 489-493.

[8] Karpenko M, Sepehri N. Hardware-in-the-loop simulator for research on fault tolerant control of electrohydraulic actuators in a flight control application. Mechatronics. 19(7)(2009): pages 1066-1067.

[9] Elton Mark D，Enes Aaron R，Book Wayne J．A virtual reality operator interface station with hydraulic hardware-in-the-loop simulation for prototyping excavator control systems . 2009 IEEE/ASME International Conference on Advanced Intelligent Mechatronics，2009：250~255

[10] Gong Wen. Hardware-in-the-loop Simulation Station and Arm Real-time Simulation in Hydraulic Excavator. Master thesis. Zhejiang University, March 2010.

Proceedings of the 8th JFPS International
Symposium on Fluid Power, OKINAWA 2011
Oct. 25-28, 2011

1D3-3

DEVELOPMENT OF LARGE SCALE BI-LATERAL MANIPULATOR FOR HEAVY INDUSTRIES

Hiroshi Yoshinada*, Shu Takeda**, Kenji Okamura*, Shinichi Yokota***

*KOMATSU Ltd., Research Division
1200 Manda, Hiratsuka-shi, Kanagawa, 254-8567 Japan
(E-mail: hiroshi_yoshinada@komatsu.co.jp)
** KOMATSU Ltd., Development Division
Tsu 23, Futsu-machi, Komatsu-shi, Ishikawa, 923-0392 Japan
*** Precision and Intelligence Laboratory
Tokyo Institute of Technology
4259 Nagatsuda-cho, Midori-ku,Yokohama-shi, Kanagawa, 226-8503 Japan

ABSTRACT

The large scale manipulator for heavy industries has been developed. The manipulator is driven by the electric-hydraulic servo mechanism and operated by the new bi-lateral master-slave control system. The new system features the combination of the symmetric type bi-lateral and the force reflection type. Additionally the variable servo stffness control method is introduced and it enables to cope with both the high payload ability and the precise controllability. The system can convey heavy weight objects (up to 2200kg), and also it can accomplish the dexterous tasks such as grinding and assembling. In this paper, the outlines of the developed manipulator are described and the results of the evaluation tests are presented.

KEY WORDS

Hydraulic manipulator, Bi-lateral Master-slave, Compliance control

INTRODUCTION

The technology of the industrial robots has matured and a large number of robots are applied for various tasks in many production lines. However due to their small payload (usually less than 100kg), the robot applications for heavy industries are practically limited. Even today slow and dangerous hoist cranes are widely used for conveying and assembling work in heavy industries. To improve these situations, the authors tried to develop a new high speed and high payload handling system for heavy industries.

ADVANTAGE AND DISADVANTAGE OF HOIST CLANE

The overhead traveling hoist cranes (Fig.1) are the most popular conveying system in heavy industries. The operation of this type crane is rather easy. Usually they have only six push buttons (up, down, north, south, east and west) on its control pendant. All the operator has to do is to push the button indicating the direction that he or she wishes to move the object. So this operation system does not require expert skills. Another advantage of the hoist crane is the literally flexibility. As a work on the hoist crane is hanged by a flexible wire rope, the position and posture of the work can be changed easily by human power. It is very convenient to precise positioning or assembling such as a pin insertion into a hole. On the other hand, to prevent swing of a work hanged by a flexible wire rope, the hoist crane can not accelerate or decelerate quickly. This is the reason that the conveying speed of the hoist crane is limited to lower range. Another disadvantage is the major problem must be solved. To operate the hoist crane, an operator has to stand by a work. This means that it is very difficult to isolate the operator from danger and harmful work environment. Some parts of the lower productivity of heavy industries is caused by these disadvantages of the hoist crane.

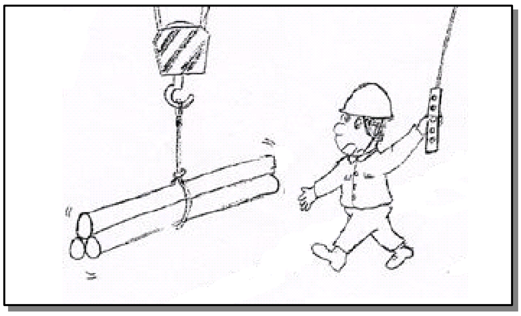

from "Japan Copper & Brass Association" Home Page

Figure 1 Overhead traveling hoist crane

DEVELOPED SYSTEM

The targets of the developing system are set as follows,

1) Easy operation system requiring no experience
2) High speed conveyance
3) Flexible and dexterous controllability
4) Operator isolation from danger and bad environment

To achieve these goals, the bi-lateral master-slave manipulator system was introduced. The bi-lateral master-slave system is well known as the control system of the manipulators for the sub-sea ROV or the nuclear power plant maintenance robot. This system can provide very intuitive operability and it is very easy to obtain the proficiency in operation. And the distinct feature of this system is the force reflection function. The force acted on the slave manipulator is fed back to the operator through the master manipulator and it makes possible to realize the dexterous controllability.

The following three types of the bi-lateral servo are known as the basic configurations.

1) Symmetric type
2) Force reflection type
3) Force feedback type

Fig.2 shows the scheme of each system.

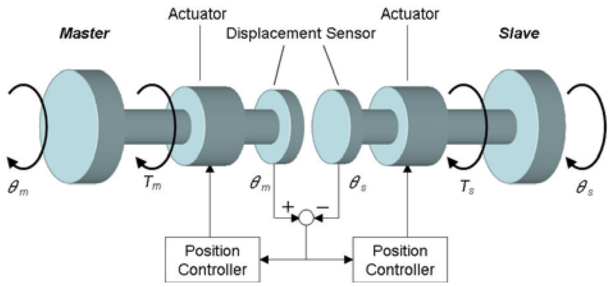

Symmetric type

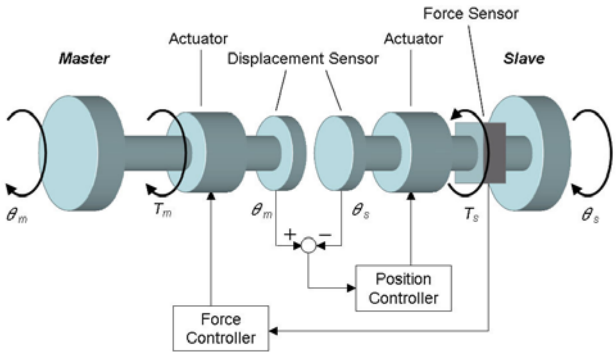

Force reflection type

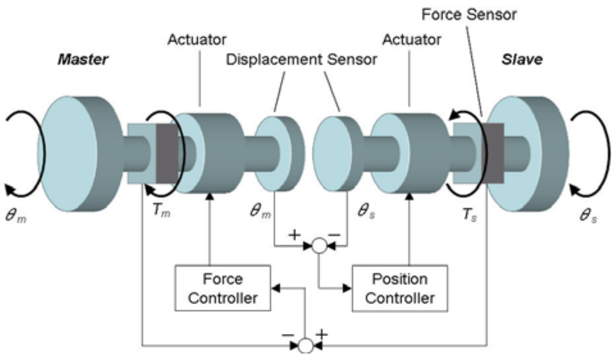

Force feedback type

Figure 2 Types of Bi-lateral servo

"Symmetric type" does not need force sensors and it is basically stable. This type provides a good sense of unity between the master and slave manipulator movement, but the force reflection ability is rather low. "Force reflection type" has good force transmissibility and "Force feedback type" is even better, but these types need some plan to make the system stable especially in the case that the slave manipulator contacts with a hard object. Taking these points into consideration, the new bi-lateral master-slave control system suitable for large scale manipulator is introduced. The scheme of the new system is shown in Fig.3. The slave manipulator which handles heavy weight objects is driven by the high output hydraulic cylinders (21MPa). The master manipulator is actuated by the electric servo motors which have the high fidelity of the reflection force. The system includes both the symmetric type and force reflection type bi-lateral servo. The symmetric type makes the system stable and the force reflection type provides the precise force reflection. The force acted on the slave manipulator is made smaller by 1/100-1/400 and reflected to an operator through the master manipulator. This brings an operator the sense of unity with the slave manipulator movements and it makes possible to move heavy weight works very smoothly.

To accomplish complicated tasks, good position and force controllability is indispensable. The hydraulic servo system has very low compliance and it has a good effect on the position controllability, but in contrast, it will become a difficult problem for precise force control. The authors perceived that the dexterous tasks such as assembling and grinding were done at rather low speed. From this observation, the variable servo stiffness control method using pressure feedback was introduced. It changes the system compliance according to the manipulator traveling speed and it provides the accurate trajectory controllability at high speed and precise force controllability at low speed. Additionally the disturbance forces such as the friction, viscosity and the deadweight of the master and slave manipulator are compensated as shown in Fig.3. As the result, it was confirmed that the non-linearity of the position controllability was less than 1% and the response delay less than 0.1sec, and as to the force controllability, they were 3% and 0.1sec respectively. Fig.4 shows the prototype manipulator. Each manipulator has 6 DOF plus a gripper. The length of the slave arm is upper 2000mm and lower 1500mm respectively. The master manipulator is one-seventh scale model of the slave manipulator. The payload of the slave manipulator is 100kg and the maximum speed is 2m/sec.

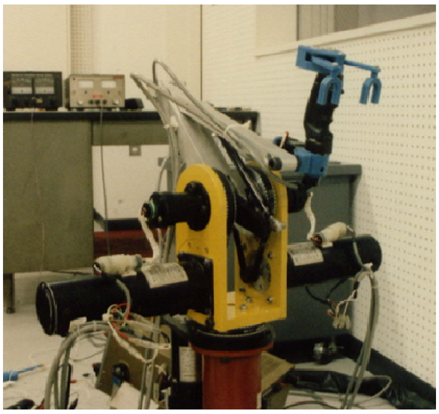

Master manipulator

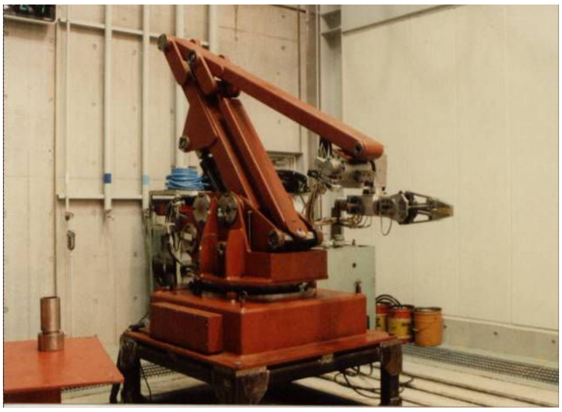

Slave manipulator

Figure 4 Prototype manipulator

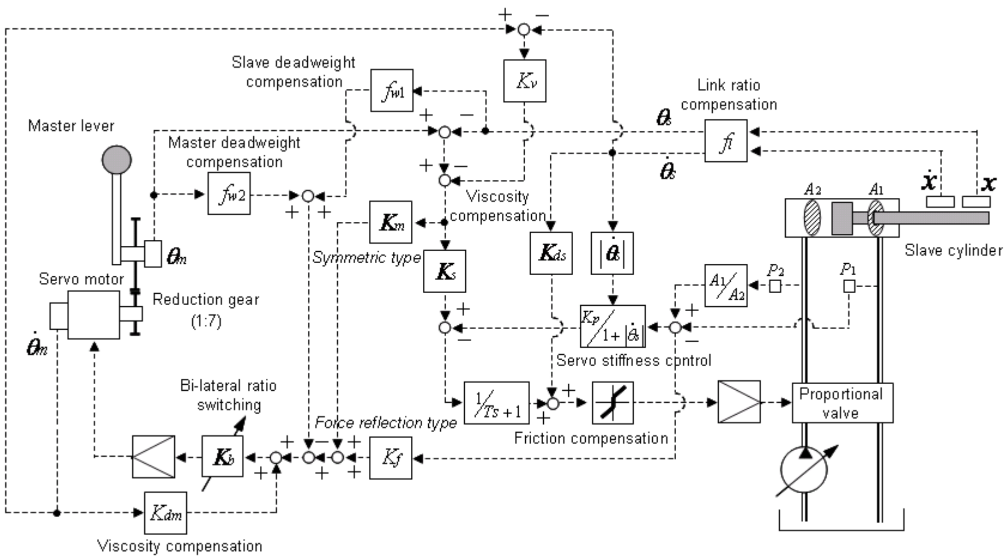

Figure 3 Scheme of the proposed bi-lateral servo system

TEST RESULTS

Using the prototype manipulator, the performance of the proposed system was evaluated.

Position traceability
It is not easy to evaluate the actual position traceability of the manual manipulator. It is not the correct evaluation to measure the linearity and the time lag of each joint. So we devised the new method shown in Fig.5. The procedure is as follows. 1)Command the adequate radius circular trajectory at a regular speed using the master manipulator. 2)Measure the horizontal acceleration at the end of the slave manipulator. 3)If the slave manipulator can trace the circular trajectory correctly, the output of the acceleration sensor shows the sinusoidal curve. 4)To compare the sensor output with the theoretical sinusoidal curve. This method is very effective to understand the operator's actual feeling of the position traceability.
The test result of the prototype manipulator is shown in Fig.5. Even at the maximum speed (2m/sec), the output of the acceleration sensor shows the good agreement with the theoretical curve. From this observation, it is considered that the developed system has the good position traceability.

Force transmissibility
Fig.6 shows the test result of the force transmissibility. The bi-lateral ratio (= the ratio of the slave manipulator load to the master manipulator reflected force) is set at 134. The force acted on the slave manipulator is reflected accurately to the master manipulator.

Peg -in- Hole task (Assembling work performance)
"Peg-in-Hole" is well-known as the representative task to evaluate the assembling work performance of the robot. We prepared the hollow steel pin as the peg and set the strain gauges on its inner surface. The outer diameter of the pin is 99.9mm. The hole has 100mm diameter and the both edge of the pin and hole are 3mm chamfered. Using this peg and hole, the "Peg-in-Hole" task was tested and the work time and the stress exerted on the peg during the insertion were measured.
The results are shown in Fig.7. The bottommost graph in Fig.7 shows the test result when the force reflection is cut off entirely. Under this condition, the work time is very long and the large stress is exerted on the peg. The top graph shows the result when the force reflection is maximum. In contrast, the work time is really short and the stress on the peg is significantly reduced. From these observations, it is understood that the force reflection by the bi-lateral control is very effective to accomplish the assembling tasks speedy and smoothly.

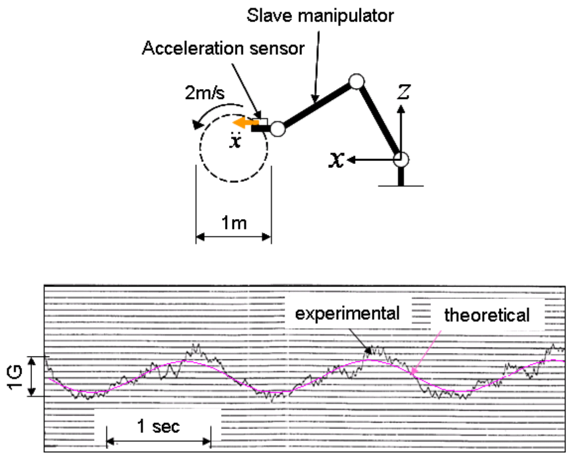

Figure 5 Test result of position traceability

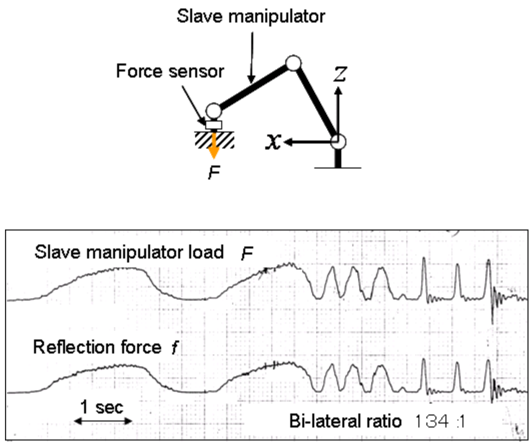

Figure 6 Test result of force transmissibility

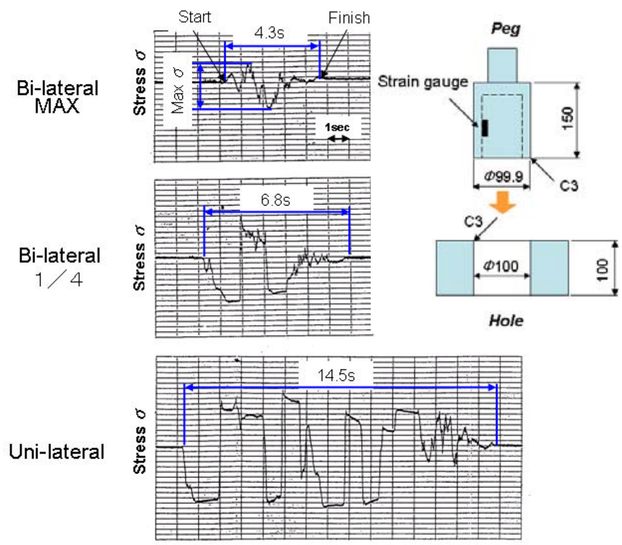

Figure 7 Test results of "Peg-in-Hole" task

Operation learning curve

To evaluate the easiness of the operation system, the test shown in Fig.8 was carried out. The task is "Peg-in-Hole", but the clearance between the peg and hole is a bid larger than one used in the assembling work performance test. The peg and the hole are set on the table at a distance of 300mm. The one set of the task is as follows. 1)Pick up the peg using the salve manipulator. 2)Carry the peg to the point above the hole. 3)Insert the peg into the hole. 4)Draw the peg. 5)Return the peg at its original position. The testee repeats this task and the changes of the cycle time are observed. The result is shown in Fig. 8. The cycle time of the expert is settled around seven or eight seconds. As the novice operator, at the beginning of the test, he required about 30 seconds to finish one set of the task. But the cycle time reduced gradually, and after 8 minutes passed, his cycle time is almost close to the expert operator. This result shows that the developed operation system is very intuitive and within half hour the novice operator learns to accomplish the complex tasks in the equal cycle time with the expert.

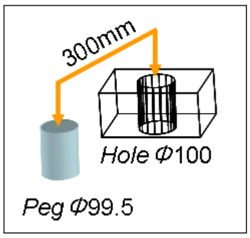

Peg-in-Hole Task

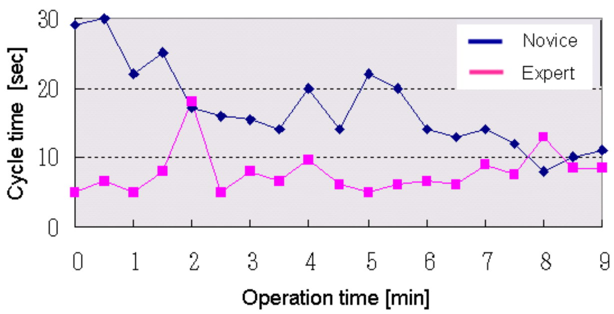

Figure 8 Operation learning curve

Fatigue characteristic

The fatigue characteristic of the developed operation system was evaluated. The tested task is the same "Peg-in-Hole" as the operation learning evaluation test. Both the testee A and B are the expert. They continued to do the task and the changes of the cycle time were recorded. The result is shown in Fig.9. Both the cycle time of A and B are slowly decreasing. During the 30 minutes continuous operation, there is no tendency of the cycle time increasing. From these results, it is considered that the developed operation system does not give the intense fatigue to the operator.

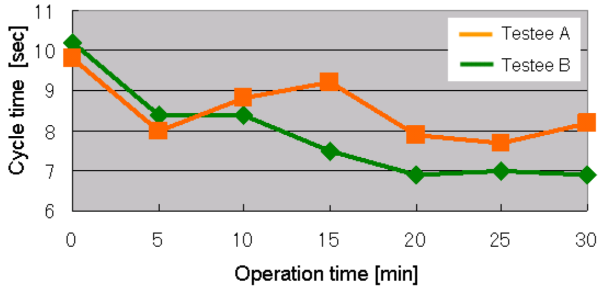

Figure 9 Fatigue characteristic

PRODUCTION MODEL

Obtaining the good results from the evaluation test of the prototype manipulator, the production models were produced. Fig.10 shows the one of the production model. The slave manipulator is equipped on the crawler vehicle, and the master manipulator is set in the air-conditioned close cabin on the vehicle. The maximum payload of this model is 700kg.

Outer view of production model

Master manipulator of production model

Figure 10 Production model

Fig.11 shows the lineup of the production models. Their payload range is from 200kg to 2200kg.

Figure 11 Lineup of production models

APPLICATIONS

The production models are received the good response from the market. The typical applications are handling and grinding in the casting and forging foundries. Some examples are shown in Fig.12. In every cases, the worker‘s environment was significantly improved and it was confirmed that the tact time was shortened by 1/7 in the case of the handling work and by 1/4 in the grinding work respectively.

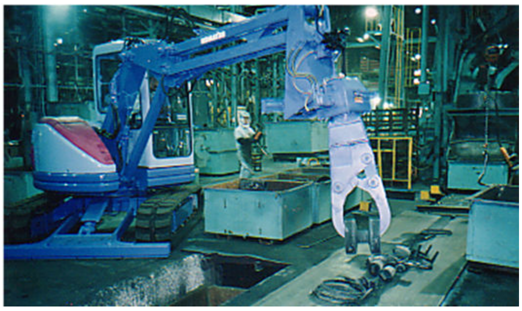

Handling in foundry

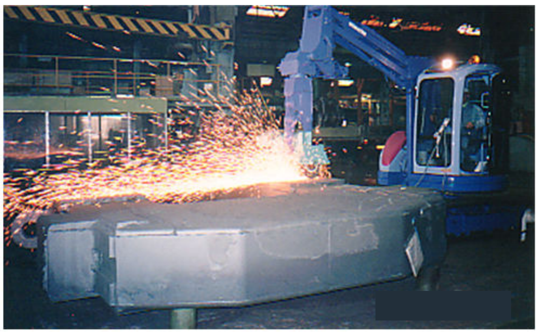

Heavy grinding

Figure 12 Examples of applications

NEXT WORK

It is conceivable that the developed technology could benefit to the future operation system for construction machinery. The authors are trying to apply the bi-lateral master-slave control method into the hydraulic excavator. As a master manipulator, the 3-dimensional joystick lever was newly designed and the new master-slave control method with different configurations was introduced. It can yield an affinity with a conventional joystick lever and give the comfortable feeling to the conservative construction machinery operators. Fig.13 shows the some examples of the test scenes. It was confirmed that complicated tasks such as the concrete cutting could be easily accomplished using the new master-slave operation system. This study is still continued and it is bringing the valuable information for the future operation system.

Handling

Ramming

Concrete cutting

Figure 13 Test scenes of master-slave excavator

CONCLUSIONS

To replace the conventional overhead hoist cranes, the high speed and dexterous manipulator for heavy industries is developed. The control method of the manipulator is newly proposed and it shows the good performances as is expected. The production models were introduced into the many factories and it was confirmed that the manipulator shortened the tact time and improved the worker’s environment significantly.

REFERENCES

1. H.Yoshinada, S.Takeda, Development of large scale bi-lateral manipulator, Proceedings of ROBOMEC’89, JSME,1989, in Japanese
2. S.Takeda, H.Yoshinada, K.ohtsubo, T. Naruse, Bi-lateral manipulator for construction work, Proceedings of 6th ISART, 1989
3. Robot society of Japan, Handbook for robotics, Coronasha, 1995, pp708-709, in Japanese
4. H.Yoshinada, Development of Large-scale handling manipulator, Journal of the Japan Fluid Power System Society, Vol.33, No.6,2002, in Japanese

Proceedings of the 8th JFPS International
Symposium on Fluid Power, OKINAWA 2011
Oct. 25-28, 2011

1D3-4

FIXED POINT VERSUS FLOATING POINT MATHEMATICS IN EMBEDDED SYSTEM PROGRAMMING FOR FLUID POWER MECHATRONIC COMPONENTS CONTROL: A REAL CASE STUDY

Massimiliano RUGGERI*, Matteo FRACASSI**, Massimo MARTELLI* and Massimo DIAN*

* IMAMOTER, Institute for Agricultural and Earthmoving Machines
National research Council of Italy
Via Canal Bianco 28, Ferrara, 44124 Italy
(E-mail: m.ruggeri@imamoter.cnr.it)
** Research and Development Dept., Tecnord S.r.l. Company
Via Malavolti 36, Modena, 41100 Italy

ABSTRACT

The increased systems complexity and performance request for electro-hydraulic applications, ask for more performing electronic systems and control functions. The new powerful microcontrollers and efficient cross compilers, encourage the floating point mathematics usage in the software control routines, useful to directly reuse the routines generated by the simulation tools, despite the lack of control for precise resulting routine execution.

The paper describes a practical experience of system performance optimization on a microcontroller installed on electro-hydraulic systems for mobile applications. A deeper analysis carried out on execution time occupied by floating point mathematic operations, working on the software side of the mechatronic component, led to a considerably better performance. Here it is demonstrated that, without lack of precision, fixed point mathematics are more performing, if executed by modern microcontrollers, even if more instructions are executed by the software routines due to the necessary rescaling of factors needed by the requested precision.

KEY WORDS

Floating Point, Fixed Point, Electronic Valve Control, Embedded Systems, Real Time

NOMENCLATURE

I	:	current (A)
ms	:	milliseconds
ns	:	nanoseconds
P	:	Pressure (bar)
µs	:	microseconds
Q	:	Flow rate (l/min)
SP	:	Spool Position (mm)
V	:	Voltage (V)

INTRODUCTION

In the last years the complexity of digital control of electro-hydraulic components and systems increased, due to the continuous request for better performance, efficiency and safety. Moreover, due to the increased quality and reliability of the simulation environment the electronic control of Mechatronic systems is moving away from maps and vectors towards a model based approach, in order to model in a better way the controlled actual systems and to reduce the dependency on control parameterization. In this scenario, useful tools allow to generate in various automatic ways C/C++ language code or pseudo-code, that can be transferred into embedded systems compiled binary files, or in hardware-in-the-loop platforms (HWIL), in order to test, on the physical bench or directly in the machine, the designed control strategies. This productivity increment brings with it a design habit: the floating point mathematic usage. Floating point mathematic is a powerful method to calculate and to perform the control actions, once the system is simulated or treated by a HWIL powerful platform, but very difficult to be managed by an embedded microcontroller not featuring a Floating Point Unit (FPU). Sometimes it can be though that a limited usage of Floating Point mathematic in a software program doesn't affect its real-time; this paper demonstrates that this is normally a risky approach, due to the high CPU load resulting from floating point to fixed point conversions and vice-versa and due to the uncertainty related to time required by the floating point / fixed point data conversion. A real case study of a product whose control was optimized, and its performance increased, is presented, analyzing the performance and performance comparison from the floating point mathematic to fixed point mathematic used in two versions of embedded software in the mechatronic component electronic control unit.

THE SYSTEM

The paper describes a real case study of a Two Stage Directional Valve Spool Position Control.

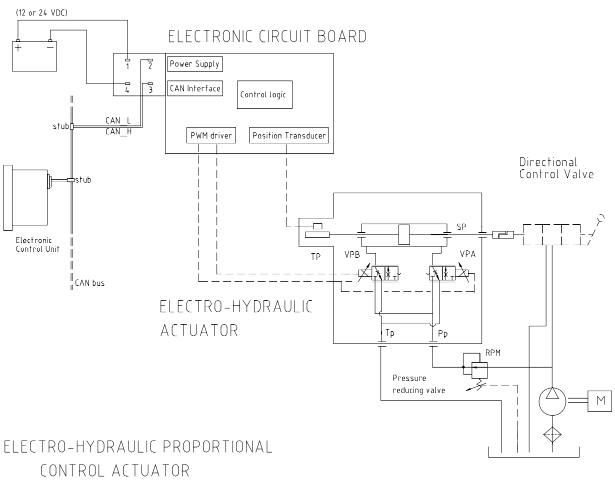

Figure 1 The Multidrom System Structure with electro-hydraulic valves and the flow regulation spool

The directional valve is a CAN controlled remote of an agricultural tractor and the spool position is controlled by a couple of three-way flow regulation valves, electronically and independently controlled on the basis of the spool position feedback from a contactless position sensor. As shown in Figure 1, the two proportional flow regulation valves are controlled by two electronically controlled PWM signals, regulated by a Freescale HCS12 series microcontroller, a powerful 16-bit core microcontroller widely used in mobile and automotive applications. The only feedback related to the position of the two proportional flow regulation valves is the current feedback acquired through the Analog to Digital Converter (ADC) of the microcontroller, while the current regulation is realized through an hardware circuitry, directly controlled by the PWM signal, by the specialized output of the microcontroller. The two proportional flow regulation valves are totally independent, and can be separately controlled, in order to increase the spool dynamic control performance. This first stage valve configuration gives the possibility to reduce the spool speed during transients, opening the opposite valve in respect to the desired direction of the spool movement, in order to avoid spool position overshoot, that is not desirable in a flow control of actuators. In fact a second stage spool position overshoot can result in a damage in some applications, due to a possible wrong actuator final position caused by an excess of oil flow in the final stage of actuators (e.g. hydraulic cylinders). The control module that is studied in the paper is composed by the two first stage valves, the electronic control unit embedded in the valves enclosure and the second stage valve spool position sensor. The module, called Multidrom®, is produced by Tecnord Company and is mounted in a wide number of directional valves and widely used both in agricultural machines and in earthmoving and construction machines, all over the world. The Multidrom® module adaptability is a challenging characteristic because of the control stability and robustness for the entire range of applications.

In fact the control is the same for all applications, and the tuning is realized only through a different parameter set for each different application and valve section.

Figure 2 The Multidrom Module coupled with a Directional Valve

THE STATE OF THE ART

The Multidrom module is produced in various versions and it is provided with a complex control strategy that is based on a feed forward function implementing the model of the electro-hydraulic flow control valves and the second stage flow regulation valve; moreover, in order to compensate the model uncertainties and the environment variables, a feedback function based on a PID with variable gains and a differentiated anti-windup strategy is implemented, coupled with the feed forward function. The PID was optimized on a test bench and an important dependency from oil temperature was observed. Thus, in order to reach a good compromise between control stability and performance various parameter sets were defined, as a function of the second stage configuration. From the software point of view, all strategies, implemented in standard C language, were written using floating point mathematics, allowed by the Metrowerks CodeWarrior compiler and by the Freescale microcontroller used for the application. That mathematics setting is a modern choice, allowed by the increased calculation power of the new microcontroller products on the market, protects from some kind of data type error, leaving the control for data dimension to the microcontroller, while implies a considerably greater time to execute the requested operations with the Arithmetic Control Unit (ALU) of the Microcontroller.

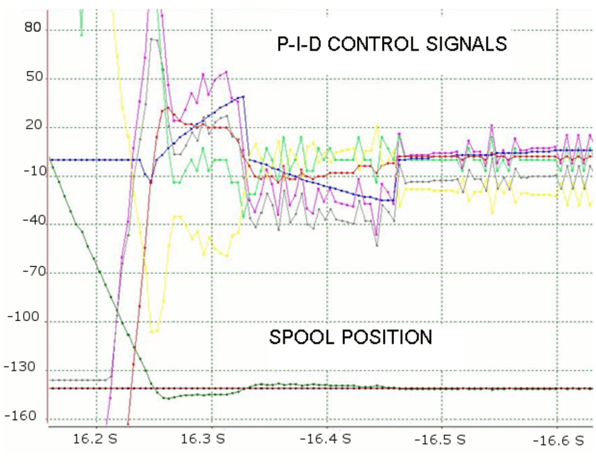

Figure 3 Step Response with Floating Point Software

The resulting maximum rate for the control function execution and the necessary controls for diagnosis and communication was 5 ms (cycle period). This 200 Hz control frequency is apt to control a classic second stage dynamic of the flow regulation valve coupled with Multidrom modules, whose step response was measured to be 110 ms from central neutral position to the complete open position both in extend and retract direction, as shown in Figure 3; but the control dynamic can result unable to take advantage of the higher dynamics of the electro-hydraulic controlled valves of which is provided the Multidrom module. Tests performed on a test bench demonstrated that, in some high dynamic working condition, the control was unable to avoid flow regulated valve spool position overflow and that the steady state error was difficult to be nullified; in fact the control reactivity, needed for dynamic performance, created a bigger reaction on small dynamics and near the steady state spool position (in Dark-Green in Figure 3). This is the classic demonstration of the limits of linear controls, like the PID (Red, Light-Green and Blue lines respectively in Figure 3) even if provided with variable gains and anti-windup system, that is unable to be tuned for highly non-linear systems. The main idea of this work is to reduce the CPU control time in order to increase the frequency of the control function execution, in order to observe the dynamics of the controlled systems in a shorter time period, where the model linearization is allowed and then the linear controller is apt to regulate the system behavior.

THE CONTROL IMPLEMENTATION

The control strategy was primarily designed using a mathematical model of the system, and, in a second phase, was translated in ANSI C language and cross-compiled for the HCS12 Freescale microcontroller family using the CodeWarrior C/C++ compiler.

Many calculations are executed using single precision float data type, 32 bits, 8 for the exponent, 23 for the significand and 1 for the data sign as stated in [1] and [2], that are expressed in the form:

$$value = (-1)^{sign} \cdot \left(1 + \sum_{i=1}^{23} b_i \cdot 2^{-i}\right) \cdot 2^{(e-127)} \qquad (1)$$

Where *sign* is the most significant bit, b_i are the base fractional binary values and e is the exponential binary value. The microcontroller converts all data using Eq. (1) for each control function run using shift, multiplier and divider functions of the ALU (Arithmetic Logic Unit) both for direct and for reverse conversions.

For each addition/subtraction the ALU converts the floating point numbers in order to obtain the same exponent for all operation's elements and then execute the addition or subtraction; after the operation another shift can be executed in order to normalize the result in case of overflow or underflow of the operation executed; similarly for multiplication and division. To multiply for example, the significands are multiplied while the exponents are added, and the result is rounded and normalized. Thus, the floating point mathematic need for more instruction to be executed by the microcontroller ALU, in order to normalize the numbers before and after the operation over the mantissa in fixed point mode.

 ISBN 4-931070-08-6

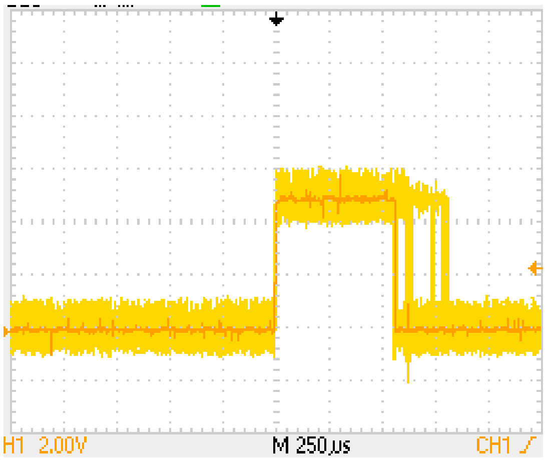

Figure 4 Uncertainty in Floating Point Control Task Duration

The resulting control function task execution time can vary considerably from the best to the worst case from 550 µs to 820 µs, depending on the number of floating point operations that need shift for normalizing data to the standard format. Figure 4 shows the multiple acquisition of the control function execution time, obtained using an Oscilloscope with the "persistency" function activated at 2 seconds of period. The signal shown is the status of an hardware output pin of the Freescale microcontroller activated in the first instruction of the control function and deactivated in the last instruction of the control function; the task execution time is then affected by the introduction of two new instruction for switching the hardware pin status: the time for each switch is around 25 ns at 80 MHz clock.
The real need for floating point was evaluated as suggested in [3], and it was found that, using integer numbers with 32 bit precision in the intermediate computations of the control function, the range of values was sufficient to cover the entire range of intermediate calculations of the actual control implementation (also solved in [4]). In fact fixed point mathematics does not reduce the precision with respect to single precision float data, if the value of variables does not change for more than 7 orders of magnitude if, when necessary, 32 bit variables are used; nevertheless the microcontroller executes faster the control strategy.
Moreover a fixed point algorithm requires the designer to write much more controlled code, because of the need to verify the absence of overflows in fixed point operations, while in floating point mathematics the designer can lose the feeling on the data dimension in the control function implementation.
Last but not least, considering the embedded systems structure and method to design, tune and test digital control systems, it is clear that a large number of floating to fixed point and vice-versa are necessary, in order to perform the complete software structure. Data to be transmitted to a data logger over CAN network, for example, are converted from floating point to fixed point, in order to be sent in a readable format to the logger through CAN messages; in the same way, control parameters are sent and stored in memory in fixed point format, as usual for human thinking. Moreover looking at the sensor inputs and at the output of the control system and analyzing the microcontroller peripheral structure, the spool position is acquired by a 10 bit ADC channel and the control action is actuated through a PWM signal by a peripheral where a control register must be filled with a 10 bit duty cycle value in real time. All these values are in fixed point format and a conversion is necessary to pass from/to floating point format in control function.

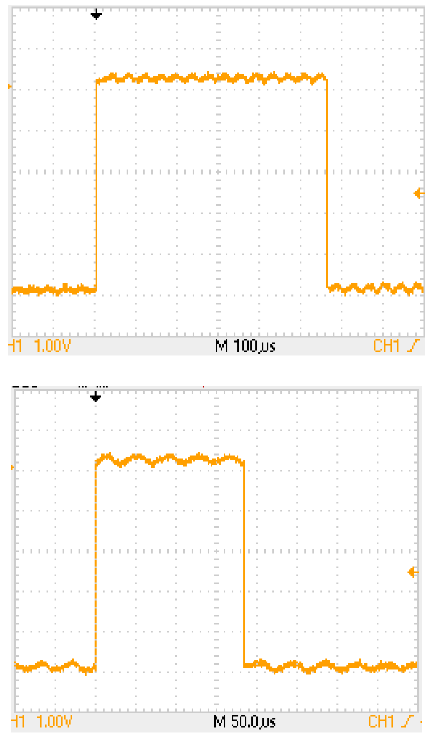

Figure 5 Task Control Duration with Floating and Fixed Point Mathematics

All these conversions and the strategies required by the application limits the repetition time for the control task at 5 ms at least. The mean value of the pure control function time occupation with floating point mathematics is shown in the Figure 5 above and is around 550 µs.
The new control was then implemented, modifying the software control code by replacing all floating point computation and variables with equivalent fixed point, thus reducing the data dimension to 16 bit integer, when possible, and using 32 bit variables where needed for computation requirements.
The result for the mean value of the control function time occupation with fixed point mathematics is shown in the

Figure 5 below and is around 180 µs.
This performance increase was similarly obtained in the other functions of the application, where floating/fixed point conversions were operated.

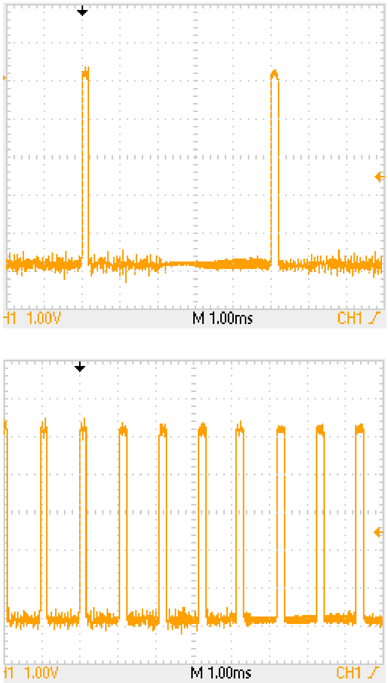

Figure 6 Task Control Period and precise repeatability at 5 ms and 1 ms timing (new software)

The result in terms of occupation time by the main control function is shown in Figure 6, where in the above image is presented the result for control action time distribution at 5 ms, while in the below image the control function time distribution at 1 ms is shown. The figures demonstrate that no delay due to other tasks is present in the control function time distribution and then that the control is executed at deterministic time intervals. In order to ensure the equivalence of the new software a test version was created where, for each computation modified both versions were implemented and a control was added in order to evaluate both the consistency of the new software version and the precision.

```
ResultFloatX = float_functionX();
ResultFixedX = fixed_functionX();
if ( ResultFloatX != (float) ResultFixedX )
{
        error_management_function();
}
```

After the new and old versions comparison, the final software version was settled at 500 µs of cycle time for the main control function, resulting in a 10 factor for control dynamic in respect to the original control.

This software configuration increased considerably the dynamic and steady state system performance.

COMAPRATIVE TESTS AT TEST BENCH

A Multidrom equipped flow regulation valve was installed at test bench and tested in various working conditions, using both software versions reloaded on the same unit for each test. The monitoring of control task execution time and cycle time was maintained using a probe directly connected on a software controlled pin of the microcontroller (the red cable in the Figure 7), while all other data, both from sensors and from control corrections, were acquired through the Multidrom CAN network with Vector Canalyzer at 500 µs frequency.

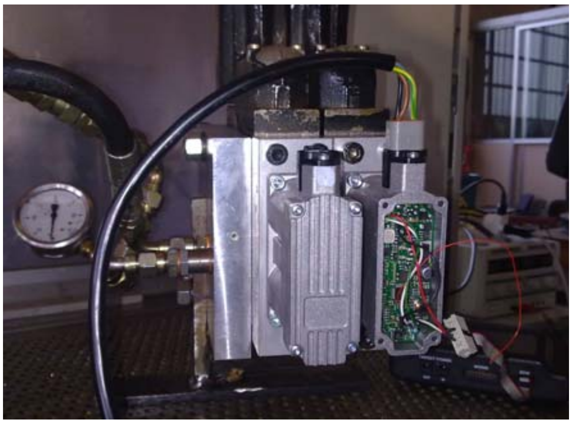

Figure 7 The System under test at the test bench

The same CAN network analyzer was used to simulate CAN commands to the module through a dynamic script that simulated time histories of set point for flow regulation commands automatically sent by the same tool.

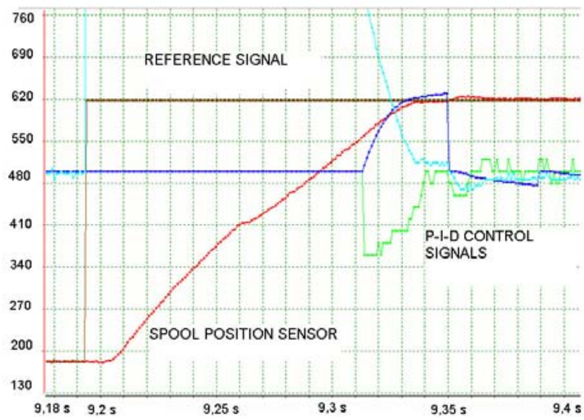

Figure 8 Step full displacement response with control contribution and Peak strategy: Integral term Blue line, D term Green line, P term light blue line.

Figure 8 shows the main control strategy behavior, that applies a fully powered command for big errors in set point spool position, while starting to use the variable gains PID for small errors [5].
In the figure a full extend to retract transient is presented, in order to show the second stage spool dynamics.
A very small spool position overflow is observed and it can be noted that it does not result in a higher flow because it is in the fully opened spool displacement region.

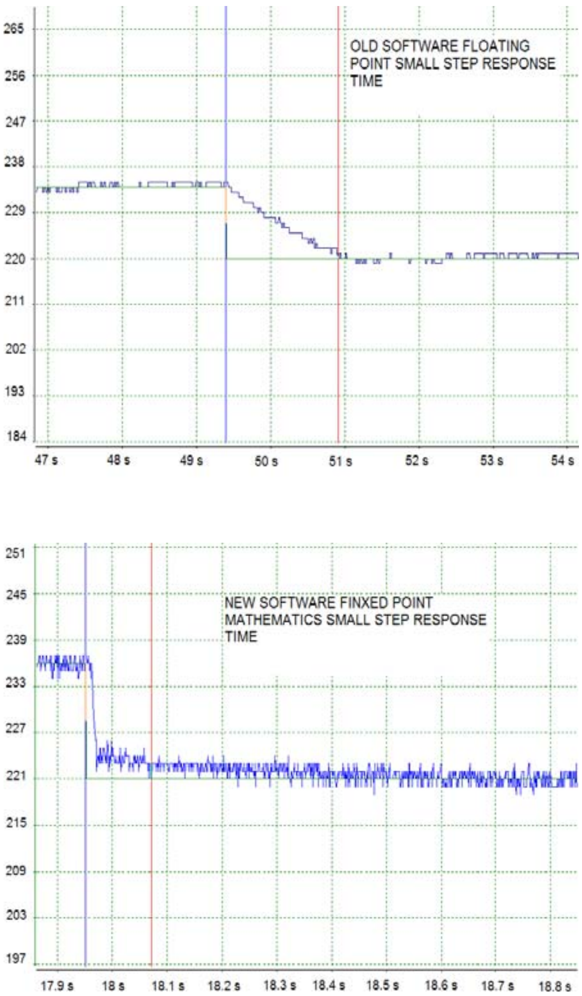

Figure 9 Small step response

The green line is the derivative correction, the light blue is the proportional correction (saturated) and the blue is the integral term correction. The values in the vertical axis are the ADC acquisition values in 10 bit resolution. The total spool displacement is 16 mm (at 0,02 mm/bit).The best results are in the small set-point variations and in steady state error, that results stable with the new control.
As show in the comparison in the two graphics in Figure 9 for small step response, here 0,35 mm, the faster control action results in a 10 times reduced time for reaching the 90 % of the difference and absence of overshoot (new software with fixed point mathematics: below graphic; old software with floating point mathematics: above graphic). In both graphics the green line is the set-point for spool position and the blue line is the spool position direct acquisition through the Hall effect sensor in the Multidrom module.

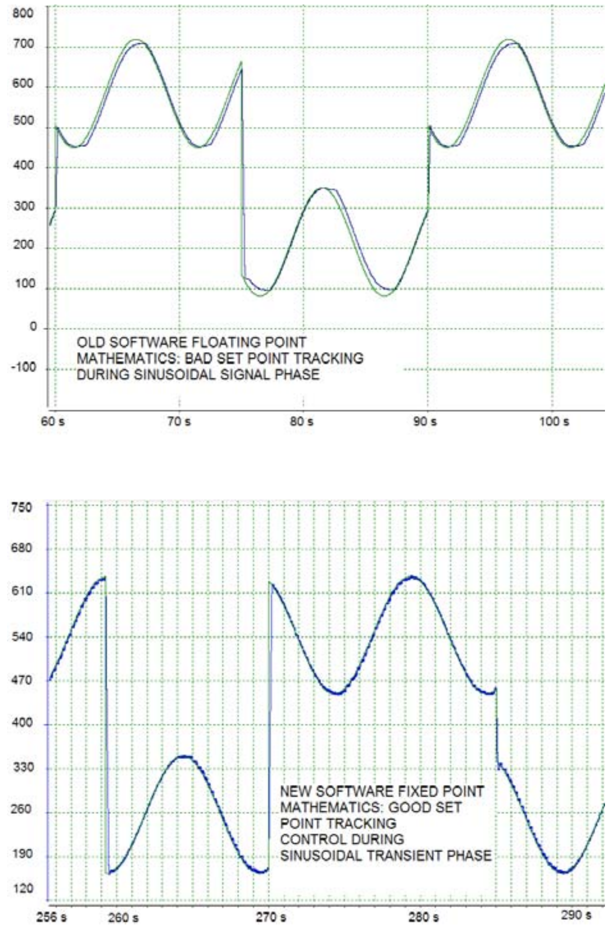

Figure 10 Sinusoidal Set-point with Step dynamic

As presented in Figure 10 a variable set-point with steps response and a sinusoidal waveform results in a better dynamic response in the new software (below graphic in the Figure) and in a uncorrected spool position error in the old software version (above graphic in the Figure), while the dynamic response at big steps are comparable for the two software versions.
In both graphics the green line is the set point command and the blue line is the spool position sensor signal.
The same differences can be found in Figure 11, where step response coupled with a saw-tooth set-point time history was generated (new software in the below graphic in the Figure). The most remarkable result is the control robustness in function of the control pressure that should be optimal at 20 bar, but that can be varied in a

range of values without lack of precision in flow regulation, except for the dynamic performance.
With the new software version the Multidrom module allows the control pressure reduction to 8 bar, while the original software is unable to reach the set-point value and the diagnostic strategies lead it to protection condition in safe state (neutral spool position).

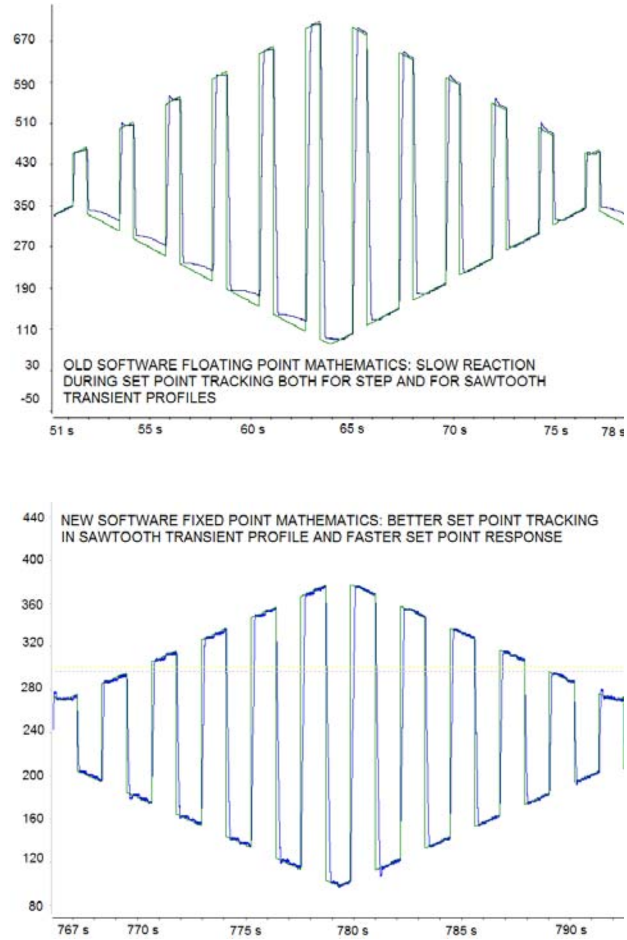

Figure 11 Saw-Tooth Set-point with Step dynamic

As shown in Figure 12 a complete retract to extend transient was generated with low dynamics in 30 s time, in order to characterize the steady state error with 8 bar of control pressure in the Multidrom flow control valves.
In the above graphic in the Figure, it can be noted that the old software strategies, based on Floating point mathematics, are unable to reach the set-point and, after a diagnosis time the control valves are switched off by the module, in order to lead the spool of the controlled vale in the neutral position (safe state).
Conversely in the below graphic in the Figure, it can be observed the entire stationary characteristic of the spool position control response, that is lead by the new software based on fixed point mathematics, through the neutral position at 400 ADC value, that corresponds to 8 mm (0,02 mm/bit for the spool position acquisition), with no error in steady state control even if in low (degraded) pressure condition. In the graphic are also in evidence the two dead-band and the two polarization currents near by the valve center rest position.
A higher dynamic without spool position overflow, the absence of steady state error, the complete spool position hysteresis and an increased robustness against the control pressure variation are the most remarkable results; all these performance increase are due to the PID feedback correction, that results easier for smaller errors that are observed in shorter time between two control actions.

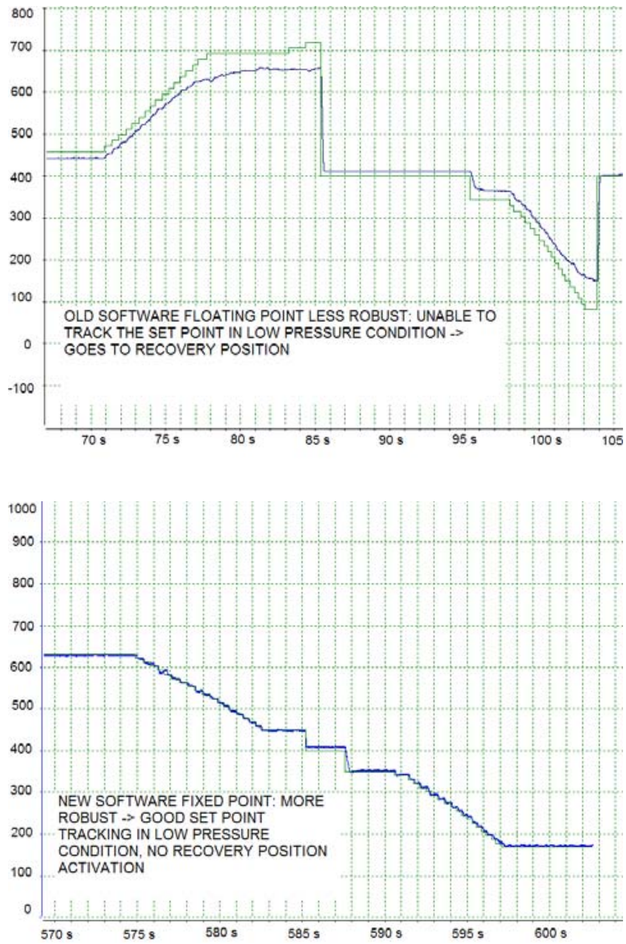

Figure 12 Low pressure quasi-static characteristic

CONCLUSIONS

The optimization of the control function, obtained with the sole mathematics optimization performed on a real product case, represents an important case study for all research groups that need for more performance for an embedded control system.
The limited computing power available in the embedded systems and microcontrollers, even if in continuous

growth, is not sufficient to implement floating point mathematics based control functions, obtained for example as output products of widely used simulation tool-suites.

Conversely fixed point mathematics, the standard embedded mathematical library in the automotive sector today, is suitable for optimal control and fits the data field for the most part of applications without lack of precision in respect to floating point mathematics and represents a good compromise for real time control of mechatronic components in electro-hydraulic applications.

The next step for fixed point mathematics test and validation, in our study for electro hydraulic controls design, will be the direct synthesis of fixed point control blocks in simulation environment and their test on models and in control function translation for embedded systems programming [6]. This method should allow a direct comparison on control performance compared with floating point mathematics control blocks and functions directly on simulation environment.

REFERENCES

1. IEEE 754, ed. 2008: IEEE Standard for Binary Floating-Point Arithmetic, IEEE
2. IEC 60559 ed. 2.0: 1989, Binary floating-point arithmetic for microprocessor systems, IEC, Swiss.
3. James W. Gray, PID Routines for MC68HC11K4 and MC68HC11N4 Microcontrollers, AN1215/D Freescale Semiconductor Inc., 2004.
4. Elmenreich W., Rosenblatt M., Wolf A., Fixed Point Library Based on ISO/IEC Standard DTR 18037 for Atmel AVR Microcontrollers, 5th Workshop on Intelligent Solutions in Embedded Systems, June 2007,Madrid, Spain, pages 101 – 113.
5. Kum K.; Kang J.; Sung W; AUTOSCALER for C: an optimizing floating-point to integer C program converter for fixed-point digital signal processors, IEEE Transactions on Circuits and Systems II, Vol. 47/9, 2000, Page(s): 840 – 848.
6. Goossens G., Van Praet J., Lanneer D., Geurts W., et al., Embedded software in real-time signal processing systems: design technologies, Proceedings of the IEEE, Vol. 85, Issue 3, 1997, pages 436 -454.

Proceedings of the 8th JFPS International
Symposium on Fluid Power, OKINAWA 2011
Oct. 25-28, 2011

1D3-5

BUNDLING SEVERAL EXTENDING/CONTRACTING MUSCLES TO POWER SOFT MECHANISMS

Kazuhiro IWATA*, Koichi SUZUMORI*, and Shuichi WAKIMOTO*

* Department of Graduate School of Natural Science and Technology
Okayama University
3-1-1 Tsushima-naka, Okayama, Okayama, 700-8530 Japan
(E-mail: iwata8@act.sys.okayama-u.ac.jp)

ABSTRACT

Recently, there has been increasing researches on light weight and high power robot hands that use the artificial muscles. In this research, to hold heavy loads with various shapes, we have developed a new bending soft mechanism that uses artificial muscles. We have developed two different types of slim hydraulic artificial muscles, contracting type and extending type. Both types can be applied high hydraulic pressure, and have a great advantage on the ratio of the generated force / mass. Bundling these high hydraulic artificial muscles has a great potential to realize soft bending mechanisms which have high generated power, stiffness variable in wide range and shape adaptability.

In the previous report, we showed experimentally that combining two muscles of extending and contracting motion realizes much higher stiffness than combining the muscles of same motions. In this paper, we develop a power soft mechanism bending in any direction which consists of a contracting muscle and six extending muscles and evaluate its performance experimentally. Applying hydraulic pressure of 1.0[MPa] causes the bending angle of 160[deg] and the force of 40 [N] at the mechanism top.

KEY WORDS

McKibben actuator, Soft Mechanisms, Hydraulic actuator

INTRODUCTION

Recently, many researchers are rather more focused on the development of artificial muscles as a source of actuating forces to replace conventional pneumatic and hydraulic cylinders. Above all, McKibben type artificial muscles developed by Shulte et al in the 1961 [1] are typical ones, they are light in weight, but can generate considerably large contraction forces. Thus, there has been increasing researches on light weight and high power robot hands that use the rubber actuators [2] [3] [4].

In this research, we intend to develop hydraulic artificial muscle based on McKibben muscle. They are not only contraction type but also extension one, and to apply them to new soft mechanisms generating high power with high compliance. Applying hydraulic pressure causes the big amount of motion and force of mechanisms.

Previously two types of water-driven artificial muscles namely contraction type and extension type, were developed, and by using them we realized soft mechanisms generating bending motion with high stiffness as shown in Figure 1, the mechanism can generate high force at mechanism top and big amount of bending motion. As a result, we showed experimentally that combining two muscles of extending and contracting motions realizes much higher stiffness than combining the muscles of same motions. However previous mechanism can bend in only one direction

In this report, we apply this design method to a new power soft mechanism bending in any direction which consists of a several extending/contracting muscles and evaluate its performance experimentally.

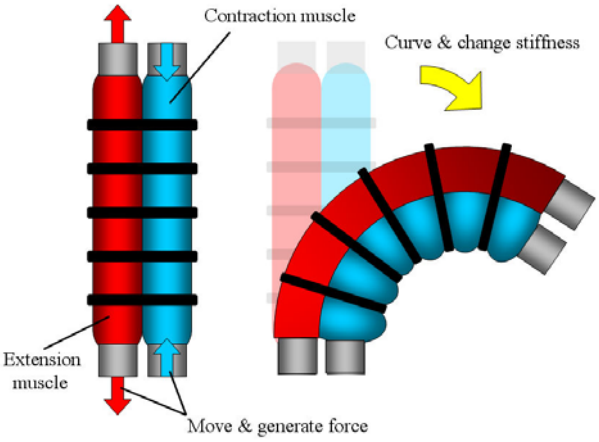

Figure 1 Basic concept of high stiffness bending rubber mechanism

WORKING PRINCIPLE

Here we explain the hydraulic artificial muscles for the proposed soft mechanisms mentioned above.

Yokota et al. applied McKibben type muscle to the hydraulic artificial muscles, which have an advantage in power mass ratio over the any actuators [5]. We also have applied McKibben muscle to hydraulic ones, and uniquely our muscle can generate not only contracting motion but also extending one individually. Figure 2 shows the composition of a hydraulic artificial muscle and its operating principles.

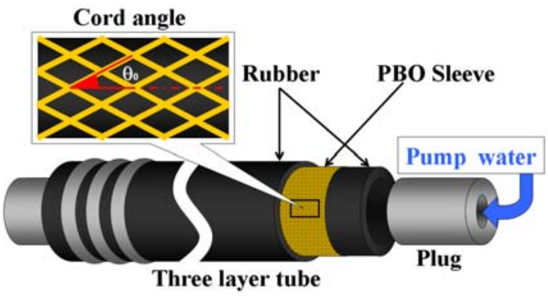

Figure 2 Constitution of the hydraulic artificial muscle

The Hydraulic artificial muscle consists of a rubber tube covered with fiber sleeves and two terminals fixed at both ends. One terminal has a plug for inlet of working fluid from pumps as shown in the above Figure. Generally McKibben type muscles generate contraction forces expressed by the following equation [1], and the equation can also be applied to the hydraulic artificial muscles. Additionally the equation is effective for not only contracting force but also extending force.

$$F = \frac{\pi}{4} D_0^{\,2} P \left(\frac{1}{\sin \theta_0} \right)^2 \left\{ 3(1-\varepsilon)^2 \cos^2 \theta_0 - 1 \right\} \quad (1)$$

D_0, denotes diameter of artificial muscle; P, applied pressure; θ_0, initial knitting angles of sleeve; ε, contraction rates. This equation indicates that variation of forces, and generated forces vary with the initial knitting angles. Given that generated forces are proportional to applied pressure, the developed artificial muscles, using water instead of air as working fluid to apply high pressure, can generate large forces.

STRUCTURE

Figure 3 shows the overview of knitting sleeve fibers of two types of artificial muscles, (a) is contraction type and (b) is extension type. In the previous report, we clarified that artificial muscles of contraction type show a good result of a balance in expansions in radial direction and contractions in axial direction when knitting angles are around 25 [deg] and extension type show a good result of best extensions displacement when knitting angles are around 65 [deg][6][7][8]. Depending on specifications of cord-making machines, knitting angles of the artificial muscles were 23.5 [deg] for the contraction type and 66.5 [deg] for the extension type. Fibers of the sleeves are p-Phenylene-2, 6-Benzobis Oxazole (PBO) fibers, which have the highest levels of tensile strength and elasticity modulus among organic fibers as well as high decomposition temperatures and fire resistance.

(a) θ_0=23.5 [deg]

(b) θ_0=66.5 [deg]

Figure 3 Overview of the PBO sleeves

The three-layered tubes are of such structure to have PBO sleeves in Figure 3 inserted between the tube and chloroprene rubber. Figure 4 shows cross section of the actuator. The three-layered tube has an outside diameter of 21 [mm], an inner layer of 2.0 [mm] thick rubber, a middle layer of 1.0 [mm] thick sleeve, and an outer layer of 1.0 [mm] thick rubber. PBO fibers, which are likely to deteriorate due to ultra-violet light and water, are protected by the inner and outer layers of rubber. Moreover, rubber getting into gaps of fiber bundles to eliminate clearance between rubber and sleeve seems to work for prevention of local changes.

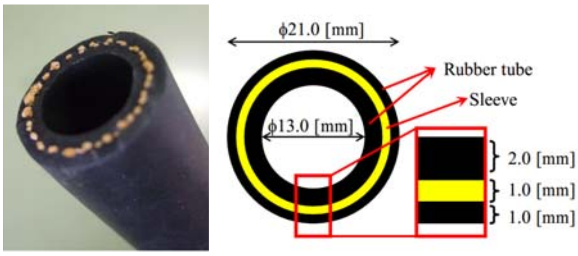

Figure 4 Cross-section of the three layer rubber tube

Figure 5 shows components of the artificial muscles developed in this research. The artificial muscles consist of three-layered tubes, special terminal plugs, hose bands, and parts to apply hydraulic pressure. The terminal plugs are of such shape that lots of small inverted truncated cones are piled up to prevent the plugs from falling off due to application of high pressure and to prevent the inner layer of rubber from getting damaged due to water leakage.

Figure 5 Parts of high hydraulic artificial muscle

EXPERIMENTS

Artificial muscle

We have conducted experiments to actuate the developed two types of artificial muscles. In the experiments, we have applied hydraulic pressure of 1.5 [MPa] to the each type of artificial muscle having effective actuation part of 300[mm]. Figure 6 shows the appearances of the developed artificial muscles when hydraulic pressure of 1.5 [MPa] is applied; the upper artificial muscle in the Figure is of extension type and the bottom one is of contraction type. Details of the two types of artificial muscles are given in Table 1 together with their experimental results: both artificial muscles of extension and contraction types have got displacements of around 70 [mm] in

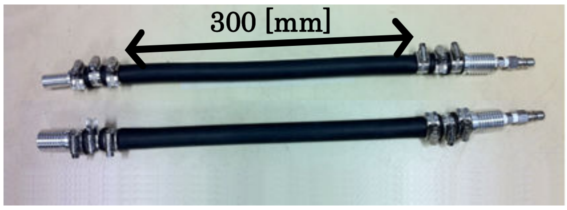

(a) 0 [MPa]

(b) 1.5 [MPa]

Figure 6 Driving experiments of three kinds of artificial muscles

Table 1 Details of artificial muscles

	Contraction Type	Extension Type
Knitting Angle [deg]	23.5	66.5
Effective changeable Part [mm]	300	300
Displacement [mm] of 1.5 [MPa]	75	68
Generative force [N] of 1.5 [MPa]	2285	230

We have also measured forces generated in the axial direction as well as variations in length. Figure 7 shows the overview of the experimental setup to measure the generating force. A hydraulic cylinder is used for generating the pulling or pushing load onto the muscles. One end of the each muscle is fixed and the other end is connected to the cylinder rod. The artificial muscles are driven by a water hand pump. Water is supplied to the muscle through hydraulic tube. The contraction and extension force is calculated from hydraulic pressure in the cylinder measured by a pressure sensor.

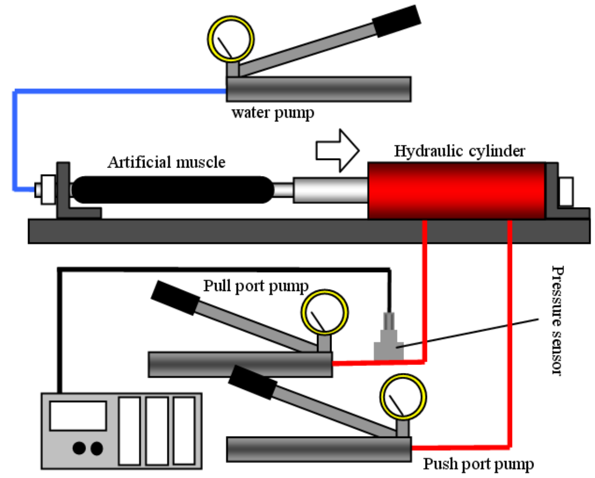

Figure 7 Experimental setup for generating force test

The contraction muscle endures the pressure of 1.5 MPa to achieve maximum contracting force of 2.3 [kN] and contraction ratio of 25%. On the other hand, the extension muscle endures the pressure of 1.5 [MPa] to achieve maximum extending force of 0.23 [kN] and extension ratio of 23%. Those experimental results are shown in Table 1. The experimental data agrees well to theoretical data.

Basic bending mechanism

In order to increase stiffness of the mechanism consisting of rubber actuators, the structure needs to have two parts to bear contraction forces and to bear tensile forces. Mechanism consisting of a combination of either extension type actuators or contraction type actuators will fail to give high stiffness. For example, Flexible Micro Actuators (FMA) [9], a mechanism consisting of a combination of three actuators of extension type, has difficulties in increasing stiffness in the vertical direction to the axis. In this research, we have developed bending rubber actuators with high stiffness, in which high stiffness and large curvature are both achieved through a combination of multiple artificial muscles of extension and contraction types. Figure 8 shows simple models of such bending actuators before and after being actuated. We denoted the length of artificial muscle before actuation at L; its radius, at r; variation rates of the artificial muscle after actuation, at α; curvature radius of the actuator, at R; and bending angles at the tip, at θ, bending angles R and curvature radii θ are expressed by Equations (2) and (3) respectively.

$$R = \frac{100}{\alpha} r \tag{2}$$

$$\theta = \frac{\alpha}{100} \cdot \frac{L}{r} \tag{3}$$

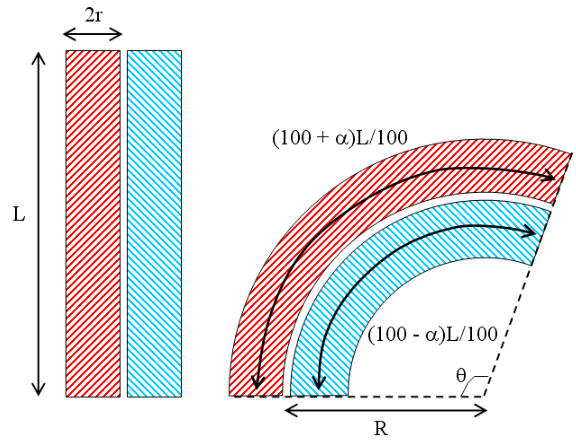

Figure 8 Simple model of bending actuator

Figures 9, 10 show the design and overview of developed actuators. This actuator uses the slim artificial muscle with one contraction type muscle on the upper side and two extension type muscles on the lower side. As their variation rates become identical if the same pressure is applied, it is possible that they will make similar motions with the structures. They are made up of 600[mm] in length of artificial muscles bound together with binding bands, so that hydraulic pressure application makes them bend towards the upper side. Although variation rates of artificial muscles of extension and contraction types may differ in certain pressure bands, flexibility of the artificial muscles works for prevention of any play or bucking.

Figure 9 Design of muscles for high stiffness bending actuator

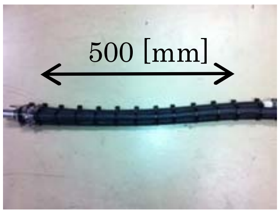

(a) 0 [MPa]

(b) 0.3 [MPa]

(c) 0.6 [MPa]

(d) 0.8 [MPa]

Figure 10 Driving experiments of high stiffness bending actuator combining one contraction and two extension muscles

Based on the initial state, the bending actuator bends 0 [deg] at the central axis of the tip when no hydraulic pressure is applied and 270 [deg] when hydraulic pressure of 0.8 [MPa] is applied, representing a variation rate of about 10%. Substitution of these values in Equation (2) will make the curvature of the actuator 330 [deg]. With attenuation of forces due to frictions or others taken into account, theoretical values and actual measurements are nearly identical with each other, which validate the basic concept. This type of actuators can make larger-angled curvatures and higher stiffness than the ones made by a combination of artificial muscles of either extension type or contraction type.

Power soft mechanism bending in any direction

Based on this result, we have developed the power soft mechanism bending in any direction. The design is shown in Figure 11. This mechanism is composed of the radial arrangement of six extension muscles in surroundings of one contraction muscle. Seven artificial muscles are bundled at intervals of 50[mm], and the length of the effective bent Part of the mechanism is 500mm. This composition makes it possible to bend in any directions by driving two adjoining extension muscles and contraction muscle at the center. Interference of non-drive muscle during bending in a certain direction does not influence so much and actually it is possible to bend in any direction, because all the artificial muscles have flexibility.

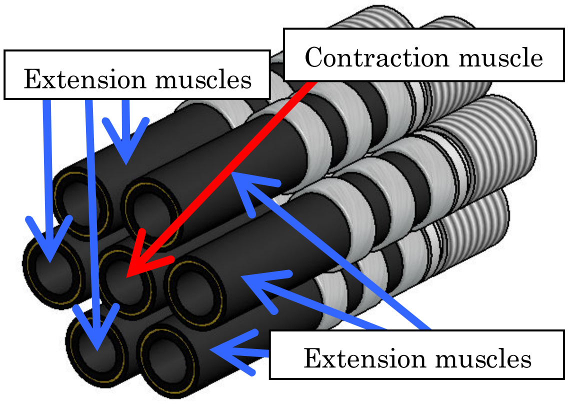

Figure 11 Design of muscles for a power soft mechanism bending in any directions

Figure 12 shows the initial state and driving state of the developed new mechanisms. The mechanism bends 160 [deg] when hydraulic pressure of 1.0 [MPa] is applied, we were able to confirm this mechanism bent in any direction.

We measured forces generated at the mechanism tip of the axial vertical direction as well as amount of bending. Those experimental results are shown in Figure 13.

(a) 0 [MPa]

(b) 1.0 [MPa]

Figure 12 Overview and driving experiments of power soft mechanisms bending in any directions combining one contraction and six extension muscles

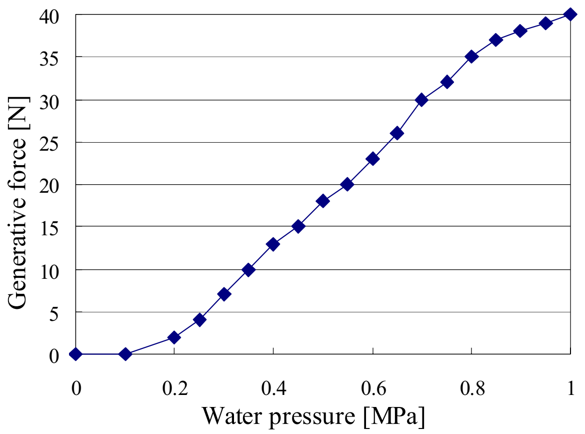

Figure 13 Experimental results of generative force to hydraulic pressure

The experimental result showed that applying hydraulic pressure of 1.0[MPa] causes the maximum force of 40 [N] at the mechanism top. However, the problem that the response was low because the difference of the generation power of the extension type and the contraction type was great remained.

CONCLUSION

We have developed power soft mechanisms bending in any direction by bundling artificial muscles of contraction and extension types. Through the experiments on such mechanisms, we have confirmed that they realize bending in any direction and high force in the bending direction. This design is based on concept of combining contraction/extension muscles.

In the future, we will establish the design method of a soft mechanism by the optimization of the arrangement of the artificial muscles using nonlinear finite element method with a different direction of the drive. The mechanism for the heavy loads with various shapes will be achieved by combining power soft mechanisms bending in any direction with constructing the hydraulic pressure control system.

REFERENCES

1. Schulte, H. F., “The Characteristics of the McKibben Artificial Muscle” The Application of External Power in Prosthetics and Orthetics, 1961, pp. 94-115
2. Lei Gao, Toshiro Noritsugu, “Development of Wearable Waist Power Assist Device Using Curved Pneumatic Artificial Rubber Muscle” The Japan Fluid Power System Society, Vol. 36, No. 6, pp. 143-151 (2005)
3. Mari Nakatani, Taro Nakamura “The development of super-thin-type pneumatic rubber artificial muscle and the application to the robot hand” ROBOMEC 2009, 2P1-A15(2009)
4. Toshio Fukuda, Kenichi Miyahara, “POSITION AND FORCE CONTROL OF MANIPULATORS WITH PNEUMATIC DRIVEN RUBBER ACTUATORS” Society of Biomechanisms (SOBIM). Vol. 10, 1990, pp. 271-280
5. Shinichi Yokota, Takehiro Komatsu, “A Study on a Flexible Hydraulic Actuator for Space Manipulators” Transactions of the Japan Society of Mechanical Engineers Series C, Vol. 57, No. 542, pp. 3222-3227, 1991.
6. Mori Mayuko, Suzumori Koichi, Takahashi Masayuki, Hosoya Takashi, “Very High Force Hydraulic McKibben Artificial Muscle with a p-Phenylene-2,6-benzobisoxazole Cord Sleeve” Advanced Robotics, Vol. 24, No. 1-2, 2010 , pp. 233-254(22)
7. Kazuhiro Iwata, Koichi Suzumori, “Development of high hydraulic pressure McKibben artificial muscle and its application to light spreader” ROBOMEC 2009, 2P1-A17(2009)
8. Kazuhiro Iwata , Koichi Suzumori , Shuichi Wakimoto “Combination of extending/ contracting artificial muscles realizing power soft mechanisms”, The 4th International Conference on Manufacturing, Machine Design and Tribology, D1-03, (2011)
9. Koichi Suzumori, Shoichi Iikura and Hirohisa Tanaka, “Applying A Flexible Microactuator to Robotic Mechanism” IEEE Control Systems, Vol. 12, No. 1, (Feb.1992), pp. 21-27

Proceedings of the 8th JFPS International
Symposium on Fluid Power, OKINAWA 2011
Oct. 25-28, 2011

2A1-1

DEVELOPMENT OF DIGITAL SERVO VALVE WITH SELF-HOLDING FUNCTION

Tetsuya AKAGI*, Shujiro DOHTA* and Hirofumi UEDA**

* Department of Intelligent Mechanical Engineering, Faculty of Engineering,
Okayama University of Science
1-1 Ridai-cho, Kita-ku, Okayama, 700-0005 Japan
(E-mail: akagi@are.ous.ac.jp)

** SMC Corporation
Akihabara UDX15F, 4-14-1,Sotokanda, Chiyoda-ku, Tokyo, 101-0021 Japan

ABSTRACT

Recently, power assisted nursing care systems have received much attention and active research. In such control system, an actuator and a control valve are mounted on the human body. In such designs, the size and weight of the valve become serious concerns. At the same time, the valve should be operated with lower energy consumption using limited electrical power. The purpose of our study is to develop a small-sized, lightweight and lower energy consumption control valve. In our previous study, a new type of fluid control valve with a self-holding function using a permanent magnetic ball in a check valve, a cylindrical magnet and two solenoids was also proposed and tested. In this study, a digital servo valve with self-holding function is proposed and tested. As a result, we can confirm that the tested digital servo valve can control output flow rate in both supply and exhaust.

KEY WORDS

Wearable Control Valve, Self-holding Function, Low Energy Consumption, Digital Servo Valve, Permanent Magnet

INTRODUCTION

Recently, force feedback devices in virtual reality and power assisted nursing care systems[1][2] have received much attention and active research. In such a control system, an actuator and a driving device such as a control valve are mounted on the human body[3]-[5]. When we consider the development of a wearable control valve that can drive pneumatic actuators to support the multi-degrees of freedom of human motion, the size and weight of the valve become serious concerns. The typical electromagnetic solenoid valve drives its spool using a larger solenoid to open the flow passage. The solenoid valves have a complex construction to keep a seal while the spool is moving. This complex construction makes its miniaturization and the fabrication of a low cost valve more difficult. The purpose of our study is to develop a small-sized and lightweight control valve that can be safe enough to mount on the human body at a lower cost. In our previous study, we proposed and tested a small-sized control valve that can be driven using a vibration motor[6]. In the valve, the orifice and the steel ball are inserted into a flexible tube. The vibration motor is set on the outer side of the flexible tube. When the vibration motor is driven, the tube is oscillated. It, then, gives a horizontal direction force to the ball. Then the inner ball starts to move and rotate along to the inner wall of the tube. When the vibration motor is stopped, the steel ball automatically moves toward the orifice as in a check valve. This method is more useful to supply a stable flow rate compared with other methods of opening the valve using vibration[7]-[9]. We had also investigated the output flow characteristics of the tested valve. In the next step for development of a wearable control valve, we should consider to develop a valve with lower electric power consumption. In order to decrease the electric power consumption of the valve, it is useful to reduce electric power to keep the valve open or close. Therefore we proposed and tested the valve with self-holding function that can hold the state of opening and closing with no electrical power[10]. In addition, if the valve can operate many flow lines, it can decrease even more the energy consumption per port. So, we improved the valve with self-holding function so that it can operate many directions of flow line, such as a supply port or an exhaust port, at the same time[11].

However, in the case to adjust the analog output flow rate of the tested valve, the tested valve must be driven by the PWM method. In this case, the electric power consumption of the tested valve increases according to the driving time. In addition, to decrease the electric power while the valve holds the inner pressure constant, it is better that the valve has a function of cutting off the output port without supply and exhaust. Therefore, in this paper, we propose and test a digital servo valve with self-holding function to control the output flow rate from the valve and cut off the output port in order to control the pressure in the pneumatic actuator.

FUNDAMENTAL CONCEPT

Figure 1 shows the fundamental concept of the proposed control valve. The figure shows the model of the tested valve using the check valve which is composed of a steel ball and an orifice. Figure 1 (a) and (b) illustrate the operational image of a typical electro magnetic on/off control valve and the proposed valve, respectively. In both valves, the supply pressure is applied from the lower inlets as shown in Fig.1. The steel ball is always applied by the upper force according to the differential pressure between the inlet and the outlet of the orifice and its sectional area. To open the typical on/off valve as shown in Fig.1 (a), it needs a larger longitudinal pulling force that can overcome the pushing force of the ball generated by the supplied pressure. Therefore, the typical electro-magnetic solenoid valve needs a relatively larger solenoid to open the valve surely, which prevents the miniaturization of the valve. In addition, in order to pull the steel ball while keeping the seal between the inside and the outside of the valve, it needs some complex mechanisms which prohibit reducing the cost of the valve. In the proposed valve as shown in Fig.1 (b), to increase the opening of the valve, we apply horizontal force to the steel ball. Using this method, it becomes possible to open the valve using a smaller force. When closing the valve, we stop applying the horizontal force and the inner steel ball automatically moves toward the orifice by the generated force of momentum of the flow, such as in a check valve. Then, the ball closes the orifice as in the stable condition of a check valve.

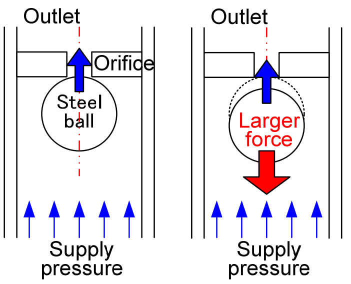

(a) Concept of typical valve

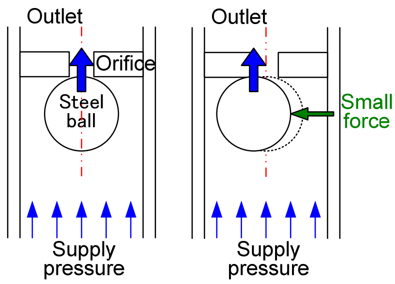

(b) Concept of proposed valve

Figure 1 Fundamental concept of the tested valve

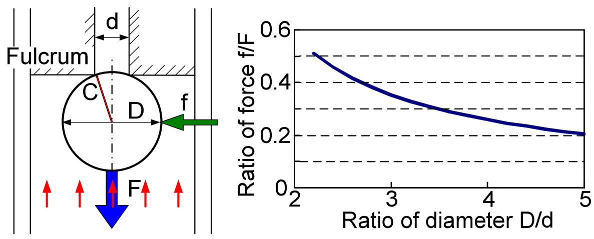

(a)Model of the valve (b) Theoretical force to open

Figure 2 Theoretical model and calculated result to open the valve

Figure 2 (a) shows the model of the proposed valve. The model shows a check valve that includes the steel boll with an outer diameter D and a narrow orifice with an inner diameter d. The longitudinal force F to open the valve is equal to the generated force by the pressure calculated by multiplication of the differential pressure and the sectional area of the orifice. In order to open the valve using the horizontal force f, the generated torque using the horizontal force at the point of the fulcrum C as shown in Fig.2 (a) must overcome the torque calculated by the longitudinal force and radius of the orifice (d/2). Therefore, the ratio of the force f to F to open the valve is given by the following equation.

$$\frac{f}{F} = \frac{1}{\sqrt{\left(\frac{D}{d}\right)^2 - 1}}$$

Figure 2 (b) shows the relation between the ratio of the force f/F and the ratio of diameter D/d calculated by Eq. (1). From Fig.2 (b), the required horizontal force f to open the valve is about 1/4 compared with the longitudinal force in the case using diameter D of 2 mm and diameter d of 0.5 mm. This means that the proposed method is very effective to open the valve.

CONTROL VALVE WITH SELF-HOLDING FUNCTION

Construction and operating principle

For such a valve mentioned above, the one that consumes electric power only when it changes states, such as opened or closed, might be ideal. Therefore, we aimed to develop a valve using permanent magnetic force in order to open or close the valve. Therefore, we proposed and developed a valve with self-holding function without any electric power in holding the state.

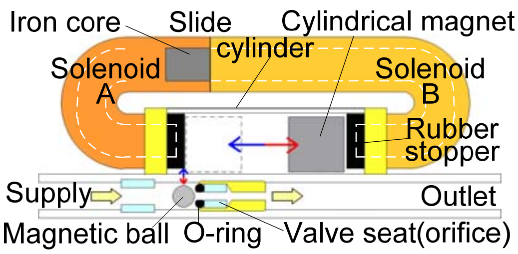

(a) Schematic diagram of the tested valve

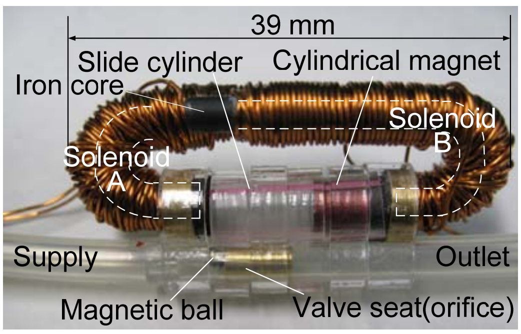

(b) Photograph of the tested valve

Figure 3 Construction of the valve with self-holding function

Figure 3 (a) and (b) show the schematic diagram and a photograph of the tested valve, respectively. The valve consists of a flexible tube whose inner diameter is 2.5 mm and outer diameter is 4 mm, a brass valve seat (orifice) with an inner diameter of 0.7 mm, a permanent magnetic ball with an outer diameter of 2 mm, a cylindrical permanent magnet with an outer diameter of 5 mm and a length of 5 mm, a shin plastic cylinder (straw) with an inner diameter of 5 mm and two handmade solenoids. The valve seat and the magnetic ball are inserted into the flexible tube in order to make a check valve. Each handmade solenoid consists of a J-shaped iron center core with an outer diameter of 3 mm and 250 turns of coil made of enameled wire with an outer diameter of 0.35 mm and the internal resistance of 1.2 ohms. The end of each iron core has a shin rubber shock absorber with a thickness of about 1mm. The cylindrical magnet is inserted into the thin plastic cylinder so that the magnet can slide along the cylinder with a stroke of 14 mm. They are connected to both ends of the thin plastic cylinder and set on the outer side of the flexible tube by acrylic connectors. The valve including the two solenoids has a length of 39 mm, a width of 11mm and a height of 18mm. The mass of the tested valve is 12.7 g.

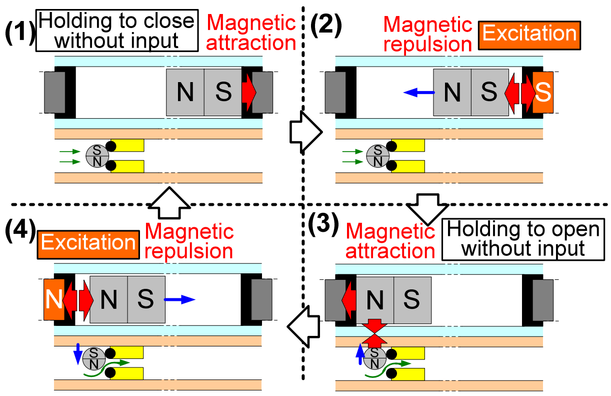

Figure 4 Operating principle of the valve with self-holding function

Figure 4 shows the operating principle of the tested valve. The operating principle of the valve is as follows: In the case of closing the valve as shown in Fig.4 (1), the iron core of solenoid A and the cylindrical permanent magnet are naturally attracted to each other. Then the magnetic ball makes the valve seat (orifice) closed by the generated force of momentum of the flow, as in a check valve. In this condition, the valve holds the state of closing with no electrical input by the permanent magnetic force. When the electric input is applied to the solenoid B for about 0.01 seconds as shown in Fig.4 (2), the magnetic repulsive force is generated between the iron core and the cylindrical magnet. Then, the cylindrical magnet moves toward the end of solenoid A, and they are attracted to each other by the permanent magnetic force as shown in Fig.4 (3). In the condition as shown in Fig.4 (3), the cylindrical magnet also attracts the magnetic ball so as to move the vertical direction of the tube. Then, the valve opens and holds it open state with no electrical input. In the same manner of opening the valve, when the electrical input is applied temporarily to the opposite side solenoid A, the cylindrical magnet moves toward the iron core of solenoid B, and they are attracted to each other. After the cylindrical magnet moves by the repulsive force as shown in Fig.4 (4), the magnetic ball automatically moves toward the center of the valve seat (orifice) by the generated force of momentum of the flow. Using this method, the valve can hold both states of closing and opening with no electrical power. It means that the valve has an excellent characteristics of low energy consumption. In addition, using the repulsive force instead of pulling force between the cylindrical magnet and the solenoids in order to slide the cylindrical magnet, the electrical power of the tested valve becomes lower. It is caused by the fact that the magnetic force becomes larger in reverse proportion to the distance between both objects.

Characteristics of the valve

In order to confirm the performance of the tested valve, such as the lower electrical input for opening or closing, we investigated the dynamic response of the valve by alternately changing states. Figure 5 shows the transient response of the input current of solenoid A and B, and output pressure of the valve, respectively. In the experiment, the valve is connected to a chamber with volume of about 30 cc that has an exhaust port with a constant sectional area.

The input current was calculated using the internal resistance of 1.2 ohms and the impulse input voltage of 5 volts. The electrical input voltage was applied for 0.008 seconds to the solenoid only when the valve began to open or close. Then, as a result of the experiment for static characteristics of the valve, the maximum output flow rate is 13.4 liters per minute for the supply pressure of 500 kPa. The value is almost the same as the output flow rate of the small-sized commercially available on/off valve. From the transient response of the output pressure in Fig.4, it can be seen that the valve can be held opened or closed after applying momentary electrical input. We also find that the dead time for opening the valve is 0.021 seconds, the dead time for closing is 0.016 seconds. The dead time of the valve is related to the moving speed of the cylindrical magnet. The difference of the dead time between the cases of opening and closing is caused by the time the cylindrical magnet moves and reaches point of attracting or repulsion to the magnetic ball. From the geometric arrangement between the magnetic ball and the cylindrical magnet as shown in Fig.4, it is easy to recognize that the time delay for closing is faster than that for opening. From Fig.5, it can be also seen that the induced current in the non-operating side solenoid occurs when the opposite solenoid is driven.

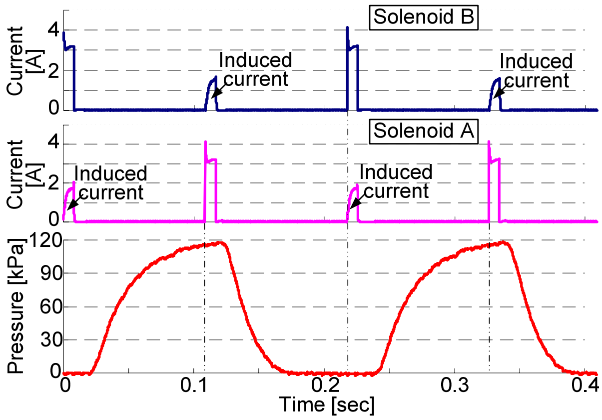

Figure 5 Transient response of input current and output pressure using the valve

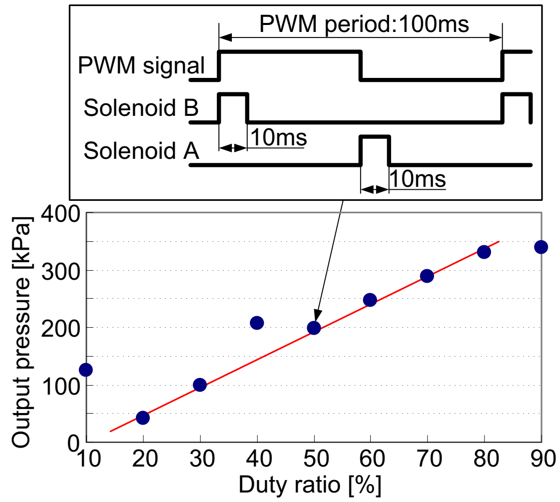

Figure 6 Relation between duty ratio of PWM signal input and output pressure of the valve

Figure 6 shows the relation between the duty ratio and the output pressure of the valve with self-holding function. In the experiment, the valve is also connected with a chamber with a volume of about 30 cc that has an exhaust port with a constant sectional area. The period of input PWM signal is selected as 0.1 seconds by considering the response time of the valve as shown in Fig. 5. In the tested valve, the time for driving the current of each solenoid is 0.01 seconds

(10ms). For example, the PWM signal with a duty ratio of 50 % is made as follows: In the beginning of the PWM period, first, solenoid A is driven for 0.01 seconds. After that, both solenoid A and B are stopped to apply the input voltage for 0.04 seconds. Next, solenoid B is driven for 0.01 seconds. At last, both solenoids are stopped for 0.04 seconds. By repeating these operations, we can realize the PWM input signal for the tested valve with self-holding function. The signal is created by using a micro-computer (Renesas Co. Ltd. H8/3664). In the case of making the other duty ratio of the PWM signal, the stopping time of both solenoids is changed. In other words, the electric power consumption does not change even if the duty ratio is changed in the same PWM period. In addition, the longer the PWM period is used, the lower electric power consumption can be realized. From Fig. 6, we can see that the output pressure of the valve is almost proportional to the duty ratio of PWM signal. It means that the tested valve has relatively good dynamics, so much so that it can be used as a pressure control valve even if the valve has a self-holding function.

DIGITAL SERVO VALVE WITH SELF-HOLDING FUNCTION

Construction of digital servo valve

In order to drive a control valve for a long time using a limited battery supply, the valve with the self-holding function mentioned above is one effective solution. However, in the case to adjust the analog output flow rate of the tested valve, the tested valve must be driven by the PWM method. In this case, the electric power consumption of the tested valve can not be ignored according to the driving time. In addition, in the case of controlling a wearable actuator such as a pneumatic artificial muscle, the pressure control valves that can hold constant pressure in the actuator are required. To decrease the electric power while the valve holds the inner pressure constant, it is better that the valve has a function of cutting off the output port without supply and exhaust. Therefore, we aim to develop a digital servo control valve with self-holding function that can consume less electric power to adjust the output flow rate and cut off the output port. Figure 7 shows the construction of the digital servo valve that we proposed and tested. The valve consists of a servo motor (Kondo Co. Ltd., KRS-2352 ICS, speed: 0.14s/60deg.), a disk with two cylindrical magnets and six check valves that each consists of an orifice in the flexible tube with an inner diameter of 2.5 mm and a steel ball or a magnetic ball with outer diameter of 2mm. The center of the disk is connected with the shaft of the motor. The eight check valves are set on parallel to the surface of the disk. The rotational angle of the disk is easily controlled by a micro-computer (Renesas Co. Ltd., H8/3664) with PWM timer function. The mass of the tested valve is about 80 g, and the valve has a length of 41 mm, a width of 55 mm and a height of 61 mm.

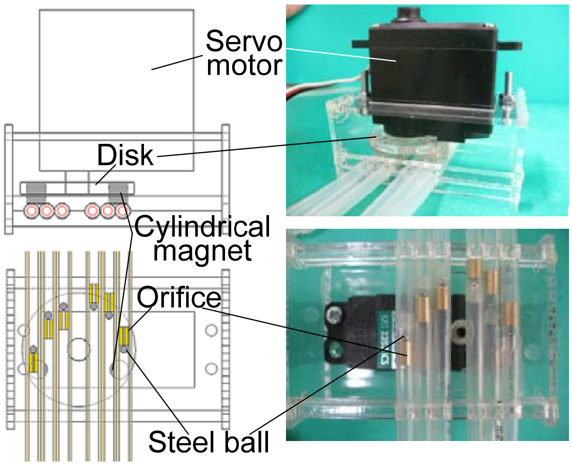

Figure 7 Schematic diagram and view of the digital servo valve with self-holding function

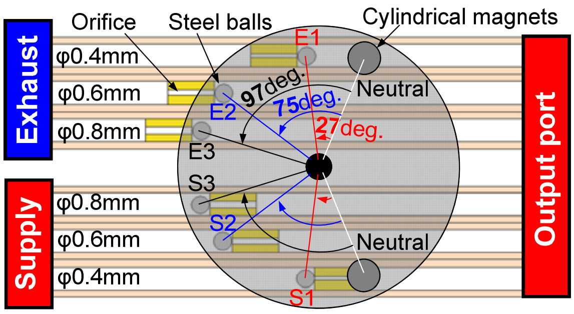

Figure 8 Schematic diagram and location of the elements in the digital servo valve with self-holding function

Figure 8 shows the schematic diagram and the location of the elements in the digital servo valve with self-holding function. The two cylindrical magnets are located at the point of the center angle of 120 degrees and radius of 12 mm from the center of the disk. In the neutral position, each cylindrical magnet is positioned at an angle of 60 degrees to the longitudinal direction of the check valve. The three check valves are used as exhaust ports. The other three check valves are used as supply ports. The tube end of all check valves are connected to each other as an output port. The other three ends of the check valves for supply ports are connected with a tank with a high pressure of 500 kPa. The others are not connected to anything. So, the direction of natural flow of the check valves between the supply ports and exhaust ports are reversed. In both supply and exhaust ports, the steel balls or the magnetic balls in the check valves are set at specific angle on the orbit so that the cylindrical magnet can move as shown in Fig.8. Each center angle from the cylindrical magnet at the neutral position to the ball is 27, 75 and 97 degrees, and each inner diameter of the orifices is 0.4, 0.6 and 0.8 mm, respectively. The value of the inner diameter in each orifice is selected so that the flow rate through the orifice becomes about two or three times as large as the lowest flow rate through the narrowest orifice in the valve. Each location of the balls is selected so as not to be attracted to the other balls by the cylindrical magnet while the only one is attracted. It means that the cylindrical magnet can attract each ball independently. In the case of the check valve with the inner diameter of 0.8 mm, the magnetic ball is used instead of the steel ball, because a larger magnetic force is required to open the check valve.

Operating principle of digital servo valve

Figure 9 shows the operating principle of the tested digital servo valve. The valve has seven states. One is the neutral state in which the valve can close the output port without supply and exhaust as shown in Fig.9 (a). The others are three exhaust stages as shown in Fig.9 (b) to (d) and three supply stages as shown in Fig.9 (e) to (g). Each figure in Fig.9 shows the location of two cylindrical magnets in the disk for each state of the valve, respectively. The operating principle of the valve is as follows. First, two cylindrical magnets stay at the neutral position as shown in Fig.9 (a). To increase the output flow rate from the servo valve, the servo motor rotates the disk from the neutral position to 27 degrees clockwise. The lower cylindrical magnet attracts the ball in the check valve. Then, the check valve (S1) as shown in Fig.12 (e) opens. By rotating the disk an additional 38 degrees (75 degrees from the neutral position) clockwise using the servo motor, the check valve (S2) as shown in Fig.12 (f) opens. At the same time, the ball in the check valve (S1) loses the attracting magnetic force. Then, the ball automatically moves toward the orifice by the momentum of the flow and closes the check valve (S1) as shown in Fig.9 (f). Then, the larger flow rate at the output port can be obtained according to the sectional area change from S1 to S2. In the same manner of increasing the output flow rate from the valve, the output flow rate can be decreased by rotating the disk counterclockwise. In the case of exhaust, the upper cylindrical magnet as shown in Fig.8 is used. The other cylindrical magnet does not act as shown in Fig. 9. The tested digital servo valve can realize seven states that include holding the pressure and three types of output flow rate in both conditions of supply and exhaust. In addition, while the disk rotates between two balls gives the overlap function to the valve. It means that this time delay prevents opening two check valves at the same time. The geometric configuration of check valves with various sizes of orifices as shown in Fig.8 introduces the proportional stepwise change of the output flow rate according to the rotational angle of the disk in both supply and exhaust. The neutral position is used to hold the pressure in the output port constant by cutting off both the supply and exhaust ports. The position of the cylindrical magnets can be held at a specific position without electrical input by turning off both the electrical supply voltage and the duty signal to the servo motor at the same time. It means that the tested valve can control the flow rate of both supply and exhaust in digital control with lower energy consumption.

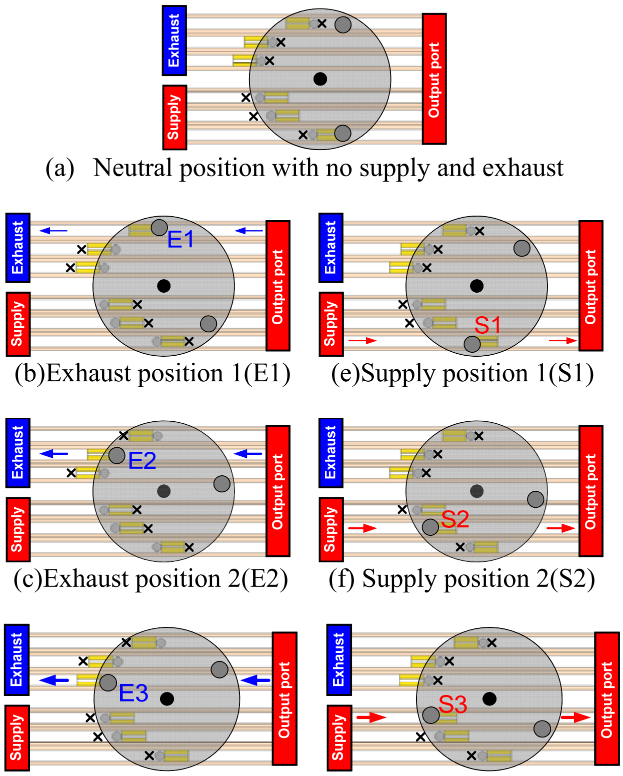

(a) Neutral position with no supply and exhaust

(b)Exhaust position 1(E1) (e)Supply position 1(S1)

(c)Exhaust position 2(E2) (f) Supply position 2(S2)

(d)Exhaust position 3(E3) (g) Supply position 3(S3)

Figure 9 Schematic diagram and view of the digital servo valve with self-holding function

Characteristics of digital servo valve

Figure 10 shows the relation between the output flow rate from the valve and the valve state. In Fig.10, each character E1,E2 or E3 refers to the active check valves as shown in Fig.9. In the experiment, the output flow rate was measured by a digital flow meter (SMC Co. Ltd., PF2A750-01-27). In the measurement of the supply flow rate, the supply pressure of 500 kPa is applied at the supply port in the condition that the output port is not connected with anything, that is, to use the output port as an exhaust port. The flow rate from the output port to the atmosphere is measured by the digital flow meter. In the case of measuring the flow rate for exhaust, the output port is pressurized to 500 kPa in the condition that the supply ports cut off the output port of the valve. From Fig.10, it can be seen that the relation between the output flow rate from the valve and the valve state is proportional in both cases of supply and exhaust states.

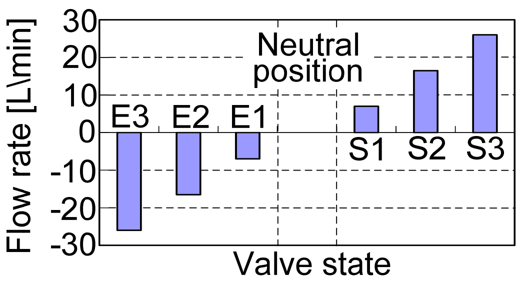

Figure 10 Relation between the valve states and output flow rate from the tested valve

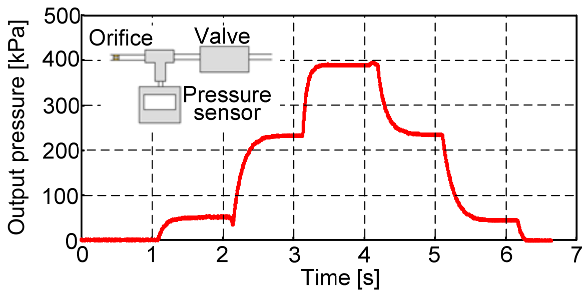

Figure 11 Transient response of the output pressure in the output port of the valve for stepwise change of the valve states

Figure 11 shows the transient response of the output pressure in the output port of the valve for stepwise valve state change, that is, a stepwise angular change of the disk. In the experiment, the output port is released to the atmosphere through the orifice with the inner diameter of 0.7 mm. The pressure in the output port was measured by a pressure sensor (Keyence Co. Ltd., AP-33). The valve state was changed according to the order of the neutral position, S1, S2, S3, S2, S1 and the neutral position every 1 second. From the pressure change in Fig.11, we can confirm that the tested valve can control the output flow rate according to the valve state. It can be also seen that the valve can adjust the flow rate in both cases of increasing and decreasing the output flow rate smoothly. The time delay of the valve for stepwise change is from 0.063 to 0.083 seconds. These values depend on the rotational speed of the servo motor and the distance between the two check valves. Therefore, it is possible to improve the dynamics of the valve by changing the geometric configuration of the check valves and using a high speed servo motor.

CONCLUSIONS

This study, aimed at improving the performance of the small-sized wearable control valve that can be operated with lower energy consumption, can be summarized as follows.

1) We proposed and tested the digital servo valve with self-holding function using a servo motor, a disk with two cylindrical magnets and check valves with steel balls or magnetic balls. The operating principle of the digital servo valve was introduced. The simple control system of the valve using a micro-computer was produced.
2) We investigated the performance of the digital servo valve. As a result, we can confirm that the tested valve can change the output flow rate in seven stages that they include holding the pressure and three types of output flow rate in both conditions of supply and exhaust.
3) As for the dynamics of the digital servo valve, it can be also seen that the valve can adjust the flow rate in both cases of increasing and decreasing the output flow rate smoothly. The time delay of the valve for stepwise change is from 0.063 to 0.083 seconds.

ACKNOWLEDGMENT

This study was supported by the Ministry of Education, Culture, Sports, Science and Technology of Japan through a Financial Assistance Program for Social Collaborative Research(2006-2010) and a Grant-in-Aid for Young Science (B) (Subject No. 22760201). It was also supported by a research-aid fund from SMC Co. Ltd. in Japan.

REFERENCES

1.Ishii,M., Yamamoto,K. and Hyodo,K., "Stand- Alone Wearable Power Assist Suit -Development and Availability-", Journal of Robotics and Mehatronics, Vol.17, No.5, 2005, pp.575-583.
2. Nagata,Y. ed., "Soft Actuators -Forefront of Develop ment-", NTS Ltd., 2004, pp.291- 335(in Japanese).
3. Akagi,T. and Dohta,S., "Development of a Rodless Type Flexible Pneumatic Cylinder and Its Application", Transaction of JSME, Series C, Vol.73, No.731,2007, pp.2108-2114.
4. Akagi,T. and Dohta,S., "Development of McKibben

Artifical Muscle with a Long Stroke Motion", Transaction of JSME, Series C, Vol.73, No.735, 2007, pp.2996-3002.
5. Akagi,T. and Dohta,S., "Development of Wearable Pneumatic Actuator and Multiport Pressure Control Valve", Journal of Robotics and Mechatronics, Vol.17, No.5, 2005, pp.529-536.
6. Akagi,T., Dohta,S. and Katayama,S., "Development of Small-sized Flexible Pneumatic Valve Using Vibration Motor and Its Application for Wearable Actuator", Proc. 15th. Int. Conf. on Mechatronics and Marin Vision in Practice, 2008, pp.487-491.
7. Uehara,S. and Hirai,S., "Unconstrained Vibrational Pneumatic Valves for Miniaturized Proportional Control Devices", Proceedings of 9th International Conference on Mechatronics Technology, 2005.
8. Jing,S., Kitagawa,A., Lui,C. and Tsukagoshi,H., "A Study on a Sound Operated Valve for a Wearable Pneumatic System : 1st Report: Development of a Pilot Valve a Sound Operated Direction Control Valve", Journal of the Japan Fluid Power System Society, Vol.39, No.3, 2008, pp.54-60(in Japanese).
9. Nishioka.Y, Suzumori,K., Kanda,T. and Wakimoto,S., "A New Pneumatic Control System using Multiplex Pneumatic Transmission", Proc. of 7th. JFPS International Symposium on Fluid Power Toyama 2008 ,2008, pp.439-442.
10. Akagi,T. Dohta,S. and Ueda,H., "Development of Small-sized Fluid Control Valve with Self-holding Function Using Permanent Magnet", Journal of System Design and Dynamics, Vol.4, No.4, 2010, pp.552-563.
11. Ueda,H., Akagi,T. and Dohta,S., "Development of 2-Position 3-Port Control Valve with Self-holding Function", Proceedings of SICE Annual Conference 2010, 2010, pp.1239-1243.

Proceedings of the 8th JFPS International
Symposium on Fluid Power, OKINAWA 2011
Oct. 25-28, 2011

2A1-2

REPEATED POSITIONING OF A PNEUMATIC RODLESS CYLINDER USING PROXIMITY SWITCHES

Mohammad TAUFIQ MUSTAFFA*, Hidetoshi OHUCHI*

*Interdisciplinary Graduate School of Medical and Engineering
University of Yamanashi
4-3-11 Takeda, Kofu, Yamanashi, 400-8511 Japan
(E-mail: g09dm004@yamanashi.ac.jp, ohuchi@yamanashi.ac.jp)

ABSTRACT

Applications requiring accurate position control of cylinders are in increasing use in industry. High speed, reliability and significantly low cost of the pneumatic cylinder are the characteristics more often required to all components in the automation field. In this research, a technique of repeated positioning of a pneumatic rodless cylinder is evaluated through experiment and simulation. The basic control algorism is a sequential on-off action of the air valves. In this scheme, deviation of stop position can be reduced by braking at a certain velocity which can affect the positioning performance. It has been experimentally suggested that there is an optimal velocity when the braking should be started to apply. The aim of this paper is to validate through numerical simulation that the optimal velocity exists and it is strongly related to the frictional fluctuation and the braking characteristics.

KEY WORDS

Pneumatics, Rodless cylinder, Positioning, Braking, Proximity switch

INTRODUCTION

This paper deals with a technique of repeated positioning of a long stroke pneumatic cylinder. This system is suitable for a long stroke cylinder when the desired intermediate stop positions are fixed and the same operation may be repeated as in automatic production lines.

The design of an air servo system is not intended. Without constructing a feedback loop, it is possible to maintain the simplicity of the air positioning system.

The basic control algorism is a sequential on-off action of directional air valves. There is a fact that a clear relationship exists between the slider velocity and its braking distance with a strong braking [1]. For one desired position, three proximity switches are installed to detect the slider passing as well as its velocity. After passing the first switch the slider is weakly decelerated, and after passing the second switch it is strongly decelerated. The third switch is installed to detect the final positioning result which is used in the next run by a learning scheme. Another switch is also installed to confirm the slider return to the starting point.

As a matter of course, the positioning accuracy depends strongly on the frictional condition [2-5]. There is another factor such as the load or the setting direction of the cylinder. In the experiment, the cylinder was set in horizontal direction on a table in the laboratory.

A high positioning accuracy cannot be expected without a feedback loop. Our final goal is that the stop positions converges to the desired region in several operations and maintain the accuracy in each time of operations.

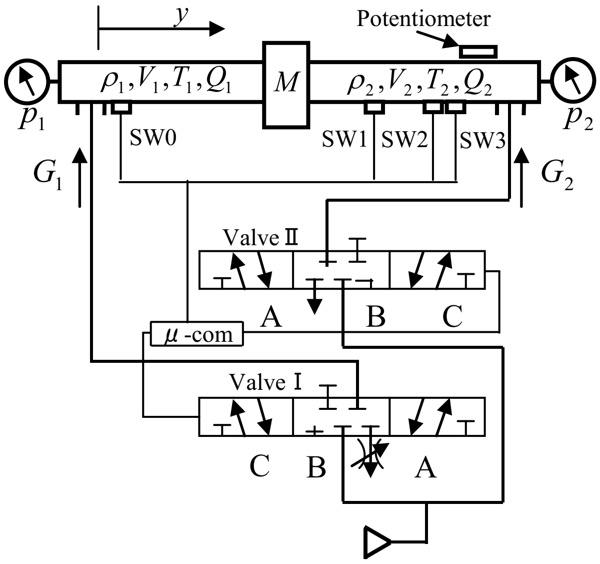

Figure 1 Experimental circuit

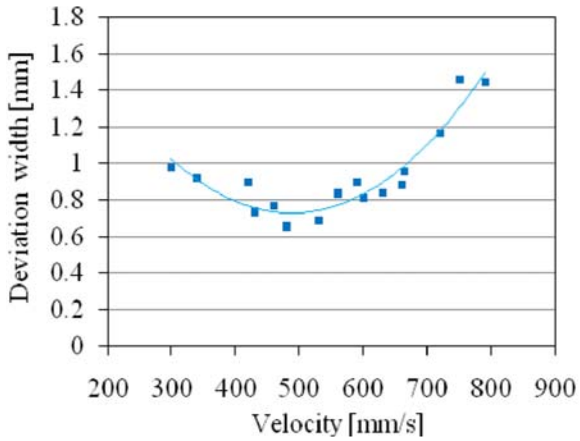

Figure 2 Optimal velocity for starting strong braking

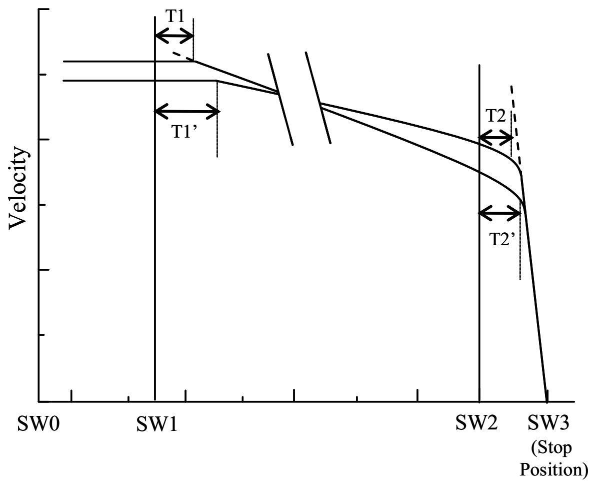

Figure 3 Sequence of two-stage braking method

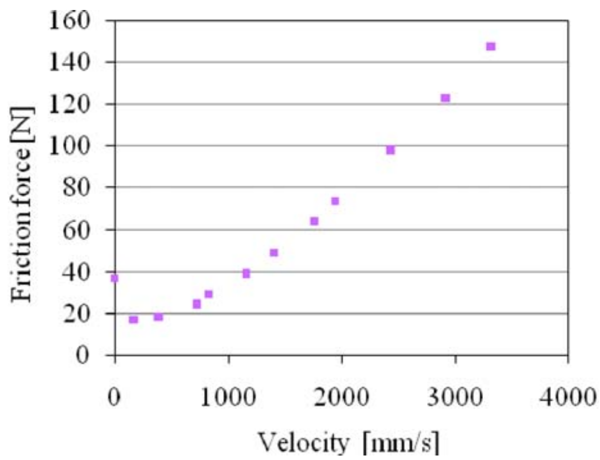

Figure 4 Frictional Force

EXPERIMENTAL SETUP

The outline of experimental apparatus is shown in Fig. 1. The cylinder is installed horizontally on a table in the laboratory. The cylinder is of a rodless band type and has a stroke of 2000mm in length and a bore of 25mm in diameter. Four proximity switches are installed. SW1, SW2, SW3 are used for motion control, and SW0 is used only for detecting the return of the slider to the starting point. A potentiometer with length of 50(mm) is installed near the SW2 and SW3. Therefore, the potentiometer output can only be recorded when the slider approaches near SW2.

Optimal velocity

In our research, deviation of stop position can be reduced by braking at a certain velocity which can affect the positioning performance. It is experimentally proven that there is an optimal velocity when the braking should be started to apply. In our cylinder system, deviation width of stop position becomes much smaller if the strong braking started at slider velocity of 500(mm/s) as shown in Fig.2. One plot indicates deviation width of stop position for 30 times of operation. Thus, a method of braking is suggested in this research to make the slider stop by braking at about 500(mm/s) in order to obtain better positioning accuracy in each time of operations.

Sequence of two-stage braking method

For the cylinder positioning, we propose a two-stage braking method as shown in Fig.3. In this method, a weak braking and a strong braking are applied in sequence. At the first stage, a weak braking is applied, and a strong braking is applied in the second stage. To apply the weak braking, the valve I is kept on connecting to supply port and only the valve II is closed. To apply the strong braking, the valve I is still kept on connecting to the supply port and the valve II is switched to the supply port. In order to obtain slider's velocity of 500(mm/s) at the time it passes through SW2, timer T1 is used to adjust the timing for the weak breaking. The purpose of Timer T2 is for fine adjustment before applying the strong braking. To perform this sequence smoothly, two 3-position 5-port valves are utilized for keeping the air flows as desired. Valve operations are controlled by a micro-computer.

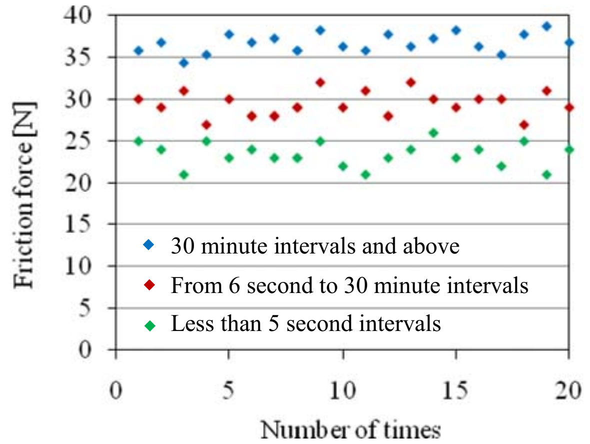

Figure 5 Static forces in different time intervals

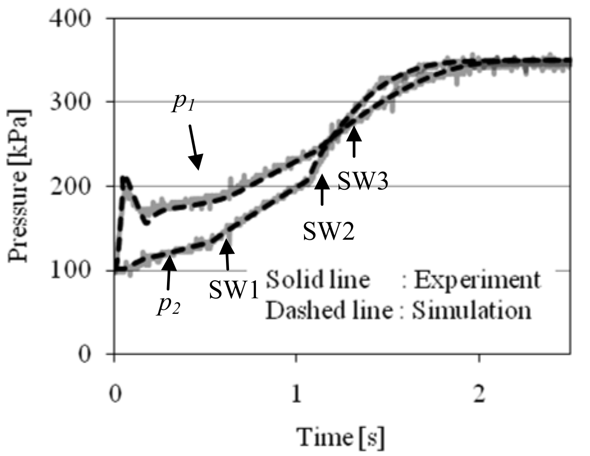

Figure 6 Air pressure changes in chambers

Frictional condition

In general, the friction force depends on the velocity due to the surface mechanics and the lubricants between the two surfaces. Fig.4 shows a result of an experiment performed to measure the friction force as the slider moving in varying velocity. The force was measured by the set air pressure that will be pushing against the piston multiplied by the contact area of the piston. It shows that the friction force may decrease continuously from the static friction level to Coulomb friction level. Afterward, the force increase with increased sliding velocity due to viscous friction. Measured maximum static force F_0, Coulomb force F_1, and viscous force were 37(N), 18(N) and 10(Ns/m), respectively.

Fig.5 shows friction force required to move the cylinder under different time intervals in 20 times of operations. The friction force was measured experimentally as same as stated above. This indicates that with a time interval in between operation there is a range of friction force due to the different lubrication conditions between the sliding surfaces. Repeated positioning experiments were conducted with less than 5 second gap between two operations. The aim for static force measurements is to find the possibility of friction fluctuation during operation.

NOMENCLATURE

p : Pressure [Pa]
y : Displacement of the slider [m]
y_{10}: Equivalent length of upstream at starting point [m]
R : Gas constant [J/(kg·K)]
M : Mass of the slider [kg]
V : Volume of chamber [m^3]
T : Temperature [K]
T_a : Atmospheric temperature [K]
A : Area of piston [m^2]
c_v : Isometric specific heat [J/(kg·K)]
G : Mass flow rate [kg/s]
h : Heat transfer coefficient [W/(m^2·K)]
κ : Adiabatic index [—]
ρ : Density [kg/m^3]
B : Viscous resistance coefficient[Ns/m]
Q : Heat flow [W]
S_h: Heat transfer area [m^2]
s : effective sectional area of flow passage [m^2]
$D\left(\dot{y}\right)$: Friction force [N]

PLANT MODEL

In order to model an approximate dynamics of the pneumatic cylinder, the aerodynamic and thermodynamic analysis of the system is presented. The relationship among the mass flow rate of air, the change of pressure, the temperature and the volume in chamber can be found as below. The equations shown below are only for upstream chamber.

$$\frac{dp_1}{dt} = \frac{RT_1}{V_1}G_1 + \frac{p_1}{T_1}\frac{dT_1}{dt} - \frac{p_1}{y + y_{10}}\frac{dy}{dt} \qquad (1)$$

$$c_v \rho_1 V_1 \frac{dT_1}{dt} = RT_1 G_1 - p_1 \frac{dV_1}{dt} + Q_1 \qquad (2)$$

where 1 and 2 are subscripts denoting the upstream and downstream chambers. Heat transfer equation can be formulated as

$$Q_1 = hS_{h1}(T_a - T_1) \qquad (3)$$

The equation of motion for the system can be represented as follows,

$$M\frac{d^2y}{dt^2}+B\frac{dy}{dt}+D\left(\dot{y}\right)=A\left(p_1-p_2\right) \quad (4)$$

Further, p_d, p_u denote the downstream and upstream pressure respectively.

If $\quad 0.528 \le p_d / p_u \le 1$

$$G = sp_u\sqrt{\frac{2\kappa}{RT_u(\kappa-1)}\left(z^{\frac{2}{\kappa}}-z^{\frac{\kappa+1}{\kappa}}\right)} \quad (5)$$

If $\quad 0 \le p_d / p_u < 0.528$

$$G = sp_u\sqrt{\frac{2\kappa}{RT_u(\kappa+1)}\left(\frac{2}{\kappa+1}\right)^{\frac{2}{\kappa-1}}} \quad (6)$$

In this friction model, $D\left(\dot{y}\right)$ is a function where

$$D\left(\dot{y}\right)=\begin{cases} F_0 & \text{if } \dot{y}=0 \text{ (mm/s)} \\ F_1 & \text{if } \dot{y}>200 \text{ (mm/s)} \end{cases} \quad (7)$$

if $\dot{y} \ge 0$. For $0 < \dot{y} \le 200$ (mm/s), $D\left(\dot{y}\right)$ decreases from F_0 to F_1 in a straight line.

EXPERIMENTAL RESULT AND NUMERICAL SIMULATION

The main objectives of the simulation are to validate the existence of optimal velocity and to know whether the characteristic is also common in pneumatic cylinder systems. Fig.6 indicates an example of the experimental result and numerical simulation of pressure in the downstream and upstream chamber. From the starting point at SW0, pressure in the upstream chamber, p_1 increases continuously until it overcomes the maximum static friction. The slider starts moving and it decelerated when passing through SW1. The strong braking applied at SW2 and the slider stops at SW3.

Since friction has a very strong influence on the performance and behavior of mechanical systems, prediction of friction phenomena are important in all simulations and analyses. Most sliding contacts are lubricated during operation. The friction force will then vary with the sliding velocity depending on the extent to which the interacting contact surfaces are running under boundary, mixed, or full film lubrication [6].

The behaviors of friction models during the strong breaking are presented in Fig. 7. For the operation at zero fluctuation of friction along the stroke with F_0=37(N) and F_1=18(N), the stop position is taken as a reference point. When friction fluctuates the deviation width of stop position is defined as a distance from the reference point. Fig.7(a) shows deviation width for varying velocity when F_1 is decreased 3%. The braking distance of stop position increases as the strong braking applied at higher velocity, which results deviation width becomes wider.

For 7(b), a large fluctuation is considered to occur as the velocity is decreased, where the condition of static friction force estimated to decrease up to 50%. Fig.5 is a factor to be taken into consideration of decreasing

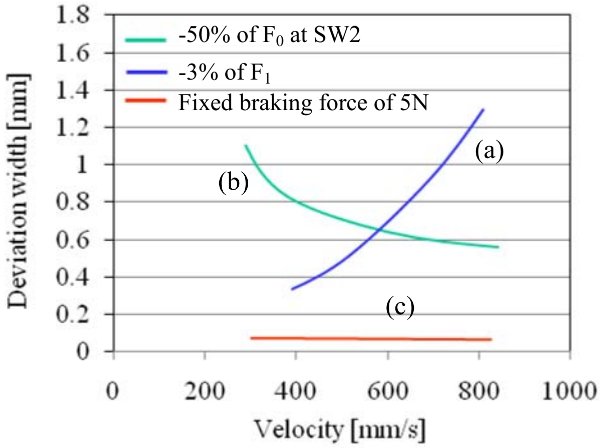

Figure 7 Deviation width of stop position (simulation)

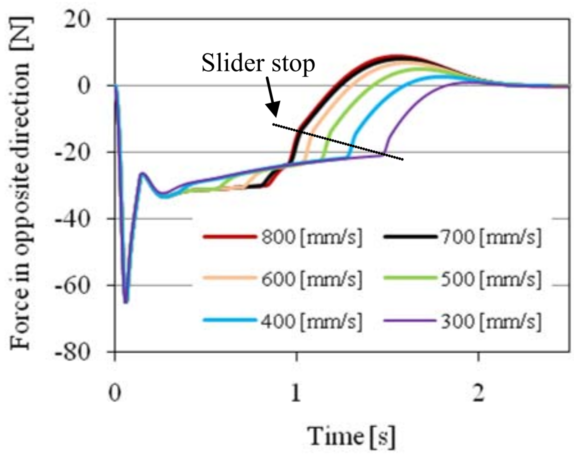

Figure 8 Force in opposite direction, A(p_2-p_1) (simulation)

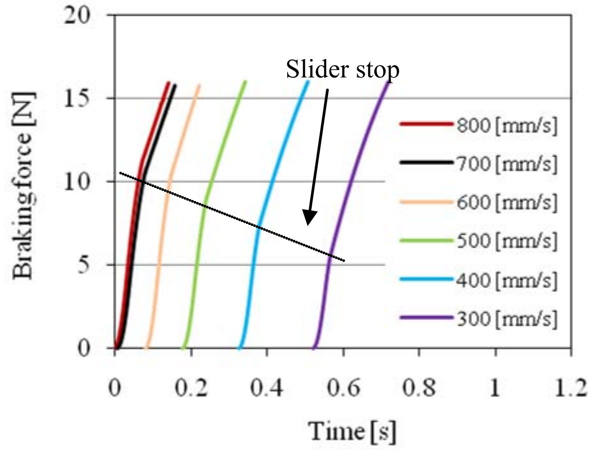

Figure 9 Force required to stop slider after strong braking applied (simulation)

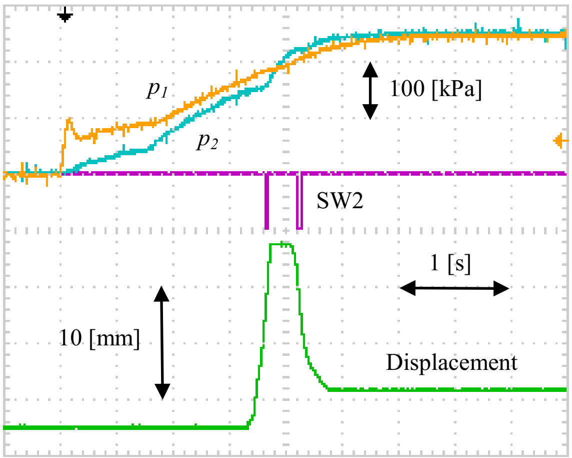

Figure 10 Sudden backward movement of slider

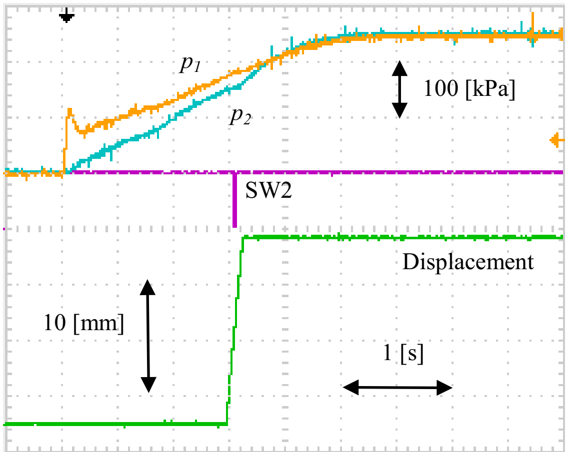

Figure 11 After tube length adjusted

percentage. Opposite to 7(a), as the sliding velocity becomes slower, the deviation width becomes larger. The reason that the deviation width becomes smaller on strong braking at higher velocity is difficult to be explained with only Fig.7, because the sliding velocity certainly will drop to low velocity before stopping.

Fig.8 indicates the simulated value of the opposite force, $A(p_2\text{-}p_1)$ during the sliding. It takes more than 60(N) to overcome the maximum static force. The opposite force is becomes higher as the slider moving due to the increased p_2. After about one second, the force increases rapidly, which is the time when the strong braking is applied. After that, p_2 increases rapidly than p_1 and the pressure difference between both chambers becomes smaller.

Fig.9 shows the re-arranged opposite force shown in Fig.8 from the moment the strong braking applied at SW2 for varying velocity. At that time, the braking force is not sufficient to stop the slider immediately. It takes time for the pressure difference to be increased to the level of strong braking. This may be the reason that the stop positions fluctuate in the low velocity region.

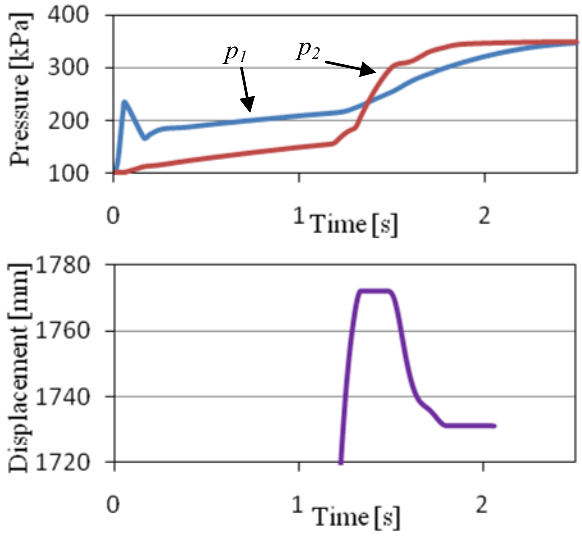

Figure 12 Simulation when SW2 set at 1760(mm)

To validate the statement, another simulation is conducted by increasing 5N of braking force immediately at SW2 for varying velocity. The result is shown in Fig.7(c). Deviation widths for any velocity when the constant strong braking applied are almost the same and small. It can be concluded that there are two reasons for the wide deviation width in the low velocity region. The first is that the friction force fluctuates in wide range and the second is that it takes time for the braking force to be increased.

Sudden backward movement of slider

Although the cylinder is 2000(mm) of length, the stop position is not able to be fixed on all any desired position. In the experiment, SW2 cannot be located on more than 1.3(m) position. Fig. 10 shows the air pressures for chambers, SW2 signal, and the slider displacement when SW2 was located at 1760(mm). Fig.10 shows p_2 increases rapidly compared to p_1 right after the slider passed through SW2. In a moment, p_2 becomes higher than p_1 and the slider made a stop afterward. The pressure difference becomes bigger than the friction force at that moment, which results in pushing the slider backward.

It is assumed that the occurrence of this phenomenon is because of the unbalance pressure between both chambers when the strong braking applied. To tackle the problem in easiest way, the tube lengths of both sides are adjusted. The tube length adjustment results in not only the change of tube resistance but also the change of chamber volume. The length adjustments for upstream and downstream before and after the adjustment are 4.4(m)→1.8(m), 1.75(m)→10.5(m) respectively. The result after adjustment has been made is shown in Fig.11. The problem of backward movement of the slider was solved because the pressure difference after the slider made a stop was less than the fiction force. The phenomenon was also simulated and the result is

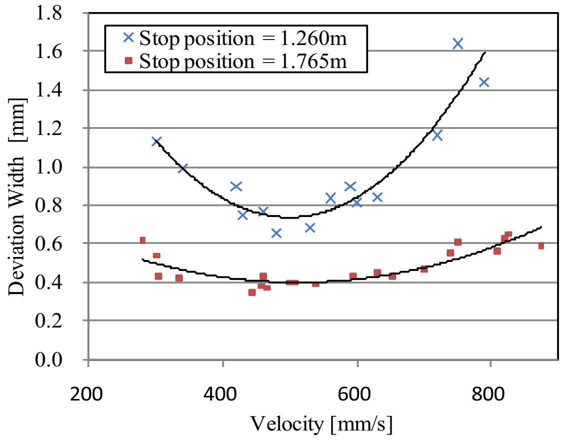

Figure 13 Optimum velocity to start applying the strong braking

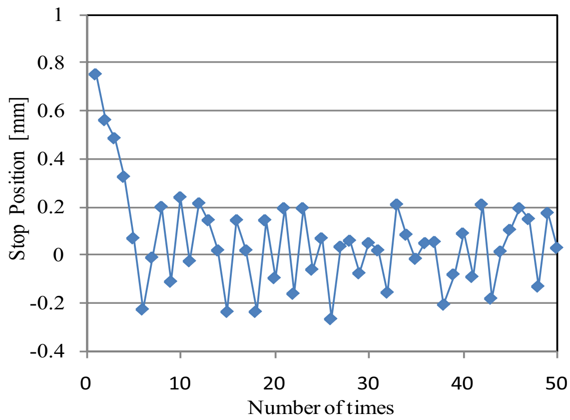

Figure 14 Convergence of the stop position

shown in Fig.12. p_2 increases rapidly after strong braking applied as same as in Fig.10. It also indicates the slider has been pushed backward as like in the experiment.

Repeated positioning of pneumatic cylinder

Before the tube length adjustment, the slider was unable to stop at position of more than 1.3(m) due to rapid increase in p_2. With adjustment made, an optimal velocity for strong braking at SW2=1760(mm) can be found and it is shown in Fig.13. The optimal velocity is also about 500(mm/s), however, the deviation width of stop positions become small due to the increased strong braking. It can also be concluded if the stop position was set near the stroke end, to increase the tube resistance might be one of the solutions. Fig. 14 shows that stop position converged after about 5 times of operation within about +/-0.2mm of accuracy. Information of the stop position in each time of operations will be detected by SW3.The obtained information will be used for fine adjustment of the timer T2 in the next operation to maintain the convergence.

CONCLUSIONS

From the above experimental results and simulation analysis, the following conclusions can be drawn:

1) Friction has a strong influence on both the behavior and performance of a system. This paper presents the relevance of friction condition and the positioning accuracy by experiments and numerical simulations. Simulation shows that the optimal velocity to start strong braking exists because the friction fluctuates largely and the braking force requires time to increase.

2) Sudden backward movement of slider occurs on the condition when the pressure differences in upstream and downstream chambers overcome the friction force after slider made a stop. However, this can be prevented by adjusting the tube length, which affects the volume in both sides and resistance for air to flow through.

ACKNOWLEDGMENTS

The authors would like to acknowledge SMC Corporation and the persons concerned who offered great supports to this research.

REFERENCES

1. Mustaffa, M.T. and Ohuchi, H., Repeated Positioning of a Long Stroke Pneumatic Cylinder using Proximity Switches, Proceedings of the 7th JFPS International Symposium on Fluid Power, 2008, pp.443-448.
2. Zhang, B.H., Ma, Y.F., Cheng, H. F. and Peng, G.Z., A New Method to Predict the Occurrence of Stick-Slip in Pneumatic Cylinders, Proceedings of the 6th JFPS International Symposium on Fluid Power, 2005, pp. 812-816
3. K. Hamiti, A.V.Besancon and H.R.Buisson, Position Control of a Pneumatic Actuator under the Influence of Stiction, Control Eng. Practice, Vol.4, No.8,1996, pp.1079-1088
4. M. Sorli, L. Gastadi, E. Codina, S.Heras, Dynamic analysis of pneumatic actuators, Simulation Practice and Theory 7, 1999, pp.589-602
5. S.C. Fok, E.K. Ong, Position control and repeatability of a pneumatic rodless cylinder system for continuous positioning, Robotics and Computer Integrated Manufacturing 15, 1999,pp. 365-371
6. S.Andersson, A. Soderberg, S. Bjorklund, Friction models for sliding dry, boundry and mixed lubricated contacts,Tribology International 40, 2007, pp.580-587

Proceedings of the 8th JFPS International
Symposium on Fluid Power, OKINAWA 2011
Oct. 25-28, 2011

2A1-3

EFFICIENCY MEASURES OF COALESCING FILTERS FOR PNEUMATIC EQUIPMENT

Guido BELFORTE, Terenziano RAPARELLI and Andrea TRIVELLA

Department of Mechanics, Politecnico di Torino, Technical University
C.so Duca degli Abruzzi 24, 10129, Torino, Italy
(E-mail:guido.belforte@polito.it, terenziano.raparelli@polito.it, andrea.trivella@polito.it)

ABSTRACT

This paper describes an experimental study on industrial coalescing filters to drain oil from compressed air. An appropriate test bench has beeen developed to reproduce several operating conditions of a compressed air distribution system and able to measure the efficiency of commercial and non-commercial coalescing filters. Tests have been conducted on filter cartridges of different type and grade, in particular are shown some results relative to three cellulose cartridges, one commercial and two experimental protoypes.

KEY WORDS

Filter, Coalescing, Aerosol, Pneumatic

INTRODUCTION

Filters are used to remove the impurities from a gas or liquid, thus achieving a variety of advantages. In industrial installations, filters maintain system and component cleanliness, optimizing operating efficiency and ensuring that the work environment is free from contaminants that could pose a hazard to health. In industrial pneumatic systems, the air is filtered and dehumidified prior to use. Depending on the type of application, this is accomplished by means of particulate filters of appropriate grade, normally with a porosity between 50 and 5 micrometers, which can retain contaminants of varying size and traces of rust forming in the system. As the compressor is normally lubricated, the compressed air also contains a certain amount of oil in the form of aerosol and vapor. Most of this oil is in aerosol form, and can reach concentrations by weight ranging from hundreds to thousands of PPM in the air, depending on the state of wear of the machine's moving parts. Particle size can range from a few micrometers to hundreds of micrometers after the oil has gone through successive heating and condensation cycles. Oil aerosol can be separated by means of coalescing filters, while oil in vapor form can be separated using activated carbon filters. In the following only coalescing filters are examined.

COALESCING FILTERS

A schematic view of a coalescing filter for pneumatic systems is shown in Figure 1. The filter element is an annular cartridge made up of a matrix of fibers embedded in a binder featuring a certain porosity. Air flows through the cartridge, moving from the interior outwards, and the oil droplets intercepted by the fibers coalesce together and are pushed to the outer surface of the filter, where they fall by gravity into the collection chamber at the bottom of the filter (Figure 2).

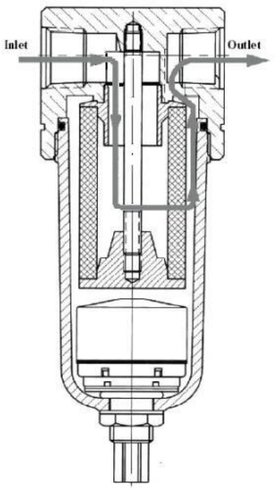

Figure 1 Schematic view of a coalescing filter

A variety of phenomena may be involved in capturing droplets, depending on the latter's size and velocity [1-2]. In general, particles over 1 μm in size are more readily intercepted by the fibers, while the smaller particles, traveling in random directions, are less likely to be captured. The ability to hold the intercepted liquid also depends on the liquid's surface tension on the fibers and hence on the nature of the fiber material as compared to the liquid to be collected.

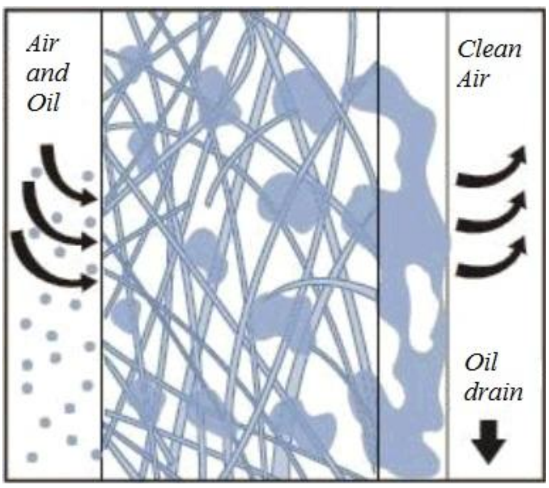

Figure 2 Coalescence process

Currently, the materials that are most commonly used for the fibers in coalescence filtration are borosilicate glass and cellulose. Several theoretical and experimental studies are conducted on the types of filter media employed.

Borosilicate filter media consist of thin glass fibers with controlled dimensions in a high-porosity resin binder that ensures adequate structural stiffness [3-4]. They may feature inner and outer layers performing prefiltration and drainage functions, and normally consisting of synthetic fibers. Depending on the required filtration grade, cartridges are available with varying average fiber diameters, generally between 5 and 30 microns [5-6] .

Cellulose filter media are widely employed in HEPA filters (High Efficiency Particulate Air filters) to remove solid particles [7-9]. They are also used in coalescent filters to remove oil in industrial compressed air lines.

In coalescent filters cellulose cartridges consist of several layers of special paper rolled in metallic mesh for stiffening purposes and adhesive bonded to two end plates [4], the upper one is provided of the inlet hole for the air flow passage. The first and last layers are more porous in order to retain or drain the largest droplets, while the intermediate layer performs the filtration function per se. Compared to glass fiber filters, they are less porous and thus are more efficient at separating small fibers, but also offer greater resistance to the passage of air. In some cases, the paper is pleated to increase the surface area exposed to the passage of air. Paper is produced in different filter grades, and may be coated with appropriate resins to improve absorbency. To improve the draining effect, an appropriate coating of open cell polyurethane foam on the exterior of the metal mesh is normally used. In fact oleophilic properties of some type of polyurethane foams make them particularly able to absorb and drain the oil droplets [10-12].

With the development of the nanotechnologies both on the borosilicate and cellulose fibers can be added polymeric nano fibers to improve the filtering action [13-14].

The efficiency *E* of a coalescing filter is measured as the ratio of the quantity of liquid separated and the quantity of liquid entering the filter over a certain time period: $E=(m_{in}-m_{out})/\ m_{in}$ where m_{in} and m_{out} are the masses of the oil at filter inlet and outlet [15]. Defining penetration *P* as the ratio of the mass at filter outlet to the mass at filter input per unit of time, we have $E = 1-P$.

Efficiency depends both on the material of the fibers in relation to the liquid to be filtered, and on fiber size and concentration. Pressure drop across the filter depends on the resistance introduced by the cartridge and thus on the fibers' concentration, or Packing Fraction (ratio of the volume of fibers to the volume of the cartridge). In turn, this parameter influences filter efficiency; consequently, it is useful to define the parameter *QF*, or Quality Factor [15], as the ratio of the logarithm of penetration to pressure drop: $QF = -\ ln(P)\ /\Delta p$. This formulation expresses filter efficiency as a function of the pressure drop introduced by the filter.

TESTS TO DETERMINE FILTER EFFICIENCY

A frequently used test for measuring filter efficiency is the DOP method, which takes its name from the liquid used for the test: dioctyl phthalate, an oil with high boiling point and thermal stability [5]. The liquid is nebulized and mixed with hot air, and the vapor thus formed is then condensed using controlled amounts of cold air to produce a DOP aerosol in the desired concentration, normally 67 PPM by weight, with droplets whose size is controllable in a range of 0.04 to 0.7 microns (and normally 0.3 to 0.6 microns) passing through the filter under test. The velocity of the air crossing the filter is very low. Aerosol concentrations upstream and downstream of the filter are measured using a forward light scattering photometer. These measurements are used to determine the quantity of aerosol captured and hence filter efficiency, as a function of aerosol particle diameter. Other instruments employed to measure aerosol concentration include photoionization and infrared detectors.
This test requires sophisticated instrumentation capable both of generating oil aerosols in which particle size and concentration can be regulated, and of measuring the quantity of aerosol separated by the filter with a high degree of accuracy, particularly with minimal liquid concentrations. However, it is also useful to investigate the behavior of filters in industrial pneumatic systems, where air velocity may be very far from that required for the DOP test, and oil aerosol is present in concentrations that are not negligible and with a wide range of particle sizes (from a few units up to several tens of μm), depending on the complex phenomena whereby the particles coalesce along the circuit.
For example in [16] is studied the coalescing efficiency and pressure drop of some cellulose media for industrial filtering application. The study shows the effects of the speed of the airflow and concentration of oil whose values differ from those provided by the DOP method.
Often the tests are conducted on samples of shapes and sizes other than those provided on the real filtering systems avoiding to consider the effects related to the geometry of the housing of the depurator.
Actually, the filtration efficiency depends also on the size of the ducts inside the filter and of the cup of oil collection, as well as the shape of the inlet port of the cartridge.
In this work efficiency and drop pressure measurements on several coalescing filters were performed, simulating actual service in an industrial pneumatic system under different operating conditions. Tests were conducted using commercial and prototype interchangeable cartridges in commercial filter housings.

TEST BENCH DESCRIPTION

For the purpose, a test bench based partially on previous works was set up [17] [18]. As shown schematically in Figure 3, the test bench consists of a filter-pressure regulator (1), a lubrifier (2), flexible tubing (3) of appropriate length (5 meters) and inside diameter (6 mm) to simulate the resistance of a user circuit, the filter under test (4) with 3/8'' fittings, a variable resistance (5) and the discharge filter (6). A flowmeter (7) is installed upstream of the lubricator to measure air flow rate. Two pressure gauges (8) are provided on flow regularizing tubes (9) to measure pressure p_U upstream and pressure p_D downstream of the filter under test. By means of the pressure regulator and discharge resistance, flow rate and pressure p_U are established in accordance with the operating conditions to be simulated. The test method entails introducing a defined quantity of oil into the fluid current by means of the lubricator. At predetermined operating intervals, both the lubricator and the filter are weighed, thus determining operating efficiency. The length of flexible tubing is also weighed to take oil circuit filling or emptying during transients into account. To minimize weight measurement errors, operating intervals are selected in accordance with the accuracy of the precision balance. Different oil concentrations can be established, normally between 1 and 0.1 g/m^3 A.N.R., in relation to the selected air flow rate and pressure p_U. To obtain lower oil concentrations, a small-displacement volumetric metering system controlled by a pneumatic solenoid valve and a PLC can be used instead of the lubricator. In this way, oil concentrations between 0.05 and 0.1 g/m^3 A.N.R. can be achieved.

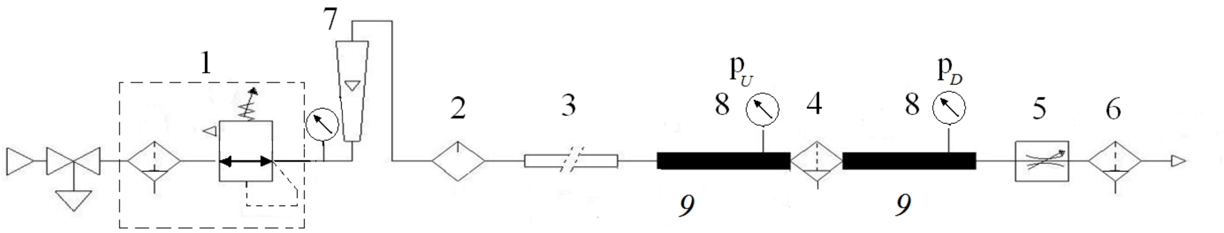

Figure 3 Coalescing filter test bench

Air flow rate can be regulated to guarantee a certain average velocity across the filter under test and a certain relative pressure p_U. Filter efficiency can thus be compared for any given average air velocity.

MEASURED EFFICIENCIES

Tests were conducted to evaluate the efficiency of one commercial cartridge (specimen 1) and two prototype cartridges (specimens 2 and 3) made with commercial filtering paper. Commercial cartridge 1 (fig. 4 left) has nominal filtration efficiency equal to 95% for diameter particles equal or greater to 0.01 µm. It consists of three cylindrical layers of paper of different porosity impregnated with phenolic resin and two cylindrical perforated metal guards to reinforce the papers' layers (fig 4 right). Metal guards have internal and external diameters equal to 15 mm and 23 mm, length equal to 35 mm. The actual air passage section is equal about to 1270 mm^2. Externally, the cartridge is provided with a drainage foam whose pores measure 250 µm on average. In Figure 5 is shown an enlargement under the microscope of the outer layer. Cartridge 1 is mounted in a commercial housing filter, ports G 3/8", by means of a thread hole made in the lower end plate.
The commercial papers used for prototypes 2 and 3 have nominal filtration grads equal respectively to 1 µm and 10 µm corresponding with DOP efficiencies (0.05 m/s flow velocity, particle size 0.3 µm) equal to 99% and 72% (single layer).
Specimens 2 and 3 feature a single layer of paper with no resin treatment. Aspect and dimensions of specimens 2 and 3 are identical and were selected in order to obtain an air passage section similar to that of specimen 1.

Figure 4 Specimen 1 (left), without upper end plate and drainage foam (right).

Also for the specimens 2, 3 the paper is wound several times and enclosed within two cylindrical perforated metal reinforcing guards. For both the specimens the internal and external diameters of the guards are equal to 7 mm and 20 mm, the length is equal to 65 mm. Cartridges 2, 3 are mounted in a housing filter with ports G 3/8" by means of M20 thread on the upper end plate. One of the two tested specimens is depicted in Figure 6.
For specimens 2 and 3, several types of foam with porosity and thicknesses similar to those of specimen 1 were tested. A commercial polyurethane foam was selected to reproduce similar oleophilic properties of the foam of the specimen 1. The selected foam is made in polyester base, specifically for filter's application, and the mean dimension of the cells is about equal to 300 µm (number of pore: 75 PPI).
Figure 7 shows enlargements of the open cell structure of the polyurethane foam on specimen 1 and selected for specimens 2 and 3 respectively.
All tests were carried out with an air velocity across the filter v = 0.4 m/s and pressure p_U = 4 bar gauge. Air flow rate imposed was 170 l/min A.N.R. for specimen 1 and 150 l/min A.N.R. for specimens 2 and 3, according to the actual air passage section. Average oil concentration was 0.6 g/m^3 A.N.R., while the kinematic viscosity of the oil used was 22 cSt at 40°C.
On all specimens, starting from the new cartridge, efficiency measurements were repeated more times in order to obtain results with sufficient accuracy. Effective values were the average of all the efficiencies measured at the end of each operating interval. Measurements were carried out both with and without foam.

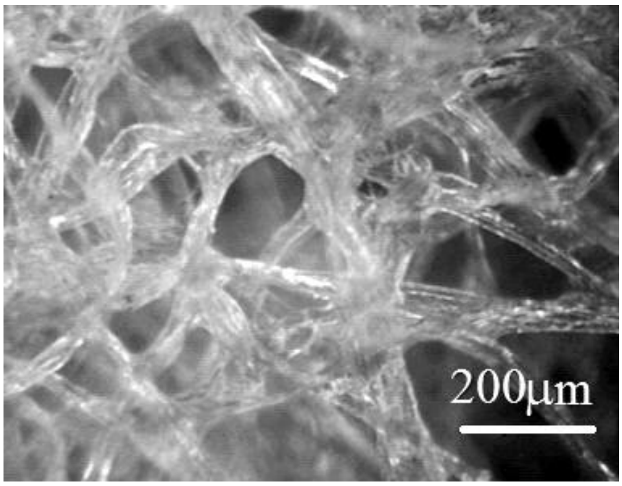

Figure 5 Enlarged view of the treated outer layer on specimen 1.

Figure 6 Specimen 2 , with and without drainage foam (specimen 3 has same geometry).

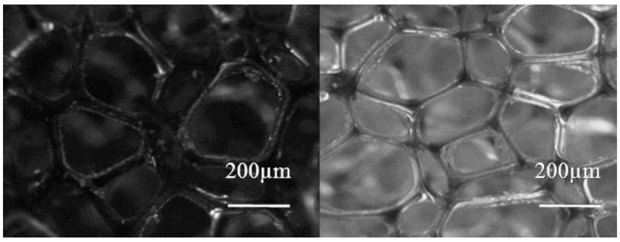

Figure 7 Enlarged view of the foam used for specimen 1 (left) and for specimens 2 and 3 (right).

The graph in Figure 8 shows efficiency versus time for different examined cases.

Specimen 1 was found to have excellent efficiency even without the outer foam, thanks to the special resin treatment used for the paper. The values obtained for specimens 2 and 3 without foam are lower than those for specimen 1 and show a certain instability, probably because the untreated paper fibers have difficulty in retaining the captured oil droplets. The lowest recorded efficiency values are those obtained for the smallest untreated paper fibers (specimen 2). However, it was found that the use of suitable foam, appropriately combined with papers of a certain filter grade (though not necessarily treated) significantly improves results.

As can be seen from the graph, the selected foam material, because of its ability to hold liquid, provided specimen 3 with efficiency values that were much more stable and close to those of specimen 1. Good results were also achieved with the specimen 2 that use the same type of foam. Measurements repeated more times confirmed these performances.

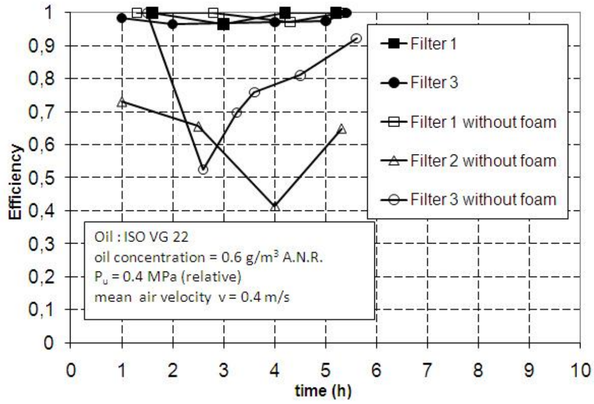

Figure 8 Efficiency versus time in different cases.

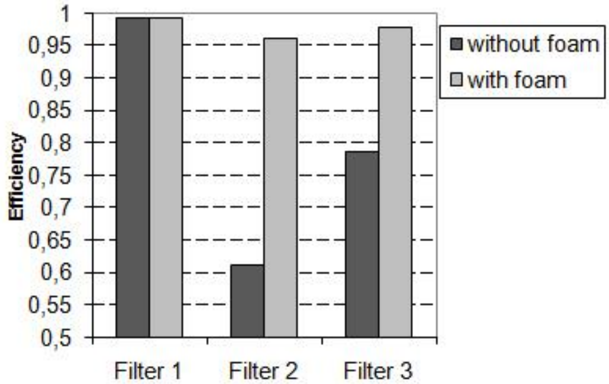

Figure 9 Effective efficiency for tested specimens (mean values).

Scatter in effective values obtained with foam did not exceed 5%. Effective efficiency values are shown in Figure 9 for all the examined cases, while Figure 10 shows pressure drops recorded at the beginning of the test for all specimens. All three cases exhibited the same operating efficiency, but a significant difference in pressure drop.

CONCLUSIONS

A test bench for measuring the efficiency of coalescing filters was designed and constructed. The bench can simulate different operating conditions encountered in pneumatic systems, and test a variety of cartridge types. A test method was developed that can be used to compare results with different samples, considering the cartridge mounted in the actual housing filter.

To investigate the performance of cellulose filters, tests were conducted on three cartridges of this type with different filter papers, including one commercial cartridge and two prototypes constructed in the laboratory.

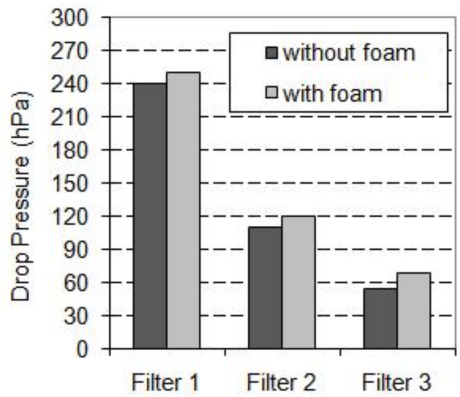

Figure 10 Pressure drop p_U-p_D at start of test.

Measurements indicated that both paper type and foam type have a significant influence on performance. An appropriate polyurethane foam ensure a distinct improvement in filter efficiency, and can also compensate for poor retention on the part of the filter paper. Further work can be carried out to investigate the effect of varying parameters such as air velocity, oil aerosol dimensions and operating time on filter efficiency.

REFERENCES

1. Gianluca Zanovello, Filtrazione vantaggiosa se ben fatta, I quaderni dell'Aria Compressa, September 2001, pp. 33-35

2. Thomas P. Colcombe, The why and how of coalescing type oil removal filter, Advances in Filtration and Separation Technology, 13b, 1999, pp. 940-944.

3. G. Vasudevan, G.G.Chase. Performance of B-E-glass fiber media in coalescence filtration. Journal of Aerosol Science, 35, 2004, pp. 83-91.

4. Filters and Filtration Handbook - Trade & Technical Press, 1987.

5. C. Billiet. Necessary Protection for Sensitive Separation Equipment. Filtration & Separation, 1991, May/June, pp.153-157.

6. P.C.Raynor, D.Leith. The influence of accumulated liquid on fibrous filter performance. J.Aerosol Sci. ,31, (1), 2000, pp.19-34.

7. B.M. Verdegan, B.W.Schwandt, S.L.Fallon, J.Malik. Preferential attachment of contaminants to filter media in oil. Filtration & Separation, 12, 1997, pp.1061-1064.

8. L. Boskovic, I.E.Agranovski, R.D.Braddock. Filtration of nanosized particles with different shape on oil coated fibres. Journal of Aerosol Science, 38, 2007, pp.1220-1229.

9. J.Steffens, J.R. Coury. Collection efficiency of filters operating on the removal of nano-sized aerosol particles II. Heterogeneos fibers. Separation Purification Technology, 58, 2007, pp.106-112.

10. N.J. Mils. Air flow in open-cell foams. Polymer Foams Handbook, 2007, pp.177-203.

11. Changhong Su. Highly hydrophobic and oleophilic foam for selective absorption. Applied Surface Science, 256, 2009, pp.1413-1418.

12. B.H.Park, M.H..Lee, S.B.Kim, Y.M.Jo. Evaluation of the surface properties of PTFE foam coating filter media using XPS and contact angle measurements. Applied Surface Science, 257, 2011, pp.3709-3716.

13. R.S.Barhate, S.Ramakrishna. Nanofibrous filtering media: Filtration problems and solution from tiny materials. Journal of Membrane Science, 2007, pp.1-8.

14. M.G. Hajra, K. Mehta, G.G. Chase. Effects of humidity, temperature, and nanofibers on drop coalescence in glass fiber media. Separation and Purification Technology, 30, 2003, pp. 79-88.

15. R.C. Brown. Air Filtration, An Integrated Approach to the Theory and Applications of Fibrous Filters, 2005, Pergamon Press.

16. A.Charvet, Y.Gonthier, A.Bernis, E.Gonze. Filtration of liquid aerosol with a horizontal fibrous filter. Chemical Engineering Research and Design, 86, (2008), pp.569-576.

17. G. Belforte, C. Ferraresi, T. Raparelli. Analisi della nebulizzazione dell'olio in un circuito pneumatico. Notiziario tecnico AMMA, 41, (9), 1986, pp. 31-35.

18. G. Belforte, C. Ferraresi, T. Raparelli. Testing the performance of oil fog lubricators. 7th Inter. Fluid Power Symp., Bath, 1986, pp. 359-368.

Proceedings of the 8th JFPS International
Symposium on Fluid Power, OKINAWA 2011
Oct. 25-28, 2011

2A2-1

DEVELOPMENT OF FLEXIBLE MECHANISMS USING FLEXIBLE PNEUMATIC CYLINDERS

Ayaka ANDO*, Shujiro DOHTA*, Tetsuya AKAGI*, Feifei ZHAO**
and Takahiro FUJIKAWA***

*Department of Intelligent Mechanical Engineering, Faculty of Engineering
Okayama University of Science, 1-1 Ridai-cho, Kita-ku, Okayama, 700-0005 Japan
(E-mail: dohta@are.ous.ac.jp)
**Tsuyama National College of Technology, 624-1 Numa, Tsuyama, Okayama, 708-8509 Japan
***Sanki Engineering Co. Ltd., 2-1-1 Nihonbashi-Muromachi, Chuo-ku, Tokyo, 103-8331 Japan

ABSTRACT

A wearable actuator needs to be flexible so as not to injure the human body. The purpose of our study is to develop a flexible and lightweight actuator which can be safe enough to be attached to the human body, and to apply it to a flexible mechanism and rehabilitation device. New types of flexible pneumatic actuator that can be used even if the actuator is deformed by external force have been developed in our previous studies. In this paper, we propose and test two kinds of flexible mechanisms using the novel flexible pneumatic cylinders. One is a flexible robot arm using three cylinders, and the other is a simple spherical actuator using two cylinders. The control systems using the tested quasi-servo valves and a micro-computer were also developed. As a result, both flexible mechanisms could be controlled well by the simple controller and the tested valves.

KEY WORDS

Flexible mechanism, Flexible pneumatic cylinder, Attitude control, Quasi-servo valve

INTRODUCTION

Recently, it has been desired strongly to develop a system to aid in nursing care [1][2] and to support the activities of daily life for the elderly and the disabled [3]. The actuators required for such a system need to be flexible so as not to injure the human body [4]. The purpose of this study is to develop a flexible and lightweight actuator and to apply it to a flexible robot arm, a rehabilitation device and so on. So far, new types of flexible pneumatic actuator that can be used even if the actuator is deformed by external forces have been proposed and tested in our previous studies [5]. Also, several kinds of rod-less type flexible pneumatic cylinder were tested, and the tested flexible pneumatic cylinder was utilized as a rotary actuator [6]. In this paper, we propose and test two kinds of flexible mechanisms using the novel flexible pneumatic cylinders. One is a flexible robot arm, and the other is a spherical actuator. The flexible robot arm with simple structure can realize a natural flowing movement by using the pneumatic cylinders. As a result of the experiment using the tested robot arm, it is confirmed that the tested robot arm can easily work for various directions, and shows a natural flowing movement without complex arrangement of actuators. Furthermore, a simple analytical model of the robot is proposed for attitude control. The effectiveness of the attitude control method by use of the proposed analytical model and the quasi-servo valve that we had developed is confirmed. The novel spherical actuator using two flexible pneumatic cylinders has a simple structure. By driving two cylinders, the actuator can bend largely for every direction. The bending control system using a micro-computer and the quasi-servo valve is proposed and tested.

FLEXIBLE PNEUMATIC CYLINDER

We have developed two types of novel rod-less type flexible pneumatic cylinder [6]. Figures 1 (a) and (b) show the constructions of the cylinder; (a) “Single type” and (b) “Double type”. Both types have the similar construction and the same operating principle. The difference of their properties is as follows. The single type has less frictional force, and the double type has higher flexibility. The single type cylinder consists of a flexible tube as a cylinder and gasket, one steel ball as a cylinder head and a slide stage that can slide along the outside of the tube. The steel ball is pinched by two pairs of brass rollers from both sides of the ball. The operating principle of the rod-less type flexible pneumatic cylinder is as follows. When the supply pressure is applied to one side of the cylinder, the inner steel ball is pushed. At the same time, the steel ball pushes the brass rollers and then the slide stage moves while it deforms the tube. We investigated the minimum driving pressure of the tested rod-less type flexible pneumatic cylinder using various center distance D (shown in Fig.1) and distance W between two pairs of rollers as a design parameter. From the experiments, we found that D of 14.4mm and W of 10mm were the best [6]. Table 1 shows the properties of the tested single type cylinder as a pneumatic cylinder compared with an ordinary pneumatic cylinder. The specifications of the cylinder such as a minimum radius of curvature of the cylinder, a maximum working pressure and an allowable working temperature depend on the properties of the soft polyurethane tube (SMC Co. Ltd., TUS 1208).

The minimum driving pressure of the double type cylinder is 130kPa for the best distance D of 14.6mm. This is a little higher than that of the single type, because the frictional force becomes larger due to the increase of the contact area between inner two balls and the inner bore of the tube.

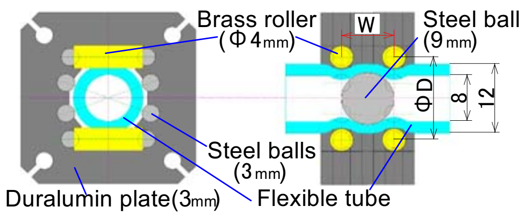

(a) Single type

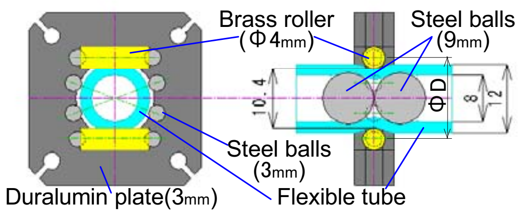

(b) Double type

Figure 1 Construction of rod-less type flexible pneumatic cylinder

Table 1 Properties of flexible pneumatic cylinder

Min. driving pressure	120kPa
Generated force	16N(input:500kPa)
Max. moving speed	> 1m/s
Weight (stroke of 1m)	< 0.1kg
Min. radius of curvature	about 30mm
Max. working pressure	600kPa
Working temperature	From -20 to +60 deg.C
Movement	Push-pull actions

FLEXIBLE ROBOT ARM AND CONTROL SYSTEM

Flexible Robot Arm

Figure 2 shows a flexible robot arm using flexible cylinders for bending control. The robot arm consists of two ring-shaped stages and three single type flexible pneumatic cylinders with the slide stages. The outer diameter of the ring-shaped stage is 100mm, the initial

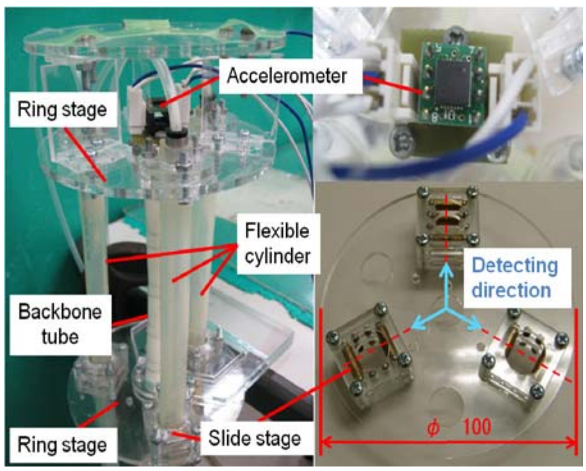

Figure 2 Construction of flexible bending robot arm

distance between the upper and lower ring-shaped stage is about 100mm. Each flexible pneumatic cylinder is arranged so that the central angle of two adjacent slide stages becomes 120 degrees on a ring-shaped stage. Also, an edge of each flexible cylinder is fixed in the upper ring-shaped stage. Two on/off control valves (Koganei Co. Ltd., G010HE-1) or quasi-servo valves are used to drive one flexile pneumatic cylinder. In the control of the robot, we used six control valves. In addition, this robot arm has a flexible tube in the center of ring-shaped stage as a backbone in order to deal with the bending motion as an attitude control of the robot. The both ends of the backbone tube are connected with upper and lower ring-shaped stages.

Master-Slave Control System

In order to control the movement of the robot arm, we tried an attitude control of upper ring-shaped stage using an accelerometer. Figure 3 shows the schematic diagram of the master-slave control system based on the attitude of the upper ring-shaped stage. It consists of a slave arm and a master arm. The slave arm consists of the tested robot arm mentioned above, an accelerometer, a micro-computer (Renesas Co. Ltd., H8/3664) and six quasi-servo valves mentioned later. The master arm consists of an accelerometer that is set on the top of a flexible tube to give the reference attitude. The attitude of the upper ring-shaped stage is detected with the accelerometer installed in the upper ring-shaped stage. The accelerometer can detect the bending angle of the upper stage by measuring the change of gravity for X,Y, and Z axis. From these values, the bending direction angle α and the bending angle β (shown in Fig. 4) are calculated by Eq. (5) and Eq. (6) shown in later section. The control of the tested flexible robot arm is carried out as follows. The micro-computer gets the output voltage of the bending angles, the micro-computer calculates the desired length and the present length of each flexible

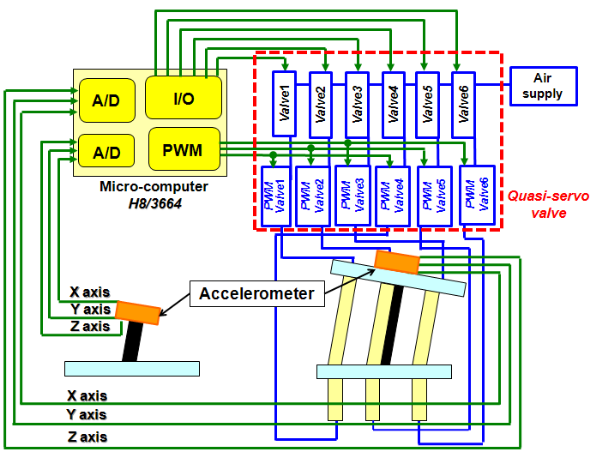

Figure 3 Schematic diagram of control system

cylinder by Eqs. (1)-(4) based on the simple analytical model of the flexible robot arm mentioned later. Where, the "length of the flexible cylinder" is defined as a distance between the upper ring-shaped stage and the lower stage. By using this method, each length of the cylinder can be controlled as a position control, and consequently, a master-slave control can be realized. Therefore, the analytical model of the robot that can calculate the bending angle of the robot and the length of each flexible cylinder from the output signals of the accelerometers is very important. In a control with a micro-computer, we need a device to record or output several variables (angle, displacement and so on) during the control. In our control system, they are recorded by a recorder (GRAPHTEC, GL200) through a handmade D/A converter connected with the micro-computer.

Analytical Model for Control

Figure 4 shows an analytical model for the attitude control of a flexible robot arm. In this model, we assumed that the shape of each flexible pneumatic cylinder becomes a circular arc when the arm bends. From the geometrical relationship shown in Fig.4, the desired length (in a master arm) and the present length (in a slave arm) of each cylinder L are calculated by the following equations (1)-(4) by using the bending direction angle α and the bending angle β.

$$L_{1i} = (R_i - r \cdot \cos\alpha_i) \cdot \beta_i \qquad \text{(i=m,s)} \qquad (1)$$

$$L_{2i} = \{R_i - r \cdot \cos(\tfrac{2\pi}{3} - \alpha_i)\} \cdot \beta_i \qquad \text{(i=m,s)} \qquad (2)$$

$$L_{3i} = \{R_i - r \cdot \cos(\tfrac{4\pi}{3} - \alpha_i)\} \cdot \beta_i \qquad \text{(i=m,s)} \qquad (3)$$

$$R_i = L_{0i}/\beta_i \qquad \text{(i=m,s)} \qquad (4)$$

Where, L_0 means the fixed length of a backbone tube installed between the upper and lower ring-shaped stage, that is 100mm. Subscripts m, s, and i indicate the desired (master arm), the present (slave arm) and the location number of the cylinder, respectively. R and r mean the radius of curvature of the cylinder and the distance from the center of the ring-shaped stage to the center of the slide stage in the cylinder, respectively. Radius r is 33mm. On the other hand, the bending direction angle α, and the bending angle β are given by following equations using the output signal from the accelerometer.

$$\alpha_i = \cos^{-1}\frac{V_{xi}}{\sqrt{{V_{xi}}^2+{V_{yi}}^2}} \qquad \text{(i=m,s)} \qquad (5)$$

$$\beta_i = \cos^{-1}(\frac{V_{zi}}{V_{zmaxi}}) \qquad \text{(i=m,s)} \qquad (6)$$

Where, V_x, V_y, and V_z mean the accelerometer output differential voltage from the initial value. The voltages V_x and V_y correspond to the angle from the horizontal plane and V_z corresponds to the angle from the vertical plane. Then, V_{zmax} means the difference of V_z between the values in horizontal and vertical planes. By using Eqs. (1)-(6), we can calculate the length of the six cylinders for every bending state of the robot arm. In our previous study [7], we confirmed that the calculated angle agreed well with the measured value. The error between both angles was less than 1 degree.

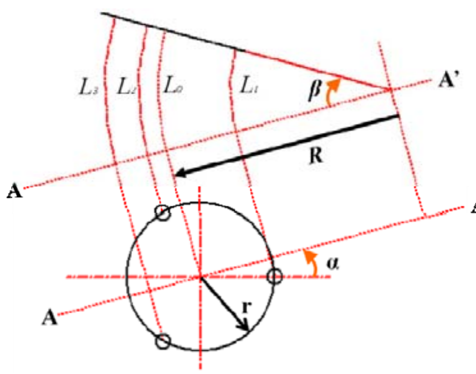

Figure 4 Analytical model of flexible robot arm for attitude control

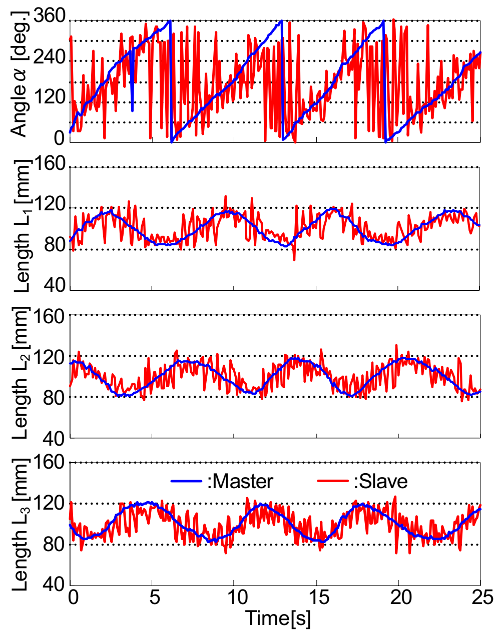

Figure 5 Transient response of the length of each flexible pneumatic cylinder and bending direction angle of robot arm

Control Scheme and Experimental Results

As a control method for the attitude control of the robot, first, we apply the on/off control scheme to the master-slave control system. In the control, the micro-computer drives the suction or exhaust control valves through the transistors according to the deviation between two sensor voltages. We used the following on/off control scheme.

$$u_j = e_j = L_{jm} - L_{js} \qquad (j=1,2,3) \quad (7)$$

$u_j<0$ Valve(j): on, Valve(j+3):off (j=1,2,3)

$u_j=0$ Valve(j):off, Valve(j+3):off (j=1,2,3) (8)

$u_j>0$ Valve(j):off, Valve(j+3):on (j =1,2,3)

Where, u_j means the control input, e_j means the error of each cylinder length.

Figure 5 shows the transient responses of the length of each flexible pneumatic cylinder L_1,L_2,L_3 and bending direction angle α of the robot arm. The blue line shows the desired length of the virtual cylinder and bending direction angle of the virtual master robot and the redline shows those of the slave robot. From Fig.5, we can find that there is very large oscillation in the slave robot arm: the control performance is not good. It is because that the feedback control gain becomes too high by using a simple on/off control valve whose output flow rate is too large for the small volume of the cylinder. In order to prevent the oscillation caused by larger input, it is better to use the lower input. But the lower input makes the dynamics of the actuator slower. In ideal, the output flow rate in both cases of supply and exhaust should be adjusted according to the control input. In such a situation, a servo valve is used commonly, but the servo valve is large and very expensive. Therefore, we use the quasi-servo valve using on/off valves.

Figure 6 shows the schematic diagram of the inexpensive quasi-servo valve which was developed in our laboratory [8]. The quasi-servo valve consists of two on/off control valves (Koganei Co. Ltd., G010HE-1) whose both output ports are connected each other. One valve was used as a switching valve to exhaust or supply, and another was used as a PWM (pulse width modulation) control valve that can adjust output flow rate like a variable fluid resistance. The valve connected with the actuator is a two-port valve without an exhaust port. Another is a three-port valve that can change the direction of fluid flow from the supply port to the output port or from the output port to the exhaust port.

The two-port valve is driven by PWM method in order to adjust the valve opening per time. It becomes a quasi variable orifice. Then, the latter valve is called as "PWM valve", and the former is called as "Switching valve". The size of the on/off valve is 33mm×20mm×10mm, and the mass is only 15g.

In the attitude control of the robot arm, the two PWM

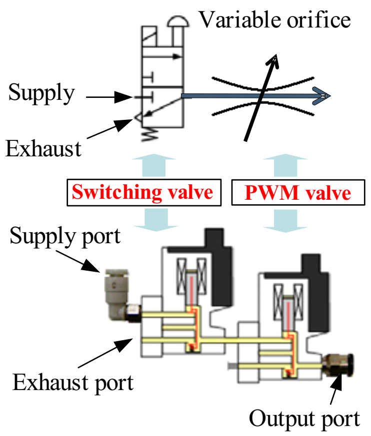

Figure 6 Schematic diagram of the tested quasi-servo valve

valves for each cylinder are driven at the same time, that is, the input duty ratio for two valves are same. As an analog control method using the tested quasi-servo valve to improve the bending control performance, the following typical PID control scheme was used.

$$u_i = K_P e_i + K_I \int e_i \, dt + K_D \frac{de_i}{dt} \qquad (i=1,2,3) \qquad (9)$$

Where, K_P (=1.5[%/mm]), K_I (=0.003[%/mm/s]) and K_D(=0.025 [% s/mm]) indicate the proportional gain, the integral gain and the differential gain, respectively. These control parameters are adjusted based on the ultimate sensitivity method. Using the lower duty ratio as a control input to PWM valve, there exists the dead zone for output flow rate of the valve. Therefore, the input duty ratio of the PWM valve is always added 23% to the absolute value of the control input calculated by Eq. (9). In addition, the state of switching valve (on or off) is decided by the sign (positive or negative) of the control input. As this control method is embedded into the micro-computer, we can use the valve like a typical servo valve without complex operations. Figure 7 shows the transient response of the length of each flexible cylinder L and bending direction angle α of the robot arm using the quasi-servo valve and the PID control scheme mentioned above. The blue line shows the desired length of the virtual master flexible cylinder and the red line shows the length of the slave flexible pneumatic cylinder. From Fig.7 we can find that the oscillation of the slave cylinders are remarkably decreased compared with the previous result using on/off control method as shown in Fig.5 It can be also seen that the tracking performance of the attitude control system is improved. We can confirm the effectiveness of the control method based on the simple analytical model and the tested quasi-servo valve.

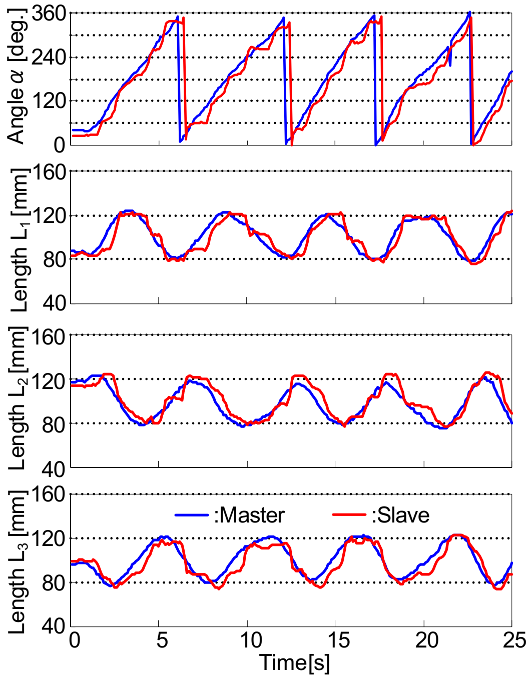

Figure 7 Transient response of the length of each flexible pneumatic cylinder and bending direction angle of robot arm

SPHERICAL ACTUATOR

Construction

Figure 8 shows the construction of the tested spherical actuator. The actuator consists of two ring-shaped flexible pneumatic cylinders (the double type cylinder). They are intersected at right angle and are fixed on the base. The diameter of each ring-shaped cylinder is 148mm. And they can bend by being supplied the air to the cylinder. Two slide stages of each cylinder are connected by a right angle so that the bending movement with 2 degrees-of-freedom can be realized. The size of

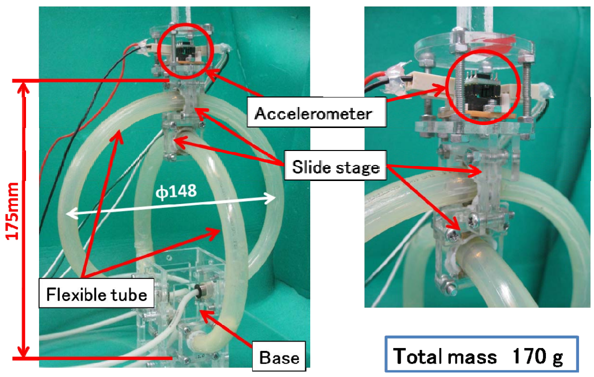

Figure 8 View of tested spherical actuator

the actuator is 160mm in width and 175mm in height. The total mass of the actuator is 170g. The tested actuator can bend over the range of 240 degrees around the center of circle of the cylinder.

Fundamental Characteristics

Figures 9 (a) and (b) show the experimental setup for measuring the generated force of the spherical actuator. In Fig.9 (a), the supply pressure is 0kPa, and in Fig.9 (b), the supply pressure is 300kPa. The measuring procedure is as follows. The wire is fixed at a certain height of the actuator, then the tensile force is measured with a force gauge when the cylinder is pressurized. The measurement is carried out for four direction; ±x-direction and ±y-direction. Here, x axis is taken in a parallel direction to the lower cylinder, y axis is taken in a parallel direction to the upper cylinder. Figure 10 shows the relation between the generated force and the supply pressure. From Fig.10, we can see that there exists a dead zone within ±100kPa by the friction of the rod-less type flexible pneumatic cylinder. From Fig.10, we can also see that the maximum generated force in x-direction is 3.5N, and the y-direction is 7N. Such a difference of the maximum force between x-direction and y-direction is caused by the fact that the wire fixed point was the same in both directions as shown in Fig.9. Therefore, the torque is compared. Figure 11 shows the generated torque. They are calculated based on the distance from a circular center of the cylinder to the wire fixed point. The distance in x-direction is 105mm, and the distance in y-direction is 75mm. As a result, we can confirm that the maximum toque in x-direction is 0.36Nm and that of y-direction is 0.5Nm although the tested actuator has flexibility. Although the difference of the toque between x-direction and y-direction becomes smaller compared with the case of generated force, we can find that the toque of x-direction is still smaller. This is because that the frictional toque of x-direction is larger than that of y-direction due to the longer distance from a circular center of the cylinder to the slide stage. Moreover, from a constructional point of view of the actuator, the posture in Fig.9 seems to be the lowest rigidity of the actuator.

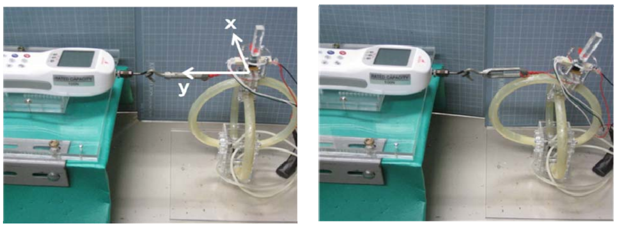

(a) Pressure: 0kPa (b) Pressure: 300kPa

Figure 9 Experimental setup

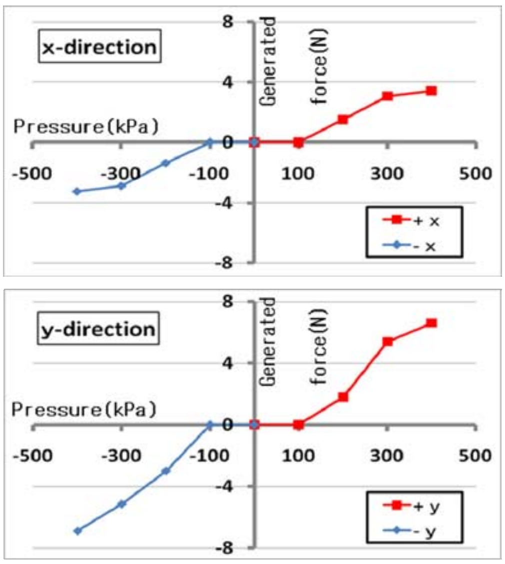

Figure 10 Measured generated force

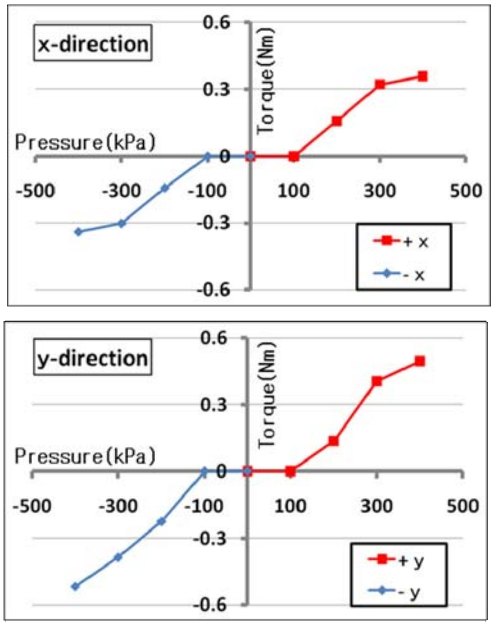

Figure 11 Measured generated torque

Master-Slave Control System

Figure 12 shows the construction of the master-slave control system of the spherical actuator using accelerometers, and Fig.13 shows the view of the system. The slave consists of the spherical actuator, an accelerometer, four quasi-servo valves to operate two flexible pneumatic cylinders and a micro-computer as a controller. The master consists of an accelerometer for the desired attitude on the ring-shaped stage with a diameter of 100 mm as shown in Fig.13. The control is done as follow. The micro-computer gets the output voltage from two accelerometers. By a control scheme based on the difference of the voltages, the quasi-servo valves are driven, the flexible pneumatic cylinders are driven and then the attitude of the spherical actuator is controlled. As a control scheme, an on-off control scheme and a PD control scheme were used.

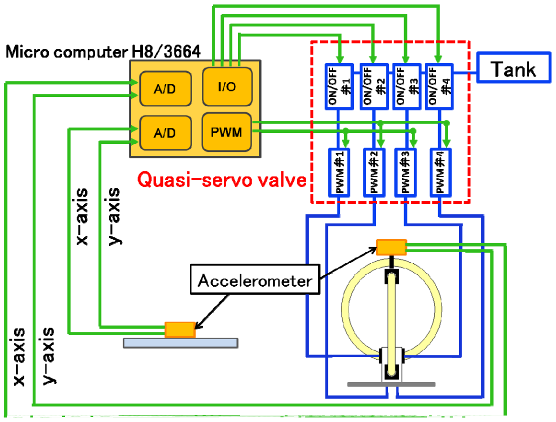

Figure 12 Schematic diagram of control system

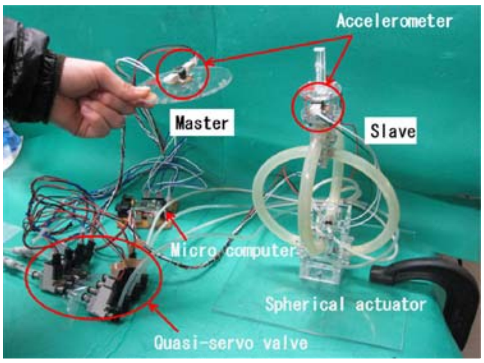

Figure 13 View of master-slave control system

Control Scheme and Experimental Results

Figure 14 shows the transient response of the bending angles of the actuator using the on/off control scheme. In the experiment, the desired angles were given so as to rotate the master device with a certain period. In Fig.14, the upper figure shows the transient response of the bending angle of x-axis direction, the middle one shows the results of y-axis direction, and lower one shows the result of the bending direction angle. In Fig.14, the broken line shows the master, and the solid line shows the slave. From Fig.14, we can see that the bending angle and the bending direction angle of the slave have a larger oscillation compared with the master. Moreover, the accelerometer also detects an acceleration of the spherical actuator, and the result shows the larger change including the acceleration change than the real movement of the spherical actuator. This appears in the result of the bending direction angle such as larger angular change compared with the actual movement. It is caused by using the higher gain such as an on-off control scheme. Therefore, we need to apply the analog control method in order to improve the control performance.

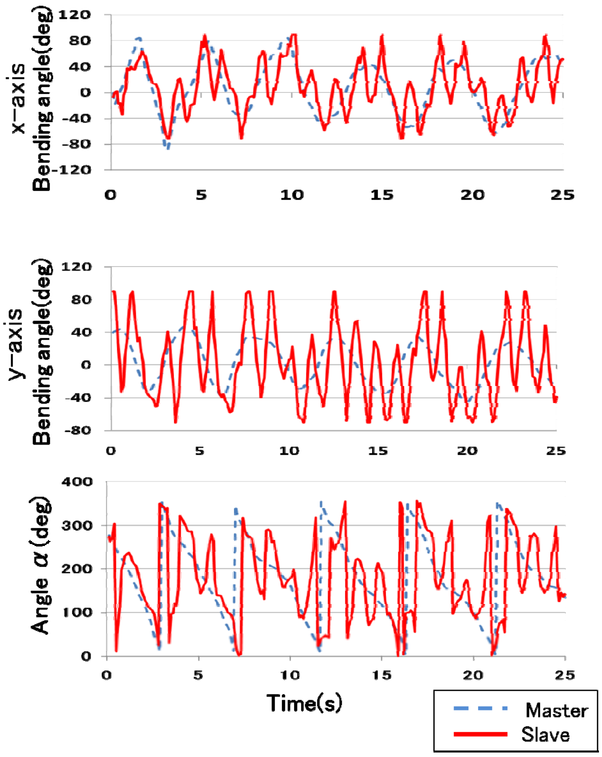

Figure 14 Transient response for on/off control

In the experiment using PD control scheme, as a same manner of on/off control, the desired angles were given so as to rotate the master device. Then, the PWM period of the quasi-servo valve is 10ms. Figure 15 shows the view of movement of the actuator using the PD control scheme. Figure 16 shows the transient response of each bending angle of the actuator. Each figure in Fig.16 shows the result of the bending angle of x and y direction and the bending direction angle, respectively. From Fig.16, compared with on/off control result, the vibration of each angle became smaller. We found that the slave spherical actuator can trace the movement of the master device. However, it needs to improve the control performance, because there is a step wise change of the slave bending angle. We think that it is caused by the larger friction in the rod-less type flexible pneumatic cylinder. Therefore, it will be possible to improve the control performance by decreasing the friction of the cylinder.

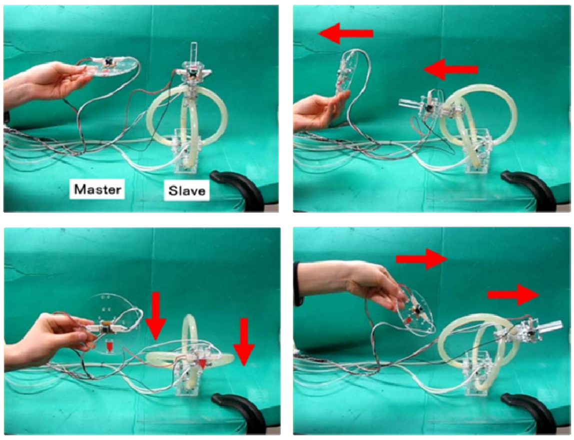

Figure 15 View of master-slave control

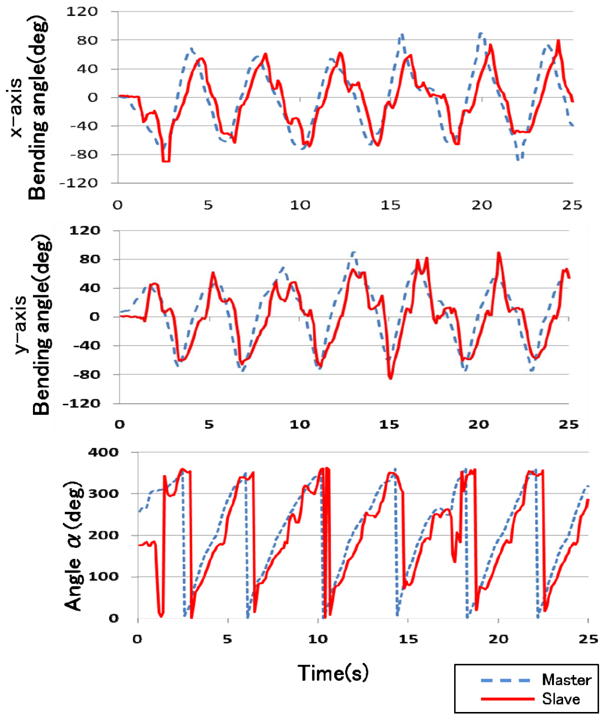

Figure 16 Transient response for PD control

CONCLUSIONS

The study aiming at developing the flexible mechanisms using flexible pneumatic cylinders is summarized as follows.

1) The simple-structured flexible robot arm using the novel flexible pneumatic cylinders was proposed and tested. For an attitude control of the arm, a simple analytical model that can calculate the displacement of the flexible cylinder and the control system using a micro-computer were proposed and tested.
2) In order to improve the control performance of the robot arm, the quasi-servo valve using inexpensive on/off control valves developed in our laboratory was used. The attitude control system using the quasi-servo valve and PID control scheme was tested. As a result, the tracking control performance of attitude control system was improved. The effectiveness of the control method by using the proposed analytical model of the flexible robot arm and the tested quasi-servo valve was confirmed.
3) The simple-structured spherical actuator that it consists of two flexible pneumatic cylinders was proposed and tested. The master-slave control system using the tested actuator, four quasi-servo valves and a micro-computer was also proposed and tested. As a result, the control performance of the actuator could be improved by using PD control method and quasi-servo valves compared with the results using on/off control scheme.

REFERENCES

[1] Ishii, M., Yamamoto, K. and Hyodo, K., "Stand-Alone Wearable Power Assist Suit -Development and Avail-ability-", Journal of Robotics and Mehatronics, 2005, 17-5, pp.575-583.
[2] Noritsugu, T., Takaiwa, M. and Sasaki, D., "Development of Power Assist Wear Using Pneumatic Rubber Artificial Muscles", Journal of Robotics and Mechatronics, 2009, 21-5, pp. 607-613.
[3] Kobayashi, H., Shiban, T. and Ishida, Y., "Realization of all 7 motions for the upper limb by a muscle suit", Journal of Robotics and Mechatronics, 2004, 16-5, pp.504-512.
[4] Nagata, Y. ed., "Soft Actuators -Forefront of Development-", NTS Ltd., 2004, pp.291- 335.
[5] Akagi, T. and Dohta, S., "Development of McKibben Artificial Muscle with a Long Stroke Motion", Transactions of JSME, Series C, 2007, 73-735, pp.2996-3002.
[6] Akagi, T. and Dohta, S., "Development of a Rodless Type Flexible Pneumatic Cylinder and Its Application", Transactions of JSME, Series C, 2007, 73-731, pp.2108-2114.
[7] Fujikawa, T., Dohta, S. and Akagi, T.,"Development and Attitude Control of Flexible Robot Arm with Simple Structure Using Flexible Pneumatic Cylinders", Proceedings of 4th Asia International Symposium on Mechatronics, 2010, pp.136-141.
[8] Zhao, F., Dohta, S. and Akagi, T., "Development and Analysis of Small-Sized Quasi-Servo Valve for Flexible Bending Actuator", Transactions of JSME, Series C, 2010, 76-772, pp. 3665-3671.

Proceedings of the 8th JFPS International
Symposium on Fluid Power, OKINAWA 2011
Oct. 25-28, 2011

2A2-2

A PRELIMINARY EXPERIMENT FOR A FASTENING EQUIPMENT DESIGN ON THE VERTICAL WALL OF HIGH-RISE BUILDINGS

Byung-Ju Lim*, Young-Bog Ham*, Chang-Dae Park*[1], Dae-Myoung Kim** and Ji-Suk Gu**

*Energy Plant Research Division, Korea Institute of Machinery and Materials
171 Jang-dong, Yuseong-gu, Daejeon, 305-343, Korea
(E-mail: bzoo77@kimm.re.kr, hyb665@kimm.re.kr)
[1](Corresponding author: parkcdae@kimm.re.kr)

** Department of Intelligent Mechanical Engineering
Kumoh National Institute of Technology
Sanho-ro 77, Gumi, Gyeongbuk, 730-701, Korea

ABSTRACT

In order to perform maintenance on the outer walls of a high-rise building, including sweeping, painting and repairs, a device that enables the easy attachment/detachment of working equipment such as a gondola to the outer wall of a building is necessary. Though vacuum suction pads are able to fasten items of working equipment without causing damage to a building's outer wall, their necessary suction force to fasten the equipment on the wall should be designed by considering various conditions such as wind force, the own weight of each item of working equipment, and suction capacity. The suction force is changed by the internal vacuum pressure of pads, and the materials and shapes of an outer wall's surface have a considerable influence on vacuum pressure.
In this study, we performed the preliminary experiment for the vertical force of vacuum suction pads against the vertical wall of concrete material under various loads and wall surface shapes. The experiment results are supposed to be useful as fundamental datum for development of fastening equipment on vertical wall of high-rise building.

KEY WORDS

Suction pads, Maximum Vacuum suction force, High-rise building, Vertical outer wall, Fastening equipment

INTRODUCTION

The outer walls of high-rise buildings are made of various materials such as steel, red block, marble, glass, and so forth, and their surfaces can contain many grooves of irregular shapes and sizes. Table 1 presents the diverse materials used in the outer walls of buildings, as reported in previous studies [1]. The outer walls of high-rise buildings require regular maintenance including cleaning and painting. Conventionally, gondola systems are used to carry on platforms the workers who conduct maintenance work on the outer walls of high-rise buildings. However, for super-high-rise buildings, i.e., higher than 30 stories, it is very difficult to perform such works on their outer walls using a gondola due to external disturbances including squalls.

Table 1 Various outer wall materials

Type	Materials
A	Wood, stone, concrete, red block, glass, ceramic, plastic, fiber, metal, paper
B	Stone, block, tile, glass
C	Aluminum composite panel, stone, porcelain enamel panel, red block, cement

Also, it is difficult for workers using gondola systems suspended by wires to carry out precision works such as painting as gondolas tend to sway around in the wind. Even in an environment without an external load, the gondola platform has to be fixed onto a wall to perform such works as sweeping or painting. To perform these kinds of work on outer walls using gondolas, considerable attachment force (to the wall) is required, taking into consideration the external loads and own load. Since the fixing must not damage a wall requiring such work, vacuum suction pads are used as fixing devices

Many researchers have been studying about robot travelling and working on the vertical wall, and the robot is practically used suction pad to attach the wall. Dong Gwang L., et al. developed and tested a robot system using vacuum suction technology for cleaning the window panes of a building's outer walls [2]. Kun Chan S., et al. designed a suction unit for a robot system which can climb up irregular vertical surfaces [3]. Siyoul J conducted a study on the design of a vacuum suction pad which can provide a uniform contact shape in large-scale imprinting [4]. However, robots traveling on vertical walls have limitations in terms of the shape of the walls and their adhesive force [5-7]. Therefore, the vacuum suction ability with the various wall shapes should be evaluated and applied in the outer wall work system. Guido La Rosa et al. developed a low-cost, lightweight robot system which can travel in a vertical direction using 8 suction cups [8]. The NINJYA BIPED developed by Nishi al Miyazaki can travel along a wall's surface using small suction cups [9-11]. Hwang Kim et al. developed a robot system which can travel along vertical walls stably and continuously, using endless tracks attached with vacuum pads [12]. The vacuum suction pads used in preceding studies for movment and work on vertical walls are lightweight, making them easy to use in various applications. However, for systems where additional heavy loads are applied, such as a gondola, the performance of the vacuum pads has to be investigated precisely.

In this paper, a testing apparatus is developed to test the maximum absorption forces of suction pads on various vertical wall surfaces according to pressure change. Also, the absorption forces were measured according to four types of wall surface shapes.

TEST EQUIPEMENT SETUP

Test Apparatus

Test apparatus to measure absorption force of suction pad on concrete sample surface was manufactured. Main components of the apparatus compose of pneumatic cylinder, load cell, suction pad, and concrete wall as presented in Figure 1. Two pneumatic cylinders function as traveling bi-directionally suction pad in the vertical and horizontal direction against wall. If the pad moves by the cylinder under the condition suction pad is absorbed on the wall, load cell between the pad and cylinder is loaded to compressive or tensile force. And calculating load value of load cell is same as absorbing force of suction pad. Sliding block between load cell and pad enables to move to both vertical and horizontal direction. But the pad is not able to move simultaneously to the two directions. Sliding block is presented in Figure 2. The measurement data is collected using LabVIEW software and data acquisition system. The specifications of the sub-components of the test equipment are presented in Table 2.

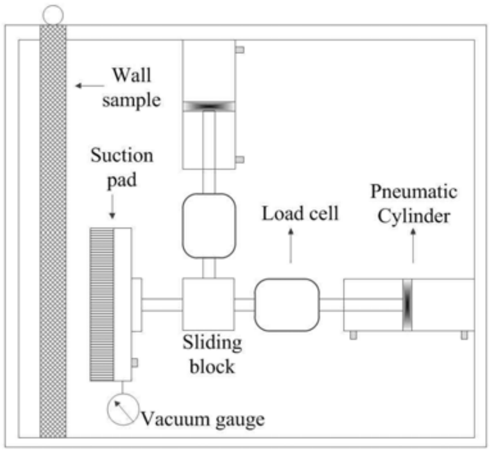

Figure 1 Schematics of test equipment

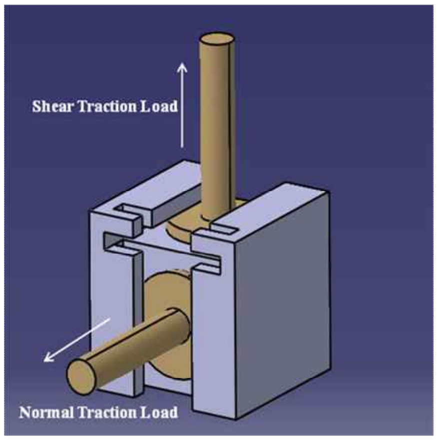

Figure 2 3D design of sliding block

Table 2 Specifications of the sub-components

Contents	Specifications
Load cell	Range: max. 2,000 N
Vacuum sensor	-Range: $10^{-3} \sim 10^{3}$ Torr -Accuracy: 0.1 % of indicated decade
Pneumatic cylinder	Max pressure : 1 MPa
Compressor	Max. pressure: 1 MPa
DAQ	Model: NI SCXI 1520(8 ch)

Concrete Wall Sample

To simulate the various wall shapes of high-rise buildings, four types of wall samples - including Flat, Step, Rib, and Embossing - were prepared. Material of the wall samples was fabricated with concrete as shown in Figure 3.

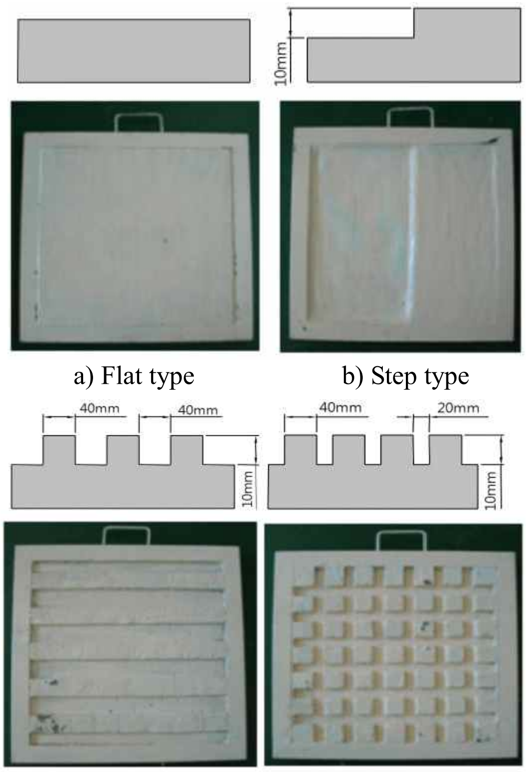

a) Flat type b) Step type

c) Rib type d) Embossing type

Figure 3 Shapes of the outer wall samples

Suction Pad

The suction pad used in this study was based on the ejector principle, whereby the air inside the pad is removed by the ejection of compressed air. Ejectors are often used to suck up and discharge, transfer or mix gases, liquids or powders. The vacuum pressure inside the pad is higher as supply air pressure increase. A multi-step nozzle-type VMECA vacuum cartridge was inserted to maintain constant vacuum pressure even under low and irregular input pressure. Figure 4 shows the structure of the suction pad. The size of the suction pad was 300 mm x 130 mm and its cross-section 390 cm^2. The suction pad was made of flexible sealing foam with multiple holes measuring 12 mm in diameter and 20 mm in depth. The suction pad, which could be attached to the irregular surfaces of vertical walls, had a maximum relative vacuum pressure of -555 mmHg.

EXPERIMENTAL RESULTS

The performance test of suction pad was conducted according to the following procedures:

a. Set the air pressure with the regulator.
b. Move the suction pad on surface of the concrete wall sample using the cylinder.
c. Attach the suction pad on the wall surface by supplying air pressure.
d. Apply a force perpendicular to the wall to the suction pad by injecting compressed air into the cylinder.
e. Increase the air pressure in cylinder until the suction pad detaches from the wall.
f. Repeat the test on regulating increase velocity of air pressure in cylinder.

To determine suction performance of the suction pad, the tensile force of load cell was measured by varying the supply pressure of the compressed air between 0.4 to 0.6 MPa. Figure 5 shows the graphic depiction of the tensile force according to changes in compressed air pressure. Table 3 presents the vacuum pressure in the pad and the tensile force at the respective air pressure. The relative vacuum pressure of the suction pad was found to be between -350 ~ -540 mmHg. At this time, the average tensile force was between 1790 ~ 2770 N.

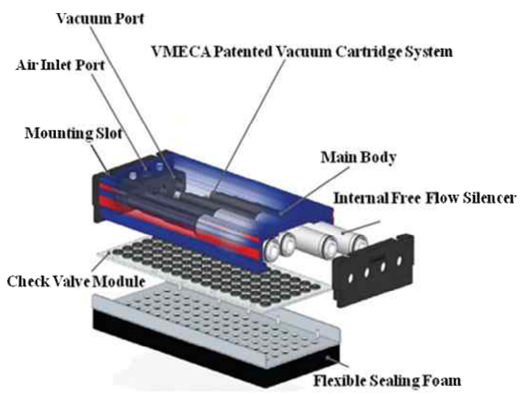

Figure 4 View of the disassembled suction pad

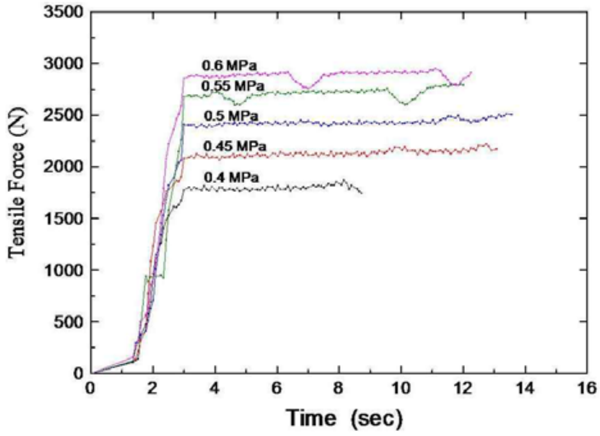

Figure 5 Results graph of tensile force with air pressure

Table 3 Result data of tensile force with air pressure on the flat surface

Supply Pressure (MPa)	Vacuum Pressure (Torr)	Vacuum Pressure (-mmHg)	Avg. Tensile Force (N)
0.4	410	350	1790
0.45	383	377	1930
0.5	274	486	2490
0.55	260	500	2560
0.6	220	540	2770

In the previous test, an increase rate of air pressure inside cylinder was very slow less than about 100 N/s. The increase rate varied to simulate environmental condition as squalls and shortly strong winds. Figure 6 shows the graph of the tensile forces at the cylinder load rates of 255 N/s, 602 N/s, and 1652 N/s at the constant air supply pressure of 0.5 MPa into suction pad. Table 4 presents the vacuum pressures and maximum tensile forces (when detaching from the wall) at the load rates. The maximum attachment forces of the vacuum suction pad were measured according to surface shapes. Figure 7 shows the maximum attachment forces according to the shapes of the walls and compressed air pressure. Tables 4~7 present the vacuum pressure and maximum attachment forces of the pad according to air pressure. The results of the test showed that the ranges of vacuum pressure and attachment forces on the flat-type wall were -355 ~ -605 mmHg and 86.9~121 N, respectively. Those observed for the other types were as follows: 1) step-type: -232 ~ -280 mmHg and 13.4~15.8 N; 2) rib-type: -222 ~ -254 mmHg and 7.3~11.2 N; and 3) embossing-type -209 ~ -216 mmHg and 2.7~5 N. On the flat-type wall, the vacuum pressure and attachment force increased proportionally with the increase in the amount of input air pressure. However, for the step-type, while the maximum vacuum pressure was -280 mmHg, the maximum attachment force was 15.6 N at -259 mmHg of vacuum pressure; for the rib-type, while the maximum vacuum pressure was -254 mmHg at 0.5 MPa of air pressure, the maximum attachment force was 11 N at -242 mmHg of vacuum pressure; and for the embossing-type wall, the maximum attachment force was obtained at the lowest vacuum pressure of -209 mmHg.

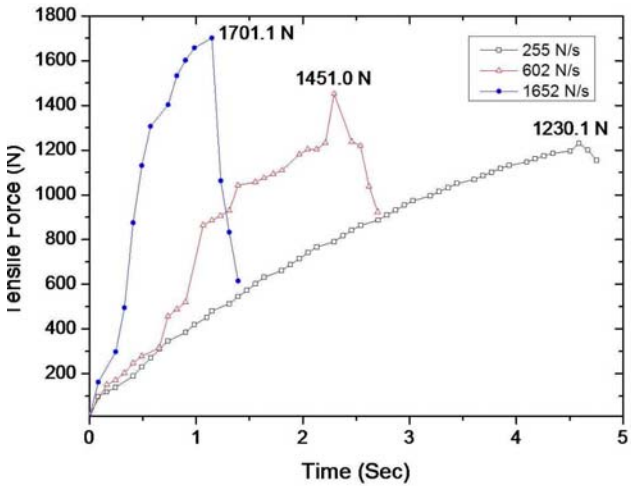

Figure 6 Results graph with dynamic load

Table 4 Results data with load rate

Load Rate (N/s)	Vacuum Pressure (-mmHg)	Max. Tensile Force (N)
255	429	1230.1
602	477	1451.0
1652	520	1701.1

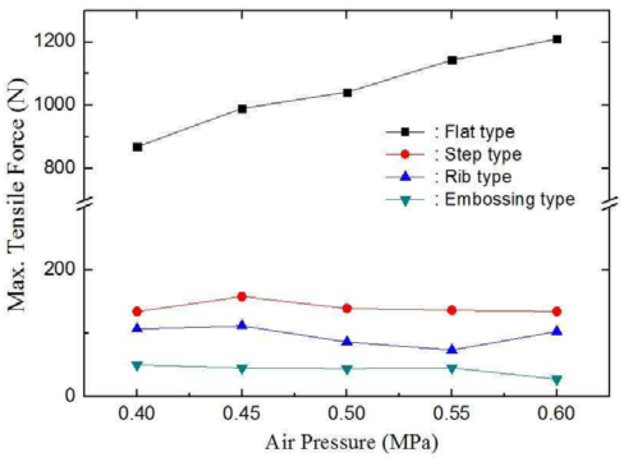

Figure 7 Results graph of max. tensile force with various surface shapes

Table 4 Result data of flat-type sample

Input Pressure (MPa)	Vacuum Pressure (-mmHg)	Max. Tesile Force(N)
0.4	355	868.7
0.45	421	989.9
0.5	500	1041.2
0.55	585	1142.7
0.6	605	1209.7

Table 5 Result data of step-type sample

Input Pressure (MPa)	Vacuum Pressure (-mmHg)	Max. Tesile Force(N)
0.4	232	134.4
0.45	259	158.1
0.5	259	139.4
0.55	280	136.4
0.6	245	134.4

Table 6. Result data of rib-type sample

Input Pressure (MPa)	Vacuum Pressure (-mmHg)	Max. Tesile Force(N)
0.4	223	106.8
0.45	242	111.8
0.5	254	86.1
0.55	222	73.3
0.6	235	102.9

Table 7. Result data of embossing-type sample

Input Pressure (MPa)	Vacuum Pressure (-mmHg)	Max. Tesile Force (N)
0.4	209	49.9
0.45	215	45
0.5	216	44
0.55	213	45.1
0.6	216	27.2

CONCLUSIONS

In this study, testing equipment was fabricated to test and measure the attachment performance of a vacuum suction pad on various configurations of wall surface, i.e., flat, step, rib, and embossing types, formed with concrete material. Since the suction pad was based on the ejector principle, the higher the air pressure, the higher the vacuum pressure. The testing equipment was designed to allow insertion of the concrete wall sample and to measure both the vertical and horizontal attachment forces using a slide block. The attachment force of an ejector-type vacuum suction pad in a perpendicular direction to the wall's surface of flat shape was tested. It was found that the higher the compressed air pressure, the higher the vacuum pressure in the suction pad and, proportionally, the maximum attachment force of the suction pad. The rate of increase of the air pressure in the cylinder was varied, which in turn led to variations in the rate of the force pulling the pad perpendicularly from the wall, to measure the attachment force of the suction pad under a sudden external load. The load rates were varied by 255 N/s, 605 N/s, and 1652 N/s, and it could be confirmed that the higher the load rate, the higher the maximum attachment force. However, the force was lower than 2490 N, which was the maximum force under a static load, by about 50%. This means that the suction pad yields a higher attachment force under a static load than under a dynamic load.

Also, the test results showed that, while the attachment force on the flat-type wall was 868.7 N or above, that on the other types of wall were 160 N or less, showing that the performance of the suction pad decreases greatly on irregular wall surfaces. On the step, rib, and embossing types of surfaces, the vacuum pressure in the pad did not increase while the air pressure was being increased, but showed irregular values within a certain range. The attachment performance became increasingly inferior in the flat, step, rib, and embossing types of wall configuration in that order.

The test results show that the performance of the suction pad depends more on the shape of a wall's surface than on the attachment force generated by air pressure. As such, it could be concluded that the performance of the vacuum suction pad is reliable on flat surfaces, but not on stepped, ribbed or embossed surfaces due to the loss of vacuum pressure via their irregular grooves.

The results disclosed in this paper could serve as useful data when determining the specifications of suction pads to be used in gondola or robot systems for work on a building's outer walls. However, further tests should be conducted on a greater variety of suction pads (in terms of their types and shapes) and another wall surface shape.

ACKNOWLEDGEMENTS

The work presented in this paper was funded by the BMRC (Building-Façade Maintenance Robot Research Center), and supported by the Korea Institute of Construction and Transportation Technology Evaluation and Planning (KICTEP) under the Ministry of Land, Transport and Maritime Affairs (MLTM).

REFERENCES

1. Ji-Seok, J. et al, A Study on Choice of the Type of

Curtain Wall and the Exterior Material according to Commercial Building Images by using the AHP, 2006, Vol. 22(11), pp.89-96.
2. Dong-Kwang L. et al, An instrument of building an outer-wall window-cleaning robot and controller layout using vacuum adsorption technology, 2007, pp. 259-260.
3. Kunchan S. et al, Design of an attachment device for robotic systems that climb rugged vertical surfaces, KSPE, 2007, pp. 99-100.
4. Siyoul Jang, A study on the enhancement of uniform contact technology for large-scale imprinting with the design of a vacuum gripping pad, Journal of the KSTLE, 2008, Vol.24(6), 99. 623-331.
5. M. Elliot, W. Norris, J.Xiao, City-Climber: A new generation of wall-climbing robots, Proceedings of the IEEE International Conference on Robotics and Automation, 2007.
6. S. Hirose, A. Nagakubo, R. Toyama, A machine that can walk and climb on floors, walls and ceilings, International Conference on Advanced Robotics, 1991, Vol. 1, pp. 753-758.
7. Alan T. et al, "Scaling hard vertical surfaces with compliant microspine arrays", The International Journal of Robotic Research, 2006, Vol. 25, pp. 1165-1179.
8. Guido La Rosa, Michele Messina, Giovanni Muscato, R. Sinatra, A low-cost lightweight climbing robot for the inspection of vertical surfaces, Mechatronics, 2002, Vol 12, pp. 71-96.
9. Nishi A., A biped walking robot capable of moving on a vertical wall, Mechatronics, 1992, Vol. 2(6), pp. 543-554.
10. Nishi A., Development of wall-climbing robots, Compute Electron Eng, 1996, Vol. 22(2), pp. 123-149.
11. Nishi A., Miyagi H., A wall climbing robot using the thrust force of a propeller mechanism and control in a strong wind, JSME Int J Ser C, 1994, Vo1. 37, pp. 172-178.
12. Hwang Kim, Dongmok Kim, Hojoon Yang, Kyouhee Lee, Kunchan Seo, Doyoung Chang, Jongwon Kim, A wall climbing robot with a vacuum caterpillar wheel system operated by a mechanical valve, Proceedings of the 9th International Conference on Climbing and Walking Robots, 2006, pp. 28-33.

Proceedings of the 8th JFPS International
Symposium on Fluid Power, OKINAWA 2011
Oct. 25-28, 2011

2A2-3

TRANSIENT PRESSURE AND FLOW RATE MEASUREMENT OF THE VACUUM TOILET SYSTEM FOR TRAIN

Kenji FUJINO*, Masahiko ITO**, Chongho YOUN**, Li Xin**, Kenji KAWASHIMA**,
Toshiharu KAGAWA**, Nobuaki YAMAMOTO***, Koji TANIGUCHI****
and Hiroshi YAMAMOTO*****

*EAST JAPAN RAILWAY COMPANY, Research and Development Center of JR East Group,
2-479, Nisshin-cho, Saitama-shi, Saitama-pref. 331-8513, Japan
(E-mail: k-fujino@jreast.co.jp)
** Tokyo Institute of Technology, Precision and Intelligence Laboratory, Japan
*** TOKYO METER CO., LTD, Engineering Department, Japan
**** Tokyu Car Corporation, Development Planning Department Railway Division, Japan
***** Tesika Co., Ltd., Japan

ABSTRACT

The pneumatic system which is called a vacuum toilet is used for the toilet for train to make a car interior comfortable. So far, a pneumatic system design of the vehicle was much based on the experience. In this paper, in the efficiency of this pneumatic system, using the quick flow sensor which has a high response, it measured the pressure and the flow rate of the vacuum toilet for train. Also, it confirmed that it is possible to attempt vacuum toilet feature improvement by the change of the pneumatic element and that the simulation result agreed with the experiment data approximately.

KEY WORDS

Pneumatic system, Vacuum toilet system, Energy consumption

NOMENCLATURE

P	:	Pressure [kPa]
Q	:	flow rate [L(ANR)]
t	:	Time [sec]

Subscript

s	:	supply line
c	:	the reserve filth tank
H	:	ejector
2	:	upstream of ejector

INTRODUCTION

A pneumatic system is used for the wide field in addition to the industrial field. In recent years, a pneumatic system is used to realize the lightening of a vehicle, and comfortable car interior environment at the toilet for train, too.

The system which is called a vacuum toilet is composed of the mechanism to transfer to the filth tank in the positive pressure after sucking filth with the negative pressure. A vacuum toilet for train is shown in Figure 1.

However, as for such a pneumatic system, the measurement of the pressure and the flow rate isn't sufficiently done and as for the design, most are based

on the experience. It thinks that it is necessary to review about the validity of the design from the viewpoint of the efficiency and the energy consumption.
On the other hand, by the research of the authors, the evaluation of the air pressure energy is done in case of measurement of the compressed fluid. First, we define a concept with the valid energy of the air to have considered the compressibility of air. The energy and the efficiency of the pneumatic-system become able to be evaluated using this concept.[1]
Also, we proposed quick flow sensor(QFS) which has a high response. Then, using QFS, it showed that the flow rate measurement by the compressed air about the static state and the non-steady state became possible.[2] The static characteristic of QFS is shown in Figure 2. Also, the frequency response of QFS is shown in Figure 3.
Therefore, in the this report, it reviews about the measurement technique for the pneumatic system at the toilet for train.
First, it measures pressure and flow rate about the non-stationary flow of the vacuum toilet of the initial condition by the experiment.
Next, we aim at the efficiency improvement and the energy consumptio restraint at the vacuum toilet, and based on the measuring result, it reviews the pneumatic equipment change, the pipe size and the route change which composes a vacuum toilet, and it evaluates the efficiency of the system.
Then, it compares between the simulation result based on the pneumatic characteristic of this system and the result of the experiment .

Figure 1 Vacuum toilet for train

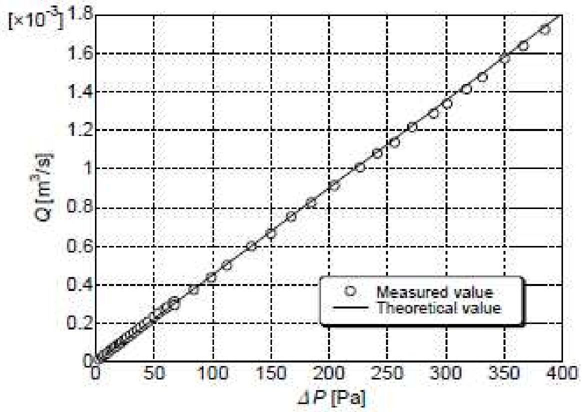

Figure 2 The static characteristic of QFS

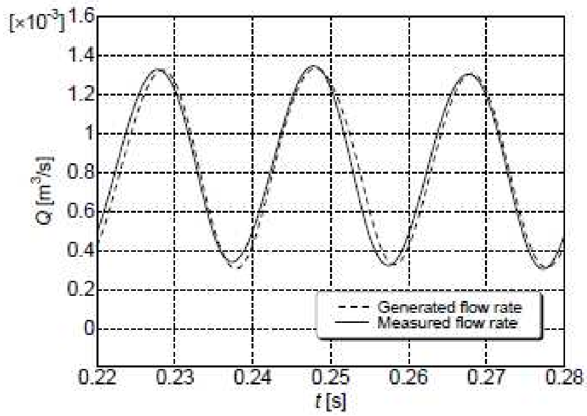

Figure 3 The frequency response of QFS

The vacuum toilet system for train

The history at the toilet for train

The toilet is the facilities which have the feature to dispose filth such as the excrement which has the fear to stain environment around, giving off a bad smell. Specifically, as for the means of transportation such as the airplane and the railway which does a long movement, a wide range of devices were so far made a restroom. [3,4]
In the past, at the railcar, the way of making the track inside and outside of the country slip filth was used for a transit-time after washing a toilet in water but became a problem very much hygienically. In the 1960s, A shattering type excrete-disposer was developed. This equipment mixed a treatment agent to the filth and disinfected and firmed the filth, and then had the feature the filth shattering and scattering and was applied to the vehicle of the part. However, as the sanitary problem, there was not qualitative improvement and this equipment was abolished by the 1980s. After that, the collection type toilet which installed a filth tank in the vehicle lower part was used. Because the amount of

consumption of water was much at the toilet of the type of washing in water, and the weight of the vehicle which had a great deal of rinse waters and the collection tank of the filth increased, and became a problem when aiming to lighten in the vehicle. To solve this problem, A circle-method toilet was used by much since the 1970s. This toilet has the feature to filter and disinfect the moisture which was collected at the filth tank and to reuse for washing a toilet in water. However, the solid which is caused by the feces and the toilet paper and so on was contained in reused moisture, adhered to the drainpipe inside and sometimes caused the stuff. Also, it gives an unpleasant feeling because the treat-water itself smell is hard and it isn't possible to finish preventing the peculiar smell of the vehicle toilet. From the 1990s, A vacuum toilet was introduced into the means of transportation such as the airplane. At the previous toilet for train, it needed 5 - 6 liters of water for every the use of the taking. On the other hand, at the vacuum toilet, the filth in the toilet is sucked into the filth tank with the vacuum pressure. Therefore, it gets to use only about 0.3 liters of water in taking operation and the amount of consumption of water can be suppressed to the minimum. Therefore, it connects with the weight reduction by the vehicle, too. Moreover, the vacuum toilet is comfortable because the smell of the filth isn't left because it absorbs the atmosphere of the neighborhood with the filth and the slide-valve closes after that. And, to compared with the conventional restroom., the vacuum toilet gets to arrange pipe levelly to convey filth with the negative pressure and it becomes possible to arrange in the looking up.

The vacuum toilet system for train

There is a vehicle by which a vacuum toilet is loaded into the Shinkansen vehicle which East Japan Railway Co., possesses and operates. Figure 4 is Series E3 Shinkansen vehicle which has a vacuum toilet.

An example at the vacuum toilet for train is shown in Figure 5. After use, the vacuum toilet operates in the following order. Valve 3 operates and compressed air is sent to the ejector and makes a vacuum occur to the reserve filth tank. Also, valve 1 operates and accumulates 300 cc water to the buffer tank(water). Valve 2 operates after Valve 3 and 1 closes, and pressurizes the buffer tank(water) and washes a seat by the water. At the same time, it changes an air-circuit with valve 6 and slide valve 2 operates. When slide valve 2 operates, with the negative pressure, filth in the seat is sucked by the reserve filth tank. After that, slide valve 2 closes and isolates the seat and the reserve filth tank. Next, after Valve 4 operates and pressurizes the reserve filth tank, valve 5 operates and slide valve 1 opens. Then, the filth is transferred to the filth tank.

Figure 4 Series E3 Shinkansen vehicle

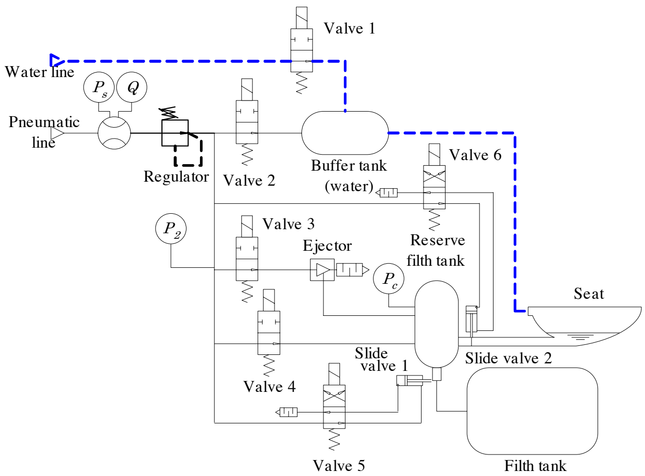

Figure 5 The scheme of vacuum toilet system for train

The measurement of the vacuum toilet

From the preceding chapter, it finds that a vacuum toilet for train is composed of the air actuator of the ejector and the air cylinder and so on, and control valve, pipe. Therefore, we measured pressure and flow rate about the wash cycles such as the filling of the tank, the operation of the cylinder and the vacuum generation by the ejector. Incidentally, we used QFS(Quick Flow Sensor) which is excellent about the linearity and the response for the measurement.

Measuring point of the experiment

As shown in Figure 5, we measured the pressure and the flow rate of the supply source at the vacuum toilet, the pressure of the valve 2 inlet to send compressed air to the ejector, and the pressure in the reserve filth tank .

The test condition

Test condition list is shown in Table 1. In addition to the measurement in the initial condition, we measured

with the change of the decompression-valve size and the change of the main line size and the reroute. Test number A-07 is initial condition and isn't changing a circuit. As for test number B-07, we changed a decompression-valve. Test number C-07 is the test to have changed the size and the route of the pipe in addition to the change of the decompression-valve. Also, at test number C-06, we changed the set-pressure of the decompression-valve 0.6 MPa, too.
The list of the equipment used for the experiment is shown in Table 2.

Table 1 The test condition list

Test number	Supply Pressure [MPaG]	Size of reducing valve	Size of pipe	Pipe route
A-07	0.7	original	original	no change
B-07	0.7	big flow	original	no change
C-07	0.7	big flow	up	change
C-06	0.6	big flow	up	change

Table 2 The list of measuring equipment

Mark	Model	Maker
Ps	APM-L-400	TOKYO METER CO., LTD
Q	APM-L-400	TOKYO METER CO., LTD
P2	AP-13S	KEYENCE CORPORATION
Pc	KL-80	Nagano Keiki CO., Ltd

The experimental result

Result of pressure
The experimental result of the reserve filth tank pressure is shown in Figure 6. The experimental result with 4 conditions is being described in the figure at the same time. There is change of state in a few steps floor in the operation of the vacuum toilet, but in this paper, we aim at the pressure variation of the reserve filth tank. Incidentally, the decrease of the vacuum pressure emission rate is seen from the 2.5 second. This is because the operation to send water to the seat was begun from this time. When comparing with the vacuum pressure emission rate of the initial condition, to make the decompression-valve a big flow rate is increasing a vacuum pressure emission rate. Moreover, it is that the pipe size up and the change of the pipe route decreased pressure loss and the vacuum pressure emission rate is increasing.
The change of the supply pressure is shown in Figure 7. From this figure, the supply pressure of test number B-07 and C-07 are higher than test number A-07. It thinks that this leads to the increase of the vacuum pressure emission rate in the reserve filth tank. Also, the supply pressure declines around 2.5 seconds. We think that this is the purpose that compressed air supply operation to the ejector and the pressurization operation of the water to wash a toilet are done at the same time.
At experiment, because the air pressure part of the system is composed efficiently, the improvement of the suction performance which is the important feature of the vacuum toilet is attempted. Also, even if it changes a supply pressure into 0.6 MPa by the configuration status with test number C-06, there is not a big difference with the vacuum pressure emission rate in the initial condition. From this thing, it was possible to confirm that there was not a problem in the performance of the vacuum toilet even if the supply pressure was declined by decreasing the delta-pressure of the component of the system.

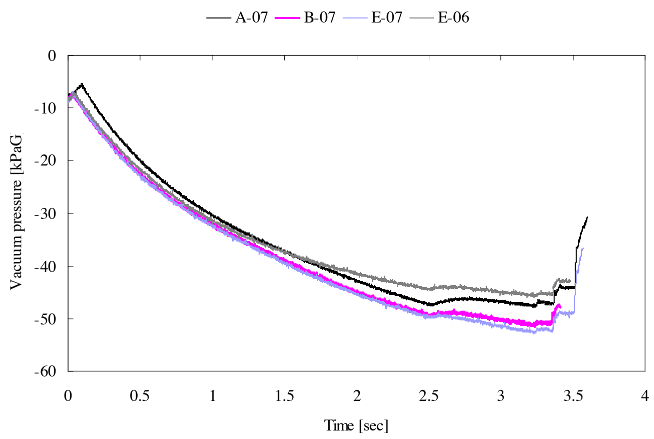

Figure 6 Experimental result of the reserve filth tank pressure

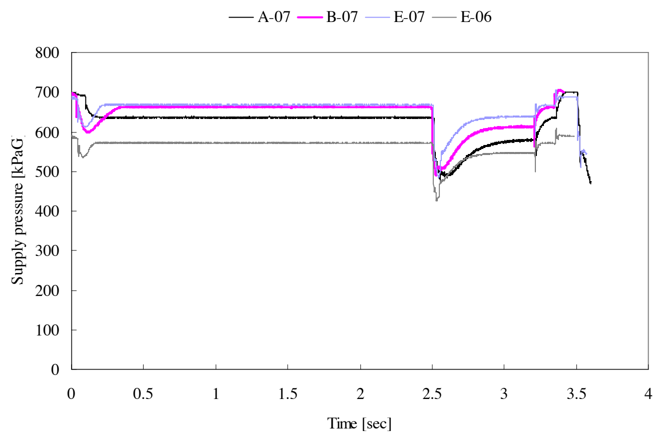

Figure 7 Experimental result of the supply pressure

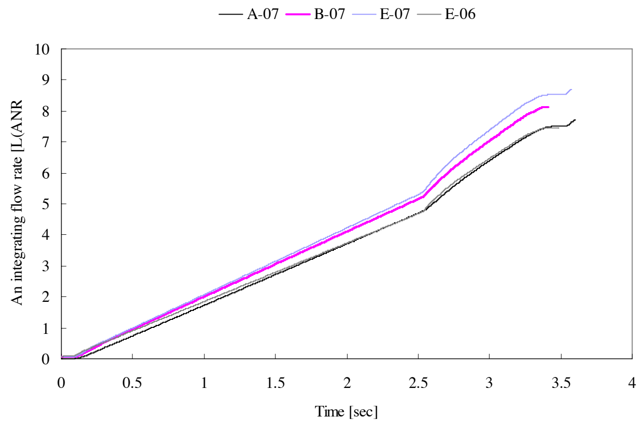

Figure 8 Experimental result of the integrating flow rate

Result of flow rate

The integrating flow rate which was measured in the supply line at the vacuum toilet is shown in Figure 8. The experimental result with 4 conditions is being described in the figure at the same time. Also, to compare with the pressure result of the reserve filth tank, the flow rate change makes elapsed time the same. As shown in this figure, to compare with the initial condition flow rate, the flow rate to be supplying a vacuum toilet with making the decompression-valve a big flow rate, line size up and changing of the pipe route is increasing. Because the pressure loss of the pipe and so on was decreased, this is because it became easy for air to flow.

Therefore, when changing a supply pressure into 0.6 MPa in the condition which is the same as test number C-06, the flow rate can be restrained as initial condition. This shows that the vacuum toilet can be worked, being no-problem functionally even if it makes a supply pressure decline in arranging plumbing and so on efficiently. Incidentally, the decline of the supply pressure and the decrease of the flow rate get to suppress energy consumption at the vacuum toilet, too.

Simulation of toilet system

To do a simulation with spare filth tank pressure, we measured the vacuum characteristic of the ejector. The vacuum characteristic of the ejector is shown in Figure 9. A vacuum characteristic is found from the upstream pressure of the ejector and the pressure of the vacuum port.

It is therefore shown by the following equation.

$$G_H = f(P_2,\ P_c) \tag{1}$$

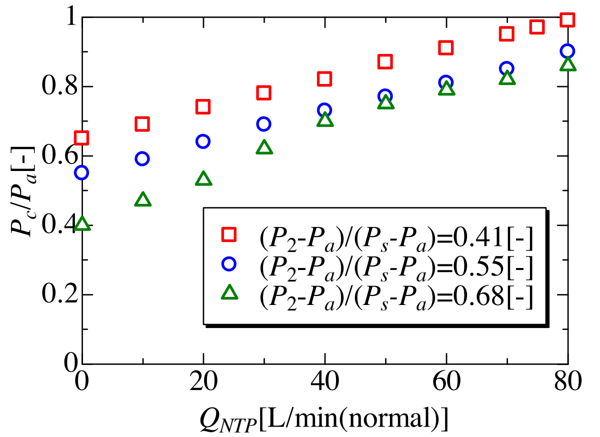

Figure 9 Vacuum characteristic of the ejector

We simulated with the reserve filth tank pressure from the vacuum characteristic of the ejector which was measured by the experiment. The simulation result is shown in Figure 10. The experimental result and the simulation result showed approximately the same pressure variation.

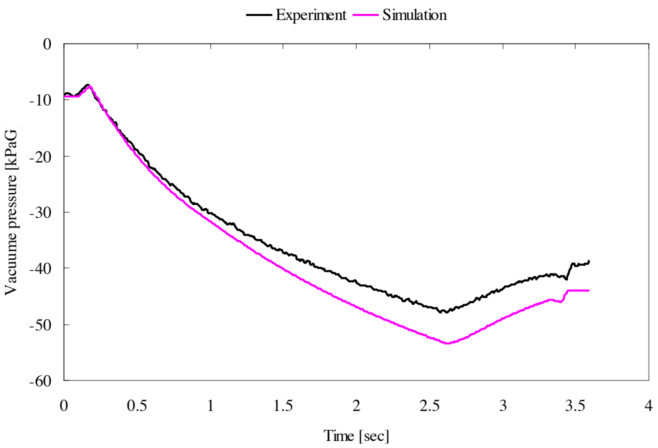

Figure 10 The simulation result of the reserve filth tank

Summary

In this paper, we measured the pressure and the flow rate of the vacuum toilet for train, being first. The following matters could be confirmed from this measuring result.

The decompression-valve change, and the line size change, and the pipe route change, when doing all of them, it became excellent about the vacuum pressure emission rate.

For the large consumption flow rate of the ejector and the large consumption flow rate in water tank pressurization, at the present equipment size, this is because the pressure loss had occurred. The efficiency of the vacuum toilet became good in doing an equipment size roughly, and as a result, the higher performance could be shown.

Also, when the decompression-valve and the pipe are size up, the vacuum pressure emission rate becomes big, but the whole consumption flow rate becomes big and the energy consumption has increased. However, if composing pneumatic equipment efficiently, supply pressure becomes low and the thing by which it is possible to make energy consumption decrease was shown.

Moreover, we simulated the pressure of the reserve filth tank from the vacuum characteristic of the ejector. We think that the simulation result is same as the experimental result approximately, and that it is possible to utilize for increase in efficiency at the vacuum toilet for train in the future by it.

The railway vehicle is using pneumatic system for the brake, the suspension, the door and the toilet and so on. There is a problem with the space and the cost, and built-in number of the air compressor is limited. That is, there is a limit in the air volume which the air pressure equipment can be supplied with. And, the brake operation must make not be influenced by the other pneumatic equipment. Therefore, we want to make the consumption air volume of the service equipment like the vacuum toilet as little as possible.

REFERENCES

1. M.Cai, T.Fujita, T.Kagawa, Energy Consumption and Assessment of Pneumatic Actuating Systems, Transactions of the Japan Hydraulic & Pneumatic Society, 2001, 32-5, 118/123
2. T.Funaki, K,Kawashima, T,Kagawa : Characteristic Analysis of Laminar Flow Meter for Gases with High Speed Response, Transactions of the Society of Instrument and Control Engineers, 2004, 40-10, 1008/1013
3. Homepage of Japan Toilet Lab. : http://www.toilet.or.jp
4. Tanaka : Applicability of sustainable sanitation technology at the watershed of reservoir(1), Report of Water Resources Environment Research Institute, 26/30, 2004
5. T.Funaki, K,Kawashima, T,Kagawa: Development of Unsteady Flow Controller for Gases , Transactions of the Society of Instrument and Control Engineers, Vol.42, No.5, 461/466, 2006

Proceedings of the 8th JFPS International
Symposium on Fluid Power, OKINAWA 2011
Oct. 25-28, 2011

2A2-4

CONTROL ANALYSIS OF AN ELECTROPNEUMATIC ACTUATOR WITH FULL CONVECTION MODEL: TOWARD MINIMUM ENERGY ACTUATION

Mouchira ABIDI*, Eric BIDEAUX*, Xavier BRUN*, and Sylvie SESMAT*

Ampère Lab, UMR CNRS 5005, INSA Lyon,
University of Lyon
25 avenue Jean Capelle, Villeurbanne, F-69621, FRANCE
(E-mail: eric.bideaux@insa-lyon.fr)

ABSTRACT

Today it is no more reasonable to think that air is free. In order to increase energy efficiency, the control of electropneumatic actuator requires the energy balance in terms of air flow delivered by the power modulators to be optimized during tasks such as trajectory tracking. This paper tries to tackle two essential difficulties when dealing with pneumatic actuation. First, the modeling of the heat transfer phenomena in the cylinder chambers and second, control syntheses taking into account a realistic representation of the temperature dynamic. As a consequence, this approach enables to address properly the optimization of the overall actuation efficiency.

KEY WORDS

Electropneumatic, heat transfer, model analysis, linear control, energy efficiency

NOMENCLATURE

h	specific enthalpy (J/kg)
m	mass of gas (kg)
U	internal energy (J)
$\frac{dQ}{dt}$	heat exchange (J/s)
P	pressure (Pa)
T	temperature (K)
q_m	mass flow rate (kg/s)
u	servo-distributor input voltage (V)
y	piston position (m)
v	piston velocity (m/s)
V	chamber volume (m^3)
F	force (N)
c_v	specific heat capacity at constant volume (J/kg/K)
c_P	specific heat capacity at constant pressure (J/kg/K)
r	perfect gas constant per mass unit (J/kg/K)
γ	adiabatic index
k	polytropic constant
k_{air}	air thermal conductivity (J/s/K/m)
μ	air dynamic viscosity (Ns/m^2)
g	gravity acceleration (m/s^2)
b	viscous coefficient (N/m/s)
M	moving load (kg)
S	area of the piston (m^2)
A	heat exchange area (m^2)
λ	heat exchange coefficient (J/K/m^2)
t	time (s)
$\underline{x}$	state vector
δ	variation

Subscripts and superscripts

0	external or wall
ext	external
N	chamber N
P	chamber P
S	supply pressure
E	exhaust pressure
e	equilibrium
f	friction

INTRODUCTION

For pneumatic applications, the overall energy balance must be made in terms of power consumption of the compressor supplying the fluid. In hydraulic and electric applications, energy consumption can easily be evaluated but, when dealing with compressible fluids [1, 2, 3], the energy is related to mass flow rate [4] but also to temperature [5, 6]. However, temperature measurement is still a bottleneck in terms of time constant in regard with the dynamic of the actuation and the modeling of heat transfer behavior is usually drastically simplified.
Recent works on modeling heat transfer in reservoir have resulted in simulation models with detailed convection phenomena according to air flow behavior [6, 7]. These models have been validated experimentally in different configurations and air flow conditions. One of the main interests of these results is that the real energy consumption can now be evaluated on line and in real time using state observers based on cheap and large bandwidth measurement equipments as pressure sensors.
The aim of this work is to explore the interest of temperature dynamic in the synthesis of the control law in order to tackle different drawbacks of electropneumatic actuation such as stick-slip [9] and energy efficiency. Consequently, a model with full heat transfer phenomena and temperature dynamic is proposed. Then, this model is used to perform the synthesis of linear laws taking into account these phenomena.

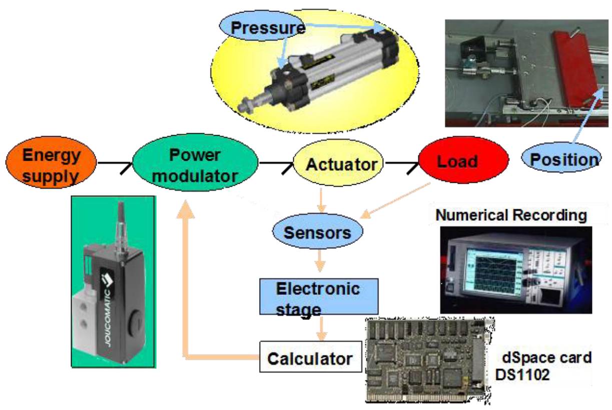

Figure 1: Experimental rig

The first section is dedicated to the modeling of the system where a model taking into account a full convection model for air in the cylinder is proposed. Then the next sections focus on the comparison of two modeling approaches: the first model is based on the classical polytropic hypothesis, whereas the second model takes into account heat exchanges. The first step consists in the comparison of the open-loop dynamic of the linearized models according to piston position. A state feedback control is then designed for each model. This enables the comparison of the system behavior according to the model used for the control synthesis. In this last part, a virtual prototype of the actuator is used and the results are discussed in terms of temperature evolution and energetic performances.

SYSTEM MODELING

The experimental bench (Fig. 1 and 2) is an in-line electropneumatic servodrive controlled by two three-way servo-distributors.

Mechanical part:
The stroke length is half a meter and the total moving load is 17 kg. The electropneumatic system model uses classical assumptions [10]: by considering the pressure behavior in a chamber with variable volume and the mechanical equation which includes pressure force, viscous friction and dry friction (F_f) and an external force (F_{ext}) due to atmospheric pressure.

$$\begin{cases} M\dfrac{dv}{dt} = S_P P_P - S_N P_N - F_{ext} - F_f \\ \dfrac{dy}{dt} = v \end{cases} \qquad (1)$$

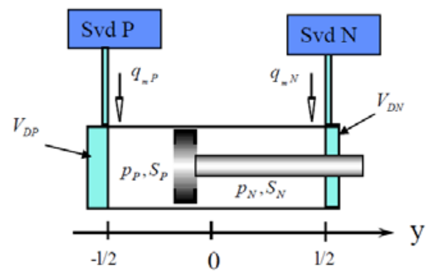

Figure 2: Scheme and notation

Using the theory of multi-scale systems, the dynamics of the servo-valves can be neglected [9]. Then the model can be reduced to a static characteristic for given supply and exhaust pressures and is described by two relationships $q_{mP}(P_P, u_P)$ and $q_{mN}(P_N, u_N)$ between the mass flow rates q_{mP} and q_{mN}, the input voltages u_P and u_N, and the output pressures P_P and P_N.

The following assumptions are taken into account for establishing the thermodynamic model:

- air is a perfect gas,
- pressure and temperature are homogenous in the chambers,
- kinetic and gravitational energy of the fluid, as well as viscous work and cylinder flow leakages are considered as negligible.

The thermodynamic model obtained by applying the thermodynamic principles and mass conservation is defined as follow:

Chamber N:

$$\begin{cases} \dfrac{dU_N}{dt} = q_{mSN}h_S - q_{mNE}h - P_N\dfrac{dV_N}{dt} + \dfrac{dQ_N}{dt} \\ \dfrac{dm_N}{dt} = q_{mSN} - q_{mNE} \\ \dfrac{dV_N}{dt} = -S_N v \end{cases} \tag{2}$$

and

$$\begin{cases} P_N = \dfrac{r}{c_v}\dfrac{U_N}{V_N} \\ T_N = \dfrac{1}{c_v}\dfrac{U_N}{m_N} \end{cases} \tag{3}$$

Chamber P:

$$\begin{cases} \dfrac{dU_P}{dt} = q_{mSP}h_P - q_{mPE}h - P_P\dfrac{dV_P}{dt} + \dfrac{dQ_P}{dt} \\ \dfrac{dm_P}{dt} = q_{mSP} - q_{mPE} \\ \dfrac{dV_P}{dt} = S_p v \end{cases} \tag{4}$$

and

$$\begin{cases} P_P = \dfrac{r}{c_v}\dfrac{U_P}{V_P} \\ T_P = \dfrac{1}{c_v}\dfrac{U_P}{m_P} \end{cases} \tag{5}$$

Thermal Exchange:

The thermal exchange from the gas in each chamber and the cylinder is developed. The proposed macroscopic model is based on the dimensional analysis theory and takes into account free-forced convection phenomena as well as wall thermal conduction. The model gives the equivalent macroscopic temperature in a chamber according to chamber state, flow conditions, and external temperature. It has been validated experimentally for charge and discharge tests, which justify the proposed estimation.

$$\frac{dQ_N}{dt} = \lambda(T_N, P_N)\cdot A_N(y)\cdot(T_0 - T_N) \tag{6}$$

$$\frac{dQ_P}{dt} = \lambda(T_P, P_P)\cdot A_P(y)\cdot(T_0 - T_P) \tag{7}$$

where $A(y)$ is the heat exchange area between gas and walls according to the piston position, and $\lambda(T,P)$ is the heat transfer coefficient obtained using the dimensionless number listed below :

- Nusselt number, $Nu = \dfrac{\lambda D}{k_{air}} = \xi \cdot Gr^{\beta} \cdot \Pr^{\beta'}$
- Grashof number, $Gr = \dfrac{gD^3(T_0 - T)P^2}{r^2\mu^2T^3}$
- Prandtl number, $\Pr = \dfrac{c_P\mu}{k_{air}}$

In this relations, β and β' are coefficient experimentally determined and D is a characteristic length for the convection phenomena.

In the pressure and temperature range for this application, the Prandtl number for the gas can be considered as constant. Then, the heat transfer coefficient can be expressed for each chamber as:

$$\lambda\left(T_{P\,(\text{or N})}, P_{P\,(\text{or N})}\right) = \lambda_{P\,(\text{or N})} = \xi\frac{k}{D}\frac{\left[gD^3\left(T_{cyl} - T_{P(\text{or }N)}\right)P^2_{P(\text{or }N)}\right]^{\beta}}{r^2\mu^2T^3_{P(\text{or }N)}} \tag{8}$$

Using (3) and (5) enables the substitution in (2) and (4) of the natural state variables (internal energy and mass) by pressure and temperature in each chamber. The obtained model has 6 state variables and is given by the following equations:

$$\begin{cases} \dfrac{dy}{dt} = v \\ \dfrac{dv}{dt} = \dfrac{1}{M}\left(S_PP_P - S_NP_N - F_{ext} - F_f\right) \\ \dfrac{dP_N}{dt} = \dfrac{\gamma rT_N}{V_N(y)}\left(q_{mSN} - q_{mNE}\right) - \dfrac{\gamma r(T_N - T_0)}{V_N(y)}q_{mSN} \\ \qquad + \dfrac{\gamma S_NP_N}{V_N(y)}v + (\gamma-1)\dfrac{A_N(y)\lambda_N}{V_N(y)}(T_0 - T_N) \\ \dfrac{dP_P}{dt} = \dfrac{\gamma rT_P}{V_P(y)}\left(q_{mSP} - q_{mPE}\right) - \dfrac{\gamma r(T_P - T_0)}{V_P(y)}q_{mSP} \\ \qquad - \dfrac{\gamma S_PP_P}{V_P(y)}v + (\gamma-1)\dfrac{A_P(y)\lambda_P}{V_P(y)}(T_0 - T_P) \\ \dfrac{dT_N}{dt} = \dfrac{(\gamma-1)T_N}{P_NV_N(y)}\left[\left(\gamma\dfrac{T_0}{T_N} - 1\right)c_vT_Nq_{mSN}\right. \\ \left. -(\gamma-1)c_vT_Nq_{mNE} + P_NS_Nv + \lambda_NA_N(y)\cdot(T_0 - T_N)\right] \\ \dfrac{dT_P}{dt} = \dfrac{(\gamma-1)T_P}{P_PV_P(y)}\left[\left(\gamma\dfrac{T_0}{T_P} - 1\right)c_vT_Pq_{mSP}\right. \\ \left. -(\gamma-1)c_vT_Pq_{mPE} - P_PS_Pv + \lambda_PA_P(y)\cdot(T_0 - T_P)\right] \end{cases} \tag{9}$$

EQUILIBRIUM SET AND LINEARIZED MODEL

The previous physical model of the electropneumatic system is too complex for an analytic approach. A linearized model has to be established first for analyzing the modal characteristic of the model, and second for the synthesis of a state feedback control law. Let us assume that:

- the heat transfer coefficient is nearly constant at equilibrium,
- the mass flow rate characteristic of the servovalve is not depending on the temperature and is given by:

$$\begin{cases} q_{mN}(P_N,u) = -q_{mSN}(P_S,T_S,P_N,u) + q_{mNE}(P_N,T_N,P_E,u) \\ q_{mP}(P_P,u) = q_{mSP}(P_S,P_P,T_S,u) - q_{mPE}(P_P,T_P,P_E,u) \end{cases} \tag{6}$$

For a single input non-linear model $\underline{\dot{x}} = f(\underline{x},u)$, the equilibrium set is defined by $E = \{(\underline{x}_e,u^e) \in \Re^n \times \Re / f(\underline{x}_e,u^e) = 0\}$. In our case the equilibrium set can be deduced from (9):

$$\begin{cases} y^e \\ v^e = 0 \\ T_N^e = T_P^e = T_0 \\ q_{mN}(P_N^e,-u^e) = 0 \\ q_{mP}(P_P^e,u^e) = 0 \\ S_P P_P^e - S_N P_N^e - F_{ext}^e = 0 \end{cases} \tag{10}$$

The three unknown variables (P_P^e, P_N^e, u^e) are determined by solving graphically the three last equations in (10) using the mass flow rate characteristic of the servovalve.
Let us note the variations in a neighborhood of the equilibrium set as:

$$\begin{cases} \delta x = x - x^e \\ \delta u = u - u^e \end{cases} \tag{11}$$

The linearized model is then defined by (12) using following notations for the flow characteristics of the servovalve around the equilibrium point:

$$\begin{aligned} & G_{uN}^e = -\left.\frac{\partial q_{mN}(P_N,u)}{\partial u}\right|_{(P_N^e,-u^e)}, C_{P_N N}^e = \left.\frac{\partial q_{mN}(P_N,u)}{\partial P_N}\right|_{(P_N^e,-u^e)} \\ & G_{uP}^e = \left.\frac{\partial q_{mP}(P_P,u)}{\partial u}\right|_{(P_P^e,u^e)}, C_{P_P P}^e = -\left.\frac{\partial q_{mP}(P_P,u)}{\partial P_P}\right|_{(P_P^e,u^e)} \\ & \tau_P^e = \frac{V_P(y^e)}{krT_0 C_{P_P P}^e}, \tau_N^e = \frac{V_N(y^e)}{krT_0 C_{P_N N}^e} \end{aligned} \tag{12}$$

In most of the cases, for control purposes, the thermodynamic transformation of the gas in the cylinder is assumed to be polytropic and heat transfer with walls is neglected. Taking into account those simplifications, it allows the reduction of the model to a 4th order model defined by (14). The two models can now be compared analytically according to the formulation shown bellow.

$$\frac{d}{dt}\begin{bmatrix} \delta y \\ \delta v \\ \delta P_N \\ \delta P_P \\ \delta T_N \\ \delta T_P \end{bmatrix} = \underbrace{\begin{bmatrix} 0 & 1 & 0 & 0 & 0 & 0 \\ 0 & -\frac{b}{M} & -\frac{S_N}{M} & \frac{S_P}{M} & 0 & 0 \\ 0 & \frac{\gamma S_N P_N^e}{V_N(y^e)} & -\frac{\gamma r T_N^e}{V_N(y^e)} C_{P_N N}^e & 0 & -\frac{(\gamma-1)A_N^e \lambda_N^e}{V_N(y^e)} & 0 \\ 0 & -\frac{\gamma S_P P_P^e}{V_P(y^e)} & 0 & -\frac{\gamma r T_P^e}{V_P(y^e)} C_{P_P P}^e & 0 & -\frac{(\gamma-1)A_P^e \lambda_P^e}{V_P(y^e)} \\ 0 & \frac{(\gamma-1)S_N T_N^e}{V_N(y^e)} & -\frac{(\gamma-1) r T_N^e}{P_N^e V_N(y^e)} C_{P_N N}^e & 0 & -\frac{(\gamma-1)T_N^e A_N^e \lambda_N^e}{P_N^e V_N(y^e)} & 0 \\ 0 & -\frac{(\gamma-1)S_P T_P^e}{V_P(y^e)} & 0 & -\frac{(\gamma-1) r T_P^e}{P_P^e V_P(y^e)} C_{P_P P}^e & 0 & -\frac{(\gamma-1)T_P^e A_P^e \lambda_P^e}{P_P^e V_P(y^e)} \end{bmatrix}}_{A_{heat}} \begin{bmatrix} \delta y \\ \delta v \\ \delta P_N \\ \delta P_P \\ \delta T_N \\ \delta T_P \end{bmatrix} + \underbrace{\begin{bmatrix} 0 \\ 0 \\ -\frac{\gamma r T_N^e}{V_N(y^e)} G_{uN}^e \\ \frac{\gamma r T_P^e}{V_P(y^e)} G_{uP}^e \\ -\frac{(\gamma-1) r T_N^e}{P_N^e V_N(y^e)} G_{uN}^e \\ \frac{(\gamma-1) r T_P^e}{P_P^e V_P(y^e)} G_{uP}^e \end{bmatrix}}_{B_{heat}} \delta u \tag{13}$$

$$\frac{d}{dt}\begin{bmatrix} \delta y \\ \delta v \\ \delta P_N \\ \delta P_P \end{bmatrix} = \underbrace{\begin{bmatrix} 0 & 1 & 0 & 0 \\ 0 & -\frac{b}{M} & -\frac{S_N}{M} & \frac{S_P}{M} \\ 0 & \frac{k P_N^e S_N}{V_N(y^e)} & -\frac{1}{\tau_N^e} & 0 \\ 0 & -\frac{k P_P^e S_P}{V_P(y^e)} & 0 & -\frac{1}{\tau_P^e} \end{bmatrix}}_{A_{poly}} \cdot \begin{bmatrix} \delta y \\ \delta v \\ \delta P_N \\ \delta P_P \end{bmatrix} + \underbrace{\begin{bmatrix} 0 \\ 0 \\ -\frac{krT_0}{V_N(y^e)} G_{uN}^e \\ \frac{krT_0}{V_P(y^e)} G_{uP}^e \end{bmatrix}}_{B_{poly}} \cdot \delta u \tag{14}$$

OPEN LOOP STABILITY

In this section a comparative study of both 4th and 6th order open loop systems is presented. In linear system, poles have influence on stability system response, transient response and bandwidth. For both linearized models (12) and (14), the stability can be analyzed according to the considered equilibrium state (10), which depends on pressures and piston position. Here the polytropic index *k* has been set equal to 1.2 in the polytropic model (14); this value is generally the one

used for control purposes as it gives a good approximation of the cylinder dynamic in most of the cases.
Fig. 3 and 4 show respectively the evolution of the poles of the 4th and 6th order models for different piston positions. Fig. 5 presents a comparison of the dynamic of the poles calculated at middle stroke.

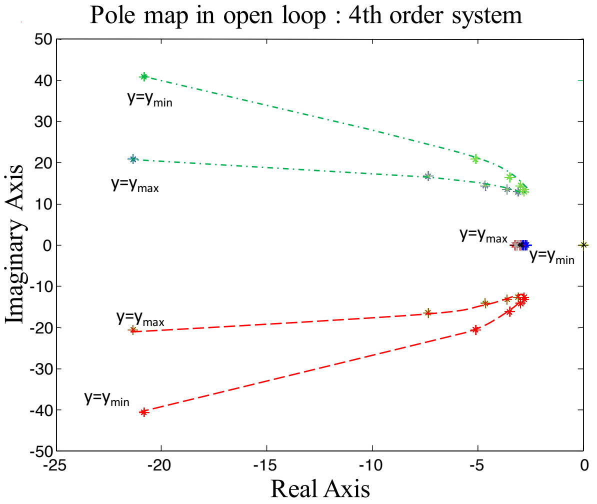

Figure 3: Pole evolution in open loop for the 4th order model at different equilibrium position

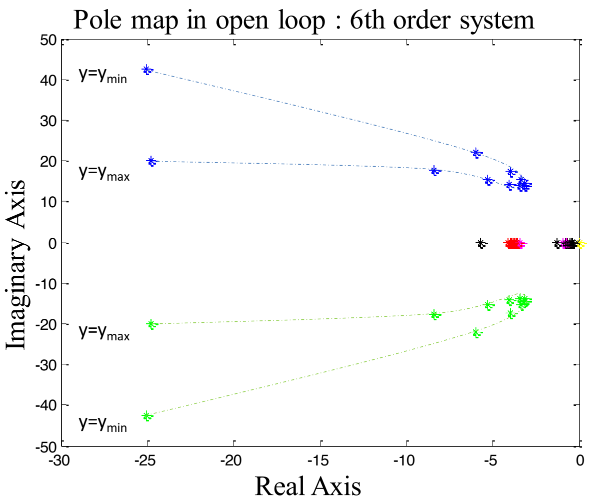

Figure 4: Pole evolution in open loop for the 6th order model at different equilibrium position

These two figures show clearly that the piston position plays a crucial role on the system dynamic. We can also remark that poles at y_{min} and y_{max} are naturally not identical since the cylinder has a rod on only one side and the chambers are consequently non symmetrical.
The influence of the temperature dynamic can clearly be observed with the two new real poles at low frequency, but also because it changes the location of the other poles. These changes are more clearly shown on Fig. 5 where the dynamic of the poles calculated at middle stroke is compared for both models.

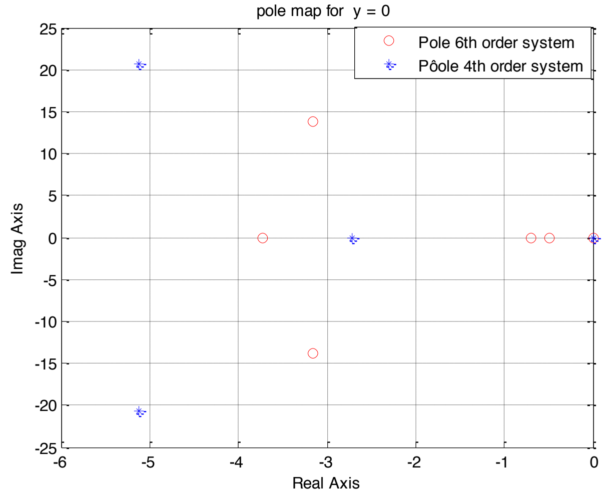

Figure 5: Comparison of the pole in open loop for both models at half-stroke

It can be concluded that classical hypothesis that states that the temperature dynamic can be neglected is not so obvious. All the dynamics are of the same order of magnitude. Nevertheless, the polytropic model with a polytropic index k = 1.2 seems to catch properly the main effects.
In the next section, basic control laws are designed in order to outline the differences between the two approaches (models).

STATE FEEDBACK CONTROL LAW

The position control of pneumatic actuators has widely been studied and many linear and non linear techniques have been successfully applied [11, 12, 13]. Our goal is not here to design a control law leading to high performances, but rather to consider a linear control approach, such as state feedback, that allows all the information provided by the model to be taken into account, and the system to be studied in the linear domain. Of course, the implementation of such a control law is not considered here, as feedback on all states is not realistic on real systems, especially for temperatures.
In this section, the state feedback control law with pole placement is synthesized in order to reach about the same kind of step response for both linearized models. For the polytropic model, the polytropic index k is set equal to 1.2, and for the model taking into account the temperature dynamic, the heat exchange coefficient is fixed to 15 J/s/m^2/K.
The first step in the pole placement approach is to define the pole locations for the closed loop. For high order system, which cannot be approximated by second order systems (it is the case here, especially at half-

stroke), this choice can be complex. The ITAE [14] is one of the techniques that can be applied at the pole selection step. In our case, in order to avoid command saturation, the following closed loop pole locations have been chosen:

Prototype Response Poles: ITAE transfer functions		
order	**Pole locations for w_0=1rad/s**	
4	$s+0.4240 \pm 1.2630\,j$ $s+0.6260 \pm 0.4141\,j$	$w_n = 1.33$ rad/s, $\zeta = 0.32$ $w_n = 0.75$ rad/s, $\zeta = 0.83$
6	$s+0.3099 \pm 1.2634\,j$ $s+0.5805 \pm 0.7828\,j$ $s+0.7346 \pm 0.2873\,j$	$w_n = 1.30$ rad/s, $\zeta = 0.24$ $w_n = 0.97$ rad/s, $\zeta = 0.59$ $w_n = 0.79$ rad/s, $\zeta = 0.93$

By substituting $\boldsymbol{s}$ by s/w_0, pole location can be obtained for any values of w_0, the open-loop natural frequency.

From the state feedback control defined as $\delta u = -K \cdot \delta x$, the chosen closed loop poles are also the eigenvalues of the closed loop state matrix $(A - BK)$. This leads to the following feedback gain matrix K for both models at half-stroke.

order	**Feedback gain matrix (K)**
4	$[0.9637 \quad -1.5072 \quad 0 \quad 0]$
6	$[29.6804 \quad -17.7596 \quad -0.0001\ldots$ $\ldots 0.0022 \quad -10.5847 \quad 1.2379]$

The state feedback gains can also be calculated for different piston positions. Fig. 4 and 5 show the pole evolution in closed loop for the 4th and 6th order models with the choice made for each model.

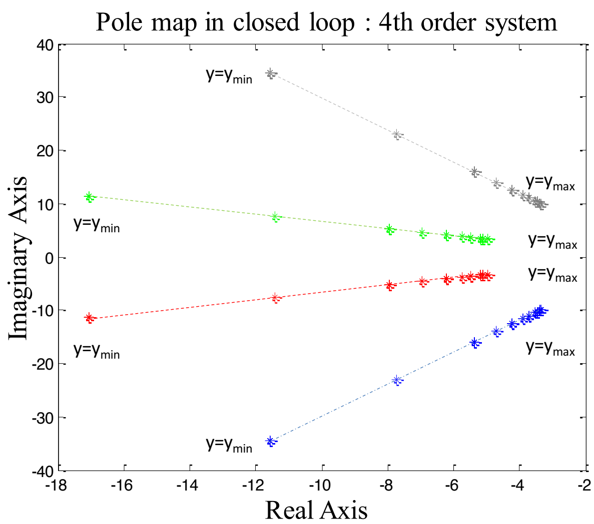

Figure 6: Pole evolution in closed loop for the 4th order model at different equilibrium position

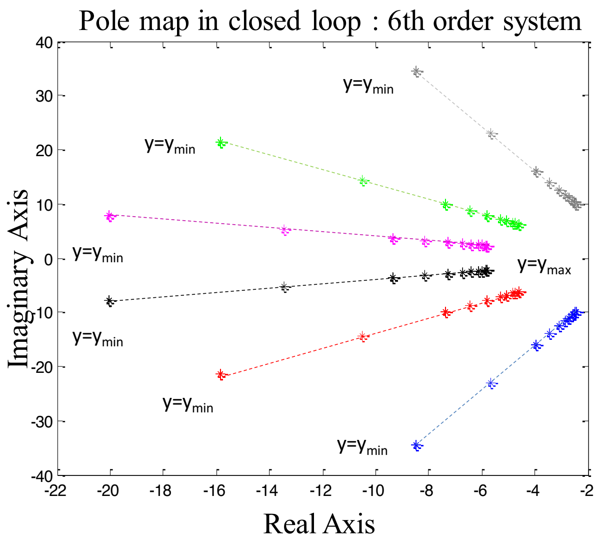

Figure 7: Pole evolution in closed loop for the 6th order model at different equilibrium position

A completer ….

SIMULATION

In order to compare the two synthesized control laws, a simulation model of the actuator has been implemented in the LMS Imagine.Lab AMESim (Fig. 8). This model takes into account several phenomena, which have been neglected at the control design step:

- the heat transfer coefficient is variable according to (8),
- dry friction with Stribeck effects is considered: stiction force is equal to 50 N, and Coulomb friction force is equal to 30 N,
- leakages between chambers are taken into account,
- the dynamic and the real flow characteristics [15] of the servovalves are fully modeled.

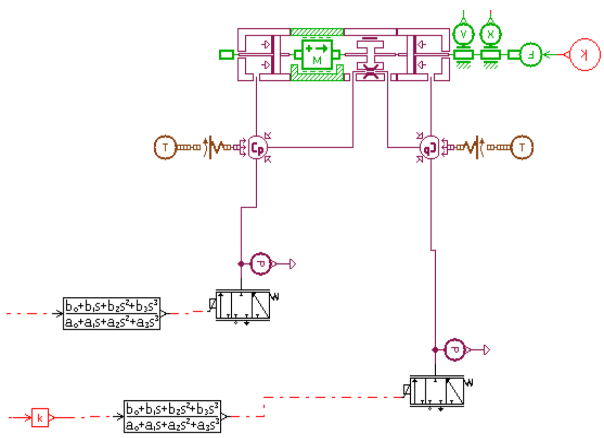

Figure 8: AMESim model

The feedback gain matrix calculated for half-stroke is used for step responses around this position. Fig. 9 shows the position of the piston in both cases.

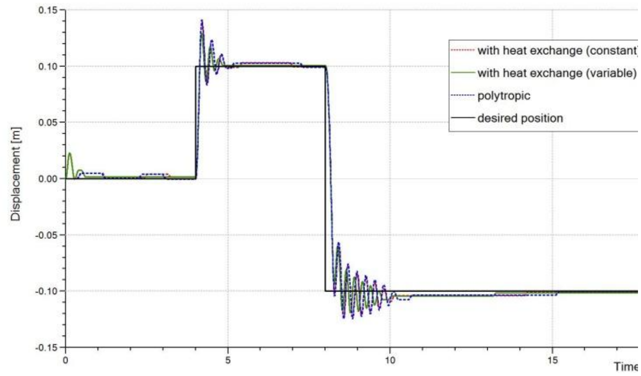

Figure 9: Comparison of the piston displacement for step inputs with the same control law

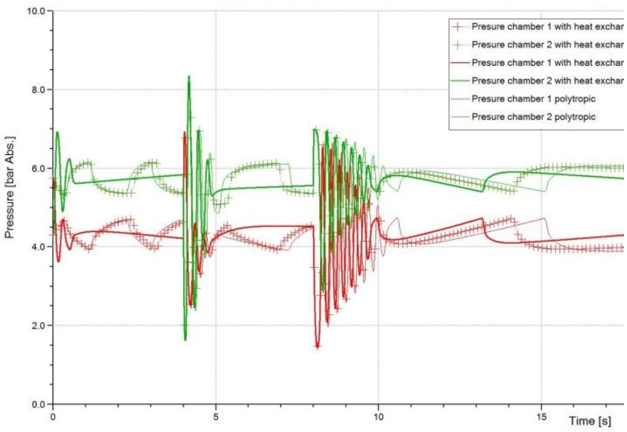

Figure 10: Comparison of the pressures in the cylinder chambers

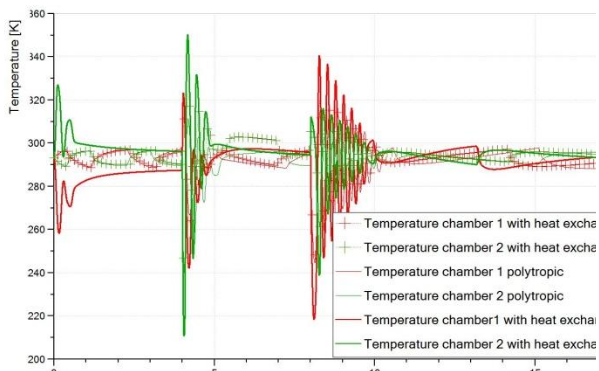

Figure 11: Comparison of the temperatures in the cylinder chambers

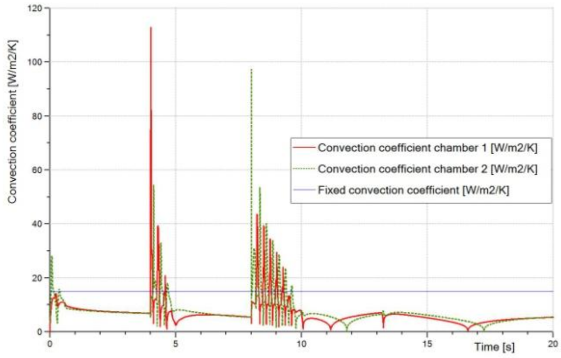

Figure 11: Evolution of the heat transfer coefficient in the cylinder chambers

CONCLUSION

In this paper, we have shown that it could be worth to take into account the temperature dynamic for the design of the control law. First, the influence of temperature dynamic is significant; second, it leads to a better control of the system. The simulations have shown that neither the polytropic approach, neither a model with a constant heat exchange coefficient can properly represent the temperature magnitude or dynamic.

This type of approach allows now the energy efficiency problem to be studied in details. Further works should now revisit energy efficient control law, which have already been discussed in previous work [16]; thermal share could be an answer to the minimization of energy. On the proposed model basis, the adequate path planning can be developed and the choice of the structure of the system can also be questioned, for example in terms of energy recovery. This development will however require more advanced control strategy, such as flatness theory or backstepping control techniques [17, 18].

REFERENCES

[1] B.W. Andersen, "The analysis and design of pneumatic systems", New-York: John Wiley and Sons, 1967, 302p.

[2] D. Mc Cloy D. and H.R. Martin, "Control of Fluid Power: Analysis and Design", Chichester (England), Ellis Horwood, 1980. 510p.

[3] L.A. Zalmanzon, "Components for pneumatic control instruments", Oxford: Pergamon press, 1965, 320 p.

[4] International Standard ISO 6358, "Pneumatic Fluid Power Components using Compressible Fluids – Determination of Flow-rate Characteristics", 1989. 15p.

[5] T. Kagawa, K. Kawashima, and T. Fujita, "Effective area measurement method using isothermal chamber", *Hydraulics and Pneumatics*, Vol. 26(1), pp. 76–78, 1995.

[6] K. Kawashima, T. Kagawa, and T. Fujita, "Instantaneous flow rate measurement of ideal gases", *Journal of Dynamic Systems, Measurement and Control*, vol. 1222:174–178, march 2000.

[7] R. de Giorgi, E. Eric Bideaux, and S. Sesmat, "Using inverse models for determining orifices mass flow rate characteristics", 6th JFPS Japan International Symposium on Fluid Power, Tsukuba, Japan, November 7-10, 2005.

[8] R. De Giorgi, E. Bideaux, S. Sesmat Dynamic thermal model of a discharging process of a pneumatic chamber, 4th FPNI PHD Symposium, Sarasota, 2006.

[9] Study of "Sticking and restarting phenomenon" in electropneumatic positioning systems, Brun X., Sesmat S., Thomasset D., Scavarda S., *Journal of Dynamic Systems Measurement and Control*, Transaction of the ASME 127, 1, pp. 173-184, 2005.

[10] Shearer, J.L., "Study of pneumatic processes in the continuous control of motion with compressed air. Parts I and II", *Trans. Am. Soc. Mech. Eng*., 78, 233-249, 1956.

[11] Bachmann, J.R., Surgenor, B.W., "On design and performance of a closed circuit pneumatic positioning system", fifth Scandinavian International Conf. on Fluid Power, Linköping, Sweden, Vol.1, pp 309-322, May 28-30, 1997.

[12] Richard, E., Scavarda, S., "Comparison between Linear and Nonlinear control of an eletropneumatic servodrive", *Jour. of Dyn. Syst. Meas. & Control*, June 1996, Vol. 118, p 245-252.

[13] Brun X., Belgharbi M., Sesmat S., Thomasset D., Scavarda S., "Control of an electropneumatic actuator, comparison between some linear and nonlinear control laws", *Jour. of Syst. and Control Engineering*, 1999, Vol. 213, N°I5, p 387-406.

[14] G. F. Franklein, .J.D. Powell, A. Emami-Naeini, "Feedback control of dynamic systems", Prentice Hall; 4 edition, January 15, 2002.

[15] Belgharbi, M., Thomasset, D., Scavarda, S., & Sesmat, S. "Analytical model of the flow stage of a pneumatic servo-distributor for simulation and nonlinear control", 6th Scandina. Int. Conf. on Fluid Power, SICFP'99, pp. 847-860, 1999, Tampere, Finland.

[16] Brun, X., Thomasset, D., Sesmat, & S., Scavarda, S., "Limited energy consumption in positioning control of electropneumatic actuator", Bath Workshop on Power Transmission & Motion Control, 1999, pp 199-211, Bath, England.

[17] Isidori, A., "Nonlinear control systems", New York: Springer Verlag, 2nd edition, 479 p., 1989.

[18] M. Smaoui, X. Brun, D. Thomasset, "A study on tracking position control of an electropneumatic system using backstepping design", *Control Engineering Practice*, Vol. 14, Issue 8, August 2006, Pages 923-933.

Proceedings of the 8th JFPS International
Symposium on Fluid Power, OKINAWA 2011
Oct. 25-28, 2011

2A3-1

PERFORMANCE CHANGES DUE TO DIRECTION OF PARALLEL LINK MECHANISM WITH SIX DEGREES OF FREEDOM USING ELECTRO-HYDRAULIC SERVO CYLINDERS

Yuki SAGAWA*, Tomoya WATANABE**, Masahiro KAWAMURA**,
Yuki OHASHI**, Katsumasa SUZUKI**

* Graduate school of Tokyo City University
** Department of Mechanical Systems Engineering,
Tokyo City University
1-28-1 Tamazutsumi Setagaya, Tokyo, 158-8557 Japan
(E-mail: ksuzuki@tuc.ac.jp)

ABSTRACT

The Stewart platform type parallel link mechanism with 6 degrees of freedom is a structure which arranges six single rod hydraulic cylinders parallel between the base platform and the end effecter as the controlled object. By controlling the length of each link with the hydraulic cylinder, the position and posture of the end effecter is controlled with six degrees of freedom in three-dimensional space. In this report, I give a desired sinusoidal signal to a coordinate axis direction and I measure the frequency response of each coordinate axis direction. The difference depending on the axis direction and interference are examined. The experimental results are compared with the simulation results.

KEY WORDS

Parallel Link, Six Degrees of Freedom, Electro-Hydraulic Servo Cylinders

1. INTRODUCTION

Parallel link mechanism is considered that a tire testing equipment for airplane of the 1950's is a first mechanism with six degrees of freedom in the world. In recent years, a research and a development of a parallel link were done from 1990 in Japan because the control computer performance became a speedup and higher.

Now the parallel link mechanism is used for the position control of the pedestal part for the amusement equipment in amusement parks by the development of the amusement industry in the world. It is also used for flight simulator of airplanes. The development in the field such as welfare and medicine which needs precise positioning that is hard to perform with the serial link mechanism is expected. The parallel link mechanism is also expected to be used for a construction machine.

2. PARALLEL LINK MECHANISM USED ROR EXPERIMENT

Parallel link mechanism is structure which arranges six single rod hydraulic cylinders parallel between the base platform and the end effecter. The motion of the end effecter with six degrees of freedom is enabled by moving six cylinders independently. The picture of the experimental machine is shown in Fig.1. The constitution of the single rod hydraulic cylinder control system is shown in Fig.2. The servo amplifier output six single rod hydraulic cylinders, after PC is given desired value. The desired lengths, of six hydraulic cylinders are calculated with inverse kinematics from desired value of position and posture. Two pumps are used. The pump pressure (Ps1) of a pushing side is fixed. Pump pressure (Ps2) is sent to servo valve and the cylinder pressure in pulling side is changed. Each cylinder is attached potentiometer and value of potentiometer is read by PC. The advantage of parallel mechanism is high rigidity by using the hydraulics and truss. A frame of reference of parallel link is shown in Fig.3.

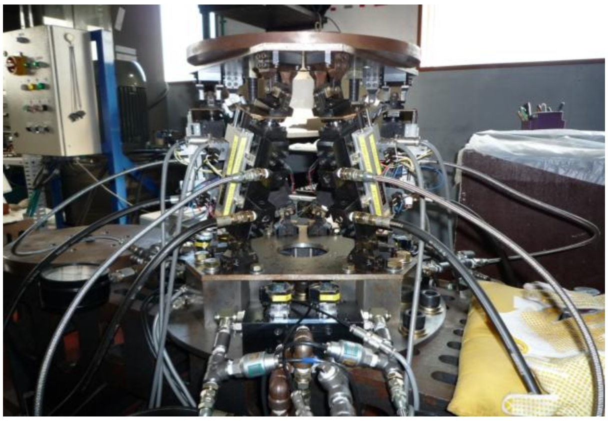

Fig.1 Experimental equipment

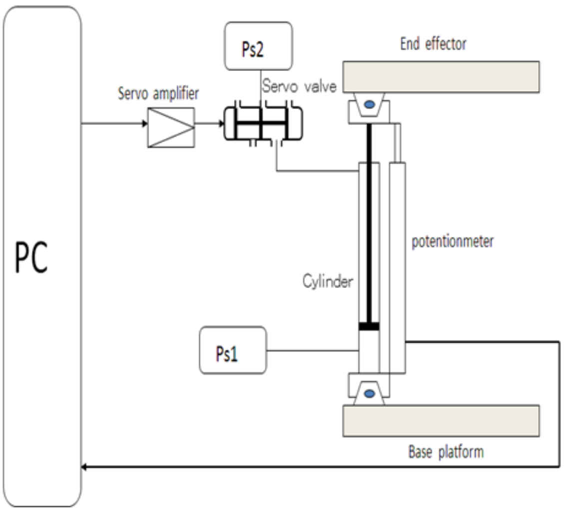

Fig.2 Constitution of single rod hydraulic cylinder control system

3. NOMENCLATURE

A_1, A_2: effective sectional area of pushing side and pulling side of cylinder

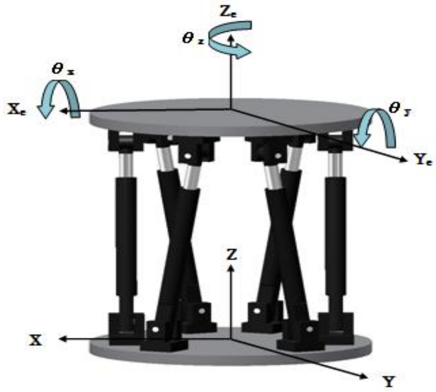

Fig.3 Parallel link mechanism and coordinate system

A_d: amplitude of dither
B_0: coulomb friction force of electro-hydraulic servo cylinder
C: center point of gravity of end effecter
$\boldsymbol{C}$: vector of position and posture of C
f_d: frequency of dither
f_m: thrust of cylinders
F_x, F_y, F_z: force of x,y,z axis of end effecter
g: gravitational acceleration
h: function of inverse kinematics calculation
i_m: applied current to servo valve
$\boldsymbol{J}_l$: Jacobian matrix of parallel link mechanism with six degrees of freedom
J_x, J_y, J_z: moment of inertia of X_e, Y_e, Z_e axis of end effecter
K: bulk modulus of hydraulic oil
k_1: ratio of link length to output current of servo amplifier
k_2: constant about output flow of servo valve
l_m: length of link
l_{max}: critical length of link
M: mass of end effecter
O: origin of reference coordinate system
p_{2m}: pressure in pulling side of cylinder
P_{s1}: supply pressure in pushing side of cylinder
P_{s2}: supply pressure in pulling side of servo valve
q_{2m}: output flow of servo valve
R_{im}: desired value of link length
t: time
$T_\alpha, T_\beta, T_\gamma$: torque of X_e, Y_e, Z_e axis of end effecter
V_{2m}: volume of pulling side of cylinder
V_{sp}: piping volume between servo valve and cylinder
x, y, z: XYZ coordinates of C
α, β, γ: Eulerian angle

· vector

$\boldsymbol{C}=[x\ y\ z\ \alpha\ \beta\ \gamma]^T$, $\boldsymbol{f}=[f_1 \cdots f_6]^T$
$\boldsymbol{F}=[F_x\ F_y\ F_z\ T_\alpha\ T_\beta\ T_\gamma]^T$, $\boldsymbol{l}=[l_1 \cdots l_6]^T$
$\boldsymbol{M}=\mathrm{diag}(M\ M\ M\ J_x\ J_y\ J_z)$

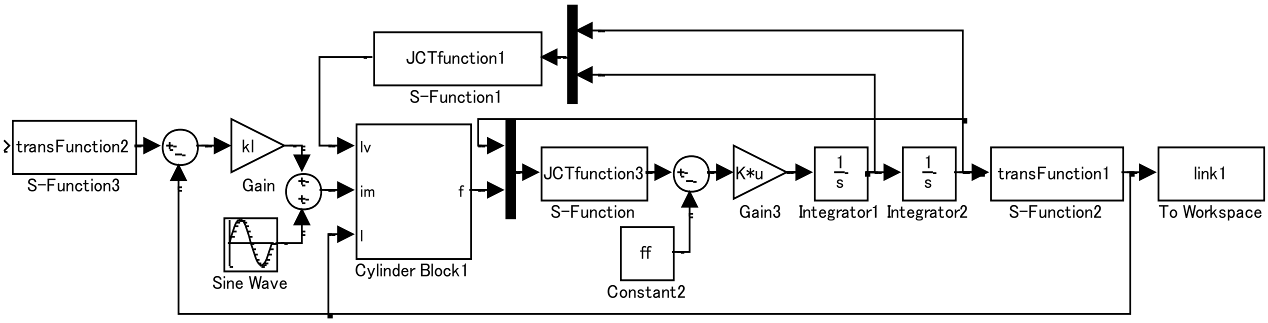

Fig.4 Block diagram of parallel link mechanism

4. SIMULATION

In this study, simulation results using Matlab/Simulink are compared with experiment results. Fundamental equations of parallel link mechanism are shown. Equation for motion of end effecter is

$$F = M\ddot{C} - M(0\ 0\ g\ 0\ 0\ 0)^T \quad \cdots(1)$$

Function to calculate the length of links from position and posture of end effecter.

$$l = h(C) \quad \cdots(2)$$

Relation between link speed and position and pasture of end effecter is obtained by time derivative for both sides of equation (2).

$$\dot{l} = J_1(C)\dot{C} \quad \cdots(3)$$

J_1(c) is called Jacobian.

$$J_1(C) = \frac{\partial h(C)}{\partial C}$$

Relation between thrust of cylinders and force and torque which affects on target point.

$$F = J_1^T(C) f \quad \cdots(4)$$

It is assumed that the servo valve is zero lap and the displacement is proportional to the current. The relation between the output flow rate and the pressure drop is expressed by

$$q_{2m} = k_2 i_m \sqrt{P_{s2}\,\mathrm{sgn}(i_m)(P_{s2} - 2p_{2m})} \quad \cdots(5)$$

Relation between compression of fluid and pressure change is

$$\dot{p}_{2m} = \frac{K}{V_{2m}}(A_2\dot{l}_m - q_{2m}) \quad \cdots(6)$$

where

$$V_{2m} = A_2(l_{\max} - l_m) + V_{sp} \quad \cdots(7)$$

Force for cylinder piston is

$$f_m = A_1 P_{s1} - A_2 p_{2m} - B_0\,\mathrm{sgn}(\dot{l}_m) \quad \cdots(8)$$

Current to servo valve is represented by the following equation,

$$i_m = k_1(R_{lm} - l_m) + A_d \sin(2\pi f_d t) \quad \cdots(9)$$

where $A_d \sin(2\pi f_d t)$ is overlapped dither signal. Relationships of above-mentioned equations are expressed by the block diagram as shown in Fig.4.

5. EXPERIMENTAL METHOD

The desired sinusoidal signal of the end effecter is inputted and the frequency response of each axis direction is measured. The gain is obtained by computing basic components of Fourier coefficient of the measured signal. Control method is proportional control. Frequency response is measured from 0.1 Hz to 20Hz.The parameter values of the system are shown in table1.

Table1 Parameter values

A_1	3.14×10^{-4}m^2	A_2	1.37×10^{-4}m^2
A_d	0.09mA	B_0	90.0N
f_d	200Hz	K	385MPa
k_1	0.30A/m	k_2	1.00×10^{-6}m^{3}Pa$^{-1/2}$s^{-1}A^{-1}
l_{max}	377mm	l_{min}	282mm
M	30kg	P_{s1}	2.01MPa
P_{s2}	7.30MPa	V_{sp}	2.50×10^{-5}m^3

6. EXPERIMENTAL RESULT

6.1 WAVE FORM

The displacement of each axis direction is measured when the oscillating desired value is given to z-axis direction.

The wave forms of each axis direction are shown in Fig.5, when the desired amplitude of z-axis direction is 30mm and the frequency is 0.1Hz. The amplitude of z-axis direction is close to desired amplitude. The desired amplitude of other direction is 0. The amplitude of about

3mm in other direction is observed at most.

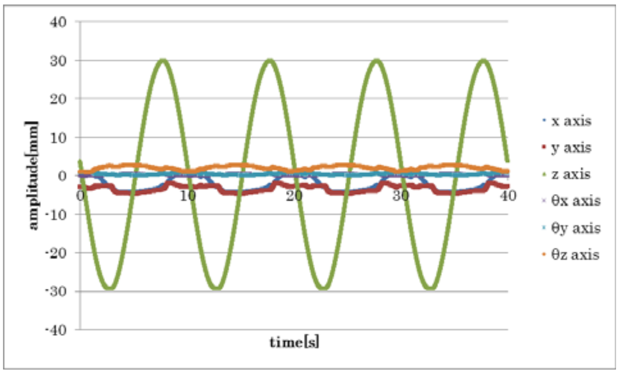

Fig.5 Wave form of each axis direction when desired value is inputted in z-axis direction
(frequency is 0.1Hz, desired amplitude is 30mm)

6.2 FREQUENCY RESPONSE OF EACH AXIS DIRECTION WHEN DESIRED SINUSOIDAL SIGNAL IS IMPUTED TO ONE AXIS

The frequency response is measured when the desired value is given to only one axis direction. These are measured for all axis directions.

The frequency response of each axis direction is shown in Fig.6 when the desired sinusoidal signal of amplitude 30mm is given to z-axis direction. Some amplitude of oscillation in the x and y-axis directions are observed. From this, the x and y-axis directions receive interference from z-axis direction.

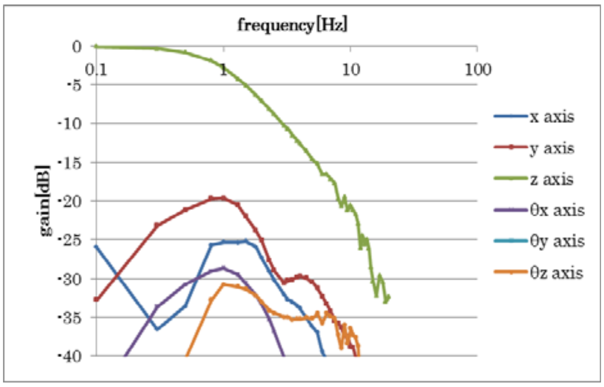

Fig.6 Frequency response of each axis direction when oscillating desired value is given to z-axis direction
(desired amplitude is 30mm)

The frequency response of each axis direction is shown in Fig.7 when the desired sinusoidal signal of amplitude 30mm is given to x-axis direction. The desired amplitude in z-axis direction is 0. But some amplitude of oscillation is observed in this direction in low frequency until approximately 3Hz. The gain in θ_y-axis direction increases when the frequency becomes higher than 3Hz. When the desired oscillating signal is given only to y-axis direction, some interference oscillation in z-axis direction is observed in low frequency and the amplitude of oscillation in θ x-axis increases in higher frequency.

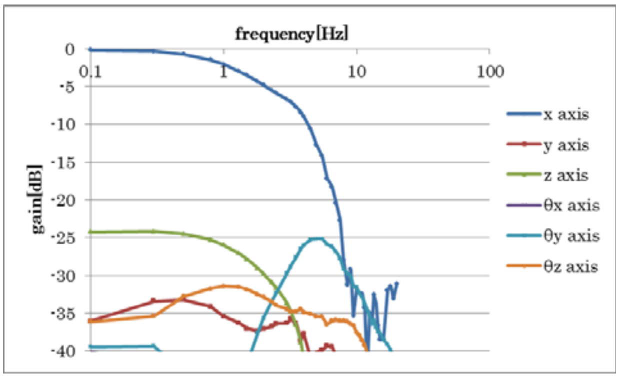

Fig.7 Frequency response of each axis direction when oscillating desired value is given to x-axis direction
(desired amplitude is 30mm)

Frequency response of each axis direction is shown in Fig.8 when the oscillating desired amplitude of 10degrees is given to θ_x-axis direction. The oscillation of y-axis direction becomes large when the frequency becomes higher than approximate 5Hz. When the desired oscillating signal is given to θ_y-axis direction the vibration of x-axis direction becomes large in high frequency in the same way.

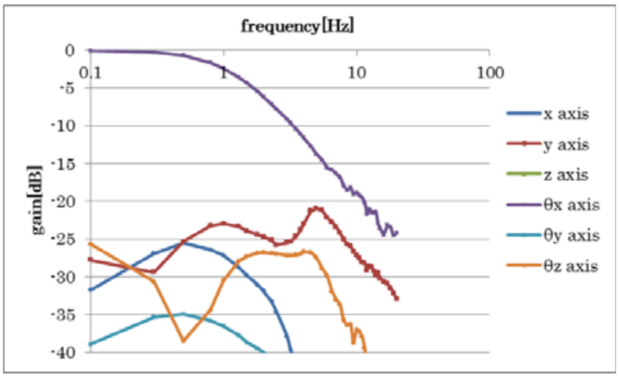

Fig.8 Frequency response of each axis direction when oscillating desired value is given to θ_x-axis direction
(desired amplitude is 10deg)

The frequency response of each axis direction is shown in Fig.9 when the oscillating signal of amplitude 10 degrees is given to θ_z-axis direction. The amplitude of other axis direction from the axis which the desired oscillating signal is given is very small in Fig.9 compared with Fig.5 to Fig.7.

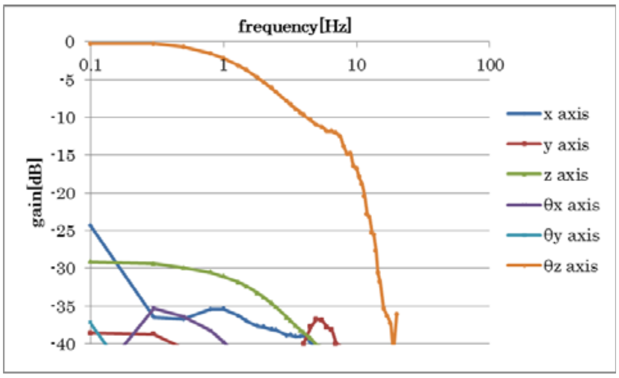

Fig.9 Frequency response of each axis direction when oscillating desired value to is given θ_z-axis direction (desired amplitude is 10deg)

6.3 FREQUENCY RESPONSE OF EACH AXIS WHERE DESIRED SINUSOIDAL SIGNAL IS IMPUTTED

The frequency responses of the coordinate axis direction where the desired oscillating signal is given are shown.

The desired amplitude is 30mm for x, y and z –axis direction respectively. It is 10degrees for θ_x, θ_y and θ_z-axis direction respectively. The results are shown in Fig.10. The frequency response of x-axis direction is similar to that of y-axis direction. Also, the frequency response of θ x-axis direction is similar to that of θ_y-axis direcrion. The band widths of x and y-axis are apploximately 4Hz. From the frequency, the gain decreases suddenly.

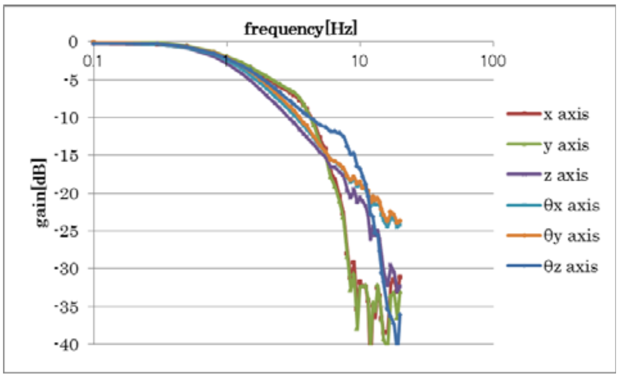

Fig.10 Frequency response of each axis which oscillating the desired value is given to (desired amplitude of x,y,z is 30mm, and θ_x, θ_y, θ_z is 10deg)

Simulation result corresponding to experimental result of Fig.10 is shown in Fig.11.Fig.10 and Fig.11 are corresponding well. Simulation results shown in Fig.11 coincide with the experimental results in Fig.10 with high accuracy.

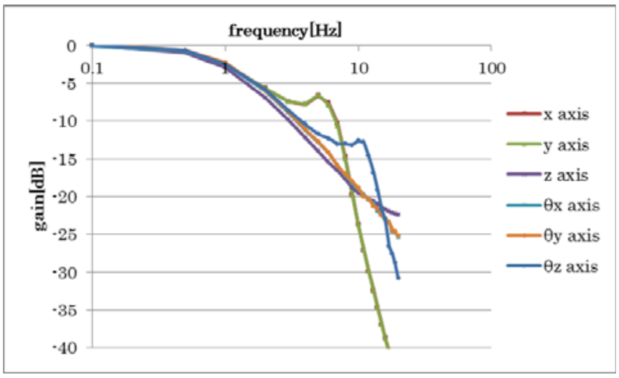

Fig.11 Simulation result of frequency response of each axis which the ocillating desired value is given to (desired amplitude of x,y,z is 30mm, and θ_x, θ_y, θ_z is 10deg)

6.4 EFFECT OF AMPLITUDE ON FREQUENCY RESPONSE

The frequency response of z-axis direction is tested when the amplitude of desired signal is changed.

The result is shown in Fig.12.The gains suddenly decrease when the desired amplitude becomes smaller than 2mm. The gains increse until amplitude 10mm, but the gains decrease at larger amplitude.

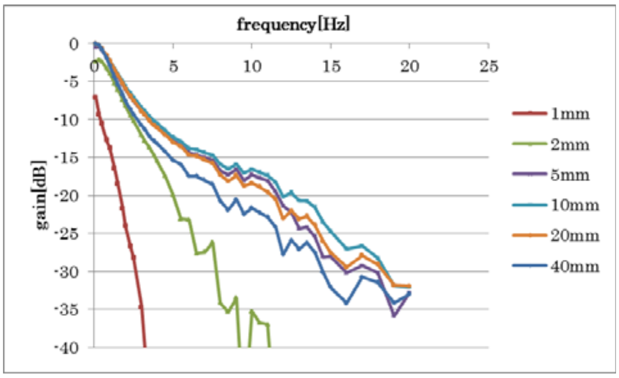

Fig.12 Effect of desired amplitude in frequency response when the desired signal is given to z-axis direction

6.5 FREQUENCY RESPONSE OF EACH LINK WHEN DESIRED SINUSOIDAL SIGNAL IS GIVEN TO Z－AXIS DIRECTION

The frequency response of each link is shown when the desired sinusoidal signal is given to z-axis direction. It is compared with simulation result. And it is compared with the result when the desired sinusoidal signal is given to one link.

The frequency response of each link is shown in Fig.13 when the desired sinusoidal signal of amplitude 30mm is given to z-axis direction. The frequency response of each link is similar each other.

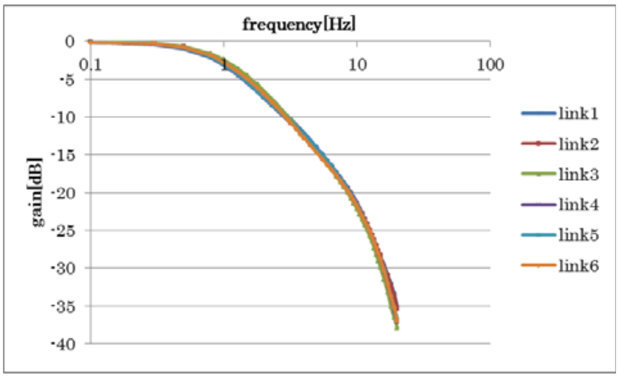

Fig.13 Frequency response of each link when desired signal is given to z-axis direction (desired amplitude of z-axis direction is 30mm)

The simulation result is shown in Fig.14. Fig.14 is similar to Fig.13. The simulation result of each link coincide each other completely.

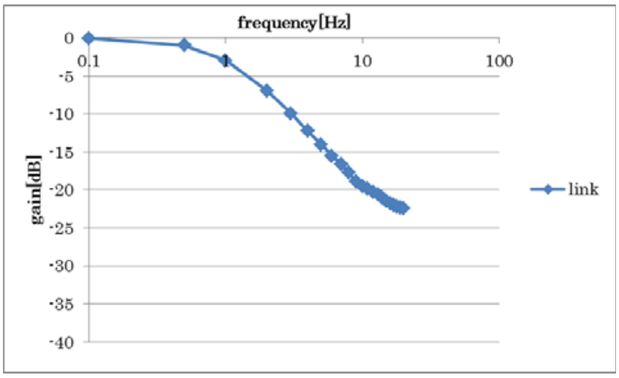

Fig.14 Simulation result of frequency response of each link when desired signal is given to z-axis direction (desired amplitude of z-axis direction is 30mm)

The frequency response of the link which is given sinusoidal signal of amplitude 30mm is shown in Fig.15 when the other link is given amplitude 0 to be at rest. The gain is changed around 9Hz compared with Fig13. The gain decreases with stability when 6 links moved togeter.

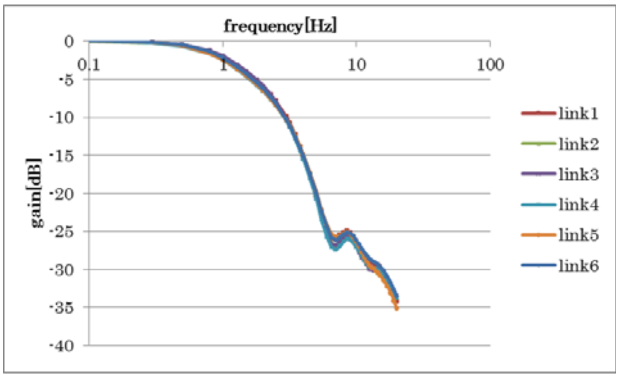

Fig.15 Frequency response of each link which desired signal is given to (desired amplitude is 30mm)

6.6 EFFECT OF THE NUMBER OF LINKS WHERE DESIRED SINUSOIDAL SIGNALS ARE INPUTED

In the section 6.5, it is confirmed that the stable frequency response is obtained when the same desired oscillating signal is given to the all 6 links at the same time. So the frequency response of each link is measured when the number of links which desired oscillating signals are given, is changed.

The frequency response when desired oscillating signal is given to link1, 2 and 3 is shown in Fig.16.The gain of link4 decreases suddenly. Oppositely, the decrease in the gain for 2 links of link5 and link6 is smaller. Link1 adjoins link2 at the joint. Link3 adjoins link4 and link5 adjoins link6 respectively. Therefore the link4 recieves the effect of adjointed link3.

The deviation of each link is reduced by moving adjoining link together.

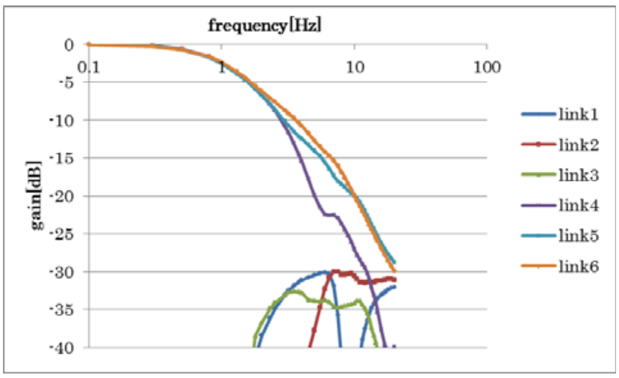

Fig.16 Frequency response of each link when the desired signal is given to link1,2 and 3 (desired amplitude is 30mm)

7. CONCLUSION

When the desired sinusoidal signal is inputted to the z-axis direction, some interference oscillation appears in x and y-axis directions. Inversely, some oscillation appears in z-axis direction, when the desired sinusoidal signal is inputted to x or y-axis direction. The desired sinusoidal signal of x or y-axis direction has an effect on the interference oscillation in θ_y or θ_x-axis direction respectively. Inversely, the desired sinusoidal signal of θ_x or θ_y-axis direction has an effect on the oscillation in y or x-axis direction respectively. However, such relation between z and θ_z-axis directions are not observed. The experimental results are computed with the simulation results. The deviation of each link is decreased by moving adjoining links together.

8. REFERENCES

1. K. Tsuchiya, S. Sato, K. Suzuki; Dynamic characteristics of parallel link mechanism with six degrees of freedom using hydraulic cylinders 1st report; Trans of JFPS, 2006,Vol.37-1, pp.1-7.
2. K. Tsuchiya, S. Sato, K. Suzuki; Dynamic characteristics of parallel link mechanism with six degrees of freedom using hydraulic cylinders 2 nd report; Trans of JFPS, 2008,Vol.39-1, pp.1-6.
3. K. Tsuchiya, S. Sato, K. Suzuki; Dynamic characteristics of parallel link mechanism with six degrees of freedom using hydraulic cylinders 3 rd report; Trans of JFPS, 2008,Vol.39-1, pp.7-12.
4. Y. Miyamoto, M. Kusakabe, K. Abe, K. Tsuchiya, K. Suzuki, S. Sato; Dynamic characteristics of parallel link mechanism with six degrees of freedom using hydraulic servo cylinders, Proceedings of the 7th JFPS International Symposium on Fluid Power TOYAMA 2008, 2008, Vol.3, pp597-602.
5. Y. Miyamoto, M. Kusakabe, K. Abe, K. Tsuchiya, K. Suzuki, S. Sato; Dynamic characteristics of parallel link mechanism with six degrees of freedom using hydraulic servo cylinders, The Proceedings on Autumn Conference of Japan Fluid Power System Society 2009, 2009, pp597-602

Proceedings of the 8th JFPS International
Symposium on Fluid Power, OKINAWA 2011
Oct. 25-28, 2011

2A3-2

COMPRESSIBLE FLOW ANALYSIS IN A CLUTCH PISTON CHAMBER

Masaru SHIMADA* , Hideharu YAMAMOTO*

* Hardware System Development Department, R&D Division
JATCO Ltd
700-1, Imaizumi, Fuji City, Shizuoka, 417-8585 Japan
(E-mail : masaru_shimada@jatco.co.jp)

ABSTRACT

In the automotive automatic transmission, the stagnated air in both the hydraulic circuit and the clutch controlling piston chamber have a bad influence on changing gears, so that understanding the mechanism of the flow field in the hydraulic system is very important. But there was no method to understand it except flow visualization experiment. So in this paper, we analyze the flow field with compressible VOF method calculation which includes an easy mesh morphing to move clutch piston. We also adapted the formulation of the boundary condition in order to reduce the calculation time. This calculation enables us to understand the mechanism of the flow field in the hydraulic system which contributes to improve controlling technology of changing gears.
-- VOF method: popular computational technique for multi-fluid dynamics / mesh morphing: a technique of continuously deforming the CFD mesh by moving vertices

KEY WORDS

VOF, Compressible, Mesh morphing, Automatic Transmission

NOMENCLATURE

A_{bleed}	:	Cross section of the air bleed [m^2]
A_{orf}	:	Cross section of the orifice [m^2]
d	:	Diameter of the cylindrical clearance [m]
h	:	Clearance height of the air bleed [m]
l	:	Length of the cylindrical clearance [m]
P_{at}	:	Pressure in the transmission [Pa] (=0.0)
p_{bleed}	:	Pressure on the air bleed boundary [Pa]
Q	:	Flow rate from the air bleed [m^3/s]
μ	:	Viscosity [Pa s]
ρ	:	Density [kg/m^3]
ζ	:	Loss coefficient :=1.25 (Inlet:0.25 + Outlet:1.0) in Eq.(1) :=2.0 in Eq.(2)

INTRODUCTION

In the automotive automatic transmission (AT), gear ratio is changed by engaging or releasing several clutches with the pistons. Since the pistons are controlled by oil pressure, highly accurate oil pressure controlling is essential for smooth and good response drive. The stagnated air in the hydraulic circuit and the clutch piston chamber has a bad influence on the hydraulic performance. Therefore, it is very important to understand the mechanism of the flow field in the hydraulic system. However, there was no method to predict the appearance (or disappearance) and the flow field of stagnated air in the hydraulic system when the clutch moves except flow visualization experiment. In this paper, we conduct the CFD with VOF method calculation which includes our various ideas and visualize the flow field of two types of clutch systems; one is a clutch which stops rotation (brake-type), another is a clutch which transmits rotation (rotary-type). We also compare the flow field of two clutch systems.

Computational fluid dynamics code STAR-CD is used in the calculation.

ANALYSIS SETTING

Outline

Fig.1 shows a computational domain of brake-type clutch. The schematic figure of all AT is shown in Fig.1 (a). The calculating clutch region is located in the end of AT which is inside the red line circle. The computational domain is composed of the output port and hydraulic circuit inside the control valve (C/V), hydraulic circuit inside the CASE, and the piston chamber. The piston surface is the green surface in the cross section as shown in Fig.1 (c). The piston surface is controlled by the spring force and moves to the left (right) when the oil pressure is high (low). The piston chamber is divided into outer and inner, and the inner piston chamber contains an air bleeding hole (air bleed) which is shown inside the black circle. Air bleed is a cylindrical hole which has 15 [μm] clearance height (h), 4 [mm] diameter (d), and 7 [mm] length (l) approximately. From this hole, although air easily leaks, oil hardly leaks due to the difference of viscosity.

In this paper, the mechanism of the air flow from the piston chamber is considered with attention to the following points.

1) Air flow from the air bleed
2) Relation between the oil flow generated by the stroke of piston and the air flow
3) Variation of the air volume by the oil pressure

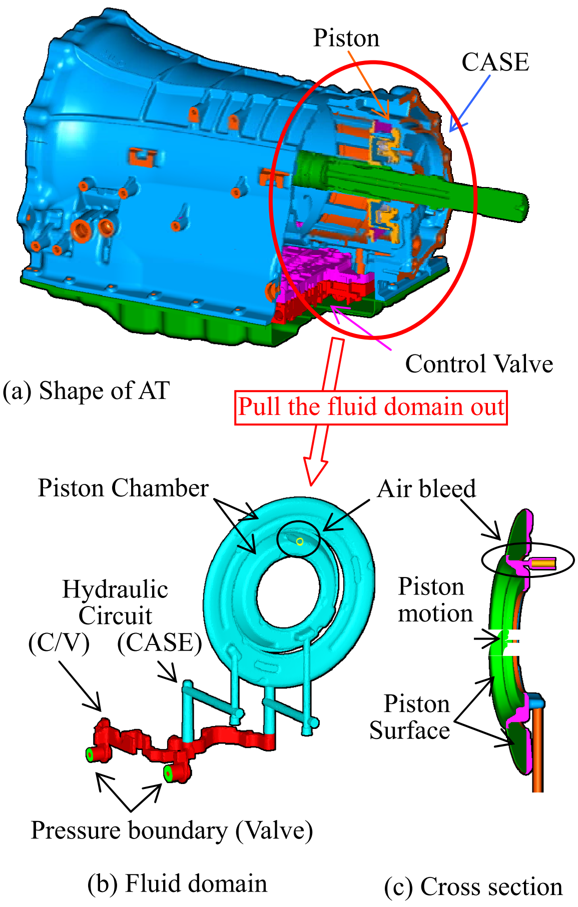

Figure 1 Computational domain

Solutions to the problems on the calculation

In this calculation, we added several ideas to VOF method as described below.

1) Compressible air flow

Since the oil pressure which controls the piston is up to 1.4[MPa] in AT, the compression and expansion of air should be taken into account. We applied the compressible VOF method to the calculation. Since it is considered that the heat has little influence to the flow field, we consider only density effect on the compressible air and ignore the heat.

2) Easy mesh morphing

Since the oil flow generated by the stroke of piston is very important for the air flow field in the piston chamber, it is necessary to deform the calculation mesh to realize the stroke of piston. However, the shape of piston chamber is so complicated that it is not easy to deform the calculation mesh. In order to solve this problem, we applied the morphing method explained below to deform the mesh without using a commercial mesh morphing program. Fig.2 shows a part of the cross section of the piston chamber.

1. Insert prism layers on the piston surface after making tetrahedral mesh
2. Deform only prism layers as solving the motion equation of the piston

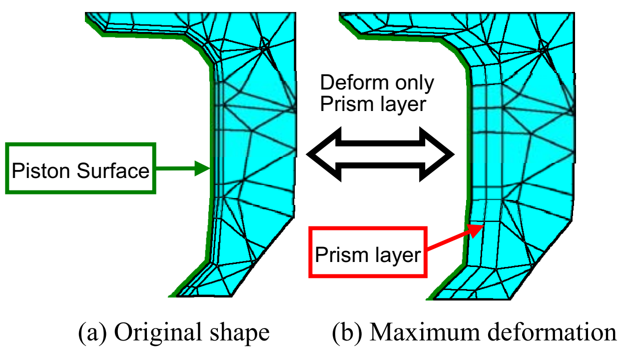

Figure 2 Easy mesh morphing method

This method enabled us to morph the mesh without breaking the topology and without making poor quality mesh. Fig.2 also shows the range of the motion.

3) Formulation of the air bleed

As mentioned above, the air bleed is a very narrow cylindrical hole in this hydraulic system. If we make grids as usual, both the number of mesh and the calculation time will be huge. In order to reduce the calculation time, we formulated the boundary condition to realize the air bleed.

The pressure loss of the air bleed is formulated as Equation (1). The first term means the friction loss of clearance and second term means the form loss of clearance inlet and outlet. Using this equation we calculated the flow rate Q from pressure at the boundary and applied it as the boundary condition. Density and viscosity are set depending on the volume fraction on the boundary. This formulation well expresses the characteristic of the air bleed such that air easily leaks and oil hardly leaks. Formulating the boundary condition enabled us to minimize the number of mesh and to reduce the calculation time.

$$p_{bleed} - p_{at} = \frac{12\mu l}{\pi d h^3} Q + \zeta \frac{1}{2} \rho \left(\frac{Q}{A_{bleed}} \right)^2 \qquad (1)$$

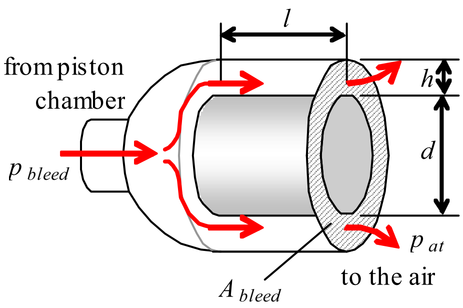

Figure 3 Air bleed

4) Formulation of the control valve (C/V)

Fig.4 shows the schematic diagram of C/V. Since orifice and valve are located in the upstream of model (in C/V), we have to take their pressure characteristics into account to calculate pressure in the piston chamber accurately. However, the number of mesh and calculation time will be huge if we try to use CFD to solve the pressure loss of the hydraulic circuit in C/V and the valve motion. So we formulated the characteristics of C/V and applied the output pressure of C/V as the boundary condition.

We assumed the orifice is the main pressure loss element in C/V, and set the boundary pressure which is obtained by subtracting the loss formulated as

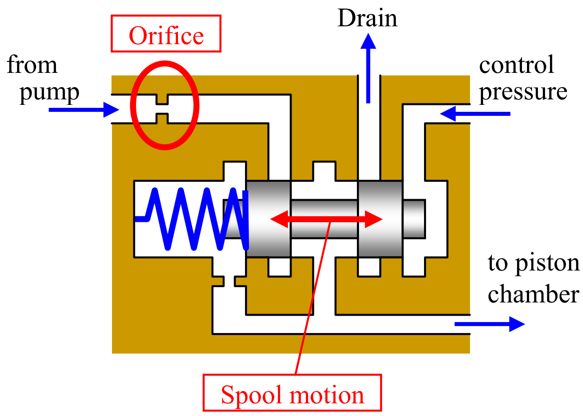

Figure 4 Valve and orifice in the C/V

Equation (2) from the output pressure. Q is the flow rate into the piston chamber. Oil density is used because there is little air in C/V. We judge the state of valve by solving the motion equation of the valve spool, and set the output pressure as zero for the closed valve condition.

$$\Delta p = \zeta \frac{1}{2} \rho \left(\frac{Q}{A_{orf}} \right)^2 \qquad (2)$$

5) Δt control

Finally we focus on the calculation time-step, since reducing the calculation time is essential to apply this calculation to the development of AT.

In this hydraulic system, the oil velocity is high when the piston moves, but it is low when the piston stops. Therefore we tried to reduce the calculation time by controlling the time-step depending on the flow field. To be concrete, we changed the time-step depending on the maximum courant number. We set the time-step small when the courant number is high, and set the time-step large when the courant number is low. As a result, we were able to reduce the calculation time to 1/10 or 1/20 compared with the time when time-step is not controlled.

RESULTS & VERIFICATION

Stroke of piston and air bleed

Fig.5 shows the transient data in 1-cycle of output pressure of C/V. The data are pressure in the piston chamber, stroke of piston and flow rate into the piston chamber, respectively. The piston moves fast when the pressure is increasing, and moves relatively slowly when the pressure is decreasing. Although the graph of pressure looks like a shelf when the piston moves, this means that spring force and oil pressure force are balancing. From this figure, we can say that this calculation basically simulate the typical clutch motion.

Fig.6 shows the relation between the pressure in the piston chamber and the flow rate goes through the air bleed. The red line indicates the flow rate of air calculated by Eq. (1), the points indicate the flow rate (air and oil) calculated in CFD, and the bars indicate

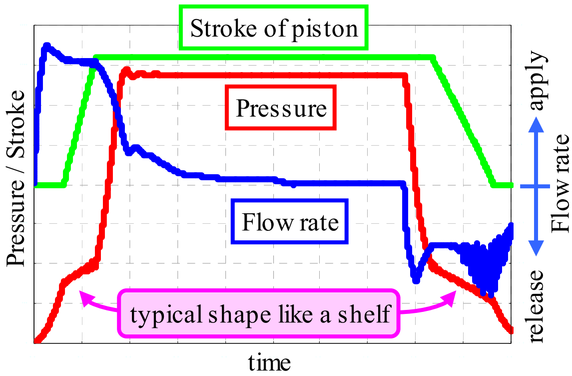

Figure 5 Transient data in 1-cycle

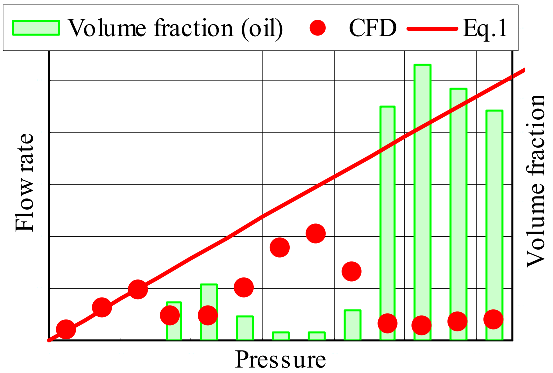

Figure 6 Flow rate from the air bleed

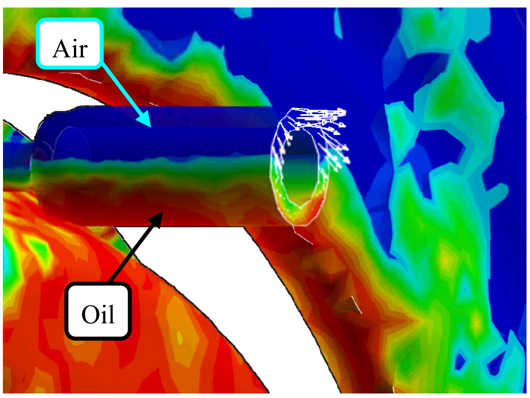

Figure 7 Velocity vector from the air bleed
Contour: volume fraction
Red = Oil / Blue = Air

the volume fraction of oil on the air bleed boundary. This graph means that the flow rate decreases when the oil reaches the boundary. Fig.7 shows the velocity vector which flow out through the air bleed, and the contour indicates the volume fraction; red is oil and blue is air. The vector shows that though air leaks, oil hardly leaks. These results mean that the formulated boundary condition simulates the characteristic of air bleed well.

Comparison with the experiment

We conduct the experiments and calculations with two different cases and compare the relation between the stagnated air volume in the piston chamber and the response of oil pressure. In the first case, the air volume was checked before the response measurement. Fig.8 shows the volume fraction, and Fig.9 shows the pressure in the piston chamber compared with experimental results. The waveform of pressure rise is basically the same in both CFD and experiment, so we realize this calculation method is useful to visualize the flow field in the hydraulic system.

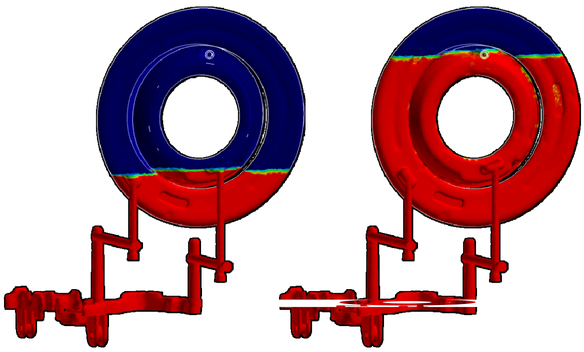

(a) Before the measurement (b) Final state

Figure 8 CFD result: Volume fraction
(Air volume before the measurement is known)

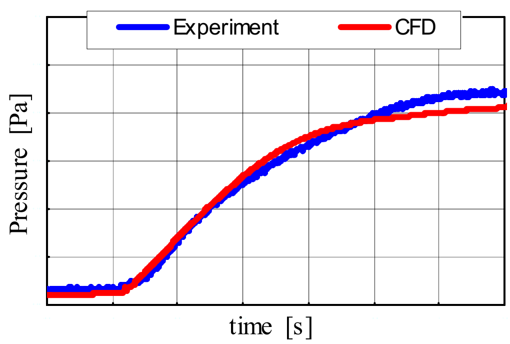

Figure 9 Comparison of CFD and experiment
(Air volume before the measurement is known)

In the second case, the oil was fully discharged from the piston chamber initially, and then oil pressure was applied and released 5 times with the maximum range. The difference with the first case is that the air volume before the response measurement is unknown. Fig.10 shows the volume fraction, and Fig.11 shows the pressure in the piston chamber compared with experimental result. Compared with the first case the pressure rises faster because the air flows out from the piston chamber by applying and releasing oil pressure. Since the pressure rise rate seems to be the same in both CFD and experiment, we realize that this calculation method is useful to visualize the air flowing out from the piston chamber.

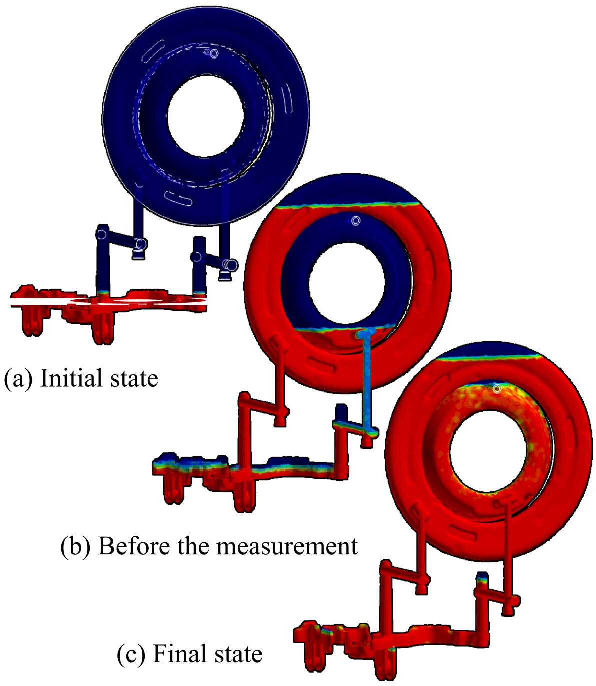

Figure 10 CFD result: Volume fraction
(Air volume before the measurement is unknown)

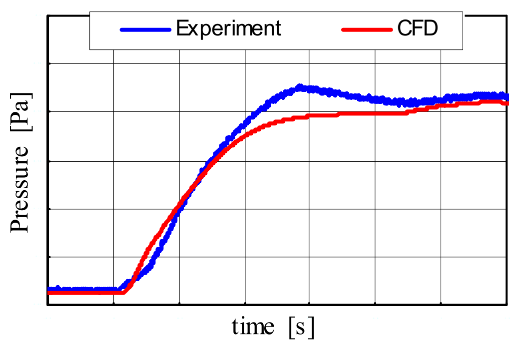

Figure 11 Comparison of CFD and experiment
(Air volume before the measurement is unknown)

These results show this calculation method is very useful for the design of AT.

CONSIDERATION OF THE MECHANISM (BRAKE CLUTCH)

We made calculations of two patterns of output pressure of C/V in order to understand how the stagnated air flows out from the piston chamber. Fig.12 shows pressure pattern diagram. We applied five times high pressure in the pattern1 and two times high pressure after once low pressure in the pattern2, and compared the flow field in the piston chamber which is shown in Fig.13. The timing of each figure is shown in Fig.12; 1)-4): the pressure applied, 5): after the pressure released, and 6): the final state.

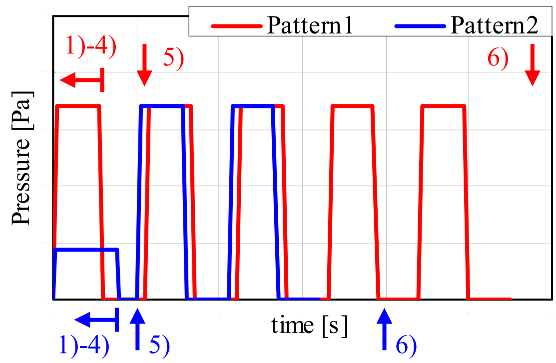

Figure 12 Pressure pattern

With the air bleed (inner piston)

From Fig.13 (6), we can see that the difference of the air volume of final state in the inner piston chamber is large between two patterns. Paying attention to the oil flow, from Fig.13 (3), we can see that oil reaches the air bleed in pattern1. Once oil has reached the air bleed, air hardly leaks. As a result, the air bleed doesn't work effectively and the air stagnates in the piston chamber. In contrast, the oil level of pattern2 rises gradually, and compressed air leaks from the air bleed steadily. This means that the air bleed works effectively when the initial moderate oil injection is applied. From these results, it is important to apply low pressure and inject oil gradually at first in the case of piston chamber with the air bleed.

By the way, a little air must remain in the piston chamber even if the air bleed worked effectively as pattern2. It is because the compressed air stagnated in a volume above the air bleed (Fig.14) is expanded by releasing pressure. The stagnated air volume after releasing pressure can be calculated by Boyle's law (pV=const.).

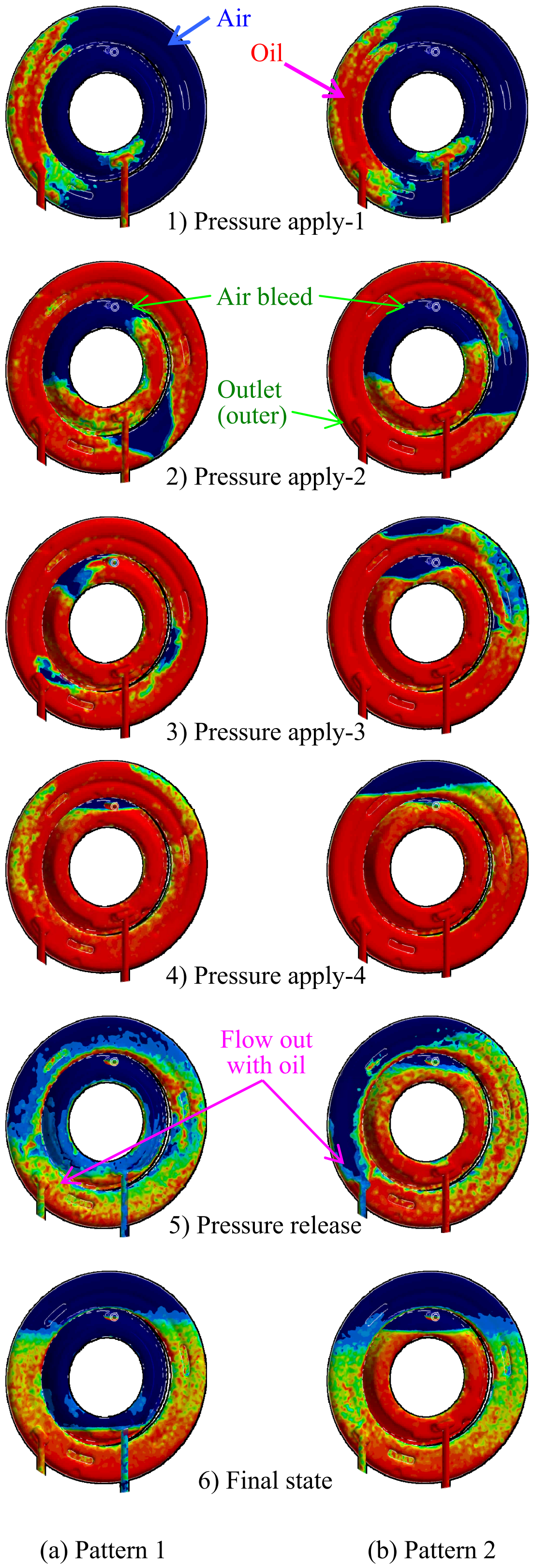

Figure 13 Motion of oil and air
(Red = Oil / Blue = Air)

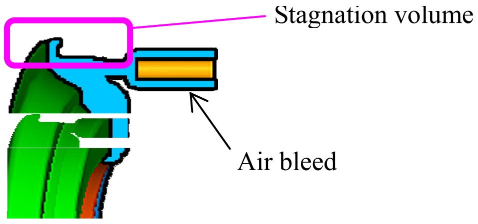

Figure 14 Volume above the air bleed

Without the air bleed (outer piston)

In the outer piston chamber which has no air bleeding hole, air is mixed by oil when applying pressure. Then, the mixed air flows out of the piston chamber as bubbles or the mass of air with the stream which is generated by stroke of piston and by expansion of air when releasing pressure. However, a large volume of air remains even after oil pressure is applied and released.

In order to understand the effect of outlet position on the flow field, we calculated two cases which are shown in Fig.15. In both cases, we can see that the air stagnates in upper part of the piston chamber after mixing with oil when the pressure is applied. When the pressure is released, a large volume of expanded air stagnates in the piston chamber in the case that the outlet is set at the bottom. On the other hand, the stagnated air flows out of the piston chamber in the case that the outlet is set at the top. This means that it is important to set the outlet as high as possible when a brake-type clutch is used.

These results gave us the following knowledge to reduce the air volume in the piston chamber of brake-type clutch.

i. The outlet should be set as high as possible at the piston chamber.
ii. For the piston chamber with the air bleed
   a) Low pressure and initial moderate oil injection should be applied.
   b) The volume above the air bleed should be minimized.

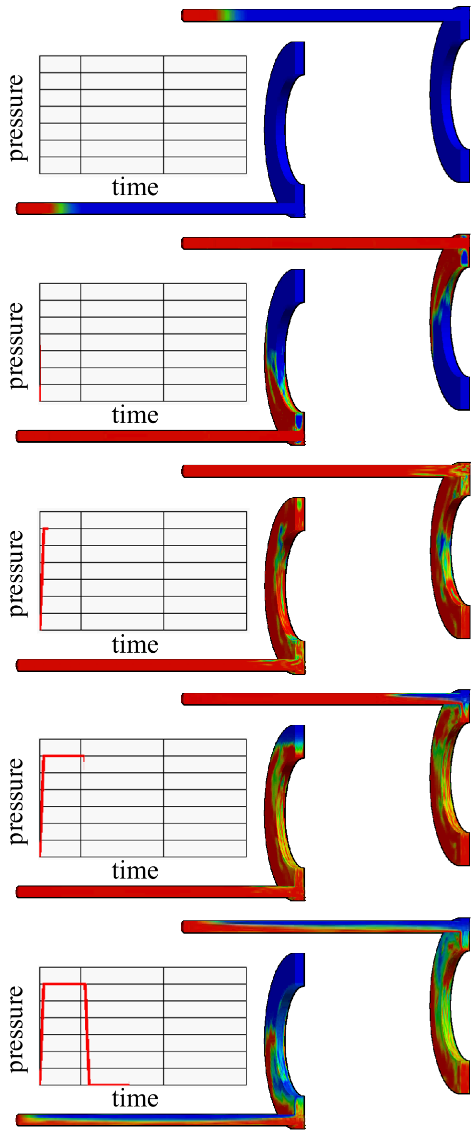

Figure 15 Difference by the outlet position

APPLICATION TO THE OTHER PART (ROTARY CLUTCH)

We applied the same calculation method to the rotary-type clutch as well as brake-type clutch. Fig.16 shows the results. In this case, the piston chamber and the shaft are rotating. Although the air stagnates in upper part of the piston chamber for the brake-type clutch, the air moves toward the shaft, which is rotation center, under the influence of centrifugal force for the rotary-type clutch. The stagnated air inside the shaft finally leaks from gap of the seal ring.

This calculation enabled us to visualize the flow field in the rotary clutch for the first time.

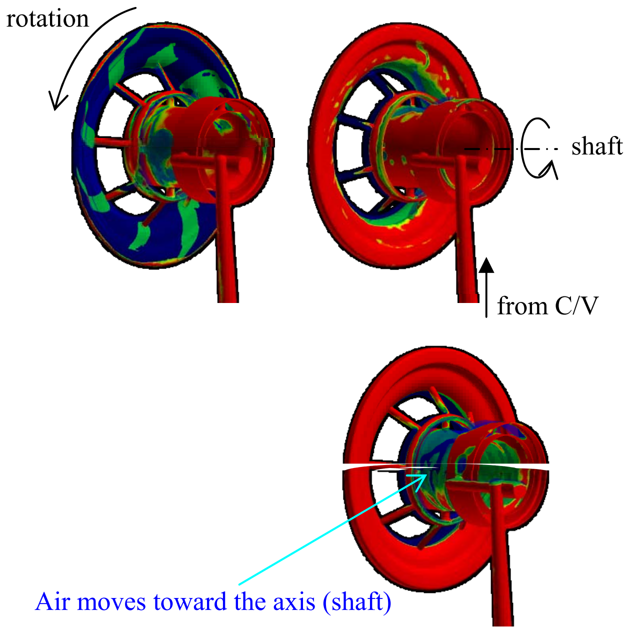

Figure 16 Motion of oil and air in the rotary clutch piston chamber

CONCLUSIONS

In this calculation, we adapted the compressibility, easy mesh morphing and formulation of the boundary conditions to the VOF method, so that we succeeded in visualizing the flow field inside the hydraulic system that conventionally required experiments. And it enabled us to understand the flow field and the air volume, and to get design knowledge of minimizing the stagnated air volume.

We are planning to apply this technology to the other parts in the transmission and achieve the performance improvement and the shortening of development period.

Proceedings of the 8th JFPS International
Symposium on Fluid Power, OKINAWA 2011
Oct. 25-28, 2011

2A3-3

HYDROSTATIC DRIVE IN RENEWABLE ENERGY FIELD

Yoshikazu Homma* and Takahiro Urai*

* Industrial Application Engineering Department
Bosch Rexroth Corporation
5-1 Higashi-nakanuki Tsuchiura-shi Ibaraki-ken 300-8588 Japan
(E-mail: yoshikazu.homma@boschrexroth.co.jp)

ABSTRACT

People are facing up to the problem of the increasing energy supply demand and but request decreasing greenhouse gases. The take off the renewable energy is necessary to satisfy the both requirements. Wind energy and ocean energy is useful energy in development. The drive train of the power take off should be improved. The conventional drive train is usually mechanical transmission. Hydrostatic drive system is a useful power take off system. In this paper some references and the development of hydrostatic drive system are introduced.

KEY WORDS

No frequency converter, Damping characteristics, Efficiency, Reliability, Over load protection

INTRODUCTION

Hydrostatic drive system is a reliable long time proofed system. It is able to cover wide power range and speed range. Consequently, hydrostatic drive system is useful to drive the generator of Wind/Current/Tidal turbine, and wave generator. In this paper, some reference and development of Wind/Current/Tidal turbine generators are described. In the second part of this paper, some reference and development of wave generator are described.

1 Wind/Current/Tidal turbine generator

The turbine driven by wind or water flow is rotated in low speed (Only a very small wind turbine turns at even 50min^{-1}). The standard solution of generation needs to drive the generator in high speed (more than 1000min^{-1}).

1.1 Conventional mechanical transmission

The conventional mechanical transmission (Gear box) has to be installed inline between turbine rotor and generator. It is designed to transfer the power of turbine rotor to generator with good efficiency at rated power. Figure 1 shows the typical configuration of wind turbine with mechanical transmission.

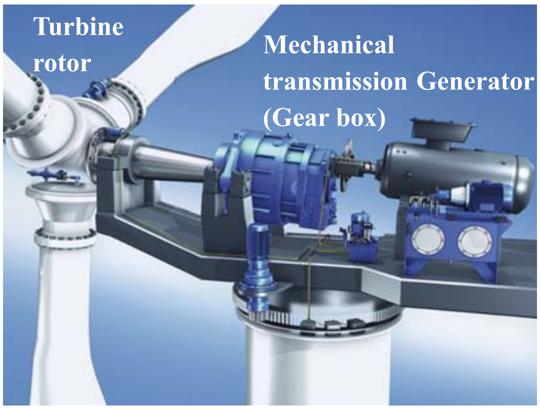

Figure 1 Configuration of wind turbine with mechanical transmission

Turbine rotor speed is changed by wind speed variation. General mechanical transmission has one gear ratio. Usually a frequency converter is installed between generator and grid due to this and fed constant frequency electric power to grid. Figure 2 shows the power transmission flow of turbine generator with mechanical transmission.

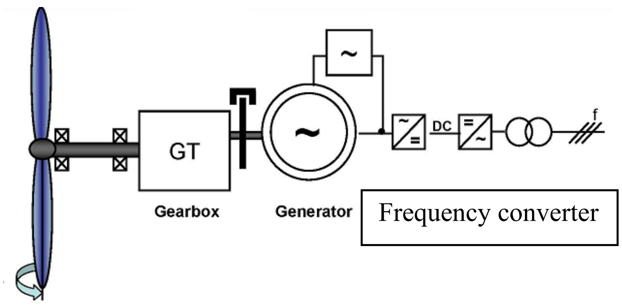

Figure 2 Power transmission with mechanical transmission and frequency converter

The mechanical transmission mounted direct on shaft which transfers all forces directly through gearbox and generator. Therefore it is difficult to install an over load limiter into a mechanical transmission. Some failures of the mechanical transmission occur due to this reason. Especially the electric part is dominating and it is related to power electronics required to convert from power from asynchronous generator to grid. Figure 3 shows the cause of failure of existing wind turbine.

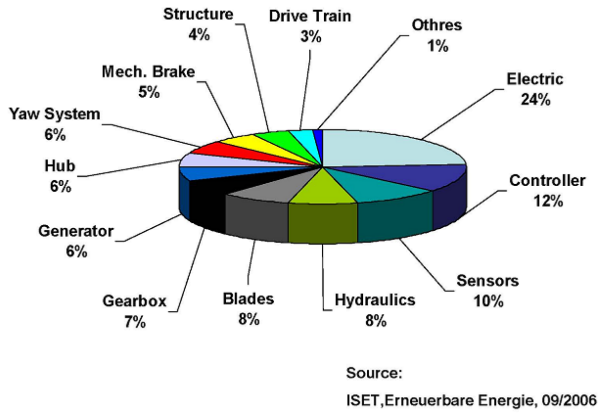

Figure 3 Failures of wind turbine

The traditional concept is also heavier which have impact on structure design. The weight of gear box for 1MW generator input is around 5000~5500kg. Figure 4 shows the example of gearbox.

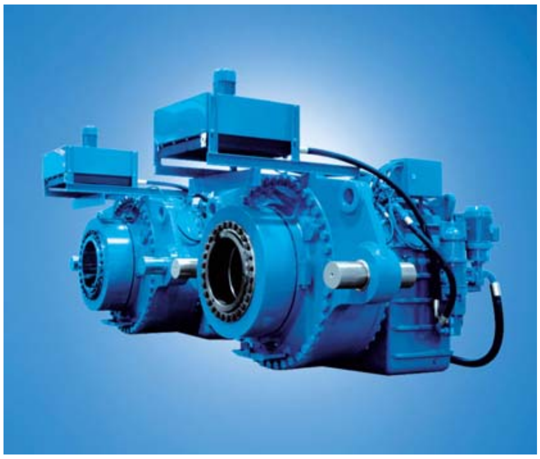

Figure 4 Gear box for wind turbine generator

1.2 Basic of Hydrostatic drive transmission

One of the alternative solutions of the power train of turbine generator is the Hydrostatic drive technology. The low speed high displacement hydraulic pump is driven by the turbine and high speed low displacement motor drives the generator. The generator can be synchronous type and directly connected to grid elimination medium voltage transformers. Figure 5 shows the concept of hydrostatic drive transmission.

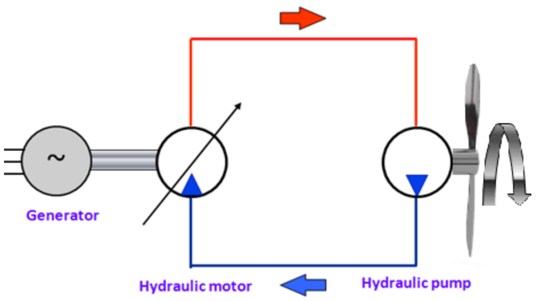

Figure 5 Concept of hydrostatic drive

Using the variable displacement motor achieves the constant drive speed of generator. The variable high speed small size motors are available in market so the solution with variable motor is a reasonable selection. Figure 6 shows the concept of hydrostatic drive with this arrangement.

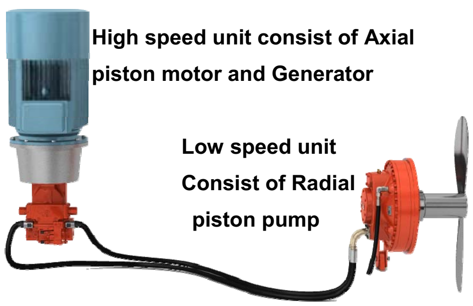

Figure 6 Concept of hydrostatic drive

The intense torque fluctuations impacting on the turbine cause changes in rotation speed of turbine rotor. Compared to the stiffness of a mechanical transmission, the hydrostatic drive transmission has a much lower stiffness because of compression of oil and the low inertia of its components. The elastic modulus of oil is 1.6 kN/mm^2 compared to 210kN/mm^2 for steel. Consequently, due to the elastic connection of turbine and generator, the rotation speed of turbine may changes on a small scale. Figure 7 shows the simulation result of dynamic analysis and it is proven by measurement [1]. Hydrostatic drive transmission has good damping characteristics.

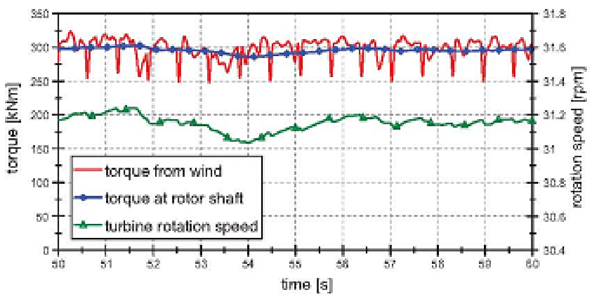

Figure 7 Simulation result of dynamic analysis about torque fluctuation

Above result shows the rotation speed of generator may be constant with suitable control of variable motor. In this system, frequency converter is redundant. Figure 8 shows power transmission flow of turbine generator with hydrostatic drive transmission.

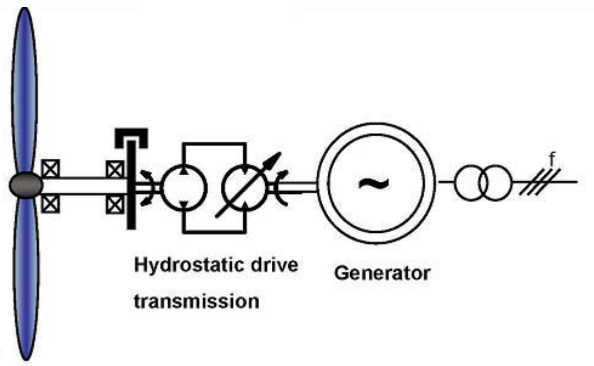

Figure 8 Power transmission with hydrostatic drive transmission

Mechanical transmission has good efficiency at rated point, but usually no efficiency data of mechanical transmission , especially at partial load, is available. It is easy to calculate and measure the overall efficiency of hydrostatic drive transmission. Because the efficiency of each item of equipment including losses in hoses, piping and valves as well as in the cooler are known. Figure 9 shows the overall efficiency and the input and output power of the hydrostatic transmission versus wind speed[1].It can be seen , that from the rated wind speed of 15m/s down to 9m/s the overall efficiency is nearly constant at 85%. This means the hydrostatic drive transmission has a constant efficiency over the power range from 20% to 100% of the rated power.

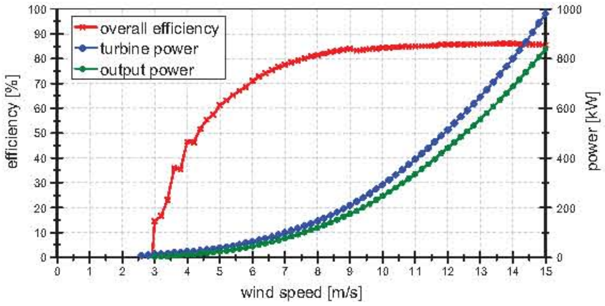

Figure 9 Simulation result of overall efficiency

This graph shows the example of the efficiency. The efficiency of hydrostatic transmission is depends on configuration and control.

1.3 Development of hydrostatic drive transmission

Development of hydrostatic drive transmission is done by certain institutes and companies. In this paper the development in IFAS (Institute for Fluid Power Drives and Controls) in Aachen University is introduced for example. IFAS have made a test bench of 1MW wind turbine. Figure 10 shows the test bench layout. It consists of fixed displacement 13200cc pump, 52800cc pump(P1 and P2) , and variable displacement 180cc motor, 250cc motor, 355cc motor, 500cc motor(M1,M2,M3 and M4) and additional fixed displacement 250cc motor.

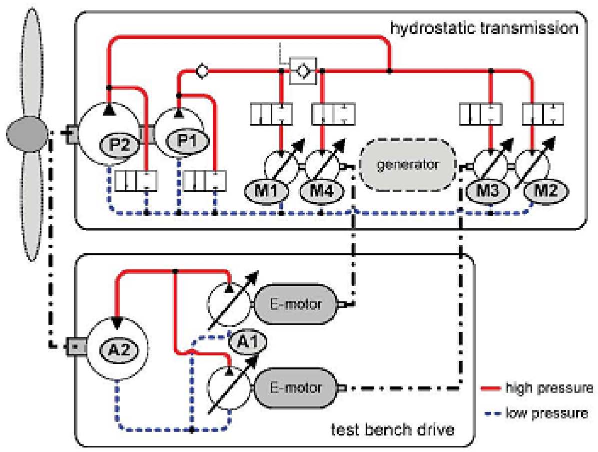

Figure 10 test bench layout

Figure 11 shows the configuration of test bench.

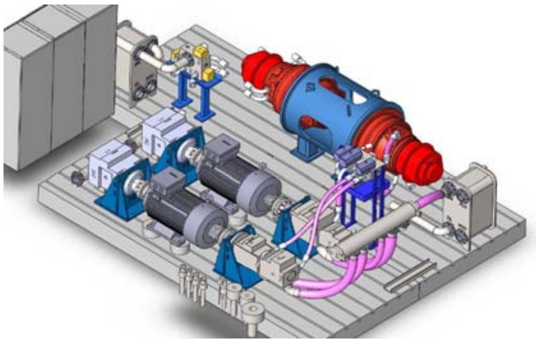

Figure 11 Configuration of test bench.

IFAS measured the overall efficiency. Figure 12 shows efficiency versus rotor rotation speed and Figure 13 versus input power.

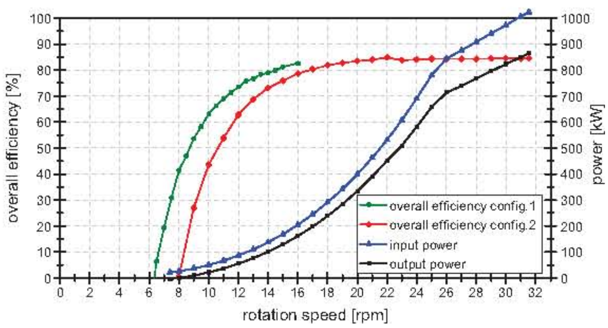

Figure 12 Overall efficiency versus rotation speed

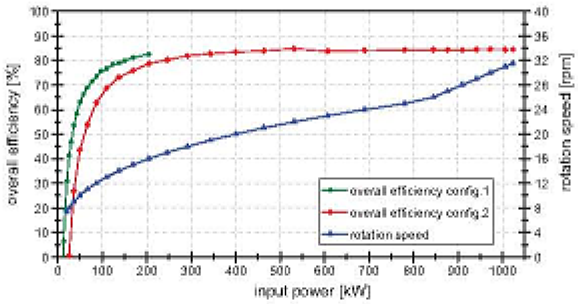

Figure 13 Overall efficiency versus input power

1.4 Hydrostatic drive transmission in wind turbine

The low speed pump should be connected to turbine rotor directly, and the high speed motor should be connected to generator directly. However the pump and motor are able to be installed separately. It allows the installation of the high speed motor and generator on the ground. Figure 14 shows the concept of hydrostatic transmission in wind turbine.

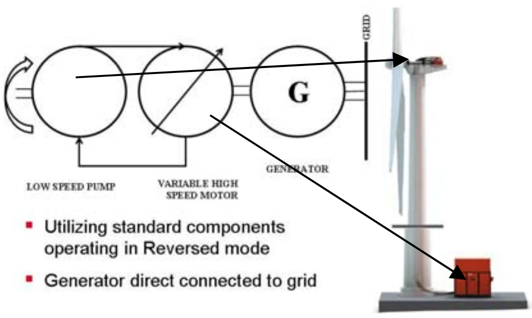

Figure 14 Concept of wind turbine

In this configuration, only the low speed pump should be installed in nacelle. The weight of fixed displacement 13200cc pump and 52800cc pump for 1MW wind turbine is 2700kg. It is almost 30% of mechanical transmission and generator for 1MW. Lower weight on top of the tower allows reducing the strength, weight and cost of tower. Figure 15 shows the detail of nacelle configuration.

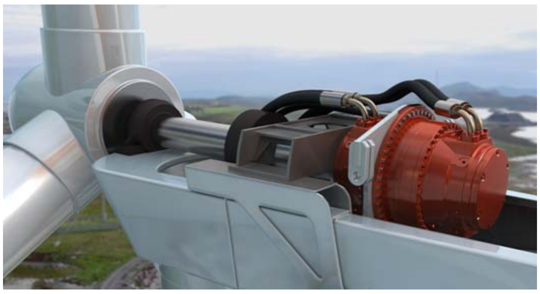

Figure 15 Nacelle configuration with hydrostatic drive transmission from ChapDrive in Norway

A reference of hydrostatic drive transmission in wind turbine can be seen in Figure 16.

Figure 16 Reference of wind turbine

Two wind turbines are installed in Norway. Specification of one turbine is power 225kW, fixed displacement pump 11314cc and variable displacement motor 500cc. Specification of another one is power 900kW, fixed displacement pump 100529cc and variable displacement motor 1000cc.

1.5 Hydrostatic drive transmission in Current/Tidal turbine

Main philosophy of current/tidal turbine is the same as wind turbine. Flexible mounting opportunities is good for easy maintenance and easy installation. Figure 17 shows the concept with one single turbine tidal turbine..

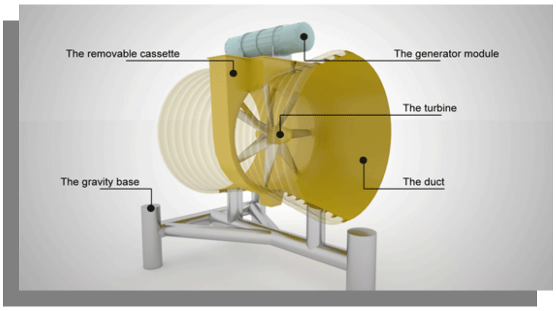

Figure 17 Concept of single current/tidal turbine

Figure 18 shows the multi concept where 4 turbines together acting against a common centralized positioned.

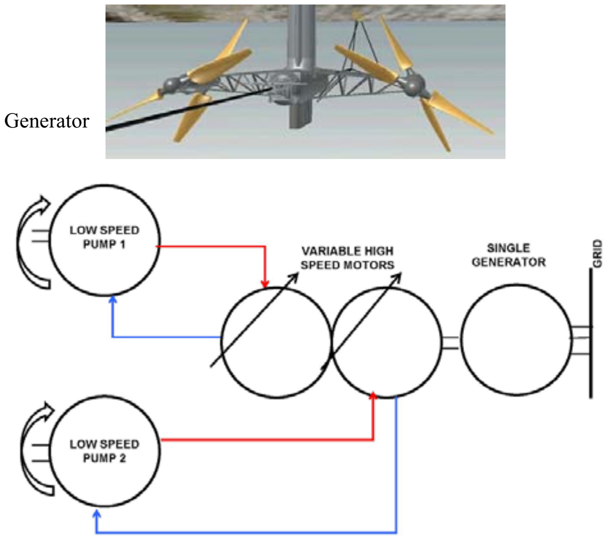

Figure 18 Concept of multiple current/tidal turbine

2 Wave generator

Wave movement usually transfers to movement of buoy /float/vane in the wave generator. Buoy/float/vane movement transfers to rod movement of hydraulic cylinder or rotation of hydraulic winch or others. The hydraulic power transfers to a hydraulic motor and finally it rotates the generator. The movement of buoy/float/vane is alternating. The hydraulic system is able to compensate the fluctuation of direction and power into a useable range by using accumulator and other devices. Figure 19 shows a concept of wave generator with a direct coupling of the cylinder. Linear Motion to a rotating. Generator via variable motor. The concept needs a flywheel and frequency converter.

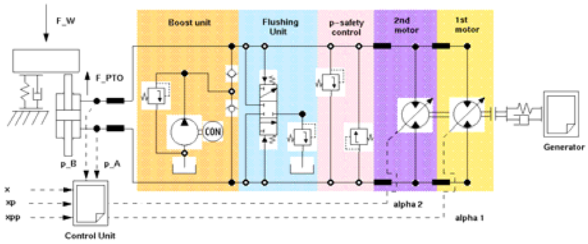

Figure 19 Concept of wave generator[2]

Some simulation and test of hydraulic system was done. Figure 20 shows the test bench and measurement.

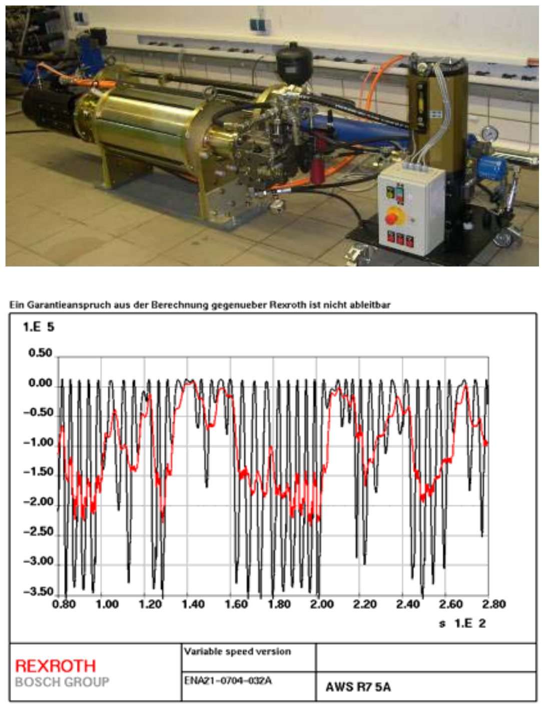

Figure 20 Test bench and measurement of wave generator

Conclusion

Merits of Hydrostatic drive transmission in turbine generator are bellow.

-Constant speed to generator without power electronics.

-Synchronous generators directly can be fed to grid without transformers.
-Weight and space saving.
-Flexible mounting opportunities.
-System reliability.
-Easily over load protection by limitation of the pressure.
The general solution for wave generator is not appeared now. Hydrostatic drive is reliable system and it will be good solution of drive system of wave generator. The Hydrostatic drive has good opportunity to improve the drive technology in Renewable Energy field.

REFERENCES

1. Jochannes Schmitz, Nils Vatheuer and Hubertus Murrenhoff, Hydrostatic drive train in Wind Energy Plants, RWTH Aachen University, Germany, Institute for Fluid Power Drives and Controls(IFAS)
2. Nik Scharmann and Christian Langenstein, German international patent DE102009012108(A1), Robert Bosch GmbH.

Proceedings of the 8th JFPS International
Symposium on Fluid Power, OKINAWA 2011
Oct. 25-28, 2011

2A3-4

ANALYSIS OF FAILSAFE HYDRAULIC ACTUATION SYSTEM USING PASSIVE RELIEF VALVES; APPLICATION FOR POWER ASSISTING DEVICES

Kotaro ISHIGURI*, Keisuke SHIMODA, Yusuke YAMANAGA,
Shogo KAMOSHITA and Makoto ISHIGE

* Railway Technical Research Institute
2-8-38 Hikari-cho, Kokubunji-shi, Tokyo, 185-8540 Japan
(E-mail: ishiguri@rtri.or.jp)

ABSTRACT

This paper presents a hydraulic circuit to ensure safety actuation mechanically. The system includes passive valves for safety operation. When the actuation system moves toward intended direction discharged hydraulic fluid from pump goes through the proposed passive valves and flows into the actuator cylinder to assist movement of the actuator. Consequently, supplied pressure from the pump is correctly loaded to the cylinder. On the other hand, when the actuation system moves for unintended direction, relief port to relieve pressure of the actuator is formed and at the same time bypass channel from higher pressure side of the pump to lower pressure side of the pump is formed by the proposed passive valve. As a result, the supplied flow is bypassed by the valve and pressure of the cylinder is kept on lower than the discharged pressure of the pump. Simulations are carried out to evaluate the effectiveness of the circuit.

KEY WORDS

Hydraulic, Actuator, Failsafe system, Passive valve

NOMENCLATURE

A_{D1}, A_{D2}, A_{P1}	:	Area of orifice (Spool valves)
A_s	:	Area of spool valve end
A_{c1}, A_{c3}	:	Area of orifice (Check valves)
A_p	:	Area of piston
a_0	:	Ratio of cylinder area of rod-side and head-side
c	:	Coefficient of discharge
c_S	:	Damping coefficient of spool valves
c_L	:	Leakage coefficient
K_e	:	Bulk modulus of oil
k_S	:	Spring constant of spool valves
m_S	:	Mass of spool valves
$p_{CL}, p_{CR}, p_{P1L}, p_{P1R}, p_{D2L}, p_{D2R}, p_{AL}, p_{AR}, p_{BL}, p_{BR}$, p_{a1}, p_{a2}	:	Circuit pressure of each port
$Q_{D1L}, Q_{D1R}, Q_{D2L}, Q_{D2R}, Q_{AL}, Q_{AR}, Q_{P1L}, Q_{P1R}, Q_{BL}, Q_{BR}$, Q_{CL}, Q_{CR}	:	Circuit flow of each port
Q_{a1}, Q_{a2}	:	Inflow of cylinder
$Q_{c1}, Q_{c2}, Q_{c3}, Q_{c4}$	:	Circuit flow of check valves
Q_P	:	Discharge flow of pump
Q_L	:	Leakage flow of piston
ρ	:	Density of oil
x_p	:	Displacement of piston
y_{SL}, y_{SR}	:	Displacement of spool valves
W_{BP}	:	Volume of channel near the pump
W_{b1}, W_{b2}	:	Cylinder volume of rod-side and head-side
W_{p0}	:	Cylinder volume of head-side

		at neutral position
W_{SL}, W_{SR}	:	Total volume of the channel near the spring side of spool valves with the end of spool valves
W_{BL}, W_{BR}	:	Volume of channel near the spring side of spool valve
W_{BM}	:	Volume of bypass channel

INTRODUCTION

Hydraulic and pneumatic actuators are used for controlling power assisting devices. Those are often used for the part where safety is secured by other mechanism. In automotive systems, power assisting actuation mechanism for steering wheels has been installed to assist steering torque. In the system, the steering shaft is directly connected with handling shaft to ensure safety driving [1], [2]. For this reason, if the power assisting system does not work correctly, we can avoid danger by overriding the actuator torque with the power of ourselves. The system is an example of ensuring safety by mechanical system and human power. However, there are some systems that cannot be supported by other source of power. Considering further applications of those actuators, it is necessary to ensure safety by itself. Therefore, this paper presents the hydraulic circuit for power assisting devices to ensure safety actuation mechanically.

MECHANISM

This actuation system has a cylinder for power assisting. The actuator is initially moved by external force and then the assisting movement is followed by the initial movement of the actuator. On the contrary, when the system moves for unintended direction (fault operation), valves connect pump with bypass channel and actuator with relief channel at the same time, then the power assisting function is invalidated. The system has an actuator cylinder and a pump. Figure 1 shows relationships between pressure and movement of the actuator. In the correct operation, it is necessary to load pressure constantly to assist motion of the actuator. When we set ordinary relief valves for this actuation system, it is impossible to set relief pressure lower than the actuation pressure for the correct operation, because the supplied pressure from the pump will be loaded also in the fault operation. For this reason, it is necessary to set up special valves. The valve has two functions, one is to load hydraulic pressure to the actuator in the correct operation, and another is to relieve pressure from the actuator with bypassing hydraulic fluid from delivering side to suction side of the pump by the bypass channel.
Figure 2 shows an actuation system including proposed passive valves for safety operation. The system has two passive valves and four check valves. In addition, Figure 3 shows valve unit of the actuation system. The valve unit has six ports for controlling hydraulic flow and pressure. P_1 is a port for supplying fluid from the pump. A is a port connected with the actuator cylinder. In the correct operation, hydraulic fluid flows from the pump to the actuator through the port P_1 and A. D_2 is a port for bypass channel. C and D_1 are ports to relieve pressure of

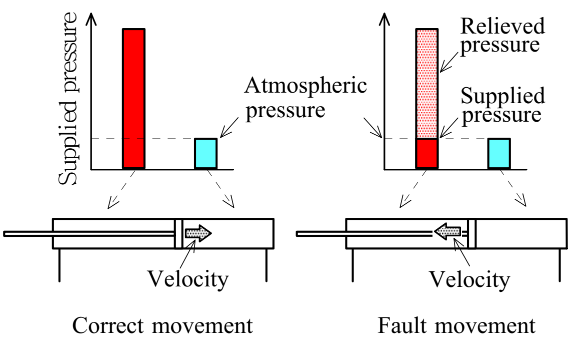

Figure 1 Pressure of the cylinder

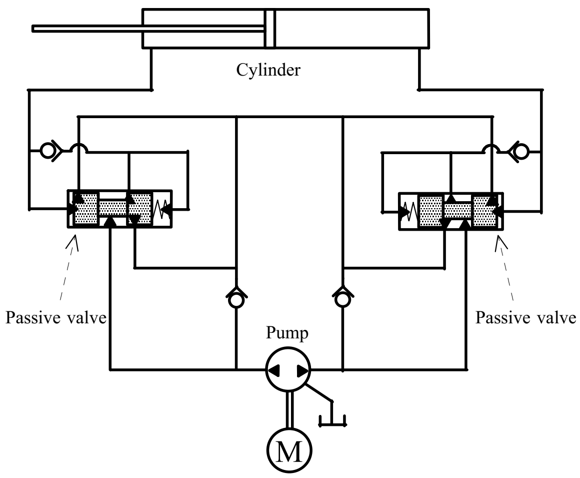

Figure 2 Schematic configuration of failsafe hydraulic actuation system

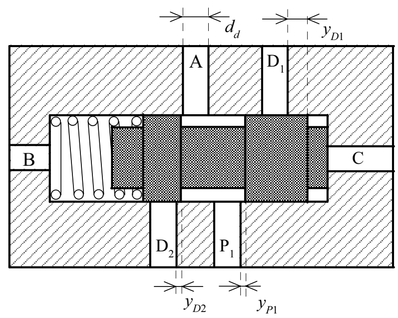

Figure 3 Valve unit

the actuator. In the fault operation, bypass channel through port D_2 and relief channel through port C and D_1 work as safety systems. B is for the preload port to load the same pressure as the actuator to the spool. The preload port works to maintain position of the spool.

Figure 4 shows flow of the actuation system in the correct operation. This is an example that the actuator moves toward rod-side. Under this condition, supplying fluid from the pump comes into the port P_{1R}, and then through the port A_R of the spool valve unit to the actuator. In addition, returned fluid from opposite side of the cylinder comes into the port C_L of another valve, and then through the port D_{1L} of the valve to lower pressure side of the pump. Consequently, it is possible to load appropriate pressure to the cylinder in the correct operation.

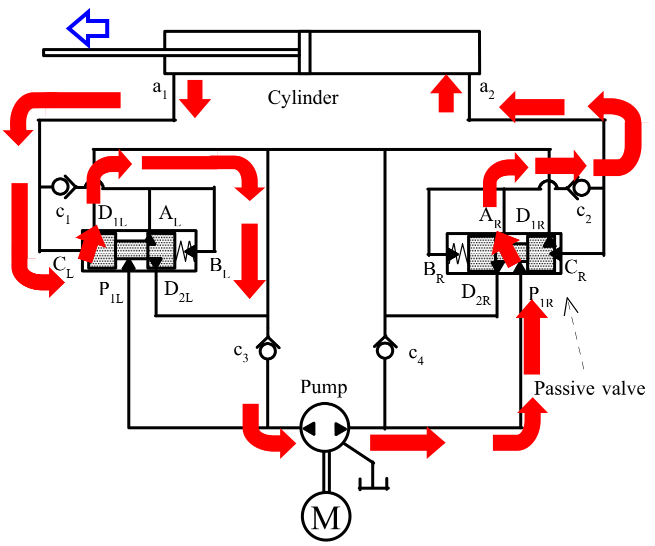

Figure 4 Flow of the actuation system in the correct operation

On the other hand, Figure 5 shows flow of the actuation system in the fault operation. This is an example that the actuator moves toward head-side. Under this condition, supplying fluid from the pump comes into the port P_{1R}, and then through the port D_{2R} of the spool valve unit to the lower pressure side of the pump. At that time, bypass channel from higher pressure side of the pump to lower pressure side of the pump was formed. Consequently, the actuation system did not produce force for actuation under the fault condition.

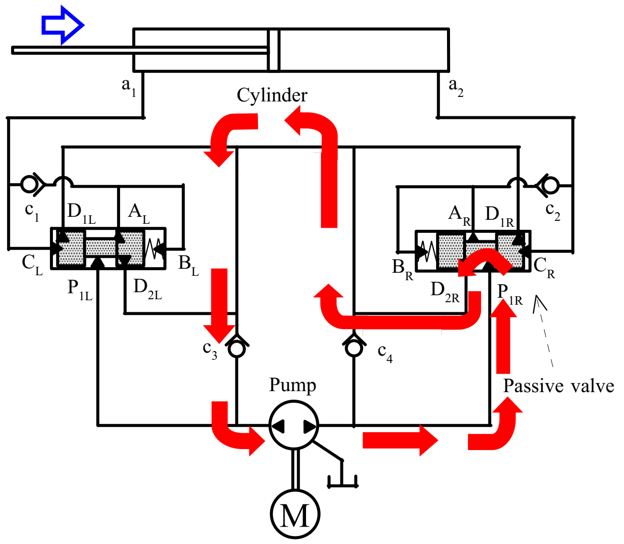

Figure 5 Flow of the actuation system in the fault operation

SIMULATION SETTINGS

Figure 6 shows direction of hydraulic flow and pressure of the actuation system. Positive direction of the fluid flow is indicated by the arrow in the Figure. Moreover, black circles indicate connecting points of the path. We set displacement of the piston x_p, and displacement of the passive valve elements y_{SL} and y_{SR}, where the neutral position of the piston correspond to x_p=0. And displacement y_{SL}=0 and y_{SR}=0 correspond to the position that springs of spool valves are extended.

Fluid flow at port D_{1L} and D_{1R} are calculated from following equations,

$$Q_{D1L} = c\,A_{D1}(y_{SL})\sqrt{\frac{2\left|p_{CL}-p_{D1L}\right|}{\rho}}\,\mathrm{sign}\left(p_{CL}-p_{D1L}\right) \quad (1)$$

$$Q_{D1R} = c\,A_{D1}(y_{SR})\sqrt{\frac{2\left|p_{CR}-p_{D1R}\right|}{\rho}}\,\mathrm{sign}\left(p_{CR}-p_{D1R}\right) \quad (2)$$

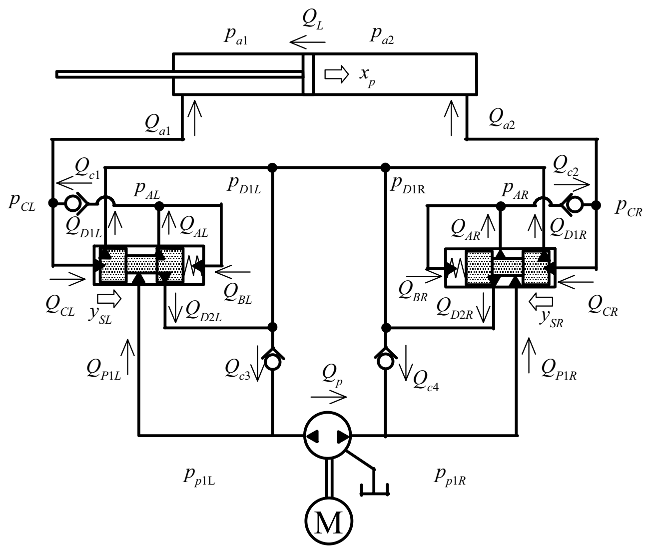

Figure 6 Definition of hydraulic flow direction and pressure of the actuation system

where c is coefficient of discharge, ρ is density, $A_{D1}(y_{SL})$ and $A_{D1}(y_{SR})$ are the area of orifice relative to the displacement of the spool valves. Fluid flow at port A_L and A_R are shown as follows:

$$Q_{AL} = c\,A_{P1}(y_{SL})\sqrt{\frac{2|p_{P1L}-p_{AL}|}{\rho}}\,\mathrm{sign}\left(p_{P1L}-p_{AL}\right) \quad (3)$$

$$Q_{AR} = c\,A_{P1}(y_{SR})\sqrt{\frac{2|p_{P1R}-p_{AR}|}{\rho}}\,\mathrm{sign}\left(p_{P1R}-p_{AR}\right)\ . \quad (4)$$

Where $A_{P1}(y_{SL})$ and $A_{P1}(y_{SR})$ are the area of orifice relative to the displacement of the spool valves. By the same way, fluid flow at port D_{2L} and D_{2R} are given as follows:

$$Q_{D2L} = c\,A_{D2}(y_{SL})\sqrt{\frac{2|p_{P1L}-p_{D2L}|}{\rho}}\,\mathrm{sign}\left(p_{P1L}-p_{D2L}\right) \quad (5)$$

$$Q_{D2R} = c\,A_{D2}(y_{SR})\sqrt{\frac{2|p_{P1R}-p_{D2R}|}{\rho}}\,\mathrm{sign}\left(p_{P1R}-p_{D2R}\right). \quad (6)$$

Where $A_{D2}(y_{SL})$ and $A_{D2}(y_{SR})$ are the area of orifice depending on the displacement of the spools. Fluid flow at port P_{1L} and P_{1R} are sum of the fluid flow at port A and D_2

$$Q_{P1L} = Q_{AL} + Q_{D2L} \quad (7)$$

$$Q_{P1R} = Q_{AR} + Q_{D2R}\ . \quad (8)$$

Check valves are set up from the valve and spring, for this reason, fluid flow of the valve are calculated from equations (9) to (12).

$$Q_{c1} = c\,A_{c1}(y_{c1})\sqrt{\frac{2|p_{AL}-p_{CL}|}{\rho}} \quad (9)$$

$$Q_{c2} = c\,A_{c1}(y_{c2})\sqrt{\frac{2|p_{AR}-p_{CR}|}{\rho}} \quad (10)$$

$$Q_{c3} = c\,A_{c3}(y_{c3})\sqrt{\frac{2|p_{D1R}-p_{P1L}|}{\rho}} \quad (11)$$

$$Q_{c4} = c\,A_{c3}(y_{c4})\sqrt{\frac{2|p_{D1L}-p_{P1R}|}{\rho}}\ . \quad (12)$$

Where $A_{c1}(y_{c*})$ and $A_{c3}(y_{c*})$ are the area of orifice depending on the state of the check valves. Inflow of cylinder at rod-side and head-side are as follows:

$$Q_{a1} = Q_{c1} - Q_{D1L} \quad (13)$$

$$Q_{a2} = Q_{c2} - Q_{D1R} \quad (14)$$

Swept volume at the spring end of the spool valve are

$$Q_{BL} = -A_S\,\dot{y}_{SL} \quad (15)$$

$$Q_{BR} = -A_S\,\dot{y}_{SR}\ . \quad (16)$$

Supplied pressure from the pump p_{p1L} and p_{p1R} are

$$p_{p1L} = \frac{K_e}{W_{BP}}\int\left(-Q_P + Q_{c3} - Q_{p1L}\right)dt \quad (17)$$

$$p_{p1R} = \frac{K_e}{W_{BP}}\int\left(Q_P + Q_{c4} - Q_{p1R}\right)dt \quad (18)$$

where K_e is modulus of elasticity of volume, W_{BP} is channel volume near the pump; Q_p is discharge flow of pump. Inflow of bypass channel is same as the fluid flow at port D_{1L} and D_{1R},

$$Q_{CL} = Q_{D1L} \quad (19)$$

$$Q_{CR} = Q_{D1R}\ . \quad (20)$$

Acceleration of spool valves are as follows:

$$\ddot{y}_{SL} = \left\{A_S\left(p_{CL}-p_{BL}\right) - c_S\dot{y}_{SL} - k_S y_{SL}\right\}/m_S \quad (21)$$

$$\ddot{y}_{SR} = \left\{A_S\left(p_{CR}-p_{BR}\right) - c_S\dot{y}_{SR} - k_S y_{SR}\right\}/m_S\ . \quad (22)$$

Where m_s, c_s and k_s are mass, damping coefficient and spring constant of the spool valve. Pressures of the cylinder are

$$p_{a1} = \frac{K_e}{W_{b1}(x_p)}\int\left(Q_{a1} - a_0 A_p \dot{x}_p + Q_L\right)dt \quad (23)$$

$$p_{a2} = \frac{K_e}{W_{b2}(x_p)}\int\left(Q_{a2} + A_p \dot{x}_p - Q_L\right)dt\ . \quad (24)$$

Where a_0 is a ratio between pressure receiving area of rod-side and head-side of the cylinder, Q_L is leakage flow of the piston due to the gap between cylinder and piston

$$Q_L = c_L\,(p_{a1} - p_{a2})\ . \quad (25)$$

Volume of the cylinder of rod-side W_{b1}, and volume of the cylinder of head-side W_{b2} are shown in equations

$$W_{b1}(x_p) = a_0 W_{p0} + a_0 A_p x_p \quad (26)$$

$$W_{b2}(x_p) = W_{p0} - A_p x_p \quad . \tag{27}$$

Pressure of the channel of spring side of the proposed valves are as follows:

$$p_{BL} = p_{AL} = \frac{K_e}{W_{SL}(y_{SL})} \int \left(Q_{AL} - Q_{BL} - Q_{c1} \right) dt \tag{28}$$

$$p_{BR} = p_{AR} = \frac{K_e}{W_{SR}(y_{SR})} \int \left(Q_{AR} - Q_{BR} - Q_{c2} \right) dt \tag{29}$$

where W_{SL} and W_{SR} are total volume of the channel near the spring side of spool valves with the end of spool valves

$$W_{SL}(y_{SL}) = W_{BL} - A_S y_{SL} \tag{30}$$

$$W_{SR}(y_{SR}) = W_{BR} - A_S y_{SR} \quad . \tag{31}$$

Pressure of the bypass channel is

$$p_{D1L} = \frac{K_e}{W_{BM}} \int \{ \left(Q_{D1L} + Q_{D2L} - Q_{c4} \right) + \left(Q_{D1R} + Q_{D2R} - Q_{c3} \right) \} dt . \tag{32}$$

Where W_{BM} is the volume of bypass channel. Pressures of the port connected with the bypass channel are the same as the pressure p_{D1L}

$$p_{D1R} = p_{D2L} = p_{D2R} = p_{D1L} \quad . \tag{33}$$

Parameters for simulation are listed on Table 1. This setting is used to verify fundamental operation of the proposed passive valves under the correct operation and the fault operation.

SIMULATION RESULT

We set two conditions for the simulation. One is the correct operation and another is the fault operation. In addition, the time, we set the actuator forced to move toward the correct and fault direction to emulate conditions that the actuator moves to the commanded direction and unintended direction. Simulation results of correct operation are shown in Figure 7. The top Figure shows displacement of the actuator. In this Figure, positive displacement means shrinking. Therefore the actuator forced to shrink from two to 12 seconds and to return toward neutral position from 17 to 27 seconds, under this setting. The middle Figure shows hydraulic flow from the pump. In the Figure, positive flow of the pump corresponds to supply hydraulic fluid to head-side of the actuator. Under this setting, the pump discharges hydraulic fluid toward rod-side of the actuator from two to 12 seconds, and then after the 5-second stop, the pump discharges hydraulic fluid toward head-side of the actuator from 17 to 27 seconds. The bottom Figure

Table 1 Parameters for simulation

Parameters	Symbol	Value	Unit
Atmospheric pressure	p_{sa0}	100	kPa
Pressure of discharge side of pump	p_{sb0}	4000	kPa
Density of oil	ρ	860	kg/m^3
Bulk modulus of oil	K_e	1.6	GPa
Coefficient of discharge	c	0.7	
Diameter of spool valve	d_s	27.0	mm
Mass of spool valve	m_s	0.245	kg
Spring constant of spool valve	k_s	1.981	N/mm
Damping coefficient of spool valve	c_s	300.0	Ns/m
Diameter of spool port	d_d	8.0	mm
Overwrap of spool port D_1	y_{D1}	6.5	mm
Overwrap of spool port P_1	y_{P1}	0.0	mm
Overwrap of spool port D_2	y_{D2}	1.5	mm
Diameter of actuator piston	d_p	40.0	mm
Ratio of cylinder area of rod-side and head-side	a_0	0.68	
Leakage coefficient	C_L	0.0	$(L/min)/(kgf/cm^2)$
Volume of channel near the pump	W_{BP}	100.6	cm^3
Volume of bypass channel	W_{BM}	158.5	cm^3
Volume of channel near the spring side of spool valve	W_{BL}	31.7	cm^3

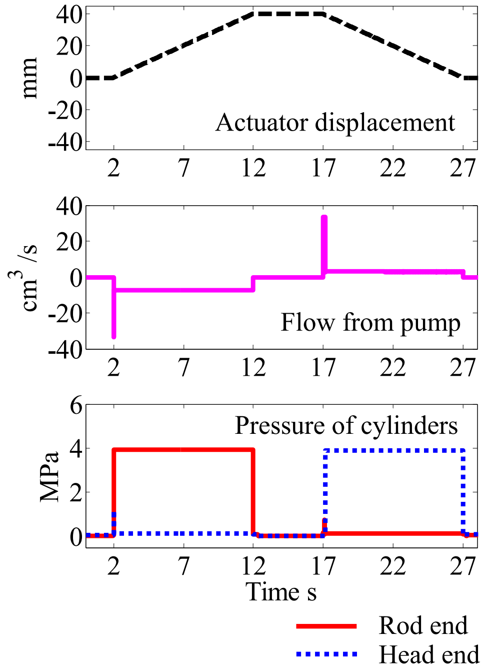

Figure 7 Correct operation

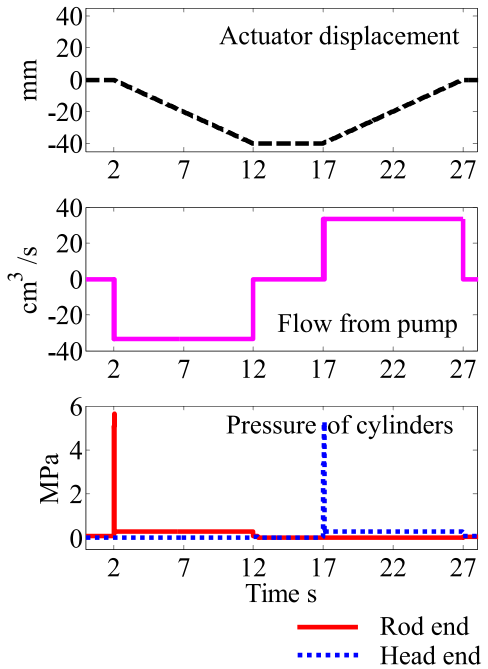

Figure 8 Fault operation

shows pressure of the actuator cylinders. Continuous line corresponds to pressure of rod-side of the cylinder. In addition, dotted line corresponds to the pressure of head-side of the cylinder. As shown in this Figure, discharged hydraulic fluid goes through the proposed passive valves and flows into the actuator cylinder to assist actuator motion. Consequently, supplied pressure is correctly loaded to the cylinder under this condition.

On the contrary, simulation results of fault operation are as shown in Figure 8. Specifications of lines are same as that of the Figure 7. Under this setting, discharging direction of the pump is same as the correct operation. By contrast, direction of the actuator displacement is opposite from the setting of the correct operation. The bottom Figure shows pressure of the actuator cylinder. As shown in this Figure, surging response is inevitable at the transition time instantaneously. However, except for the transitional period, pressure of the cylinder is kept on lower than the discharged pressure of the pump at the condition. At that time, bypass channel from higher pressure side of the pump to lower pressure side of the pump is formed by the proposed passive valve. As a result, the supplied flow is bypassed by the valve and pressure of the cylinder is kept on lower than the discharged pressure of the pump. Consequently, the actuation system did not produce force for actuation under the fault condition. In addition, it is possible to ensure safety operation by using the proposed passive relief valve.

CONCLUSION

In this paper, we studied hydraulic circuit for power assisting devices to ensure safety actuation. Two passive valves are installed in this system. When the actuation system moves toward intended direction, supplied pressure from the pump is correctly loaded to the cylinder to assist movement of the actuator. On the contrary, when the actuation system moves for unintended direction, the supplied flow is bypassed by the valve and pressure of the cylinder is kept on lower than the discharged pressure of the pump. Simulation results show that the actuator works just as intended both in the correct operation and the fault operation. Consequently, it is possible to ensure safety operation of power assisting devices by using the proposed passive valve.

REFERENCES

1. Baharom, M. B., Hussain, K. and Day, A. J., Design concepts and analysis of a semi-active steering system for a passenger car, Proceedings of the Institution of Mechanical Engineers, Part K: Journal of Multi-body Dynamics, 2009, Vol.223, No.4, pp. 283-292
2. Nong, Z., and Mial, W., Dynamic Modeling of Hydraulic Power Steering System with Variable Ratio Rack and Pinion Gear, JSME International Journal, Series C, 2005, Vol.48, No.2, pp.251-260

Proceedings of the 8th JFPS International
Symposium on Fluid Power, OKINAWA 2011
Oct. 25-28, 2011

2A4-1

SELF-TUNING FUZZY-SLIDING CONTROLLER DESIGN OF VARIABLE DISPLACEMENT HYDRAULIC MOTOR SYSTEM WITHOUT POSITION FEEDBACK OF REGULATING CYLINDER

Tsai De-Lung, Kei-Ren Pai, Ming-Chang Shih and Yue-Lin Guo

*Department of Mechanical Engineering
National Cheng Kung University
701, No.1, Da-She Rd., Tainan, Taiwan
(E-mail:mcshih@mail.ncku.edu.tw)

ABSTRACT

In this paper, a hydraulic save-energy driven system is built by using a variable displacement hydraulic motor without the swashplate angle feedback. It can change the output torque suitably in accordance with the demand of the external load torque by adjusting the motor's swash plate to achieve the objective of high control and low power consuming. Furthermore, a self-tuning fuzzy sliding mode controller is developed in this study to add the control accuracy and performance under the external variable load. In order to verify the feasibility of the control systems, the dynamic simulation and experiments are implemented respectively. From the results, the control system has very good performance.

Keywords

Hydraulic secondary control, Variable displacement hydraulic motor, Fuzzy sliding mode control.

INTRODUCTION

Hydrostatic drives are used in mobile, industrial and aircraft applications when typical advantages such as a high power density, good controllability, flexibility in the system set-up, the efficient and easy generation of linear movements (especially under high forces) and the excellent dynamic performance give this kind of drive technique a clear advantage over electrical or mechanical solutions. This kind of the hydrostatic drives control is divided into resistance and displacement control. Resistance-controlled drives use a control valve or servo-valve in the main circuit thus inducing losses by throttling. These losses lead to oil heating and must be considered as an irreversible loss, decreasing the system efficiency. These losses can be avoided using displacement control. To reduce energy consumption, one hydraulic pressure energy-saving transmission, secondary regulation hydrostatic transmission technology, is adopted in industrial. This technology is the regulation on the secondary component that makes conversion between hydraulic pressure energy and mechanical energy in the constant voltage network [1]. Regulation on torsion and rotate speed of load is realized through changing the displacement of the secondary component.

If a load change occurs, the secondary control reacts immediately by accelerating or decelerating the process, thus maintaining a constant speed. And, in the system with secondary control there is almost loss-free conversion of hydraulic energy into mechanical energy and of mechanical energy into hydraulic energy.

In this paper, a secondary-regulating hydrostatic transmission system without the swashplate angel feedback is built. A self-tuning fuzzy sliding mode control strategy is designed to execute the speed control under the external variable load.

the variable hydraulic motor are derived as follows.

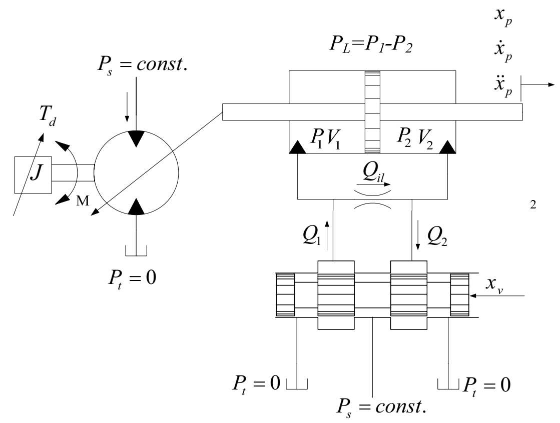

Figure 2 The scheme of speed control system of the variable displacement hydraulic motor.

THE BASIC THEORY AND MATHEMATIC MODEL OF SECONDARY REGULATION

(1) The organization of the proposed system

There are two types of hydraulic power supply, which are constant flow system with volume invariability and constant pressure system with volume regulable. There are also two types of control way for hydraulic executors, which are restriction control and displacement control. It will be four types of hydraulic system by assembling the two types of power supply and two types of control way. The secondary regulation technology is the type assembled by constant pressure power supply and displacement control.

The traditional organization of the secondary regulation transmission control is showed in Figure 1(a). The displacement of the secondary unit is controlled by the variable cylinder to change its slope angle with the swashplate angle feedback, the movement of variable cylinder is controlled by servo valve, changing the slope angle can change the displacement of the secondary unit, and can control the position, rotation rate and torsion, etc. However, under cost consideration, the variable displacement hydraulic motor without the swashplate angel feedback is developed and built. Its organization is shown as Figure 1(b). The slope angle of the swashplate is modified through the designed controller and the only speed sensor.

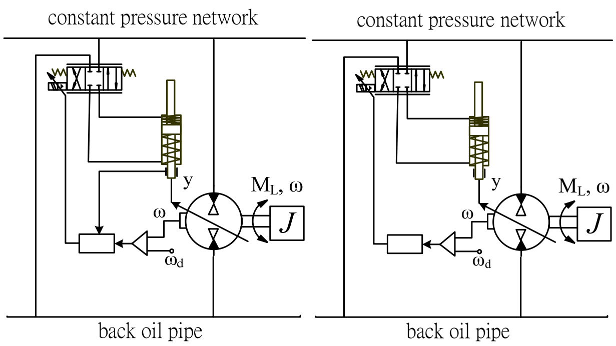

(a) (b)

Figure 1 The secondary regulation system
(a) with the swashplate angel feedback
(b) without the swashplate angel feedback

(2)The Mathematic Model of the variable displacement hydraulic motor system

The scheme of speed control system of the variable displacement hydraulic motor is shown in Fig. 2. The hydraulic variable motor is driven and controlled by regulating the piston stroke. The dynamic equations of the variable hydraulic motor are derived as follows.

The hydraulic variable motor is driven and controlled by regulating the piston stroke. The dynamic equations of the variable hydraulic motor are derived as follows. The dynamic equation of the spool displacement of a servo valve can be described by a first-order dynamic equation and the transfer function of the spool of the servo valve can be written as

$$\dot{x}_v = -\frac{1}{T_v} x_v + \frac{K_v}{T_v} u \tag{1}$$

Where K_v 、T_v are separately expressed the gain of servo valve and the time constant of the servo valve.

Servo-valve linearization flow equation is,

$$Q_L = K_q x_v \sqrt{1 - sign(x_v) \cdot P_L / P_s} \tag{2}$$

Where Q_L , K_q , x_v, P_s and P_L are separately expressed load flow, flow gain, variety hydraulic cylinder displacement, flow-pressure coefficient, load pressure.

Hydraulic cylinder continuity flow equation is,

$$Q_L = C_t P_L + A_p \dot{x}_p + \frac{V_t}{4\beta_e} \dot{P}_L \tag{3}$$

Where A_P, C_t, V_t and β_e are separately expressed variety hydraulic cylinder area, variety hydraulic cylinder whole leak coefficient, whole compress volume, oil volume module.

Hydraulic balance equation between output power and load is,

$$P_L A_p - F_L - B_p \dot{x}_p - K_p x_p = m_p \ddot{x}_p \tag{4}$$

Where m_p , B_p , K_p and F_L are separately expressed piston mass variety hydraulic cylinder, stickiness damping coefficient of piston and load, load spring rate, random external load.

The displacement of the variable hydraulic motor is

$$V_g = \frac{V_{g\max}}{x_{p\max}} x_p \tag{5}$$

Where V_g , V_{gmax} and $x_{p\max}$ are separately expressed the displacement of the variable hydraulic motor , the maximum displacement of the variable hydraulic motor and maximum position of the regulating piston.

The output torque of the variable hydraulic motor can be expressed as

$$M = \frac{P_s V_{g\max}}{2\pi x_{p\max}} x_p \tag{6}$$

The torque balance equation for the Motor can be expressed as

$$J_t \dot{\omega} + B_m \omega = \frac{P_s V_{g\max}}{2\pi x_{p\max}} x_p - T_d \tag{7}$$

Where P_s , J_t , ω, B_m and T_d are separately expressed pressure of the constant pressure network, secondary unit rotation inertia, motor speed, coefficient of damping, random load torque.

LAYOUT OF THE EXPERIMENTAL DEVICES

The layout of the experimental devices for the speed control system of the variable displacement hydraulic motor system is shown in Figure 3. The motor is pushed by constant pressure power supply. The displacement of the motor is controlled by the variable cylinder to change its slope angle, the movement of variable cylinder is controlled by servo valve, changing the slope angle can change the displacement of the secondary unit, and can control rotation rate. For the rotation rate feedback, a encoder with 1024 pulse/rev resolution is employed. A microcomputer acts as a controller and is used for the experimental data acquisition. The rotation rate of the motor is measured by a encoder and feedback to the computer through the data acquisition and control board. The control input signal is calculated in the microcomputer through the designed software and set to the proportional control valve by the D/A capability of the data acquisition and the control card. So that the oil mass flow rate can be regulated and the pressure difference of the cylinder can be built up to drive the cylinder. Therefore, the swashplate can move toward the target position. Then, in order to test the robust of building variable displacement hydraulic motor system, a variable torque load system consists of a oil pump and a pressure control valve is used to make the load torque for variable displacement hydraulic motor. The variable torque is generated by the variable command signal to the pressure control valve. Two pressure sensors set up on the inlets of the torque simulator are used to measure the pipe pressures. The measured pressure signals will be amplified and transferred by interface card, and stored in the PC.

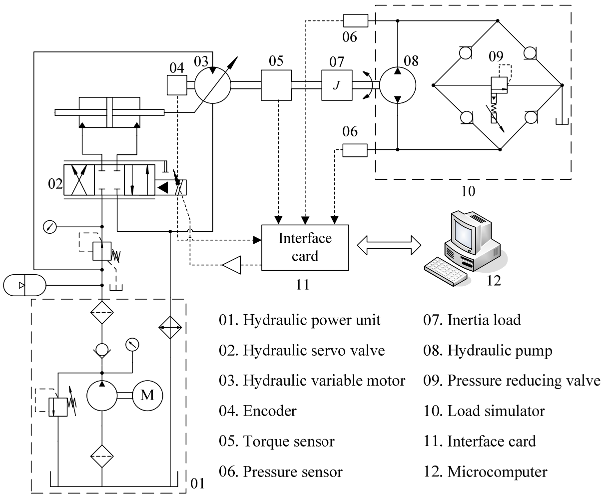

Figure 3 The layout of the experimental devices for the speed control system of the variable displacement hydraulic motor system.

CONTROLLER DESIGN

To obtain the better transient and steady-state response at the same time, in this study a self-tuning fuzzy sliding mode controller (SFSMC) is designed, and is applied to execute the precise control. Besides, a dead-zone compensator is designed to compensate the dead zone of the system and to reject the external load, respectively. Those compensation signals are added directly the designed controller to raise the positioning precision and the robustness of system. The block diagram of the pneumatic control system is shown in Figure 4.

(1) Self-tuning fuzzy sliding mode control (SFSMC)

Fuzzy control theory was combined with sliding mode control theory in the study to control the variable displacement hydraulic motor system. The structure of the fuzzy control includes four parts: fuzzification inference, knowledge base, decision logic and defuzzification. In the article, Mamdani control rules and maximum-minimum algorithm are applied, and the "center of the gravity" method is used to defuzzify and to get the accurate control signal. For sliding mode control, the sliding surface S and the change of sliding surface dS are defined as

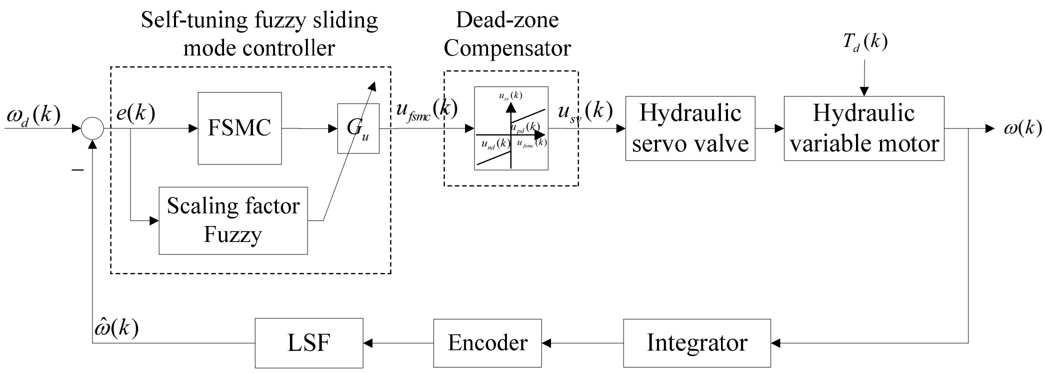

Figure 4 Block diagram of the control system.

$$S(k) = de(k) + \lambda \times e(k), \tag{8}$$

$$dS(k) = S(k) - S(k-1), \tag{9}$$

where e(k) is the error, de(k) is the change of error and λ is the slop of sliding surface S.

The variables $S'(k)$, $dS'(k)$ and $U(k)$ are chosen to be the two inputs and one output of the fuzzy controller, respectively. The variables $S'(k)$ and $dS'(k)$ are defined by

$$S'(k) = S(k) \times Ge, \tag{10}$$

$$dS'(k) = dS(k) \times Gv, \tag{11}$$

where Ge and Gv are the scaling factors of sliding surface and change of sliding surface. The control output signal $u_{fsmc}(k)$ is defined as:

$$u_{fsmc}(k) = U(k) \times Gu(k), \tag{12}$$

where $U(k)$ and $Gu(k)$ denote the controller output and the output scaling factor of the controller at time instant *kT*. In this paper, the triangular membership function is applied to define the fuzzy sets of the inputs and the output, as *Figure 5* illustrated. Three linguistic fuzzy sets are applied for the input and output variables. The control rules are illustrated in *Table 1*. The “max-min” and “center of gravity“ methods are adopted for fuzzy inference logic and defuzzification algorithm.

For the conventional fuzzy inference, its control parameters as rules table, scaling factors and membership functions are usually obtained by trial-and-error method. The method is time-consuming and difficult to obtain the optimum parameters. And, the conventional controller has not the adaptive resource to supervise and modify its control parameters to reject the

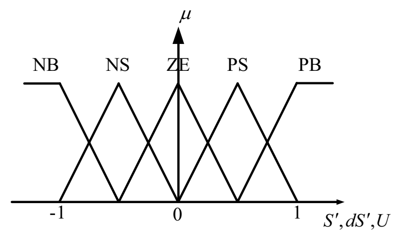

Figure 5 Membership function of $S'(k)$, $dS'(k)$ and $U(k)$.

Table 1 Fuzzy reasoning rules.

dS' \ S' (U)	NB	NS	ZE	PS	PB
NB	NB	NB	NS	NS	ZE
NS	NB	NS	NS	ZE	PS
ZE	NS	NS	ZE	PS	PS
PS	NS	ZE	PS	PS	PB
PB	ZE	PS	PS	PB	PB

disturbance. Therefore, in this paper the output scaling factor *Gu(k)* of fuzzy sliding mode controller is tuned on-line by a real-time gain updating factorα(k) to raise the positioning precision and robustness of the control system. The new scaling factors are modified by

$$Gu(k+1) = Gu(k) \times (1 + \alpha(k)), \tag{13}$$

where α(k) is the real-time gain factor. The value of real-time gain factor α(k) is computed on-line using a model independent fuzzy rule-base defined by error and change of error of the controlled variable. The most important point to note is that real-time gain factor is not dependent in any way, on any process parameter. The value of real-time gain factor depends only on the input variable of controller at the sampling instant. The membership functions for input variables *e(k)* and *de(k)* and output variable α(k) are shown in Figure 6. The membership function for α(k) is also a triangular type and the rule-base in Table 2 is used for the computation of α(k).

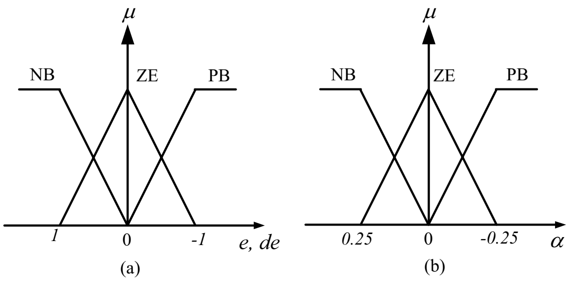

Figure 6 (a) Membership function of e(k) and de(k). (b) Membership function of α(k).

Table2 Rule table of real-time gain factor

de \ e (α)	N	ZE	P
N	ZE	N	ZE
ZE	P	ZE	P
P	ZE	N	ZE

(2) Dead-zone compensations

Finally, in order to avoid the dead-zone of the system, a dead-zone compensator is designed. The algorithm of dead-zone compensator is expressed by the following equations:

$$u_{sv}(k) = \begin{cases} u_{fsmc}(k) + u_{pd}(k) & ,if \quad u_{fsmc} > 0 \\ u_{fsmc}(k) - u_{nd}(k) & ,if \quad u_{fsmc} < 0 \end{cases} \tag{13}$$

where u_{sv} is the real driven signal after compensation , u_{pd} is the positive compensation signal of dead-zone and u_{nd} is the negative compensation signal of dead-zone. The signal u_{sv} is shown as Figure 7 illustrated

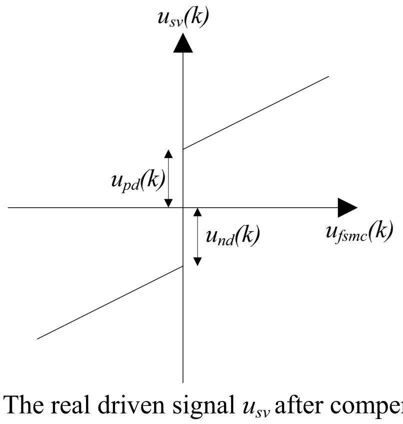

Figure 7 The real driven signal u_{sv} after compensation.

SIMULATION RESULTS

The tracking control system of the variable displacement hydraulic motor has been described. The time responses of the speed control of the motor under variant load torque are simulated. The parameters of the variable displacement hydraulic motor are illustrated in Table 3. Simulation and results are shown as follows:

Table 3 Parameters of the variable displacement hydraulic motor

Parameter		Value
Supply pressure	P_s	100 bar
Return pressure	P_t	0 bar
Moment of Inertial	J_t	0.065 *kg-m²*
Viscous friction coefficient	B_m	0.01 *N-m-s/rad*
Maximum motor Displacement	$V_{g\max}$	40 c.c/rev
Cylinder piston area	A_p	8.1×10^{-4} m²
Maximum cylinder stroke	$x_{p\max}$	0.0142 m
Maximum no-load servo-valve flow-rate	$Q_{o\max}$	10.2 L/min

(1) Step input

In the simulation, the reference input is set to be 1200 rpm and a sudden load torque 20 N-m is acted from the time 4 to 8 s. Time response of the system with step input is shown in Fig. 8. The simulation results have shown that the speed of the motor can be adjusted to the steady state value very quickly under the loading effect.

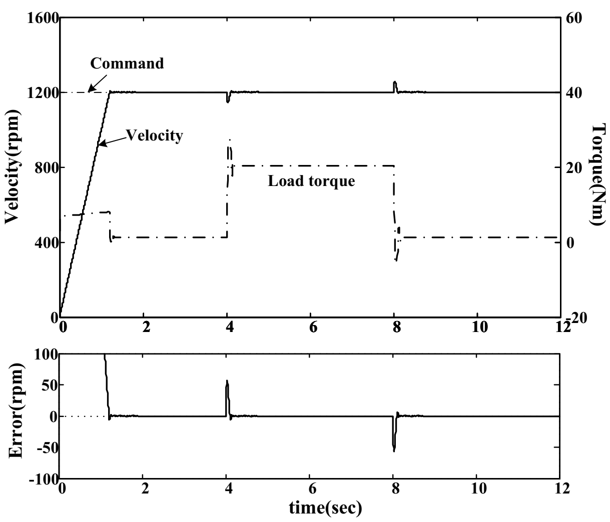

Figure 8 Time response of the system with step input.

(2) Square wave speed tracking

In order to prove the robustness of the control system, the speed tracking of a square wave is performed. The amplitude range of the desired speed is ±1200 rpm. The load torque of the sine wave is acted during control. The amplitude range of the load torque is 20 Nm and the frequency of the sine load torque is 1 Hz. Fig. 9 shows the time responses of Square wave speed tracking of variable displacement hydraulic motor. The control system still has the good responses under variable input command and load torque.

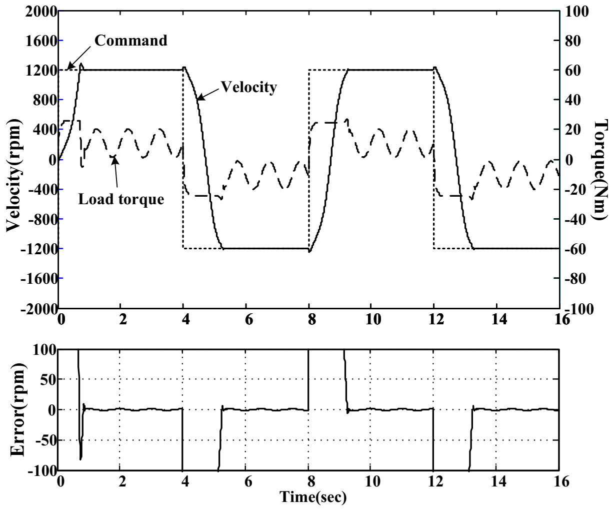

Figure 9 Time response of the system with square wave speed tracking.

EXPERIMENTAL RESULTS

With the same control conditions, the experiments have been performed. The control characteristics of the system are shown in Figure10 to Figure11. The experimental results and simulation results are very match. From the experiment curves, the speed of the variable displacement hydraulic motor can be controlled to a little error range under variable input command and load torque. The steady state errors are within 50 rpm.

CONCLUSIONS

In the paper, a variable displacement hydraulic motor without position feedback of regulating cylinder is built. A self-tuning fuzzy-sliding control method is applied to control the speed of the motor successfully. From the experimental results, one can make conclusions as follows:

(1) The speed of the motor can be adjusted to the steady state value very quickly under the loading effect.The robustness of the control system is very good under such a design controller.

(2) The control accuracy of the motor is always under 50 rpm, i.e. the control performance is satisfactory.

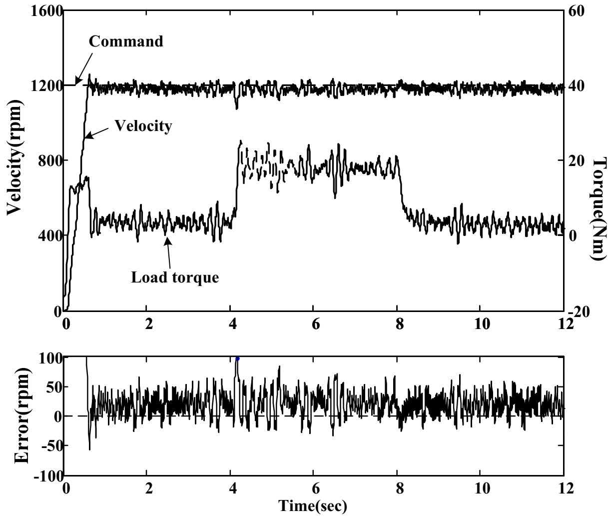

Figure10 The experimental results for step input.

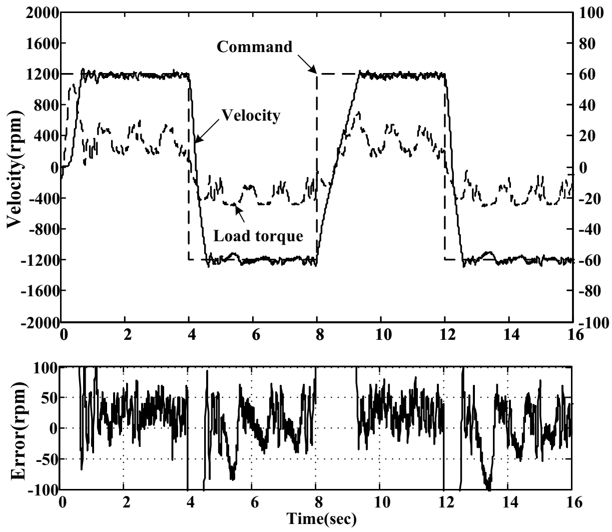

Figure11 The experimental results for square wave speed tracking.

ACKNOWLEDGEMENT

This research was supported by National Science Council Taiwan, ROC, under the Grant NSC 100-3113-E-006 -008

REFERENCES

[1] W. Backé and Ulrich, Design of electrohydraulic speed control for variable displacement motors on different pressure networks, Society of Automotive Engineers Transactions, 1990, 99(Sect 2), 394-403.

[2] Backé W. and Feigel H.-J., “Neue Möglichkeiten beim electrohydraulischen Load-Sensing” (in German), O+P Ölhydraulik undPneumatik 34, Nr. 2, pp. 106-114, 1990.

[3] Michael J. Plahuta, Matthew A. Franchek and Hansjoerg Stern, Robust controller design for a variable displacement hydraulic motor, American Society of Mechanical Engineers, The Fluid Power and Systems Technology, 1997, 4, 169-176.

[4] H. Berg and M. Ivantysynova, Design and testing of a robust linear controller for secondary controlled hydraulic drive, Proc. of the Institution of Mechanical Engineers. Part I: Journal of Systems & Control Engineering, 1999, 213(I5), 375-386.

[5] Chul Soo Kim and Chung Oh Lee,” Design of Electrohydraulic Speed Control for Variable Displacement Hydraulic Motors on Different Pressure Networks”, Transactions of the ASME.Vol.122,MARCH 2000.

[6] M.C.Shih, K.Dluzik, " Geschwindigk eitssteuerung eines Cylinders am Constant-Drucknetz durch Hydro-Transformator", Zeitschrift Oelhydraulik u. Pneumatic, 05.1985. pp.281-286, Germany.

[7] Murrenhoff, H. Systematic approach to the control of hydrostatic drives. Proc. IMechE, Part I: J. Systems Control Engineering, 1999, 213(I5), 333–347. DOI: 10.1243/0959651991540197.

Proceedings of the 8th JFPS International
Symposium on Fluid Power, OKINAWA 2011
Oct. 25-28, 2011

2A4-2

DEVELOPMENT OF AN ENERGY SAVING ELECTRIC EXCAVATOR

Jong Il YOON*, Dinh Quang TRUONG**, Kyoung Kwan AHN**

* Graduated School of Mechanical and Automotive Engineering,
University of Ulsan
San 29, Namgu-Muger2dong, Ulsan, 680-749 Korea
(E-mail: hero9825@mail.ulsan.ac.kr)
** School of Mechanical and Automotive Engineering
University of Ulsan
Muger 2-Dong, Nam-Gu, Ulsan, 680-749 Korea
(E-mail: kkahn@ulsan.ac.kr ; truongdq@mail.ulsan.ac.kr)

ABSTRACT

This paper is to propose a new type of excavator - electric excavator (ELEX) - with energy saving capacity using six quasi independent electro-hydraulic actuators (EHAs). The quasi-independent configuration minimizes hydraulic interferences among the actuators and losses which occur in HYEXs. In addition, the potential energy accumulated at "up" positions can be recuperated and converted into electric energy when the boom/arm/or bucket goes down, respectively. Kinetic energy of the upper slewing body also can be recovered and converted into electric energy when a slewing stop happens. A 5-ton excavator including a hybrid boom system (HBS) is analyzed, developed as an experimental ELEX (EELEX) with its validation model for evaluating the proposed ELEX. A control strategy for the 5 ton EELEX is built to operate the machine to follow desired performances. Performance of the EELEX is clearly verified through simulations and experiments in comparison with the conventional 5 ton HYEX.

KEY WORDS

Hydraulic excavator, Electric excavator, Electro-hydraulic actuator, Energy saving, Control

NOMENCLATURE

$de(t)$	: Derivation of error
$e(t)$	: Error between the desired and current speed
$I_{generated}$	: Generated current [A]
$I_{supplied}$	: Current supplied from main electric power [A]
K_p, K_i, K_d	: Proportional, Integral, Derivative gains
P_{elec}	: Electric power supply [W]
P_{gen}	: Generated electric power [W]
P_{lost}	: Lost power [W]
P_{pot}	: Potential power [W]
$R_{breaking}$	: Breaking resistor
t_{finish}	: Simulating time [s]
$T_{generated}$	: Generated torque [Nm]
T_m	: Torque of the electric motor [Nm]
T_{m1}, T_{m2}	: Torque generated by the CBS fixed and variable pumps [Nm]
$U_{generated}$	: Generated voltage [V]
$U_{supplied}$	: Voltage supplied from the main electric power [V]
u_{PID}	: Control signal for the electric motor
$\omega_{generated}$	: Generated angular velocity [rpm]
ω_m	: Angular velocity of the electric motor [rpm]

INTRODUCTION

Nowadays with the high fuel prices, demands for energy saving and green emission of construction machineries, without sacrifice of working performance, safety and reliability, especially for hydraulic excavators (HYEXs), have been highly increased. Hydraulic systems are indispensable components of many modern work machines. Excavators are subjected to large variations in workloads while repeating high work load operations, such as excavation, and low work load operations, such as leveling. In a conventional HYEX, hydraulic power, corresponding to the maximum workload, is always supplied from a pump and excessive power is dissipated as heat. In addition, potential and kinetic energies at the times of lowering and slewing stoppage of the excavator are also dissipated as heat. Hence, reductions of energy consumption and pollution become necessary and urgent demands. And hybrid electro-hydraulic vehicles, especially hybrid construction machines, are feasible solutions [1-5]. However, performances of these machines in comparison with corresponding conventional machines have been not much considered.

This paper proposes one effective solution for excavator design - electric excavator using EHAs. In this ELEX, it is recognized that the EHAs consume less energy than conventional hydraulic valve-controlled actuators. In addition the potential energy derived from gravity of the EHAs with/without working loads during their operations may be stored and later returned to the system as needed. A 5-ton experimental excavator with a modification - hybrid boom system was then implemented for validating the performance of the proposed ELEX. Based on the EELEX structure and working conditions, a control strategy was designed to control the HBS with high working efficiency and energy saving capacity. Simulations and practical experiments have been then carried out to investigate the efficiency of the proposed EELEX machine.

ELECTRIC EXCAVATOR (ELEX)

Design concept for ELEX

In the literature, several structures of hybrid excavators have been proposed. For example, in a series type of hybrid excavators as shown in Fig. 1a [2-3], all power generated by an engine is converted into electric energy by a generator, and this energy is converted again into mechanical power by electric motors to drive hydraulic pumps. Since hydraulic lines of the boom system are separated, the boom potential energy can be recuperated. In addition, the swing actuator is driven by an electric motor. As a result, a recuperation of regenerative power in this system is also possible. A storing system including capacitors and a battery is charged when load power is light or the swing and boom systems are operated in regenerative mode. On the contrary, the storing device is discharged when load power is heavy. In another design of hybrid excavators as a parallel type shown in Fig. 1(b) [3-5], the engine and actuators are directly connected to each other by mechanical shafts or hydraulic lines. Here, the engine speed should be decided by the speed that hydraulic pump requires, and the recuperation of regenerative power at the swing actuator is impossible. Thus, in the parallel type, less improvement of fuel economy is expected than in the series type. But the generator does not need to have the same capacity as the engine, so it can be designed smaller than that in the series type. As a result, the additional cost for the hybridization as the parallel type is much less than that of the series type.

From above analyses, the new electric excavator is suggested in this paper. Configuration of the suggested electric excavator is suggested as shown in Fig. 1c. The ELEX comprises six quasi-independent EHAs [6] driven by electric motor/generators and pumps which represent for the swing, left traveling, right traveling, boom, arm and bucket system. Therefore, the quasi-independent configuration of the ELEX minimizes hydraulic interferences among the actuators and losses which occur in conventional excavators [6]. With the suggested excavator design, the boom/arm/or bucket cylinder is driven by a closed system comprising an EHA, so that potential energy accumulated at "up" positions can be recuperated and converted into electric energy via the hydraulic motor and the generator when the boom/arm/or bucket goes down, respectively. The slewing motions are driven by an electric motor, instead of a hydraulic actuator. Consequently, kinetic energy of the upper slewing body can be recovered and converted into electric energy when a slewing stop happens. Power source of the ELEX is an external battery and capacitors inside motor drivers of the EHAs. To realize the energy saving capacity of the excavator, the internal capacitors stores the electric power generated by the potential energy or kinetic energy. The battery is automatically recharged when the amount of generated electric energy is more than the capacitor capacity.

Experimental electric excavator (EELEX)

To verify the effectiveness of the ELEX design idea suggested in the previous section, the 5 ton experimental electric excavator was analyzed and re-fabricated from a 5-ton hydraulic excavator. Here, the EELEX is a combination of the HYEX using a conventional boom system (CBS) and a hybrid boom system (HBS). The integrated HBS-CBS circuit is depicted in Fig. 2.

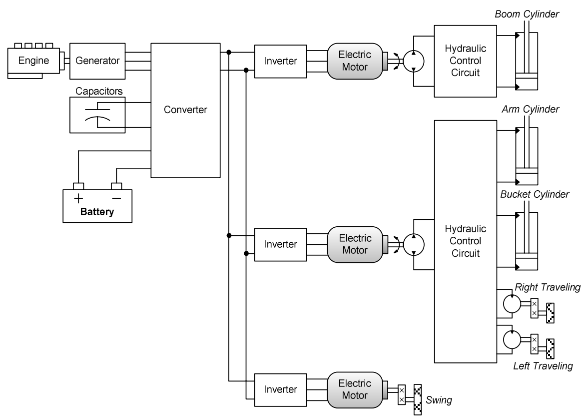

Figure 1(a) Series type of hybrid excavator

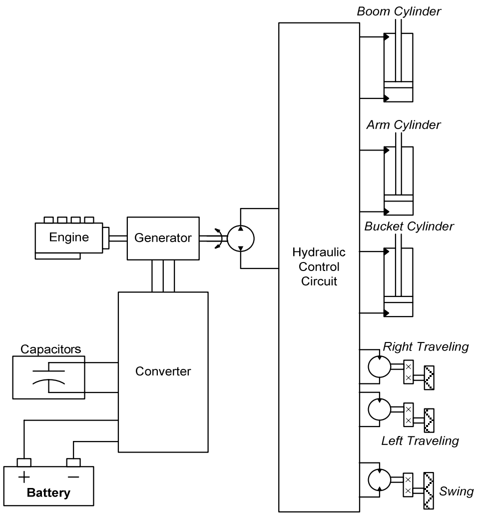

Figure 1(b) Parallel type of hybrid excavator

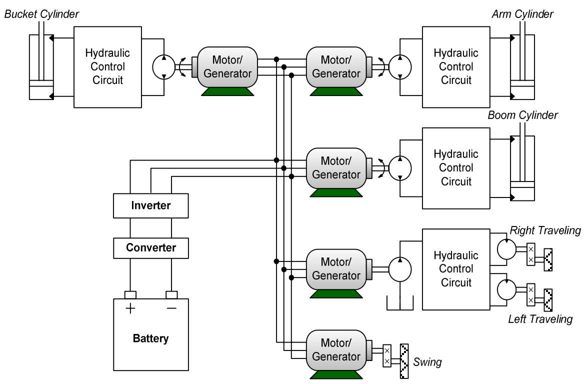

Figure 1(c) Proposed electric excavator

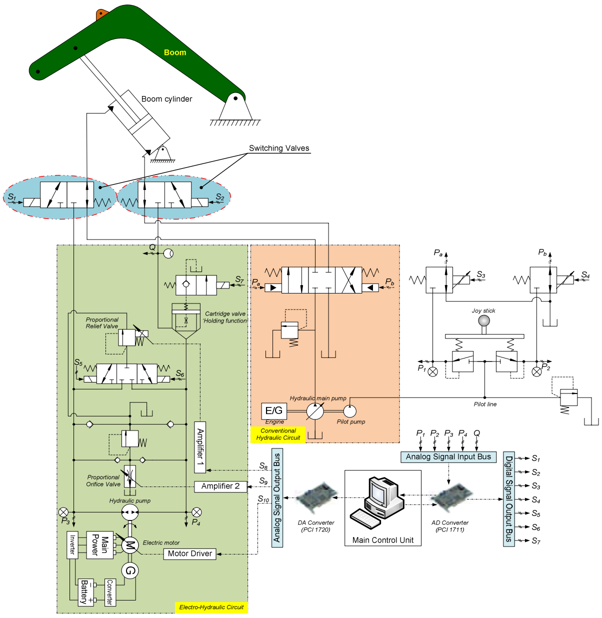

Figure 2 Integrated control circuit for HBS and CBS

In this figure, the HBS is depicted as the 'green' block. The boom cylinder can be driven in both directions by the electric motor/generator combined with the bi-directional hydraulic pump/motor and the hydraulic control circuit. In this circuit, a 3/3 solenoid valve with a proportional pressure relief valve were installed to distribute flow lines. In addition, a proportional orifice valve was employed in the HBS to adjust the boom down speed. In order to make the load holding function for the boom cylinder, an orifice cartridge valve was used and connected between the port of the cylinder large chamber and one port of the pump/motor. The combined HBS-CBS circuit was designed to be controlled with a user-interface program from a PC. It helps the user can easily switch the excavator from using the CBS to using the HBS and vice versa by using two solenoid 3/2 switching valves (S_1 and S_2). The excavator works as the HYEX when these valves are OFF. On the contrary, the excavator works with the hybrid boom system. Based on the circuits proposed in Fig. 2, components needed to construct the system were chosen to satisfy the working requirements of the EELEX. Subsequently, the specifications and setting parameters for the integrated HBS-CBS boom system are listed in Table 1.

CONTROL STRATEGY FOR BOOM SYSTEM

Working principle

Conventional boom system

In case of 'Boom Up' mode, the signal P_2 is high pressure (at that time, $P_1 = 0$) and sent to the control line P_b on the right hand side of the 4/3 main control valve. As a result, hydraulic oil is pumped from the main pump system to the boom cylinder large chamber to cause it to extend.

On the other hand, with a rising pressure of P_1 (at that time, $P_2 = 0$), the main supply oil line is connected with the cylinder small chamber, consequently, causing the cylinder to retract. It is called 'Boom Down' mode of the CBS.

Hybrid boom system

The HBS operation is divided into four modes: 'Boom Up', 'Boom Slow Down', 'Boom Fast Down', 'Digging' mode.

a) Mode 1 - 'Boom Up' mode

In this mode, the electric motor/generator works as an electric motor while the hydraulic pump/motor functions as a bi-directional hydraulic pump. The motor generates the speed and torque for the hydraulic pump in the direction to supply the high pressure oil (P_4) into the cylinder large chamber. The motor speed affects directly the cylinder moving speed. The pump inlet flow with low pressure (P_3) is from the low pressure lines connected from the cylinder small chamber and the tank. The orifice cartridge with the holding function only allows the flow to get into the cylinder large chamber which causes the boom to move up.

b) Mode 2 - 'Boom Slow Down' mode

Here, the electric motor/generator functions as an electric generator while the hydraulic pump/motor becomes a hydraulic motor. Because of gravity of the boom with or without load, the boom is automatically lowered, consequently, converting the potential energy generated during the 'Boom Up' mode into mechanical energy by the hydraulic motor. The mechanical power is then converted into electric energy and stored in the battery by the generator. In order to increase the energy saving capacity in this mode, the line connected from the hydraulic motor to the cylinder small chamber needs to be a low pressure line (P_3) as the tank with atmospheric pressure. Hence, setting pressure of the proportional relief valve is set to zero while the orifice of the flow control valve is closed. The generated electric power (P_{gen}) can be calculated as

$$P_{generated} = U_{generated} \times I_{generated} = P_{pot} - P_{lost}\,[W] \qquad (1)$$

c) Mode 3 - 'Boom Fast Down' mode

Contrary to mode 2, in this case the electric motor/generator works as the electric motor while the hydraulic pump/motor works as the hydraulic pump when the boom cylinder is commanded to retract fast. The piston is retracted by both the potential energy and power supplied from the motor which runs in the direction to lower the boom. Therefore, the hydraulic line from the cylinder large chamber to the pump is a low pressure line (P_4) while the line connecting between the cylinder small chamber and the pump has high pressure (P_3). Moreover, control signals are sent to the proportional relief valve and the flow control valve to set the relief pressure and the orifice area, respectively, proportional to the given joystick command. The input power (P_m) for the electric motor to cause the boom to lower is taken from the main power supply and the potential energy as:

$$P_m = T_m \times \omega_m = P^*_{elec} + P^*_{pot} - P^*_{lost}\,[W] \qquad (2)$$

d) Mode 4 - 'Digging' mode

In this mode, the electric motor generates the torque and speed for the pump to supply high pressure oil (P_3) to the small chamber of the boom cylinder (as in mode 3). An electric control signal (S_6) is sent to the solenoid on the right hand side of the control valve which is opposite energizing side when compared to the energizing side of the control valve in the modes from 1 to 3. The return line from the cylinder large chamber to the pump inlet port is then connected to the tank through the proportional relief valve with a small setting pressure and it becomes a low pressure line. Therefore, the different volume between fluid in the large chamber and in the small chamber is returned to the tank to make a balance of fluid lines.

To make the HBS to be automatically switched between its operating modes to satisfy the driver commands, a control strategy was necessary and designed as presented in Fig. 3.

Motor speed control

In order to ensure that the motor as well as the boom cylinder can follow the desired speed, an auto-adjustable proportional-integral-derivative (PID) controller, was applied to control the motor speed. The control signal for the electric motor (u_{PID}(t)) can be then

Table 1. Specifications and setting parameters of the modified boom system

Modified Boom System		Parameters	Values
Common Parts	Boom Cylinder	Piston diameter (mm)	110
		Rod diameter (mm)	60
		Length of stroke (m)	0.72
Conventional Boom System	Engine	Speed (rpm)	2300
	Main pump	Variable displacement (cc/rev)	16+2x25
	Servo pump	Fixed displacement (cc/rev)	4.5
	Control Valve	Ports/Positions (Hydraulic control)	4/3
	Relief valve	Relief pressure (bar)	210
Hybrid Boom System	Brushless servo motor (MPP2308P)	Input voltage (VAC)	400
		Rated speed (rpm)	1805
		Rated torque (Nm)	73.757
	Breaking resistor	Resistance (Ohm)	27
	Bi-directional	Displacement (cc/rev)	45
	Relief valve	Relief pressure (bar)	320
	Proportional Relief valve	Relief pressure (bar)	0~315
	Proportional	Percentage of maximum	0~100
Main Control Unit (MCU)	PC	Intel CoreTM2 duo	2.4GHz
	PCI 1711	Advantech multifunction card	A/D
	PCI 1720	Advantech multifunction card	D/A

expressed as:

$$u_{PID}(t) = K_p e(t) + K_i \int_0^t e(t)\,dt + K_d \frac{de(t)}{dt} \tag{3}$$

To make the controller more adaptive, the PID gains need to be switched corresponding to the working conditions. Hence, a switching algorithm using a learning vector quantization neural network (LVQNN) was proposed and designed in this paper. The LVQNN was constructed by a hidden competitive layer and a linear output layer. The LVQNN estimates the PID gains based on the current working mode of the boom which are determined by the pressure sensor signals from the joystick (P_1, P_2) and from the HBS circuit (P_3, P_4). The detailed design process as well as training process of the switching algorithm was referred from the previous research [7]. As a result, the control scheme for the motor speed tracking task is depicted in Fig. 4.
For each of the HBS working mode, a set of the PID gains, K_p, K_i, and K_d, was derived by 'trials and errors' method with respect to reduce the control error. Consequently, the gain sets corresponding to the HBS working modes were found as given in a look-up table – Table 2.

Table 2 Look-up table for tuning the PID gains

HSB modes	Kp	Ki	Kd
Boom Up	100	0.1	0.01
Boom Slow	10	0.1	0
Boom Fast	100	0.1	0.01
Digging	100	0.1	0

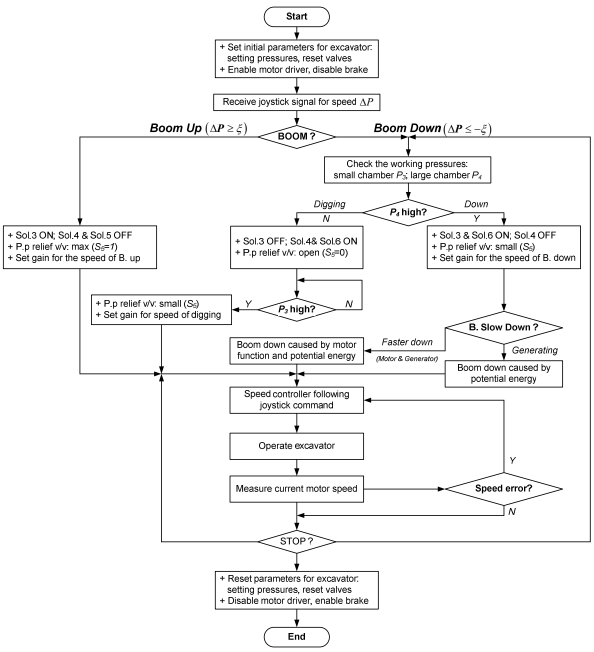

Figure 3 Overview of the EELEX control strategy

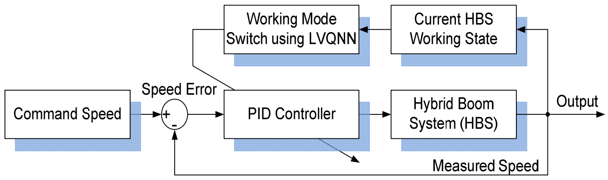

Figure 4 Overview of the auto-adjustable PID controller for speed control of EELEX

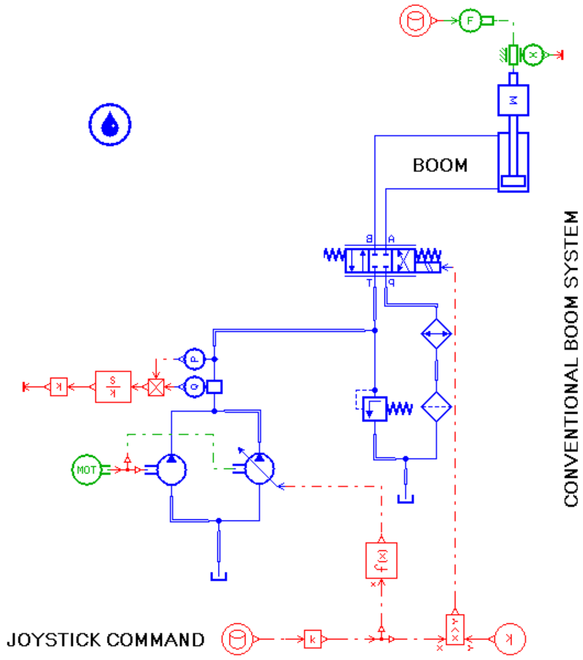

Figure 5(a) AMESim model for the CBS system

SIMULATIONS

In order to verify working efficiency of the proposed excavator, two models representing for the CBS and HBS circuits have been built using AMESim software version 4.3.0 as shown in Fig. 5a and 5b, respectively. The setting parameters for these models were obtained from the information of the real boom systems in Table1.
The input parameters for the boom models were joystick command and loading force attached to the piston rod. The input data was obtained from a real experiment done by a well-working driver on the 5-tons excavator for only boom up and down process in several times with maximum moving speed and without working load at the bucket. Simulations were then performed with this input data. To investigate the effect of using the flow control valve in the HBS, the HBS model has been tested with two cases: without and with using the flow control valve.
The reduction in energy consumption of the HBS when

compared with that of the CBS can be computed as:

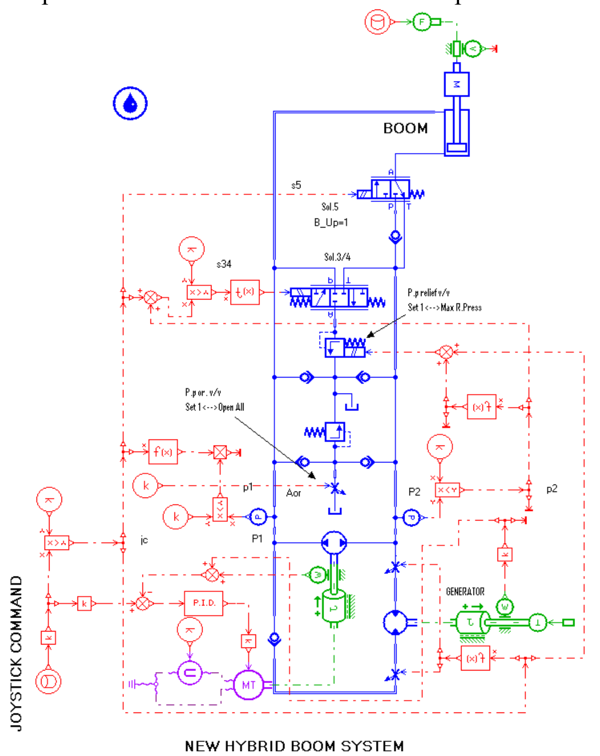

Figure 5(b) AMESim model for the HBS system

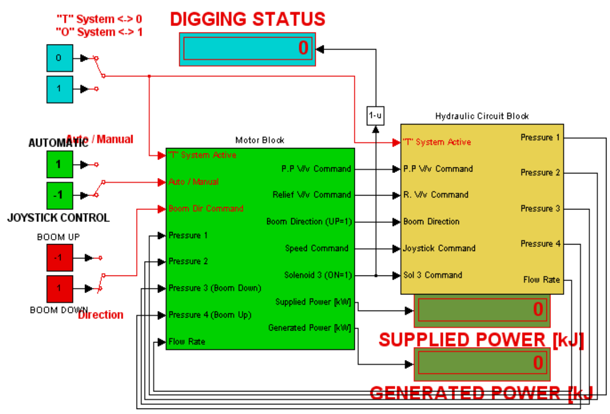

Figure 6 EELEX control program built in Simulink

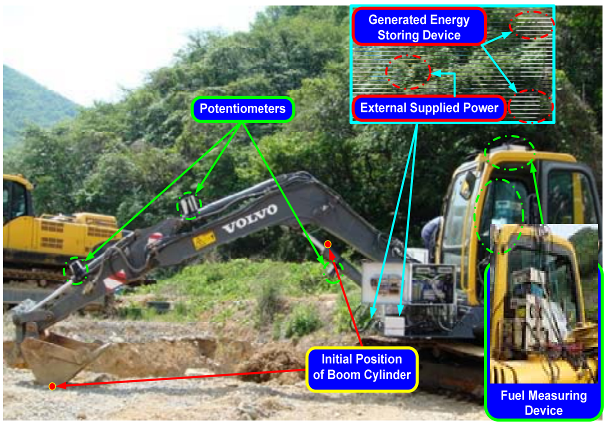

Figure 7 A photograph of the 5-tons EELEX

$$\%SavedEnergy = \frac{\left(\sum E_{used}\right)_{CBS} - \left(\sum E_{used}\right)_{HBS}}{\left(\sum E_{used}\right)_{CBS}} \times 100\%$$
$$= \frac{\left[\left(\sum E_{used}\right)_{CBS} - \left(E_{supplied} - E_{generated}\right)_{HBS}\right]}{\left(\sum E_{used}\right)_{CBS}} \times 100\% \tag{4}$$

$$\left(\sum E_{used}\right)_{CBS} = \int_0^{t_{finish}} \left(T_{m1} + T_{m2}\right)\omega_m dt \tag{5}$$

$$\left(\sum E_{used}\right)_{HBS} = \int_0^{t_{finish}} U_{supplied} I_{supplied} dt \tag{6}$$

$$\left(\sum E_{generated}\right)_{HBS} = \int_0^{t_{finish}} T_{generated}\,\omega_{generated} dt \tag{7}$$

The simulated performances of the CBS and HBS were obtained and analyzed as in Table 3. As seen in this table, the simulated energy consumption of the HBS model without using the flow control valve was reduced by 55.14% comparing with that of the CBS model. Meanwhile, by using the flow control valve in the HBS, the simulated energy consumption was significantly reduced up to 75.12%. It proves clearly that the high working efficiency could be realized in the proposed HBS, especially in case of using the flow control valve. In addition, the HBS had the ability in saving energy as depicted in Table 3.

EXPERIMENTS

To investigate the ability of the proposed ELEX in the real working environment, experiments with the 5-tons EELEX using both of the HBS and CBS were carried out. The control strategy introduced in Section 3 was built within Simulink environment combined with Real-time Windows Target Toolbox of MATLAB as displayed in Fig. 6. The control program contains two main blocks: 'Motor Block' and 'Hydraulic Circuit Bock'. The user can manually switch the EELEX to work with the CBS or the HBS to perform tests by 'Manual Switch' component. Here, the power supplied to the HBS was electric power while the power supplied to the CBS was gasoline fuel. A photo of the EELEX with all the measurement devices is displayed in Fig. 7. Experiments have been carried out for the EELEX with fast full up and down strokes of the boom (without working load) in two cases: using the CBS and the HBS. The reduction in energy consumption of the EELEX using the HBS when compared with using the CBS is obtained by (4) in which the total energy used in each the system can be calculated as (8), (6) and (9).

$$\left(\sum E_{used}\right)_{CBS} = \left(\sum GasolineFuel_{used}\right)_{CBS} \tag{8}$$

$$\left(\sum E_{generated}\right)_{HBS} = \int_0^{t_{finish}} R_{breaking}\left(I_{generated}\right)^2 dt \tag{9}$$

Finally, the boom working performances were analyzed through the experiment results as given in Table 4. From this table, it clearly shows that the high working efficiency could be enhanced in case the EELEX using the HBS. Here, the recuperated energy from the boom potential energy was 0.734kJ. This generated energy is small because the EELEX is 5-tons type in which the boom weight was small and the excavator was tested without working load. The more working load, the bigger potential energy as well as recuperated energy could be obtained. Moreover, the experiments with the boom down and fast moving speed caused the HBS to operate mostly in 'Boom Fast Down' mode in which the generated energy is un-considered.

CONCLUSIONS

This paper presents the new idea design of ELEX using EHAs. The 5-tons excavator was re-assembled with the HBS in order to improve the working efficiency. In addition, the proper control strategy was designed to manage the operation of the experimental electric excavator with the high working performance.

The AMESim models have been built to verify the designed hybrid circuit and the control strategy. The simulations and experiments have been done to evaluate the ability of the suggested boom system. The results prove that the boom cylinder controlled by the HBS circuit could reduce remarkably energy consumption when compared with the boom cylinder controlled by the traditional circuit.

This proposed ELEX can become an optimal selection for the heavy industry in a near future with energy saving and green emission purpose.

ACKNOWLEDGEMENTS

This work was supported by Korea Evaluation Institute of Industrial Technology (KEIT).

REFERENCES

1. Ochiai, M., Technical Trend and Problem in Construction Machinery, Construction Machinery, 2002, **38**- 4, pp. 20-24.
2. Kagoshima, M., Komiyama, M., Nanjo, T. and Tsutsui, A., Development of new hybrid excavator, Kobelco Technology Review, 2007, **27**, pp. 39-42.
3. Wang, D., Guan, C., Pan, S., Zhang, M. and Lin, X., Performance analysis of hydraulic excavator powertrain hybridization, Automation in Construction, 2009, **18**-3, pp. 249-257.
4. Xiao, Q., Wang, Q. and Zhang, Y., Control strategies of power system in hybrid hydraulic excavator, Automation in Construction, 2008, **17**-4, pp. 361-367.
5. Lin, X., Pan, S. X. and Wang, D. Y., Dynamic simulation and optimal control strategy for a parallel hybrid hydraulic excavator, J. of Zhejiang University Science A, 2008, **9**-5, pp. 624-632.
6. Truong, D. Q. and Ahn, K. K., Force control for hydraulic load simulator using self-tuning grey predictor – fuzzy PID, Mechatronics, 2009, **19**-2, pp. 233-246.
7. Ahn K. K. and Chau N. H. T, Intelligent switching control of a pneumatic muscle robot arm sing learning vector quantization neural network, Mechatronics, 2007, **17**-4-5, pp. 255−262.

Table 3 Simulation results – Energy consumption analysis

Simulation cases	Energy analysis for the boom models with up-down motion			
	Total supplied energy	Generated energy	Total energy	Saved
CBS	669.2	0	669.2	0
HBS without flow control valve	304.7	4.453	300.247	55.14
HBS with flow control valve	167.6	1.099	166.501	75.12

Table 4 Real-time experimental results – Working performance analysis

Test case: Boom Fast Up-Fast Down Motions	Comparison factors for one cycle time T of boom system operation				
	Cycle Time	Total supplied	Generated	Total used	Saved
CBS	5.625	78.136	0	78.136	0
HBS	7.375	41.539	0.734	40.809	47.772

Proceedings of the 8th JFPS International
Symposium on Fluid Power, OKINAWA 2011
Oct. 25-28, 2011

2A4-3

ENERGY SAVING OF OIL HYDRAULIC PUMP UNIT BY IDLING STOP WITH ACCUMULATOR

Sinpei OTA*, Ken SUGIMURA* and Katsumasa SUZUKI**

*Graduate school of Tokyo City University
(E-mail: accum_kenkyuusitu@hotmail.co.jp)
**Department of Mechanical systems Engineering
Tokyo City University
1-28-1, Tamazutumi, Setagaya-ku, Tokyo, 158-8557 Japan

ABSTRACT

If an accumulator is coupled with a hydraulic pump unit, idling stop operation can be attained by using a pressure switch and pressure-holding function. In this research, an intermittently operated hydraulic pump unit coupled with an accumulator (ACC pump unit), an inverter control-type hydraulic pump unit (INV pump unit), and a variable displacement-type hydraulic pump unit (VD pump unit) are tested, and the efficiencies of these pump units are compared. In the experiment that changes the duty ratio, the efficiency of ACC pump unit is about eight times as high as an INV pump unit and 18 times as high as VD pump unit. In addition, ACC pump unit is hardly influenced by the duty ratio, and almost constant efficiency is obtained. Therefore, ACC pump unit has the best energy-saving effect.

KEY WORDS

Energy Saving, Oil Hydraulic Pump Unit, Accumulator, Idling Stop, Efficiency

1. INTRODUCTION

Energy saving has been made in a number of fields due to the shortage of energy resources and the need to protect the earth's environment. The hydraulic field is not an exception.

If an accumulator is coupled with a hydraulic pump unit, intermittent operation of the electric motor powering the pump drive, called idling stop operation, can be attained by using the pressure switch and the pressure-holding function. As a result, unneeded power consumption can be reduced.

In this research, an intermittently operated hydraulic pump unit coupled with an accumulator (ACC pump unit), an inverter control-type hydraulic pump unit (INV pump unit), and a variable displacement-type hydraulic pump unit (VD pump unit) are tested. The efficiencies of these pump units are compared, and it is clarified that the ACC pump unit has the best energy-saving effect.

2. EXPERIMENTAL SYSTEM

A bladder-type accumulator with a capacity of 3 L is used in ACC pump unit as shown in Fig.1. ACC, INV, and VD pump unit uses the same pump. When the pump output pressure exceeds upper bounded pressure of the pressure switch, the pump drive motor of the ACC pump unit is turned OFF. It keeps the OFF state until the pump output pressure falls below the lower bounded pressure of the pressure switch. When the pump output pressure falls below the lower bounded pressure, the pump drive motor is turned ON. The pump used in ACC pump unit is a variable displacement vane pump. However, it works as a fixed displacement type because the cutoff pressure of the pump is set at much higher value.

INV pump unit is shown in Fig.2. The load pressure detected by the pressure sensor is input into the inverter controller. The pressure is kept constant by changing the frequency of the electricity supplied to the electric motor, changing the pump rotation speed, and adjusting the flow rate.

VD pump unit is showed in Fig.3. VD pump unit removes an accumulator and pressure switch from ACC pump unit.

The hydraulic circuit of a simplified load model is shown in Fig.4. This is connected with the discharge side and tank side of each pump unit as shown in Fig.1, 2, and 3 respectively. The flow rate and duty ratio are changed in this experiment.

3. EXPERIMENTAL METHOD

First, the hydraulic fluid flows into the load side intermittently by turning the solenoid-operated valve ON or OFF. The characteristic of each pump unit was examined by changing the duty ratio and flow rate into the load side. The period of ON-OFF operation is 10s. The necessary pressure to the load side was assumed to be 2.6 MPa.

Next, we changed the period to 50s to test with smaller duty ratio. These experimental conditions are shown in Table.1.

Lastly, we tested ACC pump unit with the upper bounded pressure changed.

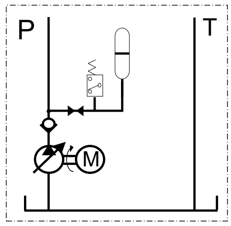

Figure 1 ACC pump unit

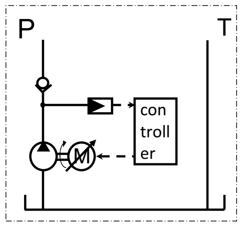

Figure 2 INV pump unit

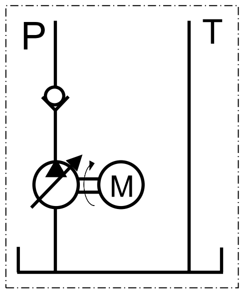

Figure 3 VD pump unit

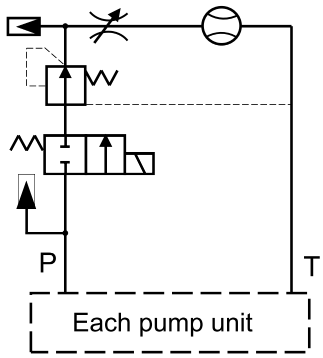

Figure 4 Hydraulic circuit of the load side

4. RESULT

The duty ratio was set between 10 to 100 percent. The experimental results of ACC, INV, and VD pump unit are shown in Fig.5, 6, and 7, respectively when duty ratio is 50 percent and flow rate is 16l/min. In Fig.5, 6, and 7, the vertical axis is electric power, rotation speed, load side pressure, output pressure, and flow rate, and the horizontal axis is time.

When solenoid-operated valve of ACC pump unit is turned on as shown in Fig.5, it is found that the electric motor is turned on with a little delay after the hydraulic fluid begins to flow to the load. The hydraulic fluid flows from accumulator to the load side immediately after the solenoid-operated valve is turned on. Pressure in the accumulator falls gradually, and it falls below 2.9 MPa which is lower bounded pressure. Then, the electric motor for the pump drive is turned on by the pressure switch. The electric motor is stoped while the solenoid-operated valve is turned off. This is because of the pressure holding function by the accumulator. As a result, power consumption is zero.

The results of INV pump unit is shown in Fig.6. When the solenoid-operated valve is turned on, the hydraulic fluid flows to the load side, and the rotation speed of the pump increases at the same time. When the solenoid-operated valve is turned off, the rotation speed decreases. At that time, the rotation speed becomes the minimum rotation speed and the set pressure is maintained. Minimum power is consumed.

The result of VD pump unit is shown in Fig.7, the rotation speed of the pump is almost constant in VD pump unit. The frequency of the electric power for the induction motor is constant in VD pump unit, therefore, the change of the rotation speed is small. Instead, the amount of the discharge per rotation is controlled in VD pump unit.

From Fig.4, the time when power consumption becomes zero exists in ACC pump unit drived by the idling stop. On the other hand, there is power consumption to some extent in INV and VD pump unit. Therefore, power consumption in ACC pump unit is the smallest.

Next, the experimental results are obtained when the duty ratio is from 10 to 100 percent and the flow rate is changed. The relations of the duty ratio and the efficiency in each pump unit are shown in Fig.8, 9, and 10 respectively.

The efficiency of ACC pump unit is not affected so much by the duty ratio, and it is almost constant as shown in Fig.8. This is because of the idling stop.

From Fig.9 and 10, it is understood that the efficiency for INV and VD pump unit increases as the duty ratio increases. When the solenoid-operated valve is turned on, working fluid flows to the load. Therefore, output power increases when the duty ratio increases. And, the efficiency rises.

The relation among electrical power consumption, efficiency and duty ratio for flow rate 16 l/min are shown in Fig.11. The efficiency of ACC pump unit is high compared with INV and VD pump unit in the area where the duty ratio is low. When the duty ratio is 10 percent, ACC pump unit is about twice higher than INV pump unit and about three times higher than VD pump unit. As ACC pump unit is drived using the idling stop, power consumption is reduced. Moreover, the efficiency of ACC pump unit is not affected by duty ratio as INV and VD pump unit, and it is almost constant.

Table 1 Experimental conditions when flow rate and duty ratio are changed

ACC pump unit	Upper bounded pressure	3.4 MPa
	Lower bounded pressure	2.9 MPa
INV pump unit	Pressure where rotation speed begins to decrease	2.9 MPa
VD pump unit	Pressure where displacement begins to decrease	2.9 MPa
Load side necessary pressure		2.6 MPa
Period		10 s (Fig.5~11,16) 50 s (Fig.12~15)
Oil temperature		30 ℃ ± 2 ℃

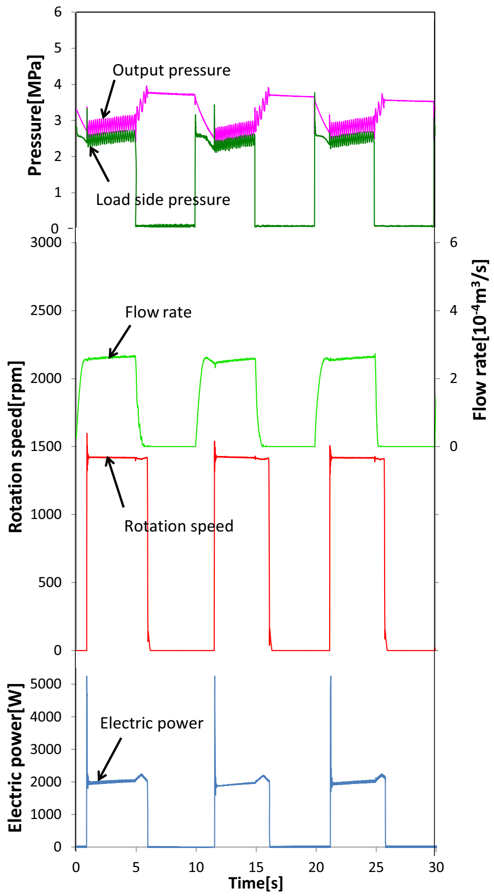

Figure 5 Output pressure, load pressure, rotation speed, and electric power of ACC pump unit

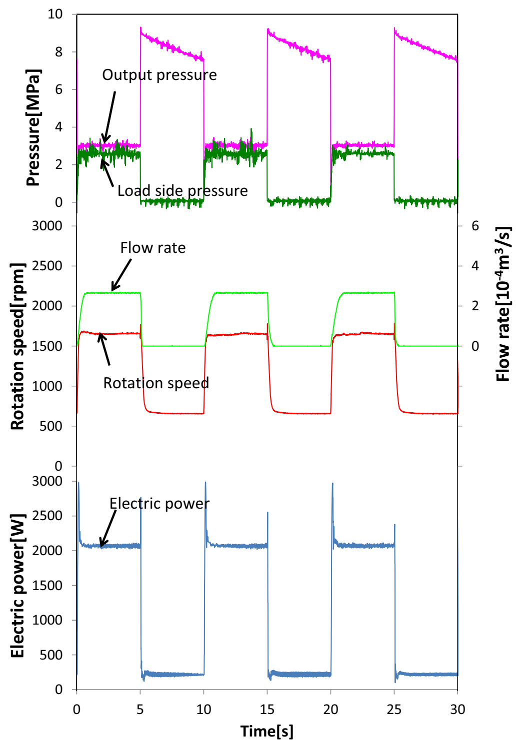

Figure 6 Output pressure, load pressure, rotation speed, and electric power of INV pump unit

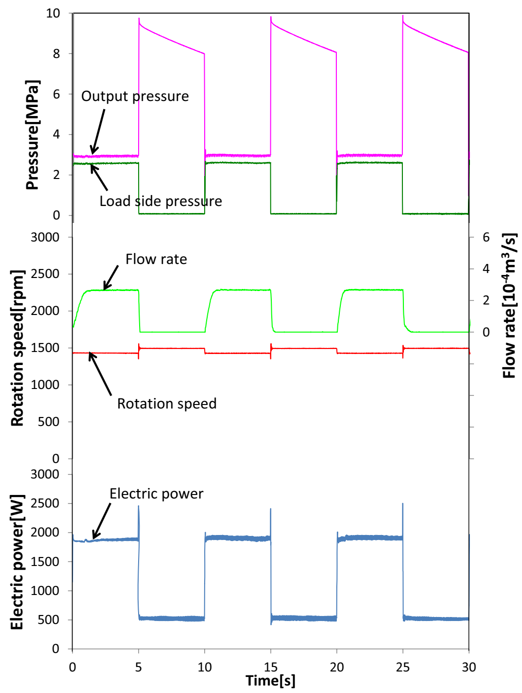

Figure 7 Output pressure, load pressure, rotation speed, and electric power of VD pump unit

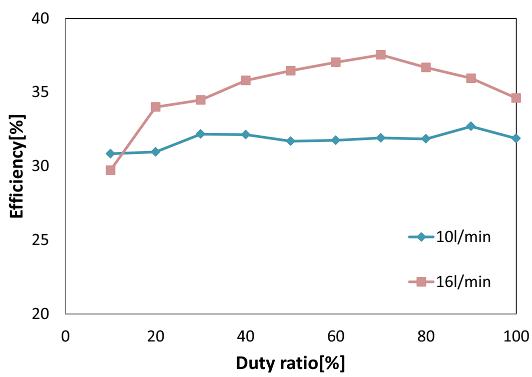

Figure 8 Duty ratio and efficiency of ACC pump unit

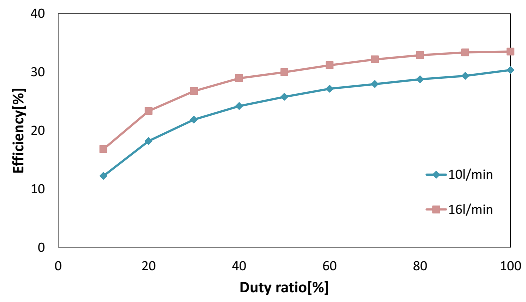

Figure 9 Duty ratio and efficiency of INV pump unit

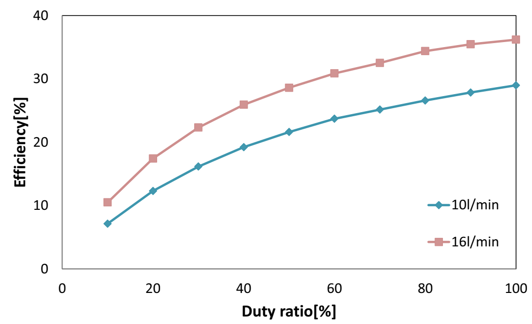

Figure 10 Duty ratio and efficiency of VD pump unit

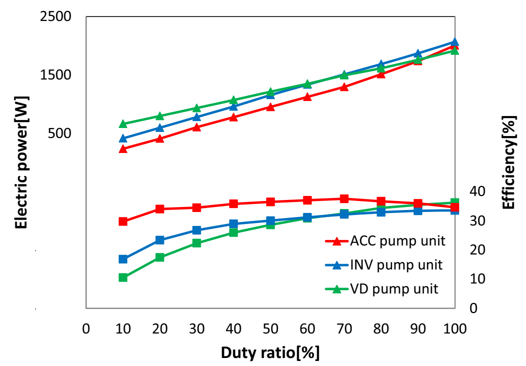

Figure 11 Electric power, efficiency, and duty ratio of each pump unit

Next, we experimented with lower duty ratio. The characteristics of each pump unit at this condition were investigated.

At first, the period is set as 50s. The results of each pump unit when duty ratio is 4 percent and flow rate to the load is 16 l/min are shown in Fig.12, 13 and 14 respectively.

The time while the fluid flows to the load of ACC pump unit is shorter in Fig.12 than that in Fig.5. As a result, the duration of idling stop is longer. In a word, it is found that power consumption is reduced more.

In Fig.13 and 14, the time while the fluid flows to the load of INV or VD pump unit is shorter than that in Fig.6 or 7. Therefore, the time while the motor is rotating without work is increased. In a word, the time while the electric power is consumed uselessly is increased.

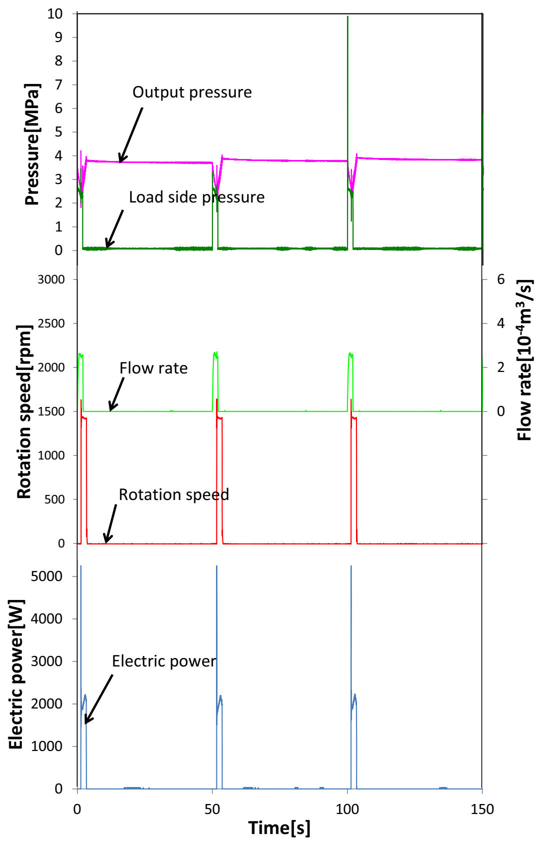

Figure 12 Output pressure, load pressure, rotation speed, and electric power of ACC pump unit

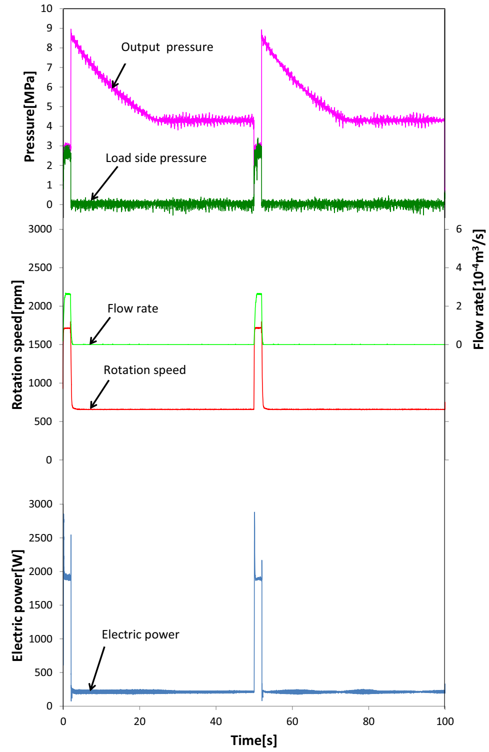

Figure 13 Output pressure, load pressure, rotation speed, and electric power of INV pump unit

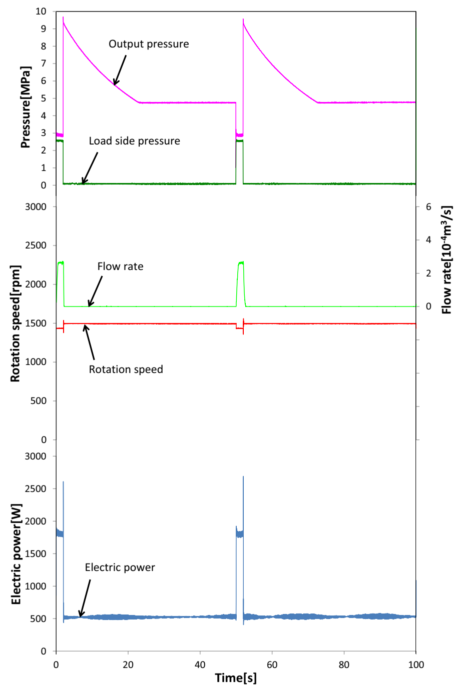

Figure 14 Output pressure, load pressure, rotation speed, and electric power of VD pump unit

Electric power consumption and efficiency of each pump unit for duty ratio from 2 to 10 percent are shown in Fig.15.

The difference of efficiency between the ACC pump unit and INV or VD pump unit grows as duty ratio lowers further. When the duty ratio is 2 percent, the efficiency of ACC pump unit is about eight times higher than that of INV pump unit and about 18 times higher than that of VD pump unit. It is because useless power consumption does not decrease so much though an effective output decreases in INV and VD pump unit when the duty ratio decreases further. Contrarily, almost constant efficiency is obtained for ACC pump unit within this range because useless power consumption also decreases by the idling stop.

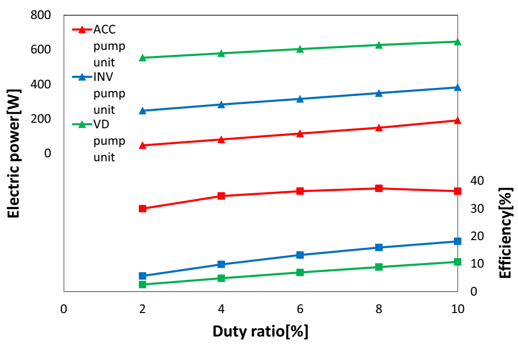

Figure 15 Electric power, efficiency, and duty ratio of each pump unit

We measured electric power and efficiency of ACC pump unit when the upper bounded pressure was changed. The lower bounded pressure was fixed as before. The duty ratio was 90 percent in this experiment. And flow rate was 12 l/min. The result is shown in Table.2.

Pressure ratio is 1.15 and 1.3 is almost the same. But, when pressure ratio is 1.4, its efficiency becomes smaller. The reason is that the pump output pressure is higher when pressure ratio is higher. Then, electric power consumption of the pump increases. Therefore, the efficiency is worse when pressure ratio is higher.

Table 2 Pressure ratio and Efficiency

Pressure ratio	Efficiency[%]
1.15	33.3
1.30	32.4
1.40	30.4

5. CONCLUSION

The efficiency of ACC pump unit is about twice higher than INV pump unit and about three times higher than VD pump unit when the duty ratio is 10 percent. The efficiency of ACC pump unit is about eight times higher than INV pump unit and about 18 times higher than VD pump unit when the duty ratio is 4 percent. ACC pump unit is not affected so much by the duty ratio, and almost constant efficiency is obtained. The efficiency of ACC pump unit decreases as the upper bounded of pressure switch increases. ACC pump unit has the best energy-saving effect.

6. REFERENCES

1. K.Suzuki, K.Sugimura: Energy Saving of Oil Hydraulic Pump Unit by Idling Stop Using accumulator, 7th International Fluid Power Conference, Aachen Germany, 2010
2. K.Suzuki, K.Sugimura: Energy Saving of Oil Hydraulic Pump Unit by Idling Stop Method Using An Accumulator, 10th International Conference on Fluid Control, Measurements and Visualization, Moscow Russia 2009
3. K.Suzuki, K.Sugimura, S.Ota, T.Doi: Energy Saving of Oil Hydraulic Pump Unit by Idling Stop Using Accumulator (1st Report), Trans. of JFPS, Vol.42, No.3, 2011

Proceedings of the 8th JFPS International
Symposium on Fluid Power, OKINAWA 2011
Oct. 25-28, 2011

2A4-4

A STUDY OF THE MECHANISM AND CHARACTERISTICS OF A PWM-BASED VALVE CONTROL SYSTEM WITH NO THROTTLE LOSS

Zhang Yongqiang*, Shi Guanglin* and Wang Ruigang*

*School of Mechanical Engineering, Shanghai Jiao Tong University, 800 Dong Chuan Road, Shanghai, China

ABSTRACT

For the problem of low efficiency of conventional valve control systems, an economical PWM-based valve control system with no throttle loss is put forward and examined in this paper. There are four no-throttling-loss units used to control a single rod cylinder in this fixed displacement pump system, which breaks the mechanical linkage of meter-in and meter-out flow in the traditional four way directional valve. The no-throttle-loss valve control unit includes a normal opened 3/2 high speed ON/OFF valve as a pilot valve and a two-way cartridge valve as a main valve. Due to the special designs, the maximum pump flow could run through the unit with no throttle loss. The high response frequency of the unit allows to control the average flow of the main valve, as well as the position and speed of the load by regulating the duty cycle of PWM signal. Parallel to the main oil circuit, an energy recovery device is used to absorb the high pressure pump oil when the main valve is closed during a control period, which would ensure the relief valve works as a safety valve and avoid the overflow loss. First, the paper proposes a concept of no-throttling-loss valve control unit. And then, the principle of achieving the dual objectives of energy saving and fast dynamic response is illustrated. Finally, the system model is established based on AMESim, and the feasibility of the system program is verified by the simulation in this paper. Besides, the influence of the control frequency of PWM signal and the pilot valve frequency is discussed. The simulation results ensures the system's merits of high dynamic response and energy saving.

KEY WORDS

PWM, No Throttle Loss, Valve Control System, Mechanism, AMESim

NOMENCLATURE

A_V:valve flow area

A_u:outlet port of no-throttling-loss unit

C_q:valve flow coefficient

P_u:inlet port of no-throttling-loss unit

p_R: opening pressure of relief valve
$p_{Motor:}$ driven pressure of hydraulic motor
p_{AccMin}: minimum operating pressure of accumulator
p_{Load} :load pressure
q :valve flow
$\overline{q}$: average flow
τ : duty cycle of PWM signal
Δp:valve pressure drop
ρ :oil density

INTRODUCTION

Traditionally, we have two methods to control an actuator in hydraulic system. They are valve control and pump control. Hydraulic servo valve control system has high response frequency, which makes it easy to get perfect motion control effect. However, a relief valve is needed to keep the system pressure constant. So, the throttling loss and relief loss are inevitable, which reduces the system efficiency to a very low level and increases the oil temperature. The other method is pump control. By changing the pump displacement or motor speed or changing them harmoniously at the same time, the outlet flow rate and pressure could adapt to the load [1]. This kind of load sensing control method could largely improve the system efficiency [2,3]. However, both varying pump displacement and varying pump speed would not get high response frequency, which restricts the application areas of this energy saving method. In recent years, in order to achieve the goal of fast dynamic behavior and energy saving simultaneously, a lot of researches have been done about the combination of valve control method and pump control method [4,5,6]. Besides, Emanuele Guglielmino etc applied the switch control technology to the hydraulic actuation. A hydraulic switching converter inspired by the electric DC-DC Buck converter was prototyped and its performance was tested in experiments. An energy saving of 75% is achieved compared to a classical proportional valve-controlled system [7].

In conventional constant pressure hydraulic control system, a great portion of the hydraulic power supplied by the pump is lost on the pressure relief valve and the flow control valve. The portion is 42.3 % and 19.2 % [2]. That is to say, the relief loss is more than two times of the throttling loss. Thus reducing the relief loss could improve system efficiency greatly. In order to maintain the fast dynamic behavior of traditional valve control system and avoid the throttling loss and relief loss, a PWM-based energy saving valve control cylinder system with no throttling loss is put forward and examined in this paper. First, the no-throttling-loss valve control unit is proposed. Second, the PWM-based energy saving valve control cylinder system is described. Finally, the system model is established in AMESim and simulation is implemented, and the effect of the system parameters is analyzed.

NO-THROTTLING-LOSS VALVE CONTROL UNIT

As a flow rate control component, traditional valve could regulate the flow rate through it by changing its opening area. The valve orifice flow equation can be written as

$$q = C_q A_V \sqrt{\frac{2}{\rho}\Delta p} \tag{1}$$

In the traditional valve control system, the pressure drop through the valve Δp is determined by relief valve's working pressure p_R and load's working pressure. p_L Because the flow area of traditional proportional and servo valve is small, the pressure drop is very large, even when fully opened. However, if the full opened flow area is so large that the whole system flow rate could run through the valve port without pressure drop or with a tiny pressure drop, we call that no-throttling-loss. However, if we keep the valve fully open all the time, the load velocity would not be regulated in fixed displacement pump system. And if we regulate the flow area continuously to change load velocity as traditional proportional and servo valve do, pressure drop will appear inevitably, which is not desired. So, we use the Pulse Width Modulated (PWM) control method to regulate the average flow rate, which would also regulate the load velocity. According to the Eq. (2), what we need to do is changing the duty ratio τ . PWM signal has only two states 0 and 1.When the signal is 1, the valve is fully opened, which is no-throttling-loss state, and the signal 0 corresponds to completely close.

$$\overline{q} = \tau \cdot q \quad (0 \le \tau \le 1) \tag{2}$$

Two way cartridge valves have a wide range of applications in the field of high pressure and large flow rate. Based on two way cartridge valve, we developed a no throttling loss control unit, which consists of a normal open 2/3 high speed ON/OFF valve and a two way cartridge valve.

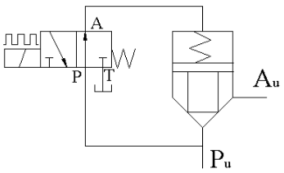

Figure 1 No-throttling-loss valve control unit

In the unit, the normal opened 2/3 high speed ON/OFF valve works as a pilot valve and the 2 way cartridge valve as main valve. The control chamber and inlet port of the main valve is connected to the port A and port P of the pilot valve separately. When the pilot valve of the unit is not energized, high pressure flow could run through the pilot valve to the control chamber of main valve. Because the working area of control chamber is larger than the inlet port and the spring of main valve has a preload, the main valve closed completely. When the pilot valve receives signal 1, the left position of pilot valve works and the high pressure flow promote the poppet moving up, and the oil in the control chamber could run through the pilot valve to the tank. When the pilot valve receive signal 0, the right position of pilot valve works and the high pressure oil run through the pilot valve to the control chamber. The fluid force and the spring force act on the poppet together, which would shut up the main valve rapidly.

In order to use PWM control method, the no-throttling-loss unit must have high response frequency. However, the frequency of the unit is restricted by the pilot valve response frequency and pilot flow rate. First, during a period of PWM signal, main valve always acts after the pilot valve and the opening and closing process of main valve need a short time. So, the frequency of no-throttling-loss unit must be lower than the pilot valve. Second, the opening and closing process of main valve employ the pilot valve to fill and empty the control chamber of the main valve. The larger of the pilot flow rate, the higher the response frequency of the unit. Actually, the proposed no-throttling-loss valve control unit is a high speed ON/OFF valve with large flow rate.

PWM-BASED ENERGY SAVING VALVE CONTROL CYLINDER SYSTEM

Traditionally, a typical four-way proportional directional valve or servo valve is used to control a hydraulic cylinder. The four inlet or outlet port of the directional valve are equivalent to four controllable orifices, which are mechanically linked together. If we break the mechanical linkage between the meter-in and meter-out orifices, the dual objectives of high performance motion tracking and energy savings could be achieved [8,9].

In this paper, four no-throttling-loss valve control units are used to control a double acting single rod cylinder. By coordinating the average flow of four units through PWM signal ratio, we can control the meter-in and meter-out flow of the cylinder. As shown in figure 2, a fixed displacement pump driven by a three-phase AC induction motor is used to supply oil to the system. In the pink frame of dot dash line, there are four no-throttling-loss valve control units. In the red elliptical frame, there is an energy reusing device, including a check valve, an accumulator, a hydraulic pump and a generator. The relief valve acts as a safety valve. In order to ensure the system work properly, the relief valve opening pressure p_R, the driven pressure of hydraulic motor p_{Motor}, the minimum operating pressure of accumulator p_{AccMin} and the load pressure p_{Load} should satisfy the following relations.

$$p_{Load} < p_{Motor} < p_{AccMin} < p_R \tag{3}$$

During a control period, when the PWM signal is 1, the high pressure runs through the main valve with no throttling loss. When the PWM signal is 0, main valve is closed completely. As a result, the high pressure flow runs through the check valve to fill the accumulator and drive the hydraulic motor to generate electricity. When the next PWM signal 1 is received, the check valve would be closed because p_{AccMin} is higher than p_{Load}. That means, the safety valve is always closed except extreme conditions. Thus, there are no throttling loss and relief loss in the system.

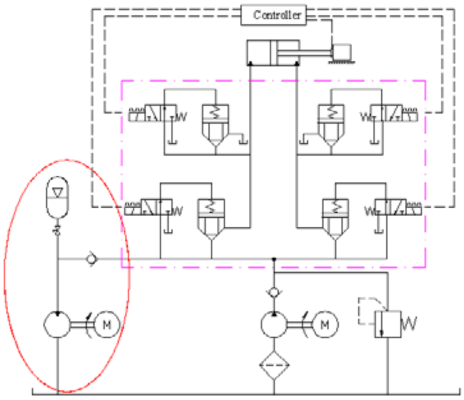

Figure 2 Schematic of PWM-Based energy saving valve control system with no throttling loss and no relief loss

SYSTEM MODEL AND SIMULATION

In order to verify the feasibility of the PWM-based energy saving valve control cylinder system, the system model is established in AMESim.

In this paper, the load pressure is 20MPa, and the maximum flow rate is 100L/min。According to a company's product samples of cartridge valve, nominal diameter 16mm could guarantee a tiny pressure drop of 0.2MPa. Compared with traditional valve pressure drop, we declare this tiny pressure drop no throttling loss. Because the control chamber of cartridge valve is large, the flow rate must be greater than 12L/min.

Figure 3 presents the model of the PWM-based energy saving valve control system with no throttling loss and no relief loss. Four no-throttling-loss valve control units are used to control the movement of cylinder rod. The models of pilot valve and main valve are established by Hydraulic Component Library of AMESim. The generator is simulated by a rotating load for covenience.

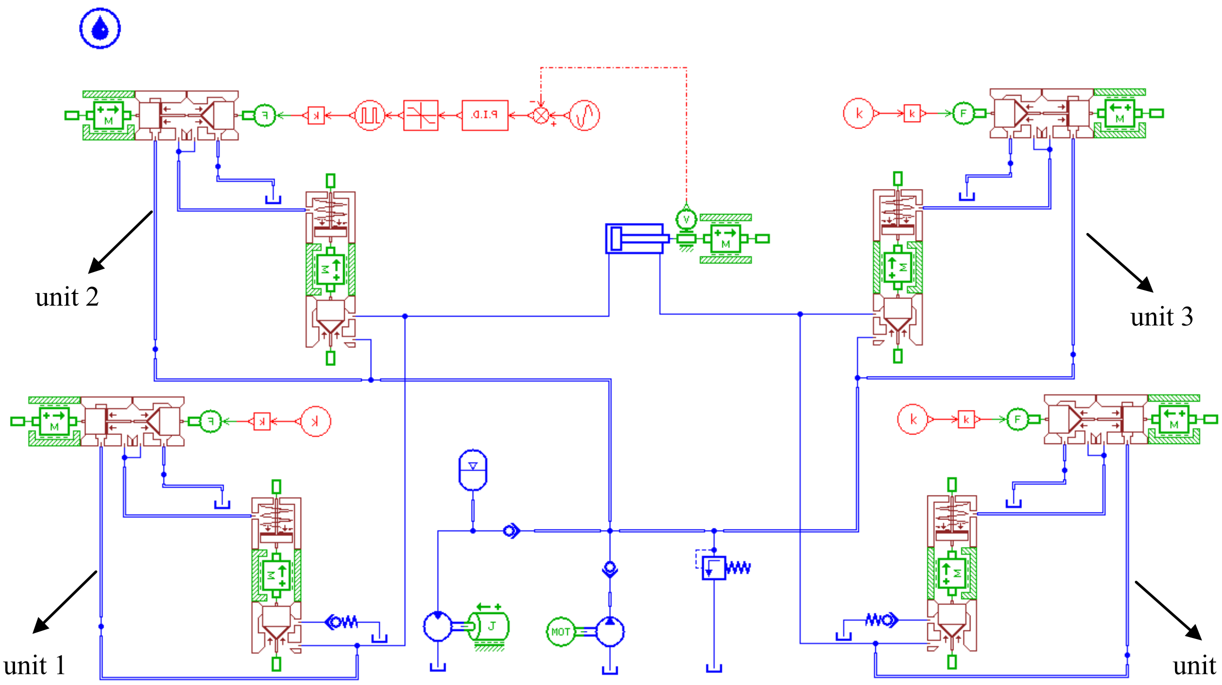

Figure 3 AMESim model of PWM-based energy saving valve control cylinder with no throttling loss and no relief loss

To get the correct simulation result, the specification of simulation parameters is very important. Some important simulation parameters are listed in Table 1

Table 1 Specification of some important simulation parameters

Load mass	20000kg
Friction	150796N
Pump rated pressure	20MPa
Pump displacement	63mL/r
Pump rotation speed	1600r/min
Relief valve opening pressure	25MPa
Minimum working pressure of accumulator	23MPa
Hydraulic motor working pressure	22.5MPa
Cylinder diameter	100mm
Rod diameter	20mm

For convenience, we consider the right and left movement of the cylinder rod respectively in the simulation. In this case, the four no-throttling-loss valve control units can be defined as outlet unit of rod-less chamber, inlet unit of rod-less chamber, inlet unit of rod chamber and outlet unit of rod chamber in numerical order. The Table 2 describes the control mode of four no-throttling-loss valve control units.

Table 2 Control modes of four units in different movement direction

	unit 1	unit 2	unit 3	unit 4
right	OFF	PID	OFF	ON
left	ON	OFF	PID	OFF

According to the Table 2, when the cylinder moves in the right direction, we just need to control the PWM signal duty ratio of inlet unit of rod-less camber of the cylinder with PID control strategy. At the same time, unit 1 and unit 3 are set to completely closed, and unit 4 fully opened. The left direction is similar to the right direction.

Figure 4 is the sinusoidal velocity response when the cylinder moves in the right direction. As shown in the figure 4, the cylinder could track the ideal sinusoidal velocity command at 0.05Hz. And the tracking error gradually stabilizes between 0 and 0.005m/s.

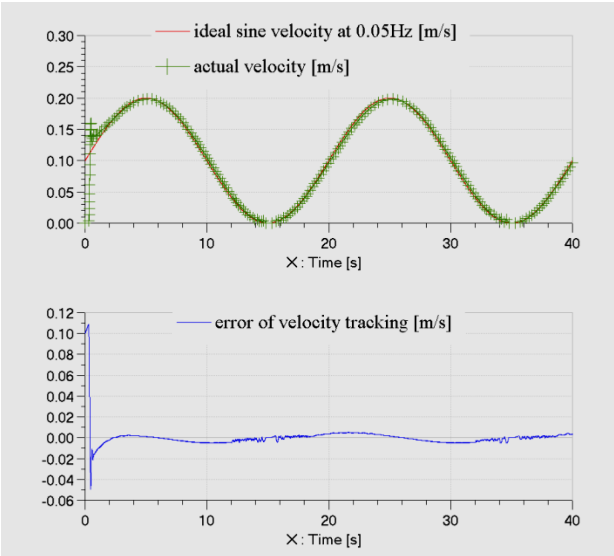

Figure 4 Tracking performances and tracking error corresponding to 0.05Hz sinusoidal velocity command

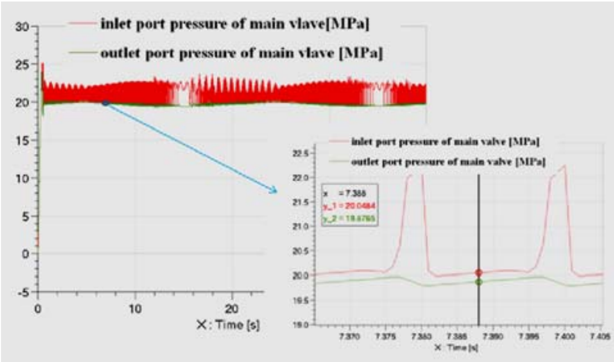

Figure 5 Inlet and outlet port pressure of main vlave

Figure 5 presents the inlet and outlet port pressure of main valve. During a control period, when the PWM signal is 1, the pressure drop is less than 0.2MPa, as shown in the right side of the graph, which is called no throttle loss. When the PWM signal is 0, the main circuit to the cylinder is closed, and the high pressure flow drives the hydraulic motor, which is connected to an electricity generator. Thus, the inlet pressure of main valve is about 22.5MPa, which is the hydraulic motor working pressure. Generally speaking, the outlet pressure of main valve remains constant basically.

Figure 6 and figure 7 present the system instantaneous power distributions and average power distributions. From the two figures, especially the average power distributions, we can see that there is nearly no throttling loss and relief loss. In the figure 6 and 7, pink line represents the power to the hydraulic motor, which used to generate electricity. This part of power is very large and usually is wasted in the traditional valve control system.

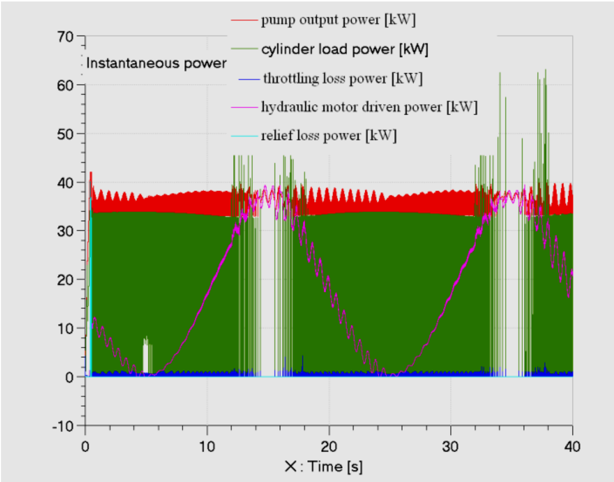

Figure 6 System instantaneous power distributions

Figure 8 is the sinusoidal velocity response when the cylinder moves in the left direction. This case is similar to the right direction.

Figure 9 is the sinusoidal velocity response at 0.6Hz when the cylinder moves in the right direction. With the increasing of frequency of ideal command, it's more and more difficult to get satisfactory tracking performance. As shown in figure 9, the system already has much difficulty tracking the ideal velocity at 0.6Hz. If we want to get satisfactory results, the response frequency of the no-throttling-loss unit must be improved.

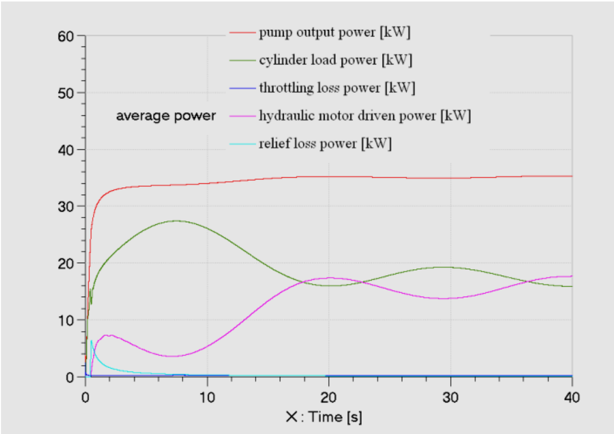

Figure 7 System average power distributions

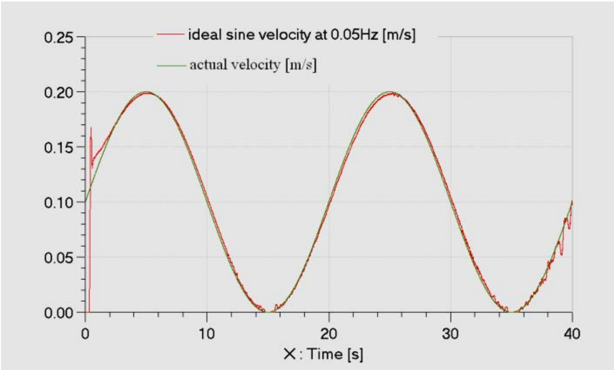

Figure 8 Tracking performances corresponding to 0.05Hz sinusoidal velocity command

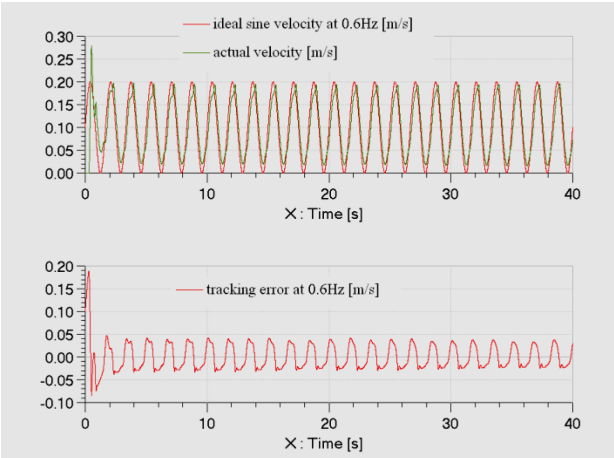

Figure 9 Tracking performances corresponding to 0.6Hz sinusoidal velocity command

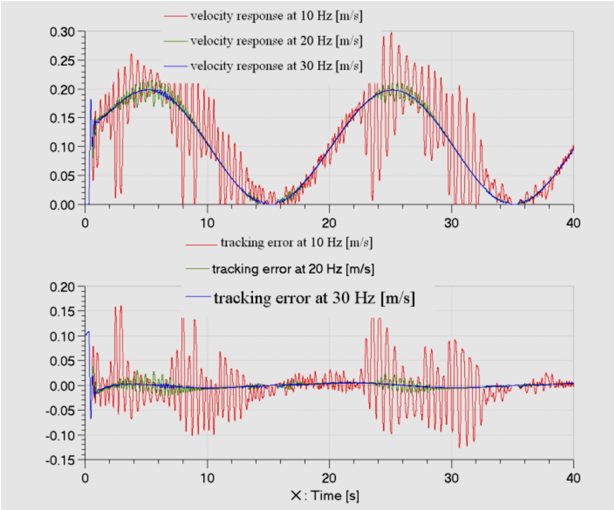

Figure 10 Tracking performances at different control frequency

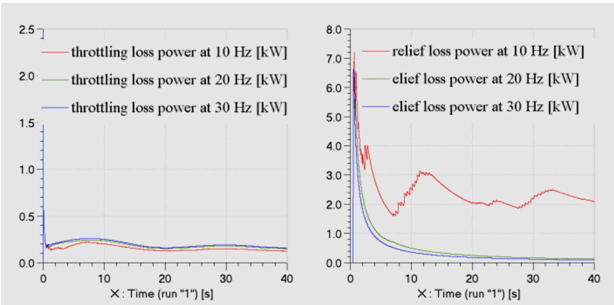

Figure 11 Throttling and relief loss power at different control frequency

Figure 10 and 11 present the influence of control frequency of PWM signal, which implies us the system could not track the ideal sine velocity when the control frequency is below 20Hz. However, the decrease of control frequency has little impact on the throttling loss. As for relief loss power, there is a rapid increase when the control frequency is below 20Hz. Generally speaking, increasing the control frequency of PWM signal is helpful for system response characteristics. But, the maximum control frequency is restricted by the inherent response ability of the system.

Figure 12 and 13 display the influences of pilot valve frequency to the system response characteristics. In the simulation, control frequency of PWM signal is 50Hz. When the pilot valve frequency is less than 50Hz, there is much velocity fluctuation on the tracking performance, which is shown clearly in the figure 14. The velocity fluctuation is caused by the flow pulse of the main valve, which also results in the fluctuation of pressure at the inlet port of relief valve. Thus, the relief loss power also increases rapidly with the decreasing of the pilot valve frequency.

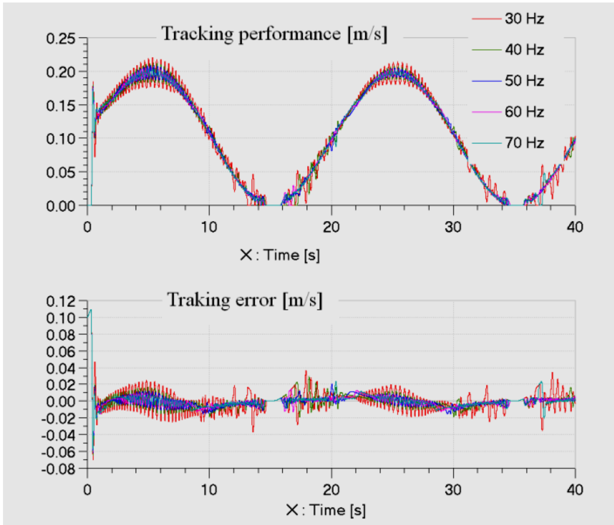

Figure 12 Tracking performances at different frequency of pilot valve

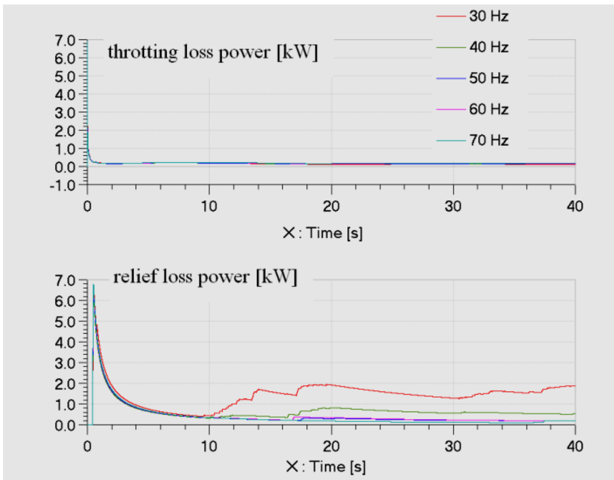

Figure 13 Throttling and relief loss power at different frequency of pilot valve

CONCLUSIONS

In order to resolve the conflicts between low efficiency of traditional valve control system and low dynamic response of pump control system, a novel PWM- based no-throttling-loss valve control system is proposed in this paper. The paper illustrates the principle of energy conservation without deterioration to the dynamic response. The system model is established in AMESim, and the simulations verify that the new system could reduce the throttling and relief loss power to the minimum extent. Thus, the system efficiency could be improved greatly. According to the simulation, the control frequency of PWM signal and pilot valve frequency have great impacts on the tracking performance and relief loss power. For a satisfactory performance, the pilot valve should have a response frequency 80Hz or higher when the control frequency is 50Hz.

REFFERENCES

1. Chiang, M.H., etc, A comparison of an AC-servo motor driving variable rotational speed and a variable displacement pump-controlled system for velocity control, Proceedings of the 7th JFPS International Symposium on Fluid Power, 2008, pp.629-634.
2. Çalişkan, H., Balkan, T., Platin, B.E. Hydraulic position control system with variable speed pump. Proceedings of the ASME Dynamic Systems and Control Conference 2009, DSCC2009 (PART A), pp. 275-282
3. Aoki Y., Uehara K., Hirose K., Karakama T.. Loadingsensing fluid power systems[J]. SAE Transactions, 1994,103(2):139-153
4. DING Haigang, etc, Performance Simulation of VC Variable Frequency Hydraulic Compound Speed Regulation System with High Inertia, Machine Tool & Hydraulics,2009,pp.219-226.
5. QIU Ai-zhong, NIE Hui-juan, A compound speed regulation system based on vector control and throttle speed governing, Chinese Hydraulics & Pneumatics, 2010,pp.27-30
6. QIU Ai-zhong, NIE Hui-juan, A compound speed regulation system based on vector control and throttle speed governing, Chinese Hydraulics & Pneumatics,2011, pp.27-30
7. Guglielmino, E., Semini, C., Kogler, H., Scheidl, R., Caldwell, D.G. Power hydraulics - Switched mode control of hydraulic actuation. IEEE/RSJ 2010 International Conference on Intelligent Robots and Systems, IROS 2010 - Conference Proceedings , art. no. 5653181, 2010, pp. 3031-3036
8. S. Liu and B. Yao. Automated Modelling of Cartridge Valve Flow Mapping. IEEE/ASME International Conference on Advanced Intelligent Mechatronics, 2005, pp. 789-794
9. S. Liu and B. Yao. Coordinate Control of Energy Saving programmable valves, IEEE Transactions on Control Systems Technology ,2008, pp. 34-45

Proceedings of the 8th JFPS International
Symposium on Fluid Power, OKINAWA 2011
Oct. 25-28, 2011

2B1-1

STUDY ON LIQUID CRYSTALLINE FLOW INDUCED BY DIRECT CURRENT ELECTRIC FIELD

Kenta KODAMA*, Tetsuhiro TSUKIJI* and Shun NISHIMURA*

* Faculty of Science and Technology
Sophia University
7-1 Kioi-Cho, Chiyoda-Ku, Tokyo, 102-8554, Japan
(E-mail: t-tukiji@sophia.ac.jp)

ABSTRACT

A functional fluid flows by itself when electric fields are applied to the functional fluid. This phenomenon is called EHD (electrohydrodynamics) phenomenon, and research and developments are being made to apply this phenomenon on to motors and pumps. We use a liquid crystal as a functional fluid and observe the behavior of the liquid crystal as well as flow in the flow channel when steady electric fields are generated through a direct current by two electrodes in the bottom of the flow channel. Moreover, we observe how the behavior and flow change as a result of the shape of the electrodes being changed. Furthermore, we research the possibility to design the motors using EHD phenomenon.

KEY WORDS

Liquid crystal, EHD phenomenon, Electric field, Direct current, Electrode

NOMENCLATURE

a	:	distance between two electrodes
E	:	electric field strength of between two electrodes
v	:	flow velocity in the whole flow channel
w	:	width of electrodes
ε_{para}	:	the same direction as axis of the liquid crystalline molecule
ε_{per}	:	the vertical direction against axis of the liquid crystalline molecule
ϕ_A	:	electric potential of electrode-A
ϕ_B	:	electric potential of electrode-B

INTRODUCTION

A functional fluid such as a liquid crystal flows when electric fields are applied to the functional fluid. This phenomenon is called EHD (electrohydrodynamics) phenomenon, and research and developments are being made to apply this phenomenon to motors and pumps [1]. However, the mechanism of liquid crystalline flow induced by electric fields is not yet made clear. Therefore, whether there is influence of shape of electrodes and electric fields on generated flow still needs to be investigated. We observe flow of the liquid crystal in the vicinity of electrodes as well as flow in the whole flow channel when steady electric fields are generated through direct current by two electrodes at the bottom of the flow channel. Especially, we observe the velocity of flow in the whole flow channel and flow of the liquid crystal in the vicinity of electrodes causing flow in the whole flow channel when a one-directional flow is generated. Moreover, we observe changes in flow when the shape of the electrodes is changed. First, we demonstrate the physical properties of the liquid crystal used in this study. Next, we explain the experimental apparatus and method, and describe liquid crystalline flow induced by direct current electric field.

PHYSICAL PROPERTIES OF THE LIQUID CRYSTAL

The liquid crystal used this time is mixed liquid crystal MJ-0669 (Merck & Co., Inc.). The physical properties of MJ-0669 are shown in Table 1, where ε_{per} is the vertical direction against axis of the liquid crystalline molecule, and ε_{para} is the same direction as axis of the liquid crystalline molecule.

Table 1 Physical properties of MJ0669

Operating temperature region [°C]	~45.9
Kinematic viscosity (25[°C]) [mm^2/s]	11.0
Dielectric constant ε_{per} (20[°C]) [F/m]	3.5×10^{-11}
Relative permittivity ε_{per} (20[°C])	3.9
Dielectric constant ε_{para} (20[°C]) [F/m]	9.9×10^{-11}
Relative permittivity ε_{para} (20[°C])	11.2
Density (25[°C]) [g/cm^3]	0.95

EXPERIMENTAL APPARATUS AND METHOD

Experimental apparatus

The flow channel is shown in figure 1. It is made of transparent acrylic, and the flow channel of 4 mm width and 2 mm depth is put between the top and the bottom. The electrode is made by etching and as thin as paper, and set up at the bottom of the flow channel. Then, electric field is generated at the bottom of the flow channel by applying voltage to electrode-A connected with the anode of DC power source and electrode-B with cathode as shown in figure 2.

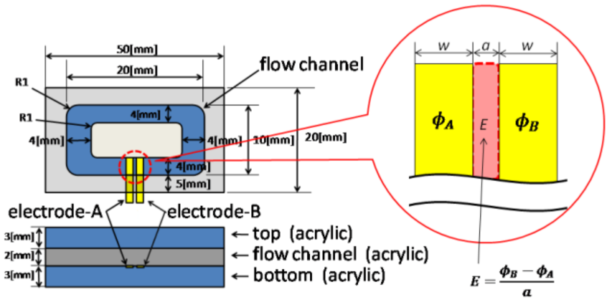

Figure 1 Flow channel

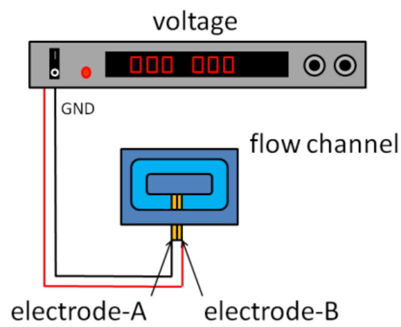

Figure 2 Experimental apparatus

Experimental method

First, the liquid crystal mixed with particle M-600 (Matsumoto Yushi-Seiyaku Co., Ltd, particle diameter 5~50μm) for making flow visible is poured into the flow channel; the flow channel is set up on the hot plate, and the temperature of the liquid crystal is kept constant (30±1°C) with the hot plate and thermometer. Next, the voltage is applied to two electrodes (electrode-A and electrode-B), and electric field is generated at the bottom of the flow channel. Then, the laser sheet is shone from the top through the center of the flow channel where the influence of the viscosity is the weakest, and the behavior of the liquid crystalline flow is recorded on video from the front of the flow channel as shown in figure 3. The recording is done for 3 minutes after the voltage is impressed. Similarly, the laser sheet is shone from side of the flow channel, and the flow in the flow channel is recorded on video from the top of the flow channel as shown in figure 4.

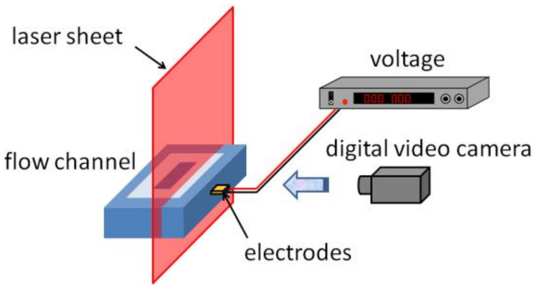

Figure 3 Observing from the front

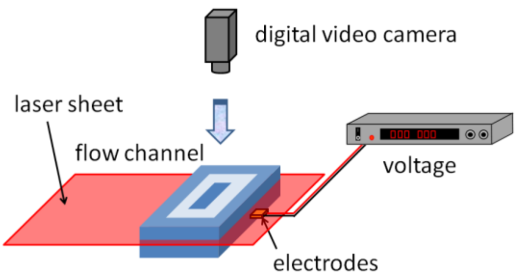

Figure 4 Observing from the top

When a one-direction flow is generated in the flow channel, flow velocity is measured. The measurement is done in the time zone when flow velocity is the steadiest. The area for measuring flow velocity is the area at the center of the flow channel on the other side of the flow channel where the electrodes are set up as shown in figure 5. Flow velocity is calculated from the video by using the width of the flow channel as 4 mm. Concretely, the time taken by the particle to move by 4 mm is measured with the help of stopwatch, and the speed of the particle is calculated by using that time. This is done once with five separate particles in the area where flow velocity is measured, and the average of these speeds is assumed to be flow velocity.

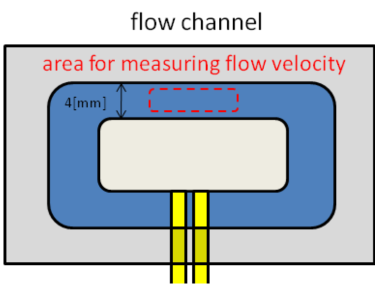

Figure 5 Area for measuring flow velocity

Moreover, experimental conditions for each experiment are shown in Table 2, where w is width of electrodes, a is distance between two electrodes, ϕ_A is electric potential of electrode-A, ϕ_B is electric potential of electrode-B, and E is electric field strength of between two electrodes.

Table 2 Experimental conditions

No.	w [mm]	a [mm]	ϕ_A [V]	ϕ_B [V]	E [V/mm]
1	1	0.2	0	1000	5000
2	1	0.2	0	500	2500
3	1	0.2	0	1500	7500
4	0.5	0.2	0	1000	5000
5	1.5	0.2	0	1000	5000
6	1	0.3	0	1000	3333
7	1	0.4	0	1000	2500
8	1	0.3	0	1500	5000
9	1	0.4	0	2000	5000

RESULT OF EXPERIMENTS

Result of experiments

Figure 6 shows the results for experiment No.1. Referring to (a) front view, we observed that rotational flows (Vortex-A, B, and C) are generated between electrodes and on the edge of each electrode. We noticed a one-directional flow over electrode-B by being involved with the counterclockwise rotational flow (Vortex-B) generated in the right edge of electrode-B, brought from over electrode-B to on electrode-A by being involved with the counterclockwise rotational flow (Vortex-A) generated between electrodes, and sent at the left of electrode-A by being involved with the clockwise rotational flow (Vortex-C) generated in the left edge of electrode-A. Referring to (b) top view, we observed that a one-directional flow occurs in the flow channel clockwise. The flow velocity was comparatively steady with 0.29 mm/s.

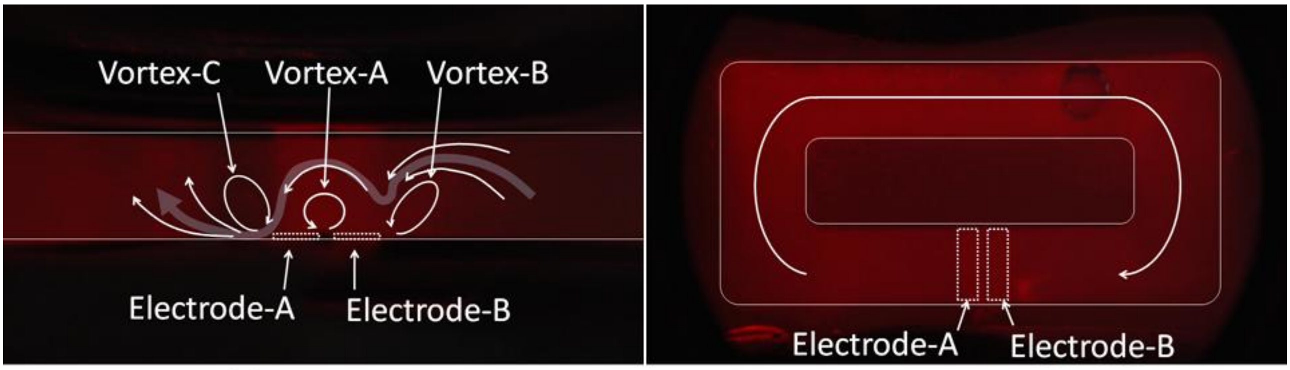

(a)Front view (b)Top view

Figure 6 Results of experiment No.1

Similarly, the results of experiments Nos.2~9 are shown in figures 7~14. Moreover, flow velocity of a one-directional flow in the flow channel in each experiment is shown in table 3, where v is flow velocity.

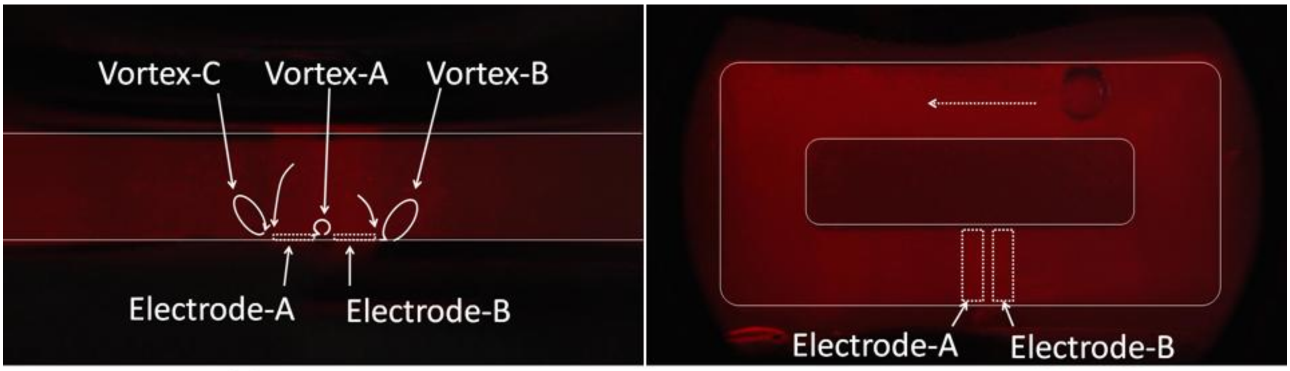

(a)Front view (b)Top view

Figure 7 Results of experiment No.2

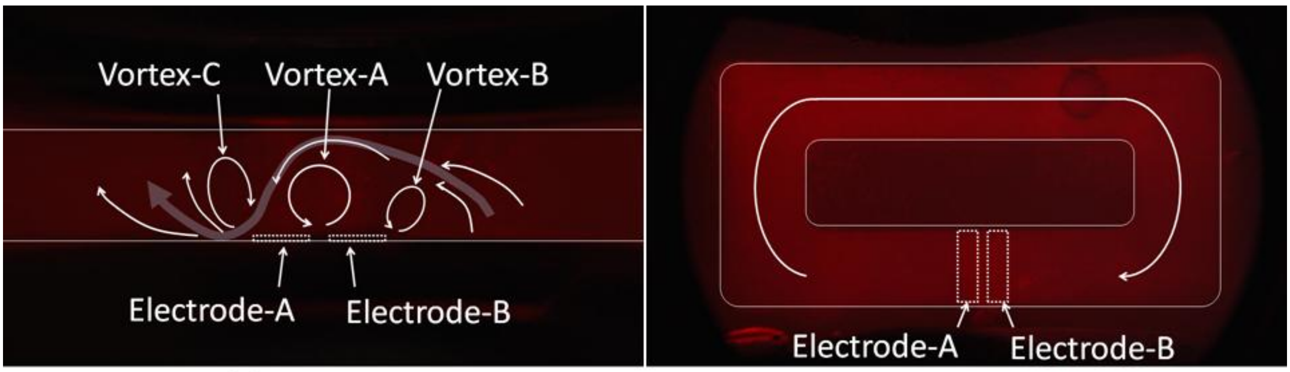

(a)Front view (b)Top view

Figure 8 Results of experiment No.3

Figure 9 Results of experiment No.4

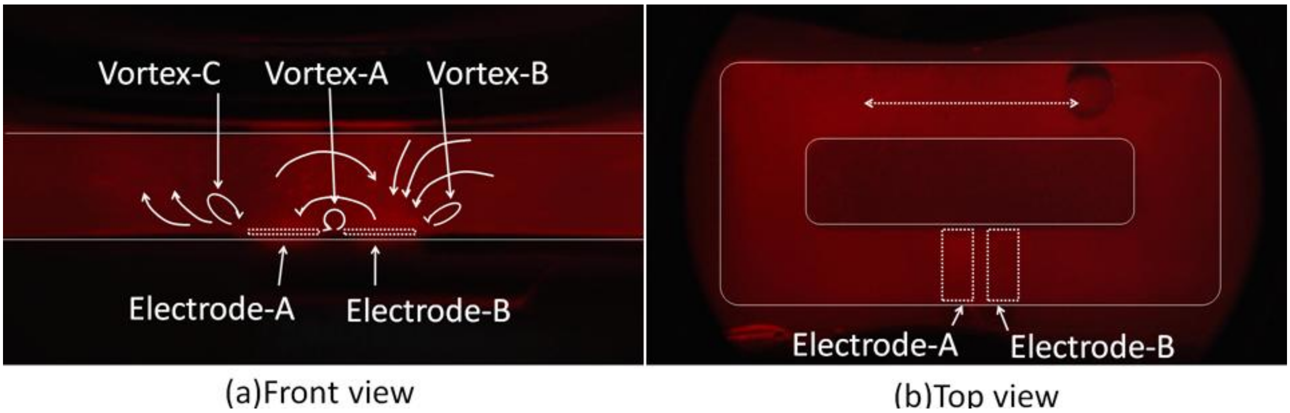

Figure 10 Results of experiment No.5

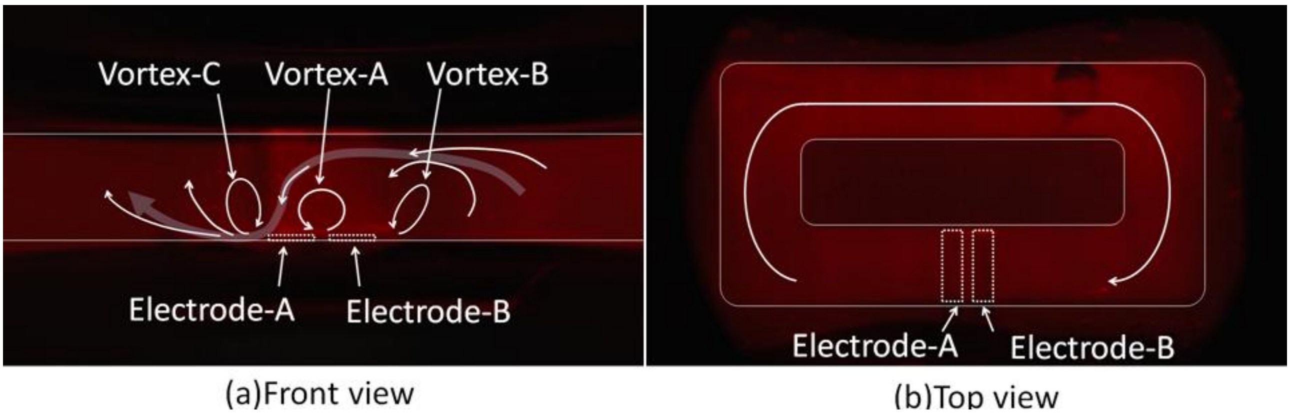

Figure 11 Results of experiment No.6

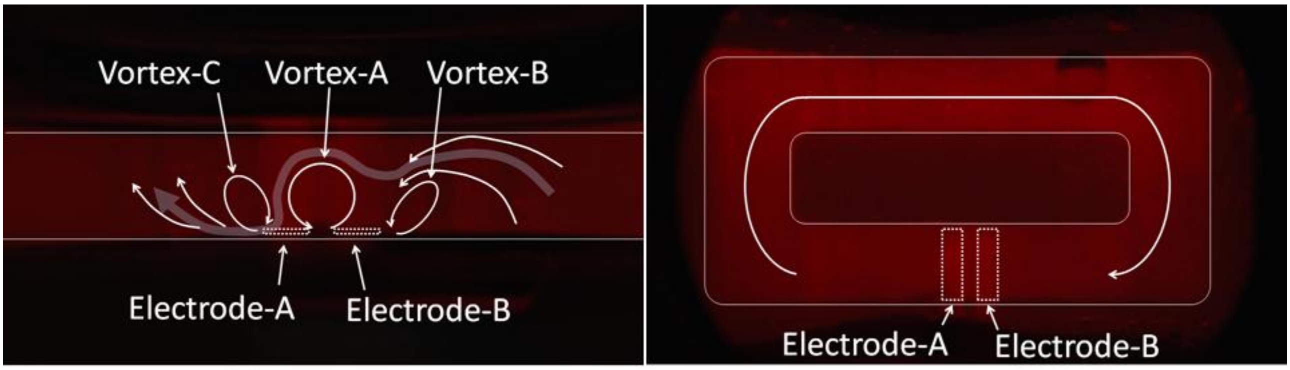

(a)Front view (b)Top view

Figure 12 Results of experiment No.7

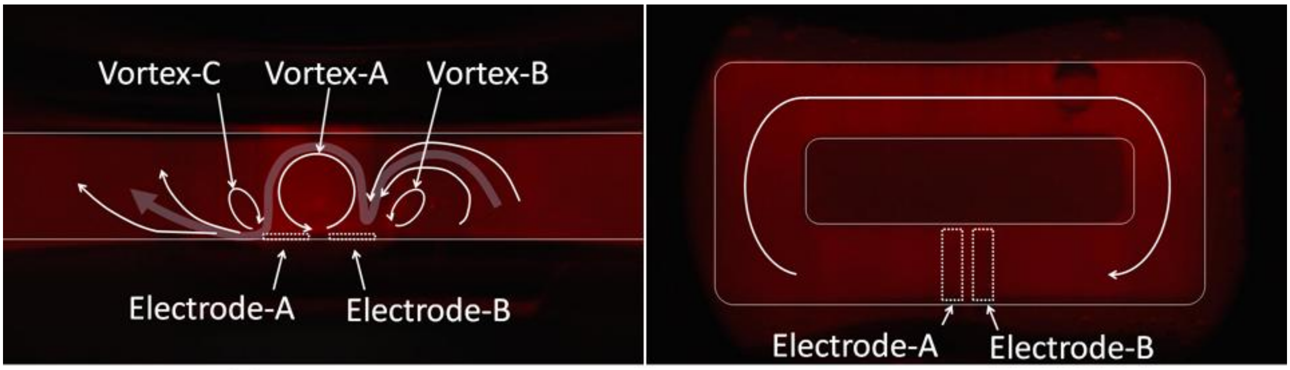

(a)Front view (b)Top view

Figure 13 Results of experiment No.8

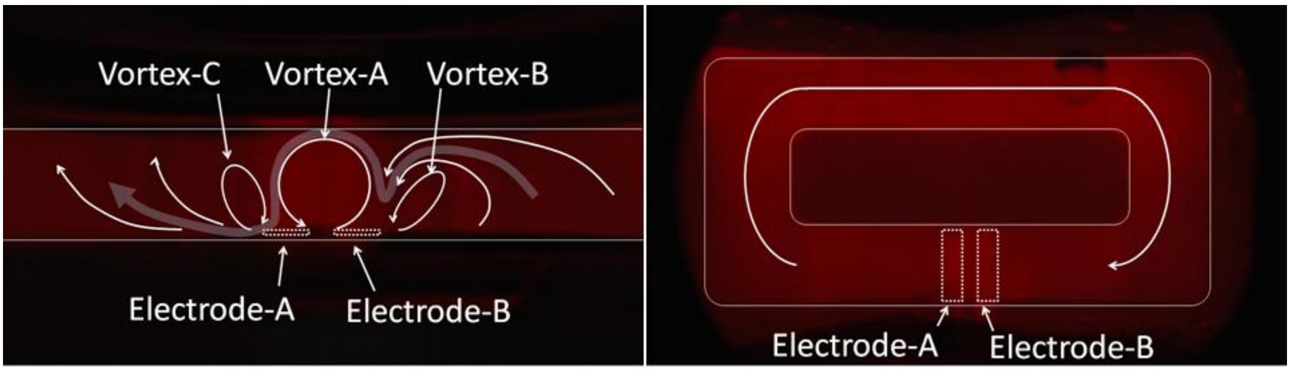

(a)Front view (b)Top view

Figure 14 Results of experiment No.9

Table 3 Flow velocity

No.	v [mm/s]	Flow direction
1	0.29	Clockwise
2	-	None
3	0.48	Clockwise
4	0.13	Clockwise
5	-	None
6	0.13	Clockwise
7	0.10	Clockwise
8	0.60	Clockwise
9	0.90	Clockwise

Influence of voltage
(comparison among experiments Nos.1, 2, and 3)
When experiments Nos.1, 2, and 3 were compared, it turned out that rotational flows are generated between electrodes and on the edge of each electrode for all experiments, that those rotational flows are weak in case of experiment No.2, and that the stronger the voltage in experiments Nos.1 and 3, the stronger the rotational flow. Therefore, it is believed that the strength of rotational flows generated between electrodes and on the edge of each electrode is proportional to the strength of voltage or electric field strength. Moreover, it is thought that rotational flows between electrodes and on the edge of each electrode cause a one-directional flow in the flow channel; therefore, flow velocity of a one-directional flow in the flow channel in case of experiment No.3 in which rotational flows are stronger than those in case of experiment No.1 is higher.

Influence of width of electrodes
(comparison among experiments Nos.1, 4, and 5)
When experiment No.4 in which the width of electrodes is less than that in case of experiment No.1 was compared with experiment No.1, it turned out that rotational flow between electrodes and on the edge of each electrode in case of experiment No.4 is less than that in case of No.1. In other words, electric fields become low because the width of electrodes in case of experiment No.4 is less than that in case of experiment No.1; therefore, rotational flow between electrodes and on the edge of each electrode also becomes low. Moreover, it is thought that power of rotational flow to cause a one-directional flow in the flow channel weakens because rotational flow becomes small; therefore, flow velocity of a one-directional flow in the flow channel becomes low. On the contrary, when experiment No.5 in which width of electrodes is less than that in case of No.1 was compared with experiment No.1, it turned out that flow in the vicinity of electrodes is complex in case of experiment No.5 unlike the case of No.1. Hence, electric fields expand because the width of electrodes increases and therefore flow that obstructs rotational flow causes a one-directional flow in the flow channel.

Influence of distance between two electrodes in case of voltage is constant
(comparison among experiments Nos.1, 6, and 7)
When experiments Nos.1, 6, and 7 were compared, it turned out that the wider the distance between electrodes, the bigger the rotational flow between electrodes. Hence, the area of electric fields between electrodes that generates rotational broadens when distance between electrodes increases, so that rotational flow between electrodes is more. Moreover, it turned out that the wider the distance between electrodes, the weaker the rotational flow between electrodes. Hence, electric fields between electrodes weaken when distance between electrodes is increased, so that rotational flow between electrodes reduces when the distance between electrodes is increased. Also, the wider the distance between electrodes, the slower the one-directional flow in the flow channel. In other words, rotational flow between electrodes that causes a one-directional flow in the flow channel weakens when distance between electrodes is increased, so that one-directional flow in the flow channel slows when distance between electrodes is increases.

Influence of distance between two electrodes in case of electric fields strength is constant
(comparison among experiments Nos.1, 8, and 9)
When experiments Nos.1, 8, and 9 were compared, it turned out that the wider the distance between electrodes, the more the rotational flow between electrodes even in the case of experiment Nos.1, 6, and 7, but it is different in case of experiments Nos.1, 6, and 7. Strength of the rotational flow remains stable even if distance between electrodes is increased. It is thought that this is because voltage is raised so that electric field strength between electrodes is constant even if distance between electrodes increases. The wider the distance between electrodes, the faster the one directional flow in the flow channel. Because distance between electrodes is increased keeping electric field strength between

electrodes constant, rotational flow between electrodes increases; therefore, a one-directional flow in the flow channel increases because power of rotational flow to cause one-directional flow in the flow channel increases.

APPLICATION TO MOTOR

We research the possibility to design the motors using EHD phenomenon. By placing two electrodes along equal intervals inside a cylinder as shown in figure 15, voltages will generate a one-directional rotation inside the cylinder as shown in figure 16.

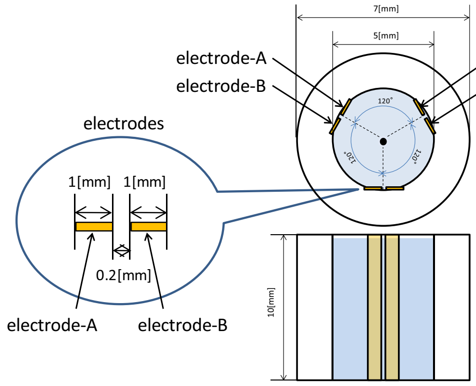

Figure 15 Two electrodes inside a cylinder

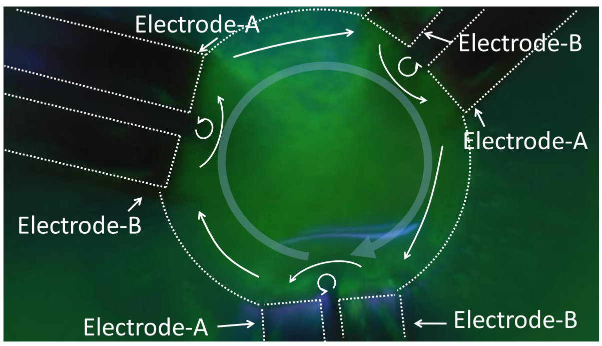

Figure 16 One-directional flow inside the cylinder

We research if motors can be designed using this phenomenon as shown in figure 17.

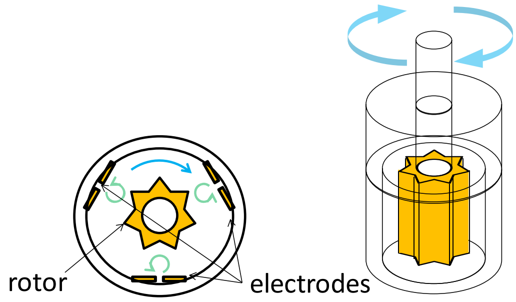

Figure 17 Concept of motor

CONCLUSIONS

In this study, a variety of electric fields were generated by varying voltage, width of electrodes, and distance between electrodes set up at the bottom of the flow channel, and we compared liquid crystalline flows in the vicinity of electrodes as well as flows in the flow channel in each electric field. The conclusions are given as follows.

1. When voltage is applied on two electrodes set up at the bottom of the flow channel filled with liquid crystal, rotational flows are generated between electrodes and on the edge of each electrode, causing a one-directional flow in the flow channel.

2. When electric field strength between electrodes increases, rotational flow between electrodes increases too. When width of electrodes is reduced, rotational flow between electrodes decreases. When width of electrodes is increased, flow in the vicinity of electrodes becomes complex. When distance between electrodes is increased, rotational flow between electrodes increases. A one-directional flow in the flow channel changes depending these changes.

3. By placing two electrodes along equal intervals inside a pipe, voltages will generate a one-directional flow inside the cylinder.

ACKNOWLEDGMENTS

Authors thank Merck & Co., Inc. for their generous support.

REFERENCES

1. Tetsuhiro T., “Characteristics and Application of Liquid Crystalline Flow under Application of External Fields”, Journal of the Japan Society of Applied Electromagnetics and Mechanics, Vol. 18, No. 3, (2010), in Japanese.

Proceedings of the 8th JFPS International
Symposium on Fluid Power, OKINAWA 2011
Oct. 25-28, 2011

2B1-2

AN IN-PIPE MOBILE ROBOT USING ELECTRO-CONJUGATE FLUID

Akihiro YAMAGUCHI*, Kenjiro TAKEMURA**,
Shinichi YOKOTA*** and Kazuya EDAMURA****

* Graduate School of Science and Technology, Keio University, 3-14-1, Hiyoshi Kouhoku-ku, Yokohama, Japan (phone/fax: +81-45-566-1826, e-mail: b_l_h_1987@yahoo.co.jp)
** Department of Mchanical Engineering, Keio University, Japan
*** Precision and Intelligence Laboratory, Tokyo Institute of Technology, 4259-R2-41, Nagatsuta-cho, Midori-ku, Yokohama, Japan
**** New Technology Management Co., Ltd., 2-9-1-306, Higashi-shinkoiwa, Katsushika-ku, Tokyo, Japan

ABSTRACT

An electro-conjugate fluid (ECF) is a kind of functional fluid, which produces a jet flow (ECF jet) when subjected to high DC voltage. This study introduces the ECF jet to develop a novel inchworm like in-pipe mobile robot which mainly consists of two clamping units (a clamping actuator, an ECF jet generator and an ECF tank) and a propelling unit (a propelling actuator, an ECF jet generator and an ECF tank). First, we characterize the actuators composed of a silicone rubber tube and aramid fibers. Next, we characterize the ECF jet generator which could be a micro fluid pressure source of the actuator, and confirm the effect of the number of electrode pairs on its performance. Finally we develop the ECF in-pipe mobile robot and demonstrate that the robot can move in a ϕ14 mm acrylic pipe with 0.043 mm/s. The robot is 200mm long with the diameter of 10mm.

KEY WORDS

In-pipe mobile robot, Functional fluid, Electro-conjugate fluid, Soft actuator, Artificial muscle

1. INTRODUCTION

It has been required for robots to contribute to inspection and repair of industrial plants including nuclear facilities, because the modern facilities are composed of innumerable narrow pipes, which are difficult to be manually inspected. Therefore, development of an in-pipe mobile robot which works in a small space is required.

Hence several types of in-pipe mobile robots using micro motors, shape memory alloys, piezoelectric actuators etc. have been developed [1]-[6]. In addition, an in-pipe mobile robot driven by pneumatic soft actuators is also actively developed because of its advantages as flexibility, compactness and high generative force [7]-[9]. The pneumatic soft actuator such as McKibben artificial muscle [9][10] is mainly consists of a rubber tube covered with a fiber sleeve, a pneumatic power source, and a valve. The rubber tube configuration, control method and applications of the pneumatic soft actuators have widely been investigated so far, however, the essential problem with pneumatic actuators is the requirement for bulky power sources apart from the actuator itself. Furthermore, it requires pneumatic lines to supply air pressure to each actuator. Therefore the entire system must be large.

On the other hand, there is an attractive functional fluid or an electro-conjugate fluid (ECF). The ECF is a kind of dielectric fluid, which generates a powerful jet flow when subjected to high DC voltage. The ECF

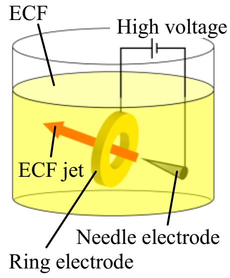

Fig. 1. Schematic diagram of ECF jet

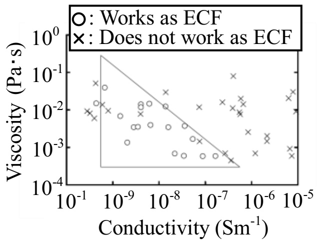

Fig. 2. ECF qualification

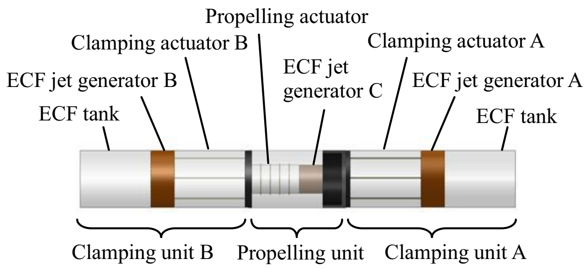

Fig. 3. Concept of the ECF in-pipe mobile robot

could be an appropriate fluid power source for downsizing and lightening an in-pipe mobile robot, because ECF jet becomes more powerful as the electrode pair becomes more compact (the power density increases as the size decreases), and configuration of the electrode pair is quite simple [11]. Furthermore, using the ECF jet pressure together with flexible balloon actuators enables an actuator to have constructive flexibility.

Hence, the purpose of this study is to develop a novel inchworm like in-pipe mobile robot using electro-conjugate fluid.

2. ELECTRO-CONJUGATE FLUID

The electro-conjugate fluid is a dielectric fluid, which works here as a smart/functional fluid. Applying a high voltage of several kilovolts between electrodes inserted into the fluid with an interelectrode gap of several hundred micrometers, we can observe a powerful jet flow (an ECF jet) between the electrodes as shown in Fig. 1, and this phenomenon observed with the electro-conjugate fluid is called an ECF effect in particular [11]. Although a high voltage is required to generate the jet flow, the current is quite low at several microamperes. The ECF jet may be observed especially under a non-uniform electric field produced, for example, by a needle–ring electrode pair as shown in Fig. 1. Although the mechanism of ECF effect has yet to be fully clarified [12][13], dielectric fluids plotted by white circles in Fig. 2 show the jet flow [14]. As can be seen from the figure, the dielectric fluids showing the ECF effect are obviously within a particular triangular region on the conductivity vs. viscosity plot. This means

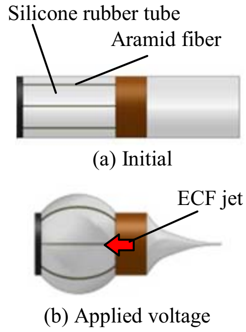

Fig. 4. Concept of the clamping unit

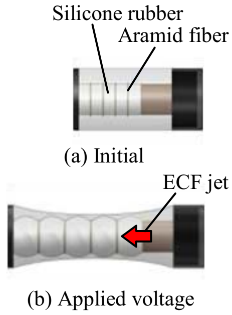

Fig. 5. Concept of the propelling unit

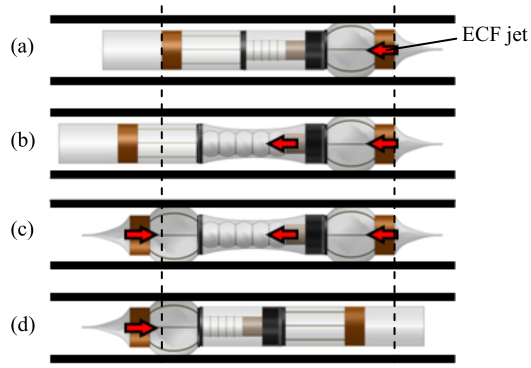

Fig. 6. Principle of operation

that plotted in this triangle is a necessary condition for fluids to show the ECF effect.

3. CONCEPT

Fig.3 shows a conceptual view of the in-pipe mobile robot, composed of ECF jet generators, two clamping units, and a propelling unit. The following sections detail each component of the in-pipe mobile robot.

3.1 Configuration and operating principle of the units

1) Clamping unit

Fig.4 (a) shows the clamping unit composed of the ECF jet generator, a clamping actuator, and an ECF tank. Each component is connected in alignment. Inside of the unit is filled with ECF. The ECF jet generator has a needle-ring electrode pair. The clamping actuator is composed of a silicone rubber tube and aramid fibers. The tube of the clamping actuator is reinforced with fibers along its axis. The actuator contracts and expands as the inner pressure increases due to an expansive force caused by the pressure increase and restrains by the fibers. Consequently, when high voltage is applied to the ECF jet generator, the ECF moves from the tank to the actuator by the ECF jet, resulting in making the actuator contract in the axial direction and expand in the radial direction as shown in Fig.4 (b).

2) Propelling unit

Fig.5 (a) shows the propelling unit composed of the

ECF jet generator, a propelling actuator, and an ECF tank. Inside of the unit is filled with ECF. The tank and the actuator compose a bicylindrical structure, and the ECF jet generator is located at the end of the actuator. Namely, the actuator and the ECF jet generator are located inside the tank. The propelling actuator is composed of a silicone rubber tube and aramid fibers. The tube of the propelling actuator is reinforced with fibers on its circumferential surface. The actuator extends as the inner pressure increases due to an expansive force due to the pressure increase and restrains by the fibers. Consequently, when a high voltage is applied to the ECF jet generator, the ECF moves from the tank to the actuator by the ECF jet, resulting in making the actuator extend in the axial direction as shown in Fig.5 (b). Note that the operating principle of the propelling unit is quite similar to that of the clamping unit, however, the motion is different.

3.2 Operating principle of the in-pipe mobile robot

It may be possible for the robot to move by pressurizing each actuator using ECF jet when following steps (a)-(d), corresponding to these in Fig. 6.

(a) The clamping actuator A expands by applying high voltage to the ECF jet generator A.
(b) The propelling actuator extends by applying high voltage to the ECF jet generator C. Note that, the robot does not move backward because of the frictional force between the clamping actuator A and the inner surface of pipe.
(c) The clamping actuator B expands by applying high voltage to the ECF jet generator B.
(d) The propelling actuator contracts (restores to the initial state) by stopping applying voltage to the ECF jet generator A and C. Then the clamping actuator A and the propelling actuator move forward because there exist a frictional force between the clamping actuator B and the inner surface of the pipe.

Hence, by appropriately switching the electrical input pattern as time step goes, the pressurized actuator is switched step by step, resulting in making the in-pipe robot move forward. There are several similar in-pipe mobile robots using pneumatic pressure [8][9], however, the proposed robot differs from these robots in the following points. First, the working fluid is completely enclosed in the robot itself. Second, the actuator and the pressure sources are integrated. Finally, the configuration is quite simple in comparison with the pneumatic robots, which require bulky compressors/valves outside. Hence, we believe that the proposed robot has advantages for integration, downsizing and lightening. Furthermore it is believed that the configuration of the robot is quite simple so that the robot overcomes the difficulty of spaghetti cord problems of other robot.

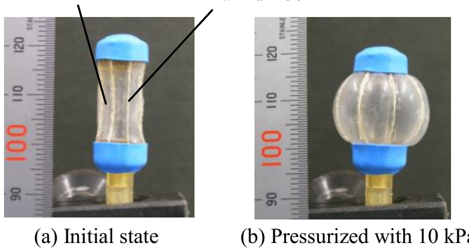

Fig. 7. Motion of the clamping actuator

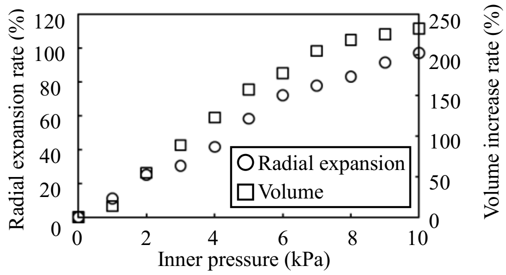

Fig.8. Characteristics of the clamping actuator

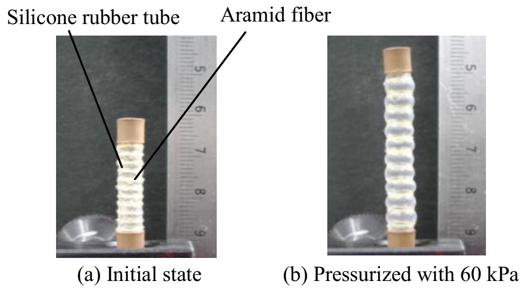

Fig. 9. Motion of the propelling actuator

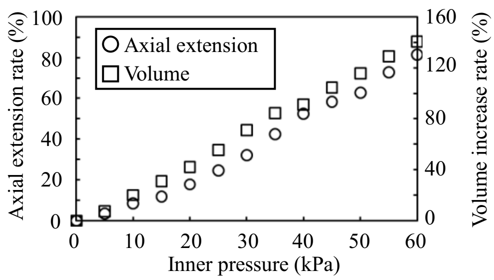

Fig.10. Characteristics of the propelling actuator

4. ACTUATORS

4.1 Clamping actuator

Fig.7 shows the actual view of the clamping actuator. Fig. 7 (a) shows a basic configuration and Fig. 7 (b) shows its actual view when it contracts and expands due to pressurization with 10.0 kPa using a pneumatic syringe. The actuator is composed of a silicone rubber tube reinforced with eight aramid fibers on its axis with equal spacing. The length and the inside diameter of the actuator are 15 mm and 10 mm, respectively. The thickness of the tube is approximately 0.1 mm.

In order to confirm the basic characteristic of the clamping actuator, we measured the inner pressure

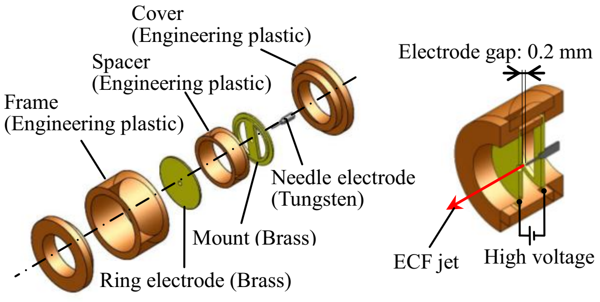

(a) Exploded view (b) Cross sectional view

Fig. 11. ECF jet generator

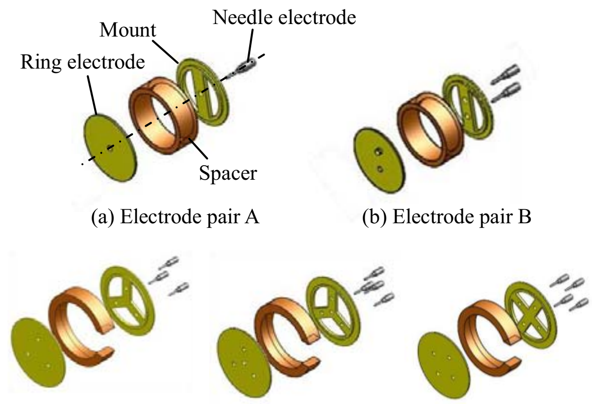

(a) Electrode pair A (b) Electrode pair B

(c) Electrode pair C (d) Electrode pair D (e) Electrode pair E

Fig. 12. Electrode pairs

versus radial expansion rate and volume increase rate of the actuator. However, the radial expansion rate means the ratio of radial expansion against the initial diameter of the actuator, and the volume increase rate means the ratio of the volume increase against the initial volume of the actuator. The results are shown in Fig.8. Note that, the inner pressure was increased using a pneumatic syringe. We confirmed the radial expansion rate and the volume increase rate increase as the inner pressure of actuator increases as can be seen in Fig. 8. The maximum radial expansion rate and the maximum volume increase rate are 97.2 % and 232.4 %, respectively, when pressurized with 10 kPa. This means the maximum radial expansion and the maximum volume increase are 9.4 mm and 2.7 ml, respectively.

4.2 Propelling actuator

Fig.9 shows the actual view of the propelling actuator. Fig. 9 (a) shows a basic configuration and Fig. 9 (b) shows its actual view when it extends due to pressurization with 60.0 kPa using a pneumatic syringe. The actuator is composed of a silicone rubber tube reinforced with eleven aramid fibers on its circumferential surface. The length and the inside diameter of the actuator are 20 mm and 5.0 mm, respectively. The thickness of the tube is approximately

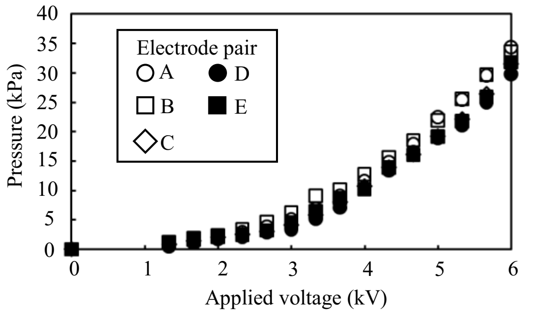

Fig. 13. Relationship between the pressure and applied voltage

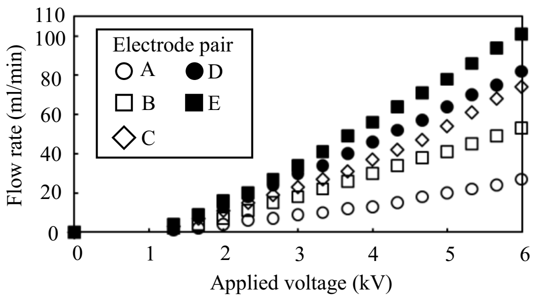

Fig. 14. Relationship between the flow rate and applied voltage

TABLE I
Physical properties of FF-101EHA2

Physical property	FF-101EHA2
Relative permittivity [-]	7.2
Electrical conductivity [S/m]	2.20E-07
Density [kg/m^3]	1540
Viscosity [mPa・s]	1.7

0.1 mm. The distance between each fiber is 2.0 mm.

In order to confirm the basic characteristic of the propelling actuator, we measured the inner pressure versus axial extension rate and volume increase rate of the actuator. However, the axial extension rate means the ratio of axial extension against the initial length of the actuator. The results are shown in Fig.10. Note that, the inner pressure was again applied using a pneumatic syringe. We confirmed the axial extension rate and the volume increase rate increase as the inner pressure of the actuator increases as can been seen in Fig. 10. The maximum axial extension rate and the maximum volume increase rate are 81.4 % and 140.6 %, respectively, when pressurized with 60 kPa. This means the maximum axial extension and the maximum volume increase are 17.1 mm and 0.6 ml, respectively.

5. ECF JET GENERATOR

5.1 Configuration

The ECF jet generator could be a micro fluid pressure source of the actuator. There can be several types of electrode pairs which may generate the ECF jet, for example, a bar-shaped electrodes pair, a ring and needle

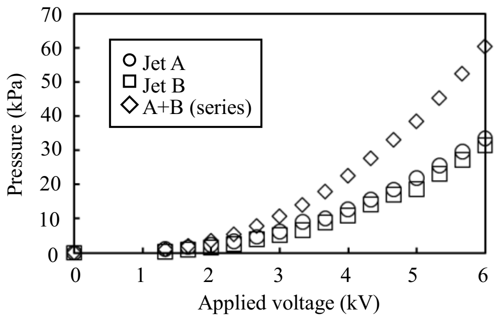

Fig. 15. Relationship between the pressure and applied voltage

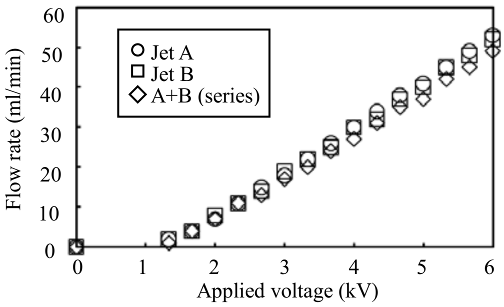

Fig. 16. Relationship between the flow rate and applied

electrode pair etc. In this study, we adopted the pair of ring and needle electrodes because this pair can easily be located in a channel and generates relatively high pressure [11]. Fig. 11 shows the schematic illustration of the ECF jet generator we designed. It is mainly composed of a needle-ring electrode pair, an electrode spacer, a frame, and covers. The electrode pair is of a brass ring, a tungsten needle, and a needle mount made of brass. The other parts are made of engineering plastic. The spacer keeps a gap of the electrode pair to an appropriate distance. The electrode pair and the spacer which are inserted into the frame are fixed by covers. The ECF jet is generated from the tip of needle through the ring bore when a high DC voltage is applied as shown in Fig.11 (b).

5.2 Experiment

We investigated the pressure and the flow rate characteristics with five types of electrode pairs shown in Fig. 12. Note that the electrode pairs B-E have several needle-bore pairs in parallel. Diameter of needle electrode, bore diameter of ring electrode and electrode gap are 0.13mm, 0.3mm, and 0.2mm, respectively. The experimental results are shown in Fig. 13 and Fig. 14. We used the ECF called FF-101EHA2 (New Technology Management Co. Ltd., Japan) as a working fluid. The physical properties of FF-101EHA2 are shown in Table I. Fig. 13 shows the generated pressure of each electrode has little difference, possibly showing a slight decrease as the number of electrode pairs (needle-bore pairs) increases. We attribute this to the following reason. The maximum pressure may depend on the lowest pressure generated by a certain pair of

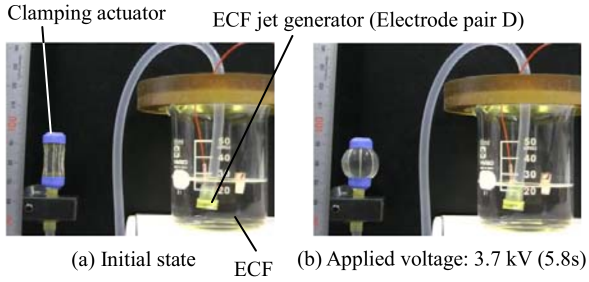

Fig. 17. Motion of the clamping actuator

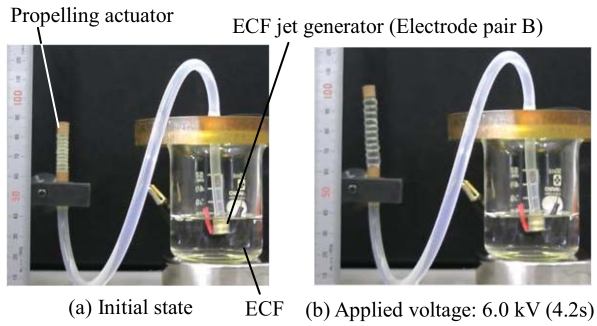

Fig. 18. Motion of the propelling actuator

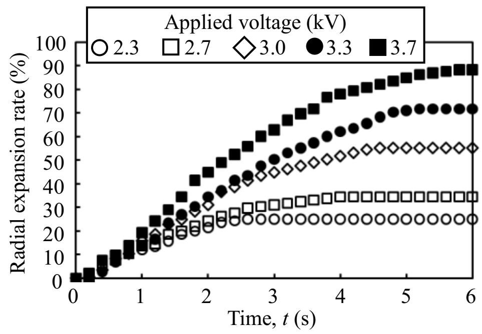

Fig.19. Characteristics of the clamping actuator

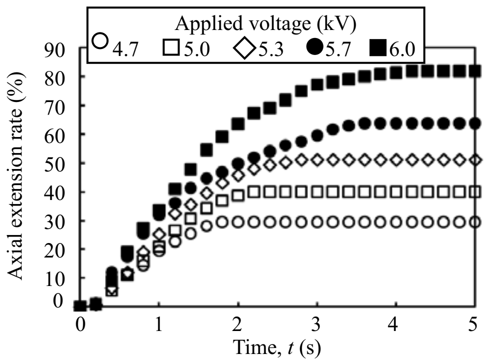

Fig.20. Characteristics of the propelling actuator

needle and bore, that is, there must be some difference between pressures generated by each pair of needle and bore due to the manually assembling error.

On the other hand, Fig. 14 shows that the flow rate obviously increases as the number of the ring-bore pairs increases. Fig. 14 also shows that the flow rate is

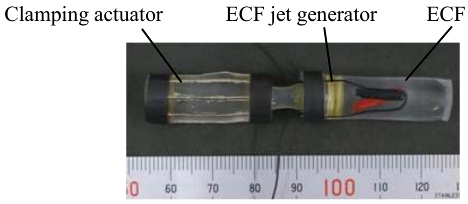

(a) Initial state

(b) Applied voltage: 3.7 kV (5.4s)

Fig. 21. Motion of the clamping unit

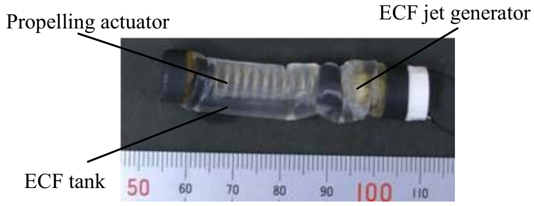

(a) Initial state

(b) Applied voltage: 6.0 kV (3.4s)

Fig. 22. Motion of the propelling unit

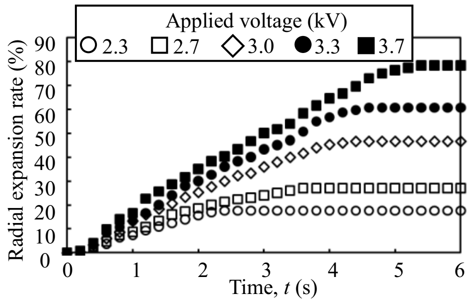

Fig.23. Characteristics of the clamping unit

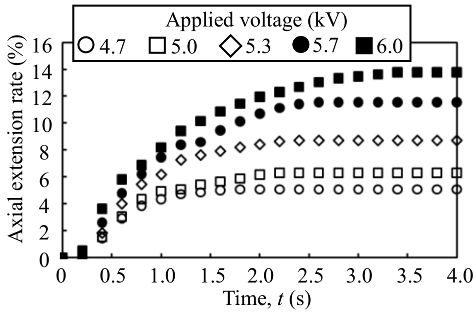

Fig.24. Characteristics of the propelling unit

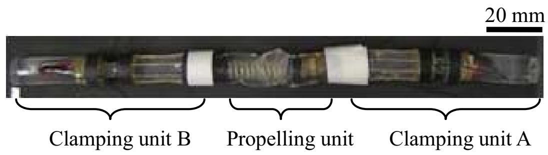

Fig.25. The ECF in-pipe mobile robot

approximately proportional to the number of needle-bore pair except the case with the electrode pair D. The flow rate with the electrode pair D is approximately three times higher than that with the electrode pair A, despite the electrode pair D has four ring-bore pairs in parallel. This may be because of the influence of the location of needle-bore pairs. Namely, the ECF jet generated by the ring-bore pair located at the center does not work adequately. Consequently, the flow rate with the electrode pair D is almost the same as that with the electrode pair C. The maximum flow rate, 103.0 ml/min, was measured with the electrode pair E with the applied voltage of 6.0 kV.

As mentioned above we indicated the characteristics of the ECF jet generator, and it can be seen that the pressure generated by the ECF jet generator is large enough to drive the clamping actuator in Fig.8 and Fig.13. However, the pressure by the ECF jet generator is not large enough to drive the propelling actuator because the propelling actuator requires approximately 60 kPa to drive as shown in Fig. 10. Hence, we confirmed the characteristics of the ECF jet generators when arranged in series because it is theoretically clear that pressure may double by arranging two pressure sources (ECF jet generator) in series. The experimental results are shown in Fig. 15 and Fig. 16. Note that we use the Electrode pair B which has relatively high flow rate characteristics and simple configuration among five types of electrode pairs investigated in this study (cf. Fig. 12 and Fig. 14) because the propelling actuator does not require the large volume increase compared to the clamping actuator (cf. Fig.8 and Fig.10). In this experiment we used two ECF jet generators in total ("Jet A" and "Jet B"), and we arranged "Jet B" at the upstream of "Jet A". A distance between the rear end of needle electrode of "Jet A" and the ring electrode of "Jet B" is 1.4 mm. Owing to this arrangement, ECF jet may possibly be generated to unwanted direction (from "Jet A" to "Jet B"); therefore we coated the rear end of needle electrode with an insulator. Fig. 15 and Fig. 16 show that the characteristics of two ECF jet generators are nearly equal. Fig. 15 also shows that the generated pressure doubles by arranging two ECF jet generators in series. The maximum pressure was 60.5 kPa with the applied voltage of 6.0 kV. This means the pressure generated by two ECF jet generators arranged in series is large enough to drive the propelling actuator. On the other hand, Fig. 16 shows that the flow rate slightly decreased by arranging two ECF jet generators in series. Hence we determined that we use the electrode pair E to

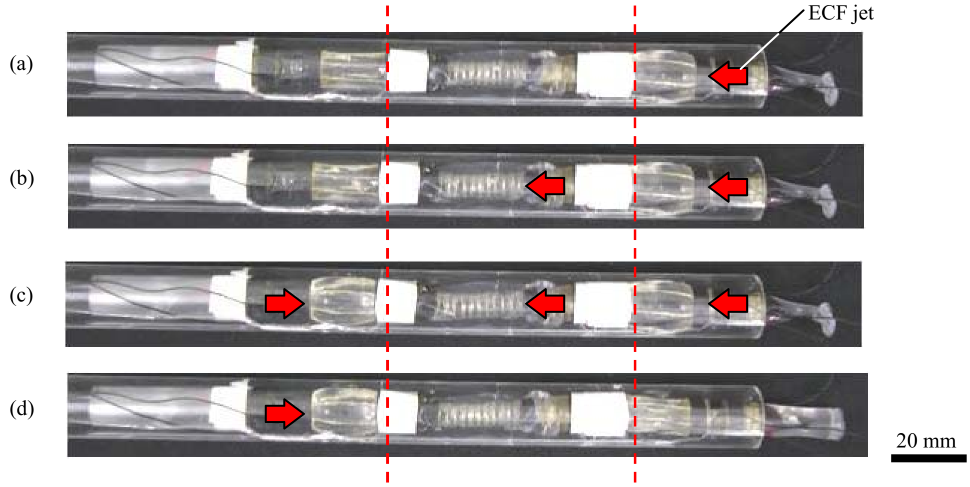

Fig.26. Motion of the ECF in-pipe mobile robot

drive the clamping actuator, and two electrode pair B arranged in series to drive the propelling actuator.

6. DRIVING EXPERIMENT USING ECF JET

6.1 Actuators

In order to measure basic performances of the actuators, we constructed an experimental setup shown in Fig. 17(a) and Fig. 18(a). The main purpose of this experiment is to confirm the characteristics of the actuators when driven by ECF jet, so that the actuators, the ECF jet generator and the ECF tank are arranged separately, and they are connected with rubber tubes. Inside of the actuator, ECF jet generator, and rubber tube are filled with the ECF.

Fig. 17(b) and Fig. 18(b) shows an actual view of the motion of the actuators when a high voltage was applied to the ECF jet generator. However, the initial state is shown in Fig. 17(a) and Fig. 18(a). We measured the radial expansion rate of the clamping actuator and the axial extension rate of the propelling actuator with every 0.2 s in order to confirm step response of the actuators. The experimental results are shown in Fig. 19 and Fig. 20. It can be seen that the maximum radial expansion rate of the clamping actuator is 88.3 % when the applied voltage to the ECF jet generator is 3.7 kV as in Fig.19. It is also confirmed the rise time of the clamping actuator with 3.7 kV step input is 3.5 s as can be seen in Fig. 19. On the other hand, it can be seen that the maximum axial extension rate of the propelling actuator is 81.8 % when the applied voltage to the ECF jet generator is 6.0 kV as in Fig.20. It is also confirmed the rise time of the propelling actuator with 6.0 kV step input is 2.4 s as can be seen in Fig. 20.

From this experiment, we confirmed that the actuator could be driven by the ECF jet as we proposed.

6.2 Units

The clamping unit and the propelling unit we developed are shown in Fig.21 (a) and Fig.22 (a). Each unit is composed of the actuator, the ECF jet generator, and the ECF tank. Inside of the unit is filled with ECF. The ECF tank is made of silicone rubber tube. The thickness of the ECF tank is approximately 0.1 mm.

The basic driving performance of each unit is confirmed by experiments. The experimental results are shown in Fig. 21 (b), Fig. 22 (b), Fig. 23, and Fig. 24, respectively indicating the motion of the clamping unit, the motion of the propelling unit, the step response of the clamping unit, and the step response of the propelling unit. From this experiment, we confirmed that each unit could be driven by the ECF jet as we proposed.

7. ECF IN-PIPE MOBILE ROBOT

7.1 Configuration

Fig. 25 shows an ECF in-pipe mobile robot we developed. The in-pipe mobile robot is composed of the clamping units and the propelling unit as shown in Fig.25. The in-pipe mobile robot is 200mm long with the diameter of 10mm.

7.2 Experiment

Characteristics of the in-pipe mobile robot were confirmed by experiment in a ϕ14 mm acrylic pipe. In the experiment, we applied the voltage of 3.7 kV to the ECF jet generator for the clamping units and 6.0kV to the ECF jet generator for the propelling unit. Fig. 26 shows a photocopy of a motion of the robot. The symbols (a)-(d) in Fig.26 correspond to the symbols (a)-(d) in Fig.6 which shows the designed operation. As shown in Fig.26, we demonstrated that the robot could move in the ϕ14 mm acrylic pipe as we proposed. The experimental results confirm the robot moves in the ϕ14 mm acrylic pipe with 0.043 mm/s. Note that, we appropriately switched the electrical input pattern manually, since the main purpose of this experiment is to confirm the operating principle.

However it may be required for the robot to move much faster. The moving velocity of the robot can be faster by improving the response of the actuators and the axial extension rate of the propelling actuator. The response can be improved by placing several electrode pairs in parallel in order to increase the flow rate of the ECF jet as we tested in Sec. 5.2. The axial extension rate of the propelling actuator can be improved by increasing the generated force of the propelling actuator. The force to extend the actuator itself is also used to extend the ECF tank in our prototype. So the axial extension rate of the propelling unit (Fig. 24) decreases compared to that of the propelling actuator itself (Fig.10). Furthermore, when the in-pipe mobile robot moves, the force to extend the propelling actuator is also used to move the clamping actuator forward. The force of the propelling actuator can improved by placing several electrode pairs in series in order to increase the generated pressure of the ECF jet as we tested in Sec. 5.2. Note that, the electrode pair required is extremely compact compared with the actuator itself.

8. CONCLUSIONS

This study proposed a novel inchworm like in-pipe mobile robot using the ECF. First, we proposed the concept of the in-pipe mobile robot. Second, we investigated the characteristics of the clamping actuator, propelling actuator, and the ECF jet generator, which are the essential components of the proposed robot. Third, we developed the clamping unit and the propelling unit, and confirmed our concept is reasonable. Finally, we developed the ECF in-pipe mobile robot and demonstrated that the robot can move in a ϕ14 mm acrylic pipe with 0.043 mm/s.

Our future study focuses on the improvement of configuration of the actuator, the unit, and the ECF jet generator, and controlling the ECF in-pipe mobile robot.

REFERENCES

[1] Koichi Suzumori, Toyomi Miyagawa, Masanobu Kimura, and Yukihisa Hasegawa, “Micro Inspection Robot for 1-in Pipes”, IEEE/ASME Transactions on mechatronics, Vol. 4, No. 3, pp. 286-292, 1999.

[2] Shuichi Wakimoto, Jun Nakajima, Masanori Tanaka, Takefumi Kanda, Koichi Suzumori, “A micro snake-like robot for small pipe inspection”, International Symposium on Micromechatronics and Human Science, pp.303-308, 2003.

[3] Byungkyu Kim, Moon Gu Lee, Young Pyo Lee, YongIn Kim, GeunHo Lee, “An earthworm-like micro robot using shape memory alloy actuator”, Sensors and Actuators A: Physical, Vol. 125, pp. 429-437, 2006.

[4] Takaharu Idogaki, Hitoshi Kanayama, Nobuyuki Ohya, Harumi Suzuki and Tadashi Hattori, “Characteristics of Piezoelectric Locomotive Mechanism for an In-Pipe Micro Inspection Machine”, Sixth International Symposium on Micro Machine and Human Science, pp.193-198, 1995.

[5] A. Menciassi, S. Gorini, G. Pernorio, P. Dario, “A SMA Actuated Artificial Earthworm”, Proceedings of the 2004 IEEE International Conference on Robotics and Automation, pp. 3282-3287, 2004.

[6] A. Menciassi, S. Gorini, G. Pernorio, Liu Weiting, F. Valvo, P. Dario, “Design, Fabrication and Performances of a Biomimetic Robotic Earthworm”, Proceedings of the 2004 IEEE International Conference on Robotics and Biomimetics, pp.274-278, 2004.

[7] Pal Liljeback, Oyvind Stavdahl, Kristin Y. Pettersen, “Modular Pneumatic snake robot 3D modeling, implementation and control”, Modeling, Identification and Control, Vol. 29, No. 1, pp. 21–28, 2008

[8] Jinwan Lim, Hyunjun Park, Sunmoo Moon Byungkyu Kim, “Pneumatic Robot Based on Inchworm Motion for Small Diameter Pipe Inspection”, Proceedings of the 2007 IEEE International Conference on Robotics and Biomimetics, pp. 330-335, 2007.

[9] Norihiko Saga, Taro Naksmura and Shlnya Ueda, “Study on Peristaltic Crawling Robot Using Artificial Muscle Actuator”, Proceedings of the 2003 IEEE/ASMElmemationd Conference on Advanced Intelligent Mechatronics, pp.679-684.

[10] B. Tondu, P. Lopez, “Modeling and Control of McKibben Artificial Muscle Robot Actuators”, IEEE Control Systems Magazlne, Vol. 20, Issue. 2, pp. 15-38, 2000.

[11] Kenjiro Takemura, Humiya Yajima, Shinichi Yokota and Kazuya Edamura, “Integration of micro artificial muscle cells using electro-conjugate fluid”, Sensors and Actuators A: Physical, Vol. 144, Issues 2, pp. 348-353, 2008.

[12] Hideki Yamamoto, Kento Mori, Kenjiro Takemura, Leslie Yeo, James Friend, Shinichi Yokota and Kazuya Edamura, “Numerical modeling of electro-conjugate fluid flows”, Sensors and Actuators A: Physical,Vol.161, pp.152-157, 2010

[13] Kento Mori, Hideki Yamamoto, Kenjiro Takemura, Shinichi Yokota and Kazuya Edamura, “Dominant factors inducing electro-conjugate fluid flow”, Sensors and Actuators A: Physical, Vol. 167, pp. 84-90, 2011.

[14] R. Abe, K.Takemura, S. Yokota and K.Edamura, “Concept of a Micro Finger using Electro-conjugate Fluid and Fabrication of a Large Model Prototype”, *Sensors and Actuators A: Physical,* Vol. 136, Issue 2, pp. 629-637, 2007.

Proceedings of the 8th JFPS International
Symposium on Fluid Power, OKINAWA 2011
Oct. 25-28, 2011

2B2-1

DEVELOPMENT OF MEMS-BASED ECF MICRO RATE GYRO

Tsunehiko IMAMURA**, Toshiya SUZUKI*, Joon-wan KIM*, Shinichi YOKOTA*,
and Kazuya EDAMURA***

* Tokyo Institute of Technology, Precision & Intelligence Laboratory
4259-R2-41 Nagatsuta-cho Midoriku Yokohama 226-8503 Japan
(E-Mail: syokota@pi.titech.ac.jp)
**Tamagawa Seiki Co., Ltd. Spacetronics Laboratory
1879 Ohyasumi Iida Nagano 395-8515 Japan
(E-Mail: tsunehiko-imamura@tamagawa-seiki.co.jp)
***New Technology Management Co., Ltd.
2-9-1-306 Higashi-shinkoiwa Katsushika Tokyo 124-0023 Japan

ABSTRACT

We are proposing a liquid rate gyro named "ECF micro rate gyro". Although the sensing principle is based on that of a conventional gas rate sensor, the liquid micro rate gyro works by an electro-conjugate fluid (ECF) instead of a gas. The electro-conjugate fluid is a dielectric fluid that works as a functional fluid, generating a powerful jet flow (ECF jet) when subjected to a high DC voltage. In our concept model, an ECF micro rate gyro was made by machines and handwork. In this study, we propose a MEMS fabrication process of ECF jet generator, flow channel and sensing hot wire, which are parts of the ECF micro rate gyro. By using MEMS technology, we can downsize and integrate an ECF micro rate gyro. Then we perform functional test of the fabricated prototype and confirmed a function as a rate gyro.

KEY WORDS

Rate Gyro, Functional Fluid, MEMS, ECF

INTRODUCTION

A rate gyro is a sensor which detects angular rate of moving objects and is widely used in various mechanical systems. It has some subtypes depending on their operation principles [1] (Fig.1). Optical gyros and mechanical gyros have high accuracy and can detect very small angular rate such as daily or orbital motion of the earth. They are used for aircraft navigation and north seeking and their prices are high. Gas rate gyros have middle accuracy and are used for high-dynamic application such as flying objects and space ships. But their bulky size and high cost make their application limited. Vibration gyros fabricated by MEMS technology have relatively low accuracy but their low cost makes themselves standard rate gyros in recent consumer applications including car navigation and digital cameras [2-4]. But they have some problems due to having vibrating element inside such as sensitivity to outer vibration and low impact resistance. And about 20 years have passed since the emergence of the MEMS based vibratory gyro, desire for a new type of rate gyro has arisen.

The authors introduced an electro-conjugate fluid or ECF [5] to realize a promising candidate for new type of rate gyro [6-9]. The ECF is a kind of smart fluid which generates a powerful jet flow when subjected to high DC voltage. This means the ECF could be used for fluid power systems without any bulky pumping systems [10-15]. The proposed "ECF liquid rate gyro" which measures the drift of the ECF jet due to Coriolis force when an angular rate is applied. We confirmed the

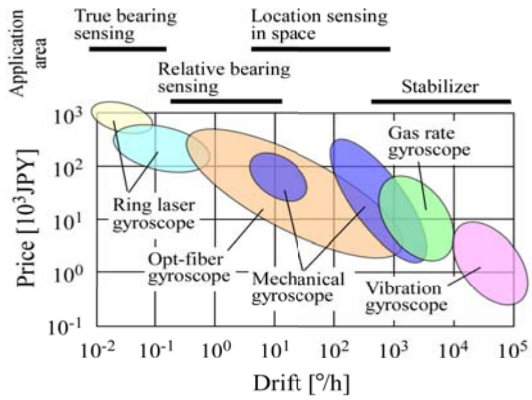

Fig.1 Performance vs. price relation of gyroscope [1]

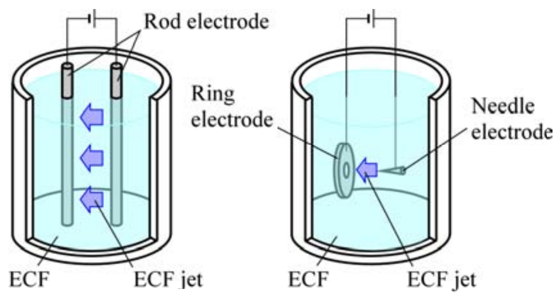

Fig.2 Schematic of ECF jet

rotation detection function of our concept model and addressed some practical problems found in the concept model [6-8]. These results show the possibility of the ECF rate gyro as a next generation standard micro rate gyro. Then we tried to fabricate some of the parts for ECF rate gyro by MEMS fabrication process and have gotten MEMS-based ECF jet generator and sensing flow channel [9]. In this study, in addition to an ECF jet generator and sensing flow channel, we try to fabricate a sensing hot film by MEMS technology and have an ECF micro rate gyro fully made by MEMS technology.

Principle of the ECF rate gyro

Fig.3 shows the schematic view and operation principle of an ECF rate gyro. The ECF rate gyro mainly consists of ECF jet generators, channel separation walls and hotwires. When a high DC voltage is applied to the ECF jet generators, the ECF jet is generated to form the total jet flow which circulates inside the channel. The jet stream ejected from a nozzle moves to sensing hotwires and cools them. In static condition, each sensing hotwire is cooled equally and no output change is observed from the bridge circuit. When a rotation is applied, the ECF stream drifts due to Coriolis force and resulted in unbalanced cooling of the hotwires. And we can know the angular rate from the output change from the bridge circuit (Fig.4). A functional test result of our previous

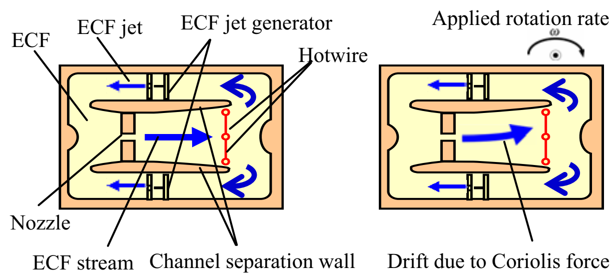

Fig.3 Schematic view of ECF micro rate gyro and principle of scanning angular rate

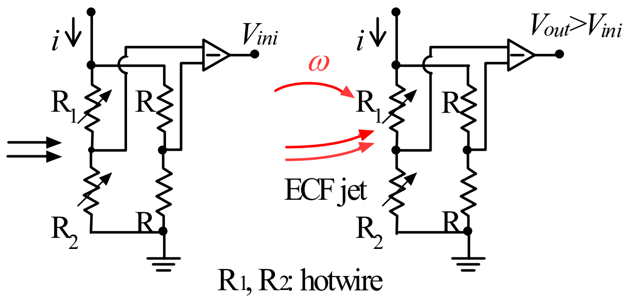

Fig.4 Sensing principle of ECF micro rate gyro

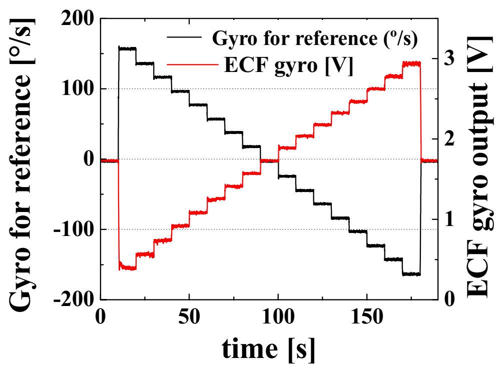

Fig.5 Functional test of previous ECF micro rate gyro

ECF micro rate gyro [8] is shown in Fig.5. As can be seen, the ECF micro rate gyro (red line) outputs a voltage in response to the input rotation rate, which is calibrated by a reference MEMS gyro (black line).

Fabrication process of MEMS-based ECF micro rate gyro

In our concept model (Fig.3), we used a needle-plate electrode pair as an ECF jet generator (Fig.6 (a)), tungsten hot wire for sensing and PEI (polyetherimide) channel wall. Each part is processed by machines and assembled by hand. The use of a machined

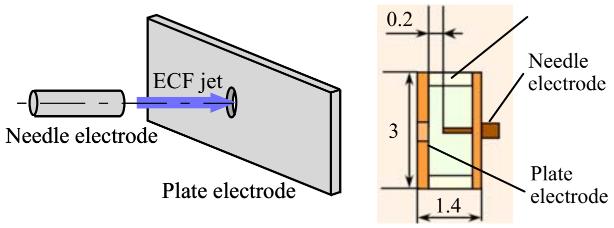

(a) Needle-plate electrode pair

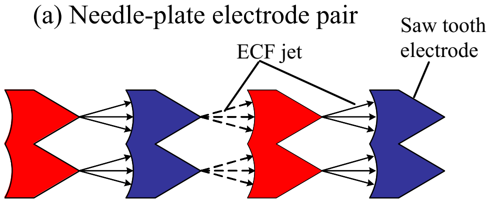

(b) Planar saw tooth electrode

Fig.6 Examples of the ECF jet generator electrode

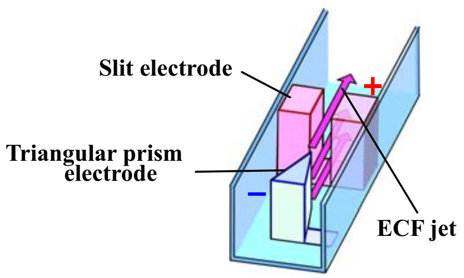

Fig.7 Triangular prism and slit electrode

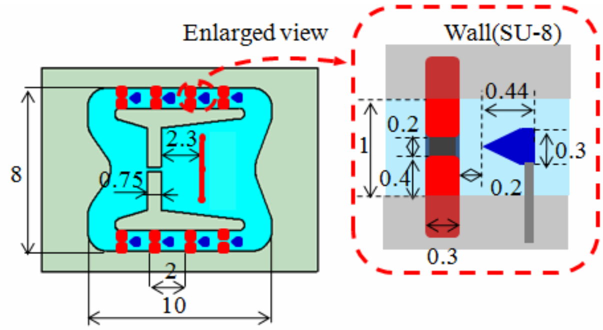

Fig.8 Dimensions of wall and electrodes [mm]

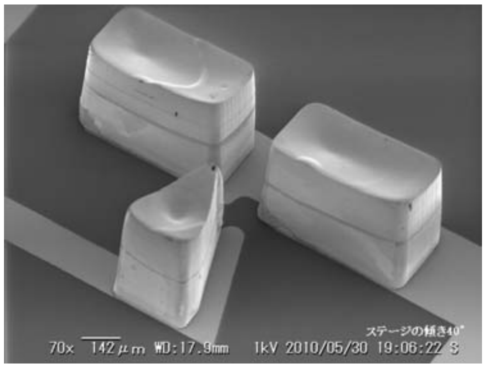

Fig.9 SEM image of fabricated triangular prism and slit electrode pair

part limits miniaturization and mass productivity. And the hand assembly can easily be a cause of error and also be a barrier for mass production. So we here fabricate all of these parts by MEMS process to overcome above mentioned problems.

ECF jet generator

There are some types of electrode pairs which generates the ECF jet [15, 16]. Among them, a needle-plate electrode pair produces strong ECF jet but has bulky size. A planar saw tooth electrode has thin structure and suitable to be fabricated by MEMS process, but it generates relatively weak ECF jet. As a combined form of the needle-ring electrode pair (Fig.6 (a)) and the planar saw tooth electrode (Fig.6 (b)), we proposed a triangular prism and a slit electrode pair (Fig.7) as it has adaptability to MEMS fabrication process and is supposed to generate strong ECF jet [9]. In this case the ECF jet is thought to be generated in the direction from the apex of the triangular prism electrode to the slit electrode. Fig.8 (right) shows the dimensions of electrode pair used in this study. The height of the electrodes is set to 0.5mm as in our partly MEMS-based model [9]. We fabricate these electrodes by a kind of electroforming process as described in ref. [9]. SEM image of fabricated electrode is shown in Fig.9.

Flow channel for sensing

Channel separation walls and a nozzle are constructed by a negative resist SU-8. This process is done by coating SU-8 on glass wafer followed by patterning of it to form channel separation walls and a nozzle (Fig.8 (left)). Height of fabricated channel separation walls was 1mm. Finally we fabricate ECF jet generator electrodes and the flow channel within 1mm thickness, which is much thinner than our previous ECF micro rate gyro fabricated by machines and handwork, by using MEMS fabrication process.

Hot film for sensing

In addition to an ECF jet generator and sensing flow channel, we try to fabricate a sensing hot film, instead of tungsten hot wire in our previous model, by MEMS technology. It is difficult to construct such a 3D structure like a hot wire used in our previous model by

MEMS fabrication process because it has a stand-off structure which is aligned in the center of flow channel's height. So here we propose a hot film formed on a bridge between posts both of which are constructed by SU-8 (Fig.10).

A glass wafer is used as a base for the hot film. First, negative resist SU-8 is coated on the glass base followed by patterning to form three posts (Fig.11 (a)). Next a light blocking material (Cu) is deposited on SU-8 to form bridges between the posts (Fig.11 (b)). Coating a thin layer of SU-8 and patterning to complete SU-8 posts and bridges after removing unexposed SU-8 (Fig.11 (c) (d)). Then a stencil mask, which is patterned to form a sensing hot film, is overlaid and sputtering Cr and Au over it (Fig.11 (e) (f)). Then conductive epoxy is put between the metal film and electrode pad on the glass base for output wiring (Fig.11 (g)). And finally Ni plating is performed on the conductive area to confirm conductivity (Fig.11 (h)). Dimension and SEM image of the fabricated sensing hot film is shown in Fig.12.

Preparation of the test sample

We construct a test sample by mounting fabricated electrodes and flow channel on the base and fill the channel with ECF (FF8-EHA2; New Technology Management). After that cover with the hot film is overlaid on the base (Fig.13). A silicon rubber sheet is used as a shim to fill the gap between the jet generator and the cover. Fig.14 is a schematic of fabricated test sample. This sample has the channel volume of $10\times 8\times$ t1mm^3, much less volume than that of our machined model ($16.6\times 10.6\times$ t1.5mm^3). Fig.15 shows a schematic of operation of the fabricated ECF micro rate gyro.

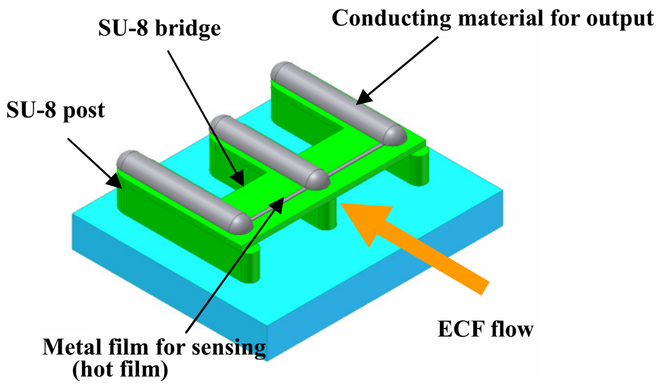

Fig.10 Conceptual illustration of sensing hot film

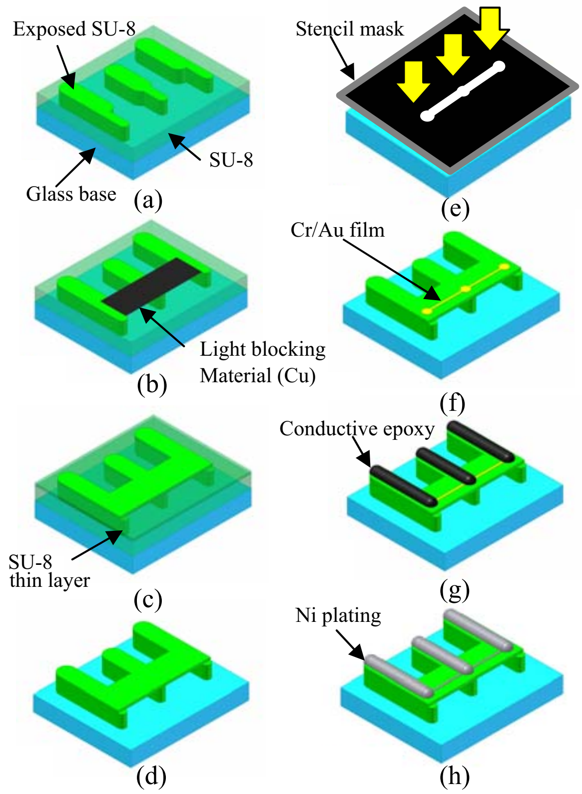

(a) Coating SU-8 on a glass and patterning to form three posts.
(b) Light blocking material is deposited to form bridges between the posts.
(c) Coating thin SU-8 and patterning to form final form of posts and bridges.
(d) Developing SU-8.
(e) A stencil mask is overlaid.
(f) Sputtering Cr and Au over a stencil mask to form hot film for sensing.
(g) Wiring hot film to electrode by conductive epoxy.
(h) Ni plating to confirm conductivity.

Fig.11 Fabrication process of sensing hot film

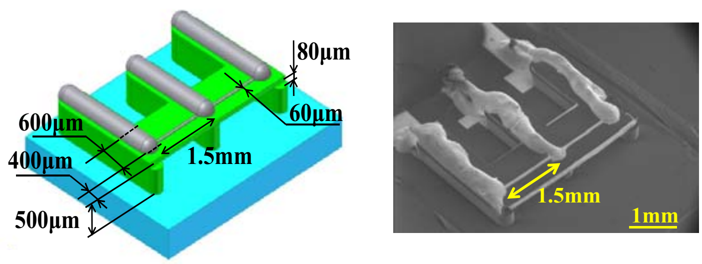

(a) Dimensions (b) SEM image

Fig.12 Fabricated sensing hot film

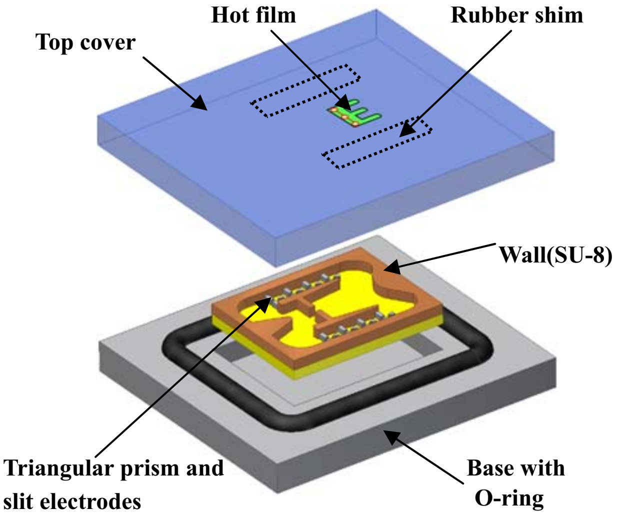

Fig.13 Preparation of Test Sample

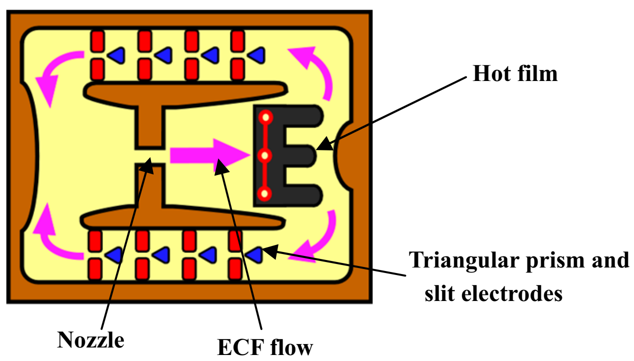

Fig.14 Schematic of operation of the fabricated ECF micro rate gyro

Functional test of ECF micro rate gyro

Functional Test Setup

Functional test of the fabricated ECF micro rate gyro is performed on a rotation rate table. The setup is shown in Fig.15. The fabricated test sample, a high voltage power source (HV-10P, Matsusada Precision Co., Ltd., Japan), and a reference gyro with accuracy of <0.2 %F.S. (AU4522, Tamagawa Seiki Co., Ltd.) are located on a rotary table. The angular rate of the rotary table can manually be controlled. The input voltage to the jet generator is up to 6 kV. The input current to the hotwires can be varied (set to 80mA in this study). Since the output from the hot wire bridge V_{out} is very low, we amplify the signal at a signal converter which is also located on the rotary table. In addition, we can insert a first order low pass filter to the signal if necessary. The output signal from the concept model is expected negative against the signal at 0°/s when the rotary table rotates in clockwise (CW) with observing from the upper side. On the other hand, it is expected positive when rotating in counter clockwise (CCW).

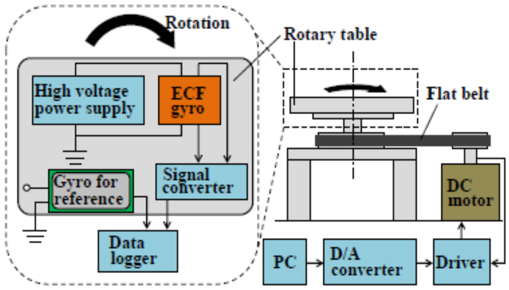

Fig.15 Functional test setup

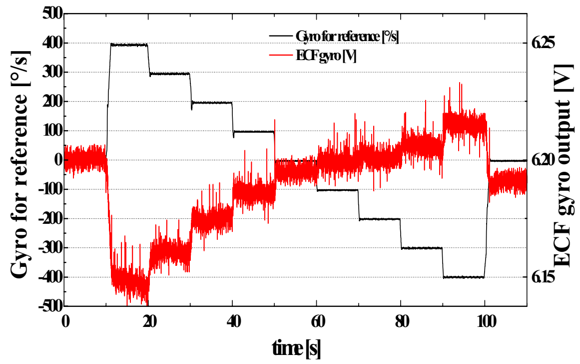

Fig.16 Functional test result of ECF micro rate gyro

Functional Test Results

The ECF jet can be generated when a high voltage is applied to the ECF jet generator located on the channel base as mentioned above. In our concept model, when the needle is connected to the ground and the plate is to the positive, we obtained higher sensitivity and lower noise property [6]. Hence we connected the triangular prism electrode to the ground instead of connecting the needle electrode to the ground, and the slit electrode to the positive instead of connecting the plate electrode to the positive. Fig.16 shows the output signals from the test sample and the reference gyroscope, where the gain at the signal converter is 550, the cutoff frequency is 8.6 Hz, ECF drive voltage is 0.31kV and the hotwire current is set to 80mA. From Fig.16, fabricated fully MEMS-based ECF micro rate gyro is functional as a rate gyro. But a sensitivity of the rate gyro (0.1mV/°/s) is much lower than those of our machined model (11.7 mV/°/s) and our partly MEMS-based model (3.9 mV/°/s). This may be caused by a lower resistance of fabricated sensing hot film than tungsten hot wire used in our machined and partly MEMS-based ECF rate gyro as discussed later. And there exists asymmetry between output for CW and CCW rotation rate. This is also attributed to resistance of fabricated hot film.

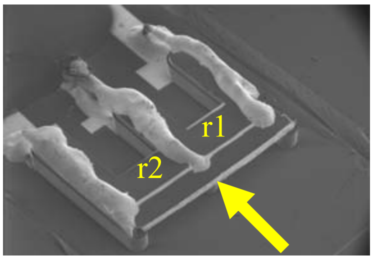

(a) Total view of fabricated hot film

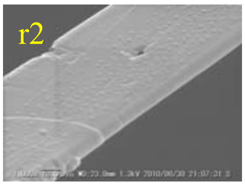

(b) r2 side(Expanded)

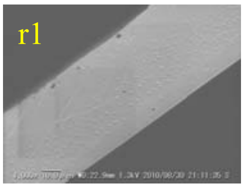

(c) r1 side(Expanded)

Fig.17 Detailed examination of fabricated hot film

Characterization of fabricated hot film

Magnified view of fabricated hot film is shown in Fig.17. There exists unbalanced film thickness between left side (r2; Fig.17 (b)) and right side (r1: Fig.17 (c)), approximately 10μm for r1 and 1μm for r2. And measured resistance is 0.2Ω for r2 and 0.4Ω for r1. Measured resistance is much lower than that of tungsten hot wire used in our machined and partly MEMS-based model, approximately 5Ω each. This may be a cause of lower sensitivity observed in Fig.16 because the low resistance hot film has low ability to generate heat and differential of resistance against temperature change (dR/dT), which is caused by cooling sensing hot film by ECF flow might also be low. As a same manner, because r2 has lower resistance than r1, differential of resistance r2 against temperature change (dR_2/dT) might be lower than that of r1 (dR_1/dT). This explains the output asymmetry also observed in Fig.16. When CW rotation is applied, ECF flow is drifted to the direction for r1. And when CCW rotation is applied, ECF flow is drifted to the direction for r2. So sensitivity for CW rotation (flow drifts to r1 direction) is higher than CCW rotation (flow drifts to r2 direction).

These results show that uncontrolled thickness of metal for sensing hot film may have affected the property of the rate gyro. So the precise control of the metal film thickness is required to improve the property of sensing hot film. And for highly sensitive hot film, stand-off metal film is desirable [17, 18]. The hot film fabricated in this study is laid on 80μm SU-8 layer. This might also be a cause of low sensitivity as a part of generated heat is absorbed by SU-8. To have improved sensing hot film, we are planning to fabricate stand off metal hot film, which will be designed to have higher and uniform resistance.

CONCLUSIONS

In addition to previously proposed ECF jet generator and the channel separation wall, we here fabricate the sensing hot film by MEMS process and has achieved fully MEMS-based ECF micro rate gyro. And we perform functional test of the rate gyro constructed by these parts. Functional test results show that this fully MEMS-based ECF rate gyro is functional but has a low and asymmetrical sensitivity. They are attributed to low and asymmetric resistance of fabricated sensing hot film. Further study is necessary to have a sensing hot film which has higher and uniform resistance.

ACKNOWLEDGEMENTS

A part of the research was supported by Grant-in-Aid for Exploratory Research #21656044 of the Ministry of Education, Culture, Sports, Science and Technology of Japan.

REFERENCES

1. Introduction of Gyro Technology, Tamagawa Seiki Co. Ltd. (in Japanese).
2. R. Oboe, R. Antonello, E. Lasalandra, G. Spinola Durante, L. Prandi, “Control of a z-axis MEMS vibrational gyroscope”, IEEE/ASME Transactions on Mechatronics , 10, (4), (2005) , pp. 364–370.
3. T. Rogers, N. Aitken, K. Stribley, J. Boyd, “Improvements in MEMS gyroscope production as a result of using in situ, aligned, currentlimited anodic bonding” , Sensors and Actuators, A, 123, (124), (2005) pp.106–110.
4. S. Lee, S. Park, J. Kim, S. Lee, D.I. Cho, “Surface/bulk micromachined singlecrystalline silicon micro-gyroscope”, J. Microelectromechanical Systems, 9, (4), (2000), pp.557–567.
5. S.Yokota, Y. Otsubo, K. Edamura, “Electro-sensitive movable fluids, method of using the same and motors for the electro-sensitive movable fluids”, USP6, 030, (2000), 544.
6. K. Takemura, S. Yokota, M. Suzuki, K. Edamura, H. Kumagai, T. Imamura, “A Liquid Rate Gyroscope using Electro-conjugate Fluid”, the Journal of Sensors and Actuators, A, Vol.149, issue2, (2009), pp.173-179.
7. K. Takemura, T. Imamura, K. Edamura, H. Kumagai, S. Yokota, “The Practical Design of a Liquid Rate Gyroscope using Electro-conjugate Fluid”, the Journal of Systems and Control Engineering, Part I of the Proceedings of the IMechE, Vol.223, No.6, (2009), pp.727-736.
8. S. Yokota, M. Hongo, K. Takemura, K. Edamura, T. Imamura, H. Kumagai, “ECF Liquid Rate Gyroscope”, 14th International Symposium on Applied Electromagnetics and Mechanics (ISEM2009), Xian, China, (2009), pp.625-626

9. T. Imamura, T. Suzuki, J -W. Kim, S. Yokota, K. Edamura, “Miniaturization of ECF Micro Rate Gyro by using MEMS technology”, Proc. of the 14th International Conference on Mechatronics Technology (ICMT2010) , Osaka, (2010), pp.303-308.
10. S. Yokota, Y. Kondoh, A. Sadamoto, Y. Otsubo, K. Edamura, “A micro motor using electro-conjugate fluids (ECF) (proposition of stator electrode-type (SE-type) micro ECFmotors)”, International Journal of JSME Series C, 44, (3), (2001) pp.756–762.
11. S. Yokota, “A 2mm ECF micromotor”, Proc.of the 7th International Conference on Mechatronics Technology (ICMT’03), (2003), pp.361–366.
12. R. Abe, S. Yokota, “A micro actuator using ECF-jetwith needle-type electrode”, Proc. of FLUCOME’03, (2003), CD-ROM.
13. K. Takemura, S. Yokota, K. Edamura, “A micro artificial muscle actuator using electro-conjugate fluid”, Proc. of the IEEE International Conference on Robotics and Automation (ICRA2005), (2005), pp.534–539.
14. S. Yokota, K. Kawamura, K. Takemura, K. Edamura, “A high-integrated micromotor using electro-conjugate fluid (ECF)”, J. Robotics and Mechatronics (2005) pp.142–148.
15 W.-S. Seo, K. Yoshida, S. Yokota, K. Edamura, “A high performance planar pump using electro-conjugate fluid with improved electrode patterns”, Sensors and Actuators A, 134, (2), (2007), pp.606–614.
16 K. Takemura, H. Kozuki, K. Edamura, S. Yokota, “A Micromotor using Electro-conjugate Fluid - Improvement of motor performance by using saw-toothed electrode series” ,Sensors & Actuators A, Vol. 140, (2007), pp.131-137.
17. U. Buder, J.-P.v. Klitzing, E. Obermeier, “Bulk micromachining of polyimideby reactive ion etching”, Sensors & Actuators A, Vol. 132, (200), pp.393-399.
18. U. Buder, J.P.v. Klitzing, E. Obermeier, “Bulk micromachining of polyimide for AeroMEMS flowsensors using reactive ion etching” , Proc. of Eurosensors XIX, Barcelona, Spain, September 11–14, 2005, Paper No.MC 11.

Proceedings of the 8th JFPS International
Symposium on Fluid Power, OKINAWA 2011
Oct. 25-28, 2011

2B2-2

A MICRO MOBILE HYDRAULIC SYSTEM USING ELECTRO-RHEOLOGICAL FLUID

Kazuhiro YOSHIDA*, Takafumi ANZAI**, Joon-wan KIM* and Shinichi YOKOTA*

* Precision and Intelligence Laboratory
** Graduate School
Tokyo Institute of Technology
R2-42, 4259 Nagatsuta-cho, Midori-ku, Yokohama, 226-8503 Japan
(E-mail: yoshida@pi.titech.ac.jp)

ABSTRACT

The paper presents a novel micro mobile hydraulic system using ERF (electro-rheological fluid) for in-pipe working micromachines, etc. The hydraulic system generates high power motion irrespective of the system posture. First, a micro rolling diaphragm actuator (MRDA) equipped with an ER valve is proposed and developed. The MRDA is a fluid power microactuator which has long stroke and large output force. The ER valve controls ERF flow by the apparent viscosity increase due to the applied electric field. Second, an FI micropump for high viscosity fluids like ERFs is developed, which generates high output fluid power utilizing fluid inertia (FI) effect in a pipe. In addition, a sealed flexible tank is developed to adapt the posture and the ERF amount changes of the tank. Finally, a micro mobile hydraulic system is constructed using the above-mentioned elements and the validity is confirmed through experiments.

KEY WORDS

Micromachine, Mobile hydraulics, ERF (electro-rheological fluid), Microactuator, Micropump

INTRODUCTION

For micromachines performing power-needed tasks such as in-pipe working micromachines as shown in Figure 1 [1][2], etc., micro mobile hydraulic systems which generate high power motion irrespective of the system posture are required. In this paper, we propose and develop a micro mobile hydraulic system using ERF (electro-rheological fluid). The ERF increases its apparent viscosity remarkably and reversibly when subjected to electric field.

We have been developing ER microactuators which are combinations of ER valves and fluid power microactuators [3][4]. The ER valve controls the ERF flow by the electric field applied with fixed electrodes.

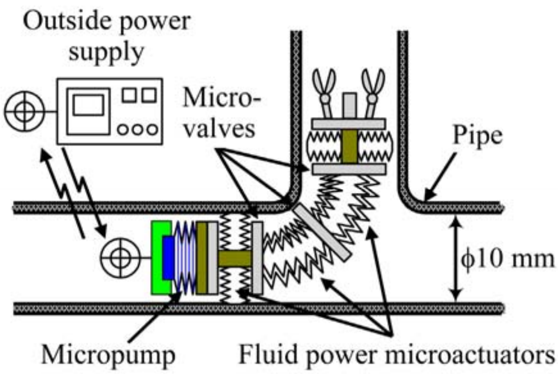

Figure 1 In-pipe working micromachine using fluid power

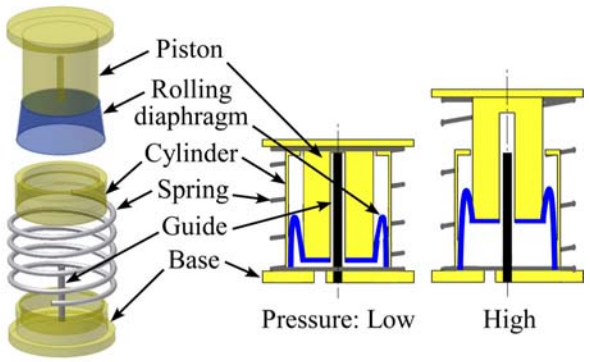

Figure 2 Proposed micro rolling diaphragm actuator (MRDA)

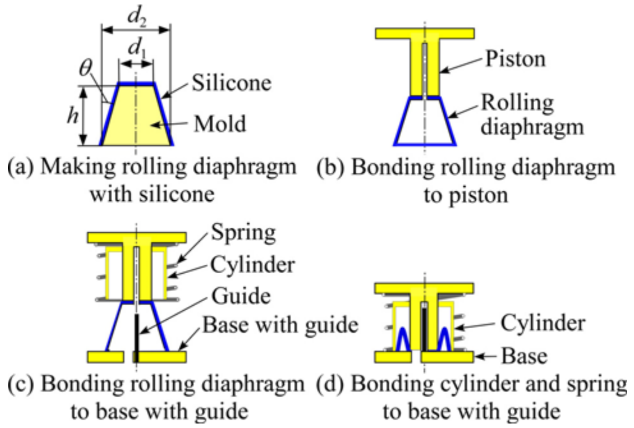

Figure 3 Fabrication process of MRDA

The ER microactuator controls the high density fluid power [5] with simple and miniaturizable structure.

As fluid power microactuators, bellows are the promising candidates, however, ratio of the extension to the free length, which is called the "extension ratio," hereafter, of conventional metal bellows is about 20 % due to the permanent deformation and large free length is required for the sufficiently long stroke. Rubber bellows have large extension ratio, however, the allowable pressure and the output force are not so high.

In this study, a micro rolling diaphragm actuator called "MRDA" is proposed, which utilizes a rolling diaphragm which can linearly extend long stroke with enclosing the working fluid. Then an MRDA equipped with an ER valve is proposed and developed, which has compact structure, large extension ratio, and large output force.

As a fluid power source, an FI micropump [6] is developed for high viscosity fluids like ERFs. The FI micropump utilizes fluid inertia (FI) effect in a pipe and has realized high output fluid power in water pumping. In addition, a sealed flexible tank is developed to adapt the posture and the ERF amount changes of the tank.

Finally, a micro mobile hydraulic system is constructed using the above-mentioned elements. The characteristics and the validity are investigated experimentally.

MICRO ROLLING DIAPHRAGM ACTUAOTR (MRDA) EQUIPPED WITH ER VALVE

Proposition of MRDA equipped with ER valve

There are several fluid power actuators such as piston-cylinders, diaphragms, metal bellows, rubber bellows, and rolling diaphragm-cylinders [7]. The piston-cylinders have long stroke and high output force due to high allowable pressure, however, the miniaturization needs special improvements to prevent leak and friction [8]. The diaphragms have simple structure and high output force, however, the strokes are very small for in-pipe working micromachines, etc. The metal bellows have high output force due to high allowable pressure and miniaturizable simple sealed structure without sliding parts, however, the extension ratio is up to 20 % due to the permanent deformation. The rubber bellows have large extension ratio and miniarturizable simple structure, however, they can not generate high output force due to low allowable pressure. The rolling diaphragm-cylinders have large extension ratio and high output force, however, the miniaturization potential has not been investigated yet. Hence, in this study, miniaturization of the rolling diaphragm-cylinder is investigated.

Figure 2 shows schematics of the proposed MRDA. The MRDA consists of rolling diaphragm, piston, cylinder, base, guide, and spring. With increasing the inner pressure of the MRDA, it extends with decreasing the overlap part length. With decreasing the inner pressure, it contracts due to the outside spring force. Different from the conventional rolling diaphragm-cylinders [7], with locating the spring outside, the small free length is realized. The extension ratio is expected to realize up to 60 % based on the geometry. Also, as the rolling diaphragm is in a cylinder, high pressure can be applied, which results in high output force.

The ER valve for the MRDA is a three-port type which has two pairs of parallel plate electrodes and changes the control pressure due to the viscosity change with the applied electric field. With maintaining the sum of electric field strengths in the upstream and downstream electrode pairs constant, increase/decrease of the downstream electric field strength results in increase/decrease of the control pressure and in extension/contraction of the MRDA.

Fabrication of MRDA

Figure 3 shows schematics of the fabrication process of the MRDA. As the material of the rolling diaphragm, silicone rubber was employed due to the high flexibility and the easiness of fabrication. The content ratios of silicone rubber, silicone solution, and diluent were determined experimentally. The piston, cylinder, and

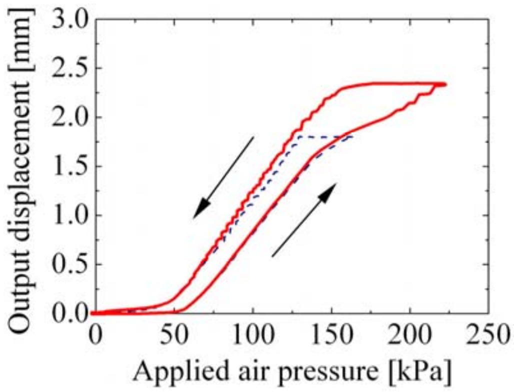

Figure 4 Measured static characteristics of MRDA

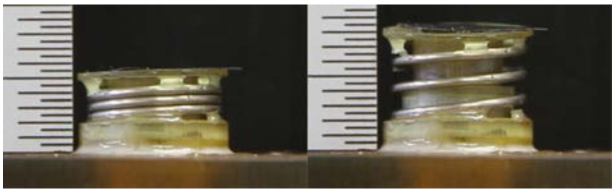

Figure 5 Fabricated small length MRDA

base were made of engineering plastic. The guide was made of tungsten.

In the fabrication, first, the mixture of the silicone rubber was applied to the vertically supported taper mold, thermally cured, and peeled off (Figure 3(a)). Second, the rolling diaphragm was bonded to the piston and a guide hole was dug (Figure 3(b)). Third, the rolling diaphragm was bonded to the base with guide (Figure 3(c)). After this process, molybdenum disulfide was applied on the rolling diaphragm outside as lubricant. Finally, the cylinder and the spring were bonded to the base with guide.

The optimal structural parameters were investigated through experiments. As a result, thickness 0.10 mm and taper angle θ=9.5 ° of the rolling diaphragm were obtained.

Static characteristics of the MRDA

In considering application to small in-pipe mobile machines, an MRDA was fabricated with 10 mm diameter, 15 mm length, and designed extension ratio of 17 % (2.5 mm stroke). In this fabrication, for simplicity, a standard spring with large free length was used and the extension ratio is small. The rolling diaphragm has height h=3.0 mm, top diameter d_1=6.0 mm, bottom diameter d_2=7.0 mm (taper angle θ=9.5 °) and thickness 0.10 mm. The spring constant is 1.8 kN/m. The MRDA is used as a part of the MRDA equipped with an ER valve in the next section.

The static characteristics were experimentally investigated. The output displacement of the MRDA was

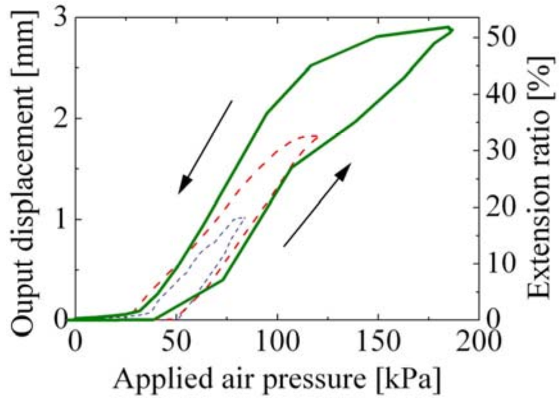

Figure 6 Measured static characteristics of small length MRDA

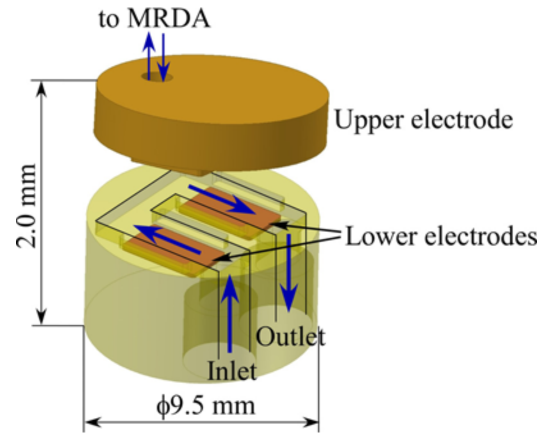

Figure 7 Fabricated ER valve

measured without load using pneumatic pressure. Figure 4 shows the measured results. The output displacement begins to increase about at 50 kPa which is the balanced point between the force due to pressure and the spring contraction force to the minimum length. It has hysteresis due to the friction and deformation. The increasing rate of the output displacement is decreased about at 150 kPa because the overlap part of the rolling diaphragm extends due to the excessive pressure and it contacts with the upper plate of the cylinder.

To verify the larger extension ratio, small length MRDA was fabricated as shown in Figure 5. The MRDA has 10 mm diameter, 5.6 mm length, and designed extension ratio of 54 % (3.0 mm stroke). Figure 6 shows the measured output displacement without load. At pressure 50 kPa, the MRDA begins to extend. The measured extension ratio is 52 %, which agrees well with the designed value. It was confirmed that the MRDA has large extension ratio.

Fabrication of MRDA equipped with ER valve

An ER valve was fabricated with 9.5 mm diameter and 2.0 mm length as shown in Figure 7. The ER valve has

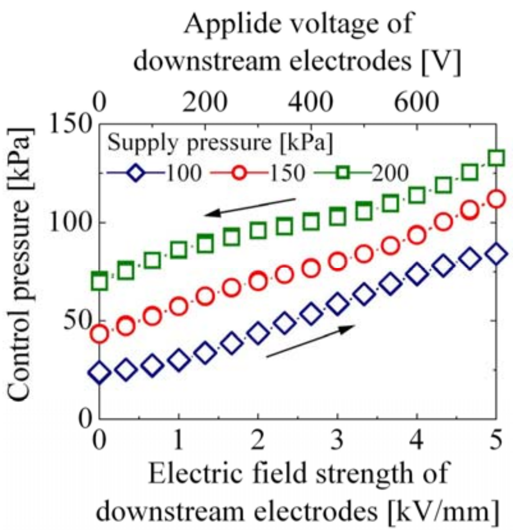

Figure 8 Measured static characteristics of ER valve

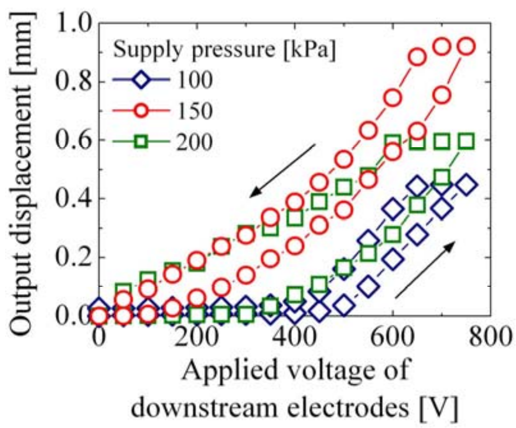

Figure 9 Measured static characteristics of MRDA equipped with ER valve

upstream and downstream flow channels, each of which has 2.5 mm width, 3.4 mm length, and 0.15 mm height that is the electrode gap length.

Figure 8 shows the measured static characteristics with different supply pressures as a parameter. The ERF was a nematic liquid crystal (MLC-6457-000, Merck Ltd., Japan. Base viscosity 23 mPa·s at 23 °C). The sum of electric field strengths in the upstream and downstream flow channels was 5 kV/mm. Based on the results, it was confirmed that there are no hystereses for every supply pressures. The control pressure range are 61, 68, and 62 kPa for supply pressures 100, 150, and 200 kPa, respectively. The control pressure range to the supply pressure decreases with increasing supply pressure, which is due to lower ER effect for higher flow velocities.

An MRDA equipped with an ER valve was fabricated with 10 mm diameter and 17 mm length using the

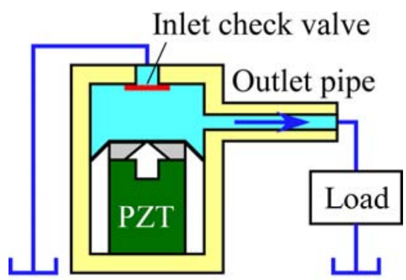

(a) Pumping period

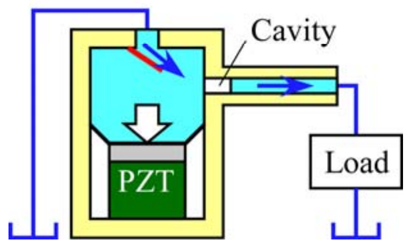

(b) Suction period

Figure 10 Working principle of FI micropump

MRDA fabricated in the previous section and the ER valve mentioned above. Figure 9 shows the measured static characteristics. As the control pressure range is almost same for the different supply pressures, the maximum output displacement is 0.9 mm at supply pressure 150 kPa at which the MRDA has linear characteristics without saturation. The output displacement has also hysteresis due to the characteristics of the MRDA.

FI MICROPUMP AND SEALED FLEXIBLE TANK

A piezoelectric micropump using fluid inertia (FI) effect in a pipe called the “FI micropump” [6] was newly developed for high viscosity fluids like ERFs.

Figure 10 shows schematics of the FI micropump. The pump consists of a reciprocating pump chamber driven by a multilayered PZT actuator, an inlet check valve, and an outlet pipe with small diameter. An accumulator, which consists of a flexible tube in this study, is attached to the outlet in the actual device and the outlet pressure is constant. In the chamber above the inlet check valve, a plastic diaphragm is installed as a buffer to maintain the inlet pressure constant in the actual device.

In a pumping period shown in Figure 10(a), the PZT actuator contracts the pump chamber, the inner pressure increases, the inlet check valve closes, and the working fluid flows out through the outlet pipe at a high flow velocity. In the subsequent suction period shown in Figure 10(b), the PZT actuator expands the pump chamber, the inner pressure decreases, and the working fluid flows in through the opened inlet check valve. At the same time, in the outlet pipe, the flow is going to

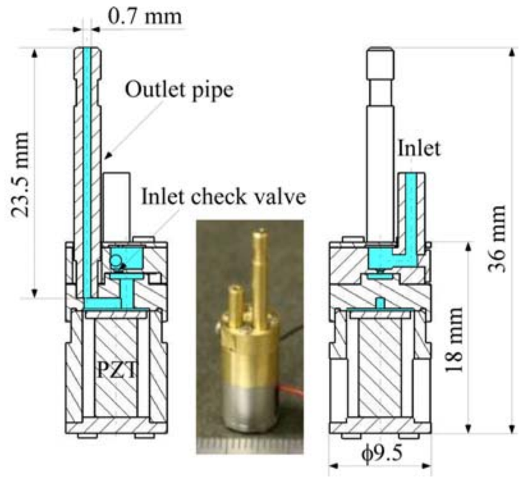

Figure 11 Fabricated FI micropump

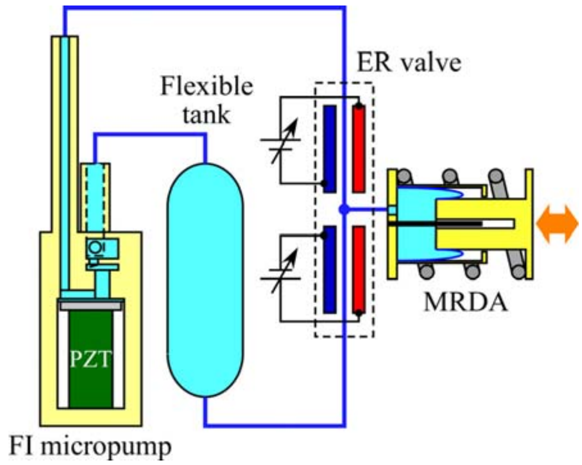

Figure 13 Micro mobile hydraulic system using ERF

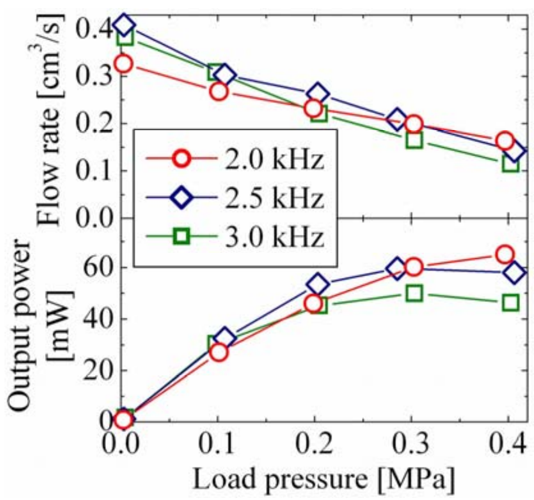

Figure 12 Measured load characteristics of FI micropump

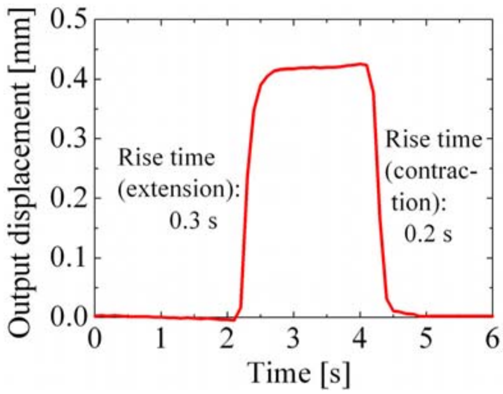

Figure 14 Measured output displacement of micro mobile hydraulic system

maintain due to the fluid inertia (FI) effect in the outlet pipe with a liquid column separation. Thus, the pump flows out the working fluid in not only the pumping but also the suction periods and realizes an outlet flow rate higher than the value estimated with the displacement. Through experiments, an output fluid power up to 0.22 W for water pumping has been realized by an FI micropump with 2.3 cm^3 in volume [6].

For pumping high viscosity fluids like ERFs, a multi-reed valve was proposed as the inlet check valve. Also, the size of the outlet pipe was optimized [9]. Figure 11 shows the fabricated FI micropump with 10 mm in diameter. The volume is 1.3 cm^3 which is 60 % of the previous pump [6].

Figure 12 shows the measured load characteristics of the FI micropump. The working fluid was silicone oil which had viscosity 19 mPa·s similar to the nematic liquid crystal used in this study. The driving voltage of the PZT actuator had 100 V_{pp} amplitude, 70 V offset, and frequencies of 2.0, 2.5, amd 3.0 kHz. The maximum output fluid power of 65 mW was obtained.

Furthermore, to adapt the posture and the ERF amount changes of the tank, a sealed flexible tank made of polyethylene film was fabricated with 1.5 cm^3 in volume.

MICRO MOBILE HYDRAULIC SYSTEM

By integrating the MRDA equipped with an ER valve, the FI micropump, and the sealed flexible tank, a micro mobile hydraulic system was constructed as shown in Figure 13.

Figure 14 shows an example of the measured step responses. The stroke 0.4 mm was successfully obtained, which shows the sealed tank system can work similar to a conventional open tank system. The rise times were 0.3 s for extension and 0.2 s for contraction.

CONCLUSIONS

In this paper, we proposed and developed a micro mobile hydraulic system using ERF which generates high power motion irrespective of the system posture. The main results are summarized as follows:

1) A micro rolling diaphragm actuator (MRDA) was proposed, which has compact structure, large extension ratio, and large output force.

2) An MRDA equipped with an ER valve was fabricated with 10 mm in diameter and experimentally characterized.

3) An FI micropump using fluid inertia (FI) effect in a pipe was developed with 9.5 mm in diameter for high viscosity fluids like ERFs.

4) A micro mobile hydraulic system was constructed by integrating the above-mentioned elements and the validity was confirmed experimentally.

REFERENCES

1. Takeda, M., Applications of MEMS to Industrial Inspection, Proc. MEMS 2001, 2001, pp. 182-191.
2. Yoshida, K., Takahashi, K. and Yokota, S., An In-Pipe Mobile Micromachine Using Fluid Power (A Mechanism Adaptable to Pipe Diameters), JSME Int. J.(Ser. B), 2000, **43**-1, pp. 29-35.
3. Yoshida, K., Park, J.-H., Yano, H., Yokota, S. and Yun, S., Study of Valve-Integrated Microactuator Using Homogeneous Electro-Rheological Fluid, Sensors and Materials, 2005, **17**-3, pp. 97-112.
4. De Volder, M., Yoshida, K., Yokota, S. and Reynaerts, D., The Use of Liquid Crystals as Electrorheological Fluids in Microsystems: Model and Measurements, J. of Micromechanics and Microengineering, 2006, **16**-3, pp. 612-619.
5. Yoshida, K. and Yokota, S., Study on High-Power Micro-Actuator Using Fluid Power, Preprints of the 6th Int. Conf. on Flow Measurement (FLOMEKO'93), 1993, **1**, pp. 122-130.
6. Yoshida, K., Jung, Y.-O., Seto, T., Takagi, K., Park, J.-H. and Yokota, S., A Piezoelectric Micropump Using Fluid Inertia in Pipe and Its Application, Proc. 6th JFPS Int. Symp. on Fluid Power, Tsukuba 2005, 2005, pp. 688-693.
7. March Bellofram homepage: http://www.marshbellofram.com/
8. De Volder, M. and Reynaerts, D., Pneumatic and Hydraulic Microactuators: A Review, J. of Micromechanics and Microengineering, 2010, **20**-4, 043001 (18pp).
9. Yoshida, K., Muto, T., Kim, J. W. and Yokota, S., An ER Microactuator with Built-in Pump and Valve, Proc. ACTUATOR 2010, 2010, pp. 556-559.

Proceedings of the 8th JFPS International
Symposium on Fluid Power, OKINAWA 2011
Oct. 25-28, 2011

2B2-3

PARAMETER OPTIMIZATION OF MEMS-BASED MICRO TRIANGULAR-PRISM-SLIT ELECTRODE PAIR AS AN ELECTRO-CONJUGATE FLUID JET GENERATOR

Hai-bo Wang*, Joon-wan Kim*, Shinichi Yokota* and Kazuya Edamura**

* Precision and Intelligence Laboratory
Tokyo Institute of Technology
R2-42, 4259 Nagastuta-cho, Midori-ku, Yokohama 226-8503, Japan
(E-mail: wang.h.ac@m.titech.ac.jp)
** New Technology Management Co. Ltd
2-9-1-306 Higashi-Shinkoiwa, Katsushika-Ku, Tokyo 124-0023, Japan

ABSTRACT

Study on electrodes, which are inserted into electro-conjugate fluid (ECF) and generate ECF jet, is still in progress. A sort of so-called triangular-prism-slit (TPS) electrode structure was proposed and it is often thought as a promising candidate for future ECF effect applications thanks to its relatively high performance and easy fabrication. Besides considering power density characteristic of ECF effect and miniaturization demands, micro TPS electrodes as minimal as several hundred micrometers show more attractive and significant. This paper is primarily about parameter optimization for micro TPS electrodes at a common operating point. The four researched structure parameters include thickness and slit width of slit electrode, tip angle of triangular-prism electrode and gap between them, while performance is evaluated by output pressure, flow rate and power. The micro TPS electrodes are fabricated by MEMS technology and the optimization work is realized by four corresponding groups of comparison experiments.

KEY WORDS

Functional fluid, Electro-conjugate fluid, Micro triangular-prism-slit electrode pair, Parameter optimization, MEMS

INTRODUCTION

Electro-conjugate fluid (ECF) is a kind of dielectric and functional fluid, which generates a powerful jet named ECF jet when electrodes inserted into it are subjected to a constant voltage of less than one thousand volts, as shown in Fig.1. Accordingly, this phenomenon that appears in the ECF is called ECF effect and electric energy is converted directly to kinetic energy of the ECF. Moreover it should be noticed that even though it is necessary to generate ECF jet with a high voltage, the current is always as low as several microamperes after voltage is applied.

Apart from the complicated theoretical principal on ECF effect temporarily, based on such interesting energy transformation process of ECF, various engineering applications have been proposed and studied. For examples, Fig.2 (a) presents a cylindrical-rotor-electrode type micromotor with 2mm inner diameter. A rotor with pairs of electrodes located on the surface is inserted in a cylindrical vessel. When high voltage is applied to the electrodes, the reaction force of the generated ECF jet flow is directly converted to rotation [1]. Fig.2 (b) demonstrates a liquid micro rate gyroscope with good impact resistance. ECF jet flow is produced by electrode array and continuously cools down two hot wires. If angular rate is applied to the gyroscope, the flowing ECF jet drifts due to Coriolis force, resulting in temperature difference for the hot wires. As a result, the output voltage from hot wire bridge will change because the electrical resistance of hot wires is related to temperature [2].

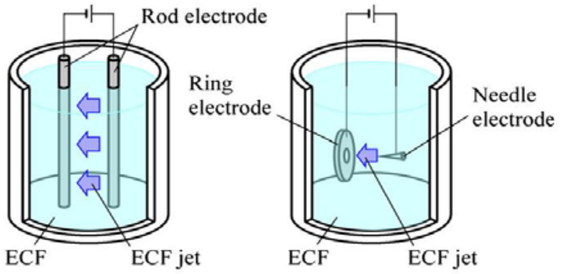

Figure 1 ECF effect

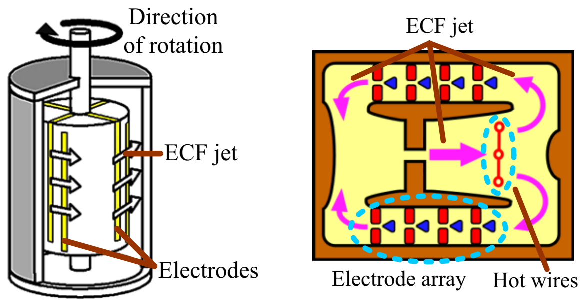

(a) (b)

Figure 2 Examples of ECF effect applications

According to numerous instances including the mentioned above, it is obvious that electrodes producing ECF jet possess a major influence on the performance of all ECF applications. Consequently, they have been investigated attentively since researchers were interested in the ECF phenomenon. Several electrode structures were proposed and developed, e.g. planar parallel rod-like electrode array as well as its derivatives, ring-needle electrode pair, and triangular-prism-slit (TPS) electrode pair or array, as shown in Fig. 3.

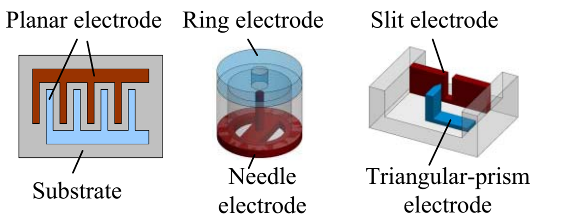

(a) Planar parallel electrode array (b) Ring-needle electrode pair (c) Triangular-prism-slit electrode pair

Figure 3 Electrode structure

Among these electrode varieties, the TPS electrode structure elongating vertical height of planar electrode patterns is often considered as the most promising electrode structure candidate for future's ECF effect applications, thanks to its great merits of combining relatively high performance and easy fabrication by MEMS technology or traditional machining [3, 4, 5].

Using ECF named FF-1EHA2 as working fluid, structure parameter optimization research for the TPS electrode structure at some operating points in several millimeters feature size was finished by a series of comparison experiments. Several significant design rules were well summarized. By reviewing this study, it shows that structure parameters, including thickness and slit width of slit electrode, tip angle of triangular-prism electrode and electrode gap between two electrodes, play great roles in performance of the usual TPS electrode pair [6]. However, in consideration of miniaturization demands of ECF effect applications and power density characteristic of ECF effect as shown in Fig.4, micro TPS electrodes as minimal as several hundred micrometers have higher power density and show more attractive, compared to electrodes in several millimeters or above feature size [7]. Therefore, this research conducts parameter optimization of micro TPS electrodes fabricated by MEMS technology in tiny dimension. Referring to the former research, structure parameters such as thickness, slit width, tip angle and electrode gap are still selected as studied parameters.

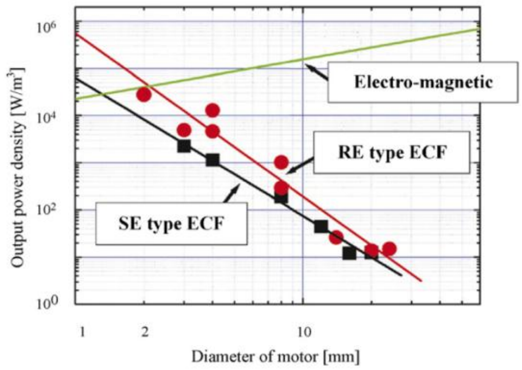

Figure 4 Comparison between ECF motors and electromagnetic motors

In this paper, research scheme and micro TPS electrode array are described in section 2. Then fabrication procedure of ECF jet generator is presented in section 3. Section 4 describes experimental apparatus. Finally, conclusion is given in section 5.

RESEARCH SCHEME AND MICRO TPS ELECTRODE ARRAY

Research scheme

As mentioned in introduction section, the researched parameters of the micro TPS electrode pair contain thickness, slit width, tip angle and gap which are indicated respectively by symbols t, w, θ and d illustrated in Fig.5.

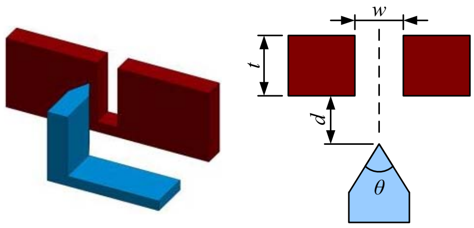

Figure 5 Structure parameters

Allowing for previous parameter optimization research scheme and conclusions on TPS electrode pair in several millimeters feature size, a common operating point shown in Table 1 is selected for the micro TPS electrode pair as well, and the influence of every parameter on its performance is evaluated by many comparison experiments in which every parameter is set to a series of discrete values near the operating point.

Table 1 Values of the operating point

Parameter	Thickness [μm]	Slit width [μm]	Tip angle [°]	Gap [μm]
Value	200	200	45	200

Moreover, an important assumption that the four structure parameters are independent and uncoupled is made to simplify our research issue. Consequently, all comparison experiments are divided into four groups corresponding to four parameters. In every group, the researched parameter varies near the operating point value and the other three parameters are equal to their corresponding values of the operating point. The parameter values of four comparison experiment groups corresponding to four researched parameters are listed respectively in Table 2.

Table 2 Parameter values of all comparison experiments

Group number	Corresponding parameter	Other parameters
1	Thickness t=200, 300, 400 μm	Slit width w=200 μm Tip angle θ=45° Gap d=200 μm
2	Slit width w=100, 200, 300 μm	Thickness t=200 μm Tip angle θ=45° Gap d=200 μm
3	Tip angle θ=30°, 45°, 60°	Thickness t=200 μm Slit width w=200 μm Gap d=200 μm
4	Gap d=150, 200, 250μm	Thickness t=200 μm Slit width w=200 μm Tip angle θ=45°

Micro TPS electrode array

For the purpose of generating relatively higher output pressure and flow rate, four pairs of micro TPS electrodes with high aspect-ratio is designed. One pair of electrode indicated here consists of one minus triangular-prism electrode and one plus slit electrode. All minus and plus electrodes are connected by their own thin copper conductor layer, respectively.

In addition, allowing for it difficult to finish sharp edge for MEMS fabrication process and we intend to reduce resistance of electrode shape to ECF jet flow, each intersection of plane surfaces on electrodes is change to arc transition. The final structure of micro TPS electrode array is illuminated in Fig.6.

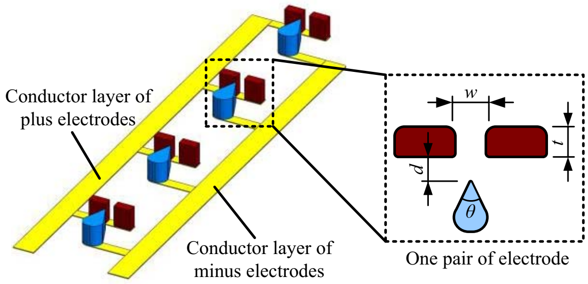

Figure 6 Structure of micro TPS electrode array

FABRICATION OF ECF JET GENERATOR

The fabrication processes of ECF jet generator, which is an assembly of micro TPS electrode array, case and sealing component, mainly contain production of micro TPS electrode array and final assembly.

Production of micro TPS electrode array

The micro electrode array is produced by ultraviolet (UV) photolithography. In order to obtain electrodes with high aspect-ratio, negative photoresist KMPR 1035 is used as a micromold for nickel electroplating to form the main part of electrodes. The height of electrodes is determined by thickness of the micromold and is designed to 500 μm to achieve higher aspect-ratio. In addition, all micro electrode arrays in twelve comparison experiments as shown in Table 2 are designed in one glass wafer to guarantee that all electrode arrays are finished in the same conditions and have nearly the same electrode height.

The complete fabrication process is illuminated in Fig.7 and explained as follows: (a) deposition of a titanium layer and a gold layer on a glass wafer successive; (b) spin coating, exposure and development of positive photoresist S-1805 and etching of gold layer and titanium layer one after another; (c) removal of unexposed photoresist S-1805; (d) nickel electroplating; (e) spin coating of negative photoresist KMPR 1035; (f) exposure and development of KMPR 1035; (g) RIE treatment and nickel electroplating; (h) removal of exposed KMPR 1035; (i) gold electroplating; (j) spin coating of negative photoresist SU-8; (k) exposure and development of Su-8 to form micro fluidic channels; (l) dicing wafer with electrode array.

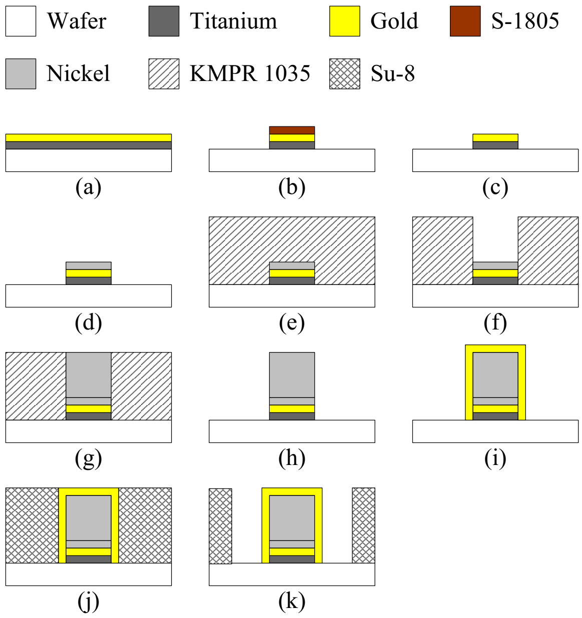

Figure 7 Fabrication process of micro electrode array

The finished twelve micro TPS electrode arrays in one wafer and one cutting electrode array with Su-8 fluidic channels, which correspond to step (i) and step (l) of fabrication process mentioned above, are given in Fig.8 and Fig.9, respectively.

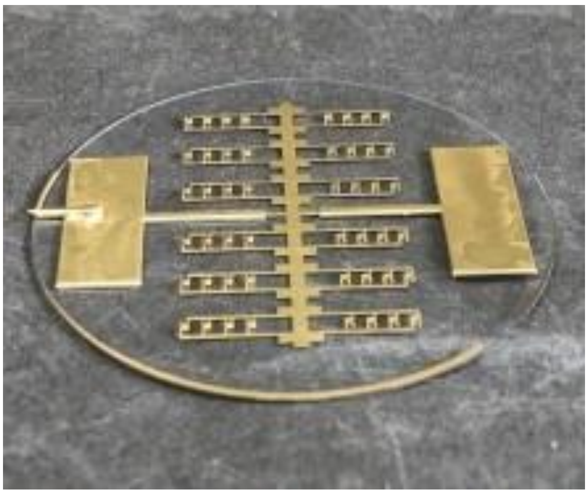

Figure 8 Finished micro TPS arrays

Assembly

Following finishing micro TPS electrode array with Su-8 micro fluidic channels, engineering plastic case and silicon sealing sheet, ECF jet generator is assembled as shown in Fig.10. The dimensions of finished ECF jet generator is 24mm×36mm×6mm.

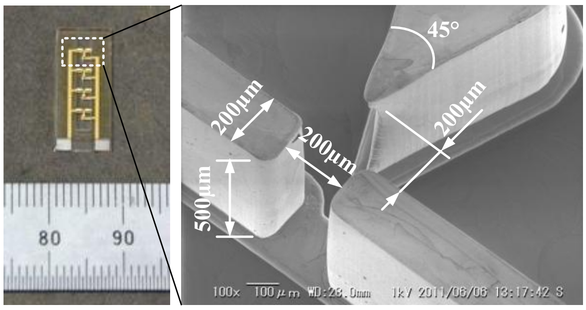

Figure 9 One micro TPS electrode array

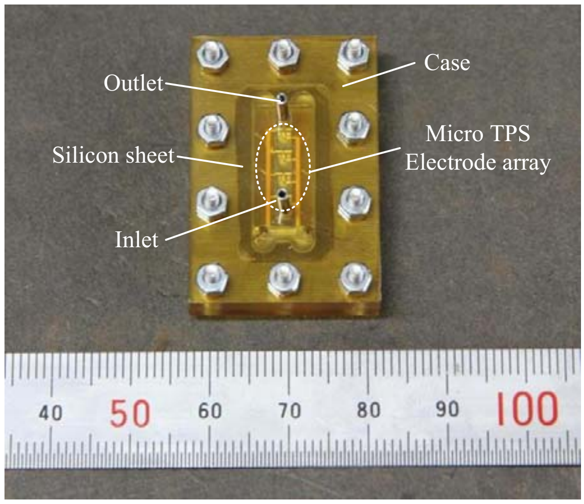

Figure 10 Assembly of an ECF jet generator

EXPERIMENTS

As the ECF, fluid named FF-8EHA2 is selected as the working fluid and its physical properties are listed in Table 2.

Table 2 Physical properties of ECF FF-8EHA2

Property	Value
Boiling point [°C]	61
Density [kg/m^3]	1.52×10^{3}
Viscosity [Pa·s]	0.58×10^{-3}
Electric conductivity [S/m]	1.20×10^{-6}

Among all comparison experiments, performance of ECF jet generator is evaluated by output pressure, flow rate and power. As shown in Fig.11, the experimental apparatus consists of an ECF jet generator, a high voltage power supply, a digital ammeter, a pressure sensor and a flow rate meter. Output pressure and flow rate of the ECF jet generator are measured by pressure sensor and flow rate meter, while output power is calculated by experimental data. The height h of tube outlet can be changed to apply load on output of ECF jet generator and get its flow rate with load.

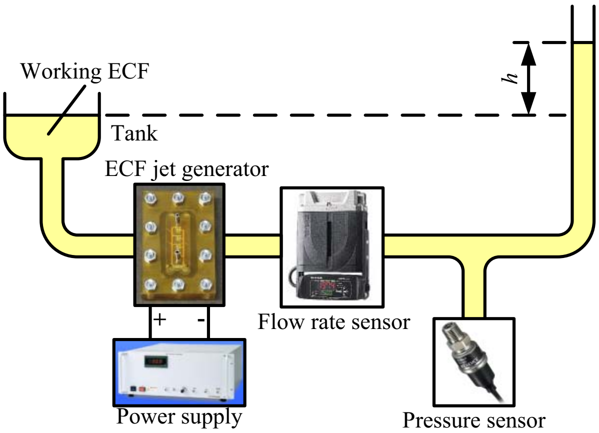

Figure 11 Experimental apparatus

Because of the slow plating speed of nickel electroplating step, the comparison experiments have not completely finished on time before the paper submission. So in the near future, all comparison experiments and parameter optimization work for micro TPS electrode pair will be conducted using experimental system shown in Fig.11.

CONCLUSIONS

Compared to usual TPS electrode pair in several millimeters feature size, study on micro electrode pair as minimal as several hundred micrometers shows more significance for future's ECF effect related applications in consideration of characteristic of ECF effect and miniaturization demands of corresponding devices. As a result, parameter optimization of micro TPS electrode pair near a common operating point (thickness 200μm, slit width 200 μm, tip angle 45° and gap 200μm) was carried on by four groups of comparison experiments in this paper. Moreover, whole twelve micro TPS electrode arrays with four pairs of high aspect-ratio electrodes were fabricated on one wafer to maintain the nearly same electrode height and production conditions. Finally, in the near future, all comparison experiments will be conducted and some useful design rules for micro TPS electrode structure will be obtained as well.

ACKNOWLEDGEMENT

This work was supported in part by a Grant-in-aid for Encouragement of Young Scientists (B) #21760108 of the Ministry of Education, Culture, Sports, Science and Technology of Japan.

REFERENCES

1. S., Yokota, and K., Edamura, New construction of an electro-conjugate fluid-jet driven micromotor with an inner diameter of 2 mm, Proc. of IMechE, Part I: J. Systems and Control Engineering, 220, 4, pp.251-256.
2. Tsunehiko, Imamura, Toshiya, Suzuki, Joon-wan, Kim et al, Miniaturization of ECF Micro Rate Gyro by using MEMS technology, Proc. of 14th ICMT2010, pp.303-308.
3. Woo-Suk, Seo, Kazuhiro, Yoshida, Shinichi Yokota et al, A high performance planar pump using electro-conjugate fluid with improved electrode patterns, Sensors and Actuators A, 2007, 134(2), pp. 606-614.
4. Joon-wan, Kim, Toshiya, Suzuki, Shinichi, Yokota et al, Tube-type micropump by using electro-conjugate fluid (ECF), Proc. of 13th ICMT2009, CD-ROM.
5. Ryutaro, Abe, Kenjiro, Takemura, Kazuya, Edamura et al, Concept of a micro finger using electro-conjugate fluid and fabrication of a large model prototype, Sensors and Actuators A, 2007, 136(2), pp. 629-637.
6. Hai-bo, Wang, Joon-wan, Kim, Shinichi, Yokota et al, Performance evaluation of a triangular-prism-slit electrode pair as an ECF-jet generator, Proc. of JSME ROBOMEC2010, CD-ROM.
7. Kenjiro, Takemura, Hiroto Kozuki, Kazuya Edamura et al, A micromotor using electro-conjugate fluid—improvement of motor performance by using saw-toothed electrode series, Sensors and Actuators A, 2007, 140(1), pp. 132-137.

Proceedings of the 8th JFPS International
Symposium on Fluid Power, OKINAWA 2011
Oct. 25-28, 2011

2B2-4

NEEDLE-RING ELECTRODE PAIR AS AN ECF-JET GENERATOR BY USING MEMS TECHNOLOGY

Joon-wan KIM *, Shinichi YOKOTA * and Kazuya EDAMURA **

* Precision and Intelligence Laboratory
Tokyo Institute of Technology
R2-42, 4259 Nagatsuta-cho, Midori-ku, Yokohama 226-8503 Japan
(E-mail: woodjoon@pi.titech.ac.jp)
** New Technology Management Co. Ltd
2-9-1-306 Higashi-Shinkoiwa, Katsushika-Ku, Tokyo 124-0023, Japan

ABSTRACT

We are studying microactuators using an electrode-conjugate fluid (ECF). ECF is a functional fluid that produces a powerful flow (ECF-jet) between an electrode pair which is subjected to high DC voltage. In our past experiments, we realized that pressure generated by this ECF-jet increased with downsizing of the electrode pair. Therefore it is considered that the pressure due to ECF-jet is useful as a driving source of the microactuator. We confirmed that high pressure was obtained by a needle-ring electrode pair composed of a needle-shaped electrode and a ring-shaped electrode, but there were the problems in the reproducibility and downsizing of the electrode pair in a current method. In addition, one needle-ring electrode pair is insufficient for high flow rate. In order to solve those problems, we propose a MEMS fabrication method for multiple needle-hole electrode pairs.

KEY WORDS

MEMS, Electro-conjugate fluid (ECF), ECF-jet generator, Microactuator, Integration

INTRODUCTION

Numerous microactuators have been studied and developed, since microactuators are the key devices to give rise to fundamental movement in the world of microscale. There have been many kinds of microactuators, such as electromagnetic, electrostatic, piezoelectric, shape memory alloy, pneumatic, and functional fluid-driven microactuators. Among microactuators, we have focused on an electro-conjugate fluid (hereafter ECF) as a driving force of advanced microactuators. ECF is a kind of functional and dielectric fluid. A strong and active jet flow of ECF is generated between electrodes surrounded by ECF when high DC voltage is applied to the electrodes. This phenomenon called as ECF effect shown in Figure 1 is a promising candidate for micro actuation, thanks to the advantages of miniaturization and high output power density. The previous experimental results of ECF motors whose diameters of their stators are down to 1 mm proved that the smaller ECF motors had the characteristic of the higher output power density, being remarkably desirable for miniaturization [1]. In addition, a needle-ring electrode pair designed for high electric field intensity at the tip of the needle electrode was developed, showing its effectiveness and suitability in micro size [2].

Although the needle-ring electrode pair was confirmed as an ECF-jet generator for high pressure, there were the problems in the reproducibility and the downsizing for reliable microactuators due to difficulties in the tradition way of precision machining process and hand-assembling. At the same time, one needle-ring electrode pair is insufficient for high pressure and high flow rate in the field of some applications.

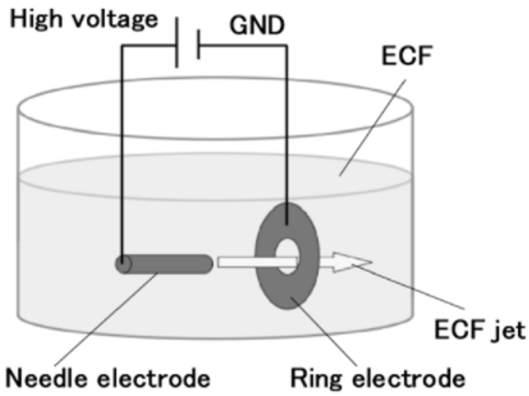

Figure 1 ECF-jet effect by a needle-ring electrodes

In order to overcome these difficulties, MEMS fabrication technology can be an effective candidate, thanks to the following advantages: (a) miniaturization, to create very small electrodes for ECF-jet; and (b) batch process, to produce many identical ECF-jet generators at the same time on one wafer. The miniaturization makes it possible to easily and reliably fabricate multiple needle-hole electrode pairs in an ECF-jet generator, resulting in parallel ECF-jets for the higher flow rate and quicker dynamic response. In addition to the advantage of parallelization, high pressure can be realized by serializing these identical ECF-jet generators resulting from the batch process.

Although MEMS fabrication technology has these advantages mentioned above, there is a difficult problem to have to overcome. Since the ordinary MEMS technique using photolithography is basically a plane geometry process, inducing the shape-limit of simple 3D structures whose aspect ratio is low, it is difficult to fabricate micro needle structure of high aspect ratio at once. Therefore we conceive and utilize an advanced MEMS fabrication method based on the combination of micro-mold formation by thick photoresist and Ni electroplating. In addition, we propose a multilayer fabrication that divides complex 3D microstructures into several layers of column-limited microstructures and builds one layer by one layer. Before realizing MEMS-fabricated needle-hole electrode pairs, in section 2, we investigate the characteristics of serialized and parallelized electrode pairs by using the prototypes fabricated by the precision machining process and hand-assembling. Based on the optimal values investigated experimentally in section 2, multiple needle-hole electrode pairs as an ECF-jet generator is proposed in section 3 and fabricated by using MEMS technology in section 4. Finally, this study is concluded in section 5.

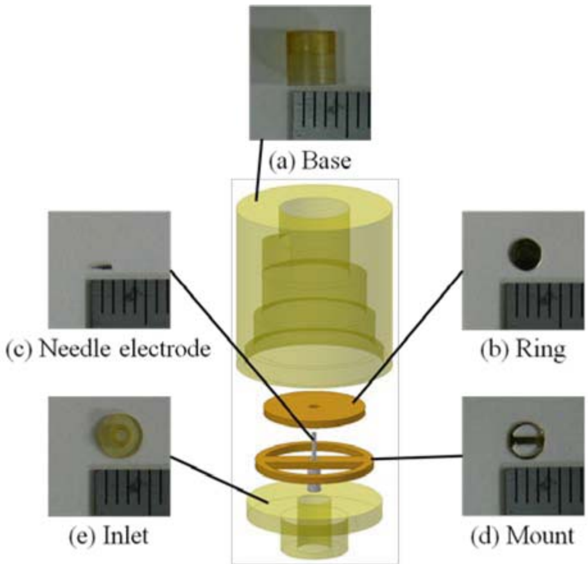

(A) Structure and components of ECF-jet generator

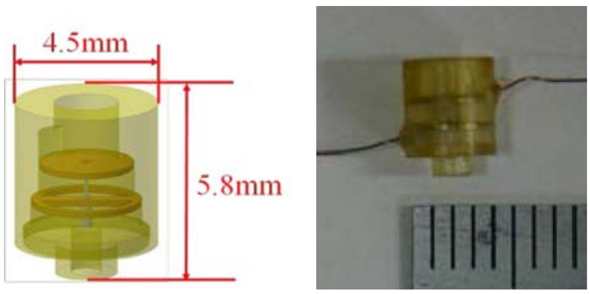

(B) Dimensions (C) Assembled ECF-jet generator

Figure 2 ECF-jet generator
with a needle electrode and a ring electrode

SERIALIZATION AND PARALLELIZATION OF ECF-JET ELECTRODE PAIRS

In order to realize micro hydraulic power source, an ECF-jet generator with a needle-ring electrode pair has been studied. According to the assumption that one pair of a needle electrode and a ring one can make the same performance, the serialization of needle-ring electrode pairs will induce the increase of pressure, while the parallelization will increase the flow rate. By using the prototypes made by precision machining process and hand-assembling, we investigate the effectiveness and feasibility of the serialization and parallelization of ECF-jet electrode pairs.

Fabrication of prototypes

Based on our previous research [3], main dimensions of a needle-ring electrode pair are as follows: 0.13 mm in diameter of a needle electrode; 0.3 mm in inner diameter of a ring electrode; 0.2 mm in thickness of a ring electrode; 0.25 mm in the gap between a needle electrode and a ring one. The needle electrode is made of tungsten, while the ring electrode is made of brass. The other plastic components are made of polyetherimide resin (UL-1000). The needle electrode is fixed to the mount by using electrically-conductive adhesive. Both electrodes are attached to the base by two-component epoxy adhesive. The schematic diagram and components of a prototype are shown in Figure 2. In addition to ECF-jet generator with only one pair of the electrodes, ECF-jet generators with two needles and three needles in parallel are fabricated and shown in Figures 3 and 4, respectively. These three types of ECF-jet generator, shown in Figures 2, 3, and 4, have the same dimensions except number of needles and different shapes of mounts. The prototypes with three types of needles are formed in one unit for the parallelization, while the prototypes for the serialization are realized by directly connecting these two units.

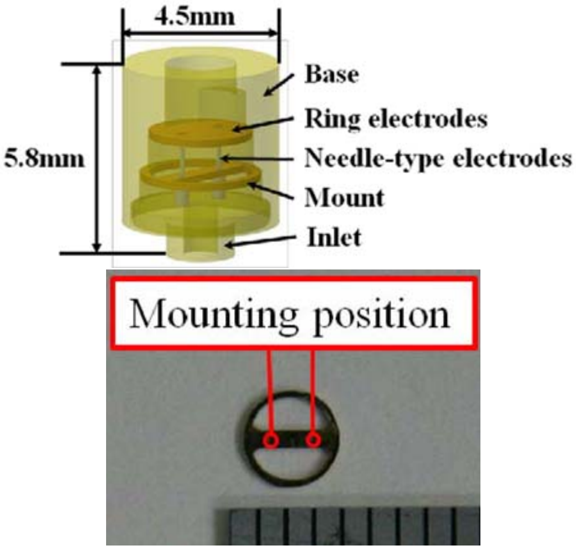

Figure 3 ECF-jet generator with two needle electrodes

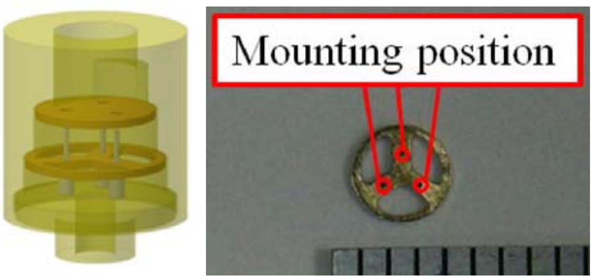

Figure 4 ECF-jet generator with three needle electrodes

Characteristics of the serialization and parallelization

We calculated the output pressure generated by the prototype, by measuring the height of liquid surface in a tube, shown in Figure 5. The flow rate was obtained by using the experimental setup shown in Figure 6. By measuring weight in fixed time, we can calculate the flow rate of ECF-jet generators. The load pressure can be adjusted by changing the height of an outlet tube.

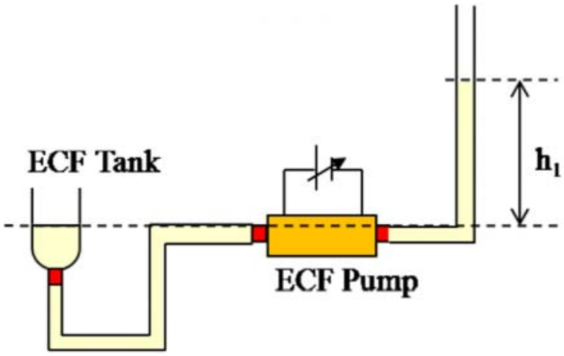

Figure 5 Experimental setup to measure the output pressure (by measuring the height of ECF level)

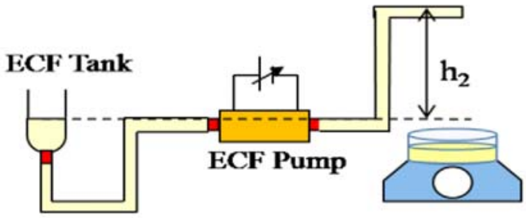

Figure 6 Experimental setup to measure the flow rate (load pressure adjusted by the position of outlet tube)

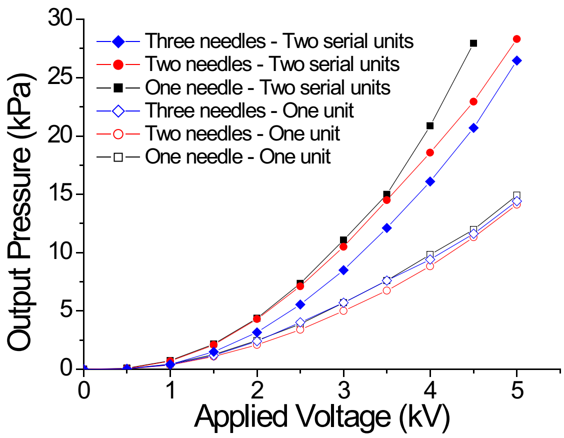

Figure 7 Output pressure without flow of ECF

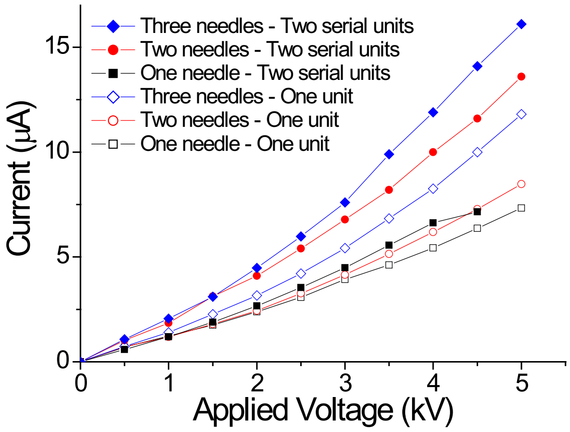

Figure 8 Electric current vs applied voltage (in case of output pressure measurement)

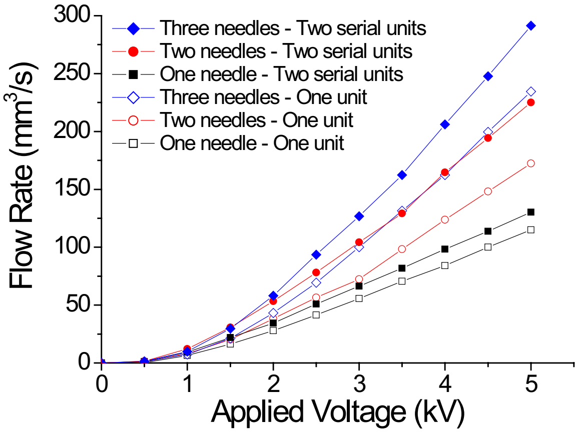

Figure 9 Flow rate without load pressure

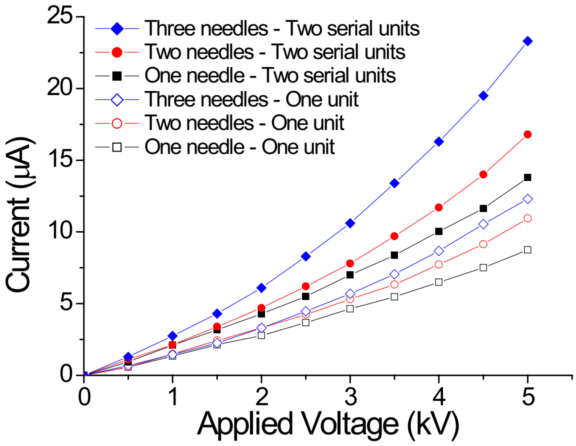

Figure 10 Electric current vs applied voltage (in case of flow rate without load pressure)

To investigate the output pressure and flow rate of the serialization and parallelization, we used six types of ECF-jet generators: one needle-hole electrode pair and one unit of ECF-jet generator; two needle-ring electrode pairs in parallel and one unit; three needle-ring electrode pairs in parallel and one unit; one needle-hole electrode pair and two units; two needle-ring electrode pairs in parallel and two units; and three needle-ring electrode pairs in parallel and three units.

The output pressure and its corresponding electric current are shown in Figures 7 and 8, respectively. As shown in Figure 7, output pressures of two units are approximately twice larger than those of the one unit at the applied voltage of 5 kV in all types of parallelized electrode pairs, respectively. On the other hand, output pressures of parallelized electrodes are almost same in case of the one unit. Although output pressure slightly decreases with parallel increase of the electrode pairs in case of two serial units, output pressure has not significant difference as well. The electric current also increase, as the number of the parallel electrodes pairs and the serial units of ECF-jet generators.

In addition to the characteristics of output pressure, the flow rate characteristics of ECF-jet generators are also investigated experimentally, shown in Figures 9 and 10. The serialization as well as the parallelization makes the flow rate to increase dramatically. The electric current shown in Figure 10 is also proportion to the numbers of the serial and parallel electrode pairs.

According to these experimental results mentioned above, we found that the serialized ECF-jet generator can increase the output pressure and the flow rate, while the parallelized one can make the flow rate higher.

PROPOSITION OF MEMS-FABRICATED ECF-JET GENERATOR

The ECF-jet generator in this paper consists of the needle electrode on the support structure, spacer, and the hole electrode, shown in Figure 11. To realize the ECF-jet generator by MEMS fabrication technology, we used two kinds of thick photoresists: KMPR (Microchem Corp.) as a micromold for nickel electroplating; and SU-8 (Microchem Corp.) as a spacer material. The fabrication procedure is shown in Figure 12. First, sacrificial layer of fluoro-carbon and seed layer of Au/Ti are formed, in order to release the needle electrode from a wafer and to raise the nickel structure through a micromold, respectively (Figure 12, A). The mold is formed by KMPR process and a support structure is made by the electroplating of nickel (Figures 12, B and C). By electroplating nickel as the needle electrode after laminating and patterning KMPR as a micro-mold, the needle electrode is formed on and unified with the support structure. After the mold is removed, MEMS-fabricated needle electrode for the ECF jet is completed (Figures 12, D and E). To make the ECF-jet generator, the spacer is formed after the needle electrode fabrication (Figure 12, F). The hole electrode is separately fabricated and combined with the needle electrode by using bonding layer (Figures 12, G and H).

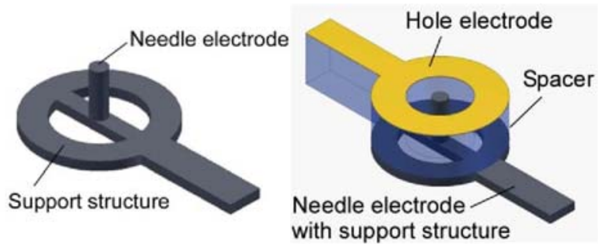

Figure 11 Schematics of ECF-jet generator proposed by MEMS fabrication technology

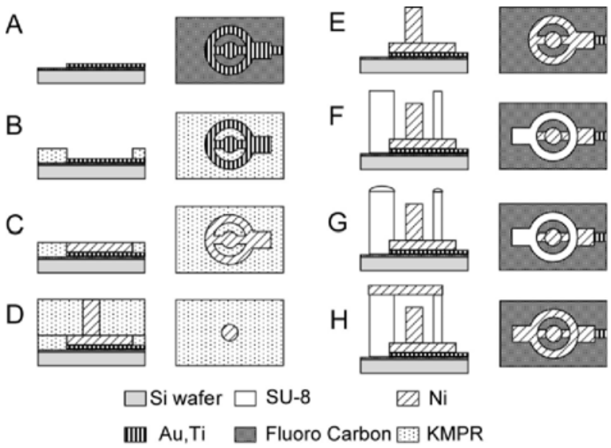

Figure 12 Fabrication procedure of the MEMS-based needle-ring electrode pair

FABRICATION OF MULTIPLE NEEDLE ELECTRODE FOR ECF-JET GENERATION

Inner and outer diameters of the support structure are 1.4 mm and 2 mm, respectively, while the thickness of the structure is 70 μm. In order not to reduce the flow rate, supporting arms are designed to have narrow width that is 100 μm. Instead of reducing the width, the number of supporting arms should be increased, as shown in Figure 13 and 15. The targeted dimensions of the needle are 200 μm in diameter and 130 μm in height. The micro-molds shown in figure 13 were formed by KMPR (MicroChem Corp.) and the support structures, whose height is about 70 μm were made by the electroplating of nickel. By forming micro-molds shown in Figure 14 and electroplating nickel, the multiple needle electrodes were fabricated. Removing micro-mold, we successfully fabricated the multiple needle electrodes shown figure 15, whose height is about 130 μm.

Figure 13 Micromolds for support structures

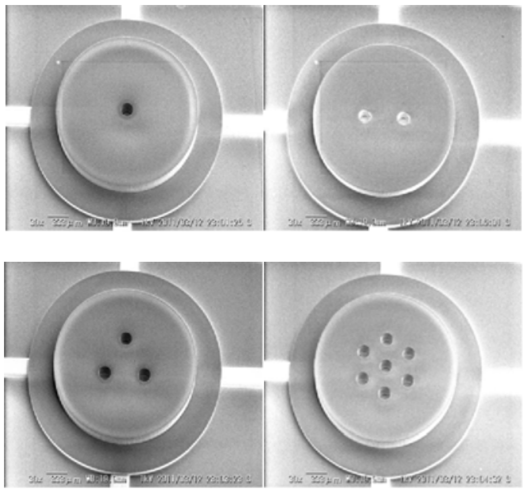

Figure 14 Micromolds for multiple needles

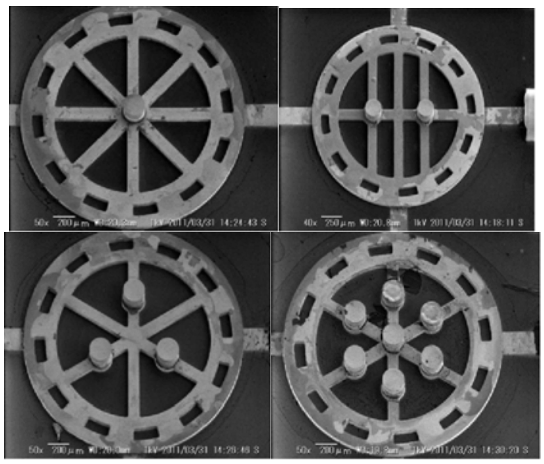

Figure 15 Fabricated needle electrodes

All dimensions of fabricated electrodes are in good agreement with designed dimensions.

CONCLUSIONS

To realize the easy fabrication and high performance, a novel ECF-jet generator with multiple needle electrodes was proposed and micro-needles were successfully fabricated by MEMS technology. The serialization and parallelization of ECF-jet generators was investigated experimentally by using the prototypes fabricated by mechanical machining and hand assembly. The experimental result proved that the serialization and parallelization is very effective to improve the performance. The MEMS-fabricated structure and the experimental results showed the feasibility of an advanced ECF-jet generator.

REFERENCES

1. Yokota, S., Kawamura, K., Takemura, K., and Edamura, K., A High-Integrated Micro-motor Using Electro-conjugate Fluid (ECF), the Journal of Robotics and Mechatronics, 2005, Vol.17, No.2, pp.142-148.
2. Yokota, S., Abe, R., Takemura, K., and Edamura, K., Micro Finger Driven by Electro-conjugate Fluid jet (ECF-jet) and Characteristics Evaluation of a Large Model, Sensors and Actuators A, 2007, Vol.136, issue.2, pp.629-637.
3. Yokota, S., Yajima, F., Takemura, K., and Edamura, K., ECF-jet driven Micro artificial antagonistic muscle actuators and its integration, the Journal of Advanced Robotics, 2010, Vol.24, No.14, pp.1929-1934

Proceedings of the 8th JFPS International
Symposium on Fluid Power, OKINAWA 2011
Oct. 25-28, 2011

2B3-1

THE CONTROL OF A BELLOWS ACTUATOR USING ELECTRO-CONJUGATE FLUID

Kento Mori*, Akihiro Yamaguchi*, Kenjiro Takemura**
Shinichi Yokota***, Kazuya Edamura****

* School of Integrated Design Engineering
Keio University
3-14-1 Hiyoshi, Kohoku-ku, Yokohama, 223-8522 Japan
(E-mail: k.wave81.4@gmail.com)
** Department of Mechanical Engineering
Keio University
3-14-1 Hiyoshi, Kohoku-ku, Yokohama, 223-8522 Japan
*** Department of Mechano-micro Engineering
Tokyo Institute of Technology
4529 Nagatsuta-cho, Midori-ku, Yokohama, 226-8503 Japan
**** New Technology Management Co., Ltd
2-9-1 Higashishinkoiwa, Katsushika-ku, Tokyo, 124-0023 Japan

ABSTRACT

An electro-conjugate fluid (ECF) is a kind of dielectric fluid which generates a powerful flow when subjected to high DC voltage. The ECF is a promising micro fluid power source (an ECF pump) for actuators including soft actuators, bellows actuators etc. For today control method of these actuators has not been investigated well. In almost all ECF researches, ECF actuators have been controlled only by ON/OFF control except the research reporting PD control for an ECF artificial muscle. In the research the gains of controller are determined just by experiment. Thus a control system designed by the control model has yet to be developed for ECF actuators. In this research we propose the control model of the ECF pump. By using this model, we develop a bellows actuator control system for ECF pump to realize good response.

KEY WORDS

Electro-conjugate fluid, Electrohydrodynamics, Functional fluid, Control system, Bellows actuator

NOMENCLATURE

t: Time
p: Pressure
p_T: Target pressure
p_O: Output pressure
V: Voltage
V_E: Estimated Voltage
V_{PI}: Voltage calculated by PI controller
T: Time constant

K: Gain
K_P: P gain of PI controller
K_I: I gain of PI controller
f: Frequency
m: Weight
μ: Viscosity
k: Spring coefficient
A: Area of bellows head

INTRODUCTION

The electro-conjugate fluid or ECF is a dielectric fluid. Applying a high voltage of several kilovolts between electrodes inserted into the fluid with an interelectrode gap of several hundred micrometers, we can observe a powerful flow between the electrodes as shown in Fig. 1. This flow can be used as a micro fluid power source (an ECF pump). A mechanism of the ECF flow generation could be found in Ref. [1, 2]. Although a high voltage is required to generate the ECF flow, the current is quite low at several microamperes.

Some actuators (motors [3], soft actuators [4], etc.) are driven by the ECF pump. For today the control of these actuators has not been investigated well. In almost all ECF researches, the ECF actuators have been controlled only by ON/OFF control. Since repeatability of pressure generated with ECF pump is limited, the control system should be constructed as a feedback system. There is the research reporting PD control for ECF artificial muscle [5]. However in this research the gains of controller are determined just by observing experimental responses. Thus a control system designed using the control model has yet to be developed for ECF actuators.

In this research we propose the control model of the ECF pump. By using this model, first, we develop an ECF pump control system. Then we develop a bellows actuator control system to realize good responses.

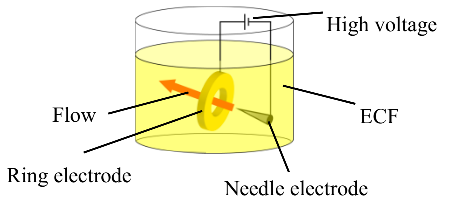

Figure 1 Schematic diagram of ECF flow

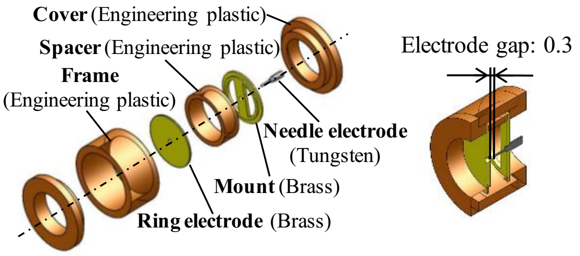

(a) Exploded view (b) Cross sectional view

Figure 2 ECF Pump

THE CONTROL OF PRESSURE GENERATED WITH THE ECF PUMP

Experimental Setup

First, we develop an ECF pump control system. In this system, pressure generated with the ECF pump is controlled by voltage applied to the ECF pump. The ECF pump is shown in Fig. 2. This pump which has a pair of needle-ring electrode is generally used as power source for actuators. Fig. 2 (a) is an exploded view of an ECF pump, and Fig. 2 (b) is a cross sectional view when constructed. The dimensions of electrodes are determined based on the experimental data reported in the previous report [6]. The outer diameter of a needle electrode is 0.13 mm, the inner diameter of a ring electrode is 0.3 mm, and the electrode gap is 0.3 mm. The polarity of needle electrode is GND, and that of ring electrode is positive. The flow is generated from the needle tip to the ring when applied high DC voltage. In this research we use FF-101EHA2 (New technology management) as a working fluid.

Fig. 3 shows an experimental setup of the ECF pump control system. High voltage is applied to the ECF pump via a high voltage amplifier (HV-10P (A), Matsusada precision). The pressure generated by the ECF pump is measured with a pressure gauge (PSE563-01, SMC). Note that an ECF tank, an ECF pump and a pressure gauge are filled with ECF. The output signals from the pressure gauge are sent to a computer through an A/D converter (AD112-16 (PCI), CONTEC). An applied voltage to the ECF pump is calculated in the computer, and applied to the ECF pump via a D/A converter (AIO-160802AY-USB, CONTEC) and high voltage amplifier.

The Control Model

First, we propose a model of ECF pump. The relation between the applied voltage and the pressure of ECF pump is shown in Fig. 4. According to this graph, pressure is almost proportional to the square of applied voltage. In addition the responses of pressure when applied step input from 0 to 1-6 kV voltage are shown in

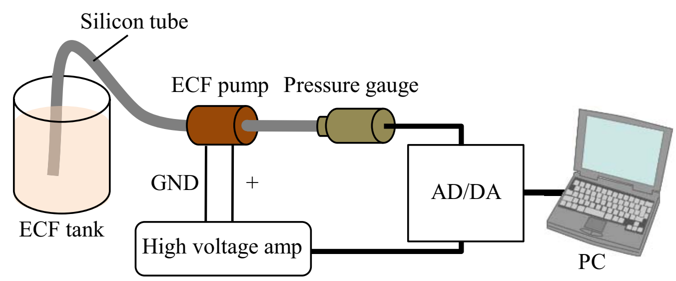

Figure 3 Experimental setup (The ECF pump control system)

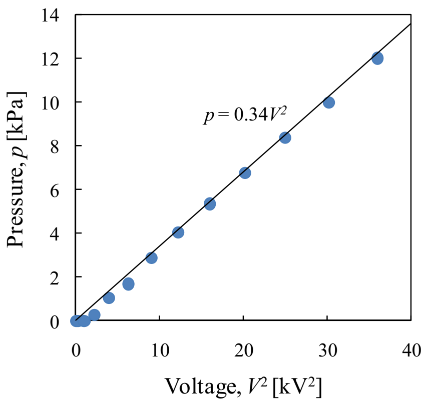

ssure

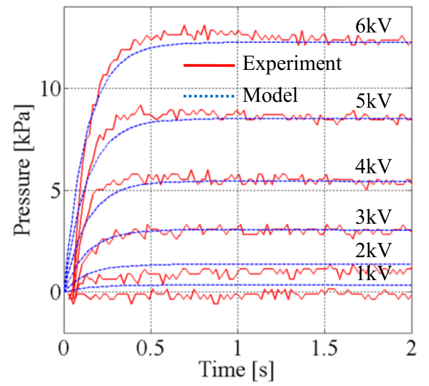

Figure 5 Step responses of pressure

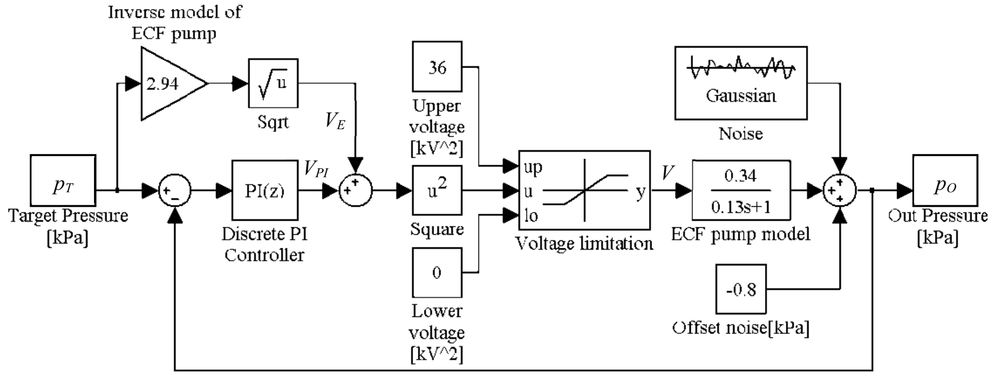

Figure 6 The ECF pump control model

Fig. 5. According to this graph, the pressure response could have first order lag. Thus we propose the model of ECF pump as,

$$T\frac{dp}{dt} + p = KV^2 \tag{1}$$

where t, p, V, T and K represent time, pressure, voltage, time constant, and gain. T, K is determined from the relation of Fig. 4 and Fig. 5. In Fig. 5 the response of the ECF pump model is shown as dash line. According to Fig. 5 the responses of the model fit closely with experimental results.

Then, a control model is constructed using the ECF pump model. A block diagram of a control model is shown in Fig. 6. First, estimated voltage V_E is calculated by target pressure p_T as,

$$V_E = \frac{1}{K}\sqrt{p_T} \tag{2}$$

This equation can be obtained from the relation shown in Fig. 4. Second, voltage V_{PI} is calculated from the difference between the target pressure p_T and the output pressure p_O by the PI controller as,

$$V_{PI} = K_P(p_T - p_O) + K_I\int(p_T - p_O)dt \tag{3}$$

where K_P and K_I are P gain and I gain, respectively. Finally, the voltage V calculated as the following equation is applied to the ECF pump.

$$V = V_E + V_{PI} \tag{4}$$

The applied voltage V should not be higher than 6kV in order to prevent electric discharge. Then, the pressure generated with the ECF pump is calculated using voltage V by Eq. (1). Finally, offset noise and Gaussian noise are added. The offset noise represents the instability of pressure generated with the ECF pump. In addition, the Gaussian noise represents the noise observed in the output signal of pressure gauge.

The Control Response

We aim to improve the step response by appropriately adjusting PI gains. The PI gains are adjusted by observing the step responses of the control model shown in Fig. 6. Fig. 7 (a) shows the step responses of the model with/without the PI controller. In this graph, the target pressure is a step input from 0 to 6 kPa. Fig. 7 (b)

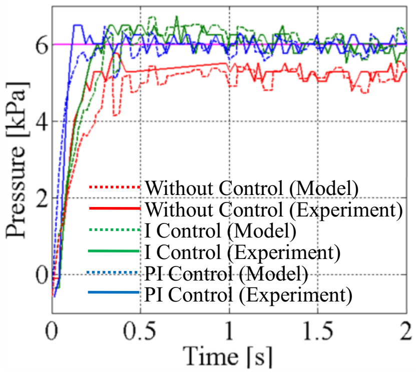

(a) Pressure

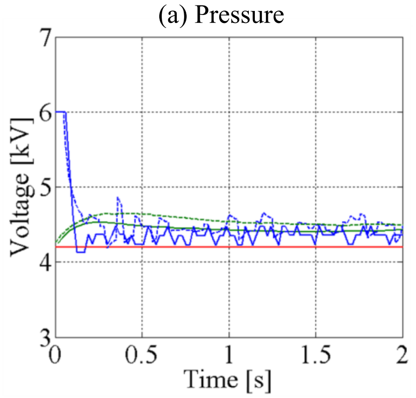

(b) Voltage

Figure 7 Step responses

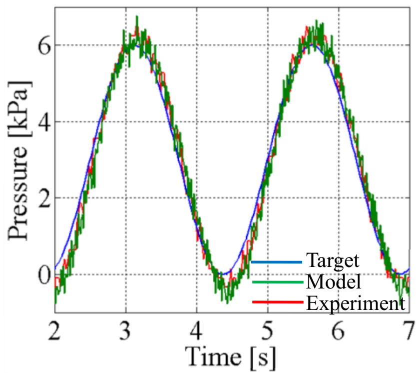

(a) 0.4 Hz

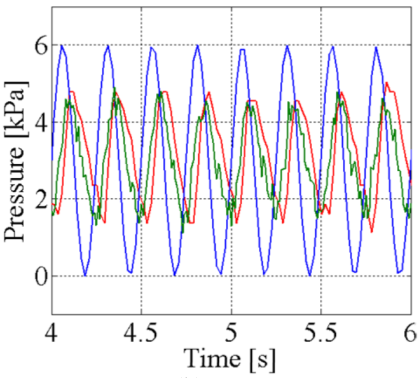

(b) 4 Hz

Figure 8 Frequency responses

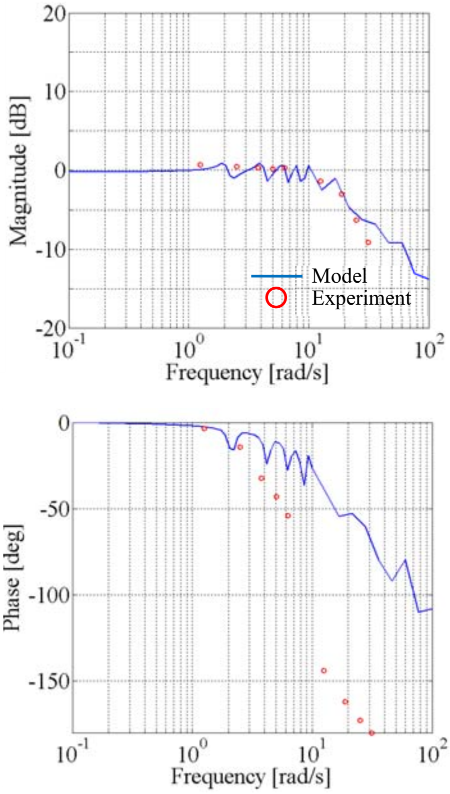

Figure 9 Bode diagram

shows the time history of the applied voltage. Without PI control, steady state error was observed. This error occurs due to offset noise which represents the instability of pressure generated with the ECF pump. Then with I control, steady state error is resolved. Furthermore with PI control, response speed improves, and rise time decreases by half. According to the time history of applied voltage, maximum voltage 6 kV is applied to ECF pump just after control starts. This causes the improvement of the response speed.

The experiment is also conducted with the same control condition. These results are shown in Fig. 7. In this graph, the pressure responses and the time history of applied voltage are corresponding to those of simulation results. Hence we could effectively design a control system using the proposed control model.

Then we observed frequency response using the same control system. The target pressure p_T is defined as,

$$p_T = 3\sin(2\pi f t) + 3 \quad \text{kPa} \tag{5}$$

where f is frequency [Hz]. Fig. 8 shows the responses when frequency f is 0.4 Hz and 4 Hz. When frequency f is 0.4 Hz the pressure p_T follows the target pressure p_T, i.e., the amplitude reduction and the phase lag are not observed. On the other hand, the phase lag and the

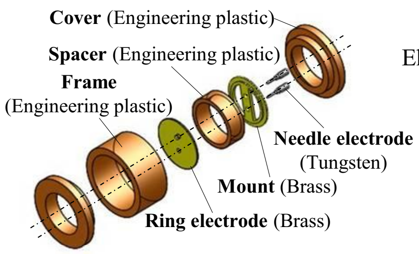

(a) Exploded view

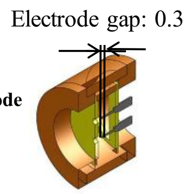

(b) Cross sectional view

Figure 10 Two needle ECF Pump

amplitude reduction are observed with the frequency of 4 Hz. In this frequency, the amplitude reduction of experiment is almost corresponding to that of the model. However the phase lag of experiment is slightly bigger than that of the model. We observed responses in wider frequency range, and these results are shown in Fig. 9 as a form of bode diagram. As in the Fig. 9, the phase lag of experiment is bigger than that of the model with relatively high frequency. This result suggests the ECF pump model might be comprehended the second order lag.

CONTROL OF BELLOWS ACTUATOR USING ECF PUMP

Experimental Setup

Next, we develop a bellows actuator control system

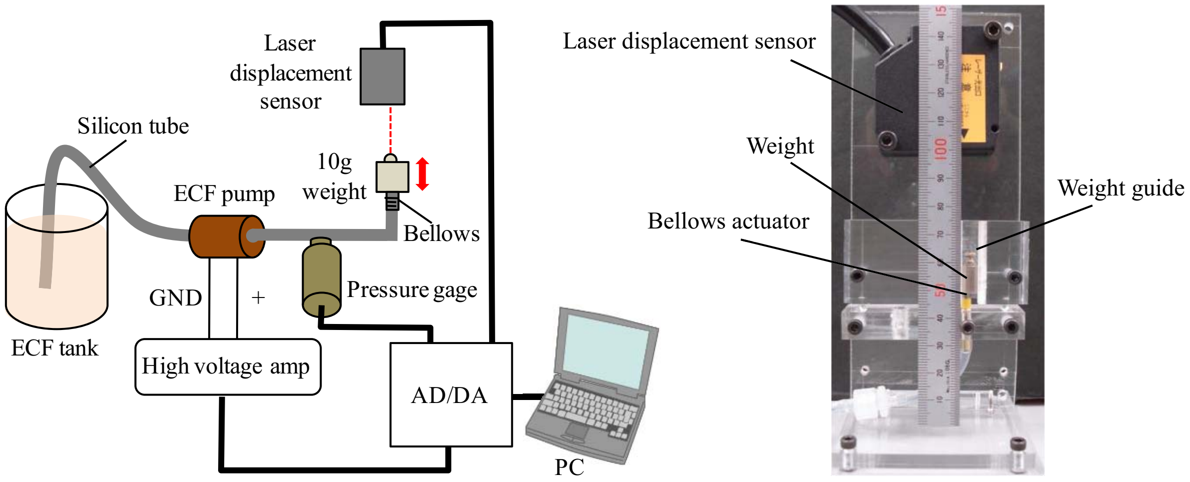

(a) Overall view (b) View around the bellows actuator

Figure 11 Experimental setup (The bellows actuator control system)

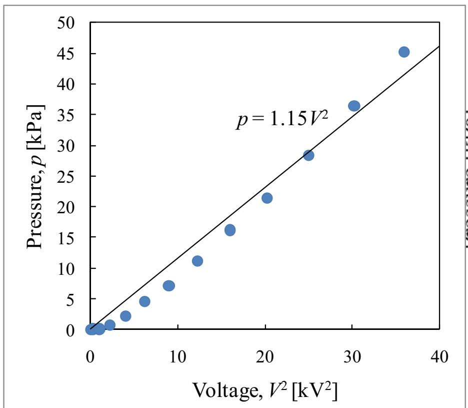

Figure 12 Relation between voltage and pressure

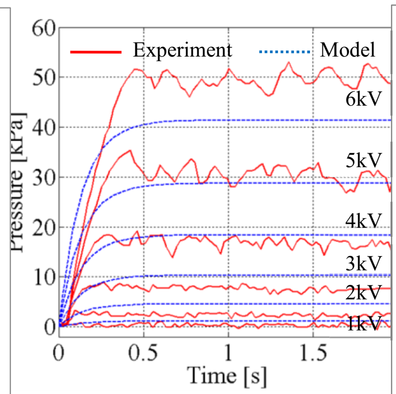

Figure 13 Step responses of pressure

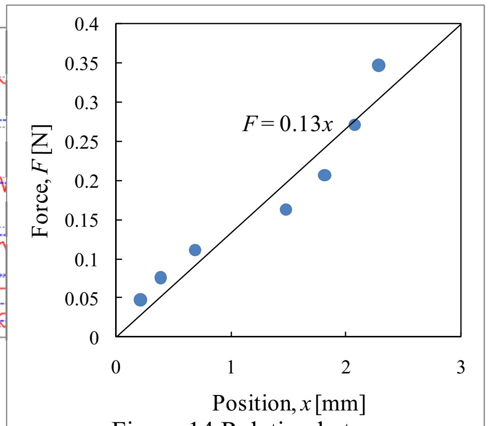

Figure 14 Relation between force and position

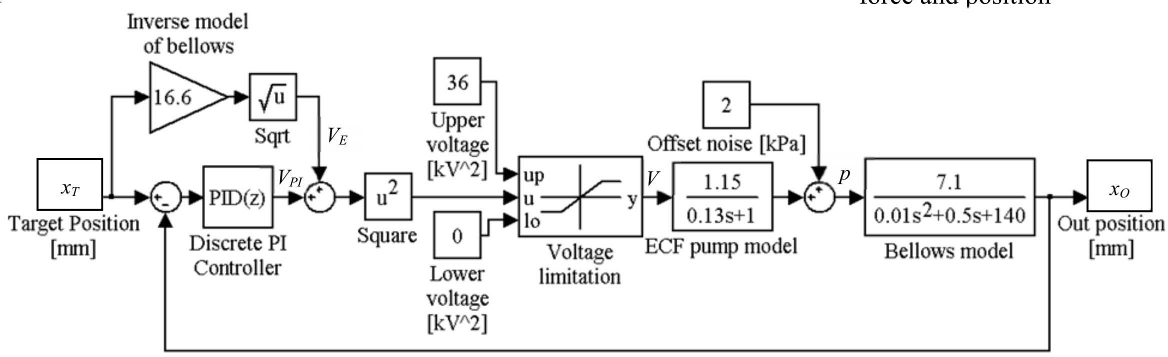

Figure 15 The Bellows actuator control model

using an ECF pump. In this system, two ECF pumps, each of them has two pairs of needle-ring electrode shown in Fig. 10 are connected in series. The size of each electrode is the same as Fig. 2. This ECF pump can generate enough pressure and flow rate in order to drive a bellows actuator described as follow. Note that FF-101EHA2 is used as working fluid in this experiment, as well.

Fig. 11 (a) shows an overview of experimental setup, and Fig. 11 (b) shows a closed up view around the bellows actuator. The bellows actuator (SK-27929, Servometer) expands in axial direction when inner pressure is changed by the ECF pump. The diameter and length of the bellows actuator are 3 mm and 3.5 mm, respectively. As shown in Fig. 11 (b), 10 g weight is located on the bellows actuator. The position of the weight is measured with a laser displacement sensor (LB-02, Keyence). This weight is driven in the axial direction of bellows actuator

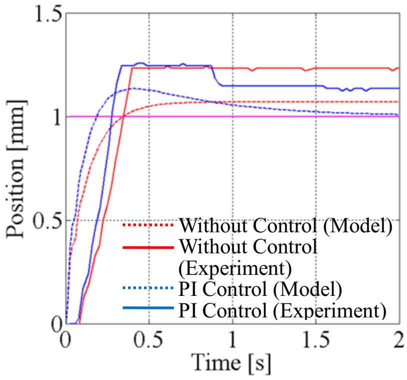

(a) Pressure

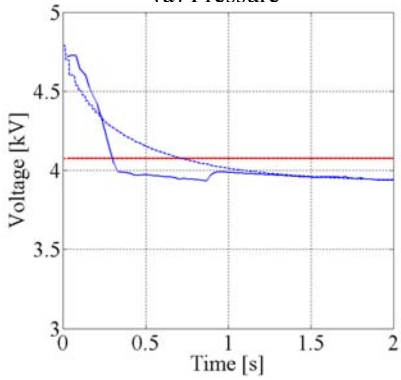

(b) Voltage

Figure 16 Step responses

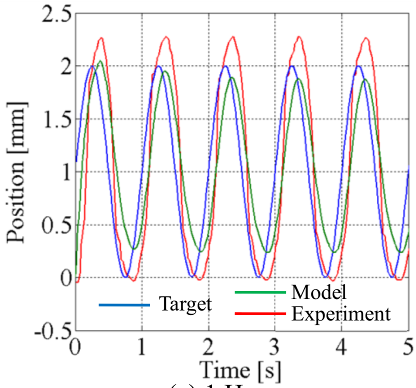

(a) 1 Hz

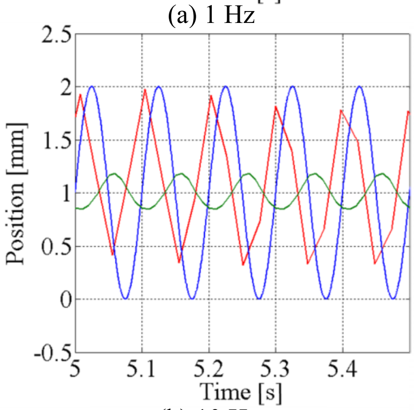

(b) 10 Hz

Figure 17 Frequency responses

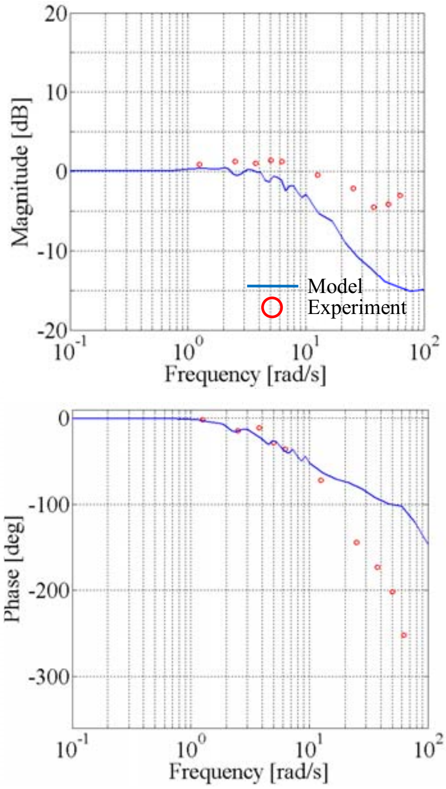

Figure 18 Bode diagram

along a guide rail. The position signal obtained by the laser displacement sensor is send to PC via the A/D converter.

The Control Model

In this model the ECF pump model is same as Eq. (1), as well. The time constant T and the gain K are determined from the relations shown in Fig. 12 and Fig. 13. The responses of the model are shown in Fig. 13 as dash line. Then we propose the model of bellows actuator as,

$$m\frac{dx^2}{d^2t}+\mu\frac{dx}{dt}+kx=Ap \tag{6}$$

where m, x, μ, k and A represent weight, position, viscosity, spring coefficient and area of bellows head, respectively. Eq. (6), the first term of left side is the inertia force, the second term is the frictional force, the third term is the spring force, and the right side is the external force applied to the bellows actuator. The spring coefficient k is determined by relation of the external force applied to the bellows actuator and the displacement shown in Fig. 14.

Next we propose the model of the bellows actuator control system using the ECF pump model and the bellows actuator model.

Fig. 15 shows a block diagram of the bellows actuator control system. In this control system an estimated voltage V_E is calculated from the target position x_T as,

$$V_E=\frac{1}{K}\sqrt{\frac{kx_T}{A}} \tag{7}$$

Note that Eq. (7) is developed using the relation shown in Fig. 12 and Fig. 14. Second, voltage V_{PI} is calculated from the difference between the target position x_T and the output position x_O by the PI controller as,

$$V_{PI}=K_P(x_T-x_O)+K_I\int(x_T-x_O)dt \tag{8}$$

where K_P and K_I are P gain and I gain, respectively. Finally, the applied voltage V to the ECF pump is calculated by Eq. (4).This voltage should not be higher than 6kV in order to prevent an electric discharge. The pressure generated with the ECF pump is calculated using by Eq. (1). Then, an offset noise which represents the instability of pressure generated with the ECF pump is added. Finally the position of the bellows actuator is calculated by Eq. (6).

The Control Response

We aim to improve the step response of the bellows actuator by appropriately adjusting PI gains. The PI gains are adjusted by observing the step responses of the control model shown in Fig. 15. Fig. 16 shows the responses of the model and experiment when the target position is a step input from 0 to 1 mm. Fig. 16 (a) is the responses of position, and Fig. 16 (b) is the time history of the applied voltage. Note that the control condition of experiment is corresponding to that applied to the model. As you can see in Fig. 16 (a), with PI control the steady state error is slightly observed, and response speed is improved compared to that without control. In addition, the responses of the model and experiment are almost corresponding. This means that we can effectively construct the bellows actuator control system using the proposed control model.

Furthermore frequency responses are observed as well with the same PI control. The target position x_T is

$$x_T = \sin(2\pi f t) + 1 \quad \text{mm} \tag{9}$$

The frequency responses of the model and experiment when frequency f is 1 Hz and 10 Hz are shown in Fig. 17. As in the graphs, when f is 1 Hz the position x_O follows the target position x_T, i.e., the amplitude reduction and the phase lag are not observed. On the other hand, they are observed with the frequency of 10 Hz with the model. However, the amplitude reduction is hardly not observed in the experiment. Accordingly we observed responses with wider frequency range, and these results are shown in Fig. 18 as a form of bode diagram. As in Fig. 18, the amplitude reduction of experiment is quite low. Furthermore the responses of the model disagree with experimental results especially in the high frequency region. This is caused by the following reason. The frictional force of the bellows actuator model does not represent well with the actual friction between the weight and the guide rail.

CONCLUSION

We proposed the ECF pump model which has first-order lag element. Then we constructed the ECF pump control model, and designed PI controller by observing the response of control model. This control system has a better response of pressure than that without control.

In addition we constructed the bellows actuator control model using the ECF pump model and the bellows actuator model. Then we designed the PI controller for the bellows actuator. Finally we constructed the bellows actuator control system which may improve the actuator response.

ACKNOWLEDGEMENT

The work reported in this article was supported in part by a Grant-in-Aid for Encouragement of Young Scientists (A) #21686017 awarded by the Ministry of Education, Culture, Sports, Science and Technology of Japan.

REFERENCES

1. H. Yamamoto, K. Mori, K. Takemura, S. Yokota and K. Edamura, Numerical modeling of electro-conjugate fluid flows, Sensors and Actuators A, 2010, Vol. 161, pp. 152–157.
2. K. Mori, H. Yamamoto, K. Takemura, S. Yokota, K. Edamura, Dominant Factors Inducing Electro-conjugate Fluid Flow, Sensors and Actuators A, 2011, Vol. 167, pp. 84-90.
3. K. Takemura, H. Kozuki, K. Edamura, S. Yokota, A micromotor using electro-conjugate fluid -Improvement of motor performance by using saw-toothed electrode series-, Sensors and Actuators A, 2007, Vol. 140, pp.131-137.
4. K.Takemura, F. Yajima, S. Yokota, K. Edamura: Integration of micro artificial muscle cells using electro-conjugate fluid, Sensors and Actuators A, 2008, Vol. 144, Issue 2, pp.348-353.
5. K. Takemura, S. Yokota, K. Edamura: Development and control of a micro artificial muscle cell using electro-conjugate fluid, Sensors and Actuators A, 2007, Vol. 133, pp.493-499.
6. R. Abe, S. Yokota: A micro actuator using ECF-jet with needle type electrode, Prpc. FLUCOME,2003, CD-ROM

Proceedings of the 8th JFPS International
Symposium on Fluid Power, OKINAWA 2011
Oct. 25-28, 2011

2B3-2

NUMERICAL SIMULATION OF ION DRAG PUMP CHARACTERISTICS

Hideki YANADA*, Yuta ISOHATA** and Kazuhiro TSURUTA*

* Department of Mechanical Engineering, Graduate School of Engineering
Toyohashi University of Technology
1-1, Hibarigaoka, Tempaku-cho, Toyohashi, 441-8580 Japan
(E-mail: yanada@me.tut.ac.jp)
** Chiyoda Corporation
12-1, Tsurumichuo 2-chome, Tsurumi-ku, Yokohama, 230-8601 Japan

ABSTRACT

This paper deals with numerical simulation of ion drag pump characteristics. Electrohydrodynamic (EHD) phenomena have recently been applied to pumps and actuators utilizing the so-called functional fluids. The configurations of the electrodes and flow passage are designed by trial and error and it is not easy to find out a better configuration of pump or actuator. In this paper, the effects of the configurations of the electrodes and flow passage on ion drag pump characteristics are investigated by numerical simulation. Two-dimensional configurations of pump are treated. The effects of the electrode spacing, the distance between electrode pairs, the depth of flow passage, etc. on the pump characteristics are made clear. In addition, the effect of the electrostriction force is shown.

KEY WORDS

Electrohydrodynamics, Ion drag pump, Numerical simulation

NOMENCLATURE

$\boldsymbol{E}$	electric field strength [V/m]
E_{static}	electrostatic field strength [V/m]
E_{thres}	threshold electric field strength [V/m]
$\boldsymbol{f}$	electric force per unit mass [m/s^2]
f_x	x component of $\boldsymbol{f}$ [m/s^2]
f_y	y component of $\boldsymbol{f}$ [m/s^2]
$\boldsymbol{j}$	current density [A/m^2]
k	proportional constant for injected charge density [C/(V・m^2)]
p	pressure [Pa]
q	charge density [C/m^3]
q_e	charge density injected from emitter electrode [C/m^3]
Q	flowrate generated by ion drag pump [m^3/s]
u	x component of flow velocity [m/s]
v	y component of flow velocity [m/s]
V	applied voltage [V]
$\boldsymbol{V}$	flow velocity [m/s]
x	x coordinate [m]
y	y coordinate [m]
ε	permittivity [F/m]
ε_0	permittivity of the vacuum [F/m]
ε_r	relative permittivity [-]
μ	viscosity [Pa・s]
μ_i	ionic mobility [m^2/(V・s)]
μ_{iw}	ionic mobility determined by Walden's rule

	$[m^2/(V \cdot s)]$
ρ	mass density [kg/m^3]
σ	conductivity [S/m]
ϕ	electric potential [V]

INTRODUCTION

When an electric field is applied to a fluid in which excess charges exist, a motion of the fluid is caused by the Coulomb force acting on the charges. Such a phenomenon is classified into electrohydrodynamics (EHD), which covers both of hydrodynamics and electrodynamics, and has been applied to heat transfer enhancement [1, 2], pumps [1-7], and actuators [8, 9], etc.

Ion drag pump is typical of EHD pumps and for the pump, the excess charges are generated by the so-called charge injection phenomenon [10]. Many investigations into ion drag pump have been conducted so far. Recently, research on ion drag micropump [11-14] or micropumps of which working principle may be different from ion drag pump [15-18] have been conducted. Various configurations of the electrodes and flow passage have been proposed by trial and error. If the pump performance can be predicted by numerical simulation, the configurations of the electrodes and flow passage suitable for a high-performance pump can be designed with minimum trial manufactures. However, numerical simulation of EHD pump has been limited [13, 19] and the simulation method has not been established yet.

Darabi and Rhodes [13] conducted numerical simulation of two-dimensional ion-drag micropump and examined the effects of mechanical factors such as electrode gap, etc. on the pump performance and showed a relatively good agreement with experimental results. However, the simulation procedure is not clear and the factors that were examined are limited.

For the numerical simulation of ion drag phenomenon, only the Coulomb force has been taken into consideration. However, it has been shown recently that the electrostriction force can cause a fluid motion [20].

In this paper, the effects of the configurations of the electrodes and the depth of the flow passage on the performance of two-dimensional ion drag pump are numerically examined. The numerical simulation method used in the paper is the same as that used in the previous papers [19, 21] and is based on the assumption that the excess charges are injected from the point and its vicinity where the electric field strength takes the maximum value on the emitter electrode. In addition, the effect of the electrostriction force on the ion drag pump performance is examined.

ION DRAG PUMPS AND EXPERIMENT

In order to make the visualization of the flow pattern and the numerical simulation easy, a pump with an approximately two-dimensional configuration is used as a standard pump and is shown in Figure 1. The pump was inserted in a closed pipeline circuit and the pressure and flow rate generated by the pump were measured. The pressure was measured using an inverse U-tube manometer and the flow rate was measured using the relation between the flow rate and the pressure drop across a cylindrical choke inserted in the pipeline. The pressure drop was measured using another inverse U-tube manometer. The flow field was measured by a particle image velocimetry (PIV) technique. Particle motions were captured by a charge-coupled device (CCD) camera (DITECT Corp., HAS-220R, 500 flames/s) and were analyzed using a PIV software (DITECT Corp., DIPP-FLOW).

The test liquid used in the experiment is Dibutyl sebacate (DBS) and its physical properties measured at the experimental temperature (293K) are as follows: mass density ρ=938 kg/m^3, viscosity μ=8.67×10^{-3} Pa·s, conductivity σ=4.43×10^{-10} S/m, and relative permittivity ε_r=4.7.

Figure 2 shows the ion drag micropumps treated and they are used only in numerical simulation. The effects

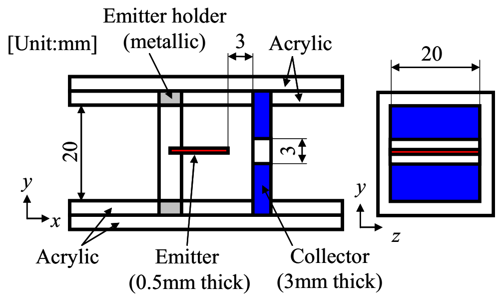

Figure 1 Standard ion drag pump

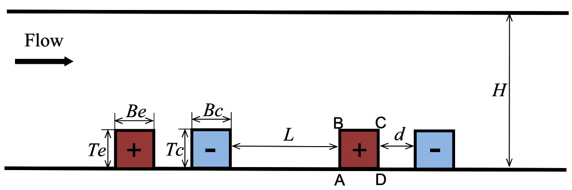

(a) One side array

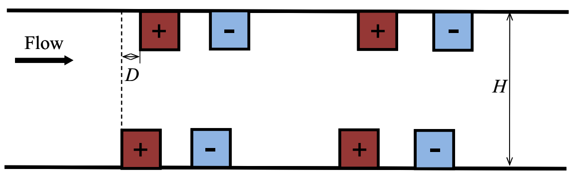

(b) Two-side array

Figure 2 Ion drag micropump

of the dimensions of the electrodes, electrode spacing, etc. on the pump characteristics are examined. This configuration of micropump was treated in several papers [12, 13, 15, 16, 18].

THEORY

The electric body force acting on a dielectric fluid per unit mass is given by

$$\boldsymbol{f} = \frac{q}{\rho}\boldsymbol{E} - \frac{1}{2\rho}\boldsymbol{E}^2\nabla\varepsilon + \frac{1}{2\rho}\nabla\left(\boldsymbol{E}^2\rho\frac{d\varepsilon}{d\rho}\right) \quad (1)$$

For a homogeneous fluid under a uniform temperature, there is no permittivity gradient in the fluid and the derivative of permittivity with respect to mass density in the third term can be given by the Clausius-Mossoti equation. Therefore, Eq.(1) is simplified as follows [22]:

$$\boldsymbol{f} = \frac{q}{\rho}\boldsymbol{E} + \frac{1}{6\rho}\varepsilon_0(\varepsilon_r - 1)(\varepsilon_r + 2)\nabla\boldsymbol{E}^2 \quad (2)$$

The third term in Eq.(1) or the second term in Eq.(2) is called the electrostriction force and is usually omitted when a charge injection phenomenon is treated. In this paper, the effect of the electrostriction force on the ion drag pump characteristics is investigated by numerical simulation.

NUMERICAL SIMULATION SCHEME

The numerical simulation scheme used is the same as that in the previous papers [19, 21] except for the inclusion of the electrostriction force and is described again in this paper.

Fundamental equations

Two-dimensional, laminar, and steady flow is assumed. The fundamental equations that describe the flow field and electric field are as follows:

(a) Continuity equation:

$$\frac{\partial u}{\partial x} + \frac{\partial v}{\partial y} = 0 \quad (3)$$

(b) Navier-Stokes equation:

$$u\frac{\partial u}{\partial x} + v\frac{\partial u}{\partial y} = -\frac{1}{\rho}\frac{\partial p}{\partial x} + \frac{\mu}{\rho}\left(\frac{\partial^2 u}{\partial x^2} + \frac{\partial^2 u}{\partial y^2}\right) + f_x \quad (4)$$

$$u\frac{\partial v}{\partial x} + v\frac{\partial v}{\partial y} = -\frac{1}{\rho}\frac{\partial p}{\partial y} + \frac{\mu}{\rho}\left(\frac{\partial^2 v}{\partial x^2} + \frac{\partial^2 v}{\partial y^2}\right) + f_y \quad (5)$$

(c) Charge conservation law:

$$\nabla \cdot \boldsymbol{j} = 0 \quad (6)$$

(d) Current density:

$$\boldsymbol{j} = q\mu_i\boldsymbol{E} + q\boldsymbol{V} + \sigma\boldsymbol{E} \quad (7)$$

(e) Gauss' law:

$$\frac{\partial^2\phi}{\partial x^2} + \frac{\partial^2\phi}{\partial y^2} = -\frac{q}{\varepsilon} \quad (8)$$

(f) Relation between electric field and potential:

$$\boldsymbol{E} = -\nabla\phi \quad (9)$$

All the equations were discretized by a finite volume method and the SIMPLE (Semi-Implicit Method for Pressure-Linked Equations) algorithm [23] was used to solve the discretized equations. The third term in Eq.(7) hardly affects the ion drag flow field and electric field and, therefore, can be neglected. However, the third term has to be included when calculating the current.

Injected charge density

One of the difficulties in the numerical simulation of ion drag phenomena lies in the determination of the value of the density of the charges injected from the electrodes. It is assumed that the charge density injected from the emitter electrode obeys the following function [19, 21]:

$$q_e = k(E_{static} - E_{thres}) \quad (10)$$

where E_{thres} stands for the threshold electric field strength and E_{static} stands for the electrostatic field strength on the emitter surface. When charges are injected, the electric field strength on and near the injecting surface is decreased to a great or some degree from that for no charge injection case. However, it is assumed for simplicity that the quantity of the injected charge density is determined by the electrostatic field strength.

The value of the proportional constant, k, is determined by comparing the experimental results with the simulated ones using the standard pump shown in Figure 1 at a certain experimental condition. The threshold electric field strength, E_{thres}, was determined experimentally and was 0.25 kV/mm, which is usually significantly small compared with the electrostatic field strength applied to the emitter electrode [19, 21].

Boundary conditions

Figure 3 shows the electrostatic field strength distribution on the surface of the emitter electrode. The electric field strength becomes extremely high at the two corners, B and C shown in Figure 2 and takes the maximum at corner C. Therefore, for the emitter electrodes except for the first stage emitter, charges may be injected from the two corners, B and C in Figure 2(a). Numerical simulation is done first for the two cases where charges are injected (i) from the two corners (B, C) and (ii) only from the corner C. For the other boundary conditions, refer to [19, 21].

Ionic mobility

A standard value of the mobility of positive ions in test liquid was estimated by using the following relation given by Adamczewski [24]:

$$\mu_{iw} = 2.0\times10^{-11}\mu^{-1} \quad (11)$$

where the subscript w stands for the Walden's rule. When μ=8.67×10^{-3} Pa·s, the ionic mobility calculated by Eq.(11) is μ_{iw}=2.31×10^{-9} m^2/(V·s).

Another difficulty in the numerical simulation of ion drag phenomena is the lack of the information on the correct value of the ionic mobility. It is essential to assign a much larger value to μ_i than μ_{iw} and an appropriate value of μ_i is determined by comparing the

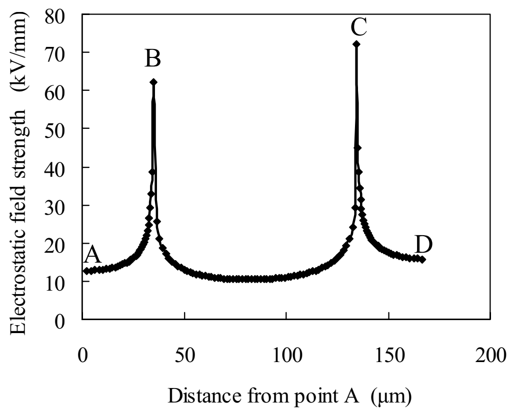

Figure 3 Electrostatic field strength distribution on emitter electrode (V=2.5 kV, d=100μm, L=H=500μm, T_e=T_c=35μm, B_e=B_c=100μm)

measured flow field and pressure-flow rate (p-Q) characteristic with simulated ones [19].

RESULTS AND DISCUSSION

Standard pump

Figure 4 shows the comparison of the p-Q characteristic of the standard pump between experiment and simulation. The measured characteristic is relatively accurately simulated by the method used. For this case, the value of k in Eq.(10) is 4.27×10^{-9} C/(V·m^2), which corresponds to the injected charge density of q_e=0.0330 C/m^3 at V=10 kV. In addition, the value of the ionic mobility is μ_i=20μ_{iw} and this value is used in all the simulations in this paper.

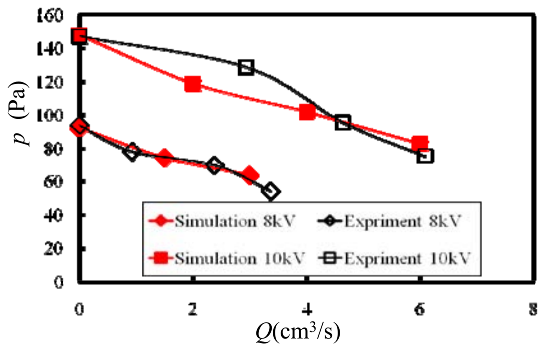

Figure 4 Comparison of p-Q characteristic of standard pump between experiment and simulation

Charge injection condition of micropump

As described above, numerical simulation was done for the two cases where charges were injected (i) from the two corners (B, C) and (ii) only from the corner C. In the following simulations, the applied voltage is fixed at 2.5 kV.

Figure 5 shows the charge density distribution for the above two conditions. When the charges are injected from the two corners, B and C, the charges injected from corner B spread out in y direction more widely than those injected from corner C. This is because the distance between corner B and its facing collector electrode is longer than that between corner C and its facing collector electrode. For condition (i), due to the wider spread of the charges at the upstream of corner B than at the downstream of corner C, the Coulomb force acting in the upstream direction at the upstream of corner B may become larger than the Coulomb force acting in the downstream direction at the downstream of corner C. Therefore, the calculated pressure becomes negative for the majority of the simulation conditions used. This is contrary to the experimental results obtained in [12, 13, 15, 16, 18].

The discrepancy between the results shown in Figure 5 and the results shown in [12, 13, 15, 16, 18] shows that condition (i) is not correct. It may be considered that charges are apt to be injected at and in the vicinity of the point where the electric field strength becomes the maximum, though charges may be injected also at corner B to some degree. In what follows, the numerical simulation is conducted using condition (ii).

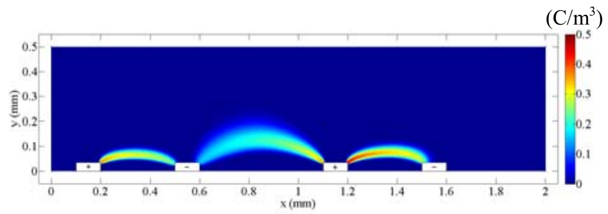

(a) Condition (i) (charges are injected at B and C)

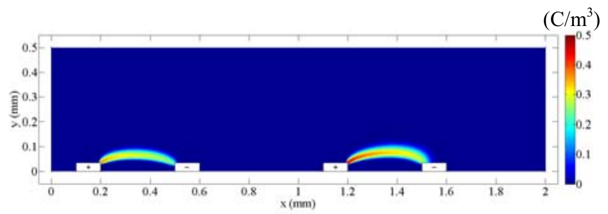

(b) Condition (ii) (charges are injected only at C)

Figure 5 Charge density distribution for two injection conditions (V=2.5 kV, d=300μm, L=H=500μm, T_e=T_c=35μm, B_e=B_c=100μm)

Effects of micropump configurations

Figures 6 to 10 show the effects of the electrode spacing, d, the distance between two stages, L, the electrode width, B, the electrode height, T, and of the depth of the flow passage, H, on the pressure generated per stage of electrode arrays when Q=0.

As can be seen from Fig.6, the pump pressure is increased with the electrode spacing. The increase in the electrode spacing brings about the decrease in the electric field strength on the emitter and in the space between electrodes but makes the charge spread wider. It seems that the latter effect surpasses the former effects and, therefore, the pump pressure is increased

with increasing electrode spacing.
The distance between the neighboring electrode stages hardly affects the pump pressure as shown in Figure 7. The pump pressure tends to be increased with decreasing electrode width and to be saturated at small and large electrode widths as shown in Fig.8.
In addition, the pump pressure is increased with increasing electrode height (Figure 9) and is steeply increased with decreasing depth of the flow passage (Figure 10). The simulation shows that the misalignment, D, between the top and bottom electrode arrays hardly affects the pump pressure.

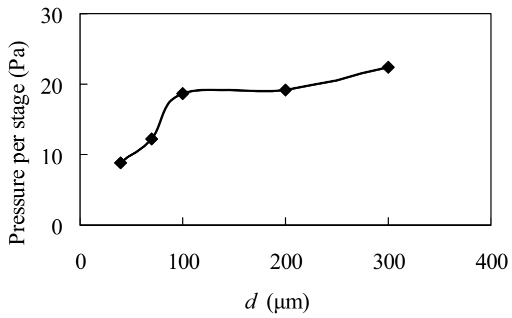

Figure 6 Effect of electrode spacing on pump pressure at Q=0 (L=H=500µm, T_e=T_c=35µm, B_e=B_c=100µm)

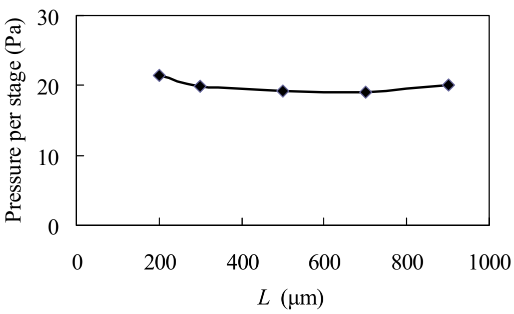

Figure 7 Effect of distance between neighboring electrode pairs on pump pressure at Q=0 (H=500µm, d=100µm, T_e=T_c=35µm, B_e=B_c=100µm)

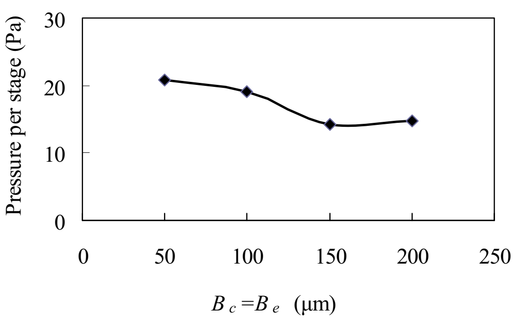

Figure 8 Effect of electrode width on pump pressure at Q=0 (L=H=500µm, d=100µm, T_e=T_c=35µm)

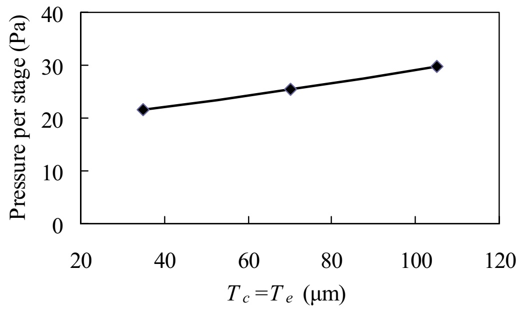

Figure 9 Effect of electrode height on pump pressure at Q=0 (L=H=500µm, d=100µm, B_e=B_c=100µm)

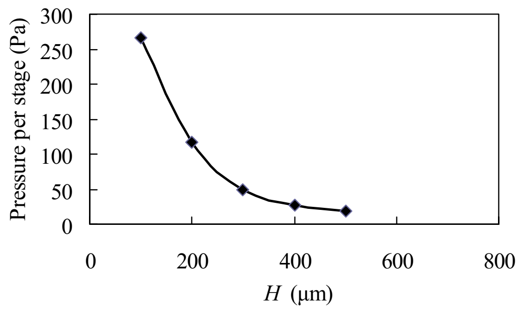

Figure 10 Effect of depth of flow passage on pump pressure at Q=0 (L=500µm, d=100µm, B_e=B_c=100µm, T_e=T_c=35µm)

Effect of electrostriction force
Numerical simulation for the standard pump shown in Figure 1 shows that the electrostriction force tends to shift the p-Q curve upward and the pressure is increased by about 8 percent. For the micropump shown in Figure 2, the electrostriction force slightly decreases the pump pressure and its effect is negligible.
The Coulomb force is augmented in proportion to the injected charge density and, therefore, for fluids in which lots of charges are easily injected, the effect of the electrostriction force becomes negligible.

CONCLUSIONS

The characteristics of two-dimensional micropump are investigated under various conditions by numerical simulation. The effects of the dimensions of electrodes, the pitch of electrode pair and the depth of the flow passage are made clear. It is confirmed that the electrostriction force has a small or negligible influence on the pressure generated by ion drag pump. The numerical simulation scheme in the paper uses an assumption that charges are injected only from the point and its vicinity of the maximum electric field strength on the emitter electrode. This needs an experimental verification.

ACKNOWLEDGEMENTS

The authors would like express their gratitude to S. Mamiya and Y. Teramoto for their help in part of the numerical simulation. This work has been financially supported by the Japan Society for the Promotion of Science through the Grant-in-Aid for Scientific Research (C) (No. 22560141).

REFERENCES

1. Allen, P. H. G. and Karayiannis, T. G., Electrohydrodynamic enhancement of heat transfer and fluid flows, Recovery Systems & CHP, 1995, 15-5, pp.389-423.
2. Seyed-Yagoobi, J. and Bryan, J. E., Enhancement of heat transfer and mass transport in single-phase and two-phase flows with electrohydrodynamics, Advances in Heat Transfer, 1995, 33, pp.95-186.
3. Stuetzer, O. M., Ion drag pumps, J. Applied Physics, 1960, 31-1, pp.136-146.
4. Sharbaugh, A. H. and Walker, G. W., The design and evaluation of an ion-drag dielectric pump to enhance cooling in a small oil-filled transformer, IEEE Trans. Industry Applications, 1985, 21-4, pp.950-955.
5. Bryan, J. E. and Seyed-Yogoobi, J., An experimental investigation of ion-drag pump in a vertical and axisymmetric configuration, IEEE Trans. Industry Applications, 1992, 28-2, pp.310-316.
6. Asano, K. and Yatsuzuka K., Fundamental study of EHD pump with needle-cylinder electrodes, Conf. Rec. IEEE/CEIDP Annual Meeting, Austin, 1999, pp.785-788.
7. Yanada, H., Hakama, S., Miyashita, T. and Zhang, N., An investigation of an ion drag pump using a needle-mesh electrode configuration, Journal of Mechanical Engineering Science (Proc. Instn. Mech. Engrs., Part C), 2002, 216-C3, pp.325-335.
8. Kang, S., Hallinan, K. P. and Kashani, R., Electrohydrodynamic pumped hydraulic actuation, ASME DE, 1998, 97, pp.193-200.
9. Tsuchida, N, Makiuchi, H., Ohosawa, J. and Ohohashi, A., Studies on reversible drive ion drag micro-actuator with subsidiary electrodes, The Transactions of The Institute of Electrical Engineers of Japan, 1999, 119-C8/9, pp.985-990.
10. Felici, N. J., D.C. conduction in liquid dielectrics - A survey of recent progress (Part I), Direct Current, 1972, 2-3, pp.90-99.
11. Richter, A., Plettner, A., Hofmann, K. A. and Sandmaier, H., Electrohydrodynamic pumping and flow measurement, Proc. IEEE Micro Electro Mech. Syst., 1991, 271-276.
12. Ahn, S. H. and Kim, Y. K., Fabrication and experiment of a planar micro ion drag pump, Sensors and Actuators A, 1998, 70, 1-5.
13. Darabi, J., Rhodes, C., CFD Modelling of an ion-drag micropump, Sensors and Actuators A, 2006, 127-1, pp.94-103.
14. Kazemi, P. Z, Selvaganapathy, P. R. and Ching, C. Y., Effect of micropillar electrode spacing on the performance of electrohydrodynamic micropumps, Journal of Electrostatics, 2010, 68-4, 376-383.
15. Yokota, S., Seo, W. S., Yoshida, K. and Edamura, K., A thin-planar pump using electro-conjugate fluid (ECF) for liquid cooling of electronic chips, Trans. JSME, Ser. C, 2005, 71-709, 2798-2804. (in Japanese)
16. Sakurai, Y., Kadoi, H., Nakada, T. and Edamura, K., Development of printed circuit board multi-layered type ECF pump and its application to liquid cooling system, Trans. JSME, Ser. C, 2006, 72-715, 991-996. (in Japanese)
17. Seo, W. S. , Yoshida, K., Yokota, S. and Edamura, K., A high performance planar pump using electro-conjugate fluid with improved electrode patterns, Sensors and Actuators A, 2007, 134-2, 606-614.
18. Sakurai, Y., Nakada, T. and Edamura, K., Development of tube type ECF-pump and its application to liquid cooling system for CPU, Trans. JSME, Ser. B, 2009, 75-753, 966-971. (in Japanese)
19. Yanada, H., Yamada, T., Asai, Y. and Terashita, Y., Measurement and numerical simulation of ion drag pump characteristics, Journal of Fluid Science and Technology, 2010, 5-3, 617-631.
20. Ohtomo, Y., Ando, A., Ogiura, K., Hattori, K. and Inutake, M., Characteristics of the electrohydrodynamic (EHD) pump working with an electrostriction force, IEEJ Trans. FM, 2007, 127-9, 531-536.
21. Tran, K. D., Kojima, Y., and Yanada, H., Measurement and numerical simulation of flow and electric fields in charge injection type of electrostatic oil filter, Transactions of the Japan Fluid Power System Society, 2009, 40-1, pp.8-15.
22. Takeyama, S., Theory of Electromagnetic Phenomena (in Japanese), Maruzen Co. Ltd., 1950, 121-123.
23. Patankar, S. V., Numerical heat transfer and fluid flow, New York: Hemisphere Publishing Corp., 1980
24. Adamczewski, I., Ionization, Conductivity, and Breakdown in Dielectric Liquids, London: Taylor and Francis, 1969, 219-228.

Proceedings of the 8th JFPS International
Symposium on Fluid Power, OKINAWA 2011
Oct. 25-28, 2011

2B3-3

DEVELOPMENT OF HYBRID MAGNETIZING DEVICES FOR MR FLUID CONTROL

Yasukazu SATO*

* Department of Mechanical Engineering, Faculty of Engineering
Yokohama National University
79-5 Tokiwadai, Hodogayaku, Yokohama, kanagawa, 240-8501 Japan
(E-mail: yasukazu@ynu.ac.jp)

ABSTRACT

This paper proposes three types of mechanism to control the viscosity of magneto-rheological fluid (MR fluid) from the viewpoints of the expansion of controllable viscosity range and electric power-saving of magnetizing devices. The first type is configured by two MR fluid chambers which are connected by four tubes, which is effective to expand the controllable viscosity range. Each tube acts as a valve by the MR effect. The equivalent viscosity of MR fluid flowing through this device is controlled by the flow resistance of tubes. The magnetic field controlled by the combination of the digital and analog magnetizing system can change the viscosity of MR fluid in each tube. The second one utilizes the magnetization/demagnetization property of permanent magnet material. It consumes no electric power while maintaining the external magnetic field. The third one utilizes the magnetic field generated by the moving permanent magnet with less electric power consumption.

KEY WORDS

Functional fluid, MR fluid, Magnetizing, Viscosity, Electric power-saving

INTRODUCTION

Magneto-rheological fluid (MR fluid) is the one of functional fluid, which changes its viscosity according to the intensity of an external magnetic field. Because the viscosity of MR fluid can be controlled by applying the magnetic field to the fluid, some MR fluid applications such as a damper, resistive force device, clutch mechanism, and so on, are put to practical use [1-3]. For the source of external magnetic field applied to MR fluid, an electromagnet such as a solenoid is generally used. Electric current of a solenoid is digitally switched on and off based on the demand of the magnetic field. On contrary, the current changing continuously is applied to a solenoid for the demand of continuous field change. It is not common to use a permanent magnet for magnetizing MR fluid except applying the constant offset field to MR fluid.

For applying the magnetic field to MR fluid effectively, a pair of magnetic pole forms the field crossing the conduit of MR fluid at right angles. Typical magnetic pole is coaxial inner/outer cylinders or a pair of plate facing each other. The distance between the poles is required to be narrow for increasing the intensity of field applied to MR fluid. However, from the viewpoint of expansion of controllable viscosity range, it is required to be wide for reducing the fluid resistance by viscosity of non-magnetized MR fluid. It is the one of purposes of this paper to develop a new magnetizing device which copes with both conflict requirements.

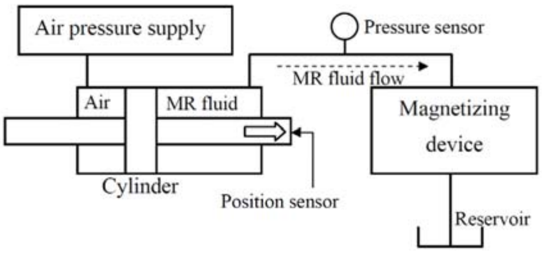

Figure 1 Testing apparatus for evaluation of MR fluid viscosity control

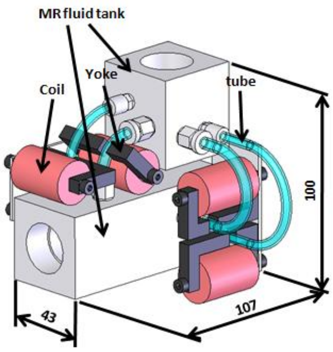

Figure 2 Digital / analog hybrid magnetizing device for MR fluid control

Furthermore, since the magnetic field is generally applied to MR fluid by an electromagnet, a magnetizing device has a problem of electric power consumption for maintaining the field in a long period.

Aiming to include properties both of the controllable viscosity range expansion and the electric power-saving into the magnetizing device development, the author proposes new design concept with hybridization of different magnetizing principles. This paper presents three types of new mechanism magnetizing MR fluid, and shows their performance and evaluation.

TESTING APPARATUS FOR EVALUATION OF MAGNETIZING DEVICES

All of hybrid magnetizing devices developed in this study are evaluated by the testing apparatus shown in Figure 1. It consists of an air compressor, a double rod cylinder and a reservoir for MR fluid. The air pressure is supplied to one chamber of the cylinder. The other chamber is filled with MR fluid. MR fluid is discharged from the cylinder via the piston pushed by air pressure, and passes through the magnetizing device. In order to measure the pressure drop at the magnetizing device, a pressure transducer is installed into upstream of it. The flow rates of MR fluid flowing through the device can be measured using the velocity of the piston rod. In this study, the rheological property of MR fluid is evaluated by the flow rates under the constant pressure drop, and its viscosity is not measured directly.

Table 1 Dimensions of tube and its flow resistance

Ratio of flow resistance R	Ratio of inner diameter of tube d_0	Ratio of tube length l	Magnetizing command u
2^0	$\sqrt{2}$	2	u_0
2^1	$\sqrt{2}$	1	u_1
2^2	1	2	u_2
2^3	1	1	u_3

DIGITAL / ANALOG HYBRID MAGNETIZING DEVICE FOR EXPANSION OF CONTROLLABLE VISCOSITY RANGE

Configuration of Digital/Analog Hybrid Magnetizing Device

The conduit in this magnetizing device satisfies both requirements to put the magnetic poles close and to have large cross-sectional area, by dividing a single conduit into some parallel tubes. The prototype device is shown in Figure 2. It consists of four parallel tubes, each of which has a solenoid coil and a yoke. Because the viscosity of magnetized MR fluid is very large, the tube in which the solenoid is active acts like a stop valve. Due to the viscosity of non-magnetized MR fluid, the tube has a flow resistance when the solenoid is not active. As to the approximate stop valve, the maximum pressure difference at the tube is given by [4];

$$\Delta p_{MR} = \frac{2L}{h}\tau_{MR} \qquad (1)$$

where, Δp_{MR}, h, L and τ_{MR} are the pressure difference at the tube, the gap between the magnetic poles, the width of the pole and the yield stress of MR fluid, respectively.

The flow resistance ratio of the tubes is designed to be $2^0:2^1:2^2:2^3$. Assume the laminar flow, a set of the inner diameter of tube and tube length is selected as shown in Table 1. Applying the PCM (Pulse Code Modulation) to the control of the equivalent viscosity of MR fluid, the relation between the pressure difference Δp at the device and flow rates Q through it is given by;

$$Q = \frac{\Delta p}{R_0}\left(2^3,\ 2^2,\ 2^1,\ 2^0\right)\begin{pmatrix} u_3 \\ u_2 \\ u_1 \\ u_0 \end{pmatrix} \qquad (2)$$

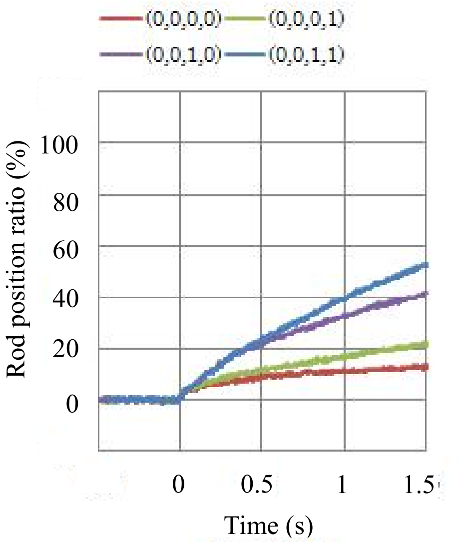

Figure 3 Measured velocity of the cylinder piston rod controlled by the digital / analog hybrid magnetizing device under the pressure difference Δp of 0.04MPa at PCM signals (u_3, u_2, u_1, u_0) of (0, 0, 0, 0), (0, 0, 0, 1), (0, 0, 1, 0) and (0, 0, 1, 1)

where, each u is the PCM signal which is 0 or 1, and R_0 is the flow resistance of the tube in which (d_0, l) is ($\sqrt{2}$, 2). Applying a conventional PCM, the equivalent viscosity of MR fluid can be controlled in 16 levels between the minimum and maximum, but the viscosity change is discontinuous due to digital command input.

In this study, a modified PCM in which only LSB (least significant bit) u_0 is controlled between 0 and 1 continuously is applied to the magnetizing command of (u_3, u_2, u_1, u_0). Because u_3, u_2 and u_1 are digital signal and only u_0 is analog one, this magnetizing device is named the digital/analog hybrid system.

Testing of Viscosity Control Using Digital/Analog Hybrid Magnetizing Device

As to the command u in PCM signals, "0" means that MR fluid is fully-magnetized, and "1" means non-magnetized. Figure 3 is an example that the flow rates Q flowing through the device under the constant pressure difference Δp of 0.04MPa at (u_3, u_2, u_1, u_0)=(0, 0, 0, 0), (0, 0, 0, 1), (0, 0, 1, 0) and (0, 0, 1, 1). The slope of the flow rate is equivalent to the viscosity of MR fluid. The flow of MR fluid in all tubes should stop at (u_3, u_2, u_1, u_0) = (0, 0, 0, 0), but slight flow is recognized. Figure 4 shows the measured result of the cylinder rod velocity equivalent to the viscosity of MR fluid for all combination of PCM signals. It is confirmed that the cylinder rod velocity can be controlled in 16 levels by the viscosity change of MR fluid. Since the flow of the

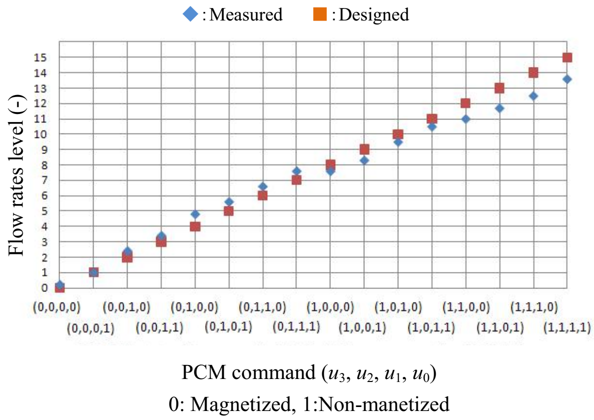

Figure 4 Measured flow rates equivalent to the viscosity of MR fluid controlled by the digital / analog hybrid magnetizing device under the pressure difference Δp of 0.04MPa at PCM signals

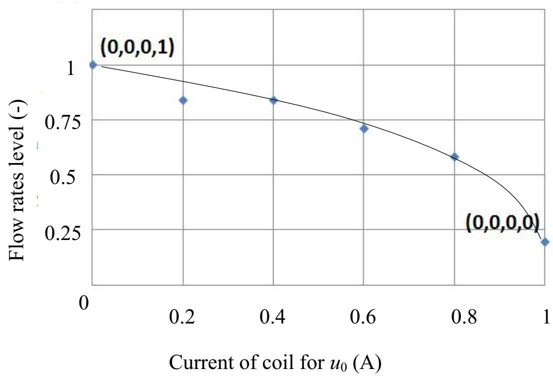

Figure 5 Measured flow rates equivalent to the viscosity of MR fluid controlled by the digital / analog hybrid magnetizing device under the pressure difference Δp of 0.04MPa by the modified PCM signals in which LSB is controlled continuously

magnetized MR fluid cannot stop completely, the measured rod velocity is a little bit faster than the designed one in the case of below (0, 1, 1, 1) in the PCM signals. And it is a little bit slower in the case of above (1, 0, 0, 0) because of the flow resistance in other conduit except the tubes.

In the modified PCM control, only LSB u_0 is controlled between 0 and 1 continuously. Figure 5 shows the measured result when the electric current for u_0 is varied from 0 to 1A continuously. This continuous change of the viscosity fills the signal gap between 0 and 1. Consequently, it is confirmed that this device can control the viscosity of MR fluid continuously from (0, 0, 0, 0) to (1, 1, 1, 1) by the modified PCM signals.

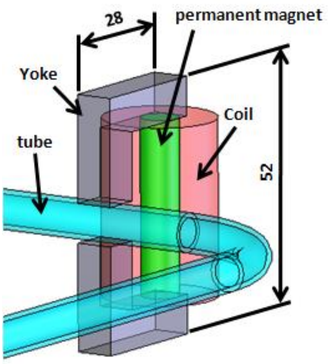

Figure 6 Electromagnet / permanent magnet hybrid magnetizing device for MR fluid control

Table 2 Specification of the permanent magnet used in the electromagnet/permanent magnet hybrid magnetizing device

Material	Al-Ni-Co (Alnico5)
Magnetic saturation	240 kA/m
Remanent magnetic flux density	1.2 T
Coercive force	50 kA/m

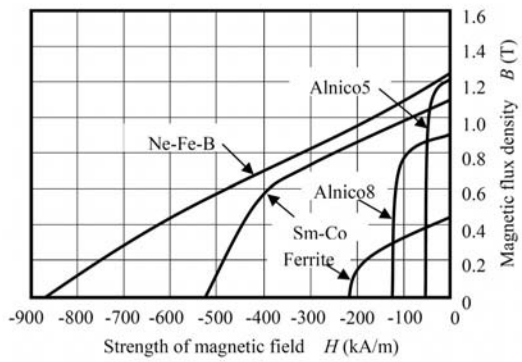

Figure 7 Demagnetization curve of various permanent magnets

ELECTROMAGNET / PERMANENT MAGNET HYBRID MAGNETIZING DEVICE FOR ELECTRIC POWER-SAVING

Configuration of Electromagnet / Permanent Magnet hybrid Magnetizing Device

The prototype magnetizing device consists of a tube which is the conduit of MR fluid, a yoke, a permanent material rod and a solenoid coil as shown in Figure 6. This coil is not used for magnetizing MR fluid, it used only for magnetizing or demagnetizing the permanent magnet material. Since the external magnetic field applied to MR fluid is generated by the magnetized permanent magnet material, no electric power is consumed during magnetizing MR fluid.

The permanent magnet material in this device is Al-Ni-Co (Alnico 5) as shown in Table 2. Figure 7 shows the demagnetizing properties of typical permanent magnet materials, in which Alnico 5 has double residual magnetic flux density and a half coercive force compared with a ferrite magnet. This means that Alnico 5 can apply a magnetic field of large intensity to MR fluid and be easy to be demagnetized by the coil with small electric power.

The state of the permanent magnet material with MR fluid is shown in Figure 8 (a) [5], and the yield stress of MR fluid in the magnetic field is shown in Figure 8(b). When magnetizing MR fluid, an instantaneous electric current is applied to the coil. Then the permanent magnet material in natural condition (State (1)) is fully-magnetized, and its state moves to State (2). After

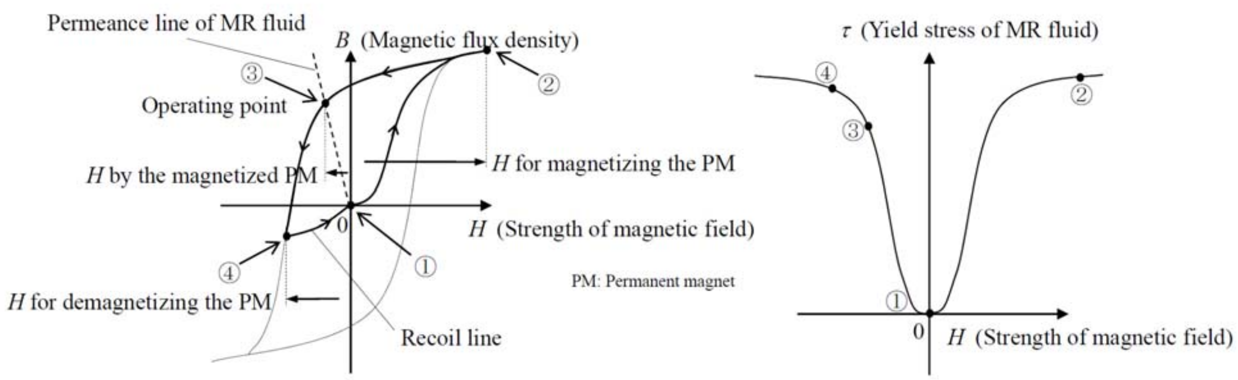

(a) Magnetic characteristics of permanent magnet material in the magnetic circuit with MR fluid

(b) Yield stress of MR fluid under the magnetic field

Figure 8 Principle of power-saving magnetizing for MR fluid using magnetization/demagnetization of permanent magnet material electric current is turned off, its sate moves to State (3). The intersection point of the demagnetization curve and permeance line is the operating point for maintaining magnetic field to MR fluid without electric power consumption. When demagnetizing MR fluid, the instantaneous electric current of counter direction at magnetizing is applied to the coil. Then the state of the permanent magnet material moves from State (3) to State (4). After the current is turned off, its state returns to the origin (State (1)) along with the recoil line. In this case, the operating point is fixed because the state moves on the major loop of magnetizing/demagnetizing property of the permanent magnet material. It is possible to control the intensity of magnetic field applied to MR fluid. The electric current supplied to the coil should be controlled so that the state could move on the minor loop. The concept of magnetic field intensity control is shown in Figure 9.

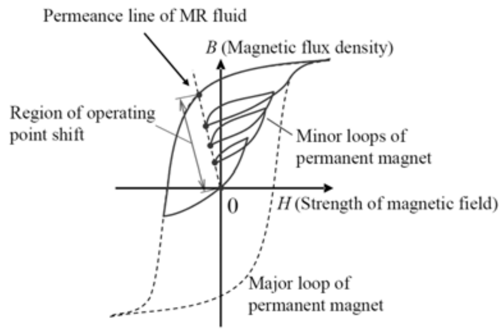

Figure 9 Concept to control the intermediate magnetic field applied to MR fluid using magnetization / demagnetization of the permanent magnet in the minor loop of B-H curve.

Testing of Viscosity Control Using Electromagnet / Permanent Magnet Hybrid Magnetizing Device

Figure 10 shows the measured results of the cylinder rod velocity under the constant pressure difference (Δp=0.1MPa). The energizing time width of electric current both for magnetizing and demagnetizing is set at 10ms constant. The amplitude of current varies at 0, 4, 5, 6, 8 and 10A. Over the current of 8A, the permanent magnet material is fully-magnetized and magnetizing state moves on the major loop. On contrary, the state moves on the minor loop in case of the current below 8A. In Figure 10, the slope of each curve is equivalent to the viscosity of MR fluid. The minimum viscosity is as same as that of non-magnetized MR fluid without magnet. It is confirmed that this device can control the viscosity of MR fluid without electric power consumption during maintaining the field.

The electric power consumption of the prototype device in one cycle of magnetizing and demagnetizing can be calculated by the followings; this device consumes the electric power only at magnetizing and demagnetizing the permanent magnet material. The electric power consumption H(W) is estimated with the current i (A) and coil resistance $R(\Omega)$ by $H=i^2R$. The consumed energy E is derived from the integral of H with the current of 10A and the energizing time width of 10ms. In this case, E marks 1.7J/cycle.

Assuming the permanent magnet material rod is replaced by the iron rod and the constant current is applied to the coil continuously, the current of 0.8A is required for the same magnetic field intensity as this device. The electric power consumption H is 2.4W and the consumed energy E is proportional to the time width of maintaining the field. It reaches to 1.7J by time width of 0.7s.

Over 0.7s for maintaining the magnetic field, this device is superior to a conventional magnetizing device from the viewpoint of the electric power-saving. It is remarkable when the time width for maintaining the field

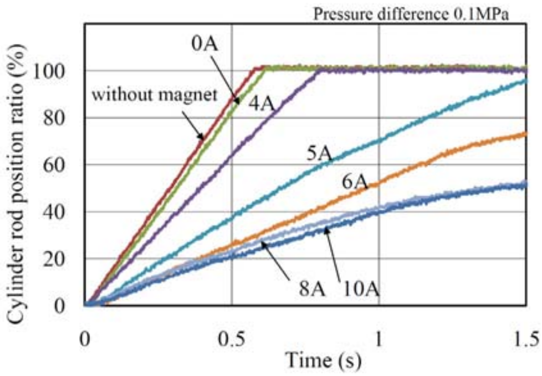

Figure 10 Measured result of MR fluid viscosity change controlled by the electromagnet / permanent magnet hybrid magnetizing device at every magnetizing current

becomes longer.

MECHANICALLY DRIVE / PERMANENT MAGNET HYBRID MAGNETIZING DEVICE FOR ELECTRIC POWER-SAVING

Configuration of Mechanically Drive / Permanent Magnet hybrid Magnetizing Device

Though a permanent magnet can apply the constant magnetic field intensity to MR fluid, it is difficult to vary the intensity of the field if the permanent magnet is fixed. On contrary, the magnetic field applied to MR fluid can be controlled if a permanent magnet can move in a yoke because the reluctance between the magnet and yoke is varied by the relative position of them. For example, the maximum magnetic field intensity is applied to MR fluid when the permanent magnet and yoke are fully overlapped. The overlap of them becomes smaller, the

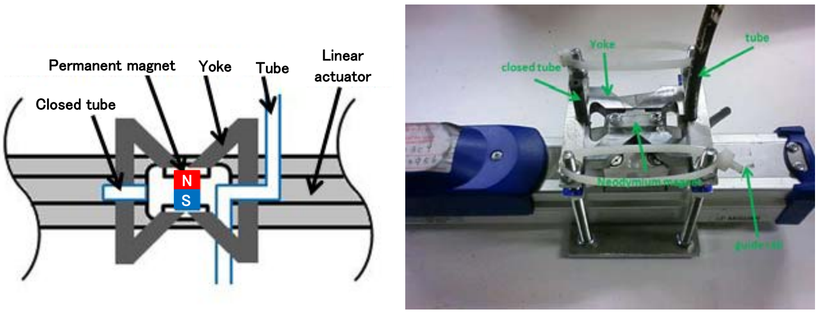

Figure 11 Mechanically drive / permanent magnet hybrid magnetizing device for MR fluid control

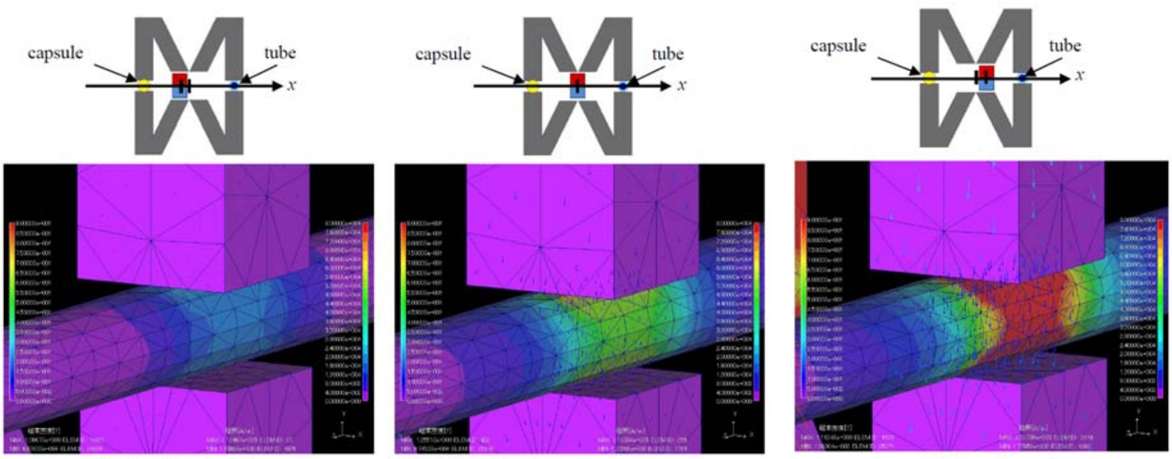

(a) left end (x=-4mm) (b) center (x=0mm) (c) right end (x=+4mm)

Figure 12 Simulated result on the position of the permanent magnet
(The magnetic field to MR fluid varies from 20kA/m to 80kA/m which is equivalent to the yield stress of MR fluid from 4kPa to 18kPa)

intensity of the field weaker. The simple idea is that an actuator moves a permanent magnet against the yoke. However, a restoration force, which attracts to maximize the overlap of a yoke and magnet, always acts on the magnet when it protrudes from the yoke. The restoration force is caused by the change of reluctance due to the magnet movement. In order to maintain the position of the magnet, a brake mechanism which consumes the electric power is required in the actuator. The electric power consumption increases when the intensity of magnet is large and the time width maintaining the magnet position is long. In this study, a new configuration of magnetizing device in which the restoration force can be reduced against the large intensity magnet is proposed. This prototype device is shown in Figure 11. In this device, the permanent magnet can be moved by an electrical linear actuator. The width of the yoke end covers the range of the magnet movement, and they are always fully overlapped to reduce the restoration force. The yoke separates into two symmetrical magnetic circuits. A tube is inserted into each magnetic circuit. The tube in the right side magnetic circuit in Figure 11 is the conduit for MR fluid flowing through the device, another tube in the left side circuit is a capsule containing MR fluid and its diameter is the same as the right side tube. Because this capsule acts like a dummy conduit with the same magnetic property of MR fluid in the right side tube, the reluctance is almost constant regardless of the magnet position.

A strong magnet, Neodymium (Ne-Fe-B) magnet, is used for this prototype device. Figure 12 shows the simulated result on the position of the magnet. From the simulation, it is estimated that this device applies the magnetic field to MR fluid from 20kA/m to 80kA/m. It means that this device can control the yield stress of MR fluid from 4kPa to 18kPa.

Testing of Viscosity Control Using Mechanically Drive / Permanent Magnet Hybrid Magnetizing Device

The center of the yoke, in which the width is 16mm, is defined as x=0, and the side of MR fluid conduit is defined as x>0, the dummy capsule side as x<0. Figure 13 shows the measured result of flow rates of MR fluid under the constant pressure difference (Δp=0.1MPa), when the center of the magnet with 8mm width moves from x= - 4mm to x=4mm. When the magnet moves closer to MR fluid conduit side, the magnetic field intensity and its viscosity in this side become larger, and the flow rates decrease. When the magnet is placed closest to the dummy capsule side, the flow rates of MR fluid are the almost same as that of non-magnetized MR fluid.

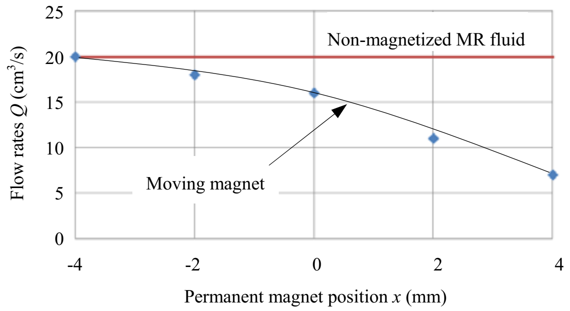

Figure 13 Measured flow rates equivalent to the viscosity of MR fluid controlled by the mechanically drive / permanent magnet hybrid magnetizing device under the pressure difference Δp of 0.1MPa

CONCLUSION

For the purposes both of the controllable viscosity range expansion and the electric power-saving at magnetizing MR fluid, this study proposed new magnetizing devices as following; (1) Digital / analog hybrid magnetizing device controlled by the modified PCM, (2) Electromagnet / permanent magnet hybrid one which utilizes the magnetizing and demagnetizing property of the permanent magnet material and (3) Mechanically drive / permanent magnet hybrid one in which the magnetic field is controlled by the strong permanent magnet movement with less electric power consumption. The digital / analog hybrid one is effective to expansion of the controllable viscosity of MR fluid, both the electromagnet / permanent magnet hybrid one and the mechanically drive / permanent magnet hybrid one are effective to the electric power-saving in maintaining the magnetic field. Those three hybrid magnetizing concepts are not independent each other, and can be combined to realize both requirements in one device.

ACKNOWLEDGEMENT

The author is thankful to Mr. Yusuke Tomotaka for his assistance to the trial manufacture of the magnetizing devices.

REFERENCES

1. Fujita T., Shimada K., Characteristics and Apprilcations of Magnetorheological Fluids, Journal of the Magnetic Society of Japan, 2003, 27-3, pp.91-100. (in Japanese)
2. Takesue N., Furusho J., Kiyota Y., Fast Response MR-Fluid Actuator, JSME international journal, 2004, Series C, 47-3, pp.783-791.
3. Murakami T., Sakai M., Nakano M., Study on the Development of Passive MR Damper with Displacement-Dependent Damping Characteristics, Journal of Fluid Science and Technology, 2010, 5-2, pp.86-97.
4. Yoshida K., Jung Y., Yokota S., A Microvalve Using MR Fluid Valve-Body, Transactions of the Japan Society of Mechanical Engineers, 2003, Series C, 69-682, pp.1633-1639. (in Japanese)
5. Sato Y., Shinohara K., Power Saving Drive in 2-position Control of Giant- magnetostrictive Actuator, IEEE Transactions of Magnetics, 2009, 45-10, pp.4554-4557.

Proceedings of the 8th JFPS International
Symposium on Fluid Power, OKINAWA 2011
Oct. 25-28, 2011

2B4-1

REDUCING THE STEADY-STATE ERROR BY TWO-STEP CURRENT INPUT FOR A FULL-DIGITAL PNEUMATIC MOTOR SPEED CONTROL

Chin-Yi Cheng *, Jyh-Chyang Renn **

* Department of Mechanical Engineering
National Yunlin University of Science and Technology
No. 123, University Road Sec. 3, Douliou, 640 Yunlin, Taiwan, R.O.C.
（E-mail: g9511706@yuntech.edu.tw）
** Department of Mechanical Engineering
National Yunlin University of Science and Technology
No. 123, University Road Sec. 3, Douliou, 640 Yunlin, Taiwan, R.O.C.

ABSTRACT

In this paper, a novel technique to reduce the steady-state error of a full-digital pneumatic motor speed control system by two-step variable current input is proposed and realized. One feature of such a control system is the utilization of a full-digital control valve (FDCV) consisting of 12 parallel-connected 2/2 pneumatic on-off valves. Obviously, the employed FDCV is intended to replace the expensive proportional or servo valve. In addition, compared to the conventional PWM-controlled proportional flow control scheme, the new FDCV possesses several advantages like medium operating noise, long life, ease of control and low cost. The conventional binary coding system together with the FDCV is chosen for this study. However, the major fault of the FDCV is its nonlinear saw-toothed flow-rate characteristic which generally results in the limit-cycle oscillation and the undesirable steady-state error. Therefore, a novel technique to reduce the steady-state error is further developed in this paper. The basic idea of the proposed novel technique is to adjust the opening areas of on-off valves in the FDCV by applying two-step current input structure to the valve coils. Consequently, without any hardware modification, an alternative saw-toothed flow-rate characteristic with higher resolution but less maximal flow-rate is available in the steady-state response. Finally, experimental results show that the steady-state error is significantly reduced by the proposed novel current switching control structure.

KEY WORDS

Pneumatics, Pneumatic Motor, Proportional Technology, Full-digital Control

NOMENCLATURE

$u(k)$: actuating signal,
$e(k)$: error signal,
K_P : gain of the proportional controller,
K_I : gain of the integral controller,
K_D : gain of the derivative controller.

INTRODUCTION

Nowadays, applications of pneumatic system may be found in many different engineering fields, like the automation technology, mechatronics, pneumatic tools, rehabilitation devices used by human being, clean room technology and so on [6, 7]. In a conventional position or speed control system, servo or proportional valve is generally utilized to achieve precise, linear and

continuously variable position or speed control. However, such valves are generally expensive and they are analogue components that are sensitive to noise or disturbance. To reduce the cost, another digital proportional control structure is proposed [2], in which four or more fast-switching 2/2 on-off valves using PWM-control are employed. A significant advantage of the fast-switching PWM-control structure is the lower cost. Its major faults, however, are noisy operation, short life and the obvious steady-state error. In this paper, therefore, a novel full-digital proportional pneumatic motor speed control system is developed and realized. The newly presented full-digital control valve (FDCV) consists of 12 parallel-connected 2/2 pneumatic on-off valves. In addition, a SSR relay module and binary coding system are also necessary components. Compared to the conventional PWM-control fast-switching proportional flow control structure, the new full-digital control system possesses several advantages like medium operating noise, long life and ease of control [3, 4]. Similar to the simple sequence control structure, the basic principle of the developed FDCV is that the number of actuated 2/2 pneumatic on-off valves depends on the actual demand of the volumetric flow-rate [6, 7]. In details, if the demanded volumetric flow-rate is quite low, then only few switching valves will be energized to supply low amount of airflow to the system. On the other hand, if the speed control system demands large amount of airflow, then more 2/2 switching valves will be switched to ON position. Table 1 shows some comparisons between aforementioned three control structures.
Surveying some previous reports, it can be found that the concept of full-digital control scheme proposed in this paper can be found in early 1980s [1]. However, this control scheme was not considered to be promising because the global digital revolution just began and was not fully developed at that time. On the other hand, the commercial products of 2/2 pneumatic on-off valve in 1980s were generally slow, expensive and bulky, which were definitely not suitable for the realization of the full-digital proportional pneumatic speed control system. Nowadays, however, the digital revolution covers all fields of technology, entertainment and other aspects. In addition, some fast, low-cost and small-sized sectional 2/2 pneumatic on-off valves are developed and commercialized. Thus, it may be concluded that the full-digital control scheme is ready for the application to the pneumatic motor speed control system. However, the major fault of the FDCV is its nonlinear saw-toothed flow-rate characteristic which generally results in the limit-cycle oscillation and the undesirable steady-state error. Therefore, a novel technique to reduce the steady-state error is further developed in this paper. The basic idea of the proposed novel technique is to adjust the opening areas of all on-off valves in the FDCV by applying two-step current input structure to the valve coils. Consequently, without any hardware modification, an alternative saw-toothed flow-rate characteristic with higher resolution but less maximal flow-rate is available in the steady-state response if the lower current is applied to the solenoid valve coils. In details, after reaching the pre-set quasi steady-state response, the control scheme is then switched from the larger maximal flow-rate mode to the higher resolution mode so that the steady-state error can be effectively reduced. In the following, the coding system as well as the designed test bench for the full-digital pneumatic motor speed control system is outlined.

CODING SYSTEM AND TEST BENCH

In this paper, the simple but effective binary coding system is utilized [3, 4]. Figure 1 shows the details of the binary coding system. The nonlinear and discontinuous saw-toothed air flow-rate output is depicted in Fig. 2. Obviously, the more 2/2 on-off valves are used, the higher control resolution could be achieved. However, more 2/2 on-off valves means also higher cost, which is generally not acceptable in most real applications. Therefore, a trade-off must be made. In this paper, the number of utilized on-off valves is chosen to be 12 to meet the trade-off. Figure 3 shows the real picture of the designed FDCV consisting of 12 small-sized 2/2 on-off valves (SMC V114 series). To achieve the synchronous actuation of all valves, it is essential that all 12 2/2 on-off valves are of the same type and manufactured by the same company.
The circuit diagram of the full-digital pneumatic motor speed control system is shown in Fig. 4. The speed of the pneumatic motor is controlled by only one set of FDCV shown in Fig. 3, which controls the airflow rate for P->A position. At the beginning, the FDCV is fully opened. Thus, the pneumatic motor is accelerated. However, if the motor runs too fast meaning that the control overshoot happens, the FDCV is then switched off and the motor slows down gradually due to inertia and friction force. To measure the speed of the pneumatic motor, a simple digital encoder is utilized. The measured speed signal is then fedback to the PC-based controller to form a closed-loop control scheme. In addition, a SSR module consisting of 12 solid-state relays serves as the drive unit in the test device.

Due to the discontinuous saw-toothed airflow-rate characteristic shown in Fig. 2, the limit-cycle oscillation is generally inevitable and exists in the steady-state response [7]. This is chiefly because that one or two 2/2 on-off valves of FDCV are still switched on and off continuously trying to reduce the steady-state error in the closed-loop steady-state response. Surveying some previous relevant studies, it is found that different coding systems in full-digital control structure can be used to reduce steady-state error [3, 4]. In this paper, however, a simple but novel full-digital current switching control structure based on conventional binary coding system is proposed to reduce the amplitude of the undesired limit-cycle oscillation. Referring to the force/stroke family curves of a general switching solenoid as shown in Fig.5, it is clear that different force output can be obtained if the input current is changed. An example is also given in Fig.5. That is, if the input current is changed from i_1 to i_2, then the spool stroke of the switching valve is varied from S_1 to S_2. Therefore, the opening area and the volumetric airflow rate output of the switching valve will also be changed accordingly. In summary, the basic idea of the proposed current switching control structure is to reduce the opening areas of all 2/2 on-off valves in the FDCV simultaneously by applying lower input excitation current to the coils. Consequently, in the steady-state response, an alternative saw-toothed flow-rate with higher resolution but less maximal flow-rate is available as shown in Fig.6. The most suitable switching timing has to be obtained by trial-and-error and is found to be the time when the transient response reaches around 50 % of its final value for the tested pneumatic motor. This is also defined as the beginning of the quasi steady-state response in this paper. At this moment, the control scheme is switched from high speed mode to high resolution mode so that the steady-state error is expected to be reduced effectively.

NOVEL TWO-STEP CURRENT CONTROLLER DESIGN

Figure 7 shows the block diagram of the closed-loop motor speed control system. To show the validation of the proposed full-digital proportional pneumatic motor speed control scheme, a simple PID controller is utilized in this paper as shown in Eq. (1). The chosen gains for the PID controller are obtained by trial-and-error approach. As shown in Fig. 7, it is observed that the first-step current input (0.8A) is supplied to the on-off valves if the actual motor speed, ω, is lower than the pre-set switching timing, that is, ω < 0.5 R, where the symbol R denotes the desired speed input to the system. At this time, the orifice areas of all on-off valves are fully open with maximal airflow-rate output to achieve fastest response. Therefore, it is called the high-speed mode in this paper. On the other hand, if the motor speed exceeds the pre-set switching timing, that is, ω > 0.5 R, the input current is then switched to the second-step current (0.5A). At this moment, the orifice opening areas of all on-off valves are reduced. This is called the high-resolution mode. Meanwhile, the airflow- rate output is also reduced by nearly 50%.

$$u(t) = K_p e(t) + K_I \int_0^t e(\tau) d\tau + K_D \frac{de(t)}{dt}. \tag{1}$$

Where
$u(t)$: Actuating signal,
$e(t)$: Error signal,
K_P : Gain of the proportional controller,
K_I : Gain of the integral controller,
K_D : Gain of the derivative controller.

EXPERIMENTAL RESULTS OF MOTOR SPEED CONTROL AND DISCUSSION

Owing to the nonlinear saw-toothed airflow-rate characteristic shown in Fig. 2, it can be seen that the airflow-rate output between 1Q and 2Q (for example: 1.5Q) is practically impossible due to the inherent, poor resolution of the full-digital control system. Consequently, the limit-cycle oscillation is inevitable and exists in the steady-state response because one or two 2/2 on-off valves of FDCV are still switched on and off continuously trying to reduce the steady-state error in the closed-loop steady-state response. In this paper, a novel current switching control structure is proposed that makes the higher resolution of airflow-rate possible. In details, the original 12-step resolution of the saw-toothed airflow-rate shown in Fig. 2 is successfully doubled by switching the input current between the normal (24V, 0.8A) and the smaller current value (24V, 0.5A). In this paper, the former is named the first-step current and the latter is called the second-step current. Consequently, the value of the parameter K in Fig. 6 is found to be 0.5 approximately and the airflow-rate output of 1.5Q becomes possible. Figure 8 shows the open loop speed control performance of the tested pneumatic motor. There are two curves in this figure. The upper curve represents the motor speed output using the first-step input current (0.8A) and the lower curve indicates the motor speed output using the second-step input current (0.5A). Obviously, the resolution is increased from 12 steps to 24 steps without any hardware modification if both current levels are switched properly. However, it is also noticeable that two kinds of nonlinearity, that is the dead-zone and saturation, exist in the open loop speed control performance. Such nonlinearities can be effectively compensated by the closed-loop control scheme. Figure 9 shows the closed-loop motor speed control responses. The desired motor speed input is set to be 750 rpm. From the enlarged response curves shown in Fig. 10, it is observed that the limit-cycle oscillation exists. To quantify the control error, the root-mean-square method is chosen. After some calculations, the root-mean-square steady-state error is decreased from 8 rpm to 2 rpm if the proposed two-step current switching control structure is utilized. That is, the steady-state error is decreased by 75%. In addition, it is also observable that the amplitude of the limit-cycle oscillation is reduced significantly. The PID controller gains for the experiments are chosen to be K_P = 0.16 V/m, K_I = 0.003 V*s/m and K_D = 0.001 V*s^2/m respectively and the switching timing is set to be 50%. However, the proposed full digital two-step current switching control structure introduces inevitably some phase lag in the transient response. This is reasonable because the maximal flow-rate output is reduced by half when the high resolution mode is switched on.

CONCLUSION

In this paper, a full-digital control scheme for pneumatic motor speed control system is successfully developed and implemented. Compared to the fast-switching PWM-control proportional flow control scheme, the full-digital control scheme possesses several remarkable advantages like medium operating noise, long life and ease of control. From the experimental results, it is also proved that the amplitude of the steady-state limit-cycle oscillation is significantly reduced by using the proposed two-step current switching control structure as compared to the utilization of a conventional control scheme. Besides, it is also expected that such a full-digital switching control structure together with the proposed FDCV has the potential to replace some traditional proportional or servo valves in the future.

ACKNOWLEDGEMENT

The financial support of the National Science Council under grant number NSC-98-2221-E-224-040-MY2 is greatly appreciated.

ILLUSTRATIONS

Net flow	Valve 1,Q	Valve 2,Q	Valve 3,Q	Valve 4,Q	Valve 5,Q	Valve 6,Q	Valve 7,Q	Valve 8,Q	Valve 9,Q	Valve 10,Q	Valve 11,Q	Valve 12,Q
0	0	0	0	0	0	0	0	0	0	0	0	0
1xQ	1	0	0	0	0	0	0	0	0	0	0	0
2xQ	1	1	0	0	0	0	0	0	0	0	0	0
3xQ	1	1	1	0	0	0	0	0	0	0	0	0
4xQ	1	1	1	1	0	0	0	0	0	0	0	0
5xQ	1	1	1	1	1	0	0	0	0	0	0	0
6xQ	1	1	1	1	1	1	0	0	0	0	0	0
7xQ	1	1	1	1	1	1	1	0	0	0	0	0
8xQ	1	1	1	1	1	1	1	1	0	0	0	0
9xQ	1	1	1	1	1	1	1	1	1	0	0	0
10xQ	1	1	1	1	1	1	1	1	1	1	0	0
11xQ	1	1	1	1	1	1	1	1	1	1	1	0
12xQ	1	1	1	1	1	1	1	1	1	1	1	1

Fig.1. Details of the binary coding system

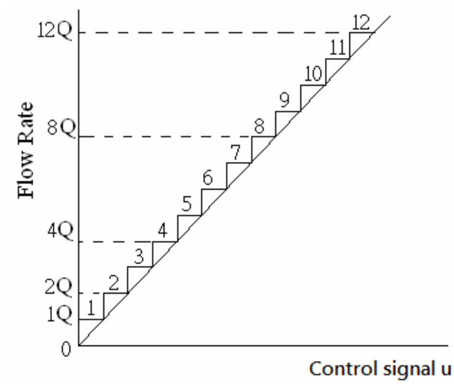

Fig.2. Discontinuous saw-toothed airflow rate

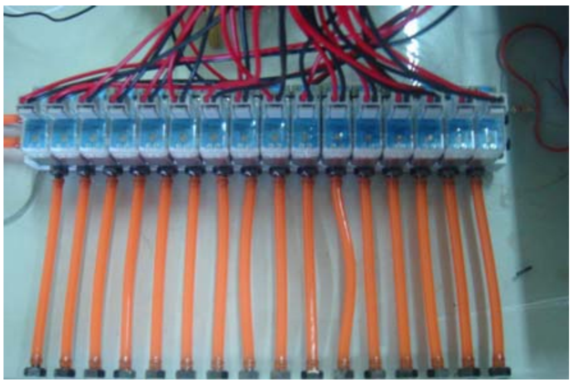

Fig. 3 The real picture of designed FDCV speed control system of an air

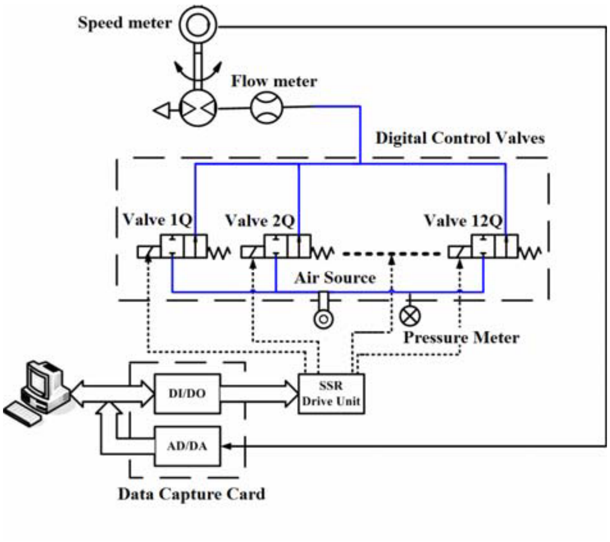

Fig.4. Proposed circuit diagram for the full-digital pneumatic motor speed control system.

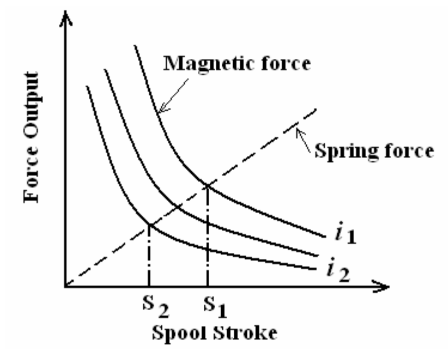

Fig.5. Force/stroke family curves of a general switching solenoid.

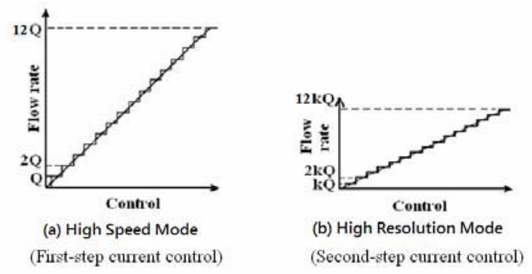

Fig.6. Comparison between the discontinuous airflow rate output for high speed mode and high resolution mode

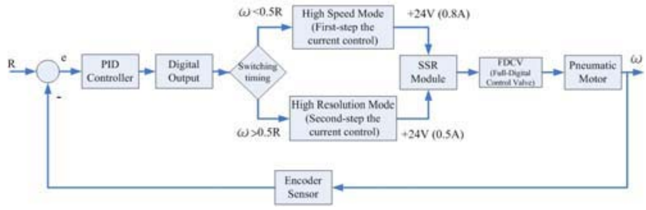

Fig.7. Block diagram of the full-digital closed-loop motor speed control system

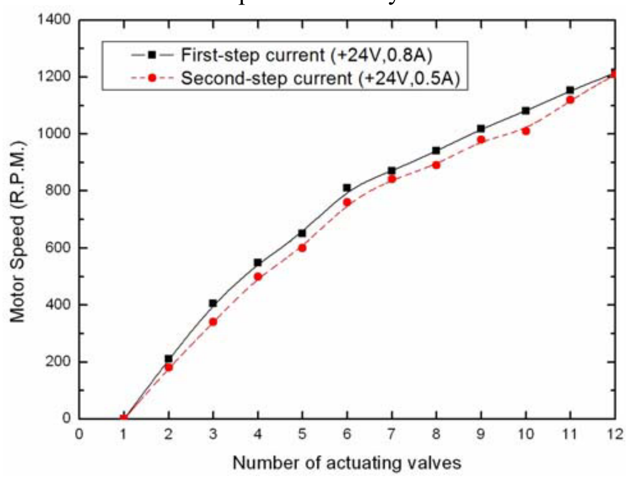

Fig.8. Comparison of motor speed control between the one-step current controller and two-step current switching controller

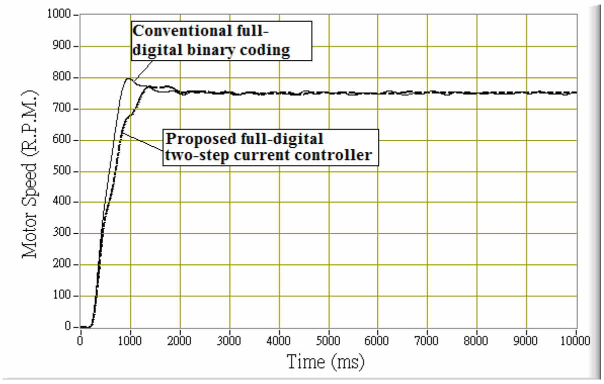

Fig.9. Experimental comparison between the conventional binary coding controller and the proposed full-digital two-step current switching controller (switching timing: 50%).

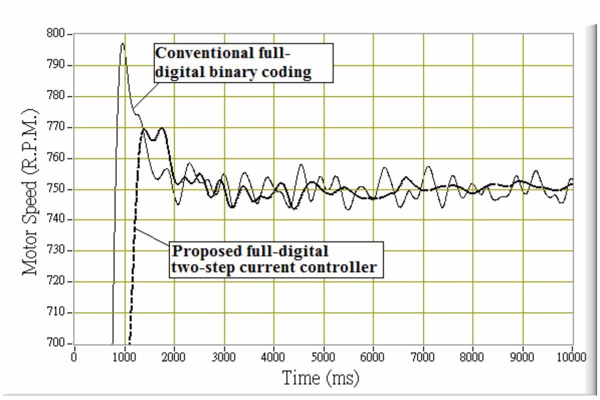

Fig.10: Enlarged comparison between the 700 rpm to 800 rpm.

Table 1: The comparisons between aforementioned three control schemes

	Full-digital proportional control	PWM fast-switching on/off control	Traditional proportional/ servo valve control
Cost	Medium	Low	High
Life	Long	Short	Long
Noise	Medium	High	Low
Dimension	Medium	Small	Small

REFERENCES

1. N.N., "Electro-hydraulic Proportional Valves and Closed Loop Control Valves Theory and Application," Robert Bosch GmbH, 1989.
2. Yuan Lu, "Elektro-pneumatischer Positionierantrieb mit schnellen Schaltventilen," Dissertation, RWTH Aachen, Germany, 1992.
3. Arto Laamanen, Matti Linjama and Matti Vilenius, "On The Pressure Peak Minimization In Digital Hydraulics," Proc. of Tenth Scandinavian International Conference on Fluid Power, Tampere, Finland, Vol.1, 2007, pp. 107-114.
4. Matti Linjama and Matti Vilenius, "Digital Hydraulics-Towards Perfect Valve Technology," Proc. of Tenth Scandinavian International Conference on Fluid Power, Tampere, Finland, Vol.2, 2007, pp.181-190.
5. Ziegler, J. G. and Nichols, N. B., "Optimum Settings for Automatic Controllers," Trans. of ASME 64, 1942, pp. 759-768.
6. Jyh-Chyang Renn, " Position Control of A Pneumatic Servocylinder Using Fuzzy-sliding Surface Controller," Int. J. of Fluid Power, Vol. 3, No. 3, 2002, pp. 19-25.
7. Jyh-Chyang Renn, Shigeru Ikeo, Chin-yi Cheng, "A Simple Switching Control Structure for Improving the Steady-State Error of a Full-Digital Water-Hydraulic Cylinder Position Control," Proc. of 4th Asia International symposium on Mechatronics, 2010, No.132.

Proceedings of the 8th JFPS International
Symposium on Fluid Power, OKINAWA 2011
Oct. 25-28, 2011

2B4-2

A DISTRIBUTED OBSERVER BASED ON NUMERICAL SIMULATION FOR A PIPELINE CONNECTING TO PNEUMATIC CYLINDER

Yu Okamoto*, Mitsuhiro Nakao**, Kotaro Tadano***, Kenji Kawashima***, Toshiharu Kagawa***

*Department of Mechano-Micro Engineering, Tokyo Institute of Technology
4259 Nagatsuta, Midori-ku, Yokohama 226-8503, Japan
(Email : okamoto.y.ae@m.titech.ac.jp)
**Department of Mechanical Engineering, Kagoshima University
1-21-40, Korimoto, Kagoshima, 890-0065, Japan
***Precision and Intelligence Laboratory, Tokyo Institute of Technology
4259 Nagatsuta, Midori-ku, Yokohama 226-8503, Japan

ABSTRACT

Time delay caused by pipelines connected to a pneumatic cylinder makes the controllability of the cylinder worse. Usually, pipelines are treated as lumped parameter systems. However, the pressures and flow velocities in the pipeline are distributed. If the pipeline is given as a distributed model, the controllability of the pneumatic cylinder can be improved. Usually, sensors are used to measure the state of a cylinder chamber. However, the sensors at the cylinder chambers are not desirable in terms of explosion and water proof. A distributed observer based on numerical simulation for a valve-cylinder connecting pipeline can estimate the real-time state of the cylinder chamber without the sensors. In this paper, we propose a real-time pressure estimation at cylinder chamber by using distributed observer for a valve-cylinder connecting pipeline. The effectiveness of the method is demonstrated experimentally.

KEY WORDS

Pneumatic Cylinder, Pipe Flow, Distributed Observer

NOMENCLATURE

A	:	Cross section	[m^2]
C_v	:	Specific heat at constant volume	[J/(kgK)]
D	:	Pipe diameter	[m]
f	:	frequency	[1/s]
G	:	Mass flow rate	[kg/s]
h	:	Heat transfer coefficient	[W/(m^{2}K)]
k	:	Thermal conductivity	[W/(mK)]
L	:	Pipe length	[m]
P	:	Pressure	[Pa]
P_r	:	Prandtl number	[ ]
R	:	Gas constant number	[J/(kgK)]
R_e	:	Reynolds number	[ ]
S_h	:	Heat transmission area	[m^2]
t	:	Time	[s]
u	:	Velocity of air	[m/s]
V	:	Volume of cylinder chamber	[m^3]
x	:	Position	[m]
ρ	:	Density	[kg/m^3]
γ	:	Ratio of specific heat	[ ]
λ	:	Coefficient of pipe friction	[ ]
θ	:	Temperature of air	[K]

Subscripts

a	:	Atomosphere
c	:	Cylinder
d	:	Discharge side
u	:	Charge side
p	:	Pipeline
$1, \cdots, n$	:	Mesh index of pipeline

INTRODUCTION

Time delay caused by pipelines connected to a pneumatic cylinder makes the controllability of the cylinder worse. Usually, pipelines are treated as lumped parameter systems[1]. However, the pressures and flow velocities in the pipeline are distributed. If the pipeline is given as a distributed model, the controllability of the pneumatic cylinder can be improved. Many studies for obtaining approximate solutions were conducted by solving the equations numerically with a computer. Usually, sensors are used to measure the state of a cylinder chamber. However, the sensors at the cylinder chambers are not desirable in terms of explosion and water proof.

The method of characteristics is a well known technique for solving partial differential equations, and is applied to compute the response of fluid pipelines. Even though the method of characteristics shows excellent agreement with experimental results in small amplitude wave [2][3][4][5], it can not be applied to a flow computation when the bulk velocity is not negligibly small. The authors have proposed pressure control of a pipeline-chamber system using an observer for the pipeline without sensors at the chamber [6]. A distributed observer based on numerical simulation for a valve-cylinder connecting pipeline can estimate the real-time state of the cylinder chamber without the sensors. In this paper, we propose a real-time pressure estimation at cylinder chamber by using distributed observer for a valve-cylinder connecting pipeline. The effectiveness of the method is demonstrated experimentally.

DISTRIBUTED MODEL OF PIPELINE

The pipeline is given as one dimensional distributed model. The governing equations of the pipelines are motion equation(1), continuity equation(2), energy equation(3), and state equation of gas(4). We use distributed observer by solving these equations by difference method.

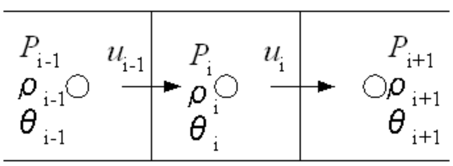

Fig. 1 The staggered grid system

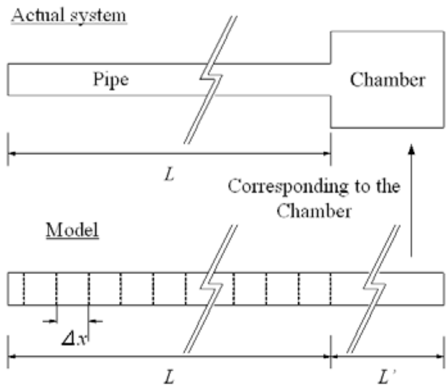

Fig. 2 The actual system and the computation model of the distributed observer

$$\frac{\partial u}{\partial t} + u\frac{\partial u}{\partial x} = -\frac{1}{\rho}\frac{\partial P}{\partial x} - H \tag{1}$$

$$\frac{\partial \rho}{\partial t} + u\frac{\partial \rho}{\partial x} = -\rho\frac{\partial u}{\partial x} \tag{2}$$

$$\frac{\partial p}{\partial t} + u\frac{\partial P}{\partial x} = -\gamma\rho\frac{\partial \rho}{\partial x} + \rho(\gamma-1)(uH+T) \tag{3}$$

$$P = \rho R\theta \tag{4}$$

where

$$H = \lambda|u|u/(2D) \tag{5}$$

$$\lambda = 0.3164R_e^{-0.25} \tag{6}$$

$$T = -h(\theta-\theta_a)/(\rho D)) \tag{7}$$

$$h = 0.023R_e^{0.8}P_r^{0.4}k/D \tag{8}$$

$$k = 7.95\times10^{-5}\theta + 2.0465\times10^{-3} \tag{9}$$

Pressure loss due to friction along a pipe to the average velocity of the fluid flow is described with the Darcy-Weisbach equation as shown in (5). As a flow coefficient of turbulent flow, the Blasius friction factor described in (6) is employed. The rate of convective heat transfer between the pipe wall and the air is given by (7). Heat transfer coefficient is described in the formulation given as (8). The Dittus-Boelter equation is employed for describing Nusselt number. Thermal conductivity is approximated by (9) .

A staggered grid system as shown in Fig.1 is employed for a stable computation. Fig.2 shows the actual system and the computation model of the distributed observer. The distributed observer regards the cylinder chamber as a part of the pipeline and decide length of the last grid L' to equal the volume of cylinder chamber. As the inlet boundary condition, the measured pressure is used and regards gradient of flow velocity as 0. As the outle boundary condition, we calculate state of cylinder chambers by solving following equations by difference method. Time derivative of the state equation of the cylinder chambers are written as follows

$$V_{cu}\frac{dP_{cu}}{dt} = -A_{cu}\frac{dx_c}{dt}P_{cu} + R\theta_{cu}G_{cu} + \frac{P_{cu}V_{cu}}{\theta_{cu}}\frac{d\theta_{cu}}{dt} \tag{10}$$

$$V_{cd}\frac{dP_{cd}}{dt} = A_{cd}\frac{dx_c}{dt}P_{cd} + R\theta_{cd}G_{cd} + \frac{P_{cd}V_{cd}}{\theta_{cd}}\frac{d\theta_{cd}}{dt} \tag{11}$$

The energy equation of the cylinder chambers can be written as follows

$$\frac{C_vP_{cu}V_{cu}}{R\theta_{cu}}\frac{d\theta_{cu}}{dt} = C_vG_{cu}(\theta_{pun} - \theta_{cu}) + R\theta_{pun}G_{cu} - A_{cu}\frac{dx_c}{dt}P_{cu} + h_{cu}S_{hcu}(\theta_a - \theta_{cu}) \tag{12}$$

$$\frac{C_vP_{cd}V_{cd}}{R\theta_{cd}}\frac{d\theta_{cd}}{dt} = R\theta_{cd}G_{cd} + A_{cd}\frac{dx_c}{dt}P_{cd} + h_{cd}S_{hcd}(\theta_a - \theta_{cd}) \tag{13}$$

This method is an explicit method. For a stable computation, the CFL condition described as the following equation must be satisfied:

$$c\Delta t \leq \Delta x \tag{14}$$

When pipe length is 2 m, the tested pipeline is separated to 4 computation meshes which have a grid spacing of 0.5 m to satisfy the CFL condition. When pipe length is 9 m, The tested pipe line is separated to 9 computation meshes which have a grid spacing of 1.0 m to satisfy the CFL condition.

EXPERIMENT

Apparatus

Fig.3 shows the experimental apparatus of pneumatic cylinder system. The cylinder is controlled by a five port servo valve.

The apparatus consists of a servo valve(FESTO MPYE-5-MS-010B-30L-SA), pipelines, pneumatic cylinder(SMC CJ2L6-100), four pressure sensors(JTEKT PD64S), encorder(MTL MLS-12-1500pst), an AD converter, a DA converter and a personal computer(Intel(R) Core(TM) i3 CPU M370 @ 2.40GHz). The servo valve controls the inlet mass flow to the piplines. The AD converter and the four pressure sensors

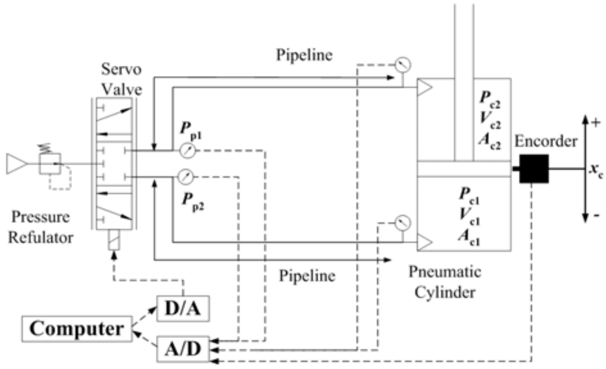

Fig. 3 Experimental apparatus

Table 1 Specification of the Pipeline connecting to cylinder

	Pipe length L[m]	Pipe diameter D[m]
I	2.0	1.0×10^{-3}
II	2.0	2.0×10^{-3}
III	2.0	4.0×10^{-3}
IV	9.0	1.0×10^{-3}
V	9.0	2.0×10^{-3}
VI	9.0	4.0×10^{-3}

Table 2 Specification of the cylinder

Inner Diameter	$A_{c1} = 78.53 \times 10^{-6}$[m^2], $A_{c2} = 65.97 \times 10^{-6}$[m^2]
stroke	100×10^{-3} [m]

are used to obtain the pressure at the inlets of the pipelines and in the cylinder chambers. Pressure supply to the servo valve was set at 600 kPa. Sampling time of the AD converter and the DA converter is 1 ms.

Method

We evaluate the computation accuracy and time of the distributed observer. And, we also compared the distributed observer with the 2nd order model expressed as follows[1].

$$\frac{P_{c1}}{P_{p1}} = \frac{\omega_n^2 e^{-T_d s}}{s^2 + 2\zeta\omega_n s + \omega_n^2} \tag{15}$$

where, ω_n is natural angular frequency, ζ is damping facter and T_d is time delay. These parameters were identified by measured pressure at the inlet of the pipelines and at the cylinder chambers.

- **Step input**
  A step input of 4.0, 3.5 and 3.0 V has been applied to the valve. In order to make same initial condition, initial input voltage applied to the valve is set to 9.0 V . After 2 s, change the input voltage to 4.0 V, 3.5V and 3.0V . Neutral position of the valve is 5.0 V . V_1 is discharge side and V_2 is charge side if the input voltage is 9.0V.

- **Position controlled**
  To evaluate validity of the distributed observer when the cylinder periodically moves, we compare pressure at the cylinder chambers among the three methods with the position controlled cylinder. Reference of position control is set to $x_c = 10 \times 10^{-3} \sin(2\pi f t)$, f=1 and 2 Hz. Fig.4 shows the block diagram of control system of the pneumatic cylinder. Table.4 shows control parameters of the controller. These parameters are determined by trial and error.

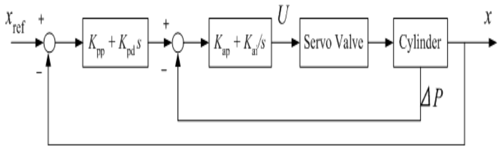

Fig. 4 Block diagram of the pressure control

RESULTS AND DISCUSSIONS

Step input

Table.3 shows the identified parameters of the 2nd order model. we can see the parameters are different among even same condition but with different input voltages.

Fig.5 shows cylinder displacement and comparison of pressure P_1, P_2 at cylinder chambers among three methods: distributed observer, 2nd order model and experiment, versus time when input of 4.0 V has been applied to the valve with V (the pipe length L=9 m, the pipe diameter D=2 mm). In Fig.5, P_1 is charge side pressure of the cylinder chamber and P_2 is discharge side pressure of the cylinder chamber. The experimental data shows time delay caused by the pipelines. P_1 raise rate and P_2 drop rate decrease when the cylinder is moving. A difference is large between pressure at inlet of pipeline and at cylinder chambers when the cylinder is moving. The distributed observer can estimate the condition but the 2nd order model can not. Fig.6 shows comparison of pressure P_1 at cylinder chamber among the 3 methods when input of 4.0,3.5 and 3.0 V has been applied to the valve. Fig.6 shows the distributed observer can reproduce real pressure response but 2nd order model can not.

Table 3 Parameters of 2nd order model

	Input Voltage [V]	ω_n [rad/s]	ζ	$T_d[s]$
I	4.0	112	1.2	0.001
	3.5	1000	0.0018	0.030
	3.0	113	1.2	0.020
II	4.0	208	0.40	0.000
	3.5	118	0.43	0.000
	3.0	108	0.51	0.000
III	4.0	215	0.13	0.000
	3.5	229	0.13	0.000
	3.0	230	0.13	0.000
IV	4.0	10	1.50	0.040
	3.5	8	1.80	0.035
	3.0	8	1.80	0.035
V	4.0	15	0.60	0.000
	3.5	13	0.64	0.000
	3.0	17	0.88	0.014
VI	4.0	200	0.58	0.000
	3.5	100	0.59	0.000
	3.0	34	0.35	0.000

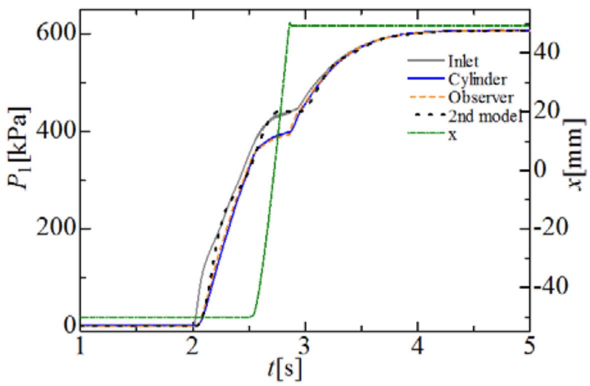

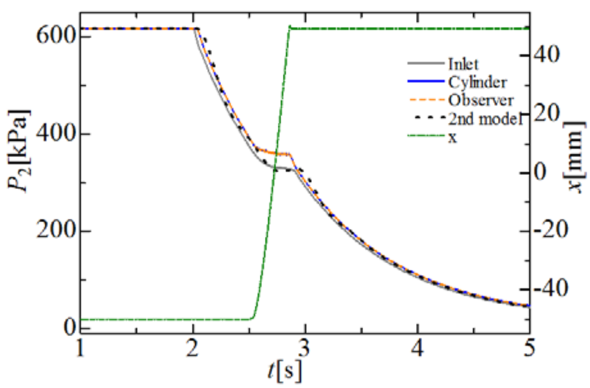

Fig. 5 Pressure responses of the cylinder chamber (V : L = 9 m, D = 2 mm)

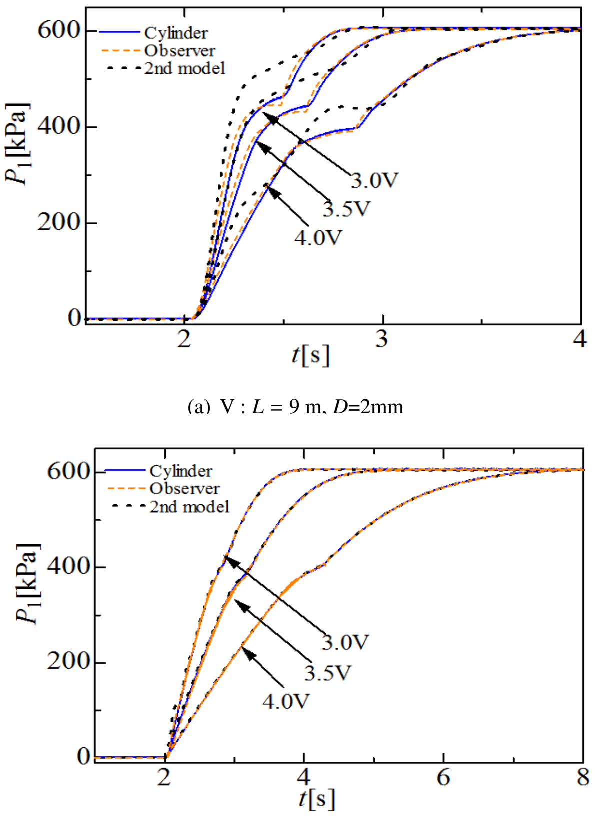

(a) V : L = 9 m, D=2mm

(b) VI : L = 9 m D= 4mm

Fig. 6 Pressure responses of the cylinder chambers (V, VI) against the three type of the applied input voltages to the valve

In order to apply the observer to real-time pressure estimation, computation times of the observer must be faster than the real time. 1 s computation times of the observer separated to 4 computation meshes less than 0.017 s and separated to 9 computation meshes less than 0.075 s. Since computation time of explicit method depends on only time increment and grid space, we confirmed that the distributed observer can estimate real-time pressure at the cylinder chambers.

Position control

Fig.7,Fig.8 show comparisons among the three methods versus time when the cylinder is position contorlled. with IV (the pipe length L=9 m, the pipe diameter D=1 mm) and with V (the pipe length L=9 m, the pipe diameter D=2 mm). Reference of position control is set to $x_c = 10 \times 10^{-3} \sin(2\pi f t)$, f=1 and 2 Hz. The pressure estimation at the cylinder chambers by using the observer has a good agreement with experimental result except III(f = 2 Hz, D = 1 mm). On the other hand, the 2nd model can not reproduce the real pressure response.

Fig.7 shows large difference occured when the cylinder velocity is large. Possible cause of that difference is flow velocity distribution in the cylinder chambers. The distributed observer regards the cylinder chambers as one grid and calculate the state of the chambers by solving (10)-(13) and ignores flow velocity disitribution in the chambers. However, there are flow velocity in the actual cylinder chambers. Especially, when the cylinder velocity is large, there are complex flow velocity in the cylinder chambers. Flow velocity distribution in the cylinder chambers effect the pipelines if volume of the pipelines is small compared to the cylinder chambers. Since volume of the pipelines of III are small compared to the cylinder chambers, the distributed observer can not reproduce the real pressure. In order to calculate more precise pressure, the observer needs to consider flow velocity distribution in the cylinder chamber. However, calculation the flow velocity distribution is very difficult because the flow velocity distribution is very complex.

Another possible cause of that difference is the boundary layer effect in the pipelines. In order to calculate more precise pressure, observers need to consider flow in the pipelines as three dimensional flow. More complex model is needed to solve these problem. However, making model more complex may make real-time pressure estimation impossible.

It is verified that distributed observer can estimate real-time pressures at the cylinder chambers except the volume of the pipelines are small compared to the cylinder chambers

Table 4 Specification of the Pipeline connecting to cylinder

f [Hz]		K_{pp}	K_{pi}	K_{pd}	K_{ap}	K_{ai}
1	I	1.0	20	0.08	0.10	0.20
	II	1.0	30	0.08	0.15	0.30
	III	1.0	30	0.08	0.15	0.30
	IV	1.2	0	0.06	0.11	0.10
	V	1.2	0	0.02	0.22	0.00
	VI	2.5	0	0.03	0.20	0.30
2	I	1.5	0	0.06	0.15	0.30
	II	1.5	0	0.06	0.15	0.30
	III	1.3	0	0.08	0.20	0.30
	IV	1.5	0	0.04	0.10	0.00
	V	1.3	0	0.06	0.10	0.30
	VI	2.0	0	0.05	0.20	0.30

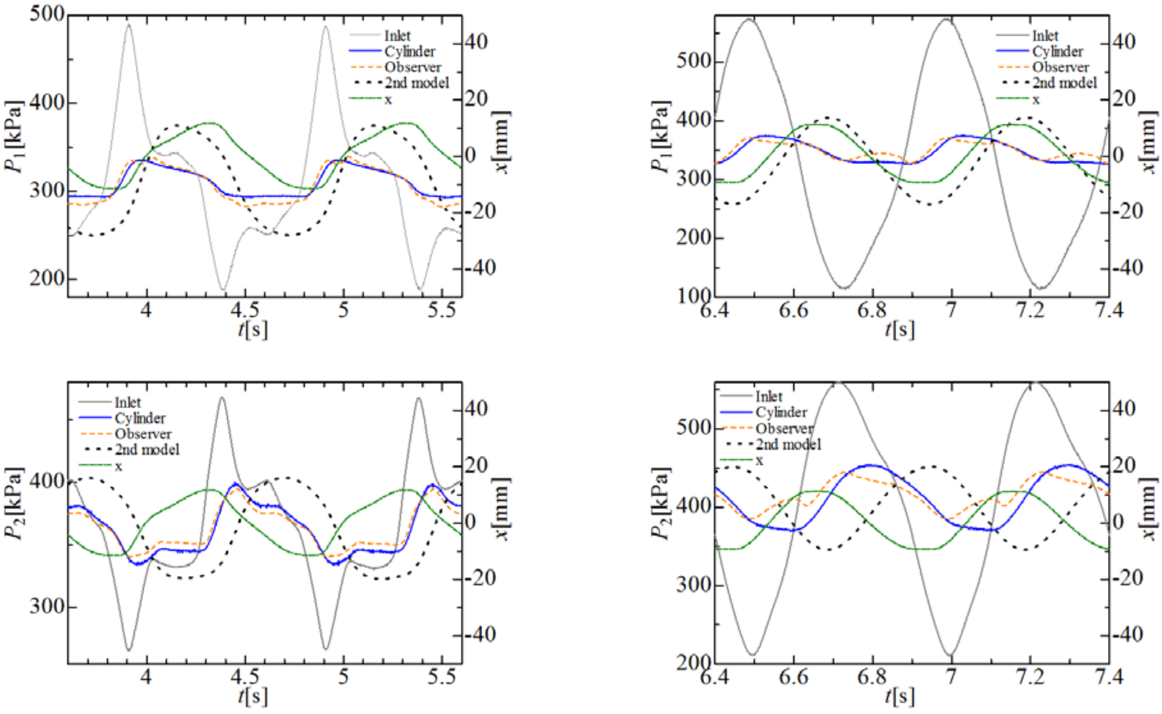

(a) f=1Hz (b) f=2Hz

Fig. 7 Pressure responses of the position controlled cylinder chambers with IV (L=9[m],D=1[mm])

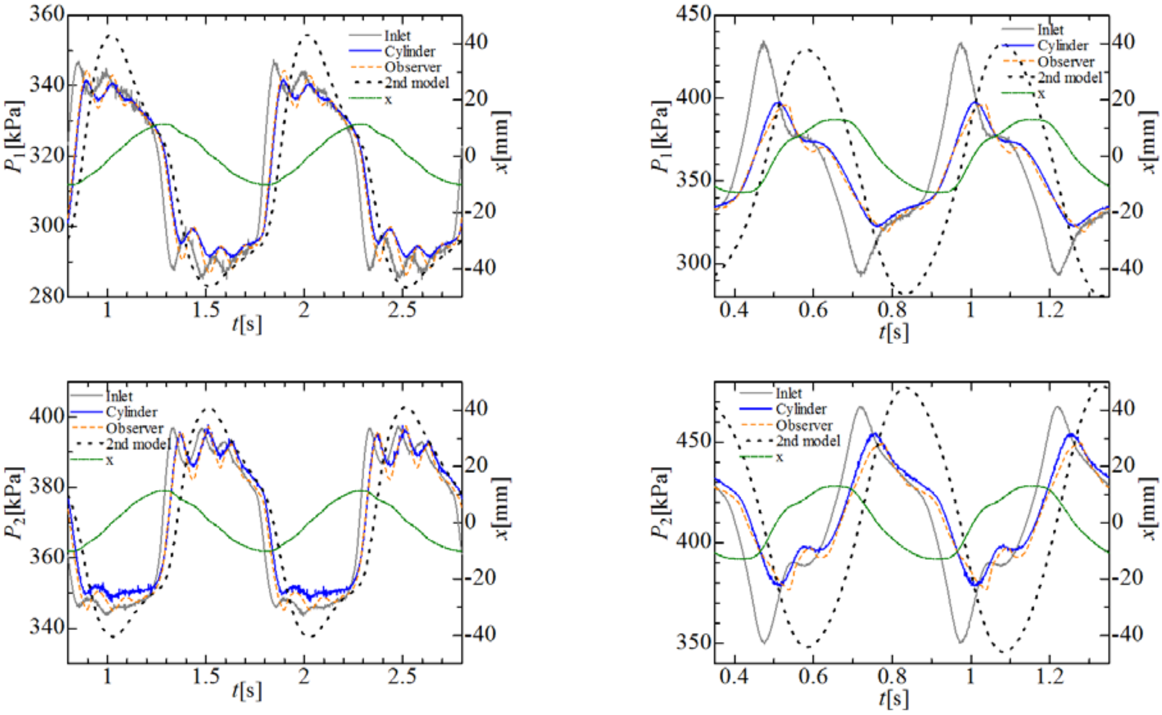

(a) f=1Hz (b) f=2Hz

Fig. 8 Pressure responses of the position controlled cylinder chambers with V (L=9[m],D=2[mm])

CONCLUSION

In the present study, we proposed a real-time pressure estimation at the cylinder chambers by using the distributed observer. The effectiveness of the method is demonstrated experimentally. At first, we construct the distributed observer for a pipeline connecting to pneumatic cylinder. Then, we compare pressure at the cylinder chambers among three methods: the distributed observer, the 2nd order model and experiment when step input voltage has been applied to the valve and position controlled cylinder. The distributed observer has better agreement with experimental result than the 2nd order model. We confirmed the distributed observer distributed observer can estimate real-time pressures at the cylinder chambers except the volume of the pipelines are small compared to the cylinder chambers.

REFERENCE

1. Kagawa T. et al, A Study of a Reduced Model for a Dynamics of a Pneumatic Transmission Line , Trans. Jpn. Soc. Instrum. & Control Eng. , vol.21 (p.9) , 1985. (in Japanese)
2. Brown, F.T., The Transient Response of Fluid Lines, Trans. ASME, J. Basic Engineering, 84(4), pp. 547-553, 1962.
3. Zielke, W.,Frequency—Dependent Friction in Transient Pipe Flow, Trans. ASME, Ser. D90—1,109/115. 1968.
4. Kitagawa A. et al, High Speed and Accurate Computing Method for Transient Response of Pneumatic Transmission Line Using Characteristics Method, Transactions of the Society of Instrument and Control Engineering, 20(7), pp. 648-653, 1984.(in Japanese)
5. Kagawa T. et al, High Speed and Accurate Compating Method of Frequency-Dependent Friction in Laminer Pipe Flow for Characteristics Method, Trans. Jpn. Soc. Mech. Eng., 49(447), pp. 2638-2643, 1983. (in Japanese)
6. Nakao M, Okamoto Y, Kawashima K, Kagawa T 2010 Pressure Control of Pneumatic Pipe-Chamber System Using a Distributed Observer, 11th SICE Symposium on Industrial Application Systems 35-40 (in Japanese)

Proceedings of the 8th JFPS International
Symposium on Fluid Power, OKINAWA 2011
Oct. 25-28, 2011

2B4-3

Research and Development of New Opto-Fluidic Transducer

Keisuke NAGASHIMA*, Osamu OYAMA* and Toshihiro YOSHIMITSU**

* Mechanical Engineering
Meiji University
1-1-1 Higashimita, Tama-ku, Kawasaki-shi, Kanagawa-ken, 214-8571 Japan
(E-mail: ce02068@meiji.ac.jp)
** Robotics and Mechatronics
Kanagawa Institute of technology
1030 Shimoogino, Atsugi-shi, Kanagawa-ken, 243-0292 Japan

ABSTRACT

A purpose of this study is building the system which can perform remote control only with light and a fluid for a transmission signal by simple mechanism without using electricity and an electric wave. In this way, we realize high reliability and environmental performance, and we aim at the thing which is expected of the activity in the healthcare, severe environment and the micromachine. For the summary of the system, it converts light intensity into air pressure signal and drive an air actuator. Therefore the development of the opto-fluidic transducer which could convert light into air pressure was necessary. In this study, we focus on photothermal effect and thermo-magnetic materials which could control the putting on and taking off of the magnet by heat. We inspected distance and the temperature in thermo-magnetic materials and the magnet to make the most suitable element. As a result, we could realize an objective opto-fluidic transducer.

KEY WORDS

Photothermal Effect, Thermo-Magnetic Materials, Air Pressure

NOMENCLATURE

F	: Force	[N]
r	: Distance	[m]
m	: Strength of the magnetic pole	[Wb]
μ_0	: Magnetic permeability in a vacuum	[H/m]

INTRODUCTION

The developments of the super minute processing technique and the electronics technology of lately years are remarkable. Thereby, the microminiaturization of various devices has been enabled. In addition, it has become possible to achieve a compact, complex, precise and reliable electronic equipment. With it, the development of the micromachine is expected in various fields, and the development of the microactuator is indispensable. However, it is very difficult to make the micro device which has a complicated electronic circuit and a motor. Besides, the reliability of machinery equipped with an electronic circuit has a limitation. As long as it uses electricity, it can't avoid the environmental obstacles and the influence on surrounding. Further influence of frictional force swells for generated power in the micro world. Therefore fluid pressure without the mechanical contact such as the gear is suitable for the transmission of the energy. From these reason, it is ideal to build the system that has simple mechanism and can transmit signals by using air pressure without electrical signals. This can be achieved with the opto-fluidic control system. If the device which is controlled only by light and air pressure and simple mechanism, without electrical signal the attractive system which is independent of the environmental obstacles and has high reliability can come out.

In this study, we aim at the realization of the opto-fluidic control system by using materials called the thermo-magnetic materials which can control magnetic induction by heat. In this report, we describe a structure of the opto-fluid transducer which is the pivot of this system, a theory and a property of thermo-magnetic materials.

THERMO-MAGNETIC MATERIALS

A paramagnet has temperature to lose the magnetism called the Curie point. This temperature varies by a kind of the paramagnet. In the general iron this is 770 [℃]. If the iron reaches this temperature the iron loses magnetism and does not adhere to a magnet. In addition, when the iron cools down from a high temperature state and is less than 770 [℃] (Curie point), it gains magnetism again and comes to adhere to the magnet. Under low temperature, because the magnetic moment of the atom can stand in line in same direction, the magnetic moment adheres to the magnet. However, a course of the magnetic moment is disturbed because the heat vibration occurs when it becomes the high temperature. Therefore the magnetic moment can't stand in line in same direction, and paramagnet loses magnetism. In higher temperature than Curie point, it is not in this way adhered to a magnet. Fig.1 shows the image of the state of the magnetic moment before and after the Curie point.

The thermo-magnetic materials refer to the thing which set the Curie point mentioned above from the normal room temperature to a high temperature level optionally. Because the magnetism properties change in approximately a Curie point greatly, depending on a temperature change, it can control the putting on and taking off of the magnet. The thermo-magnetic materials include a Fe - Ni alloy, a Fe - Ni - Cr alloy. A Curie point can be set optionally by changing the combination ratio of the materials of this alloy.

The thermo-magnetic materials are generally used for temperature sensor and Heating element for IH heating.

In this time, we focus on the low temperature type that the Curie point is normally room temperature, and tried the application of the opto-fluidic transducer.

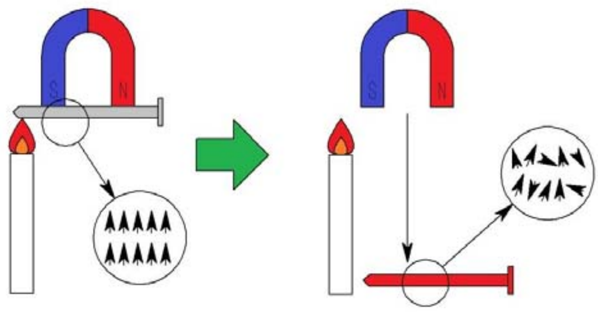

Fig.1 State of the magnetic moment

OPTO-FLUIDIC TRANSDUCER

The Fig.2 shows the schema of the opto-fluidic transducer.

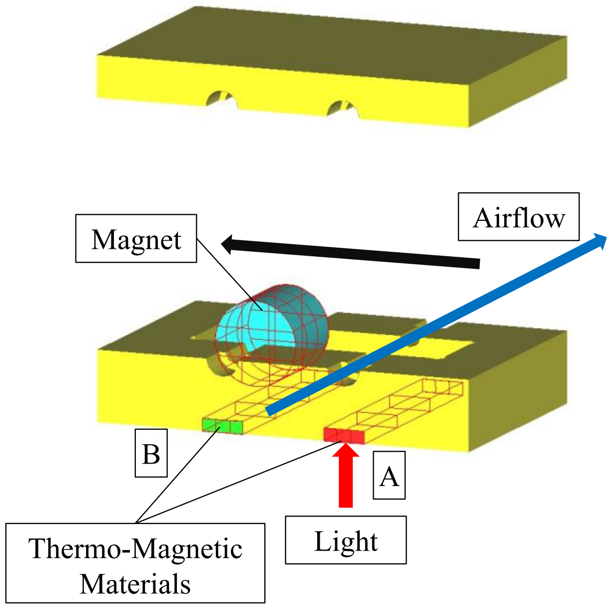

Fig.2 Schema of the opto-fluidic transducer

The new opto-fluidic transducer changes the flow pass by the positioning of the magnet. The positioning of the magnet is performed by changing magnetic induction of thermo-magnetic materials by the heat of light. In this way, the control of the fluid by the light is realized.

Fig.3 shows the structure of a new opto-fluidic transducer.

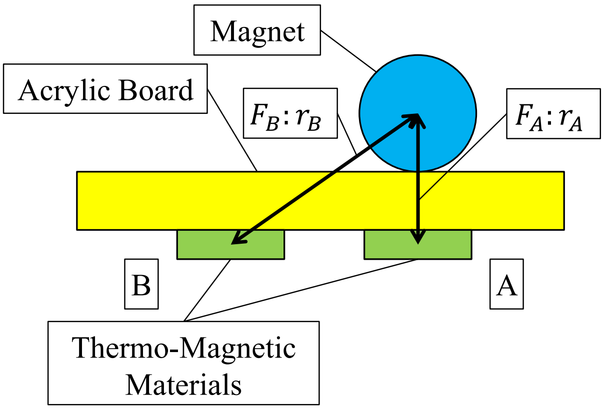

Fig.3 Component of opto-fluidic transducer

In this study, the new opto-fluidic transducer consists of column-shaped neodymium magnet, acrylic board and two thermo-magnetic materials. The neodymium magnet composes the valve body, the acrylic board composes the spacer and thermo-magnetic materials move the valve. We distinguish two thermo-magnetic materials from A, B each.

MAIN PARAMETER

Eq. (1), Eq. (2), Eq. (3) express Coulomb's low.

$$F = \frac{m_1 m_2}{4\pi\mu_0 r^2} \quad (1)$$

$$\mu_0 = 4\pi \times 10^{-7} \quad (2)$$

$$F = 6.33 \times 10^4 \times \frac{m_1 m_2}{r^2} \quad (3)$$

Understanding from this expression, the gravitation occurred between particles on two magnetic charges is proportional to the strength of the magnetic pole, and inversely proportional to square of the distance. We decided to inspect size of the magnet and thermo-magnetic materials, distance between the magnet and thermo-magnetic materials, and two thermo-magnetic materials as a main parameter. We aim at finding the most suitable combination from this inspection.

PRINCIPLES OF MOVEMENT

Fig.4 and Fig.5 show a process of the movement of a new opto-fluidic transducer.

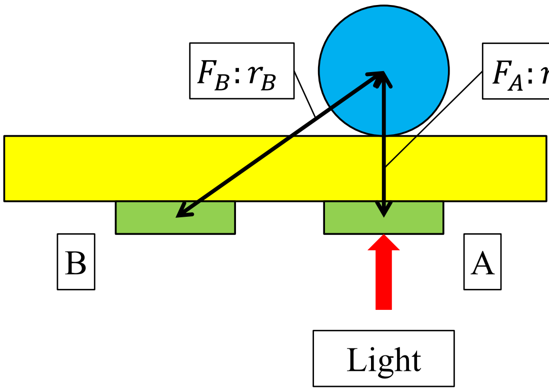

Fig.4 Theory 1 of the opto-fluidic transducer

Understanding from the Eq. (3), if the strength of the magnetic pole is the same, gravitation of the one closing the magnet becomes strong. Therefore, when $r_A < r_B$, it becomes $F_A < F_B$, and the magnet is stable at the upper part of thermo-magnetic materials A.

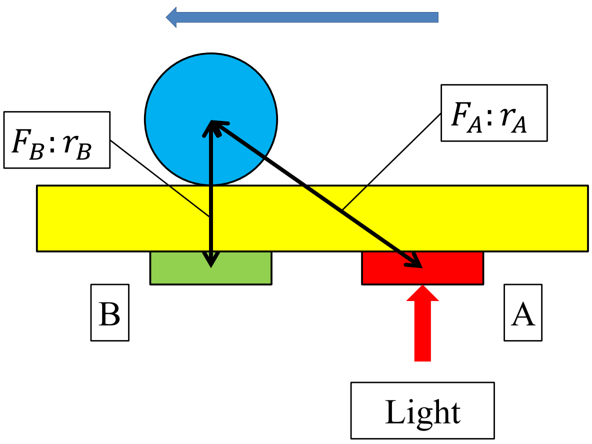

Fig.5 Theory 2 of the opto-fluidic transducer

When the thermo-magnetic materials A is warmed by light, the magnetic induction of thermo-magnetic materials decreases, and gravitation between the magnet and the thermo-magnetic materials become weak. Even if it is $r_A < r_B$, it becomes $F_A < F_B$, and the magnet is drawn to thermo-magnetic materials B.

Changing the position of the valve disc by light, the control of fluid by using above-mentioned movement is done. As a result, it realize the control of the fluid by light signal without using electricity.

THE CHOICE OF THE MAGNET

In this study, the magnet is the important element which roles and acts as the valve body. It is a part affecting the reply of the element greatly. Therefore the resistance of movement must be little as much as possible at the time of a change, and it is demanded that the magnet could cover air passage well. From these, we decided to make the shape a column-shaped. In the case of a column shape, it can perform the shut off or open state of the valve body in a rolling and not sliding, being little resistance. In the experiment, we use the magnet which a diameter and height are equal in mainly.

For the kind of the magnet, we use a neodymium magnet. The neodymium magnet has the best magnetic characteristic in a circulating magnet and can create strong magnetic fields even if small. The magnet is hard itself, and it does not break and miss, and the mechanical strength is good. By using the magnet's self moving characteristic we can switch the valve. This is the reason the magnet's force is prefer to be strong. In addition, the retention of the magnet should be strong because it affects the stability as the element. We thought that the neodymium magnet was most suitable from these points and chose it.

In the point where it should be careful about alone, the neodymium magnet is more vulnerable byheat than other magnets. By the normal use, it hardly becomes the problem, but it is necessary to consider a heat-resistant type and magnet shape, cooling under a high temperature.

THE CHOICE OF THE THERMO-MAGNETIC MATERIALS

In this study, the thermo-magnetic materials are the most important element and are the key materials of the study. Because we use the heat occurred by light this time, the Curie point of the thermo –magnetic materials are desirable for near the normal room temperature. Therefore we decided to use the low temperature type that a magnetic characteristic changed greatly in the range of 80 [℃] from -20 [℃]. For the materials fitting to above condition, we used a Fe - Ni alloy.

It was confirmed that a shape and the size of thermo-magnetic materials had a significant influence on the stability of the valve body and the position. The column magnet of the valve is magnetized axially, and long distance direction of thermo-magnetic materials and the axial direction of the column magnet make to be stable in form to agree. Fig.6 shows the construction. The shape is made as a plate-shaped rectangular solid. We change the vertical thickness and the horizontal length of the plate and inspect the characteristic.

When we inspect the influence of shape and the size of thermo-magnetic materials, cutting process of materials is necessary. We cut the thermo-magnetic materials by wire cut electric discharge method.

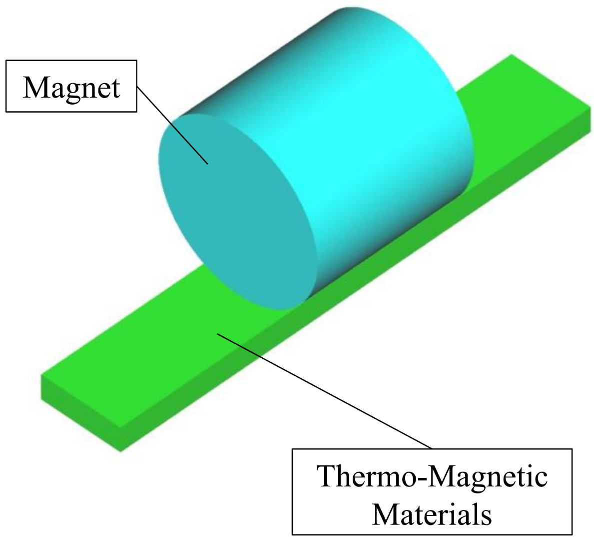

Fig.6 Stable course of the magnet

WARMING OF THE THERMO-MAGNETIC MATERIALS BY THE LIGHT

Fig.7 shows a temperature change when we warmed the plate of the thermo-magnetic materials using light.

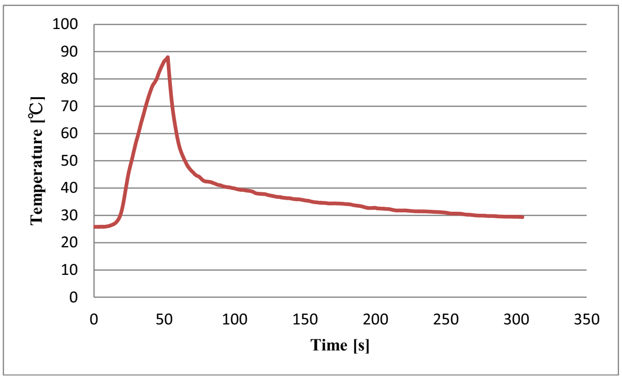

Fig.7 Warming of the thermo-magnetic materials by the light

We used a short arc metal halide lamp for a source of light. This is illumination of the luminescence source type. Because it does not include most of the infrared light, it is low fever of quarter of the halogen bulb. The wavelength spectrum properties are almost natural light of the sun.

The Fig.8 shows the set up of the experiment. In consideration of doing constantly, we tested without painting on the thermo-magnetic materials with light absorbing body such as a carbon black in a low-temperature type source of light, but it was able to warm the thermo-magnetic materials by light enough. The Fig.7 shows switched on the source of light with stating the measurement and became a certain measure of high temperature. We stopped irradiation of the light and measured the state that cooled down naturally. The warming of the thermo-magnetic materials by the irradiation of the light performs a temperature rise in the ratio of uniformity, but heat radiation efficiency fall as soon as it approached to the room temperature by the natural cooling and is supposed temperature becoming hard to decrease. When it is incorporated in the opto-fluidic transducer, we understood that it must be cooling after the warming.

On this condition, temperature control of the thermo-magnetic materials by the light was possible enough. Given these, the start of the temperature rise can earlier if we paint the thermo-magnetic materials with carbon black, and using the infrared light that is strong in a source of light. Then, if they cool off using the air flow that it can make the reply better because of improving the heat radiation characteristics.

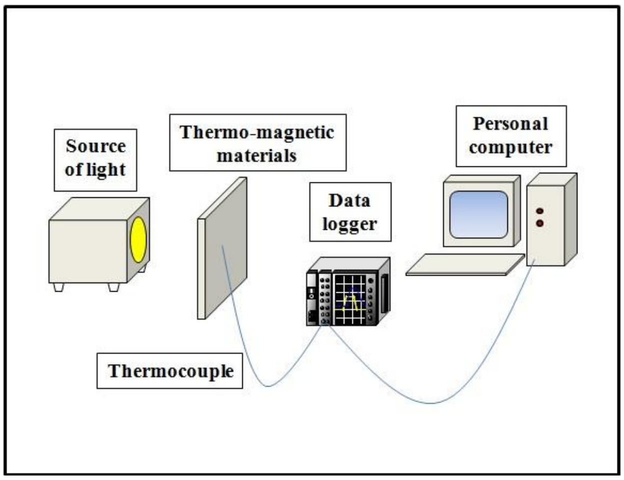

Fig.8 State of the thermometry experiment

CHARACTERISTIC

The Fig.9 shows main parameter and the Fig.10 shows relations of the distance versus difference of temperature of two thermo-magnetic materials when the valve body has switched.

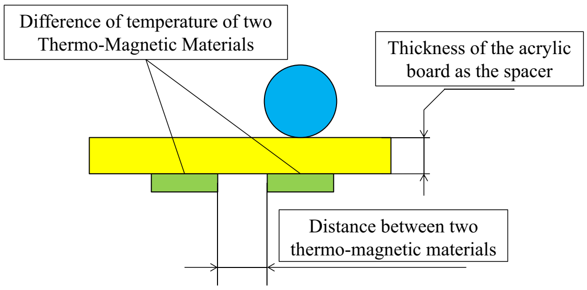

Fig.9 Main parameter

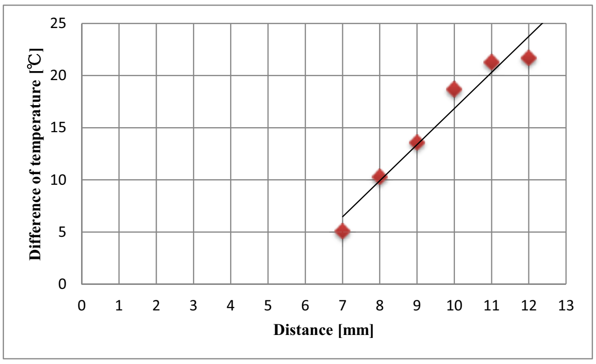

Fig.10 Relations of distance and the difference of temperature when the valve disc changed

In this figure, the size of magnet is φ 10 [mm]×10 [mm], the thermo-magnetic materials is 5 [mm]×30 [mm]×1.5 [mm], thickness of the spacer acrylic board is 2 [mm], and the atmosphere is normal room.

Initial distance of two thermo-magnetic materials begins from 7 [mm]. If the distance is smaller than this, the magnet of the valve body is stable in the vicinity of the center between two thermo-magnetic materials, and it does not work as a switching valve. In addition, it is not possible to switch without giving enough gravitation to produce between magnet and the thermo-magnetic materials when distance of two thermo-magnetic materials is too large.

In the Fig.10, it was confirmed that there was the proportional relations between difference of temperature and the distance of two thermo-magnetic materials when the valve disc has switched. If the distance between two thermo-magnetic materials is small, the difference of temperature when the valve body is switched in the thermo-magnetic materials is small. On contrary, it becomes higher if the distance is long. If the difference of temperature when the valve body has switched is lower, that is, it is easy to switch, and it means that reply is good. But it leads to increasing instability as the element. On the contrary, if distance of between two thermo-magnetic materials is large, the difference of temperature when the valve disc has switched becomes higher and the response falls, but the stability is improved. It may be said that the response has a contradicting relation with stability. Therefore both balances must be heeded. we find a condition to be able to satisfy the demand as the opto-fluidic transducer.

From the expression of the coulomb of Eq. (3), it is understands that the strength of the gravitation between magnetic bodies is proportional to the strength of the magnetic pole and inversely proportional to square of the distance. The upper limit of the magnetic induction of the thermo-magnetic materials is decided. From these, the factor to affect the switch of the valve (stability and reply of the element) greatly is the strength of the magnet, size, the thickness of the spacer, the distance of between two thermo-magnetic materials, and we should inspect chiefly. Above all, distance between two thermo-magnetic materials is the most important factor. In other words, to choose the nearest distance is ideal, while the valve is stable to secure stability and the reply of the selector valve.

MERIT

The opto-fluidic transducer in this study has very simple mechanism, and does not include an electrical element at all with using only light and air for the transmission signal. From these, the opto-fluidic transducer has a merit such as that the trouble tolerance is very high, it is strong in influence from the outside, it is very clean, it does not pollute the neighborhood even if damages, do not have to worry about the electric shock, flexibility is high, it does not need a power supply to be driven, and so on. In other words, it may be said that the transducer is superior to environment resistance, and safe for people.

OPTO-FLUID CONTROL SYSTEM

Fig.7 shows schema of the opto-fluid control system. This system can be remote controlled without transmitting the electrical signal, and completely isolates an exact control part from a drive working outside. As a control process, it controls the source of light first and the input light signal into the opto-fluidic transducer changes. Then, the input light intensity is converted into air pressure, and the air actuator is driven. In this way, the control of the actuator by light signal is realized. The electrical element is not included in a drive at all.

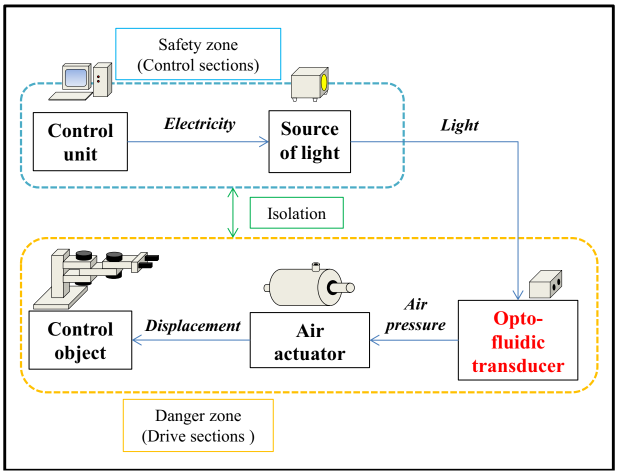

Fig.7 Schema of the opto-fluid control system

APPLICATION OF THE OPTO-FLUID CONTROL SYSTEM

Because this system is independent of the environmental disorder under the severe environment such as the medical field that is sensitive to the influence of the electromagnetic wave, the nuclear reactor that are affected by the strong electromagnetic wave and radiation from the outside, various applications are expected. In addition, it is very simple. it is suitable for downsizing and hides the possibility of the application to the field of micromachine.

CONCLUSION

We described about the new opto-fluidic transducer. As described, the opto-fluid control system can realize the high environment resistance and environmental performance by simple mechanism. It is hard to be influenced by the external environment and new applications are expected. The opto-fluidic transducer in this study will be further improved, and we want to make it pushing of the development of various fields.

REFERENCES

1. Harada, Masakazu and Ozaki, Shotaro, *Ryushi Kougaku*. Yokendo, 1971.
2. Ozaki, Shotaro and Hara, Yoshiaki, *Jyun Ryutai Soshi Nyumon*. Nikkan Kougyou Shinbun Sha,1967.
3. Hujiwara, Akito A development research of the opto-fluidic converter by LPA, 2007.

Proceedings of the 8th JFPS International
Symposium on Fluid Power, OKINAWA 2011
Oct. 25-28, 2011

2B4-4

PNEUMATIC HIGH SPEED SPINDLE WITH AIR BEARINGS

Terenziano RAPARELLI, Federico COLOMBO and Rodrigo VILLAVICENCIO
Department of Mechanics, Politecnico di Torino
Corso Duca degli Abruzzi 24, Torino, 10129 Italy
(E-mail: terenziano.raparelli@polito.it)

ABSTRACT

This article describes different experimental tests performed on a pneumatic spindle with gas bearings in order to evaluate its maximum rotational speed and stability. In particular the rotor unbalance response, the power losses calculated from deceleration tests, the thermal transient due to viscous losses are calculated and analyzed.

KEY WORDS

Pneumatic Spindle, Air Bearings, Feed hole, Thermal transient

INTRODUCTION

These applications are related both to high precision devices, e.g. for measuring machines, both to high speed rotating machines, e.g. high speed spindles for operations of finishing or drilling. During the last fifty years the use of no contact air bearings in rotating machines has been the object of interest by part of the researches in order to obtain bearings that support rotational speeds out of the range of conventional ball bearings [1].

Limitations on the maximum rotational speed are represented by centrifugal forces and by the well-know whirl instability of gas bearings. Nevertheless gas bearings enable to reach higher rotational speeds than rolling bearings, compared at the same diameter. Focusing the attention on the high rotational speeds, a broad spectrum of applications demand the use of gas bearings, in manufacturing industry (high speed machining, printed circuit boards drilling, micro-milling and wafer dicing) and not only (high speed compressors and turbines). In the first case the high speed is aimed to obtain high quality surface finishing or the correct tangential cutting speed with micro-tools; in the second case it is due to a reduction of the dimensions of the turbomachines.

The drawbacks of pneumatic bearings can be summarized in the following phenomena: the air-hammer [4], the unstable whirl [5][6], the relative low damping. All these problems must be solved to design such systems and obtain a stable operation of the rotor to contain its dynamic runout.

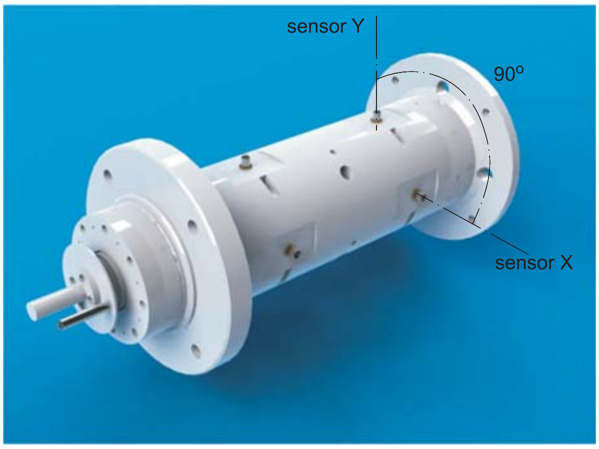

Figure 1: Sketch of the pneumatic spindle.

In this paper, a completely pneumatic spindle (Figure 1) designed and realized at the Mechanical Department of Politecnico di Torino [2] was tested experimentally. The stability of the spindle was verified monitoring the dynamic runout by means of displacement sensors facing the rotor and positioned along perpendicular radial directions. The bearings air consumption [3] and the external surface temperature were registered at different rotating speeds. The air turbine used to accelerate the rotor was also characterized.
Particular attention was given to the thermal analysis to evaluate the effects of temperature on the air clearance and prevent any rotor grip.

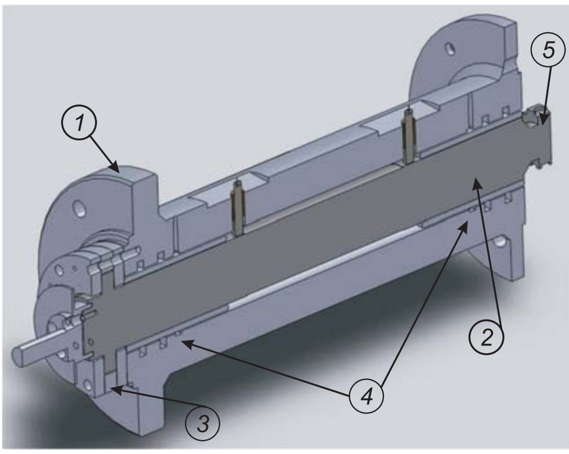

Figure 2: Prototype pneumatic spindle.

PROTOTYPE AND TEST BENCH

Figure 2 depicts the cross section of rotor (2), which is sustained by two radial bearings (4) of axial length 100 mm and a double thrust bearing (3) composed by three rings. The bearings are supplied by means of channels drilled in the housing (1) and in the three rings of the thrust bearing. The thrust bearing has inner and outer radius 49 mm and 79 mm respectively. The thickness of the central ring defines the axial air gap. The nominal radial and axial clearance are 27 μm and 19 μm respectively. The rotor is accelerated by a pneumatic turbine (5) machined on the rotor itself.

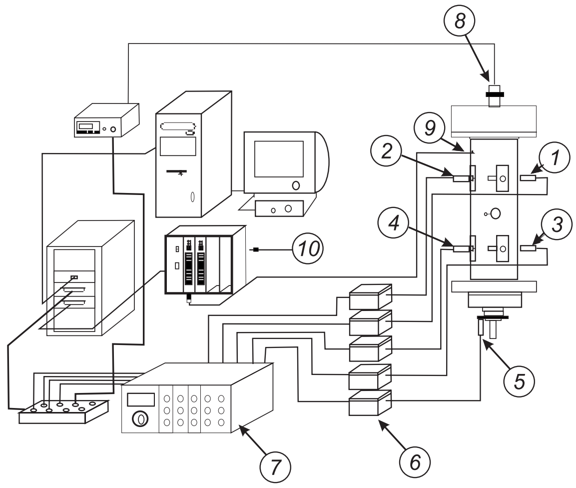

Figure 3: Transducers and Data Acquisition system.

The test bench designed to measure the performance of the pneumatic spindle was endowed of a data acquisition system and of pneumatic supply lines. Displacement capacitive transducers, see Figure 3 are arranged radially and axially facing the rotor. Four radial transducers are placed in two planes (close to each bearing) along X and Y directions. In Figure 3 are represented the measuring planes on which sensors (1) and (2) are set on the turbine side and sensors (3) and (4) on the thrust side. Sensor (5) is set along the axial direction on the thrust side. The sensors are connected to the amplifiers (6) and to the signal conditioner (7), whose analog output is detected by means of the data acquisition system. An optical tachometer (8) is placed in front of the spindle along the axial direction. The pulse train signal of the sensor is sent to counters that calculate the spindle rotational frequency. A series of thermocouples type T (9) are disposed on the carter surface to measure its external temperature distribution; their signal is amplified by means of amplifier (10). The temperature of the discharged air is also measured next to the axial and radial bearings.

The pneumatic system (Figure 10) consists of two supply lines: one for the turbine and the other for the bearings. This last is endowed of a 100 l tank with non-return valves, which is inserted downstream the pressure regulator. It can be useful in case the supply line fails to prevent a spindle damage.

The output signal of the displacement transducers is acquired with a 50 kHz sampling rate. The signals of two perpendicular sensors are composed in an XY plot to visualize the spindle orbits on the measuring planes. In this way the conical and cylindrical modes are visualized. By means of a FFT algorithm the Fourier spectrum of the signal is obtained in order to study the unbalance spindle response and verify the absence of sub-synchronous whirl. Six thermocouples were set in correspondence of the following points (see the Figure 4):

1-turbine housing,
2-air discharge next to the turbine,
3-measuring plane on turbine side,
4-measuring plane on thrust side
5-rotor flange,
6-air discharge next to the thrust bearing.

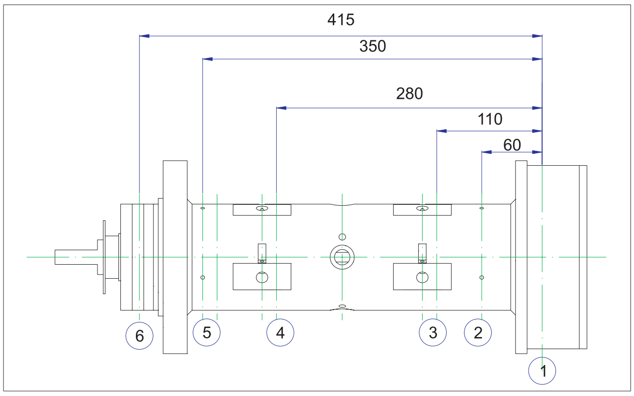

Figure 4: Thermocouple measuring points.

EXPERIMENTAL ACTIVITY

The experimental activity involved beforehand the measure of the air gaps, then were carried out:

1) the unbalance spindle response,
2) the bearings air consumption,
3) deceleration tests,
4) temperature tests,
5) the turbine characterization.

The measuring of the rotor and bearings dimensions was intended to evaluate the radial and axial air clearance, to which the bearing stiffness, the viscous losses and the spindle stability during operation are very sensitive. The mean values obtained after many dimensional tests are reported in Table 1:

Table 1: Dimension of bearings and air gaps.

Rotor dia. on turbine side	49.454 mm
Rotor dia. on thrust side	49.452 mm
Bushing dia. on turbine side	49.508 mm
Bushing dia. on thrust side	49.507 mm
Radial gap on turbine side	27 μm
Radial gap on thrust side	27 μm
Thickness of spindle flange	11.181 mm
Thickness of central ring	11.218 mm
Axial gap	19 μm

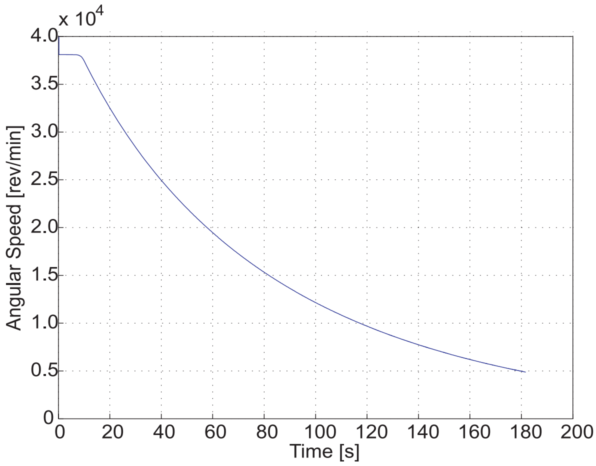

Figure 5: Deceleration test.

To calculate the friction torque, deceleration tests were carried out. The deceleration was started at 40000 rpm by closing the spheric valve that intercepts the turbine supply line. Figure 5 displays the spindle rotational speed vs time, while Figure 6 plots the torque due to viscous losses on bearings, that was obtained as a function of the rotational speed considering the mass moment of inertia of the spindle.

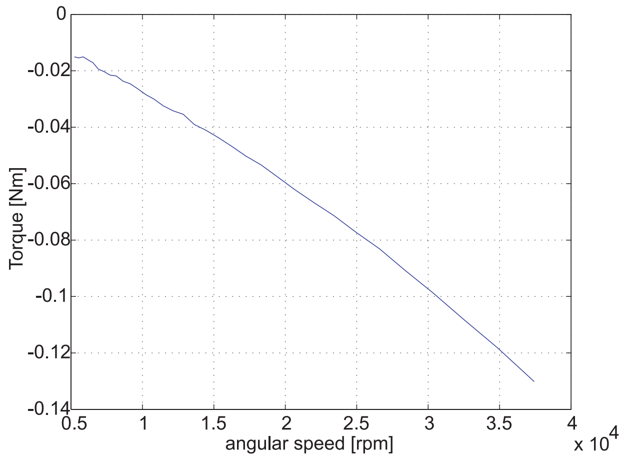

Figure 6: Friction viscous torque.

The temperature trends vs time are reported in Figure 7. They refer to a gauge supply pressure of 5 bar to the bearings and an initial rotational speed of 40000 rpm. After 110 minutes the spindle was shut down. It was observed that the temperature increases moving from the turbine to the thrust bearing, where the tangential speeds are higher. After the spindle shut down the temperature becomes uniform and begins to decrease, with the exception of the turbine housing, that presents an initial increase of temperature.

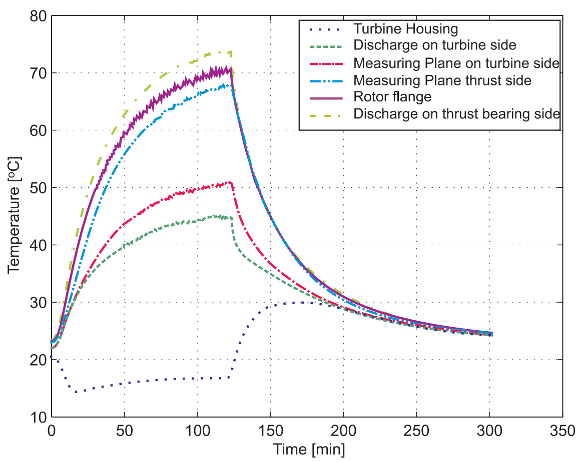

Figure 7: Curves of temperature vs. time.

The spindle orbits were measured every 1000 rpm starting from 0 to 42000 rpm. The spindle during operation suffers from centrifugal expansion; for this reason its surface approaches to the sensors, that are fixed to the housing. This displacement is visible in the spindle orbits show in, Figure 8 and Figure 9.

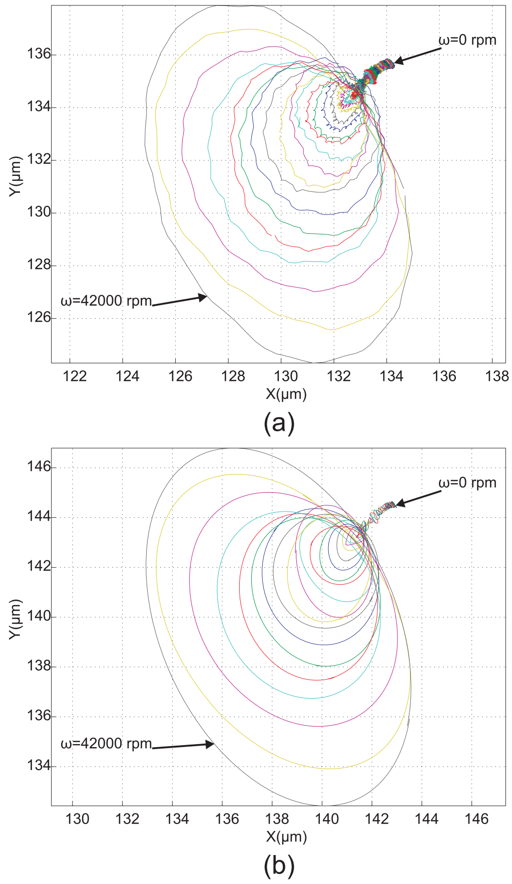

Figure 8: Spindle orbits measured on the turbine side plane at different rotational speeds; (a)non filtered, (b) filtered.

The driving turbine was characterized as a function of the rotational speed. Its air consumption was measured with a rotameter and the pressure was detected at the input and output of the turbine, Figure 10. In Table 2 it is shown the correspondence between the air consumption and the supply pressure of the turbine and the steady rotational speed without external payload. In these conditions it is calculated the power absorbed by the turbine, that is equal to the power dissipated.

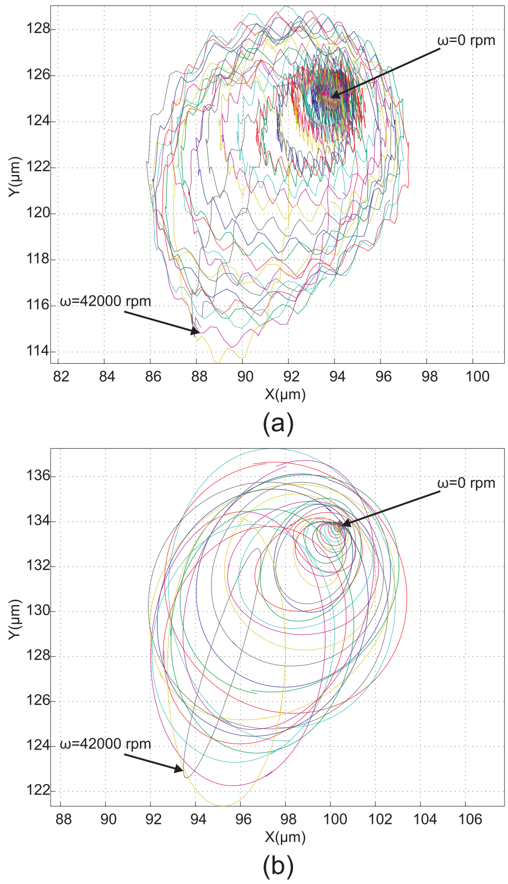

Figure 9: Spindle orbits measured on the thrust side plane at different rotational speeds; (a)non filtered, (b) filtered.

Table 2: Power Consumption

rpm	turbine air flow(l/min)ANR	gauge press (bar)	power (kW)
10000	394.66	0.25	0.16
15000	416.65	0.425	0.30
20000	460.54	0.525	0.40
25000	435.60	0.8	0.58
30000	414.32	1.09	0.75
35000	417.10	1.325	0.92
40000	382.82	1.75	1.12

RESULTS

The orbits of the spindle during rotation are plotted

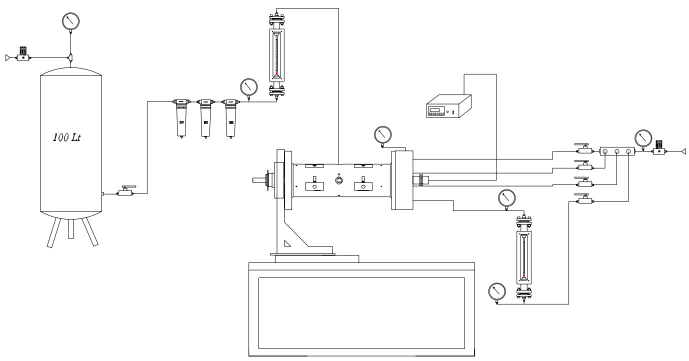

Figure 10: Pneumatic system used to characterize the driving turbine.

in Figure 8 for the measuring plane on the turbine side and in Figure 9 for the measuring plane on the thrust side. The figures compare the original signal with the signal obtained with a low pass filter. The dynamic runout is confined under 7 μm. In Figure 11 the amplitudes of the runout measured by the four radial sensors are plotted against the rotational speed. The first critical speed is about 35000 rpm. The effect of centrifugal forces is visible in Figure 12, where the mean displacement values detected from radial sensors is plotted against the rotor speed.
In Figure 12 it is represented the displacement the rotor center around the mean value.

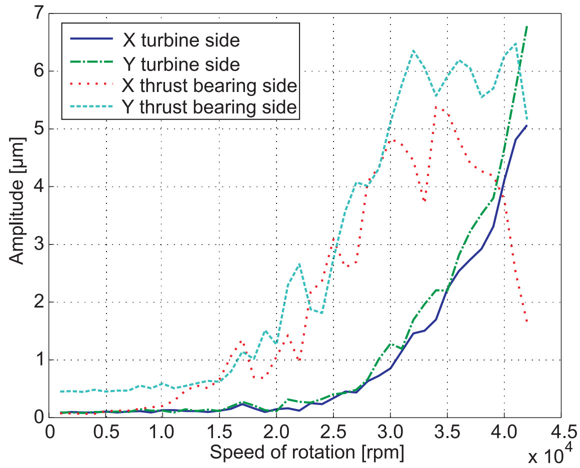

Figure 11: Amplitude displacement.

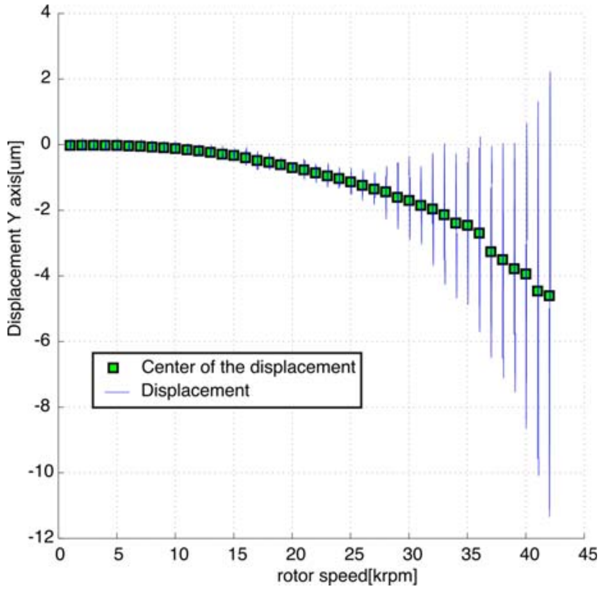

Figure 12: Displacement of Y axis around the center of the orbit (turbine side).

The unbalance response evidences both cylindrical and conical modes. In Figure 13 and Figure 14 are represented examples of conical modes at 30000 rpm and 40000 rpm respectively.

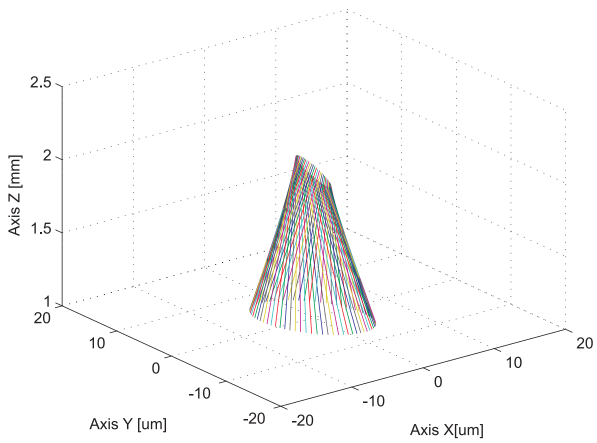

Figure 13: Mode of rotation at 30000 (rpm).

The waterfall diagram of Figure 15 shows that the unbalance response is only synchronous and the sub-synchronous whirl is absent in the tested range of speed.

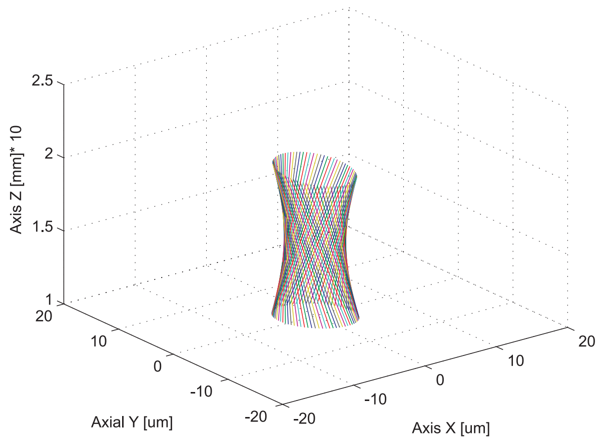

Figure 14: Mode of rotation at 40000 (rpm).

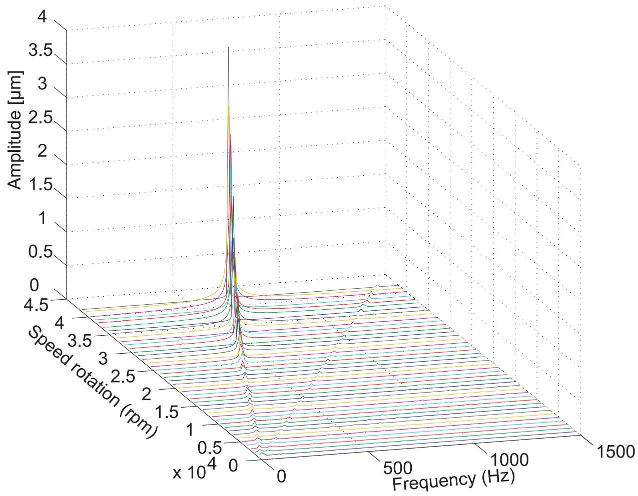

Figure 15: Waterfall Diagram.

The temperature of the rotor increase during operation due to viscous losses in the air gap. It remains in a safety range in which the spindle can operate for a long time without problems.

CONCLUSIONS

An experimental activity was developed to evaluate the performance of a turbo pneumatic spindle with gas bearings. In synthesis the following conclusions can be listed:

- the spindle rotates in stable conditions up to 40000 rpm;
- the spindle temperature in steady conditions at 40000 rpm remains under 75^{o}C and the thermal effects due to viscous actions do not compromise the operation of the spindle;
- the friction torque of gas bearings is very low (around 0.13 Nm at the maximum speed) due to the low air viscosity.

REFERENCES

[1] Krzysztof, Czolczynski, "Rotordynamics of gas-lubricated journal bearing systems, New York. (1999), Springer.

[2] Belforte G., Raparelli T., Viktorov V., Trivella A., Colombo F., An experimental study of high-speed rotor supported by air bearings: test rig and first experimental results, Tribology International, 2006, 39-8, pp.839-845.

[3] Belforte G., Raparelli T., Viktorov V., Trivella A., Discharge coefficients of orifice type restrictor for aerostatic bearings, Tribology International, 2007, 40, pp.512-521.

[4] Tauler H.M.,Stowell T.B., Pneumatic hammer in an externally pressurized orifice-compensated air journal bearing, Tribology International, 2003, 36, pp.585-591.

[5] Waumans T., Peirs J., Reynaerts D., Al-Bender F., On the dynamic stability of high-speed gas bearings: Stability study and experimental validation, 2011, Laboratory Soete

[6] Brzeski L.,Kazimierski Z., Experimental investigation of precision spindles equipped with high stiffness gas journal bearings, Precision Engineering, 2003, 23, pp.155-163.

Proceedings of the 8th JFPS International
Symposium on Fluid Power, OKINAWA 2011
Oct. 25-28, 2011

2C1-1

STUDY ON OIL FILM CHARACTERISTICS OF SLIPPER WITHIN AXIAL PISTON PUMP UNDER DIFFERENT WORKING CONDITION

Yi Sun, Jihai-Jiang.

Harbin Institute of Technology, School of Mechtrionics Engineering, China

ABSTRACT

In order to accurate master lubrication condition between slipper and swash-plate under practical operation condition, pressure field and oil film characteristics of slipper were studied. By analysis motion and force of slipper, establishing mechanics model of it, and simulated in Matlab software, variation laws of the film thickness with rotation angle, angle of swash plate, rotational speed and pressing force in different position were obtained, The simulation results show that in the range of general working conditions, rotational speed and swashplate angle of piston pump will not exceed bearing capacity of oil film, but it will have influence on hydrostatic bearing of slipper if exceed certain range, especially rapid change of inertia force because of increasing rotate speed.

KEY WORDS

Slipper, Mathematical model, Oil film

NOMENCLATURE

f_p : Vertical component force of high-pressure oil from piston that act on the slipper
d_1 : Diameter of the piston
p : Discharge oil pressure.
f_t : Horizontal force from the spring
f_a : Precompression force from center-spring
Z : Number of the pistons in the pump
f_g : Horizontal inertia force from single pair of the slipper and the piston

m : Weight of the single piston pair
φ : Angle rotating instantaneous.
f : The total pressing force
R_2 : Inner radius of slipper's sealing region
R_1 : Outer radius of slipper's sealing region
p_s : Pressure of oil groove under the slipper.
Q : Leakage from sealing region under the slipper
Q_1 : The oil flowing into the slipper through damping orifice from piston
h : Oil film thickness
μ : Oil viscosity.
d : Diameter of damping orifice
l : Length of damping orifice.

INTRODUCTION

The axial piston pump is widely used in hydraulic systems to provide pressure and flow for various machines in industry, but there are some several challenging issues associated with it, such as conflicts between lubrication and wear. The slipper pad and swashplate form a key friction pair in the axial piston pump, excessive wear between them may significant influences the performance of the pump. Hydrostatic slipper bearing is an effective way to maintain a fluid film between slipper pad and swash plate that slide against each other, and to thereby mitigate direct surface-to-surface contact.

There have been many publications in hydrostatic slipper bearing over the past 30 years, many concerned with improving the slipper performance of the piston pumps. Most of the work has focused on analyzing the formation mechanism of hydrostatic bearing over the slipper [1-4]. The effects of slipper spin, tangential velocity, tilt, slipper non-flatness, inlet orifice, and conditions for metal to metal contact, were investigated in [5-9]. The fluid-film thickness between the thrust bearing and the running surface were also measured within an actual application, this work was conducted under high speed conditions and showed that a slightly convex bearing design was required for successful operation[10]. A good analytical understanding of slipper behaviour in piston pumps is crucial to good design, and a large amount of work has been done in this area [11-13].

Here we developed a mathematical model that reflected the lubrication condition between slipper and swash-plate, and the performance of the hydrostatic slipper bearing was analyzed through system simulation.

STRUCTURE AND WORKING PRINCIPLE OF HYDROSTATIC BEARING

The principle of the hydrostatic slipper bearing is shown in fig 1. High-pressure oil from piston pass through damping orifice and then flow into the slipper groove, thus generate the bearing force. The bearing force can balance the pressing force which act on the slipper if design reasonable, and thus form a certain thickness oil film. The pressing force is always changing during the pump operation, but because of damping effect, that is damping from throttle orifice and damping from gap between the slipper and the swashplate which created by the oil film, it ensure the oil film will maintain stable with load variation. Consequently, reliable fluid lubrication is assured and wearing between the slipper and the swashplate can be reduced.

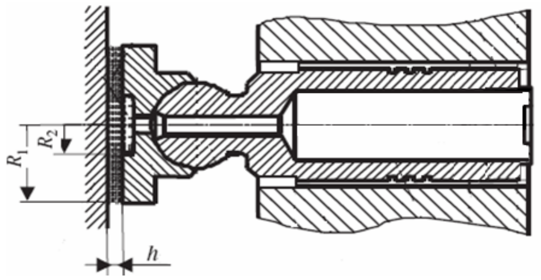

Fig.1 Structure profile of hydrostatic slipper bearing

MOVEMENT AND FORCE OF THE SLIPPER

Because the slipper bears the high-pressure oil and great pressing force in the oil discharge port , and severe wear of the slipper mainly occurred in this region too, so this paper mainly study the state of movement and force of the slipper when it in the oil discharge port.

The motion trajectory of the slipper is shown in fig 2. Suppose the swashplate angle is γ, the radius of distribution circle in the cylinder is R_f, if regards oxyz as coordinate system, then we can see the trajectory of the slipper perpendicular to the direction of axis is a circle, while the trajectory in the $o'y'z'$ plane is a ellipse. If the piston rotary as angular velocity ω, and takes top dead center as initial position, then the pump will absorb oil in interval of 0°~180°, and discharge oil in interval of 180°~360°.

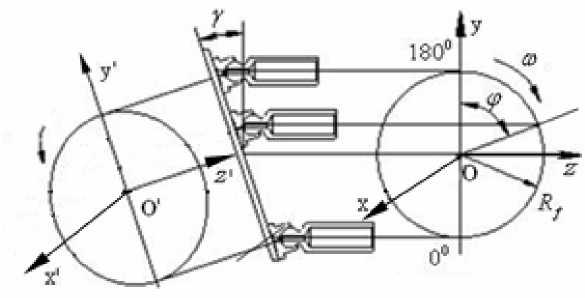

Fig.2 Motion trajectory of the slipper

The force received by the slipper can be seen in fig 3, the slipper mainly bears component force from piston, spring force, inertia force of the piston and hydraulic supporting force from oil film.

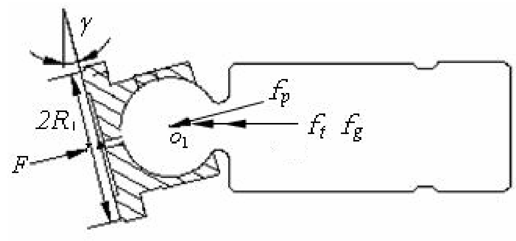

Fig.3 Bearing force condition of the slipper

Vertical component force of high-pressure oil from piston that act on the slipper can be expressed as formula (1)

$$f_p = \frac{\pi d_1^4}{4\cos\gamma} p \qquad (1)$$

Horizontal force from the spring can be written as equation (2).

$$f_t = \frac{f_a}{Z} \quad (2)$$

Horizontal inertia force from single pair of the slipper and the piston can be expressed as formula (3)

$$f_g = mR_f \omega^2 \tan(\gamma)\cos(\varphi) \quad (3)$$

Then the total pressing force can be written as equation (4).

$$f = f_p + \frac{f_t}{\cos\gamma} + \frac{f_g}{\cos\gamma} \quad (4)$$

From equation (4) can be seen that the total pressing force is constantly changing with rotation angle of the slipper, so pressure of oil groove under the slipper is also changing constantly, and finally affect the oil film thickness under the sipper.

MATHEMATICAL MODEL OF SLIPPER IN THE OIL DISCHARGE PORT

The hydraulic supporting force of hydrostatic slipper bearing is shown in fig 4.

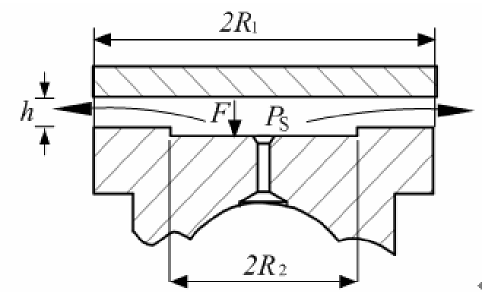

Fig.4 Hydraulic supporting force under the slipper

According to the literature [3], the supporting force can be written as equation (5)

$$F = \pi R_2^2 p_s + \int_{R2}^{R1} 2\pi r \frac{\ln\frac{R_1}{r}}{\ln\frac{R_1}{R_2}} p_s dr$$

$$= \frac{\pi(R_1^2 - R_2^2)}{2\ln\frac{R_1}{R_2}} p_s \quad (5)$$

According to the hydrostatic bearing theory, supporting force should equal to the total pressing force, so pressure of oil groove under the slipper can be expressed as formula (6)

$$p_s = \frac{2\ln\frac{R_1}{R_2}\cdot f}{\pi(R_1^2 - R_2^2)} \quad (6)$$

According to hydrodynamic theory, leakage from sealing region under the slipper can be expressed as formula (7)

$$Q = \frac{\pi h^3 p_s}{6\mu\ln\frac{R_1}{R_2}} \quad (7)$$

The oil flowing into the slipper through damping orifice from piston can be denoted as formula (8)

$$Q_1 = \frac{\pi d^4}{128\mu l}(p - p_s) \quad (8)$$

On the basis of flow rate continuation equation, Q is equal to Q_1, and then it can be expressed as formula (9)

$$\frac{\pi d^4}{128\mu l}(p - p_s) = \frac{\pi h^3 p_s}{6\mu\ln\frac{R_1}{R_2}} \quad (9)$$

From formula (9) we can obtain relationship between p and p_s , it can be written as formula (10)

$$\frac{p_s}{p} = \frac{1}{1 + \frac{64}{3\ln R_1/R_2}\frac{l}{d^4}h^3} \quad (10)$$

Then puts the formula (10) into formula (6), and then obtains a new formula (11).

$$\frac{2\ln\frac{R_1}{R_2}\cdot f}{\pi(R_1^2-R_2^2)}=\frac{p}{1+\frac{64}{3\ln R_1/R_2}\frac{l}{d^4}h^3} \qquad (11)$$

We can see from formula (11), that once the strcture of pump is fixed, several parameters can be determined. If suppose

$$\frac{64}{3\ln R_1/R_2}\frac{l}{d^4}=\mathrm{k1}, \quad \frac{2\ln\frac{R_1}{R_2}}{\pi(R_1^2-R_2^2)}=\mathrm{k2}$$

then we can abtained the formulat as follws

$$\mathrm{k1}\cdot h^3=\frac{p}{\mathrm{k2}\cdot f}-1 \qquad (12)$$

From formula (12) we can see, if the strcture of pump is determined, the oil film thickness of slipper can be expressed as the function of p and f, that is to say the oil film thickness will be influenced by outside factor in operating, such as the load, the inclination angle of the swashplate or the rotation speed.

ANALYSIS ON CHARACTERISTICS OF OIL FILM UNDER DIFFERENT WORKING CONDITIONS

From above analysis we can see, hydrostatic bearing is an effective way to solve severe wear, while by analysis of oil film thickness we can estimate whether or not the hydrostatic bearing can be formed.

Fig 5 shown the oil film thickness of the slipper follow with rotation angle, it is obtained based on formula(12). The parameter of simulation is shown in table 1, load and revolution speed is 12MPa and 1500r/m respectively, and inclination angle is 12°.

Table 1 Main parameters of the slipper pair

Parameters	Nominal value	Dimension
Oil viscosity	0.073222	Pa·s
Weight of the single piston pair	85	g
Radius of piston	8.5	mm
Density of oil	870	kg/ m^3
Inner radius of sealing region	14.1	mm
Outer radius of sealing region	21.4	mm
Length of orifice	3.4	mm
Diameter of orifice	0.8	mm

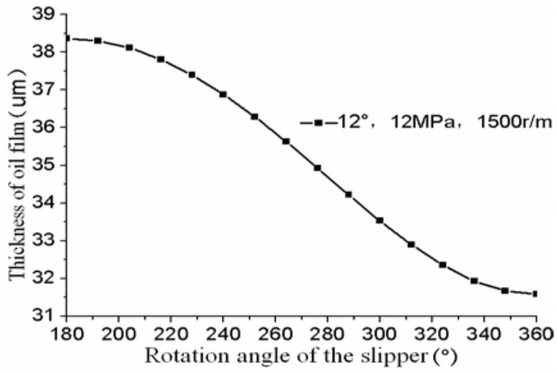

Fig.5 Variaton of oil film thickness follow with rotation angle

Because the axial piston pump structure is compact and flow state under complex, it is difficult to installation measurement device inside the pump, especially to the high-speed slipper, it almost impossible to measure flow parameters which is continuous variation. Due to the limitation of experiment condition, we use experimental data in references [10] proved the accuracy of our simulation, the references [10] measuring oil film thickness of the slipper when the pressure is 12Mpa and rotate speed is 1500 rpm, and indicated that " the average thickness of the oil film when the slipper in the oil discharge port is about 35um", this conclusion is conformity with our simulation results, it has fully proven the slipper's mechanical model in the oil discharge port this paper provides is correct.

The influence of inclination angle

From formula(12) we can see that the pressing force act on the slipper could be affected by rotation speed of the pump, the swashplate angle and the system load, and eventually influence the oil film thickness, so it is necessary to analyse the oil film of the hydrostatic slipper bearing under different conditions. Fig 6 shows variation of the pressing force with rotation angle in the oil discharge port under different inclination angle. Fig 7 shows variation of the oil film thickness with rotation angle corresponding to the pressing force in fig 6.

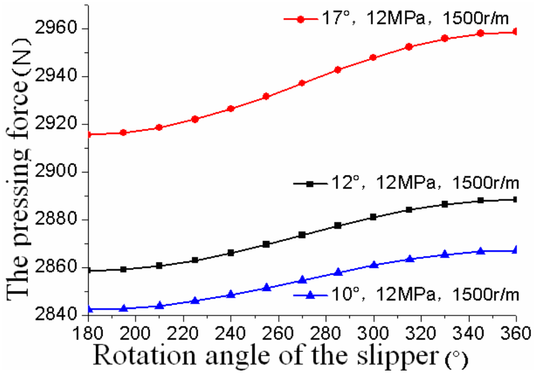

Fig.6 Variaton of pressing force follow with rotation angle under different inclination angle

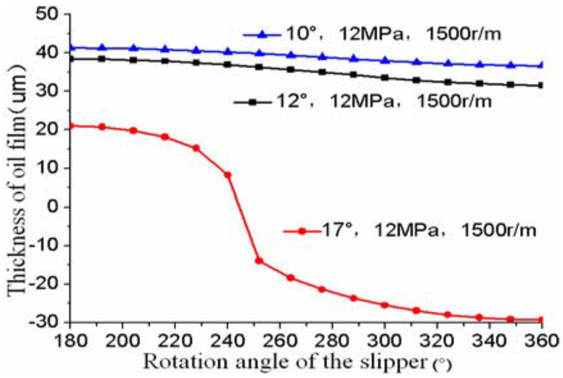

Fig.7 Variaton of oil film thickness follow with rotation angle under different inclination angle

From fig 6 we can see, the generally trend of the pressing force increase gradually with rotation angle in the oil discharge port, because according to formula (3), the inertia force of the slipper and piston is directly proportional to square of the rotation speed, and varies with the rotation angle, especially in the case of high rotation speed, the inertia force increased gradualy in the oil discharge port. When the rotation speed and the system load keep invariant, the pressing force increases with increasing inclination angle, this is consists with formula(1), formula (3) and formula (4), in that both the pressing force and the inertia force increase with the increasing inclination angle.

From fig 7 we can see, the oil film thickness decrease gradually as the pressing force increased, and even reached negative when the inclination angle is 17°. The answer is: based on the formula (12), the pressing force is denominator, while numerator remains unchanged, this time their ratio will reduction with increased pressing force, when the ratio< 1, the theory value of oil film thickness will less than zero. Surely the oil film thickness can not reach negative in practice, the simulation results only illustrate the pressing force have already overtaken the ultimate load that the oil film can endure at the moment, that is to say the hydrostatic bearing is difficult to form, and the slipper can only operate in redundant pressing force condition this time.

The influence of rotation speed

From equation (12) can be seen that the rotation speed also have an effect on the pressing force and oil film thickness. When the inclination angle and the system load remain unchanged, variation of the pressing force with rotation angle is shown in fig 8. Fig 9 shows variation of the oil film thickness with rotation angle corresponding to the pressing force in fig 8.

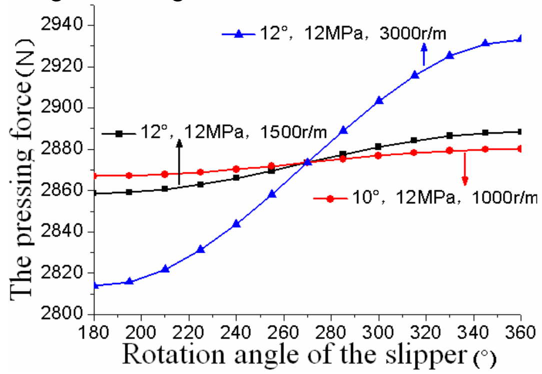

Fig.8 Variaton of pressing force follow with rotation angle under different rotation speed

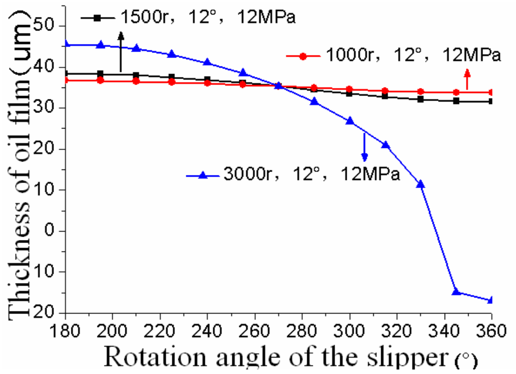

Fig.9 Variaton of oil film thickness follow with rotation angle under different rotation speed

We could see from fig 8, though the generally trend of the pressing force increase gradually, it decrease with increasing rotation speed before the slipper reached 270°

when the inclination angle and the system load remain unchanged, only after rotating 270°, the pressing force rose sharply with rotation angle. Because according to formula (3), the inertia force not only proportional to square of the rotation speed, but also directly as cosine of rotation angle, in interval of 180~270° cosine of rotation angle is negative, while it is positive in interval of 270~360°. So when the slipper just rotated in the oil discharge port, the inertia force decrease as the rotation angle increase, until the slipper rotated to 270°, the inertia force increase with the rotation angle.

Fig 9 also shows the oil film thickness decrease as the pressing force increase, while it appearance negative when the rotation speed reached 3000rpm. This situation is similar to the preceding, when the pressing force is more than a certain extent, the oil film can not support the pressing force, this shows that the oil film can not form this time. From above analysis we can see, the inertia force of the slipper and piston has a great influence on the oil film, especially at high rotation speed.

CONCLUSION

In this research, the mathematical model that reflected the lubrication condition of the hydrostatic slipper bearing is presented, through analyzing the characteristics of the oil film under different working conditions, some conclusions are obtained as follows:

1. Though bearing capacity of the oil film of the hydrostatic slipper can applies to a wide range of working condition, it is not infinite, once exceed the extreme, it will affec the formation of the oil film, and hydrostatic bearing status of the slipper will be destroyed at this time.
2. When the working conditon remains unchanged, inertial force of the slipper and piston is the key factor affecting the thickness of the bearing of the oil film, especially in the high rotaton speed condtion, the oil film will be greatly changed by the inertial force.

REFERENCES

1. Shengwu XU. Hydraulic Pump of Piston Type. Beijing, 1985,pp.35-57.
2. Desheng Wen. Open-Circuit Axial Piston Pumps of Swashplate. Beijing, 1993.53-60
3. Desheng Wen. Innovation and Development of Hydraulic Components. Beijing,2009.96-128
4. Peixiang Qu. Design Method of Axial Piston Pumps. Beijing, 1989.54-65
5. E. Koc, C. J. Hooke. Considerations in the Design of Partially Hydrostatic Slipper Bearings. Tribology International, 1998, 11(30), pp.815–823.
6. E. Koc, C. J. Hooke. Investigation into the Effects of Orifice Size Offset and Overclamp Ratio on the Lubrication of Slipper Bearing .Tribology International, 1996, 4(29), pp. 299–305.
7. Koc E, Hooke CJ, Li KY. Slipper Balance in Axial Piston Pumps and Motors. ASME J Tribol 1992, 114(4), pp. 766–72.
8. Hooke CJ. The Lubrication of Slippers in Axial Piston Pumps and Motors-the Effect of Tilting Couples[J]. Proc Inst Mech Eng Part C:J Mech Eng Sci 1989, 203(C), pp. 343–50.
9. Li KY, Hooke CJ. Note on the Lubrication of Composite Slippers in Water-Based Axial Piston Pumps and Motors. Wear 1991, 147(2), pp. 413–37.
10. Tanaka, Nakahara. Motion Characteristics of Slipper Bearing in Swash plate Type Piston Pump and Motor. Transactions of the Japan Society of Mechanical Engineers Par.2007, pp. 1236-1244
11. Yulin Li. Hydraulic Components and Systems Design.Beijing:1989,pp.43-59
12. Bihai He, JianguoSun. Calculation and Analysis on Film Thickness of the Slippers Based on Hydrostatic Bearing in the Aeronautical Fuel Piston Pump. Journal of aerospace power. 2009,24(12),pp.2821~2827
13. Yongge Pan, Decai Han, Tienong Zhou. Experimental Study on Dynamical Characteristics of Slippers in Axial Piston Pump. Journal of Yanshan University, 1990, 6(1),pp.9-14

Proceedings of the 8th JFPS International
Symposium on Fluid Power, OKINAWA 2011
Oct. 25-28, 2011

2C1-2

NOISE CHARACTERISTICS IN SPOOL VALVE WITH V-NOTCHES

Xin FU, Liang LU and Jun ZOU
State Key Laboratory of Fluid Power and Control
Zhejiang University
Hangzhou, 310027 China

ABSTRACT

Experimental investigations on the noise characteristics in spool valve with v-notches are conducted in this paper. Cavitation noise with frequency peak forms when the flow state changes form single phase turbulent to cavitating. The peak frequency decreases with the increase of the flowrate. On the other hand, jet flow develops intensely from the notches. Self-sustained flow oscillation produces whistling noise with pure tones, which is much more powerful than the cavitation noise. The pure tone frequency jumps with the outlet pressure, in each jump range, which has good monotonicity with the outlet pressure.

KEY WORDS

Cavitation, Self-sustained oscillation, Whistling noise, Frequency peak

NOMENCLATURE

x	:	throttling opening
L_h	:	length of the salient part of the valve seat
L_s	:	length of the concave part of the valve spool
L	:	notch length
U	:	jet flow velocity
f_p	:	peak frequency of the cavitation noise
f_s	:	pure tone frequency whistling noise

INTRODUCTION

In recent years, with the development of the hydraulic industry, the noise problem has been addressed with much attention for the evaluation of the product quality. Throttling valves, usually fixed in the operation cab, the noise comes from which affects directly to the operators' comfort and health [1]. It is important to make analyses to the noise mechanisms.

Throttling valves are fluid power components, noises from which are mainly the product of the flowing process. As we know, the flow will be accelerated when getting through the vena contract area, leading the drop of the local pressure. Which triggers the nucleus or small bubbles develops to form cavitation bubbles. The bubbles travel to high pressure region and implode to form cavitation noise [2]. From the traditional notion, cavitation noise is considered as the prominent source of fluid power acoustics. Literatures on cavitation noise in hydraulic components are abundant [3-7]. The cavitation noise is based upon on the bubble implosion, which is basically taken as a monopole source due to the volume changes [8]. The acoustical power usually distributes in relatively high frequency range in the spectra with one or more frequency peaks [9]. Though the frequency peak exists, the cavitation noise is much broad in the spectra, which hardly present any whistling characteristics.

In the presenting valves, the whistling noise with pure tone frequently occurs, the frequency and intensity of which is relatively small and sometime much higher compared with the cavitation bubble noise respectively. The mechanism can be considered as the flow self-sustained oscillation. The phenomenon of which is firstly observed by Sondhaus in 1854 with edge-tone noise [10]. Any flow configurations with shear-layer instability can cause self-sustaining oscillations [11-13], which is another important source of flow noise. Though the literatures are lot, investigations on the valve whistling noise is rarely referred.

In this paper, the noise induced by the cavitation bubble implosion and the flow self-sustained oscillation in spool valve with v-notches are mainly investigated. Noise from the vibration of valve shell and the flow turbulence are out of concern. Frequency peak forms in the spectra when the flow state changes form single phase turbulent to cavitating. The flow self-sustained oscillation exists in both non-cavitating and cavitating conditions, the pure tone frequency produced by which jumps with the outlet pressure.

EXPERIMENTAL FACILITY

The experimental facility is composed by three parts (fig 1). Firstly, the hydraulic system, to sustain the flow circulation, liquid cooling and up-down stream pressure control. Secondly, the data acquisition system, to measure the up-down stream pressure, flowrate and acceleration. Finally the experimental object, the spool valve, with two v-notches symmetrically fixed on the spool. Where, x is the throttling opening, Lh is the length of the salient part of the valve seat, Ls is the length of the concave part of the valve spool, L is the length of the valve notch. In this paper, L=5mm, Ls =7mm, Lh =4mm or 10.5 mm, x is within the range of 0 to 5mm.

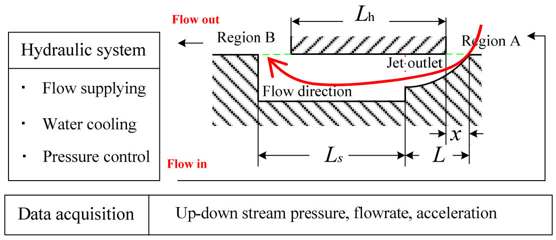

Figure 1 Experimental facility

Fig. 1 (a) provides the profile of the flow configuration of the valve. Narrow flow passage of Region A leads the acceleration of the local flow speed, the drop the local pressure and the inception of cavitation. Jet flow occurs at the outlet of the notch, leading the shear-layer instability. Something needs to make out is that not any kind of notch configuration can produce jet flow. The gradually divergent configuration is probably needed.

CAVITATION NOISE IN V-NOTCHES

Experimental results prove that the inception of cavitation in spool valve with v-notches is relatively difficult compared with that of spool valves with U-notches, which may be the consequent of the good negotiability of the v-notch structure characteristic. On the other hand, the level of cavitation noise in v-notches is comparatively much higher, which implies that the valves with v-notches have more serious problems of noise. In order to get good understandings of the properties of the cavitation noise, it is necessary to make the spectra analysis. In this paper, the acceleration on valve wall is detected as the corroborative evidence of the noise, for we emphasize mostly on the spectra distribution properties.

For the convenience of comparison, fig. 2 only provides the spectra pictures within 10kHz to 18kHz, the cavitation noise spectra range. It is obvious to find that with the increasie of the flowrate, notable frequency peak appears in the curve when cavitation incepts, which is produced by the coherent collapse of the cavitation bubbles [14]. The spectra curve presents hill shapes in cavitating flow states. When the flow goes choked, the frequency peak disappear, the spectra curve goes flat again.

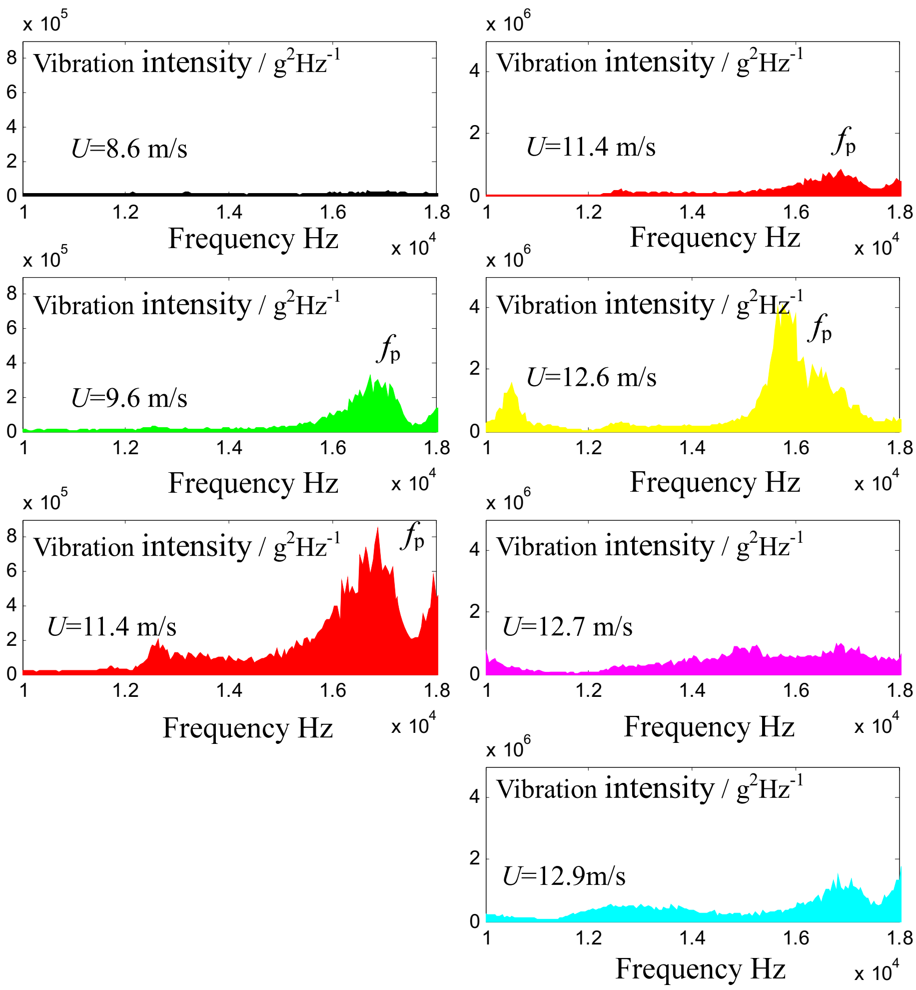

Figure 2 Cavitation noise spectra in spool valve with v-notches (x=1mm, Lh =4mm)

The value of the peak frequency can be roughly estimated by the bubble collapse time [4]. Experimental results prove that the peak frequency decreases with the increase of the flowrate on cavitating flow conditions, as shown in fig.3.

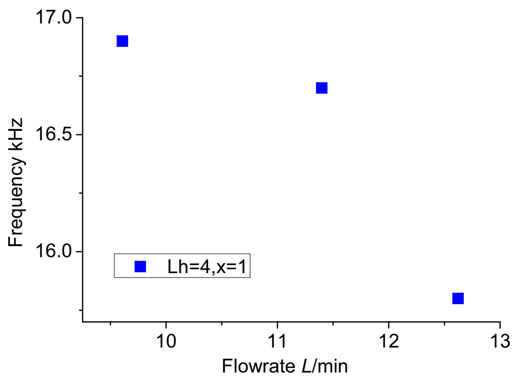

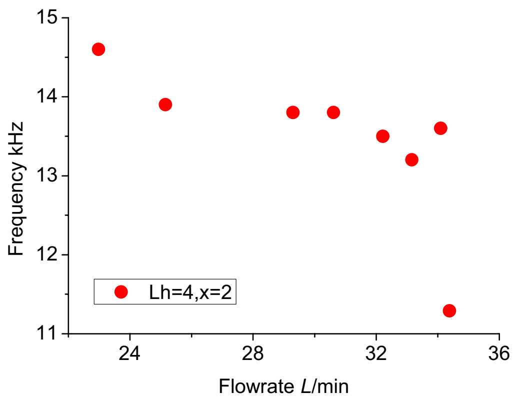

Figure 3 Peak frequency with the flowrate

SELF-SUSTAINED OSCILLATION IN V-NOTCHES

In most hydraulic cavitation component, the cavitation noise plays the main role of the valve noise. In some flow configurations, like spool valve with v-notches, the flow speed difference between the jet flow from the outlet of the notches and the flow in the valve chamber leads the shear-layer instability, which magnifies the pressure fluctuations forms by the up-stream flow contract area (Fig. 1 Region A,). The noise induced by the shear-layer instability sometime is much larger than the traditional cavitation noise. In the presenting spool valve flow channel, the flow outlet area (Fig. 1 Region B) and the spool down steam wall may play the hydrodynamic feedback role to the up-stream pressure fluctuations, leads highly organized oscillations, which could be the reason of the whistling noise with pure tones [15].

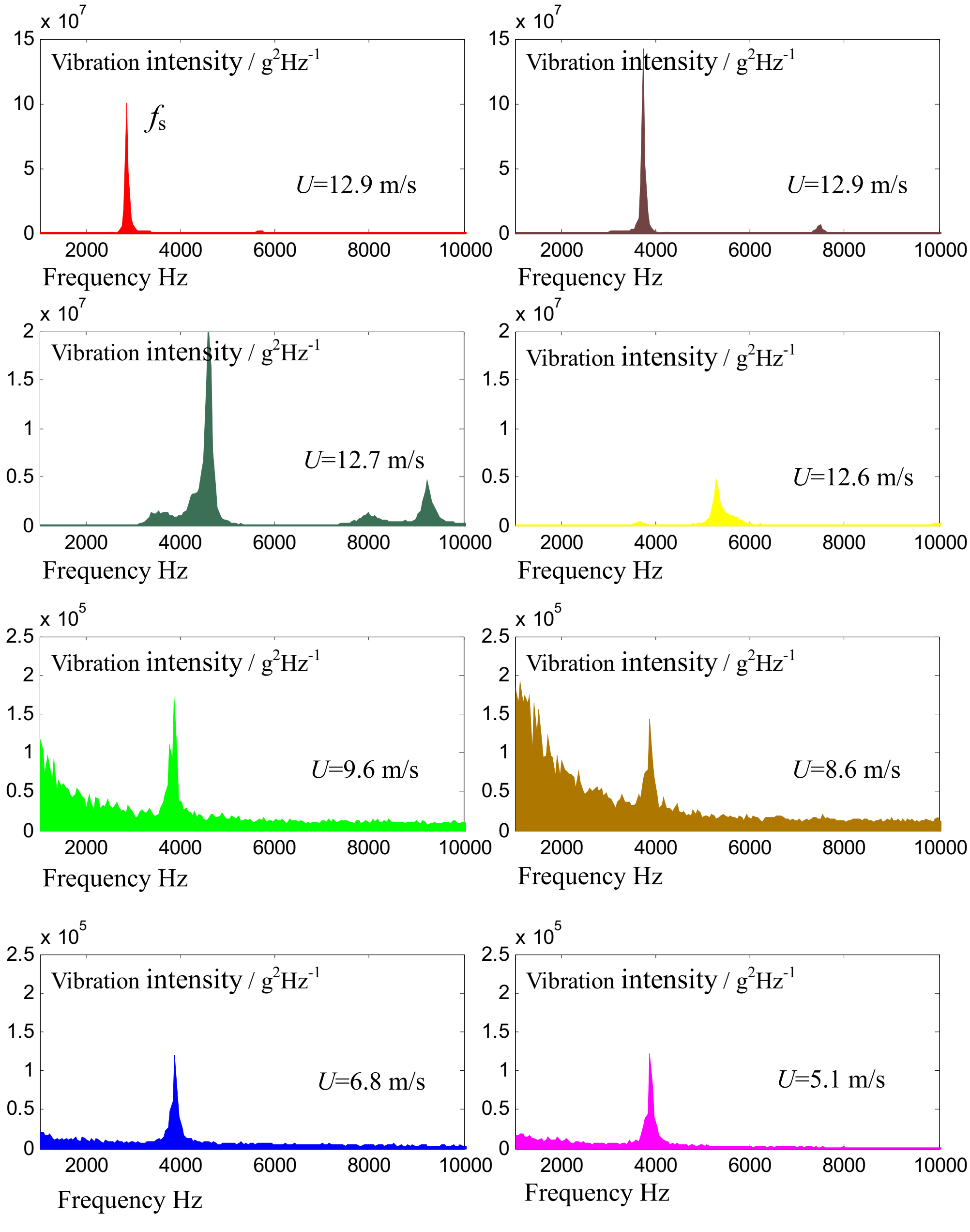

Figure 4 Self-sustained oscillation spectra in spool valve with v-notches (x=1mm, Lh=4mm)

As mentioned in the introductions, literatures on shear-layer oscillation noise is abundant, the mechanism of this phenomenon is still unclarified. Generally, the pure tone frequency is the function of the flow configuration and the flow speed.

Fig. 4 proves the shear-layer oscillation spectra in spool valve with v-notches, which exist in both non-cavitating ($U \leqslant 9.6$ m/s, presenting case) and cavitating flow ($U \geqslant 12.6$ m/s, presenting case) conditions. Obvious frequency peak appear in the spectra, which is much narrow compared with that of cavitation noise frequency peak, leading the noise whistling property. Besides the main peak frequency, one or more harmonic frequencies can be observed.

In this paper, the flow in the spool valve may be made an analogy with the labial flow model. The initial pressure fluctuation occurs in the notch area (Fig.1 Region A), the shear-layer instability makes which amplified. Pressure fluctuation in the flow outlet area (Fig.1, Region B) plays the feedback role. Experiments on the flow velocity, the length of the impingement area to the shear separation area and the feedback configuration is considered for investigation.

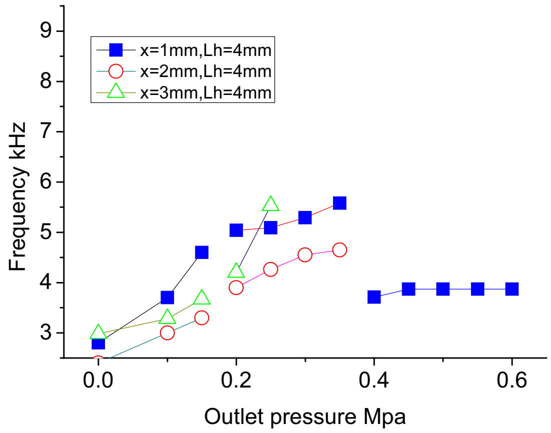

Figure 5 Pure tone frequency with outlet pressure and x (with constant inlet pressure)

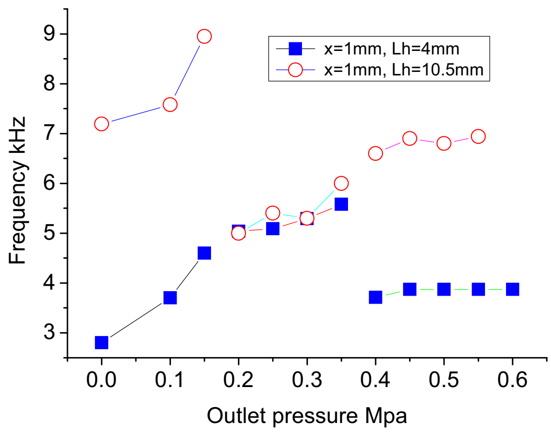

Figure 6 Pure tone frequency with outlet pressure and Lh (with constant inlet pressure)

As shown in Fig.5 and Fig. 6, in any configuration cases, the pure tone frequency presents similar jump property with the outlet pressure, in each jump range, which has good monotonicity with the outlet pressure. The variation of the opening x only changes the character length of the impingement area to the shear separation area. The properties of the pure frequency with outlet pressure shows similarity when changes the opening. While the variation of Lh leads difference of the frequency trend with the outlet pressure. It assumes the variation of Lh changes not only the feedback configuration but also the character length.

CONCLUSIONS

Noise characteristics in spool valve with v-notches are investigated in this paper. Because of the jet cavitating flow phenomenon within the valve channel, both cavitation noise and whistling noise induced by the flow self-sustained oscillation can be observed. In spool valves with v-notches, the latter type noise plays the predominant role for its pure tone and large intensity properties.

With the decrease of the outlet pressure, cavitation noise occurs when the flow state changes from turbulent to cavitating flow. Frequency peak forms in relatively higher spectra range, which decreases with the increase of the flowrate. Finally, the frequency peak disappears nearly simultaneous when the flow goes choked. Whistling noise produced by the flow self-sustained oscillation exist in both non-cavitating and cavitating flow conditions, which is triggered by the pressure fluctuations in the flow contract area, and amplified by the shear-layer instability. The hydrodynamic feedback leads highly organized oscillations, makes the noise whistling with pure tones.

The pure tone frequency presents jump property with the outlet pressure, in each jump range, which has good monotonicity with the outlet pressure. It seems that the flow configuration influences importantly to the pure tone distributions. However, the mechanism of this phenomenon is still unclarified, further investigations will be conducted.

ACKNOWLEDGEMENTS

The authors are grateful to the National Natural Science Foundation of China (no. 51075361) and the Major Research plan of the National Natural Science Foundation of China (no. 91023015) for financial support. Thanks are also given to Shohei RYU and Masami OCHIAI for their helps with this research, who work at the technical research laboratory of Hitachi Construction Machinery Co. Ltd. Tsuchiura, Ibaraki, Japan.

REFERENCES

1 Skaistis S., Noise Control of Hydraulic Machinery, 1988.
2 Christopher E. B., Cavitation and Bubble Dynamics, 1995.
3 Plesset, M. S., the Dynamics of Cavitation Bubble.

Trans. ASME, Jr. Appl. Mech., 1949, 16, 277-282.
4 Fitzpatrick H. M. and Strasberg M., Hydrodynamic Sources of Sound. First symposium on naval hydrodynamics, 1956.
5 Koivula, T., on Cavitation in Fluid Power. Proc. of 1st FPNI-PhD Symp., Hamburg, 2000, 371–382.
6 Hans, D. B. and George, W. P., a Method to Predict Sound Levels from Hydrodynamic Sources Associated with Flow through Throttling Valves. J. Noise Control Eng., 1995, 43(5), 145–158.
7 Martin, C. S., Medlarz, H. and Wiggert, D. C., Cavitation Inception in Spool Valves. Journal of Fluids Engineering, 1981, 103, 564–576.
8 Marboe, R.C. and Billet, M. L., Some Aspects of Traveling Bubble Cavitation and Noise. International symposium on Cavitation and Multiphase Flow, ASME, 1986, 119-126.
9 Li, S. C., Cavitation of Hydraulic Machinery, 2000.
10 Sondhaus, C. 1854. Ann. Phys. 9 1 : 2 1 4-40
11 Betts, P. L., Self-Induced Oscillations in an Open Water-Channel with Slotted Walls, J. Fluid Mech., 1972, 55, 401-417.
12 Brown, G. B., the Mechanism of Edge-Tone Production. Proceedings of the Physical Society of London, 1937b, 49, 508-521.
13 Holger, D. K., Wilson, T. A. & Beavers, G. S., the Fluid Mechanics of the Edge Tone. Journal of the Acoustical Society of America, 1977, 62, 1116-1128.
14 Lu L., Zou J. and Fu X., the Acoustics of Cavitation in Spool Valve with U-notches, Proc. IMechE, Part G: J. Aerospace Engineering, 2011.
15 Rockwell D. and Naudascher E., Self-Sustained Oscillations of Impinging Free Shear Layers, Ann. Rev. Fluid Mech., 1979, 11, 67-94.

Proceedings of the 8th JFPS International
Symposium on Fluid Power, OKINAWA 2011
Oct. 25-28, 2011

2C1-3

PRACTICAL PERFORMANCE OF HIGH BULK MODULUS OIL

Toshiyuki TSUBOUCHI* and Jitsuo SHINODA**

* Advanced Technology Research Laboratories, Idemitsu Kosan Co., Ltd.
1280 Kami-izumi, Sodegaura, Chiba, 299-0293, Japan
(E-mail: toshiyuki.tsubouchi@si.idemitsu.co.jp)
** Lubricants Research Laboratory, Idemitsu Kosan Co., Ltd.
24-4 Anesaki-kaigan, Ichihara, Chiba, 299-0107, Japan

ABSTRACT

Practical performance of high bulk modulus oil was studied. Besides high bulk modulus oil has advantages in pressure response and volumetric efficiency of pumps, has an advantage in terms of oil temperature control, because oil temperature rise is 20% smaller than that of mineral oil due to large volumetric heat capacity. Since high bulk modulus oil has extremely low gas solubility, no air bubble generation occurs even by ultrasonic wave vibration. Therefore high bulk modulus oil has an advantage in low pressure hydraulics as well. The new oil has sufficient practical performances, such as oxidation stability and anti-wear property. Various new applications of the new oil are promising.

KEY WORDS

bulk modulus, hydraulic fluid, volumetric efficiency, air bubble, anti-wear

INTRODUCTION

In order to improve performances of hydraulic servo systems, we have addressed primary function of hydraulic oil, namely transmission of power, and developed high bulk modulus oil, of which bulk modulus is as high as that of water, successfully [1].

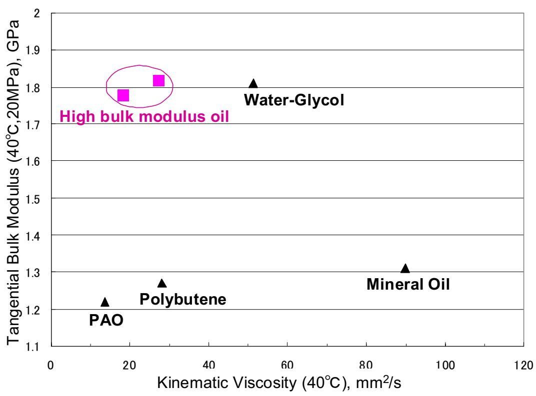

Figure 1 Bulk modulus vs kinematic viscosity of conventional oil and high bulk modulus oil

Figure 1 shows bulk modulus of newly synthesized oil compared to conventional base oil.

The new oil has been verified to have advantages of pressure response and pump efficiency because of high bulk modulus from the basic experiments [2].

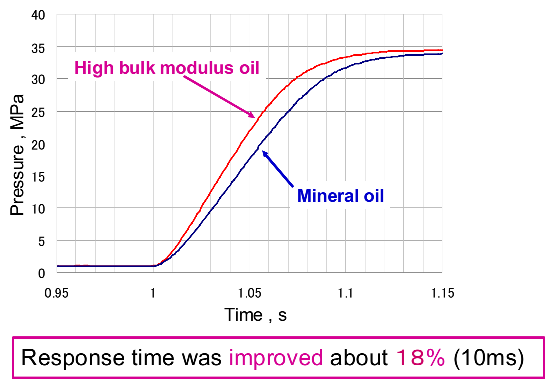

Figure 2 Result of pressure response experiment

Figure 2 shows pressure response time of high bulk modulus oil compared to mineral oil.

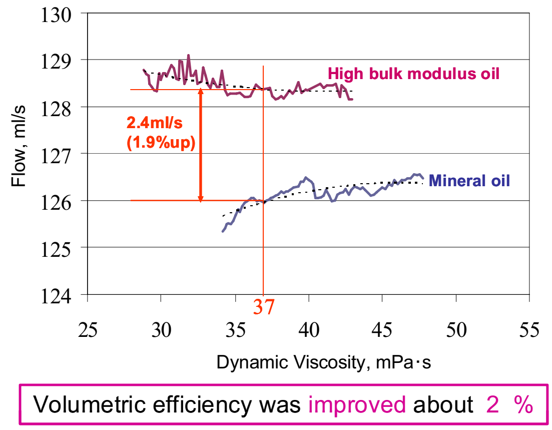

Figure 3 Result of pump efficiency experiment

Figure 3 shows flow volume of high bulk modulus oil compared to mineral oil by pump efficiency experiment.

The new oils have also been examined the principle of high bulk modulus and low pressure-viscosity coefficient [3].

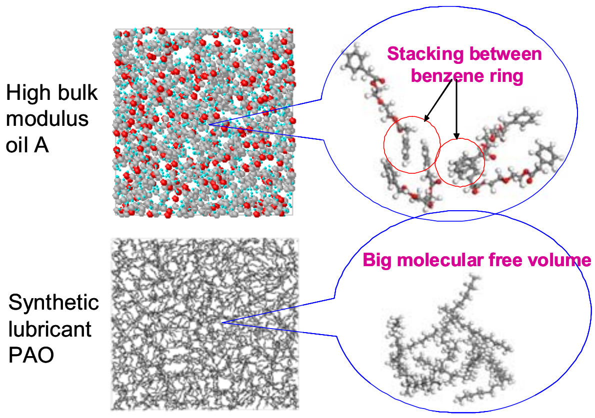

Figure 4 Prospective exact liquid structure obtained by MD simulation

Figure 4 shows prospective exact liquid structure which explains principle of high bulk modulus compared to conventional synthetic lubricant PAO. The new oil has thick liquid structure of which benzene rings situate closely each other, on the other hand PAO has thin liquid structure of which molecular structural regularity is low and molecular free volume is big.

Besides above mentioned qualities, extremely low gas solubility and low traction coefficient have been confirmed in previous studies. This paper describes some practical performances of high bulk modulus oil.

EXPERIMENTS

A rise in oil temperature during pump test

When pump efficiency tests of high bulk modulus oil and mineral oil were carried out, oil temperatures at pump-in and pump-out were measured. Figure 5 shows oil measurement points of hydraulic circuit for pump efficiency test.

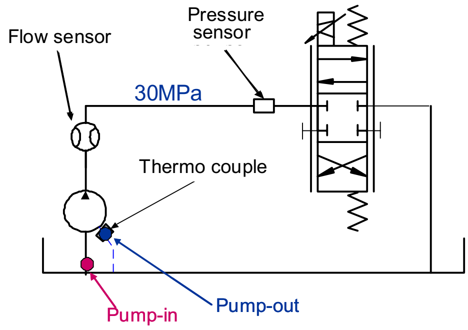

Figure 5 Hydraulic circuit for pump efficiency test

Figure 6 shows results of oil temperature measurement.

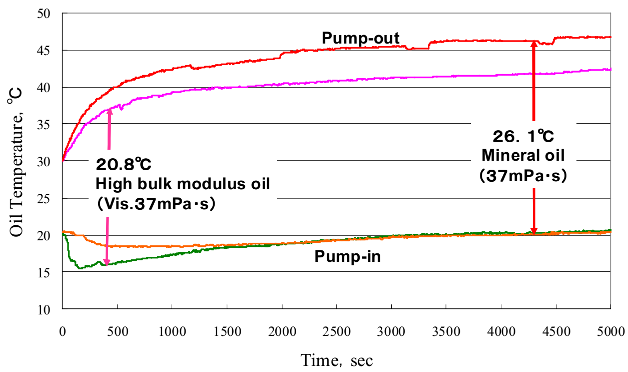

Figure 6 Oil temperature rise at pump-out

Figure 6 shows temperature rise of the new oil is about 21℃, on the other hand that of the mineral oil is about 26℃. The oil temperature rise of the new oil is smaller than that of the mineral oil by 20%, which comes from about 20% larger volumetric heat capacity of the new oil. The new oil can have advantages in terms of precise temperature control and reduction of energy loss for cooling.

Air bubbles generation by vibration

Even small inclusions of unsolved air, namely air bubbles, can have a large effect on system dynamics at low pressure. In theory 0.1vol% of air bubble content reduces 17% of effective bulk modulus at 1MPa [4].

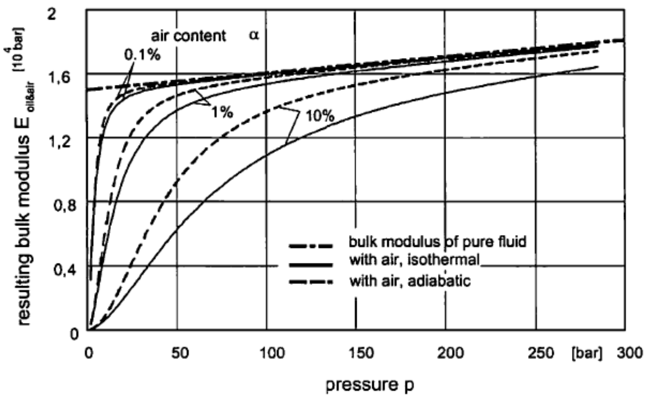

Figure 7 Resulting bulk modulus of oil with air bubbles [4]

Figure 7 shows large effect on bulk modulus of oil with air bubbles under low pressure.

Accordingly in the case of low pressure hydraulic systems, especially hydrostatic bearing in ultra-precision machine tools and so on, existing air bubbles can deteriorate system performance. Except for air bubbles caught in oil, air bubbles generation occurs from solved air in oil by vibration. In this case low gas solubility in oil is advantage.

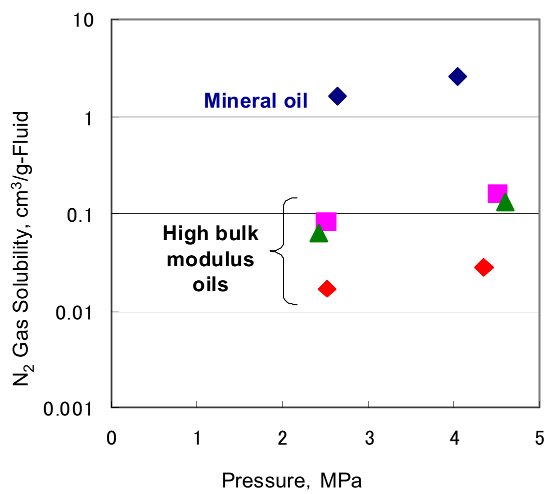

Figure 8 Nitrogen gas solubility of high bulk modulus oils

Figure 8 shows nitrogen gas solubility of high bulk modulus oil and mineral oil, and it says the new fluids have extremely low gas solubility compared to mineral oil [1].

Air bubbles generation was observed by supersonic wave vibration given to the air-saturated oils. As a result of the test, 7 minutes of supersonic wave vibration gave air bubbles generation in the case of air-saturated mineral oil, on the other hand no bubble generation in the case of air-saturated high bulk modulus oil because of extremely low gas solubility.

Figure 9 shows result of the air bubble generation test, no bubble generation was observed in the new oils.

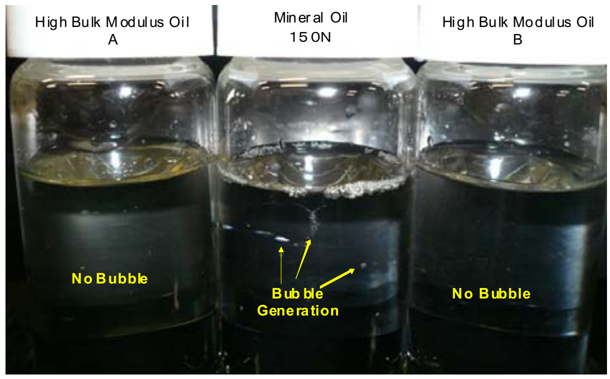

Figure 9 Result of the air bubble generation test

Oxidation stability

Table 1 shows oxidation stability test results of experimentally formulated high bulk modulus hydraulic oil. Compared to conventional biodegradable hydraulic fluid, the new oils have sufficient oxidation stability.

Pump wear test

Pump wear test was carried out by using vane pump V104C (TOKYO KEIKI INC.) under the condition of 13.7MPa, 65℃ and 1200rpm. Figure 10 shows wear amount after 100hrs and 250hrs compared to conventional anti-wear hydraulic oil. Figure 10 says the new hydraulic oil has an excellent anti-wear property. Figure 11 shows wear track of cam ring. Clear wear tracks are observed in that of conventional oil, on the other hand little wear track is observed in that of the new oil.

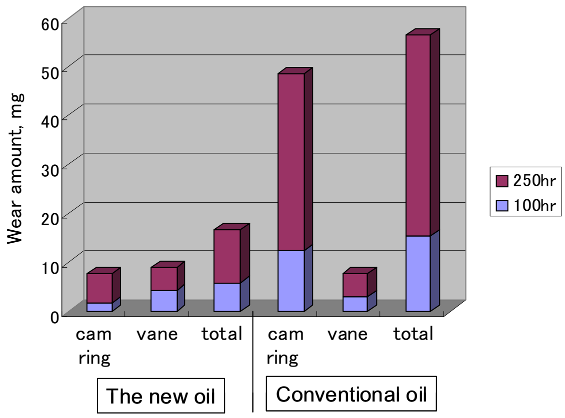

Figure 10 Wear amount of pump wear test

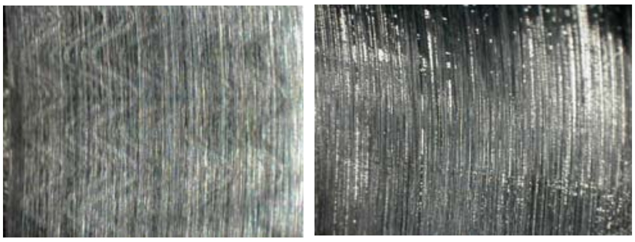

The new oil

Conventional oil

Figure 11 Wear track of cam ring

SUMMARY

1) Besides high bulk modulus oil has advantages in pressure response and volumetric efficiency of pumps, has an advantage in terms of oil temperature control, because oil temperature rise is 20% smaller than that of mineral oil due to large volumetric heat capacity.
2) Since high bulk modulus oil has extremely low gas solubility, no air bubble generation occurs even by ultrasonic wave vibration. Therefore high bulk modulus oil has an advantage in low pressure hydraulics as well.
3) The new oil has sufficient practical performances, such as oxidation stability and anti-wear property.
4) Various new applications of the new oil are promising.

ACKNOWLEDGEMENT

We thank Prof. Kitagawa and Dr. Liu of Tokyo Institute of Technology for hydraulic performance evaluation.

REFERENCES

1. T.Tsubouchi, H.Kamimura and J.Shinoda, "Development of Oily High Bulk Modulus Fluid", Proc. 7th JFPS International Symposium on Fluid Power, Toyama, 2, 2008, 329-334
2. C.Liu, A.Kitagawa, K.Uraguchi, S.Minematsu, J.Lu and T.Tsubouchi, "Improvement of Hydraulic Servo System with High Bulk Modulus Oil", Proc. Spring Conference of JFPS, Sendai, 2009, 53-55 (in Japanese)
3. T.Tsubouchi and J.Shinoda, "Characterization of Oily High Bulk Modulus Fluid", Tribology Online, 5, 5 (2010), 230-234
4. H.Teissen and H.Murrenhoff, "Determination of Effects of a High Bulk Modulus Fluid", IFAS/RWTH Aachen undisclosed report, 2006

Table 1 Oxidation stability test results of experimentally formulated oil

General Properties	Unit	Test Fluid A	Test Fluid B (Biodegradable)	Conventional Biodegradable Fluid
Kinematic Viscosity(40℃)	mm^2/s	47.26	46.01	45.69
Kinematic Viscosity(100℃)	mm^2/s	7.128	7.185	8.767
Viscosity Index		109	116	175
Acid Number (Indicator Method)	mgKOH/g	0.03	0.49	0.84
Base Number (HCl Method)	mgKOH/g	–	0.15	0.06
Density(15℃)	g/cm3	1.0596	1.1481	0.932
Flash Point(COC)	℃	254	250	312
Pour Point	℃	−47.5	−32.5	−50.0>
Copper Corrosion Test 100℃×3h		1(1b)	1(1b)	1(1b)
RBOT(Fall time to 1.75kg/cm2)	min	927	651	123
ISOT 165.5℃×72h Properties After 72hrs				
Kinematic Viscosity(40℃)	mm^2/s	47.43	48.16	99.19
Acid Number	mgKOH/g	3.02	1.07	10.9
Viscosity Change Ratio	%	0.36	4.67	117.09
Increase of Acid Number	mgKOH/g	2.99	0.58	10.06

Proceedings of the 8th JFPS International
Symposium on Fluid Power, OKINAWA 2011
Oct. 25-28, 2011

2C2-1

DEVELOPMENT OF WATER HYDRAULIC PROPORTIONAL VALVES DRIVEN BY POSITIVE CAM MECHANISM

Kenji SUZUKI*, Sho AKAZAWA*, Toshiki HATAYAMA* and Yohichi NAKAO*

* Department of Mechanical Engineering, Faculty of Engineering
Kanagawa University
3-27-1 Rokkakubashi, Kanagawa-ku, Yokohama, 221-8686 Japan
(E-mail: suzuki@kanagawa-u.ac.jp)

ABSTRACT

This paper describes development of water hydraulic proportional valves. The valves are spool-type and the spool is driven by a stepping motor and positive cam mechanism. The cam is always placed between two cam followers and the return spring is omitted. The rotational angle of the cam and the displacement of the spool is linear. The experimental results of static characteristics are also shown: internal leakage and pressure gain against spool displacement, flow rate characteristics with no load and flow rate against load pressure. Although the spool is overlap, the dead band was not observed in the flow rate characteristics with no load because of the leakage passing through the clearance around the spool. In addition, non-linearity of the spool displacement against the rotational angle of the cam was below 0.2% and the hysteresis was hardly observed even though the spool displacement was not feed backed.

KEY WORDS

Proportional Valve, Positive cam, Water hydraulics

NOMENCLATURE

p_A : Pressure at port A [Pa]
p_B : Pressure at port B [Pa]
p_s : Supply pressure [Pa]
p_t : Tank pressure [Pa]
r : Radial distance of cam follower [m]
x : Spool displacement [m]
θ : Rotational angle of cam [-]

INTRODUCTION

The proportional valve is a kind of the valve that controls the movement of the fluid actuator. The valve to control the movement of the spool by the pressure difference generated by the nozzle flapper system is called a servo valve. The valve to drive the spool directly with the electromagnetic proportional solenoid is called a proportional valve. Those neither name nor structure are clearly defined. In general, the servo valve is used for a high-speed, highly accurate control, though it is expensive because the structure is comparatively complex. The proportional solenoid valve is for use that

high-speed response like the servo valve is not necessary, and is comparatively cheap. As for both types, the valves with the wide range of the performance have been produced for the oil hydraulics. Some the water hydraulic servo valves are marketed, and the research example [1-3] and the example of practical use are found. The proportional valve with good response is preferable for the spread of the water hydraulic system. However, the water hydraulic proportional valve in the market is only a little kind, and the research examples are also few [4, 5].
The response of the proportional solenoid valve is inferior compared with the servo valve because the core of the solenoid is heavy. For the improvement of the response, the proportional valve that drives the spool by using a voice coil motor or a linear motor has been marketed for the oil hydraulics though it is a relatively costly. However, the proportional valve that intends the high-speed response is rarely found for water hydraulics [6].
This paper describes development of water hydraulic proportional control valve driven by positive cam mechanism and stepping motor. The experimental results and one of the applications are also shown.

VALVE STRUCTURE

Figure 1 shows the photograph of the developed valve. The internal structure of the valve is shown in Figure 2. The mounting surface dimensions agree with ISO code: 4401-03-02-0-05 and JIS B 8355 code: D-03-02-0-94.

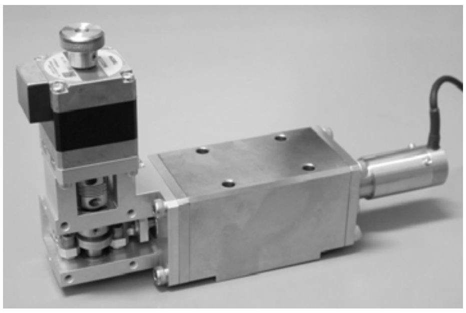

Figure 1 Photograph of the developed valve

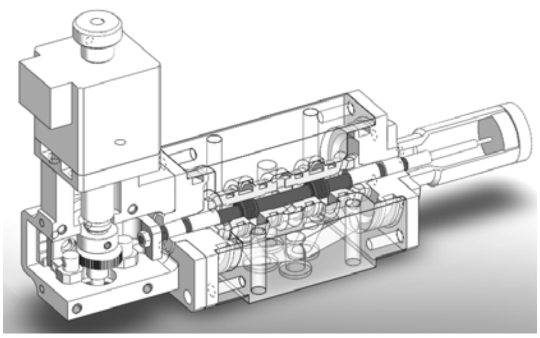

Figure 2 Structure of the developed valve

Spool driver
In the spool drive mechanism of the developed valve, the rotation of the stepping motor is converted into a linear movement with the cam for the spool. The reason why these mechanism were adopted are described as follows.
Firstly, the mechanism to obtain the linear motion of the spool was examined. The demand in the design is to achieve the high-speed response of the stroke of several mm with a cheap, small mechanism as much as possible.
To obtain the linear motion of the spool directly from electromagnetic force, the following mechanisms became candidates. It was judged, however, that neither was suitable.

(1) Electromagnetic proportional solenoid: the core is heavy and the high-speed response cannot be obtained.
(2) Linear motor: expensive; suitable for long-stroke.
(3) Voice coil motor: large-scale.
(4) Piezoelectric device: the displacement expansion mechanism is required; large hysteresis; expensive.

Next, to convert from the rational motion of a rotation-type motor on the market into the linear motion, the following mechanisms became candidates.

(5) Clank mechanism: rotational angle and displacement is not linear.
(6) Ball-screw: suitable for long-stroke.
(7) Cam: suitable for short-stroke and high-speed response

As a result of examining these mechanisms, the rotation-type motor and the cam mechanism were combined to obtain the linear motion.
Finally, the kind of the rotation-type motor was examined. The AC servo motor is suitable for the use to position accurately in the long distance combining with the ball screw. However, it was judged that the stepping motor was suitable for the usage in which only the half rotation of the cam was used.
Positive cam mechanism
In a usual cam mechanism, the cam follower is made not to part from the cam by pressing it against the cam by the return spring. However, because a stiff spring is necessary to achieve the high-speed response, useless power is consumed to displace the spring. In the eccentric disc cam often used, the rotational angle of the cam and the displacement of cam follower are nonlinear. Therefore, it is required to calculate the rotational angle to obtain necessary displacement by trigonometric function, and the load of the controller becomes larger.
Then, the present study employed a positive cam mechanism, in which the cam is always placed between two cam followers. As a result, the return spring is omitted and hysteresis is excluded. In addition, the rotational angle to obtain necessary displacement is computable with a simple linear equation because the cam shape is provided as the rotational angle of the cam

and the displacement of cam follower becomes completely linear.
The cam shape becomes the envelope curve of the end mill for machining as shown in Figure 3. When the diameter of the end mill is different from the cam follower, the calculation of center tracks of the end mill becomes complex. However, when their diameters are identical, the cam follower's displacement against the rotational angle of the cam can be specified directly.
As for the cam profile adopted in the present study, the cam follower's displacement to the rotational angle of the cam was made to become to 25 μm/deg. The center tracks of the end mill of the same diameter with the cam follower is given by equation (1) in which the base circle radius is 9 mm.

$$r\,[\mathrm{mm}] = 9 + 0.025 \times |\theta| \quad (-180^\circ \le \theta \le 180^\circ) \qquad (1)$$

As a result, the displacement of ±2 mm is obtained for the rotational angle of ±80 deg. Because the basic step angle of the stepping motor used is 1.8 deg, the resolution of displacement is 45 μm/pulse. The step angle can be divided into 16 by the motor driver's setting. In this case, the resolution of displacement becomes about 3 μm/pulse. The stroke and the resolution of the spool displacement can be easily changed by the cam profile and the specification of the stepping motor.

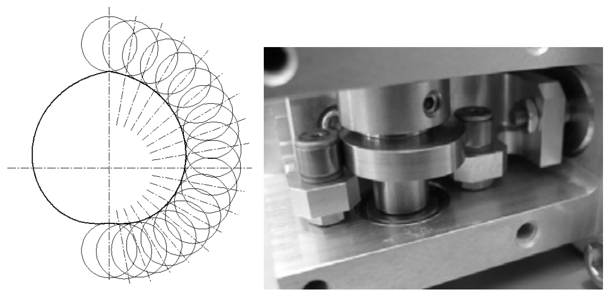

Figure 3 Cam profile and positive cam mechanism

CONTROL OF MOTOR

As for the stepping motor, the given pulse number is proportional to the rotational angle. Therefore, if the origin of the spool position has been surely detected, the feedback of the spool displacement is unnecessary. However, it decided to detect the spool displacement and feed backed because there was a possibility of the step out by disturbance. Moreover, as shown in Figure 4, the voltage from variable resistance is added to the targeted value of the spool position to fine-tune the neutral position.
The driver of the stepping motor is a marketed commodity. The microcomputer named Arduino was used as a controller to generate the pulse to the motor driver. The Arduino is an open-source electronics prototyping platform based on flexible, easy-to-use hardware and software [7]. The microcontroller on the board is programmed using the Arduino programming language and the Arduino development environment.
To make the algorithm in the controller general, the rotational direction of the motor was decided according to the sign of the difference between the present value and the targeted value, and only one pulse was output. It is possible to make the motor work with stability though the response is slow because the A/D conversion and leveling for the noise removal are done whenever one pulse is output.
Figure 5 shows one example of the step response of the motor angle. The overshoot is not observed and there is not a vibration after settling though it takes about 0.1 seconds to settle.

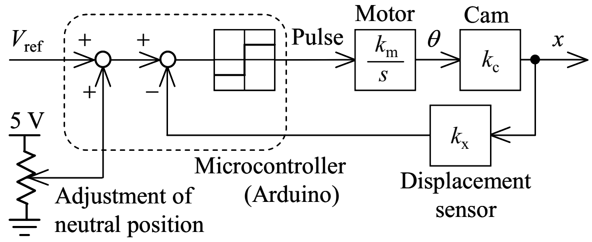

Figure 4 Block diagram

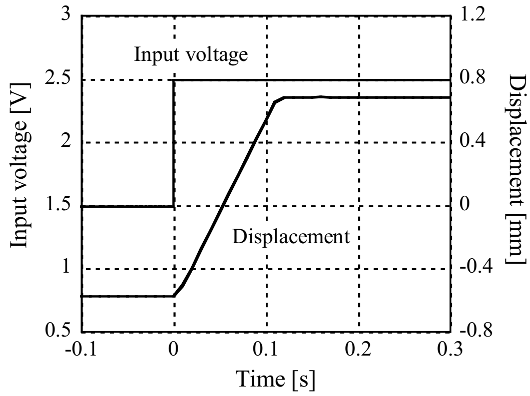

Figure 5 Step response of motor with controller

STATIC CHARACTERISTICS OF CAM MECHANISM

First of all, the displacement sensor for the spool was calibrated. The spool displacement to the rotational angle of the stepping motor was measured by using the result. The resolution of the step angle was set to 1/4 (0.45 deg) of the basic step angle. The pulse number and the rotational angle of the motor were assumed to be proportional.
Figure 6 shows the result of the measurement. (b) shows the nonlinearity to full-scale (4 mm). The nonlinearity is almost a range of ±0.1% over the whole stroke though it

increases to about 0.2% on the stroke ends. Moreover, the hysteresis is within 0.1%, and almost negligible. Therefore, the positive cam mechanism adopted in the present study has very excellent linearity.

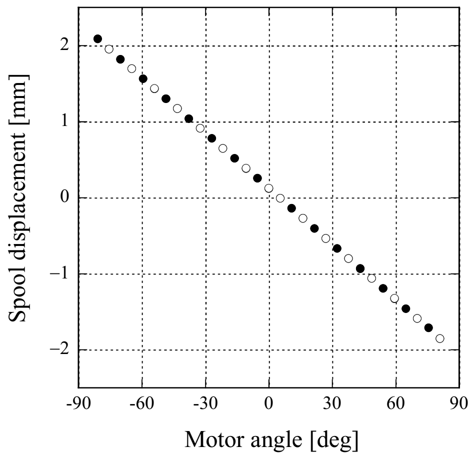

(a) Spool displacement vs. motor angle

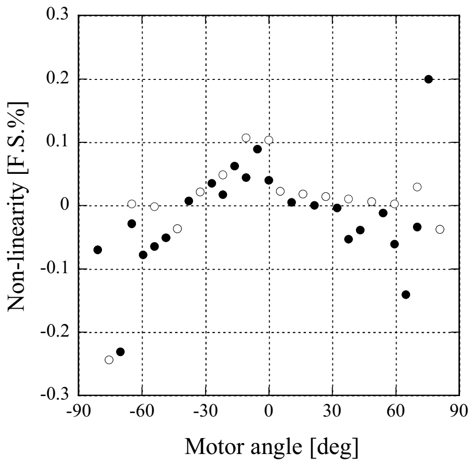

(b) Non-linearity of spool displacement vs. motor angle

Figure 6 Static characteristics of positive cam mechanism

STATIC CHARACTERISTICS OF VALVE

This chapter shows the experimental results of the static characteristics of the valve. Figure 7 shows the schematics of experimental setup for the measurement. The supply pressure was set to 3.5 MPa with the pressure relief valve that authors had developed [8]. The all flow rate was measured with the flow meter of the turbine type. Two kinds of flow meters with different measurement range were switched according to the amount of flow rate.

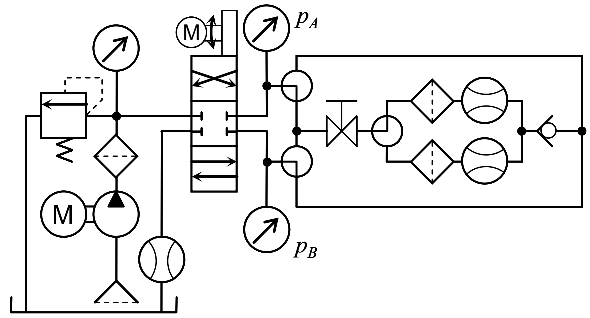

Figure 7 Experimental setup

First of all, the pressure gain characteristic is shown in Figure 8. (b) is the expansion of the neutral position neighborhood. The neutral position was slightly shifted because it doesn't feed back the spool displacement to the rotational angle of the motor. However, the pressure gain of the neutral position neighborhood was almost linear and symmetric.

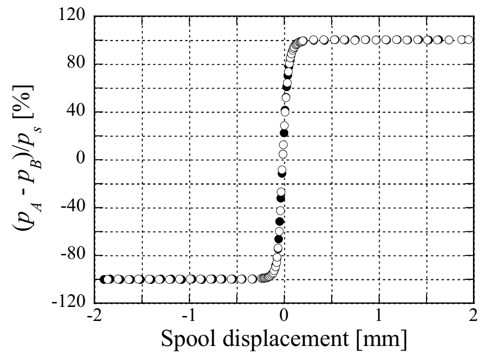

(a) Full scale

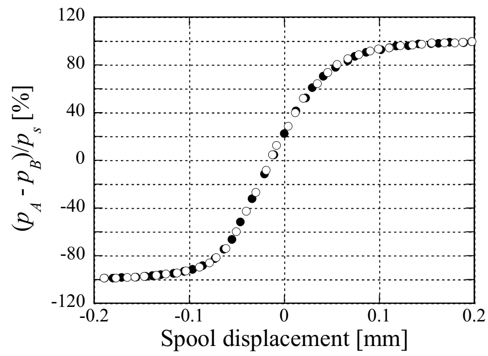

(b) Nearby neutral position

Figure 8 Pressure gain characteristics

Next, the internal leakage characteristic is shown in Figure 9. The reason to show unnatural behavior to the displacement of the spool is circumferential grooves on the spool and the asymmetric diversity of the clearance between the spool and sleeve.

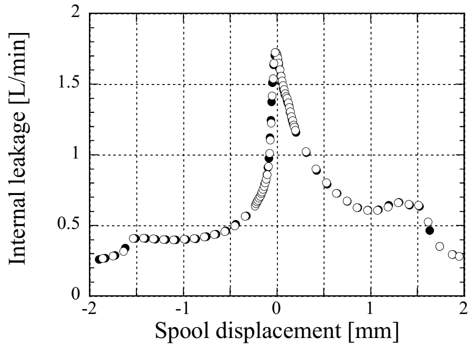

Figure 9 Internal leakage

Figure 10 shows the flow rate characteristic with no load. Although the spool is overlap within the range of ±0.1 mm for the decrease of the internal leakage, the dead band was not observed. This is because a radial clearance was large.

Finally, the flowing rate characteristic with load is shown in Figure 11. Flow rate doesn't increase so much when the spool displacement becomes 1.5 mm or more. This is because the part of smaller diameter of the spool is too large, and the passage area of the fluid was not enough.

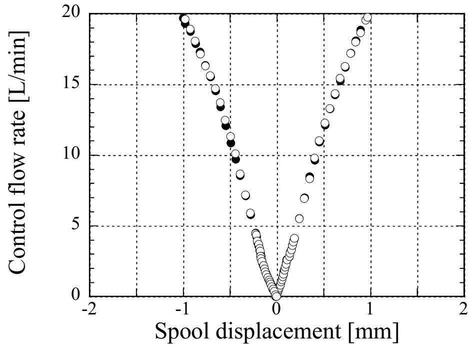

Figure 10 Flow rate characteristic with no load

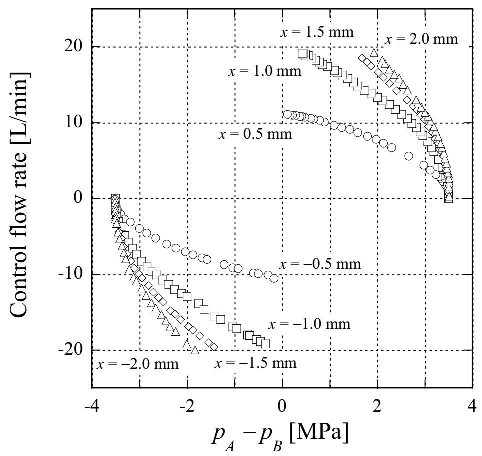

Figure 11 Flow rate characteristic with load

APPLICATION

As an example of applying the water hydraulic proportional valve developed in the present study, the water hydrostatic bearing was actively controlled to improve the support stiffness. Figure 12 shows the schematic drawing of the hydrostatic support mechanism. The pressures supplied to the hydrostatic bearings confronting the supporting plate are controlled with the proportional valve.

Vertical both control pressures are equal when the spool is at a neutral position. When the spool is displaced, the amount of the overlap changes, and this part functions as variable restrictors.

When a downward load is impressed to the supporting plate, the supporting plate is displaced below. Then, the spool is displaced below, and the recess pressure of the lower hydrostatic bearing increases, thus the displacement of the supporting plate can be returned to zero. That is, displacement can be adjusted to zero regardless of the amount of the load, and the support stiffness can be made infinity.

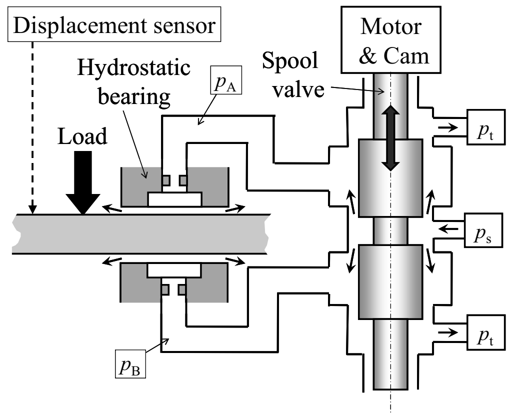

Figure 12 Active control of displacement of hydrostatic support

Figure 13 shows the change in control pressure p_A and p_B supplied into the hydrostatic bearing to the spool displacement. The control pressure p_A to the upside hydrostatic bearing decreases as the spool is displaced, and the lower pressure p_B increases. Therefore, the pressure difference between upper and lower sides increases, and the load capacity increases.

Figure 14 shows the experimental results of the displacement of the supporting plate to the load. When the supply pressure is not controlled to the hydrostatic bearing, the displacement of about 4 μm has been generated for the load of 400 N. However, the displacement was able to be adjusted to almost zero by actively controlling the supply pressure to the hydrostatic bearings.

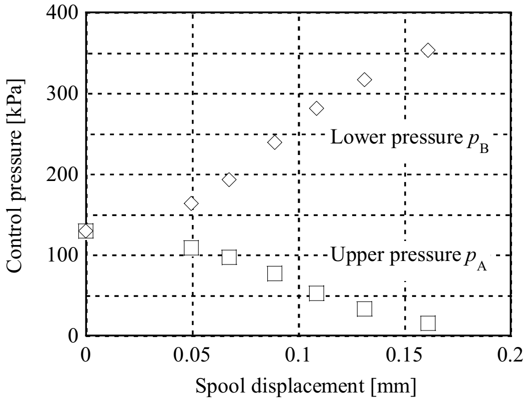

Figure 13 Control pressures vs. spool displacement

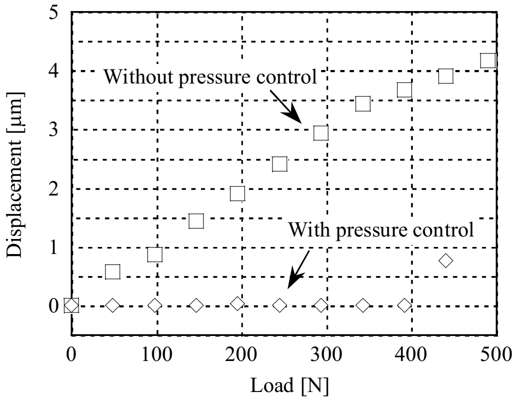

Figure 14 Displacement of hydrostatic bearing vs. load

CONCLUSIONS

The prototype of water hydraulic proportional valve that the spool is driven by the stepping motor and positive cam mechanism is developed. the experimental results of the valve are measured: internal leakage and pressure gain against spool displacement, flow rate characteristics with no load and flow rate against load pressure.

Although the spool is overlap, the dead band was not observed in the flow rate characteristics with no load because of the leakage passing through the clearance around the spool. In addition, non-linearity of the spool displacement against the rotational angle of the cam was below 0.2% and the hysteresis was hardly observed even though the spool displacement was not feed backed.

As an application example, the water hydrostatic bearing was actively controlled to improve the support stiffness. keeping zero-displacement was achieved to some degree of the load; the support stiffness was able to be made infinity.

ACKNOWLEDGEMENT

We thank Messrs. Tetsuka and Tamura for their assistance on the experimental work in this study.

REFERENCES

1. Urata, E., Miyakawa, S., Yamashina, C., Nakao, Y., Usami, Y. and Shinoda, M., Development of a water hydraulic servovalve, Jpn. Soc. Mech. Engrs, Intl. J., Ser. B, 1998, **41**-2, pp. 286-294.
2. Oomichi, T. and Tanaka, A., Development of water hydraulic servo control system considering water characteristics, Trans. Jpn. Soc. Mech. Engrs, Ser. C, 1996, **62**-599, pp. 2612-2619.
3. Watanabe, T., Inayama, T. and Oomichi, T., Development of the small flow rate water hydraulic servo valve, J. Robotics and Mechatronics, 2010, **22**-3, pp. 333-340.
4. Takahashi, T. and Yamashina, C., Development of Water Hydraulic Proportional Control Valve, Ebara Engineering Review, 2001, **193**, pp. 3-9.
5. Yoshida, F. and Miyakawa, S., Characteristics of proportional control valve using tap water, Proc. Seventh Intl. Fluid Power Conf., Group H, Aachen, Germany, 2010, pp. 445-456.
6. Park, S.-H., Kitagawa, A. and Kawashima, M., Water hydraulic high-speed solenoid valve, Part 1: development and static behaviour, Proc. Instn. Mech. Engrs, Part I: J. Systems and Control Engineering, 2004, **218**, pp. 399-409.
7. http://www.arduino.cc/
8. Suzuki, K. and Urata, E., Development of a direct pressure-sensing water hydraulic relief valve, Intl. J. of Fluid Power, 2008, **9**-2, pp. 5-13.

Proceedings of the 8th JFPS International
Symposium on Fluid Power, OKINAWA 2011
Oct. 25-28, 2011

2C2-2

THE CO-SIMULATION OF THE AXIAL PISTON PUMP FOR SEAWATER REVERSE OSMOSIS DESALINATION

ZHAI Jiang* ZHOU Hua*

* State Key Lab of Fluid Power Transmission and Control
Zhejiang University
38 Zheda Road, Hangzhou, 310027 P. R. China
(E-mail: jiangzhai@sina.com)

ABSTRACT

One of the most important components for Seawater Reverse Osmosis Desalination (SWRO) system is the high pressure pump. The axial piston pump based on water hydraulics technology can be developed as a high pressure pump in small and medium scale SWRO system. To reduce the cost in the development process, a comprehensive simulation for the pump is critical to evaluate its mechanical characteristics and hydraulic performance before the prototype is made. In this paper, mechanics simulation tools such as ADAMS, and ANSYS were used to evaluate the kinematics and dynamics characters, stress and strain of critical components of the pump, and hydraulic simulation tool such as AMESim was used to evaluate the pressure of the cylinder. In conjunction with these simulation tools, the co-simulation of the pump provided an accurate estimation of the kinematics, main parts loading, hydraulic flow and pressure of the pump.

KEY WORDS

Axial Piston Pump, Sea Water Desalination, Simulation

NOMENCLATURE

$\sum \overline{F_P}$: total force acting on the piston [N]
$\overline{N_S}$: reacting force of the slipper acting on the piston [N]
$\overline{N_C}$: reacting force of the cylinder bush acting on the piston [N]
$\overline{f_C}$: friction force of the cylinder bush acting on the piston [N]
m_P : mass of the piston [kg]
$\overline{P_P}$: hydraulic force acting on the piston [N]
$\overline{a_r}$: component of piston acceleration in r direction [m/s^2]
$\overline{a_z}$: component of piston acceleration in z direction [m/s^2]
V_{P0} : dead volume of a single cylinder chamber [m^3]
A_P : pressurized area of a single piston [m^2]
R : piston pitch radius [m]
θ_i : circular position of the piston [rad]
α : swash plate angle [rad]
ω : angular speed of the cylinder of the pump [rad/s]
$A_{I,O}$: orifice area of the cylinder chamber connected with portplate [m/s^2]

$p_{I,O}$: the intake/output pressure at the port plate [Pa]
ρ : density of seawater [kg/m^3]
C_d : throttling coefficient [-]
B : bulk modulus of seawater [Pa]
Q_{PLi} : leakage flow from the clearance of the piston and the cylinder bush [m^3/s]

INTRODUCTION

It is well-known that seawater desalination is an important technique for getting fresh water from sea. Compared to other methods, the reverse osmosis process is an energy-saving technology in seawater desalination projects. [1, 2] One of the most important components in Sea Water Reverse Osmosis (SWRO) desalination system is the high pressure pump. Compared with reciprocating pump and centrifugal pump, the axial piston pump based on water hydraulics technology has remarkable virtues such as high efficiency, low noise and small size. So this type pumps can be developed as high pressure pumps for small and medium scale SWRO desalination projects. Commercial products such as DANFOSS APP series [3] now are available in the markets of China. In order to develop domestic axial piston pumps for SWRO and reduce the cost in the development process, a comprehensive simulation for the pump is critical to evaluate its mechanical characteristics and hydraulic performance before the prototype is made.
With the development of simulation technology, the so-called Virtual Prototype Technology (VPT) was used to comprehensive simulate the main characters of oil hydraulic piston pumps. [4-7] But for water hydraulic piston pumps, simulation studies were rarely reported in literatures. Because the working fluid and materials of the axial piston pump for SWRO are quite different from that of oil pump, it is meaningful to simulate the pump for SWRO based on VPT technology.

STRUCTURE AND SOLID MODELING

At present, the maximum flow of axial piston pump can not be compared to multi-stage centrifugal pump and even can not be compared to reciprocating pump, so multi-stage centrifugal pumps' status in large-scale SWRO projects are still irreplaceable. The high-pressure pump which is axial piston structure should depend on its small size, high efficiency, low noise, all water lubrication and other advantages, and compete with multi-stage centrifugal pumps and reciprocating pumps in small and medium scale SWRO desalination projects. So its application is mainly targeted at the SWRO desalination projects of which the water production is about 120 ~ 150 m^3/d. The general anti-osmotic pressure in SWRO system is about 5.5 ~ 8MPa. For these reasons, the main technical parameters of the pump are showed in Table 1.

Table 1 Main technical parameters of the pump

Rated pressure [MPa]	8.0
Maximum pressure [MPa]	10.0
Nominal displacement [mL/r]	80
Rated speed [rev/min]	1500

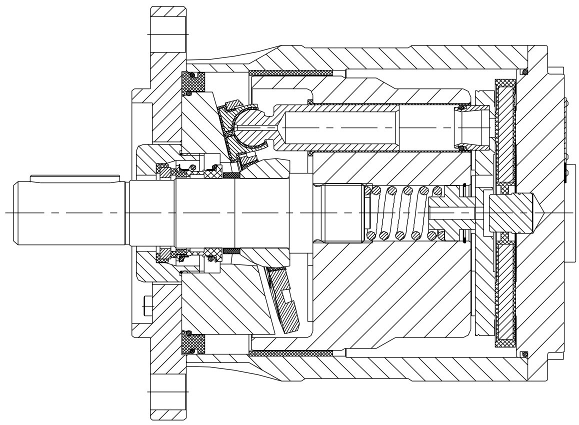

Figure 1 The structure of the pump

The structure of the pump for SWRO is shown in Fig. 1. The pump is base on axial piston principle. When the main shaft drives the cylinder to rotate, the structure can make the plungers for reciprocating movement along the cylinder axis. With the action of port plate, the water flow can be continually sucked from the inlet and discharged at the outlet. Compared with other structure, the pump using port plate as its flow distribution mechanism can have a better self-priming ability, can run at higher speeds. All this can make a result in a smaller size for a larger flow. The pump is lubricated by water directly, so the materials of port plate pairs, slipper pairs, piston pairs and ball joints are surface treated stainless steel and engineering plastic. Due to the restrictions of current development level of water-lubricated bearing, the pump is so called "half-axle" structure and only one engineering plastic bearing is adopted to support the cylinder-pistons group. The plate at the end of the cylinder is floating installed and has certain "flexibility". The floating plate under the action of the spring can contact with the port plate well, thereby this structure can reduce the internal leakage and improve volumetric efficiency. The pump's shaft seal is different from the oil one which widely used lip seal and it adopted mechanical seal structure, so the housing of the pump

can withstand greater pressure. The pump parts (including housing) are made of high quality stainless steel and engineering plastics, have excellent resistance to seawater corrosion and long service life.
The geometrical characters of the main parts of the pump are complicated and many parts are manufactured with different materials. In order to acquire the accurate data of the geometrical and inertial characters of the pump, the solid model of the pump was created by Pro/Engineer. After solid modeling in Pro/Engineer, the centers of gravity, masses, moments of inertia of the main moving parts can be automatic generated. Table 2 presents the main inertia information of the moving parts of the pump for simulation.

Table 2 Inertia information of the pump 's main moving parts

Main parts	Mass [kg]	Moment of inertia					
		I_{xx} [kg·m^3]	I_{yy} [kg·m^3]	I_{zz} [kg·m^3]	I_{xy} [kg·m^3]	I_{zx} [kg·m^3]	I_{yz} [kg·m^3]
Main shaft	1.218	1.751×10^{-4}	3.069×10^{-3}	3.065×10^{-3}	0	3.661×10^{-5}	0
Cylinder group	6.341	1.573×10^{-2}	1.332×10^{-2}	1.332×10^{-2}	4.989×10^{-7}	1.897×10^{-6}	-7.457×10^{-6}
Single piston	0.136	7.843×10^{-5}	7.843×10^{-5}	1.133×10^{-5}	0	0	0
Single slipper	0.036	2.587×10^{-6}	2.587×10^{-6}	3.437×10^{-6}	0	0	0
`Floating plate	0.851	8.511×10^{-4}	8.516×10^{-4}	1.673×10^{-3}	0	0	6.121×10^{-8}

MECHANCIAL MODEL

In order to seamlessly export the solid model files of the pump of Pro/Engineer to ADAMS, an ADAMS module named as Mech/Pro in Pro/Engineer environment was used to do this. In the environment of Mech/Pro and Pro/Engineer, the rigid bodies of moving parts of the pump were created and other all fixed parts such as swash plate, port plate, housing with the cylinder slide bearing were created as a ground. Different types of joints were used between the moving and fixed parts, such as cylindrical joints, fixed joints, planar joints and spherical joints. After this, the model can be transport from Pro/Engineer to ADAMS. Figure 2 presents the models of the pump in Pro/Engineer and in ADAMS respectively. Table 3 illustrates the joints between the moving and fixed parts.

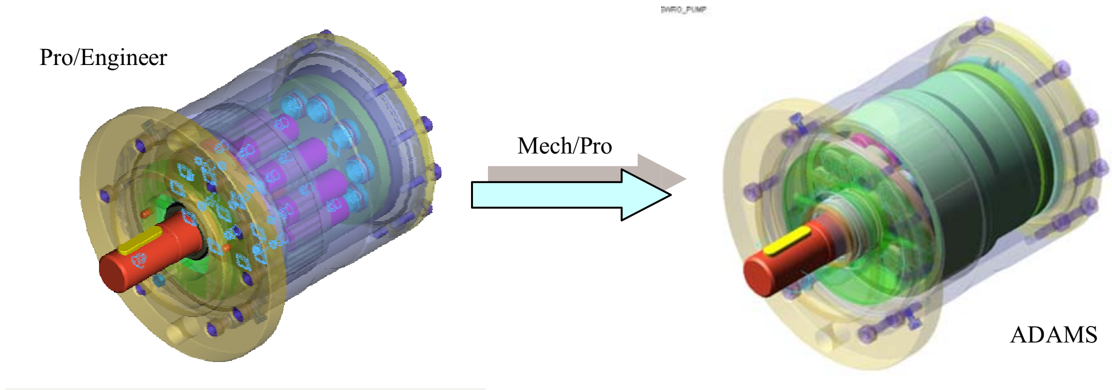

Figure 2 The solid model of the pump in Pro/Engineer and in ADAMS

Table 2 Joints between moving and fixed parts

Parts of the pump	Ground	Main shaft	Cylinder group	Single piston	Single slipper	Valve plate
Ground	-	Cylindrical	Cylindrical	-	-	Planar
Main shaft	Cylindrical	-	Fixed	-	-	-
Cylinder group	Cylindrical	Fixed	-	Cylindrical	-	Cylindrical
Single piston	-	-	Cylindrical	-	Spherical	-
Single slipper	-	-	-	Spherical	-	-
Floating plate	Planar	-	Cylindrical	-	-	-

For the body of one piston, shown in Figure 3, the instantaneous force on the piston is given by:

$$\Sigma\overline{F_P} = \overline{N_S} + \overline{N_C} + \overline{P_P} + \overline{f_C} = m_P(\overline{a_z} + \overline{a_r}) \tag{1}$$

From Eq.(1) and Figure 3, we can know that the force acting on the piston is due to the geometry structure of the pump, the rotation velocity and the hydraulic pressure in the cylinder. The forces on other parts, such as slippers, cylinder, valve plate, and main shaft, have the similar mechanical characters. For these reasons, the accurate profile of cylinder pressure is necessary for the mechanical model.

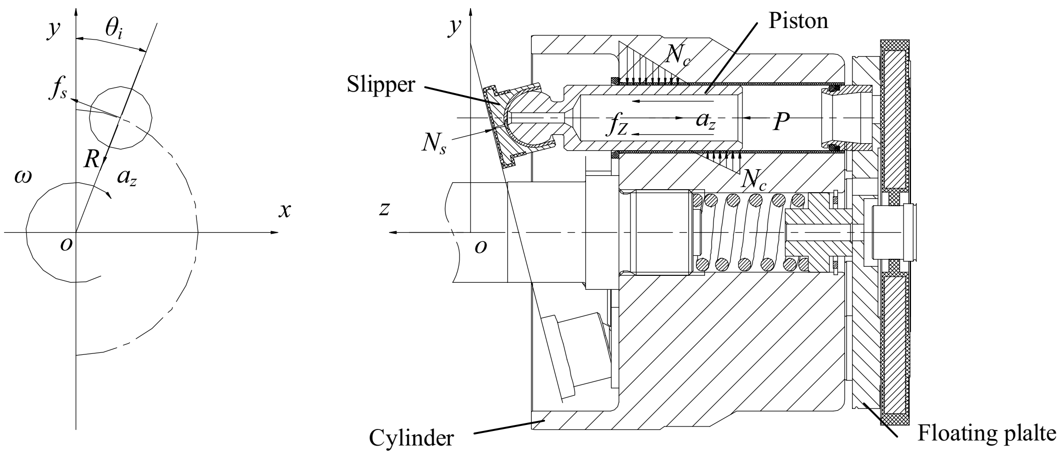

Figure 3 Diagram of the piston with instantaneous force

HYDRAULIC MODEL

Figure 3 also showed the sectioned view of the one piston within the cylinder block as it operates within the pump. From the kinematics and geometrical character of the pump, the volume of a single cylinder chamber V_{ci} is given by

$$V_{Pi} = V_{P0} + A_P R(1+\cos\theta_i)\tan\alpha \tag{2}$$

If i represent the sequence number of the piston from the up dead point and the pump has N pistons, we can get

$$\theta_i = \omega t + (i-1)\frac{2\pi}{N} \tag{3}$$

Because of the low viscosity of the seawater, a high Reynolds number tends to characterize the seawater flow in and out of the cylinder chamber. This flow Q_i may be modeled using an orifice pressure-flow equation, and this result is given by

$$Q_{Pi} = C_d A_{I,O}\sqrt{\frac{2}{\rho}\left|p_{Pi} - p_{I,O}\right|}\,\mathrm{sgn}(p_{Pi} - p_{I,O}) \tag{4}$$

Figure 4 presents two kidney ports connected to the suction and delivery volumes and two silencing grooves that allow the cylinder to pass smoothly from inlet to delivery. The areas of the variable orifices A_i and A_o depend on the position of the cylinder block with respect to the port plate. The pressure of the cylinder chamber varies with time to account for the periodicity change from the output pressure to the intake pressure. The intake pressure can set to be as the value of the inlet pressure of the pump, and the output pressure can be controlled by an orifice.

Considering the continuity equation and ignoring the leakage of the cylinder, the dynamic pressure of each cylinder chamber is determined for the cylinder volume, so one can obtain

$$\frac{\mathrm{d}p_{Pi}}{\mathrm{d}t} = \frac{B}{V_i}\left(\frac{\mathrm{d}V_{Pi}}{\mathrm{d}t} - Q_{Pi} - Q_{PLi}\right) \tag{5}$$

and

$$\left|\overline{P}\right| = p_{Pi}A_p \tag{6}$$

According the principle represented by Eq. (2) - Eq. (5), the AMESim model which simulate the dynamic pressure of the cylinder chamber can be constructed. Figure 5 presented the schematic of the model in AMESim environment.

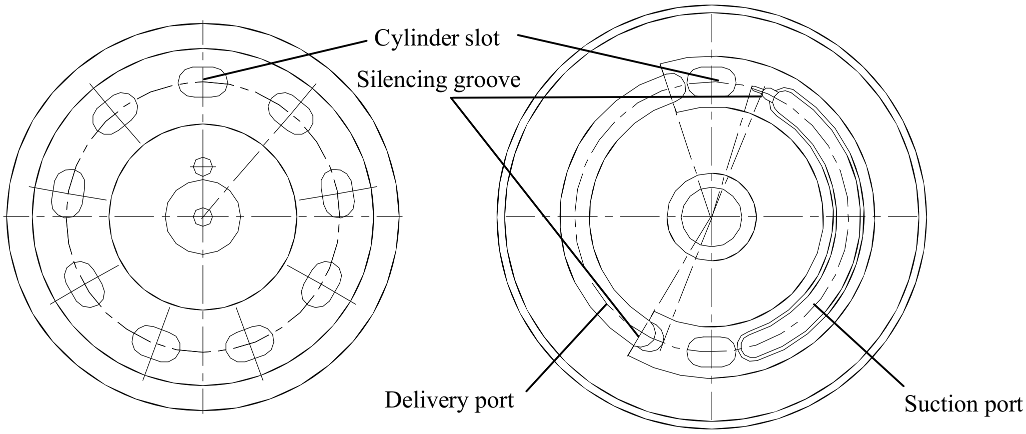

Figure 4 Diagram of the piston with instantaneous force

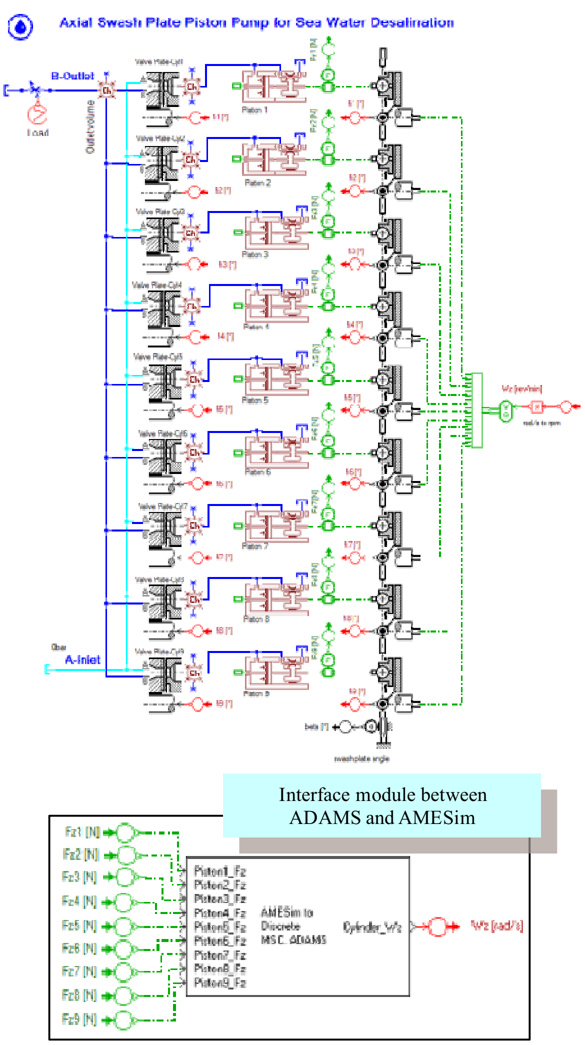

Figure 5 The hydraulic model of the pump in AMESim

From Figure 5, we can see that the pressure at the pump's outlet is due to the variable orifice. The rotation velocity of the cylinder is due to the output of the pump's mechanical model in ADAMS, and the hydraulic force acting on the piston will be calculated and transfer to ADAMS. These data exchanging process is implemented by the interface module in AMESim.

FEM MODEL

In order to analyze the stress and deformation of the main parts such as pistons and main shaft, the rigid bodies of these parts have to be made to be flexible. This work can be implemented by the interface between ADAMS and ANSYS. The models of the parts in Pro/Engineer can seamlessly transfer to ANSYS without geometrical error. After the elements type, materials' properties, tagged point, rigid region and meshing method were set in ANSYS environment, the FEM models of the main parts such as the piston and main shaft would be generated and could be exported as MNF files. In ADAMS environment the rigid bodies of the pistons and main shaft were replaced by these FEM models, and the models of pistons, main shaft were flexible. By this method, the mechanical model of the pump in ADAMS was created as a mixture model with rigid and flexible bodies.
Figure 6 presented the FEM model of the pistons and main shaft in ANSYS. Figure 7 presented the rigid model and the rigid-flexible mixture model in ADAMS respectively.

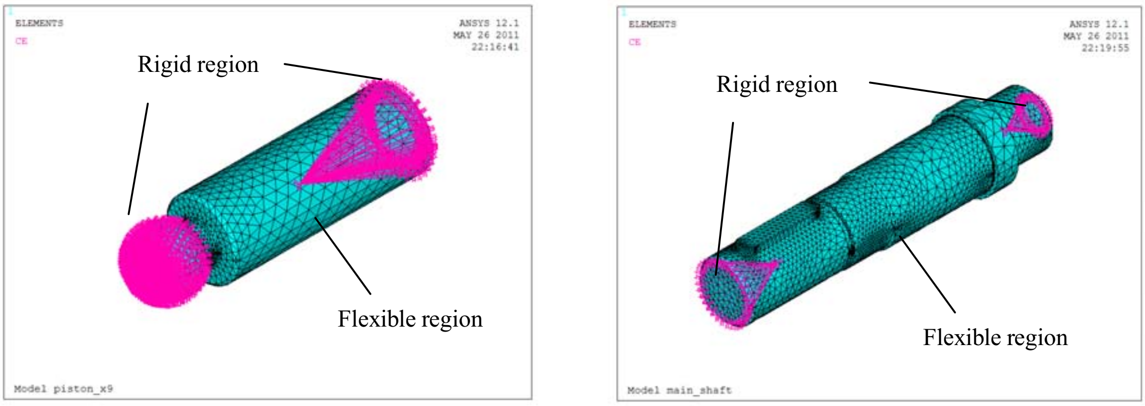

Figure 6 FEM models of the piston and main shaft in ANSYS

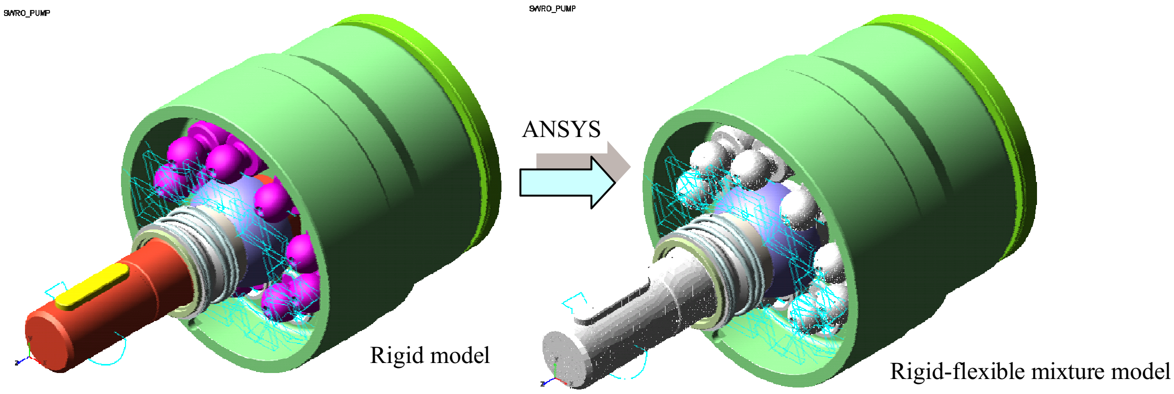

Figure 7 Models of main parts of the pump in ADAMS

CO-SIMULATION RESULTS

The co-simulation model of the pump was run in ADAMS environment with the communication between AMESim. Many simulation results can be acquired.

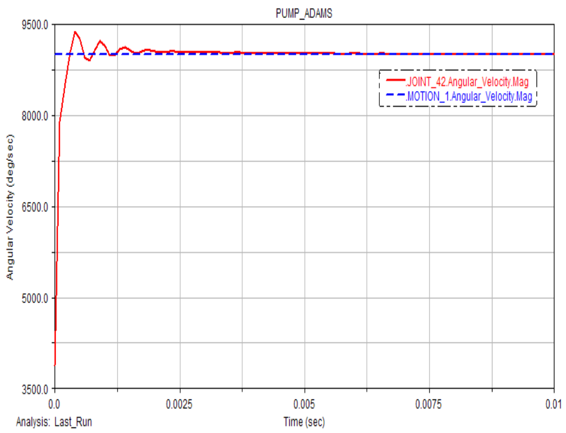

Figure 8 Angular velocities of the cylinder and the motor

Figure 8 presented the curves of angular velocities of the cylinder and the motor. The motor is a idealized driver which can keep a constant angular velocity at 1500rpm. We can see that the angular velocity of the cylinder have an overshoot at the initial time and will be stable after 0.005s. The reason for this phenomenon is that the main shaft model is flexible and its stiffness is finite.

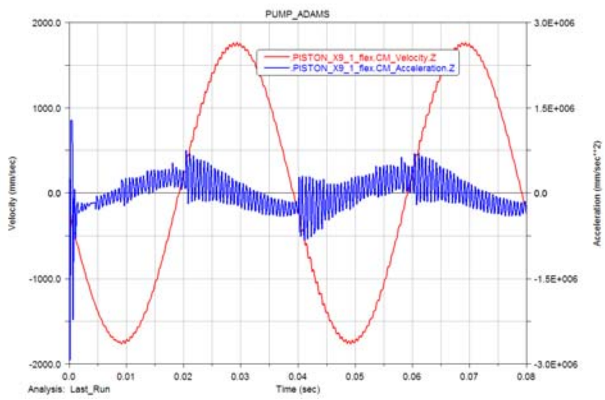

Figure 9 Velocity and acceleration of one piston in *z* direction

Figure 9 showed the velocity and acceleration of the center gravity on one piston in z direction. The piston and main shaft models are flexible, so the kinematic characters are obviously different. The acceleration curve has many high-frequency ripple and the velocity curve is not a strict sinusoid.

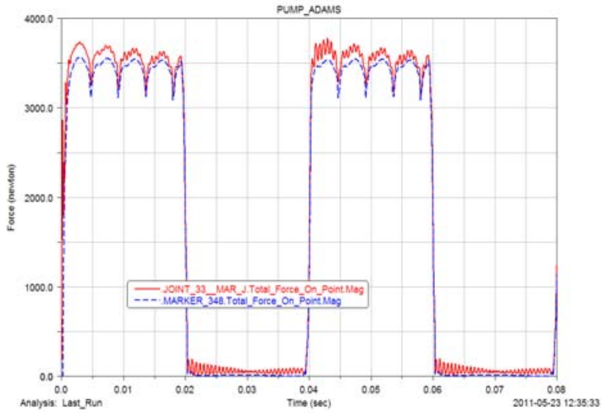

Figure 10 Hydraulic and inertia force in z direction acting on one piston

Figure 10 presented hydraulic and inertia force components in z direction acting on one piston. The red curve represented the sum of hydraulic force and inertia force, and the blue represented the hydraulic force. The inertia force can be omitted when it compared with the hydraulic force.

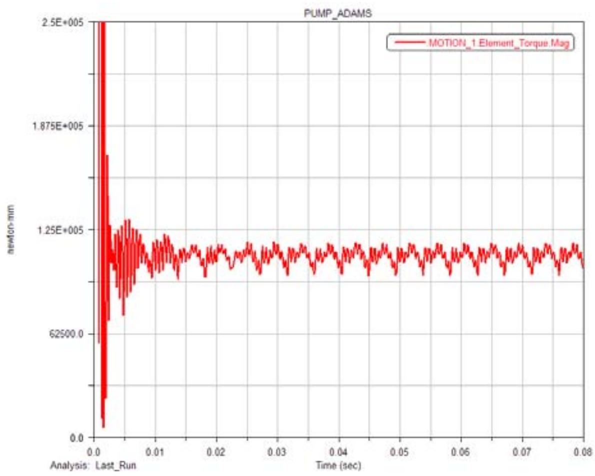

Figure 11 Driving torque on the main shaft

Figure 11 presented driving torque on the main shaft. The initial torque is about 2 order magnitude of the stable driving torque, the reason is that the driving motor is idealized and the main shaft is flexible.

Figure 12 presented the flow rate and pressure at on the outlet of the pump, these curves have similar trend.

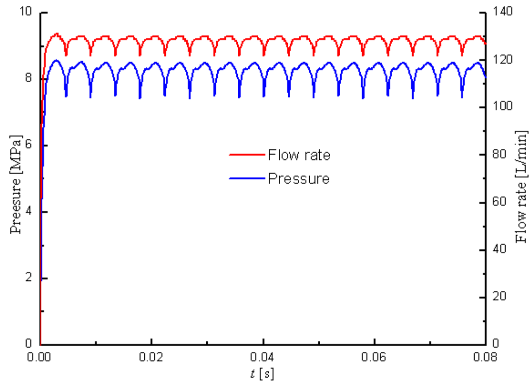

Figure 12 Pressure and flow rate at the outlet

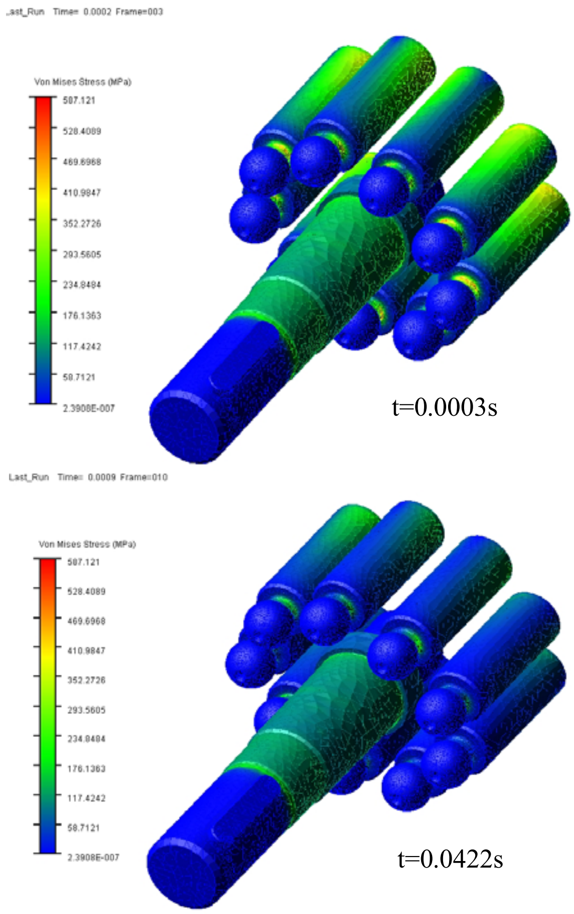

Figure 12 Von Mise stress of the flexile body

Figure 12 presented the Von Mise stress of the flexile body at 0.0003s and 0.0422s. From the simulation results, the maximum Von Mise stress of the piston was occurred at 0.0002s and the value is 587.121 MPa. The maximum Von Mise stress of the main shaft was occurred at t=0.003s and the value is 429.401 MPa. But when the rotation velocity of the pump is stable, the value of maximum stress is sharply decreased. The maximum Von Mise stress of the piston was 209.318 MPa and the danger point was on its neck. The maximum Von Mise stress of the main shaft was only 82.322 MPa.

CONCLUSION

This article illustrated the co-simulation process of an axial piston pump for SWRO. With the mechanical and hydraulic simulation tools such as ADAMS, ANSYS and AMESim, the kinematics and dynamics characters of the pump, stress and strain of critical components, the hydraulic characters such as the flow rate and pressure can were acquired. The results would benefit the improvement and optimal design of the pump.

ACKNOWLEDGEMENT

The authors would like to thank the Ministry of Science and Technology of PRC for the National "Eleventh Five-Year" Technology Support Program (No. 2006BAF01B03-02), the Ministry of Education of PRC for the Program for New Century Excellent Talents in University (No. NCET-06-0529). Both these research projects provide the funding for this work.

REFERENCES

1. Wang S. Seawater Desalination Engineering. Beijing: The press of chemical industry, 2003, pp. 73-74
2. Gao C., Chen G. Handbook of Seawater Desalination Technology and Engineering. Beijing: The press of chemical industry, 2004, pp.131-245
3. http://www.danfoss.com
4. A. Peter, P. Martin. Simulation of a hydraulic variable axial piston double pump of bent axis design with subsystems. The 1st MSC.ADAMS European User Conference, London, November 13−14, 2002, pp. 10-17.
5. M. Deeken, Using modern CAE tools to simulate hydrostatic displacement units. Ölhydraulik und Pneumatik (O+P), 2002, 46. pp. 6-12.
6. H Zhang, L Kasper, K Rich. Development of a virtual prototype of piston pump for hydrostatic transmission. Proceedings of the 6th International Conference on Fluid Power Transmission and Control, Hangzhou, China, April 5-8, 2005. pp. 485−489.
7. Zhang B, Xu B, Xia C, et al. Modeling and simulation on axial piston pump based on virtual prototype technology. Chinese Journal of Mechanical Engineering, 2009,22-1: pp. 84-90.

Proceedings of the 8th JFPS International
Symposium on Fluid Power, OKINAWA 2011
Oct. 25-28, 2011

2C3-1

DESIGN OF SPEED CONTROL SYSTEM OF WATER DRIVEN STAGE

Toshiaki SANO*, Midori NAGASHIMA**, Yohichi NAKAO*, Kenji SUZUKI*

*Department of Mechanical Engineering, Kanagawa University
3-27-1, Rokkakubashi, Kanagawa-ku, Yokohama 045-481-5661, Japan
**KYB Corporation
World Trade Center Bldg., 4-1, Hamamatsu-cho, 2-chome, Minato-ku, Tokyo 105-6111, Japan
(E-mail: nakao@kanagawa-u.ac.jp)

ABSTRACT

The water driven stage is developed for ultra-precision machine tool, especially for machining small parts in size, such as optical mirrors and lenses. The water driven stage is composed of the water hydrostatic bearings and the water hydraulic piston mechanism. In order to finish fine diamond turned surfaces, it is needed to maintain the speed of the stage during machining processes. The speed of the water driven stage can be controlled by the supplied flow rate into the piston-cylinder. In this paper, mathematical models of the water driven stage and the flow control valve are first derived. The derived mathematical models are verified through experiments and calculation. A conventional feedback controller is then designed based on the derived mathematical models. The feedback control system represented by the second-order system is then introduced. Performances of the designed feedback control system are studied through experiments and simulations.

KEYWORD

Precision machine tools, Water hydrostatic bearing, Water hydraulics,
Feedback control system, Single-point diamond turning

NOMENCLATURE

A: area of piston [880 mm^2]
$A_{b1,b2}$: area of piston
$A_{p1,p2}$: area of piston
a: height of piston [8 mm]
b: size of piston [110 mm]
c_c: coefficient of viscous friction due to water viscosity
c_v: coefficient of discharge
D: diameter of valve [1 mm]
e: thickness of plate [3 mm]
F_c: cutting force
$h_{b1\sim4}$: gap of bearing
$h_{p1\sim5}$: gap of piston
K_s: characteristic of water driven stage
k_p: characteristic of pressure-flow rate of valve
k_u: characteristic of voltage-flow rate of valve
K_1: feedback gain
K_2: feedback gain
L: size of piston [8 mm]
M: mass of table [15 kg]
p_c: downstream pressure of valve

p_{c0}: downstream pressure of valve
p_s: supplied pressure of valve
$p_{1,2}$: pressure in cylinder room
q_l: leakage flow rate of cylinder-piston
q_p: supplied water flow rate
R: flow resistance of gap between piston and cylinder
T_c: time constant of the stage
$T_c^{'}$: time constant
u: input voltage of valve
u_0: input voltage of valve
v : speed of stage
v_d: desired speed
x_v: displacement of valve
μ : viscosity of water [1.02×10^{-3} Pa s]
ρ: density of water [0.998×10^3 kg/m^3]

INTRODUCTION

The ultra-precision machine tools are essential for machining precision parts such as various lenses and mirrors. There are increasing demands for improving machining accuracy of the ultra precision machine tools[1]. One of the important components of the machine tools is the stage of the machine tool. For achieving precise machining accuracy, the precise linear motion of the stage is inevitable. Hydrostatic bearings are effective to achieve precise motion of the stage. Therefore, the hydrostatic bearings have been studied and used for the ultra-precision machine tools. In general, the tables supported by hydrostatic oil or air bearings are generally used in the ultra-precision machine tools.

However, the air pressurized bearing has low bearing stiffness due to the compressibility of air. Contrarily, the oil hydrostatic bearings are disadvantage in the positioning accuracy as well as the thermal stability, because of its higher viscosity. Water is the incompressible fluid unlike air, and water has less viscosity than oil. It is thus considered that the water hydrostatic bearing is advantageous in order to design the hydrostatic bearing with higher stiffness, compared to the air pressurized bearing. In addition, low viscosity of water is effective to give precise linear motion and reduce the heat generation compared to the oil hydrostatic bearings. The machine tool stage with water hydrostatic bearings have thus been reported[2],[3]. These machine tools used a liner-motor[2] or belt driven mechanism[3]. In contrast, we developed the water driven stage[4] that is composed of the water hydrostatic bearings and a water hydraulic piston and cylinder. Because of the piston cylinder designed in the moving table, we could successfully design the stage so that the driving force can act at the center of gravity of the moving table.

The water driven stage was developed for ultra-precision machine tool. In this case, the speed of the stage must be controlled in order to obtaining fine finishing surfaces. In general, in the ultra-precision machining by a single-point diamond cutting tool, it is noted that the feed rate is quite low and it is about 10-20 μm/rev[5]. Thus, the paper deals with the design of speed control system for the water driven stage. In this paper, the mathematical model of the water driven stage is first derived. A conventional PI controller is then designed based on the derived mathematical model. Performance of the designed feedback control system is studied through experiments and simulations.

WATER DRIVEN STAGE

The structure of water driven stage[4] is shown in Fig. 1. The guide-way of the water driven stage is fixed on the base, consequently the table of the stage is moved by the driving forces generated by the pressure difference of the piston and cylinder. It should be mentioned that the piston has a rectangular shape as shown in Fig. 2. A feature of the stage is that the hydraulic piston and cylinder is fabricated inside a moving table of the stage. Because of the structure of the stage, no additional components, such as an electric motor and a ball screw, are needed. In general, the additional components degrade the linear motion accuracy of stage. Another feature of the stage is that the stage has a symmetrical structure. Particularly, the pressures in the upper and bottom cylinder rooms can be cancelled because both cylinder rooms are connected by vertically fabricated flow channel in the guide-way. Accordingly, the driving force acts on the center of gravity of the moving table as illustrated in Fig. 3, minimizing undesirable pitching and yawing motions. It is therefore expected that the water driven stage achieves precise straightness motion.

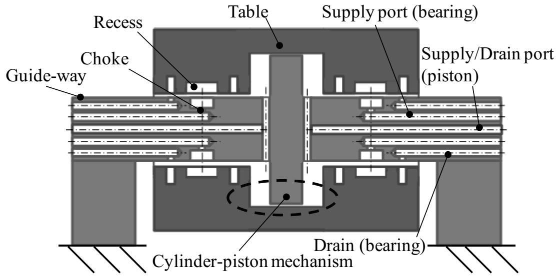

Fig. 1 Schematic drawing of water driven stage

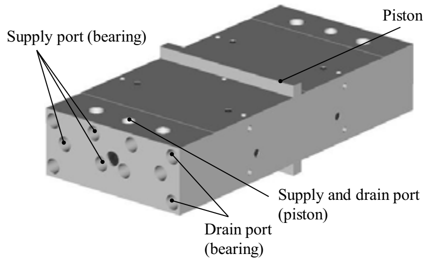

Fig. 2 3D model of guide-way of water driven stage

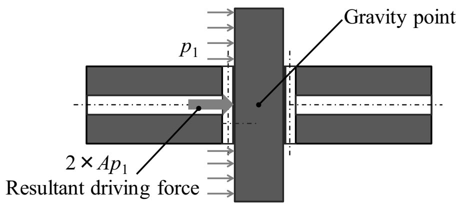

Fig. 3 Resultant driving force

MODEL OF WATER DRIVEN STAGE

The equation of motion of the water driven stage is given by Eq. (1).

$$M\frac{dv}{dt}+c_c v = A(p_1-p_2)-F_c \tag{1}$$

The relationship between the pressure difference and the leakage flow rate of the piston and cylinder is given by Eq. (2).

$$p_1-p_2 = q_l \bullet R \tag{2}$$

It is considered that the compressibility of water in the stage is negligibly small. Thus, the continuity equation gives the speed of table and the flow rate as Eq. (3).

$$Av = q_p - q_l \tag{3}$$

By substituting Eq. (2) and Eq. (3) into Eq. (1), the equation of motion of the stage can be given by Eq. (4).

$$T_c\frac{dv}{dt}+v=\frac{AR}{c_c+A^2R}q_p-\frac{F_c}{c_c+A^2R} \tag{4}$$

In Eq. (4), the time constant of the stage is given by Eq. (5).

$$T_c=\frac{M}{c_c+A^2R} \tag{5}$$

In Eq. (1) ~ Eq. (5), the flow resistance, R, of the gaps between the piston and cylinder is given by Eq. (6).

$$R=\frac{12\mu L}{b\left(h_{p1}^3+h_{p2}^3\right)+2a\left(h_{p3}^3+h_{p4}^3\right)+4eh_{p5}^3} \tag{6}$$

The coefficient of viscous friction due to water viscosity is given by Eq. (7).

$$c_c=\mu\left\{\left(\frac{1}{h_{p1}}+\frac{1}{h_{p2}}\right)A_{p1}+\left(\frac{1}{h_{p3}}+\frac{1}{h_{p4}}\right)A_{p2}\right.$$
$$\left.+4\left(\frac{1}{h_{b1}}+\frac{1}{h_{b2}}\right)A_{b1}+2\left(\frac{1}{h_{b3}}+\frac{1}{h_{b4}}\right)A_{b2}\right\} \tag{7}$$

EXPERIMENTAL SETUP

An experimental set up of the water driven stage is shown in Fig. 4. As shown in Fig. 4, the speed of the stage is measured by a laser interferometer with 0.6 μm resolutions. The signal of the sensor is fed into a PC. Proportional flow control valves, described later, are used to control the flow rate in the designed feedback control system. The proportional control valve is controlled by input voltage by the PC. The temperature of water is controlled by a temperature control unit that connected to the water tank. The temperature during experiments was controlled to be 20 – 21 degrees Celsius.

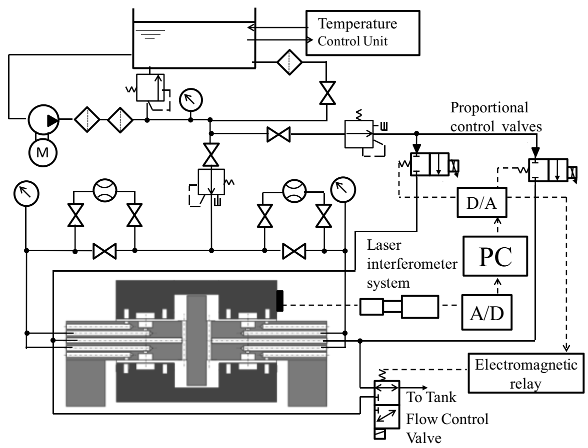

Fig. 4 Structure of control system of water driven stage

SPEED OF WATER DRIVEN STAGE

The supplied flow rate into the water driven stage can control the speed of stage, as represented by Eq. (4). The displacenment of the stage was studied through experiments and calculation for various flow rate from 20 mL/min to 50 mL/min, as shown in Fig. 5. In addition, the relationship between the speed of stage and the supplied flow rate is shown in Fig. 6.

The displacements obtained by the derived mathematical model agree with the experimental results until 15 seconds. It is however observed that the speed obviously changed afterward, due to slight difference of the gap between the table and other factors. This implies that a feedback control mechanism should be added to maintain the speed of stage.

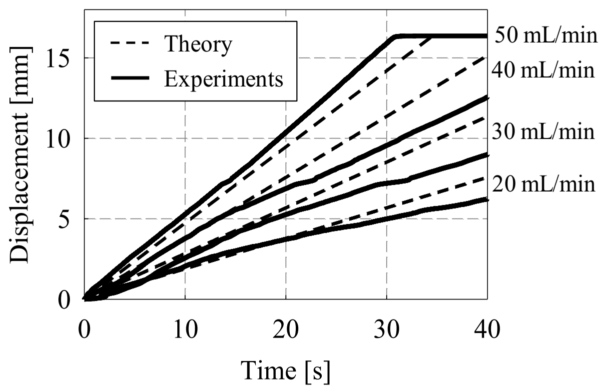

Fig. 5 Stage displacement vs. time

Figure 6 represents the speed of the stage for various supply flow rate from 20 mL/min to 100 mL/min. It is clearly observed that measured speed in the lower flow rate less than 40 mL/min becomes lower than the calculations. This is mainly due to a difficulty of controlling lower flow rate. In addition, geometrical errors of the gap between the cylinder and piston affect the speed of table. It is however verified that the table speed calculated by the derived mathematical model has a same tendency with the experimental results.

In general, the feed rate is about several tens micrometer per revolution of the spindle in the single-point diamond turning. If the rotational speed of the spindle is 3,000 min^{-1}, the required speeds of stage become about 1.0 mm/s. Thus the required speed for the diamond turning can be obtained by supplying water of several tens milliliter per minutes.

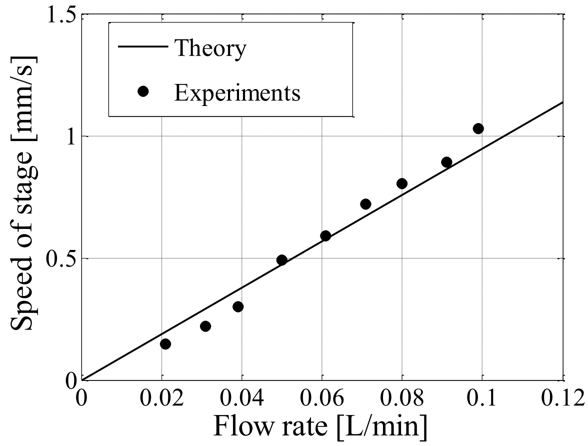

Fig. 6 Speed of stage vs. flow rate

SPEED CONTROL SYSTEM OF WATER DRIVEN STAGE

In order to control the flow rate into the water driven stage, proportional flow control valves were used in this study, a structure of the valve is illustrated in Fig. 7. The proportional control valve is a solenoid flow control valve. The orifice diameter of valve is 1 mm, and the valve-opening area is 0.33 mm^2. The rated flow rate is 0.55 L/min at the input voltage of the valve is 10 V. For designing a feedback control system, the pressure-flow characteristic of the valve given by Eq. (8) is linearized as Eq. (9).

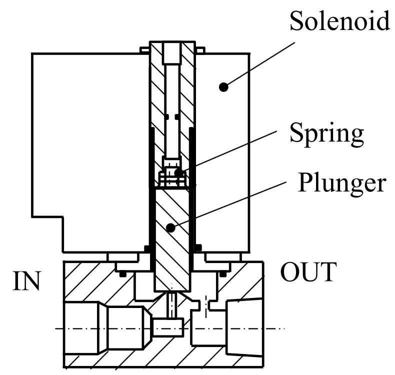

Fig. 7 Structure of proportional control valve

$$q_p = c_v \pi D x_v \sqrt{\frac{2(p_s - p_c)}{\rho}} \tag{8}$$

$$q_p = k_u u - k_p p_c \tag{9}$$

In Eq. (8) and Eq. (9), the coefficients k_u and k_p are given by Eq. (10) and Eq. (11), respectively.

$$k_u = k_v \sqrt{\frac{2(p_s - p_{c0})}{\rho}} \tag{10}$$

$$k_p = \frac{k_v u_0}{\sqrt{2\rho(p_s - p_{c0})}} \tag{11}$$

EXPERIMENTS

Leakage flow rate

As represented in Eq. (4), the resistance, R, affect the speed of the stage. Thus, we measured the flow resistance of the gap between the piston and cylinder. Figure 8 represents the leakage flow rate of the gap between the cylinder and piston. The flow resistance of the gap between the piston and cylinder is the reciprocal of the slope of the relationship between leakage flow rate and pressure difference. In the experiment, the flow resistance is 2.63×10^9 Pa s/m. In the calculation, it becomes 1.86×10^9 Pa s/m if the gap sizes are 40 μm and 43 μm as designed. However, the exact control of the gap in assemble process of the stage is quite difficult. For instance, if the gap sizes are assumed to be 10% smaller than that of the designed sizes, the calculated flow resistance agree with the experimental result, as shown in Fig. 8.

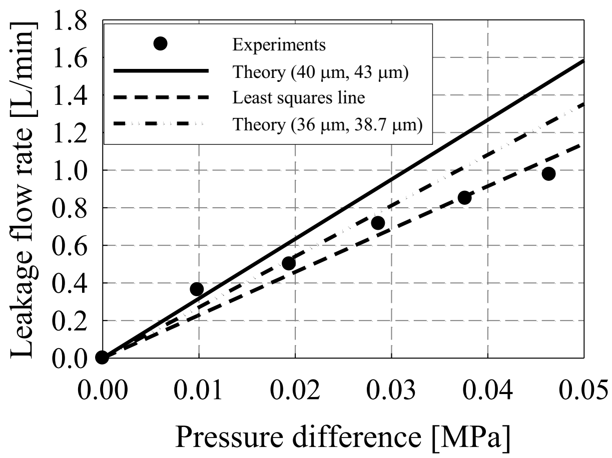

Fig. 8 Leakage flow rate vs. pressure difference

Step response of water driven stage

The step response of water driven stage is shown in Fig. 9. The input voltage of the control valve was changed at 15 s. As a result, the time constant of stage was measured approximately to be 0.5 s.

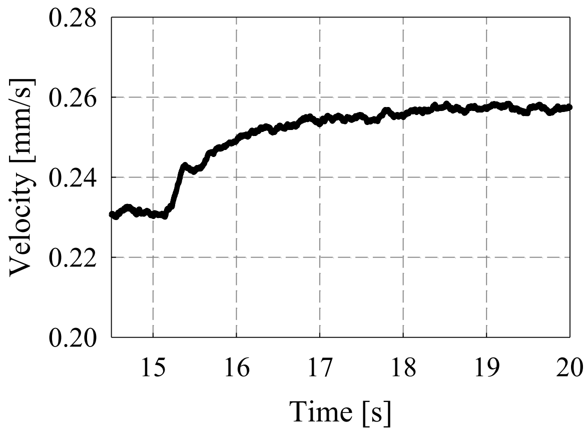

Fig. 9 Step response of water driven stage

Flow control valve

The characteristics of the proportional control valve k_u and k_p in Eq. (9), are experimentally determined. The relationship between the input voltage of the proportional control valve and the flow rate is shown in Fig. 10, then we verified that k_u=2.11×10^{-7} m^3/sV. In addition, the relationship between the downstream pressure of the proportional control valve and the flow rate is shown in Fig. 11, accordingly k_p=4.33×10^{-12} m^5/sN is obtained.

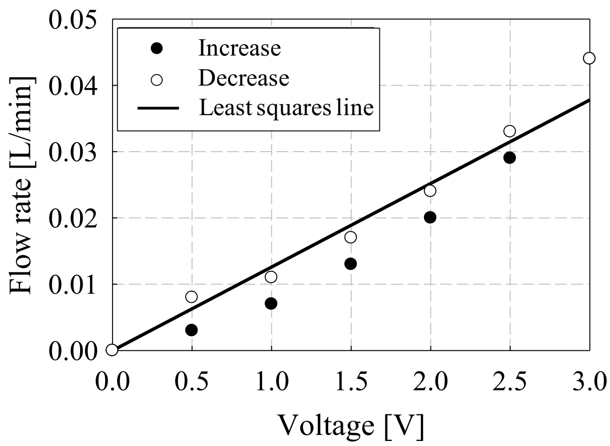

Fig. 10 Flow rate vs. voltage

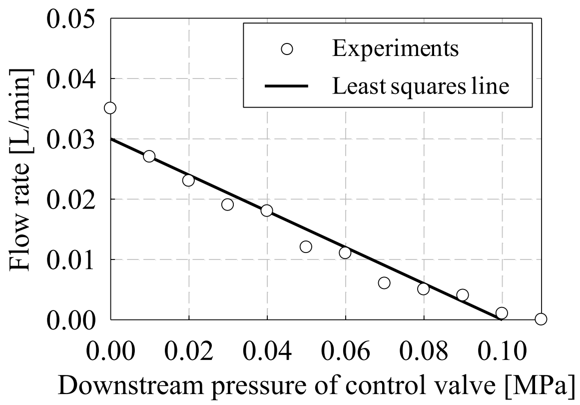

Fig. 11 Flow rate vs. downstream pressure of control valve

DESIGNED FEEDBACK CONTROL SYSTEM

As shown in Fig. (4), for the controlling the speed of stage, the speed of stage is first measured by the laser interferometer, then the signal is fed into the PC. The block diagram of the open loop control system of the water driven stage is given in Fig. 12.

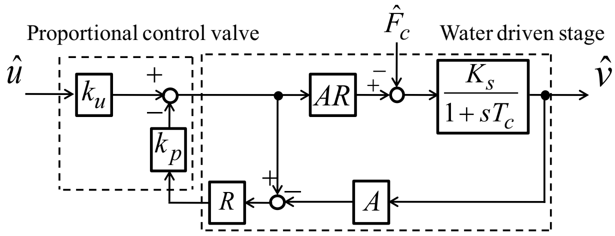

Fig. 12 Open loop system of water driven stage

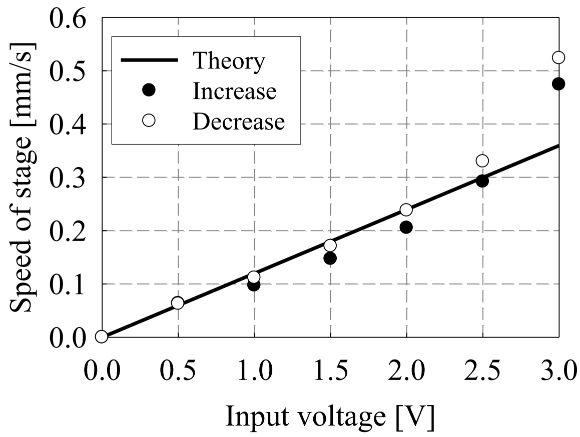

Fig. 13 Speed of stage vs. input voltage

The characteristic of the open loop control system was obtained as shown in Fig. 13.The result shows that the calculated speed of the stage good agreed with experimental result if the input voltage was less than 2.5 V. The required speed of the stage for diamond turning is about 0.3 mm/s as described. In the low speed ranges, the derived mathematical model is capable of predicting the speed of the stage.

The feedback control system of the water driven stage is thus designed based on the derived mathematical models. A feedback control system was designed so that the zero steady state error can be achieved in the step response.

As shown in Fig. 12, no integrator is included in the open loop control system. Accordingly, a feedback controller with an integrator must be designed so that no steady state error can be made as shown in Fig. 14. The transfer function of the feedback control system is represented by Eq. (12). The damping coefficient and the natural frequency are given by Eq. (13) and Eq. (14), respectively.

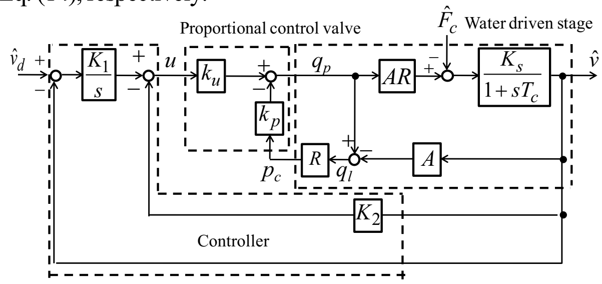

Fig. 14 Feedback control system

$$G_c(s) = \frac{1}{1 + 2\zeta \frac{s}{\omega_n} + \frac{s^2}{\omega_n^2}} \tag{12}$$

$$\omega_n = \sqrt{\frac{K_1 K}{T_c'}} \tag{13}$$

$$\zeta = \frac{1}{2} \frac{1 + K_2 K}{\sqrt{K_1 K T_c'}} \tag{14}$$

In Eq. (13) and Eq. (14), K and $T_c^{'}$ is described by Eq. (15) and Eq. (16), respectively.

$$K = \frac{k_u A}{A^2 + c k_p + c/R} \tag{15}$$

$$T_c' = \frac{T_c}{\dfrac{1 + k_p R - k_p K_s (AR)^2}{1 + k_p R}} \tag{16}$$

The feedback gains K_1 and K_2 can accordingly be determined so that the desired control performance can be obtained by designating appropriate ω_n and ζ in Eq. (13) and Eq. (14).

FEEDBACK CONTROL SYSTEM

Figures 15 and 16 represent the performance of the designed feedback control system of the water driven stage. In the experiments, the damping coefficient and the natural frequency were specified as 3.5 rad/s and 0.8, respectively. For comparison, a response of the open loop control system is also represented in Fig. 15. In this case, it can be observed that the open loop control system control not maintain the constant speed. In contrast, the designed feedback controller achieved the constant speed of the stage.

In addition, a transient response of the feedback control system was also investigated as shown in Fig. 16.

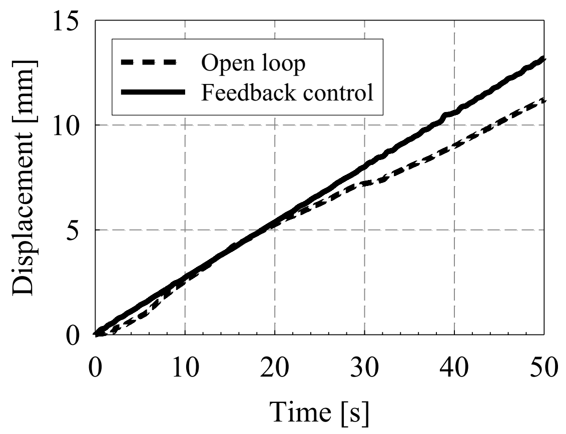

Fig. 15 Displacement vs. time

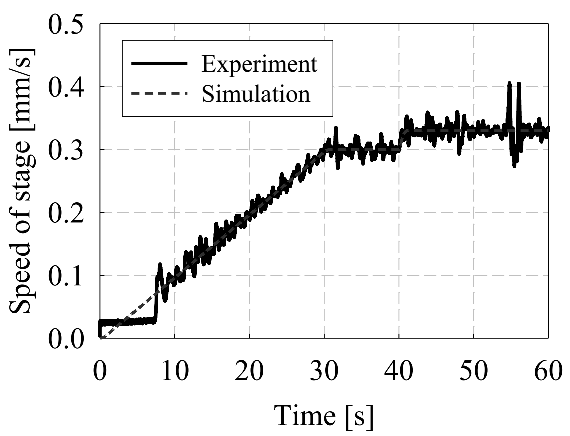

Fig. 16 Speed of stage vs. time

The experiment of the speed of the stage has the fluctuation in its speed, with the frequency of 1 Hz, due to an experimental environment. However, the speed of the stage can follow the designed signal. In addition, the small steady state error of 0.002 mm/s was obtained.

CONCLUSIONS

In the present paper, a speed control of the water driven stage was discussed. Mathematical model of the water driven stage was derived, together with that of a flow control valve. Predicted performance of the open loop control system using the derived mathematical model was then compared with experimental results, showing validity of the derived model. Based on the derived mathematical model, a conventional PI control system was introduced for the water driven stage. Performances of the feedback control system were tested through simulations and experiments. The results indicated that the designed feedback control system achieved zero steady state error. The designed feedback control will be tested for the actual diamond turning experiments.

This research work is financially supported by the Grant-in-Aid for Scientific Research (C) of the Japan Society for the Promotion of Science.

REFERENCES

1. TANIGUCHI, N., Construction and Idea of Nanotechnology, The Japan Society for Precision Engineering, Vol. 56, No. 3, 1990, pp. 427-431, (in Japanese).
2. YUI, A., et al., Development of a Linear-Motor-Driven Table with Hydrostatic Water Bearing, Transaction of Japan Society of Mechanical Engineers(C), No.752, 2009, pp. 364-370, (in Japanese).
3. KUSUI Naoki, et al., A Study on Linear Motion Stage Using Water-hydrostatic Bearing, Transaction of Japan Society of Precision Engineering, Vol.65, No. 8, 1999, pp.1153-1157 (in Japanese).
4. NAKAO, Y., and KAWAKAMI, M., Design of water driven stage, Proceedings of 9th International Conference of the European Society for Precision Engineering and Nanotechnology, Vol. 1, 2009, pp. 200-203.
5. SHAMOTO, E., and MORIWAKI, T., Ultraprecision Diamond Cutting of Hardened Steel be Applying Elliptical Vibration Cutting, Annals of the CIRP, Vol. 48, 1999, pp. 441-444.

Proceedings of the 8th JFPS International
Symposium on Fluid Power, OKINAWA 2011
Oct. 25-28, 2011

2C3-2

SENSITIVITY ANALYSIS OF DATA ANALYSIS PROCESS IN HYDRAULIC FORKLIFT

Tomi KROGERUS, Markus ROKALA and Kari T. KOSKINEN

Department of Intelligent Hydraulics and Automation
Tampere University of Technology
P.O.Box 589, FIN-33101, Tampere, Finland
(E-mail: tomi.krogerus@tut.fi)

ABSTRACT

The goal of this paper is to study the sensitivity of data analysis process in hydraulic forklift. Based on earlier studies of forklift, it was noticed that there were changes between different instances of use. Therefore, a simulation model of the lifting movement of the forklift was made because it is stable between different instances of use and the repeatability of the tests is good. The simulation model was verified with measurements from the forklift with two different loading conditions. After that it was driven to obtain 10 sequences from each state that were used in training and testing of the data analysis methods. The Self-Organizing Maps (SOM) with unsupervised learning was used to classify measurement data. Before classification feature extraction using wavelet analysis is performed to extract relevant and discriminating information from the measurement data and to reduce data dimensionality. The extracted features are then used for training and testing the SOM.

KEYWORDS

Data analysis, Sensitivity analysis, Hydraulic systems, Water hydraulics, Forklift

NOMENCLATURE

F	:	Force [N]
f_{max}	:	Bandwidth [rad/s]
K_{leak}	:	Flow gain [-]
p	:	Pressure [Pa]
p_A	:	Pressure in actuator port A [Pa]
p_B	:	Pressure in actuator port B [Pa]
p_S	:	Supply pressure [Pa]
p_T	:	Tank pressure [Pa]
Q	:	Flow rate [l/min]
Q_A	:	Flow rate in A line [l/min]
Q_B	:	Flow rate in B line [l/min]
Q_i	:	Internal leakage of cylinder [l/min]
Q_T	:	Tank flow [l/min]
t_c	:	Correlation time [s]
u	:	Control signal in simulation model [-]
x	:	Position [m]

INTRODUCTION

Analysis of hydraulic systems is based on the measured variables from these systems. These variables are measured in various operating and loading conditions.

Changes of operating conditions are common in hydraulic systems. In addition, the loading conditions change frequently, for example in mobile machine systems. The generalization capability of the data analysis process is important if only some of the operating conditions and/or loading conditions are used in the training phase. Also in the case of a fault situation, fault levels that are between the trained ones should be detected as the closest fault level.
Analysis of hydraulic systems consists of several phases between physical inputs and the final decision about the state of the system. This process [1] is shown in Figure 1. A sensor measures a physical quantity and converts it into a signal which can be read by an observer or by an instrument. A feature extractor extracts features from the measurement data which are then used in classification. After this a classifier uses extracted features to assign sensed inputs to a category. Finally, a post processor uses the output of the classifier to make a decision about the state of the system and it can also decide what actions to take. In this study the focus is on feature extraction and classification parts, including the post processed state of the system.

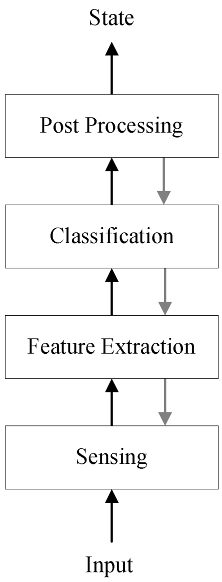

Figure 1 Process of data analysis [1].

Failure mechanisms and different condition monitoring techniques to detect emerging fault situations of hydraulic components and systems have been widely studied, and lots of various condition monitoring methods have been developed and tested with different systems. But only few of these studies consider the sensitivity of the methods to the changes of operating and loading conditions [2, 3].
A forklift, reach stacker [4], has been used in a previous study [5] as a research platform to study the operation of the data analysis process. The oil hydraulic components from the work hydraulics of the forklift have been replaced with water hydraulic ones [6]. The test platform is shown in Figure 2 and its hydraulic circuit of work hydraulics in Figure 3.

Figure 2 Used research platform (forklift).

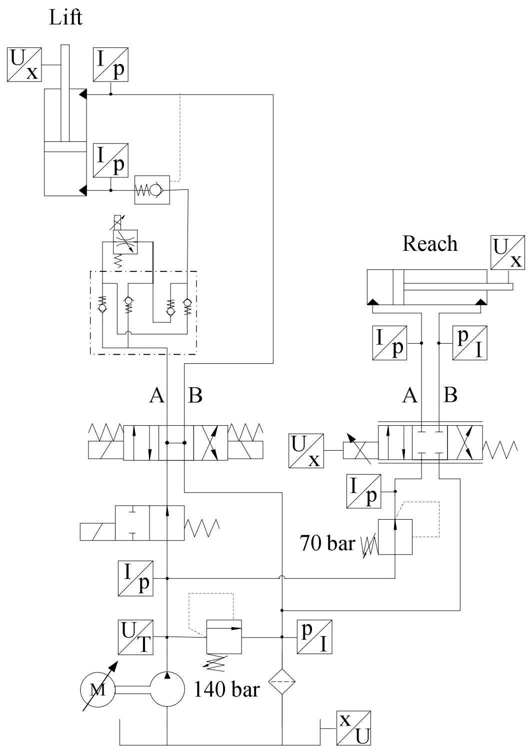

Figure 3 Hydraulic circuit of work hydraulics of forklift.

Based on earlier studies of forklift, it was noticed that there were changes between different instances of use. Therefore, a simulation model of the lifting movement of the forklift, based on physics equations, was made

because it is stable between different instances of use and the repeatability of the tests is good. By means of this model the effects of changes in the loading and operating conditions on the performance of the data analysis methods were studied. Using this simulation model data were generated which were then used in training and testing of the data analysis methods. The Self-Organizing Maps (SOM) with unsupervised learning was used to classify measurement data. Before classification feature extraction using wavelet analysis was performed.
In this study Matlab Simulink [7] was used for the simulation, the SOM Toolbox [8] was used to create and use the neural network and Mathworks' Wavelet Toolbox [7] was used in wavelet analysis.

SIMULATION MODEL OF THE LIFTING MOVEMENT

The simulation model of the working hydraulics of the forklift is a tool used to describe the behavior of the hydraulic system so accurately that a reliable sensitivity analysis could be made. The basic structure of the simulation model and the signal connections between the components are shown in Figure 4.

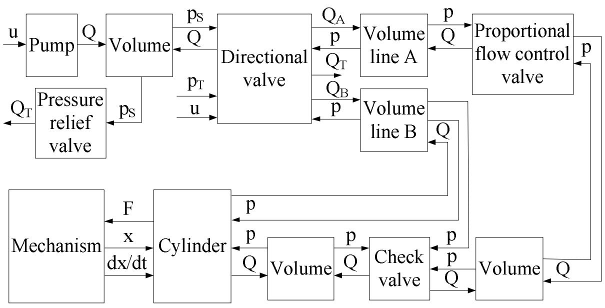

Figure 4 Structure of simulation model of lifting movement of forklift.

The control signal of the pump and valves in the simulation model was taken from the actual tests. The hydraulic pump of the system is a fixed displacement pump. The flow rate of the pump is generated by the rotational speed of the electric motor multiplied by the theoretical displacement of the pump. The losses were taken into account by the function of pressure difference over the pump. The dynamics of the pump are defined with the control signal and the measured supply pressure signal. The pressure relief valve was simply modeled as a table without the dynamics of the valve. The flow through the valve depends on the supply pressure of the system.
The 4/3-directional valve of the system is an on/off-valve. Pressure difference versus flow over every direction of the flow was measured in a test rig and those values were used in modeling the orifices. The dynamics of the valve were taken into account by adding a delay and limiting the maximum opening speed. The check valves in the Wheatstone bridge, shown in Figure 3, were taken into account only as a pressure drop. The flow control valve was modeled as an orifice, which opening was controlled with the control signal. The dynamics of the opening and closing situations were also modeled. The pilot operated check valve was used to hold the load in place when the lifting movement is not operated because the 4/3-on/off valve has an open center position and the flow control valve is not leak-proof. The pilot operated check valve was modeled as an orifice, the flow area of which was dependent on the pressures. The dynamics of the pilot operated check valve were also modeled.
The lifting cylinder was modeled with two volumes, whose pressure and area difference generates the force. The cylinder ends were modeled with stiff springs and the friction of the cylinder is dynamic. Hoses and tubes were taken into account as volumes which generate the pressure. The mechanism of the lifting was modeled with a simple mass model. The mass of the mechanism, added mass, effect of the mechanism and the roller friction curve were taken into account to generate the force to the lifting cylinder.
The modeling of the components was really challenging because the behavior varied between test runs. Especially the behavior of the flow control valve was inconsistent and the variation was quite significant with small openings. Also the flow of the pump was slightly different between tests.
Pressure dependent laminar flow was used to model the leakage in the cylinder to study the fault level changes in the data analysis process, see Eq. 1. In the rest of the flows a combined laminar and turbulent flow model was used [9].

$$Q_i = K_{leak}\,(p_A - p_B) \qquad (1)$$

After verification, measurement noise was added to the simulated pressure signals A and B, which were used in the data analysis. White noise was used to simulate the measurement noise. The effect of the white noise was simulated by using a random sequence with a correlation time much smaller than the shortest time constant of the system. The correlation time was calculated according Eq. 2, where f_{max} is the bandwidth of the system. The amplitude of the noise was estimated from the measurements. [7]

$$t_c = 1/100 \cdot 2\pi / f_{max} \qquad (2)$$

The model was verified with supply pressure, cylinder chamber pressures, pressure between directional valve and Wheatstone bridge connection, and position and velocity of the cylinder. Verification process is described in [10].

SIMULATED DATA USED IN THE SENSITIVITY ANALYSIS

The simulation model was used to acquire data that is then used in the sensitivity analysis. Example of the used control signal of the driven sequence and the position of the cylinder, when there is no added load and no leakage, are shown in Figure 5.

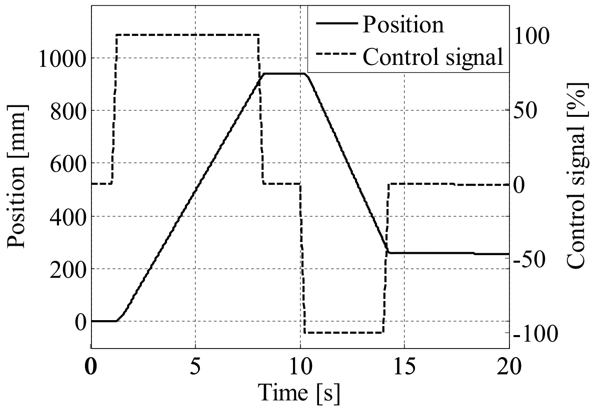

Figure 5 Example of cylinder position and control signal from extending and retracting strokes.

The simulation model was driven to obtain 10 sequences for training and 10 sequences for testing from each state that were used in training and testing. Table 1 and 2 shows the levels of fault and load which are used to study the effect of fault level change and different loading conditions. When the effect of the changes in the fault level was studied, data from the normal situation was used in training on the first level. The fault levels that were used in training or testing are marked with X in the table.

Table 1 Levels of fault and their use in data analysis process.

Level	Fault	Training		Testing	
		1st	2nd	1st	2nd
1	Leakage 0.50 l/min	-	X	X	X
2	Leakage 0.75 l/min	-	-	X	X
3	Leakage 1.00 l/min	-	X	X	X
4	Leakage 1.50 l/min	-	-	X	X
5	Leakage 2.00 l/min	-	X	X	X

Table 2 Levels of loading conditions and their use in data analysis process.

Level	Load	Training	Testing
		1st	1st
1	0 kg	X	X
2	250 kg	-	X
3	500 kg	X	X
4	750 kg	-	X
5	1000 kg	X	X

The variables used in the data analysis were pressures A and B from the actuator ports. The measurement frequency with the pressure measurements was 100 Hz. Figures 6 and 7 show examples of the pressure signals in the case of simulated leakages, and Figures 8 and 9 in the case of different loading conditions. Pressure signals are composed of 50 points of the beginning of pressure A, 50 points of pressure A after the control signal of the lifting movement has been cut off, 50 points of the beginning of pressure B and 50 points of pressure B after the control signal of the lifting movement has been cut off.

Before classification, level 2 discrete wavelet analysis was used in extracting approximation coefficients in the case of the pressure signal. The extending and retracting strokes were processed separately. The parts of the pressure signals A and B were first merged, resulting in a signal of 200 points. Then 52 coefficients were extracted from the merged signal. Therefore, a training vector consists of 52 values.

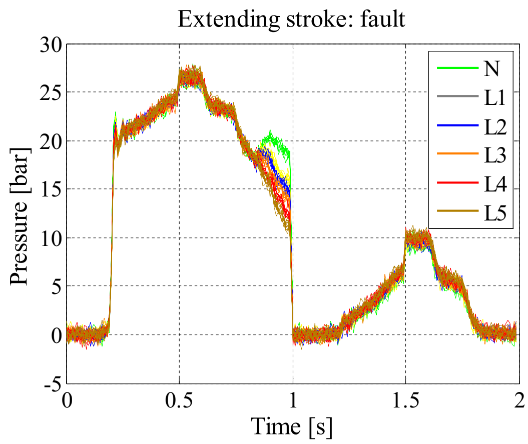

Figure 6 Examples of measured pressures A and B from extending strokes in normal and different fault levels. N is normal and L1 to L5 are different fault levels.

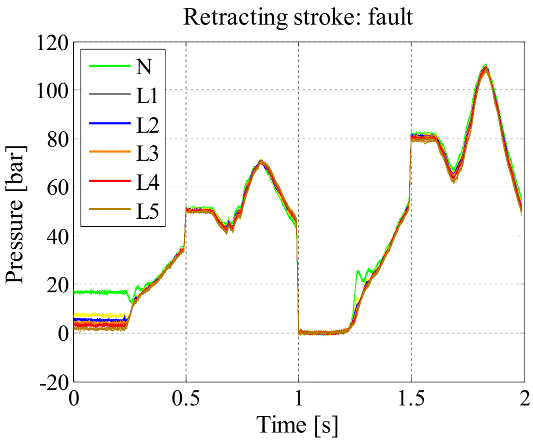

Figure 7 Examples of measured pressures A and B from retracting strokes in normal and different fault levels, N is normal and L1 to L5 are different fault levels.

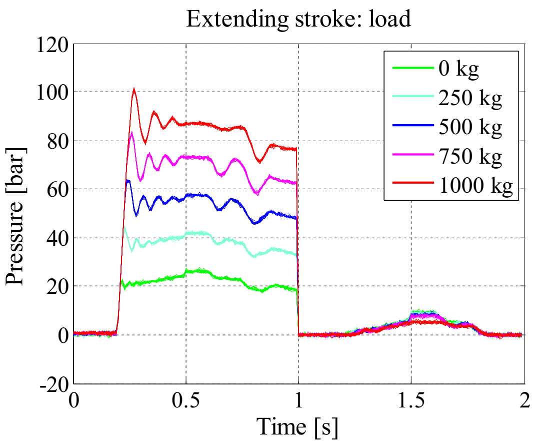

Figure 8 Examples of measured pressures A and B from extending strokes in different loading conditions.

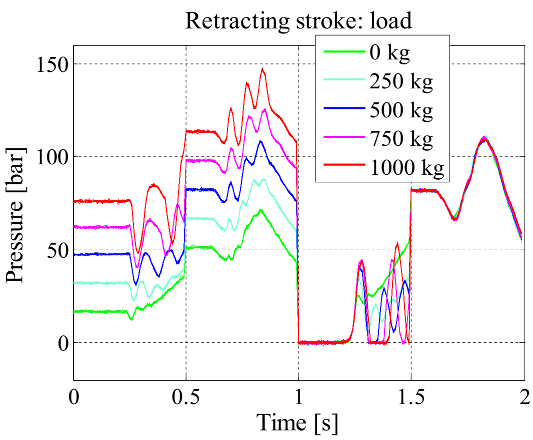

Figure 9 Examples of measured pressures A and B from retracting strokes in different loading conditions.

CLASSIFICATION RESULTS OF THE SENSITIVITY ANALYSIS

The Self-Organizing Map (SOM) with unsupervised learning is used to classify measurement data. On the first level, the so called fault-detection map is used and the fault detection is based on the quantization error method. The categorization method is used on the second level to define specific faults and their levels. Classification process is described more detailed in [5, 10].

Two different cases were studied. In the first one, leakage levels L1, L3 and L5 are used in the training and levels L1 to L5 are used in the testing. The levels were determined by the maximum leakage during the driven sequence and were the following: 0.5, 0.75, 1.0, 1.5 and 2.0 l/min. Levels L2 and L4 were studied in terms of how well they are classified as a normal or fault state on the first level of the SOM and how well they were classified as the closest possible fault level on the second level of the SOM. In the second one, loading levels, 0 kg, 500 kg and 1000 kg, were used in the training and in the testing it was studied whether untrained levels, 250 kg and 750 kg, are classified as normal states on the first level of the SOM. It was also tested whether the distance between the best-matching unit (BMU) and the vectors from different normal loading conditions were smaller than the distance between the BMU and the vectors from fault situations.

Effect of Changes in Fault Level

On the first level, two different maps were trained. One was for extending strokes and the other one for retracting strokes. The number of map units on the first level is 4 x 4 in both maps. Figures 10 and 11 show the distances between the BMUs and the testing vectors. In the extending stroke the threshold was set to 1.9 so that all the normal state sequences were classified correctly. This, however, results in few sequences of the smallest fault level being classified as normal. The distance clearly increases when the fault level gets higher. In the retracting stroke the difference between the normal and fault situation was clear. However, the differences between the fault levels were very small. Table 3 shows the quality of the state recognition on the first level. 94 % of the sequences are classified correctly in the extending stroke if the threshold is set to 1.9. Respectively, in the retracting stroke 100 % of the sequences are correct if the threshold is set to 2.5.

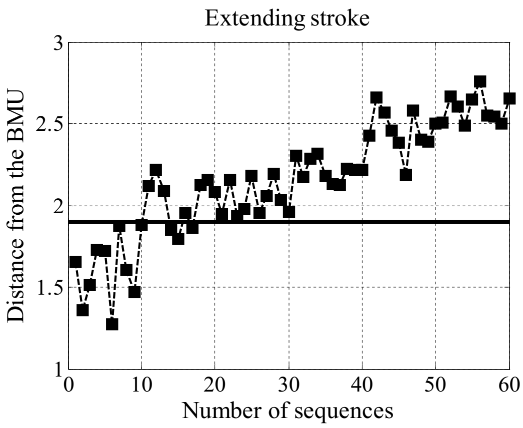

Figure 10 BMU distances from extending strokes. Sequences are in order normal, fault levels 1, 2, 3, 4, 5.

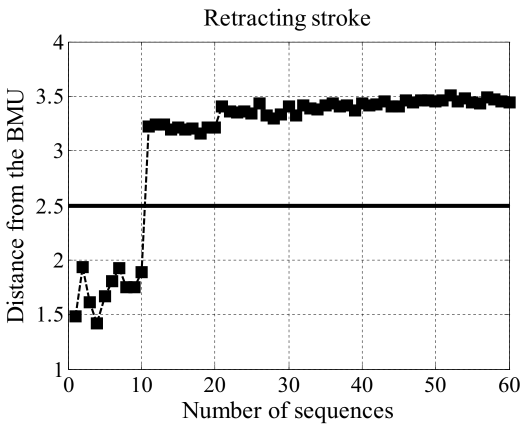

Figure 11 BMU distances from retracting strokes. Sequences are in order normal, fault levels 1, 2, 3, 4, 5.

Table 3 Quality of state recognition on the first level in case of extending and retracting strokes. N is normal, ND is not defined and L1 to L5 are different leakage levels of cylinder. Dark grey areas are classified correctly.

	Detected state of the system			
	Extending		Retracting	
State	N	ND	N	ND
N	10	0	10	0
L1	3	7	0	10
L2	0	10	0	10
L3	0	10	0	10
L4	0	10	0	10
L5	0	10	0	10

On the second level, the number of map units in extending stroke is 2 x 5 and in retracting stroke 3 x 3. Table 4 shows the results of the quality of the state recognition on the second level. The levels that are not used in training are better classified, as the closest fault level, in the extending stroke. In the retracting stroke about half of the sequences that are not used in training are correctly classified and half of those are classified as a not defined fault level (NDFL). 90 % of the sequences in the extending strokes are classified correctly with fault levels that are used in training and 90 % of the sequences are classified as the closest fault level with fault levels that are not used in training. Respectively, in the retracting stroke 100 % of the sequences are correct in the case of the fault levels that are used in training and 55 % of the sequences are classified as the closest fault level in the case of fault levels that are not used in training.

Table 4 Quality of state recognition on the second level in case of extending and retracting strokes. N is normal, L1 to L5 are different leakage levels of cylinder and NDFL is not defined fault level. Dark grey areas are correct states. Light grey areas are closest correct states.

	Identified state of the system							
	Extending				Retracting			
State	L1	L3	L5	NDFL	L1	L3	L5	NDFL
L1	7	3	0	0	10	0	0	0
L2	5	5	0	0	2	3	0	5
L3	0	10	0	0	0	10	0	0
L4	0	4	4	2	0	3	3	4
L5	0	0	10	0	0	0	10	0

Figure 12 shows the distribution of neurons according to the state. On the second level, it is obvious that the levels not used in training are better detected in the extending stroke because the areas, especially levels 1 and 3, are adjacent neurons. In the retracting stroke there is not such a situation and the classification result is inferior.

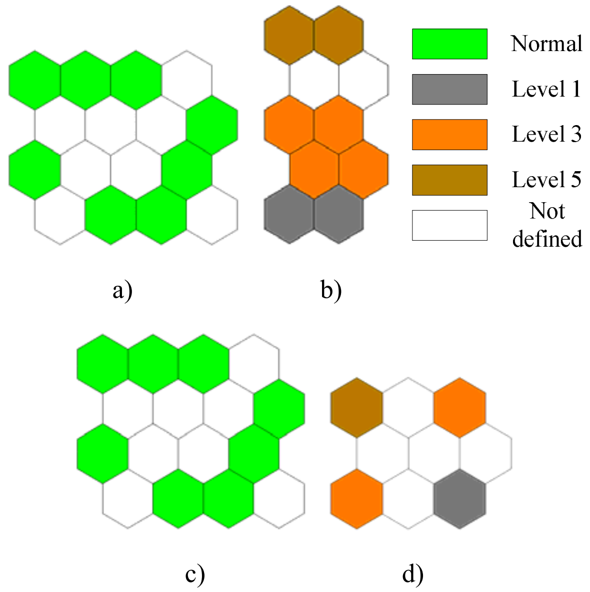

Figure 12 Distribution of neurons according to the state of the system: a) extending: first level, b) extending: second level, c) retracting: first level, d) retracting: second level.

Effect of Changes in Loading Conditions

Besides the levels that were used in training, two other loading conditions are used in testing. The number of map units is 3 x 10 in extending and retracting strokes. BMU distances on the first level were calculated to prove that the normal state is classified correctly even in untrained loading conditions. Figures 13 and 14 show the distances between the BMUs and the testing vectors. When 250kg and 750 kg are used in testing, the distance is higher in both cases. In the extending stroke the change is still far smaller than in the retracting stroke, where the difference can be clearly seen. If Figures 13 and 14 are compared to Figures 15 and 16, where different fault levels were tested with the maps of loading conditions on the first level, it can be seen that some of the lower levels of the fault can be confused with the normal situation of untrained loading conditions. Overall, the distance is higher with a fault situation. If the thresholds are set to 1.25 in the extending stroke and to 1.38 in the retracting stroke, all different loading conditions are classified as normal states. In this case, 52 % of the faulty sequences in the extending stroke shown in Figures 15 and 16 are classified correctly as faults. Respectively, in the retracting stroke 98 % of the sequences are classified as faults. It can be noticed that in the extending stroke especially the lower levels of fault were hard to distinguish from the normal state. In the retracting stroke the loading conditions that were not used in training were close to the smallest fault level, but all the other fault levels have a higher distance.

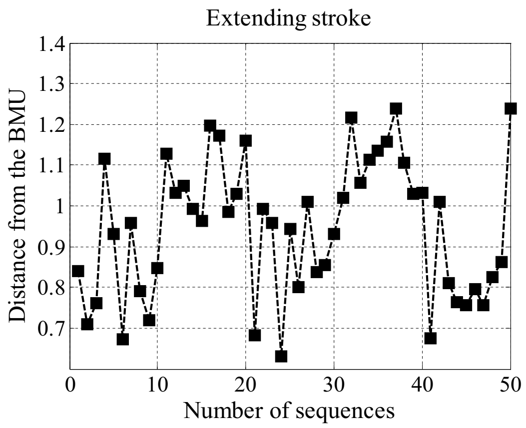

Figure 13 BMU distances from extending strokes. Sequences are in order 0 kg, 250 kg, 500 kg, 750 kg and 1000 kg.

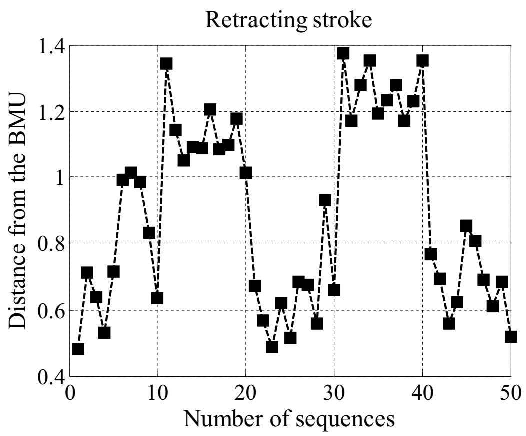

Figure 14 BMU distances from retracting strokes. Sequences are in order 0 kg, 250 kg, 500 kg, 750 kg and 1000 kg.

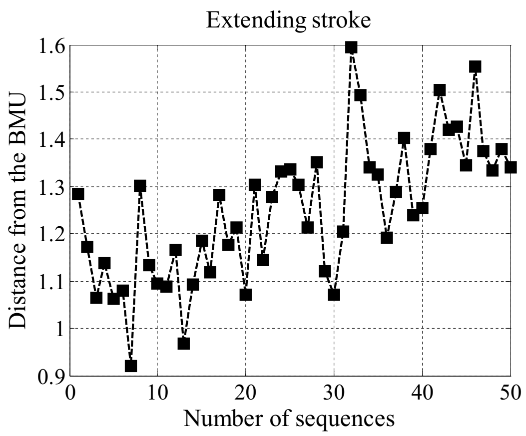

Figure 15 BMU distances from extending strokes. Sequences are in order fault levels 1, 2, 3, 4, 5.

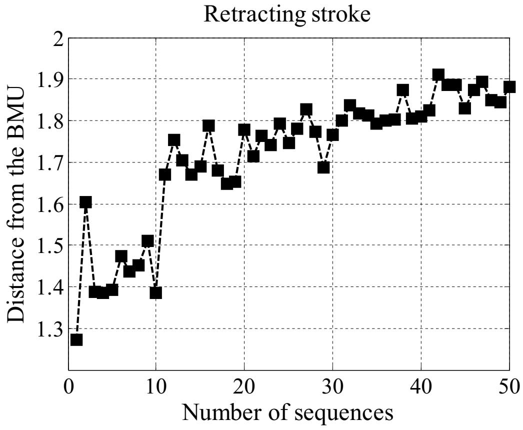

Figure 16 BMU distances from retracting strokes. Sequences are in order fault levels 1, 2, 3, 4, 5.

CONCLUSIONS

The main goal of this research was to study the sensitivity of data analysis process in hydraulic forklift. For this purpose a simulation model of the lifting movement of the forklift was made. This model was used to produce data for analysis purposes. It was noticed from the results of the analysis that it is possible to use only few fault levels and loading conditions in the training phase and still maintain the performance of the data analysis process.

When the effect of fault level change was studied, 94 % of the sequences in the extending stroke and 100 % in the retracting stroke were classified correctly on the first level of analysis. On the second level, 90 % of the sequences in the extending stroke and 55 % in retracting stroke were classified as the closest fault level, with fault levels that are not used in training.

The loading conditions that are not used in training can still be classified as normal state on the first level with good results but some of the lower levels of the fault can be confused with the normal situation of untrained loading conditions. When fault levels L1 to L5 were tested with the maps of loading conditions on the first level, 52 % of the faulty sequences in the extending stroke were classified correctly as faults. Respectively, in the retracting stroke 98 % of the sequences were classified as faults.

These results prove the generalization capability of the used data analysis process.

REFERENCES

1. Duda, R., Hart, P. and Stork, D. 2001. Pattern Classification. A Wiley-Interscience Publication, New York, USA, 2nd edition.
2. Alhoniemi, E., Hollmén, J., Simula, O. and Vesanto, J. 1999. Process Monitoring and Modeling Using the Self-Organizing Map. Integrated Computer-Aided Engineering, Vol. 6, No. 1, pp. 3-14.
3. Ramdén, T. 1998. Condition Monitoring and Fault Diagnosis of Fluid Power Systems - A Approaches with Neural Networks and Parameter Identification. Dissertation. Linköping, Sweden. Linköping University. No. 514. 195 p.
4. SFS-EN 1726-1. 1999. Safety of industrial trucks. Part 1: Self-propelled trucks up to and including 10 000 kg capacity and industrial tractors with a drawbar pull up to and including 20 000 N. Helsinki, Finland, Suomen standardisoimisliitto. 146 p.
5. Krogerus, T. and Koskinen, K.T. 2011. Testing of Data Analysis Process in Hydraulic Forklift. Proceedings of the Twelfth Scandinavian International Conference on Fluid Power, SICFP'011, Tampere, Finland, May 18-20, 2011. Vol. 3, pp. 105-118.
6. Krogerus, T., Sairiala, H. and Koskinen, K.T. 2008. Water Hydraulic Forklift with Intelligent Condition Monitoring System. Proceedings of the 51st National Conference on Fluid Power, Las Vegas, Nevada, USA, March 12-14, 2008. pp. 337-344.
7. Mathworks Inc. 2010. www.mathworks.com [Referred 27.6.2010].
8. SOM Toolbox. 2010. www.cis.hut.fi/projects/somtoolbox [Referred 27.6.2010].
9. Ellman, A., Piché, R. 1999. A Two Regime Orifice Flow Formula for Numerical Simulation, Journal of Dynamic Systems, Measurement and Control, Vol. 121, No. 4, pp. 721-724.
10. Krogerus, T. 2011. Feature Extraction and Self-Organizing Maps in Condition Monitoring of Hydraulic Systems. Dissertation. Tampere, Finland. Tampere University of Technology. Publication 949. 126 p.

Proceedings of the 8th JFPS International
Symposium on Fluid Power, OKINAWA 2011
Oct. 25-28, 2011

2C3-3

STUDY ON ENERGY EFFICIENCY OF WATER HYDRAULIC FLUID SWITCHING TRANSMISSION

Wataru KOBAYASHI*, Kazuhisa ITO*, Shigeru IKEO**
Tsuyoshi YAMADA*** and Koji TAKAHASHI**

* Mechanical Engineering, Graduate School of Engineering
Shibaura Institute of Technology
307, Fukasaku, Minuma-ku Saitama-shi, Saitama, 337-8570 Japan
(E-mail: kazu-ito@shibaura-it.ac.jp)
** Department of Engineering and Applied Sciences, Faculty of Science and Technology
Sophia University
7-1, Kioicho, Chiyoda-ku, Tokyo, 102-8554 Japan
*** Former student, Mechanical Engineering Course, Graduate School of Engineering
Tottori University
4-101, Koyamacho-minami, Tottori-shi, Tottori, 680-8552 Japan

ABSTRACT

Water hydraulic fluid switching transmission (FST) has lower environmental load and lower energy loss in valves for using only ON/OFF valves. In addition, improvement of transmission efficiency can be expected by using accumulator as the second driving source and making use of waste energy by energy recovering action. This paper concerned with experimental results and a design of simulator of the FST system. First, it was shown from experimental results that the error rate was within 5 percent and the recovered energy during the deceleration phase was more than 25-38% of the kinetic energy of the load. Next, the FST simulator was developed for designing the key parameters to achieve higher transmission efficiency. As a result, the effects of design parameters of FST system were clarified and design standard of water hydraulic FST was established.

KEY WORDS

Key words, Water hydraulics, FST, Energy recovery, ON/OFF valve, Accumulator

NOMENCLATURE

p_i	: pressure in pipe (i = 1, 2, 3)
p_s	: supply pressure
p_{ACC}	: pressure in accumulator ACC
q_i	: volumetric flow rate (i = 1, 2)
q_{ACC}	: flow rate to accumulator ACC
I	: inertia load
ω_{FW}	: rotational velocity
ω_{const}	: rotational velocity at the end of Phase 2
E_{FW}	: kinetic energy of load
E_{recovery}	: recovery energy in Phase 3
$E_{\mathrm{sup\_ac}}$	: supplied energy in Phase 1

INTRODUCTION

Water hydraulics is recognized as the forth drive systems for more than ten years because of its lower environmental load and high cleanness. This system can be widely applied to various fields. Its control performance have already discussed in many papers and it was shown that the control performance was comparable with oil hydraulics [1][2]. On the other hand, as a drive system, not only the control performance but also the energy efficiency is very important in application. For water hydraulics, while the proportional or servo valves are proper to achieve higher control precision, these kinds of valves dissipate the energy at their throttle part. As a result, this leads to lower energy saving performance [3]. In this situation, the fluid switching transmission inspired by electrical power switching control was introduced for fluid power transmission these ten years. Its key concept is to transmit power by applying the switching control with ON/OFF valves and store the surpass energy to accumulator. Therefore the higher energy loss components such as proportional or servo valves are not adopted. Since only ON/OFF valves are used in this system, the energy dissipation at their throttle part is less than conventional valve control system.

This system was examined in oil hydraulics and its energy balance and loss were discussed in the literature [4]. As described above, from the viewpoint of environment load and working conditions, it is useful to apply FST system to industrial fields, for example, food, cosmetic and pharmaceutical factories which are required high cleanness. Moreover, in water hydraulic FST, as energy loss at pipe line is small due to lower viscosity, it is hoped that energy recovering is more effective than in oil hydraulic FST. The authors has already reported the feasibility of the water hydraulic FST [5].

In this research, a simple drive pattern was introduced for a production process, and then the rotational velocity control performance and the energy efficiency were examined by experiments. At first, control performance was examined by experiments. The comparison with conventional systems was focused on and the cause of rotational velocity error was examined to improve the control performance. Secondly, using FST simulator, two key parameters on energy transmission efficiency were analyzed to examine the ability for transmission of the FST system. Especially, recovered energy which was dissipated in conventional transmission was focused on.

FST EXPERIMENTAL SYSTEM

The water hydraulic circuit used in this study is shown in Fig.1. This is composed of a fixed displacement pump (P), a fixed displacement pump/motor (PM), three ON/OFF valves (VS_i, i =1, 2, 3) and two accumulators (ACC_i , i =1, 2) as key components. These ACC_1 and ACC_2 are used as a surge absorber and energy storage, respectively. The flywheel (FW) connected to PM is the rotating load. The specifications of each components and instruments for measurement are listed in Table 1. In this research, the input energy is defined as the fluid energy which is supplied from the pump P through the valve VS_1. On the other hand, the output energy is defined as the transmitted energy to the flywheel FW. The supply pressure p_s is 12MPa in all experiments and as a reference rotational velocity the drive pattern of load is given as seen in Fig.2 which is composed of three phases; acceleration phase (Phase 1), constant velocity phase (Phase 2) and deceleration phase (Phase 3). In this research, considering the response time of ON/OFF valves and their control relays, ±10rpm threshold around reference rotational velocity is introduced in Phase 2.

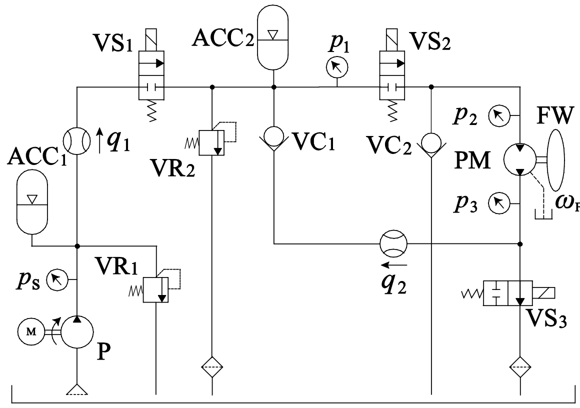

Figure 1 Water hydraulic FST circuit

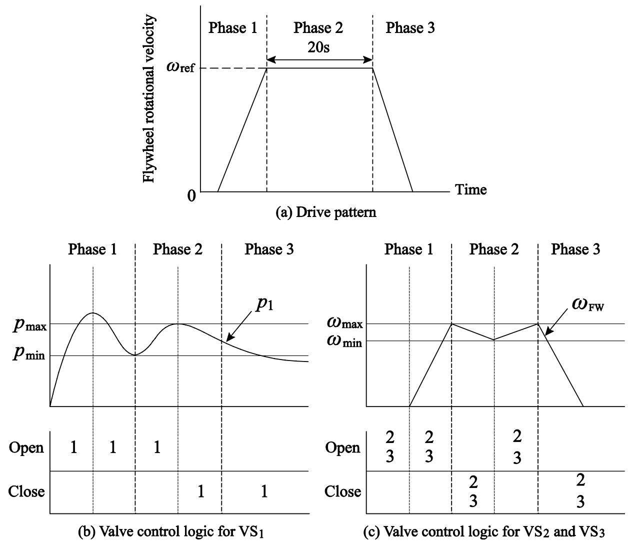

Figure 2 Logic charts of each ON/OFF valves

Table 1 Specifications of experimental devices

P	Displacement volume	30×10^{-6} m^3
PM	Displacement volume	15×10^{-6} m^3
ACC_1	N_2 gas volume	0.005 m^3
	Preload pressure	5.0 MPa
ACC_2	N_2 gas volume	0.01 m^3
	Preload pressure	8.4 MPa

FW	Total inertia	1.58 kgm^2
	Mass	78.9 kg
	Diameter	0.4 m
	Thickness	0.08 m
Drive motor	Revolution	500 rpm
Flow meter	Range of measurement	0-15 L/min
Rotational speed meter	Time constant	63 ms
	Range of measurement	1-20000 rpm

EXPERIMENTAL RESULTS

The experimental results on control performance are summarized in Table 2 for the reference velocity 600-1000rpm. Fig.3 and Fig.4 show the experimental results of flywheel velocity ω_{FW} and recovery flow rate q_2, respectively. Especially, Fig.3 contains the comparison of two cases; with and without energy recovering operations.

Table 2 Comparison for various reference velocities

	ω_{min} [rpm]	ω_{max} [rpm]	e_{min} [%]	e_{max} [%]	ω_{const} [rpm]
600rpm	561	639	6.42	6.55	601
700rpm	664	740	5.09	5.68	700
800rpm	761	841	4.86	5.09	801
900rpm	864	941	3.94	4.53	899
1000rpm	964	1043	3.58	4.25	1001

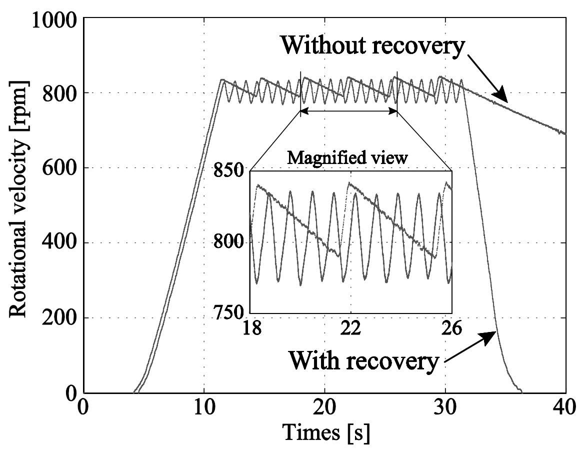

Figure 3 Experimental results of flywheel velocity

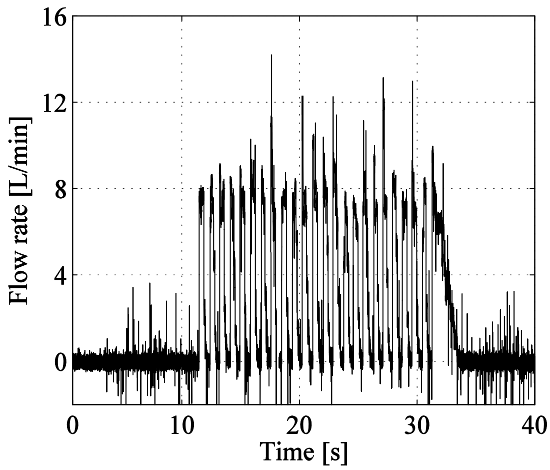

Figure 4 Experimental result of flow rate q_2

Table 2 shows that the rotational velocity ω_{max} and ω_{min} in Phase 2 are different from reference velocity irrespective of reference velocity. This is due to two reasons; 1) the time lag and response time in ON/OFF valves (see Fig.5), and 2) the response time of velocity transducer. From Fig.5, which represents ON/OFF valve characteristics, the maximum opening time is about 40ms and the maximum closing time about 100ms. These correspond to 15-30% of the rotational velocity error ratio. The latter has relatively larger effect on the results because time constant of velocity transducer is about 63ms as in Table 1. The settling time of this sensor seems to be about 300ms, this implies that the rotational velocity is highly depending on the performance of velocity transducer compared with valve response lags.
On the other hand, comparing the performance with recovery to the one without recovery, it is shown that maximum errors of both are almost same. Therefore, energy recovering has little relationship with the rotational velocity control performance.

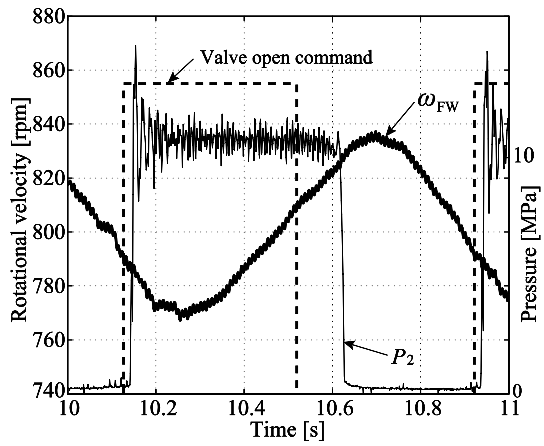

Figure 5 Pressure response in experiment

EVALUATION OF ENERGY EFFICIENCY

In this chapter, two indices will be defined to evaluate the energy recovery of FST system. Note that these indices are valid during Phase 3 because the energy recovery is operated only in this phase.

Efficiency index η_1

The index η_1 is defined as

$$\eta_1 = \frac{E_{\text{recovery}}}{E_{\text{FW}}} \tag{1}$$

where E_{FW} is the kinetic energy possessed by the flywheel at the end of Phase 2, and E_{recovery} the recovered energy to the accumulator ACC$_2$ during Phase 3. This evaluates how much energy will be recovered from the kinetic energy of flywheel which is dissipated in conventional operation and can be reused in next operation in real application. In this case, E_{FW} is defined as

$$E_{\text{FW}} = \frac{1}{2} I\omega_{\text{const}}^2 \tag{2}$$

where ω_{const} is the final value of rotational velocity of flywheel at the end of Phase 2. On the other hand, E_{recovery} is the pressure energy in the accumulator ACC$_2$ which can be calculated with the pressure p_{ACC} in the accumulator ACC$_2$ and its flow rate q_{ACC} as follows.

$$E_{\text{recovery}} = \int_{t_{\text{start}}}^{t_{\text{end}}} p_{\text{ACC}} \cdot q_{\text{ACC}} dt \tag{3}$$

where t_{start} and t_{end} are the time at the beginning and the end of the Phase 3, respectively. Because the pressure p_{ACC} is same to the pressure p_1 and the flow rate q_{ACC} into the accumulator ACC$_2$ is only q_2, Eq. (3) can be rewritten in

$$E_{\text{recovery}} = \int_{t_{\text{start}}}^{t_{\text{end}}} p_1 \cdot q_2 dt \tag{4}$$

Efficiency index η_2

Another evaluation index η_2 is defined as

$$\eta_2 = \frac{E_{\text{recovery}}}{E_{\text{sup\_ac}}} \tag{5}$$

where $E_{\text{sup\_ac}}$ is supplied energy to FST system by opening ON/OFF valve VS$_1$ during Phase 1. This index η_2 indicates the ratio of recovered energy to the total supplied energy to FST system. This is supplementary for η_1 because even if the η_1 is supposed to be higher, there is a possibility that FST could transmit the small portion of supplied energy to the load. Therefore the η_2 is also required to evaluate the FST system performance as a transmission. In Eq. (5), $E_{\text{sup\_ac}}$ is obtained as

$$E_{\text{sup\_ac}} = \int_0^{t_{\text{end}}} p_{\text{s}} \cdot q_1 dt \tag{6}$$

where p_{s} is supply pressure and q_1 the supplied flow rate. Based on these two indices, the energy and transmission performances will be evaluated in the following section.

Efficiency analysis

The results on efficiency analysis are shown in Fig.6 and Table 3. These results are the average of 5 times experiments. First, from Fig.6, it can be observed that the energy recovery efficiency η_1 is improved for higher reference rotational velocity of load. This is due to the characteristics of volumetric efficiency of the pump/motor PM which is connected to the flywheel. The index η_2 also shows similar property and this reason can be explained as follows. For higher reference velocity, the kinetic energy in flywheel is higher at the end of Phase 2, and this implies that the recovered energy in the accumulator is also larger. Therefore, for higher reference velocity, η_1 will be improved and the FST will achieve better energy performance. Moreover, higher pump/motor efficiency makes η_1, η_2 higher.

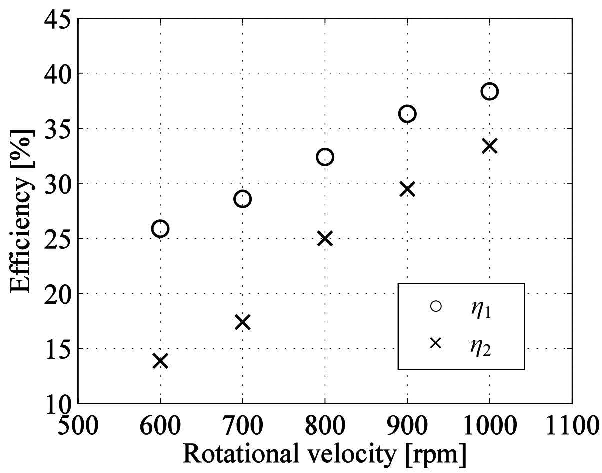

Figure 6 Efficiency comparisons for various reference rotational velocities

Table 3 Analysis of energy efficiency η_1, η_2

ω_{FW} [rpm]	E_{FW} [kJ]	$E_{recovery}$ [kJ]	E_{sup_ac} [kJ]	η_1 [%]	η_2 [%]
600	3.10	0.80	5.78	25.9	13.9
700	4.23	1.21	6.95	28.6	17.4
800	5.52	1.79	7.15	32.4	25.0
900	6.98	2.54	8.60	36.3	29.5
1000	8.61	3.30	9.89	38.4	33.4

As mentioned above, η_1 shows the recovered energy ratio to the energy possessed by flywheel at the end of Phase 2. This FST system achieves more than 25-38% recovery of energy depending on reference velocity of flywheel. However, if recovered energy exceeds the capacity of the accumulator ACC_2, the surplus energy will be dissipated through the relief valve VR_2. This leads to lower energy recovery. Therefore, for volume of ACC_2, which depend on drive pattern of load, are very important to minimize this dissipative energy.

SIMULATION ANALYSIS

In this chapter, the validity of FST simulator based on mathematical model is confirmed by comparing with experimental results. Fig.7 and Fig.8 show the simulation and the experimental results on rotational velocity ω_{FW} and the pressure p_1, respectively. Both results agree well.

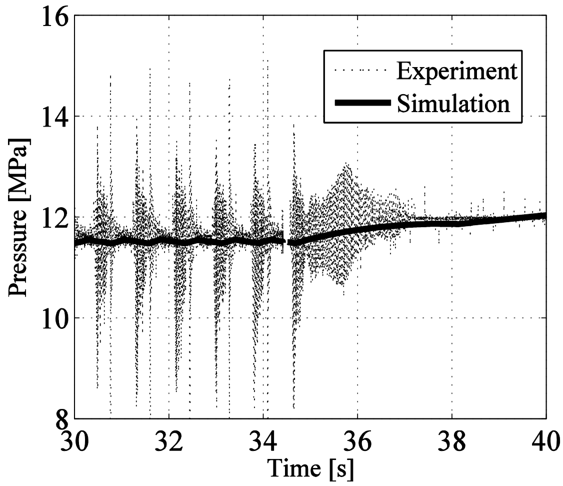

Fig.8 Comparison of pressure p_1

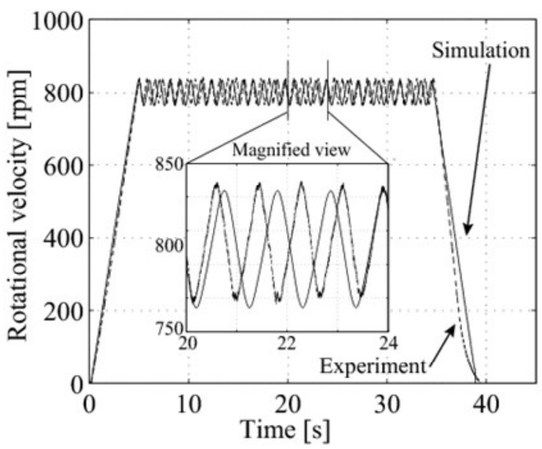

Figure 7 Comparison of rotational velocity ω_{FW}

The simulation results on control performance and energy efficiency are compared with experimental results. The control performance means rotational velocity error ratio e_{max} and e_{min} in Phase 2 which is constant velocity phase. For energy efficiency, two indices η_1 and η_2 are also used (see Eq. (1) and (5)). The results are shown in Table 4. Note that experimental methodology in this chapter different from the previous chapter. Even when the reference velocity is changed 600-1000rpm, the simulation results show good agreement with the experimental results. For this reason, the FST simulator which is possible to adequately reproduce actual phenomenon is constructed.

Table 4 Simulation analysis

	e_{min} [%]	e_{max} [%]	E_{FW} [kJ]	$E_{recovery}$ [kJ]	E_{sup_ac} [kJ]	η_1 [%]	η_2 [%]
Experiment	3.94	4.53	5.52	1.79	12.1	34.2	15.5
Simulation	3.58	4.25	5.51	1.78	12.4	32.4	14.4

DESIGN KEY PARAMETERS

In this chapter, time constant of velocity transducer and design parameters of accumulator ACC_2 are examined as key parameters of the FST system. These will improve control performance of rotational velocity and energy efficiency.

Consideration of control performance

In this section, improvement of control performance is examined with the FST simulator. In the previous chapter (see chapter EXPERIMENTAL RESULTS), two reasons are pointed out as rotational velocity error. Focusing on time constant of transducer which is dominant consider to which level the control performance can be improved. Fig.9 shows simulation results on rotational velocity ω_{FW} in a part of Phase 2. Note that Fig.9 contains the comparison of two cases; transducer time constant 63ms and 0ms.

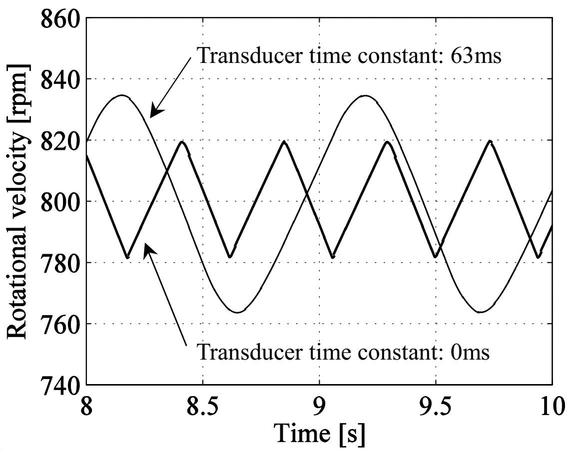

Figure 9 Comparison for different time constants

Table 5 Number of valve switching on simulation for different time constants

Time constant [ms]		63	0
error ratio [%]		4.25	2.56
Number of switching	VS_1	1	1
	VS_2	34	67
	VS_3	34	67

It is seen from Fig.9 that the rotational velocity error ratio is reduce to about 2% from 4% of experimental result for the reference velocity 800rpm. Therefore, one of key parameter of control performance is clarified. On the other hand, from Table 5, it is confirmed that number of switching of ON/OFF valves with transducer time constant 0ms are more than with transducer time constant 63ms. Because too many valve switching may lead to shorten of life of valve, it is necessary to optimize both the control performance and number of switching of ON/OFF valves. Table 5 shows the control performance and number of switching of ON/OFF valves. Note that 'number of switching' stands for all of the switching number of ON and OFF in Phase 2, not the pair of ON/OFF.

Consideration of energy efficiency

In this section, to clarify drive performance of the FST system, the key parameters of energy efficiency are discussed. In this research, intended parameters are focused preload pressure p_a and volume V_a of accumulator ACC_2. First, preload pressure is examined with experiment and simulation. Energy efficiency η_1 and η_2 are summarized in Table 6 for various preload pressures 6.0-9.6MPa. These results were the average of 3 times experiments.

Table 6 Comparison for different preload pressures

p_a [MPa]	Experiment		Simulation	
	η_1 [%]	η_2 [%]	η_1 [%]	η_2 [%]
6.0	34.7	7.6	34.2	6.1
7.2	34.9	10.0	34.2	9.8
8.4	34.2	15.5	34.4	14.8
9.6	34.6	22.1	34.6	22.5

From Table 6, the value of preload pressure has no direct effect on energy efficiency η_1. Although the energy recovering is made only in Phase 3, ACC_2 have completed to store enough energy before this phase. In fact, the pressure of ACC_2 in Phase 3 was almost constant irrespective the preload pressure p_a in the experiments. On the other hand, energy efficiency η_2 is greatly affected by the value of preload pressure. For higher preload pressure, from Table 6, the energy efficiency η_2 becomes higher in both experiment and simulation. This is due to the experimental methodology that initial value of stored energy in ACC_2 is zero. In other words, it is necessary to supply energy to ACC_2 before supplying energy to flywheel. Therefore, for higher preload pressure, the supply energy which accumulator ACC_2 needs is smaller and supply energy E_{sup_ac} is also smaller. As noted from Eq. (5), energy efficiency η_2 can be improved by decreasing E_{sup_ac}.
Accumulator volume which is another key parameter is examined with only simulation. Energy efficiency η_1 and η_2 are summarized in Table 7 for various accumulator

volumes 6-14L.

Table 7 Comparison for different accumulator volumes

V_a [L]	η_1 [%]	η_2 [%]
6	32.6	17.1
8	32.2	15.3
10	32.4	14.4
12	32.5	13.8
14	32.6	13.3

From Table 7, the accumulator volume also has no direct effect on energy efficiency η_1 same as the situation of preload pressure. As seen from Fig.8, pressure in ACC_2 raised by recovery flow rate q_2 to accumulator ACC_2 is a little. Hence, there is no difference in recovery energy $E_{recovery}$ for various accumulator volumes.

On the other hand, energy efficiency η_2 is affected by the value of accumulator volume. For larger accumulator volume, energy efficiency η_2 becomes lower. For larger volume of accumulator ACC_2, pressure fluctuation in ACC_2 becomes smaller. Therefore, it is necessary to supply more energy to accumulator ACC_2 in Phase 1. For this reason, it is expected to improve the energy efficiency of the FST system by minimizing the accumulator volume. However, smaller volume of accumulator ACC_2, the capacity of ACC_2 becomes smaller and a part of recovery energy is may be wasted through the relief valve VR_2.

CONCLUSIONS

This paper deals with water hydraulic FST and examines the rotational velocity control performance and the energy efficiency with two indices. In addition, the FST simulator is developed for designing the key parameters. For the constant reference velocity, the proposed simple valve control logic achieved control accuracy within ± 40rpm for given reference velocity, that is, within 5% error ratio. This error ratio is highly depending on the time constant of velocity transducer and the response of ON/OFF valves. Also, it is confirmed that the energy recovery performance of FST system is more than 25-38% of kinetic energy of the load, but this depends on the reference velocity. In conventional fluid power transmission, this energy is all dissipated at orifices. This result implies that a part of this energy can be used to compensate the power required by load. These results show the effectiveness of water hydraulic FST system.
To improve control performance of the FST system, the effect of the time constant of velocity transducer is examined. It is confirmed that the rotational error ratio can be improved to more than 40% of previous result while the number of ON/OFF valve switching becomes almost double, therefore this is a criteria for users.
To improve energy efficiency, two key parameters of ACC_2 are clarified with the FST simulator and design indices η_1 and η_2 of water hydraulic FST system is established. As the preloaded pressure of ACC_2 increases, η_2 increases. On the other hand, as the volume of ACC_2 increases, η_2 decreases. Both have little effect on η_1.

REFERENCES

1. Sanada, K., A method of designing a robust force controller of a water-hydraulic servo system, Proc. Instn. Mech. Eng. Vol.216, Part I:J Systems and Control Engineering, pp.135-141, 2002
2. Ito, K., Ikeo, S., Takahashi, H., Kanamori, N., Robust Control Performance Comparison on Water Hydraulic Servo Motor System, in Dr.D,N,Johnston, Prof.A.R.Plummer ED., Fluid Power and Motion Control FPMC2008, pp.149-162, Bath, UK, 2008
3. Linjama, M., Vilenius, M., Energy-efficient motion control of a digital hydraulics joint actuator, Proc. of the 6th JFPS International Symposium on Fluid Power, TSUKUBA, pp.640-645, 2005
4. Sanada, K., A Study on HILS of Fluid Switching Transmission, Proc. of International Joint Conference SICE-ICASE, pp.4668-4671, 2006
5. Ito, K., Kobayashi, W., Pham Noc Pha, Ikeo, S., A Control and Energy Saving Performance of Water Hydraulic Fluid Switching Transmission, Proc. of the 12th Scandinavian International Conference on Fluid Power, Vol.1, pp.103-114, 2011

Proceedings of the 8th JFPS International
Symposium on Fluid Power, OKINAWA 2011
Oct. 25-28, 2011

2C4-1

RESEARCH ON THE VISCOUS LOSS OF UNDERWATER TOOL

Yinshui LIU, Defa WU, Shudong YANG, Xinjun WANG

School of Mechanical Science and Engineering
Huazhong University of Science and Technology, Wuhan, Hubei, 430074, China

ABSTRACT

Underwater tools are widely used in underwater work. Usually, underwater tools are driven by oil hydraulics, pneumatics or electricity. Compared with the tools used in the air, viscous loss of water for the rotary underwater tools with larger tools head, such as the abrasive disk saw and brush, must be considered because the dynamic viscosity of water is about 50 times more than that of air. Especially when the rotational speed is very high and the disk very large the energy loss due to viscous loss accounts for a very large ratio of the output power of the motor. In the paper, an abrasive disk saw driven by seawater hydraulics was used as the example to research the viscous loss of underwater tool. The influences of the rotary speed and the diameter of disk on the viscous loss were researched experimentally and theoretically and then a formula was built to estimate the viscous loss.

KEY WORDS

Water Hydraulics, Underwater Tool, Abrasive Disk Saw, Viscous Loss

1. INTRODUCTION

The underwater tool is necessary to accomplish underwater work as the ocean is more and more important to human's development. Generally, underwater tools can be divided into two kinds according to the moving ways: one is the reciprocal tool such as steel cable cutter, torque wrench etc., the other is rotary tool driven by motor. Compared with the tools used in the air, the viscous loss of water for the rotary underwater tools with larger tools head, such as abrasive disk saw and brush, must be considered because the dynamic viscosity of water (1×10^{-3}kg/ms at 20℃ and 1atm) is about 50 times more than that of air (2.03×10^{-5} kg/ms at 20℃ and 1atm). Especially when the rotational speed is very high and the diameter of disk very large the energy loss due to viscous loss accounts for a very large ratio of the output power of the motor.

Underwater tools can be divided into several kinds according to their driving ways: manual tools, electric tools, pneumatic tools and hydraulic tools. Compared with electric tools and pneumatic tools, the hydraulic tools have stronger working capacity and higher reliability and so are most often used underwater. Traditionally, mineral oil is used as the working media of hydraulic tools. However mineral oil is not compatible with seawater and so the system must be as a closed-circuit which has some insurmountable drawbacks such as pollution, leakage, erosion and pressure compensation when working at deep sea. Recently, underwater tools driven by seawater hydraulics，which uses seawater instead of mineral oil as the pressure media in hydraulic power systems, are a new development direction. When seawater hydraulics is used to drive underwater tool, the following advantages can be obtained compared with the underwater tools powered by pressurized air, hydraulic oil or electricity[1,2,3]:

1) No risk of leakage.
2) No pollution to environment.
3) Less pressure loss due to the less viscosity of seawater than mineral oil.
4) Simpler system because of open-circuit system without return lines, reservoirs etc.
5) No need of storage of working media.

In addition, underwater tools driven by seawater hydraulics have no need of pressure compensators. Generally, oil hydraulic tools are a closed-circuit and a pressure compensator is needed to improve the effective working pressure if they are used in a deep sea. Comparatively, a seawater hydraulic system is open and the inlet pressure is the one produced by the sea depth and so the practical pressure is still the one that the system can produce.

In this paper, the underwater tools driven by seawater hydraulics were taken as the example to research the influences of viscosity on the underwater tool.

2. THEORETICAL ANALYSIS

Fig.1 shows a seawater hydraulic abrasive disk saw, in which an abrasive disk is driven by a seawater hydraulic motor. According to the boundary layer theory, the viscous resistance of water on the disk can be expressed by:

$$M_D = 1.935 \frac{\rho\omega^2 R^5}{\sqrt{R_e}} \qquad (1)$$

In which, $R_e = \dfrac{\omega R^2}{v}$ is the Reynolds number, ρ is the density of water, ω is the rotary speed, R is the radius of disk, M_D is the resistant torque of water.

Formula (1) is correct for laminar flow and not suitable for turbulent flow. If the tangential speed across the boundary layer follows the 1/7 power law, the viscous torque on the disk is [4,5]:

$$M_D = 0.073\rho\omega^2 R^5 (v/\omega R^2)^{1/5} \qquad (2)$$

Besides, the thickness of abrasive disk also has influences on the viscous resistance. If the thickness is Δmm then a thickness coefficient can be defined as follows:

$$\frac{M_R}{M_D} = \frac{2\Delta}{R} = \frac{4\Delta}{d} = K \qquad (3)$$

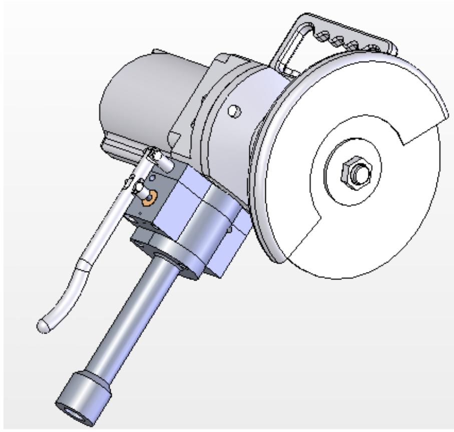

Fig.1 Seawater hydraulic abrasive disk saw

Then the total viscous resistant torque is

$$\begin{aligned} M &= (1+K)M_D \\ &= (1+K)0.073\rho\omega^2 R^5 (v/\omega R^2)^{1/5} \end{aligned} \qquad (4)$$

And the power loss due to viscous resistance is

$$P_s = M\omega \qquad (5)$$

For an abrasive disk with the rotary speed n=2000r/min, radius R=100mm, $\Delta = 2mm$, K=1/25, and the Reynolds number

$$R_e = \frac{\omega R^2}{v} \approx 1.4 \times 10^6$$

the flow is turbulent at this time and the viscous torque and power loss according to formula (4) is as follows:

$$M \approx 2.32 \mathrm{N \cdot m}$$

$$P_s \approx 0.50 \mathrm{kW}$$

From formula (4), the influences of disk diameter, thickness, rotary speed on the power loss are shown in Fig. 2, in which, k=1/25 means the disk used to cut and k=1/2 the disk used to grind or brush.

Considering the cutting efficiency and maximum cutting diameter, an abrasive disc with 200mm diameter and 2000rpm rotary speed was selected. At this time, the viscous power loss is about 0.67 kW.

3. EXPERMENTS AND RESULTS

Based on the above theoretical analysis, the experiments were carried out to research the influences of viscosity on the power loss

3.1Test system

The test system is shown in Fig.2, which consists mainly of a water hydraulic pump, an accumulator, various rotary tools and control valves.

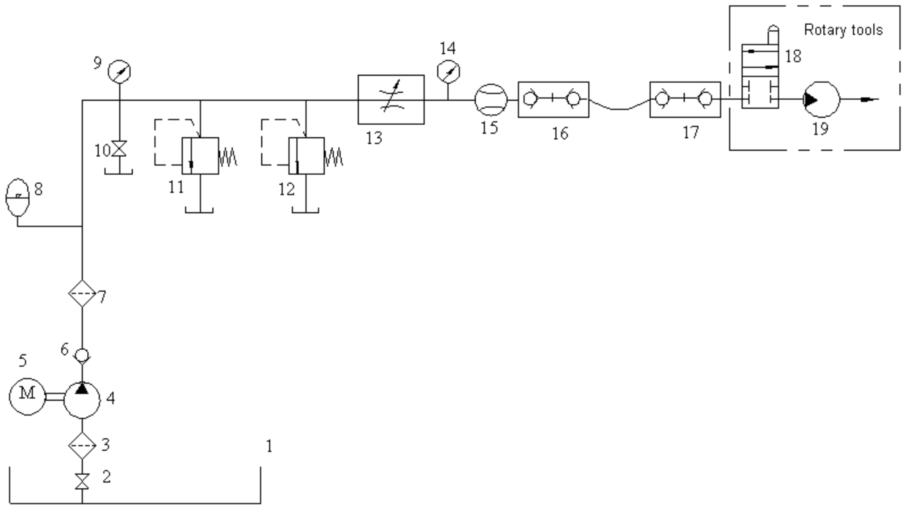

1-Water Tank 2-Shut-off Valve 3, 7-Filter 4-Water Hydraulic Pump 5-Electric Motor 6-Check Valve 8-Accumulator 9,14-Manometer 10-Unloading Valve 11-Safety Valve 12-Relief valve 13-Flow Control Valve 15-Flowmeter 16, 17-Fast Fitting Connector 18-Control Valve of Tool 19-Motor and Tool

Fig.2 The hydraulic scheme of the test system

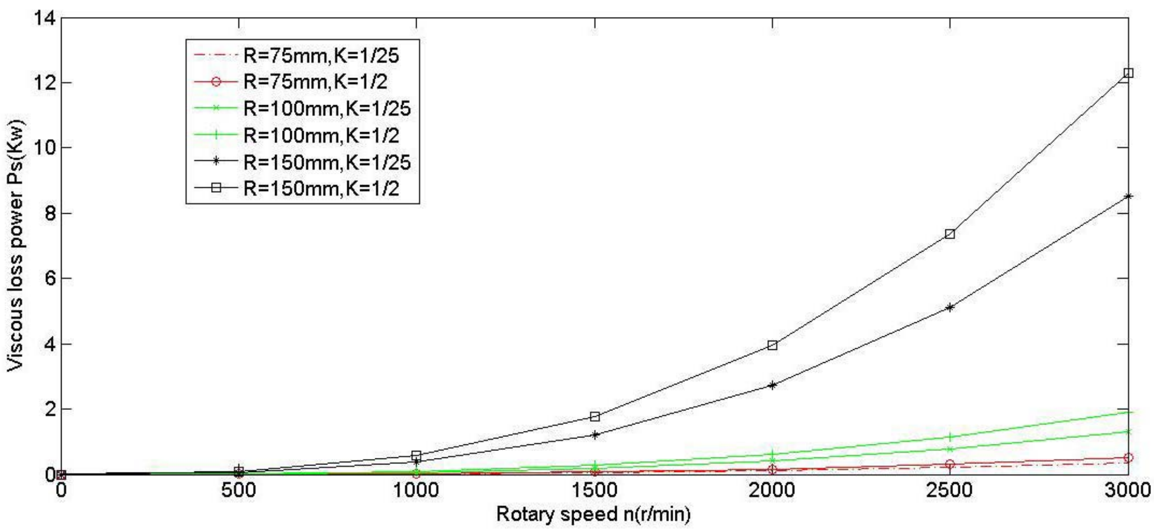

Fig.3 The power loss due to viscosity for different disks

The unloading valve should be open before starting and ending the system in order to protect the pump. Besides, the system also needs to be unloaded when changing different tools in order to replace the fast-fitting connector easily. The relief valve is used to adjust the working pressure of the tools and the flow control valve the flow through the tools. The tests were carried out in the laboratory and the working media were tap water.

The inner diameter and length of the hose between the flow control valve and motor is 1/2 inch and 15 meters respectively.

3.2 Test results

In order to research the viscous power loss of rotary tools, an abrasive disk, steel wire brush and abrasive bowl were tested which represents underwater abrasive cutter, brush and grinder respectively. The test results are shown in Fig.4, in which, the thickness is 1.9mm for the abrasive disk with diameter 180mm, 2.6mm for the abrasive disk with diameter 125mm, 30mm for the abrasive bowl with diameter 75mm, 43mm for the steel wire brush with diameter 125 mm and 30mm for the steel wire brush with diameter 75 mm.

1) Influences of shapes on the viscous power loss

From Fig.4 it can be seen that the viscous power loss of the steel wire brush with diameter 75mm and thickness 30mm is much larger than that of the abrasive bowl with the same diameter and thickness and the former is 3.4 times larger than the latter when the rotary speed is 1900rpm.

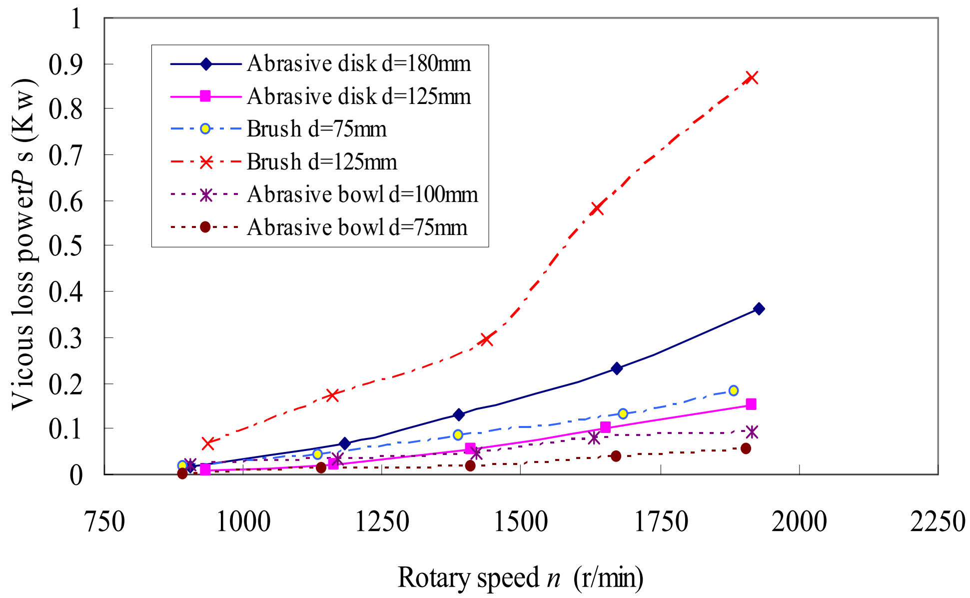

Fig.4 Viscous power loss of different tools with different scales and shapes

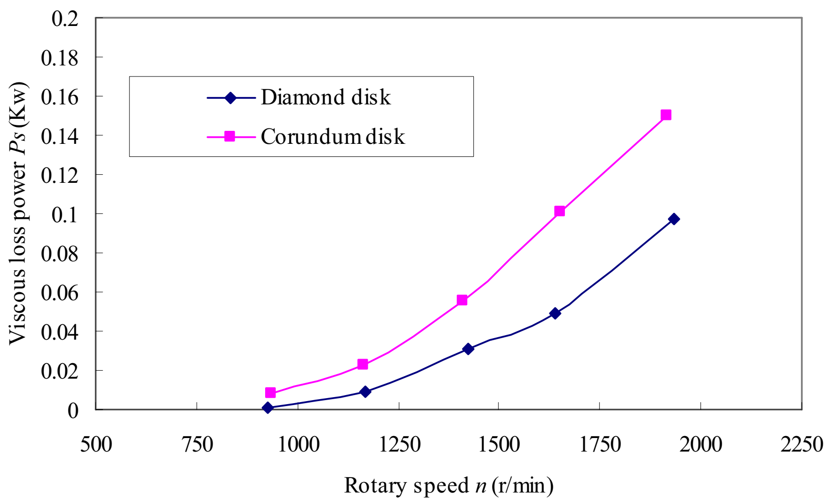

Fig.5 The influences of roughness on the viscous power loss

2) Influences of diameter on the viscous power loss

The viscous power loss of the abrasive disk with diameter 180mm is much larger than that of the one with diameter 125mm and the value of the former is 2.4 times larger than that of the latter when the rotary speed is 1900rpm even the thickness of the latter is larger than that of the former

3) Influences of roughness on the viscous power loss

In order to research the influences of roughness on the viscous power loss, a diamond and a corundum disk with the same diameter 125mm were tested. Compared with the diamond abrasive disk, the corundum disk is rougher. The test results are shown in Fig.5.

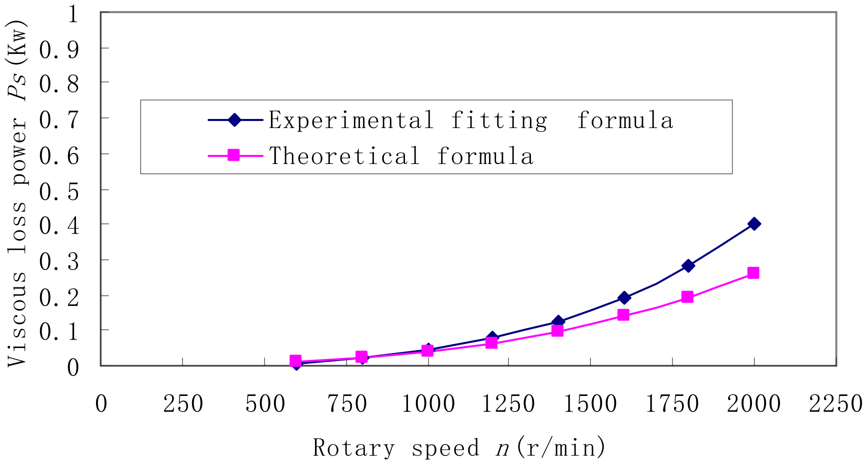

Fig.6 Comparison of the theoretical and experimental fitting values

4. DISCUSSIONS

According to the data from the test, an experimental formula of the viscous power loss for abrasive disk can be obtained by curve fitting as follows.

$$P_s = 2.72 \times 10^{-17} (K)^{0.148} n^{3.23} d^{2.53} \qquad (6)$$

In which, $K = \dfrac{4\Delta}{d}$ is the thickness coefficient, n is the rotary speed and d is the diameter of disks.

This formula can be compared with formula (4) which is obtained according to theoretical deducing. Taking a disk with diameter 180mm and thickness 1,9mm as the example, the results are shown in Fig.6. It can be seen that the value according to formula (6) is larger than the one from formula (4) when the rotary speed is high and this trend become larger with the increasing of rotary speed. These differences can be caused by the roughness of disks. Formula (4) is deduced without considering the influences of roughness. However, from Fig.6 it can be seen that roughness has obvious influences on the viscous power loss of disks.

According to the above analysis, the efficiency of a rotary seawater hydraulic underwater tool system (SWHUTS) can be estimated. Supposing the rated pressure and flow rate of the power source of the SWHUTS is 12MPa and 25L/min respectively and so the output power is 5kW. The pressurized seawater is output to the tools by a hose of 160m long and 13mm inner diameter. The velocity in the hose is 3.14m/s and the flow is turbulent. The viscous pressure loss in the hose is 1.37MPa (the viscosity of seawater is about 1 mm^2/s at 20℃) and so the power loss of the hose is 0.57 kW.

Apart from the power loss of the hose, the power loss due to the viscosity of seawater is 0.67kW for the abrasive saw with 200 mm diameter and 2000 rpm rotary speed, which can be calculated according to formula (4). So the total power loss is 1.24 kW for both the hose and viscous restriction of seawater. The total efficiency of the SWHUTS is not more than 75.2%.

For the same flow rate and hose, the flow is laminar if the working media are mineral oil (the viscosity is about 32 mm^2/s at 20℃) and the viscous pressure loss is 3.59MPa in the output line and 7.18 MPa in the output and return lines together, which means a power loss of 2.99 kW and so the total power loss is 3.66kW for both the hose and viscous restriction of seawater. The total efficiency of the SWHUTS is about 27%. Therefore, the SWHUTS using seawater as the working media has higher efficiency than the one using oil as the working media and is more suitable for the deep sea work[6].

ACKNOWLEDGEMENTS

The authors would like to thank the National Natural Science Foundation of China(No.50975101) and the National High Technology Research and Development Program of China for providing the funding for this project. Thanks are also given to Professor Zhuangyun LI, DR. Xiaofeng HE, Bihai Zhu for their contributions to this project.

REFERENCES

[1] Wu D.F., Research on Rotary Seawater Hydraulic Tools and Its Power System. Thesis for the Master Degree of Engineering. Huazhong University of Science and Technology, Wuhan, China, JUNE, 2007

[2] Terävä J., Kuikko T. and Vilenius M., Development of Seawater Hydraulic Power Pack. Proc. of 4th Scandinavian Int. Conf. on Fluid Power, Finland, Sept. 26-29, 1995, pp. 978~991

[3] Hama,F.R. Boundary layer characteristics for smooth and rough surfaces. Transaction of the Society of Naval Archtects and Marine Engineerings, 62, 1954, pp.333~358

[4] Dutton,R.A. The accuracy of measurement of turbulent skin friction by means of surface Pitot tubes and the distribution of skin friction on a flat plate. ARC RM3058, 1957

[5] Liu Y.S., Jin F.L., Wu D.F., et al. Development on the Power Pack of an Underwater Tool System Driven by Seawater Hydraulics. Proceedings of 7th ICFP'2009, Hangzhou, 2009, pp.471-475

[6] Liu Y.S., Wang X.B., Wu D.F., et al., Mobile Underwater Tool System Driven by Seawater Hydraulic Power. Machine Tools and Hydraulics, Oct. 2008, pp.14-17

Proceedings of the 8th JFPS International
Symposium on Fluid Power, OKINAWA 2011
Oct. 25-28, 2011

2C4-2

OPTIMIZATION OF FLOATING PLATE OF WATER HYDRAULIC INTERNAL GEAR PUMP

Hua ZHOU, Wei SONG

State Key Laboratory of Fluid Power Transmission and Control, Zhejiang University
38 Zheda Road, Hangzhou, 310027 China
(E-mail: songwei_zju@163.com)

ABSTRACT

Internal gear pumps have significant advantages over other types of pumps, such as, compact structure, less sensitive to contaminants, good suction capability, little flow pulsation, low noise level and long durability. However, owing to the nature of low viscosity, poor lubricity and strong corrosion of water, the performances of water hydraulic internal gear pumps are completely different from the oil ones and the design principles of oil pumps are not suitable any more. Until now, no water hydraulic internal gear pump is successfully developed in the world. Floating plate is the key component of internal gear pump, which ensures the compensation of wear and high volumetric efficiency. Based on experiment results and finite element analysis, this paper illustrates the factors of the failure of floating plate. Finally, optimization of floating plate is proposed, which can improve the performance of the pump.

KEY WORDS

Water hydraulic, Internal gear pump, Floating plate, Friction and wear

NOMENCLATURE

a	:	compensation pressure chamber
F_p	:	pressing force
F_r	:	reverse pressing force
A_{b}	:	area of compensation pressure chamber...
A_{h}	:	area of high pressure chamber
n	:	ratio of pressing force and reverse pressing force...

INTRODUCTION

Water hydraulics plays an important part in fluid power systems, which uses filtered tap water or sea water as working medium and has extraordinary advantages over traditional oil hydraulics like environmental friendliness, no-fire risk, low cost and so on. Water hydraulic pump is the fundamental components in water hydraulic systems and decides the performance of systems. A lot of investigations have been implemented about water hydraulic pumps [1, 2, 3]. With the advantages of high volumetric efficiency, variable displacement and low requirement for PV value, piston pump has become the main structure type of water hydraulic pumps. Nonetheless, the inherent characteristics of piston pump, such like, complex structure, numerous components, poor suction capability, sensitive to contaminants, large flow pulsation, high noise level and so on, restrict the application of water hydraulic technology in some fields seriously.

Internal gear pump is a new-born type of fluid power component and wildly applied in modern industry fields recently. Compared to the conventional pumps, internal gear pump has significant advantages, such as, compact structure, less sensitive to contaminants, good suction capability, little flow pulsation, low noise level and long service life, which make it welcomed in the occasions placing particular attentions on high control accuracy, environment noise level, safety and reliability. However, because of the nature of low viscosity, poor lubricity and strong corrosion of water, the performances of water hydraulic internal gear pumps are completely different from the oil ones and the design principles of oil pumps are not suitable for water ones any more. Until now, no water hydraulic internal gear pump is successfully developed in the world.

As illustrated in Figure 1 [4], an internal gear pump is mainly composed of a pinion 3 (gear shaft), a internal gear 2 meshing with the pinion eccentrically, a crescent 6, which has arc-shaped walls cooperating with the tips of the pinion and the internal gear teeth thereon in defining pressure chambers and radial seals, and two pieces of floating plates 5 arranged on both sides of the gears to form axial seals. Statistics show that 75%~80% of internal leakage of gear pumps is caused by failure of axial seals [5]. It's easily to understand that floating plate has a direct impact on performances of internal gear pump and is the key component of the pump.

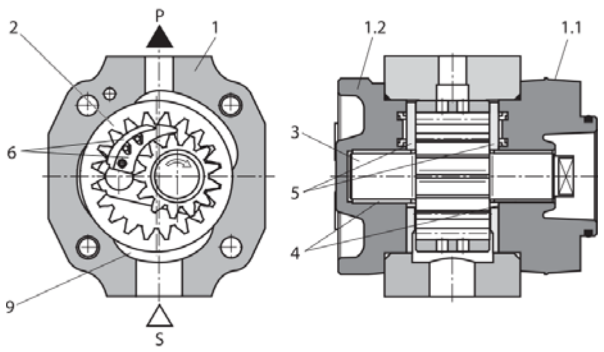

Figure 1 Section view of internal gear pump

OPERATION PRINCIPLE

In the middle-pressure and high-pressure gear pumps, plates are arranged on both sides of the gears to form axial seals with the aim to reduce internal leakage and obtain high volumetric efficiency. According to the operation principle, plates can be divided into three kinds: floating plate, flexible plate and fixed plate. Floating plate has a small hole connecting high pressure chamber with compensation pressure chamber which is located on the back surface of the plate. By this means, floating plate can utilize the output pressure to push itself firmly onto the gear surfaces so as to compensate the gap between the plate and gears. Flexible plate has a similar operation principle with floating plate. The difference lies in that flexible plate depends on its deformation, which is caused by the output pressure, to compensate the gap. Literally, fixed plate has no movement or deformation and can't compensate the gap.

As mentioned above, internal gear pump employs floating plates to keep a good performance, operation principle of which is illustrated in Figure 2 [4]. There is a compensation pressure chamber *a*, defined by seal component 8, located on the back surface of floating plate 5. With a hole connecting compensation pressure chamber with high pressure chamber, pressing force F_p is brought about, which pushes floating plate onto the gears. In order to form the effective axial seas between floating plate and gears, pressing force F_p should be great enough to overcome the reverse pressing force F_r produced from the high pressure chamber, which pushes floating plate away from surface of gears. In the meanwhile, pressing force should not be too large to increase the frictional power loss and speed wear failure of floating plate. According to the design principle of oil gear pumps, the amount of pressing force should be equal to or almost equal to that of reverse pressing force, the ratio of which usually takes a value from 1.0 to 1.1 [5]. Through this method, the load acting on floating plate can be fully neutralized or almost fully neutralized, which ensures both good axial seals and little frictional power loss.

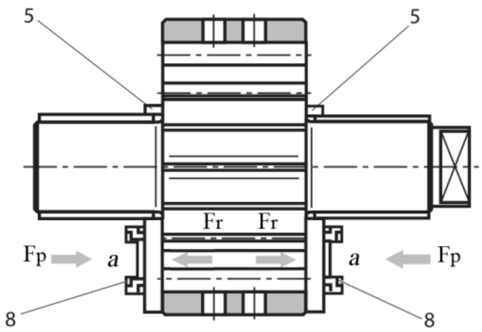

Figure 2 Illustration of operation principle of floating plates

EXPERIMENT

As the gap between floating plate and gears is very small, frictional failures, such like scratch, wear and burn, are easily to occur under conditions of incorrect design or wrong operation. Scratch is usually caused by the hard particles mixed in the fluid, for example, metal scraps cut off from the soft component. These particles are embedded on the interface between floating plate and gears and plough through the surface of floating plate as the gears rotate. Wear usually refers the semi-circle or circle traces ground by the gears on floating plates, which is mainly caused by the over-large amount of pressing force acting on floating plates. Burn mostly takes place on the interface between floating plate and gears. When the frictional force on the interface between floating plate and gears is large, surface temperature will rise rapidly, lubricant film will be crushed and hardness of surface metal will be reduced. Consequently, a cycle of adhesion, tear and adhesion happens, which is called the phenomenon of burn. Burn is the most severe damage of floating plate and leads to the rapid decrease of volumetric efficiency of the pump, which can make the pump lose the capability of work in a very short time.

With mineral oil as working medium, a thin layer of oil film will be formed on the interface between floating plate and gears, which separates them from contacting directly and makes a good lubricated movement, when the pump operate under normal conditions. In this situation, failure of floating plate is usually caused by machining error and assembly error. Compared to oil, water has lower viscosity and poorer lubricity, which makes good lubrication very difficult to achieve. The kinematic viscosity of water is only 1/30 of that of oil at the same operation conditions [1]. Hence, gap between floating plate and gears must be much smaller than that of oil pump to obtain a sufficient volumetric efficiency. However, smaller gap will cause direct contact between floating plate and gears, which leads to serious wear failure. At the same time, floating plate is usually made of copper alloy, hardness of which is softer than that of structure steel which gears is made of, and is much likely to get hurt.

To verify the analysis mentioned above, experiment is designed and carried out, which takes an oil pump as test pump and water as working medium. The test pump has a delivery of 10mL/rev and rated pressure of 16MPa measured in the oil. The water hydraulic test rig is shown in Figure 3 and the hydraulic scheme of test rig is illustrated in Figure 4 [6].

Figure 3 Water hydraulic test rig

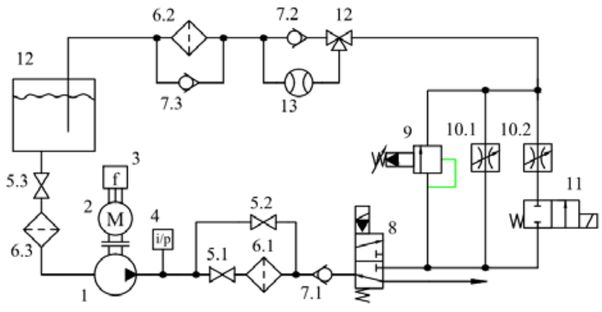

Figure 4 Hydraulic scheme of test rig

Test pump 1 is driven by motor 2, speed of which is regulated by frequency converter 3. Proportional relief valve 9, together with throttling valves 10.1 and 10.2, provides the variable load for test pump. The operating pressure and output flow can be measured by pressure transducer 4 and flow meter 13, respectively. The working medium used in the test rig is tap water and is purified through filters 6.1, 6.2 and 6.3.

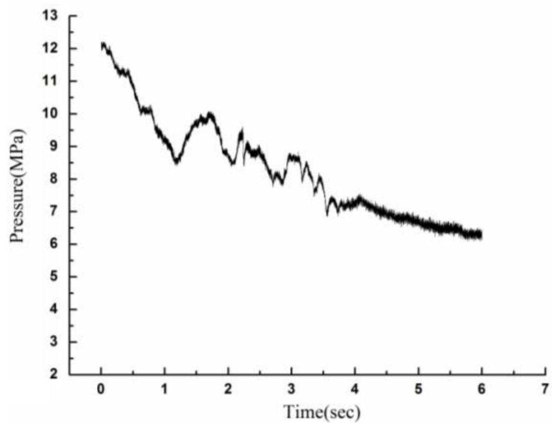

Figure 5 Pressure at speed of 1500rev/min

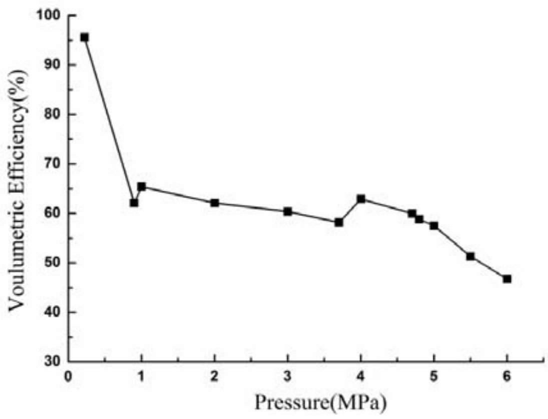

Figure 6 Volumetric efficiency after wear happens

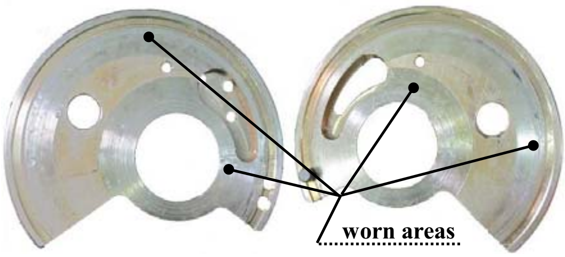

(a) back floating plate (b) front floating plate
Figure 7 Worn floating plates

Figure 5 shows that operating pressure of the pump can reach 12.1MPa at speed of 1500rev/min. However, a rapid pressure-fall occurs and the operating pressure is reduced to 6.1MPa in about 6 seconds. As illustrated in Figure 6 [6], volumetric efficiency only can only keep at a rather low level after wear failure happens, which is approximately 60% at pressure of 1.0MPa~5.0MPa and 46.8% at pressure of 6.0MPa. Figure 7 shows floating plates, which include the back floating plate and the front floating plate, are severely worn and can't form axial seals, which leads to the rapid loss of pressure.

ANALYSIS

The amounts of two forces acting on each floating plate equal the product of output pressure and area of the pressure chamber, respectively. Hence, areas of the pressure chambers are measured in order to obtain the amounts of pressing forces acting on floating plates. However, the shape of high pressure chamber is always changing owing to the meshing movement of the gears. Given that the shape of high pressure chamber varies in a rather small range, we can assume that the area of high pressure chamber is a constant value and an instant of meshing movement is chosen to analyze the pressing force and the reverse pressing force acting on floating plates. Figure 8 shows the shape of high pressure chamber at the given instant and Figure 9 shows the shapes of compensation pressure chambers of floating plates (marked in *green* color). Then, we can obtain data of these areas as depicted in Table 1 [6].

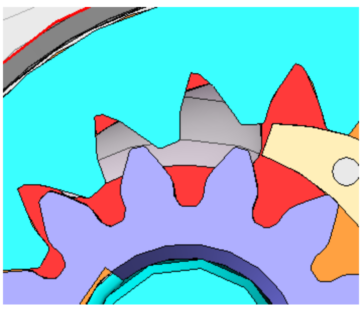

Figure 8 View of high pressure at a given instant

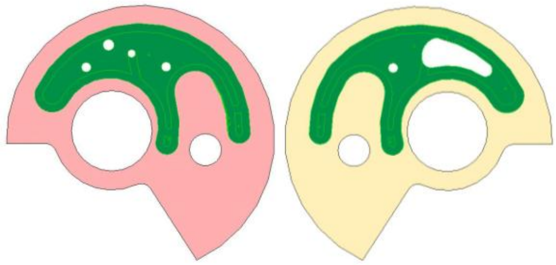

(a) back floating plate (b) front floating plate
Figure 9 Areas of compensation pressure chambers

As illustrated in Table 1[6], the ratio of pressing force and reverse pressing force is 1.87 for back floating plate and 2.39 for front floating plate. Both of them are larger than the conventional design value 1.0~1.1, which indicates that pressing forces acting on floating plates are too large, which is likely to cause badly wear failure, just like the experimental results show.

Table 1 Data of areas of pressure chambers

	A_b/mm^2	A_h/mm^2	n
back floating plate	630	337	1.87
front floating plate	502	210	2.39

With the help of *Ansys Workbench*, a FEA model is built to analyze working conditions between floating plates and gears. According to Table 1, the pressing force acting on back floating plate is larger than that acting on front floating plate. Therefore, the back surface of front floating plate, which doesn't contact with the gears, is pushed onto the pump body when the pump is operating. Hence, a fixed support is applied on the back surface of front floating plate. At the same time, a pressure of 12.1MPa is applied to the areas of pressure chambers and two no-separation contacts are built up among touching surfaces. The model is illustrated in Figure 10.

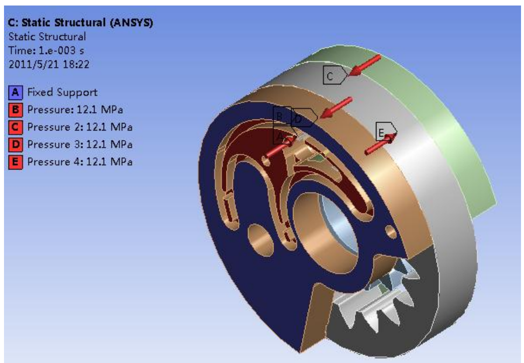

Figure 10 The FEA model of floating plates and gears

Results of contact stress are shown in Figure 11. Clearly, contact stress is much larger at the zone of high pressure chamber and the contact stress on back floating plate is larger than that of front floating plate.

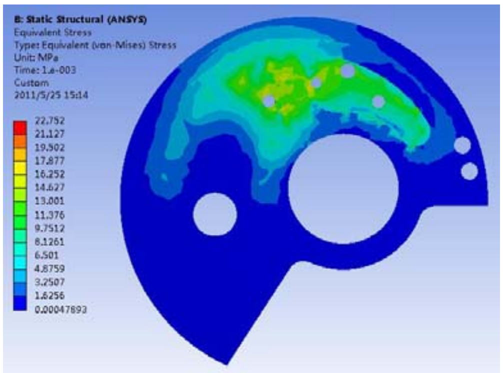

(a) back floating plate

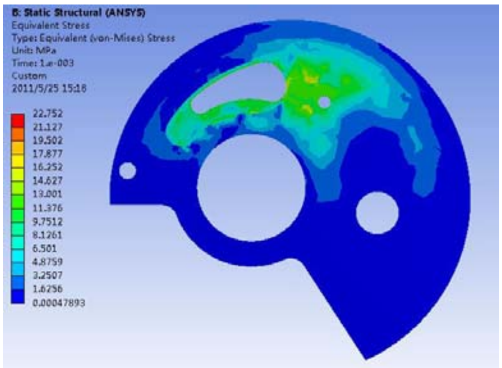

(b) front floating plate

Figure 11 Results of contact stress

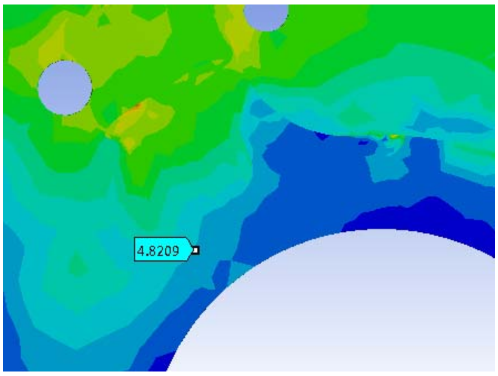

Figure 12 The chosen point to calculate PV

PV is usually taken as an index to evaluate the frictional status of contact pairs with sliding movement. When the PV value exceeds the allowable one, wear failure is likely to occur. Based on the results of contact stress, we choose a point which is located on back floating plate and with a smaller PV value and a lower sliding velocity to analyze, as shown in Figure 12. With a contact stress of 4.82MPa and a distance from rotation center of 14.8mm, PV value at this point is obtained:

$$PV=4.82\text{MPa}\times 14.8\text{mm}\times 1500\text{rev/min}=11.2\text{MPa}\cdot\text{m}\cdot\text{s}^{-1}$$

According to Mechanical Design Manual, the allowable PV value of copper is 6.25 $\text{MPa}\cdot\text{m}\cdot\text{s}^{-1}$ and clearly PV value of the picked point is almost two times of that, which indicates that wear failure occurs at that point. Since the other points at high pressure chamber have larger contact stress and higher sliding velocity, wear failure must occur, which leads to axial failure and serious internal leakage.

OPTIMATION

Based on analysis mentioned above, wear failure of floating plate is mainly caused by the large amount of pressing force. Obviously, it's helpful to reduce the area of compensation pressure chamber so as to get a proper ratio of pressing force and reverse pressing force. The shapes (marked in *blue* color) and data of improved compensation pressure chambers are shown in Figure 13 and Table 2, respectively.

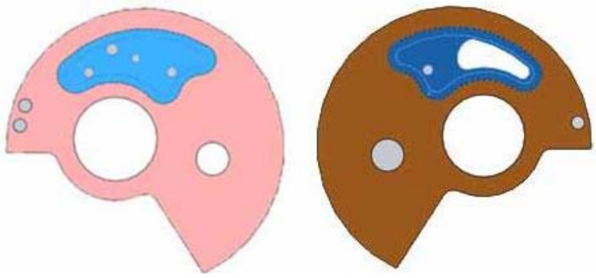

(a) back floating plate (b) front floating plate

Figure 13 Areas of improved compensation pressure chambers

Table 2 Data of areas of improved pressure chambers

	A_b/mm^2	A_h/mm^2	n
back floating plate	403	337	1.20
front floating plate	273	210	1.30

Meanwhile, as plastic has a good frictional performance sliding with metal and also can work with water, a kind of polymeric plastic with higher strength and PV value, PEEK, is chosen to build the floating plate. The material characteristics of PEEK are depicted in Table 3 [7].

Table 3 Material characteristics of PEEK

Density/g.cm^{-3}	1.44
Tensile yield strength/MPa	100
Tensile ultimate strength/MPa	134
Young's modulus/GPa	10.1
Poisson's ration	0.4
Allowable PV/ MPa·m·s^{-1}	13.23

The results of contact stress of improved floating plates are illustrated in Figure 14. Compared to Figure 11, the range of higher contact stress is smaller. Also, the average of contact stresses is about 12MPa in high pressure chamber and is a little less than that of floating plate before, which is about 13MPa. Considering the allowable PV value of PEEK is almost two times of that of copper, frictional performance of the optimized floating plates is much better. Taking the same point illustrated in Figure 12 to analysis, we get contact stress of this point as shown in Figure 14 and PV value of this point is calculated:

PV=3.57MPa×14.8mm×1500rev/min=8.30MPa·m·s^{-1}

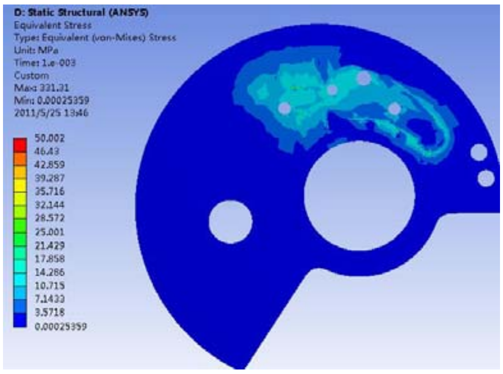

(a) back floating plate

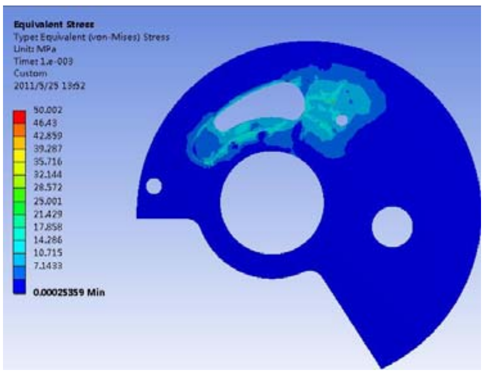

(b) front floating plate

Figure 14 Results of contact stress

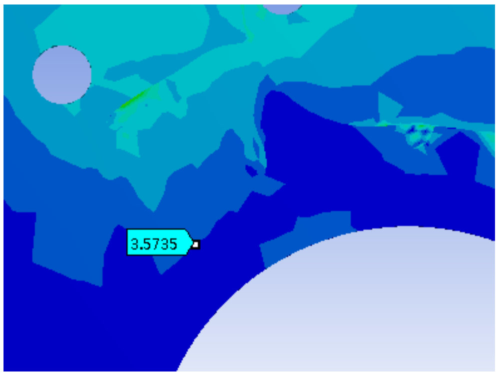

Figure 15 The chosen point to calculate PV

The PV value of the chosen point doesn't exceed the allowable PV of PEEK, which is 13.23 MPa·m·s^{-1} as illustrated in Table 3. Clearly, working condition of floating plate has been improved, which will guarantee a better performance of the pump. However, PEEK isn't as strong as metal. The application of PEEK will increase the risk of failure caused by large deformations of floating plates. Figure 16 shows the results of deformation and the largest deformation is about 0.005mm. Further researches need to be done.

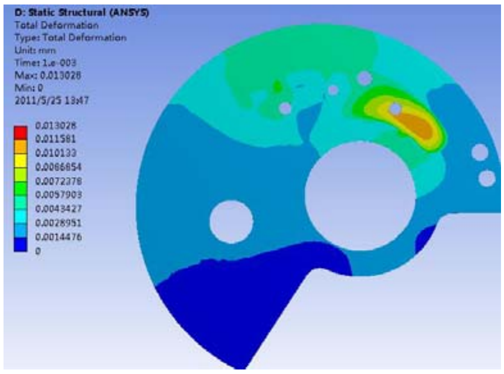

(a) back floating plate

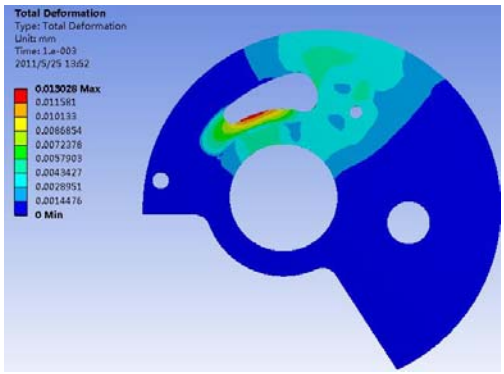

(b) front floating plate

Figure 16 Results of deformation

CONCLUSION

In this paper, performance of internal gear pump with water as medium is investigated through experimental analysis. By means of finite element method, factors of failure of floating plates are discussed and optimization is also proposed. Some conclusions are presented:
1) owing to special nature of water, design principles of oil internal gear pumps doesn't suit water hydraulic ones any more.
2) floating plate is one of the weakest components to fail in water hydraulic internal gear pump.
3) working conditions of floating plate can be improved by decreasing area of compensation pressure chamber and taking plastic to build plates. However, usage of plastic also increases the risk of failure caused by deformation of plates.

REFERENCES

1. Brookes, C.A., The Development of Water Hydraulic Pumps using Advanced Engineering Ceramics, Proceedings of the 4th Scandinavian International Conference on Fluid Power, Tampere, Finland, 1995.
2. Backé, W., Water- or oil-hydraulics in the Future. Proceedings of the 6th Scandinavian International Conference on Fluid Power, Tampere, Finland, 1999.
3. Kazama, T., Numerical Simulation of A Slipper Model for Water Hydraulic Pumps/Motors in Mixed Lubrication. Proceedings of the 6th JFPS International Symposium on Fluid Power, Tsukuba, Japan, 2005.
4. Bosch Rexroth, Catalogue Hydraulic Components for Industrial Applications (Part1), 2007, pp.701.
5. He, C., Hydraulic Components, Machine Press, Beijing, 1984, pp.64-71.
6. Song, W. and Zhou, H., Experimental Research on Performance of Water Hydraulic Internal Gear Pump. Proceedings of International Conference on Fluid Power and Mechatronics, Beijing, China, 2011 (Accepted).
7. http://sc.victrex.com.

2C4-3

EFFECT OF PARAMETERS ON FREQUENCY CHARACTERISTICS OF PROPORTIONAL CONTROL VALVE USING TAP WATER

Futoshi Yoshida*, Shimpei MIYAKAYA*

* Basic Technology R&D Center, KYB Corporation
1-12-1 Asamizodai Minami-ku Sagamihara-shi Kanagawa, 252-0328 Japan
(E-mail: yoshida-fut@kyb.co.jp)

ABSTRACT

Water hydraulic components and systems, using "tap water" as their fluid power source, are very hygienic and environmentally friendly. Because of their controllability to high output power, they are expected to be utilized as a 4th and new driving method after the conventional methods of oil hydraulic, pneumatic and electric power. The authors have also demonstrated through experiments that frequency characteristics of the proportional control valve using tap water could be approximated by a second-order lag system, and that the damping restriction could effectively work on the transient property of the valve. Furthermore, the analytical verification based on the above experimental results indicated that the second-order lag system appeared due to multiple factors including the solenoid thrust, the flow force, the damping force, and the property of a compensation circuit. This paper verifies the effect of various design parameters on the frequency characteristics through experiments and analyses.

KEY WORDS

Water Hydraulics, Proportional Control Valve, Tap Water, Frequency Response

NOMENCLATURE

μ : Viscosity [Pa s]
ν : Kinematic viscosity [m^2/s]
ρ : Density [kg/m^3]
λ : Pipe friction coefficient [-]
θ : Jet angle [degree]
L_b, L_{NT} : Length of orifice [m]
L_{bn}, L_{bT} : Length of annular clearance [m]
D_{SPL} : Diameter of spool
D_b : Diameter of hydrostatic bearing [m]
D_n : Diameter of damping orifice [m]
x : Spool displacement [m]
P_s, P_a, P_b, P_t: Pressure of supply, A, B, and return port[Pa]
P_L : Load pressure [Pa]
Q_{NT0} : Flow rate through damping restriction at the equilibrium point [m^3/s]
C : Flow coefficient

INTRODUCTION

Water hydraulic components and systems, using "tap water" as their fluid power source, are very hygienic and environmentally friendly. Because of their controllability to high output power, they are expected to be utilized as a 4th and new driving method after the conventional methods of oil hydraulic, pneumatic and electric power. Their potential markets could be extensive, including food and beverages, semiconductors, medicines and pharmaceuticals, cosmetics, chemicals, natural energy technologies, and underwater applications. As a

Copyright © 2011 by JFPS, ISBN 4-931070-08-6

fundamental technology, one of the water hydraulic components that enables water hydraulic systems to meet the requirements of sophisticated control of power, speed and positioning is the water hydraulic solenoid proportional control valve [1]. In previous papers, the authors demonstrated the effects of various design parameters on valve performance through experiment and analysis of static characteristics at a supply pressure of 14 MPa [2], and through experiment of dynamic behavior and analytical verification based on the experimental results [3]. These results further demonstrated that frequency characteristics of the valve represent the characteristics of a second-order lag system due to multiple factors including characteristics of solenoid thrust, mechanical and fluid characteristics of valve, and compensation circuit characteristics. This paper focuses on the effects of various parameters of the water hydraulic solenoid proportional valve on frequency characteristics and aims to have effective design policies to improve valve performance and achieve system optimization based on experimental and analytical verification.

STRUCTURE AND FEATURES

Figure 1 shows the structure of a water hydraulic solenoid proportional valve. Table 1 shows the main specifications of the valve.

Since low viscosity tap water is used as working fluid, it is difficult to form a water film between sliding surfaces. Therefore, the spool of this valve is supported by hydrostatic bearings at both ends and allowed to move without contact inside the sleeve, since it has a structure that reduces friction and wear due to sliding contacts.

The spool is positioned by the solenoid thrust and spring forces. While a general solenoid valve is structurally supported by compression springs at both ends of the spool, this valve uses an extension spring. The use of the extension spring can reduce the moment and lateral forces generated in the case of supports provided at both ends and obtain the full effects of hydrostatic bearings. The solenoid thrust is generated only in the extension direction, but not in the contraction direction of the rod. Consequently, when the spool is displaced in the extension direction, the solenoid thrust operates predominantly, and when the spool is displaced in the opposite contraction direction, the spring force operates predominantly.

A damping restriction is provided in the return line from pressure chambers at both ends of the spool to improve stabilization of the valve. By providing a damping restriction in this location, the valve has a meter-out circuit for a hydraulic system connected to the pressure chambers controlling the spool operation, and therefore an effective damping action can be achieved despite low viscosity.

Figure 2 shows a block diagram of the system components in the valve. This valve can be divided into components, including a compensation circuit, solenoid, and valve, the transfer function of which is referred to as C(s), S(s), and P(s), respectively. To improve valve performance, spool displacement is detected by a differential transformer which provides feedback to control the position of the spool with a compensation circuit using a PI control.

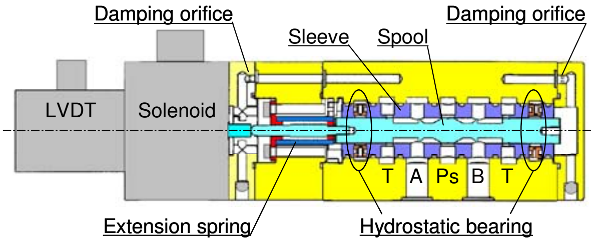

Figure 1 Structure of valve

Table 1 Specifications

Item		Specification
Rated flow rate	[L/min]	20
Rated pressure	[MPa]	14
Operating pressure range	[MPa]	3.5 to 14
Operating temperature range	[deg C]	2 to 50
Working fluid		Tap water
Input voltage	[V]	+/-10

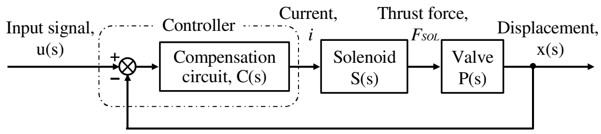

Figure 2 Block diagram

TRANSFER FUNCTION

Figure 3 shows an illustration of the parameter definition for an analysis model. Taking into consideration that according to the results of experimental verification presented in the previous papers, the valve system has the characteristics of a second-order lag system and the solenoid thrust has the characteristics of a first-order lag system, transfer functions are derived on the basis of the following assumptions [2]:

(a) Water viscosity is constant because of its low dependence on temperature.

(b) Control openings provide orifice flow.

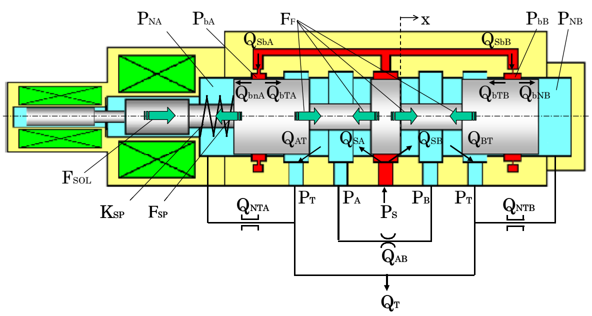

Figure 3 Parameter definition

Valve Transfer Function P(s)

The system is given with a solenoid thrust F_{SOL} as input and a spool displacement x as output relating to spool movement of the valve. Considering the frequency range used for the solenoid valve, because experiments indicated that mass effects are insignificant at the moving parts of the valve, the motion equation for this system is expressed as equation (1), where F_U is the viscous resistance, F_F is the flow force, F_{SP} is the spring force, and F_P is the pressure force at both ends of the spool.

$$F_U + F_F + F_{SP} = F_{SOL} + F_P \tag{1}$$

$$F_{SOL} = K_{SOL} \cdot i \tag{2}$$

K_{SOL} : Constant of proportion of solenoid thrust;

i : Current

$$F_{SP} = K_{SP} \cdot x \tag{3}$$

K_{SP} : Spring constant

$$F_P = (P_{NA} - P_{NB})A_{SPL} \tag{4}$$

P_{NA}, P_{NB} : Pressure at both ends of spool;

A_{SPL} : Spool cross-sectional area

$$F_U = \Gamma \cdot \dot{x} \tag{5}$$

Γ : Coefficient of viscous resistance

$$F_F = \beta \cdot x \tag{6}$$

β : Coefficient of flow force

By considering the flow at hydrostatic bearings, the flow force at control openings, the flow at the annular clearance between the spool and the sleeve, the viscous resistance, and the damping resistance in the pressure chambers at both ends of the spool, and taking the Laplace transform of equation (1) after linearization of the experimental equilibrium points, the transfer function P(s) is obtained and expressed in a standard form of a first-order lag element, as formulated in equation (7), where the coefficients are defined in equations (8) through (15). In this regard, however, the damping resistance for hydrostatic bearing restriction and damping restriction is calculated considering the experimental results and the Reynolds number by applying empirical formulas of choke restriction and Blasius, respectively.

$$P(s) = \frac{x(s)}{F_{SOL}(s)} = \frac{1}{(\Gamma - \xi)s + (K_{SP} + \beta)} \tag{7}$$

$$\Gamma = (L_{bn} + L_{bT})\frac{2\pi \cdot D_{SPL} \cdot \mu}{\delta} \tag{8}$$

$$\xi = \frac{2A^2{}_{SPL}}{\alpha \cdot \alpha_{bN}} \tag{9}$$

$$\beta = 8 \cdot C \cdot L_W \cdot (P_S - P_L)\cot(\theta) \tag{10}$$

$$\alpha = \frac{\alpha_{bN}}{\alpha_{bN} + \alpha_{bT} - \alpha_b} - \frac{\alpha_N}{\alpha_{bN}} - 1 \tag{11}$$

$$\alpha_N = \frac{\pi^2 D_N{}^5}{16\rho L_{NT} Q_{NT0} \cdot \lambda} \tag{12}$$

$$\alpha_{bN} = \frac{\pi \cdot D_{SPL} \cdot \delta^3}{12 \cdot \mu \cdot L_{bN}} \tag{13}$$

$$\alpha_b = \frac{\pi \cdot D_b{}^4}{32 \cdot \mu \cdot L_b} \tag{14}$$

$$\alpha_{bT} = \frac{\pi \cdot D_{SPL} \cdot \delta^3}{12 \cdot \mu \cdot L_{bT}} \tag{15}$$

$$\lambda = 0.3164 \cdot Re^{-0.25} \tag{16}$$

$$Re = \frac{wD_N}{\nu} \tag{17}$$

$$w = \frac{4Q_{NT0}}{\pi D_N{}^2} \tag{18}$$

In the above equations, w is the flow velocity at the restriction, and Q_{NT0} is the flow rate passing through the restriction at the equilibrium point.

Solenoid Thrust Transfer Function S(s)

The characteristics of solenoid thrust are approximated by equation (19) using the experimental results of frequency characteristics of a stand-alone solenoid for a first-order lag transfer function, where τ_{SOL} is time constant and K_{SOL} is proportional constant. Figure 4 shows comparison between measured experimental results and analytical values obtained by equation (19) for the solenoid thrust.

$$S(s)=\frac{F_{SOL}(s)}{i(s)}=\frac{K_{SOL}}{1+\tau_{SOL}\,s} \tag{19}$$

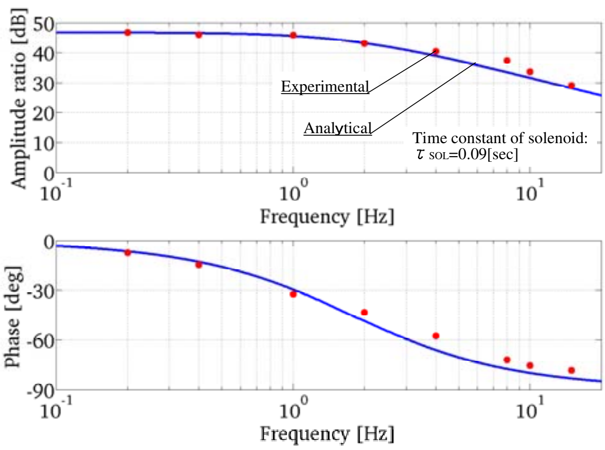

Figure 4 Frequency characteristics of solenoid thrust

Compensation Circuit Transfer Function C(s)

The transfer function C(s) for a compensator, which provides feedback of spool displacement to control the position of the spool using a PI control, is defined by equation (20) using proportional gain k_P and integral time T_I.

$$C(s)=k_P\left(1+\frac{1}{T_I\,s}\right)=\frac{k_P T_I\,s+k_P}{T_I\,s} \tag{20}$$

Transfer Function for a Valve System

By using the transfer functions P(s) and S(s) obtained above, the transfer function V(s) for a solenoid valve excluding the compensator is expressed in a standard form of a second-order lag element, as formulated in equation (21). In this regard, however, the natural angular frequency ω, the damping coefficient ζ, and the proportionality factor K are defined in equations (22) through (24).

$$\begin{aligned} V(s)&=S(s)P(s)\\ &=\frac{x(s)}{i(s)}=\frac{K\varpi^2}{s^2+2\varsigma\varpi\,s+\varpi^2} \end{aligned} \tag{21}$$

$$\varpi=\sqrt{\frac{K_{SP}+\beta}{(\Gamma-\xi)\tau_{SOL}}} \tag{22}$$

$$\varsigma=\frac{1}{2}\left(\frac{1}{\tau_{SOL}\,\varpi}+\tau_{SOL}\,\varpi\right) \tag{23}$$

$$K=\frac{K_{SOL}}{K_{SP}+\beta} \tag{24}$$

Therefore, the resonant frequency as a solenoid valve is determined based on the ratio of spring constant K_{SP}, fluid spring constant β, and damping force (Γ−ξ), and time constant τ_{SOL} of the solenoid. Furthermore, the loop transfer function $V_{SYS}(s)$ including the PI compensator can be expressed by a multi-order lag element, as formulated in equation (25).

$$\begin{aligned} V_{SYS}(s)&=\frac{x(s)}{u(s)}=\frac{C(s)V(s)}{1+C(s)V(s)}\\ &=\frac{k_P K\varpi^2\left(s+\dfrac{1}{T_I}\right)}{s^3+2\varsigma\varpi\,s^2+(1+k_P K)\varpi^2 s+\dfrac{k_P K\varpi^2}{T_I}} \end{aligned} \tag{25}$$

EXPERIMENTAL METHODOLOGY

Figure 5 shows schematically the configuration of the frequency response testing apparatus.

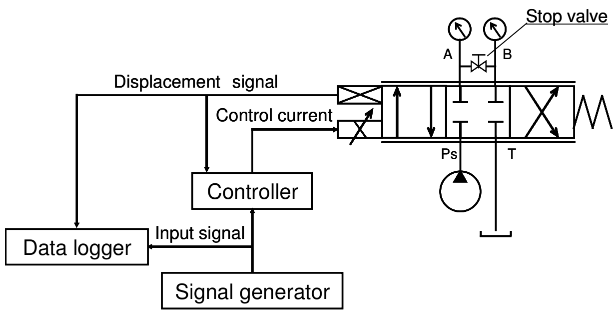

Figure 5 Experimental methodology

The neutral point of the valve has been adjusted, and the opening of the stop valve is controlled to set the load pressure difference P_L between A and B ports at 7 MPa as an experimental equilibrium point with an input signal of 50%. The input signal is a sine wave of voltage at 50%+/-10%. The input signal u and the spool displacement x are measured to calculate amplitude ratio and phase lag by FFT analysis.
All tests were conducted with a supply pressure of 14 Ma and a water temperature of 25°C +/-5 °C.

RESULTS AND CONSIDERATIONS

Effect of Proportional Gain

Figure 6 shows frequency characteristics of proportional gains ranging from 0.7 to 7 [k_P]. Other common conditions are as follows: damping restriction diameter of φ = 0.6 and integral gain of T_I = 0.03. The results show that the frequency response characteristics generally represent the characteristics of a second-order lag system, both experimentally and analytically. The experimental values and the analytical values obtained under each condition are not always quantitatively fully consistent, but sufficiently represent the qualitative characteristics. As the proportional gain k_P increases, the responsiveness improves to be in the high frequency range. As the proportional gain is smaller, the difference between the analytical results and the experimental results increases in the high frequency range. The reason of this result may be the inertial effect arising in the moving parts of the valve. The experimental results and the analytical results show that the frequency response characteristics of a second-order lag system are evident overall.

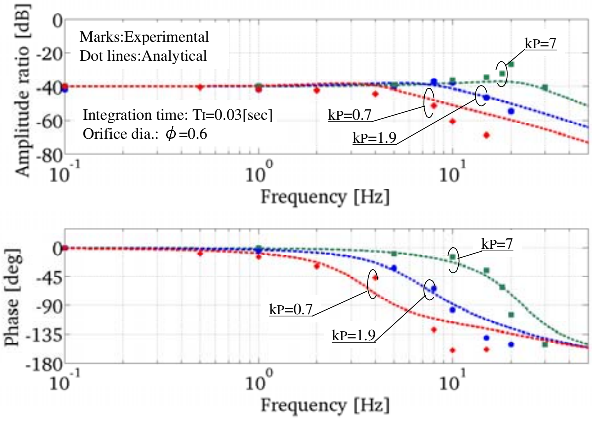

Figure 6 Effect of proportional gain

Generally, a proportional control valve is used with a frequency of approximately 10 Hz or less; however, according to the results obtained in this experiment, the responsiveness of this valve can be improved, where a frequency is approximately 20 Hz at the resonant point, by controlling the proportional gain, and the scope of application to the system can be expected to expand.

Effect of Integral Time

Figure 7 shows an example of the experimental results and the analytical results on frequency characteristics of integral time ranging from 0.1 to 0.01 [T_I, sec]. Other common conditions are as follows: damping restriction diameter of φ = 0.6 and proportional gain of k_P = 7. As a comparison, the experimental results obtained in the case of T_I = 0.03 [sec] are also plotted.
The results show that there is no significant change in the characteristics when T_I is 0.1 to 0.03 [sec], but the resonant peak increases and phase lag tends to increase when T_I is between 0.03 and 0.01 [sec]. By decreasing the integral time, resonance is more likely to occur, but the phase lag improves to be measured at a higher frequency.
Therefore, the results show that integral time has effect on frequency characteristics.

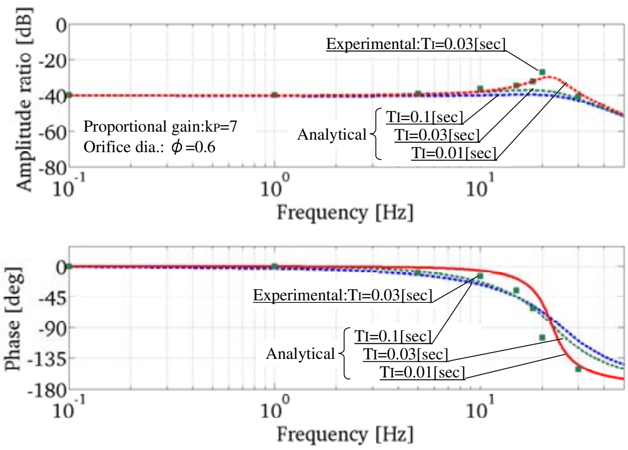

Figure 7 Effect of integral time

Effect of Damping Restriction

Figure 8 shows the results on the effect of damping restriction on frequency characteristics. The restriction diameter is φ = 0.45 and φ = 0.6, and other common conditions are as follows: proportional gain of k_P = 1.9 and integral gain of T_I = 0.03 [sec]. The experimental results show that the resonant frequency shifts to a lower frequency as the orifice diameter is smaller, indicating that damping force has an effect on frequency characteristics.
As a restriction hole diameter is smaller, the responsiveness shifts to be in the lower frequency range and the resonance is observed in the characteristics. The

reason for this result is considered to be that, as the frequency rises, the quantity of flow through the restriction increases and has more effect on the damping force, and additionally that the redundant damping force is yielded with respect to the integration constant, as expressed in Fig. 8.

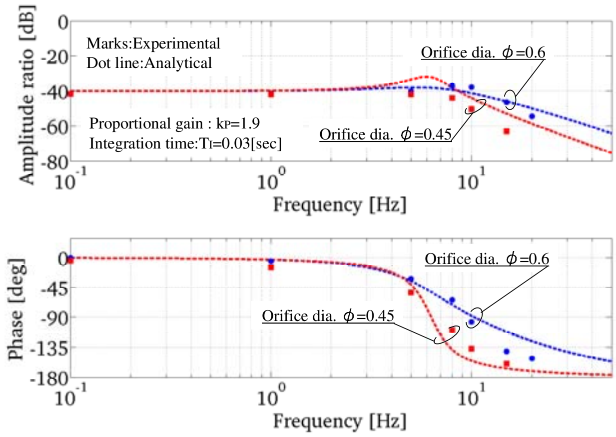

Figure 8 Effect of damping restriction

CONCLUSIONS

The following results are obtained by the experimental and analytical verification of the effects of various parameters of the water hydraulic solenoid proportional valve on frequency characteristics:

(a) The responsiveness can be improved, where a frequency is approximately 20 Hz at the resonant point, by controlling the proportional gain, and the scope of the application to the system can be expected to expand.

(b) By decreasing the integral time, resonance is more likely to occur, but the phase lag can be improved to be measured at a higher frequency.

(c) The resonant point shifts to a lower frequency as the damping restriction becomes smaller, and the valve has a meter-out circuit for hydraulic system connected to the pressure chambers controlling the spool operation, and therefore an effective damping action can be achieved despite low viscosity.

According to the above results indicating that parameters, such as proportional gain, integral time, and damping restriction, have effect on frequency characteristics, effective design policies are defined to further improve valve performance and achieve system optimization.

REFERENCES

1. Takahashi, T., Yamashina, C., Miyakawa, S., Development of Water Hydraulic Proportional Control Valve, the Fourth JHPS International Symposium on Fluid Power, ISBN4-931070-04-03.
2. Yoshida, F., Miyakawa, S., Characteristics of Proportional Control Valve Using Tap Water, the 7th International Fluid Power Conference, Group H, 445-456, 22-24 March 2010, Aachen , Germany.
3. Yoshida, F., Miyakawa, S., Dynamic Characteristics of Proportional Control Valve Using Tap Water - Experimental Examination-, the Twelfth Scandinavian International Conference on Fluid Power, Vol.2 469-480, 18-20 May 2011, Tampere, Finland.

Proceedings of the 8th JFPS International
Symposium on Fluid Power, OKINAWA 2011
Oct. 25-28, 2011

2C4-4

WATER HYDRAULIC HIGH-SPEED SOLENOID VALVE AND ITS APPLICATION

Akihito MITSUHATA*, Canghai LIU*, Ato KITAGAWA* and Masato KAWASHIMA**

* Department of Mechanical and Control Engineering, Graduate school of science and engineering
Tokyo Institute of Technology
2-12-1 Ookayama, Meguro, Tokyo, 152-8550 Japan
(E-mail: mitsuhata@cm.ctrl.titech.ac.jp)
** Tohoku Steel Co., Ltd., Japan
23, Nishigaoka, Ooazamurataaza, Murata, Shibata, Miyagi, 989-1393 Japan

ABSTRACT

This study aims at the optimization of an attenuator and the improvement of linearity of the main flow rate of water for Water Hydraulic High-speed Solenoid Valve. In this study, the parameters of optimum attenuator are defined, and verified experimentally. And the experiment of position control using a water hydraulic cylinder is performed to confirm whether the control performance is improved by the new HSSV. Though proportional poppet and attenuator improved the pressure oscillation of the control chamber, the linearity of main flow rate of water became worse than before changing the structure. In this study, the linearity of main flow rate of water is improved by adjusting a shape of control window which controls the pilot flow rate of water. Effect of new shape of window is verified experimentally.

KEY WORDS

Key words, Water hydraulics, Poppet valve, High speed solenoid valve, Attenuator

NOMENCLATURE

Q	: Pilot flow rate	[L/min]
C	: Flow coefficient of pilot valve	[－]
A	: Cross sectional area of pipeline	[mm^2]
p_s	: Supply pressure	[MPa]
p_a	: Pressure in attenuator	[MPa]
ρ	: Density of water	[kg/m^3]
V	: Volume of attenuator	[cm^3]
K_e	: Equivalent bulk modulus	[GPa]
t	: Time	[s]

INTRODUCTION

Recently, there has been great interest in the water hydraulic systems because they are not harmful to the environment. As a flow control valve of the water hydraulic systems, which have as high dynamic performance as the oil hydraulic systems, a PWM controlled water hydraulic high-speed solenoid valve (HSSV hereafter) with a two-stage mechanism has been developed by Park *et al* [1], which is shown in Fig.1. The flow characteristic of the main valve corresponding to the PWM duty ratio is linear because the main poppet valve repeats an on-off motion according to PWM signals. The on-off motion of the main poppet valve

strikes at the poppet seat and at its stroke end once every cycle of the PWM signal. Resultantly, large noise and shock are generated. To reduce that, an attenuator and proportional poppet has been applied by Minematsu *et al* [2].
In this paper, the optimum attenuator is built. In addition, the experiment of position control is performed using HSSV having the optimum attenuator for the best control performance.
Also, though proportional poppet and attenuator reduced noise and shock, the linearity of the flow rate characteristic is sacrificed to some degree. A new shape of the window of control orifice to improve the linearity of main flow rate and to reduce the noise simultaneously is introduced.

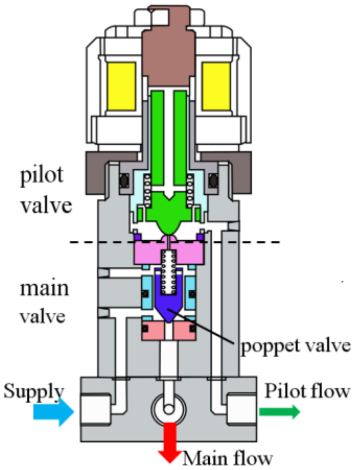

Figure 1 Water hydraulic HSSV

OPTIMIZATION OF ATTENUATOR

In this section, the optimum attenuator is defined as the smallest chamber which makes the main poppet valve not to hit the valve seat in all duty ratios. The optimization is necessary because the rapid response of the main poppet valve and the reduction of pressure oscillation in control chamber are a trade-off. The larger the attenuator is, the worse the response of the main valve is.
Figure 2 shows the experimental circuit. HSSV is divided into the pilot valve and the main valve. Attenuator, orifice, and control chamber are inserted between the pilot valve and the main valve. Displacement of the main valve is experimentally measured using the valve with attenuator and control chamber of various sizes. In this experiment, PWM signal whose duty ratio is less than 50% is given under the supply pressure of 10MPa.

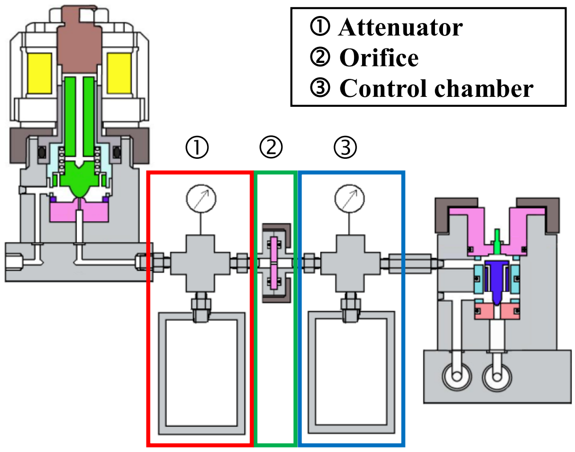

Figure 2 HSSV with attenuator for experiment

Under the conditions shown in Tabel 1, the displacement of the main valve is measured. Appropriate size of the attenuator and the control chamber which enable to reduce the pressure oscillation is verified in Measurement 1 to 5. The diameter of the orifice used in this experiment is 0.6mm.

Table 1 Conditions of Measurements 1 to 7

	Volume of control chamber [ml]	Volume of Attenuator [ml]
Meas 1	170	0
Meas 2	0	170
Meas 3	340	0
Meas 4	0	340
Meas 5	170	170
Meas 6	0	170
Meas 7	0	340

Figure 3 and 4 show the results of measurements 1 to 5. The volume of the attenuator influences the reduction of pressure oscillation in the control chamber. Meanwhile, the volume of the control chamber doesn’t reduce that sufficiently. From these results, only the attenuator is larger, it is possible to reduce the pressure oscillation.
Figure 5 shows the results of measurements 6 and 7. The pressure oscillation in measurement 7 using the larger volume is smaller than that of in 6. From this measurement, it is concluded that the larger the volume of the attenuator is, the smaller the pressure oscillation in the control chamber is. Meanwhile, the rising time of the main poppet valve of measurement 7 is 20ms longer than that of measurement 6 as shown in Fig.6.
Therefore, the optimum attenuator is revealed by increasing the volume of the attenuator gradually. As shown in Fig.7, it was revealed that the volume of the

optimum attenuator is 200ml. In this case, the main poppet valve doesn't hit the valve seat even in low duty ratio.

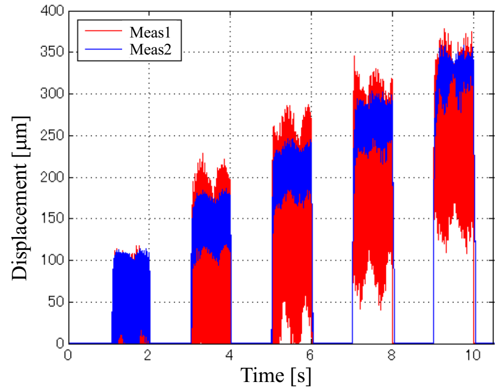

Figure 3 Results of measurements 1 and 2

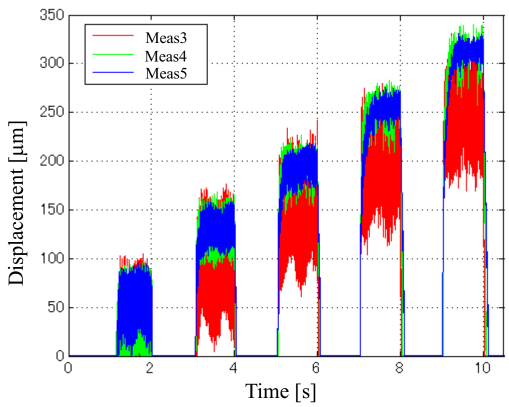

Figure 4 Results of measurements 3, 4 and 5

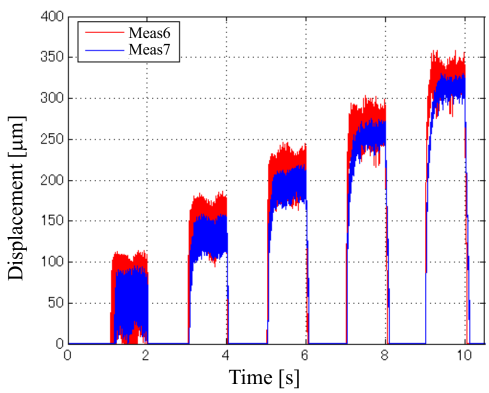

Figure 5 Results of measurements 6 and 7

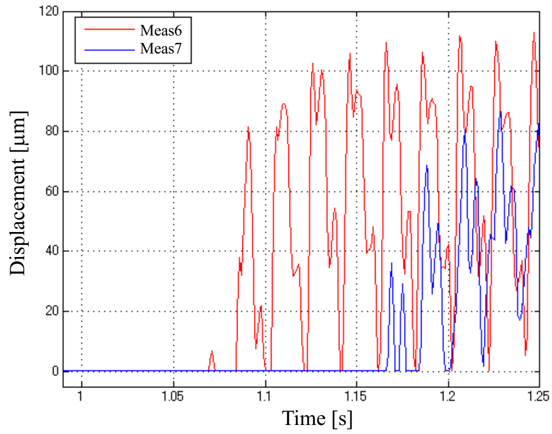

Figure 6 Comparison of displacement response

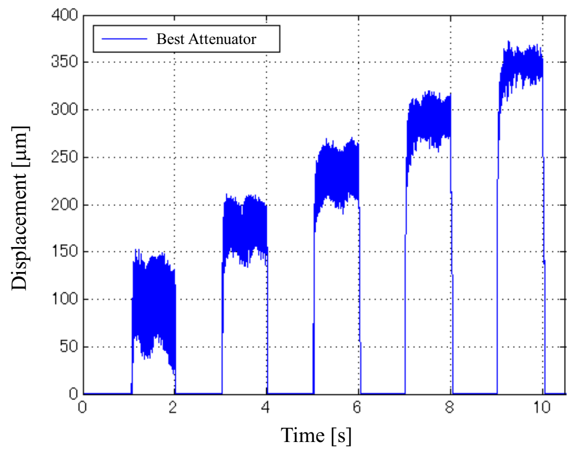

Figure 7 Displacement of main poppet with optimum attenuator

Although the volume of the attenuator is optimized, this volume is too large. If the volume of water in the attenuator increased ΔV, the rising pressure Δp can be determined from the volume of the attenuator V and the equivalent bulk modulus of the attenuator K_e. In this study, Δp is reduced by making the volume of the attenuator larger. Therefore, such a large volume is necessary.
This is explained through the following equations and an experiment.
The flow rate passing through the pilot valve is given by

$$Q = CA\sqrt{\frac{2(p_s - p_a)}{\rho}} \qquad (1)$$

The flow rate considering the equivalent bulk modulus of the attenuator K_e is expressed as

$$Q = \frac{V}{K_e}\frac{dp_a}{dt} \quad (2)$$

Using Eq. (1) and Eq. (2), the pressure response in the attenuator p_a can be expressed as in Eq. (3).

$$p_a = p_s - \frac{1}{4}\left(\frac{CAK_e}{V}\sqrt{\frac{2}{\rho}}\,t - 2\sqrt{p_s}\right)^2 \quad (3)$$

The pressure response in the attenuator p_a was acquired in the experiment. Figure 8 shows the experimental setup. The experiment was performed under 10MPa. Figure 9 shows the result.

By calculating from the equations and the result of the experiment, the equivalent bulk modulus of the attenuator K_e is 1.15GPa. The large volume of the attenuator is necessary to reduce the pressure oscillation in the control chamber because of its large bulk modulus. The volume of the attenuator is able to be reduced by reducing the bulk modulus of the attenuator.

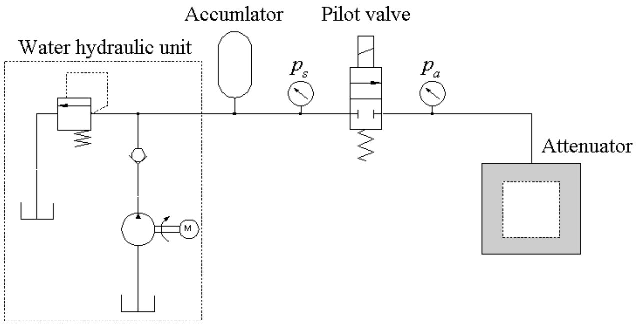

Figure 8 Experimental setup

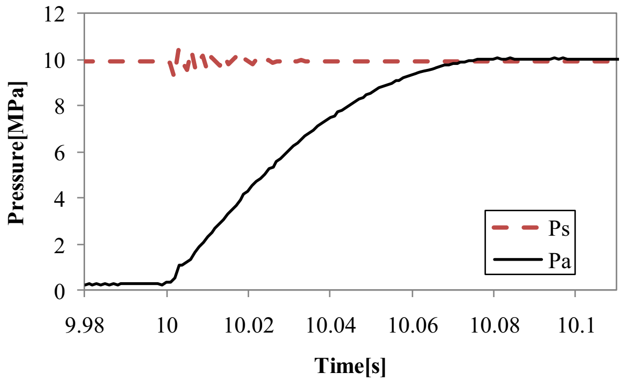

Figure 9 Pressure response

POSITION CONTROL OF WATER HYDRAULIC CYLINDER USING THE NEW VALVE

Position control experiment of water hydraulic cylinder under supply pressure of 10MPa has been performed to measure control performance and to estimate the effect of the improvement of HSSV.

Figure 10 shows the experimental setup. The cylinder has a single rod and its pressurized area ratio is 1:2. An accumulator is connected to the rod-side chamber of the cylinder. HSSV is connected to the inlet of head-side chamber of the cylinder, and the orifice whose diameter is 1.1mm is also connected to it. The cylinder moves according to the flow rate supplied from HSSV. In this experiment, a step signal or stationary signal is given as a reference, and the position of cylinder is controlled by PI control method.

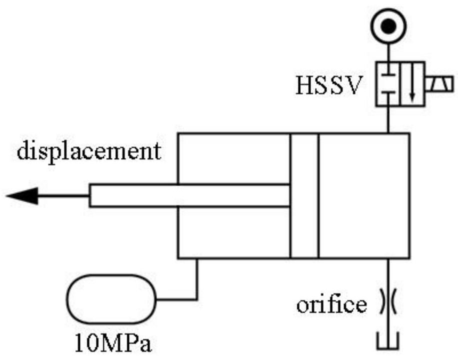

Figure 10 Experimental setup

Figure 11 shows stationary responses of the cylinder. Comparing new HSSV and original HSSV, the response of cylinder is steady with the first one, since there is a difference in pulsation amplitude of the main flow in low duty ratio between valves. In original HSSV (without attenuator), the main valve hits the valve seat in low duty ratio. Therefore, the pulsation amplitude of main flow is larger and the position of cylinder becomes unstable. On the other hand, in new HSSV (with attenuator), the pulsation amplitude of the main flow is small because main valve does not hit the valve seat. As a result, the stationary response of cylinder is stable.

Figure 12 and 13 show step responses of the cylinder. By original HSSV, response of the cylinder shows vibration because of the large pulsation, and because of the long periodical oscillation too. On the other hand, by new HSSV, the response is steady but it is a little lower than the reference, since a certain amount of water constantly flows out from the orifice. Therefore, its position is a little lower than reference.

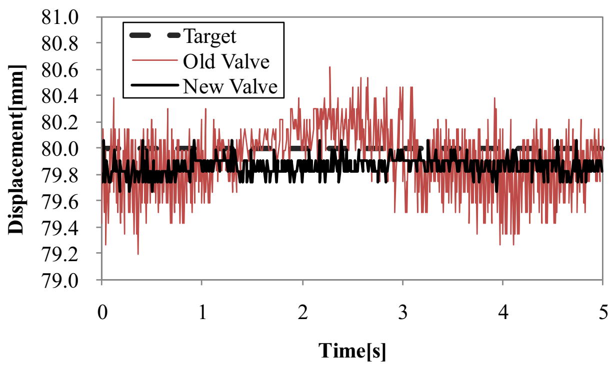

Figure 11 Comparison of displacement response

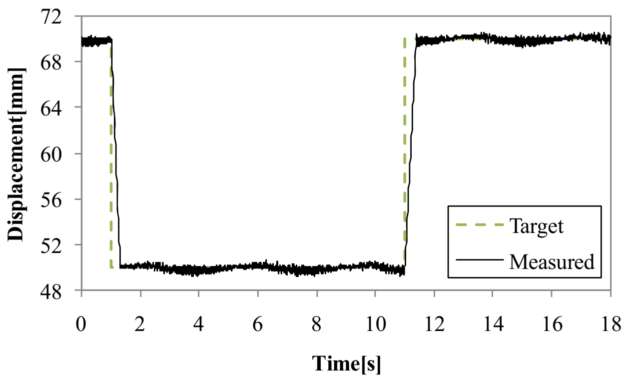

Figure 12 Step Response by HSSV without attenuator

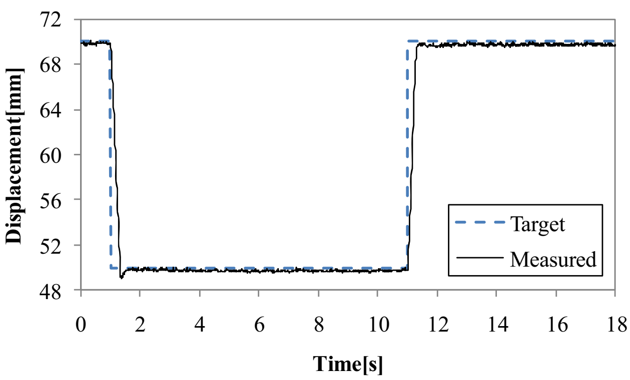

Figure 13 Step Response by HSSV with attenuator

CONSIDERATION OF MUTUALITY BETWEEN DISPLACEMENT OF MAIN POPPET VALVE AND PILOT FLOW RATE

As shown in Fig.1, the HSSV is composed of a main valve and a pilot valve. The pilot valve is controlled by a PWM signal, which supplies a pilot flow rate according to the duty ratio of PWM signal. Displacement of the main poppet valve which generate main flow rate corresponds to the pilot flow rate. As shown in Fig.14, pilot flow is composed of the leakage which passes through the clearance between the sleeve and the main poppet, and the control flow provided from the control window. Leakage through the clearance is constant.
Therefore, the displacement of the main poppet valve corresponds to the opening area of the control orifice which supplies the control flow.

So, it is possible to adjust the displacement of main poppet by adjusting the shape of control window.
Concept of displacement and control window of main poppet is shown in Fig.15. The smaller the width of control window is, the higher the displacement of main poppet is.

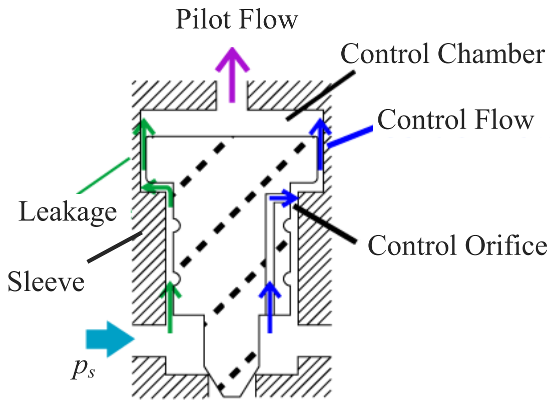

Figure 14 Water flow around main poppet

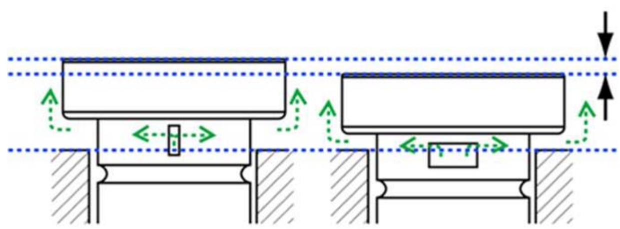

Figure 15 Relationship between displacement of main poppet and width of control window

MEASUREMENT OF THE MAIN FLOW RATE USING THE MAIN POPPET VALVE WITH THE NEW CONTROL WINDOW

As shown in Fig.16(b), a new built main poppet valve is manufactured, which improves the linearity of the main flow rate.
The main flow rate has been measured using new HSSV and original HSSV under supply pressure of 10MPa (Fig.17). Comparing the main flow rate by original HSSV and by new HSSV, the latter is a little larger than

the former because of accuracy of fabrication. However, the linearity of the main flow rate by new HSSV is improved in whole duty ratio.
It was revealed that the linearity of the main flow rate is able to be improved by adjusting the shape of the control window and the displacement of the main poppet valve.

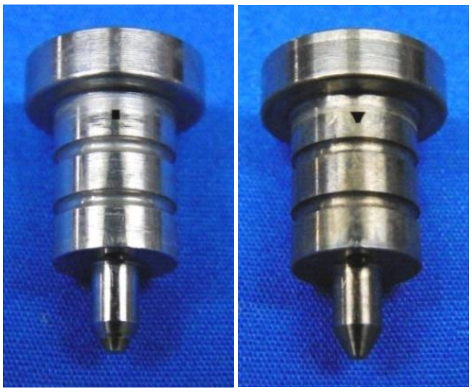

(a) Original window   (b) New window
Figure 16 Control window of main poppet

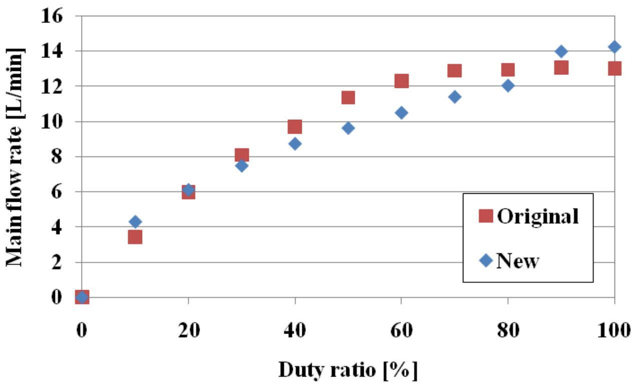

Figure 17 Average main flow rate by duty ratio

CONCLUSION

The optimum attenuator is investigated, and the smallest possible attenuator with which the poppet does not hit the valve seat has been developed.
From the experiment of position control of a water hydraulic cylinder, it is revealed that the position of actuator follows the reference accurately by the improvement of HSSV discussed in this study.
Method of adjusting the shape of control window of main poppet has been proposed to improve the linearity of main flow rate of HSSV. The main flow rate of HSSV with new shape of control window was measured. As a result, the improvement of linearity of main flow rate by adjusting the shape of control window has been verified.

REFERENCES

1. Park, S.H., Kitagawa, A. and Kawashima, M., Water Hydraulic High Speed Solenoid Valve (Part1: Development and Static Behavior), Proceedings of the Institution Mechanical Engineers, Part1, Journal of systems and Control Engineering, 2004, 218, pp.399-409
2. Park, S.H., Kitagawa, A., A Study on Noise and Flow Fluctuation Reduction of Water Hydraulic Two-Stage High Speed Solenoid Valve Using Leakage Flow around the Main Poppet as Pilot Flow, The Japan Society of Mechanical Engineers, Part C , 2005, 71-705, pp.86-93 (in Japanese)
3. Minematsu, S., Kitagawa, A., Liu, C., Fuchigami, K. and Kawashima, M., Study on Proportional Poppet Type 2-stage Water Hydraulic High Speed Solenoid Valve with Attenuator, The Proceedings on Autumn Conference of Japan Fluid Power System Society, 2009, pp.109-111 (in Japanese)

Proceedings of the 8th JFPS International
Symposium on Fluid Power, OKINAWA 2011
Oct. 25-28, 2011

2D1-1

DEVELOPMENT OF COMPLEX HYBRID 3D ROBOT WITH PARALLEL LINKS VIA NONLINEAR PNEUMATIC SERVO SYSTEM FOR PATH TRACKING CONTROL

Mao-Hsiung CHIANG[1] and Hao-Ting LIN[2]

[1] Department of Engineering Science and Ocean Engineering,
National Taiwan University
106 Taipei, Taiwan
(E-mail: mhchiang@ntu.edu.tw)

[2] Department of Engineering Science and Ocean Engineering,
National Taiwan University
106 Taipei, Taiwan
(E-mail: d97525009@ntu.edu.tw)

ABSTRACT

This study aims to develop a complex hybrid 3D robot with parallel links driven by the nonlinear pneumatic servo system for path tracking control. The mechanical system and the control system are the primary parts for developing a complex hybrid 3D robot. In the mechanical system, a complex hybrid 3D robot contains serial manipulators, parallel links, base plates, a movable platform and a pneumatic servo system. Based on the structure design theory of the robot mechanism, the structure is analyzed and the end-effector of the robot can move a 3D motion in the X-Y-Z coordinate system. According to the characteristics of the mechanism, the inverse kinematics and the forward kinematics of the robot are proposed by the coordinate transformation theory. The pneumatic actuators for the three axes are modeled by including the dynamics of the pneumatic servo valve and the cylinder. In the control system, the control scheme is applied to follow the computed trajectory for real-time control. In order to improve path tracking accuracy for a complex hybrid 3D robot, a Fourier series-based adaptive sliding mode controller with H∞ tracking performance (FSB-ASMC+ H∞) is proposed for controlling the pneumatic flows acting on the pistons of the actuators. The proposed controller first employs a Fourier series-based functional approximation technique to estimate the dynamic models and time-varying uncertainties of the system. Next, further efforts are made to improve the dynamic tracking performance by combining the H∞ tracking strategy with an adaptive sliding -mode control method to make the derived controller robust against approximation errors, un-modeled dynamics and disturbances. To verify the usefulness, simulations and experiments are carried out on a complex hybrid 3D robot based on the proposed methods. The results show that the complex hybrid 3D robot is successfully implemented with different path tracking profiles.

KEY WORDS

industrial robot, parallel mechanism, pneumatic system, kinematics analysis, path tracking control

INTRODUCTION

As labor wages increase rapidly, more and more countries have developed various kinds of robots to make our lives much easier. Robot is a kind of mechanism which can operate automatically with its components and programs. Robots are widely used in automobile, mechanical, semiconductor, electronic, and food and beverage industries, and have gradually replaced the labor force [1]. In these industries the predominant robots used are called “industrial robots,” which consists of serial type robots and parallel type robots. The serial type robot which consists of links sequentially connected forming an open chain, due to its components’ structure and placement, is able to operate within a much larger scope, and has high flexibility. However, the serial type robot has some intrinsic disadvantages such as the low accuracy affected by the accumulated errors at each joint and links, and the poor stiffness for handling heavier loads. On the contrary, the parallel type robot which has the end-effector connected to the fixed base by multiple kinematic chains has high ratio of rigidity to weight, high stiffness, high accuracy, and is able to carry heavier loads. The main drawbacks of the parallel type robot have a smaller workspace because of its structural design, complex kinematics analysis, and the closed-loop architecture [2-4, 15]. As a result, in order to complement human workers, the characteristics of high response, high accuracy and good stiffness are necessary for the robots. In recent years, for many applications, parallel type robots which represent an approach to accomplish many of these needs have become more popular in the industries due to their advantages over serial type robots, for example, high stiffness, high motion accuracy and high load-structure ratio [20-21].

Having been developed since 1950s, the pneumatic actuator system has become one of the most common actuators and been widely used in the industries, such as automation systems, which, for actuators, emphasize reliability, cost, cleanness, simplicity, easy maintenance and safety in operation. In recent years, the accessibility of low-cost microprocessors and pneumatic components has made the use of more complicated control methods in pneumatic system control possible. Many researchers, hence, have started using pneumatic actuators, such as servo-controlled pneumatic systems [16-19], to work on more complicated motion control tasks and are quite suitable to be applied in robotic fields [5-7]. Although a pneumatic actuator is inexpensive and simple, when compared with electro-mechanical actuators of equal power, it is still not competitive in a few applications that demand accuracy, versatility, and flexibility. This is due to some inherent disadvantages of a pneumatic actuator, including its nonlinearity, its low natural frequency resulting from low stiffness of the air compressibility, and its complexity in control because of its low damping associated with nonlinearities, time-varying effects, and position dependency. As a result, the pneumatic servo system which is a highly nonlinear system and hard to acquire accurate mathematic models [9] result in the pneumatic servo control much more complicate.

Research in the field of pneumatic servo control has been developed in 1960s. Some control algorithms like PID, state-space and adaptive control in pneumatic servo systems were developed via higher speed microcomputers in the 1980s. In recent years, due to the development of modern control theories, the problems of the pneumatic servo control have gradually been solved [10-12] [14]. The sliding-mode control (SMC) method has been adopted to handle system nonlinear behaviors, model uncertainty, and bounded disturbances [22-23]. However, the conventional SMC method is model-based and, hence, is dictated by a varying system model and uncertain parameter values of the system in designing a controller. To deal with these uncertainty problems, several Fourier series-based functional approximation techniques have been used. Huang *et al.* [24] suggested an adaptive sliding controller using a Fourier series-based functional approximation technique to handle a nonlinear system containing time-varying, uncertain parameters. Tsai and Huang [13] proposed a FAT-based adaptive controller for pneumatic servo systems with variable payload and uncertain disturbances. Chiang *et al.* [8] proposed a Fourier series-based adaptive sliding-mode controller with H_∞ tracking performance (FSB-AFSMC+ H_∞) for the rod-less pneumatic cylinder system. The proposed method not only is robust against approximation errors, disturbances, and un-modeled dynamics but also guarantees a desired H_∞ tracking performance for the overall system.

The aim of the present paper is to develop and implement a complex hybrid 3D robot with parallel links via nonlinear pneumatic servo system for path tracking control. In this paper, the structure of this complex hybrid 3D robot is shown. This paper describes a complex hybrid 3D robot with three vertical rod-less pneumatic cylinders combined with parallel links, such that the end-effector moves in a three dimensional coordinate system via path tracking control. Then, the kinematic analysis methods are proposed. As to the robot structure, it is designed by vertical rod-less pneumatic cylinders with parallel links, so that it is hard to calculate the kinematics of the robot. Thus, a kind of robotic coordinate system- Denavit-Hartenberg notation (D-H notation) coordinate system is proposed for solving the kinematics of the robot which includes forward kinematics and inverse kinematics. Also, the continuous path tracking control algorithm is proposed. Because the rod-less pneumatic cylinder have high nonlinearities, the accurate mathematic models of the servo pneumatic system are hard to obtain, so that it is quite difficult for path tracking control. Therefore, the intelligent controller based on a Fourier Series-based adaptive sliding mode controller with H_∞ tracking performance is proposed. The results show that the proposed complex hybrid 3D robot with parallel links via nonlinear pneumatic servo system was implemented and verified experimentally.

TEST RIG LAYOUT

The test rig layout was set up as shown in Figures1 and 2. The test system which was a three-degree-of-freedom hybrid parallel robot with parallel links via nonlinear pneumatic servo system for path tracking control is presented in this paper. The complex hybrid 3D robot primarily comprised the mechanical part and the pc-based control unit part. In the mechanical part, a complex hybrid 3D robot consisted of a three axes parallel mechanism robot which had three vertical axes arranged at 120° to each other with parallel links for end-effector in a three dimensional motion, and a pneumatic servo system which was a driving device for driving the robot with a pneumatic source, rod-less pneumatic cylinders, and proportional servo valves. The rod-less pneumatic cylinder, model DGC-25-500 FESTO AG, with a piston diameter of 25mm and a stroke of 500mm was used for three vertical axes. The proportional servo valve was made by FESTO AG with model MPYE-5-M5-010-B for each vertical axis. In the pc-based control unit part, experimental software, optical linear scales, an AD/DA interface card and a counter card were included. The air pressure was set up as five bars and the pc-based control unit part via AD/DA interface card controlled pneumatic servo valves to proper the robot. The end-effector moved in the three dimensional motion via parallel links driven by rod-less pneumatic cylinders. In addition, optical linear scales with resolution of 0.1μm were necessarily installed for each vertical axis to measure the loading mass's position that was the sum displacement of the pneumatic cylinder. The measured signals of the optical linear scales were fed back to pc-based control unit part via a counter card. The pc-based control unit part was implemented on a PC with interface cards which contained an AD/DA interface card and a counter card. The control signals of the proportional servo valves were from the pc-based control unit part with the sampling time of 1ms via an AD/DA interface card, and the control law was computed by a 32-bit Open Watcom C language program.

SYSTEM ANALYSIS

Because of the development of high technology, the fast motion and precisely accurate plate are demanded. In this paper, the complex hybrid 3D robot with parallel links via nonlinear pneumatic servo system for path tracking control was implemented. The robot which was driven by three vertical rod-less pneumatic cylinders can make the end-effector move a 3D motion in the X-Y-Z coordinate system that perform high precision,

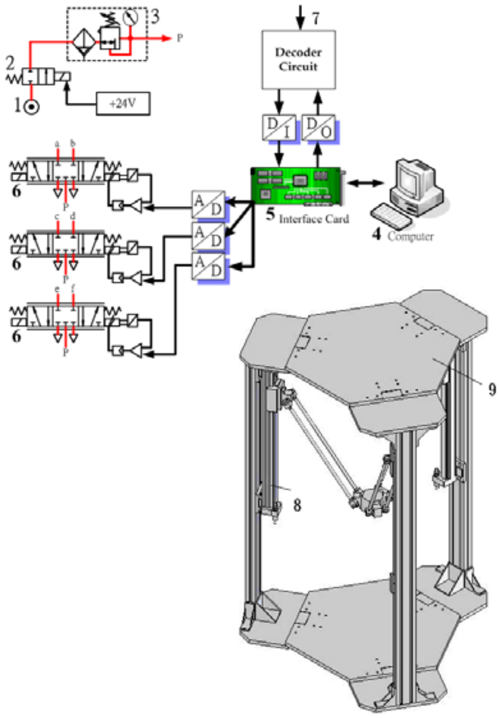

1.Air Source	2.Valve	3.Air Preparation Unit
4.Pc-Based Controller	5.Interface Card	6.Proportional Servo Valve
7.Optical Linear Scale	8.Rod-less Pneumatic Cylinder	9.Complex Hybrid 3D Robot

Figure 1 The layout of the complex hybrid 3D robot

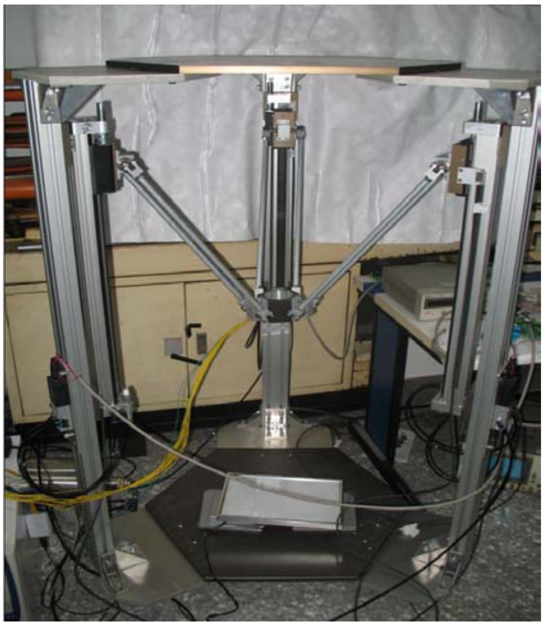

Figure 2 Prototype of the complex hybrid 3D robot

stiffness and high response. Furthermore, the robot consisted of a movable platform through three parallel links connected to the three vertical pneumatic cylinders. Each chain contained a link and joints activated by a rod-less pneumatic cylinder. The motion of the end-effector on the movable platform was transmitted through three chains with links, joints and actuators. In this section, kinematics of the complex hybrid 3D robot, dynamic models of the pneumatic servo system and controller design are presented.

Kinematics Analysis

The complex hybrid 3D robot contains a movable platform connected to a base plate through three parallel kinematic chains activated by the vertical pneumatic actuators. The motion of the mobile platform is transmitted by links and joints. In order to analyze the kinematic model of the robot, D-H notation [25] was used to resolve the geometric relation and acquired the inverse and forward kinematics. Figure 3 showed the coordinate frames of the system. P0 to P7 are denoted by different coordinate frames.

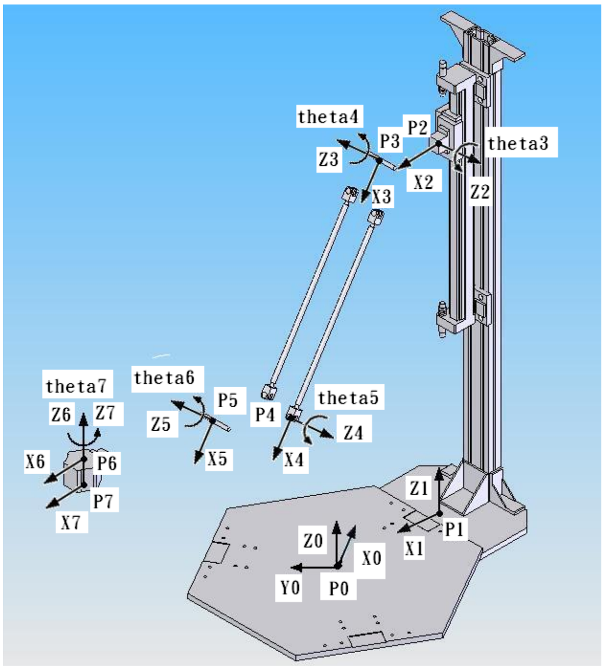

Figure 3 the coordinate frames of the complex hybrid 3D robot with parallel links via nonlinear pneumatic servo system

(a) Inverse Kinematics

The inverse kinematics analysis is mainly that given the pose of the end-effector of the moveable platform in a Cartesian space to calculate all possible set of actuated inputs and joint angles that achieve that given pose. In the inverse kinematic model, the inverse kinematics can be stated as that given the end-effector pose and the parameters of the robot, find the actuators moving. In order to analyze the inverse kinematics, the D-H notation method is used for solving the relationship of the elements on this system. The D-H notation transformation is described by the following four parameters

a_i : the distance from $\hat{Z}_i$ to $\hat{Z}_{i+1}$ measured along $\hat{X}_i$

α_i : the angle from $\hat{Z}_i$ to $\hat{Z}_{i+1}$ measured about $\hat{X}_i$

d_i : the distance from $\hat{X}_{i-1}$ to $\hat{X}_i$ measured along $\hat{Z}_i$

θ_i : the angle from $\hat{X}_{i-1}$ to $\hat{X}_i$ measured about $\hat{Z}_i$

The link transformations which define that frame {i} is relative to the frame {i-1} will be a function of the four parameters. We obtain the general form of ${}^{n-1}T_n$:

$$
{}^{n-1}T_n = \begin{bmatrix} \cos\theta_i & -\sin\theta_i & 0 & a_{i-1} \\ \sin\theta_i\times\cos\alpha_{i-1} & \cos\theta_i\times\cos\alpha_{i-1} & -\sin\alpha_{i-1} & d_i\times(-\sin\alpha_{i-1}) \\ \sin\theta_i\times\sin\alpha_{i-1} & \cos\theta_i\times\sin\alpha_{i-1} & \cos\alpha_{i-1} & d_i\times\cos\alpha_{i-1} \\ 0 & 0 & 0 & 1 \end{bmatrix}
$$

Then, the link transformations can be multiplied together to find the single transformation that relates frame {N} to frame {0}:

$$
{}^{0}_{N}T = {}^{0}_{1}T\,{}^{1}_{2}T\,{}^{2}_{3}T\ldots{}^{N-1}_{N}T
$$

${}^{0}_{N}T$ is a function of all n joint variables and the Cartesian pose of the last link will be computed. Table 1 shows the link parameters of the complex hybrid 3D robot. As a result, let P7 be an end-effector located on the moving platform, and then the mathematic models of this system in the inverse kinematics have three chains kinematics as follows

A chain kinematics:

$$
({}^{0}_{7}T)_A = ({}^{0}_{1}T)_A({}^{1}_{2}T)_A({}^{2}_{3}T)_A({}^{3}_{4}T)_A({}^{4}_{5}T)_A({}^{5}_{6}T)_A({}^{6}_{7}T)_A
$$

B chain kinematics:

$$
({}^{0}_{7}T)_B = ({}^{0}_{1}T)_B({}^{1}_{2}T)_B({}^{2}_{3}T)_B({}^{3}_{4}T)_B({}^{4}_{5}T)_B({}^{5}_{6}T)_B({}^{6}_{7}T)_B
$$

C chain kinematics:

$$
({}^{0}_{7}T)_C = ({}^{0}_{1}T)_C({}^{1}_{2}T)_C({}^{2}_{3}T)_C({}^{3}_{4}T)_C({}^{4}_{5}T)_C({}^{5}_{6}T)_C({}^{6}_{7}T)_C
$$

Table 1 Link parameters of the complex hybrid 3D robot

	A chain				B chain				C chain			
	a_{i-1}	α_{i-1}	θ_i	d_i	a_{i-1}	α_{i-1}	θ_i	d_i	a_{i-1}	α_{i-1}	θ_i	d_i
$P_0 \Rightarrow P_1$	$-R$	150^0	0^0	0	$-R$	30^0	0^0	0	$-R$	-90^0	0^0	0
$P_1 \Rightarrow P_2$	a	0^0	-90^0	hA	a	0^0	-90^0	hB	a	0^0	-90^0	hC
$P_2 \Rightarrow P_3$	0	θ_{A3}	90^0	0	0	θ_{B3}	90^0	0	0	θ_{C3}	90^0	0
$P_3 \Rightarrow P_4$	L	θ_{A4}	180^0	0	L	θ_{B4}	180^0	0	L	θ_{C4}	180^0	0
$P_4 \Rightarrow P_5$	0	θ_{A5}	-90^0	0	0	θ_{B5}	-90^0	0	0	θ_{C5}	-90^0	0
$P_5 \Rightarrow P_6$	r	θ_{A6}	-90^0	0	r	θ_{B6}	-90^0	0	r	θ_{C6}	-90^0	0
$P_6 \Rightarrow P_7$	0	-150^0	0^0	$-b$	0	-30^0	0^0	$-b$	0	90^0	0^0	$-b$

Now, by the link parameters and each chain kinematics, the inverse kinematics of the system can be obtained as follows

$$hA = b + Pz7 + L \times \sin(\theta_{A3}) \times \cos(\theta_{A4}) \quad (1)$$

$$hB = b + Pz7 + L \times \sin(\theta_{B3}) \times \cos(\theta_{B4}) \quad (2)$$

$$hC = b + Pz7 + L \times \sin(\theta_{C3}) \times \cos(\theta_{C4}) \quad (3)$$

$$\theta_{A3} = \cos^{-1}\left(\frac{R - r - a - \frac{\sqrt{3}}{2} \times Px7 + \frac{1}{2} \times Py7}{L \times \cos(\theta_{A4})} \right) \quad (4)$$

$$\theta_{B3} = \cos^{-1}\left(\frac{R - r - a + \frac{\sqrt{3}}{2} \times Px7 + \frac{1}{2} \times Py7}{L \times \cos(\theta_{B4})} \right) \quad (5)$$

$$\theta_{C3} = \cos^{-1}\left(\frac{R - r - a - Py7}{L \times \cos(\theta_{C4})} \right) \quad (6)$$

$$\theta_{A4} = \sin^{-1}\left(\frac{-Px7 - \sqrt{3} \times Py7}{2 \times L} \right) \quad (7)$$

$$\theta_{B4} = \sin^{-1}\left(\frac{-Px7 + \sqrt{3} \times Py7}{2 \times L} \right) \quad (8)$$

$$\theta_{C4} = \sin^{-1}\left(\frac{Px7}{L} \right) \quad (9)$$

where hA, hB, hC are the position of the joint along A、B、C rod-less pneumatic cylinder, b is the distance between the end-effector and the centroid of the load, ($Px7$, $Py7$, $Pz7$) is the pose of the end-effector, L is the length of the parallel link, θ_{A3}, θ_{B3} and θ_{C3} are the joint angle of the P3 on each chain, θ_{A4}, θ_{B4} and θ_{C4} are the joint angle of the P4 on each chain, R is the distance between the centroid of the bottom plate and each rod-less pneumatic cylinder, r is the distance between the centroid of the load and the P5 joint, and a is the width of the slide on the rod-less pneumatic cylinder.

(b) Forward Kinematics

The forward kinematics is to compute the pose of the end-effector of the manipulator from the known set of the actuated inputs to the unknown pose of the output platform. The forward kinematics can be stated as that given the actuators moving and the parameters of the robot, find the end-effector pose. Therefore, by the inverse kinematics, the mathematic models of the forward kinematics can be as follows

$$Px7 = L \sin(\theta_{C4}) \quad (10)$$

$$Py7 = R - r - a - L \cos(\theta_{C4}) \cos(\theta_{C3}) \quad (11)$$

$$Pz7 = hC - b - L \sin(\theta_{C3}) \cos(\theta_{C4}) \quad (12)$$

where the unknown parameters are the location of the end-effector P7=[$Px7$, $Py7$, $Pz7$] to be determined for given joint angles.

Controller Design

In the rod-less pneumatic servo system, the servo valve's orifice opening area depends on the control input to affect the air flow. When the air flows into the rod-less pneumatic cylinder, the pressure difference between two cylinder chambers is caused and results in the motion of the pneumatic cylinder. In order to analyze the rod-less pneumatic servo system, the dynamic models of the rod-less pneumatic servo system are derived. The dynamic models of the pneumatic servo system primarily comprise four parts : the dynamics of the pneumatic servo valve, the mass flow rate of the pneumatic servo valve, the continuity equation and the motion equation. The state equations of the pneumatic servo system is achieved as follows

$$\begin{aligned}
\dot{x}_1(t) &= x_2(t) \\
\dot{x}_2(t) &= \frac{(Ax_3(t) - Ax_4(t))\,\mathrm{sgn}(x_1(t)) - K_f x_2(t) - K_{S-c}(x_1(t))S(x_2(t), x_3(t), x_4(t)) - Mg\,\mathrm{sgn}(x_1(t))}{M} \\
\dot{x}_3(t) &= \frac{-kx_2(t)x_3(t)}{x_1(t) + \Delta} + \frac{kRT_s C_d C_0 wu(t) \hat{f}(x_3(t), P_s(t), P_e(t))}{A(x_1(t) + \Delta)} \\
\dot{x}_4(t) &= \frac{kx_2(t)x_4(t)}{l - x_1(t) + \Delta} + \frac{kRT_s C_d C_0 wu(t) \hat{f}(x_4(t), P_s(t), P_e(t))}{A(l - x_1(t) + \Delta)}
\end{aligned} \quad (13)$$

where

A : Piston area (m^2) ,	$P_e = 1 \times 10^5$: Exhaust pressure (N/m^2)
C_d =0.8: Discharge coefficient,	$P_s = 5 \times 10^5$: Supply pressure (N/m^2)
C_0 : Flow constant,	T_s =293 : Cylinder air temperature (K)
Δ :The general residual chamber volume,	k =1.4 : Specific heat constant
K_f : Viscous frictional coefficient,	V : Volume (m^3)
P_{atm} : Atmospheric pressure (N/m^2),	w : Port width (m)
l : Stroke (m) and $x \in [0, l]$,	M : Payload (kg)
p_r :Ratio between down- and up-stream pressure,	P_u : Up-stream pressure (N/m^2)
$R = 287$:Universal gas constant $J/(kg \cdot K)$,	P_d :Down-stream pressure (N/m^2)

In this study, FSB-ASMC+ H∞ was developed for the pneumatic servo system on each axis to solve the high non-linearity and time-varying problems. The FSB-ASMC+ H∞ contains the Fourier series-based adaptive sliding mode controller and H∞ tracking performance design technique. The Fourier series-based adaptive sliding mode controller can handle the high non-linear and time-varying problems. Furthermore, the H∞ tracking performance design technique is proposed to overcome the function approximation errors, un-modeled dynamics, disturbances, and to reduce the chattering effect affected by sliding control.

A general nonlinear system is shown as follows

$$y(t)^{(n)} = F(\mathbf{x},t) + g(\mathbf{x},t)u(t) \tag{14}$$

where $y(t)$ is the output of the system, $F(\mathbf{x},t)$ and $g(\mathbf{x},t)$ are unknown time-varying function, and $u(t)$ is the control input of the system. The functional approximation technique approximate the functions $F(\mathbf{x},t)$ and $g(\mathbf{x},t)$, and Eq. (14) can be rewritten as

$$y(t)^{(n)} = (\mathbf{W}_F^T \mathbf{q}_F(t) + \varepsilon_F(t)) + (\mathbf{W}_g^T \mathbf{q}_g(t) + \varepsilon_g(t))u(t) \tag{15}$$

where $\mathbf{W}_F^T \mathbf{q}_F(t)$ and $\mathbf{W}_g^T \mathbf{q}_g(t)$ are approximations to the uncertain time-varying functions $F(\mathbf{x},t)$ and $g(\mathbf{x},t)$, and $\varepsilon_F(t)$ and $\varepsilon_g(t)$ are the truncation errors of the approximations of $F(\mathbf{x},t)$ and $g(\mathbf{x},t)$. Define the output error as

$$e(t) = y(t) - y_m(t) \tag{16}$$

where $y_m(t)$ is a given bounded reference signal. The sliding surface is described as

$$s = a_1 e(t) + a_2 \dot{e}(t) + \ldots + e^{(n-1)}(t) \tag{17}$$

where a_i are chosen such that $\sum_{i=1}^{n} a_i \lambda^{i-1}$ is a Hurwitz polynomial. In addition, the H∞ tracking performance design technique is proposed to reduce the chattering effect affected by sliding control. Therefore, the control input is chosen as

$$u(t) = \frac{-\hat{\mathbf{W}}_F^T \mathbf{q}_F(t) - \sum_{i=1}^{n-1} a_i e_{i+1}(t) - \sum_{i=1}^{n-1} p_{(n-1)i} e_i(t) + y_m^{(n)}(t) - \frac{s}{2\rho^2}}{\hat{\mathbf{W}}_g^T \mathbf{q}_g(t)} \tag{18}$$

where $\hat{\mathbf{W}}_F^T$ and $\hat{\mathbf{W}}_g^T$ are the estimations of $\mathbf{W}_F^T$ and $\mathbf{W}_g^T$, $p_{(n-1)i}$ being elements of $\mathbf{P}$ satisfies the Lyapunov matrix equation $\mathbf{A}_1^T \mathbf{P} + \mathbf{P}\mathbf{A}_1 = -\mathbf{Q}$ and $\rho > 0$ is the design constant for attenuation level.

EXPERIMENTS

The objective of this paper is to develop a complex hybrid 3D robot with parallel links via nonlinear pneumatic servo system for path tracking control. In order to confirm the feasibility of the system development, the experiments for the end-effector in different tracking trajectories via a pneumatic servo system are implemented respectively. In this section, a ball trajectory is presented for the path tracking control in the three dimensional motion.

Ball Trajectory

In the ball trajectory experiment, the end-effector moves along a ball trajectory with a specific diameter in the three dimensional space for path tracking control. Figure 4 show the experimental results of the path tracking control for the end-effector in a ball trajectory by FSB-ASMC+ H∞. The end -effector firstly moves from (X, Y, Z)=(0,0,0) to (X, Y, Z)=(0,0,300) in 3 seconds, and then moves along a ball trajectory with a diameter of 200mm in 12 seconds. The desired path and the system response of the end-effector in a ball trajectory are shown in Figure 4(a). Figure 4(b) shows the tracking errors of the end-effector in a ball trajectory, where the maximum tracking errors can reach about 1.5mm. Figure 4(c), Figure 4(f) and Figure 4(i) show the desired paths calculated by the inverse kinematics and the system response for each axis in a ball trajectory. Figure 4(d), Figure 4(g) and Figure 4(j) show the tracking errors for each axis in a ball trajectory, where the maximum tracking errors can reach about 2mm. Figure 4(e), Figure 4(h) and Figure 4(k) show the control signals for each axis in a ball trajectory. Therefore, the desired tracking performance of the end-effector in a ball trajectory can be achieved.

CONCLUSIONS

In this study, a complex hybrid 3D robot with parallel links via nonlinear pneumatic servo system is developed and successfully implemented for path tracking control. In order to implement the motion of the robot, D-H notation is proposed to resolve the kinematics of the robot and a FSB-ASMC+ H∞ controller is developed to overcome the nonlinearities, and the time-varying problems of the pneumatic servo system. For further confirming the viability of the development on the system, the ball trajectory, is implemented experimentally. Finally, the experimental results clarify that the complex hybrid 3D robot with parallel links via nonlinear pneumatic servo system is successfully for path tracking control.

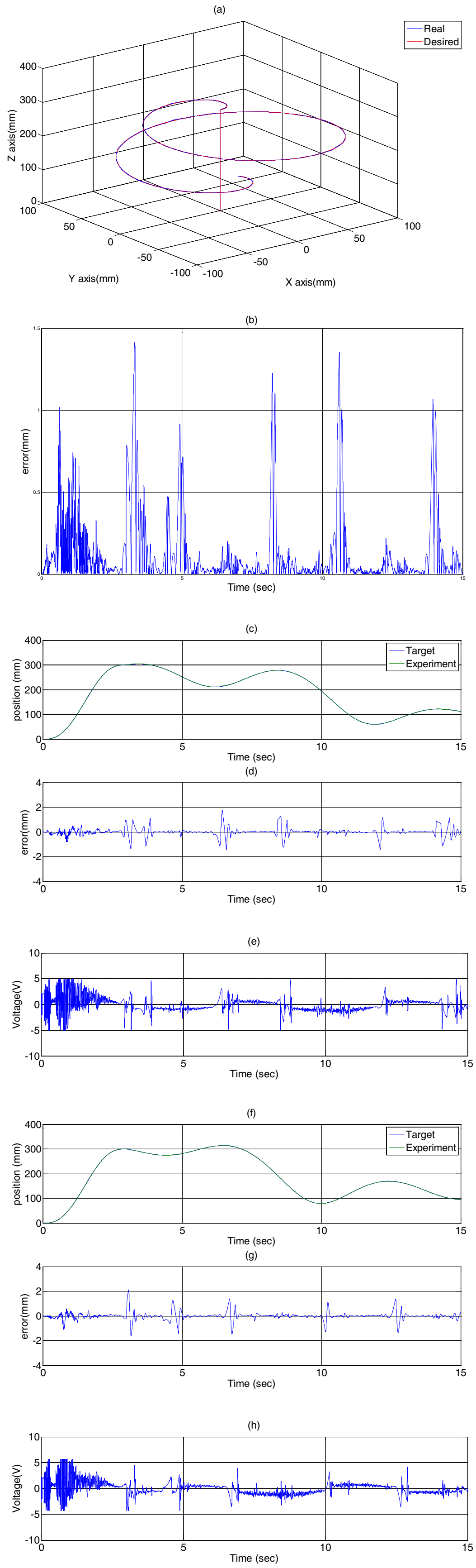

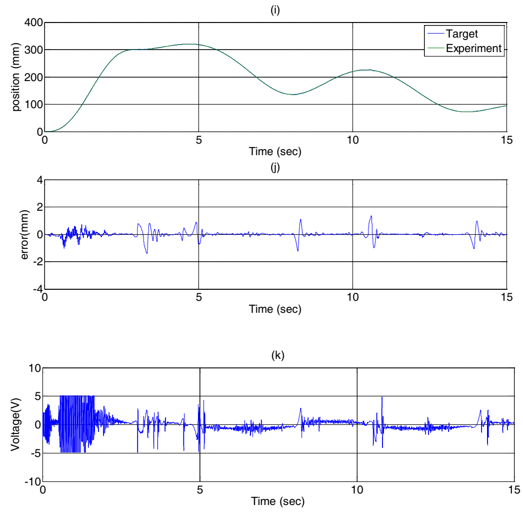

Figure 4 Experimental result of tracking control with ball trajectory (a) system response of an end point (b) tracking error of an end point (c) system response of A-axis (d) tracking error of A-axis (e) control signal of A-axis (f) system response of B-axis (g) tracking error of B-axis (h) control signal of B-axis (i) system response of C-axis (j) tracking error of C-axis (k) control signal of C-axis

ACKNOWLEDGEMENT

This research was sponsored by the National Science Council, Taiwan under the grant NSC 99-2628-E-002-021.

REFERENCES

1. T. Brogardh, Present and future robot control development- An industrial perspective, Annual Reviews in Control 31 (2007) 69-79.
2. J. Wang, X.J. Liu, Analysis of a novel cylindrical 3-DoF parallel robot, Robotics and Autonomous Systems 42 (2003) 31-46.
3. Q. Li, F.X. Wu, Control performance improvement of a parallel robot via the design for control approach, Mechatronics 14 (2004) 947-964.
4. M.A. Laribi, L. Romdhane, S. Zeghloul, Analysis and dimensional synthesis of the DELTA robot for a prescribed workspace, Mechanism and Machine Theory 42 (2007) 859-870.
5. S. KONISHI, M. NOKATA, O.C. JEONG, S. KUSUDA, T. SAKAKIBARA, M. KUWAYAMA, H. TSUTSUMI, Pneumatic Micro Hand and Miniaturized Parallel Link Robot for Micro Manipulation Robot System, in: Proceedings of the 2006 IEEE International Conference in Robotics and

Automation, Orlando, Florida, 2006, pp. 1036-1041.
6. H.-S. Choi, C.-S. Han, K.-y. Lee, S.-h. Lee, Development of hybrid for construction works with pneumatic actuator, Automation in Construction 14 (2005) 452-459.
7. M.-H. Chiang, Development of X-Y Servo Pneumatic-Piezoelectric Hybrid Actuators for Position Control with High Response, Large Stroke and Nanometer Accuracy, Sensors 10 (2010) 2675-2693.
8. M.-H. Chiang, L.-W. Lee, C.-F. J. Kuo, Y.-N Chen, A H ∞ Tracking-Based Adaptive Sliding-Mode Controller for Nonlinear Pneumatic Path Tracking Systems via a Functional Approximation Approach, Journal of the Chinese Society of Mechanical Engineers 24 (5) (2009) 507-515.
9. S. Ning, G. M. Bone, Development of a Nonlinear Dynamic Model for a Servo Pneumatic Positioning System, in: Proceedings of the IEEE International Conference on Mechatronics＆Automation, Niagara Falls, Canada, 2005, pp. 43-48.
10. Z. Rao, G. M. Bone, Nonlinear modeling and control of servo pneumatic actuators, IEEE Transactions on Control System Technology 16 (2008) 562-569.
11. L. Cai, W. Huang, Fourier series based learning control and application to positioning table, Robotics and Autonomous Systems 32 (2000) 89-100.
12. N. Shu, G. M. Bone, High steady-state accuracy pneumatic servo positioning system with PVA/PV control and friction compensation, in: Proceedings of the 2002 IEEE International Conference on Robotics＆Automation, DC, Washington, 2002, pp. 2824-2829.
13. Y.-C. Tsai, A.-C. Huang, FAT-based adaptive control for pneumatic servo systems with mismatched uncertainties, Mechanical Systems and Signal Processing 22 (2008) 1263-1273.
14. Y.-C. Tsai, A.-C. Huang, Multiple-surface sliding controller design for pneumatic servo systems, Mechatronics 18 (2008) 506-512.
15. T.K. Bera, A.K. Samantarat, and R. Karmakar, Robust overwhelming control of a hydraulically driven three-degrees-of-freedom parallel manipulator through a simplified fast inverse model, JSCE 828(2009) 169-184.
16. S. Drakunov, G. D. Hanchin, W. C. Su, and Ü. Özgüner, Nonlinear control of rodless pneumatic servo actuator, or sliding modes versus Coulomb friction, *Automatica,* Vol. 33, pp. 1401-1408, 1997.
17. R. B. Van Varseveld, and G. M. Bone, Accurate position control of a pneumatic actuator using on/off solenoid valves, *IEEE/ASME Trans. Mechatronics,* Vol. 2, pp. 195–204, 1997.
18. J. Wang, J. Pu, P. R. Moore, and Z. Zhang, Modeling study and servo-control of air motor systems, *International Journal of Control,* Vol. 71, pp. 459-476, 1998.
19. J. Wang, J. Pu, and P, R. Moore, A practicable control strategy for servo pneumatic actuator systems, *Control Engineering Practice,* Vol. 7, pp. 1483-1488, 1999.
20. S. G. Robertz, L. Halt, S. Kelkar, K. Nilsson, A. Robertsson, D. Schar and J. Schiffer, Precise robot motions using dual motor control, 2010 IEEE International Conference on Robotics and Automation, Alaska, USA, pp. 5613-5620, May 3-8, 2010.
21. T. Uchiyama, H. Terada and H. Mitsuya, Continuous path control of a 5-DOF parallel-serial hybrid robot, Journal of Mechanical Science and Technology 24 (2010) 47-50.
22. Y. C. Tsai, and A. C. Huang, Multiple-Surface Sliding Controller Design for Pneumatic Servo Systems, *Mechatronics*, Vol. 18, pp. 506-512, 2007.
23. G. M. Bone, and S. Ning, Experimental Comparison of Position Tracking Control Algorithms for Pneumatic Cylinder Actuators, *IEEE/ASME Transactions on Mechatronics*,Vol. 12, pp. 557-561, 2007.
24. A. C. Huang, Y. S. Kuo, Sliding control of nonlinear systems containing time-varying uncertainties with unknown bounds, *International Journal of Control*, Vol. 74, No. 3, pp. 252-264, 1999.
25. John J. Craig, Introduction to Robotics, Pearson Education Inc, 2005.

Proceedings of the 8th JFPS International
Symposium on Fluid Power, OKINAWA 2011
Oct. 25-28, 2011

2D1-2

DEVELOPMENT OF A PNEUMATICALLY-DRIVEN FORCEPS MANIPULATOR USING A FLEXIBLE JOINT

Daisuke HARAGUCHI*, Kotaro TADANO* and Kenji KAWASHIMA*

* Precision and Intelligent Laboratory, Tokyo Institute of Technology
4259 Nagatsuta, Midori, Yokohama, 226-8503 Japan
(E-mail: haraguchi.d.aa@m.titech.ac.jp)

ABSTRACT

This paper presents the first prototype of pneumatically-driven forceps manipulator using a simple flexible joint for future miniaturization. A high performance spring component with wire actuation is employed for two-degree of freedom (DOF) bending joint, and two-DOF tendon drive system is implemented by four pneumatic cylinders. Using a continuum model for the kinematics, PD controller with static and dynamic compensation is designed for the position control, which shows a good performance with sufficient working frequency for surgical operations. In addition, the forceps manipulator can estimate external forces using disturbance observer. A link approximation model is introduced to design the observer as the first intuitive approach. The force estimation can be achieved with an accuracy of 0.2 N in the basic straight posture.

KEY WORDS

Forceps manipulator, Pneumatic drive, Flexible joint, Force estimation

INTRODUCTION

In robotic assisted minimally-invasive surgery, miniaturization of manipulators with multi-degree of freedom (DOF) is a key technology to improve patients' quality of life, and also to enable advanced surgical techniques such as single port access surgery and microsurgery. Here the most critical issue is the mechanism of dexterous joints. Previous developments of miniaturized surgical manipulators employed rigid link joints with wire-actuation[1][2]. Rigid link mechanisms certainly provide structural stiffness and good controllability for manipulation. However, from a practical viewpoint, the complicated structure due to a lot of components may increase the cost of manufacturing and maintenance. This work therefore aims at simplification of the dexterous joint mechanism for enhanced miniaturization.

Elastic and continuum mechanisms[3][4] have a great advantage of the simple structure. Unlike rigid link mechanism, extra small parts such as shafts, bearings and pulleys are not needed, hence these are suitable for miniaturization. Simaan et al. proposed the multi-backbone continuum robot and developed manipulators with redundant DOFs for advanced surgical techniques[5][6]. However the continuum robot still has some guide disks to be assembled, and inherently has a structural weakness toward torsional loads.

On the other hand, force feedback is also very important for safer manipulation and more successful operation[7]. Though forceps manipulators with embedded force sensors were developed[8][9], these are hard to be any further miniaturized. Xu and Simaan investigated the in-

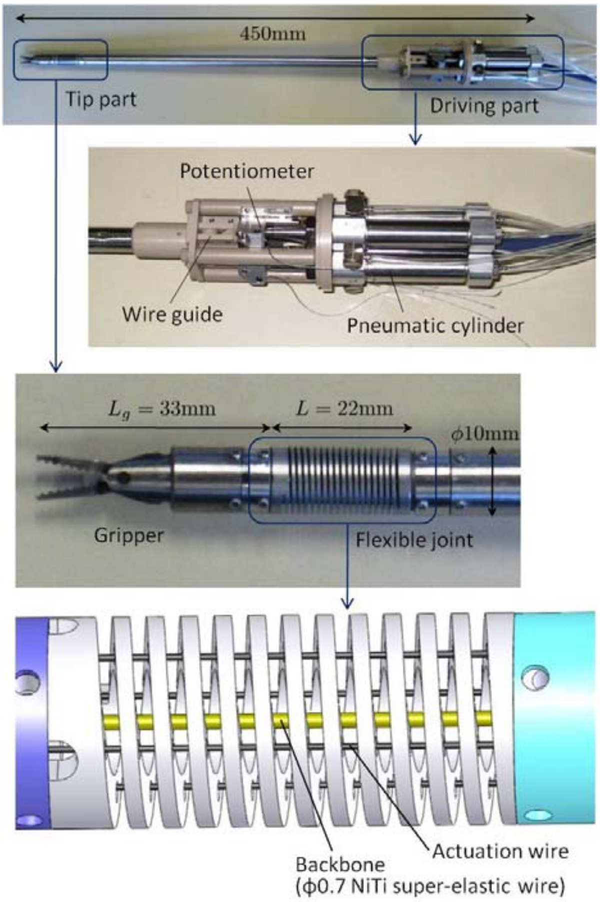

Figure 1 Overview and joint mechanism of the forceps manipulator.

trinsic force sensing capabilities of the multi-backbone continuum robots[10]. These works also required force sensors in the actuation unit placed in patient side, which makes the system large and complicated. Our approach is to estimate external forces using pneumatic driving force and identified dynamics of the forceps manipulator[11][12]. No force sensor is needed in patient side, taking advantage of the high back-drivability of pneumatic driving system.

In this work, we have developed a prototype of pneumatically-driven forceps manipulator using a highly-simplified flexible joint combined with the intrinsic force sensing technology. A high performance spring component is employed for the joint structure, which provides two-DOF bending mechanism with wire actuation. The position control system based on the kinematic and the dynamic modeling are designed, and its basic control performances are investigated. In addition, the force estimation algorithm using disturbance observer is introduced and the experimental results in specific cases are reported.

Table 1 Properties of the spring component.

Material	SUS303
Whole length	27 mm
Outer diam.	10 mm
Spring const.	2.5 N/mm
Bending range	$\pm$60 deg

DESIGN OF THE FORCEPS MANIPULATOR

An overview of the developed forceps manipulator is shown in Figure 1. Whole length of the manipulator is 450 mm and diameter of the insertable portion is 10 mm. In the driving part, four pneumatic cylinders (CJ2QB10-15, SMC) are equipped, which can directly drive the flexible joint by wires. Positions of the cylinder rod are measured by linear potentiometers. The tip part has a two-DOF bending flexible joint and a gripper. We have employed a spring component for the joint part, which is a fully-integrated, high performance spring manufactured in cutting work including attachment parts. The spring component enables the joint mechanism to be greatly simplified, therefore it provides a high potential for miniaturization as well as the cost reduction and ease of maintenance. Moreover, the excellent torque transmissibility of the spring is also a big advantage for surgical manipulation. Table 1 shows properties of the spring component used for the prototype of forceps manipulator. For the joint actuation mechanism, as shown in Figure 1, four stainless steel wires are passed into each guide hole drilled in the spring, which constitute two-DOF tendon actuation system. Furthermore, a backbone of ϕ0.7mm NiTi super-elastic wire is added to prevent compression of the spring. This reinforcement enhances the joint stiffness and back-drivability of wire-tendon actuation. The forceps manipulator can be operated with being installed on the four-DOF supporting manipulator developed in our previous work[12].

PNEUMATIC DRIVING SYSTEM

The forceps manipulator has two-DOF tendon drives with four pneumatic cylinders. Figure 2 shows a schematic of one-DOF pneumatic tendon-drive system. Each cylinder is driven and controlled by a servo valve (MPYE-M5-B SA, FESTO) with 5 ports. In order to describe the state of the tendon drive, we introduce two-DOF parameters, the actuation length $\boldsymbol{d} = [d_x, d_y]^T$ and the actuation force $\boldsymbol{w} = [w_x, w_y]^T$, which are obtained from the cylinder rod position $\boldsymbol{X}$ and pneumatic driving force $\boldsymbol{F}$ of the cylinders, respectively. In this study, $\boldsymbol{d}$ is determined by selecting the cylinder in more pulled condition of each

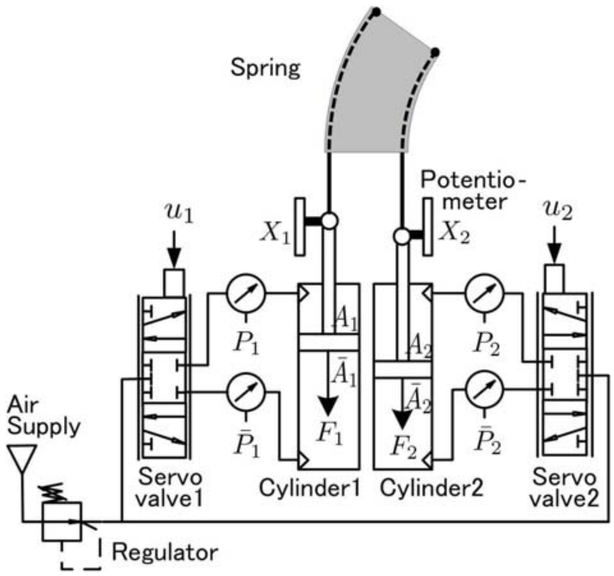

Figure 2 Schematic of one-DOF pneumatic tendon drive system.

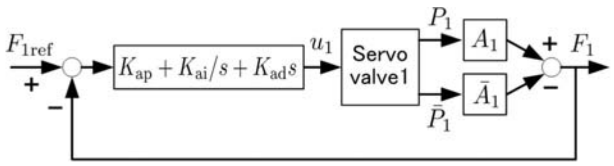

Figure 3 Block diagram of the pneumatic force control system for one cylinder.

tendon joint because the push-pull actuation is assumed to be symmetric in the flexible joint. $\boldsymbol{w}$ is calculated by taking the difference between pneumatic driving forces of the cylinder pair at each tendon joint. In the case of Figure 2 about the one-DOF system, the introduced parameters are given as follows:

$$d_x = \begin{cases} X_1 & (X_1 \le X_2) \\ -X_2 & (X_1 > X_2) \end{cases} \tag{1}$$

$$w_x = F_1 - F_2 \tag{2}$$

In the driving system, the cylinder rod positions X_1, X_2 are directly measured with potentiometers, and the pneumatic driving forces F_1, F_2 are calculated as follows:

$$\begin{aligned} F_1 &= A_1 P_1 - \bar{A}_1 \bar{P}_1 \\ F_2 &= A_2 P_2 - \bar{A}_2 \bar{P}_2 \end{aligned} \tag{3}$$

where the symbols A, $\bar{A}$ denote pressure-receiving areas of each cylinder, and the symbols P, $\bar{P}$ denote pressures measured on the output ports of each servo valve. Note that the dynamic effect of pipelines from servo valves to cylinders is not considered in this work.

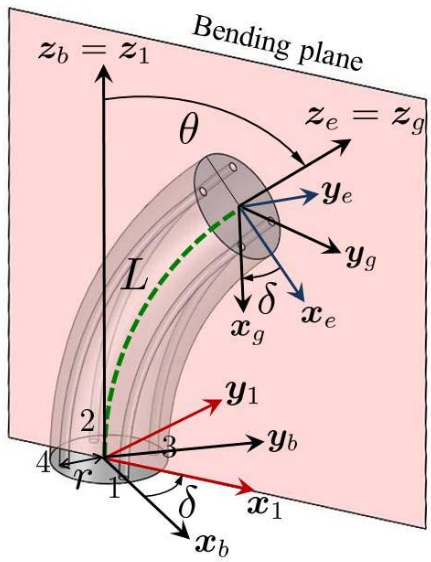

Figure 4 Nomenclature and coordinates of a continuum model.

The pneumatic driving forces are controlled based on the tendon force distribution law that keeps more than minimal tension of wires. In the case of Figure 2,

$$\begin{aligned} F_{1\text{ref}} &= F_0 + \frac{|w_{x\text{ref}}| + w_{x\text{ref}}}{2} \\ F_{2\text{ref}} &= F_0 + \frac{|w_{x\text{ref}}| - w_{x\text{ref}}}{2} \end{aligned} \tag{4}$$

where the subscript "ref" means the reference value, and $w_{x\text{ref}}$ is given by the joint position controller shown in the next section. According to the distribution law, the driving forces always become more than F_0. Therefore, the actuation wires can be kept tensioned, which maintains the back-drivability of the flexible joint. Figure 3 shows the pneumatic force control system for one cylinder. In this system, the input voltage u_1 is calculated by a PID controller to operate the servo valve. Experimental result on the pneumatic force control is shown in the next section.

JOINT POSITION CONTROL

Kinematic Modeling

In order to describe the kinematics, a continuum model studied in the previous work[13] is introduced. In this model, two-DOF joint position parameter $\boldsymbol{q} = [\delta, \theta]^T$ is defined, where δ denotes the bending direction and θ denotes the bending angle depicted in Figure 4. These are known as parameters of the spherical polar coordinates. At the same time, some local coordinate frames are defined: *Spring-Base Coordinate Frame* $\{\boldsymbol{x}_b, \boldsymbol{y}_b, \boldsymbol{z}_b\}$, *Bending-Plane Coordinate Frame* $\{\boldsymbol{x}_1, \boldsymbol{y}_1, \boldsymbol{z}_1\}$, *Spring-End Coordinate Frame* $\{\boldsymbol{x}_e, \boldsymbol{y}_e, \boldsymbol{z}_e\}$, and *Gripper Coordinate Frame* $\{\boldsymbol{x}_g, \boldsymbol{y}_g, \boldsymbol{z}_g\}$. Where $\boldsymbol{x}_b$ and $\boldsymbol{x}_g$ axes are

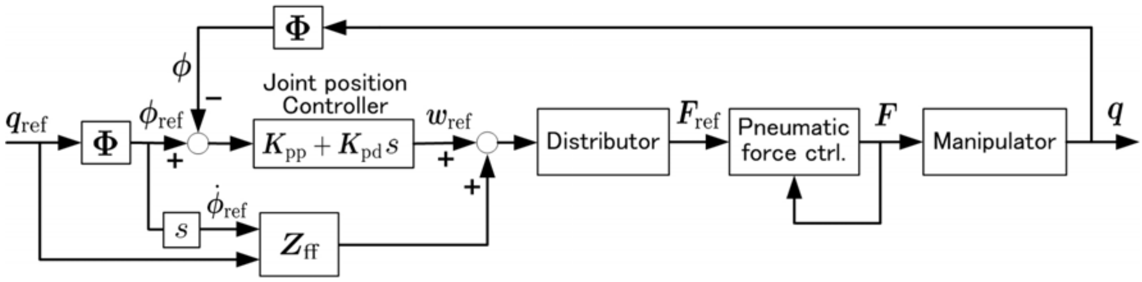

Figure 5 Block diagram of the joint position control system.

set on the No.1 wire, and $\boldsymbol{y}_b$ and $\boldsymbol{y}_g$ axes are set on the No.3 wires. Assuming that the flexible joint bends into a circular shape and the wire tendon motion is symmetric, the actuation length $\boldsymbol{d}$ is given as the forward kinematics on the joint position:

$$\boldsymbol{d} = \begin{bmatrix} d_x \\ d_y \end{bmatrix} = \begin{bmatrix} r\theta\cos\delta \\ r\theta\sin\delta \end{bmatrix} \tag{5}$$

where r denotes radius of the wire arrangement. Solving the equations about $\boldsymbol{q}$, the inverse kinematics can be obtained:

$$\boldsymbol{q} = \begin{bmatrix} \delta \\ \theta \end{bmatrix} = \begin{bmatrix} \tan^{-1}\left(\dfrac{d_y}{d_x}\right) \\ \dfrac{1}{r}\sqrt{d_x^2 + d_y^2} \end{bmatrix} \tag{6}$$

In addition, the joint position parameter $\boldsymbol{q}$ is transformed into a parameter $\boldsymbol{\phi} = [\phi_x, \phi_y]^T$ corresponding to each tendon actuation system, which can be used as the control parameter:

$$\boldsymbol{\phi} = \begin{bmatrix} \phi_x \\ \phi_y \end{bmatrix} = \begin{bmatrix} \theta\cos\delta \\ \theta\sin\delta \end{bmatrix} \tag{7}$$

The forceps tip position $\boldsymbol{p}_t$ expressed in the *Spring-Base Coordinate Frame* is given as the forward kinematics:

$$\boldsymbol{p}_t = \begin{bmatrix} \cos\delta\left(\dfrac{L}{\theta}(1-\cos\theta) + L_g\sin\theta\right) \\ \sin\delta\left(\dfrac{L}{\theta}(1-\cos\theta) + L_g\sin\theta\right) \\ \dfrac{L}{\theta}\sin\theta + L_g\cos\theta \end{bmatrix} \tag{8}$$

where L and L_g denotes the length of flexible joint and the length of gripper, respectively. In this work, the values $L = 22$ [mm] and $L_g = 33$ [mm] are used as shown in Figure 1. The detailed derivation process of the tip position is discussed in the previous work[13].

Dynamic Modeling

The joint dynamics $\boldsymbol{Z}$ is modeled in the tendon actuation system:

$$\boldsymbol{Z} = \boldsymbol{M}\ddot{\boldsymbol{\phi}} + \boldsymbol{C}\dot{\boldsymbol{\phi}} + \boldsymbol{D}\mathrm{sign}(\dot{\boldsymbol{\phi}}) + \boldsymbol{K}(\boldsymbol{q}) \tag{9}$$

The first term is the inertial term. It is sufficiently small compared to the other terms, so it can be negligible in this work. The second term comes from viscous friction and the third term comes from coulomb friction. These coefficients $\boldsymbol{C}$ and $\boldsymbol{D}$ are experimentally determined. The forth term is the potential term, which comes from static mechanics of the flexible joint. The static mechanics can be identified using the virtual work principle. First, the instantaneous kinematics is obtained by taking time-derivative of Equation (5):

$$\begin{aligned} \dot{\boldsymbol{d}} &= \boldsymbol{J}_d\dot{\boldsymbol{q}}\ , \\ \boldsymbol{J}_d &= \begin{bmatrix} r\theta\sin\delta & -r\cos\delta \\ -r\theta\cos\delta & -r\sin\delta \end{bmatrix} \end{aligned} \tag{10}$$

where the Jacobian matrix $\boldsymbol{J}_d$ is obtained. Second, considering generalized forces $\boldsymbol{\tau}_q = [\tau_\delta, \tau_\theta]^T$ about the joint position parameter, the relation between $\boldsymbol{\tau}_q$ and the tendon actuation force $\boldsymbol{w}$ can be derived using the virtual work principle:

$$\boldsymbol{\tau}_q = \boldsymbol{J}_d^T\boldsymbol{w} \tag{11}$$

Assuming that the flexible joint can be modeled as a simple elastic rod, the elastic energy should be stored only with the bending angle θ. Then, the static mechanics is obtained by solving Equation (11) under the condition of $\tau_\delta = 0$:

$$\begin{bmatrix} w_x \\ w_y \end{bmatrix} = \frac{\tau_\theta}{r}\begin{bmatrix} \cos\delta \\ \sin\delta \end{bmatrix} = \boldsymbol{K}(\boldsymbol{q}) \tag{12}$$

In this work, τ_θ is experimentally identified by linear approximation.

Design of the Control System

In Figure 5, the developed control system is shown as a block diagram. The system employs a cascade controller consisting of the outer loop for position control

Table 2 Gain parameters used for the experiments.

K_{pp}	2.0	[N/rad]	(For both x and y axis)
K_{pd}	0.01	[Ns/rad]	
K_{ap}	0.20	[V/N]	(For all cylinders)
K_{ai}	2.0	[V/Ns]	
K_{ad}	0.001	[Vs/N]	

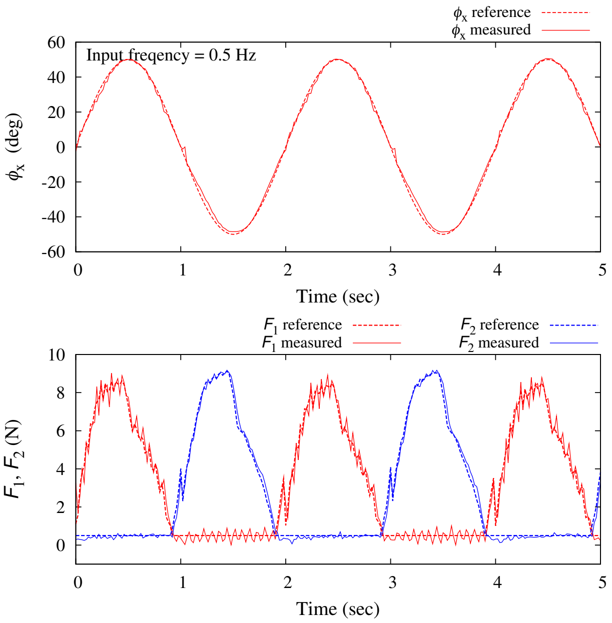

Figure 6 Experimental results of the joint position control with single DOF: joint position (upper) and pneumatic driving force of the cylinders (lower).

and the inner loop for pneumatic force control. Reference input of the joint position vector $\boldsymbol{q}_{\mathrm{ref}}$ is transformed into the angular parameter $\boldsymbol{\phi}_{\mathrm{ref}}$ expressed in the tendon-drive system by the function $\boldsymbol{\Phi}$ as shown in Equation (7). The parameters $\boldsymbol{\phi}_{\mathrm{ref}}$ and $\boldsymbol{\phi}$ are used for the feedback control, and the tendon actuation force $\boldsymbol{w}_{\mathrm{ref}}$ are calculated by a PD controller. Then, reference values of the pneumatic driving force for each cylinder $F_{\mathrm{ref}} = [F_{1\mathrm{ref}}, F_{2\mathrm{ref}}, F_{3\mathrm{ref}}, F_{4\mathrm{ref}}]^T$ are determined by the tendon-force distribution law as shown in Equation (4). Furthermore, the feed-forward compensation $\boldsymbol{Z}_{\mathrm{ff}}$ based on the dynamic model is implemented to improve the control response.

Position Control Experiment

The basic control performance was verified with some position control experiments. The gain parameters used for the experiments are shown in Table 2. First, the performance of tendon-drive with single DOF shown in Figure 2 was investigated, where sinusoidal reference input of the angle parameter ϕ_x was given and the minimum

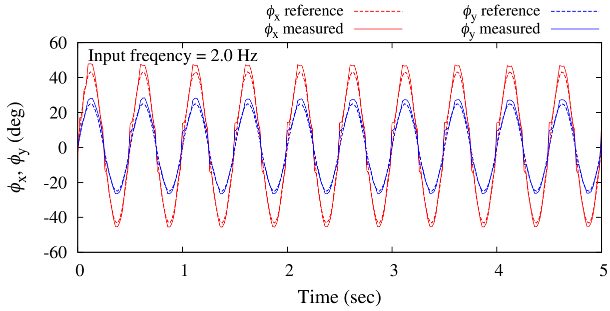

Figure 7 Experimental results of the joint position control with two DOFs. Input references are given as $\delta_{\mathrm{ref}} = 30°$, $\theta_{\mathrm{ref}} = -50° \sim 50°$ at 2.0 Hz.

wire tension F_0 was set to 0.5 N (see Equation (4)). Figure 6 shows the result: the time history of joint position and pneumatic driving force. The control response of the joint position was very good, and the driving forces of the cylinders were kept above 0.5 N despite some oscillatory responses. According to the result, desirable tendon motion was achieved without critical slack of the wires.

Next, the performance of position control was verified with two-DOF movement. Figure 7 shows the time history of joint position, where sinusoidal input of the bending angle θ_{ref} was given in the bending direction $\delta_{\mathrm{ref}} = 30°$. Although there were slight overshoots at the frequency of 2.0 Hz, the controller showed good performances as a whole. It can be said that the control bandwidth is sufficient for surgical operations.

ESTIMATION OF EXTERNAL FORCE

Disturbance Observer

The external force applied to the forceps tip can be estimated, developing a disturbance observer. The equation of motion of the flexible joint can be written in the tendon actuation system:

$$\boldsymbol{w} + \boldsymbol{w}_{\mathrm{ext}} = \boldsymbol{Z} \tag{13}$$

where $\boldsymbol{w}_{\mathrm{ext}} = [w_{xe}, w_{ye}]^T$ denotes the external force on the tendon actuations. As the actuation force $\boldsymbol{w}$ is obtained from the cylinder driving force $\boldsymbol{F}$ and the joint dynamics $\boldsymbol{Z}$ is identified as $\hat{\boldsymbol{Z}}$, the external force can be estimated by the following equation:

$$\hat{\boldsymbol{w}}_{\mathrm{ext}} = \hat{\boldsymbol{Z}} - \boldsymbol{J}_{\mathrm{a}}\boldsymbol{F} \tag{14}$$

where $\boldsymbol{J}_{\mathrm{a}}$ denotes the transformation matrix from $\boldsymbol{F}$ to $\boldsymbol{w}$. Then, it is transformed to generalized force $\hat{\boldsymbol{\tau}}_{\mathrm{ext}} = [\tau_{\delta e}, \tau_{\theta e}]^T$ using Equation (11):

$$\hat{\boldsymbol{\tau}}_{\mathrm{ext}} = \boldsymbol{J}_d^T \hat{\boldsymbol{w}}_{\mathrm{ext}} \tag{15}$$

In order to obtain external force $\hat{\boldsymbol{f}}_{\mathrm{ext}} = [f_x, f_y, f_z]^T$ applied to the forceps tip, Jacobian matrix $\boldsymbol{J}_{t(3\times2)}$ from

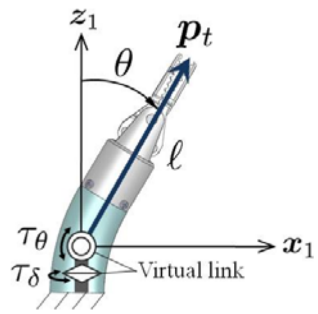

Figure 8 Concept of the link approximation in force estimation.

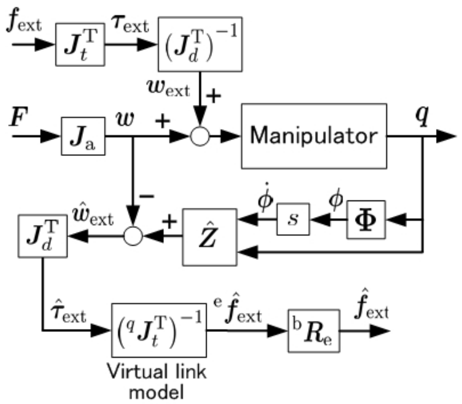

Figure 9 Block diagram of the disturbance observer.

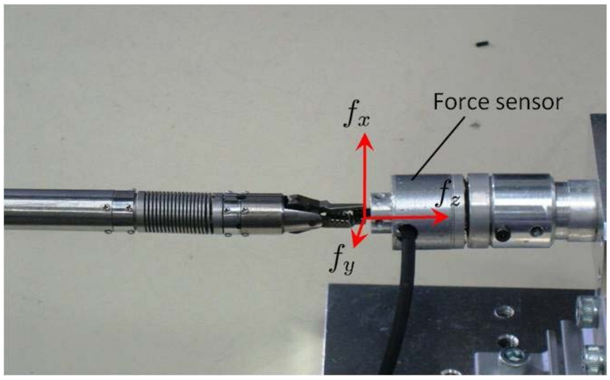

Figure 10 Experimental setup for force measurement.

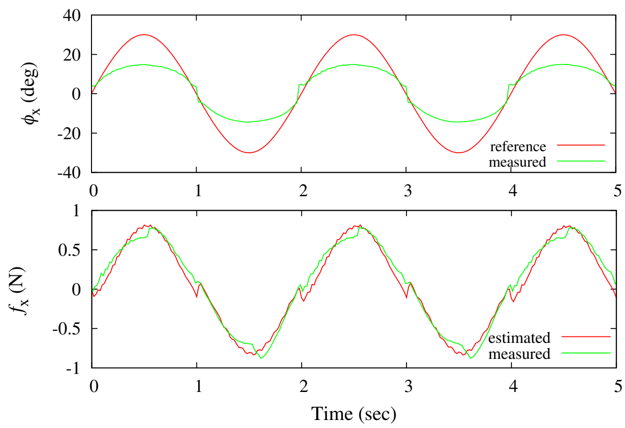

Figure 11 Result of the external force estimation with the input references of $\delta_{\text{ref}} = 0°$, $\theta_{\text{ref}} = -30° \sim 30°$ at 0.5 Hz: the corresponding joint position ϕ_x (upper) and the external force (lower).

the joint position $\boldsymbol{q}$ to the tip position $\boldsymbol{p}_t$ is used in a strict theory. However, it requires calculation of the pseudo-inverse matrix, so numerical error propagations may come up around the singular point, $\theta = 0°$. In this work as the first practical approach, a link approximation model is introduced for a kinematic alternative, which provides more intuitive solution with low calculation costs. Figure 8 shows the concept of the link approximation. In this model, two virtual link joints, rotational and bending, are assumed to be set on the center of the flexible joint. Based on this assumption, the generalized forces τ_δ, τ_θ correspond to the torque around the virtual link joints. Then the external forces ${}^q\hat{\boldsymbol{f}}_{\text{ext}} = [f_{\delta e}, f_{\theta e}]^T$ applied to the forceps tip in the direction of δ and θ are easily and analytically calculated using a diagonal matrix ${}^q\boldsymbol{J}_t$:

$$
\begin{aligned}
{}^q\hat{\boldsymbol{f}}_{\text{ext}} &= \left({}^q\boldsymbol{J}_t^T\right)^{-1}\hat{\boldsymbol{\tau}}_{\text{ext}} \\
&= \begin{bmatrix} \dfrac{r\theta}{\ell\sin\theta}(w_x\sin\delta - w_y\cos\delta) \\ -\dfrac{r}{\ell}(w_x\cos\delta + w_y\sin\delta) \end{bmatrix}, \qquad (16) \\
{}^q\boldsymbol{J}_t &= \begin{bmatrix} \ell\sin\theta & 0 \\ 0 & \ell \end{bmatrix}
\end{aligned}
$$

where ℓ denotes the virtual link length and becomes $\ell = L/2 + L_g$ from the definition. Note that ${}^q\hat{\boldsymbol{f}}_{\text{ext}}$ can be defined even at the singular point $\theta = 0°$ using the L'Hospital's rule with $\delta = \delta_{\text{ref}}$. The estimated forces $f_{\delta e}, f_{\theta e}$ is in the direction of $\boldsymbol{y}_e$ axis and $\boldsymbol{x}_e$ axis, respectively (see Figure 4). Therefore, coordinate transformation of the vector ${}^{\text{e}}\hat{\boldsymbol{f}}_{\text{ext}} = [f_{\theta e}, f_{\delta e}, 0]^T$ yields the external force $\hat{\boldsymbol{f}}_{\text{ext}}$ expressed in the inertial frame:

$$\hat{\boldsymbol{f}}_{\text{ext}} = ({}^{\text{b}}\boldsymbol{R}_{\text{e}})\,{}^{\text{e}}\hat{\boldsymbol{f}}_{\text{ext}} \qquad (17)$$

where ${}^{\text{b}}\boldsymbol{R}_{\text{e}}$ denotes the transformation matrix from the *Spring-End Coordinate Frame* $\{\boldsymbol{x}_e, \boldsymbol{y}_e, \boldsymbol{z}_e\}$ into the *Spring-Base Coordinate Frame* $\{\boldsymbol{x}_b, \boldsymbol{y}_b, \boldsymbol{z}_b\}$. The block diagram of the disturbance observer is shown in Figure 9.

Experimental Verification

The performance of external force estimation was verified, as the first step, in straight posture of the flexible joint. For the experiment, the forceps gripper was fixed to a force sensor as shown in Figure 10. With this setup, sinusoidal reference inputs θ_{ref} was given in a certain bending direction δ_{ref}. Figure 11 shows a result with the input references of $\delta_{\mathrm{ref}} = 0°$, $\theta_{\mathrm{ref}} = -30° \sim 30°$ at 0.5 Hz. The deviation of the joint position from the reference signal was caused by the physical constraint at the forceps tip. In this case, the force estimation could be achieved within the error of 0.2 N. Critical estimation errors occurred around the reference position of $\phi_x = 0°$ and $\phi_x = \pm 30°$, which were caused by bucking phenomena of the NiTi backbone. Despite the hardware problem, the effectiveness of the disturbance observer using the link approximation model has been experimentally verified at least in the straight posture.

CONCLUSIONS

A prototype of pneumatically-driven forceps manipulator with a simple flexible joint has been developed for future miniaturization. The flexible joint mechanism consists of a high performance spring component and a backbone of NiTi super-elastic wire. Two-DOF wire tendon actuation system was implemented by four pneumatic cylinders, and the performance of joint position control was sufficient for surgical operations. In addition, a disturbance observer based on the link approximation model was designed, which can estimate the external force with accuracy of 0.2 N in the straight posture. However, the buckling phenomena of the NiTi backbone gave critical errors of force estimation. Our future works are to improve the hardware problem and to verify the force estimation method in more general cases.

REFERENCES

1. Ikuta, K., Sasaki, K., Yamamoto, K., and Shimada, T., Remote Microsurgery System for Deep and Narrow Space - Development of New Surgical Procedure and Micro-robotic Tool, *Medical Image Computing and Computer-Assisted Intervention (MICCAI) 2002*, edited by T. Dohi and R. Kikinis, Vol. 2488 of *Lecture Notes in Computer Science*, Springer Berlin / Heidelberg, 2002, pp. 163–172.

2. Yamashita, H., Matsumiya, K., Masamune, K., Liao, H., Chiba, T., and Dohi, T., Two-DOFs Bending Forceps Manipulator of 3.5-mm diameter for Intrauterine Fetus Surgery: Feasibility Evaluation, *the 20th International Congress and Exhibition, Computer Assisted Radiology and Surgery*, Osaka, Japan, June 2006.

3. Hirose, S., *Biologically Inspired Robots: Serpentile Locomotors and Manipulators*, Oxford University Press, 1993.

4. Gravagne, I. and Walker, I., Manipulability, force, and compliance analysis for planar continuum manipulators, *Robotics and Automation, IEEE Transactions on*, Vol. 18, No. 3, June 2002, pp. 263 –273.

5. Wei, W., Xu, K., and Simaan, N., A Compact Two-armed Slave Manipulator for Minimally Invasive Surgery of the Throat, *Biomedical Robotics and Biomechatronics, 2006. BioRob 2006. The First IEEE/RAS-EMBS International Conference on*, 2006, pp. 769 –774.

6. Ding, J., Xu, K., Goldman, R., Allen, P., Fowler, D., and Simaan, N., Design, simulation and evaluation of kinematic alternatives for Insertable Robotic Effectors Platforms in Single Port Access Surgery, *Robotics and Automation (ICRA), 2010 IEEE International Conference on*, May 2010, pp. 1053 –1058.

7. Tholey, G., Desai, J. P., and Castellanos, A. E., Force Feedback Plays a Significant Role in Minimally Invasive Surgery: Results and Analysis, *Annals of Surgery*, Vol. 241, No. 1, 2005, pp. 102–109.

8. Seibold, U., Kubler, B., and Hirzinger, G., Prototype of Instrument for Minimally Invasive Surgery with 6-Axis Force Sensing Capability, *Robotics and Automation, 2005. ICRA 2005. Proceedings of the 2005 IEEE International Conference on*, 2005, pp. 496 – 501.

9. Takahashi, H., Warisawa, S., Mitsuishi, M., Arata, J., and Hashizume, M., Development of High Dexterity Minimally Invasive Surgical System with Augmented Force Feedback Capability, *Biomedical Robotics and Biomechatronics, 2006. BioRob 2006. The First IEEE/RAS-EMBS International Conference on*, 2006, pp. 284 –289.

10. Xu, K. and Simaan, N., An Investigation of the Intrinsic Force Sensing Capabilities of Continuum Robots, *Robotics, IEEE Transactions on*, Vol. 24, No. 3, 2008, pp. 576 –587.

11. Tadano, K., Smino, W., Kawashima, K., and Kagawa, T., Pneumatically Driven Forceps Manipulator for Laparoscopic Surgery, *SICE Annual Conference*, 2008, pp. 2993–2996.

12. Tadano, K., Kawashima, K., Kojima, K., and Tanaka, N., Development of a Pneumatic Surgical Manipulator IBIS IV, *Journal of Robotics and Mechatronics*, Vol. 22, No. 2, 2010, pp. 179–188.

13. Xu, K., Goldman, R., Ding, J., Allen, P., Fowler, D., and Simaan, N., System design of an Insertable Robotic Effector Platform for Single Port Access (SPA) Surgery, *Intelligent Robots and Systems, 2009. IROS 2009. IEEE/RSJ International Conference on*, 2009, pp. 5546 –5552.

Proceedings of the 8th JFPS International
Symposium on Fluid Power, OKINAWA 2011
Oct. 25-28, 2011

2D1-3

CONTROL OF BLOWN AIR FOR A SOPRANO-RECORDER-PLAYING ROBOT USING UNSTEADY FLOW RATE MEASUREMENTS AND CONTROL TECHNIQUES

Tomonori KATO*, Yoshiyuki KAWAMURA*, Tatsuya FUNAKI**, Kenji KAWASHIMA*** and Toshiharu KAGAWA***

* Department of Intelligent Mechanical Engineering, Faculty of Engineering
Fukuoka Institute of Technology
3-30-1 Wajiro-higashi, Higashi-ku, Fukuoka 811-0295, Japan
(E-mail: t-kato@fit.ac.jp)
** Gas Flow Standards Section, Fluid Flow Division, National Metrology Institute of Japan
National Institute of Advanced Industrial Science and Technology
Tsukuba Central 3, 1-1-1 Umezono, Tsukuba, Ibaraki 305-8563, Japan
*** Advanced Mechanical Systems Division, Precision and Intelligence Laboratory
Tokyo Institute of Technology
R2-45 4259 Nagatsuta-cho, Midori-ku, Yokohama, Kanagawa 226-8503, Japan

ABSTRACT

The purpose of this study is to construct a robot playing a soprano recorder that sounds like a human playing a soprano recorder. Recent years have seen the development of robots that entertain people by playing a variety of musical instruments. There have been many reports describing the musical expression of such robots, for example, that of robots with artificial lips for playing wind instruments. However, particularly when performing special musical effects, such as vibrato, tremolo, and tonguing, robots playing wind instruments often produce artificial sounds that differ considerably from those produced by their human counterparts. To build a soprano-recorder-playing robot that produces natural sounds matching those produced by a human player, this study employs unsteady flow rate measurements and control techniques. A spool type servo valve and a quick response laminar flow sensor (QFS), whose dynamic characteristics are calibrated using an unsteady flow rate generator, are applied for controlling the blown air for the developed recorder-playing robot.

KEY WORDS

Pneumatics, Flow Rate Measurement, Unsteady Flow Generator, Quick Response Laminar Flow Sensor, Recorder-playing Robot

NOMENCLATURE

E	:	Control signal of servo valve
f	:	Frequency
G	:	Mass flow rate
G_{out}	:	Mass flow rate from unsteady flow generator
K_v	:	Flow rate gain of servo valve
L_c	:	Sound level
P	:	Pressure
P_a	:	Atmospheric pressure
ΔP	:	Differential pressure
Q	:	Flow rate (L/min ANR)
Q_{ref}	:	Set flow rate value
t	:	Time

INTRODUCTION

Due to the rapid development of robot technology in recent years, the number of applications of robots in fields other than industrial fields has been increasing. Robots for entertaining people or encouraging social interactions have been developed[1]. For example, in recent years robots have entertained people by playing a variety of musical instruments[2]. To enable the musical expression of these robots, researchers have created many devices, including artificial lips for playing wind instruments.

However, robots playing wind instruments often produce artificial sounds that differ considerably from those produced by their human counterparts. This is particularly true for robots performing special musical effects, such as vibrato, tremolo and tonguing.

We have developed a robot that plays a soprano recorder before this research. Nevertheless, naturally expressing the special musical effects of tonguing and vibrato remain a problem.

Therefore, the purpose of this study is to build a robot playing a soprano recorder that produces natural sounds, that is, sounds matching those produced by a human player. This study employs unsteady flow rate measurements and control techniques for controlling the air blown through the soprano recorder. In the present research, the following procedure was conducted. First, not only the static but also the dynamic characteristics of the flow sensor used for measuring the blown air were calibrated using an unsteady flow generator to judge whether the performance of the flow sensor was high enough for measurement of the blown air. Second, using the flow sensor, the blown air flow rates were measured for real human players (members of Fukuoka Institute of Technology Wind Symphony) expressing vibrato with a soprano recorder. Finally, the identified blown air flow rate model was applied to the air flow rate control system of the soprano-recorder-playing robot. The flow rate was controlled by a spool type servo valve (SP valve). The recorder sounds played by a human and the sounds played by the robot were compared using a sound analyzer.

OVERVIEW OF THE DEVELOPED RECORDER-PLAYING ROBOT

We previously developed the recorder-playing robot shown in Fig. 1. The robot system consists of a computer, a musical keyboard (Edirol MIDI keyboard controller PC-50), an electronic circuit as a signal receiver and a fingering controller, an SP valve (Festo MPYE-M5-B-SA), a soprano recorder (Aulos 503B), and a fingering part consisting of solenoid plungers (Yamaha DC Solenoid MD-232) (Fig. 2). The configuration of the recorder-playing robot system is shown in Fig. 3. In the computer, MIDI (Musical Instrument Digital Interface)[3] sequencer software (Cakewalk SONAR 6 LE) generates MIDI signals for playing (controlling) the recorder. The sequencer software also generates accompaniment music in

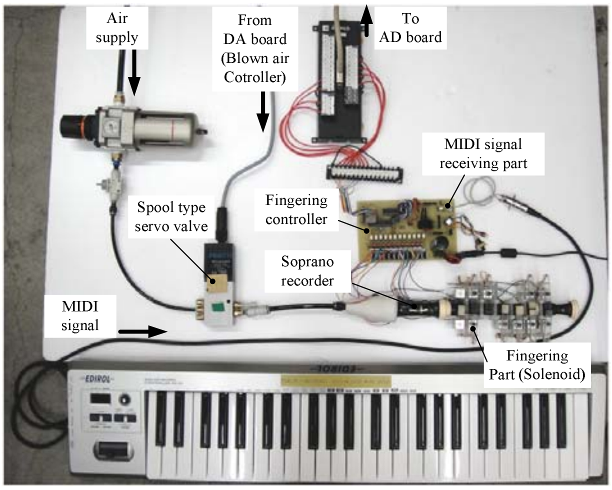

Fig. 1 Developed recorder-playing robot

Fig. 2 Fingering part (solenoid plungers)

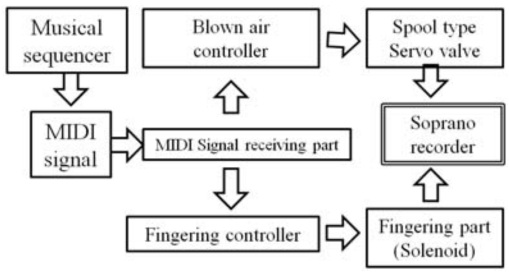

Fig. 3 Configuration of the recorder-playing robot system

synchronization with the MIDI signals. The MIDI signal is sent to the musical keyboard, which can be used both as a MIDI signal transmitter and a musical interface. Then, the MIDI signal is received by the electronic circuit. In the circuit, the MIDI signal is divided into two signals. One is the signal for controlling the blown air (i.e., the signal sent to the SP valve), and the other is the signal for controlling the fingering part (i.e., the solenoid plungers). Eleven solenoid plungers were attached to acrylic hinge plates as robot fingers. By tuning the sound by trial and error (particularly the relationship between the MIDI signal and the controlling signal of the SP valve that controls the blown air flow rate for the recorder), the robot system could play several musical songs well. For example, a demonstration at a school festival was well received. But, expressing the special musical effects of tonguing and vibrato naturally remained a problem.

QUICK RESPONSE LAMINAR FLOW SENSOR

Selection of flow sensor

To measure and control the blown air for a recorder, a flow sensor having sufficient resolution and dynamic characteristics is needed. The type of flow sensor used in this research is a laminar flow type, named "quick response laminar flow sensor" (QFS), which our research group has been developing[4)]. The QFS is composed of a laminar flow element and a differential pressure gauge. The static characteristics of the QFS used in this research are expressed in equation (1).

$$Q \quad [\text{L/minANR}] = 0.256 \frac{P}{P_a} \Delta P \qquad (1)$$

The model type of the QFS used in this research is QFS-0.3-50-30 (Tokyo Meter Co., Ltd.). Suppose, as an example, the resolution of the differential pressure gauge is 0.1 Pa; then the resolution of the QFS is 25.6 mL/min (ANR).

Dynamic characteristics test of the QFS using an unsteady flow generator

The dynamic characteristics of the flow sensor (QFS) up to 20 Hz were tested using an unsteady flow generator (UFG). The UFG is a device that can generate arbitrary oscillation air flow up to at least 50 Hz[5)]. A schematic of the UFG is shown in Fig. 4. The UFG includes two SP valves and an isothermal chamber. A schematic of the dynamic characteristics test of the QFS is shown in Fig. 5. The QFS is set downstream of the UFG. Downstream of the QFS is open to atmosphere. Both the generated flow rate from the UFG (as the standard) and

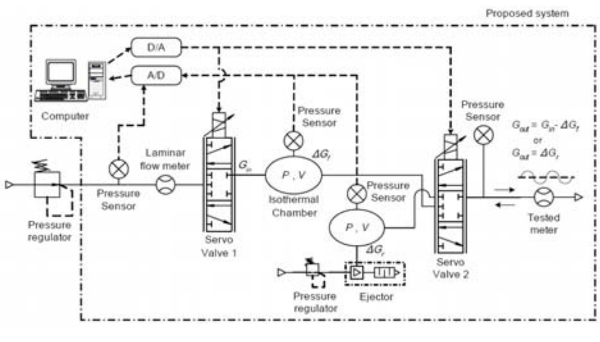

Fig. 4 Schematic of the unsteady flow generator (UFG)

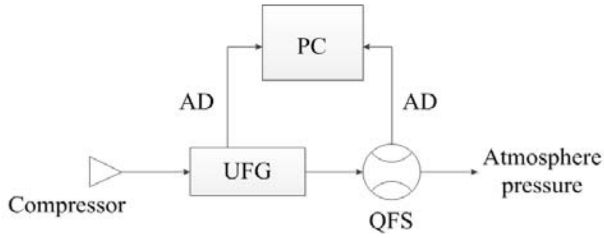

Fig. 5 Schematic of the dynamic characteristics test

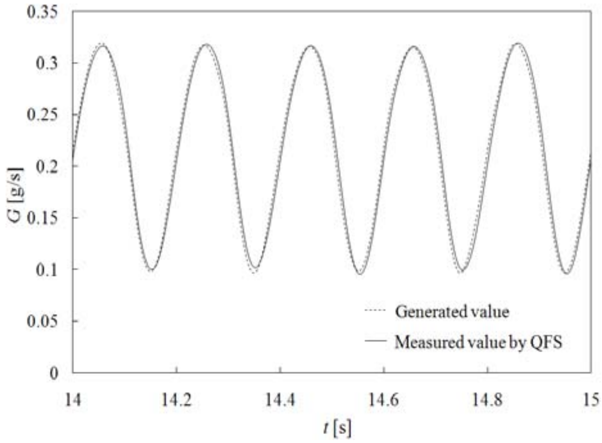

Fig. 6 Experimental results of the dynamic characteristics test (5 Hz)

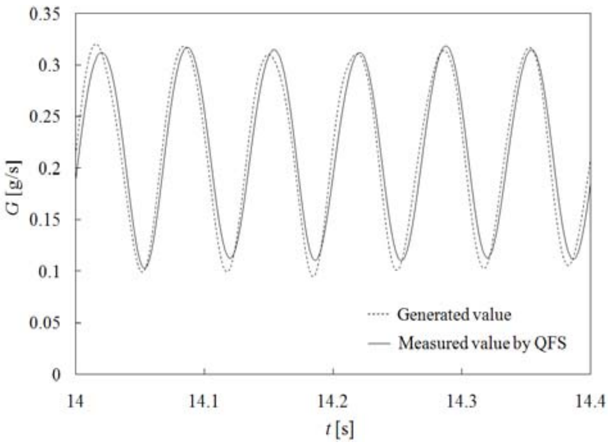

Fig. 7 Experimental results of the dynamic characteristics test (15 Hz)

the measured flow rate using the QFS are recorded and compared in a computer equipped with an AD/DA converter. In the experiments, the set value of the generated flow rate from the UFG is defined according to equation (2).

$$G \quad [\text{g/s}] = 0.216 + 0.108 \sin(2\pi f t) \qquad (2)$$

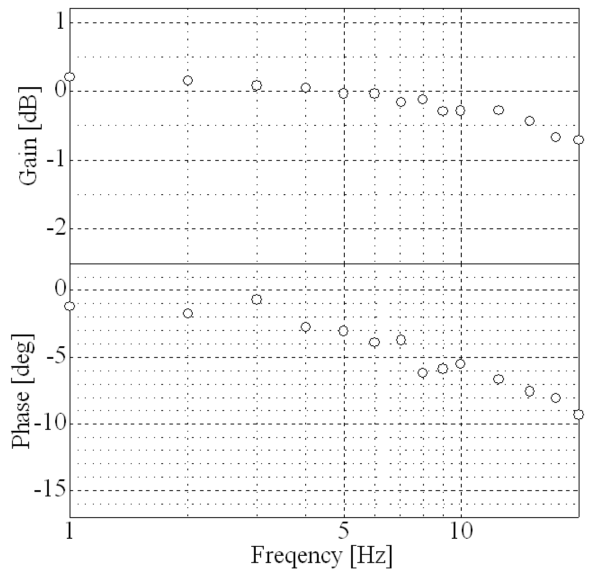

Fig. 8 Bode diagram of the dynamic characteristics of the QFS

The frequency f was varied from 1 Hz to 20 Hz. Examples of the experimental results when $f = 5$ Hz and 15 Hz are shown in Fig. 6 and Fig. 7, respectively. In Figs. 6 and 7, the broken line indicates the generated flow rate from the UFG and the solid line indicates the values measured by the QFS. The experimental results are summarized in the Bode diagram shown in Fig. 8. In the Bode diagram, the generated flow rate using the UFG is the denominator and the measured flow rate using the QFS is the numerator. The experimental results show that when $f = 20$ Hz, the gain is -0.8 dB and the phase is -9 deg. The needed frequency range for measuring the blown air into a soprano recorder when vibrato is expressed is several hertz at the highest. So, it is considered that the QFS is suitable for measurement of the blown air.

IDENTIFICATION OF RELATIONSHIP BETWEEN BLOWN AIR FLOW RATE AND MUSICAL INTERVAL USING THE QFS

When playing a recorder, an optimum blown air flow rate exists for each musical interval (tone). If the blown air flow rate is higher than the optimum value, the tone is high, and if the rate is lower, the tone is low, relative to the target tone. To identify the relationship between the optimum value of the blown air flow rate and the musical interval sounded by a soprano recorder, the experimental setup shown in Fig. 9 was used. In the experiment, the tone holes were closed by the solenoid plungers (i.e., fingers) and the blown air flow rate was adjusted using a variable throttle. The flow rate was adjusted to make the sound optimal. The flow rate was measured using the QFS, which was tested for static and dynamic

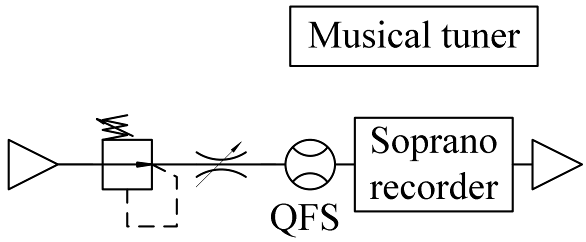

Fig. 9 Schematic of the experimental setup for the optimum flow rates for musical intervals

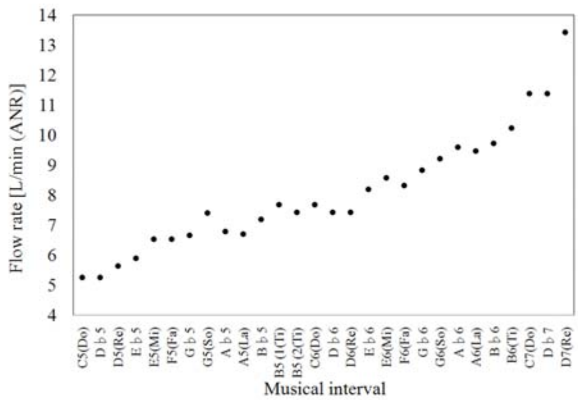

Fig. 10 Experimental results of the optimum flow rates for musical intervals

characteristics as described in the previous section. The musical tuner for discerning the musical tone was a Korg GA-1. The experimental results are shown in Fig. 10.

BLOWN AIR FLOW RATE MEASUREMENT FOR HUMAN RECOREDER PLAYERS

Definition of vibrato

Vibrato is a musical sound expressed by varying periodically tone pitch or intensity of a sound around a certain tone when playing a musical instrument or singing a song. In musical terminology, the vibration of the tone pitch is called “vibrato” and the vibration of the intensity of the sound is called “tremolo”, but the discrimination between these two terms is often difficult in practice. For a recorder especially, both the tone pitch and the intensity of the sound change as the blown air flow rate changes.

Measurement of vibrato played by human recorder players

In this section, by using the experimental setup shown in Figs. 11 and 12, the sound level and the blown air flow rate were measured when a human player expresses vibrato with a soprano recorder. Air from the player’s mouth is blown into the recorder through its windway, shown on the far left. The QFS is set between the player’s mouth and the windway of the recorder. The

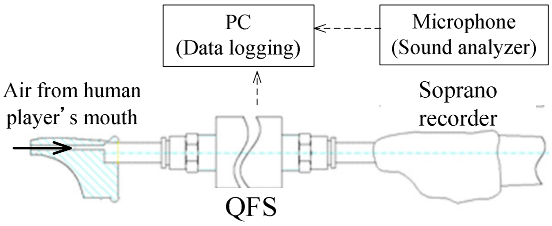

Fig. 11 Schematic of the experimental setup for measuring the sound level and blown air of a human playing a recorder

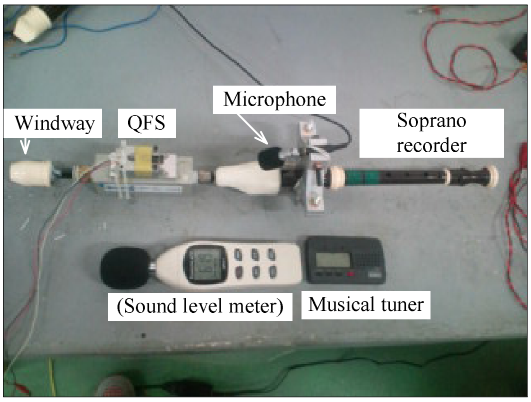

Fig. 12 Photograph of the experimental setup for measuring the sound level and blown air of a human playing a recorder

Fig. 13 Photograph of the experimental setting

blown air flow rate is measured by the QFS and the sound level is recorded and analyzed using a microphone (Sony ECO-DS30P) and a sound analyzer (Sound Engine Free).

The experiments were performed by three human recorder players. The three people were flute players of Fukuoka Institute of Technology Wind Symphony, one of the most famous university symphony orchestras in Japan. A photograph of the experimental setting is shown in Fig. 13. The experiments were conducted five times

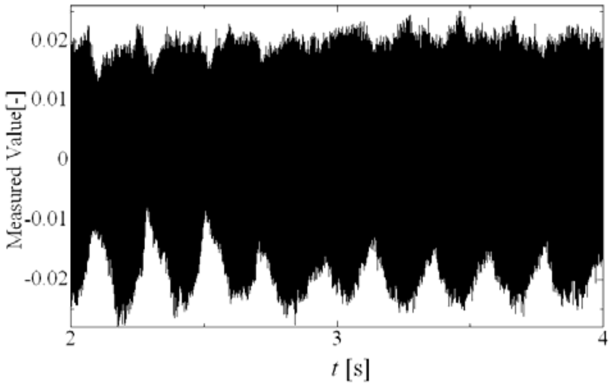

Fig. 14 Experimental data of a human recorder player playing the tone “la” (A5) measured by the microphone

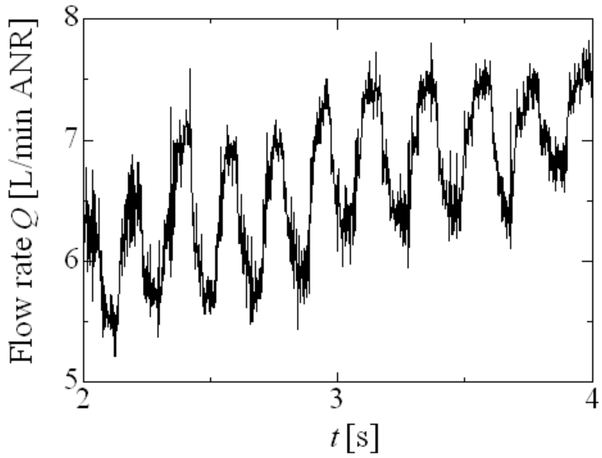

Fig. 15 Experimental data of human recorder players measured by the QFS

for each player. The tone played in the experiments was “la” (A5), since A is commonly used as a criterion in the tuning of musical instruments. One example of the experimental data measured by the microphone is shown in Fig. 14. In Fig. 14, the longitudinal axis indicates the scale of the WAV file, which by itself shows no physical characteristics to measure the sound level and blown air of a human playing a recorder. The cyclic wavy profile indicates the change of intensity of the sound. Fig. 15 shows the experimental data measured by the QFS. As shown in Figs. 14 and 15, the frequency of the blown air was approximately 5 Hz.

APPLICATION TO A RECORDER-PLAYING ROBOT

In this section, the identified flow rate model in the last section is applied to the air flow rate control system of the soprano-recorder-playing robot, shown in Fig. 16, to realize humanlike sounds produced while playing vibrato.

In the robot system shown in Fig. 16, a QFS was added between the SP valve and the recorder, in contrast with the system shown in Fig. 1.

Proposed blown air controlling method

The schematic of the controlling part of the blown air of the recorder-playing robot is shown in Fig. 17. In the digital signal process (DSP: MTT s-BOX), the measured flow rate in Fig. 15 was used as the set value of the flow rate controller. To precisely control the flow rate, feed forward control (nonlinearity compensation of the SP valve) was conducted, as illustrated in Fig. 18. Since the SP valve has nonlinearity as a characteristic, the relationship between the control signal and the sonic conductance (effective cross-sectional area) was

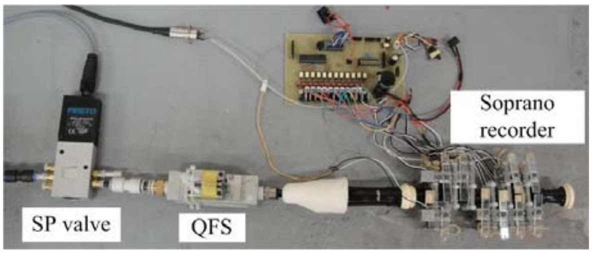

Fig. 16 Recorder-playing robot with the QFS

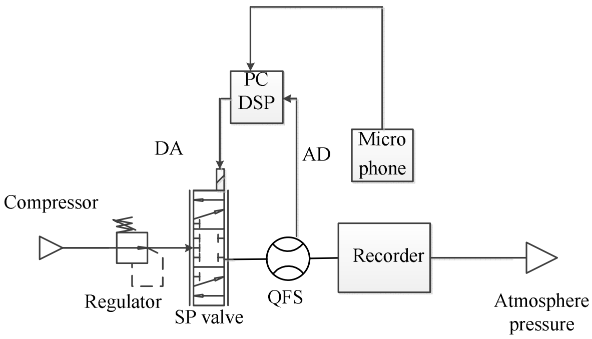

Fig. 17 Schematic of the blown air control part

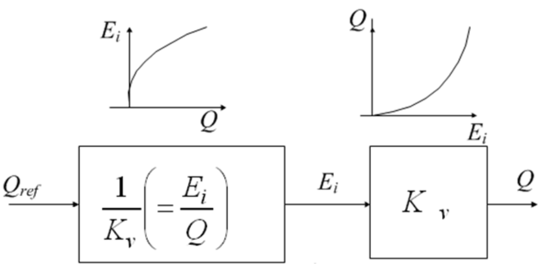

Fig. 18 Schematic of the feed forward control (nonlinearity compensation of SP valve)

preliminarily measured. Then, the inverse function ($1/K_v$) was multiplied by the set value of the flow rate Q_{ref}, as shown in the left block in Fig. 18.

Experimental results of the robot playing the recorder

In the experiment, the tone set was "la" (A5), so the MIDI signal corresponding to that tone was sent to the fingering controller. The measured flow rate stated in the last section (Fig. 15) was used as the set value of the flow rate controller.

The experimental results of the blown flow rates obtained by the QFS are shown in Fig. 19. As shown, the measured value of the flow rate of the human player performing vibrato and that of the recorder-playing robot correspond very well. Figs. 20 and 21 show the results of the frequency analysis. Since the tone is "la" (A5), the 1st mode frequency is 880 Hz. The analyzed results obtained by the human player and the robot correspond very well.

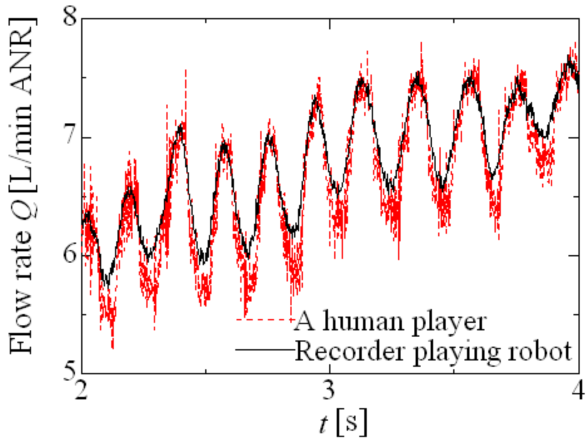

Fig. 19 Measured flow rates obtained by the QFS while vibrato was expressed

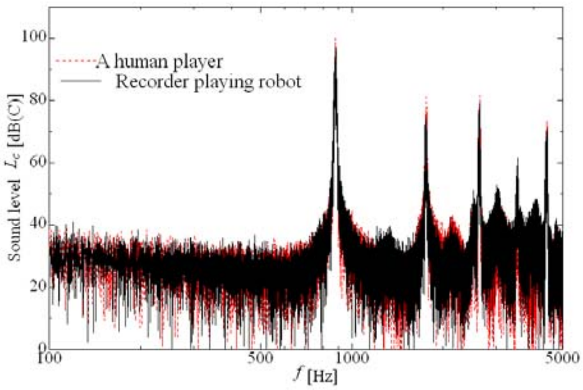

Fig. 20 Experimental results of the sound level

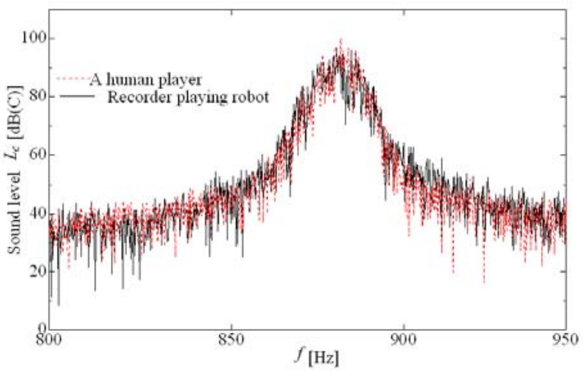

Fig. 21 Experimental results of the sound level (magnified)

CONCLUSIONS

To realize a soprano-recorder-playing robot that produces natural sounds matching those produced by a human player, this study employs unsteady flow rate measurements and control techniques to control the blown air for a soprano recorder. In the present research, the following procedure was conducted. First, not only the static but also the dynamic characteristics of the flow sensor used for measurement of the blown air were calibrated using an unsteady flow generator to judge whether the performance of the flow sensor was high enough to measure the blown air. Second, using the flow sensor, the blown air flow rates were measured when real human players (members of a brass band) performed vibrato with a soprano recorder. Finally, the identified blown air flow rate model was applied to the air flow rate control system of the soprano-recorder-playing robot. The flow rate was controlled by a spool type servo valve. The sounds played by the real human player and those played by the robot were compared using a sound analyzer. The experimental results showed that the results obtained for the human player and for the recorder-playing robot agreed very well.

In future work, the measured flow rate waves for human players should be modeled and applied to the control of the blown air flow rate of the recorder-playing robot when playing a song.

ACKNOWLEDGMENT

The authors would like to give special thanks to the members of Fukuoka Institute of Technology Wind Symphony for their cooperation in the experiments.

REFERENCES

1. http://www.toyota.co.jp/en/special/robot/
2. Kaneko Y., Mizuhara S, Mizutani K., Nagai K. : Artificial Lips for Automatic Trombone Blower (Biomimetics & Innovative Design) : Proc. of the Asian Pacific Conference on Biomechanics : emerging science and technology in biomechanics, 2004, pp.23-24
3. http://www.midi.org/
4. Kato T., Kawashima K., Cai M., Funaki T., Takayama K., Kagawa T. : Development of Dynamically Calibrated Quick Response Flow Sensor and Its Application to Pressure Servo Control System, Proceedings of 7th Triennial International Symposium on Fluid Control, Measurement and Visualization, 2003, CD-ROM
5. Funaki T., Kawashima K., Kagawa T. : Generator of variable gas flows using an isothermal chamber, Measurement Science and Technology, Vol.18, 2007 pp.835-842

Proceedings of the 8th JFPS International
Symposium on Fluid Power, OKINAWA 2011
Oct. 25-28, 2011

2D1-4

SOFTNESS DISPLAY BASED ON LOW FRICTION PNEUMATIC CYLINDER*

Zhongsheng SUN, Xiaoning LI, Liangpeng Kou and Yan TENG

SMC Pneumatics (Nanjing) Technical Center
School of Mechanical Engineering
Nanjing University of Science & Technology
200 Xiaolingwei Street, Nanjing 210094, China
(E-mail:billsun1978@163.com)

ABSTRACT

Now the researches of haptic display mainly focus on the simulation of force, roughness, geometrical shape and texture, whereas the research about softness display is paid less attention. This paper introduces a softness display based on low friction pneumatic cylinder, which not only has the advantages of simple structure, big stiffness changing range, but also has the merits of pneumatic actuation such as compliance and safety. The compliant softness display is quantificationally realized by the force servo-control of low friction cylinder, namely, controlling the cylinder output force proportional to its displacement. Firstly, the nonlinear mathematical model of valve controlled cylinder is built, and its linear model is deduced by linearization with the method of general approximate linearization of working-point. At last, the control accuracy, stability, force response rate and fidelity of softness display is researched by experiment. By the research in this paper, we hope that the designed softness display system based on low friction cylinder not only promotes the design of the compliant haptic interface and the application in the virtual reality, but also contributes to the application in the medical field (for example, virtual surgery).

KEY WORDS

softness display, low friction cylinder, virtual reality

INTRODUCTION

Haptic perception is the important information channel to explore and recognize an object by conveying several physical information to mechano-receptors and thermo-receptors lying into our skin throughout the body[1]. Moreover the haptic perception is a combined activation of two groups of physiological sensations: force and tactile sense. The former refers to the information about joint angle or muscle contractile force mediated by the sensory receptors in the muscle, articular capsules, and the tendon. The latter is mainly by cutaneous perception, and can be divided into two groups according to its characteristic. The first is sliding perceptions of geometric properties such as shape, size, texture, etc. Another is the dynamic perception perpendicular to the interface between the finger and object, namely the compliance haptic display about the softness or stiffness of virtual object. The softness rendering or display

* Supported by NUST Research Funding,（NO: 2010ZYTS010）, National Natural Science Foundation of China (No: 50905089) and Qing Lan Project

appears to be of particular importance in application of simulation of soft object in virtual environment or soft tissue in virtual operation.

At present, various types of display devices to simulate the softness perception have been developed by regulating certain physical parameter such as elasticity, pressure or contact area. That is to say, the level of elasticity can be associated with a specific force-displacement or force-area behavior [1]. Mavroidis designed a compliance haptic interface using electro-rheological fluids [2], which enable a remote operator to feel the stiffness of virtual object by regulating the electric intensity in the Electro- Rheological fluid to change its damping force. Fujita developed a force feedback glove to display the hardness of virtual object by applying force to the fingertip as the displacement of object deformation [3]. Song aiguo realized the softness display device actuated by a motor to reproduce the stiffness of virtual object from very soft to hard by adjusting the length of thin elastic beam [4]. The softness display devices mentioned above adopt the force- displacement method. Fujita also designed a new softness display system to control the fingertip contact area dynamically based on the detected contact force with a servo controlled pump for fluid volume control [5]. Bianchi showed a new bi-elastic fabric-based display for rendering softness, and its different levels of softness is regulated by the stretching of fabric induced by a motor[1]. Bicchi thinks that the ability of humans to detect softness of different objects by tactual exploration is intimately related to both kinesthetic and cutaneous perception [6]. Based on such principle, he design a CASR display surrogating tactile information for softness discrimination, with information on the rate of spread of the contact area between the finger and the specimen as the contact force increases[6]. In order to enhance the performance of softness rendering, he also integrated the CASR display with the Delta haptic device to simultaneously replicate independent force-displacement and force-area behaviors [7].

The softness display devices based on the force-area behaviors only qualitatively reflect the elasticity of virtual object. Although the motor-actuated haptic display devices can accurately and quantitatively simulate the stiffness of virtual object, its value is relatively small. In this paper, a softness display system based on low friction cylinder is designed, which could simulate the softness of virtual object quantitatively and accurately regulate the value of stiffness in a large range. Shen already demonstrated that the pneumatic actuator can provide a significantly larger value of simulated stiffness than the motor-actuated haptic interface [8].

SOFTNESS DISPLAY SYSTEM

The schematic representation of softness display system shown in Fig.1 consists of two parts. One is the softness display device; another is the virtual environment of softness rendering. When the hand doesn't tough the virtual object, namely in free space, the hand moves along with the cylinder rod, and the operator feels very small force close to zero by controlling the resistance of the pneumatic cylinder. The movement information of hand such as position is conveyed to the virtual environment for driving the probe or virtual hand. During the softness rendering, the collision detection algorithm checks continually. Once the probe or virtual hand collides with the virtual object, the force being displayed is calculated in the virtual environment according to the deformation and conveyed to softness display system. Then the softness display system controls the pressure in two chambers of pneumatic cylinder. We regard the force exerted actively by the hand as loading force. When it is in equilibrium state, the loading force is equal to the force produced by the pneumatic cylinder. If we only simulate the stiffness of virtual object, virtual object can be considered as a spring. As long as the loading force is proportional to the displacement, the operator would feel the softness sensation.

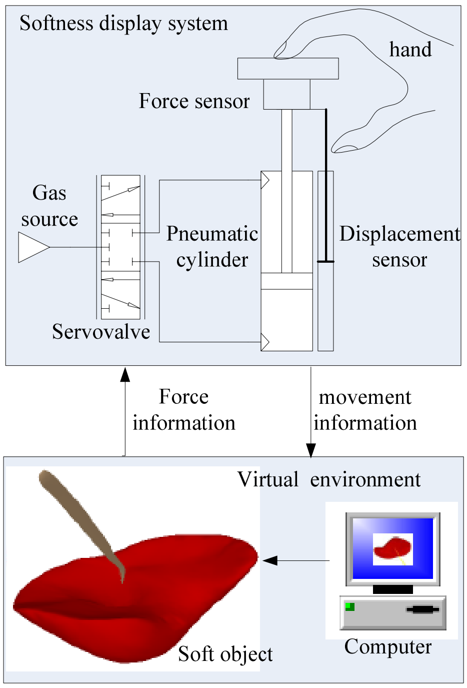

Figure 1 Schematic representation of softness display

MATHEMATIC MODEL OF SYSTEM

Softness display based on low friction cylinder can be considered as force control of pneumatic cylinder. Indeed, it is a valve controlled cylinder system. Hence, its mathematic model is established in the following.

Cross section equation of valve

Because the dynamic response frequency of valve can be up to 100Hz, and is much larger than that of the system, the valve flow can be considered as a proportional component.

$$A_u = A_u(u) = K_u(u)u \tag{1}$$

Where A_u represents the valve orifice area, u is the command voltage signal, and K_u is the gain of the valve effective opening area to the command voltage.

Flow equation of system

According to the study of Sanville F.E, the mass flow Q_{m1} into the inflation chamber and Q_{m2} out of the deflation chamber can be denoted by Eq. (2), (3).

$$Q_{m1} = \frac{A_u p_s \sqrt{1-b}}{\sqrt{RT_s}} \omega_1(\sigma, b) \tag{2}$$

Where

$$\omega_1(\sigma,b) = \begin{cases} 1, & \sigma = \dfrac{p_1}{p_s} \le b \\ \sqrt{1-\left(\dfrac{\sigma-b}{1-b}\right)^2}, & \sigma = \dfrac{p_1}{p_s} > b \end{cases}$$

$$Q_{m2} = \frac{A_u p_2 \sqrt{1-b}}{\sqrt{RT_2}} \omega_2(\sigma, b) \tag{3}$$

Where

$$\omega_2(\sigma,b) = \begin{cases} 1, & \sigma = \dfrac{p_0}{p_2} \le b \\ \sqrt{1-\left(\dfrac{\sigma-b}{1-b}\right)^2}, & \sigma = \dfrac{p_0}{p_2} > b \end{cases}$$

Where b is the critical pressure ratio, P_s is the pressure of gas source, P_1 and P_2 are the pressure of inflation and deflation chambers respectively, P_0 is the atmosphere pressure, T_s is the temperature of gas source and T_2 is the gas temperature of deflation chamber.

Differential equation of chamber pressure

In order to simplify the calculation, the following assumptions are made. a) The gas is ideal gas. b) There is no heat exchange when the gas flows through the valve ports, that is to say, the process is isoentropic adiabatic process. c) The temperature variation in the two chambers can be ignored, and the temperature is a constant value of T. d) the leakage is ignored.

Using the law of conservation of energy, the differential equation of pressure inside each chamber of cylinder can be express as

$$\dot{p}_1 = kRT\frac{Q_{m1}}{V_1(x)} - \frac{kA_1 \dot{x} p_1}{V_1(x)} \tag{4}$$

$$\dot{p}_2 = kRT\frac{Q_{m2}}{V_2(x)} + \frac{kA_2 \dot{x} p_2}{V_2(x)} \tag{5}$$

$$V_1(x) = V_{10} + A_1 x \qquad V_2(x) = V_{20} - A_2 x \tag{6}$$

Where x is the position of cylinder piston, V_{10} and V_{20} are the initial volume of two chambers.

Dynamic equation of cylinder

According to the Newton's second law, the dynamic equation of cylinder can be expressed as

$$F = p_1 A_1 - p_2 A_2 + (m\ddot{x} + \mu\dot{x}) + f \tag{7}$$

Where F is the force exerted on the cylinder by operator, μ is the coefficient of piston viscosity damping, f is the coulomb friction.

Because the coulomb friction of the cylinder used in this paper is very small, only one tenth or one fifth of the rubber sealing cylinder, the coulomb friction f can be ignored. Eq. (1) can be converted as

$$F = p_1 A_1 - p_2 A_2 + (m\ddot{x} + \mu\dot{x}) \tag{8}$$

When the force exerted on the cylinder by operator is proportional to the displacement of the hand, the softness sensation like pushing a spring can be perceived by operator. So the softness display can be considered as a question of force servo-control.

From the mathematic model of the pneumatic force servo system, we can see that this is a seriously nonlinear system, and the model parameters change with the working point of the system. In order to analyze the system performance, the nonlinear system is linearized at its working point. And the PID control with variable arguments (shown in Fig.2) is applied to the force servo control. The arguments of PID control are chosen according to the displacement of cylinder and the error between the measured force by force sensor and the desired force proportional to the displacement.

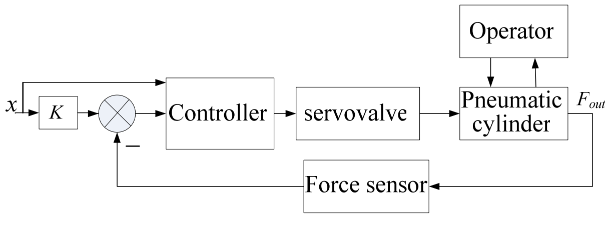

Figure 2 Schematic representation of force control

EXPERIMENT

In this paper, the softness perception like pushing a spring (shown in Fig.3) is simulated. Before hand presses the spring, the hand should not feel any force. The hand moves together with the cylinder, and the value of force sensor should be close to zero. After the hand presses the spring, the force perceived by operator should be proportional to its deformation.

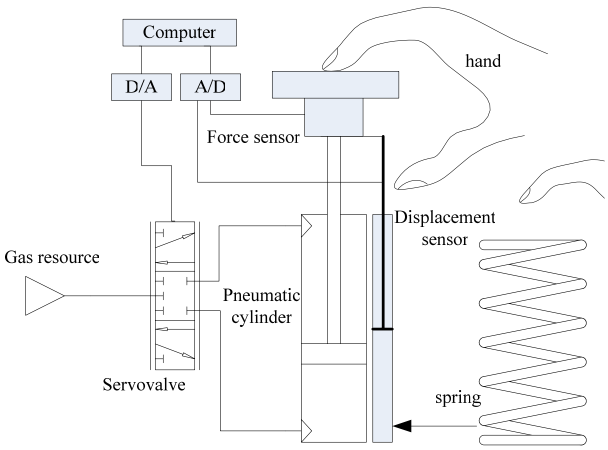

Figure 3 Schematics of experiment

The photograph of experiment is shown in Fig.4. The pneumatic cylinder (SMC MQMLB16-100D) has the characteristic of low friction, whose inner diameter and stroke are 16mm and 100mm respectively. The cylinder is controlled by a proportional flow servo-valve (FESTO MPTE-5-M5-010-B). The tension and compression force sensor is connected on piston rod to measure the loading force. The displacement of cylinder is measured by the displacement sensor of MTS R-series to generate the desired force according the contact state and the stiffness of virtual object such as spring. The supplied air is at a gauge pressure of 0.5MPa.

We assume that the position of piston rod is 0 mm when the cylinder is in the state of extrusion, and the position of piston rod is 100 mm when the cylinder is in the state of retraction. The measured and desired force charts according to the displacement are shown in Fig.5 and Fig.6 respectively when the setting stiffness is 1N/mm and 5N/mm. the dashed line at the position of 30mm denotes the contact point with virtual object. It can be seen that the perceived force by the operator is close to zero when the position is within 30mm, and is proportional to the displacement of cylinder after contacting with virtual object. So the operator can feel the softness sensation of pushing a spring. Fig.7 shows the relation between the position of cylinder and the measured force. The curve slope denotes the stiffness of simulated object.

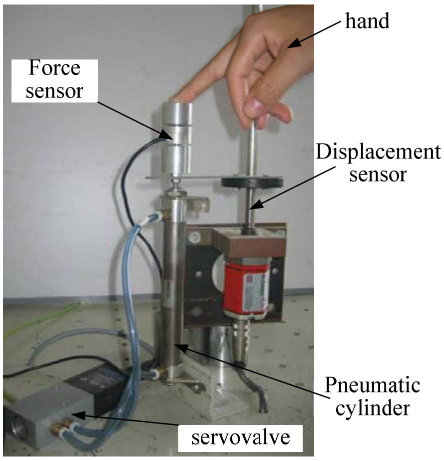

Figure 4 photograph of experiment system

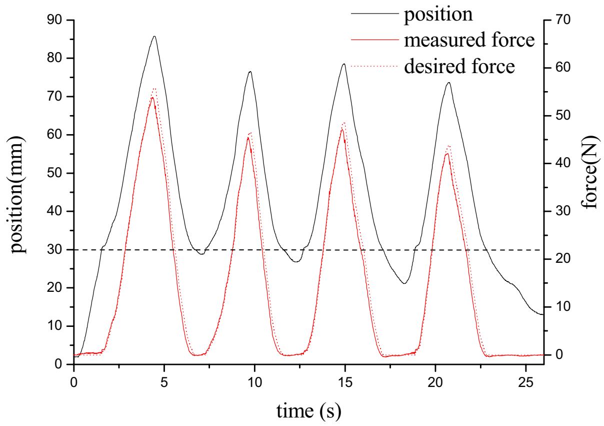

Figure 5 Desired and measured force according to the displacement of cylinder (K=1N/mm)

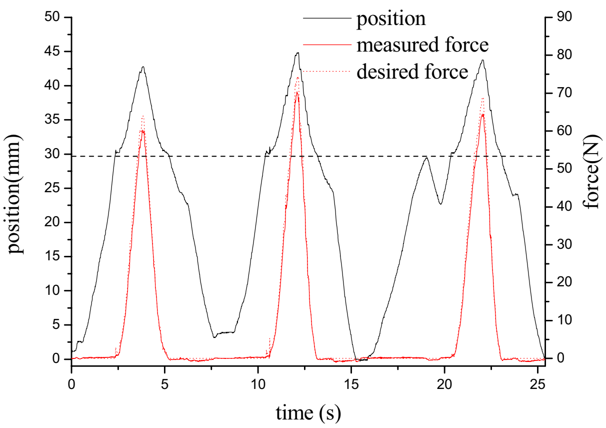

Figure 6 Desired and measured force according to the displacement of cylinder (K=5N/mm)

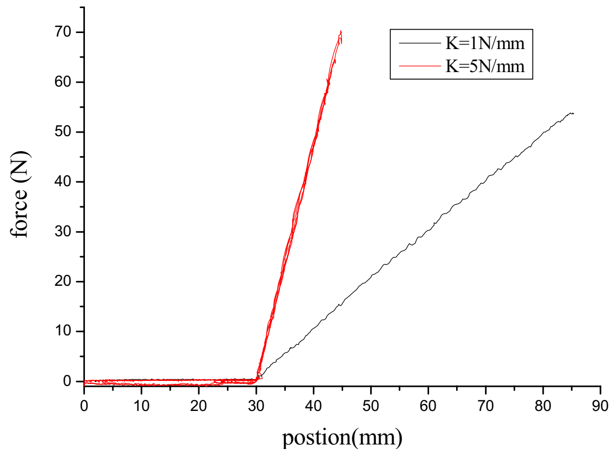

Figure 7 Relation between position and force

CONCLUSION AND FUTURE WORK

In this paper, a softness display system based on low friction pneumatic cylinder is established. The nonlinear mathematical model of valve controlled cylinder is built, and linearized with the method of general approximate linearization of working-point. The experimental results indicate that it can simulate the sensation of softness and the stiffness can be regulated according to the simulated virtual object.

The desired force is generated only by the displacement of cylinder and the assumed stiffness. And the virtual environment isn't in the control loop. In the future, we would built a realistic virtual environment and simulate the softness display in a complete control loop with the valve controlled cylinder system.

REFERENCES

1. Bianchi M., Serio A., Scilingo E. P. and Bicchi A., A New Softness Display Based on Bi-Elastic Fabric. World Haptics 2009, Salt Lake City, USA, pp.382-383.
2. Mavroidis C., Pfeifer C., Celestino J., Cohen Y. B., Controlled Compliance Haptic Interface Using Electro-Rheological Fluids. Proceedings of SPIE Conference on Electro-Active Polymer Actuators and Devices, 2000, Bellingham, WA, pp.300-310.
3. Fujita K., Development and Evaluation of Force Feedback Glove for Hardness Display of Virtual Object, Trans.IEICE, 1997, Vol. 81, No.10, pp. 2394-2400
4. Jia Liu, Aiguo Song and Haiyan Zhang, Research on Stiffness Display Perception of Virtual Soft Object, Proceedings of the International Conference on Information Acquisition, 2007, Jeju City, Korea, pp.558-562
5. K. Fujita, H. Ohmori, A New Softness Display Interface by Dynamic Fingertip Contact Area Control, Proc. of the 5th World Multiconference on Systemics, Cybernetics and Informatics, 2001, pp.78-82.
6. Antonio Bicchi, Enzo P. Scilingo, and Danilo De Rossi, Haptic Discrimination of Softness in Tele_ operation: The Role of the Contact Area Spread Rate, IEEE Transactions on Robotics and Automation, 2000, Vol. 16, No. 5, pp. 496-504.
7. Scilingo E. P., Bianchi M., Grioli G., and Bicchi A., Rendering Softness: Integration of Kinesthetic and Cutaneous Information in a Haptic Device, .IEEE Transactions on Haptics, 2010, Vol. 3, No. 2, pp. 109-118.
8. Xiangrong Shen, and Michael Goldfarb, On the Enhanced Passivity of Pneumatically Actuated Impedance-Type Haptic Interfaces. IEEE Transactions on Robotics, 2006, Vol. 22, No. 3, pp. 470-479.

Proceedings of the 8th JFPS International
Symposium on Fluid Power, OKINAWA 2011
Oct. 25-28, 2011

2D2-1

CONTROL DESIGN FOR ANTAGONISTIC DRIVE WITH PNEUMATIC ACTUATORS

Mizuki Komiya*, Kenji Kawashima*, Kotaro Tadano*, Toshiharu Kagawa*

* Tokyo Institute of Technology
4259 R2-46,Nagatsuta-cho,Midori-ku, Yokohama, Kanagawa, 229-8503 Japan
(E-mail: komiya.m.aa@m.titech.ac.jp)

ABSTRACT

Recently, pneumatic servo systems have been widely applied to mechanical systems. Because air has a number of advantages, including compressibility, high power ratio, and low heat generation. Antagonistic drive with a pair of pneumatic actuators connected by wire is widely used in robots to transform linear motion to rotation. However, wire tension affects to the drive. The drive becomes unstable when the tension is too high. The tension can be controlled with pneumatic servo valves. Therefore, control method including the configuration of servo valves for the drive is an important issue. In this paper, we focus on an antagonistic drive for joint rotation with a pair of pneumatic cylinders connected by wire. To compensate the effects of tension, two control methods using mean or minimum tension are proposed and studied experimentally. Then, the controllability is compared with three configurations of the pneumatic servo valves. The experimental results indicate that the use of minimum tension T_0 is effective for the compensation. We also confirm that the response of the system can be improved by using four 3-port servo valves.

KEY WORDS

Key words, Pneumatic actuator, Antagonistic drive, Angular control, Tension control, Valve configuration

NOMENCLATURE

F_1, F_2 : cylinder force [N]
K_{aP} : proportional gain of force control [V/N]
K_{ai} : integral gain for force control [V/N・s]
K_{PP} : proportional gain of position control [mNm/rad]
K_{Pd} : differential gain of position control [mNms/rad]
P_1, P_2 : inner pressure of cylinder [Pa]
P_0 : equilibrium pressure [Pa]
P_a : atmospheric pressure [Pa]
P_s : supply pressure [Pa]
q : angle of shaft [rad]
r :joint radius [m]
T_1, T_2 : tension of wire [N]
T_0, T_m :minimum and mean tension of wire [N]
τ : torque [mNm] u_1, u_2 : input voltage [V]

1. INTRODUCTION

Recently, pneumatic servo systems have been applied in several mechanical systems, such as pneumatic robot systems [1], aspherical glass molding machines, and a precise positioning stage [2]. Significant advantages, like low heat generation and non-magnetic make the pneumatic system become universal. In addition, the air power is compressibility with a high power ratio. Importantly, air is a clean and renewable energy source.

Pneumatic servo system control methods have been studied since the 1950s [3][4]. The performance of the system improved greatly as the pneumatic servo valve became commercially available in the late 1980s [5]. The pneumatic servo valve is the key element in the system. Its structure and parameters are important in order to achieve good performance [6][7][8][9].

Antagonistic drive is widely used in pneumatic robots to transform linear motion to rotation [10][11][12]. The drive system is affected by the friction caused by tension and becomes unstable when the stiffness of the system becomes higher. Therefore, the control method and the configuration of the valves for the drive are important issues.

In this paper, we focus on an antagonistic drive for joint rotation with a pair of pneumatic cylinders connected by wire. To compensate the effects of tension, two control methods using mean or minimum tension are proposed and studied experimentally. Moreover, the controllability is compared with three configurations of the pneumatic servo valves.

2. EXPERIMENTAL APPARATUS

Fig.1 shows the photograph of the experimental apparatus for tendon drive. Fig.2 and Fig.3 shows the schematics of tendon drive and experimental apparatus. In this experiment, we used a metal rod(ϕ 8mm) for rotating shaft. This shaft is driven by a pair of pneumatic cylinders connected by stainless steel wire(ϕ 0.36mm). Without extension and slack in the wire, and neglecting the friction of the cylinder, the wire tension T_1, T_2 are equal to the cylinder force F_1, F_2. Thus joint torque represented by the following equation.

$$\tau = (T_2 - T_1)r = (F_2 - F_1)r \tag{1}$$

The angle of the shaft is measured by an encoder installed in the joint, and the driving forces of cylinders were calculated by measuring the pressure in the cylinders. Here, we confirmed in advance that the friction of the cylinder piston is negligible small. The angle and pressure data are taken into a PC through a digital input (DI) module. The PC acts as a controller and sends the control signals to the servo valves. Experimental equipments are summarized in Table1.

3. TENSION COMPENSATION METHOD

In the antagonistic drive system, the joint was driven by two pneumatic cylinders with wire. Without extension and slack in the wire, joint torque can be represented by Eq. (1). In this section, the effects of wire tension to the controllability of the system are studied. Two compensation methods for wire tension were proposed. An angular control was applied to the drive system to compare the difference between the methods.

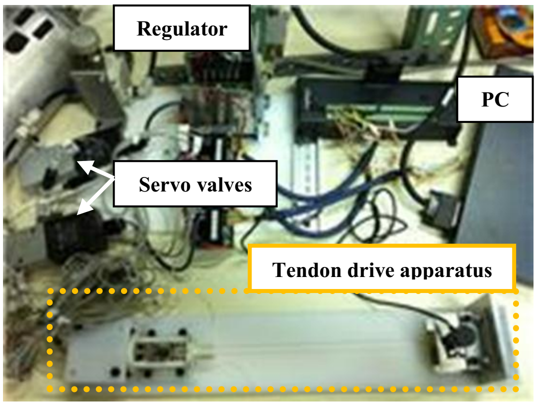

Figure 1 Experimental apparatus

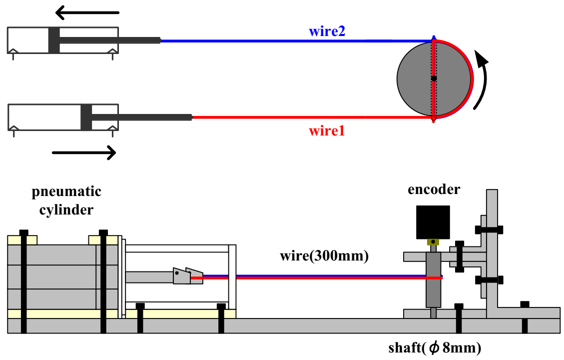

Figure 2 Schematic of tendon drive apparatus

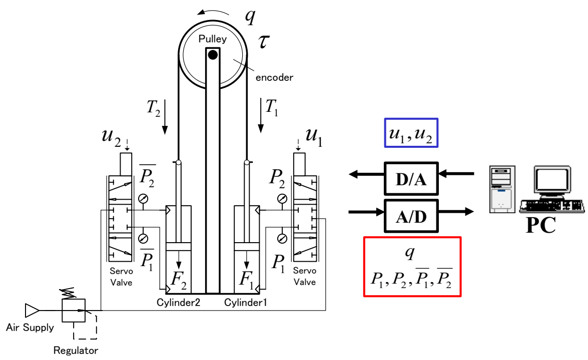

Figure 3 Schematic of experimental apparatus

Table 1 Experimental equipments

Servo valve	FESTO, MPYE-5-M5-010B
Pressure sensor	SMC,PSE510-R06
encoder	MTL,ME-12-2000P16
wire	Stenless wire (ϕ 0.36mm)

3.1 Angular control methods

The block diagram of the angular control is shown in Fig.4. A PD controller is used. As can be seen in Fig.4, a force control is implemented as a minor loop to the control. The reference angle q_{ref} was given as an input, and the reference torque τ_{ref} was calculated by the following equation.

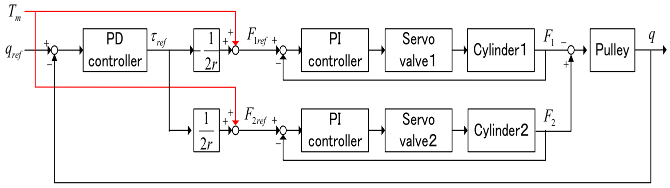

Figure 4 Block diagram of position control

$$\tau_{ref} = K_{pp}(q_{ref} - q) + K_{pd}(\dot{q}_{ref} - \dot{q}) \quad (2)$$

Here, K_{pp} and K_{pd} are the proportional gain and differential gain, respectively.

Two compensation methods were proposed to calculate the reference driving force F_{ref} of the cylinder from τ_{ref}, Those methods can be written as follows:

(a) Tension compensation method using mean tension T_m

$$F_{1ref} = -\frac{\tau_{ref}}{2r} + T_m \quad (3)$$

$$F_{2ref} = \frac{\tau_{ref}}{2r} + T_m \quad (4)$$

(b)Tension compensation method using minimum tension T_0

$$F_{1ref} = T_0 + \frac{|\tau_{ref}| - \tau_{ref}}{2r} \quad (5)$$

$$F_{2ref} = T_0 + \frac{|\tau_{ref}| + \tau_{ref}}{2r} \quad (6)$$

A relationship between T_m and T_0 can be written as Eq.(7). Since the two methods satisfy Eq.(8), wire slack can be prevented by setting T_m, T_0 high.

$$T_m = T_0 + \frac{|\tau_{ref}|}{2r} \quad (7)$$

$$\tau_{ref} = (F_{2ref} - F_{1ref})r \quad (8)$$

A PI controller is used for force control. The controller input u is calculated by

$$u = K_{ap}(F_{ref} - F) + K_{ai}\int(F_{ref} - F)dt \quad (9)$$

Here, K_{ap} and K_{ai} are the proportional gain and integral gain, respectively.

3.2 Experimental procedure

(1) Comparison of the magnitude of tension

The angular control as shown in Fig.4 is applied to the drive system. The reference sinusoidal wave with the amplitude of 0.8rad and the frequency 1Hz was inputted. The mean tension T_m was given as 2, 4, 6, and 8N and the minimum tension T_0 was given as 0, 2, 4, and 6 N to confirm the influence of the magnitude of the tension.

Table 2 Control gains

PD controller		PI controller	
K_{pp}	320[mNm/rad]	K_{ap}	0.3[V/N]
K_{pd}	1.6[mNms/rad]	K_{ai}	7.0[V/N•s]

The angular controllability was investigated. In the experiments, the supply pressure was set at 0.3MPa and the control parameters shown in Table 2 were used.

(2)Comparison of the two tension compensation methods

The angular control was applied to the drive system to compare the two methods of tension compensation. The reference sinusoidal wave with the amplitude of 0.8rad and the frequency of 1Hz was inputted. Stability limit of the proportional gain K_{pp} were investigated to compare the methods. In the experiments, the supply pressure was set at 0.3MPa and same control parameters as show in table 2 were used.

3.3 Experimental results

Fig.5 and Fig.6 shows the experimental results of angular control using mean and minimum tension, respectively. The upper, middle and lower figure shows time dependent rotation angle, driving force of the cylinder and torque at the joint with different mean or minimum tensions, respectively. Only the driving forces of a side of the cylinder are shown in the middle figure since they are almost symmetric.

The results of Fig.5 and Fig.6 show that the angle does not follow the reference at the peak point and the joint torque increases when the wire tension was set higher. With the increase of wire tension, the average force of the joint and friction increase. On the other hand, the stick-slip phenomena did not result in significant difference despite the increase of the friction. It implies that the friction in the cylinder is more influential to the stick-slip phenomena than the friction of the joint.

Fig.7 shows the stability limit of the proportional gain K_{pp}. The results of Fig7 show that the stability range increases as T_m becomes higher, while the magnitude of T_0 does not affect to the stability. In the method using minimum tension, the reference force F_{ref} keeps higher than T_0. On the other hand, the method using mean tension, F_{ref} might become smaller than the tension and there is a fear for slack of the wire. Wire slack makes the disagreement with the wire tension T and the cylinder driving force F.

The results indicate that using a minimum tension T_0 is suitable for the angular control. Moreover, the angular control results also suggested that it is better to set lower T_0 to reduce the influence of the friction.

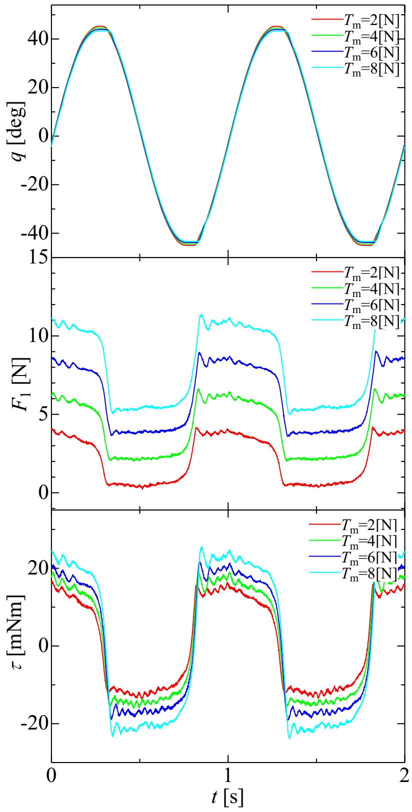

Figure 5 Experimental results with mean tension T_m

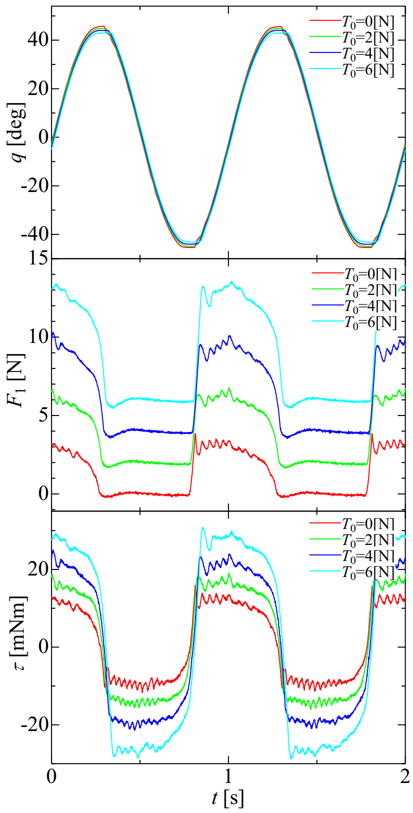

Figure 6 Experimental results with minimum tension T_0

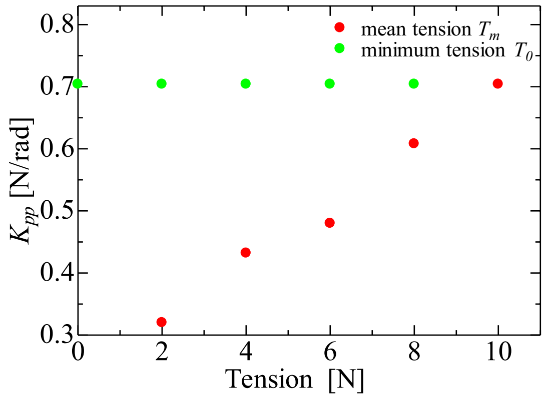

Figure 7 Stability limit of the proportional gain K_{pp}

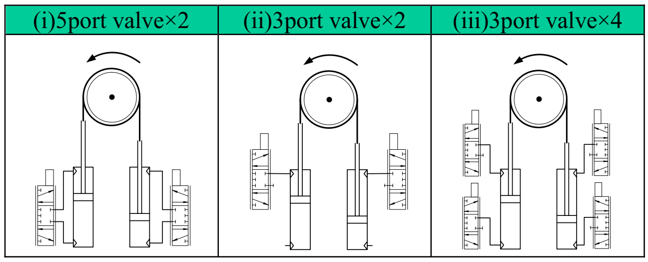

Figure 8 Control methods

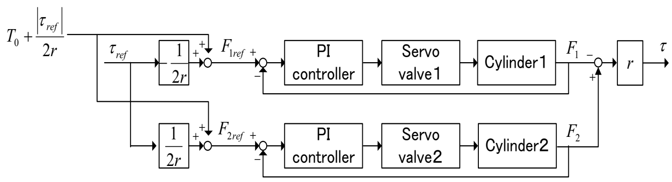

Figure 9 Block diagram of torque control

4. CONFIGURATION OF SERVO VALVE FOR ANTAGONISTIC DRIVE

Configuration of the servo valves to control the antagonistic drive with a pair of cylinders will cause a big effect to the controllability. Therefore, in this section, three configurations of the servo valves were considered. Fig.8 shows the schematics of configurations. The configurations can be summarized as follows:

(i) A 5- port servo spool-type valve is used to control the pressure difference of a pneumatic cylinder.

(ii) A 3-port spool-type servo valve is used to control only the rod side of the pneumatic cylinder. The head side is set as atmospheric pressure.

(iii) Two 3-port spool-type servo valves are used to control the pneumatic cylinder both for the rod and head side. Therefore, totally four servo valves are used to control the drive system. The equilibrium pressures were set at 0.2MPa and 0.3MPa.

A torque control and angular control were applied to the drive system to compare the configuration differences. The apparatus as shown in Fig.2 was also used in the experiments. The 3-port servo valve was realized by shutting the two ports of the 5-port servo valve. Therefore, the dynamics of the servo valves were the same for all configurations.

4.1 Control method

The cascade loop shown in Fig.4 was used for the torque control. The block diagram of the torque control is shown in Fig.9. The reference torque τ_{ref} was given as an input. The minimum tension of the wire T_0 as shown in Eq.(5) and Eq.(6) were used to obtain the reference force F_{ref}. The PI control as shown in Eq.(9) was used for the control.The angular control was applied with the control method as shown in Fig.4.

4.2 Experimental procedure

(1)Torque control

The frequency responses of the control system were investigated. The amplitude of the reference torque was given as 10mNm. The sinusoidal inputs from 1 to 40 Hz were given. The supply pressure was set at 0.3MPa and the minimum tension of 4N was applied. The joint was fixed at the center during the experiments. The control parameters shown in Table 2 were used in the experiments.

(2)Angular control

The angular control was performed with the three configurations. The angular controllability and observation of the stick-slip phenomena were investigated. The reference sinusoidal wave with the amplitude of 1rad was inputted. The frequencies from 1 up to 10Hz were given. The experiments were executed with no load.

4.3 Experimental results

Fig.10 shows the experimental results of torque control with the frequency of 10Hz. The experimental results are summarized in the bode diagram as shown in Fig.11. Fig.10 shows that the configuration (ii) is inferior to other control methods. This is because the stiffness of the cylinder is the lowest as the head side remains atmospheric pressure. The configuration (iii) with the equilibrium pressure 0.2MPa shows the best performance. The bandwidth becomes wider compared with the others as shown in Fig.11. This is considered to be because the charge and discharge from the servo valves becomes well-balanced with the configuration. The equilibrium pressure becomes about 0.15MPa with the configuration (i). Therefore, the charge becomes faster than the discharge. The opposite condition occurs with the configuration (iii) with 0.3MPa, i.e. unbalanced occurs.

The experimental results of the angular control at the frequency of 2Hz are shown in Fig.12. The stick-slip phenomena can be observed with the configuration (i) and (ii). On the other hand, smooth response was realized with the configuration (iii). This is because the force control loop can be improved with the configuration. As the response of the cascade loop affects to the main loop, the results are reasonable.

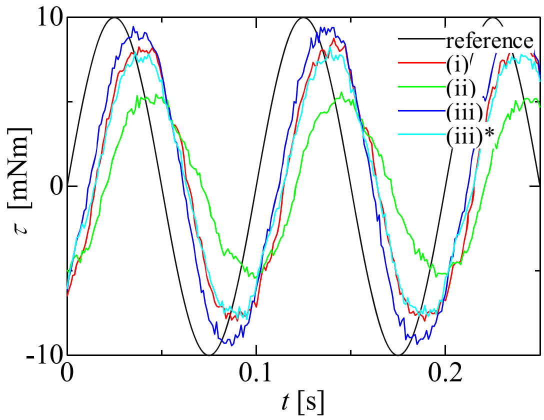

Figure 10 Experimental results of torque control(10Hz)

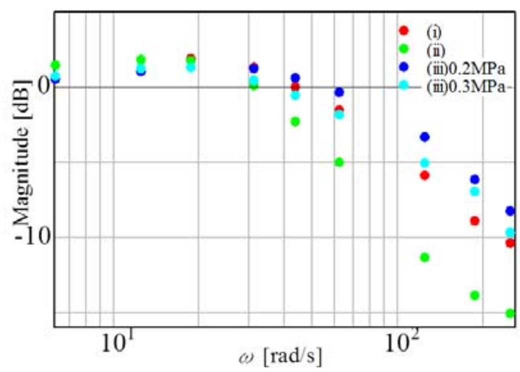

(a) Gain

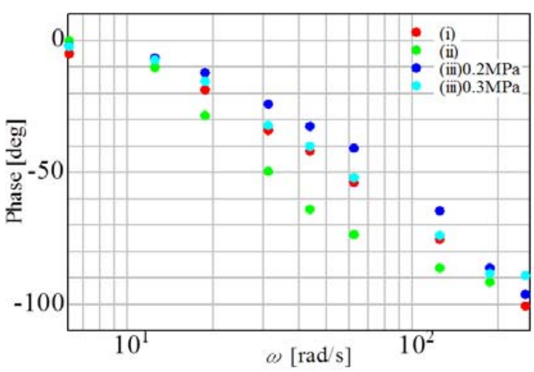

(b) Phase

Figure 11 Bode diagram

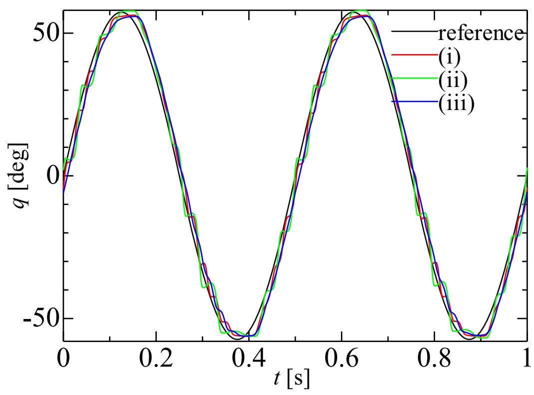

(a) q

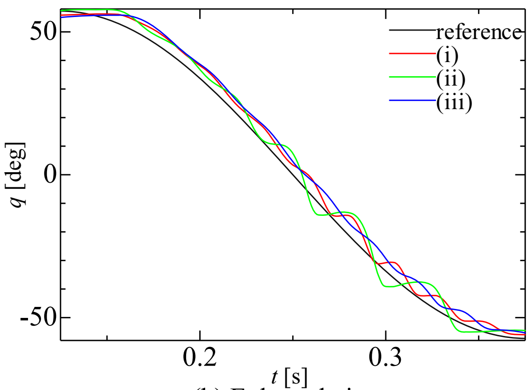

(b) Enlarged view

Figure 12 Experimental results of angular control

It became clear from the torque and angular control experiments that the use of four 3-port servo valve with suitable equilibrium pressure to realize well-balance between charge and discharge flow can realize good performance. However, the use of four valves costs and need space compared with the use of two servo valves.

5. CONCLUSION

In this paper, we focused on antagonistic drive with a pair of pneumatic cylinders. The control method of the system, the influence of tension to the controllability and the configuration of the servo valves were studied.

First, the effects of wire tension to the controllability of the system were investigated. Two types of tension compensation methods were considered. An angular control was applied to the drive system to compare the difference between the methods. The experimental results demonstrated that the use of minimum tension T_0 was effective to compensate the effect of wire tension.

Then, the configuration of servo valves was also studied. Three configurations of the servo valves were considered for the antagonistic drive with a pair of pneumatic cylinders. A torque control and angular control were applied to the drive system to compare the configurations difference. The experimental results show that the response of the system can be improved by using four 3-port servo valves. This was considered to be because the charge and discharge from the servo valves becomes well-balanced with the configuration.

REFERENCE

1. S. Liu , J. E. Bobrow, An Analysis of a Pneumatic Servo System and Its Application to a Computer-Controlled Robot, Transactions of the ASME Journal of Dynamic Systems, Measurement and Control, 1988, pp. 228-235.
2. T. Fujita, L. R. Tokashiki, T. Kagawa, Stick-Slip Motion in Pneumatic Cylinders Driven by Meter-Out Circuit; Proceedings of The 4th JHPS International Symposium on Fluid Power, 1999, pp. 131-136.
3. J. L. Shearer, Study of pneumatic processes in the continuous control of motion with com-pressed air-I,II. Transactions of the ASME, 1956, pp. 233–249.
4. C.R.Burrows and C.R.Webb, Use of the root loci in design of pneumatic servo-motors, Control, 1966, pp. 423–427.
5. Festo.http://www.festo.com/INetDomino/coorp_sites/en/index.htm.
6. I. L. Krivts, Optimization of performance characteristics of electropneumatic (two-stage) servo valve. Transactions of the ASME Journal of Dynamic Systems, Measurement, and Control, Vol.126, 2004, pp.416–420.
7. B.W.Andersen, The Analysis and Design of Pneumatic Systems. John Wiley & Sons, Inc, 1967
8. W. Backe, The application of servo pneumatic drives for flexible mechanical handling techniques. Robotics, Vol. 2, No.1, 1986, pp.45–56.
9. J. Pu and R H.Weston, A new generation of pneumatic servo for industrial robot, Robotica, Vol.7, 1988, pp.17–23.
10. T. Sasaki and K. Kawashima, Remote Control of Backhoe at Construction Site with Developed Pneumatic Robot System, Automation in Construction,2009,Vol.17,Issue 8,pp.907-914.
11. K. Tadano, K. Kawashima, K. Kojima, N. Tanaka, Development of a Pneumatic Surgical Manipulator IBIS IV, Journal of Robotics and Mechatronics 2010,Vol.22 No.2, pp.179-187.
12. N. Vitiello, T. Lenzi, S. Marco Maria De Rossi, S. Roccella, M. C. Carrozza, A sensorless torque control for Antagonistic Driven Compliant Joints, Mechatronics Volume 20,Issue 3, 2010, pp 355-367.

Proceedings of the 8th JFPS International
Symposium on Fluid Power, OKINAWA 2011
Oct. 25-28, 2011

2D2-2

BURROWING RESCUE ROBOT REFERRING TO A MOLE'S SHOVELING MOTION

Takashi KOBAYASHI*, Hideyuki TSHUKAGOSHI*,
Shunsuke HONDA*, Ato KITAGAWA*

* Department of Mechanical and Control Engineering,
Tokyo Institute of Technology,
S5-106, 2-12-1, Meguro-ku, Ookayama, Tokyo, 152-8552, Japan
(E-mail: t-kobayashi@cm.ctrl.titech.ac.jp)

ABSTRACT

In this study, a novel inspecting robot is proposed, which is aimed to move into the soil on its own, and inspect survivors more efficiently. This inspector is useful at landslide disaster sites, which occur after earthquakes, heavy rain, and accidents. Inside the soil, this inspector aims to be able to generate the necessary propulsion force as well as to steer by itself. The proposed propulsion method is inspired by the movement of a mole, which advances efficiently by pushing aside the soil with the shoveling motion. The characteristics and the efficiency of the proposed method are verified through basic experiments. Then, the verification of the behavior through burrowing as well as the possibility of steering is verified through experiments. In addition, the burrowing inspector is equipped with sensors, and it is verified the efficiency of information gathering through the landslide.

KEY WORDS

Key words, Biomimetic, Rescue Robot, Burrowing, Shoveling Motion, Pneumatics

NOMENCLATURE

a	:	Width of palm
b	:	Length of palm
x	:	Displacement of movement
z	:	Depth
θ	:	Angle of arm
φ	:	Angle of tilting

INTRODUCTION

The rapid search for survivors is required at landslide disaster sites, which occur after earthquakes, heavy rain, and accidents. Rescuers search for survivors by inserting a rigid bar into the soil and judging if there are any survivors by feeling the resistance force from the bar. However, it is difficult to search deep into soil because the insertion of the bar suffers resistance from the soil mass which is generated by pushing the soil. In addition, it can only search in a straight direction, so it is difficult to search behind a hard rock. Moreover, it is not enough to search for survivors only with the felling of the rescuer.

In this study, a novel type of robot is proposed, which generates propulsion on its own, steers propulsive direction and gathers the information with some sensors for searching for survivors covered by soil (Figure 1).

MECHANISM FOR BURROWING INTO SOIL

Methods for Pushing Aside Soil

The inspector is prevented from moving by the soil mass made by compressing the soil with the inspector itself. It is effective to push aside soil with the head of the inspector for efficient propulsion. The methods for pushing aside soil are classified into six methods as follows: peristaltic action, shaking motion, air injection, vacuuming, drilling motion and shoveling motion (Figure 2).

Authors have proposed a search and rescue robot which could be inserted into the soil with less force by pushing aside the soil using air injection [1]. It can steer its direction of movement by changing the direction of air injection. However, this robot could not generate propulsion force by itself.

The lunar exploration robot proposed by Nagaoka *et al* [2], uses the drilling motion to burrow into the soil, but it is difficult to steer the direction of movement.

Shoveling Motion

In this study, shoveling motion is proposed, which makes it possible to generate propulsion on its own as well as steer its direction of movement. This motion is realized by two arms with palms, and each of them pushes aside the soil by rotating the arms. Shoveling motion consists of two motions: digging motion with which the robot push aside soil, and recovery motion with which it recovers the position of the arms. This robot is inspired in the movement of a mole shown in Figure 3, but it has no hind legs to simplify the structure.

Shoveling motion is classified into three types according to the method of recovery motion: Rotating Motion Type which recovers the position of the arms by rotating them in one direction shown in Figure 4, Swing Motion Type which recovers the position of the arms by rotating it into another direction shown in Figure 5, and Rotating and Slide Motion Type which recovers the position of the arms by sliding the palms and rotating the arms shown in Figure 6.

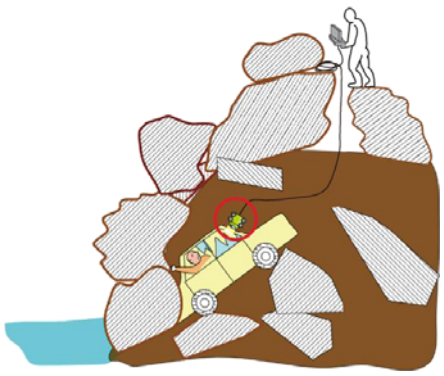

Figure 1 Image of the rescue operation in the soil

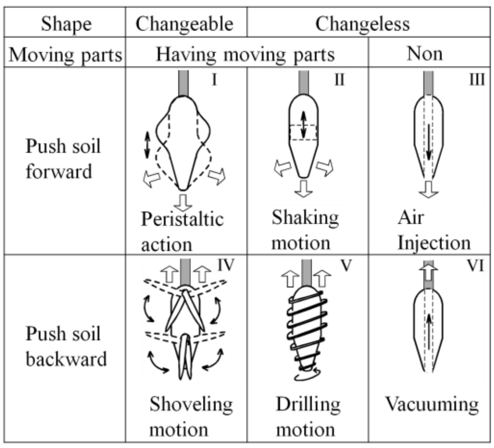

Figure 2 Methods for pushing aside soil

Figure 3 Shoveling motion of a mole

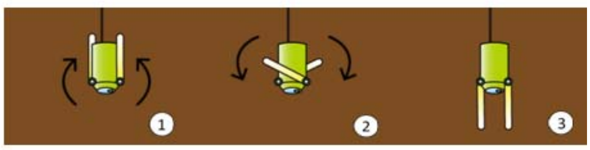

Figure 4 Rotating Motion Type

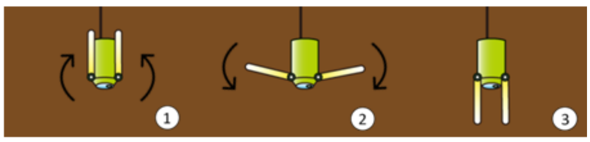

Figure 5 Swing Motion Type

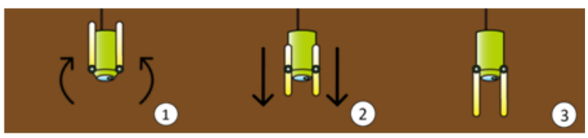

Figure 6 Rotating and Slide Motion Type

PROTOTYPE-1 ROTATING MOTION

Basic Motion

This prototype-1 takes Rotating Motion Type which is the simplest method to realize the shoveling motion. This motion is realized by rotating two arms with the palms in one direction shown in Figure 7. The palms are perpendicular to the arms to move into the soil efficiently. However, the inspector moves backward during the recovery motion, and the interference between the body and the palms prevent the rotation of the arms. A mole holds on with its hind legs to prevent from moving backward during the recovery motion, but it is impossible for this robot to do so.

Therefore, a cam mechanism is proposed to turn these arms parallel during the recovery motion shown in Figure 8. With this mechanism, the palms turn parallel to the rotation of the arms when the angle θ of the arms (shown in Figure 11) is πrad, and the palms turn perpendicular to the rotation of the arms again when θ is 0rad just by rotating the arms.

Structure

Structure of the prototype-1 is shown in Figure 9 Two arms are driven synchronously by an electric motor through a worm gear.

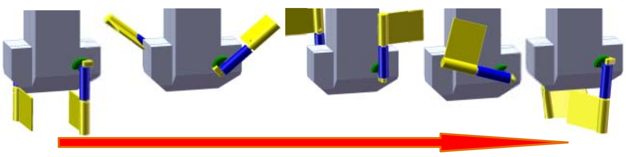

Figure 7 Target motion of the Rotating Motion Type

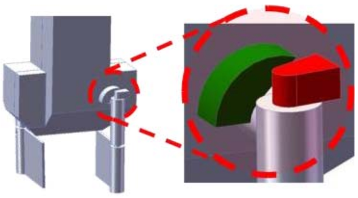

Figure 8 Cam mechanism

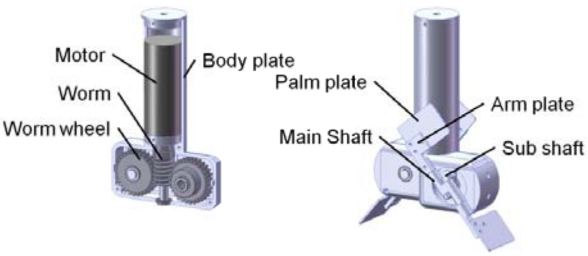

Figure 9 Structure of Prototype-1

Motion of the Rotating Type is realized by rotating the motor in one direction. Each arm has two palms for effective movement. These palms prevent from moving backward, as one palm is in digging motion while the other is in recovery motion in place of mole's hind legs.

Experiment

This prototype can move into the soil without any extra force down to 2 meter deep at a speed of 0.67mm/s. This experiment is shown in Figure 10. However, its propulsive speed and ability to borrow deep into the soil are not enough to search efficiently. In addition, a stone can get stuck between an arm and the body. Moreover, waterproof and dustproof are inadequate.

BASIC EXPERIMENT

Forward Movement

To solve these problems, characteristics of the movement needed to be revealed through experiments. Prototype of the burrowing inspector was used to make basic experiments of shoveling motion shown in Figure 11. The arms were rotated from the angle of 0rad to 3rad, simulating the digging motion, and the corresponding displacement of the movement was measured.

First, the inspector was set perpendicular to the soil and moved to a downward direction into the soil. The relationship between the angle of the arms θ and the displacement of the downward movement x is shown in Figure 12.

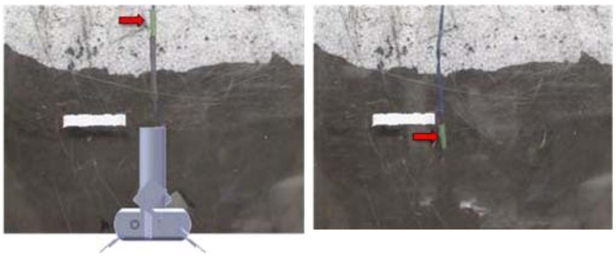

Figure 10 Digging motion of Prototype-1

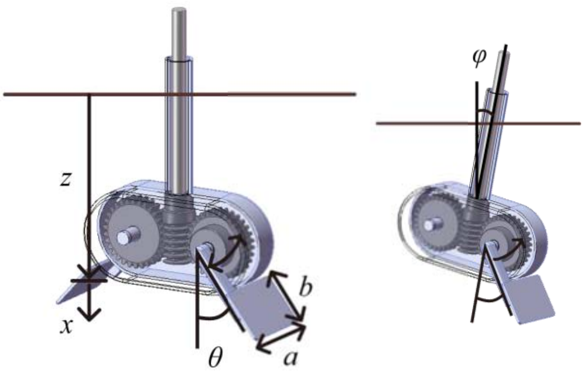

Figure 11 Experimental apparatus

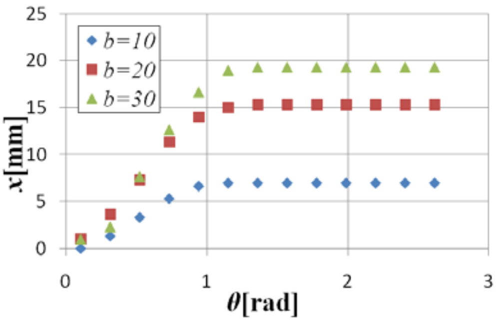

Figure 12 Displacement of downward movement

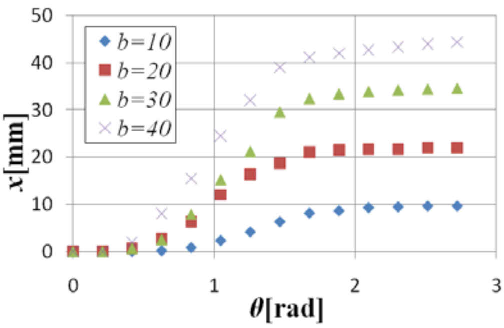

Figure 13 Displacement of horizontal movement

As a result, at the digging motion, the inspector made propulsion while θ was from 0rad to 1.2rad, and it could not make propulsion while θ was over 1.1rad. The motion of rotating the arms over 1.2rad is not effective for pushing aside soil mass. And the inspector was not able to get enough propulsive force while θ was over 1.2rad, because the palms push the soil which has less soil pressure, though the soil pushed by the body has higher soil pressure. Therefore, it seems more effective to swing the arms between the angles of 0rad to 1.2rad.

Second, the inspector was set horizontally in the soil and moved to a horizontal direction in the soil. The relationship between the angle of the arms θ and the displacement of the horizontal movement x is shown in Figure 13. The inspector did not make propulsion while the angle of the arms θ was from 0rad to 0.4rad, made propulsion while θ was from 0.4rad to 1.7rad, made little propulsion while θ was over 1.7rad. In this case, the inspector could not make adequate propulsive force while θ was from 0rad to 0.4rad, because force of gravity was not acting on it in the direction of its movement. And the inspector could make propulsion while θ was over 1.2rad, because it could generate enough force to make propulsion as the soil pressure at the palms and at the body were the same.

Backward Movement

Then, the arms were rotated in the opposite direction from the angle of 1.2rad to 0rad, simulating that the arms

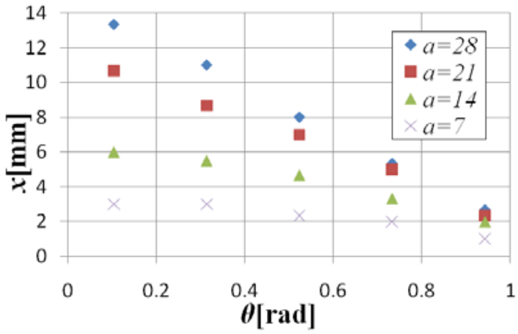

Figure 14 Displacement of backward movement

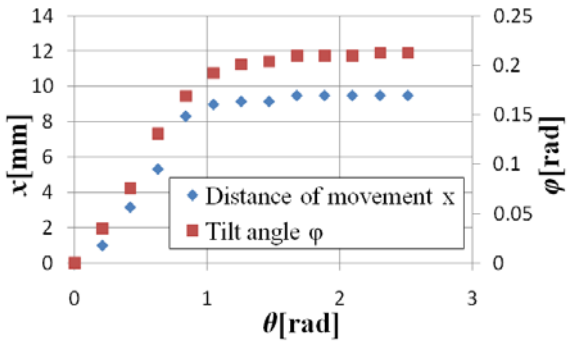

Figure 15 Displacement and tilt of steering motion

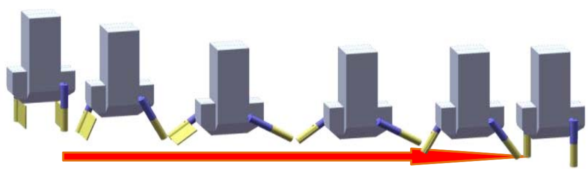

Figure 16 Target motion of the Swing Motion Type

were recovered by swinging them. The inspector was set perpendicular to the soil and the angle of the arms θ and the corresponding displacement of the backward movement x were measured. The width of the palms a was changed from 7mm to 28mm. The result is shown in Figure 14. As a result, the shorter the widths of the palms were, the shorter the displacement of the backward movement was, and the relationship between them was linear. Therefore, the efficiency of prototype-1's method was verified to change the effective width of the palms by changing the angle of the palms.

Steering Motion

Finally, simulating the steering motion, the inspector pushed aside soil by rotating only one palm. The inspector moved downward to the soil and angle of the arm θ, displacement of the movement x and the tilt angle of the body φ were measured (Figure 15). The inspector made propulsion while θ was from 0rad to 1.2rad in the same way as the usual propulsion. And the inspector

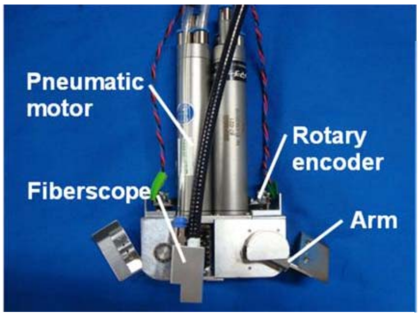

Figure 17 Structure of Prototype-2

Specifications	
Weight	830[g]
Length	170[mm]
Height	36[mm]
Width(arm part)	84[mm]
Width(body part)	44[mm]
Palm size	20x36[mm]

Figure 18 Specifications of Prototype-2

steered its direction also while θ was from 0rad to 1.2rad. Therefore, possibility of the steering is verified by rotating one arm from the angle of 0rad to 1.2rad.

PROTOTYPE-2 SWING MOTION

Basic Motion

From these results, Prototype-2 takes Swing Motion Type whose arms are swung between the angle of 0rad to 1.2rad aiming for the efficient downward propulsion and steering motion. Faster movement is expected by swinging only in the effective range for the movement.

In order not to move backward during the recovery motion, the palm turns parallel to the arms' rotation, and the palm turns perpendicular to the arm's rotation during the digging motion. Using this method, it is expected that displacement of the backward movement becomes shorter. This motion is shown in Figure 16.

Structure

Structure and specification of Prototype-2 are shown in Figure 17 and Figure 18. Shoveling motion can be realized by using two arms which are driven independently by two pneumatic motors through worm gears. This structure makes it possible to steer its direction by swinging only one arm and stopping the other. It wears a dry-suit made of latex for dustproof and waterproof and searches survivors in the soil with a fiberscope.

The hinge and angled palm mechanism, shown in Figure 19 is proposed to prevent from moving backward. The palms can be rotated around the arms freely in the range of $\pi/2$rad. And the palms turn parallel to the rotation of the arms during the recovery motion, as the whole areas of each of the palms are subjected to reactive force from the soil. And palms turns perpendicular to the arm's rotation during the digging motion, as the angled areas of the palms are subjected to reactive force. With this mechanism, motion to prevent from moving backward is realized just by swinging the arm.

Experiment

The basic motion of Prototype-2 is shown in Figure 20. The arms are swung in a speed of 2.4rad/s with the 0.2MPa pneumatic supply. In the experiment shown in Figure 21, it can move into the soil without any extra force down to 5 meters deep at a speed of 4mm/s. In the darkness in the soil, a letter covered by the soil was recognized using the fiberscope. It could move into the gravel without any stucks using the Swing Motion Type.

The steering motion was also verified in the experiment shown in Figure 22. The robot can turn its direction of movement by swinging one arm and stopping the other.

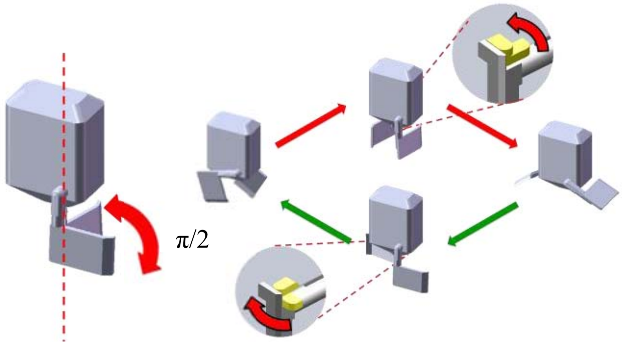

Figure 19 Hinge and angled palm mechanism

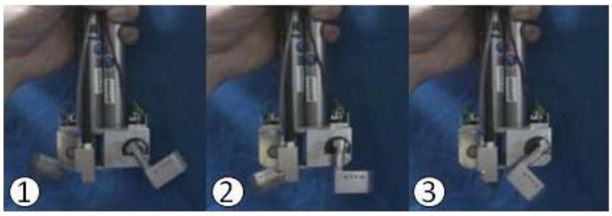

Figure 20 Basic motion of Prototype-2

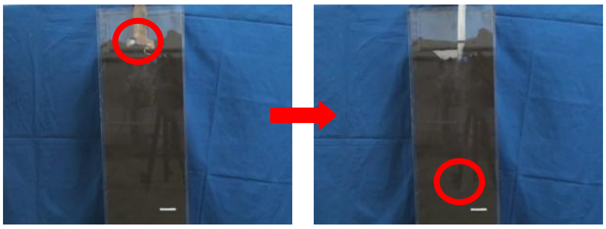

Figure 21 Digging motion of Prototype-2

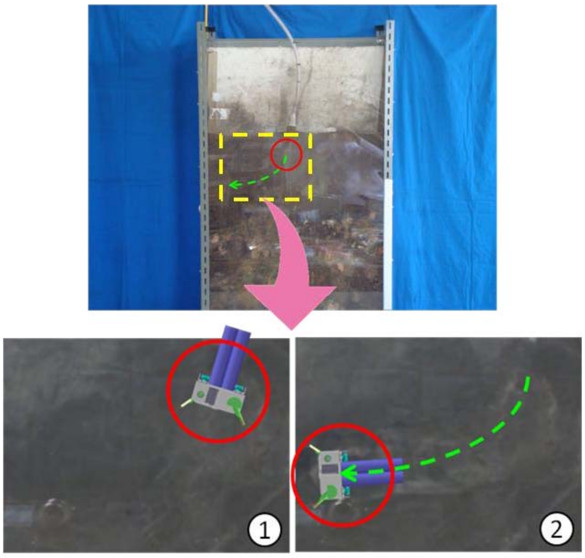

Figure 22 Steering motion

Figure 23 Different types of soils

We made the experiment to make propulsion into some types of soil. The robot moved into the dry soil, wet soil and mud soil. The results are shown in Figure 24. This inspector could make propulsion more efficiently in the wet soil and mud soil. Wet soil and mud soil have high viscosity, therefore less soil flows into below the inspector. Therefore, it is expected to be able to move into dry soil by injecting water from the inspector.

CONCLUSION

Shoveling motion is proposed to move into the soil efficiently. Its characteristics and the efficiency are verified through basic experiments. Then, using the Swing Motion Type, the effectiveness of propulsion on its own as well as steering its direction of movement are verified through experiments. In addition, the burrowing inspector is equipped with sensors, and it is verified the efficiency of information gathering through the landslide. As the next steps, we aim at 3-dimentional steering to search effectively in the soil. Then, for practical use, we will make it easy to operate it by measuring the position of the inspector with sensors inside the soil.

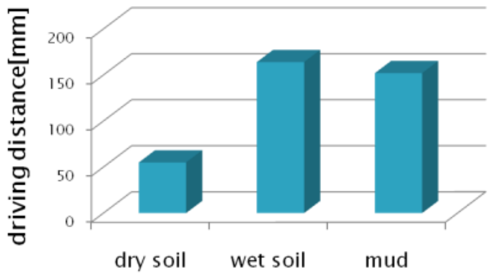

Figure 24 Influence of the moisture content

REFERENCES

1. Hideyuki Tsukagoshi, Terunori Koyama, Ato Kitagawa,Development of an Earth-propelling Hose Aimed to Search Victims : Study on Reduction of the Insertion Resistance and Steering Method, Dynamics and Design Conference, 2005-4, pp.1334-1341.
2. Kenji Nagaoka, Takashi Kubota, Masatsugu Otsuki, Satoshi Tanaka, An Experimental Study on Contra-Rotor Screw Drilling Mechanism : Effective Screw Mechanism for Lunar Subsurface Exploration Robot(Mechanical Systems), Dynamics and Design Conference, 2009-8, pp.2295-2300.
3. Kazuya Yoshida, Hiraku Kudou, Yasuhiro Kawakatsu, Takaaki Yokoyama, Minoru Sonoyama, Development of a Mole-like Robot for Lunar Subserface Exploration, The Robotics and Mechatronics Conference, 2000, 1P1-07-019.
4. Susumu Yasuda, Keiji Komatsu, Research for Regolith Drilling Mechanism Using Reactive Torque, Space Engineering Conference 2009(18), 75-79, 2010-01-28.
5. Taro Murakami, Taro Nakamura, Takayuki Yada, Hayato Omori, Examination of Excavation Mechanism for a Lunar Underground Explorer Robot using a Peristic Crawling, The Robotics and Mechatronics Conference, 2009, 1A2-F15.
6. Hiroaki Nagai, Hayato Omori, Taro Murakami, Taro Nakamura, Development of Peristaltic Crawling Excavation Robot, The Robotics and Mechatronics Conference, 2010, 1A2-B20.
7. Agathe Koller-Hodac, Daniel P. Germann, Alexander Gilgen, Katja Dietrich, Maik Hadorn, Wolfgang Schatz, Peter Eggenberger Hotz, Actuated Bivalve Robot Study of the Burrowing Locomotion in Sediment, 2010 IEEE International Conference on Robotics and Automation Anchorage Convention District.
8. Tadaaki Imai, Biological Animal Guide, Gakken.
9. Riichi Hirai, Have a Slight Acquaintance with Soil Engineering, Soil Mechanics as General Knowledge for Architectural Engineer.

Proceedings of the 8th JFPS International
Symposium on Fluid Power, OKINAWA 2011
Oct. 25-28, 2011

2D2-3

A STUDY ON FORCE REFLECTING JOYSTICK CONTROL USING VIRTUAL FORCE SENSOR FOR APPLICATIONS TO EXCAVATORS

Nguyen Thanh TRUNG**, Dinh Quang TRUONG* and Kyoung Kwan AHN*

* School of Mechanical and Automotive Engineering
University of Ulsan
San 29, Namgu-Muger2dong, Ulsan, 680-749 Korea
(E-mail: kkahn@ulsan.ac.kr)
** Graduated School of Mechanical and Automotive Engineering
University of Ulsan
San 29, Namgu-Muger2dong, Ulsan, 680-749 Korea

ABSTRACT

Nowadays, tele-operation robotic systems, especially in construction machinery such as automated excavators become an urgent demand which help improving productivity, safety, and reducing of operation costs. The aim of this paper is to develop a novel force reflecting joystick control (FRJC) method using virtual force sensor for applications to excavators. Here, the suggested system is a combination of a master system – force reflecting joystick mechanism (FRJM) and a slave system – real excavator which is integrated with potentiometers at its active joins. Two non-linear black box models (NBBM) are proposed for identifying dynamic behaviors of the excavator and FRJM. Once, the optimized models are obtained, they can be used in a combination with potentiometers to estimate loading forces without using any force sensor as well as to monitor current states of the excavator in the virtual environment. A test rig employing a pneumatic actuator was used in this study for investigating the proposed NBBM models.

KEY WORDS

Force reflecting joystick, Excavator, Non-linear black box model, Virtual environment

NOMENCLATURE

b	: Biases of neural network
d	: Target outputs of neural network
e	: Errors between neural network outputs and target values
f	: Transfer functions of neural network
$F(x)$	: Performance function
$J(x)$	: Jacobian Matrix
K, N, P	: Numbers of neurons in the input layer, hidden layer and output layer
u	: Inputs of neural network
v	: Nonlinear functions of vector x
x	: Parameters vector of neural network
y	: Outputs of neural network
μ_k	: Damping parameter

INTRODUCTION

There are hundreds of thousands of excavator machines manufactured every year and widely used in the construction, forestry, and mining industries. As a new trend, tele-operation of excavation helps improving productivity, safety, and reducing of operation costs, consequently, making construction works become feasible even in hostile environment. In the teleoperated

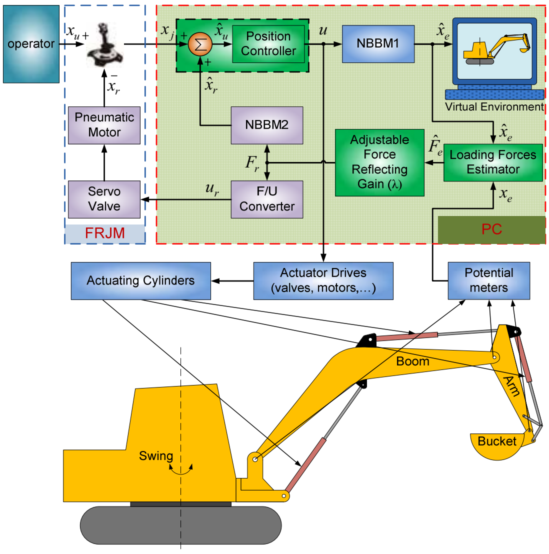

Figure 1 Schematic diagram of proposed FRJC method

excavator design, when there is a contact between the bucket and the environment at the remote site, a proper force signal fed back to operator is important to make operator feel as the physically present at the remote site. Therefore, there were many studies in the literature relating on force reflecting control methods [1-2]. In these studies, the force sensors were used to measure the contacting force. However, the system cost was high and the control accuracy was reduced due to using lots of sensors.

The aim of this paper is to develop a novel force reflecting joystick control method using virtual force sensor for applications to excavators. In order to construct the proposed method, designing the NBBM model and building the excavator 3D model have been considered as the first two generation steps. As the first step, the test rig employing a pneumatic actuator was used for investigating the proposed NBBM model. And the second step to build the 3D excavator also was also described in this paper.

DESIGN CONCEPT OF FRJC SYSTEM FOR EXCAVATORS

This section gives a detail description of FRJC system for excavators as shown in Fig. 1. The suggested system is the combination of the master system – force reflecting joystick mechanism and the slave system – real excavator. Here, the FRJM includes an electrical joystick to generate driving commands, and a pneumatic motor controlled by a pneumatic servo valve to produce force reflection information sensed from the loading conditions. The excavator has four degrees of freedom consisting of the wing, boom, arm, and bucket, which are actuated by cylinders. The positions of cylinders are driven by control signals, u, which are sent from a position controller built in a personal computer (PC) through the D/A converter to cylinder drives such as valves, motors, etc. The excavator coordinate, x_e, can be determined by potentiometers attached on the active joints of the excavator. Consequently, to implement the proposed control method, the two non-linear black box models based on multi-player perceptron neural network (MLPNN) are proposed. Here, the NBBM1 model is used to estimate the dynamic behavior of the excavator and the NBBM2 model is exerted to identify the dynamic behavior of FRJM. Once, these optimized models are obtained, they can be used in a combination with the potentiometers to estimate the machine loading forces without using any force sensor as well as to monitor current states of the excavator in the virtual environment.

During tele-operation, the operator provides the trajectory commands, x_u, to the real excavator through interacting with the joystick. The joystick motion, x_j, is converted to a voltage signal, which is then acquired and fed through an A/D converter to the position controller. Here, according to the measured value, the controller attempts to make the excavator track the operator commands via u. The real excavator performance, x_e, which is caused by u, is measured by the potentiometers and fed through an A/D converter to a loading forces estimator built in the PC. The relationship between u and x_e can be represented by the NBBM1. In no-load condition, if the NBBM1 is well optimized, the estimated excavator performance, $\hat{x}_e$, yielded from this model is similar with that of the real excavator, x_e. Otherwise, in the case the bucket end-point contacts with the working environment, the loading forces are attacked to the excavator links. Subsequently, there exists a position difference between $\hat{x}_e$ and x_e. Based on this different value, the loading forces, $\hat{F}_e$, can be estimated and scaled by a adjustable force reflection gain λ to produce a reflection force, F_r, to the FRJM. Thus, the operator can feel the real working conditions as directly-driving method. However, the joystick movement, x_r, which is reasoned by the force feedback, causes a deviation between x_u and x_j. This phenomenon makes the real excavator acts unlike the operator intention, even induces the control system become unstable when the value of λ is high. Hence, to overcome this problem, the NBBM2 is utilized to identify the relationship between F_r and x_r. Once, the optimized NBBM2 is obtained, its output estimated value, $\hat{x}_r$, is fed to the position controller to combine with x_j to estimate the true operator commands, $\hat{x}_u$. By this way, the operator can feel the working conditions through the joystick while the excavator is still driven by the true operator intention. In addition, to

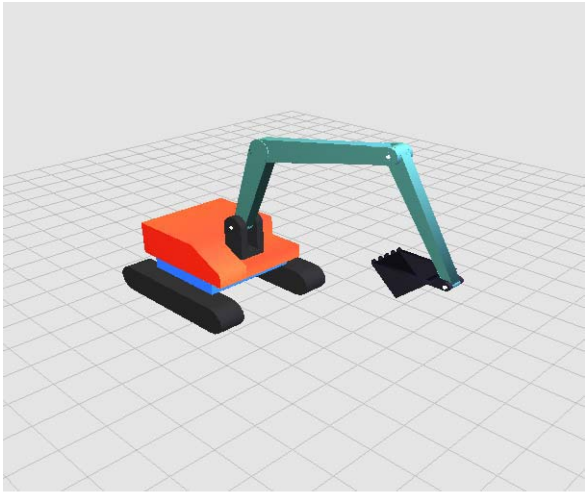

Figure 2 Excavator in virtual environment

make a visual feeling for the operator to control the excavator more easily and safely, the virtual excavator is also graphically rendered and viewed upon the computer screen by using the output values from the optimized NBBM1 model, $\hat{x}_e$.

To prepare for the proposed FRJC method, the following sections describe first two generation steps of this method: the implementation of the virtual excavator environment, as well as the procedure to design, optimize, and verify the proposed NBBM model.

VIRTUAL ENVIRONMENT DESIGN

In order to make the visual feeling for the operator during driving the real excavator, it is necessary to construct a virtual excavator, whose manner imitates the real excavator posture. Therefore, a combination of the Visual Basic program and the graphics library built upon OpenGL was implemented to create the virtual environment as displayed in Fig. 2.

By employing this virtual environment, the virtual excavator actuation is defined by the optimized NBBM1 model and the joystick commands.

IDENTIFICATION METHODOLOGY USING NBBM MODEL

Multi-layer Perceptron Neural Network

In this study, the NBBM is a general MLPNN and was built in the M-files environment of Matlab 2006a. The MLPNN structure consists of three layers: one input layer, one hidden layer and one output layer, as seen in Fig. 3. With this structure, the MLPNN can approximate virtually any input-output map. In addition, the MLPNN structure is programmed flexibly and can be adjusted easily by changing three effective factors: N, K, P corresponding to numbers of neurons in the input layer, hidden layer and output layer, respectively.

Considering the working principle of the MLPNN, the input layer is represented by a vector of input variables ($u_1, u_2, \dots, u_N$). The input layer distributes these values to the neurons in the hidden layer. At neuron k^{th} in the hidden layer, the values from the input layer are multiplied by weights ($w^1_{k,n}$) and added together with a bias factor b^1_k to produce a combined value (Sh^1_k) . The weighted sum (Sh^1_k) is then fed into an transfer function, f^1, to obtain the output value (Oh^1_k) of neuron k^{th}. This calculating process is expressed as:

$$\begin{cases} Sh_k^1 = \sum_{n=1}^{N} w_{k,n}^1 u_n + b_k^1, \\ Oh_k^1 = f^1(Sh_k^1) = \dfrac{1}{1+e^{Sh_k^1}}. \end{cases} \quad with\ k = \overline{1,K} \qquad (1)$$

The outputs from the hidden layer are then distributed to the output layer. At neuron p^{th}, these values are multiplied by weights ($w^2_{p,k}$) and added together with a bias factor b^2_p to produce a combined value (Sh^2_p) . The weighted sum (Sh^2_p) is then fed into an transfer function, f^2, to obtain the output value (y_p) of neuron p^{th}. The set of all the output values, y_p, comprises the outputs of the MLPNN. And each of the output variables from the MLPNN can be obtained as:

$$\begin{cases} Sh_p^2 = \sum_{k=1}^{K} w_{p,k}^2 Oh_k^1 + b_p^2, \\ y_p = f^2(Sh_p^2) = Sh_p^2. \end{cases} \quad with\ \ p = \overline{1,P} \qquad (2)$$

The training purpose is to find a set of weights and biases that minimize the error between the neural network outputs and the desired outputs. The MLPNN parameters are trained with the back propagation algorithm and Lerverberg-Marquardt (LM) method.

Levenberg-Marquardt algorithm

The LM algorithm is a standard technique used to solve

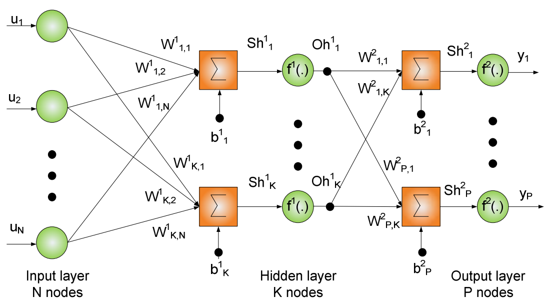

Figure 3 Structure of the MLPNN

non-linear least squares problems. The LM algorithm is actually a combination of two minimization algorithms: the gradient descent algorithm and the Gauss-Newton algorithm. In the gradient descent algorithm, the sum of the squared errors is reduced by updating the parameters in the direction of the greatest reduction of the least squares objective. In the Gauss-Newton algorithm, the sum of the squared errors is reduced by assuming the least squares function is locally quadratic, consequently finding the minimum of the quadratic. The LM algorithm acts more like a gradient-descent method when the parameters are far from their optimal values, and it acts more like the Gauss-Newton algorithm when the parameters are close to their optimal values.
Assuming that performance function $F(x)$ required to be minimized is a sum of squares function:

$$F(x) = \sum_{h=1}^{H} v_h^2(x) \, . \tag{3}$$

where, x is parameters vector $x = \left[x_1 \, x_2 \ldots x_m \right]$.
The LM algorithm minimizes the performance function $F(x)$ by updating the parameters vector as the following equation:

$$x^{k+1} = x^k + \Delta x^k = x^k - [J^T(x^k) J(x^k) + \mu_k I]^{-1} J^T(x^k) v(x^k) \tag{4}$$

where, x^k is the parameters vector at time k; μ_k is a adaptive parameter and $J(x)$ is Jacobian matrix, which is expressed by:

$$J(x) = \begin{vmatrix} \frac{\partial v_1(x)}{\partial x_1} & \frac{\partial v_1(x)}{\partial x_2} & \cdots & \frac{\partial v_1(x)}{\partial x_m} \\ \frac{\partial v_2(x)}{\partial x_1} & \frac{\partial v_2(x)}{\partial x_2} & \cdots & \frac{\partial v_2(x)}{\partial x_m} \\ \vdots & \vdots & & \vdots \\ \frac{\partial v_H(x)}{\partial x_1} & \frac{\partial v_H(x)}{\partial x_2} & \cdots & \frac{\partial v_H(x)}{\partial x_m} \end{vmatrix} \tag{5}$$

In Eq. (4), as the adaptive parameter μ_k is increased, the LM algorithm approaches the steepest descent algorithm with small learning rate. Conversely, as μ_k is decreased to zero the algorithm becomes Gauss-Newton. Therefore, this algorithm provides a nice compromise between the speed of Newton's algorithm and the guaranteed convergence of steepest descent algorithm.

NBBM model optimization using LM

In order to train the NBBM model using the LM, the training set is specified by:

$$Z^Q = \left\{ [u_1(t) \ldots u_n(t), d_1 \ldots d_p(t)] t = 1 \ldots Q \right\} . \tag{6}$$

The performance function for the NBBM is given as:

$$F(x) = \sum_{q=1}^{Q} \sum_{i=1}^{P} (d_{i,q} - y_{i,q})^2 = \sum_{q=1}^{Q} \sum_{i=1}^{P} e_{i,q}^2 = \sum_{h=1}^{H} v_h^2 \tag{7}$$

Eq. (7) is equivalent to the performance function in Eq. (3). Where, v and x are expressed as:

$$\begin{aligned} v^T &= [v_1 \, v_2 \ldots v_H] = [e_{1,1} \ldots e_{P,1} \ldots e_{1,Q} \ldots e_{P,Q}], \\ x^T &= [x_1 \, x_2 \ldots x_m] = [w_{1,1}^1 \ldots w_{K,N}^1 \, b_1^1 \ldots b_K^1 \, w_{1,1}^2 \ldots w_{P,K}^2 b_1^2 \ldots b_P^2] \end{aligned} \tag{8}$$

Therefore, the NBBM parameters can be optimized by using Eq. (4). The key step in updating the network parameters is the computation of the Jacobian matrix. Substituting Eq. (8) into Eq. (5), the Jacobian matrix for NBBM training can be written and calculated as:

$$J(x) = \begin{vmatrix} \frac{\partial e_{1,1}}{\partial W_{1,1}^1} & \frac{\partial e_{1,1}}{\partial W_{1,2}^1} & \cdots & \frac{\partial e_{1,1}}{\partial b_P^2} \\ \frac{\partial e_{2,1}}{\partial W_{1,1}^1} & \frac{\partial e_{2,1}}{\partial W_{1,2}^1} & \cdots & \frac{\partial e_{2,1}}{\partial b_P^2} \\ \vdots & \vdots & & \vdots \\ \frac{\partial e_{P,Q}}{\partial W_{1,1}^1} & \frac{\partial e_{P,Q}}{\partial W_{1,2}^1} & \cdots & \frac{\partial e_{P,Q}}{\partial b_P^2} \end{vmatrix} \tag{9}$$

$$\frac{\partial e_{i,q}}{\partial W_{p,k}^2} = \begin{cases} -\frac{\partial y_{i,q}}{\partial Sh_p^2} \frac{\partial Sh_p^2}{\partial W_{p,k}^2} = -Oh_k^1, \, for \, i = p \\ 0, \, for \, i \neq p \end{cases} \tag{10}$$

$$\frac{\partial e_{i,q}}{\partial b_p^2} = \begin{cases} -\frac{\partial y_{i,q}}{\partial Sh_p^2} \frac{\partial Sh_p^2}{\partial b_p^2} = -1, \, for \, i = p \\ 0, \, for \, i \neq p \end{cases} \tag{11}$$

$$\frac{\partial e_{i,q}}{\partial W_{k,n}^1} = -W_{i,k}^2 . Oh_k^1 (1 - Oh_k^1) u_n \tag{12}$$

$$\frac{\partial e_{i,q}}{\partial b_k^1} = -W_{i,k}^2 . Oh_k^1 (1 - Oh_k^1) \tag{13}$$

Finally, the training process of NBBM using the LM algorithm can be described as follows:

- Step 1: Present all inputs to the MLPNN and compute the corresponding network outputs using Eqs. (1)~(2) and performance function, $F(x)$, using Eq. (7).
- Step 2: Compute Jacobian maxtrix by Eqs. (9)~(13).
- Step 3: Solve Eq. (4) to obtain Δx^k
- Step 4: Re-compute the sum of squared errors $F(x)$ using $x^k + \Delta x^k$. If $F(x)$ is smaller than that computed in step1, then divide μ_k by factor ξ >1, let $x^{k+1} = x^k + \Delta x^k$ and go back step 1. If $F(x)$ is not reduced, the multiply μ_k by factor ξ and go back step 3.

The above process is implemented repeatedly until the desired NBBM is obtained.

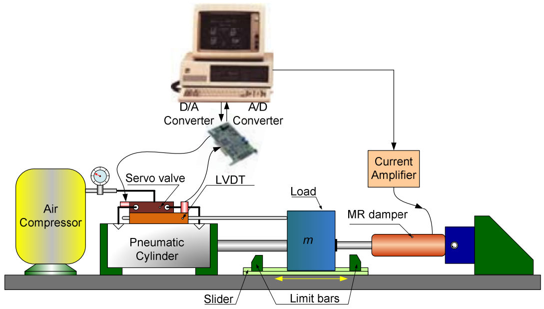

a) Test rig diagram

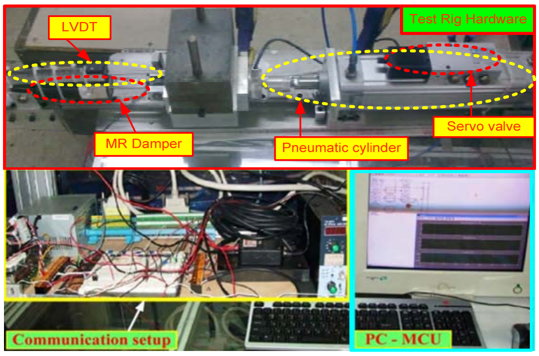

b) Photograph of test rig

Figure 4 Test rig setup of pneumatic actuator

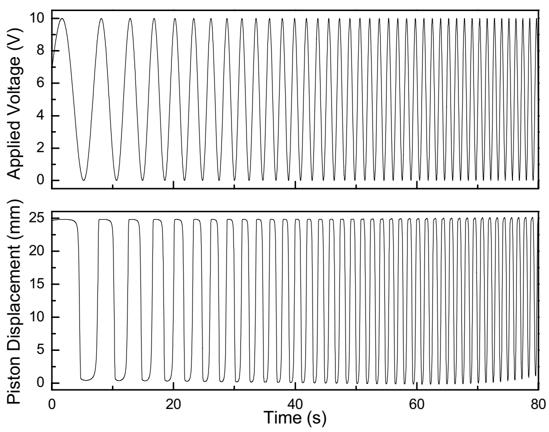

Figure 5 Pneumatic actuator response with respect to a chirp voltage input signal

INVESTIGATION OF PROPOSED NBBM MODEL

Test rig setup

To investigate the identification ability of the proposed NBBM, the test rig was setup as in Fig. 4a. Here, a pneumatic cylinder was driven by a 5/3-way proportional valve manufactured by Festo Corp. The spool motion of this servo valve is proportional to its control signal sent from the PC through a D/A converter of the Advantech card PCI-1711 which was installed on a PCI slot of the PC. A linear variable differential transformer (LVDT) was fixed on the rig base to measure the displacement of the cylinder piston rod. A processing system was built in the PC with a CoreTM2 Duo 1.8 GHz processor within the Simulink environment combined with Real-time Windows Target Toolbox of MATLAB 2006a. In addition, a magneto-rheological (MR) fluid damper from Lord Corp. was installed in series with the cylinder piston to create the working environment. Here, the loading condition can be varied by adjusting the current value applied to the MR damper. For safety of experiments, two limited bars were positioned on two sides of a slider to restrict the piston movement which protects MR damper from damages. A real photograph of the test rig is described in Fig. 4b.

Generation of training data

To obtain data for the pneumatic actuator identification using NBBM model, a series of experiments on the test rig in the Fig. 4 were conducted by using the opened-loop control system. For these experiments, a chirp voltage signal was applied to the servo valve. The chirp signal was a sine wave signal whose frequency increased from 0.1Hz to 2Hz at a linear rate with time and amplitude varied from 0 to 10V. The control system was built within Simulink/Matlab 2006a. Here, the sampling time was set to 0.01ms. The voltage signal, applied to the servo valve, and the piston displacement were collected as the training data. One of the experimental results for pneumatic actuator is plotted in Fig. 5.

NBBM model training process

The NBBM model training process is depicted in Fig. 6. As seen in Fig. 6, the input vector of NBBM model was a set of past values of the voltage applied for the servo valve and the piston displacement. The collected training data was used to train the NBBM model. After training, the training results were evaluated by the successful training rates (%) for the different NBBM structures as shown in Table 2 and Fig. 7.

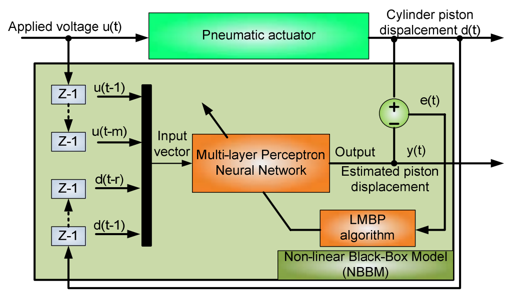

Figure 6 Block diagram for training NBBM model

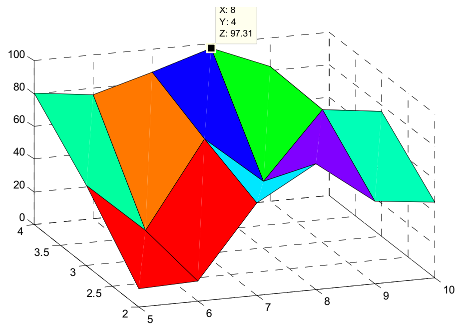

Figure 7 Fitness surface of the NBBM with different MLPNN structures

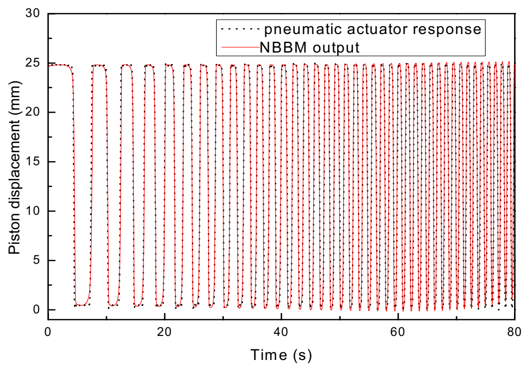

Figure 8 Pneumatic actuator identification result using NBBM model

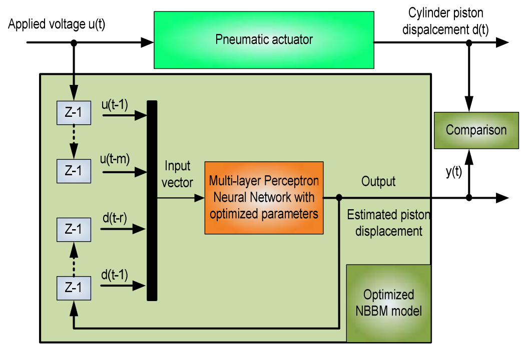

Figure 9 Block diagram for verifying the optimized NBBM

From these table and figure, the optimized NBBM, with four neurons in the input layer (three past applied voltage values and one past piston displacement value) and eights neurons in the hidden layer, could estimate the cylinder piston displacement with the highest accuracy (97.31%).

The optimal NBBM parameters were obtained as in the Table 3. As a result, the pneumatic actuator identification result is displayed in Fig 8. This figure points out that the designed model has enough ability to represent the actuator dynamic behavior with high accuracy.

Table 2 Fitness table of the NBBM with different MLPNN structures (*Highest successful training rate)

NBBM model fitness		Number of nodes in hidden layer					
Inputs vector	Number of inputs	5	6	7	8	9	10
[u(t-1),d(t-1)]	2	10.90	12.93	56.45	76.67	50.12	45.95
[u(t-1),u(t-2),d(t-1)]	3	48.72	17.89	70.21	40.96	80.99	76.72
[u(t-1),u(t-2),u(t-3),d(t-1)]	4	80.35	75.92	85.95	**97.31***	82.31	28.71

Table 3 Weights and bias values of the optimized NBBM model

	W^1_{ji}-weights of hidden layer					W^2_{ji}-weights of output layer	
i	1	2	3	4	0 (for bias 1)	1	0 (for bias 2)
j							
1	1.4879	-0.1596	-1.7700	-1.3735	2.6836	1.3099	-2.1464
2	1.8619	0.0700	-2.1026	-3.3930	0.1666	1.4606	
3	1.6708	0.3012	-1.3575	-2.0326	0.1458	-1.6944	
4	-0.3543	-0.1000	0.6073	1.4458	-0.1775	7.8706	
5	0.0045	-0.2148	-0.4751	-0.5700	-0.4018	1.1862	
6	-0.9995	-0.1106	0.7257	2.0349	-0.1183	-4.7452	
7	1.9447	0.6566	-0.6531	-3.15	0.2151	-0.0410	
8	2.2526	0.0835	-1.9890	-3.3761	0.1182	-1.4585	

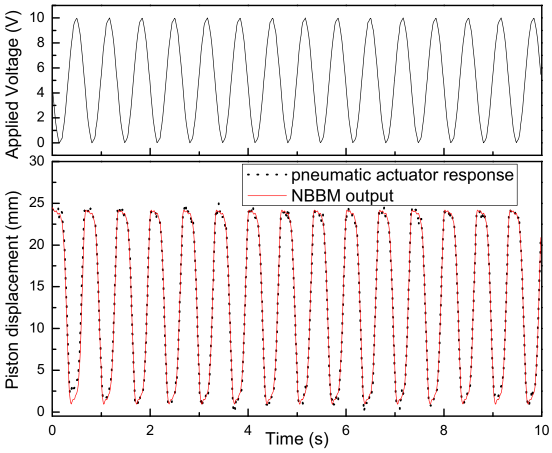

Figure 10 Comparison between estimated and actual responses of the pneumatic actuator with respect to an applied sinusoidal voltage signal

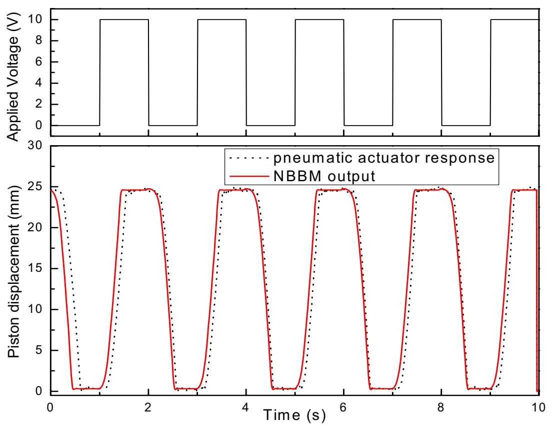

Figure 11 Comparison between estimated and actual responses of the pneumatic actuator with respect to an applied square voltage signal

NBBM model verification

The NBBM model with its optimal design shown in the previous section was then verified by a comparison of the estimated and real pneumatic actuator performance. The verification diagram is displayed in Fig.9.

At first, the comparison was performed with the sinusoidal applied voltage signal of which the frequency was 1.5 Hz and the voltage value was varied from 0-10V. As a result, the comparison result was obtained as in Fig. 10.

Next, a different type of the applied voltage signal was generated for pneumatic actuator to investigate the modeling accuracy when using the designed model. A square voltage signal with 0.5Hz of frequency and 0-10V of amplitude was varied from was then applied to the pneumatic actuator. Consequently, the actual and estimated responses were obtained as in Fig 11.

From the comparison results in Fig. 10~11, it is convincing that the proposed NBBM could identify the dynamic behavior of the pneumatic actuator well.

CONCLUSIONS

In this article, the novel force reflecting joystick control method for applications to excavators was described. To implement this proposed method, the two first generation steps were also presented. The first step is building the excavator 3D model in virtual environment. As the second step, the NBBM was proposed and designed for identifying dynamic behaviors of the FRJM and excavator. To verify the effectiveness of the designed NBBM, the test rig employing the pneumatic actuator was then setup. The identification results prove that the proposed NBBM has strong potential to be applied to the presented FRJC method. Consequently, completing the proposed method is the subject for future research.

ACKNOWLEDGEMENTS

This work was supported by University of Ulsan, School of Excellence in Mechanical Engineering

REFERENCES

1. Hirata, M., Yuichi, N., Fumio M. and Tsugito, Design of Teleoperation System with a Force-Reflecting Real-time Simulator, 3rd International Symposium on Artificial Intelligence, Robotics and Automation in Space, 1994, pp. 125-135.
2. Cha, D. H. and Cho, H. S., Design of a force reflection controller for telerobot systems using neural network and fuzzy logic, Journal of Intelligent and Robotic Systems, 1996, **16**, pp. 1-24.
3. Ahn, K. K. Development of force reflecting joystick for hydraulic excavator, KSME International Journal C, 2004, **47**-3, pp. 858-863.
4. Truong, D. Q. and Ahn, K. K., Design and verification of a nonlinear black-box model for ionic polymer metal composite actuator, Journal of intelligent material systems and structures, 2011,**23**-3, pp. 253-269.
5. Katherine, J. K. and Gunter N., Induced master motion in force-reflecting teleoperation, the ASME Journal of Dynamic Systems and Controls, 2011,**128,** pp. 800-810.

Proceedings of the 8th JFPS International
Symposium on Fluid Power, OKINAWA 2011
Oct. 25-28, 2011

2D2-4

DYNAMIC FRICTION CHARACTERISTICS OF PNEUMATIC ACTUATORS AND THEIR MATHEMATICAL MODEL

Xuan Bo TRAN* and Hideki YANADA**

* Mechanical & Structural Systems Engineering
Toyohashi University of Technology
1-1, Hibarigaoka, Tempaku-cho, Toyohashi 441-8580, Japan
(E-mail: t089102@edu.imc.tut.ac.jp)
** Department of Mechanical Engineering
Toyohashi University of Technology
1-1, Hibarigaoka, Tempaku-cho, Toyohashi 441-8580, Japan

ABSTRACT

This paper deals with dynamic friction characteristics in the gross-sliding regime of pneumatic cylinders. Using three pneumatic cylinders, friction characteristics are investigated and modeled under various conditions of velocity and pressures. It is shown that a hysteresis loop behavior can be seen at low velocities in the friction force-velocity relation and the friction force varies nearly linearly with the velocity at high velocities. The hysteresis loop is expanded to higher velocity when the frequency of the velocity variation is increased, and its size increases with increasing driving pressure and decreases with increasing resistance pressure. It is shown that these behaviors can be relatively accurately modeled by the modified LuGre model. The pressures have influence on the maximum static friction force, the Coulomb friction force and the Stribeck velocity of the model.

KEY WORDS

Friction, Dynamic behavior, Pneumatic actuator, Mathematical model

NOMENCLATURE

a	:	acceleration
A_i	:	piston area (i=1,2)
F_c	:	Coulomb friction force
F_L	:	force acting on load cell
F_r	:	friction force
F_{rss}	:	steady-state friction force
F_s	:	maximum static friction force
g	:	Stribeck function
h	:	dimensionless dynamic
	:	lubricant film thickness
h_{ss}	:	dimensionless steady-state
	:	lubricant film thickness
K_f	:	proportional constant for
	:	lubricant film thickness
m	:	mass of the pneumatic piston
n	:	exponent for Stribeck curve
p_i	:	pressure (i=1,2)
p_s	:	supply pressure
v	:	velocity
v_b	:	velocity at maximum film
	:	thickness
v_s	:	Stribeck velocity

z	:	mean deflection of bristles
σ_0	:	stiffness of bristles
σ_1	:	micro-viscous friction
	:	coefficient for bristles
σ_2	:	viscous coefficient
τ_h	:	time constant for lubricant
	:	film dynamics
τ_{hp}	:	time constant for acceleration
	:	period
τ_{hn}	:	time constant for decelation
	:	period
τ_{h0}	:	time constant for dwell time

INTRODUCTION

Friction is always present in pneumatic actuator systems and makes the dynamics of pneumatic position/velocity control systems rather complex and precise position/velocity control is usually difficult. It is, therefore, necessary to investigate the friction characteristics and develop a suitable friction model for pneumatic actuators to improve the control performance of pneumatic actuator systems. However, it is extremely difficult to obtain friction characteristics of a pneumatic actuator when the actuator is pneumatically operated due to the difficulties in controlling the velocity of the actuator.

Several experimental methods have been proposed to investigate the friction characteristics of pneumatic actuators [1-3]. Schoroeder and Singh [1] proposed an experimental test setup in which the friction force was calculated by detecting the force exchanged by the rods of the tested pneumatic cylinder and of a load pneumatic cylinder assembled with a reversed working direction. Belforte et al. [2] proposed an experimental test setup in which the velocity of the test pneumatic cylinder was controlled by a driving hydraulic cylinder and the pressures of the chambers were controlled by pressure-proportional valves in order to measure the friction force under a broad range of operating conditions of velocity and pressures. Nouri [3] proposed an experimental test setup to identify the friction force in both the pre-sliding and gross-sliding regimes of a rodless cylinder. However, these experimental methods mainly focused on investigating the friction characteristics under steady-state conditions. To the best of the authors' knowledge, the friction characteristics of pneumatic actuators under dynamic conditions have not fully been investigated.

Several mathematical models that describe the dynamic behaviors of friction have been proposed so far [4-9] and among them, the LuGre model [6] is most widely utilized. However, all these models cannot simulate well the friction behaviors of a hydraulic cylinder in the gross-sliding regime as shown in [10]. Yanada and Sekikawa [10] have made a modification to the LuGre model by incorporating lubricant film dynamics into the model and it has been shown that the proposed model, called the modified LuGre model, can simulate dynamic behaviors of friction observed in hydraulic cylinders with a relatively good accuracy [10-12]. However, the validity of the modified LuGre model in simulating the dynamic friction characteristics of pneumatic cylinders has not been investigated.

In this paper, first a new experimental test setup is developed to examine dynamic friction characteristics of pneumatic cylinders under various operating conditions of velocity variation and pressures in the cylinder chambers. The modified LuGre model is then used to simulate the dynamic friction characteristics measured. A parameter investigation is also conducted to identify the influence of the pressures in the cylinder chambers on the modified LuGre model's parameters.

TEST SETUP AND EXPERIMENTS

The test setup used in this investigation is shown in Figure 1. It consists of a pneumatic cylinder under test and an electro-hydraulic servo cylinder system. The pneumatic piston was driven by the hydraulic piston in order to precisely control the velocity of the pneumatic piston. Pressures in two chambers of the pneumatic cylinder were independently controlled by using two proportional valves (pressure type). The valves provide air flow up to 0.025 m^3/s and allow controlling the pressures up to 0.65 MPa. The motion of the hydraulic cylinder was controlled by a computer through an amplifier and a servovalve. The supply pressure of the servovalve was set at 2 MPa, providing enough force to drive the pneumatic piston.

A load cell with a rated output of 500 N and with an accuracy less than 0.15% R.O., which was set between the rod of the pneumatic cylinder and the rod of the hydraulic cylinder, was used to measure the force acting on the pneumatic piston. Two pressure sensors with an accuracy less than 2% F.S. were used to measure the pressures, p_1, p_2, in the cylinder chambers, and the piston velocity, v, was measured using a tachometer generator with a ripple of less than 2% by converting linear motion of the piston to rotational motion through a pulley and belt system.

The values of velocity, pressures, and force from the sensors were read into a computer through an A/D converter and the computer provided the control signals to the proportional valves and servovalve though a D/A converter. The acceleration, a, of the piston was calculated by an approximate differentiation of the piston velocity accompanied by a first-order low pass filter with 50 Hz cutoff frequency. The velocity of the pneumatic cylinder, v, and the pressures, p_1, p_2, were controlled by using PID control laws. Experimental data, i.e., velocity, v, pressures, p_1, p_2, and acceleration, a, were recorded at the interval of 0.5 ms (2 kHz).

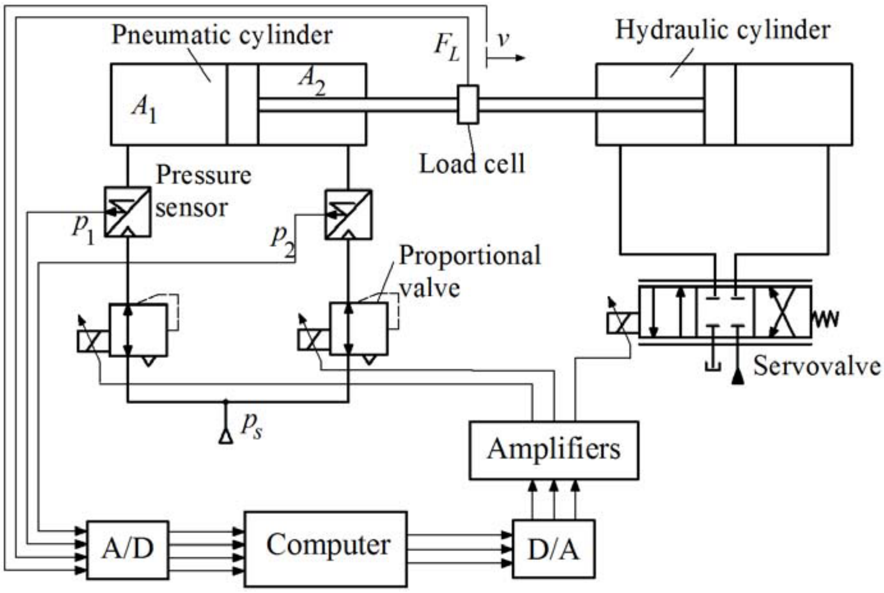

Figure 1 Schema of experimental test setup

The friction force, F_r, is obtained from the equation of motion of the pneumatic piston using the measured values of the pressures in the cylinder chambers, the inertia force and the force acting on the load cell as follows:

$$F_r = p_1 A_1 - p_2 A_2 - ma + F_L \tag{1}$$

where m is the mass of the pneumatic piston, A_1, A_2 are the piston areas, and F_L is the force acting on the load cell.

Three different pneumatic cylinders were used for the experiments: standard, smooth, and low speed cylinders. They are of the same size but have different operating conditions of the velocity and pressure as shown in Table 1. In this experiment, dynamic friction force-velocity characteristic was measured under different conditions of the velocity and pressures. The input velocity of the pneumatic piston was varied sinusoidally in both the extending and retracting strokes of the cylinder between 0.005 and 0.12 m/s at three different frequencies of 0.5, 2, and 4 Hz. Pressures, p_1 and p_2, in the cylinder chambers were varied between 0 and 0.6 MPa. Every experiment was conducted three times to verify the repeatability of the experimental result.

MODIFIED LUGRE MODEL

Yanada and Sekikawa [10] have extended the LuGre model [6], called the modified LuGre model, for simulating the dynamic friction behaviors of hydraulic cylinders by incorporating a dimensionless lubricant film thickness parameter, h, into the Stribeck function. The model is described by

$$\frac{dz}{dt} = v - \frac{\sigma_0 z}{g(v,h)} v \tag{2}$$

$$F_r = \sigma_0 z + \sigma_1 \frac{dz}{dt} + \sigma_2 v \tag{3}$$

where z is the mean deflection of the elastic bristles, v is the velocity between the two surfaces in contact, F_r is the friction force, σ_0 is the stiffness of the elastic bristles, σ_1 is the micro-viscous friction coefficient, and σ_2 is the viscous friction coefficient. $g(v,h)$ is a Stribeck function that expresses the Coulomb friction and the Stribeck

Table 1 Specifications of pneumatic cylinders tested

Specifications	Standard cylinder	Smooth cylinder	Low speed cylinder
Bore diameter (mm)	25		
Rod diameter (mm)	10		
Stroke (mm)	300		
Operating velocity (mm/s)	50 - 750	5 - 500	0.5 - 300
Operating pressure (MPa)	0.05 - 1	0.02 - 1	0.005 - 1

effect and is given by

$$g(v,h) = F_c + \left[(1-h)F_s - F_c\right]e^{-(v/v_s)^n} \tag{4}$$

where F_c is the Coulomb friction force, F_s corresponds to the maximum static friction force, v_s is the Stribeck velocity, and n is an appropriate exponent. The lubricant film dynamics can be given by

$$\frac{dh}{dt} = \frac{1}{\tau_h}(h_{ss} - h) \tag{5}$$

$$\tau_h = \begin{cases} \tau_{hp} & (v \neq 0,\ h \leq h_{ss}) \\ \tau_{hn} & (v \neq 0,\ h \geq h_{ss}) \\ \tau_{h0} & (v = 0) \end{cases} \tag{6}$$

$$h_{ss} = \begin{cases} K_f\,|v|^{2/3} & (|v| \leq |v_b|) \\ K_f\,|v_b|^{2/3} & (|v| > |v_b|) \end{cases} \tag{7}$$

$$K_f = (1 - F_c/F_s)|v_b|^{-2/3} \tag{8}$$

where h_{ss} is the dimensionless steady-state lubricant film thickness parameter, K_f is the proportional constant for lubricant film thickness, v_b is the velocity at which the steady-state friction force becomes minimum, and τ_{hp}, τ_{hn}, and τ_{h0} are the time constants for acceleration, deceleration, and dwell periods, respectively. In Eq. (6), $h<h_{ss}$ corresponds to the acceleration period, $h>h_{ss}$ to the deceleration period.
For steady-state, friction force is given by

$$F_{rss} = F_c + \left[(1-h_{ss})F_s - F_c\right]e^{-(v/v_s)^n} + \sigma_2 v \tag{9}$$

The static parameters of the modified LuGre model, F_s, F_c, v_s, v_b, n, and σ_2, can be identified experimentally from steady-state friction force-velocity characteristic and the dynamic parameters, σ_0, σ_1 and τ_h, can be identified experimentally by the methods proposed in [11].

RESULTS AND DISCUSSION

Figure 2 shows dynamic friction force-velocity characteristics measured in the extending stroke of three pneumatic cylinders. Figure 2(a) shows the sinusoidal velocity variation of the pneumatic piston and Figure 2(b) shows the friction force versus velocity curves. The pressures, p_1 and p_2, in the cylinder chambers were controlled and kept constant at 0.3 and 0 MPa, respectively. It is shown in Figure 2(b) that a hysteresis behavior can be obtained from the friction force-velocity curves at small velocities ($v \leq 0.02$ m/s) for all the three

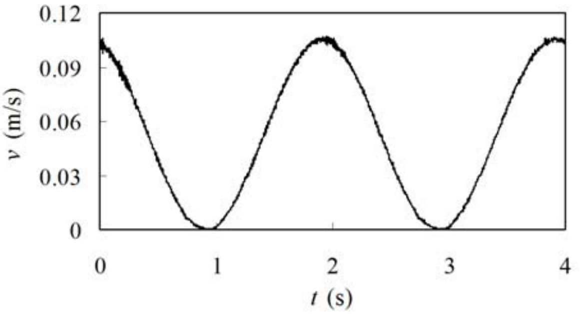

a) Velocity variation (f=0.5 Hz)

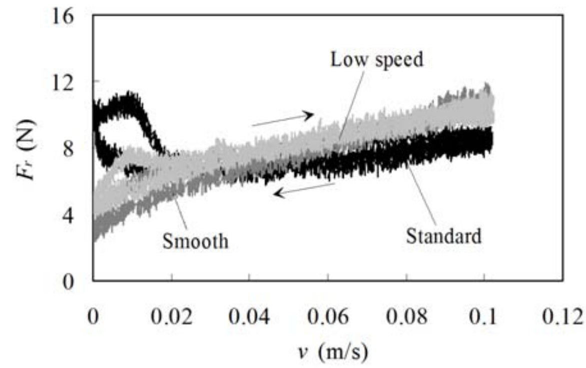

b) Friction force vs. velocity

Figure 2 Dynamic friction force-velocity characteristics for three pneumatic cylinders in extending stroke (p_1=0.3 MPa, p_2=0 MPa)

pneumatic cylinders. The hysteresis loops of the smooth and low speed cylinders are relatively small as compared to the one of the standard cylinder. At high velocities, the friction forces are increased nearly linearly with the velocity.

Figure 3 shows dynamic friction force-velocity characteristics measured in the retracting stroke of three pneumatic cylinders. In this case, the pressures, p_1 and p_2, in the cylinder chambers were kept constant at 0 and 0.3 MPa, respectively. As can be seen from Figure 3(b), the hysteresis behavior can be obtained only for the standard cylinder at small velocities. For the smooth and low speed cylinders, the friction force varies almost linearly with the velocity in the whole velocity range.

Figure 4 shows dynamic friction force-velocity characteristics of the standard cylinder measured at three different frequencies of velocity variation: 0.5, 2, and 4 Hz, for both the extending and retracting strokes. It is shown in Figure 4(a) for the case of extending stroke that when the frequency is increased, the hysteresis loop is expanded to higher velocities and becomes larger. In addition, a reduction of the friction force at small velocities can be seen when the frequency is increased. For the case of retracting stroke in Figure 4(b), it is shown that the hysteresis loop is also expanded to higher velocities but becomes smaller when the frequency is increased. The effects of the frequency of velocity

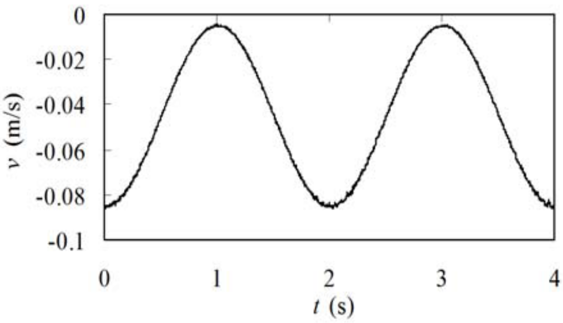

a) Velocity variation (f=0.5 Hz)

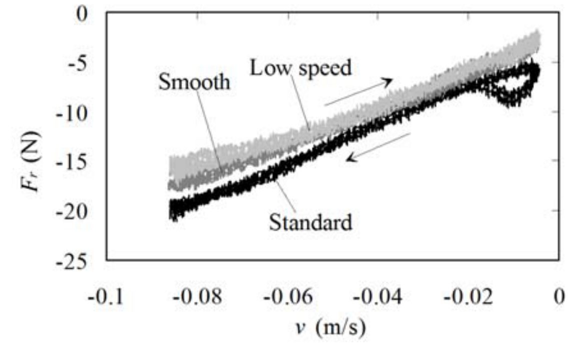

b) Friction force vs. velocity

Figure 3 Dynamic friction force-velocity characteristics for three pneumatic cylinders in retracting stroke (p_1=0 MPa, p_2=0.3 MPa)

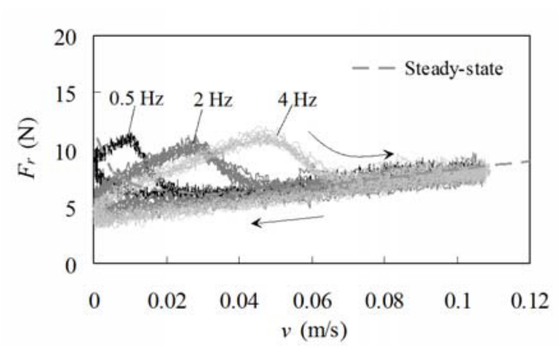

a) Extension (p_1=0.3 MPa, p_2=0 MPa)

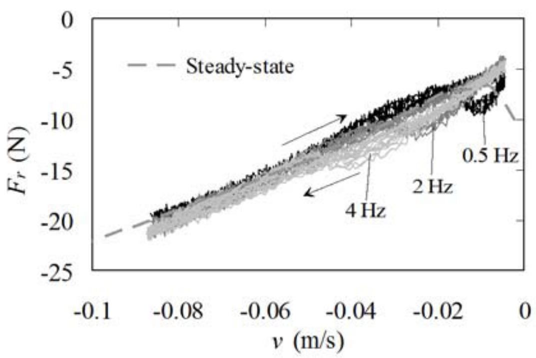

b) Retraction (p_1=0 MPa, p_2=0.3 MPa)

Figure 4 Dynamic friction force-velocity characteristics under different frequencies (standard cylinder)

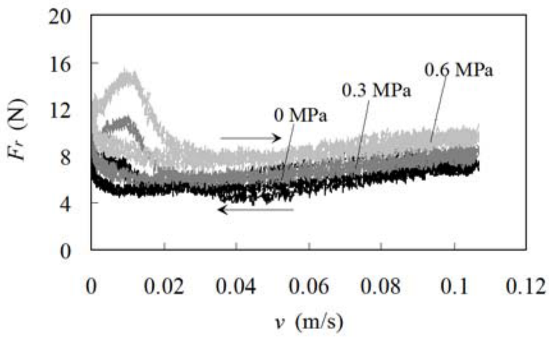

a) Effect of p_1 (p_2=0 MPa, f=0.5 Hz)

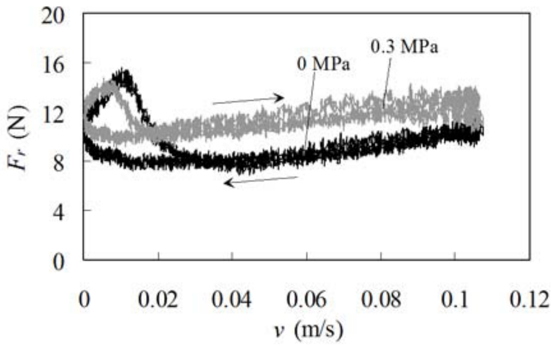

b) Effect of p_2 (p_1=0.6 MPa, f=0.5 Hz)

Figure 5 Dynamic friction force-velocity characteristics under different pressures in extending stroke (standard cylinder)

variation on the dynamic friction force-velocity characteristics for the smooth and low speed cylinders are similar to those for the standard cylinder.

Figure 5 shows the effects of pressures, p_1 and p_2, on the dynamic friction force-velocity characteristics for the standard cylinder in the extending stroke. In this case, p_1 is the driving pressure and p_2 is the resistance pressure. Figure 5(a) shows the effect of pressure, p_1, when the pressure, p_2, is kept constant at 0 MPa, and Figure 5(b) shows the effect of pressure, p_2, when the pressure, p_1, is kept constant at 0.6 MPa. As can be seen from Figures 5(a) and 5(b) that the hysteresis loop becomes larger with increasing pressure, p_1, and becomes smaller with increasing pressure, p_2.

Figure 6 shows the effects of pressures, p_1 and p_2, on the dynamic friction force-velocity characteristics for the standard cylinder in the retracing stroke. In this case, p_2 is the driving pressure and p_1 is the resistance pressure. Figure 6(a) shows the effect of pressure, p_2, when the pressure, p_1, is kept constant at 0 MPa, and Figure 6(b) shows the effect of pressure, p_1, when the pressure, p_2, is kept constant at 0.6 MPa. As can be seen from Figures 6(a) and 6(b) that the hysteresis loop becomes larger with increasing pressure, p_2, and becomes smaller with increasing pressure, p_1. From the results obtained in Figures 5 and 6, it can conclude that the driving pressure makes hysteresis loop larger and the resistance pressure

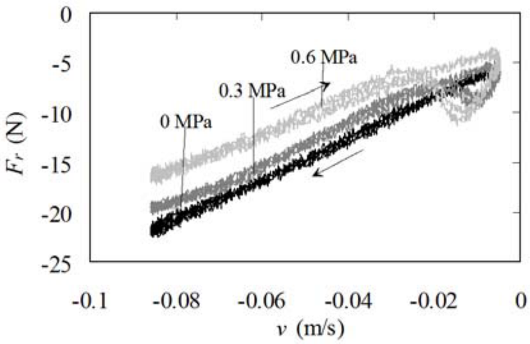

a) Effect of p_2 (p_1=0 MPa, f=0.5 Hz)

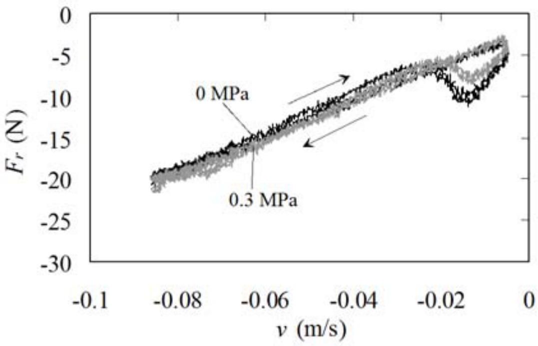

b) Effect of p_1 (p_2=0.6 MPa, f=0.5 Hz)

Figure 6 Dynamic friction force-velocity characteristics under different pressures in retracting stoke (standard cylinder)

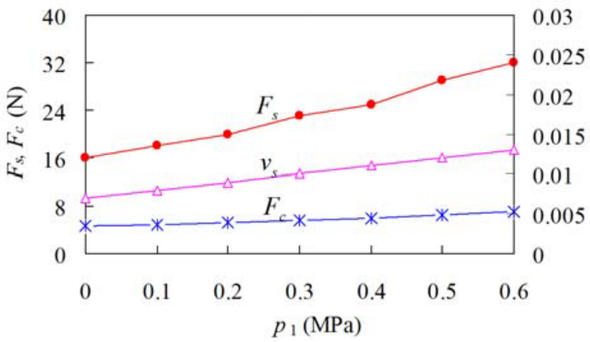

a) Effect of p_1 (p_2=0 MPa)

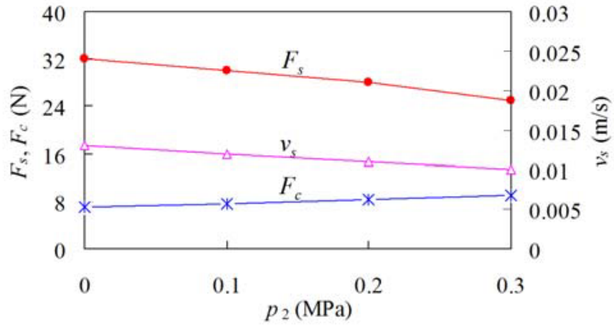

b) Effect of p_2 (p_1=0.6 MPa)

Figure 7 Relations between the pressures and the model parameters in extending stroke (standard cylinder)

makes hysteresis loop smaller. The effects of the pressures on the dynamic friction force-velocity characteristics for the smooth and low speed cylinders are similar to those for the standard cylinder.

Based on the experimental results, all the parameters of the the modified LuGre model were identified at different conditions of the pressures, p_1 and p_2, for three cylinders. In this paper, only the identification results for the case of extending stroke are shown. The results identified for three cylinders at a condition of p_1=p_2=0 MPa are shown in Table 2. For other conditions of pressures, the identification results show that the values of the maximum static friction force (F_s), the Coulomb friction force (F_c) and the Stribeck velocity (v_s) of the modified LuGre model are changed with the pressures while other parameters are unchanged. Figure 7 shows the relations between the values of the parameters, F_s, F_c, v_s, and the pressures, p_1, p_2 for the standard cylinder. It is shown in Figure 7 that the value of F_c increases with both p_1 and p_2, while the values of F_s and v_s increase with p_1 and decrease with p_2.

Table 2 Values of parameters of the modified LuGre model for three cylinders at p_1=0 MPa, p_2=0 MPa

Parameters	Standard cylinder	Smooth cylinder	Low speed cylinder
F_{s0} [N]	16	3.6	4.5
F_{c0} [N]	5	3.6	4.5
v_{s0} [m/s]	0.005	0.005	0.005
v_b [m/s]	0.025	0.025	0.025
n	2.5	0.5	0.5
σ_2 [Ns/m]	25	72	53
σ_0 [N/m]	1.5×10^4	1.5×10^4	1.5×10^4
σ_1 [Ns/m]	0.1	0.1	0.1
τ_{hp} [s]	0.02	0.01	0.01
τ_{hn} [s]	0.15	0.2	0.2
τ_{h0} [s]	20	20	20

Figure 8 shows comparisons between the dynamic friction characteristics measured and the ones simulated by the modified LuGre model for the standard, smooth and low speed cylinders. The simulations were done using MATLAB/Simulink. As can be seen from Figure 8, all the simulated results are in good overall agreement with the measured results. However, the hysteresis behaviors of the smooth and low speed cylinders at small velocities are hardly simulated by the modified LuGre model.

Figures 9 shows the simulation results obtained by the modified LuGre model and needs to be compared with the experimental results shown in Figure 4(a) for the effect of the frequency. The comparison shows that the modified LuGre model cannot predict the expansion of the hysteresis loop in the measured result when the

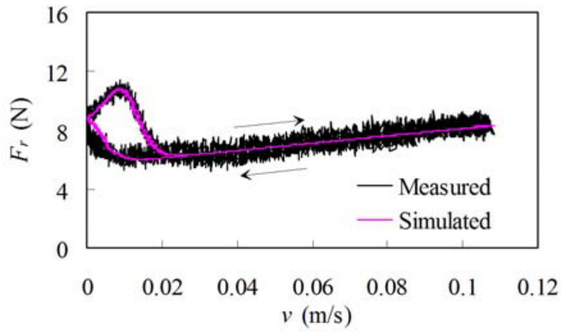

a) Standard cylinder

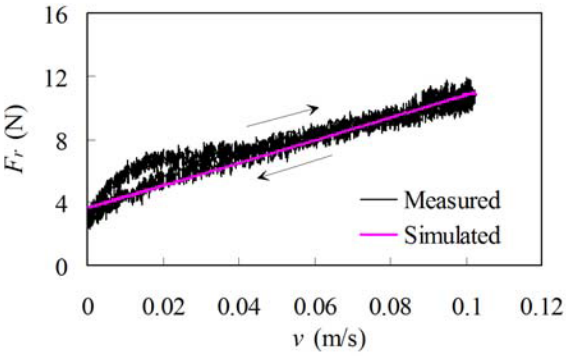

b) Smooth cylinder

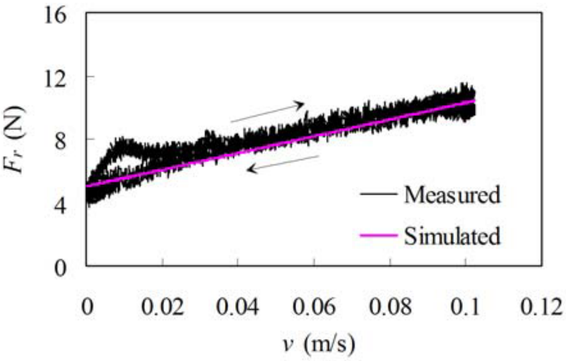

c) Low speed cylinder

Figure 8 Comparison between measured and simulated results for three pneumatic cylinders (p_1=0.3 MPa, p_2=0.0 MPa, f=0.5 Hz)

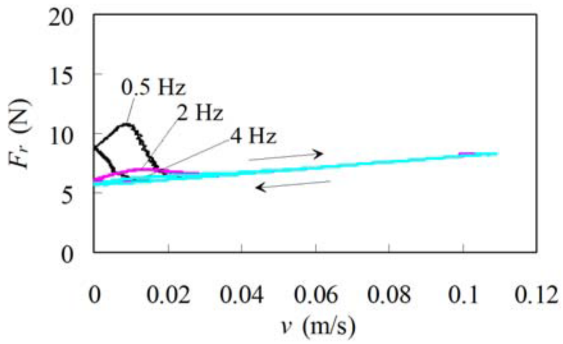

Figure 9 Simulation results corresponding to Figure 4(a)

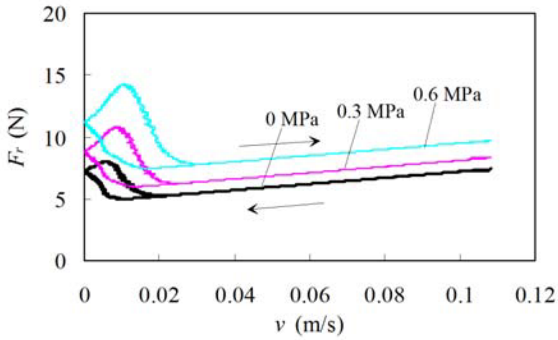

a) Effect of p_1 (p_2=0 MPa)

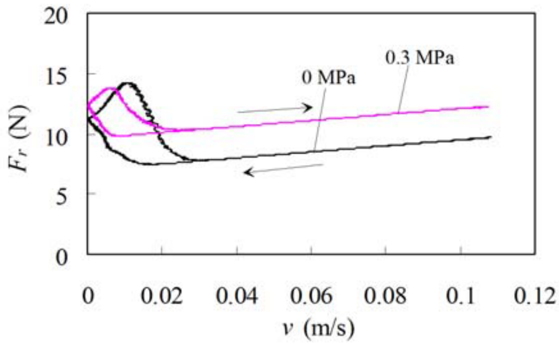

b) Effect of p_2 (p_1=0.6 MPa)

Figure 10 Simulation results corresponding to Figure 5

frequency is increased; as shown in Figure 9, the hysteresis loop predicted by the modified LuGre model becomes smaller by increasing the frequency. However, the model can predict the reduction of the friction force at small velocities when the frequency is increased. The reason for the discrepancy between the simulated results and measured ones obtained in Figures 8 and 9 may be due to the effects of other factors of mechanism, which is not clear at present and are not taken into account in the modified LuGre model.

Figure 10 shows the simulation results obtained by the modified LuGre model and needs to be compared with the experimental results shown in Figure 5. The comparison shows that the modified LuGre model can predict accurately the variation of the hysteresis loop when the pressures are varied.

CONCLUSION

In this paper, dynamic behaviors of friction of pneumatic cylinders are experimentally investigated at various conditions of velocity and pressures. The experimental results show that a hysteresis behavior can be obtained at low velocities in the dynamic friction force-velocity relation and the friction force varies nearly linearly with the velocity at high velocities. The hysteresis loop is expanded to higher velocity when the frequency of the velocity variation is increased, and its size increases with the driving pressure and decreases with the resistance pressure. It is shown that these behaviors can be relatively accurately modeled by the modified LuGre model. The pressures have influence only on the maximum static friction force, the Coulomb friction force and the Stribeck velocity.

ACKNOWLEDGEMENT

The authors would like to express their gratitude to Prof. Y. Wakasawa for his help in part of the experiments and to SMC Corporation for donating the major pneumatic components used in the investigation.

REFERENCES

1. Schroeder, L.E. and Sigh, R., Experimental Analysis of Friction in a Pneumatic Actuator at Constant Velocity, ASME J. Dynam. Syst. Meas. Contr., 1993, **115**-3, pp.575-577.
2. Sc Belforte, G., Mattiazzo, G., and Mauro, S., Measurement of Friction Force in Pneumatic Cylinders, Tribol. J., 2003, **10**-5, pp.33-48.
3. Nouri, Bashir M. Y., Friction Identification in Mechatronic Systems, ISA Trans., 2004, **43**, pp. 205-216.
4. Armstrong-Helouvry B., Dupont P., and Canudas de Wit C., A Survey of Models, Analysis Tools and Compensation Methods for the Control of Machines with Friction, Automatica, 1994, **30**-7, pp.1083–138.
5. Haessig Jr D.A., and Friedland B., On the Modeling of Friction and Simulation, J Dynam Syst Measurement Control, 1991, **113**-3, pp.354–62.
6. Canudas de Wit, C., Olsson, H., Åström, K. J., and Linschinsky, P., A New Model for Control of Systems with Friction, IEEE Trans. Automatic Control, 1995, **40**-3, pp.419-425.
7. Dupont, P.E. and Dunlop, E.P., Friction Modeling and PD Compensation at Very Low Velocities, J Dynam Syst Measurement Control, 1995,**117**-1, pp.8–14.
8. Swevers, J., Al-Bencer, F., Ganseman, and C.G., Prajogo, T., An integrated friction model structure with improved presliding behavior for accurate friction compensation, IEEE Trans Automatic Control, 2000, **45**-4, pp.675–86.
9. Dupont, P., Hayward, V., Armstrong, B., and Altpeter, F., Single state elastoplastic friction models, IEEE Trans Automatic Control, 2002, **47**-5, pp.787–92.
10. Yanada, H., and Sekikawa, Y., Modeling of Dynamic Behaviors of Friction, Mechatronics, 2008, **18**-7, pp.330-339.
11. Yanada, H., Takahashi, K., and Matsui, A., Identification of Dynamic Parameters of Modified LuGre Model and Application to Hydraulic Actuator, Trans. Japan Fluid Power System Society, 2009, **40**-4, pp.57-64.
12. Tran, X. B., Matsui, A., and Yanada, H., Effects of Viscosity and Type of Oil on Dynamic Behaviors of Friction of Hydraulic Cylinder, Trans. Japan Fluid Power System Society, 2010, **41**-2, pp.28-35.

Proceedings of the 8th JFPS International
Symposium on Fluid Power, OKINAWA 2011
Oct. 25-28, 2011

2D3-1

DEVELOPMENT OF PORTABLE ENERGY-SAVING TYPE AIR SUPPLY SYSTEM USING VARIABLE VOLUME TANK

Tatsuyuki Iwawaki*, Toshiro Noritsugu*, Daisuke Sasaki* and Masahiro Takaiwa*
*Graduate School of Natural Science of Technology
Okayama University
1-1-1 Tsushimanaka Okayamacity Okayama, 700-8530 Japan
(E-mail: iwawaki@mcrlab.sys.okayama-u.ac.jp)

ABSTRACT

The purpose of this study is to develop a portable energy-saving type air supply system. A variable volume tank is developed in order to drive a pneumatic actuator with a low discharge pressure in a tank. The developed tank composed of flexible materials can store a pneumatic energy by converting it to an elastic energy. In this paper, the composition of the system, the structure and characteristic of a variable volume tank and experiment of driving actuator with constant and variable volume tanks are discussed. As a result, a variable volume tank can drive the actuator at low pressure compared with the constant volume tank.

KEYWORDS

Pneumatic, Portable air supply system, Variable tank, Energy conservation

INTRODUCTION

At present, the age of the population is advancing in Japan. According to publication of Cabinet Office, the rate of elderly person to total population reached the level of an aging society 7.0[%] in 1970. After that, the rate of it had increased 21[%] in 2007 [1]. Therefore, it is a problem that a care load increases. To decrease a care load, the wearable robot which can decrease a physical load has been developed. The wearable robot is used by human on a body. So the structure of the wearable robot is required to have a human friendliness. Therefore, the many wearable robots constructed with a pneumatic actuator have been developed. The pneumatic actuator has flexibility, a light weight and a high power weight ratio. And it has the advantage that this actuator does not effect on a human body and surrounding environment compared with the electric and the hydraulic actuators. However, the air supply system to send the compressed air to the actuator is required to drive the pneumatic actuator. The air supply system is configured with a compressor, a tank, a control valve. It is desirable that the air supply system should have a portable size to use a wearable robot in a daily life.

The purpose of this study is to develop a portable energy-saving type air supply system. A variable volume tank is developed in order to drive a pneumatic actuator with a low discharge pressure in a tank. The developed tank composed of flexible materials can store a pneumatic energy by converting it to an elastic energy. In this paper, the definition of the pneumatic energy is discussed, and then the problem of a constant volume tank and the structure and the characteristic of the variable volume tank are discussed. Finally, the experiments of supplying a compressed air to the actuator with the constant or the variable volume tanks are described.

PNEUMATIC ENERGY

The air power included the compressed air is necessary to drive the pneumatic actuator. The air power [2] is a total of the time derivative power transmission energy and expansion energy. The power transmission energy is a power to transmit the mechanical energy in the compressed air to downstream. The expansion energy is a power to expand the compressed air. The air power is calculated from a pressure and a flow rate as follow:

$$W_{ap}[k] = \mathrm{P_a} Q_a[k] \ln \frac{P[k]}{\mathrm{P_a}} \quad (\mathrm{k} = 0,1,2\cdots) \quad (1)$$

W_{ap}, P_a, P and Q_a are shown an air power, an atmospheric pressure, an absolute pressure and flow rate under the atmospheric state, respectively. The pneumatic energy is calculated as follow:

$$E_{air}[k] = \mathrm{t_s} \sum_{k=0}^{n} W_{ap}[k] \quad (2)$$

E_{air}, t_s, and n are pneumatic energy, sampling time and sampling number, respectively. In this paper, the air system is evaluated from the view point about the above pneumatic energy.

CONSTANT VOLUME TANK

Figure 1 shows the flow of the compressed air of usual air supply system. The air compressed by compressor is saved in the tank as shown in Figure 1 ①. The compressed air is supplied through the control valve as shown in Figure 1 ②. The compressed air is released through the valve when the pressure is decreased as shown in Figure 1 ③. Decreasing the charged pressure in the tank to drive the actuator is the target of this study. In this study, the power assist glove shown in Figure 2 is used as the pneumatic actuator in this system [3]. A required pressure (P_m) to drive a power assist glove is 200[kPa].

In order to develop energy-saving type air supply

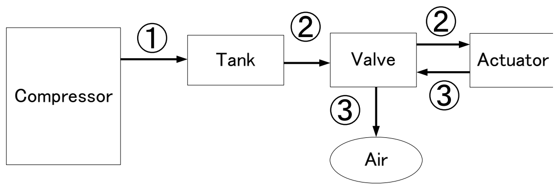

Figure 1 Previous supply system

Figure 2 Power assist glove

system based on a pneumatic energy, the pneumatic energy to drive a power assist glove is measured. In addition, the pneumatic energy charged in a tank at several constant inner pressures is also measured.
Figure 3 shows the experimental setup to measure a pneumatic energy. A pressure sensor, a flowmeter and A tank are connected to output of pressure control valve. The tank shown in Figure 3 is changed to a power assist glove when the required energy is measured to drive for a glove.
The maximum inner pressure of a power assist glove is 200[kPa] when a required pneumatic energy to drive the glove is measured. Figure 4 shows the relation between pressure and consumption pneumatic energy in the glove at the each pressure. From this result, a required pneumatic energy to drive a glove is about 70[J].
Figure 5 shows the image about the pressure state before and after supplying the compressed air form the tank to the actuator. In Figure 5, the diagonal line represents the compressed air. If a tank charged the compressed air is connected with a power assist glove, compressed air is supplied from a tank to a power assist glove, then the all energy in the tank and the glove is kept at the initial charged energy in the tank if the energy loss does not occur. It is required to increase pneumatic energy 70[J] further from the energy in 200[kPa] in order that the inner pressure becomes 200[kPa], which is required pressure to drive the glove. In this experiment, the compressed air is supplied until the maximum charged pressure in Figure 4. In addition, several constant volume tank, 0.2, 0.75, 0.95, 1.5, 1.7[l] are measured. Figure 6 shows the relation between the pressure and the charged pneumatic energy in the each tank and Table 1 shows pressure when the pneumatic energy 70[J] to drive the glove is charged. A large constant volume tank is required when a low discharge pressure compressor is used. On the other hand, the system portability decreases when a large constant volume tank issued. The pneumatic energy in 200[kPa], which is shown the broken line arrow, can not be used to drive the glove. This energy can be considered like an energy loss because this energy can not be used to drive the glove.

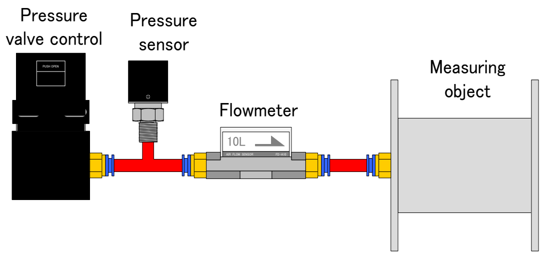

Figure 3 Experimental setup to measure pneumatic energy

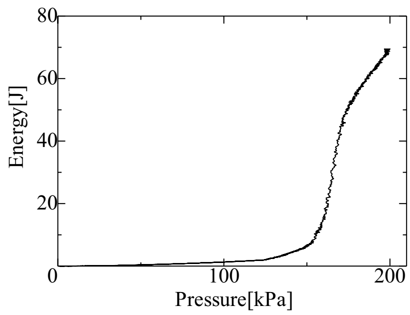

Figure 4 Result of energy (glove)

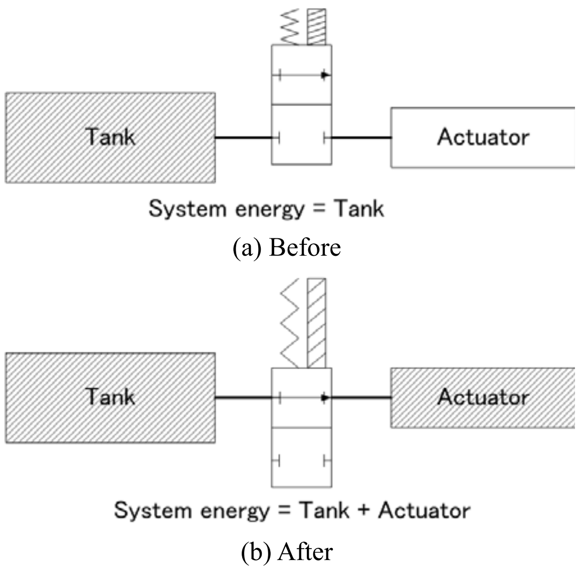

Figure 5 Drive of actuator

VARIABLE VOLUME TANK

The required pressure decreases as the tank volume increases. However, the above remaining energy also increases as the volume increases.

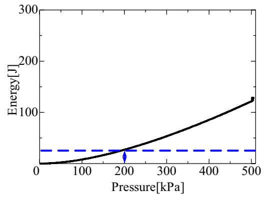

(a) 0.2[l]

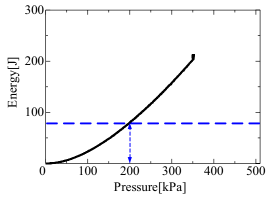

(b) 0.75[l]

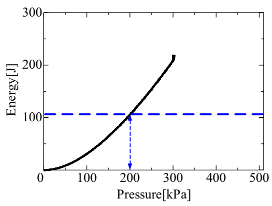

(c) 0.95[l]

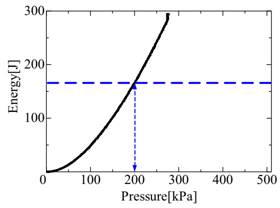

(d) 1.5[l]

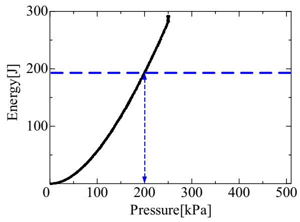

(e) 1.7[l]

Figure 6 Result of energy (glove and constant tank)

Table 1Tank volume and required charged pressure

Tank volume[l]	Required charged pressure[kPa]
0.2	440
0.75	290
0.95	270
1.5	245
1.7	240

In this study, a variable volume tank is developed. The developed tank can be increased the tank volume by supplying the compressed air. The volume of this tank is decreased after supplying a compressed air to a target object, which is glove in this study. Therefore, it can be expected by decreasing the volume that the remaining energy in the tank can be decreased.

Figure 7 shows the ideal charged energy characteristic compared with the constant volume tank. P_d, E_d represent the required pressure (200[kPa]) and the consumption energy to drive the glove. P_t represents

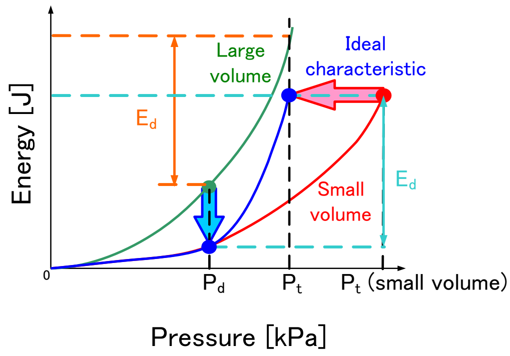

Figure 7 Ideal variable tank

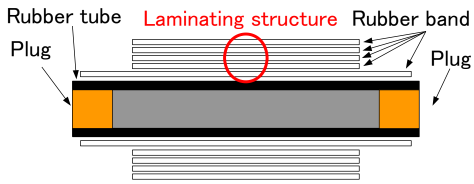

(a) Structure

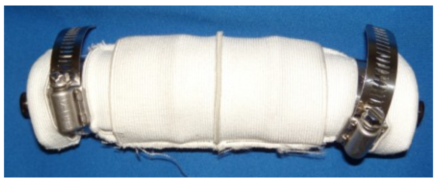

(b) Over view

Figure 8 Variable volume tank

the maximum charged pressure in the each tank. It is desirable that the charged energy is small under P_d in order to decrease the remaining energy. Therefore, the volume must be small under P_d. In order to decrease the charged pressure P_t in the tank, the volume over P_d must be large.

Figure 8 shows the structure and the overview of developed tank. This tank can realize flexibility and a light weight and can charge a pneumatic energy by converting it to an elastic energy. This tank is composed with a rubber tube, and rubber bands. The rubber tube is covered with the rubber band. This rubber tube is prevented the expansion to the length direction by the rubber band. By covering with the rubber band, the rubber tube can expand to only the radial direction when the compressed air is supplied. The charged energy characteristic can be changed by increasing or decreasing the number of the rubber

band. The outer and inner diameters of the rubber tube are 33 and 24[mm]. The inner length between the plugs is 100[mm]. The initial inner volume is about 0.045[l]. The weight is about 185[g]. The circumference length is limited about 240[mm] by a nylon band to prevent an excessive expansion.
The energy characteristic is measured by the same system shown in Figure 5. The developed tank is pressurized until 280[kPa] in this experiment. The number of the rubber band is single and double layers. Figure 9 shows the charged energy characteristic. From Figure 9, the developed tank can be almost realize a ideal characteristic shown in Figure 7.

EXPERIMENT TO SUPPLY PNEUMATIC

The power assist glove is driven using the constant and the variable volume tanks. In this experiment, the inner pressure of the tank and the power assist glove are measured when the compressed air is supplied from the tank to the glove. Figure 10 shows the experimental setup. In order to supply the pressure stably, the pressure control valve is used as a power source for the tank in this system. In an actual system, the compressor is used instead of this pressure control valve. Three constant volume tanks, 0.2 and 0.95, 1.7[l], are used in this experiment. The maximum charged pressures in each tank considered an energy loss, which is decided experimentally, are shown in Table 2. The tank is pressurized until the maximum charged pressure by the pressure control valve for 20[s]. The air flow between the pressure control valve and the tank is shut off by the ON-OFF valve 1 at 25[s]. The compressed air in the tank is supplied by the ON-OFF valve 2 to the glove at 28[s]. Figure 11 shows the overview of the experimental system before and after the compressed air is supplied. From these pictures, it can be confirmed that the glove is pressurized by decreasing the glove is pressurized by decreasing the volume of the developed tank.
Figure 12 shows the experimental results when the each tank is used. From the results, the variable volume tank has the almost same result of the constant volume 0.95[l] even though the initial volume of the

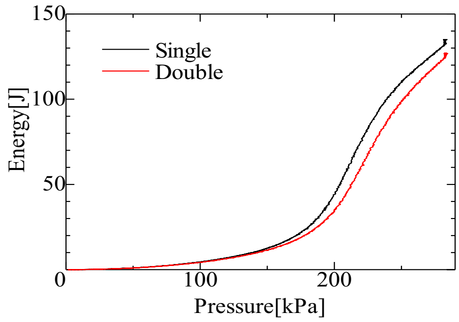

Figure 9 Charged energy characteristic

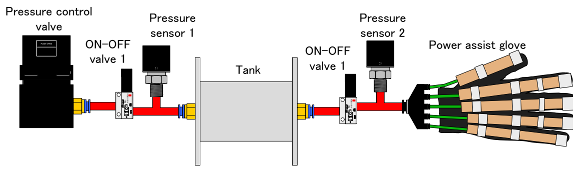

Figure 10 Experimental setup

Table 2 Maximum charged pressure

	Tank	Volume[l]	Pressure[kPa]
(a)	constant	0.2	500
(b)	constant	0.95	280
(c)	constant	1.7	245
(d)	variable	-	280

variable one is 0.045[l]. In addition, the glove can be pressurized by using the developed tank at the lower charged pressure than the constant volume 0.2[l].
The same experiment is verified when the small size compressor (SQUSE MP-2-C) is used instead of this pressure control valve. Three constant volume tanks, 0.75 and 0.95, 1.7[l], are used in this experiment. The maximum charged pressures in each tank are shown in Table 3. The tank is pressurized until the maximum charged pressure by the compressor. When the charged pressure arrives to the maximum charged pressure, the compressor is stopped. The compressed air in the tank is supplied by the ON-OFF valve 2 to the glove after stopping the compressor. The ON-OFF valve 1 is used to exhaust the compressed air in the tank after the experiment.
Figure 13 shows the experimental results. From the results, the variable volume tank can be pressurized

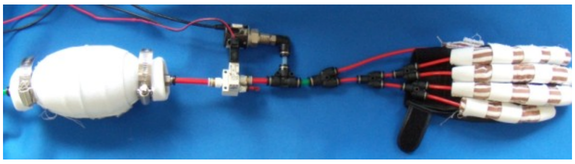

(a) Before

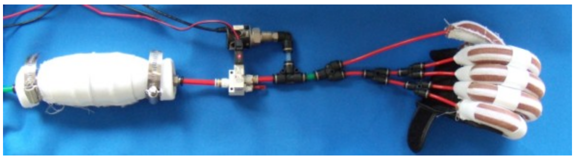

(b) After

Figure 11 State of volume shift

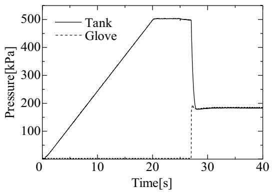

(a) 0.2[l]

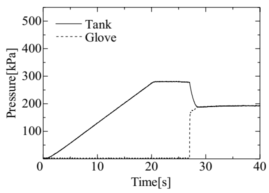

(b) 0.95[l]

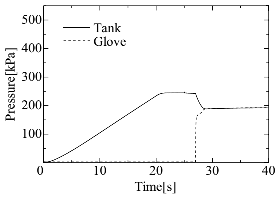

(c) 1.7[l]

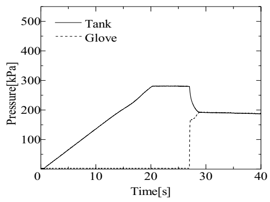

(d) Variable

Figure 12 Pressurized experiment using pressure control valve

until the maximum charged pressure in a short time compared with the constant volume tank. The variable volume tank has the small volume under the low charged pressure, then this tank can be pressurized in a short time. The above is the advantage when the portable air supply system is constructed by using the small size compressor, which has the low discharge performance.

CONCLUTION

From the results, the variable volume tank can be used at low charged pressure compared with a constant volume tank. In addition, the variable volume tank can

Table 3 Maximum charged pressure

	Tank	Volume[l]	Pressure[kPa]
(a)	constant	0.75	300
(b)	constant	0.95	280
(c)	constant	1.7	245
(d)	variable	-	280

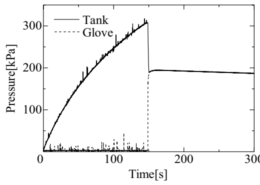

(a) 0.75[l]

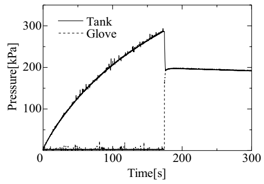

(b) 0.95[l]

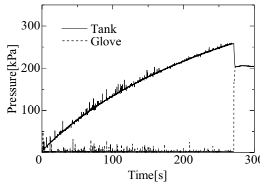

(c) 1.7[l]

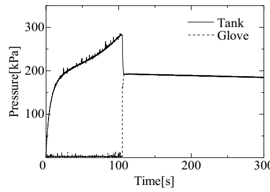

(d) Variable

Figure 13 Pressurized experiment using compressor

be pressurized until the maximum charged pressure in a short time compared with the constant volume tank. These are the advantages when the portable air supply system is constructed by using the small size compressor, which has the low discharge performance.

REFERENCES

1. Cabinet Office, White Paper of Age of the Population, 2010
2. Kagawa and Matsuri, Compressibility of Air, Hydraulic Technology, 2005, December, Vol.44, No.10, pp.46-50
3. Kadowaki, Noritsugu, Takaiwa and Sasaki, Development of soft power assist glove and its control based on human intention, Journal of Robotics and Mechatronics, Vol23, No.2, 2011

Proceedings of the 8th JFPS International
Symposium on Fluid Power, OKINAWA 2011
Oct. 25-28, 2011

2D3-2

MOBILE ROBOT BY A DRAWING-OUT TYPE ACTUATOR FOR SMOOTH LOCOMOTION INSHIDE NARROW AND CURVING PIPES

Kenichi HOSAKA*, Hideyuki TSUKAGOSHI* and Ato KITAGAWA*

* Department of Mechanical and Control Engineering
Tokyo Institute of Technology
Ookayama, 2-12-1-S5-107, Tokyo, Japan
(E-mail: k-hosaka@cm.ctrl.titech.ac.jp)

ABSTRACT

This study discusses the search and rescue mobile robot which is aimed to go through narrow and curving routes and pipes inside the collapsed houses. This robot is inspired by the action of the octopus drawing out its arms. Since it uses the part of the arm that was drawn out as support for its advancing motion, it is expected to carry a camera without depending on the size of pipes. To realize this action, this robot is composed of a flat tube and a slider named Λ-drive. In Λ-drive the tube is bent, forming a buckling point on it, which helps to cut off the fluid passage in order to provide the driving force to the slider when pressurizing one side of the tube. Finally, it is experimentally verified through experiments that this robot is able to go through some narrow and curving pipes.

KEY WORDS

Key words, Pneumatic actuator, Rescue Robot, Flat tube, Flexible actuator, Octopus

INTRODUCTION

A long pole with a camera and a fiberscope are used as methods to find someone who is left inside collapsed buildings when an earthquake occurs. But the search area of the long pole with a camera is limited within the reachable distance of the pole. Besides, it can only approach through linear paths. The fiberscope can follow the route for its flexibility. However, it can get stuck because it is pushed from the entrance of the route to go through. Although mobile rescue robots using wheels or crawlers [1-2] might be capable of searching much wider region in 3D, they are still hard to traverse over irregular terrain with the obstacles higher than their own size. The method of letting the whole body going forward at the same speed [3] has the problem that the moving direction of the whole body tends to be unstable on the bumpy terrain, for the driving direction at each contact point on the ground varies with the contact condition.

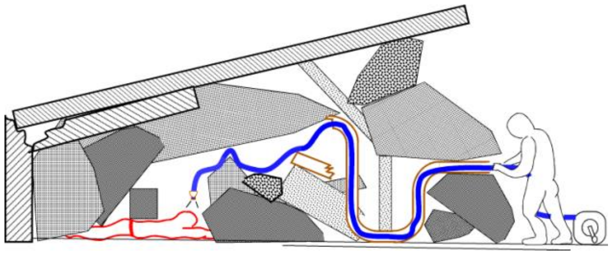

Figure 1 Image of the rescue operation by a hose-shaped robot passing through a water pipe to search for survivors

On the other hand, as the method of moving each part of the body intermittently with different phase, the gait composed of the moving mode and the fixed mode, motivated by the behavior of an earthworm and an inchworm [4-8], is one of the examples. The problem is how to enable the part of the body to being fixed to the bumpy path stably in the fixed mode and how to reduce the friction in the moving mode. To solve these problems, Grow-hose-I [9] is proposed. It can go through some narrow and curving routes. However, in order to be able to go through narrower routes and smaller curving radius routes, its structure needs to be simpler. Therefore, we refer to the drawing out action of an octopus shown in Figure 2 [10]. Since it uses a part of the arm that was drawn out as support for its advancing motion, it is expected to carry a camera without depending on the inside state of the routes and the size of pipes. To realize this action, we use the flat tube and head unit which is composed of a camera and a slider called Λ-drive [11].
In this paper, we compare the difference between the existing drawing out type drive and the Λ-drive. Next, we explain how to reduce the friction. Moreover, we show experimental results of its basic operation and the validity of the analysis is verified. Finally, it is experimentally verified that this robot is able to go through some narrow and curving pipes.

Figure 2 Drawing out action of an octopus

OUTLINE OF THE DRAWING OUT TYPE DRIVE

A drawing out type drive using a round tube and pinch roller is one of the methods to realize the drawing out action like an octopus [12]. One side of the round tube which is pinched by two rollers to cut off the fluid passage is pressurized, and it goes forward. But in order to cut off the fluid passage completely, it needs to pinch the tube with a strong force. This causes the friction between the two rollers and the round tube.
Therefore, we use a flat tube and Λ-drive. The cross section of a flat tube forms the flat shape in non-pressurized condition, while it approaches the round shape in pressurized condition keeping its peripheral length approximately constant. When it bends and its one side is pressurized, the buckling point which can cut off the fluid passage without pinch roller occurs (Figure 3). But the pressurized tube tends to be linear shape. So, in order to keep the tube bent, we use two rollers as shown in Figure 4. The stopper roller and cover roller prevents the flat tube from slipping out. The composition like this is called Λ-drive. Since the tube is not pinched in it, it is expected to generate more strong force than the pinch roller mechanism.

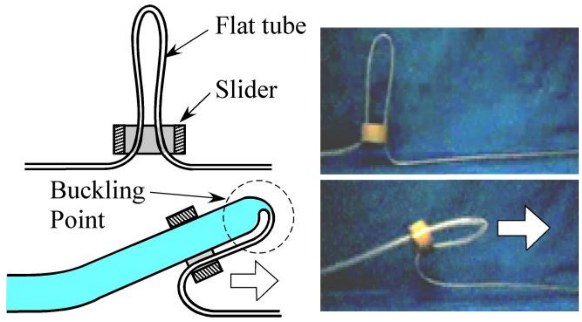

Figure 3 Basic principle of Λ-drive

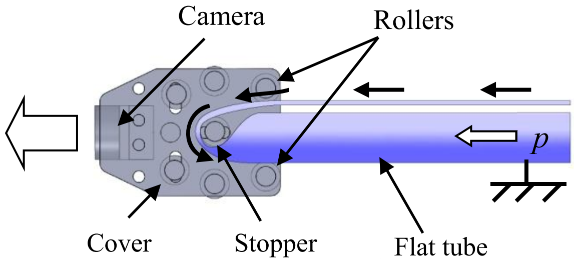

Figure 4 Image of the robot

ANALYSIS OF THE DRIVING FORCE

The driving force at the buckling point is derived as follows. Let us assume that the flow rate ΔQ with the pressure p flows into the tube, while the displacement Δl_b with the force F_b is produced at the buckling point as the output. Assuming a perfect state with no energy loss from input to output, the following equation holds from the conservation law of energy.

$$p \cdot \Delta Q = F_b \cdot \Delta l_b \tag{1}$$

At the same time, the next equation can also be obtained, assuming that the most expanded part in the tube, whose cross sectional area is expressed as A, becomes long for Δl_b with the buckling shape kept constant, shown in Figure 5.

$$\Delta Q = A \cdot \Delta l_b \tag{2}$$

Considering the above two equations, the following relationship can be derived.

$$F_b = p \cdot A \tag{3}$$

While the buckling point moves a distance Δl_b, the downstream tube is pulled by $2\Delta l_b$. Therefore, Eq. (4) holds, where F_b is the traction. As a result, the relationship in Eq. (5) can be deduced.

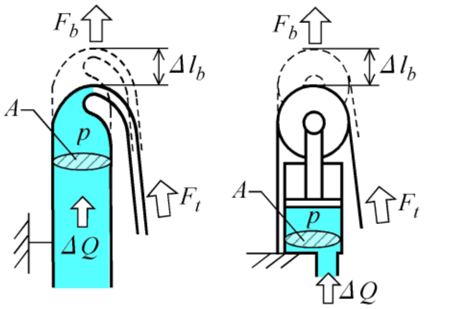

(a) Model of the flat tube (b) Model using a pulley and a wire

Figure 5 Model of the flat tube and its equivalent model

$$F_b \cdot \Delta l_b = F_t \cdot (2\Delta l_b) \tag{4}$$

$$F_t = F_b / 2 = (p \cdot A) / 2 \tag{5}$$

This equation shows the pulling force F_t is not affected by the angle between the upstream tube and the downstream tube.

To be exact, the energy is consumed to deform the cross-section of the tube, and therefore may be smaller than the values in Eq. (3) and (5). However, in this work we use Eq. (3) and (5) as approximations valid when flat tubes that are soft enough are used.

The driving force of the robot is smaller than the force at the buckling point because the contact area between the flat tube and the stopper is smaller than the cross sectional area of the most expanded part in the tube. The contact area can be approximated by the part of the ellipse shown in Figure 6. As shown in it, the distance of its major axis a, minor axis b and the height of the contact area h can be obtained from the flat tube and the stopper which are used in the robot. It is made from a round tube whose outer diameter is 12mm and inner diameter is 10mm. Therefore, the contact area A_c is less than 59% of the area A which is shown in Figure 5.

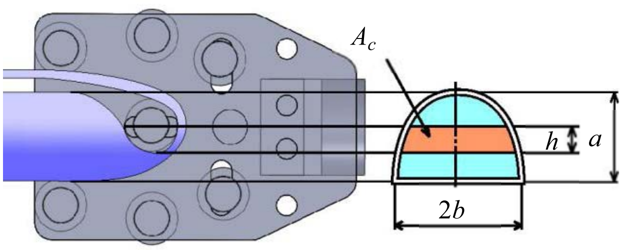

Figure 6 The contact area between the tube and stopper

CLASSIFICATION OF THE DRIVING MODE

The motion of the robot depends on which side of the tube is fixed and which side of the tube is pressurized. As shown in Figure 7-(a), when one side of the tube is fixed on the ground and pressurized, the head unit advances. In this case, two modes are possible. When the downstream tube is tensioned, the head unit advances with its stopper pushed by the tube. This is called stopper mode. The other is called cover mode, and the downstream is not tensioned (Figure 7-(b)). Usually, the robot advances in stopper mode because of the weight of the tube and the friction between the tube and the other place. When the one side of the tube is pressurized and the other side is fixed, the robot goes backwards as shown in Figure 7-(c). It is called back mode. When the both sides of the tube are pressurized, the robot stays still (Figure 7-(d)). It is called stop mode. Surely, to quit pressurizing, the robot stops advancing, but stop mode can break quicker.

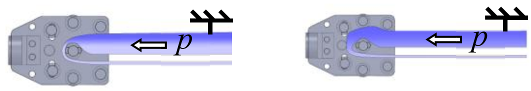

(a) stopper mode (b) cover mode

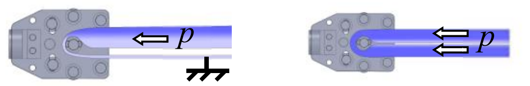

(c) back mode (d) stop mode

Figure 7 Driving mode of the robot

EXPERIMENTS ON DRIVING FORCE AND FRICTION

As shown in Figure 6, the bigger the stopper roller is, the larger the contact area is. However, if the stopper roller is too big, a leakage flow rate occurs at the buckling point. The leakage flow rate causes the reduction of the pressure applied to the buckling point. The relation between the diameter of the stopper roller and the leakage flow rate is shown in table 1. Accordingly, 6mm is the best in this case because it is the largest diameter without the leakage flow rate. So the driving force is produced as shown in Figure 8. It is less than 57% of the ideal value which is shown in Eq. (5).

Table 1 Leakage flow rate at the buckling point

	Diameter of the stopper roller [mm]		
	4	6	8
0.1MPa	○	○	○
0.2MPa	○	○	○
0.3MPa	○	○	×

○Leakage flow rate does not occur
×Leakage flow rate occurs

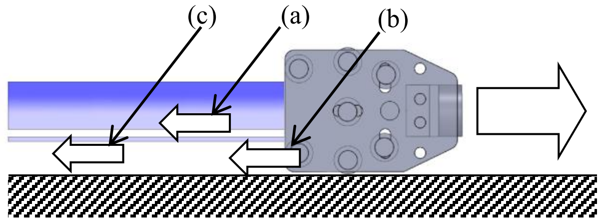

Figure 10 Three kinds of frictions

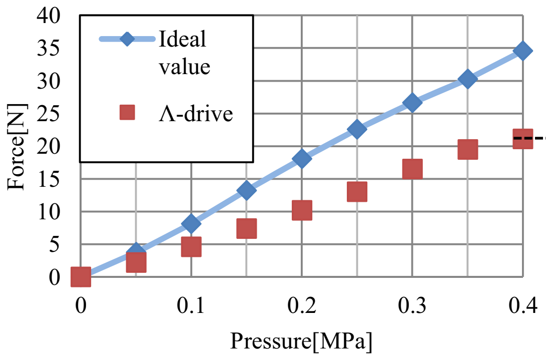

Figure 8 Result of the experiment of the driving force

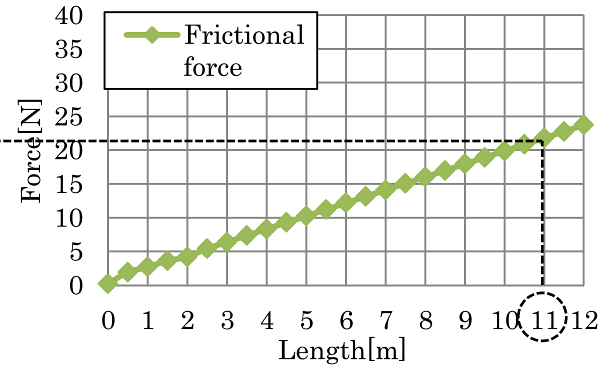

Figure 11 Result of the experiment of friction

When the robot advances through inside the pipes called duct hose, whose inner diameter is 50mm as shown in Figure 9, three kinds of frictions act on the robot against the driving force which can be produced from the flat tube. The frictions are as follows,

(a) friction between non-pressurized side of the flat tube and inner wall of the duct hose
(b) friction between the head unit and inner wall of the duct hose
(c) friction between pressurized side of the flat tube and non- pressurized side of the tube (Figure 10)

So we conducted the experiments to measure the frictions and summed them. The experimental results are shown in Figure 11.

Accordingly, the robot with a pneumatic pressure of 0.4MPa can advance 11m inside the straight duct hose.

Figure 9 Image of the duct hose

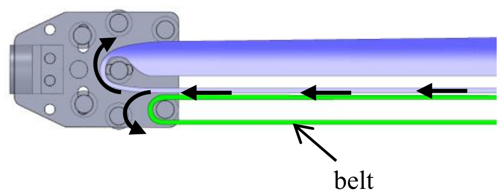

Figure 12 Image of the robot with a belt

However, in the curve section, the friction (a) and (b) especially increase. Therefore, the head unit is equipped with the outer roller and the belt against the non-pressurized side of the flat tube (Figure 12).

OVERVIEW OF THE PROTOTYPE

The prototype robot is shown in Figure 13, and the specification is shown in table 2. The air can be supplied to the both sides of the flat tube. However, when the robot advances, the air is supplied to only one side of the tube. The head unit is equipped with a camera which is used to see inside of the duct hose. The images taken from the camera can be seen by using a monitor as shown in Figure 15.

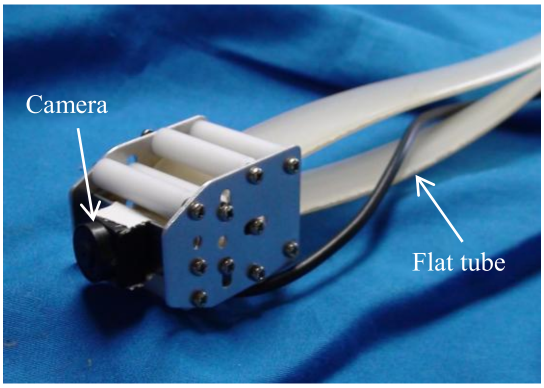

Figure 13 Image of the prototype robot

Table 2 Specification of the prototype

Robot size	Length:43mm Width:26mm Height:29mm
Mass	34.0g

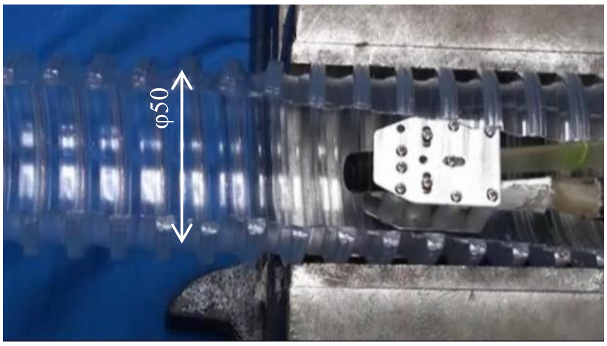

Figure 14 Prototype robot in the duct hose

EXPERIMENTS OF THE PROTOTYPE

We conducted the following experiments to find out the ability of the prototype to go through inside pipes. Inside straight pipes, the prototype whose tube is then internally pressurized with a pneumatic pressure of 0.3MPa is able to advance at the velocity of about 1.5m/s and the velocity can be reduced by using a throttle valve. Next, inside the curving pipes whose curvature radius is 70mm, shown in Figure 15-(a), the prototype can advance without belt. However, the velocity with belt is more efficient than the velocity without belt. In the S-shaped pipes, shown in Figure 15-(b), it is difficult for the prototype to advance by only one side of the tube pressurized since it is not symmetric as shown in Figure 16. The right side of the tube is pressurized (Figure 16-b), and therefore the prototype tends to go to the left side. The same occurs with the left side (Figure 16-c). By using this characteristic, when we want the prototype to go to the right side, the opposite side of the tube is pressurized. Then, the prototype can go through the S-shaped curving pipe. The prototype is able to advance into vertical direction. In this case, the above characteristic also acts. The prototype is rolled as shown in Figure 17, and then it can go through in the pipes (Figure 15-(c)). The robot also can go backwards as shown in Figure 15-(d). Furthermore, it can advance not only inside the pipes, but also on the ground with some obstacles as shown in Figure 18.

(a) Curvature radius 70mm (b) S-shaped curving pipe

(c) Vertical direction (d) Back mode

Figure 15 Propulsion experiment in the duct hose

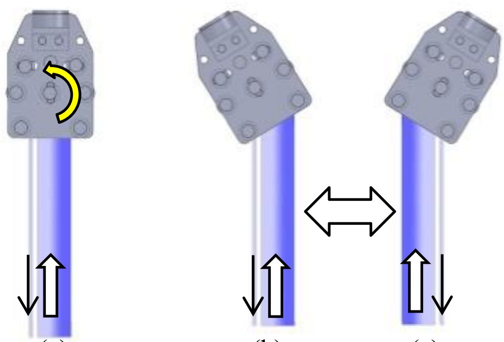

(a) (b) (c)

Figure 16 Image of the direction of the tube

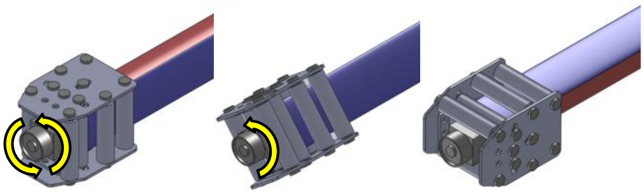

Figure 17 Image of the passive torsion of the tube

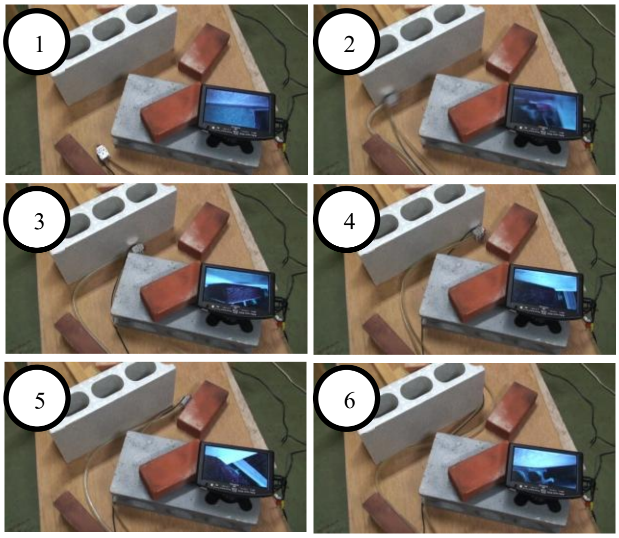

Figure 18 Propulsion experiment on the ground with some obstacles

CONCLUSION

In this paper, we show the prototype which is composed of a flat tube and Λ-drive, which can go through some narrow and curving pipes. Furthermore, it can advance on the ground with some obstacles. However, at more complex area or inside collapsed houses, it needs to steer actively and reduce the friction. The robot which is composed of a lot of tubes with downstream on the inside of the robot is one answer to solve these problems. It can reduce the friction between the robot and outer walls. As future work, we will try steering the robot by using difference of the length of each of the drawn out tubes.

REFERENCES

1. Atsushi, Nakano. and Shigeo, Hirose. Development of Souryu-VII with active slime body and multiple wheels, JSME Conference on Robotics and Mechatronics, 2009, 2P1-E19.
2. Junji, Masukawa. and Koichi, Osuka. Hybrid Operation System for Rescue Robot MOIRA2, JSME Conference on Robotics and Mechatronics, 2007, 2P1-J07.
3. Kazuna Sawata, Masashi Konyo, Satoshi Saga, Satoshi Tadokoro, and Koichi Osuka. Sliding Motion Control of Active flexible Cable using Simple Shame Information, IEEE International Conference on Robotics and Automation, 2009, SaB8.4.
4. Taro Nakamura, and Tomohide Iwanaga. Locomotion Strategy for a Peristaltic Crawling Robot in 2-Dimensional Space, IEEE International Conference on Robotics and Automation, 2008, WeA7.3
5. Richard Primerano, David Wikie, and William Regli. Toward a Multi-Disciplinary Model for Bio-Robotic Systems, IEEE International Conference on Robotics and Automation, 2008, WeA7.6
6. Menciassi, A, Gorini,S, Pernorio, G. A SMA actuated artificial earthworm IEEE International Conference on Robotics and Automation, 2004, pp.347-352
7. J.ZUO, G.YAN, and Z.GAO. A micro creeping robot for colonoscopy based on the earthworm, Journal of Medical Engineering & Technology, 2005, 29, 1, pp. 1-7
8. Alexander Boxebaum, Roger D.Quinn, Hillel J. Chel, “A New Theory and Methods for Creating Peristaltic Motion in a Robotic Platform”, Proceedings of IEEE International Conference on Robotics and Automation, TuE3.5(2010)
9. Hideyuki Tsukagoshi, Nobuyuki Arai, Ichiro Kiryu and Ato Kitagawa. Smooth Creeping Actuator by Tip Growth Movement Aiming for Search and Rescue Operation, IEEE International Conference on Robotics and Automation, 2011, 1720-1725
10. 20090320-08-Shinagawa aquarium, http://www.youtube.com/watch?v=TZKimgXhas8
11. Yotaro, Mori. Hideyuki, Tsukagoshi. and Ato, Kitagawa. Flexible Sliding Actuator Using A Flat Tube And Its Application To The Rescue Operation, IEEE International Conference on Robotics and Automation, 2010, ThA2.3
12. Akihisa, Mikawa. Hideyuki, Tsukagoshi. Ato, Kitagawa. Tube Actuator with Drawing Out Drive Aimed for the Inspection in the Narrow and Curved Path, IEEE/ASME International Conference on Advanced Intelligent Mechatronics, 2010, FrC3.2

Proceedings of the 8th JFPS International
Symposium on Fluid Power, OKINAWA 2011
Oct. 25-28, 2011

2D3-3

DEVELOPMENT OF JUMP ASSIST SYSTEM USING PNEUMATIC RUBBER MUSCLE

Kotaro TADANO*, Hiroshi ARAYA**,
Kenji KAWASHIMA*, Chongo YOUN *, Toshiharu KAGAWA*

* Precision and Intelligence Laboratory,
Tokyo Institute of Technology
4259 R2-46, Nagatsuta-cho, Midori-ku, Yokohama, 226-8503 Japan
(E-mail: tadano@pi.titech.ac.jp)
** Technology Development Division HQ, NSK Ltd.

ABSTRACT

In this paper, we develop a jump assist system that can generate instantaneous force using pneumatic artificial rubber muscles (PARMs) since such quick motion is required in the rescue activities. The device extends the knee joint using PARMs. Moreover, bi-articular mechanism between the knee and ankle joint is realized using PARMs. Assist timing with the device is detected with an acceleration meter installed in the device. The timing is investigated both theoretically and experimentally. The experiments are performed with three subjects to demonstrate the effectiveness of the device.

KEY WORDS

Key words, Pneumatic artificial rubber muscle, Power assist system, Bi-articular muscle, Instantaneous force

INTRODUCTION

A number of power-assist robots have been developed for amplify human muscle strength. These robots are widely expected to apply for various fields such as medical welfare, rescue, agriculture, physical labor in the factory and so on. Most of conventional wearable power-assist systems propose a method based on the biological signals such as EMG signals or hardness of skin surface [1][2]. However, the noises included in these biological signals make it difficult to identify the motions of the user accurately. Moreover, in the case of using electric motor at each joint, joint parts become heavy and bulky, and need to prepare an electric circuit.

Pneumatic actuators have advantages such as high weight-power ratio, compressibility, low heat generation and clean energy. Therefore, the actuators have applied to drive power assist robots. Yamamoto et al. developed a power assist suit for nurse caring with pneumatic actuator utilizing pressure cuffs [3]. Load cells are used to detect the muscles to realized harmonic motion of the robot to the wearer.

Pneumatic artificial rubber muscles are often used in the power assist robot since the characteristics of the muscles are well studied [4-7]. In order to support activity of daily living of aged or disable person safety and easily, a wearable power assist device for hand grasping have been developed [8]. By using the rubber muscles, the glove can assist various daily finger tasks owing to its flexibility and light weight [9]. In order to provide muscular support for the manual worker, a “muscle suit” has been developed. The muscle suit consists of a mechanical armor-type frame and McKibben artificial muscle. Using a new link mechanism for the shoulder joint which consists of two half-circle links with for universal joints, all motion for upper limb has been realized [10].

Most of the power assist systems are focused on relatively slow motion such as walking or lift up motion. However, the systems are expected to use in various situations such as rescue activities. In the activities, quick motion is sometimes required. Therefore, we have intended to assist jumping with a power assist device which is one of quick motion. In this paper, we develop a jumping assist system that can generate the instantaneous force using pneumatic artificial rubber muscle (PARM). A servo control is applied to the system. The effective start timing of the assist detected by an acceleration sensor is investigated experimentally.

JUMP ASSIST SYSTEM

Design

The developed jump assist system composed of an ankle and knee joint. Especially, we focused on the extension of the knee joint since the joint contribute highly for jumping.

Figure 1 shows the designed jump assist device. A user wears the device on his/her lower legs. The device mainly consists of three parts, thigh, shin and foot frames as shown in Figure1. Both the user and arm unit are fastened with hook-and-loop at three points, thigh, second thigh and ankle.

Pneumatic artificial rubber muscle (PARM) is known as an effective actuator for assist devices since it has flexibility and a high mass-power rate. Therefore, PARM is selected as actuators for the jump assist system. It is known from our previous research [11] that the generated force F by the PARM can be given as

$$F = aP - b\varepsilon - c\dot{\varepsilon} - df \qquad (1)$$

here, P indicates the inner pressure, ε is the contraction ration and f is the friction force of PARM. a, b, c and d are the constant parameters obtained from experiments.

Joint mechanism

Figure 2 shows a side view of the extension mechanism for the knee joint. The joint extend with the contraction of PARM. The extend torque τ_{gk} with the device at the knee joint can be given as

$$\tau_{\mathrm{gk}} = Fr \qquad (2)$$

here F is the generated force by the PARM and r is the radius of the pulley at the knee joint. The PARM is installed at the both side which suggest the knee joint is pulled with two PARMs. The PARM is actively controlled by pneumatic servo valves.

In human, bi-articular muscles exist and act on the both end joints simultaneously in addition to the mono-articular muscles. The antagonistic pairs of bi-articular muscles could positively contribute to the compliant properties of the multi-articular extremity, leading to smooth, fine and precise movements [12]. Therefore, in the developed device, bi-articular mechanism is realized as shown in Figure3. The PARM for bi-articular mechanism (shown as bi-articular muscles in Figure 3) is passively controlled at a certain pressure to generate constant pulling force. As the mechanism is so called parallel mechanism, the torque at the knee and ankle joint τ_{k} and τ_{a} have the following relation with the length of the links.

$$\frac{\tau_{\mathrm{k}}}{\tau_{\mathrm{a}}} = \frac{h_{\mathrm{k}}}{h_{\mathrm{a}}} \qquad (3)$$

here, h_{k} and h_{a} are the length defined in Figure 3.

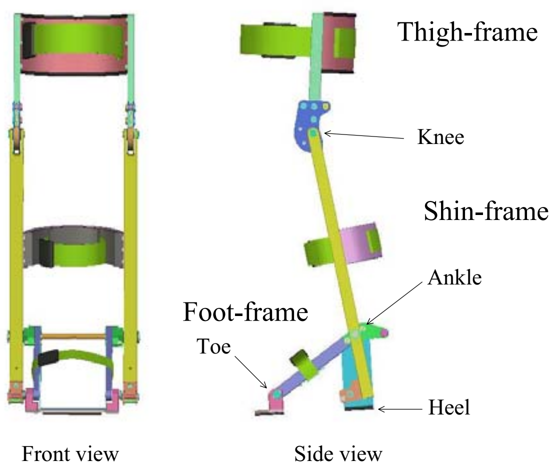

Figure 1 Design of Jump assist device

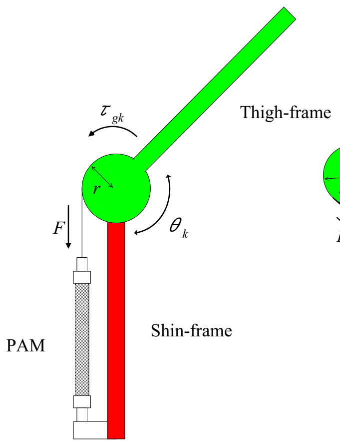

Figure 2 Knee extension Mechanism

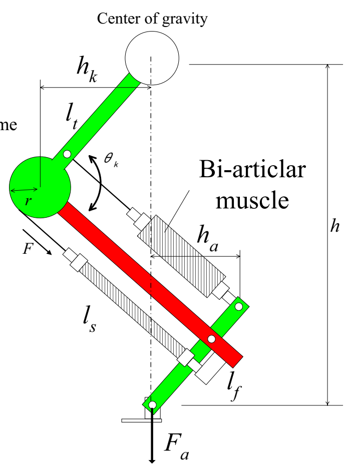

Figure 3 Bi-articular muscle mechanism

The following equation is obtained from the balance of torques.

$$\tau_{\mathrm{k}} + \tau_{\mathrm{a}} = \tau_{\mathrm{gk}} \tag{4}$$

The force to the ground F_{a} generated by the device can be written as

$$\mathrm{F_a} = \frac{1}{(h_{\mathrm{k}}+h_{\mathrm{a}})}\tau_{\mathrm{gk}} \tag{5}$$

The photograph of the developed jump assist device is shown in Figure 4. The left photograph shows when a user mounted the device. As can be seen in the figure, the ankle and knee joint is assisted with four PARMs with the diameter of 20 mm. The weight of the device is 7.28 kg with both legs including the actuators. The size and specification of the device is summarized in Table 1. The device is designed to generate maximum torque of 90 Nm at the knee joint.

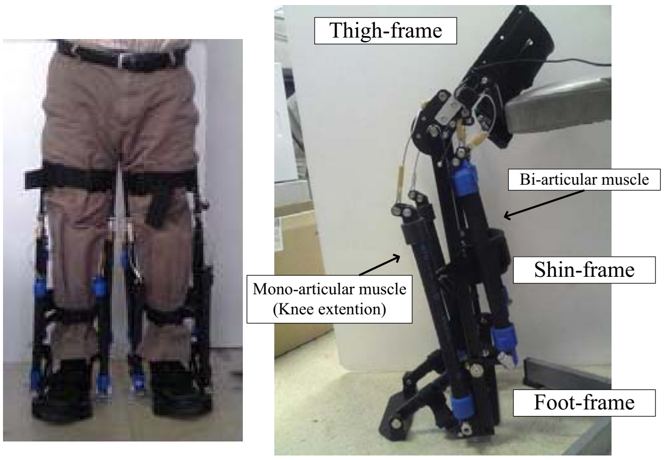

Figure 4 Jump assist device

Table 1 Specification of jump assist suit

Length [mm]	Thigh-frame	200
	Shin-frame	350
	Foot-frame	170
Available angle [deg]	Knee joint	117
	Ankle joint	125
Maximum torque [Nm]	Knee joint	90
Weight [kg]	Both legs	7.28

SIMULATION

The timing to start assist for jumping is an important issue with the developed device. Therefore, we developed a simulation model and investigated the timing.

Generated force by the subject for jumping

The kinematic equation when a subject wearing the assist device but with no assist can be written as

$$(m_{\mathrm{h}} + m_{\mathrm{a}})a = F_{\mathrm{h}} - (m_{\mathrm{h}} + m_{\mathrm{a}})g \tag{6}$$

here, m_{h} and m_{a} are the weight of the subject and the assist device, respectively. a is the acceleration and F_{h} denotes the generated force of the subject.

Using the developed device as shown in Figure4, the experiments of jump with no assist were executed for two subjects to measure the generated force of the subjects F_{h}. A rotary encoder is installed at the knee joint. The acceleration a was calculated by differentiating the position data obtained by the encoder.

An example of experimental results is shown in Figure 5. The upper figure shows the calculated acceleration and the movement of the knee joint. The lower figure shows the calculated force F_{h} from Eq.(6) using the acceleration data. The upward direction is defined as positive value for acceleration. The lateral axis shows the time. We selected the initial time 0s when the acceleration becomes 9.81m/s^2 (1G). It is clear from the upper figure that the subject bends the knee joint to generate the upward acceleration for jump.

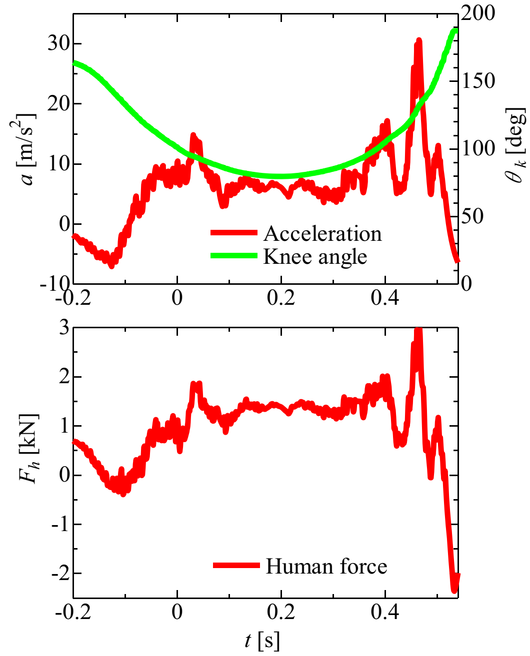

Figure 5 Experimental results of measurement of generated force of the subject for jump

Simulation model

The kinematic equation with the assist device can be given as

$$(m_\mathrm{h}+m_\mathrm{a})a = F_\mathrm{h}+F_\mathrm{a}-(m_\mathrm{h}+m_\mathrm{a})g \quad (7)$$

here F_a is the generated force by the assist device.

The relation between the contraction ratio of the PARM ε and the joint angle θ can be given in the following equation.

$$\mathrm{d}\theta = \frac{L_0}{r}\mathrm{d}\varepsilon \quad (8)$$

Here, L_0 is the initial length of the PARM and r is the radius of the knee joint.

The height from the ground to the center of gravity h as shown in Figure 3 has the following relationship with the knee joint angle.

$$\mathrm{d}h = (h_\mathrm{k}+h_\mathrm{a})\mathrm{d}\theta \quad (9)$$

h_k and h_a are defined as shown in Figure 3.

The following equation can be derived by substituting Eq.(4) and (5) to Eq.(3).

$$(m_\mathrm{h}+m_\mathrm{a})\frac{h_\mathrm{k}+h_\mathrm{a}}{r}L_0\ddot{\varepsilon} = F_\mathrm{h}+F_\mathrm{a}-(m_\mathrm{h}+m_\mathrm{a})g \quad (10)$$

The following conditions are assumed for the simulation.

1. The state change of air in the PARM is assumed to be adiabatic condition.
2. The static characteristics of the servo valve used in the experiment are measured in advance. The dynamics of the valve is fast enough compare with that of the PARM, only the statics of the valve is considered.
3. F_h is assumed to keep the same value as that of no assist even the assist device generated force.

Then, the assist force F_a is calculated from Eq.(1) to (5) and (10). The assisted energy E can be given by integrated the assisted force F_a until the knee joint extended.

$$E = \int F_\mathrm{a}\,\mathrm{d}h \quad (7)$$

The simulations were performed by changing the assist start timing.

Figure 6 shows the simulation results. The lateral axis shows the start timing. Initial time was as same as Figure 5. The longitudinal axis shows the energies calculated by Eq.(7). The simulations were executed with two subjects those weights were 55kg and 80kg.

It is clear from Figure 6 that the most effective assist timing is around 80ms to 125ms after the acceleration becomes 1G.

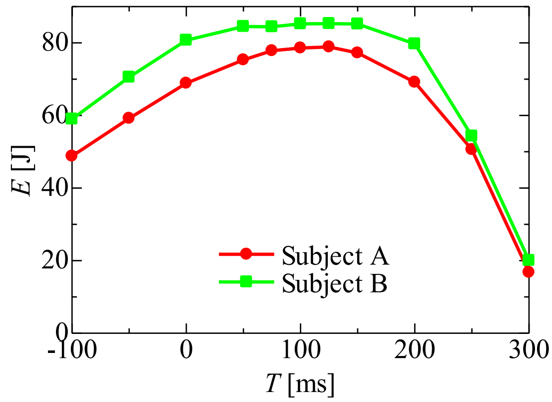

Figure 6 Simulation results (Energy)

Table 2 Weight and height of jump

Subject	A	B
Wight[kg]	80	55
Height of jump without assist[mm]	359	390
Calculated height of jump with assist[mm]	421	484

The calculated jumping height is shown in Table 2 when the energy is totally used for jumping. The results suggest that theoretically the jump height can be increased more than 20% with the developed jump assist device.

JUMP ASSIST EXPERIMENTS

System configuration

The system setup of the assist device is shown in Figure 7. An acceleration sensor installed at the waist of the subject is used for the trigger to start assist. The PARMs for the bi-articular mechanism are controlled at a constant pulling force by the servo valves.

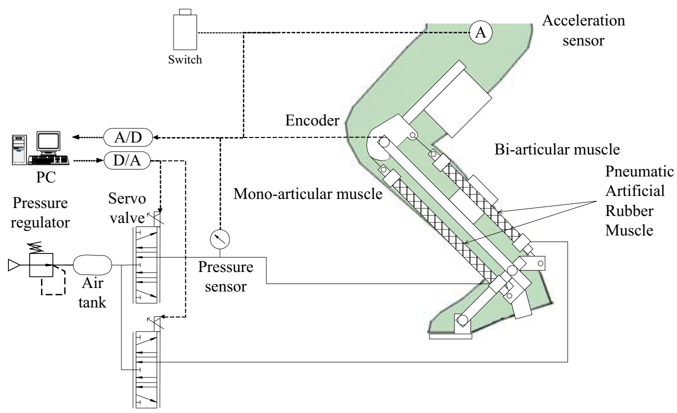

Figure 7 Configuration of the jump assist system

The PARMs to extend the knee joints are controlled with servo valves. The valves were full opened depended on the timing. The supply pressure was set at 600kPa abs. The knee angle is measured with a rotary encoder attached on the joint. The measured data were taken into personal computer through a counter. The height of jump was measured using a 3D position measurement system (POLARIS). Therefore, a passive marker was putted on the wrist of the subjects.

Experimental results

Three subjects were participated in the experiment. Subject A and B are the same as shown in Table 2. The height and weight of subject C is 158cm, 50kg.

At first, the relation between the assist timing and the jump height was investigated. The subjects cross their arms in front of the chest and start jump motion from the standing posture. Therefore, arm motion has no effect for jump.

Figure 8 shows the results with subject A. The lateral axis shows the assist start timing and the longitudinal axis shows the maximum jump height. It is clear from the experimental results that the maximum height can be achieved with the start timing of 75ms to 125ms. The tendency is almost the same as the simulation results shown in Figure 6. Same tendency can be observed with other subjects as well. Therefore, in the following experiments, we selected the timing to start assist as 100ms after the acceleration becomes 1G. The valves are full opened at the time.

Figure 9 shows the photograph during the experiments. The left figure shows when the subject jumped using the assist device. The right figure shows the jumping mounted the device on the legs but without assist. Both figures show when the subject reached at the maximum height. The effectiveness of the jump assist system is clear from Figure 9. The assist system synchronizes well with the subject motion and felt no interference with the device.

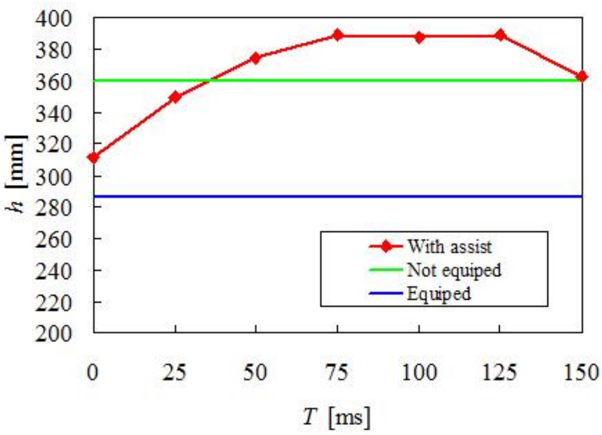

Figure 8 Experimental results of jump assist
(Results of changing the timing to start)

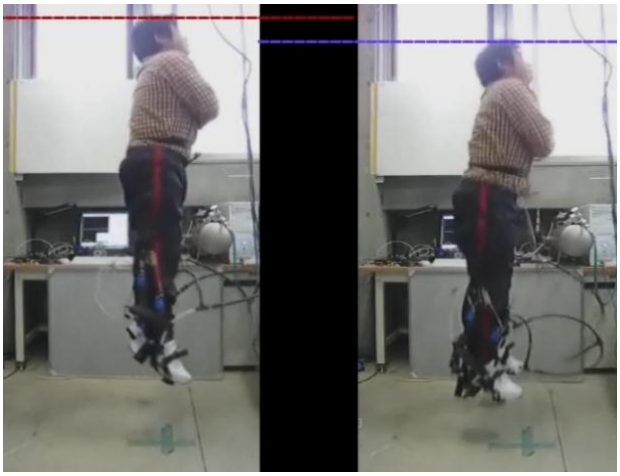

Figure 9 Experimental scenery during jumping

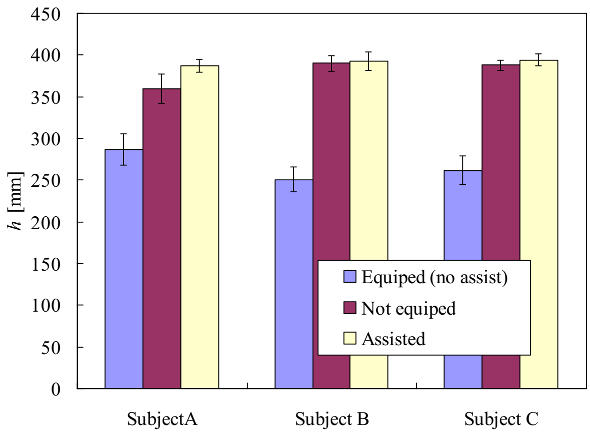

Figure 10 Experimental results of jumping height

Figure 10 shows the experimental results with the subjects. Each subject executed the experiments under three conditions: equipped the assist device but without assist, not equipped the device (free jump), and equipped the device with assist. The subjects jumped five times with the same condition those were shown in the error bars in the figure.

The effectiveness of the device is demonstrated from the experiments. Especially, the difference between with and without using the device can be clearly observed. However, the height slightly increased compared with the condition without mounted the device.

The generated energy from the PARM was calculated using Eq.(1) and the experimental results. The energy is compared with difference energy between with and without assist.

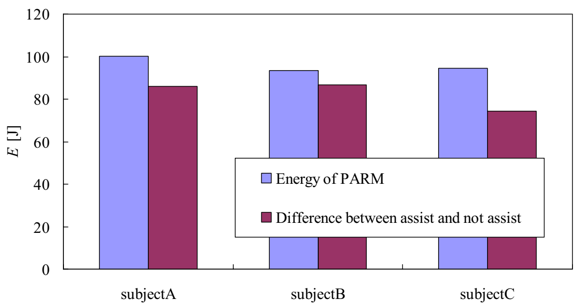

Figure 11 Effective energy used for jump

The results are shown in Figure 11. The left side shows the generated energy with the PARM and the right figure shows the difference between with and without assist. This figure suggests that about 85% of the energy generated by the PARMs was used for jump. The amount is about 85J. The potential energy for example with subject A with 500mm is 392J. Therefore, the generated energy with the device is insufficient. However, the timing of assist became clear with the developed system. The generated energy can be increased by using PARMs with larger diameters which will be our future work.

CONCLUSIONS

In this paper, we developed a jump assist system that can generate instantaneous force using pneumatic artificial rubber muscles (PARMs) since such quick motion is required in the rescue activities.

The device extends the knee joint using PARMs with the diameter of 20mm. Moreover, bi-articular mechanism between the knee and ankle joint is realized using PARMs. Assist timing with the device was detected with an acceleration meter installed in the device. The timing was investigated both theoretically and experimentally.

It became clear that the most effective assist timing with the device is around 80ms to 125ms after the acceleration of the subject becomes 1G. The experiments were performed with three subjects to demonstrate the effectiveness of the device.

REFERENCES

1. Kawamoto H., Sankai Y., Power assist method based on phase sequence driven by interaction between human and robot suit, Robot and Human Interactive Communication, 13th IEEE International Workshop, 2004, pp.491–496.
2. Tsukahara A., Kawanishi R., Hasegawa Y. and Sankai Y., Sit-To-Stand and Stand-To-Sit Transfer Support for Complete Paraplegic Patients with Robot Suit HAL, Advanced Robotics, 2010, Vol. 24, No. 11, p.1615-1638.
3. Yamamoto K., Hyodo K., Ishii M., Matuo T., Development of Power Assisting Suit for Assisting Nurse Labor, JSME international journal. Series C, 2002, Vol.45-3, pp.703–711.
4. Schulte R. A., The Characteristics of the McKibben Artificial Muscle, In The Application of External Power in Prosthetics and Orthetics, publ.874, Nas-RS, 1962, pp.94–115.
5. Chou C. P. and Hannaford B., Statics and Dynamics Characteristics of McKinbben Pneumatic Artificial Muscles, IEEE International Conference on Robotics and Automation, 1994, pp.281–286.
6. Caldwell D.G., Gustavo A. Medrano-Cerda, Goodwin M., Control of Pneumatic Muscle Actuators, Control Systems Magazine, IEEE, 1995, Vol.15–1, pp.40–48, 1995.
7. Klute G.K., Hannaford B., Fatigue Characteristics of McKinbben artificial muscle actuators, IEEE/RSJ 1998 International Conference on Intelligent Robots and Systems (IROS1998), 1998, Vol.3, pp.1776–1781.
8. Aragane M., Noritsugu T., Takaiwa M., Sasaki D., Naomoto S., Development of Sheet-like Curved Type Pneumatic Rubber Muscle and Application to Elbow Power Assist Wear, "Journal of the Robotics Society of Japan, 2007, Vol.26-6, pp.206-213.
9. Sasaki D., Noritugu T., Takizawa M., Yamamoto H., Wearable Power Assist Device for Hand Grasping Using Pneumatic Artificial Rubber Muscle, IEEE International Workshop on Robot and Human Interactive Communication, 2004, pp.655–660.
10. Kobayashi H., Suzuki H., Nozaki H., Tsuji T., Development of Power Assist System for Manual Worker by Muscle Suit, IEEE International Conference on Robot and Human Interactive Communication, 2007, pp.332–337.
11. Sasaki T. and Kawashima K., Development of Remote Control System of Construction Machinery for Rescue Activities with Pneumatic Robot, Advance Robotics, 2006, Vol.20, No.2, pp.213-232.
12. Kumamoto M., Oshima T., and Yamamoto T., Control properties Induced by the Exsitence of Antagonistic Pairs of Bi-articular Muscles-Mechanical Engineerging Model Analyses, Human Movement Science, 1994, Vol.13, pp.611-634.

Proceedings of the 8th JFPS International
Symposium on Fluid Power, OKINAWA 2011
Oct. 25-28, 2011

2D3-4

THE DECOUPLING CONTROL FOR PMA-DRIVEN SERIAL MECHANISM

Tao WANG*, Hao LIU*, Wei FAN*, Tong ZHAO*

*School of Automation, Beijing Institute of Technology, China
(E-mail: wangtaobit@bit.edu.cn)

ABSTRACT

The serial mechanism is driven by pneumatic muscle actuators (PMA) and used the tendon transmission structure. Between the various joints, the torque coupling and the location coupling seriously affect the control performance. By analyzing the location equation of tendons, a matrix which can describe the coupling is obtained. Combined with the model of PMA, the dynamic equation of the coupled system is derived. For features of the tendon drive coupling and PMA, the computed torque algorithm is improved. In order to overcome the hysteresis of PMA, the control signal is compensated ahead. Finally the decoupling control algorithm which adapted to the PMA drive and the tendon drive is proposed. Experiment proved that, compared to the PID control, improved computed-torque control can decreases the coupling, accelerates the response speed and decreases the steady-state error.

KEY WORDS

Pneumatic muscle actuator; Tendon drive; Coupling; Computed-torque control

INTRODUCTION

The load capacity of a robot end-effector is closely related with its own inertia and the drive output power. In robot design, due to the restriction of dexterity and other factors, the size of the end-effector is usually not very large. Therefore it is difficult to integrate high-power drive installed in the joints to control joint movement directly.

The usual solution is that to install the actuators in the relative open space, and make use of tendon transmission to drive power to the appropriate joints. This design provides a powerful drive and effectively reduces the inertia of the end-effector. In order to be obtained greater output power of the end of finger, tendons are used as transmission mode, such as, Utah/MIT hand[1], DIST hand[2] and UB hand[3]. Tendon transmission is usually composed of tendons and pulleys. Since tendons can only output stretching force, a rotary joint at least need two symmetric tendon pulled to form a rotary structure. Tendon has many advantages, such as light weight, good flexibility. But tendons braced by joints will have torque effects on these joints. Therefore, a control torque of a joint in the system will become a disturbance torque on another joint. In trajectory control, this coupling phenomenon is difficult to be eliminated by a simple feedback control method.

In this paper, the end-effector of a kind of 2R series rod driven by pneumatic muscle (shown as Figure 1) is studied as the object. Theory of the coupled tendon drive system is analyzed, and a decoupling control for the tendon coupling system is proposed.

Figure 1 PMA-driven serial mechanism

COUPLING MATRIX OF TENDON DRIVE

A series rod structure is composed of a group parallel revolute joints and connecting rods, shown in Figure 2. Those n+1 rods (0 is the base) form n rotational joints, which are driven by tendons. Although each tendon is connected with only one bar, on the tendon transmission path, joints which provide tendons bracing will be bear a corresponding torque.If there is not suitable tendon transmission path, the coupling is difficult to be eliminated. In the structure of tendon transmission series rods, the relationship between tendon displacements and joint angles and the relationship between tendon tensions and joint torques can be expressed by a coupling matrix[4].
To facilitate the discussion, some assumptions are given as follows: (a) Tendons are lightweight, not elastic and not stretch; (b) The contact with tendon and joint is tangent; (c) There is only one rotation radius on each joint; (d) No friction.

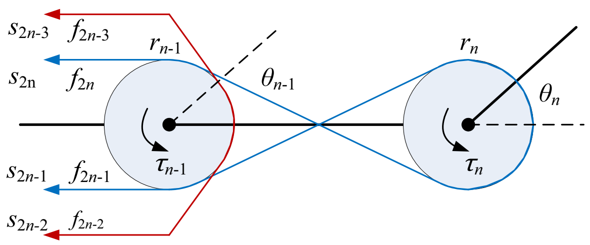

Figure 2 Schematic diagram of planar tendon drive

The working status of each tendon is represented by the displacement variable s_i,

$$s_i\left(\theta\right)=s_{0i}\pm r_1\theta_1\cdots\pm r_j\theta_j\cdots\pm r_m\theta_m\,, \tag{1}$$

where, θ_j, r_j is respectively for the joint angle and the pulley radius of the j joint; s_{0i} is the initial displacement of tendons when the joint angle vector is zero; the plus or minus sign in Eq. (1) depends on the displacement of tendon.
Based on the principle of conservation of energy, the tendon transmission coupling matrix can be derived,

$$\boldsymbol{\tau}^{\mathrm{T}}\boldsymbol{\theta}=\boldsymbol{f}^{\mathrm{T}}\boldsymbol{s}\,. \tag{2}$$

About time t, we differentiates both sides of the Eq. (2),

$$\boldsymbol{\tau}^{\mathrm{T}}\dot{\boldsymbol{\theta}}=\boldsymbol{f}^{\mathrm{T}}\frac{\partial\boldsymbol{s}}{\partial\boldsymbol{\theta}}\dot{\boldsymbol{\theta}}\,. \tag{3}$$

Definition of the matrix $\boldsymbol{P}$, so,

$$\boldsymbol{P}^{\mathrm{T}}=\frac{\partial\boldsymbol{s}}{\partial\boldsymbol{\theta}}\,. \tag{4}$$

Taking above equations, it is easy to find the description of the dynamic torque coupling and the static position coupling between each joint, as shown in Eq. (5),

$$\begin{cases}\boldsymbol{\tau}=\boldsymbol{P}\boldsymbol{f}\\ \Delta\boldsymbol{s}=\boldsymbol{P}^{\mathrm{T}}\Delta\boldsymbol{\theta}\end{cases} \tag{5}$$

where, $\boldsymbol{\tau}$ is the torque vector of joints; $\boldsymbol{\theta}$ is the angle vector of joints; $\boldsymbol{s}$ is displacement vector of tendons; $\boldsymbol{f}$ is tension vector of tendons.
In the tendon transmission coupling matrix $\boldsymbol{P}_{n\times m}$, n is the joint label, m is the tendon label, the sign '±'indicates the positive or negative sign of torque on the i joint implemented by the j tendon, and $\boldsymbol{P}$ is expressed as specific,

$$\boldsymbol{P}=\begin{bmatrix}\pm r_1 & \cdots & \pm r_1\\ \vdots & \ddots & \vdots\\ 0 & \cdots & \pm r_n\end{bmatrix}.$$

SYSTEM MODEL

1. Control System
Figure 1 shows the object is driven by the 4 PMAs, transmitted by tendons. PMAs are control by the SMC ITV0050 proportional pressure valve. Hall sensors from SENTRON company are used for the measurement of joint angles. The structure of the control system diagram is shown in Figure 3.

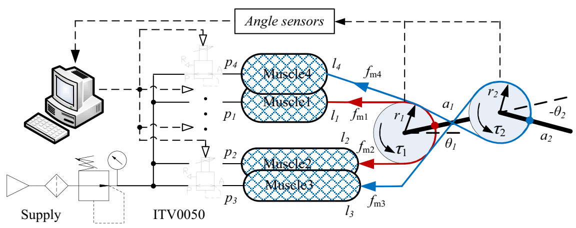

Figure 3 Structure of the control system

2. Model of Pneumatic Muscle

Because of the bound role of the outer braid, the Mckibben PMA transforms the radial expansion force of compressed air into the axial contraction force and outputs the displacement. Based on the energy conservation law and the virtual work principle of the pneumatic muscle, Ching-Ping Chou and Black Hannaford derives the static model of pneumatic muscle[5]. On this basis, considering the uncertainties in the structural parameters of pneumatic muscles[6], the static model is gained the correction and compensation.
In summary, ignoring the elastic and internal friction of rubber tube, the interaction relationships among the output force f_{m}, pressure p, the length l of pneumatic muscle is described by Eq. (6).

$$f_{mi} = k_i p_i \tag{6}$$

where, the equivalent cross-sectional area coefficient is defined as k_i,

$$k_i = \eta \frac{3l_i^2 - b^2}{4\pi N^2}.$$

In addition, the serial number of pneumatic muscle is $i \in \boldsymbol{N}$; the length of braid fiber is b; the number of filament-wound ring is N; the compensation factor of the structural parameters is η.

For the inelastic tendon, the tendon displacement is equal to the amount of the muscle's contraction. Therefore, while the initial length vector $\boldsymbol{l}_0$ is known, the length of pneumatic muscle can be described by Eq. (7).

$$\boldsymbol{l}(\boldsymbol{\theta}) = \boldsymbol{l}_0 + \boldsymbol{P}^{\mathrm{T}}\boldsymbol{\theta} \tag{7}$$

3. System Dynamics Model

Considering the actual object (shown in Figure 3) is the structure of 2R series bars in the gravity plane. In the case of ignoring friction, the open-chain robot Lagrangian dynamic equation[7] is established, as shown in Eq. (8).

$$\boldsymbol{H}(\boldsymbol{\theta})\ddot{\boldsymbol{\theta}} + \boldsymbol{C}(\boldsymbol{\theta},\dot{\boldsymbol{\theta}})\dot{\boldsymbol{\theta}} + \boldsymbol{G}(\boldsymbol{\theta}) = \boldsymbol{\tau} \tag{8}$$

where, the inertia matrix is $\boldsymbol{H}(\boldsymbol{\theta})$; the Coriolis force and centrifugal force matrix is $\boldsymbol{C}(\boldsymbol{\theta},\boldsymbol{\theta}')$; the gravitational torque is expressed by $\boldsymbol{G}(\boldsymbol{\theta})$; all elements of these coefficient matrixes are as follows:

$$h_{11} = I_{zz1} + I_{zz2} + m_1 r_{C1}^2 + m_2\left(a_1^2 + r_{c2}^2\right) + m_2 a_1 a_2 \cos\theta_2$$

$$h_{12} = I_{zz2} + m_2 r_{c2}^2 + 0.5 m_2 a_1 a_2 \cos\theta_2$$

$$h_{21} = I_{zz2} + m_2 r_{c2}^2 + 0.5 m_2 a_1 a_2 \cos\theta_2$$

$$h_{22} = I_{zz2} + m_2 r_{c2}^2$$

$$c_{11} = -0.5 m_2 a_1 a_2 \dot{\theta}_2 \sin\theta_2$$

$$c_{12} = -0.5 m_2 a_1 a_2 \left(\dot{\theta}_1 + \dot{\theta}_2\right)\sin\theta_2$$

$$c_{21} = 0.5 m_2 a_1 a_2 \dot{\theta}_1 \sin\theta_2$$

$$c_{22} = 0$$

$$g_1 = \left(r_{c2} + a_2\right) m_2 g \cos\left(\theta_1 + \theta_2\right) + a_1 m_2 g \cos\theta_1 + \left(r_{c1} + a_1\right) m_1 g \cos\theta_1$$

$$g_2 = \left(r_{c2} + a_2\right) m_2 g \cos\left(\theta_1 + \theta_2\right)$$

where, the spindle rotational inertia of the rod 1 and the rod 2 are respectively I_{zz1} and I_{zz2}; the centroid vector of the rod 1 and the rod 2 are respectively r_{c1}=-0.5a_1 and r_{c2}=0.5a_2.

Integrating Eq. (5) to Eq. (8), a second order differential vector equation can be obtained which describes the 2R series rod transmitted by tendons and driven by pneumatic muscles, as the Eq. (9) below.

$$\boldsymbol{H}(\boldsymbol{\theta})\ddot{\boldsymbol{\theta}} + \boldsymbol{C}(\boldsymbol{\theta},\dot{\boldsymbol{\theta}})\dot{\boldsymbol{\theta}} + \boldsymbol{G}(\boldsymbol{\theta}) = \boldsymbol{PK}(\boldsymbol{\theta})\boldsymbol{p} \tag{9}$$

where, the coupling matrix $\boldsymbol{P}$ represented tendon winding mode and the equivalent cross-sectional area coefficient matrix $\boldsymbol{K}$ of pneumatic muscle respectively are:

$$\boldsymbol{P} = \begin{bmatrix} r_1 & -r_1 & -r_1 & r_1 \\ 0 & 0 & r_2 & -r_2 \end{bmatrix}, \quad \boldsymbol{K} = \begin{bmatrix} k_1 & \cdots & 0 \\ \vdots & \ddots & \vdots \\ 0 & \cdots & k_4 \end{bmatrix}$$

DECOUPLING CONTROL

1. Coupling on joints

To show the effect of the coupling on system, a set of experiments is observed: Control the joints 1, but the joint 2 does not (shown in Figure 4a); Control the joint 2, but the joint 1 does not (shown in Figure 4b). According to Eq. (5), by analyzing the coupling matrix $\boldsymbol{P}$ of the actual controlled object shown in Figure 3, it is not difficult to find out : Supposing the length of muscle 3 and 4 are unchanged and muscle 1 and 2 are under control, if the joint 1 rotates θ degree, then the joint 2 will be coupling to $(r_1/r_2)\theta$ degree; Supposing muscle 3 and 4 are under control, if the joint 2 is exerted torque τ_2, then the joint 1 will be exerted coupled torque -τ_2. Results show that the coupling of the PMA-driven and tendon-transmitted series rods structure contains three parts, which are the position coupling, the torque coupling and dynamic coupling.

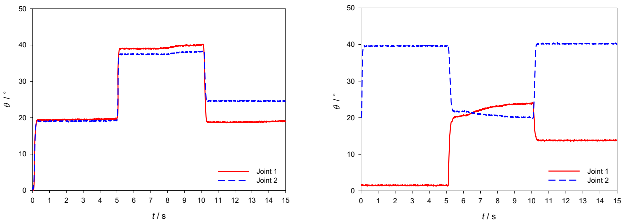

a. Position coupling for joint 1 to joint 2

b. Torque coupling for joint 2 to joint 1

Figure 4 Coupling of joints

2. The improved computed torque method based on the PMA drive and tendon transmission

The computed torque control is a typical control scheme considered the robot dynamics model. It is a "feed-forward + feedback" control method, using the robot dynamic equation to achieve the nonlinear compensation and the dynamic decoupling [8]. The coupled relation between the tendon transmission is integrated into the CTC algorithm, the control pressure of PMAs is solved and a dynamic decoupling algorithm is proposed, which is appropriate for the PMA-driven and tendon-transmitted series rods. Because of the interactions of torque between joints, according to Eq. (9), the coupling of joint torque is compensated. "p-f_{m}" feature of PMA is closely related to its length l. According to the expected angle $\boldsymbol{\theta}_{\mathbf{d}}$ of joint and making use of Eq. (7), the objective length of PMAs is calculated in advance. That is, $\boldsymbol{K}(\boldsymbol{\theta}_{\mathbf{d}})$ as a coefficient matrix of the equivalent cross-sectional area of PMA, is used for the compensation of the position coupling.

The torque control is introduced:

$$\boldsymbol{\tau} = \boldsymbol{PK}(\boldsymbol{\theta}_{\mathrm{d}})\boldsymbol{p} = \boldsymbol{H}(\boldsymbol{\theta})\boldsymbol{u} + \boldsymbol{C}(\boldsymbol{\theta},\dot{\boldsymbol{\theta}})\dot{\boldsymbol{\theta}} + \boldsymbol{G}(\boldsymbol{\theta}) \tag{10}$$

By adopting simultaneous Eq. (8) and Eq. (10), the nonlinear term of the controlled object can be eliminated. The equation of the object is changed into,

$$\boldsymbol{H}(\boldsymbol{\theta})\ddot{\boldsymbol{\theta}} = \boldsymbol{H}(\boldsymbol{\theta})\boldsymbol{u} \tag{11}$$

The PD control with a bias is introduced,

$$u = \ddot{\theta}_{d} + H^{-1}(\theta) PK(\theta_{d}) Q(K_{p}e + K_{d}\dot{e}) \tag{12}$$

where, K_p and K_d are as diagonal matrix; Q is the control pressure distribution matrix introduced to reduce the amount of the dimension.

$$Q = \begin{bmatrix} 1 & 0 \\ -1 & 0 \\ 0 & 1 \\ 0 & -1 \end{bmatrix}$$

Therefore, the equation of the closed-loop system is as follow:

$$\ddot{e} + H^{-1}(\theta) PK(\theta_{d}) Q(K_{p}e + K_{d}\dot{e}) = 0 \tag{13}$$

It is not difficult to prove that $H^{1}(\theta)PK(\theta_d)Q$ is positive definite. As long as K_p and K_d select appropriate, this algorithm can achieve global stability of the trajectory tracking.

Eq (12) substituted into (10), the control law expression will be get, as shown in Eq. (14). Δp_i is the pressure increment signal.

$$p = p_0 + Q(\Delta p_1 + \Delta p_2) \tag{14}$$

where, Δp_2 is the feed-forward component, which is the control pressure needed by the system movement along the expected trajectory; Δp_1 is the feed-back component ,which is the compensation pressure for eliminating trajectory error. Their specific expressions are as follow:

$$e_1 = \theta_d - \theta, \quad e_2 = \dot{e}_1$$

$$\Delta p_1 = K_p e_1 + K_d e_2$$

$$\Delta p_2 = Q^{+} K(\theta_d)^{+} P^{+}\left[H(\theta)\ddot{\theta}_d + C(\theta,\dot{\theta})\dot{\theta} + G(\theta)\right]$$

where, $P^{+}=P^{T}(PP^{T})^{-1}$ is the pseudo-inverse of the coupling matrix P.

Based on Eq. (14), with the integration introduced into the algorithm, the improved computed torque control algorithm based on PMA-driven and tendon -transmitted (MCTC) is obtained, which the block diagram shown in Figure 5.

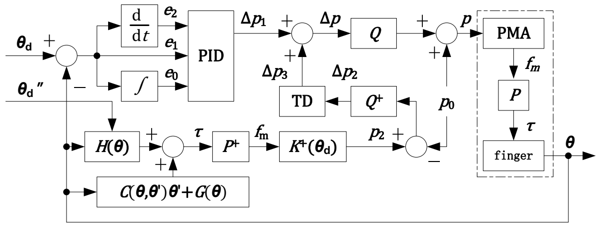

Figure 5 Control algorithm block diagram

TEST RESULTS AND ANALYSIS

In the actual control, it always has the torque coupling and the position coupling between the two joints of controlled object in any time. Moreover, the two coupling factors influence each other, as shown in Figure 3. To verify the validity of the MCTC algorithm, the two groups of contrast test reference to Figure 4 are given: The joint 1 is needed to continuously complete three step responses in 20º, 20º and -40º, simultaneously the joint 2 is expected in the 0º position, to test the torque decoupling capability; The joint 2 is needed to continuously complete three step responses in 20º, 20º and -40º, simultaneously the joint 1 is expected in the 0º position, to test the position decoupling capability. Various measured parameters of the system are list in Table 1.

Table 1 Parameters of the system

parameters	value	parameters	value
η	75%	I_{zz1}	9.866 kgmm^2
N	2.7	I_{zz2}	3.171 kgmm^2
b	188 mm	m_1	0.01170 kg
$l_{01},l_{02},l_{03},l_{04}$	160 mm	m_2	0.00433 kg
r_1,r_2	6 mm	a_1,a_2	45 mm

The performance of PID control on the two joints is shown in Figure 6. The PID algorithm is a feedback control based on the error, which will do not work in advance before disturbance arrival.

Therefore, whether in the experiment of torque decoupling (Figure 6a) or the position decoupling (Figure 6b), when the expected rotational angle of a joint has a greater step, the other joint will be pulled to leave the original equilibrium position. The coupling has been weakened, but still can not be ignored. It be seen that due to the coupling of system the self-regulation effect of PID algorithm declines, to the transition process extends and steady-state errors of the two joints are respectively 0.85º and 0.94º. Controller parameters are as follows:

$$K_p = \begin{bmatrix} 60 & 0 \\ 0 & 50 \end{bmatrix}, \quad K_i = \begin{bmatrix} 1.5 & 0 \\ 0 & 0.5 \end{bmatrix}, \quad K_d = \begin{bmatrix} 10 & 0 \\ 0 & 5 \end{bmatrix}$$

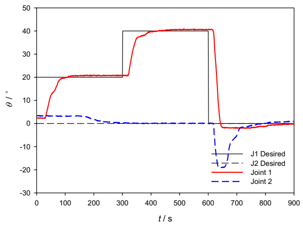

a. Step response of joint 1

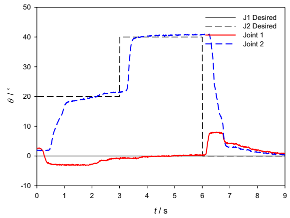

b. Step response of joint 2

Figure 6 PID control for the movement of a separate joint

Control results of MCTC on two joints are shown in Figure 7. Experiments of the torque decoupling and the position decoupling are respectively shown in Figure 7a and Figure 7b. It is clear that the coupling on the system controlled by MCTC is less unconspicuous than it on the system controlled by PID. The system on controlled by MCTC significantly has faster response and steady-state errors of the two joints decrease to 0.78º and 0.63º respectively. Their control incremental pressure curves are respectively shown in Figure 7c and Figure 7d. Parameters of PID are the same before.

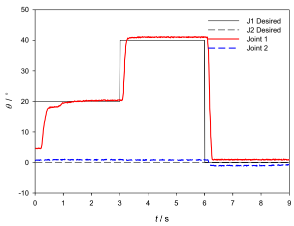

a. Step response of joint 1

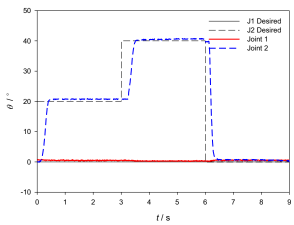

b. Step response of joint 2

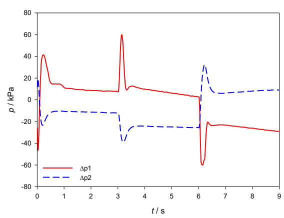

c. Control signal Δ***p***

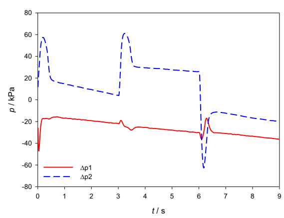

d. Control signal Δ***p***

Figure 7 MCTC control for the movement of a separate joint

CONCLUSION

The test shows that on the system of the PMA-driven and tendon-transmitted series rods, the coupling of joints is very serious in the control process. Only relying on a common feedback control, a satisfactory result is hard to obtain. The MCTC algorithm relying on the dynamic coupling model of the system, thereby a feed-forward compensation is made for the control variable, effectively weakening the coupling effect. However, the effect of MCTC algorithm relies on the accuracy of the system model. Due to the inaccurate measurement of the structural parameters or a larger friction, the model be not accurate, leading to the algorithm can not completely eliminate the coupling. In future work, a model disturbance observer is considered for the feedback compensating to further improve the system robustness.

REFERENCES

1. Jacobsen S, Iversen E, Knutti D, etc. Design of the Utah/M.I.T. Dextrous Hand [C]. Proceedings of the 1986 IEEE International Conference on Robotics and Automation. 1986, (3):1520-1532.
2. Andrea Caffaz, Giorgio Cannata. The Design and Development of the DIST-Hand Dextrous Gripper [C]. Proceedings of the 1998 IEEE International Conference on Robotics & Automation. 1998, (3):2075-2080.
3. Lotti F, Vassura G. A novel approach to mechanical design of articulated fingers for robotic hands [C]. Proceedings of the 2002 IEEE/RSJ International Conference on Intelligent Robots and Systems. 2002, (2):1687-1692.
4. Richard M, Zexiang Li, S Shankar Sastry. A mathematical Introduction to Robotic Manipulation [M]. USA Florida: CRC Press, 1994.
5. Ching-Ping Chou, Black Hannaford. Measurent and Modeling of McKibben Pneumatic Artifical Muscles [J]. IEEE Transactions on Robotics and Automation, 1996,12(1): 90-102.
6. B. Tondu, P. Lopez. Modeling and control of Mckibben artificial muscle robot actuators [J]. IEEE Control Systems Magazine, 2000, 20(2): 15-38.
7. Huo Wei. Robot Dynamics and Control [M]. Beijing: Higher Education Press, 2005.
8. Liu Deman, Liu Zangfu. Robot Adaptive Control——Computed Torque Method [J]. Robot, 1989, 3(6): 1-5.
9. Han Jing-qing. Auto-Disturbances Rejection Control for Time-Delay Systems [J]. Control Engineering of China, 2008, 15(9): 7-10.

Proceedings of the 8th JFPS International
Symposium on Fluid Power, OKINAWA 2011
Oct. 25-28, 2011

2D4-1

ANALYSIS OF EFFECTS OF REMOTE CONTROL ON USABILITY OF HYDRAULIC MOBILE MACHINES

Jarno UUSISALO and Kalevi HUHTALA

Department of Intelligent Hydraulics and Automation
Tampere University of Technology
P.O.Box 589, FI-33101 Tampere, Finland
(E-mail: jarno.uusisalo@tut.fi)

ABSTRACT

Remote control is often considered as a means of utilization when operating hydraulic mobile machines in hazardous environments. However, in some cases remote control may also improve the general usability of the machine, which is a good reason for using remote control also in normal (safe) work tasks. In this paper, the effects of remote control on the usability of a hydraulic mobile machine with an excavation function are studied by means of three experiments relating to the working efficiency and working accuracy. In the experiments, independent subjects executed work tasks with different user interfaces. Next, the user interfaces are compared. Both objective and subjective indicators to measure the effects are used. The results are evaluated through use of statistical analysis. Finally, the significance and reliability of the results are discussed. The results show that short-range remote control may improve the usability of the hydraulic excavator significantly in some work tasks.

KEY WORDS

Remote control, Usability, Experiments

NOMENCLATURE

md	:	Median	[cm], [s]
p	:	p-value	[-]
Q_1	:	First quartile	[cm], [s]
Q_3	:	Third quartile	[cm], [s]
$\bar{x}$	:	Arithmetical mean	[s], [-]
σ	:	Standard deviation	[s], [-]

INTRODUCTION

The use of electrically actuated hydraulic components in mobile applications has been limited for a long period. Now, with developments in technology and changes in needs, an electrical interface in mobile machines is becoming more common. The change enables the implementation of intelligent operations in machines, but also the utilization of old inventions in new applications, remote control among others.

The implementation of remote control of the machine will be a relatively simple and cost-effective task when an electrical interface in the machine already exists. Thus, remote control can be utilized as an alternative user interface for the machine if it improves the usability in some work tasks, due to improved visibility for instance. Previously, remote control has been utilized mainly in special applications wherein there has been a specific need for it, and in those cases remote control has been typically the only user interface for the machine or the actuator. Now, a compelling reason, such as a hazardous worksite, is not the only ground to utilize remote control anymore.

If remote control can be implemented cost-effectively so that it is an additional way to control the machine and it offers benefits in certain cases, it will be an integrated part of mobile machines. Currently, short-range remote control is widely used in commercial solutions already. However, only a few studies of the effects of remote control on the usability, working efficiency, or working accuracy have been carried out, for instance [1, 2]. In these studies the operating position has usually been fixed, that is, the operator cannot select the most suitable position, and so one of the biggest advantages of remote control, a better view, may be lost. Most existing research, for example [3, 4, 5], is related to teleoperation, level of tele-presence especially. Also, studies on the effects of force feedback in remote control applications are nonexistent.

In this study, the effects of remote control on the usability of a hydraulic mobile machine with an excavation function are studied by means of three experiments relating to the working efficiency and working accuracy. In the experiments, independent subjects executed work tasks with different user interfaces. Both objective and subjective indicators to measure the effects are used. The results are evaluated through use of statistical analysis. Additionally, the significance and reliability of the results are discussed.

RESEARCH PLATFORM

Prototypes of a remotely controlled hydraulic mobile machine with an excavator attachment and a hand-held remote control are used as a test platform in this study (see Figure 1). Both prototypes are developed at the Department of Intelligent Hydraulics and Automation (IHA) at Tampere University of Technology.

Figure 1 Mobile machine controlled remotely

Remotely Controlled Mobile Machine with Excavator Attachment

A prototype of a remotely controlled mobile machine with an excavator attachment is based on the commercial machine Avant 320+ manufactured by Avant Tecno Oy [6]. The frame of the machine is original, but the hydraulics, electronics, and control system were designed and built at IHA. The research platform, including hydraulics and control system modifications, is introduced in more details in [7].

Hand-held Remote Control

A hand-held remote control was designed and implemented to study the effects of remote control on the usability. A custom-made prototype was implemented since the existing commercial solutions do not enable the research of all issues that are considered in this study, e.g. the effects of force feedback. A casing of a game controller was exploited since the design process of mechanics was not relevant in this study. The electronics and software instead are totally re-designed. Also, the error detection and handling procedures of the wireless data transmission are custom-made. The wireless connection is implemented by means of commercial radio modems. The remote control is illustrated in Figure 2.

Figure 2 Hand-held remote control utilized in experiments

The remote control includes a vibro-tactile haptic feedback (VTHF) feature, which is a novel approach to provide cost-effectively an estimation of the load level of the machine for the operator. The system informs the operator when the load level of the machine increases by vibrating the remote control. The measurement of the load level is based on the LS (Load-Sensing) pressure of the machine. The idea of the system is not to provide an accurate proportional feedback but to provide an additional feedback information in cases where the force feedback is really useful, that is, when the force capacity of the machine approaches the limit. The remote control and VTHF feature are introduced in more details in [8].

EXPERIMENTS

Experimental Arrangements

The effects of remote control on the usability were studied by means of three experiments. The aim was to study if the usability of the machine can be improved by utilizing the remote control as a user interface. The most important factors related to the usability, that is, the working efficiency (the time taken on the task), working accuracy (steady-state error), and operators' experiences (inquired by means of questionnaires), were considered. In the experiments, a group of independent subjects carried out the same work task with different user interfaces. Then, the results were compared by means of a statistical analysis and the differences in the results caused by utilized user interfaces were considered. Statistical significances (p-values) are given for the results. The questionnaires of all experiments presented in this paper as well as operators' feedback for individual statements are presented in [7].

The work tasks were chosen so that they correspond with real life applications that are typical for excavators as well as possible. All subjects were independent and non-professional. The experiments were carried out using non-professional operators only because the background of professionals (familiar with the traditional onboard user interface) would have decreased the objectivity of the comparison. With professional operators, a long introductory period would have been needed, and in this case it was not feasible. Every subject executed the task with every user interface. The order of implementation was changed in order to compensate the effect of learning. The user interfaces and experimental arrangements are introduced in more details in [7, 9, 10].

Studied User Interfaces

In this paper, three different user interfaces were studied. The main concern was in the comparison between the cab (onboard) interface, which can be considered to be the traditional user interface for the kind of machines used in the experiments, and the remote control interface. Additionally, mechanical and robust hand levers of the control valve (called *direct manual control*) were used in the first experiment. In the experiment concerning excavation with obstructed soil, remote control with the vibro-tactile haptic feedback feature was also examined in addition to the cab interface and remote control without any force feedback. The aim was to study how lack of force feedback information affects the usability. Studied user interfaces are introduced in more details in [7].

Experiment 1: Excavation with Unobstructed Soil

The aim of the first experiment was to compare remote control to other user interfaces, the cab interface and direct manual control, in a conventional and simple work task [9]. Sakaida et al. interviewed a skilful excavator operator in [11]. According to the interview, the most frequent work executed with an excavator is digging work. In the first experiment the task was to dig a trench in a specific location, which is a very typical task. The soil to be operated on was homogenous, including no obstacles, and thus it was easy to be processed. The task was designed so that operators had to transfer the machine during the task.

Effects on the working efficiency were considered by measuring the time taken on the task. The execution time was divided in the excavation time and transfer time. The medians and quartiles of execution times are shown in Table 1.

Table 1 Elapsed times in Experiment 1

Measured variable		Cab	Direct manual control	Remote control
Excavation time [s] (p = 0.044)	Q_3	454	437	364
	Md	**368**	**359**	**315**
	Q_1	301	305	270
Transfer time [s] (p < 0.001)	Q_3	82	109	73
	Md	**62**	**89**	**51**
	Q_1	55	71	45
Total time [s] (p < 0.001)	Q_3	533	526	429
	Md	**442**	**442**	**364**
	Q_1	370	398	327

As can be seen in Table 1, utilization of the remote control decreased the time taken in the task and so improved the working efficiency compared to the cab interface. The improved working efficiency is due to the improved visibility of the work task, which can be seen in Table 2 where operators' experiences of use are shown. The differences between the cab interface and direct manual control were insignificant in this case.

The dispersion of the total execution times between different subjects while controlling the machine with the cab interface and the remote control is shown in Figure 3. Each line in Figure 3 represents the performance of an individual subject with the cab interface and remote control; time elapsed on the y-axis and user interfaces on the x-axis. In Figure 3, cases in which the cab user interface was faster than the remote control are plotted with dashed lines, and cases where the remote control improved the working efficiency are plotted with solid lines. The lines show the trend of the change in working efficiency between the user interfaces; the majority of the lines are solid lines, that is, in most cases remote control improved the working efficiency.

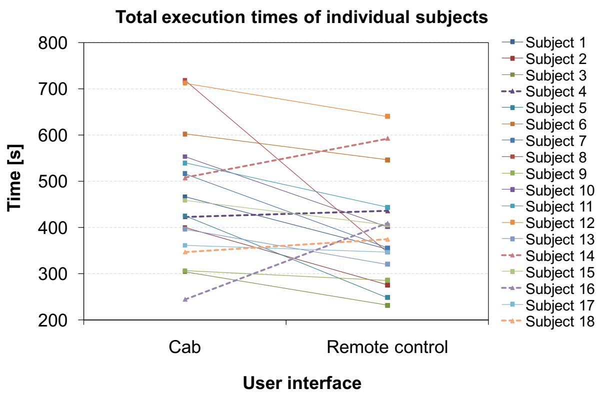

Figure 3 Dispersion of total execution times in Experiment 1

Experiences of use were obtained by means of the questionnaire. The questionnaire was divided into five subject matters, which were considered essential. Each subject matter included several statements. Finally, means were calculated. The scale is from one to five. The bigger the number is, the more positive the feedback was. Also standard deviations are shown in Table 2.

Table 2 Experiences of use in Experiment 1

Subject matter		Cab	Direct manual control	Remote control
Visibility of work task	$\bar{x}$	**2.57**	**4.37**	**4.66**
($p < 0.001$)	σ	0.69	1.08	0.62
Controllability of excavator	$\bar{x}$	**3.57**	**3.56**	**3.57**
($p = 0.845$)	σ	1.22	1.09	1.05
Transfer of machine	$\bar{x}$	**3.99**	**3.58**	**4.04**
($p = 0.312$)	σ	1.20	1.10	1.23
Comfort of working	$\bar{x}$	**4.04**	**3.04**	**4.33**
($p < 0.001$)	σ	1.26	0.92	0.82
Easiness of learning	$\bar{x}$	**3.43**	**3.33**	**3.29**
($p = 0.895$)	σ	1.27	1.27	1.17
Total	$\bar{x}$	**3.52**	**3.58**	**3.98**
($p = 0.011$)	σ	1.23	1.22	1.12

In Table 2, the most significant differences can be noticed in *visibility of the work task* (between the cab interface and remote control), otherwise the differences are relatively small. The results show that the *controllability* or *comfort of working* does not decrease while using the cost-effective remote control. Thus, the remote control is suited for controlling the mobile machine.

Experiment 2: Excavation with Obstructed Soil

In the second experiment the goal was to study the effects of force feedback [10]. The work task was to dig a trench in a specific location as in the first experiment, but in this case the soil to be processed included a hidden obstacle (stone). The obstacle was too big to be moved by the excavator. The task was to bypass the obstacle and continue digging (see Figure 4). The trench was shorter than in the first experiment and the initial position of the machine in the beginning of the task was chosen so that transfer of the machine was not required during the task.

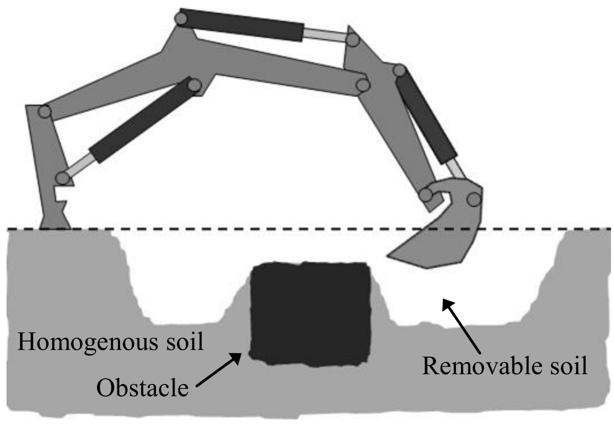

Figure 4 Task in Experiment 2

The same task was repeated in three different ways: with the cab interface, remote control interface, and remote control interface with VTHF. The goal was to study how much the operator actually benefits from secondary feelings such as vibration, which has commonly been considered to be important when controlling the machine. In addition, the goal was to find out whether the VTHF feature helps the operator.

The working efficiency was evaluated by means of the time taken, as in the first experiment. Moreover, the quality of the work was estimated visually on a scale of one to five (1 denotes the lowest quality and 5 the highest quality). The highest quality means that the trench is straight and there is no significant variation in the depth or width of the trench. The results are shown in Table 3.

Table 3 Total execution times and quality of work in Experiment 2

Measured variable		**Cab**	**Remote control**	**Remote control with VTHF**
Time [s] ($p = 0.155$)	Q_3	345	271	274
	Md	**313**	**221**	**250**
	Q_1	238	178	213
Quality of work [1-5] ($p = 0.319$)	$\bar{x}$	**2.80**	**2.93**	**3.13**
	σ	0.86	0.70	0.52

Table 3 shows that utilization of the remote control also improved the working efficiency compared to the cab interface in this experiment, just as it did in the first experiment. The VTHF feature did not improve the working efficiency while using the remote control, in fact the time elapsed was increased a little. However, VTHF slightly improved quality of the work. The improved quality of the work probably caused the increase in execution time.

The dispersion of total execution times between individual subjects with all three user interfaces is illustrated in Figure 5. Cases where remote control (without VTHF) decreased the working efficiency are plotted with dashed lines in Figure 5 and cases in which remote control improved the working efficiency are plotted with solid lines.

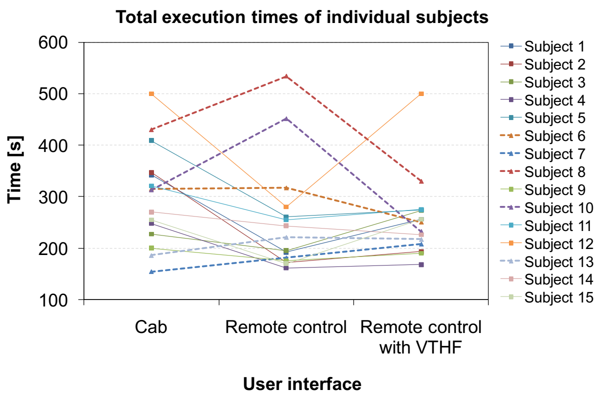

Figure 5 Dispersion of total execution times in Experiment 2

Again, subjects' feedback was inquired by means of a questionnaire. In the second experiment, the questionnaire included two subject matters. Subjects' feedback is shown in Table 4. As Table 4 shows, both *perception* and *feeling of control* were improved when using the remote control instead of the cab interface. In turn, the utilization of the VTHF feature improved both matters compared to remote control without VTHF. The results show that the force feedback information the operator receives while using the cab interface is not essential in applications of this kind. In fact, the subjects thought that improved visibility is more useful. However, since the obstacle was not visible in the beginning of the task, additional feedback information (VTHF feature) was regarded as useful even though it did not improve the working efficiency.

Table 4 Experiences of use in Experiment 1

Subject matter		**Cab**	**Remote control**	**Remote control with VTHF**
Perception ($p < 0.001$)	$\bar{x}$	**3.15**	**3.61**	**4.41**
	σ	0.75	0.65	0.53
Feeling of control ($p < 0.001$)	$\bar{x}$	**2.76**	**3.49**	**3.93**
	σ	0.91	0.65	0.42
Total ($p < 0.001$)	$\bar{x}$	**3.00**	**3.57**	**4.23**
	σ	0.74	0.58	0.44

Experiment 3: Control Accuracy

In addition to the working efficiency and comfort, the control accuracy is an important element of the usability. Improved visibility in the work task while utilizing the remote control as a user interface should facilitate accurate control. On the other hand, low-quality control devices of the remote control utilized in this study should decrease the control accuracy. In the third experiment the effects of the above-mentioned factors on the control accuracy in tasks that demand high accuracy are studied [10].

A spike was attached to the bucket of the excavator (see Figure 6). The task was to move the spike from point A to point B and then back to point A as accurately as possible. The swing movement was disabled in this experiment. Thus, the subjects controlled the excavator in a plane. The cycle was repeated five times. Errors in point B as well as in point A were measured. In addition, the time taken was considered. The means for both times and errors were calculated. The spike had to be upright when contacting a plate where the targets were marked. The machine remained stationary during the experiment.

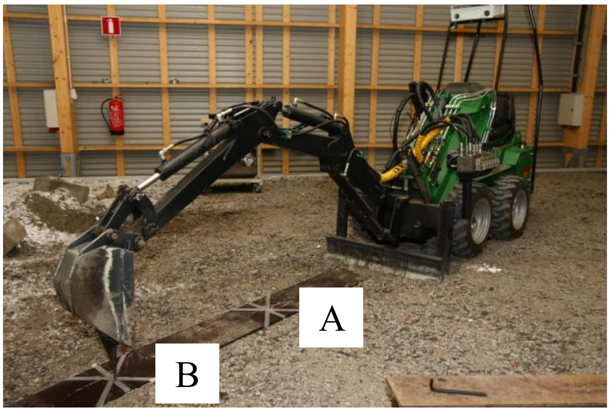

Figure 6 Setup in Experiment 3

While considering the errors, the mean of individual subject was calculated first. Then, the medians and upper and lower quartiles of the whole group, which are presented in Table 5, were found. In addition to errors, the means and standard deviations of the execution times are shown in Table 5.

Table 5 Errors and elapsed times in Experiment 3

Direction	Measured variable		Cab	Remote control
A→B	Error [cm] ($p = 0.773$)	Q_3	1.45	0.45
		Md	**-0.50**	**-0.05**
		Q_1	-2.03	-0.70
	Absolute error [cm] ($p < 0.001$)	Q_3	4.23	1.79
		Md	**3.05**	**1.30**
		Q_1	2.03	0.78
	Time [s] ($p = 0.173$)	$\bar{x}$	**27**	**23**
		σ	11	6
B→A	Error [cm] ($p = 0.096$)	Q_3	-0.50	-0.40
		Md	**-1.15**	**-0.65**
		Q_1	-2.23	-0.80
	Absolute error [cm] ($p < 0.001$)	Q_3	2.83	1.35
		Md	**2.28**	**0.80**
		Q_1	1.33	0.64
	Time [s] ($p = 0.903$)	$\bar{x}$	**26**	**27**
		σ	9	9

In Table 5, *errors* are calculated using signed values of single samples to calculate the means of individual subjects. In this case, the medians show the systematic errors. *Absolute errors* are calculated using the absolute values of single samples to calculate the means of individual subjects. *Absolute error* better describes the magnitude of error if the direction of error is ignored. The results are specified according to the direction of movement.

As presented in Table 5, utilization of the remote control decreased the errors significantly, irrespective of the direction and regardless of whether the signed values or absolute values are considered. The improvement is due to better visibility. The operator was able to have a view from the side while using the remote control, where as only depth vision could be used while operating from the cab. The differences in time taken were insignificant in this experiment.

The dispersion of errors (calculated with signed values) with both user interfaces are presented in Figure 7. If the absolute value of error of a single subject is increased in Figure 7, the results are plotted with a dashed line. Otherwise, solid lines are used. The figure shows that error increased in only a few cases while using the remote control instead of the cab interface.

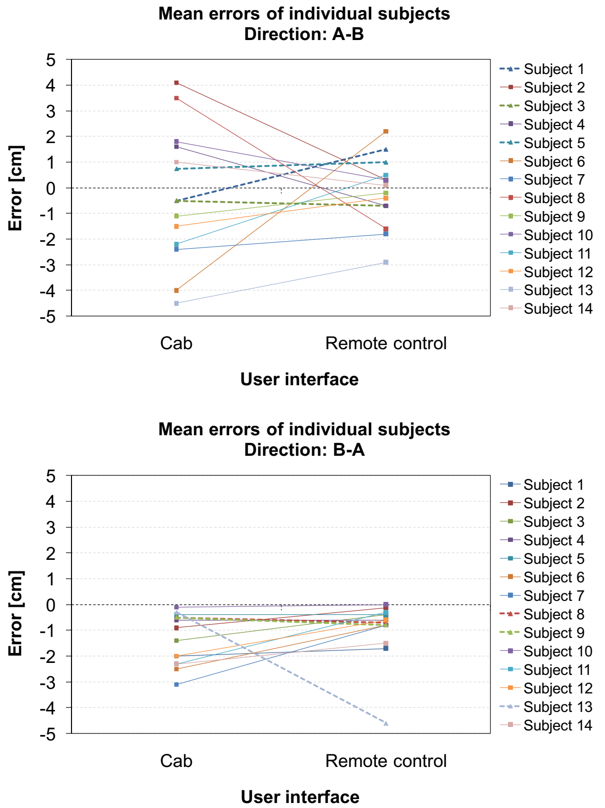

Figure 7 Mean errors of each subject in both directions: Direction is from A to B in upper part of figure and from B to A in lower part of figure

Experiences of use were also asked about in this experiment, as in the previous ones. Table 6 illustrates feedback from the subjects concerning the third experiment. The questionnaire included two subject matters. As can be seen in Table 6, the subjects felt that utilization of the remote control improved both *perception* and *feeling of control* significantly compared to the cab interface.

Table 6 Experiences of use in Experiment 3

Subject matter		Cab	Remote control
Perception ($p < 0.001$)	$\bar{x}$	**2.57**	**4.62**
	σ	0.66	0.47
Feeling of control ($p = 0.039$)	$\bar{x}$	**2.93**	**3.71**
	σ	0.73	0.75
Total ($p < 0.001$)	$\bar{x}$	**2.71**	**4.26**
	σ	0.60	0.43

DISCUSSION

Experimental studies like this include several factors of uncertainty. The utilized test platform, work tasks, subjects' background, etc. certainly have an effect to the results. Additionally, the usability of user interfaces cannot be defined or measured unambiguously but the superiority depends on the application and personal opinion among others. Thus, the results presented offer merely a suggested approach.

In this study, the experimental arrangements were aimed to made as objective as possible but still so that the most important indicators can be measured. The order of implementation was changed and the group sizes were matched to minimize the effect of learning. The user interfaces utilized are not completely identical due to practical reasons. However, the effects caused by the differences can be considered to be rather insignificant in this case.

The results show that the utilization of the remote control improved both the working efficiency and working accuracy compared to the cab interface, which was the most important point of comparison. Also, the subjects' feedback regarding the remote control as a user interface was positive in every experiment. The utilization of the remote control decreased the execution time by 18 % ($p < 0.001$) compared to the cab interface while the homogenous soil was operated (while considering the medians). The improvement is considerable and the differences are also statistically significant ($p < 0.05$, which is generally the used limit value). When the subjects' experiences in the first experiment are considered, it can be noticed that the visibility of the work task was improved significantly, as may have been expected, when using the remote control. The improvement was 81 % ($p < 0.001$) compared to the cab interface. Otherwise, the differences in the experiences between the cab interface and remote control interface were small. An interesting discovery is that the controllability of the excavator according the subjects was equal with both user interfaces.

When operating the soil with the obstacle, the corresponding improvement in the working efficiency was 29 % ($p = 0.155$), thus the lack of force feedback did not increase the execution time. However, in this case the difference was not statistically significant, probably partly due to the small number of subjects. The VTHF feature did not improve the working efficiency. However, the subjects felt that it improved the perception and feeling of control. The VTHF feature improved both the perception (22 %) and feeling of control (13 %) compared to the remote control interface without VTHF. Compared to the cab interface, the differences were even bigger (perception + 40 % and feeling of control + 42 %). Thus, it is worth exploiting.

The biggest improvement while using the remote control was achieved in the experiment in which a high working accuracy was required. While considering the medians of the absolute errors (which describes the magnitude of the error if direction of the error is ignored), the improvement was 57 % ($p < 0.001$) to one direction and 65 % ($p < 0.001$) to another. The visibility of the task, which is improved when short-range remote control is utilized, seems to have the dominating role while controlling the machine accurately. Improved visibility can be noticed when the subjects' experiences are considered. According to the feedback, the perception of the task was improved by about 80 % ($p < 0.001$).

Overall, the results presented are consistent and clearly show that the utilization of remote control may improve the working efficiency, working accuracy, and comfort, that is to say the usability of a machine, considerably in some cases. The improvements in the visibility of the work task seem to influence more than the impairments in other feedback information, such as in force feedback. However, the effects are certainly depending on the application and the worth of remote control has to be considered according to the requirements of the case in question, the work task having a dominating role in the decision-making process. Remote control is not the most convenient solution in every case. Thus, in order to maximize usability, remote control should be utilized as an alternative user interface for conventional onboard user interface, not as a substitute solution.

CONCLUSIONS

The main research contributions of this paper can be concluded as follows:

- The cost-effective hand-held remote control implemented is suited for controlling a mobile machine remotely. The low quality of the control devices does not significantly impair the controllability of the work movements of the machine.
- The effects of remote control on the usability of an excavator were estimated in three experiments by comparing the results achieved with different user interfaces. Independent non-professional subjects were utilized. The test arrangements certainly influence the results. Nevertheless, the results can be considered as broadly suggestive.
- According to the subjects' feedback, the visibility of the work task improved substantially when using the remote.
- In a typical "dig a trench" task, in the case of homogenous soil without obstacles, the working efficiency, estimated by means of the time taken, was improved considerably when using the remote control. The subjects' experiences concerning the remote control were also positive.
- The improvement was comparable in the case where the soil to be processed included an obstacle. The vibro-tactile haptic feedback feature did not improve the working efficiency, but, according the subjects' feedback, it improves the perception of the task and feeling of control, and so assists the operating.
- Better visibility of the work task consequent upon the utilization of the remote control improves the working accuracy substantially. Thus, in tasks where high working accuracy is required, the remote control is an advisable solution.

For more precise statements concerning the usability of remote control with multi-purpose mobile machines more studies would be needed. Different work tasks with various machines should be experimented since they indubitably have an influence. For instance, the controllability of the power transmission by means of a remote control have not much been studied. Also, subjects' backgrounds should be taken under consideration in order to study the precise interdependencies between different variables.

REFERENCES

[1] Sasaki, T., Miyata, T., and Kawashima, K. Development of Remote Control System of Construction Machinery Using Pneumatic Robot Arm. Proceedings of 2004 IEEE/RSJ International Conference on Intelligent Robots and Systems, Sendai, Japan, 28 September – 2 October, 2004, pp. 748-753.

[2] Sasaki, T., Nagai, T., and Kawashima, K. Remote Control of Backhoe for Rescue Activities Using Pneumatic Robot System. Proceedings of the 2006 IEEE International Conference on Robotics and Automation, Orlando, FL, USA, 15-19 May, 2006, pp. 3177-3182.

[3] Halme, A., Suomela, J., and Savela, M. Applying Telepresence and Augmented Reality to Teleoperate Field Robots. Robotics and Autonomous Systems Journal, No. 26, 1999, pp. 117-125.

[4] Suomela, J., Savela, M., and Halme, A. Tele-Existence Technics of Different Enhancement Degrees in Front End Loader Teleoperation. FSR'99 of the International Conference on Field and Service Robotics, Pittsburgh, PA, USA, 29-31 August, 1999, pp. 256-261.

[5] Minamoto, M. and Matsunaga, K. Tele-Presence Information and Remote-Controlled Task Execution. Proceedings of the 1998 IEEE/RSJ Intl. Conference on Intelligent Robots and Systems, Victoria, B.C., Canada, October 1998, pp. 1102-1106.

[6] Avant Tecno Oy. http://www.avanttecno.com

[7] Uusisalo, J., A Case Study on Effects of Remote Control and Control System Distribution in Hydraulic Mobile Machines, Dissertation, Tampere University of Technology, Publication 960, Tampere, Finland, 2011, 111 p.

[8]Uusisalo, J., Karhu, O., and Huhtala, K., Assisting Force Feedback Function for Hand-Held Remote Control of Excavator, Proceedings of the 7th JFPS International Symposium on Fluid Power, Vol. 3, Toyama, Japan, 15-18 September, pp. 653-658.

[9] Uusisalo, J., Karhu, O., and Huhtala, K. Hand-Held Remote Control as a User Interface for a Hydraulic Mobile Machine with an Excavator. Proceedings of the 51st National Conference on Fluid Power, Las Vegas, NV, USA, 12-14 March, 2008, pp. 405-411.

[10] Uusisalo, J., Huhtala, K., and Vilenius, M. Effects of Remote Control on Usability of Hydraulic Excavator. Proceedings of the ASME 2009 Dynamic Systems and Control Conference, Hollywood, CA, USA, 12-14 October, 2009, 8 p.

[11] Sakaida, Y., Chugo, D., Kawabata, K., Kaetsu, H., and Asama, H. The Analysis of Excavator Operation by Skillful Operator. Proceedings of 23rd International Symposium on Automation and Robotics in Construction, Tokyo, Japan, 3-5 October, 2006, pp. 543-547.

Proceedings of the 8th JFPS International
Symposium on Fluid Power, OKINAWA 2011
Oct. 25-28, 2011

2D4-2

ANALYSIS FOR PROCEDURE AND METHOD FOR DEVELOPMENT OF ACTUATOR OF POWER OPERATED VAVLE IN COMPLIANCE WITH IEEE STANDARD

Byung-Ju Lim*, Chang-Dae Park*, So-Nam Yun* and Kyung-Yul Chung*[1]

*Energy Plant Research Division, Korea Institute of Machinery and Materials
171 Jang-dong, Yuseong-gu, Daejeon, 305-343, Korea
(E-mail: bzoo77@kimm.re.kr, parkcdae@kimm.re.kr, ysn688@kimm.re.kr)
[1](Corresponding author:kychung@kimm.re.kr)

ABSTRACT

Equipment qualification (EQ) is to qualify that the equipment is able to operate completely safety function in both normal and accident conditions of nuclear power plant. All the electric equipment should be qualified in compliance with procedure and method of IEEE standards before applying that in nuclear power plant. The standards are separately presented according to a kind of equipment and test items and not about detailed procedure and method. Ambiguous expressions about test contents may cause misunderstanding and confusing to make a suitable test system. An actuator to operate the power operated valve (POV) is one of the critical equipment for safety in nuclear power plant. The actuator of POV uses the various actuating power sources such as motor, air and electric power and all the POV is qualified in compliance with IEEE Std. 382. Test method, test equipment and especially acceptance criteria are different each other according to power source of the actuators.
In this study, EQ test procedure, the lists and methods of operability test, normal and accident tests are thoroughly analyzed to perform EQ test of POV actuator in compliance with IEEE standards.

KEY WORDS

Actuator, Power operated valve, IEEE standard, Equipment Qualification, Nuclear power plant

NOMENCLATURE

R	: Chemical reaction rate (#/s)
A	: Pre-exponential constant
E_a	: Activation energy (J)
k	: Boltzmann constant (J/K #)
T	: Reaction Temperature (K)

Subscript

0	: Normal condition
1	: Accident condition

INTRODUCTION

It is required to verify that the safety functions of every piece of equipment used at nuclear power plants are successfully operating throughout their design lifecycle under the worst possible environmental conditions. This process of verification is called Equipment Qualification (EQ). The regulatory requirements for EQ have been corrected and supplemented based on 10 CFR 50 Appendix A, "General Design Standards" as suggested by the Nuclear Regulatory Commission. Currently, the regulatory guides and the standards of the IEEE (Institute of Electrical and Electronics Engineers) proposing the procedures and the methods of qualification stipulate the regulations for EQ. Thus, it is required to analyze and understand the legislations, guidelines, and standards for equipment for developing or performing qualification tests for the equipment at NPP (nuclear power plant). However, even the standards describing the requirements to the largest extent suggest general technical requirements such as qualification requirements or test items only, and they do not provide an in-depth description of testing equipment, testing methods, techniques, and allowable criteria. Therefore, it is essential that qualification institutes should develop technologies for EQ test and they should obtain experiences for qualification for performing actual EQ.

POV is composed of actuator part and body part. Qualification subject in IEEE standard is an actuator of POV as electrical parts. Body part is qualified by other standard such as ASME. POV's are classified into the air operated valve (AOV), the motor operated valve (MOV), and the solenoid operated valve (SOV). It is essential equipment for major system control in the common industries as well as in NPPs. It is critical to commit the best endeavors into development of POV for reliability of NPPs, and into the development of EQ technologies when considering the construction of new plants and demands for replacement of NPP.

Therefore, this thesis closely analyzes and identifies qualification standards and testing procedures for developing technologies for equipment qualification that is essential for the development and application of POV for NPPs, and it suggests an in-depth description of items, conditions, and allowable criteria for testing.

ANALYSIS OF TEST STANDARDS FOR EQUIPMENT QUALIFICATION

The CRF codes and the regulatory guides of the Nuclear Regulatory Commission, and the IEEE standards suggest a variety of legislations, guidelines, and provisions for equipment qualification testing of the SOV, and the summary of them is as shown in Table 1. The utmost super ordinate legal basis for equipment qualification is 10 CFR 50.49, which describes the equipment qualification programs for electric equipments and instrumentations related to safety [1]. There are guidelines backing the contents of the legislation such as Reg. 1.73 and Reg. 1.1, and the IEEE standards provide an in-depth description of targets and test items for qualification. The IEEE Std 323, which suggests the items and requirements for equipment qualification for all the electric equipment of safety grades, is the utmost super ordinate standard among the IEEE standards. It describes the purpose, the target, the test plans, and the documentation method for equipment qualification [2]. The IEEE Std. 382 provides the most in-depth and clear description for the qualification of the power operated valves including the items, details, and procedures for the tests [3]. Therefore, the representative standards for the equipment qualification test of the POV are IEEE Std. 323 and 382.

The various test items in IEEE Std. 382 are stipulated in other IEEE standards. As shown in Table 2, the standards for the temperature test are stipulated in IEEE Std. 1, 101, 775, 1205 and 1310. Those for the seismic qualification tests are in IEEE Std. 344; those for the voltage and the insulation tests are in IEEE Std. 4 and 43; and those for the accelerated thermal aging test are in IEEE Std. 1407.

PROCEDURES AND METHOD FOR EQUIPMENT QUALIFICATION TESTS

The equipment qualification tests are classified into the function test, the common environment test, and the accident environment test. Most of the test items for the common environment test and the accident environment test are similar to each other dependent upon the equipment for qualification. However, the items for the function test are varying within different equipment. The function test is performed for deciding if the target equipment keeps its capabilities compliant with the allowable criteria during the qualification test. The function test is performed before and after each environment test, and is also done during the accelerated thermal aging test, the vibratory aging test, and the

Table 1 Main code and standards for EQ of POV

Codes and Standards	Contents
10CFR50.49	A legal basis of EQ
REG. 1.73	Requirement of Valve EQ
REG. 1.1	Requirement of Seismic Qualification
IEEE Std. 323-2003	Mother Standard of EQ
IEEE Std. 382-2006	EQ of POV actuator

Table 2 Sub-standards for EQ test of POV

Standards	Contents
IEEE Std. 1	Temperature testing
IEEE Std. 4	High-voltage testing
IEEE Std. 43	Insulation resistance testing
IEEE Std. 101	Thermal life test
IEEE Std. 344	Seismic Qualification
IEEE Std. 775	Multi-stress aging test
IEEE Std. 1205	Thermal aging testing
IEEE Std. 1310	Thermal cycle testing
IEEE Std. 1407	Accelerated aging test

accident environment test [3]. The common environment test is a test performed under the environmental conditions that are identical with those of the aging of the valves during the design lifecycle at the installation location of the equipment in the nuclear power plant for the purpose of verifying that the capabilities of the valve are kept intact within an aging environment that involves radiation, heat, pressure and vibration. The purpose of the accident environment test is to verify that the safety of the equipment is kept intact even upon an outbreak of accidents after the expiration of the design lifecycle. The probable accidents include the seismic basis event and the design basis event (DBE). The procedures for equipment qualification for the POV are illustrated in Figure 1.

1. Function test

The items of the function test for measuring the capability of equipments vary between types of equipment, since the functions and the capability variables of each piece of electric equipment are different from one other. The major IEEE standards and the function test items are shown in Table 3 for each piece of target equipment. IEEE Std. 382 stipulates four function tests for the SOV, which are as follows: the operating voltage test, the operating pressure test, the leakage test, and the response speed test. The operating voltage test and the operating pressure test are performed before and after each environment test, while the leakage test and the response speed test are run twice before and after the equipment qualification tests [3]. The details of the test items and the systems for each function test are provided in the paragraphs below.

1.1 Operating time test

The response speed of the SOV is defined as the difference between the time of terminating the supply of the power to the SOV and the time when the pressure in the valve starting to be reduced as shown in Figure 2. In case of SOV, the valve using DC voltage is faster than the valve using AC power by about two times. It is required to use a precision location sensor along with high-speed data acquisition equipment and the storage of test data, since the typical response speed of SOV is several tens of millisecond. As aforementioned, the test is performed only twice along with the leakage test; both before and after the EQ test respectively. Operating time of AOV and MOV measures on-off time under no-load condition and simulated load condition.

1.2 Operating voltage test

The purpose of the operating voltage test is to measure the voltage when the plunger of the SOV starts moving, and when the plunger is closed again at the specific pressure. The former is called the pull-in voltage test, and the latter is called the drop-out voltage test. The pull-in voltage test measures the minimum voltage where

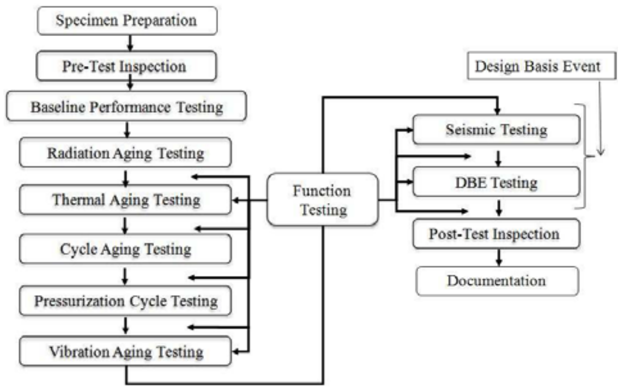

Figure 1 EQ test procedure of IEEE Std. 382

Table 3 Functional test contents of EQ equipment

Equipment		IEEE Standard No.	Functional Test
POV	SOV	382	.Operating time test .Operating voltage test .Operating pressure test .Leakage test
	AOV & MOV		.Output speed test .Operating time test .Output torque or thrust characteristics test .Leakage test
Motor		43, 112, 117, 334	.Insulation resistance test .Winding resistance test .No load test .Temperature test
Cable		383	.Insulation resistance test .Dielectric strength test
Limit Switch		572	.Insulation resistance test .Dielectric strength test .Conductor continuity test

the plunger starts moving under the maximum operating pressure conditions. The drop-out voltage test measures the maximum voltage under the maximum differential pressure and zero pressure of the valve. As for the SOV using DC voltage, the pressure where the plunger starts moving is measured by increasing or decreasing the voltage in an incremental manner.

1.3 Operating pressure test

The operating pressure test measures the minimum pressure for operating the SOV under the rated voltage. This test method is similar to the operating voltage test. Pressure is measured when the plunger starts moving, while changing the pressure in an incremental manner.

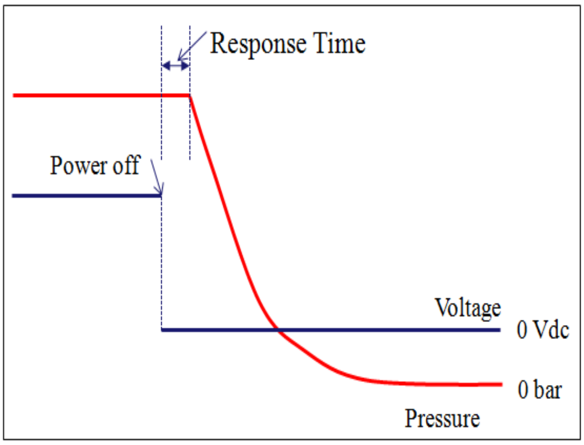

Figure 2 Concept of response time

1.4 Leakage test

The purpose of the leakage test is to verify the air-tightness of the valve. There are two leakage test types such as the internal leakage test for verifying leakage from the seat, and the external leakage test for verifying leakage from the valve body. The internal leakage test is performed as follows: the valve is installed in such a way that the outlet pipe of the valve is immersed in water in the water tank as shown in Fig. 4, nitrogen or air is then supplied to the inlet, and any air bubble is checked at the outlet tube. The external leakage test is performed as follows: the body of the SOV is installed in water, and a pressure 1.5 times that of the rate pressure is applied for verifying any air bubbles from the surface of the body. A leakage detector is often used for detecting leakage by making use of helium in lieu of air or nitrogen for the precise measurement of leakage.

1.5 Output load test

Output load test measures on load of valve stem or actuating axis when operating. Load type can be thrust or torque as operating method of valve actuator. In this test, the load test is performed under changing supply of actuating source such as fluid pressure, electric voltage or under interrupting actuator operation as shown in Table 4.

1.6 Additional function test

The SOV and MOV is a piece of electric equipment. It is an item for measuring the insulation characteristics that should be included in the function test items in addition to the four types of the tests stipulated in IEEE Std. 382. The electric insulation characteristics of the coil are a very important environmental factor for the SOV, since the characteristics directly affects the capability of the valve. The equipment qualification test of a motor includes the insulation characteristics test of the coil as one of the function test items [4].

Table 4 Test conduct of output load test of MOV and AOV

Equipment	Test conduct	Actuating source
MOV	Output torque or thrust under min. input supply	Electrical, pneumatic, hydraulic motor actuator
AOV	.The operating output thrust and torque characteristics at min. specified pressure .Max. thrust or torque in each direction at max. specified pressure	Pneumatic, electro-hydraulic, hydraulic actuator

The insulation characteristics test includes the voltage resistance test and the insulation resistance test. The voltage resistance test is to verify any current leakage by applying a high voltage of twice rated voltage plus 1000 VAC between the power cable and the valve body for one minute, while the insulation resistance test is for verifying resistance at the same point and is kept higher than the specified value [5]. Typically, it is judged normal if the resistance value is greater than 1 GΩ when applying a voltage that is higher than 500 VDC.

2. Normal condition test

The common environment test is performed after the first function test of the power operated valve. The common environment test includes the accelerated thermal aging test, the radiation aging test, the periodic operation test, and the vibratory aging test. The function test is performed before and after the individual tests. The details of the test items and the procedures for the common environment test are provided in the paragraphs below.

2.1 Radiation aging

The radiation aging test is performed by irradiating radiation doses to the POV. These does are equivalent to a radiation dose under the common environment conditions for the design cycle of the plant of about 40 years, and the exposed dose under an accident environment. The irradiation source is Co-60, which emits a gamma ray. The radiation dose of the power operated valve at new constructing plant is approx. more than 10^6 Gy, and the dose may slightly vary dependent upon the location of a plant. Since the lower the radiation dose rate is reduced, the worse aging of the nonmetal materials becomes even at same radiation dose. IEEE Std. 383 stipulates that the radiation dose is lower than 10^4 Gy/h [6].

2.2 Accelerated thermal aging test

The accelerated thermal aging test is for verifying that the POV functions safety functions normally while the valve is thermally aged in the design lifecycle of the plant. Since it is, however, not practical to perform the thermal aging test for an extended period of the design lifecycle such as 30 or 40 years, the Arrhenius equation is used for reducing the test period. This indicates the relationship between the response speed and the temperature of materials and activated energy [7].

$$\mathrm{R} = \mathrm{A}e^{\left(-\frac{E_a}{k\mathrm{T}}\right)} \tag{1}$$

Equation (1) indicates the Arrhenius Identity. The higher the temperature of the materials increases and the lower the activated energy becomes, the higher the response speed of the materials is elevated. When obtaining the reciprocals from both sides in this equation, the response speed is converted into the response time, and when obtaining the log from the reciprocals, the following value is yielded:

$$\ln t = \frac{\mathrm{E_a}}{k\,\mathrm{T}} - \ln \mathrm{A} \tag{2}$$

When converting equation (2) into the relationship between the common environmental conditions and the accelerated environmental conditions, the following results are yielded.

$$\ln \frac{t_1}{t_2} = \frac{\mathrm{E_a}}{k}\left(\frac{1}{T_1} - \frac{1}{T_0}\right) \tag{3}$$

The common environment temperature (T_0) is a sum of the environment temperature at the plant and the increased temperature due to heat generated from the POV. Since the common environment temperature at the plant has already been defined for each zone of installation of the equipment, it is allowed to define the temperature (T_1) and the time (t_1) to be accelerated during the test.

The energy activated is a unique value for the materials, and can be obtained from the existing database, or through experiments such as UTM and TGA. It is required to survey all the activated energy values of nonmetal materials used for the POV to identify the smallest value to be used. The reason is that the smaller the activated energy is reduced, the longer the accelerated aging period grows, and nuclear power plants demand equipment qualification tests under the most conservative environment for reliability.

It is allowed for testing engineers to flexibly adjust the time and the temperature of the accelerated environment test. Though the higher the test temperature elevates, the shorter test time is reduced, the test shall be performed at a temperature that is lower than the melting point of all the nonmetal materials of the POV, and IEEE Std. 323 stipulates that the accelerated thermal aging test shall be performed for longer than 100 hours [1]. These two conditions shall be considered when calculating the test conditions.

2.3 Cycle aging test

The cycle aging test is only applicable to the SOV and is performed during and after the accelerated thermal aging test respectively in the number of predicted operation for lifetime of NPP. One cycle means that out-port is fully pressurized and fully vented by energizing and de-energizing. During the thermal aging test, the SOV is subjected to a minimum of 10 % of the operating total cycle. And then, the remaining cycle numbers shall be tested. The SOV shall be repeatedly operated in condition of the maximum operating pressure differentials during the test. The schematic diagram of the systems for the periodical operation test of the SOV is as shown in Figure 3.

2.4 Pressurization test

The POV have their inlet and cylinder ports plugged so as not to subject them to atmospheric pressure during the containment pressurization aging phase. The POV is then exposed to pressurization cycles between zero and some high pressure. The high pressure value is specified as 488 kPa in IEEE Std. 382, but dependent on applicable NPP. The POV exposed to the fifteen numbers of external pressurization and the pressurization condition shall be held for a minimum of 3 min for each cycle. For the POV used in outside containment, no pressurization cycle testing is required.

2.5 Vibratory aging test

The plant facilities are exposed to vibration during the operation of the plant, since vibration is generated from rotating machinery and fluids. The vibratory aging test verifies that the capability of equipment is kept intact under the defined vibration conditions, which are installed in the vibration table. The vibration test is

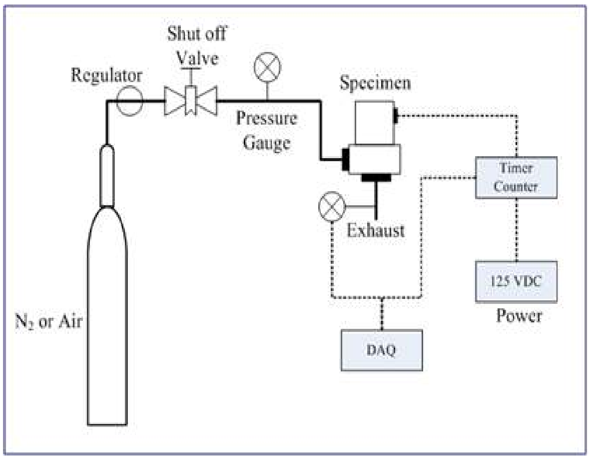

Figure 3 Cycle aging test schematic

performed at an acceleration of 0.75 g on each axis for 90 minutes. The vibration frequency is increased from 5 Hz to 100 Hz by a step of 2 octave/min, and then reduced from 100 Hz to 5 Hz.

3. Accident environment test

3.1 The seismic test

The seismic tests are classified into the operation basis seismic test and the safety shutdown seismic test. The operation basis seismic test verifies that all of the equipment is capable of operation with the safety functions kept intact upon the outbreak of an earthquake, while the safety shutdown seismic test verifies that the equipment is kept operable until the plant is safety shut down. The operation basis seismic tests shall be performed five times and the safety shutdown seismic test once.

The operation basis seismic test performs the vibration test at two-thirds the level of the seismic acceleration conditions required for the design of the plant. The frequency is increased from 2 Hz to 35 Hz by a step of 1 octave/min, and then reduced from 35 Hz to 21 Hz.

The items of the safety shutdown seismic test cover the tube mounting equipment, which are mounted on the tubes, and the facility mounting equipment, which are mounted on the structure. Sine vibration waves are applied to the sample of the tube mounting equipment at a single frequency for 15 seconds or longer the frequency is increased from 2 Hz to 32 Hz in a step of 1/3 octave/min. The composite frequency test shall be performed for the facility mounting equipment by applying vibration to the two axes or three axes. The test shall be performed three times in X-Y, Y-Z, and Z-X directions for testing on the two axes. The environment profile provided by the plant is applied for the test, and the test duration shall be longer than 30 seconds. The POV is almost tube-mounting equipment. However, it is recommended to perform both of the tests on the valve by taking into account various applicability.

3.2 Design basis event test

The design basis event tests are classified into the loss of coolant accident (LOCA) test, the high-energy line break (HELB) test, and the main steam line break (MSLB) test. The LOCA test is for the worst environment conditions for all the test items for equipment qualification. This test assumes an accident where the leakage of cooling water from a high pressure and temperature from containment building occurs, and applies the accident environment conditions to samples. When the cooling water is leaked, the containment building will be full of high temperature and high-pressure steam. In such a case, chemical solutions are sprayed from the nozzles mounted on the ceiling of the building to reduce the steam energy and the radiation dose. Therefore, the POV is subject to the environment of high temperature and high pressure

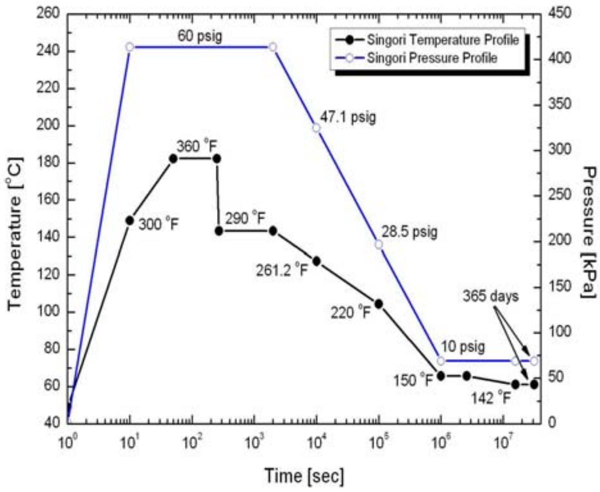

Figure 4 Loss of coolant accident test profile

steam, and chemical solutions that were sprayed during the design basis event test. The schematic diagram of the test facilities is as shown in Figure 4 illustrates the LOCA environment profile of new constructing NPP in Korea.

The function test of the POV is performed when the temperature and the pressure are highest during the LOCA test, and is to be continuously performed at a defined interval until the test is completed. Since the samples are positioned in the test chamber, the function test is replaced with the operability test.

Spraying of the chemical solutions shall start when the conditions of temperature and pressure in the test chamber reach the peak points during the LOCA. The acidity of the chemical solutions keeps in the specified range.

ACCEPTANCE CRITERIA

The acceptance criteria are for verifying that all of the equipment is qualified in the equipment tests. The equipment is considered qualified if all of the capabilities of the equipment satisfy the acceptance criteria after completion of the all the tests. The acceptance criteria is defined for verifying the appropriateness of capabilities of the equipment when planning the equipment qualification tests, and is compared with the function test results after the completion of the test. The allowable criteria makes a quantitative comparison based on the difference in data of the function test first performed during the equipment qualification test, or during specific limits. For example, as for the SOV, the acceptance criteria is decided for the leakage test and the voltage-resistance test, as well as for the operating voltage test, the insulation-resistance test and the response speed test of the limit values. Table 5 shows the items and the values of the acceptance criteria recorded in the equipment qualification report [8] of the 125 Vdc SOV that was developed by ASCO.

Table 5 Acceptance Criteria contents of SOV

Test contents		Acceptance Criteria
Leakage Test	External @ 1.5 times	pass
	Internal @ rated pressure	pass
DC operating voltage test	Pull-in voltage test @ maximum specified operating pressure drop	< 3 Vdc
	Drop-out voltage test @ maximum specified differential pressure and zero pressure	> 110 Vdc
Dielectric Strength test		Pass
Insulation Resistance test		> 10^9 Ω
Response Time Test		< 10 ms

The acceptance criteria varies dependent upon the specifications of the POV demanded by the nuclear power plants, and the product specifications developed by the manufacturers.

CONCLUSION

In this paper, the provisions and the procedures of the test for EQ of the POV actuator for NPPs were analyzed, and information on the items, the methods and the systems for the tests was identified in-depth.
The standards for EQ of the POV are hierarchically configured in the order of the legislations, guides, and provisions. The test provisions are broken down dependent upon the equipment and the items for the test. The legislations of equipment qualification are stipulated in the CFR codes and the regulatory guides of the Nuclear Regulatory Commission, and the provisions are in the standards of the IEEE. The major applicable provisions for the SOV are IEEE Std. 323 and 382. However, other IEEE standards provide an in-depth description of the temperature test, the voltage-resistance test, the insulation-resistance test, the accelerated thermal aging test, and the seismic qualification test stipulated in those two standards. Therefore, the major provisions and the detailed criteria for the test items shall be considered and applied to the qualification test.
The items of the EQ tests are classified into the function test, the common environment test, and the accident environment test. Both the common environment test and the accident environment test are applied to the equipment, while the function test has differences in the items of the function test dependent upon the functions and the capability characteristics of the equipments. IEEE Std. 382 stipulates five function tests for the POV which are as follows: the operating time test, the operating voltage test, the operating pressure test, the leakage test, and the output load test. The insulation characteristics test for assessing insulation capability is additionally included in these items. The common environment test performs the accelerated aging test, the radiation aging test, the periodic operation test, the pressurization cycle test, and the vibratory aging test, while the accident environment test performs the design basis event test and the seismic qualification test. Qualification of the test equipment after the completion of the EQ test is decided dependent upon satisfaction of the acceptance criteria by the capability of the equipment.
The manufacturer of the POV shall select the components and the materials, and shall design the valve by taking into account the items and the conditions of the EQ tests. The test institute for EQ shall demonstrate compliance with the procedures and the details of the qualification tests that are to be performed in accordance with the defined test items and with the regulatory institutes' required conditions. Therefore, the author expects that the technologies for EQ of the POV actuator analyzed in this paper will be utilized as very useful technical data for the development and application of the POV actuators.

ACKNOWLEDGEMENTS

This work was supported by the Nuclear Research & Development of the Korea Institute of Energy Technology Evaluation and Planning(KETEP) grant funded by the Korea government Ministry of Knowledge Economy(2010T100100537).

REFERENCES

1. 10 CFR 50.49, Environmental qualification of electric equipment important to safety for nuclear power plants, Nuclear Regulatory Commission
2. IEEE Std 323, IEEE Standard for Qualifying Class 1E Equipment for Nuclear Power Generating Stations, 2003
3. IEEE Std 382, Qualification of actuators for power-operated valve assemblies with safety-related functions for nuclear power plants, 2006
4. IEEE Std 334, IEEE Standard for Qualifying Continuous Duty Class 1E Motors for Nuclear Power Generating Stations, 2006
5. IEEE Std 43, IEEE Recommended Practice for Testing Insulation Resistance of Rotating Machinery, 2000
6. IEEE Std 383, IEEE Standard for Qualifying Class 1E Electric Cables and Field Splices for Nuclear Power Generating Stations, 1974
7. Park, C. D., Lim, B. J. and Song, C. S., "Methodology for modification of LOCA environmental test profile, NTHAS5, 2006
8. Shank, J. R., Report On Qualification of Automatic

Switch Co.(ASCO) Catalog NP-1 Solenoid Valves for Safety-Related Applications in Nuclear Power Generating Stations, Test Report No. AQR-67368

Proceedings of the 8th JFPS International
Symposium on Fluid Power, OKINAWA 2011
Oct. 25-28, 2011

2D4-3

COMPARISON OF TWO METHODS TO SOLVE PRESSURES IN SMALL VOLUMES IN REAL-TIME SIMULATION OF A MOBILE DIRECTIONAL CONTROL VALVE

Rafael ÅMAN*, Heikki HANDROOS*, Pasi KORKEALAAKSO** and Asko ROUVINEN**

* Laboratory of Intelligent Machines
Lappeenranta University of Technology
PL 20, 53850 Lappeenranta, Finland
(E-mail: rafael.aman@lut.fi)
** MeVEA Ltd.
Laserkatu 6, 53850 Lappeenranta, Finland
(E-mail: info@mevea.com

ABSTRACT

In fluid power systems, especially in many types of valves, there exists very small volumes which are particularly problematic in the case of dynamic analysis. Small volume with respect to the so-called normal sized orifice, formulate the system of equations which become mathematically stiff. This is a common source of numerical problems. To solve the stiffness problem, the present paper employs two alternative methods for conventional integration. Both implementations have in common that direct integration of pressures in small volumes is avoided and they are freely applicable regardless of used integration routine. Conventional numerical simulation with sufficiently small time increment is used as reference response. The valve studied is commonly available, proportional, load-sensing directional valve designed for mobile hydraulic systems, containing main spool and load-holding poppet with pilot spool. The present paper describes the methods in general level using a real-time simulation application of a relatively complex valve as a case study. Results are compared to those computed using conventional method.

KEY WORDS

Real-time, simulation, small volume, pseudo-dynamic, singular perturbation

NOMENCLATURE

B_e	Oil bulk modulus [Pa]
Cv :	Volume flow coefficient of the main spool [m^3 / s√Pa]
K:	Volume flow coefficient of the load-holding poppet valve [m^3 / s√Pa]
k:	Volume flow coefficient of the main spool depending on the input signal [m^3 / s√Pa]
L:	Cylinder stroke [m]
m:	Mass connected to the cylinder [kg]
p :	Pressure [Pa]
V:	Volume [m^3]
x :	Cylinder position [m]
x_0, x_1:	Threshold value in step function [Pa]
y_0, y_1:	Threshold value in step function [m^3 / s√Pa]
Δ :	Variable in step function [-]
Δp :	Pressure drop [Pa]
Δt :	Time step length [s]
ΔQ :	Compressional flow [m^3 / s]
Q :	Volume flow [m^3 / s]
Ψ :	Scaling factor
ε :	Typical relative volume or density change
η :	Pressure in small volume [Pa]

Subscripts

A / B:	Transmission lines A and B
cyl :	Cylinder
$inner$:	Inner loop of pseudo-dynamic model
$Leak$:	Leakage

Lock :	Lock – load-holding poppet
min :	Minimum value
Ref :	Reference model
SPT/Pseu:	SPT model and the outer loop of pseudo-dynamic model
Pseudo :	Variable in pseudo-dynamic solving method
Tol :	Pseudo-loop convergence criteria
1 :	Refers to *A1*
2 :	Refers to *B1*
A1 / B1:	Variable related to the load-holding poppet
A11 / B11:	Variable related to the main spool
η :	Variable related to the small volume between the load-holding poppet and the main spool

INTRODUCTION

In fluid power systems, especially in many types of valves, there exists very small volumes which are particularly problematic in the case of dynamic analysis. This is due the fact that from mathematical point of view small volumes in connection with larger, so-called normal volumes, formulate the system of equations which become mathematically stiff. Consequently, the system stiffness approaches infinity as the fluid volume approaches zero since it is related to fluid compressibility. For this reason, during dynamic analysis of the fluid power system the time integration of pressures in small fluid volumes is a common source of numerical problems.

The presence of relatively small time constants makes numerical integration of the ordinary differential equation (ODE) system difficult. Conventional explicit integration methods become numerically unstable unless a very small time increment is used. This leads into excessively long computational times. For stiff systems implicit, especially *L*-stable, ODE algorithms are recommended. Their drawback is that they have to solve a set of nonlinear equations at each time step, which reduces the computational efficiency of the method. To solve the problem caused by small fluid volumes, the present paper employs two alternative methods for conventional integration. Both implementations have in common that direct integration of pressures in small volumes is avoided.

Singular Perturbation Theory (SPT) is used in model reduction where the dynamics equations are pre-processed such that they can be integrated using routines for non-stiff systems. The Singular Perturbation Theory is originally introduced by Fenichel [2] and applied into fluid power simulation by Scheidl *et al.* [7]

The other implementation is the pseudo-dynamic solving method that solves the pressure as a steady-state pressure at each time step. The solution is obtained by numerical integration and iterative solution of the steady-states of the pressures after transient state. To reach the steady-state, artificial volume for the stiff part of the system is used in a cascade integration loop. Pseudo-dynamic solving method is proposed by Åman [8].

The rule of thumb for using both above-mentioned solving methods is that the nominal frequency (time constant), created by the small volume, is not significant in comparison with the dynamics of the whole system. The hydraulic capacitance V/B_e of the parts of the circuit of which stiffness is reduced should be at least ten times smaller than that of those parts whose pressures are integrated conventionally.

Both methods have the advantage of easy programming implementation and they are freely applicable regardless of used integration routine. Conventional numerical simulation with sufficiently small time increment is used as reference response when evaluating the accuracy of these two implementations.

The valve studied is commonly available, proportional, load-sensing directional valve designed for mobile hydraulic systems, containing main spool and load-holding poppet with pilot spool. Between the load-holding poppet and the main spool there exists a very small volume compared to the other volumes in the valve structure. In order to simulate the dynamic behaviour of the valve in real-time, both the pseudo-dynamic solving method and singular perturbation technique are applied.

The present paper describes the methods in general level using a real-time simulation application of a relatively complex valve as a case study. Results are compared to those computed using conventional method with a small time increment.

MODELLING OF THE COMPLEX MOBILE DIRECTIONAL CONTROL VALVE

The valve studied is commonly available, proportional, load-sensing directional valve designed for mobile hydraulic systems, containing main spool and load-holding poppet with pilot spool [5]. Between the load-holding poppet (Item no. 7 in Fig. 1) and the main spool (Item no. 2 in Fig. 1) there exists a very small volume ($V_{\eta A1}$ / $V_{\eta B1}$) compared to the other volumes in the valve structure. In order to simulate the dynamic behaviour of the valve in real-time, both the pseudo-dynamic solving method and singular perturbation technique are applied. Items no. 1 and 12 in Fig. 1 are not modelled.

Modelling of the fluid power circuit shown in Fig. 1 is started by implementing the required differential-algebraic equations for all the volumes, respectively. As an example, only equations related to one fluid power transmission line (line A) are presented. The other is then derived similarly but – naturally – oppose direction.

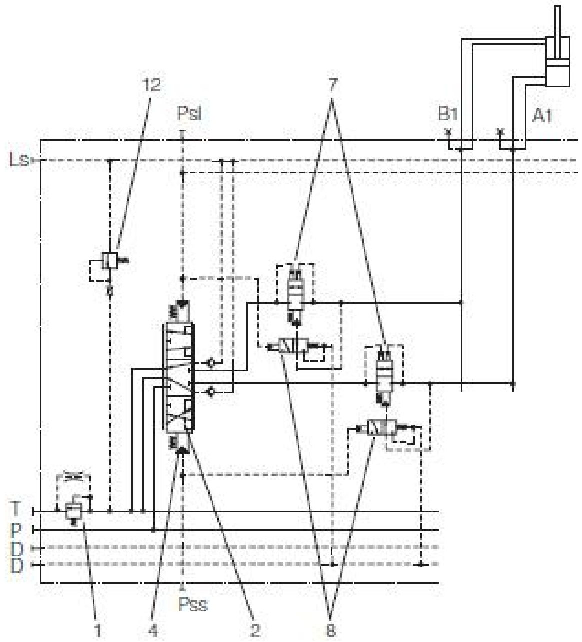

Figure 1 Modelled fluid power circuit [5]

The volume through the main spool (Item no. 2) is described using Eq. (1a…1c)

$$Q_{A11}=-U_1 Cv\sqrt{p_5-\eta_{A1}}\ ;\ U_1 < -1\times10^{-4} \quad (1a)$$

$$Q_{A11}=Cv_{Leak}\sqrt{p_5-\eta_{A1}}\ ;\ -1\times10^{-4} < U_1 < 1\times10^{-4} \quad (1b)$$

$$Q_{A11}=U_1 Cv\sqrt{p_0-\eta_{A1}}\ ;\ U_1 > 1\times10^{-4} \quad (1c)$$

It is assumed that the steady-state opening of the lock valve orifice is a third order polynomial of the pressure drop and the valve dynamics can be described by a first order differential equation. Thus, the volume flow coefficient of the load-holding poppet is solved from the Eq. (2)

$$\dot{K}_{A1}=\frac{y-K_{A1}}{\tau} \quad (2)$$

, where y according to Eq. (3a…3c)

$$y=y_0;\ \Delta p_{Lock}\leq x_1 \quad (3a)$$

$$y=y_0+(y_1-y_0)\,\Delta^2(3-2\Delta)\ ;\ 0\leq\Delta p_{Lock}\leq x_1 \quad (3b)$$

$$y=y_1;\ \Delta p_{Lock}>x_1 \quad (3c)$$

, where

$$\Delta=\frac{\Delta p_{Lock}-x_0}{x_1-x_0}$$

$$\Delta p_{Lock}=\eta_{A1}+p_1-p_{A1}-p_{ref}$$

$$p_{A1}=0\ ;\ U_1<-1\times10^{-4},\quad p_{A1}=p_1\ ;\ U_1\geq-1\times10^{-4}$$

And the volume flow through the load-holding poppet is solved from Eq. (4)

$$Q_{A1}=K_{A1}\sqrt{\eta_{A1}-p_{A1}} \quad (4)$$

The opening of the main spool of the directional control valve is solved using Eq. (5).

$$\dot{U}_1=\frac{U_{1ref}-U_1}{\tau} \quad (5)$$

The pressure build up in each volume can be described by the continuity equation of Merritt, Eq. (6) [4].

$$\dot{p}=\frac{B_e}{V}\Delta Q \quad (6)$$

The compressional flow is described by using Eq. (7).

$$\Delta Q=Q_{in}-Q_{out}+\dot{V} \quad (7)$$

, where $\dot{V}$ is externally supplied volume flow into and out of the volume (e.g. pump or actuator flow).

The flows in and out of the volume can be described by using Eq. (8).

$$Q=f(\Delta p) \quad (8)$$

SOLUTION OF PRESSURES IN SMALL VOLUMES IN DYNAMIC SIMULATION

To solve the problem caused by small fluid volumes, the present paper employs two alternative methods for conventional integration. Both implementations have in common that direct integration of pressures in small volumes is avoided. Instead the degrees of simulation models are reduced using two different methods. These methods are the pseudo-dynamic solving method [8] and the Singular Perturbation Theory [7].

Degree Reduction by Pseudo-dynamic Solving Method

The pseudo-dynamic solver is based on the basic assumption that if the volume in the system to be described is small enough, the pressure can be expressed by a steady-state pressure, as explained in [1]. The method has two key ideas. Firstly, the nominal frequency (time constant), which is created by the small volume, is not significant in comparison with the dynamics of the whole system. Secondly, instead of integrating the equations for pressure gradients in such volumes, their pressures are solved as steady-state pressures by using a pseudo-dynamic solver. The solver integrates the pressures in a separate integration loop while the volumes have pseudo-values providing a smooth and fast solution.

The key idea in the proposed method is to find steady-state solutions for the pressures in small volumes at each integration step, while the pressures in larger volumes as well as the other differential equations are integrated normally [8]. In other words, the pseudo-dynamic solver consists of two cascade integration loops, the outer and the inner loop. The outer loop consists of the ODE solvers integrating all other variables except those which are related to small volumes. Inside the outer loop, there is a separate ODE solver (inner loop) encoded to produce steady-state solutions for pressures in small volumes. The inner loop is executed by iterative means, i.e. it is controlled using the criterion for convergence, it has its own time space, the outer loop is paused during the inner loop run and only the last value of the integrated variable is returned to the outer loop. As the convergence criterion, the first derivative of pressure is used. With this predetermined condition, can be ensured that the attained solution has reached the steady-state. The influence of convergence criterion into the simulation results is studied in reference [9].

Simulation is started by defining that the pressures η_{A1} and η_{B1} are solver in their own inner loops of the pseudo-dynamic solver. Initial parameters are substituted into differential and algebraic equations and pseudo-loop is started. Integration in inner loop is carried out until the defined stopping criterion is reached. Note that the outer loop is paused during the inner loop run and these loops have their own independent time spaces. After inner loops are executed the pressures η_{A1} and η_{B1} are directed to outer loop as initial parameters. Integration in outer loop at first time step is carried out according to initial parameters. Integrated values are updated into differential and algebraic equations as new initial parameters. Results are stored and handled in post-processing after outer loop integration time has run out.

Pseudo-dynamic Solution of Steady-States of Fluid Power Circuits

The idea behind this algorithm is to consider each pressure node as finite volume. By doing so, each node represents a volume in which pressure builds up or decreases dependent on the compressional flow of the node, i.e. the sum of total flow to and from the node.
The three equations, Eq. (6), (7) and (8), make up the system formulation, which requires integration routine to update the pressures. For this a standard fixed step 4th order Runge-Kutta implementation is used, where the time steps in the solver are set sufficiently low to the account for the pseudo-dynamics in the system. This, however, also means, as oppose to the static solver, that no update algorithm is used, as the pressures are directly updated by the integration routine. For the static solver the update law also had a filtering effect. For the pseudo-dynamic solver this effect is instead replaced with pressure build up in the nodes, but to make the routine numerically more robust it may be also beneficial to add some pseudo-dynamics to the components with discrete states [6].

Degree Reduction by Singular Perturbation Theory

A system is described by a relation:

$$F(u,\varepsilon) = 0 ,$$

where u is its state from a vector or function space, ε a small non-dimensional parameter ($0 \leq \varepsilon < \varepsilon_0$; $\varepsilon_0 \ll 1$), and F some map. The system is called regularly perturbed in ε if [7]:

$$\lim_{\varepsilon\to 0} u(\varepsilon) = u_0,$$
$$F(u_0,\varepsilon) = 0.$$

Otherwise it is called *singularly perturbed.* u_0 is the solution of the so called reduced problem which is derived from the full or perturbed problem when the " is set to zero prior to solving the equation. $u(\varepsilon)$ is the solution of the full equation for different values of ε. In case of more than one solution regularity means that all solutions of the perturbed problem converge to a solution of the reduced problem [7]

Singular Perturbation Theory in Modelling Complex Mobile Directional Valve

The basic idea is to use the steady-state solution of two orifices in series connection. It is called as singularly perturbed i.e. its degree has been reduced so that the integration of the pressures η_{A1} and η_{B1} in small volumes can be avoided [3]. The drawback of this method is that the pressures of the small volumes are needed in dynamic equation for the ambient volumes. It must then be reproduced by a steady-state equation from the surrounding pressures, orifice flow and cross-section area of orifice which leads into a term in which square of flow is divided by square of cross-section area of the orifice. This again leads into numerical problems. As an example, only equations related to one fluid power transmission line (line A) are presented. The other is then derived similarly but – naturally – oppose direction.

Let us examine the transmission line A. The pressure build-up in small volume can be expressed as follows:

$$\dot{\eta}_{A1} = \frac{B_e}{V_{\eta A1}}\left(k_{A11}\sqrt{p_0 - \eta_{A1}} - K_{A1}\sqrt{\eta_{A1} - p_1}\right) \tag{9}$$

$$\dot{p}_1 = \frac{B_e}{V_{A1}}\left(K_{A1}\sqrt{\eta_{A1} - p_1} - Q_{cylA1}\right) \tag{10}$$

Let us use the following expressions:

$$\eta_{A1} = \Psi p_1, \tag{11}$$

and

$$\varepsilon = \frac{p_1}{B_e} = \frac{\eta_{A1}}{\Psi B_e}, \tag{12}$$

where Ψ is the scaling factor, B_e the effective bulk modulus of the system and ε a typical relative volume or density change. For typical hydraulic fluids and pressures its magnitude is O(10^{-2}) [7].

So, the set of equations can be written as follows:

$$\frac{V_{\eta A1}}{B_e}\dot{\eta}_{A1} = k_{A11}\sqrt{p_0 - \eta_{A1}} - K_{A1}\sqrt{\eta_{A1} - p_1} \tag{13}$$

and

$$\frac{V_{A1}}{B_e}\dot{p}_1 = K_{A1}\sqrt{\eta_{A1} - p_1} - Q_{cylA1} \tag{14}$$

From Equations (2.3) and (2.4) we get

$$\dot{\eta}_{A1} = \dot{\Psi} B_e \varepsilon \tag{15}$$

Now, by keeping Eq. (14) as it is and substituting Eq. (15) into Eq. (13), the model can be written as:

$$V_{\eta A1} B_e \varepsilon = k_{A11}\sqrt{p_0 - \eta_{A1}} - K_{A1}\sqrt{\eta_{A1} - p_1}$$

$$\frac{V_{A1}}{B_e}\dot{p}_1 = K_{A1}\sqrt{\eta_{A1} - p_1} - Q_{cylA1} \tag{16}$$

When the relation between the pressure and modulus of compressibility approaches zero, the latter term in Equation (16) takes the form:

$$\lim_{\varepsilon\to 0} \Rightarrow k_{A11}\sqrt{p_0 - \eta_{A1}} - K_{A1}\sqrt{\eta_{A1} - p_1} = 0$$

$$\Leftrightarrow k_{A11}^2\,(p_0 - \eta_{A1}) - K_{A1}^2(\eta_{A1} - p_1) = 0.$$

Then by taking the square of the both sides and solving for η_{A1}, we finally bring Eq. (16) into the form:

$$\eta_{A1} = \frac{k_{A11}^2 p_0 + K_{A1}^2 p_1}{k_{A11}^2 + K_{A1}^2}$$

$$\frac{V_{A1}}{B_e}\dot{p}_1 = K_{A1}\sqrt{\eta_{A1} - p_1} - Q_{cylA1} \tag{17}$$

The volume flows Q_{A11} and Q_{A1} can be expressed in following form, Eq. (18)

$$Q_{A11} = Q_{A1} = \frac{k_{A11}\,K_{A1}}{\sqrt{k_{A11}^2 + K_{A1}^2}}\sqrt{\Delta p} \tag{18}$$

The minimum value, k_{min}, for volume flow coefficients is defined to avoid the situation that during calculation the denominator in Eq. (18) would become zero. This would lead into immediate crash of the simulation run.

$$K_{A1} = \max(k_{min}, K_{A1})$$

Because the volume changes direction depending on the pressure drop, the following conditional statement of the directional spool position, Eq. (19) is needed. To avoid numerical problems caused by the pressure drop approaching zero, the absolute value of the pressure drop and the step function must be used.

if $U_1 < -1 \times 10^{-4}$

$k_{A11} = \max(k_{min}, (-U_1 Cv))$; $\Delta p = p_5 - p_1$

elseif $U_1 > 1 \times 10^{-4}$

$k_{A11} = \max(k_{min}, (U_1 Cv))$; $\Delta p = p_0 - p_1$

else

$k_{A11} = Cv_{Leak}$; $\Delta p = p_5 - p_1$

(19)

Finally, the steady-state equation, Eq. (20) for the pressure in small volume can be written in simpler form:

$$\eta_{A1} = \frac{Q_{A1}^{\ 2}}{K_{A1}^{\ 2}} + p_1 \tag{20}$$

NUMERICAL EXAMPLE

This study was started by modeling the fluid power circuit using three different approaches. The conventional 4th order Runge-Kutta method was used as reference response and it was implemented in Simulink. The pseudo-dynamic and SPT methods were implemented in MATLAB M-Files. To simplify the implementations of the alternative solving methods, the Euler method is selected to be used for integration of the accessory calculations and the 4th order Runge-Kutta method is only employed in the inner loop of the pseudo-dynamic solver.

In all simulation runs step function is involved in calculations of the volume flows to ensure the smooth approaches and crossings of the zero pressure drop. Its influence on results has been minimized by setting threshold pressure as low as model still stand stable (threshold pressure 1 x 10^5 Pa). Without use of step-function simulation runs failed.

To the hydraulic cylinder is connected the payload of 20 000 kg. Due to the external dynamics of the system it is difficult to adjust the initial values such that the inner pressure in small volumes remains stable during simulation run. That is why in the pressure responses of η_{A1} and η_{B1} of the SPT model there appears vibrations while the directional valve is closed (U_1=0).

To ease this phenomena the boundary values of the step function has been increased to 5x10^5 Pa. This makes the calculation of volume flows smoother near zero pressure surroundings without any degradation of model accuracy or extension in calculation time.

Reference response

As a reference model the fluid power circuit is modelled as explained in Section 2. This carried out in Simulink which enables easy employment of different integrators. The 4th order Runge-Kutta method is selected to be used for solving the equations. Time step length of Δt = 5 x 10^{-6} s was the longest possible for the use without notable changes in responses i.e. model stability. Used initial values are represented in Table 1. This method for finding the reference response is commonly acknowledged and can be stated as the most accurate one when time step length is set sufficiently short. The drawback for use of this conventional method is the computational speed. Computational times are not investigated within this study but the accuracy of different models. Naturally, the goodness criterion for employing different solving methods was at least reasonable computational time.

The simulated work cycle of the fluid power circuit is the following. First the cylinder is driven to (+) direction (out), then the movement is stopped and eventually the cylinder is driven to (-) direction. In Fig. 2 this is presented in the form of directional valve control reference signal. Also the realized valve spool opening is illustrated.

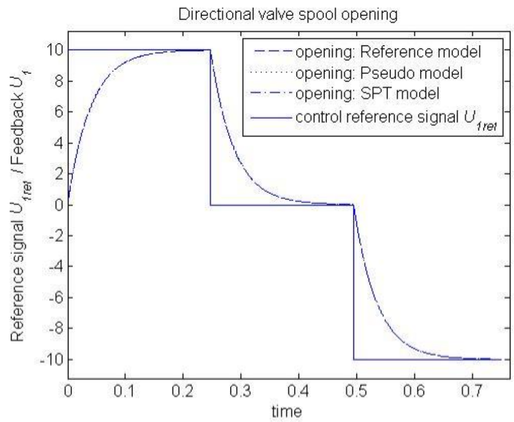

Figure 2 Control reference signal and the feedback from valve spool

Results

The following results are achieved using three alternative solving methods for the pressures in small volumes.

First, the response of the pressures in the small volumes η_{A1} and η_{B1} are studied. The responses are illustrated in Fig. 3 and 4.

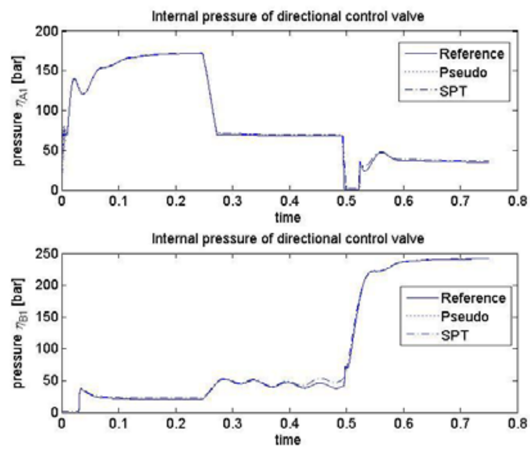

Figure 3 Internal pressures η_{A1} and η_{B1} of directional control valve.

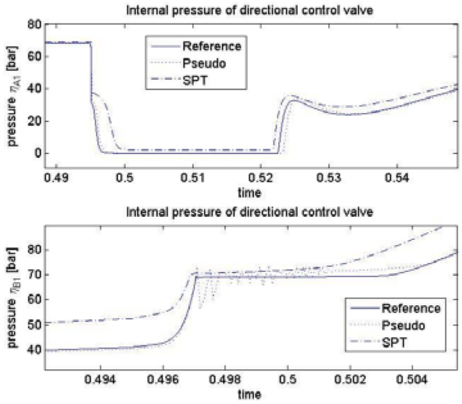

Figure 4 More focused view of Figure 3.

From Fig. 3 and 4 can be seen that responses achieved using different solving methods correspond to the reference response mainly well. Only in switching points of the control reference there exist deviations. Pseudo-dynamic solving seems to be more accurate even there exist more oscillations in switching point.

The cylinder piston position x and piston velocity $\dot{x}$ is illustrated in Fig. 5 and 6.

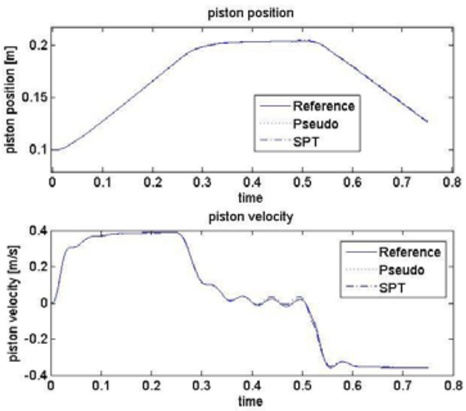

Figure 5 Cylinder piston position and velocity.

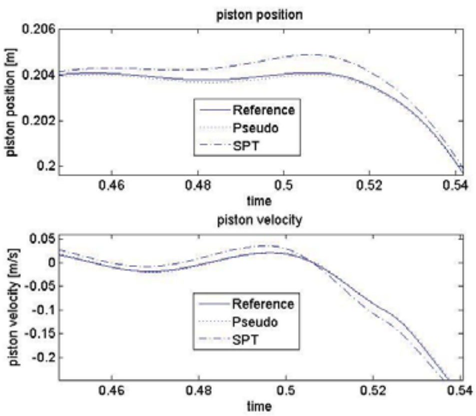

Figure 6 More focused view of Figure 5.

It can be stated that both proposed solving methods realize the piston position and piston velocity in acceptable accuracy. The responses of pseudo-dynamic solver show identical behaviour with the reference responses. In the response of piston position of SPT model there exist deviation within 1 mm tolerance.

The volume flow coefficients of the load-holding poppet K_{A1} and K_{B1} are illustrated in Fig. 7 and 8.

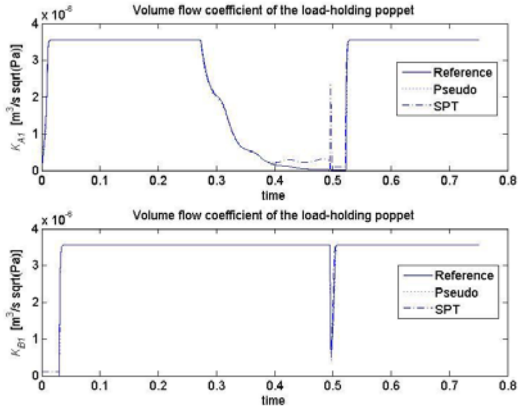

Figure 7 Volume flow coefficients of the load-holding poppet.

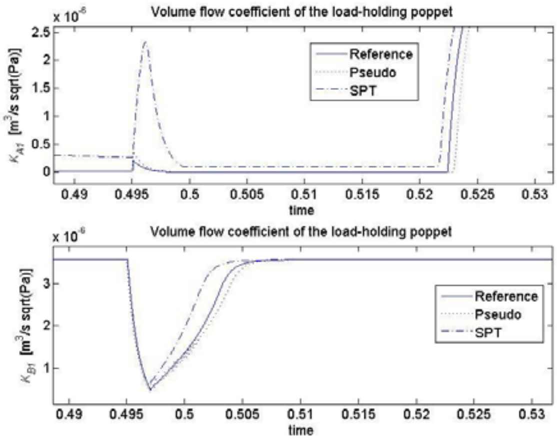

Figure 8 More focused view of Figure 7.

It can be seen from Fig. 7 and 8 that the differences between different solving methods come up in responses of the volume flow coefficients. This due to the fact that the load-holding poppet with the pilot-operated lock-up function represents the fastest dynamics in the system after the small volume in which the transients are very fast.
The responses of pseudo-dynamic method follow the reference responses with small oscillations and deviation. But the SPT model suffers from numerical noise when the value of volume flow coefficient is

lower than 3 x 10^{-7} m^3 / s√Pa. The steady-state deviation while the valve is closed is due the limitation of the minimum value of the volume flow coefficient to avoid numerical problems in SPT model.

CONCLUSIONS

Two alternative solving methods for pressures in small volumes were applied to fluid power circuit composing of mobile directional control valve and actuator. The pseudo-dynamic solving method was stated to meet the reference response more accurate. The reference response was achieved using explicit 4th order Runge-Kutta integration routine and sufficiently short time increment. The reduced model by Singular Perturbation Theory provide less oscillation but more deviation from the reference responses than appear the pseudo-dynamic model.

The pseudo-dynamic model provides better integrator stability since longer integration time steps compared to the conventional method can be used. It was then shown that using both of the proposed solving methods numerical problems apparent in calculations by conventional methods can be avoided. And both are suitable for the real-time simulation of complex mobile directional valve.

Table 1 Initial values used in system simulation

Δt_{Ref} = 5 x 10^{-6} s	$\Delta t_{SPT/Pseudo}$ = 1 x 10^{-5} s	Δt_{inner} = 5 x 10^{-5} s
$V_{\eta A1}$ = 5 x 10^{-6} m^3	$V_{\eta B1}$ = 5 x 10^{-6} m^3	V_{pseudo} = 1 x 10^{-3} m^3
V_{A1} = 4.4 x 10^{-3} m^3	V_{B1} = 16.2 x 10^{-3} m^3	L = 0.78 m
D_1 = 0.2 m	D_2 = 0.11 m	x = 0.1 m
p_0 = 290 x 10^5 Pa	p_1 = 0 Pa	p_2 = 0 Pa
p_{ref} = 5 x 10^5 Pa	Δp_{Tol} = 1 x 10^3 Pa	p_5 = 0 Pa
Cv = 3.56348 x 10^{-7} $\frac{m^3}{s\sqrt{Pa}}$	k_{min}=1 x 10^{-7} $\frac{m^3}{s\sqrt{Pa}}$	Cv_{Leak} = 1 x 10^{-7} $\frac{m^3}{s\sqrt{Pa}}$
m = 20 000 kg	x_0 = 0	y_0 = 0
b=500 $\frac{Ns}{m}$	x_1 = 1 x 10^5 Pa	y_1=10 x Cv
simtime = 0.75 s	B_e = 1.5 x 10^9 Pa	

REFERENCES

1. Ellman, A. Proposals for Utilizing Theoretical and Experimental Methods in Modelling Two-Way Cartridge Valve Circuits. PhD thesis, Tampere University of Technology, 1992.
2. Fenichel, N. Geometric Singular Perturbation Theory for Ordinary Differential Equations. Journal of Differential Equations, Vol. 31, pp.53-98, 1979.
3. Handroos, H. and Vilenius, M. Flexible Semi-Empirical Models for Hydraulic Flow Control Valves. Journal of Mechanical Design, Vol. 113, pp. 232-238, 1991.
4. Merritt, H. Hydraulic Control Systems. John Wiley & Sons, 1967
5. Parker Hannifin. Catalogueue HY17-8535/UK. PDF 07/05, 2005
6. Pedersen, H. Automated Hydraulic System Design and Power Management in Mobile Hydraulic Applications. PhD thesis, Aalborg University, 2007.
7. Scheidl, R., Manhartsgruber, B., and Kogler, H. Model Reduction in Hydraulics by Singular Perturbation Techniques. In 2nd Int. Conf. on Computational Methods in Fluid Power. Fluid Power Net Publication, pp.1-6, 2006.
8. Åman, R. Methods and Models for Accelerating Dynamic Simulation Fluid Power Circuits. PhD thesis, Lappeenranta University of Technology, 2011.
9. Åman, R. and Handroos, H. Optimization of Parameters of Pseudo-Dynamic Solver for the Real-Time Simulation of Fluid Power Circuits. In 7th International Fluid Power Conference Aachen, (Aachen, Germany, 22-24 March 2010), Vol. 1, pp. 495-507, 2010.

Proceedings of the 8th JFPS International
Symposium on Fluid Power, OKINAWA 2011
Oct. 25-28, 2011

2D4-4

Leakage-Detection System in a Liquid Pipeline

Duo FENG*, Yiqin ZHENG*,Takeshi NAKADA*,Yasuo SAKURAI **

* Tokyo Denki University, School of Information Environment, Tokyo Denki university
2-1200 Muzai Gakuendai, Inzai, Chiba, 270-1382 Japan
**Ashikaga Institute of Technology Department of Innovative Engineering
268-1 Oomae-cho, Ashikaga-shi, Tochigi, 326-8558 Japan

ABSTRACT

In this study, a novel leakage-detection system suitable for liquid pipelines is proposed in which acoustic emission (AE) sensors are used. The multiple functions of flow rate measurement and detection of acoustic emission generated by a leakage from the pipe are provided in the AE sensors for the detection of leakage from a pipeline. The characteristics of a leakage-detection system constructed on the basis of the proposed method are experimentally clarified. The experimental results showed that leakage- detection was possible for leakage flow rate of greater than 0.55 l/min by using the flow rate measurement function, and greater than 0.45 l/min by using the AE detection function. The combination of functions in the proposed method allows effective leakage evaluation of pipes.

Keywords: Leakage-detection, Acoustic emission sensor, Pressure sensor, Pipeline, Tap water

1. INTRODUCTION

Liquid pipeline systems are widely used in liquid transportation systems such as water-supply and drainage systems, water-cooling systems, and oil pipeline systems. It is estimated that in Japan, 7 % of the total water supply is lost as a result of leakage. In April 2010, a large quantity of crude oil was leaked into the sea as the result of an explosion at a subsea petroleum facility in the Gulf of Mexico. There is increased concern regarding the deterioration of the natural environment and the ecological environment arising from the use of pipeline systems. A response to these emerging social demands will require, as one measure, the development of a monitoring system that can estimate the health of a pipeline system from the viewpoint of high-efficiency operation, pipeline safety, resource savings, and environmental protection.

In this paper, a novel system for detecting leakage in liquid pipelines is proposed as the first step in the development of a system to monitor the health of liquid pipeline systems. In addition, a system for detecting leakage based on the proposed method is constructed. The constructed system consists of an acoustic emission inspection system using acoustic emission (AE) sensors and a system for checking pressure using pressure sensors. Focusing on the AE sensors, the characteristics of the leakage-detection system are experimentally clarified, and the experimental results confirm the effectiveness of the proposed system. This system can be employed to provide early warning of a pipeline leakage and failure.

2. SYSTEM for MONITORING the HEALTH of a LIQUID PIPELINE

In our concept of a system to monitor the health of a liquid pipeline, the following three functions are required.

- A function to estimate corrosion and fatigue in a pipeline, and to pinpoint corrosion and fatigue locations.
- A function to not only detect a leakage, but also to identify the flow rate and location of the leakage.
- A function to provide early warning of a pipeline leakage and failure.

The realization of these concepts requires sophisticated instrumentation such as AE sensors for the first function; flow rate sensors and pressure sensors for the second function; and computerization for the third function. In this study, a leakage-detection system having the second and the third functions is proposed. Particularly, in consideration of extensibility to include the first function, it is very important from the viewpoint of reducing the number of sensors needed that the function of measuring the flow rate is provided in the AE sensor system, which is commonly employed for the realization of the first function.

3. PROPOSAL for LEAKAGE-DETECTION SYSTEM FOR a LIQUID PIPELINE and EXPERIMENTAL APPARATUS

Figure 1 shows the concept of the leakage-detection system proposed in this study. Although AE sensors and pressure sensors need to be mounted on the pipeline at many locations, only two AE sensors and pressure sensors are shown in Fig.1.

Both a function to measure flow rate and a function to directly detect the acoustic emissions generated by a leakage from the pipe are provided to detect a leakage and ascertain its flow rate in each of the AE sensor systems, which consist of AE sensors, amplifiers shown in Fig.2, and a signal processing circuit shown in Fig.3. Leakage- detection can be conducted by two methods using the two functions provided in the AE sensor systems. It is considered that, for example, detection of major leakages can be readily accomplished by a comparison of flow rates at various locations using the flow rate measurement function in the AE sensor system. Small leakage can be detected by extracting the acoustic

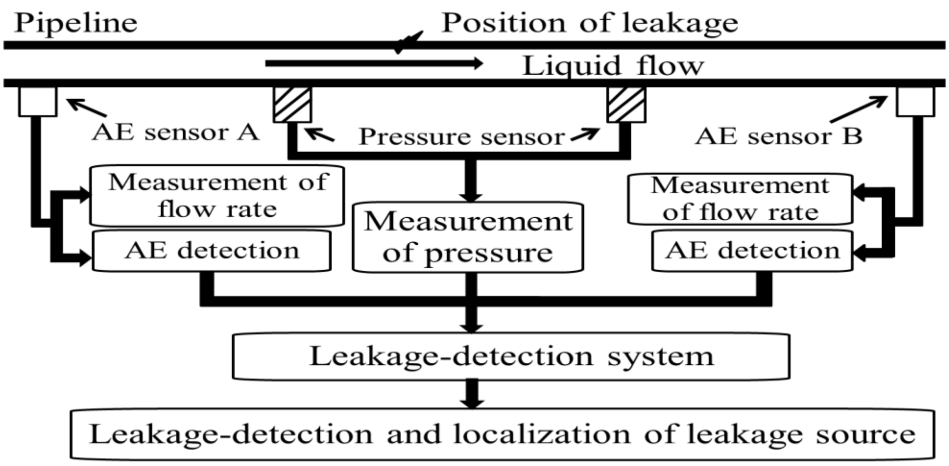

Fig.1 Concept of proposed leakage-detection system

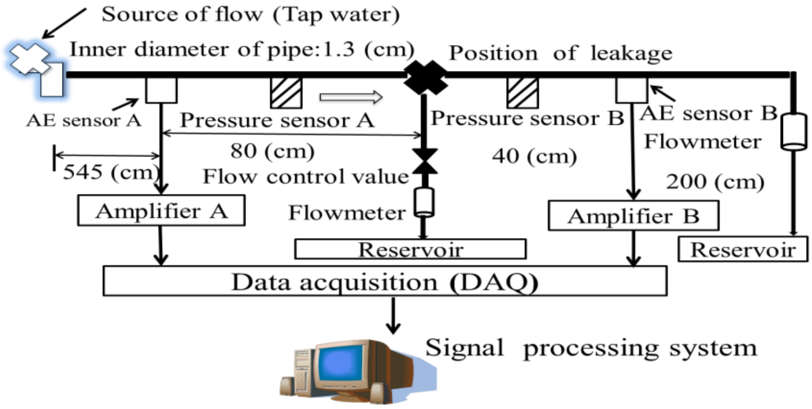

Fig. 2 Experimental apparatus for leakage-detection system

emissions generated by the leakage of a liquid from a pipeline. In this paper, the leakage-detection method using the flow rate measurement function is called the "indirect AE-leakage detection method" (IAEM), and the leakage-detection method using the extraction of acoustic emissions is called the "direct AE-leakage detection method" (DAEM). With respect to the pressure sensors, the detection of a leakage [1] can be carried out using pressure gradients and the differences in pressure at various locations along a pipeline.

In our proposed leakage-detection system, when leakages are found by methods using AE sensors and pressure sensors, the leakage flow rate are obtained, and data collected at various locations along the pipeline enable the leakages sites to be pinpointed.

Figure 2 shows an outline of the experimental apparatus for the leakage-detection system based on the concept shown in Fig. 1. The liquid used in the experiment is tap water. The main part of the experimental apparatus consists of a hydraulic pressure source that provides a flow of tap water from a reservoir into a pipeline, a steel pipeline with an inside diameter of 1.3 cm, a section of pipeline with a simulated leakage, two AE sensors to detect acoustic emissions, two pressure sensors, and a data acquisition board (DAQ) to transmit data detected by each sensor to a computer for analysis. AE sensors A and B are mounted directly on the wall of the pipe 80 cm upstream of and 40 cm downstream of the point of leakage, respectively. In the simulated leakage section, the leakage flow rate can be adjusted by a flow control valve. The pipeline is considered to be in a normal state when the flow control valve is closed, and in an abnormal state when the flow control valve is opened.

4. SIGNAL PROCESSING CIRCUIT for LEAKAGE-DETECTION USING AE SENSORS

Figure 3 shows the signal processing circuit for leakage-detection using AE sensors. It incorporates two signal processing circuits, the IAEM circuits and the DAEM circuit. The IAEM circuit is employed to diagnose leakages, based on the IAEM. In this method, measurement of the liquid flow rate is most important, and it has been already developed by the authors [2]. Using the developed flow rate measurement circuit, the flow rates are measured at the positions where AE sensors A and B are mounted on the pipeline, and the presence of a leakage is diagnosed from the difference in measured flow rates by the diagnostic circuit. The DAEM circuit is employed to diagnose a leakage directly by extracting the acoustic emissions generated by the leakage, based on the DAEM. In the DAEM shown in Fig.3 the output of the high pass filter is processed to a root mean square value (V_{rms}) with RMS circuit.

Figure 4 shows the frequency spectra of the AE signals obtained experimentally with the AE sensor A. Figure 4(a) shows the frequency spectrum of normal background noise. Most of the frequency components are lower than 700Hz. Figure 4(b) shows the frequency spectrum for the case in which the source flow rate Qs of

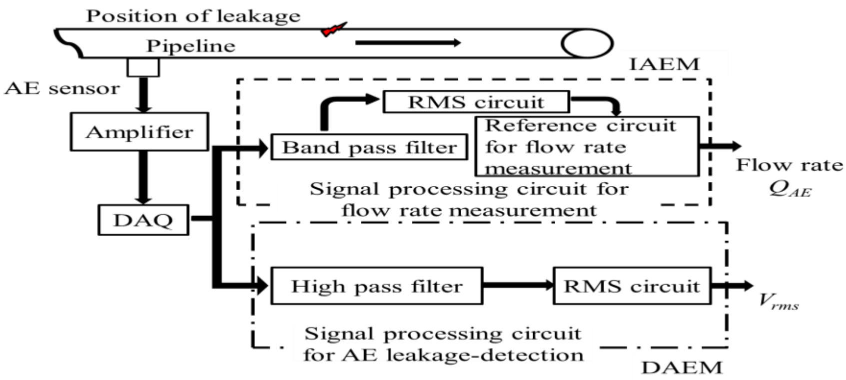

Fig. 3 Signal processing circuit for leakage-detection using AE sensor

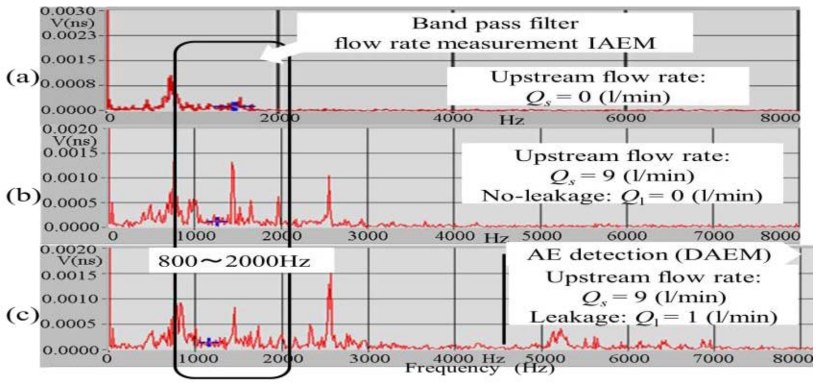

Fig. 4 Frequency spectrum analysis for AE signal

the pipeline is 9 l/min in a no-leakage condition. The results show a remarkable increase in spectrum amplitude in the frequency band between approximately 800 and 2,000 Hz with increasing flow rate. Figure 4(c) shows the frequency spectrum for the case in which Q_s is 9 l/min, and the leakage flow rate Q_l from the simulated leakage section in Fig. 2 is 1 l/min. Comparing the frequency spectrum for the no-leakage case shown in Fig. 4 (b) with the spectrum for the leakage case shown in Fig. 4 (c), shows that when there is a leakage there is a significant increase in the spectrum amplitude for frequency components higher than 4,500 Hz. Therefore, in the signal processing circuit shown in Fig. 3, the frequency band of the band pass filter in the IAEM was set from 900 to 1,800 Hz, while the frequency band of the high pass filter in the DAEM was set to higher than 4,500 Hz. The isolation of the frequency bands of the filters in the signal processing circuit means that the IAEM and the DAEM can operate independently and simultaneously in detecting a leakage. In this manner, it is possible to diagnose leakages independently by means of flow rate measurement in the IAEM, and the output magnitude of the RMS circuit in the DAEM.

5. EXPERIMENTAL RESULTS of LEAKAGE-DETECTION

Prior to the experiment to detect leakage using the IAEM, the flow rate measurement systems using AE sensors A and B were calibrated. The calibration result for the measurement system using AE sensor A is shown in Fig. 5. In this figure, Q_c and Q_{AE} are the flow rates measured using a commercial flowmeter and the flow rate measurement system with AE sensor A, respectively. It was found from the calibration result that the flow rate measurement system using AE sensor A has an accuracy of 15 % over the region in which the flow rate ranges from 5 to 10 l/min. The calibration result for the flow rate measurement system using AE sensor B was about the same as that for AE sensor A.

To evaluate the possibility of detecting leakage, the flow rates of the pipeline were measured using AE sensors A and B in the IAEM, and at the same time the RMS values (V_{rms}) of the output of the RMS circuit in the DAEM were obtained, when Q_s was 9 l/min and Q_l was varied. As the fluctuation in the leakage flow rate increased for leakages of less than 0.45 l/min due to the characteristics of the flow control valve shown in Fig. 2, the experiment was conducted for leakages greater than 0.45 l/min.

Figure 6 shows the relation between the leakage flow rate and the pipeline flow rate measured with AE sensor A mounted upstream of the leakage position, and with AE sensor B mounted downstream of the leakage position in the IAEM. The results show that detection of leakage with a flow rate of greater than about 0.55 l/min is possible using the difference in the flow rates measured by AE sensors A and B. The leakage flow rate can also be estimated in this way. However, for leakages of less than 0.55 l/min, the difference in the pipeline flow rates is so small that leakage-detection becomes inaccurate.

Figure 7 shows the relation between the leakage flow rate and V_{rms} in the DAEM. In this experiment, when there is no-leakage in the pipeline, V_{rms} is adjusted to 0 V. It can be seen from the figure that for leakages of greater

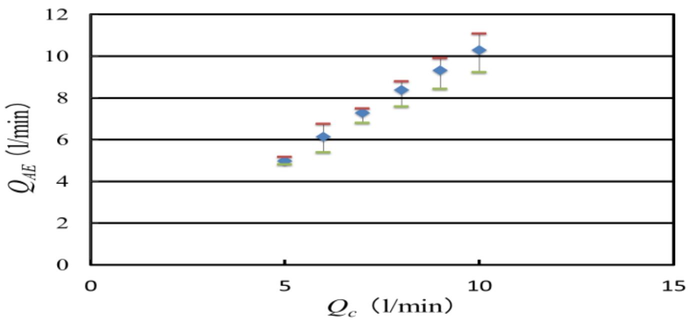

Fig.5 Calibration result of the flow rate measurement system using AE sensor A

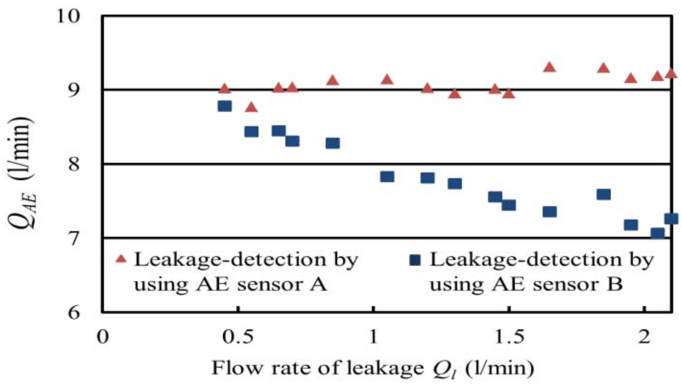

Fig. 6 Leakage flow rates and flow rates of pipeline measured with AE sensors A and B in IAEM

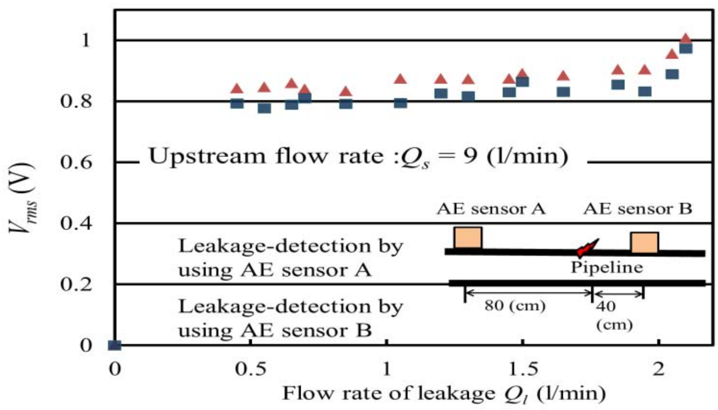

Fig.7 Relation between leakage flow rate and V_{rms} in the DAEM

than 0.45 l/min, the V_{rms} values for both AE sensors A and B have non-zero values, increasing from about 0.8 to 1.0 V with increasing leakage flow rate. Therefore, using this method, it is found to be possible to detect with certainty a leakage with a flow rate greater than 0.45 l/min.

Comparing the results for the IAEM and DAEM, a smaller leakage can be more effectively detected by the DAEM than the IAEM, but the IAEM has the advantage that the actual leakage flow rate can be measured. This study proposed the novel idea that the multiple functions of flow rate measurement and AE detection were provided in AE sensors for the detection of a leakage from a pipeline, and it was found that these multiple functions were very effective in detecting leakages.

6. CONCLUSION

In this study, a novel leakage-detection system suitable for liquid pipelines was proposed in which AE sensors were used. The multiple functions of flow rate measurement and AE detection were provided in the AE sensors for the detection of leakage from a pipeline. A leakage -detection system based on the proposed method was constructed, and an experiment was conducted to evaluate its capabilities. The experimental results showed that leakage- detection was possible for leakage flow rate of greater than 0.55 l/min by using the flow rate measurement function, and greater than 0.45 l/min by using the AE detection function. In case of the AE detection the leakage-detection may be possible even if leakage flow rate is smaller than 0.45 l/min. The system could not only detect leakage but also measure the leakage flow rate. The combination of functions in the proposed method thus allows effective leakage evaluation of pipes.

ACKNOWLEDGEMENT

The study was supported by the Japan Science and Technology Agency as part of its research and development programs.

REFERENCES

1) Fukuda, T., Mitsuoka, T.: Leakage Detection and its Localization in a Pipeline System, Proc. Of IMEKO Symposium on Flow Measurement and Control in Industry, p.193-198 (1979)

2) Zheng, Y.Q.,Nakada, T., Sakurai, Y., Tanaka, k.: Study on a Liquid Flow Measurement System using an AE sensor, Workshop Proceedings of 7th International Fluid Power Conference Aachen, p.319-328 (2010)